Fourth International Microgravity Combustion Workshop

Proceedings of a conference held at the
Cleveland Sheraton City Centre Hotel
Cleveland, Ohio
May 19–21, 1997

Fourth International Microgravity Combustion Workshop

National Aeronautics and
Space Administration

Office of Management

**Scientific and Technical
Information Program**

1997

TABLE OF CONTENTS

Gaseous Diffusion Flames

Turbulent Combustion

Soot Processes

Heterogeneous Diffusion Flames

Combustion Diagnostics

Premixed Flames

Flammability, Smoldering, Ignition, and Flame Spread

Droplet Combustion

PREFACE

This proceedings document is a compilation about work performed by a community of researchers from universities, industry and government laboratories across the United States and in Europe and Japan who have recognized the value of the reduced-gravity environment in attacking the fundamental and practical problems of combustion science. On their behalf, I am pleased to present this document to the assembled participants at the Fourth International Microgravity Combustion Workshop, to be held near the NASA Lewis Research Center in Cleveland, Ohio, on May 19-21, 1997.

The workshop is an important prelude to the release of a call for research proposals in a NASA Research Announcement (NRA) that is anticipated for the fall of 1997. This compilation of results and plans by the existing community was prepared to stimulate discussion during the workshop but also in the hope that it will spawn innovative new ideas for NRA proposals.

Since the preparations for the first workshop in 1989 and the first microgravity combustion NRA that followed, the program has grown from a small group of experimenters confined to drop towers and aircraft, to more than seventy funded efforts, many having flown in space. As we go to press with this document, the community is poised to watch as the Microgravity Science Laboratory mission of the Space Shuttle, STS-83, is launched to conduct combustion experiments including soot processes, premixed flames and droplet combustion. During the workshop we hope to hear of the success of these experiments and congratulate the participants, many of whom have worked for years bringing the experiments to fruition.

The recent fire aboard the Russian Space Station *Mir* is a clear reminder that the environment of reduced gravity is not only a tool for our research but also a living environment that our efforts might improve. Moreover, the conventional environment that we all share is influenced by combustion processes from the perspective of our comfort, health, safety, and cost of living. As we learn from each other and debate our future directions during the workshop, I urge you to consider carefully the message of Dr. Merrill King, our NASA Headquarters Enterprise Scientist for Microgravity Combustion Science. Dr. King will challenge the combustion community to consider the relevance of the fundamental knowledge gained through microgravity research to the pressing technological issues combustion science can affect.

The preparation of this document and of the workshop is an accomplishment of many people—the titular organizer only sits in the center of the bullseye. Our deep gratitude is due and expressed to the nearly ninety authors and speakers who almost without exception met a difficult deadline for paper submission and formatting. We believe that the distribution of the proceedings document at the time of the workshop will improve the technical discussions and better prepare everyone for the proposal preparations soon to come. Notably, also—the timely preparations clearly saved significant funds that might be better used for research.

It would be a mistake to miss acknowledging the effort of the staff that prepared the proceedings document and organized the workshop. The group led by Dr. Richard Ziegfeld of NYMA has performed consistently (and persistently) well in this work and with an admirable level of professionalism. We owe a large measure of our success to them:

Richard Ziegfeld
John Toma
Wilma Graham
Linda Oliver
Scharlene Schmidt

Finally, I ask that each reader enjoy the contents of this compilation of effort and the workshop. If a better job can be done in the preparations of the next workshop, we ask that you tell us your thoughts.

Dr. Kurt Sacksteder
MS 500-115
NASA Lewis Research Center
21000 Brookpark Road
Cleveland , OH 44135
216-433-2857, fax -8660
kurt.sacksteder@lerc.nasa.gov

Keynote

Page intentionally left blank

NASA MICROGRAVITY COMBUSTION SCIENCE PROGRAM

MERRILL K. KING
NASA Headquarters, Code UG
Washington, DC 20546

Introduction

Combustion is a key element of many critical technologies used by contemporary society. For example, electric power production, home heating, surface and air transportation, space propulsion, and materials synthesis all utilize combustion as a source of energy. Yet, although combustion technology is vital to our standard of living, it poses great challenges to maintaining a habitable environment. For example, pollutants, atmospheric change and global warming, unwanted fires and explosions, and the incineration of hazardous wastes are major problem areas which would benefit from improved understanding of combustion. Effects of gravitational forces impede combustion studies more than most other areas of science since combustion involves production of high-temperature gases whose low density results in buoyant motion, vastly complicating the execution and interpretation of experiments. Effects of buoyancy are so ubiquitous that their enormous negative impact on the rational development of combustion science is generally not recognized. Buoyant motion also triggers the onset of turbulence, yielding complicating unsteady effects. Finally, gravity forces cause particles and drops to settle, inhibiting deconvoluted studies of heterogeneous flames important to furnace, incineration and power generation technologies. Thus, effects of buoyancy have seriously limited our capabilities to carry out "clean" experiments needed for fundamental understanding of flame phenomena. Combustion scientists can use microgravity to simplify the study of many combustion processes, allowing fresh insights into important problems via a deeper understanding of elemental phenomena also found in Earth-based combustion processes and to additionally provide valuable information concerning how fires behave in microgravity and how fire safety on spacecraft can be enhanced.

Promising Microgravity Combustion Program Research Thrusts

(1) Turbulence and Combustion. Virtually all practical combustion devices are turbulent. The wide range of turbulence length and time scales generally precludes exact numerical simulation and also presents a significant challenge to experimental investigations. Microgravity uniquely limits the range of length and time scales to those large enough to be tractable experimentally and more readily simulated. Preliminary μg experiments reveal that buoyancy plays a role in the turbulence characteristics in regimes where it had been previously assumed that the flow field and flame behavior was independent of gravitational influence. One particularly powerful approach for treating the coupling between fluid motion and combustion chemistry based on studies of laminar flames is currently under development; this approach, referred to as laminar flamelet theory, shows promise as a tractable representation of turbulent combustion. The extension of laminar flamelet theories to predict fully turbulent flames cannot presently be exploited, however, due to limitations of our current knowledge base caused by the interferences of buoyancy during laminar flame studies. Microgravity combustion studies provide an opportunity to eliminate these interferences and, thus, markedly advance our capability to address turbulent combustion phenomena.

(2) Transient Processes in Gaseous Flames. Numerous types of instabilities are possible in combustion of flowing gases, some of these being gravity-dependent and others not. Such phenomena as ignition, extinction, and unsteady response of flames to externally imposed perturbations (e.g., pressure oscillations) are also of major importance as regards fire safety, production of pollutants, and combustion efficiency. Research studies in a microgravity environment provide for examination of fundamental phenomena involved in these transient phenomena without the confounding effects of buoyancy-induced flows which will, under normal gravity conditions, also respond in an unsteady manner to such imposed perturbations, often masking fundamental phenomena of interest. With understanding of these phenomena, strategies for controlling ignition, extinction, and responses of flames to externally imposed perturbations in practical combustion devices can better be devised.

(3) Soot Processes. Soot is a critical element in many combustion systems, strongly affecting combustor lifetime, efficiency, peak power output, and pollution generation. The short time scales and small spatial volumes affecting soot formation and destruction processes under normal gravity conditions preclude experimental probing. Furthermore, buoyancy accelerates, in an uncontrolled fashion, the flow field in which soot is formed and oxidized; this too inhibits scientific investigations. Microgravity offers a unique opportunity for controlling the flow environment and through this control extending the range of conditions involving soot processes. The lack of buoyantly-induced, accelerated flow results in longer residence times for primary soot formation, clustering, cluster-cluster agglomeration, and oxidation in a variety of flames. In addition, soot particle pathlines are strongly altered under microgravity conditions, resulting in major changes in the environmental history seen by the soot precursors and particles. From the perspective of practical benefit, the fundamental understanding of the processes controlling soot formation, aggregation, and oxidation is of vital importance since such understanding would allow us to develop methods to predict and control sooting associated with combustion processes under a wide variety of circumstances.

(4) Measurement (Species, Velocity, Temperature) Technology. A historic (and valid) criticism of microgravity experimental research is lack of quantification of meaningful variables (e.g. species concentrations). Advancement in understanding of chemical kinetic mechanisms is inhibited by an inability to measure progress of reactions and to quantify the detailed temperature and flow fields in which those reactions take place. Improved measurement methods in both 1g and µg are a growing focus of terrestrial research. Technological improvements in measurement capabilities will lead directly to improved kinetic and flow field modeling leading to enhanced capability for design of combustors with reduced pollutant generation and improved fuel efficiency. Spinoffs of these technologies can and are being used not only in laboratories distant from the inventor's own, but also in the monitoring of pollutant emissions from various sources. In the future these technologies will be used to evaluate fuel consumption, product generation, heat transfer efficiency, and pollutant control in manufacturing processes, and to serve as insitu engine performance and emission levels monitors. The resulting combination of diagnostic sensors and computational algorithms will allow electronic controls to play a larger part in practical combustion systems, enabling so-called "intelligent combustors".

(5) Droplet/Particle Combustion at Pressures Up to Supercritical. Microgravity is of particular benefit in studies of particle and liquid droplet ignition and combustion inasmuch as it permits elimination of settling effects and of buoyancy-induced flows around the droplets, thus leading to truly symmetrical (and hence one-dimensional) geometry and allowing droplets to be restrained within the field-of-view of various diagnostics. Currently, high pressure and supercritical fluid operation of combustion devices is being examined for increased efficiency. Unfortunately, pollutant (e.g., soot and oxides of nitrogen) generation increases with increasing pressure; hence military and NASA aeropropulsion research is heavily populated with studies aimed at realization of the theoretical efficiency improvements with simultaneous minimization of pollutants. Another application of this technology is in the area of hazardous waste disposal: supercritical water oxidation of hazardous wastes has been predicted as an important technology of the future, hopefully yielding only benign products (carbon dioxide and water). Much of our detailed knowledge in the area of combustion of droplets and particles has been obtained at low pressure; extension of studies to high pressure is required. For example, soot studies have mostly been performed near ambient pressures with flame temperatures of less than 2000K; diesel engines operate at over 50 atm and 2800K. Much of our knowledge of soot kinetics may not be applicable to these high temperature, high pressure regimes. High pressure operation is accompanied by increased buoyant flow effects; microgravity experiments will enable, as in other situations, an isolation of the effects of the buoyancy on flame structure, flammability, and flame speeds.

(6) Classical Model Validation/Benchmark Data. Combustion textbooks are replete with theories which are incompletely tested though widely accepted (through historical precedent). These theories often neglect buoyancy effects and utilize simplified transport processes and/or assume one-dimensional behavior in situations where buoyant effects preclude it. Microgravity continues to offer the unique ability to test, via ideal truly one-dimensional experiments, the accuracy of specific aspects of theories and to provide a benchmark data base against which extensions to existing theories and altogether new theories can be tested.

(7) Flame Structure/Elementary Mechanisms. A fruitful approach to achieving meaningful technology gains in combustion processes must be centered on development of better understanding of the fundamentals of the unit processes involved. Without such an understanding, the approach taken to improving combustion devices tends to involve incremental trial-and-error perturbations around current state-of-the-art designs, with opportunities to achieve possible major improvements with radically different approaches being missed. However, if one fully

4

understands the physics and chemistry involved in a given combustion process, including detailed understanding of the unit subprocesses and how they interact, this understanding can be combined into physically accurate models which can then be used for parametric exploration of new combustion domains via computer simulation, with possible definition of radically different approaches to accomplishment of various combustion goals. Accordingly, emphasis should be placed on studies of combustion fundamentals which are not currently well understood; gravitational effects associated with normal earthbound combustion studies have prevented study of many elementary processes which tend to be overshadowed by gravitation-induced processes such as buoyancy or settling.

(8) Direct Numerical Simulation, Large Eddy Simulation. DNS and LES are being widely pursued for definition of detailed features of the flame structure and transport processes (and their interactions) associated with combustion. Due to the large range of length and time scales, however, direct numerical simulation of practical or even idealized devices is considered to be a technology of the future, at best. DNS modeling to date has, however, shown the need to account for preferential mass diffusion even in turbulent flame environments. Microgravity experiments again lessen the range of scales and may make the problem tractable at least for model validation of laboratory-scale experiments, a first step toward DNS validation. DNS is expected to ultimately play a major role in the design of practical combustion systems and obviate the need for the expensive construction and modification of a wide range of breadboards, prototypes, and experimental models of combustion devices; it may also be used for optimization of design elements, subsystems, controls, and overall system performance at reduced cost/time.

(9) Spray and Aerosol Combustion. Realistic sprays include a liquid breakup region, dispersed multiphase flow, turbulent mixing processes, and various levels of flame interactions through the spray. Idealization of spray configurations in a quiescent environment (the starting point for models) has been impossible in 1g due to settling of large droplets and buoyant pluming of post-combustion gases. Microgravity offers the promise of such idealization, but has just begun to provide experimental data on ignition, fire spread, and interactions in idealized linear and planar arrays of monosized droplets. Spray and aerosol cloud combustion accounts for 25% of the world's energy use, yet remains poorly understood from both a fundamental and practical perspective. Improved understanding of the flammability and flame interactions of sprays can be expected to yield improved combustion efficiency in practical devices; this will only occur with an improved detailed theoretical description. In the area of combustion safety, dust clouds contribute to accidental fires and explosions (grain elevators, underground mines). Finally, improved spray technology can be applied to improvements in hazardous waste incineration.

(10) Combustion Synthesis. The use of flames to synthesize materials is expanding rapidly. Products include valuable vapors (e.g. acetylene), ultrafine particles (fullerenes, silicon oxides, titanium oxides), coatings (diamonds) or monolithic solids (boron carbide, titanium boride). Fullerene production is being investigated extensively, but the product yields of fullerenes are currently typically less than 1%, leaving tremendous potential for improvement. Sedimentation and buoyant plumes yielding limited critical residence times again interfere with present investigations into both the scientific mechanisms of material production and the quality of the actual industrial product. For example, pressure and buoyancy effects on soot-filled flames are not understood sufficiently to determine the ideal operating conditions to maximize fullerene generation in either premixed or diffusion flames. Microgravity offers the promise of isolating the effects of pressure by removing the influence of buoyancy on the material production process. A major difficulty in self-propagating, high-temperature synthesis (SHS) of materials is the control of porosity and the microstructure of the products. SHS reactions generating gaseous, liquid, or combined phases are prone to gravity-induced fluid flows, leading to non-uniform microstructure and undesirable properties of the product material due to segregation and density gradient effects. Gravitational forces have been shown to play a dominant role in controlling both the combustion-synthesis reactions and the morphologies of the synthesis products. Current research is geared towards interpreting the differences between normal- and low-gravity processing.

(11) Partial Gravity Studies. The utilization of partial gravity environments enables systematic scientific testing of effects of this parameter on fundamental processes as well as tying directly to the nation's desire for space exploration. Both the Moon and Mars are in NASA's future; microgravity and normal gravity studies have already shown that combustion processes are distinctly affected by reductions in gravity, with a conclusion that the partial gravitational levels on the Moon and Mars may yield increased flammability. In addition, partial gravity environments may have strong effects on insitu propellant production processes as well as on utilization of these products.

(12) Surface Flame Spread <----> Large-Scale Fires. Anyone who has observed the combustion of solid fuels, particularly flame spread across and burning of vertical walls, is well aware of the dominant effects of buoyancy

on such processes under normal gravity conditions, a dominance which makes understanding of other phenomena involved very difficult (an example of how buoyancy can "mask" such phenomena). Accordingly, microgravity studies of flame spread across solid fuels and liquid pools are of considerable interest from a fundamental point of view as well as being very important in terms of fire safety on various space platforms. On Earth, the fluid mechanics of large-scale fires are complicated by buoyancy-fed turbulent processes and thermal radiative interactions with surrounding materials, terrain, and building structure. Current models are still somewhat primitive, with little elucidation of the role of thermal radiation in almost any aspect of fires. Investigations of large-scale fires under microgravity conditions have yet to begin, but it has been shown that radiation takes on heightened importance in small-scale fires in microgravity, indicating that results from laboratory-scale experiments in microgravity might be utilized in modeling of large-scale fires. In terms of NASA's own direct interests, ongoing investigations of material flammability and fire behavior in microgravity have yielded vital guidance to improved fire safety aboard orbiting spacecraft. There does remain, however, a need for 1g - μg correlations of ignition, flame spread, flammability, and extinction conditions.

Current NASA Microgravity Combustion Program Content

As stated in NASA's Microgravity Research Program Strategic Management Handbook, the Microgravity Research Program mission is "To use the microgravity environment of space as a tool to advance knowledge; to use space as a laboratory to explore the nature of physical phenomena, contributing to progress in science and technology on Earth; and to study the role of gravity in technological processes, building a scientific foundation for understanding the consequences of gravitational environments beyond Earth's boundaries". For accomplishment of this mission, both a ground-based program and a flight experiments program are employed; in addition, development of facilities and experiment modules for conduct of multiple experiments is supported. The ground-based program has two major objectives: (1) nurturing and development of ideas and concepts that may be later developed into flight experiments; and, (2) providing theoretical and experimental underpinnings to support understanding of phenomena being studied in the microgravity environment. Ground-based investigations include theoretical and experimental laboratory research, drop-tower tests, and parabolic aircraft flight experiments. In the flight program experiments judged to justify use of the flight environment are developed and executed. These experiments are conducted in microgravity environments provided by suborbital sounding rockets, the Space Shuttle middeck or isolated cargo bay support structures, the Shuttle-based Spacelab or Spacehab pressurized laboratory facilities, the Russian Mir station, international Space Station facilities, and other available carriers.

Currently, the Microgravity Combustion Science program is supporting 48 ground-based studies, 7 flight definition studies, 8 flight programs, 3 Glovebox investigations, 5 Graduate Student Researcher Programs, and 2 NRC postdoctoral studies, for a total of 73 programs. In addition, two major combustion-related Advanced Technology Development programs in the area of diagnostics development are being carried out at the Lewis Research Center. In terms of the Research Thrusts described above, the number of studies involving aspects of Categories 1-12 are 7, 7, 5, 7, 11, 9, 18, 2, 8, 6, 3, and 15, respectively. [Note that this totals 97, in excess of the total number of programs being supported, since some of the programs involve aspects of more than one of the categories.]

Although the majority of the current programs are ground-based studies, centered on analytical modeling activities, testing in drop-towers and parabolic aircraft at Lewis Research Center, and testing at the Japan Microgravity Center (JAMIC) dropshaft in Hokkaido, Japan, limited flight testing has also been carried out on Sounding Rockets and on the Space Shuttle. Three Sounding Rocket tests on the Spread Across Liquids (SAL) Program of Dr. Howard Ross (Lewis Research Center) have been successfully completed to date. Each flight provided approximately six minutes of microgravity time (during which three burns were accomplished) for investigation of the flame spread characteristics across a deep pool of liquid fuel in a microgravity environment, with particle imaging velocimetry, rainbow schlieren, and flamespread data being obtained for comparison with model predictions. This program has recently been approved for five additional flights. In addition, three Sounding Rocket flights have been carried out on Prof. Robert Altenkirch's (Washington State University) Diffusive and Radiative Transport in Fires Experiment (DARTFire).

Dr. Altenkirch is also Principal Investigator on the Solid Surface Combustion Experiment (SSCE) on which eight experiments have been completed to date, with samples of PMMA being burnt in various oxygen-nitrogen atmospheres under quiescent conditions. Two additional shuttle flights have been approved for this experiment; it is expected that these will be completed during 1997. Two Getaway Special Canister (GASCAN) payload shuttle flight

6

tests on the Microgravity Smoldering Combustion experiment (MSC) of Prof. Carlos Fernandez-Pello (University of California-Berkeley) have also been recently completed, with a request for additional flights currently under review. At this time, final preparations have been completed for three major combustion experiments on the Microgravity Space Laboratory (MSL-1) on the Space Shuttle, scheduled for April, 1997; these experiments are the Droplet Combustion Experiment (DCE) of Prof. Forman Williams (UCSD), Prof. Paul Ronney's (University of Southern California) Study of Flameballs at Low Lewis Numbers experiment (SOFBALL), and Dr. Gerard Faeth's (University of Michigan) Laminar Soot Processes in Flames experiment (LSP). In addition, Dr. Yousef Bahadori's (SAIC) Turbulent Gas Jet Diffusion Flame (TGDF) experiment is tentatively scheduled to go to flight in late 1997.

To date, four Microgravity Combustion Glovebox Experiments, one on USML-2 (Oct., 1995) and three on USMP-3 (Feb., 1996), have been carried out; these were the Fiber-Supported Droplet Combustion (FSDC) experiment, the Forced Flow Flame Spreading Test (FFFT), the Comparative Soot Diagnostics (CSD) experiment, and the Radiative Ignition and Transition to Flame Spread Investigation (RITSI). In addition, a repeat of the FSDC experiment is planned for MSL-1, with two additional glovebox experiments, Opposed-Flow Flame Spread on Cylindrical Surfaces (OFFS) and Enclosed Laminar Flames (ELF), planned for the near future. Finally, additional FFFT tests and Candle Flame Combustion tests have been carried out in the Mir Glovebox facility during 1996.

Enterprise for Human Exploration and Development of Space (HEDS)--Roadmap

In early 1994, as part of ongoing reorganizations at NASA, the agency established six major enterprises, later reduced to five. In the current organization, the Microgravity Science and Applications Division (MSAD) of the Office of Life and Microgravity Sciences and Applications (OLMSA) has become part of the Human Exploration and Development (HEDS) Enterprise. In January, 1996, a Strategic Plan for HEDS was put into place and development of "roadmaps" for the future directions of activities within HEDS was initiated; the current roadmap for the Microgravity Combustion Science program is attached as Figure 1. The three major thrusts of the HEDS activities are shown in the ellipses at the left of the figure, with applications of these to the direction(s) of the Microgravity Combustion Science program over three time periods being shown in the boxes to the right of these ellipses. It is obvious from this chart that, while basic research into fundamentals is still considered to be vitally important to the program, there is a major shift of emphasis toward "mission-oriented" research; that is, research aimed at specific problems in combustion applications on Earth as well as under reduced or microgravity conditions. Thus, it is important that firmer linkages between the research being done using microgravity and applications to practical applications on Earth (e.g., increased efficiency of conversion of chemical energy contained in fuels to useful work, reduction of combustion-generated pollutants from automobile engines and other combustors, decreased fire and explosion hazards) need to be established for an increasing percentage of efforts funded under this program. In trying to steer our program into particular areas of emphasis, however, we cannot lose sight of the fact that outside peer review weighs very heavily into selection for funding of proposals submitted in response to our NASA Research Announcements (NRA's), though final selections are made by a NASA selecting official (in this case, the Director of the Microgravity Science and Applications Division). In the past, we have asked our peer reviewers to judge proposals solely on scientific merit and microgravity relevance; for future NRA's, we will likely extend the evaluation criteria to include responsiveness to specific areas of emphasis called out in these NRA's. In addition, the question of relevance to specific program goals can be used as a "tie-breaker" in choosing between proposals with similar peer review scores.

Included among the long-term goals of the HEDS microgravity combustion program are: (1) Melding microgravity combustion space experiments together with ground-based combustion studies, using gravity as an added independent variable, to provide better understanding of the physical and chemical mechanisms involved in combustion and to provide more rigorous testing of analytical models; (2) Utilizing basic research to provide technological advances in various combustion processes/devices (e.g., internal combustion engines, turbines, combustion synthesis, incinerators); (3) Creating the understanding that will permit lessons learned in microgravity combustion experiments and modeling to be used in optimizing combustion devices here on Earth; (4) Providing quantum leaps in the areas of fire safety and minimization of combustion-generated pollution; (5) Providing the understanding which will permit efficient use of alternative fuels, which will be increasingly needed as we deplete our oil and gas reserves; and, (6) Developing a better understanding of various combustion synthesis processes, opening the door to production of novel tailored materials here on Earth as well as in space.

There are numerous potential combustion technologies for terrestrial and space exploration applications delineated in the Figure 1 roadmap. These include: (1) Active control over thermal efficiency and pollutant generation (e.g., soot, NOx) through sensor development and miniaturization accompanied by development of algorithms relating sensor readings, control settings, and system performance; (2) Use of magnetic and electric fields to improve thermal efficiency (microgravity enables improved isolation of and thus understanding of field effects on electrically-charged radicals and paramagnetic molecules such as oxygen); (3) Improved atomization methods for diesel and gas turbine engines, leading to improved fuel utilization, through improved understanding of fundamentals of liquid jet breakup and droplet interactions in sprays; (4) Flame-zone pollution control in premixed and diffusion burners, reducing the need for post-combustion cleanup devices, through fundamentally improved understanding of flame structure and of mechanisms of formation of soot and oxides of nitrogen; (5) Improved exhaust gas monitoring for cars and other combustion devices combined with development of "smart" controls to compensate for fuel variations and/or degradation of engine components to decrease pollution emissions; (6) New flame-stabilization/control technologies for burners enabling reliable, ultra-lean premixed combustion through improved understanding of flame stabilization zones in engines, burners, etc.; (7) Development of improved strategies and procedures for fire prevention, detection, and suppression in the microgravity environment associated with Space Station and in the reduced gravity Lunar and Martian environments; (8) Reduction of hazards associated with gaseous fuel combustion through better mapping and understanding of flammability limit and combustion instability phenomena; (9) Development of improved protection against large-scale fires (house fires, forest fires) via better fundamental understanding of material ignition and flamespread phenomena; (10) Reduction of mine and grain silo explosion hazards through development of understanding of fundamentals associated with these phenomena; (11) Improved reliability in hazardous liquid waste incineration, resulting from studies of droplet and spray burning and of pollution generation; (12) Industrial-scale, combustion-generated fullerene production through determination of approaches for improving the yields of fullerenic material in flame systems; (13) Production of composite materials with improved strength, reliability, and ductility through better understanding of how to improve micro-structural uniformity and control porosity via gravitational control; and, (14) Development of methods for producing and utilizing alternate fuel/oxidizer combinations associated with Lunar, Martian, or other extraterrestrial habitats.

Upcoming Microgravity Combustion NASA Research Announcement

In the Microgravity Combustion Program at NASA, investigators are selected in response to a NASA Research Announcement (NRA) issued once every two years and are placed either in the Ground-based Category or in the Flight Definition Category. At this time, it is anticipated that an NRA will be released early in the Fall of this year (1997) with proposals being due approximately three months after the NRA release date; it is suggested that, even though distribution of postcards describing how to obtain the NRA will be made to an existing extensive distribution list, potential proposers contact the author to ensure that they are included on this list. Proposals received in response to this NRA will first be examined for responsiveness and divided into categories, with external peer review panels being established for each category. Next, written reviews and ratings (three per proposal) will be obtained from the reviewers, each of whom will review approximately 10 proposals, with each proposal being rated on scientific merit, microgravity relevance, and linkage to goals outlined in the HEDS Roadmap. All the reviewers on a given panel will then be assembled for discussion of the proposals within that group with the ultimate output of a consensus evaluation of each proposal and assignments into "Highly Qualified", "Qualified", or "Not Qualified" categories. For strong candidate proposals which are likely to require flight, feasibility and resource compatibility reviews will be carried out by NASA/Lewis personnel. Finally, the "Highly Qualified" and "Qualified" proposals will be assessed in terms of program balance and linkage to HEDS goals by the Enterprise Scientist for Microgravity Combustion and a list of suggested awardees for Ground-Based and Flight Definition Programs will be developed. A list of proposals recommended for funding will be generated in a meeting of the Microgravity Science Branch, with final approval by the Lead Scientist and Division Director. It is anticipated that the review process should be complete by mid-1998, with awards occurring in late 1998 (early Fiscal Year 1999).

For proposals receiving awards in the Flight Definition category, the programs may proceed, following passing of a peer-reviewed Science Concept Review (SCR) and Requirements Definition Review (RDR) and acceptance of a Science Requirements Document (SRD) generated by the Principal Investigator, into the Flight Program. In addition, there is opportunity for Ground-Based investigators to participate as "guest" investigators in Glovebox Experiments on a Space Platform based on internal NASA review of proposals submitted in response to Glovebox

Opportunity Announcements. [More details on these processes are available from the author.] In the overall (flight plus ground-based projects) Microgravity Combustion program, both experimental and theoretical modeling efforts are supported. Experimental test beds for microgravity experiments include drop-towers at NASA/Lewis, capable of providing 2.2 to 5 seconds of microgravity time, aircraft flying parabolic trajectories, providing up to twenty seconds of reduced gravity (0.001 to 0.01 g), sounding rockets which supply very low gravity for up to 6-7 minutes, and Shuttle or Space Station facilities of various types, allowing basically unlimited microgravity operating times. In addition, we are participating in cooperative studies with Japanese investigators allowing us access to a 10-second drop tower at Hokkaido, Japan.

As indicated earlier, while conduct of fundamental science investigations remains a cornerstone of the Microgravity Combustion Science program, more emphasis will be placed in the future on relevance to the goals outlined in the HEDS Roadmap, with linkage of the proposed research to attainment of these goals receiving increased emphasis. However, future proposals are not limited to the topic areas discussed in this paper; extension to combustion topics not currently included in the Microgravity Combustion program is strongly encouraged to permit us to broaden the program scope. Evaluation criteria which should be kept in mind by proposers include:

1.   Is microgravity of fundamental importance to the proposed study?

2.   Do the issues addressed by the research have the potential to close major gaps in the understanding of fundamentals of combustion processes?

4.   Is there potential for elucidation of previously unknown phenomena or interactions between phenomena?

5.   Is the project likely to have significant benefits/applications to ground-based as well as space-based operations involving combustion processes?

6.   Are the results likely to be broadly useful, leading to further theoretical or experimental studies?

7.   Can another project in the specific subarea be justified in terms of limited resource allocation?

8.   Is the project technologically feasible, without requirements for substantial new technological advances?

9.   How will this project stimulate research and education in the combustion area?

10.   How does the projected cost/benefit ratio compare with other projects competing for the same resources?

11.   What is the potential of this project in terms of stimulating future technological "spinoffs"?

12.   Are there strong well-defined linkages between the research and HEDS goals?

It appears that the most fruitful approach to achieving meaningful technology gains in processes involving combustion is to concentrate on developing better understanding of the fundamentals of the individual processes involved. With such understanding, including definition of details of the unit processes and their interactions, physically accurate models which can be used for parametric exploration of new combustion domains via computer simulation can be developed, with possible resultant definition of radically different approaches to accomplishment of various combustion goals. As discussed earlier, normal-gravity conditions have prevented study of many elementary processes which are over-shadowed by processes such as buoyancy, making it difficult to develop mechanistic understanding of unit phenomena making up overall combustion processes. It cannot be emphasized too strongly that our program is dedicated to taking advantage of microgravity to untangle these complications, allowing major strides in our understanding of combustion processes and in subsequent development of improved combustion devices leading to improved quality of life here on Earth.

Figure 1. Combustion Science Research

Strategies to Accomplish Program Objectives

1996 - 2002 **Revolutionize NASA** Deliver world-class programs and cutting-edge technology through a revolutionized NASA	2003 - 2009 **Expand our Horizons** Expand our horizons in space and aeronautics to assure continued U.S. leadership	2010 - 2020 & Beyond **Open the Frontier** Open the space frontier to international human expansion and commercial development
To advance and communicate scientific knowledge and understanding of the Earth, the environment of space, the solar system, and the universe	• Work information exchange and cooperative projects with other US agencies funding combustion research (NSF, NIST, AFOSR, ONR, ARO, DOE, EPA, FAA, DOT) • Produce significant findings from microgravity expts which will attract a vested research community of at least 100 PIs • Hold workshops to distribute information and focus activities • Delineate mechanisms associated with flammability limits and combustion instabilities • Use ground-based research and limited space experiment results to define a decade of ISS research	• Conduct ISS studies of microgravity combustion processes, focusing on problems of highest current terrestrial interest • Use results to replace and fill gaps in combustion textbooks • Develop benchmark data bases on combustion processes against which extensions to and altogether new theories can be developed, enabling a new and broad understanding of combustion science • Improve understanding of large scale fires with eye to development of means of prevention and suppression • Continue shift of emphasis to "hypothesis-driven" combustion research rather than exploratory research	• Complete data collection, reduction, and analysis of data sets to serve as standard references • Use data sets for development of unified treatments for analysis of combustion processes at all g-levels • Sustain continued development of fundamental understanding and control of combustion processes • Develop fundamental understanding of combustion-turbulence interactions • Reduce/eliminate reliance on trial-and-error design procedures for combustion devices
To explore, use, and enable the development of space for human enterprise	• Scope potential critical knowledge needs • Assume responsibilities for space fire safety • Develop understanding of and characterization methods for detection of fires in microgravity environment and develop tests for characterization of material flammability under ug • Define effects of reduced pressure and higher oxygen mole fraction on ignition and flamespread over materials for station and other reduced g environments • Develop agreements with foreign agencies regarding specific areas of cooperation and division of responsibilities	• Expand program to examine ISRU for propulsion, power generation, and combustion synthesis • Delineate mechanisms controlling material ignitability, smolder, flamespread, and extinction in normal and ug environments, with emphasis on fire safety in reduced or ug environments • Develop tools permitting accurate prediction of effects of low gravity on combustion processes in space or other extraterrestrial bodies leading to improved design tools • Perform in-space demos and validations of combustion-related technologies as preparation for Lunar and Martian habitats	• Develop extraterrestrial laboratories for combustion research and engineering development • Develop energy comversion processes optimized for use in space applications involving reduced gravity • Explore combustion processes involving alternative fuels and oxidizers which may have to replace "normal" Earth-based fuels and oxidizers • Develop, demonstrate, and enable ISRU techniques using combustion technologies for power, propulsion, and ECLSS support of Lunar and Martian habitats
To research, develop, verify, and transfer advanced aeronautics, space, and related technologies	• Steer combustion research efforts into more specific, prioritized subtopic areas (mission-oriented research) • Expand menu of diagnostic tools with emphasis on direct rather than inferential measurements • Increase capabilities of ground-based facilities • Expand research on combustion synthesis processes • Use ground-based and suborbital flight experimental studies to better scope combustion experiments requiring longer ug durations in preparation for ISS • Study soot formation, agglomeration, oxidation to define control strategies for Earthbound combustion devices	• Increase emphasis on detailed quantitative measurements with emphasis on delineation of mechanisms • Emphasize potential for high economic feedback • Increase emphasis on combustion synthesis processes for production of novel high-value materials; develop industrial-scale combustion synthesis processes • Contribute to development of low NOx emission combustors for supersonic combustion devices • Develop miniaturized instrumentation for sensing and controlling combustor performance; utilize this technology in improving terrestrial combustion processes	• Apply knowledge gained to development of ways for increasing fuel utilization efficiency and reducing pollutant emissions for many processes • Develop diagnostics/process control combinations to permit continual optimization of combustion devices • Develop strategies for improving combustion devices via smart sensors, magnetic and electric field utilization, improved mixing technologies, improved atomization, and flame-zone pollution control • Develop radically new approaches to conversion of chemical energy to useful work

10

Combustion Synthesis/ Metals Combustion

Page intentionally left blank

FULLERENES, PAH, CARBON NANOSTRUCTURES, AND SOOT IN LOW PRESSURE DIFFUSION FLAMES[*]

William J. Grieco[a], Arthur L. Lafleur[b], Lenore C. Rainey[c],
Koli Taghizadeh[b], John B. Vander Sande[c], and JACK B. HOWARD[a]

[a]Department of Chemical Engineering, [b]Center for Environmental Health Sciences,
[c]Department of Materials Science and Engineering
Massachusetts Institute of Technology, Cambridge, MA 02139

Introduction

The formation of fullerenes C_{60} and C_{70} is known to occur in premixed laminar benzene/oxygen/argon flames operated at reduced pressures[1]. High resolution transmission electron microscopy (HRTEM) images of material collected from these flames has identified a variety of multishelled nanotubes and fullerene "onions" as well as some trigonous structures[2]. These fullerenes and nanostructures resemble the material that results from commercial fullerene production systems using graphite vaporization. As a result, combustion is an interesting method for fullerenes synthesis. If commercial scale operation is to be considered, the use of diffusion flames might be safer and less cumbersome than premixed flames. However, it is not known whether diffusion flames produce the types and yields of fullerenes obtained from premixed benzene/oxygen flames. Therefore, the formation of fullerenes and carbon nanostructures, as well as polycyclic aromatic hydrocarbons (PAH) and soot, in acetylene and benzene diffusion flames is being studied using high performance liquid chromatography (HPLC) and high resolution transmission electron microscopy (HRTEM).

Experimental

Two sets of experiments have been conducted to date to test laminar, low pressure acetylene jet diffusion flames burning in air and inverted benzene diffusion flames burning in oxygen.

Acetylene Jet Diffusion Flames

A fuel jet with or without nitrogen dilution was injected vertically through a 3.5 mm diameter tube burner, located at the center of a 24 cm diameter cylindrical chamber. The fuel jet was surrounded concentrically by a flow of air, introduced uniformly across the chamber cross-section through a porous plate at the base of the chamber. Air and fuel flows were metered using critical flow orifices. Some of the exhaust was removed from the top of the burner chamber using a rotary vacuum pump, and the flames were ignited by a spark generated using a tesla coil. The flame conditions tested, shown in Table 1, were identical to those used by Sunderland and coworkers[3] in a study of soot formation in acetylene jet diffusion flames.

Table 1. Summary of Acetylene Flame Conditions. Gas flow rates and velocities are at 298 K and burner chamber pressure.

Test Flame	A1	A2	A3	A4
Pressure (torr)	190	143	95	190
C_2H_2 flow rate ($cm^3 \cdot s^{-1}$)	6.93	11.6	21.2	7.67
N_2 diluent flow rate ($cm^3 \cdot s^{-1}$)	-	-	-	5.19
Air flow rate ($cm^3 \cdot s^{-1}$)	209	401	771	209
Burner exit velocity ($mm \cdot s^{-1}$)	940	1580	2880	1740
Air velocity ($mm \cdot s^{-1}$)	5.27	10.1	19.4	5.27
Sampling location, distance from burner (mm)	10.0	10.0	30.0	10.0

13

The sampling locations were selected to be within the range of locations, corresponding to residence times between 0 and 30 ms, sampled by Sunderland and coworkers[3]. The 10 mm location for flames A1, A2, and A4 corresponds to residence times of between 5 and 7 ms, while for flame A3 the 30 mm sampling location translated to a residence time of approximately 10 ms. A longer residence time was used for flame A3 because, at the higher feed velocity, the flame tended to be unstable when sampling closer to the burner at the residence times of the other test conditions.

In all cases, the flames were sampled approximately isokinetically at a rate of ~0.2 L/min (STP) for about 10 minutes using a water-cooled quartz probe with a 1 mm orifice diameter. Combustion products, including soot and condensible compounds, were collected on a pre-weighed filter system consisting of a glass wool plug packed in an aluminum foil sleeve inside the quartz probe. After sampling, the mass of the filter system was measured to determine the amount of flame material collected. The glass wool plug including the collected flame material and the aluminum foil sleeve were placed in toluene. The resulting mixture was extracted by ultrasonication and vacuum filtered through a 0.25 μm nylon filter. The filtrate, consisting of the extractables, i.e., the toluene soluble portion of the collected flame material, in toluene, was concentrated by rotary evaporation. Extraction was carried out using toluene to take advantage of this solvent's more potent solvating capability for polycyclic aromatic compounds. The filtered extract was subjected to chemical analysis.

Inverted Benzene Diffusion Flames

The benzene flame burner, described by McKinnon[4], consists of a water-cooled body capped by a horizontal 100 mm diameter, 12 mm thick drilled copper burner plate, partitioned concentrically into a central 70 mm diameter core region surrounded by a 15 mm wide annular region. Liquid benzene was metered to a preheater and vaporizer using a syringe pump. Benzene vapor was diluted with argon in a mixing chamber and fed through the annular region of the burner, and oxygen was fed through the core region in less than the stoichiometric amount for complete combustion to CO_2 and H_2O. Oxygen and argon flows were controlled using critical flow orifices. The burner is located inside a stainless steel combustion chamber fitted with a water-cooled top flange, on which soot and other condensible flame species were deposited, and connected through ports in its base to a vacuum pump.

The flame front stabilized at the interface between the core and annular regions as an inverted truncated conical shell whose diameter increased with distance from the burner, apparently due in part to the exhaust flowing radially outward and downward. The height of the flame and the extent of the diameter increase also depend on the relative velocities of the fuel and oxidant. Typically the height was about 70 mm and the diameter increased about 30% over this vertical distance.

The flame conditions tested are shown in Table 2. This set of conditions was selected as a parametric test of the effects of pressure, argon dilution, and fuel + diluent velocity on the fractions of C_{60} and C_{70} in flame-generated condensibles. The fuel + diluent velocity was controlled by setting the benzene and argon flow rates separately. The oxygen velocity used in each case was that which resulted from feeding approximately 60% of the stoichiometric oxygen, a condition found to give a strongly sooting flame.

Table 2. Summary of Benzene Flame Conditions. Gas velocities are at 298 K and burner chamber pressure.

Test Flame	B1	B2	B3	B4	B5	B6	B7
Pressure (torr)	20.0	20.0	20.0	20.0	60.0	60.0	20.0
Benzene flow rate (SLM)	0.33	0.68	0.94	0.75	0.95	0.76	0.25
Argon dilution (mol %)	0.0	23.1	0.0	23.3	0.0	23.0	23.3
Oxygen flow rate (SLM)	1.54	3.07	4.24	3.39	4.24	3.39	1.13
Fuel + diluent velocity (cm·s^{-1})	5.21	13.3	14.8	14.5	4.99	4.90	4.85
Oxygen velocity (cm·s^{-1})	25.3	50.5	69.8	55.8	23.3	18.6	18.6

Each flame was maintained for 20 to 60 minutes. Material deposited from each flame on the top flange and walls of the combustion chamber was collected, and a representative portion was placed in toluene and extracted by ultrasonication. The resulting mixture was vacuum filtered through a 0.25 μm nylon filter, and the filtrate was concentrated by rotary evaporation in preparation for chemical analysis.

14

Analytical Methods

For both acetylene and benzene flame samples, a portion of the filtrate was exchanged into dichloromethane (DCM) and another into dimethylsulfoxide (DMSO). The filtrate contained the toluene soluble compounds, or extractables, present in the collected flame material. The mass of the extractables was determined by weighing the residue from evaporation of a measured volume of the DCM solution.

The analysis for fullerenes C_{60} and C_{70} involved injecting a portion of the original filtrate in toluene into an HPLC, equipped with a diode array detector (DAD) and a C18 reverse phase column (Vydac #201HS54). Based on the calibration for both fullerenes, chromatogram peak areas were converted to concentrations. Likewise, the PAH analysis involved injecting the DMSO solution into an HPLC, equipped with a DAD and a C18 reverse phase column (Vydac #201TP54). Chromatogram peak areas for 16 standard PAH were converted to concentrations. Concentrations of 15 additional PAH were estimated using calibration factors associated with standard PAH having similar ultraviolet absorption spectra.

HRTEM was used to characterize the morphology of the soot and carbon nanostructures present in the flame samples. For the acetylene flame samples, the toluene insoluble material left after filtration, which included the soot, was dispersed in toluene by ultrasonication. For the benzene diffusion flame samples, solids collected from the combustion chamber were suspended in toluene without undergoing an extraction step. In both cases, a drop of the suspension was placed on a holey carbon film deposited on a 200 mesh copper electron microscope grid, and the toluene was allowed to evaporate. The grids were analyzed using a TOPCON 002B microscope operating at 200 keV.

Results and Discussion

Fullerenes and Carbon Nanostructures

Fullerenes C_{60} and C_{70} were not found at a detection limit of ~250 ng/ml in samples collected from the acetylene diffusion flames. However, HRTEM analysis of flames A1 and A4 showed interesting carbon nanostructures. Figure 1a is an image of solid material from flame A1. It appears to be a nanostructure consisting of approximately 40 nested layers. It measures ~50 nm along the long axis and between ~10 and ~20 nm on the short axis. Amorphous carbon appears to be deposited at the large end of the nanostructure. Figure 1b shows an image of material from flame A4. This structure has approximately 40 nested layers and an average diameter of ~20 nm. Amorphous carbon is clearly present on this nanostructure. The nanostructures depicted in these images are fullerenic in that they are comprised of curved layers and closed shells. In addition, these structures are not unlike those in images of material from fullerene-forming premixed benzene/oxygen flames.[2] That they are formed in flames that do not produce detectable quantities of C_{60} and C_{70} is unusual, and that they are present in acetylene diffusion flame soot is both new and encouraging for the further study of fullerenes and nanostructures formation in these flames.

HPLC analyses of samples from the benzene diffusion flames identified both C_{60} and C_{70}. The yields of C_{60} and C_{70} as fraction of soot collected and the molar ratio of C_{70} to C_{60} in flames B3, B4, B5, B6, and B7 is summarized in Table 3.

Table 3. Fullerenes Identified in Benzene Diffusion Flames.

Test Flame	B3	B4	B5	B6	B7
C_{60} mass (% of soot)	0.005	0.009	0.004	0.004	0.002
C_{70} mass (% of soot)	0.012	0.015	0.008	0.007	0.006
Molar C_{70}/C_{60} Ratio	2.0	1.5	1.6	1.6	2.3

Clearly, the amount of C_{60} and C_{70} present in the flame samples varied with the flame conditions tested. The data show no significant dependence of C_{60} and C_{70} formation on pressure. A pressure increase from 20 to 60 torr, with no argon dilution, produced an increase in fullerenes yield as mass fraction of soot. With 23% argon dilution, however, increasing pressure had the opposite effect; fullerenes yield dropped to zero. The effect of dilution was marginally negative. C_{60} and C_{70} yields decreased slightly when 23% argon was added to the benzene feed. The effect of cold fuel + argon diluent velocity is striking, as shown in Figure 2. Under conditions of no argon dilution or with 23% argon in the benzene feed, increasing the fuel + diluent velocity from 5 cm/s to between 13 and 15 cm/s significantly increased C_{60} + C_{70} yield from nondetectable levels to between 0.012% and 0.023%. Similar trends for both dilution and fuel velocity have been observed in premixed benzene/oxygen flames at 40 torr.[5] HRTEM studies of samples from the benzene flame samples showed structures similar to those shown in Figure 1.

15
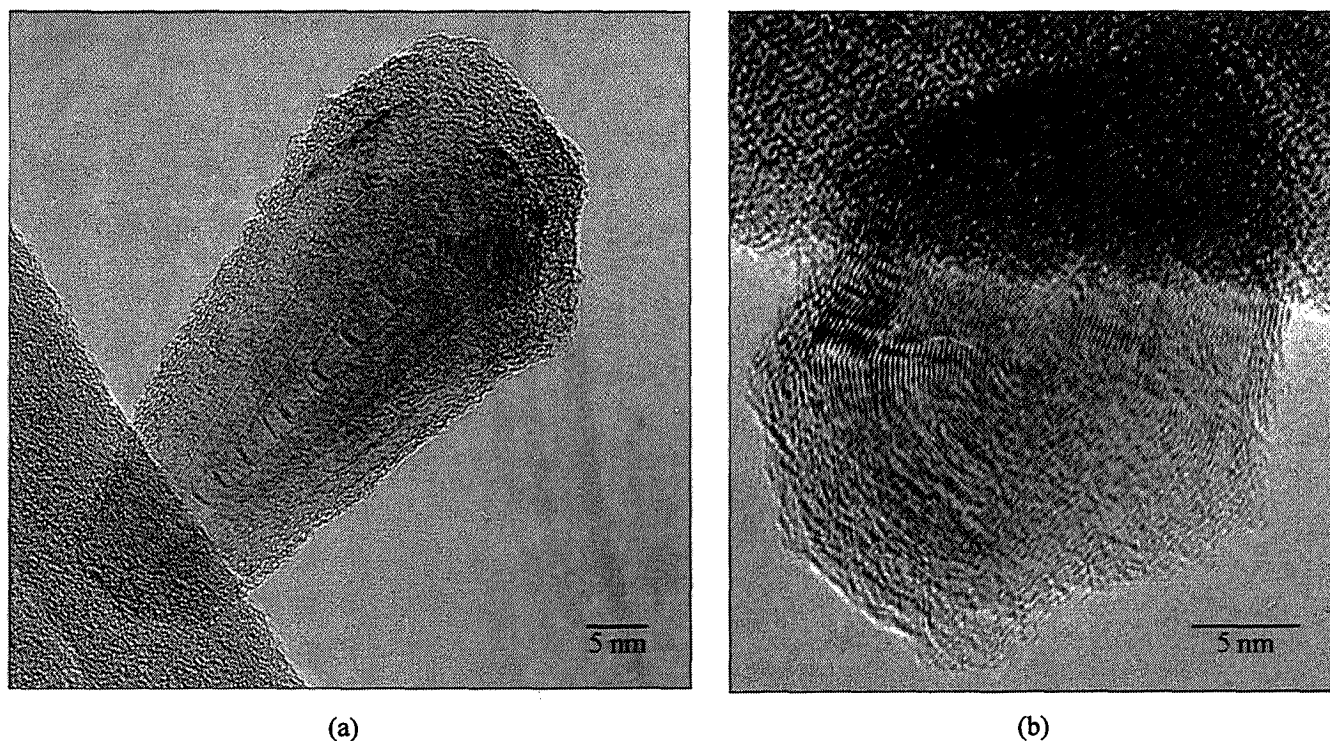
Figure 1. HRTEM images of nested fullerene nanostructures from acetylene flames (a) A1 and (b) A4.
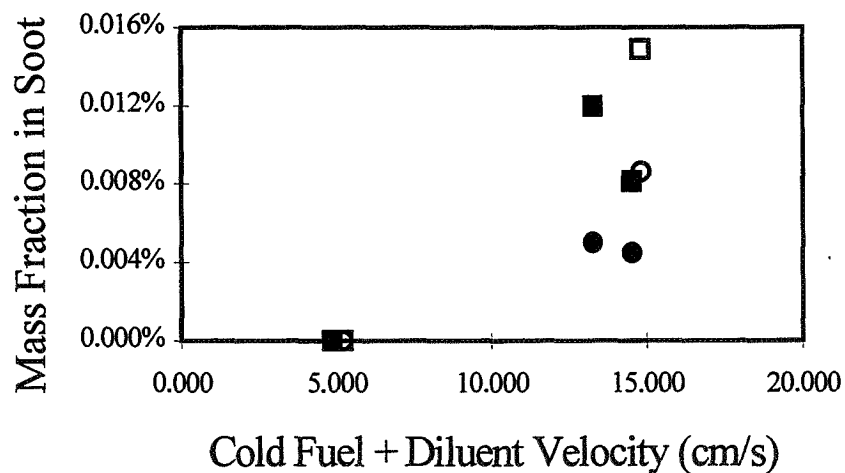
Figure 2. The effect of cold fuel + diluent velocity on C_{60} and C_{70} yield as mass fraction of soot. Data: (O) C_{60} and (□) C_{70} with 0% argon dilution and 20 torr pressure; (●) C_{60} and (■) C_{70} with 23% argon dilution and 20 torr pressure.

PAH and Soot

Samples collected from acetylene diffusion flames A1, A2, and A4 contained detectable levels of PAH. HPLC analysis identified 26 PAH species, listed in Table 4, which accounted for between 3% and 14% (by weight) of the extractables present in the collected flame material. The rest of the extractables is assumed to be high molecular weight polycyclic aromatic compounds. Of the identified PAH, twelve contained 5-membered rings on their periphery and accounted for 68, 83, and 72% of the PAH mass in samples from flames A1, A2, and A4, respectively. These compounds are interesting because they are expected to be

16

relatively reactive among PAH soot surface growth species, owing to the relative ease of radical formation by hydrogen abstraction from the exposed five-membered rings.

HPLC analysis of material from the benzene diffusion flames identified 25 PAH, many of which were present in the acetylene flame samples. These PAH are also listed in Table 4. Eight of the identified PAH, accounting for between 30 and 40% of the PAH mass in the sample, contained 5-membered rings along their periphery. It is interesting that these compounds account for a significantly higher fraction of the total quantified PAH mass in the acetylene flames, in which fullerenes were not detected.

The role of PAH in the reactions that forms fullerenes in flames is not well-characterized. However, the importance of PAH in both soot nucleation and soot surface growth has been considered. It is generally accepted that soot nucleation involves reactions of PAH, and a simple collision theory model of soot formation in premixed ethylene flames has shown that PAH can be a significant contributor to soot surface growth.[6] A similar mathematical analysis, involving both PAH and acetylene as soot growth reactants, showed that the concentrations of PAH in acetylene diffusion flames are sufficiently high to account for an important part of the soot surface growth. In a previous study[3] of these flames that did not include PAH measurements, acetylene was assumed to be the only significant soot growth reactant.

Conclusions

Fullerenes C_{60} and C_{70} were identified in material collected from benzene diffusion flames but not in samples from acetylene diffusion flames. Varying the pressure at which the benzene flames were operated had no clear effect on the fraction of C_{60} and C_{70} present in collected flame samples, while increasing argon dilution in the benzene feed reduced fullerenes yield slightly. Increasing the velocity of the fuel and diluent, however, markedly increased the combined C_{60} and C_{70} yield from a level below the detection limit of the analytical equipment to as high as 0.023% of sample collected.

High resolution transmission electron microscopy (HRTEM) revealed interesting nanostructures in the flame samples. Particularly in samples from the acetylene flames, nanostructures similar to those from premixed flames[2] were observed. The benzene flame samples contained similar nanostructures and soot particles composed of curved, or fullerenic, layers.

A variety of polycyclic aromatic hydrocarbons (PAH), several of which contained relatively reactive 5-membered rings along the periphery, were identified in both the acetylene and benzene flames. In the acetylene flames, the PAH concentrations were sufficiently high to consider PAH as important soot growth reactants. However, no information is as yet available on the significance of PAH in fullerene formation reactions.

This work was only a preliminary investigation of fullerene formation in low pressure diffusion flames. It is encouraging that C_{60} and C_{70} were present in the benzene diffusion flames and that the dependence of fullerene formation on adjustable flame conditions is consistent with observations in premixed flames. Diffusion flames, operated at different conditions from the ones tested in this study, may produce fullerenes in yields comparable to premixed flames and may represent a feasible synthesis route. Additional study of diffusion flames is clearly warranted.

References

1. Howard, J. B., McKinnon, J. T., Makarovsky Y.; Lafleur, A. L., and Johnson, M. E. *Nature* **352**, 139-141 (1991).

2. Chowdhury, K. D., Howard, J. B., and VanderSande, J. B. *Journal of Materials Research* **11:2**, 341-347 (1996).

3. Sunderland, P. B., Köylü, Ü. Ö., and Faeth, G. M. *Combustion and Flame*, **100**, 310-322 (1995).

4. McKinnon, J. M. Ph.D. Thesis, M.I.T. (1989).

5. Howard, J. B., Lafleur, A. L., Makarovsky, Y., Mitra, S., Pope, C. J., and Yadav, T. K. *Carbon*, **30:8**, 1183-1201 (1992.

6. Benish, T.G., Lafleur, A.L., Taghizadeh, K., and Howard, J.B., *Twenty-Sixth Symposium (International) on Combustion*, The Combustiion Institute, Pittsburgh, PA, 1996, (in press).

Table 4. PAH Identified in Diffusion Flames. †PAH containing 5-membered rings along their periphery.

Number	Structure	Formula	Mass	Name	Acetylene Flames	Benzene Flames
1		$C_{13}H_8O$	180	Phenalenone	✓	✓
2		$C_{10}H_8$	128	Napthalene		✓
3		$C_{12}H_8$	152	Acenapthylene†	✓	✓
4		$C_{13}H_{10}$	166	Fluorene	✓	✓
5		$C_{14}H_8$	176	Ethynyl-acenaphthylene†	✓	
6		$C_{14}H_{10}$	178	Phenanthrene	✓	✓
7		$C_{15}H_{10}$	190	Cyclopenta[def]phenanthrene†	✓	✓
8		$C_{16}H_{10}$	202	Acephen-anthrylene†	✓	✓
9		$C_{16}H_{10}$	202	Fluoranthene	✓	✓
10		$C_{16}H_{10}$	202	Pyrene	✓	✓
11		$C_{18}H_{10}$	226	Cyclopentaace-phenanthrylene†	✓	✓
12		$C_{18}H_{10}$	226	Cyclopenta[cd]pyrene†	✓	✓
13		$C_{18}H_{10}$	226	Benzo[ghi]fluoranthene		✓
14		$C_{18}H_{12}$	228	Benz[a]anthracene		✓
15		$C_{18}H_{12}$	228	Chrysene		✓
16		$C_{20}H_{10}$	250	Dicyclopenta[cd,mn]pyrene†	✓	✓
17		$C_{20}H_{10}$	250	Dicyclopenta[cd,fg]pyrene†	✓	
18		$C_{20}H_{10}$	250	Dicyclopenta[cd,jk]pyrene†	✓	
19		$C_{20}H_{12}$	252	Benzo[b]fluoranthene	✓	
20		$C_{20}H_{12}$	252	Benzo[k]fluoranthene	✓	✓
21		$C_{20}H_{12}$	252	Benzo[a]pyrene	✓	✓
22		$C_{20}H_{12}$	252	Benzo[e]pyrene	✓	
23		$C_{22}H_{12}$	276	Benzo[ghi]perylene	✓	✓
24		$C_{22}H_{12}$	276	Indeno[1,2,3-cd]pyrene	✓	✓
25		$C_{22}H_{12}$	276	Anthanthrene	✓	
26		$C_{24}H_{12}$	300	Cyclopenta[fg]benzo[ghi]perylene†	✓	
27		$C_{24}H_{12}$	300	Cyclopenta[cd]benzo[ghi]perylene†	✓	
28		$C_{24}H_{12}$	300	Coronene	✓	✓
29		$C_{24}H_{14}$	302	Dibenzo[a,e]pyrene	✓	✓
30		$C_{26}H_{12}$	324	Cyclopenta[bc]coronene†	✓	✓
31		$C_{30}H_{14}$	374	Naphtho[8,1,2-abc]coronene†		✓
32		$C_{32}H_{14}$	398	Ovalene		✓

GRAVITATIONAL EFFECTS
IN SMOLDERING AND SHS

BERNARD J. MATKOWSKY
Northwestern University
Evanston, Illinois

INTRODUCTION

Smolder waves and SHS (self-propagating high-temperature synthesis) waves are both examples of filtration combustion waves propagating in porous media. Smoldering combustion is important for the study of fire safety. Smoldering itself can cause damage, its products are toxic and it can also lead to the more dangerous gas phase combustion which corresponds to faster propagation at higher temperatures. In SHS, a porous solid sample, consisting of a finely ground powder mixture of reactants, is ignited at one end. A high temperature thermal wave, having a frontal structure, then propagates through the sample converting reactants to products. The SHS technology appears to enjoy a number of advantages over the conventional technology, in which the sample is placed in a furnace and "baked" until it is "well done". The advantages include shorter synthesis times, greater economy, in that the internal energy of the reactions is employed rather than the costly external energy of the furnace, purer products, simpler equipment and no intrinsic limitation on the size of the sample to be synthesized, as exists in the conventional technology.

When delivery of reactants through the pores to the reaction site is an important aspect of the combustion process, it is referred to as filtration combustion. The two types of filtration combustion have a similar mathematical formulation, describing the ignition, propagation and extinction of combustion waves in porous media. The goal in each case, however, is different. In smoldering the desired goal is to prevent propagation, whereas in SHS the goal is to insure propagation of the combustion wave, leading to the synthesis of desired products. In addition, the scales in the two areas of application differ. Smoldering generally occurs at lower temperatures and propagation velocities than in SHS. Nevertheless, the two applications have much in common, so that what is learned in one application can be used to advantage in the other.

We have considered a number of problem areas involving gravitational effects in filtration combustion. These are: (A) waves of reaction between a porous solid and a gas filtering through its pores, with the gas flow induced by buoyancy, (B) reaction waves in porous solids which melt prior to reaction, forming a liquid suspension containing reactive particles whose density differs from that of the liquid bath, leading to particle separation, e.g., sedimentation. Separation leads to the relative motion of one reactant through the other, as in filtration combustion. The dynamics of the process then depends on the interplay between the rates of reaction and separation, and (C) reaction waves in deformable porous media, which are used to synthesize high porosity materials in both gravity and microgravity environments.

A. BUOYANT FILTRATION COMBUSTION

We first consider the propagation of exothermic reaction waves in a porous medium through which

there is gas filtration. The porous solid is composed of both reactive and inert components. Our study describes a wide range of natural and technological combustion processes in porous media having a common mechanism of reaction front propagation. The principal feature of this mechanism is the delivery of gaseous reactant(s) to the reaction front by filtration from the surrounding environment, where it reacts with the solid reactant(s).

Filtration can be caused by two different mechanisms, referred to as forced and natural, respectively. In the former an external force pushes the gas into porous matrix, and is often used in technological processes. In natural filtration the gas flow is induced by the combustion process itself, e.g., due to consumption of gas in the reaction. Buoyant filtration, considered here, is a natural filtration process since it arises in response to the chemical reaction(s). In a gravitational field, heated gas rises, inducing a filtration flux which delivers oxygen to the reaction site from the environment below. This self sustaining process is of great importance, e.g., for fire safety because it can develop naturally, without the need for special arrangements. All that is required for its occurrence is combustible material, air and a source of heat. It is of interest to study both the ignition stage and the stage of propagation of a developed combustion wave.

Buoyant filtration is typically a slow process, since under any reasonable conditions, the buoyant flux is relatively small. Thus, large samples are required in modeling buoyant filtration systems, and there then exists the problem of relating results for large samples to those for small samples. In ordinary combustion, the characteristics of wave propagation are independent of the length of the sample. In buoyant filtration combustion systems, this is typically not the case.

Most works on filtration combustion consider forced filtration, though natural filtration has also been considered, e.g., in connection with studies of self-propagating high-temperature synthesis (SHS). In SHS the reaction front propagates through a porous sample converting filtered reactant gas, e.g., nitrogen, hydrogen, etc., and solid matrix, e.g., metal powder, into a refractory compound. Filtration of the reactant gas is sustained by a pressure difference between the environment and the reaction site where it is consumed. Note that if inert is present in the gas flow, the pressure difference cannot be maintained by the reaction. A specific feature of this type of filtration is that gas does not pass through the reaction front where the pressure is a minimum. In contrast, for buoyant filtration combustion there is gas flux (at least its inert component) through the entire porous matrix, which transports heat through the reaction site, thus affecting the temperature distribution. That is, heat carried by the gas away from the reaction site can cause the system to jump from propagating as a high temperature combustion wave to a low temperature oxidation process, when the combustion temperature is lowered sufficiently. The reverse can also occur. Additional heat transported to the reaction site can cause the system to jump from a low temperature process to a high temperature combustion wave, as also occurs in forced filtration combustion. In this sense buoyant filtration combustion is similar to forced filtration combustion where the thermal interaction of the flowing gas with the reaction front leads to various effects, such as (i) the superadiabatic effect in which heat is transported from the product region to the reaction site, inducing a burning temperature which exceeds the adiabatic burning temperature, and (ii) the subadiabatic effect in which heat is transported from the reaction site. Thus, the burning temperature can vary over a wide range. In addition, (iii) extinction can occur under adiabatic conditions, i.e. with no heat loss to the external environment, and (iv) the final temperature and depth of conversion cannot be determined from thermodynamic arguments alone. Rather, they depend on the gas flux. Moreover, the flux can (v) change the structure of the combustion wave, and also (vi) generate new instabilities. At the same time the natural mechanism of filtration distinguishes buoyant filtration combustion from forced filtration combustion where the filtration flux is prescribed, so that there is no feedback between the combustion wave and the incoming gas flux. In buoyant filtration combustion there is feedback, in that the incoming gas flux influences the combustion process, which, in turn, influences the strength of the incoming gas flux. This feedback is most important during the initial stage of the process, when interaction between filtration and reaction either reinforce or impede each other, resulting in either the propagation of a developed high temperature combustion wave or in a low temperature oxidation process. Separating these two regimes is the critical ignition condition.

For certain values of the parameters of the problem, in the absence of any external energy input, the system may self ignite, leading to the propagation of a combustion wave driven by buoyant flux. For other parameter values buoyant filtration combustion may be initiated by an external thermal pulse, which launches (e.g., at the top or bottom of the sample) the combustion wave as well as the filtration flux required to sustain it. For conventional combustion the problem of initiating a traveling combustion wave (TW) reduces to the problem of creating a preheat layer whose length scale is fixed as the width of the combustion zone (preheat layer and reaction zone). For buoyant filtration combustion, the conditions for initiating a wave are different since the wave is not a real TW. Rather, it is a quasisteady (slowly varying) wave, since the width of the hot (product) region, and therefore the buoyant flux, which affects ignition conditions, varies in time.

The buoyant filtration combustion wave may propagate either upward or downward depending on whether ignition occurs at the bottom or the top of the porous sample. In the former case the direction of wave propagation coincides with that of the buoyant flux, so that it is referred to as coflow, or forward filtration combustion. In the latter case the direction of wave propagation is opposite to that of the buoyant flux, so that it is referred to as counterflow, or reverse filtration combustion.

A model of buoyant filtration combustion consists of the basic elements of the forced filtration combustion model, supplemented by a description of the relevant hydrodynamics. Specifically, in contrast to forced filtration combustion where the hydrodynamic description is reduced to a prescribed filtration flux, in buoyant filtration combustion the flux is not known a-priori. Thus, the equations of hydrodynamics must be included in the filtration combustion model.

A cylindrical porous matrix is assumed to be set vertically in a container with both the top and bottom ends open to gas permeation, while the sides are impermeable to gas penetration. A reaction between the gas and the fuel in the porous matrix may be self-ignited in the sample if the temperature T_0 is sufficiently high. Gravity then acts as a forcing mechanism by which the hot gaseous products rise and exit the top, while fresh cool gas is pulled in through the bottom of the sample. The strength of this forcing depends on the intensity of the reaction through the amount of heat released, the temperature distribution and the density of the gaseous product. In turn, the intensity of the reaction depends on the filtration flux of gas which carries both oxidizer and heat. The role of filtration becomes very important, indeed crucial if, due to the large difference in densities of the solid and the gas, the amount of oxidizer in the pores would be insufficient for appreciable fuel conversion if there were no filtration. Thus, the principal mechanism for supplying the reaction with oxidizer is filtration. Diffusion of gas, a much slower process, cannot possibly compete with convection on large macroscopic scales.

Our goal is to gain an understanding of the principal mechanisms characteristic of buoyant filtration combustion in general. Analysis of even the simplest model of buoyant filtration combustion is of interest, due to the fact that filtration may replace chemical kinetics as the rate limiting step of the process, and thus may play a dominant role. Many features of buoyant filtration combustion are determined by processes such as flow which occur on the scale of the sample, rather than on the details of the kinetics process which occurs on the scale of the reaction zone. For example, the propagation velocity and ignition characteristics may depend on the length of the sample. Another example is the superadiabatic effect in an upward propagating buoyant filtration combustion wave, which is independent of the details of the kinetic process. Conditions for the most significant manifestation of this effect provide important information about the overall reaction scheme, which is not yet understood for many real systems.

In conventional combustion systems the combustion waves are TWs, whose wave characteristics, e.g., propagation velocity and shape, are constant, and the time and length scales for the ignition period are independent of the length L of the sample. In contrast, here the waves are not TWs. Rather, they are quasisteady waves, whose characteristics *do* depend on L. Thus, knowledge of the combustion characteristics determined from experiments on a specific sample of a given size can not be generalized to samples of larger size, as is the case in conventional combustion. Therefore, one is faced with the problem of scale up.

In order to describe the propagation of buoyant filtration combustion waves we employ both numerical simulations, and wherever possible, analytical (asymptotic) descriptions in various limiting situations, such as the large activation energy (thin reaction zone) approximation. We employ a one temperature model, assuming that the heat transfer rate between the solid and gas phases is very large compared to the reaction rate so that both phases quickly equilibrate to the same temperature. We also assume that the properties of the porous medium are homogeneous, e.g., changes in the permeability, or other characteristics, from the fresh mixture to the product region are neglected, that the kinetics are described by a strongly activated one step process, and that the propagation velocity is small compared to the gas velocity. We consider all aspects of the combustion process, including the problems of self ignition, external ignition and the dynamics of propagation of both upward and downward adiabatic and nonadiabatic waves. We determine regions of self-ignition. We find that upward propagation is more easily initiated than downward propagation, and that the superadiabatic effect occurs in upward propagation, though not in downward propagation. Where possible we compare to experimental results of A.C. Fernandez-Pello and colleagues.

In upward propagation we determine two types of wave structure, termed reaction leading and reaction trailing according as the reaction occurs at the leading or trailing edge of the heated region of the sample, respectively. That is, in each wave there are three regions in which the temperature is essentially constant, a high temperature domain (HTD) at the burning temperature, separating two regions at the low ambient temperature. The HTD is separated from each of the low temperature regions by relatively thin layers, the reaction layer, and the heat transfer layer in which there is heat transfer between the solid and the gas. The reaction leading (trailing) structure occurs when the reaction (heat transfer) layer precedes the other. For each structure, two solution modes are described, termed stoichiometric and kinetically controlled, according as the rate of oxygen supply or the kinetics controls propagation of the wave. In each of these four situations, we derive expressions for the evolution of the burning temperature, propagation velocity, incoming gas flux, degree of oxidizer consumption and degree of fuel conversion as the wave moves through the sample. In addition, profiles for temperature are described. Analysis of the case where significant heat is lost through the sides of the sample leads to extinction limits and demonstrates the sensitivity of the wave structure to changes in external heat losses.

In downward propagation we find the interesting phenomenon of wave reversal. Specifically, if the wave propagates downward under gas deficient conditions, the burned solid is not completely converted to product. As propagation continues, the HTD grows in size, inducing an increased buoyant flux. When this flux reaches a critical level, propagation can no longer continue. The front then reverses direction, traveling upward to complete the conversion of the solid fuel above it. The depth of penetration of the downward wave into the sample depends on parameters such as the buoyant flux, and decreases as the flux increases. In contrast, upward propagating waves, initiated at the bottom, always propagate through the entire sample.

We also analyze two non-adiabatic cases, distinguished by whether or not the sample is sufficiently long and the heat losses sufficiently large that the cooling region behind the reaction site is completely contained within the sample. When it is totally contained in the sample we describe traveling wave solutions whose shape does not change in time, provided there is no net production of gas in the reaction. When it is not completely contained within the sample, we describe quasi-steady combustion waves which change slowly in time due to the increasing buoyant flux as the combustion wave penetrates further and further into the sample. Solutions are categorized as gas deficient when the oxidizer is completely consumed, solid deficient when the solid fuel is completely consumed, or stoichiometric when both oxidizer and solid fuel are completely consumed. Extinction is found to occur for solid deficient and stoichiometric solutions when the buoyant flux is sufficiently large. The results of these investigations, as well as all relevant references, appear in (ref. 1) and in two additional papers, to appear.

B. "LIQUID FLAMES" IN GRAVITATIONAL FIELDS

We also consider the structure of a combustion wave propagating through an initially hard porous matrix, which is destroyed by the propagating combustion wave, due, e.g., to melting of some of the components of the mixture ahead of the reaction front. Thus, a liquid bath is formed, in which processes such as heat and mass transfer as well as chemical reactions determine the structure of the combustion wave, its propagation velocity and the composition of the reaction product. The liquid bath is a suspension containing reactive particles, either liquid or solid. In general, the particle density differs from that of the bath. Thus, under the influence of gravitational forces there is relative motion, i.e., separation, of the individual components of the mixture, e.g., sedimentation of the particles. Separation is opposed by a friction force. To gain an understanding of phenomena associated with relative motion and separation during the propagation of the combustion wave, topics which heretofore have not been considered, we formulate and analyze a relatively simple mathematical model of "liquid flame" combustion in a gravitational force field. We determine the structure of uniformly propagating combustion waves and describe the possibility of multiplicity of such solutions. We also consider nonstationary waves and show that "shock" type solutions, with jumps in the composition of the sample (though there are no jumps in the pressure field), are possible.

In addition, motivated by recent experiments of Lee and Goroshin who studied the combustion of metal particles (e.g., Zn), and Sulfur, we consider the question of ignition for the "liquid flame" problem. Clearly, if the separation rate is sufficiently smaller (greater) than the reaction rate, ignition will (will not) occur. Consider the case that the particle density exceeds that of the liquid, and the reaction is initiated from above. We analyze four regions: (i) the pure liquid layer at the top, free of all particles, which have already sedimented, (ii) the suspension region, (iii) the sediment region, and (iv) the initial solid region. The regions, and the processes occurring therein, evolve in time, due to sedimentation and reaction. Reactions occur in the suspension and sediment. We determine the interfaces between these regions and investigate the processes occurring in each region. Whether or not ignition occurs depends on the relative time scales of reaction and sedimentation. Thus, we introduce a parameter v_g, which is the ratio of the reaction and sedimentation time scales. We study the problem both analytically and numerically. We determine whether or not ignition occurs, by determining a critical ignition condition, i.e., by determining a critical value of v_g as a function of parameters such as the strength of the heat source, the initial temperature, the strength of the gravitational field, the diameter of the particles, the viscosity of the fluid, the difference in the densities of the fluid and the particles, the kinetic parameters, etc. In the case that ignition does occur, we estimate the ignition time. In addition, we numerically determine the dynamics of the ignition process as a function of the parameters of the problem. We show that it is not appropriate to employ standard ignition criteria which do not account for gravitational effects. However, it is reasonable to employ these ignition criteria, if they are appropriately modified to include gravitational considerations. Specifically, for weak gravitational fields (v_g small), the source temperature must be replaced by the temperature at the (moving) top of the reaction zone, which must be calculated. In this calculation the liquid reactant concentration and properties of the medium, e.g., the fluid volume fraction, in the reaction zone, are taken to be approximately the same as in the case without gravity, since they change very slowly. For stronger gravitational fields, it is necessary to also compute the liquid reactant concentration and the fluid volume fraction, which evolve in time and space, together with the temperature at the top of the reaction zone. Finally, we describe how to adapt the model to other heterogeneous mixtures, e.g., to gas - condensed phase suspensions. The results of these investigations, as well as all relevant references, appear in (ref. 2) and in three additional papers, to appear.

C. GRAVITATIONAL EFFECTS ON HIGH POROSITY MATERIALS SYNTHESIS

Finally, we consider a model of combustion of porous samples in a gravitational field, in which the high temperature products can deform, to describe the synthesis of high porosity materials and its dependence on parameters of the problem. It has been suggested that there are advantages to using

the method of SHS to produce bulky thermal insulation materials for use in space applications, directly in outer space, rather than producing them on earth and then transporting the bulky materials from earth to space. The method appears to offer promise for these purposes since it does not require costly external energy, it can easily be carried out in outer space, it employs simple equipment, and minimal training is required for those who will perform the task in space. The high-porosity products of the synthesis reaction of refractory compounds may be used for thermal insulation.

A number of experiments, both ground based and under microgravity conditions demonstrated that high porosity materials can indeed be produced by the SHS method. For example, in the experiments of Shteinberg, a powder mixture containing Ti, C and a small amount of a gas liberating additive was used, while in the experiments of Moore, a powder mixture of boron oxide, carbon and aluminum, was used to demonstrate the possibility of producing high porosity materials even without a gas liberating additive.

The components of such mixtures are heated to such high temperatures by the combustion wave that they change their state, e.g., melt, and can be easily deformed. The melt then solidifies into a solid product, either in the chemical reaction or by cooling, due e.g., to heat losses.

The SHS process can be used for technological applications in which various desired product characteristics e.g., porosity, structure and shape, can be achieved. These characteristics are affected by external force fields, such as gravity. However, even in microgravity the SHS process itself creates stresses in the sample, leading to self-deformation of the sample, which affects the combustion process, which, in turn, affects deformation.

We formulate and analyze a mathematical model which accounts for the principal physical mechanisms observed in experiments. In addition to the main synthesis reaction, we allow for the possibility of a gasification reaction of a special additive. We employ the model to investigate combustion synthesis of high porosity materials in both normal and microgravity environments. We describe ignition, propagation, extinction and stability of propagating combustion waves, as well as elongation of the sample, and their dependence on various factors such as heat loss, gravity, rheological parameters and amount of additive. The elongation is caused by an increase in porosity due to the gas produced in the main reaction or in the additive reaction or both. We derive an expression for the elongation, e.g., how elongation increases as gravity decreases, in accord with the experimental results of Shteinberg and of Moore. In particular, we show the advantage of a microgravity environment for the synthesis of uniformly high porosity materials. The results of this investigation, as well as all relevant references, appear in (refs. 3, 4).

References

[1] A.P. Aldushin, B.J. Matkowsky and D.A. Schult, *Downward Buoyant Filtration Combustion*, Comb. and Flame **107** (1996) p. 151.

[2] K.G. Shkadinsky, G.V. Shkadinskaya and B.J. Matkowsky, *Gravity Induced Separation in "Liquid Flames"*, Comb. Sci. & Tech. **115** (1996) p. 229.

[3] K. G. Shkadinsky, G. V. Shkadinskaya, B.J. Matkowsky and V. A. Volpert, *Self-Compaction or Expansion in Combustion Synthesis of Porous Materials*, Comb. Sci. and Tech. **88** (1993) p. 271.

[4] K.G. Shkadinsky, G.V. Shkadinskaya and B.J. Matkowsky, *Gravitational Effects on the SHS Production of High Porosity Materials*, Comb. Sci. & Tech. **118**, (1996), p. 315.

THE EFFECT OF GRAVITY ON THE COMBUSTION
SYNTHESIS OF POROUS CERAMICS AND METAL MATRIX COMPOSITES

J.J. MOORE
Department of Metallurgical and Materials Engineering
Colorado School of Mines, Golden, Colorado, 80401-1887, USA

T.C. Woodger, and T. Wolanski
Graduate Students, Department of Metallurgical and Materials Engineering
Colorado School of Mines, Golden, Colorado, 80401-1887, USA.

Collaborators: H.C. Yi, and J.Y. Guigne
Guigne International Ltd., St Johns, Newfoundland
GIL-MUN Processing, Faculty of Engineering and Applied Science
Memorial University of Newfoundland
St. John's, NF, Canada A1B3X5

Introduction

Combustion synthesis (self propagating, high temperature synthesis-SHS) is a novel technique that is capable of producing many advanced materials [1-3]. The ignition temperature (Tig) of such combustion synthesis reactions is often coincident with that of the lowest melting point reactant. The resultant liquid metal wets and spreads around the other solid reactant particles of higher melting points, thereby improving the reactant contact and kinetics, followed by formation of the required compounds. This ignition initiates a combustion propagating wave whose narrow reaction front rapidly travels through the reactants. Since this process is highly exothermic, the heat released by combustion often melts the reactant particles ahead of the combustion front and ignites the adjacent reactant layer, resulting in a self-sustaining reaction. Whenever a fluid phase (liquid or gas) is generated by the reaction system, gravity-driven phenomena can occur. Such phenomena include convective flows of fluid by conventional or unstable convection [4] and settling of the higher density phases [5,6]. A combustion process is often associated with various kinds of fluid flow. For instance, if the SHS reaction is carried out under inert or reactive gas atmospheres, or a volatile, e.g., B_2O_3, is deliberately introduced as a reactant, convective flows of the gas will occur due to a temperature gradient existing in the atmosphere when a combustion wave is initiated. The increased gas flow will produce a porous (or expanded) SHS product. Owing to the highly exothermic nature of many SHS reactions, liquid phase(s) can also form before, at, or after the combustion front. The huge temperature gradient at the combustion front can induce convective flows (conventional or unstable) of the liquid phase. Each of these types of convective fluid flow can change the combustion behavior of the synthesizing reaction, and , therefore, the resultant product microstructure. In addition, when two or more phases of different density are produced at or ahead of the propagating combustion front, settling of the higher density phase will occur resulting in a non-uniform product microstructure and properties.

Experimental Method

Elemental powders of Ni, Ti, Al, Hf, B_2O_3, graphite or lampblack (< 44 μm) and amorphous B (<1μm) were thoroughly mixed in the desired stoichiometries according to the following reactions:

$$Hf+2B+xAl = HfB_2 + xAl \tag{1}$$

$$Ti+2B + x(3Ni+Ti) = TiB_2+ xNi_3Ti \tag{2}$$

$$2B_2O_3 + C (4 + x)Al = B_4C + 2Al_2O_3 + xAl \tag{3}$$

Green reactant pellets were prepared by uniaxially pressing the powders to green densities of 65 and 75% theoretical. Each pellet had a diameter of 12.7mm and weighed between 6-8 grams. Pellets with lower densities were prepared by lightly packing the loose reactant powders. The green pellets were ignited in a cylindrical, quartz reaction chamber (579 ml in

volume) using a tungsten ignitor coil. The temperature-time profiles were recorded by a data acquisition system and the reaction chamber environment was either 1 at argon or vacuum (10^{-3} torr). The progress of the combustion reaction was recorded with a video recorder. The effects of gravity on the combustion synthesis reactions was studied by igniting the MMC green pellets from three orientations to the gravity center corresponding to top, horizontal and bottom ignitions, and on board the NASA LeRcDC9. The green pellets for reactions (3) and (4) were ignited only from the bottom on account of the expansion.

Results And Discussions

Reaction system (1) has a low density matrix and high density ceramic phase while reaction system (2) has a high density matrix and low density ceramic phase. During processing, the matrix phase for both systems is molten, which increases the potential of gravity induced segregation. When pellets for reaction (1) were ignited from the top, the combustion wave propagated with a lower velocity, the wave front appeared planar, and the wave velocity became increasingly smaller as the wave proceeded downward. Igniting these pellets at the bottom, the combustion temperature and the combustion wave velocity were considerably higher, and the combustion wave front propagated in a non-planar manner. Preheating of the green pellet proceeds the passage of the combustion front due to the heat transfer from the advancing front. Examination of the time-temperature profile confirmed that the preheating was highest when ignited from the bottom of the pellet and decreased with increasing excess metal (xAl). This preheat, in turn, produced gravity-driven convective flow of argon gas. It was found that for pellets containing 50 and 60 vol % Al, pure Al nodules gradually formed on the surface of the pellet after the combustion front had passed. This phenomenon was explained by hydrostatic pressure created by the liquid Al (head height x density x g). Settling was also confirmed from examination of the composite microstructures shown in Figure 1. The two phases present in this system, Al and HfB_2, have a density difference of 8820 kg m^{-3}. According to Stoke's law, settling of a single HfB_2 particle of radius r, under ideal conditions can be calculated by :

$$Vt = 2/9 \ g \ r^2(d_s\text{-}d_l)/\mu \qquad (3)$$

where g is the gravitational acceleration (9.81 m/s/s), d_s the density of the solid HfB_2 particle (11200 kg m^{-3}), d_l the density of the liquid Al (data taken at the melting point, 2380 kg m^{-3}), and μ the dynamic viscosity of Al (3.1×10^{-3} Pa). Under ideal conditions, the settling rate of the HfB_2 particles is calculated using equation (3) and the results are listed in Table I together with the SHS reaction data. Therefore, for a typical combustion process in which samples remained in the molten state for about 15 seconds, the total settling distance should be between about 22 μm to 837 μm under ideal conditions. However, considering the approximations used in equation (3) and that there is a large population of the HfB_2 particles, the actual settling distance would be much smaller. The settling under low gravity conditions would be three orders of magnitude less. The combustion synthesis reactions conducted under reduced gravity were carried out using parabolic flights on board a DC-9 aircraft at the NASA LeRC. All pellets were ignited from the bottom. Both the average combustion temperature (Tc) and the wave velocity (v) were considerably lower under the reduced gravity conditions than at normal gravity, as shown in Table I. The preheat temperature, Tp, was also much lower for reactions conducted under low gravity. These results confirm the role of the argon gas convection under normal gravity. Lower preheat and combustion temperatures, as well as lower propagating velocity under reduced gravity conditions were believed to result from decreased convective flows of the ambient argon gas which resulted in reduced heat transfer. There were no Al nodules observed on the surface of samples after combustion of pellets in low gravity which clearly indicated the lack of (h p g) forces on the liquid Al.

The Ni_3Ti/TiB_2 System

The combustion reactions of pellets with higher than 60% green density were characterized by high wave velocities and expansions after combustion. All pellets were ignited from the bottom of the pellet. The combustion characteristics under both normal and reduced gravity conditions for samples containing 70 vol % Ni_3Ti are listed in Table II. Under normal gravity, both the combustion velocities and temperatures were much higher for pellets of 42% green density than under reduced gravity. However, there was not much difference for samples of 65% green density. This observation again agrees with the argument presented earlier, i.e., convective flow of argon enhanced combustion. A comparison of microstructures for MMCs of 70 vol % Ni_3Ti ignited under normal and reduced gravity conditions is shown in Figures 2 and 3. Buoyancy of the TiB_2 particles and settling of the Ni_3Ti phase are clearly seen in Figure 2(a) and 3(a), whereas a more uniform distribution of the two phases can be seen in Figure 2(b) and 3(b). Simple calculations of the settling distance of TiB_2 taken from the data in Table II indicated a

26

30μm periodicity. This agrees well with the TiB_2 layered structure in Figure 2(a). The layered structure was clearly absent from samples produced under low gravity conditions.

$B_4C-Al_2O_3$ Porous Ceramic Composites

The purpose of this research is to develop a better understanding of the effects of reaction parameters on the combustion synthesis of porous boron carbide-alumina composites. The effects of reaction parameters, reaction chamber pressure and the effect of gravity on the combustion reactions were each examined. Once the variable effects are understood, they can be manipulated to produce a consistent product. Porous materials are required for a variety of applications such as: filters, lightweight structural materials, insulators, catalyst support systems, and even osteogenic support systems. By controlling the expansion and amount of porosity in a combusting (reacting) sample, its properties may be tailored for one of these applications. The reaction system (3) was selected for investigation in this research project based upon its attractive physical and mechanical properties and porous nature. The literature [7] has reported that the volumetric expansion of combusting samples is controlled by two main processes. The first process is the plasticity of the reaction zone. Increasing the plasticity of the reaction zone, through the use of a reacting component which melts, and decomposition of a gassifying additive. An approximation of the sample expansion/elongation during reaction can be written as [8]:

$$\frac{\Delta l}{l} = \frac{Pg - P\infty \Delta X}{\eta u}$$

where $\Delta l/l$ is the degree of elongation, Pg is the pressure of the gas within the pores, $P\infty$ is the gas pressure of the ambient medium, η is the material viscosity, ΔX is the size of the reaction zone and u is the rate of combustion. The parameters selected for investigation in this research project were related to $P\infty$, Pg, η, and the amount of fluid liquid at the reaction front. In the boron carbide-alumina reaction system (3), the liquid at the reaction front is composed of mixed oxides and liquid aluminum; to increase the amount of liquid at the reaction front the amount of excess aluminum present in the reactants was from 0 to 3 moles. Boron oxide is the gas forming constituent in the reaction, so to increase the amount of gas evolving in the reaction an excess of boron oxide was added. In order to prevent unreacted boron oxide from remaining in the sample and with the intention of increasing the viscosity of the liquid at the reaction front, silica was added to the excess boron oxide. Two different ratios of boron oxide to silica were used, i.e., 97:3 and 50:50. The 97 B_2O_3: 3 SiO_2 ratio corresponds to the eutectic composition which has a slightly lower melting point than pure boron oxide.

$$(2 + 0.05y)B_2O_3 + 4Al + C + 0.05(1-y)SiO_2 = B_4C + 2Al_2O_3 + 0.05yB_2O_3 + 0.05y(1-y)SiO_2 \qquad (4)$$
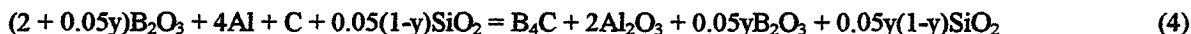
The 50 B_2O_3: 50 SiO_2 ratio contains more silica and would be expected to have a significantly higher liquid viscosity while producing less gas than the 97:3 ratio. The 50:50 ratio has a melting point between that of silica and boron oxide. Both boron oxide-silica mixtures were added to the reactants at 5 and 10 weight percent (Table III). The gravity levels (g's) experienced by the reacting compacts were varied between 0.01 and 2 g's, referred to as the reduced and enhanced gravity states, respectively. Table III provides a summary of the different reaction conditions investigated. Universally, it was seen that pellet expansions decreased with increasing reaction chamber pressure and increased with increasing combustion temperatures. Increasing the reaction chamber pressure serves to retain more of the reactive boron oxide gases within the reacting pellet, causing the reaction to approach completion and adiabatic conditions. This was confirmed by the higher combustion temperatures at elevated pressures and laser ablation ICP analysis. The form of carbon used (graphite or lampblack) did not have a significant effect on combustion temperatures. Yet the reactions which utilized graphite experienced noticeably greater expansions. This would signify that the lampblack volatiles must be released at temperatures below the melting point of aluminum, causing the volatiles to escape the pellet prior to reaction and not contribute to pellet expansion. The addition of excess aluminum caused the combustion temperatures and expansions to decrease. This same trend was observed with increasing amounts of silica. There does appear to be an enhancing effect of slight amounts of either addition on the combustion temperatures and expansions of pellets reacted in vacuum. The addition of some excess, high fluidity liquid and a slight increase in liquid viscosity or amount of a gassifying agent tended to increase combustion temperatures and expansions in a vacuum environment. In these situations the enhancement of fluid properties overcomes the accompanying decrease in exothermicity of the reaction. In reactions conducted under reduced and enhanced gravity conditions the samples reacted in low gravity conditions experienced significantly higher combustion temperatures. This stands to reason since their would be lower heat losses in low gravity than in enhanced gravity, since natural convection would be eliminated or at least greatly reduced in microgravity. Correspondingly, there was a decrease in expansion with increasing gravity levels. This can be directly linked to the temperature differences experienced, but should not exclude the possibility of other gravity-influenced factors, such as gas buoyancy. Mercury porosimetry revealed that the total area of porosity within the samples decreased with increasing chamber pressure and was roughly proportional to pellet expansion. In contrast, the average pore size within the pellets increased with

27

chamber pressure. This may indicate a tendency for the gases to remain entrapped and expand within the pellet. Therefore, the apparent density of the reacted material increased with reaction chamber pressure. In systems which contained an excess of silica-boron oxide mixture the apparent density noticeably decreased, indicating an increase in the amount of closed porosity. Evidence of segregation was seen in the excess aluminum systems reacted under enhanced gravity conditions. This segregation was minimized as gravity levels decreased. Maximum porosity and expansion were achieved under vacuum conditions and at low gravity. The graphite system exhibited an increased linear expansion than the lampblack samples but the lampblack samples contained a greater surface area porosity. In both the graphite and lampblack systems the specific porosity (m^2/g) and linear expansion (in vacuum conditions) was augmented by the addition of the silica-boron oxide mixture. The addition of the low silica-boron oxide mixture (3 SiO_2: 97 B_2O_3) increased specific porosity much more than the addition of high silica-boron oxide (50 SiO_2: 50 B_2O_3), suggesting that there may be an optimum level.

Acknowledgment

References

1. Munir, Z.A., and Anselmi-Tamburini, U., (1989), Mater. Sci. Rep., 3, pp 227-365.
2. Yi, H.C.and Moore, J.J., (1990), J. Mater. Sci., 25, pp 1159-1168.
3. Moore, J.J. and Feng, H.J., (1995), Progress. Mater. Sci., 39, pp 243-316.
4. Ostrach O., (1982), Ann. Rev. Fluid Mech., 14, pp 313-345.
5. Froyen, L. and Deruyttere, A., (1984), "Proc. of the 5th European Symposium on Materials Sciences Under Microgravity", edited by T. Guyenne and J.J. Hunt, Schloss Elmau, Germany, pp 69-78.
6. Sharma, S.C., Narayanan, P.R., Sinha, P.P., Nagarajan, K.V., (1994), J. Mater. Sci., 29, pp 5719-24.
7. Merzhanov, A.G., Combustion and Plasma Synthesis of High Temperature Materials, Eds. Z.A. Munir, J.B. Holt, pub by VHC, NY, (1990), pp. 1-53.
8. Shterburg, A.S., Shcherbakov, V.P., Martynov, V.M., Mukhoyan, M.Z. and Merzhanov, A.G., (1991), Sov. Phys. Dokl., 36,(5), pp 385-387.

Table I. Effects of Gravity for the HfB_2/Al System

VOL %AL	NORMAL GRAVITY (1g)*				REDUCED GRAVITY (ug)**		
	V (mm/s)	T_c(K)	HfB_2 (um)	Settling Rate (um/s)	V (mm/s)	T_c(K)	Settling Rate (um/s)
50	—	—	3.0	55.8	—	—	55.8×10^{-3}
60	3.1 ± 0.2	2056 ± 92	1.5	14.0	2.8 ± 0.2	1874 ± 164	14.0×10^{-3}
70	1.9 ± 0.1	1765 ± 15	0.5	1.5	0.9 ± 0.1	1403 ± 28	1.5×10^{-3}

* Bottom ignition.   ** assuming extent of gravitational force was 10^{-3} g.

Table II. Effects of Gravity for the Ni_3Ti/TiB_2 System with 70 vol % Ni_3Ti

GREEN DENSITY (%)	NORMAL GRAVITY (1G)		REDUCED GRAVITY (ug)	
	V (mm/s)	T_c (K)	V (mm/s)	T_c (K)
42	2.34 ± 0.12	1817 ± 65	1.32 ± 0.15	1690 ± 60
65	21.04 ± 0.47	1745 ± 27	21.5 ± 1.2	1724 ± 134

Table III. Reaction Conditions Under Investigation

CARBON FORM	MOLES EXCESS Al	REACTION CHAMBER PRESSURE	~g's
Graphite	0, 1, 2, 3	Vacuum, 1 atm, 2 atm	0, 1, 2
Lampblack	0, 1, 2, 3	Vacuum, 1 atm, 2 atm	0, 1, 2

Carbon Form	Excess B_2O_3-SiO_2 Mixture	η Liquid	Reaction Chamber Pressure	~g's
Graphite	5mol% (97%B_2O_3:3%SiO_2)	Low	Vacuum, 1 atm, 2 atm	0, 1, 2
Lampblack	5mol% (97%B_2O_3:3%SiO_2)	Low	Vacuum, 1 atm, 2 atm	0, 1, 2
Graphite	5mol% (50%B_2O_3:50%SiO_2)	High	Vacuum, 1 atm, 2 atm	0, 1, 2
Lampblack	5mol% (50%B_2O_3:50%SiO_2)	High	Vacuum, 1 atm, 2 atm	0, 1, 2
Graphite	10mol% (50%B_2O_3:3%SiO_2)-	Low	Vacuum, 1 atm, 2 atm	0, 1, 2
Lampblack	10mol% (50%B_2O_3:3%SiO_2)-	Low	Vacuum, 1 atm, 2 atm	0, 1, 2
Graphite	10mol% (50%B_2O_3:50%SiO_2)-	High	Vacuum, 1 atm, 2 atm	0, 1, 2
Lampblack	10mol% (50%B_2O_3:50%SiO_2)-	High	Vacuum, 1 atm, 2 atm	0, 1, 2
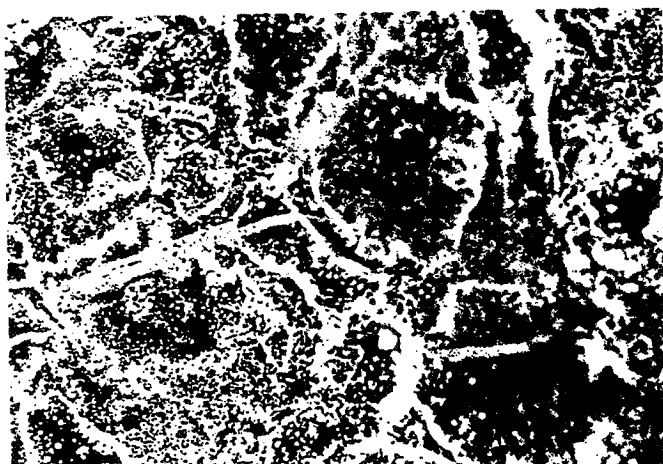
(a)   (b)
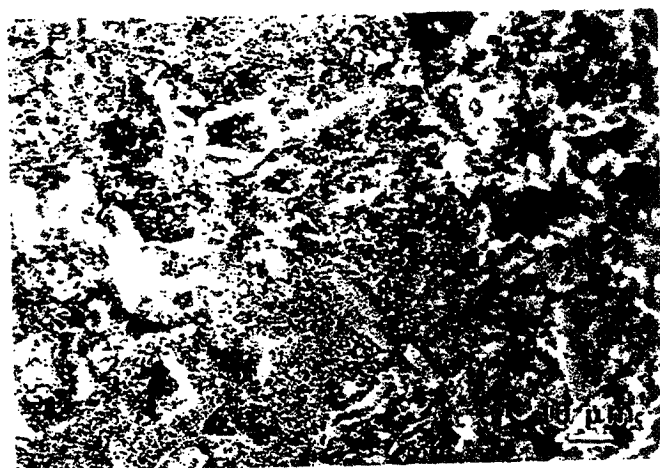
Figure 1. The effect of gravity on the microstructure of the Al-HfB_2 system showing the distribution of HfB_2 (light phase) for samples with 70 volume percent Aluminum reacted in a) 1g and b) reduced gravity conditions.
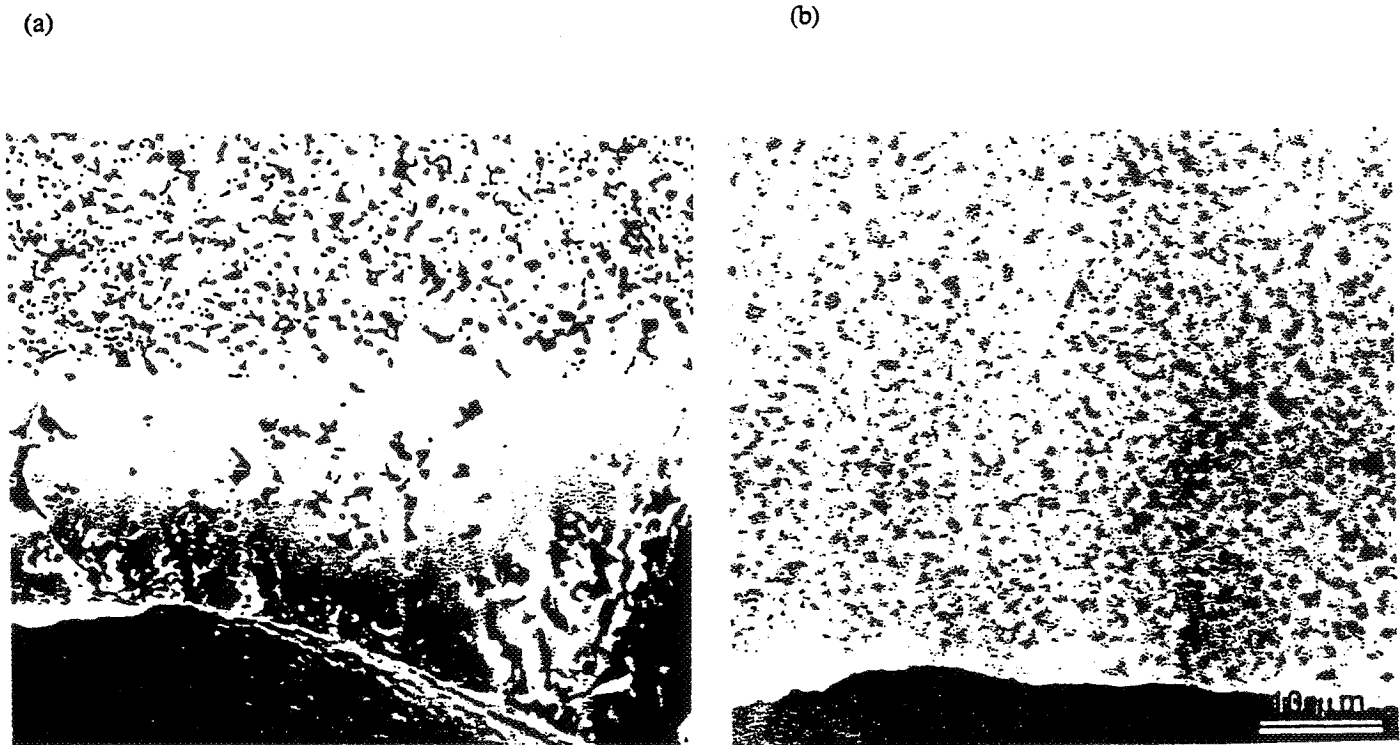
Figure 2. Bottom region of a sample containing 70 volume percent Ni₃Ti reacted in a) 1g and b) reduced gravity conditions. Gravity induced segregation of TiB₂ (dark phase) is observed for the sample reacted in 1g.

a) b)
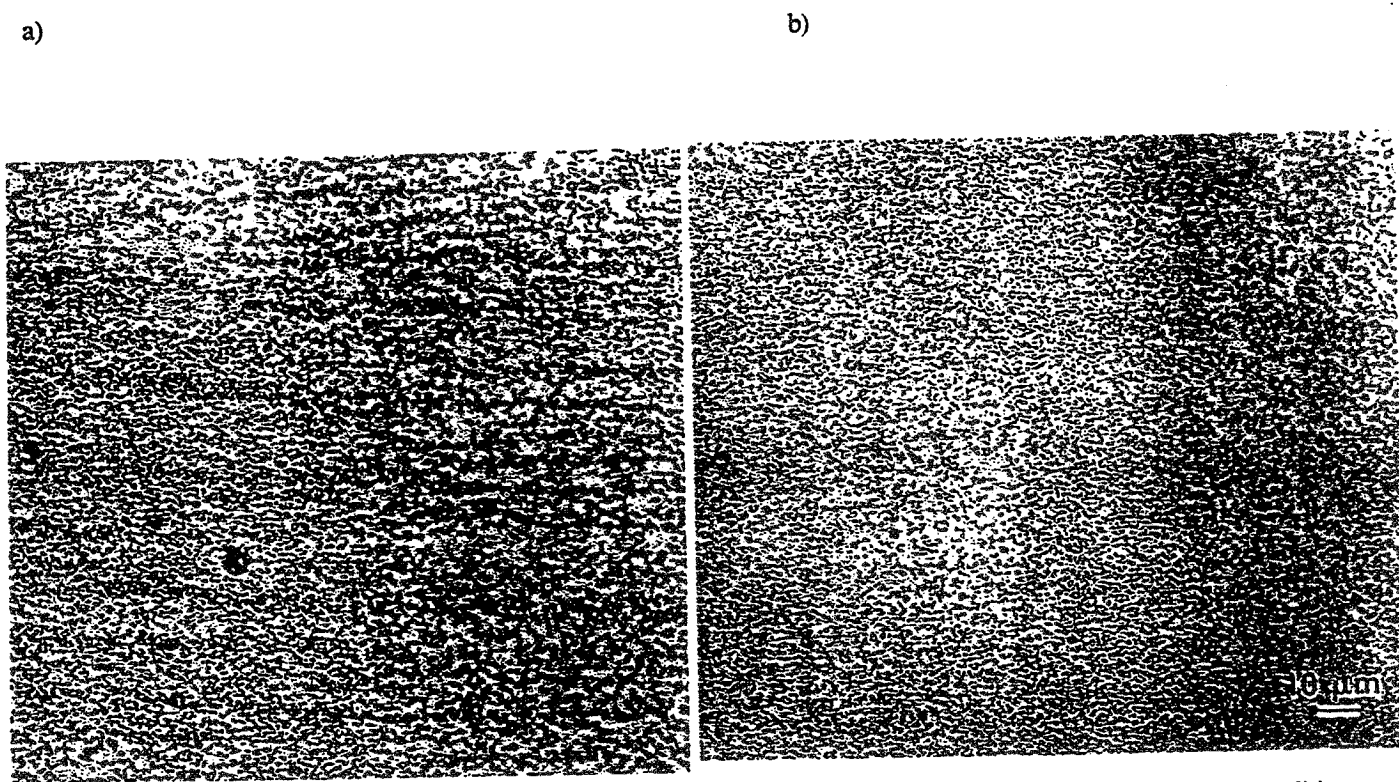
Figure 3. Central region of a sample containing 70 volume percent Ni₃Ti reacted in a) 1g and b) reduced gravity conditions. Gravity induced segregation (layering) of TiB₂ (dark phase) is observed for the sample reacted in 1g.

THE EFFECTS OF GRAVITY ON COMBUSTION AND STRUCTURE FORMATION DURING COMBUSTION SYNTHESIS IN GASLESS SYSTEMS[*]

ARVIND VARMA, Alexander Mukasyan and Aleksey Pelekh
Department of Chemical Engineering
University of Notre Dame
Notre Dame, IN 46556

Introduction

There have been relatively few publications examining the role of gravity during combustion synthesis (CS), mostly involving thermite systems (refs.1-3). The main goal of this research was to study the influence of gravity on the combustion characteristics of heterogeneous gasless systems. In addition, some aspects of microstructure formation processes which occur during gasless CS were also studied. Four directions for experimental investigation have been explored: (i) the influence of gravity force on the characteristic features of heterogeneous combustion wave propagation (average velocity, instantaneous velocities, shape of combustion front); (ii) the combustion of highly porous mixtures (with porosity greater than that for loose powders), which cannot be obtained in normal gravity; (iii) the effect of gravity on sample expansion during combustion, in order to produce highly porous materials under microgravity conditions; and (iv) the effect of gravity on the structure formation mechanism during the combustion synthesis of poreless composite materials.

Experimental Set-Up and Procedures

Our experiments were conducted primarily in the 2.2s-Drop Tower (NASA Lewis Research Center, Cleveland, OH) providing microgravity environment ($\sim 10^{-4}$ m/s^2) during 2.2 s of drop time. Some investigations were also carried out during the parabolic flights of DC-9 aircraft, yielding $\sim 10^{-2}$g condition for about 20 s. The restrictions of weight, dimensions and safety of the experimental set-up dictated its design (**Fig.1**). The reaction chamber, battery, power distribution box, specially constructed ignition module and video camera were fit into a standard NASA rig (96x84x40 cm). A microcomputer (Tattletale) controlled and synchronized ignition, temperature measurements, gravity conditions and drop processes.

Three different easily interchangeable sample holders were used in the experiments. The first was made from two boron nitride plates, with cylindrical holes for three samples and ignition electrodes. The outer part had three slits to observe wave front propagation. The entire assembly was mounted in an aluminum cup holder and installed in such a way that one of the samples could be ignited from the bottom, the second from the side, and the third from the top. Ignition occurred when electric current was applied to a tungsten filament imbedded inside an intermediate ignition mixture. This system provides relatively fast and reliable ignition, which is important in the limited time experiments. This set up was used to study the influence of gravity on the combustion behavior and microstructure of the final product. For this, experiments were conducted in both terrestrial and microgravity conditions, with the samples located under three different angles between the combustion velocity front and gravity force vectors. Another sample holder was a vertical quartz tube placed on a boron nitride support. Ignition could be initiated from either the top or the bottom of the sample. This holder was designed for studies in which the sample expands greatly during the synthesis, to yield highly porous or foam-like materials. In addition, the effect of gravity on combustion of loose reactant mixtures was investigated using this assembly. Finally, the wedged brass block was used to perform quenching experiments to investigate the microstructure formation in microgravity conditions. Initiated from the top, the combustion wave propagates in the direction of increasing heat losses and finally stops at some critical section of the wedge. The synthesized sample was examined layer-by-layer, from its tip (initial mixture) to the top (final product), to elucidate the evolution of material structure formation during combustion synthesis.

The sample fixed in the appropriate holder was placed in the reaction chamber, which was first evacuated to about 10^{-2} atm and then filled with high purity argon to 1 atm pressure. In the case of the drop tower experiments, the rig with the experimental set-up was enclosed in a drag shield and suspended using a steel wire at the top of Drop Tower. At the operator's signal, the

wire was cut and the apparatus fell freely for a distance of 27 m, followed by deceleration at the end when reaching an air bag. The video camera was connected by optic cable with the tower video system center, which allowed us to record the combustion process during the drop. For aircraft experiments, the same set-up was installed on board DC-9 aircraft, which achieves weightlessness by flying a parabolic trajectory.

After reaction, the instantaneous and average velocities of combustion front propagation as well as rate of sample expansion were determined by analysis of the video frames. The phase composition of the product was identified by X-ray diffraction and the microstructure was analyzed using scanning electron microscopy along with energy dispersive X-ray spectrometry and advanced image analysis software.

Systems Under Investigation

The systems under study (**Table I**), were chosen to investigate different aspects of the influence of gravity on combustion synthesis process. They all have the common feature that at least one liquid phase exists in the reaction front. Owing to this feature, gravity can be expected to play a role in the mechanism of combustion and structure formation.

The first system selected (S1) is the (3Ni+Al)+(Ti+2B) mixture, where a ceramic-intermetallic composite can be produced by the reaction (ref.4):

$$3 \, Ni + Al + x \, (Ti + 2 \, B) \longrightarrow Ni_3Al + x \, TiB_2 \qquad (1)$$
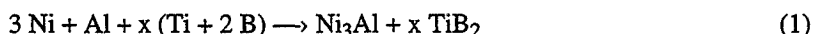
This system has a relatively high combustion velocity (~5cm/s), hence the characteristic time of combustion front propagation along the sample (length = 2.5 cm) is only ~0.5 s, which is less than the drop time (2.2 s). Thus the combustion front propagation is fully completed in microgravity conditions. Also, the combustion temperature of the investigated mixture ($x=1.95$; $T_c=1933°C$) exceeds the melting point of Ni_3Al ($1395°C$), but is lower than the melting point of TiB_2 ($2800°C$). For this reason, it is possible to investigate the role of buoyancy in the processes of nucleation and growth of TiB_2 grains in the Ni_3Al melt. It should also be noted that intermetallic matrix composites of this type exhibit superior mechanical and heat resistance properties which make them excellent candidates for high temperature applications.

Several systems have been studied (see **Table I**) in the direction of high-porous materials production in microgravity conditions. As an example, we present the results of gravity influence on CS in Ti+C+20 wt.%Ni reactant mixture. The following reaction occurs in the combustion front:

$$Ti + C + Ni \longrightarrow TiC + Ni \qquad (2)$$

The Ti powder typically contains relatively large amount of absorbed gases (mainly hydrogen); in the present experiments, we have ~0.4 mgH_2/gTi. In the combustion wave, due to the high temperature, this gas desorbs rapidly from the metal surface, resulting in sample expansion. Moreover, experiments in the normal ($g=10 \, m/s^2$) conditions show that for the Ti+C system, unconstrained samples were completely destroyed during the combustion process. In order to obtain high porous material with good mechanical properties, some excess liquid phase needs to be formed in the reaction front. The combustion temperature of Ti+C ($3200°C$) mixture is higher than melting point of Ni ($1670°C$), and for this reason we introduced some Ni powder to increase the amount of liquid phase present in the reaction zone.

The results on combustion of Ni+Al mixture are shown below as the example of gravity influence on the mechanism of combustion wave propagation in highly porous (loose powders) media. In this system, nickel aluminide is formed during the reaction in the combustion wave :

$$Ni + Al \longrightarrow NiAl \qquad (3)$$

As shown in **Table I**, various systems were also studied using the quenching technique, in order to elucidate the structure formation mechanisms. The results for the system S1 are presented here to illustrate the influence of gravity on these processes.

Some Results

All experiments were conducted under otherwise identical conditions in both normal ($g=10 \, m/s^2$) and microgravity (μG, $g=10^{-4}$ m/s^2 during free-fall and $g=10^{-1} \, m/s^2$ in parabolic flights), to make a direct comparison and to establish the effects of gravity on combustion and structure formation in the investigated systems.

Effect of Gravity on Combustion Velocity The results of combustion velocity for different systems are summarized in **Table II**. The data show that the average velocity value is somewhat larger in terrestrial conditions. More important, in all cases, the root mean square (RMS) deviations of calculated velocities, characterizing the steadiness of front propagation, are also greater in

terrestrial conditions than in microgravity. The distributions of instantaneous velocity shown in **Figure 2** illustrate this point, where a wider distribution ($\sigma=1.3$ cm/s) is observed for normal gravity as compared to microgravity ($\sigma=0.3$ cm/s). We believe that convection of inert gas, taking place in the reaction chamber during the combustion process in terrestrial conditions, leads to *instability* of combustion front propagation along the sample. These effects can be important not only for fundamentals of structure formation, but also for direct production of net-shape articles by the combustion synthesis method. Indeed, instability of combustion wave propagation usually results in undesired non-uniform properties along the surface of the produced material.

Effect of Gravity on Particle Size Growth It was observed that gravity influences not only propagation of the combustion wave, but also microstructure of the final product. The results obtained on quenched samples showed that this difference is related to the process of grain growth during CS. The characteristic dependencies of average TiB_2 particle size as a function of distance from the quenched front are shown in **Figure 3**, for normal and microgravity conditions. In both cases, very fine particles (<0.1 μm) of TiB_2 formed immediately in the reaction front. However, the rate of particle growth in μG (10^{-4} cm^2/s) condition is lower than at g=10 m^2/s. It appears that enhanced mass transfer, owing to melt convection and buoyancy in normal gravity, promotes the grain growth.

Effect of Gravity on Sample Expansion In **Table III**, data on the average measured combustion front velocity (U_c) and relative linear final expansion (l_f/l_0) for several systems are shown. For all cases, the final expansion and U_c appeared to be higher in μG than in normal gravity conditions. The dependencies of relative sample length (l/l_0) as a function of time are presented in **Figure 4**. It should be noted that in both cases, the expansion velocity (U_{ex}) remains constant as the combustion wave propagates along the sample; however, the value of U_{ex} is measurably greater under μG conditions (see also Table III). It is interesting that gravity does not influence the combustion velocity (U_c^r) measured *relative* to the unreacted part of the sample; $U_c^r=U_c-U_{ex}$. This implies that the region of sample expansion is located *behind* the combustion front (i.e. in the post-combustion zone).

Effect of Gravity on Combustion of High Porous Media To investigate the role of gravity on the mechanism of heat conduction in heterogeneous media during combustion, several systems were studied (**Table I**). We expected to find a change in the behavior of reaction front propagation due to the decrease of contact between particles in μG conditions. For this purpose, combustion of loose powder mixtures was examined. The quartz tube was half filled with reactant mixture, that was ignited from the bottom. The data obtained during combustion of loose ($\varepsilon_0=0.8$) Ni+Al mixture are shown in **Figure 5**. In terrestrial conditions, the combustion front propagates relatively steady, with an average velocity 1.6 cm/s. To describe the results obtained in μG, note that only a part of the sample was reacted at g=10^{-4} m/s^2, and in this case ignition and drop were done simultaneously. The average front velocity in μG was about 5 cm/s. This dramatic change in combustion velocity may be explained by a change in the primary mechanism of heat transfer in the reaction medium. Other experiments, with the quartz tube filled with the reaction mixture to different extents, showed that for a completely filled tube, the above mentioned effect does not occur. It is worth noting that even after impact, the velocity for the Drop Tower experiments was larger than for experiments conducted fully under normal gravity. This effect arises due to consolidation of the unreacted part of the mixture upon deceleration when reaching the air bag.

Acknowledgments

References

1. Odawara O., Mori K., Tanji A., and Yoda S., "Thermite Reaction in a Short Microgravity Environment", *J. Mater. Syn. Proc.*, 1, 203 (1993).
2. Hunter K.R., and Moore J.J., "The Effect of Gravity on the Combustion Synthesis of Ceramic and Ceramic-Metal Composites", *J. Mater. Syn. Proc.*, 2, 355 (1994).
3. Moore J.J., Readey D.W., Feng H.J., Monroe K., and Mishra B., "The Combustion Synthesis of Advanced Materials", *JOM*, November, 72 (1994).
4. Yi, H.-C., Varma, A., Rogachev, A.S., and McGinn, P.J., "Gravity-induced Microstructural Non-uniformities during Combustion Synthesis of Intermetallic-ceramic Composite Materials," *Ind. Eng. Chem. Res.*, 35, 2982 (1996).

Table I. Systems Under Investigation

Experimental Conditions	System	Comments
3-Sample set-up; initial sample porosity = 0.4	S1: 60 wt.%(3Ni+Al)+ 40wt.%(Ti+2B) 90wt.% S1+10wt.% W	U=U(angle); grain size and phase distribution in product; CS of poreless materials
Quartz tube; initial sample porosity = 0.4-0.5	Ti+0.8C Ti+0.8C+15wt.%Ni Ti+C+20%wt.Ni	sample expansion; synthesis of foam materials
Quartz tube; loose powders	Ni+Al Cladded Ni-Al particles	instantaneous velocity distribution; heat conduction mechanism
Wedged brass block; initial sample porosity = 0.3-0.4	S1; 90wt.% S1+10wt.% W Ni+Al Cladded Ni-Al particles	quenched front; mechanistic study

Table II. Characteristic Velocity of Combustion Wave Propagation in Different Gravity Conditions

System	Gravity Condition, m/s^2	Average Velocity, cm/s	RMS Deviation
(3Ni+Al)+(Ti+2B)	10	6.5	1.1
	10^{-1}	4.1	0.6
(3Ni+Al)+(Ti+2B)+W	10	8.3	1.4
	10^{-4}	7.6	0.8
(Ni+Al)+5wt% (Ti+2B)	10	15.2	0.4
	10^{-1}	14.3	0.2
(Ni+Al)+20wt% (Ti+2B)	10	3.7	1.0
	10^{-1}	3.3	0.8

Table III. Average Front Velocities and Expansion of Samples Reacted in Different Gravity Conditions

System	Gravity Conditions, m/s^2	Combustion Velocity, U_c cm/s	Expansion Velocity, U_{ex} cm/s	$U_c^r = U_c - U_{ex}$ cm/s	Final Relative Expansion, l_f/l_o
Ti+0.8C	10	1.0	0.7	0.3	3.4
	10^{-4}	1.25	0.95	0.3	4.5
Ti+C+Ni	10	3.7	2.3	1.4	2.7
	10^{-4}	4.7	3.2	1.5	3.7
Ti+C+Ni+Mo	10	8.0	3.0	5.0	1.6
	10^{-1}	14.0	9.5	4.5	3.1

34
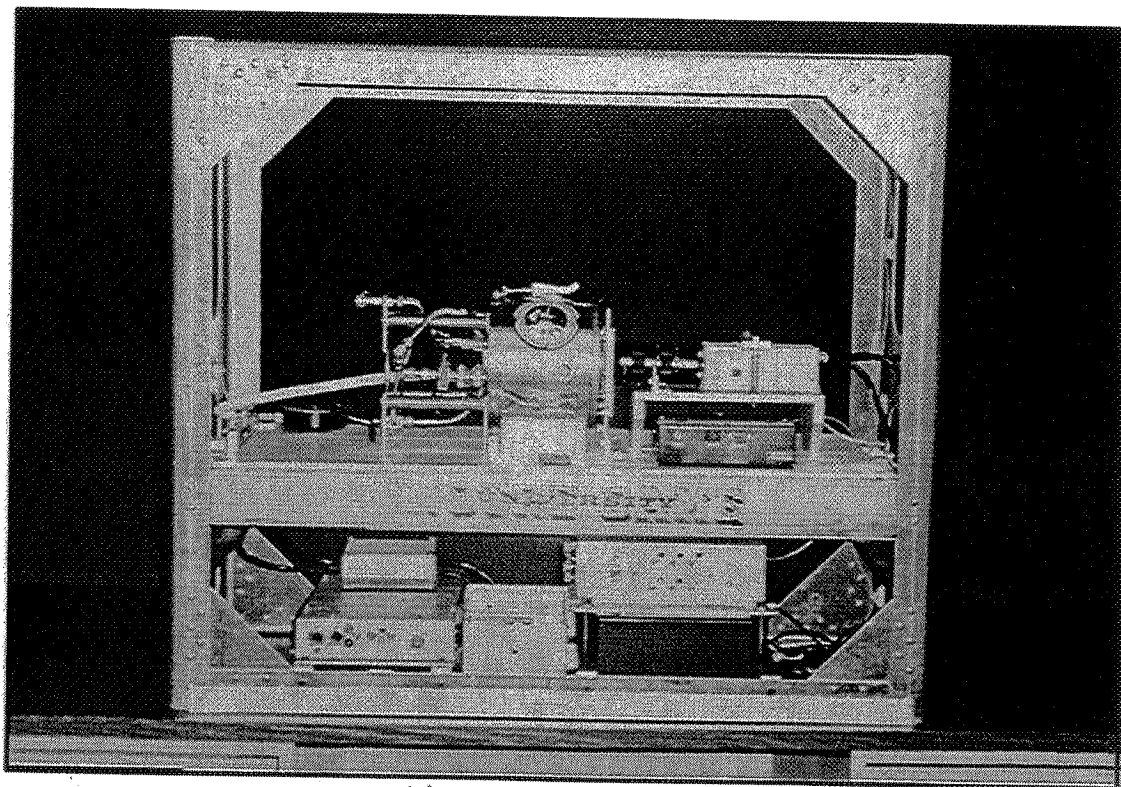
Figure 1. The experimental set-up
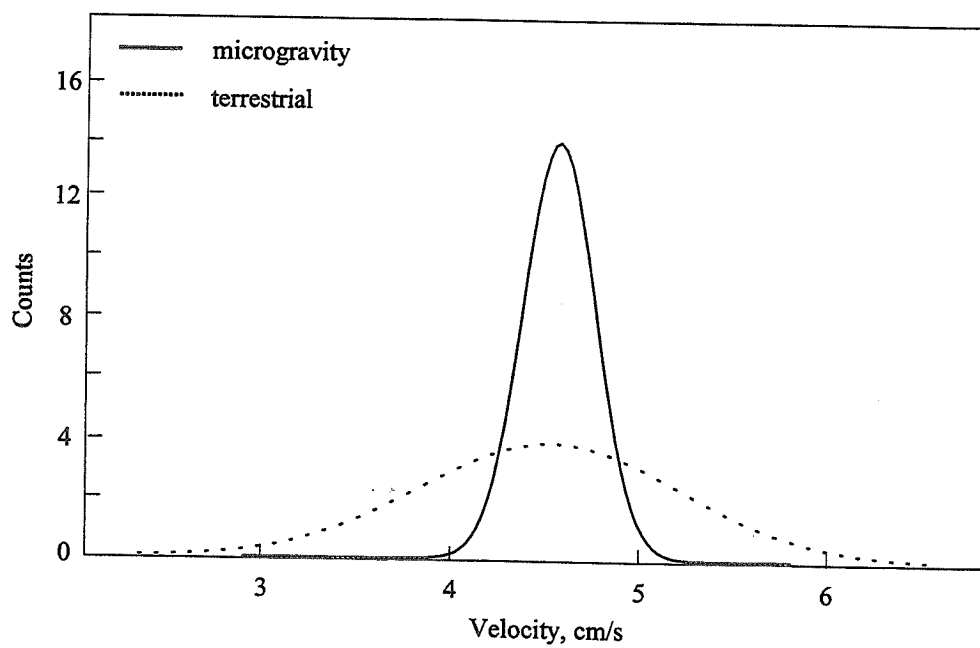

Figure 2. Distribution of instantaneous combustion front velocities in (3Ni+Al)+(Ti+2B) system

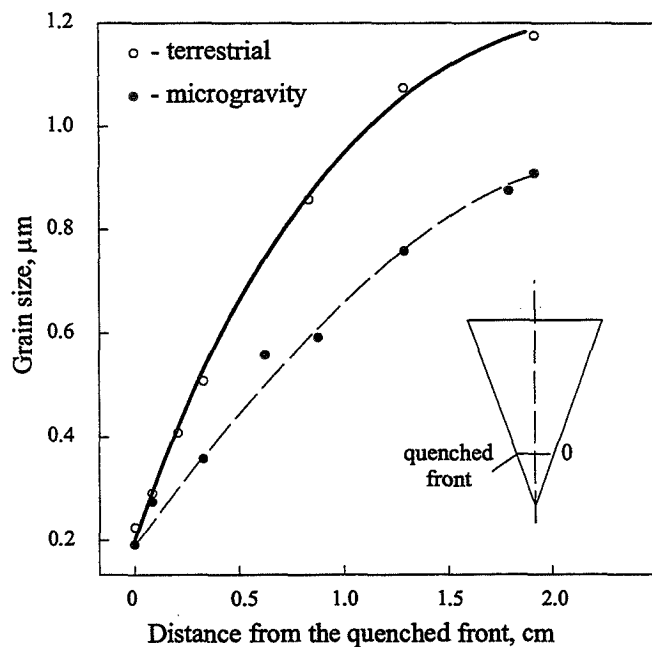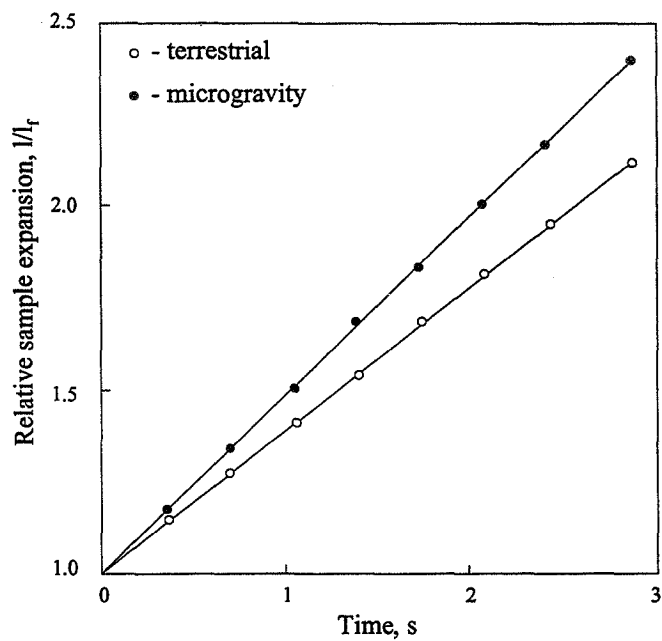Figure 3. Evolution of TiB$_2$ grain size in (3Ni+Al)+(Ti+2B) quenched sample

Figure 4. Relative linear sample expansion as a function of time during combustion of Ti+C+Ni system
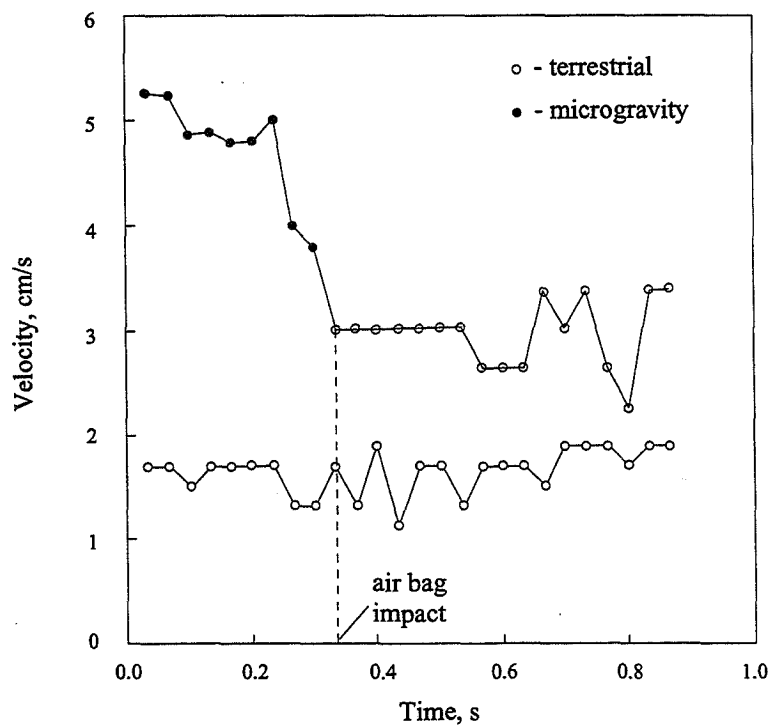

Figure 5. Instantaneous combustion velocity in (Ni+Al) system

GAS-PHASE COMBUSTION SYNTHESIS
OF METAL AND CERAMIC NANOPARTICLES*

R. L. AXELBAUM
Washington University
St. Louis, Missouri

and

B.H. Chao
University of Hawaii
Honolulu, Hawaii

Introduction

Gas-phase combustion (flame) synthesis has been an essential industrial process for producing large quantities of powder materials such as carbon black, titanium dioxide, and silicon dioxide. Flames typically produce simple oxides, with carbon black being the noted exception because the oxides of carbon are gaseous and are easily separated from the particulate matter that is formed during fuel pyrolysis. The powders produced in flames are usually agglomerated, nanometer-sized particles (nanoparticles). This is an acceptable composition and morphology for many applications. However, recently there has been interest in flames for the synthesis of metal and non-oxide ceramic *unagglomerated* nanoparticles (2 to 100 nm) for advanced materials applications. For these applications nano-powders are consolidated into bulk materials under high temperature and pressure, yielding a solid part whose grains retain the nanometer size of the starting powder. The final nanostructured materials often possess unique mechanical, electrical or magnetic properties compared to their coarse-grained counterparts. The economics of powder processing can also be enhanced with nano-powders vis-a-vis low temperature consolidation and superplastic forming.

One of the first known applications of flames for less traditional synthesis was by Lamprey and Ripley (ref. 1) where tungsten and molybdenum were synthesized by hydrogen reduction of tungsten and molybdenum chlorides. More recently Calcote and Felder (ref. 2), Glassman et al. (ref. 3) and Axelbaum et al. (ref. 4,5,6) have employed sodium/halide chemistry to produce metals and non-oxide ceramics. The list of materials that have been produced in these flames includes Si (ref. 2), TiN, TiB_2, TiC, $TiSi_2$, SiC, B_4C (ref. 3) Al, W, Ti, TiB_2, AlN, and W-Ti and Al-AlN composites (refs. 4,5,6). Many of the most important advanced materials can be produced from sodium/halide flames.

As emphasized by Zachariah in the 2nd Microgravity Workshop (ref.7) and Brezinsky in ref. 8, the main challenge that faces application of flame synthesis for advanced materials is overcoming formation of agglomerates in flames. Figure 1a illustrates the steps leading to agglomeration in a typical aerosol process. The high temperatures and high number densities in the flame environment favor the formation of agglomerates. Agglomerates must be avoided when the powders are to be consolidated because of their deleterious effect on compaction density, which leads to voids in the final part. Efforts to avoid agglomeration in flames without substantial reductions in number density (e.g. low pressure or extreme dilution), and therefore production rate, have had limited success (ref. 8,9).

Other challenges in flame synthesis processing include ensuring that the powders are high purity and that the process is scaleable. Though the containerless, high temperature environment of a flame is excellent for producing high-purity simple compounds, ultrafine metals and non-oxide ceramic powders are inherently reactive in the presence of oxygen and/or moisture. Thus the handling of these powders after synthesis poses a unique problem. Impurities acquired during handling of nanoparticles have plagued the advancement of nanostructured materials technology.

One promising approach that addresses these problems is nano-encapsulation, as schematically depicted in Fig. 1b. In this approach the *core* particles are encapsulated in a removable material while they are within the flame but before excessive agglomeration has occurred. The onset of condensation of the encapsulation material is dependent on temperature, concentration of the condensable material, and particle size. Condensation can be very rapid so that core particles are trapped within the condensed material and are subsequently protected from agglomeration. Figure 2 shows transmission electron microscope (TEM) micrographs of titanium (Fig. 2a,b) and aluminum nitride (Fig. 2c) powders produced using the nano-encapsulation process in sodium/halide flames. The NaCl by-product, the lighter material in these micrographs, acted as the encapsulation material. These results demonstrate the effectiveness of nano-encapsulation. Also, as can be seen from Figs. 2a and b, the size of the core particles can be varied by controlling process conditions.

An additional advantage of nano-encapsulation is realized when the powders are handled during post-production processing. Results have shown that when the powders are exposed to atmosphere the core particles are protected from oxidation and/or hydrolysis. Thus, handling of the powders does not require extreme care and if at the time of consolidation the encapsulation material is removed, either by washing or vacuum annealing, the resulting powders are unagglomerated and low in impurities.

An example of the relevant sodium/halide chemistry for the formation of titanium metal is

$$TiCl_4 + 4Na \rightarrow Ti + 4NaCl \tag{1}$$

To maximize yield and minimize impurities it is essential that there be sufficient sodium to fully reduce the halides. This suggests that the preferred flame configuration is one in which the halides are injected into a reducing atmosphere of sodium vapor. From this perspective the process is very similar to the Chloride process for producing TiO_2 wherein $TiCl_4$ is injected into an oxidizing atmosphere (ref. 10). When possible, halides can be introduced in the vapor phase but since many halides have high boiling points it may be desirable to employ spray combustion techniques. Consequently, sodium/halide flames share many global features of hydrocarbon flames and droplet combustion, and the experimental approaches that are being employed to study hydrocarbon combustion can be quite relevant to studying sodium/halide flames.

Despite their similarities with hydrocarbon flames, flame synthesis processes - both the sodium/halide flame and others - have many unique features. First, the reactants employed are often hypergolic and thus the flame must be nonpremixed. This dramatically limits the types of experiments that can be performed to understand chemistry. Second, the objective of the flame is not to produce heat but rather a material with a specific composition. Flame structure and particle history can have a significant impact on the composition of the final product and, thus, it is necessary to understand how flame conditions can be tailored to obtain a desired product. Third, the inlet temperatures and concentrations of the reactants are not dictated as they tend to be in hydrocarbon combustion, so there is a degree of freedom to control flame structure that is not available in traditional combustion. Fourth, the product produced at the flame front is a condensed phase. With the transformation from gaseous reactants to condensed-phase products comes a reduction in pressure and, thus, the flame front can act as a hydrodynamic sink. Furthermore, as with soot formation in hydrocarbon droplet burning, we expect a particle shell to form around the droplet. These phenomena will affect droplet burning, the flow field, and particle evolution, and, thus, the resulting product.

Objectives
The objective of this program is to gain a greater understanding of flame synthesis processes in order to control particle morphology and composition. Emphasis will be placed on the sodium/halide flame with nano-encapsulation but the fundamental understanding gained will be relevant to other flame processes as well. Since the final composition and morphology are dependent on the evolution of the aerosol and this evolution is intimately related to the flow field, microgravity affords a means of attaining a controlled investigation of many of the unique features of flame synthesis processes. The requirement that the flames be nonpremixed and the ability to produce purely one-dimensional diffusion flames with long residence times in microgravity affords a unique opportunity to understand flame synthesis. Furthermore, with a non-buoyant, spherically symmetric flame the effects of the particle shell and the hydrodynamic sink created by condensation at the reaction front can be studied to understand their effects on droplet burning.

Another unique aspect of flame synthesis that will be studied can be illustrated by consider the example of combustion of a mixture of titanium tetrachloride and aluminum trichloride with sodium. The global reaction is

$$TiCl_4 + AlCl_3 + 7Na \rightarrow TiAl + 7NaCl . \tag{2}$$
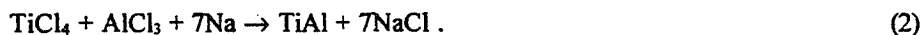
Presuming the halides are supplied in the vapor phase the stoichiometry will be largely preserved and the final product will be titanium aluminide. However, if the metal halides are supplied in the liquid phase through, e.g., spray combustion, the different volatilities of the halides can lead to a varying product throughout the droplet lifetime. This is not inherently a problem and, in fact, may be desirable for the synthesis of composite materials. Thus, the ability to control composition through reactant volatility will be explored.

This program will involve microgravity porous sphere/cylinder experiments. Thermocouple measurements and thermophoretic particle sampling will be employed to characterize the flame environment and particle history, respectively.

The combustion process and aerosol dynamics will be modeled as well. Only limited kinetic data are available (ref. 11) but fortunately the chemistry is sufficiently fast that the flame is diffusion limited and the flame location and nucleation rate can be reasonably predicted without accurate chemistry. The aerosol dynamics will be modeled with a novel multicomponent Monte Carlo scheme. The justification for such a technique and initial results will be discussed below.

Experimental Apparatus

Figure 3 is a schematic diagram of the high temperature reactor chamber that is under construction for the microgravity porous sphere experiments. The halide will be supplied through a porous sphere or cylinder into an atmosphere of sodium vapor. An inert or reactive gas (e.g. ammonia) will be mixed with the sodium. Maintaining a sufficient sodium vapor pressure will require reactor temperatures of 500 to 700 °C (T_{sat} = 883 °C). Thus, special precautions were necessary in the reactor design particularly with regards to the windows and probe system because the reactor will contain a high temperature, condensable atmosphere. One access port will be used for both the window and probe systems. The access port will be shuttered so that the cold window or probe system will only be exposed to the reactor atmosphere when needed. Sodium/halide reactions are hypergolic, which precludes the need for an ignition source yet requires a special procedure for introducing the halide. To accomplish this an inert will be fed through the porous sphere/cylinder before introducing the halides and when the system is stable the flow of inert will be discontinued and replaced with halide. Precautions are also required for TEM grid sampling because the ultrafine powders can react when exposed to atmosphere following sampling. To avoid this the probe system which contains the TEM grid will be isolated with a vacuum valve after the grid has been inserted into the flame and retracted back into the probe system housing.

Modeling

Modeling aerosol dynamics such as that represented in Fig. 1b, where core particles are encapsulated following the rapid condensation of a second component, requires that a multicomponent aerosol model be developed. The objective is to predict both the final particle size and the size of the core particles under conditions of simultaneous coagulation and condensation. The sectional method is an established technique for modeling coagulation alone and some efforts have been made to extend this technique to allow for condensation. However, the sectional method when applied to condensation suffers from numerical diffusion because condensed mass is distributed over the entire section. Efforts to avoid numerical diffusion have required hybrid schemes that couple moving sections (which address condensation) with stationary sections (which address coagulation). There are severe limitations and restrictions to such a method and the need arises for an alternative, more robust approach to modeling aerosol processes with simultaneous nucleation, coagulation and condensation. To this end, a Monte Carlo scheme is being developed which affords a statistical treatment of coagulation coupled with a deterministic treatment of nucleation and condensation. Numerical diffusion is avoided because the model keeps track of the distribution of condensed mass in any section.

The approach treats coagulation as a Markov process wherein the probability of each subsequent event is not influenced by prior events. For a given size distribution the probability of collision is determined for a discrete size interval (section) and the Monte Carlo method is used to statistically solve for the evolution due to collisions. Condensation and nucleation, on the other hand are solved classically by integrating condensation rate and nucleation rate equations and are coupled to the Monte Carlo scheme by calculating the time between collision events.

The results to-date of this modeling effort are summarized below. Coagulation results were verified by comparing to the Smulochowski solution as well as published numerical and experimental results. Figure 4 shows the evolution of aerosols with three different initially size distributions but the same aerosol mass. The mass is comparable to experimental conditions encountered during flame synthesis. These results show the well established fact that regardless of initial size distribution the aerosol quickly evolves to a log normal size distribution with a geometric standard deviation approaching 1.4.

Factors that can affect numerical accuracy of this model are the number and distribution of sections, a scale factor which defines the number of parcels that are used to represent the aerosol, and the time step for upgrading the size distribution. In Fig. 5 the sections are distributed logarithmically and the number of sections per decade is varied. With greater than 18 sections per division the results are seen to be independent of number of sections. A parcel represents an ensemble of like particles chosen to minimize computational time while providing sufficient statistics to ensure accuracy of the Monte Carlo scheme. The number of parcels decreases due to coagulation and to maintain satisfactory statistics the code allows the number of parcels to decrease by one order of magnitude and then rescales the system to the original number of parcels. The effect of parcel size is shown in Fig. 6 and it is clear that from 10^5 to 10^6 parcels is sufficient to maintain accuracy.

Figures 7 an 8 show results were condensation was added to the model. Figure 7 is for the case of pure condensation of NaCl onto the tail of an existing aerosol distribution when coagulation and the Kelvin effect are not included. The saturation ratio and temperature have been chosen to yield a critical radius for condensation r* (ref. 12) of 6 nm. As expected for condensation in the free molecular regime the growth is proportional to time. These results show that numerical diffusion has not occurred with this model. The results in Fig. 8 where coagulation and the Kelvin effect are included in the model, show that there is still a discontinuity at r* but coagulation and the Kelvin effect smooth the transition. Fig. 8b shows the mass fraction of NaCl as a function of particle size. Again, no NaCl is found on particles smaller than r* but the mass fraction grows rapidly for R > r* and tapers off for larger particles.

The Monte Carlo approach to modeling multicomponent aerosol processes is proving to be well suited for the needs of this program. After further validation of the scheme the code will be employed to study the full aerosol process in a uniform system as depicted in Fig. 1b including nucleation of the primary particles, coagulation, condensation of a second phase, particle heating and heat loss. After the aerosol process is sufficiently understood for a uniform system, a one-dimensional flame model will be developed and the Monte Carlo scheme will be incorporated into the model, allowing for comparison with the microgravity experiments.

References
1. Lamprey, H. and Ripley, R.L., *Journal of The Electrochemical Society.* 109:8:713-715 (1962).
2. Calcote, H.F. and Felder, W. *Twenty-Fourth Symposium (International) on Combustion*, The Combustion Institute, pp.1869-1876 (1993).
3. Glassman, I., Davis, K.A. and Brezinsky, K. *Twenty-Fourth Symposium (International) on Combustion*, The Combustion Institute, pp. 1-14. (1993).
4. DuFaux, D.P. and Axelbaum, R.L. *Combustion and Flame.* 100:350-358 (1995).
5. Axelbaum, R.L., Huertas, J.I., Lottes, C.R., Hariprasad, S. and Sastry, S.M.L., *Materials and Manufacturing Processes*, 11(6): 1043-1053 (1996).
6. Axelbaum, R.L., Lottes, C.R., Huertas, J.I and Rosen L.J. To appear in *Twenty-Fifth Symposium (International) on Combustion.* (1997).
7. Zachariah, M.R. "Principles of Gas Phase Processing of Ceramics During Combustion," In Proceedings of the Second International Microgravity Combustion Workshop, Cleveland, Sept. 15-17, 1992.
8. Brezinsky, K. To appear in *Twenty-Fifth Symposium (International) on Combustion.* (1997).
9. Axelbaum, R.L., DuFaux, D.P., Frey, C.A., Kelton, K.F., Lawton, S.A., Rosen, L.J. and Sastry, S.M.L., *J. Materials Research*, 11(4) 948-954. (1996).
10. Ulrich, G.D., *Chemical and Engineering News*, 62(32): 22-29 (1984)
11. Heller, W. and Polanyi, M. *Faraday Society Transactions*, 47: 84 (1936).
12. Seinfeld, J.H. *Atmospheric Chemistry and Physics of Air Pollution.* John Wiley & Sons. New York. (1986).

Typical aerosol process
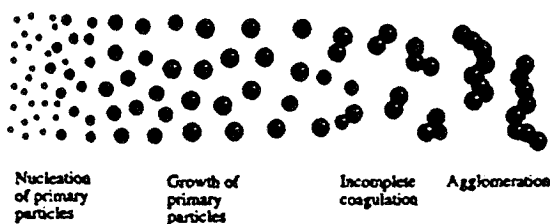
Encapsulation of primary particles

| Nucleation of primary particles | Growth of primary particles | Incomplete coagulation | Agglomeration |

(a)

| Nucleation of primary particles | Growth of primary particles | Coating of primary particles | Agglomeration of coated particles and growth of coating |
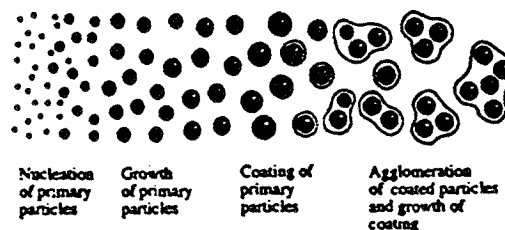
(b)

Figure 1. Schematic diagram of (a) typical aerosol process and (b) aerosol processes with nano-encapsualtion.

(a)   (b)
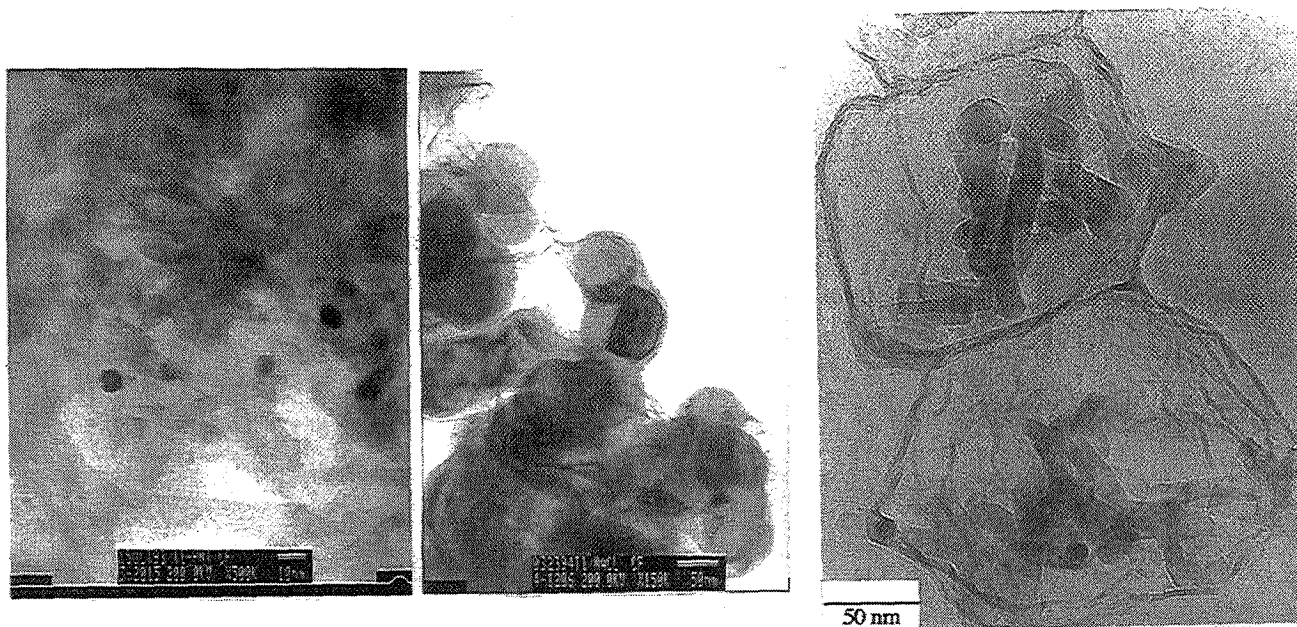
Figure 2. Transmission electron micrographs of particles produced by nano-encapsulation in sodium/halide flames (a) and (b) titanium particles encapsualted in NaCl and (c) aluminum nitride particles encapsualted in NaCl. The lighter material is NaCl. Ti particle size in (a) and (b) was varied by altering flame temperatures and concentrations.
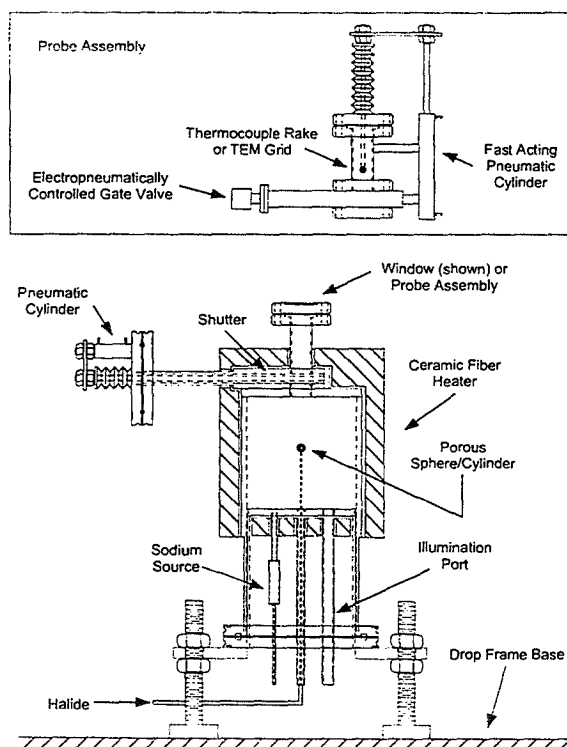
Figure 3. Schematic diagram of high-temperature microgravity combustion chamber.
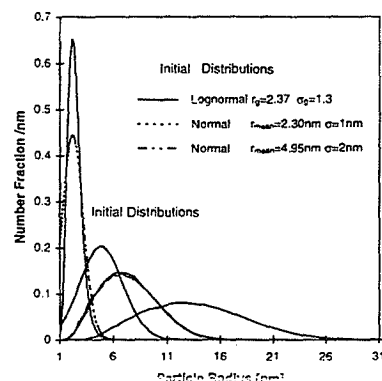
Figure 4. Evolution of particle size distribution for coagulating aerosols with three different initial size distributions.
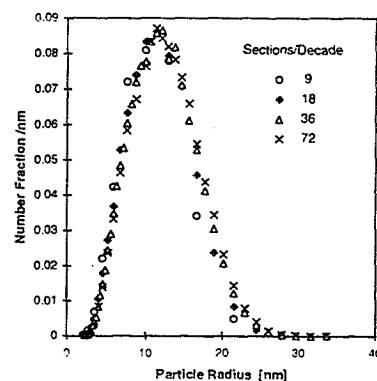
Figure 5. Effect of number of sections on particle size distribution of a coagulating aerosol.

41
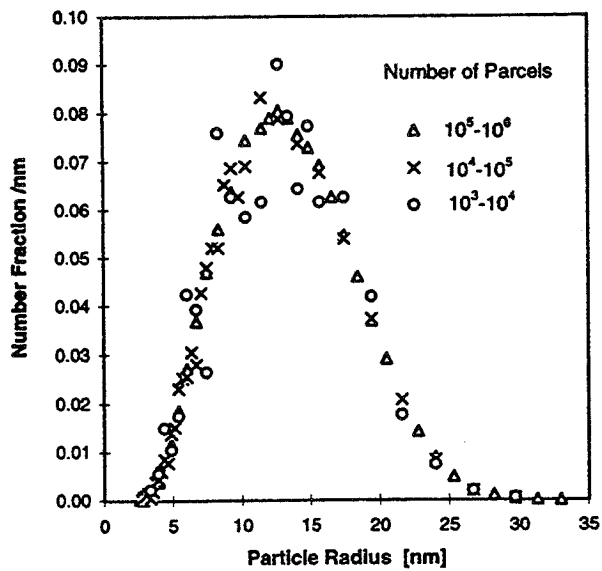
Figure 6. Effect of number of parcels on particle size distribution of a coagulating aerosol.
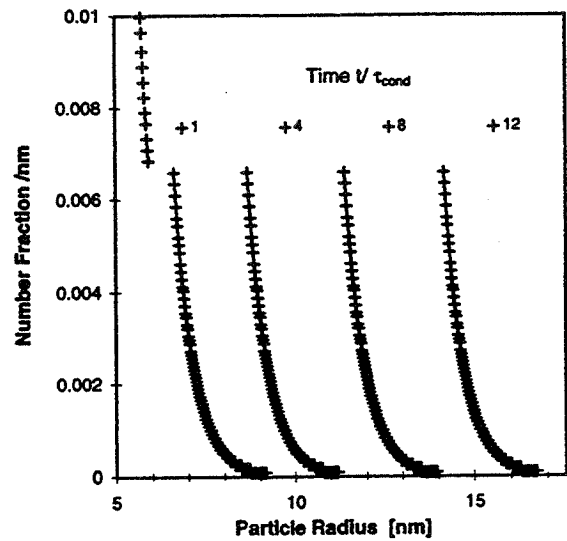
Figure 7. Evolution of particle size distribution for a non-coagulating aerosol experiencing condensation with r* = 6 nm. The Kelvin effect has not been included.
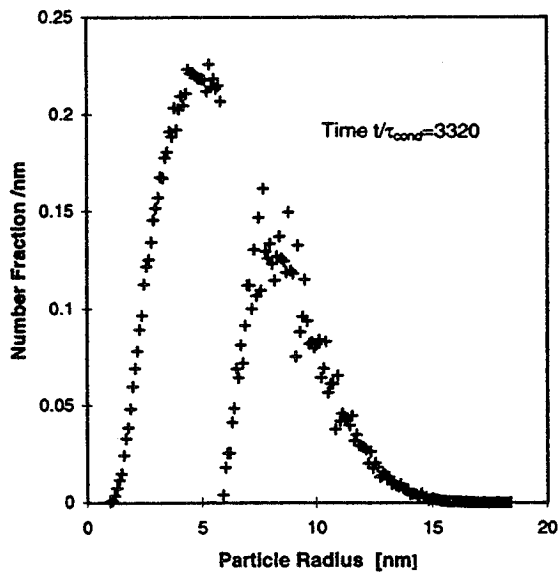
(a)
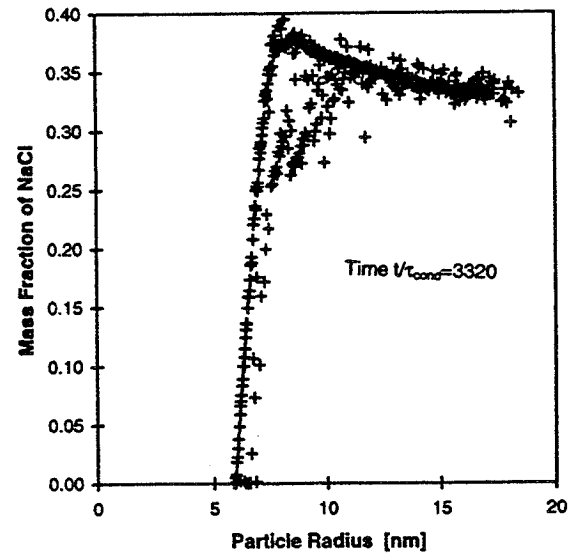
(b)

Figure 8. (a) Particle size distribution and (b) mass fraction of condensate for a coagulating aerosol experiencing condensation with r* = 6 nm, including the Kelvin effect.

42

THE EFFECT OF GRAVITY ON THE COMBUSTION OF BULK METALS*

MELVYN C. BRANCH, Angel Abbud-Madrid, and John W. Daily
Center for Combustion Research
Mechanical Engineering Department
University of Colorado at Boulder
Boulder, CO 80309-0427

Introduction

In recent years, metal combustion studies at the University of Colorado have focused on the effects of gravity (g) on the ignition and burning behavior of bulk metals. The impetus behind this effort is the understanding of the ignition conditions and flammability properties of structural metals found in oxygen (O_2) systems for space applications. Since spacecraft are subjected to higher-than-1 g loads during launch and reentry and to a zero-gravity environment while in orbit, the study of ignition and combustion of bulk metals at different gravitational accelerations is of great practical concern. From the scientific standpoint, studies conducted under low gravity conditions provide simplified boundary conditions, since buoyancy is removed, and make possible the identification of fundamental ignition and combustion mechanisms.

The influence of microgravity on the burning of bulk metals has been investigated by Steinberg et al. [1] in a drop tower simulator. All metals and alloys tested supported combustion in the absence of gravity. In general, the study found that in microgravity the upward regression rate of the melting surface of a metal rod is significantly faster than in normal gravity. Several theoretical models of bulk metal combustion [2-4] have suggested that gravity may play an important role in heat and mass transport processes that dominate metal-oxygen reactions. The possible significance of convection on mass transfer rates and on the outward transport of condensed oxides in vapor-phase metal diffusion flames was first mentioned by Brzustowski and Glassman [5].

This investigation is intended to provide experimental verification of the influence of natural convection on the burning behavior of metals. In addition, the study offers the first findings of the influence of gravity on ignition of bulk metals and on the combustion mechanism and structure of metal-oxygen, vapor-phase diffusion flames in a buoyancy-free environment. Titanium (Ti) and magnesium (Mg) metals were chosen because of their importance as elements of structural materials and their simple chemical composition—pure metals instead of multicomponent alloys to simplify chemical and spectroscopic analyses. In addition, these elements present the two different combustion modes observed in metals: heterogeneous or surface burning (for Ti) and homogeneous or gas-phase reaction (for Mg). Finally, Mg, Ti, and their oxides exhibit a wide range of thermophysical and chemical properties. Metal surface temperature profiles, critical and ignition temperatures, propagation rates, burning times, and spectroscopic measurements are obtained under normal and reduced gravity. Visual evidence of all phenomena is provided by high-speed photography.

Experimental System and Procedures

A schematic of the experimental system used is shown in Fig. 1. The ignition source consists of a 1000-W xenon lamp that generates a highly collimated beam (4° half angle) with broadband radiation (300-1100 nm). An aspheric lens focuses the beam to provide a 2-MW/m^2 power density on the top surface of a 4-mm-diameter and 4-mm-high metal specimen that sits on an alumina holder. An electric shutter permits effective control of heating time. A 4.5-L, stainless steel, cylindrical combustion vessel houses the lens, metal specimen, and alumina holder. Optical access for the movie camera and spectrograph is provided through two fused-silica side windows, while a third window is used for sample replacement. Ti and Mg metal specimens (99.95% purity) are placed in an O_2 environment (99.6% min.) at an absolute pressure of 1 atm. Evacuation and filling of the vessel is accomplished with a series of computer-controlled solenoid valves. The chamber pressure is monitored with a solid-state piezoresistive transducer. The surface temperature is measured with a 0.125-mm diameter, Type R thermocouple attached to the outer wall of the sample. A second thermocouple is sometimes used in different locations to measure temperature gradients within the sample.

43

A high-speed, 16-mm movie camera provides surface and flame visualization; the images are also used for measurement of propagation rates. With a 7.5° shutter and speeds up to 500 frames/s, exposure times as short as 1/20,000 s are obtained. A 50-mm lens and various extension tubes are used for image magnification. In addition to visible light imaging, time- and space-resolved spectral information on gas-phase reactants and products is obtained with an imaging spectrograph and a 1024-element diode array detector. Various spectral ranges are covered with two motorized gratings (300 and 2400 grooves/mm). The output signal from the detector is processed by an external controller that delivers a 15-bit dynamic range and a 150-Hz readout rate with direct memory access.

The experiment is controlled entirely by a computer, a digital/analog data acquisition board, and an interface code written in graphical programming software (LabVIEW®). In a typical run, the complete sample assembly (clean metal specimen mounted in alumina holder with attached thermocouple) is introduced into the chamber. Five evacuation and filling cycles are executed to provide a pure-O_2 atmosphere inside the vessel. The lamp is adjusted to the desired output power and the computer signals the shutter to open when the target gravity level (measured from a three-axis accelerometer located near the chamber) is achieved. Data acquisition starts (with 1-ms resolution), and the signal from the thermocouple is used to trigger all events. Immediately after ignition, the shutter is closed to remove all external heating to the sample. Temperature, pressure, energy input, gravity level, high-speed photography, and emission spectra are acquired throughout the experiment. After complete combustion, the burned or quenched samples are stored for chemical composition studies.

The low-gravity experiments were conducted onboard the NASA-Lewis DC-9 Research Aircraft in Cleveland, Ohio. Up to 20 s of reduced gravity (±0.01 g) were available in a single parabolic maneuver. A minimum of ten tests were conducted for each metal and gravity level to ensure experimental repeatability.

Results and Discussion

Heating and Ignition Behavior
For both metals under normal and low gravity conditions, higher critical temperatures (T_{crit})—the temperature at which the heat generated by oxidation first overcomes heat losses, leading to ignition—are obtained (around 1750 K for Ti and 1050 K for Mg), as compared to the values reported in the literature [6,7]; more than 200 K above the highest measured temperatures for these bulk metals. The disparity stems from the high heating rates applied in this investigation (above 100 K/s in the early stages), which are required for fast ignition during the low gravity time available in the aircraft; these rates exceed by two orders of magnitude the linear heating rates used for near-isothermal studies. The high heating rate applied to the top surface of the metal creates a significant temperature difference within the specimen (around 40 K in Mg and 150 K in Ti). In addition, the surrounding gas and vessel walls remain at a temperature close to ambient during the fast heating phase. The large increase in internal heat conduction and radiation heat losses are then responsible for the high T_{crit}.

The apparent lack of influence of gravity found on the T_{crit} measurements (and consequently on ignition temperatures) is also due to the high value of conduction (for Mg) and radiation (for Ti) heat losses versus natural convection heat loss present at these temperatures. A general theoretical model was developed to calculate the effect of low gravity on T_{crit} for a metal sample subjected to conduction, convection and radiation heat losses, as well as heat generation by oxidation [8]. For our experimental conditions, the model shows a reduction of around 10 K on T_{crit} at low g, a small value that is within experimental uncertainty.

Combustion Behavior
a) Titanium
After ignition at a point on the top rim of the sample, a molten mass consisting of a mixture of metal and oxides starts traveling across the upper surface of the specimen. As seen in Fig. 2, under normal or reduced gravity conditions, steady downward propagation of a spherical mass follows in a smooth, nonexplosive fashion until reaching the alumina base. Figure 3 shows a graph of the vertical distance traveled by the molten surface as a function of time for both samples pictured in Fig. 2. The propagation velocities inferred from the slope of the fitted lines are 16.2 mm/s and 8.7 mm/s under normal and low gravity, respectively. Similar velocities were obtained for all the samples tested (with standard deviations of 0.6 mm/s and 0.3 mm/s for the 1-g and the low-g cases). Evaluating the ratio of propagation velocities at normal (V_n) and low (V_l) gravity gives a value of 1.86. A steady regression behavior during this period at 1 g suggests that the propagation velocity has not been altered by the influence of the gravity force on the molten mass—as confirmed by its spherical shape in Fig. 2a. Furthermore, a calculation of the Bond number (Bo = gravitational force/surface tension force) under these conditions results in values below 0.1. Acceleration can occur by lateral dripping when the gravitational force overcomes the surface tension force holding the molten mass together ($Bo > 1$).

44

Following a theoretical approach similar to the one used for gaseous flame propagation, several studies [3,4] have obtained an expression of the form $V \sim (w)^{1/2}$ to calculate the propagation velocity V along metal cylinders undergoing heterogeneous surface burning with a rate of reaction w. Considering the diffusion and convection of O_2 to the sample as the rate-limiting step, the reaction rate becomes proportional to $w \sim (Gr)^{1/4}$, where Gr is the Grashof number. The propagation velocity then depends on Gr as $V \sim (Gr)^{1/8}$, so that $V \sim (g)^{1/8}$. Evaluating V_n/V_l for the normal (1 g) and low gravity (0.01 g) cases, a theoretical ratio of 1.78 is obtained. The close agreement between experimental (1.86) and theoretical (1.78) ratios of propagation velocities indicates the importance of the influence of natural convection-enhanced oxygen transport on combustion rates.

Upon reaching the end of steady-state propagation, the spherical molten mass is destroyed by the liquid-solid interfacial force as it touches the alumina holder. Once in the alumina base, Ti exhibits a more vigorous reaction with random outward expelling of small particles (possibly undergoing gas-phase reactions) and multiple fragmentation [8].

b) Magnesium
Following the first flash generated by the Mg-O_2 vapor-phase homogeneous reaction, an ignition wave runs through the sample driven by the difference between the flame temperature (near 3430 K, the vaporization-decomposition point of MgO [9]) and the temperature of the unreacted metal, which is near the Mg boiling point (1366 K). The average ignition wave speeds measured for the normal (V_n) and low (V_l) gravity cases are 220 mm/s and 115 mm/s, respectively. If the approximation used to compare propagating velocities in Ti rods is used to evaluate the V_n/V_l ratio of ignition wave speeds of Mg (similarly assuming a diffusion/convection controlled reaction rate), close agreement is again found between the experimental (1.91) and the theoretical (1.78) values. Owing to the irregularly shaped, porous, solid oxide layer surrounding the sample—a consequence of metal melting before ignition—no attempt was made to calculate surface regression rates. Instead, an evaluation of burning times and a qualitative discussion of important phenomena is given.

From the visible images and emission spectra measurements, the structure of the luminous flame that engulfs the sample after the passage of the ignition wave is in general agreement with the extended reaction zone model of Glassman et al. [2]. As seen in Fig. 4, an inner region of Mg-O_2 vapor-phase reaction is followed by MgO condensation; the solid MgO particles eventually pile up in the bright white flame front observed in the photographs. However, a thin green emission band and a wider outer diffuse blue zone (beyond the white region) are visible in addition to the prescribed features from the model. This radiation may come from Rayleigh scattering of fine oxide particles that escape the pile-up region, from excited metal vapor created by oxide dissociation in the high-temperature front, and possibly by Mg-O_2 heterogeneous reactions occurring in the oxide surface in a lower temperature region [10].

The spectroscopic measurements show similar behavior in the normal and low gravity cases. The familiar UV and green systems of MgO and Mg appear as the major radiation contributors. However, an interesting feature was captured by time-resolved spectroscopic measurements during the ignition wave propagation. Figure 5 shows the time sequence of spectra for the 285.21-nm Mg spectral line, as well as the UV and green systems of Mg and MgO, from the onset of ignition to fully developed combustion in a low gravity experiment. The lower propagation velocity of the ignition wave and the longer burning time experienced by Mg samples in reduced gravity (in combination with fast emission spectroscopy and high-speed photography) allows for a more detailed study of the Mg-O_2 flame structure and combustion mechanism. The UV bands of MgO and the UV Mg triplet appear in emission during the early stages of the ignition process, followed by an absorption and emission equilibrium towards the end of the ignition phase. The line and band systems later exhibit reversal to absorption against an intense continuum background during fully developed combustion. In contrast, the green system of MgO and the green triplet of Mg remain in emission during the combustion stage. The 285.21-nm Mg spectral line appears in absorption at all times. It is believed that in the presence of a background radiation field nonuniformly shifted towards the short-wavelength end of the spectrum (produced by Rayleigh scattering of small oxide particles), the gas-phase emitters of the Mg and MgO UV system (distributed in the inner zone of the broad flame) will disproportionally absorb more radiation than the emitters of the green system. Consequently, the spectral signal of the UV system gradually changes from emission to absorption as the density of the radiant condensed particles increases. The high intensity of the background radiation in the UV, in combination with the exceptionally high absorption oscillator strength ($f = 1.9$) of the Mg transition at 285.21 nm, is also responsible for the permanent absorption behavior of this spectral line.

During fully developed combustion, buoyancy-generated convection currents are responsible for the main differences observed in the two cases investigated. At 1 g, high convection currents enhance burning by increasing O_2 flux to the reaction zone and by removing oxide products that may constitute a barrier to O_2 diffusion (Fig. 4a). The proximity of the resulting flame front to the metal sample is an indication of fast burning rates. In comparison, at low gravity conditions, the severe reduction of

convection—threefold by the $(Gr)^{1/4}$ dependence—and the increased resistance to O_2 diffusion by combustion products diminish the oxygen transport. Figure 4b shows a broader, outer blue zone (of stagnant oxide particles in the absence of convection currents) and an increased flame standoff distance from the metal core as compared to the 1-g case. Burning times vary widely depending on the number of jets and explosions that accelerate combustion. Nevertheless, the average burning time at low gravity (3.9 s) is almost twice the average value at 1 g (2.2 s).

While in 1 g the products are swept upward by buoyancy-induced currents, condensed oxides rapidly accumulate and agglomerate in the reaction front at low gravity, producing a highly radiant flame front. Sporadic removal occurs only for large-diameter particles expulsed by inertial forces and residual accelerations during the reduced-gravity trajectory (g jitter). Particle accumulation may account for the unique, unsteady, spherically symmetric explosion phenomenon observed at low gravity—which we refer to as radiation-induced metal explosion (RIME). As shown in Fig. 6, a high particle density in the flame front generates a large heat flux to the sample. This effect raises the surface temperature and increases metal evaporation; the flexible oxide membrane that keeps Mg at temperatures below its boiling point expands as vapor pressure builds up inside the metal core. As evaporation increases, so does the flame front diameter to accommodate greater oxygen flux and maintain the stoichiometry. At the peak of the cycle, the amorphous specimen is transformed into a spherical core with twice the size of the original cylinder (Fig. 6b). Eventually, the structural integrity of the oxide layer becomes the limiting step for continued growth. At some critical diameter, the spherical shell explodes, rupturing in multiple spots and creating small jets that relieve its internal pressure (Fig. 6c). The particles of the pile-up zone are left behind as the core shrinks to its former size. These particles are later removed by the induced flow from the jets. The full cycle lasts approximately 100 ms, and depending on the recovery time of the oxide layer (to heal all ruptures), the complete process is repeated. Up to three RIME cycles were observed in a single experiment.

Conclusions

An investigation of the effects of reduced gravity on the ignition and combustion of radiatively ignited Ti and Mg bulk metals has been conducted in pure O_2 at 1 atm pressure. Reduced gravity is obtained from an aircraft flying parabolic trajectories. High applied heating rates and large internal heat conduction losses into the metal sample generate critical and ignition temperatures that are several hundred degrees above the values obtained from near-isothermal experiments. Because of high conduction and radiation heat losses, no appreciable effect on ignition temperatures with reduced convection in low gravity is detected. These findings are important from a fire-safety standpoint, since a large number of practical situations involve ignition by fast external heating.

Lower regression rates of the molten interface on Ti rods and slower propagation rates of the gas-phase ignition wave on Mg specimens are observed at reduced gravity. These rates are compared to theoretical results from heat-conduction analyses with a diffusion/convection controlled reaction. The close agreement found between experimental and theoretical values indicates the importance of the influence of natural convection-enhanced oxygen transport on combustion rates.

The lower propagation rates observed at low gravity in this study differ from the higher regression rates in microgravity given by Steinberg et al. [1]. The disagreement arises from the different experimental configurations used. In Ref. 1, propagation rates are measured for cylindrical rods ignited at the bottom. The increase in regression rates in microgravity is attributed to an increase in the temperature of the retained molten mass; cyclical detachment of this mass occurs during upward propagation at 1 g. The influence of the gravity force on the molten mass (whose detachment subsequently reduces heat transfer to the unreacted metal) is apparently greater than the influence of buoyancy-induced convection on oxygen transport to the reaction zone. In our investigation, the propagation velocity at normal g is measured while the surface tension force dominates over gravity (at low Bond numbers). In this manner, only the effect of gravity on O_2 transport rates (the limiting reaction step) is evaluated.

Convection currents also affect the burning of Mg diffusion flames. Lower oxygen flux and increased resistance to O_2 diffusion by oxide products appear to be responsible for the longer burning times observed at reduced gravity. The accumulation of condensed oxide particles in the flame front at low gravity produces a unique, unsteady, spherically symmetric explosion phenomenon in bulk Mg termed radiation-induced metal explosion (RIME). The explosions seem to be driven by increased radiation heat transfer from the flame front to an evaporating metal core covered by a porous, flexible oxide coating.

46

References

1. Steinberg, T. A., Wilson, D. B., and Benz, F. J., in *Flammability and Sensitivity of Materials in Oxygen-Enriched Atmospheres: Sixth Volume, ASTM STP 1197*, D. D. Janoff and J. M. Stoltzfus, Eds., pp. 133-145, American Society for Testing and Materials, Philadelphia, 1993.

2. Glassman, I., Mellor, A. M., Sullivan, H. F., and Laurendeau, N. M., *AGARD Conference Proceedings*, No. **52**, Paper 19, 1970.

3. Leibowitz, L., Baker, L. Jr., Schnizlein, J. G., Mishler, L. W., and Bingle, J. D., *Nucl. Sci. and Eng.,* **15**, 395-403 (1963).

4. Hirano, T., Sato, K., Sato, Y., and Sato, J., *Combust. Sci. and Technol.,* **32**, 137-159 (1983).

5. Brzustowski, T. A. and Glassman, I., in *Heterogeneous Combustion:* AIAA Progress in Astronautics and Aeronautics, Vol. **15**, H. G. Wolfhard, et al., Eds., pp. 75-116, Academic Press, New York, 1964.

6. Mellor, A. M., Ph.D. Thesis, Princeton University, Department of Aerospace and Mechanical Sciences, 1968.

7. Breiter, A. L., Mal'tsev, V. M., and Popov, E. I., *Combust. Explos. Shock Waves,* **13**, 475-485 (1977).

8. Abbud-Madrid, A., Ph.D. Thesis, University of Colorado at Boulder, Department of Mechanical Engineering, 1996.

9. Glassman, I. and Papas, P., *J. Mater. Synth. and Process.,* **2**, 151-159 (1994).

10. Markstein, G. H., *Eleventh Symposium (International) on Combustion*, pp. 219-234, The Combustion Institute, Pittsburgh, 1967.
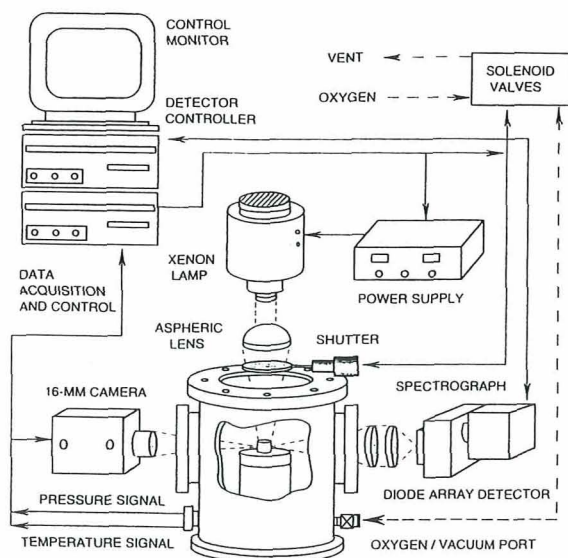
Figure 1. Diagram of the experimental system.

(a) Normal gravity

(b) Reduced gravity

5 mm
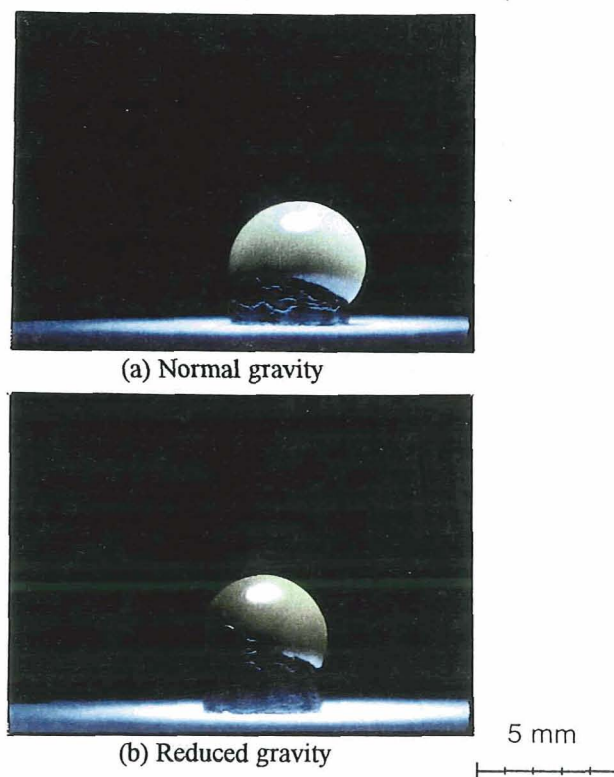
Figure 2. High-speed photographs of the steady propagation stage (200 ms after ignition) during the combustion of bulk Ti specimens in pure O_2 at 1 atm under a) normal gravity and b) reduced gravity conditions.

(a) Normal gravity

(b) Reduced gravity

5 mm
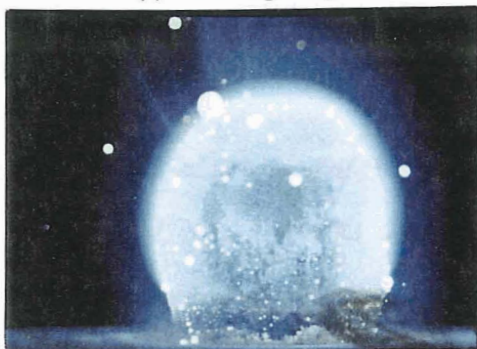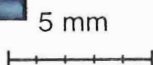
Figure 4. High-speed photographs taken during the fully developed combustion stage of bulk Mg specimens in pure O_2 at 1 atm under a) normal g and b) reduced g.
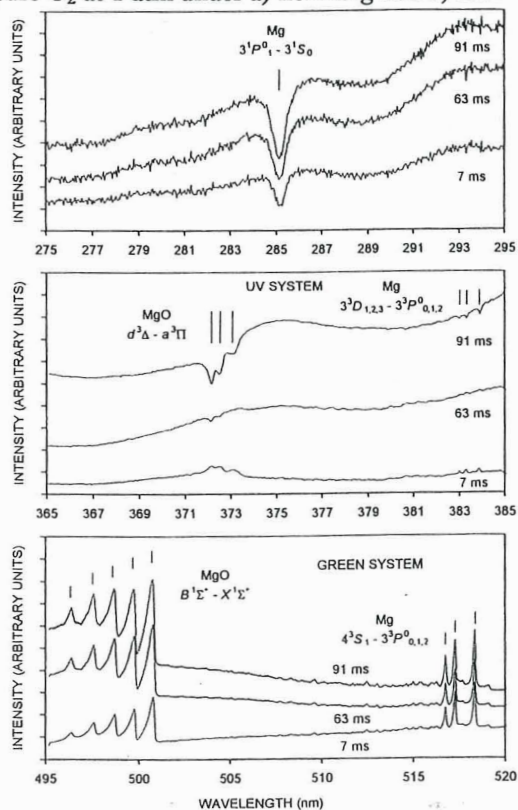
Figure 5. Time-resolved emission spectra of the 285.21-nm Mg spectral line (top) and the Mg and MgO UV (middle) and green (bottom) systems, taken at 7, 63, and 91 ms from ignition of a bulk Mg specimen in pure O_2 at 1 atm at reduced gravity.
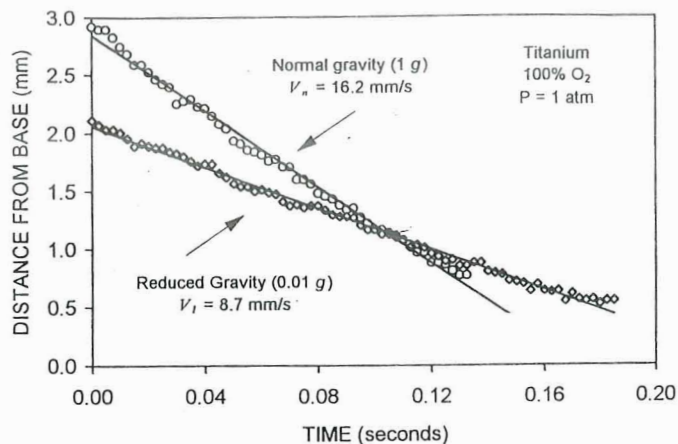
Figure 3. Propagation of the reacting molten mass of the Ti samples shown in Fig. 2 under normal and reduced gravity.

5 mm
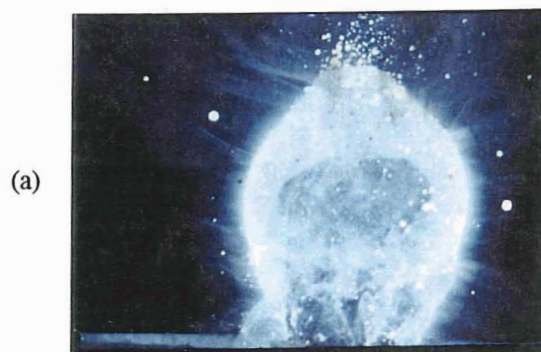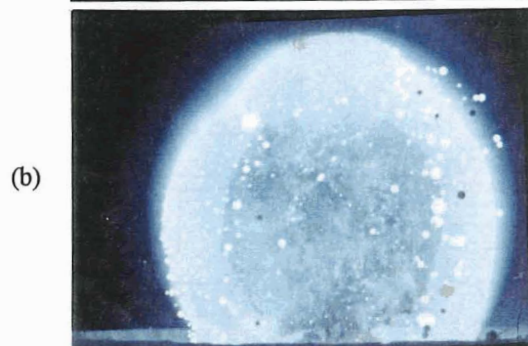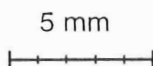
Figure 6. Radiation-induced metal explosion (RIME) in a bulk Mg specimen at reduced gravity. a) Start of cycle; b) maximum flame expansion; c) metal core explosion.

48

INTERNAL AND SURFACE PHENOMENA IN HETEROGENOUS METAL COMBUSTION

EDWARD L. DREIZIN

AeroChem Research Laboratory, Titan Research and Technology, Titan Corporation
Princeton, New Jersey

INTRODUCTION

The phenomenon of gas dissolution in burning metals was observed in recent metal combustion studies [1-4], but it could not be adequately explained by the traditional metal combustion models [5-8]. The research reported here addresses heterogeneous metal combustion with emphasis on the processes of oxygen penetration inside burning metal and its influence on the metal combustion rate, temperature history, and disruptive burning. The unique feature of this work is the combination of the microgravity environment with a novel micro-arc generator of monodispersed metal droplets, ensuring repeatable formation and ignition of uniform metal droplets with a controllable initial temperature and velocity. Burning droplet temperature is measured in real time with a three wavelength pyrometer. In addition, particles are rapidly quenched at different combustion times, cross-sectioned, and examined using SEM-based techniques to retrieve the internal composition history of burning metal particles. When the initial velocity of a spherical particle is nearly zero, the microgravity environment makes it possible to study the flame structure, the development of flame non-symmetry, and correlation of the flame shape with the heterogeneous combustion processes.

SUMMARY OF NORMAL GRAVITY EXPERIMENTAL RESULTS

Metal particle combustion experiments have been conducted in air at normal gravity with Al, Zr, and Ti particles of 90 - 350 μm diameter. These results are discussed in detail in Refs. 9-13. Particles were formed and ignited at initial velocities from 1 to 3 m/s, which correspond to the Reynolds numbers Re in the range of 5-10.

Both zirconium and titanium particle combustion experiments [9-13] showed that no oxide (or nitride) shells or inclusions formed in these burning particles. Maximum combustion temperatures were considerably lower than the boiling (volatilization) temperatures of either the metals or their oxides. For both metals, oxygen and nitrogen dissolved in the liquid metal producing a metal/oxygen/nitrogen solution. The equilibrium gas solubity limit was eventually exceeded during combustion. From that time on, the burning particles consisted of a supersaturated metal/gas solution. The final combustion products, stoichiometric oxides, formed out of the solution when a specific phase transformation temperature was reached. For zirconium combustion experiments, the phase transition was the eutectic formation of ZrO_2 and α-Zr out of the Zr-O solution; for titanium, the temperature was close to the point of eutectic precipitation of stoichiometric oxide Ti_2O_3 from the liquid Ti-O solution. In both cases, the formation of stoichiometric oxide was accompanied by a rapid temperature increase, nitrogen-gas release, and void/crack formation. When external oxygen was available, particle explosions occurred because of oxidation on the fresh surface that originated in the cracks.

Particle size and composition measurements indicated that only a negligible amount of metal evaporated during the entire titanium and zirconium particle combustion event. However, spatially resolved radiation measurements and photographs of particle streaks consistently showed a luminous zone surrounding the burning particle. The size of the luminous zone correlated well with the size of the smoke clouds observed on traces of particles quenched on foil or glass slides. The cloud was originally spherically symmetric but lost its symmetry as combustion progressed. During the entire particle combustion period, the radiation intensity from the luminous zone was considerably less than that from the particle surface.

An experimental study of the combustion of Al particles in air revealed three distinct stages in their burning histories [8,9]. The first stage was spherically-symmetric vapor phase combustion, consistent with the conventional metal vapor-phase burning model. The second stage was associated with an increase in the size and density of the smoke cloud surrounding the particle, a shift to a non-symmetric combustion regime, and initiation of oscillation in particle brightness. The finite content of oxygen built up in burning particles at that time. The particle temperature was close to the Al boiling point during the first two combustion stages. In the third combustion stage an "oxide cap" formed and grew on the burning particle, which continued to burn non-symmetrically. The particle temperature decreased continuously, and the combustion terminated after the experimentally measured temperature reached the Al_2O_3 melting point.

The transition from the first to the second combustion stage appeared to occur when the dissolved oxygen content in the Al droplet reached the saturation point (corresponding to a maximum of approximately 14 atomic oxygen percent in the solution), liquid Al_2O_3

was formed, and droplet temperature attained the three-phase (liquid Al-O solution, liquid Al_2O_3, and gaseous species, that is a mix of Al, O, O_2, and AlO) equilibrium point of $2240°C$.

MICROGRAVITY PARTICLE COMBUSTION EXPERIMENTS

Experiment justification
Microgravity experiments were limited to aluminum particle combustion tests. Aluminum was chosen because its combustion is primarily affected by the vapor-phase processes which most likely depend on the gravity environment. In addition, the non-symmetrical flame development observed in all of our normal gravity tests was most prominent in aluminum particle combustion. Therefore, the following experimental objectives were set forth for the microgravity tests:

1. Measure the combustion time of aluminum particles burning in microgravity and relate it to the combustion time of the same particles burning during free fall in air.
2. Determine whether the brightness oscillations observed during aluminum particle combustion persist in microgravity.
3. Determine whether the non-symmetric flame pattern that develops around an aluminum particle burning in air after the initial combustion stage is observed under microgravity conditions.

Experimental apparatus for microgravity tests
Aluminum particles were produced and ignited in room air using a micro-arc method [8,9]. In this method, a pulsed micro-arc is initiated between a consumable metal wire, which serves as an anode, and a tool-cathode. The tip of the metal wire is melted by a micro-arc pulse and a molten droplet is separated from the wire due to the pressure from the discharge. Each micro-arc pulse results in the production of a single metal droplet. Monodisperse metal droplets with pre-determined diameters in the 100-500 μm range were produced using this technique. An advantage of the micro-arc method is uniformity of inital diameters and temperatures of the metal droplets. However, metal droplets formed using this technique have finite initial velocities (normally, in the 1-3 m/s range) whereas stagnant metal droplets are needed to realize the advantages of the micro-gravity environment. Thus, the micro-arc apparatus was modified to produce and ignite motionless metal particles. The idea was to compensate for the droplet's initial velocity by moving the electrode unit during the micro-arc pulse in the direction opposite to that of the droplet. Both electrodes, consumable wire anode and tool-cathode, were attached to a platform positioned on a linear slide. The electrode holder was built to allow adjustment of the angular position of the electrodes, so that the direction of the droplet initial velocity could be adjusted to be parallel to the direction in which the linear slide moved. The slide was attached to the core of a solenoid with a steel cable. When the solenoid was activated, the slide started to move with nearly constant acceleration. An accelerometer was positioned on the linear slide, and its output was connected to an integrating circuit to measure the slide velocity. The signal from the integrator was sent to one of the inputs of an electronic comparator, while the other comparator's input was connected to a reference voltage source. When the voltage from the integrator, proportional to the linear slide velocity, matched the reference voltage level, the comparator produced a pulse triggering the micro-arc. The reference voltage level was chosen so that the slide velocity was equal to the initial velocity of the droplet (while the direction of the slide was opposite to that of the droplet) at the moment the micro-arc was triggered. As a result, the initial velocity of the droplet relative to the motionless environment was close to zero. Additonal circuitry was designed and built to stop the linear slide safely and prevent additional micro-arc triggering during stopping.

The diagnostics consisted of a NAC HSV-1000 high-speed video system and an optical three-wavelength pyrometer [10,11,13]. The pyrometer measured radiation at wavelengths of 458, 500, and 580 nm, chosen to minimize the effect of bands produced by the Al-O system [14].

To provide a micro-gravity environment, the experimental apparatus was mounted onboard a DC-9 aircraft and flown at NASA Lewis Research Center in October, 1996.

RESULTS

Laboratory tests in which motionless particles were produced and burned in a normal gravity environment served as a baseline for comparison with microgravity experiments. Combustion times and temperatures, measured for particles produced at normal gravity at low initial velocities and thus characterized by low Reynolds numbers ($Re < 0.25$), correlated well with our previous measurements [12,13] for particles produced for Re in the range of 5-10. Smoke traces around particles caught on glass slides at different combustion times indicated the development of non-symmetric flames (Fig. 1), similar to that reported earlier [8,9]. Non-symmetric combustion has been associated with sudden accelerations and subsequent changes in velocities of burning particles.

Twelve successful microgravity experiments were conducted in which nearly motionless aluminum particles were produced, ignited, and burned while their color temperatures were measured and combustion events were videotaped. In addition, two experiments were conducted at normal gravity in the aircraft environment to provide better reference for the microgravity tests. No effect of reduced gravity on combustion time or combustion temperatures for
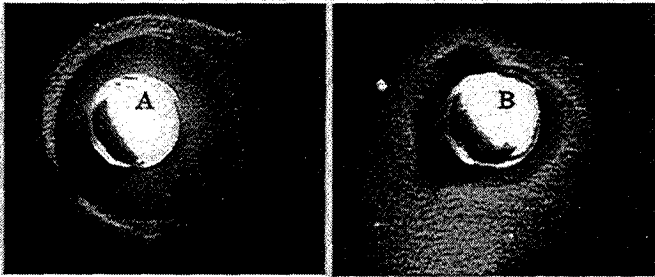
Fig. 1.
Traces of 300 μm diameter aluminum particles quenched on glass slides,
a) velocity is 0.06 m/s, quench time is 10 ms
b) velocity is 0.18 m/s, quench time is 25 ms
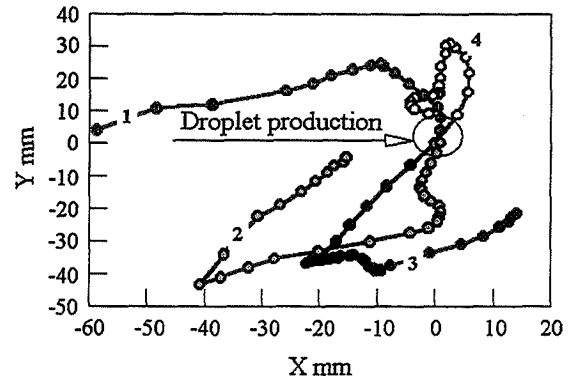
Fig. 2.
Trajectories of aluminum particles produced and burned onboard the DC-9 airplane, lines 1-3 particles at μ-gravity, 4- particle at normal gravity

aluminum particles produced at low Re was observed. Non-symmetry developed in the aluminum particle flame at both high and low Re in both normal and micro-gravity environments. The non-symmetry could be detected by analyzing video-images of burning particles as well as by observing sudden changes in particle velocities (Fig. 2). Since non-symmetry resulted in particle acceleration, particle motion was observed in the microgravity tests instead of the expected burning at a fixed location; this complicated a detailed study of the flame shape and structure. Varying particle trajectories were observed, unlike in our previous normal gravity experiments [12,13] with particles produced at higher Re, when particle trajectories were quite repeatable and were primarily governed by their initial velicities. Several trajectories of particles produced and burned in microgravity are presented in Fig. 2 (lines 1-3). For comparison, a trajectory of a particle produced and burned onboard the DC-9 airplane during a normal gravity portion of the flight is also shown in Fig. 2 (line 4). Experimental points show particle locations observed every 8 ms using the high-speed video system. There were no major difference in the trajectories of low Re particles burned at normal and reduced gravity: in both cases sudden velocity changes were observed that did not seem to correlate with the absolute velocity value. In other words, velocity could suddenly increase from zero to about 1 m/s, or, alternatively, the particle could suddenly stop after moving at about 1 m/s velocity. For example, changes of the absolute value of velocity and acceleration for a 250 μm diameter aluminum particle burning in microgravity (ca.Fig 2, line 3) are shown in Fig. 3 a, b. This particle was produced at a significant initial velocity, but it suddenly stopped and was nearly motionless during an extended period of time. After a while, the particle rapidly accelerated and then deccelerated again. It is interesting to correlate particle motion, which is apparently associated with the developing non-symmetry in the particle flame, with the particle radiation and temperature histories. A radiation trace and color temperature history measured by a three-wavelength pyrometer are shown in Fig. 3. c,d, for the same particle for which velocity and acceleration data are presented. The radiation trace clearly shows oscillations developing during particle combustion in microgravity, similar to those reported earlier [8,9]. One can see that the acceleration reaches a peak when the oscillations in the particle radiation trace are initiated and some decrease in the measured temperature is observed, which, according to Ref. 9 signifies the transition from the first to the second combustion stage. Another peak in acceleration is observed when particle temperature continuously decreases, which corresponds to the transition to the third combustion stage. Such a correlation between the acceleration, radiation, and temperature traces was repeatable; however, it was clearly noticeable only for large particles (250 μm diameter). For smaller particles, the acceleration also changed significantly at the times of transition from one combustion stage to another, but these changes were masked by strong random variations of acceleration.
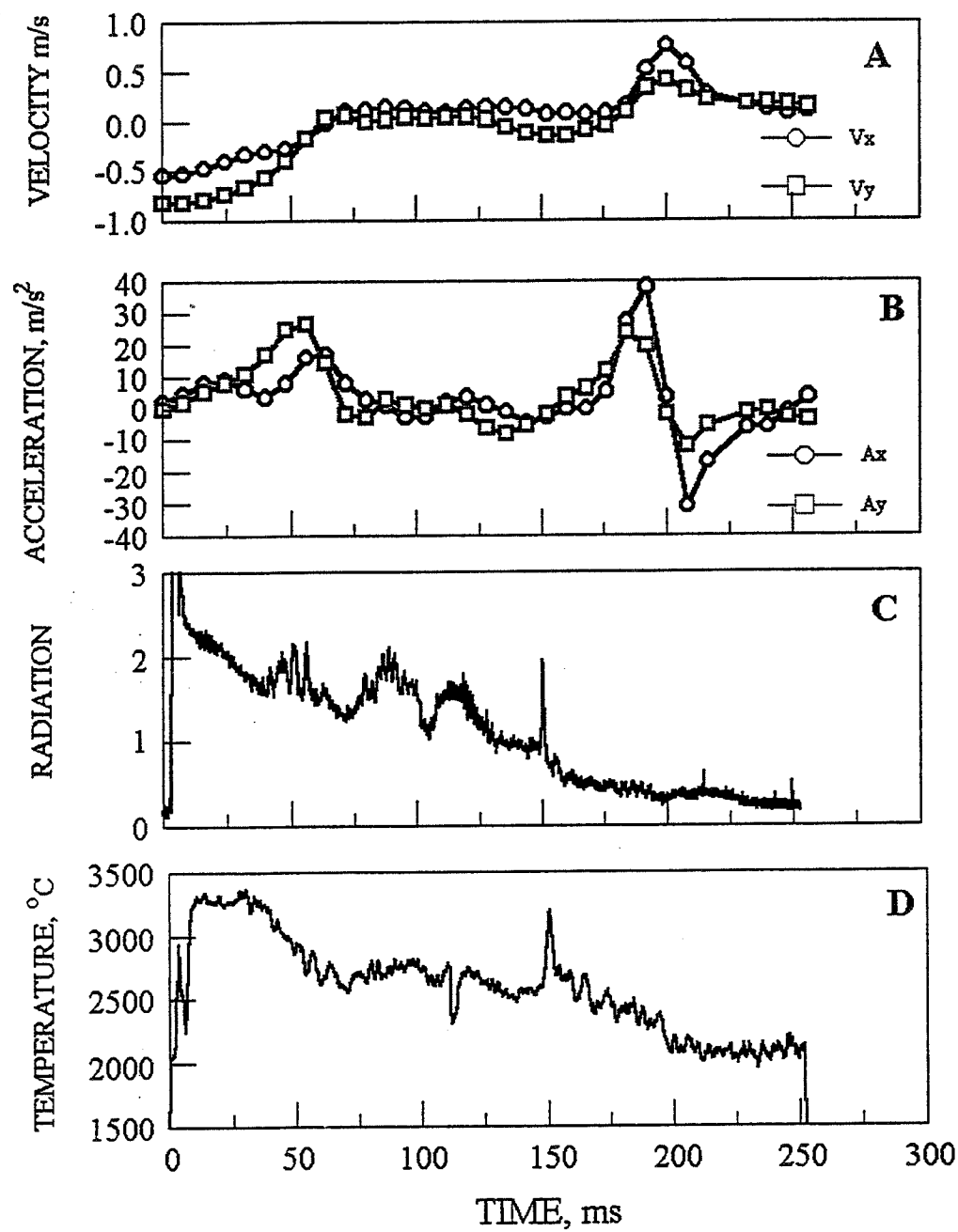
Fig. 3
Velocity, acceleration, radiation, and temperature histories of a 250 µm diameter aluminum particle burning in microgravity environment

Examination of high-speed video recordings of aluminum particle combustion in micro-gravity revealed a feature not observed before. A long radiating tail (Fig. 4) appeared and disappeared during the first 100 ms of the particle burning. The size of this tail was close to 1-1.5 cm, and is much greater than the flame zone (normally, under 1mm). At this time it is unclear whether the radiating tail was formed due to the micro-gravity environment, or was simply observed for the first time because a better and newer video-camera was used in these experiments.

DISCUSSION

Since no effects of Re number or the gravity environment on particle burning time and temperature were observed, no significant limitations of the reaction rate by convection or buoyancy exist. This is not unexpected for the particles with diameters in the 100-300 μm range, for which the rate of the gas-phase diffusion normally determines the reaction rate.
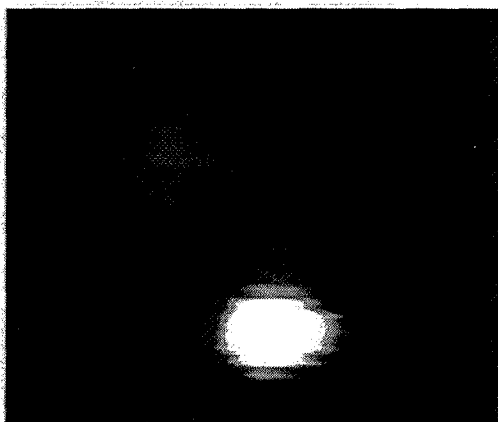
Fig. 4   Image of a 200 μm diameter aluminum particle burning in μ-gravity showing a bright radiating tail appearing and disappearing during combustion

Sudden changes in particle velocities provide important evidence and characterization of the non-symmetric burning if it is assumed that they were not a result of minor gas flows which could have existed onboard the DC-9 airplane as well as in the laboratory. An order of magnitude estimate shows how such a flow could accelerate a particle. The relaxation time (during which particle velocity reaches 1/e of the flow velocity) is given by $\tau=(2r^2\rho)/(9\eta)$, where r is particle radius, ρ is density, and η is gas viscosity. For a particle of about 100 μm radius, $\tau \sim 100$ ms. Therefore, a flow with a velocity of about 10 m/s must exist to accelerate the particle to a velocity of 1 m/s during approximately 25 ms, the time observed in our experiments. In other words, quite a strong wind (a highly unlikely event) would be required to affect the motion of a particle of 250 μm diameter; however, the particle sensitivity to gas disturbances increases greatly with decreasing particle size, which explains the random velocity changes observed for smaller particles throughout the combustion time.

The development of flame non-symmetry for the nearly motionless particles, and, in particlular, for particles burning at microgravity, shows that the non-symmetry is not a result of either forced or natural convective flows, but rather is an essential attribute of particle burning. As reported in Ref. 13, significant changes in the composition of burning aluminum particles are observed; in particlular, a saturated Al-O solution forms in the particle interior by the end of the first combustion stage. This implies that the composition of the vapor above the particle surface changes, i.e., AlO molecules appear in addition to Al atoms. Also, liquid Al_2O_3 can form in the particle, or on its surface as a result of the phase separation in the Al-O solution. These phase separation processes are, apparently, related to the particle flame non-symmetry since they both develop at the same time. The resultant effect is that the aluminum evaporation processes become non-uniform, which causes the rapid changes in particle velocity observed for initially motionless particles under both normal and micro-gravity environments. Note that similar velocity changes could not be detected in the previous experiments where particle trajectories were mostly defined by the high initial particle velocities. The experimentally measured velocities and accelerations of particles burning in microgravity allow one to evaluate the feasibility of the effect of non-symmetric evaporation on the changes in particle velocities. Similar estimates based on the results of normal gravity experiments would be complicated by the effect of convective flows on particle motion. Change in the particle impulse $m\Delta v$ is given as $m\Delta v = v_g(dm/dt)\cdot\tau$, where v_g is the unknown velocity of the evaporating gas at the particle surface, dm/dt is the particle burning rate, m is the particle mass, $m \approx 2\cdot10^{-5}$g, $\Delta v \approx 1$ m/s is the change in particle velocity during $\tau \approx 25$ ms, the typical time of the velocity change. An average burning rate dm/dt can be estimated as particle mass divided by the entire combustion time, and it is close to $9\cdot10^{-5}$ g/s. This estimate shows that v_g should be close to 5 m/s to provide the particle acceleration equal to that observed experimentally. This velocity must correlate with the bulk gas velocity at the particle surface which exists due to droplet evaportaion v_b. This velocity can be estimated

as $v_b=(dm/dt)/(4\rho_v\pi r^2)$, where aluminum vapor density, $\rho_v=MP/(RT)$, and $M=27$ g, is the molar mass of aluminum, pressure $P=10^5$Pa, the gas constant $R=8.31$ J/(mol·K), and the flame temperature, $T\approx2800$ K. For a 100 μm radius aluminum droplet, this estimate gives $v_g\approx$ 6 m/s. Therefore, the bulk gas velocity due to aluminum evaporation correlates well with the gas velocity which is needed to provide the particle acceleration observed experimentally.

Another important point can be made on the observation that repeatable brightness oscillations occurred in both normal and micro-gravity experiments using nearly motionless aluminum droplets. Previously, such oscillations were interpreted assuming droplet spinning and non-symmetric combustion. A possibility of the droplet spinning resulting from the flame non-symmetry can be evaluated by comparing torque acting on a spinning droplet due to drag forces, $T_1=8\pi\eta r^3\Omega$, where Ω is the droplet angular velocity, with the torque which can be developed if the entire mass flow from the burning particle is presented as a jet which is produced from a droplet surface perpendicular to the droplet radius. If the ratio of $T_1/T_2 <1$, particle spining could be caused by non-symmetric burning because only a portion of the entire mass flow from the particle surface could be non-symmetric and induce such a motion. The maximum torque developed from a jet representing the entire mass flow from a burning particle can be estimated as $T_2=(dm/dt)rv$, where v is the jet velocity. An estimate shows that for the experimental range of Ω from 1000 to 3000(rad/s), the ratio T_1/T_2 is in the range of 0.04–0.12 when the torque T_2 is computed using the experimental particle burning rate $dm/dt=9\cdot10^5$ g/s and $v=$ 5m/s, in accordance with the estimate discussed above for the bulk gas velocity at the droplet surface. Therefore, only a small non-symmetry of the entire vapor flow from particle surface can result in the droplet spinning with the frequencies observed experimentally.

SUMMARY

Aluminum particles were formed with initial velocities close to zero, ignited, and burned in air in normal and in microgravity environments. Combustion times and temperatures were similar to those measured in the previous normal gravity laboratory experiments. The present experiments demonstrated that the non-symmetric flame develops around a nearly motionless aluminum particle burning in air. The development of such flame non-symmetry in microgravity shows that it is an intrinsic feature of aluminum burning rather than the result of forced or natural convection flows. Burning particle brightness oscillations were also observed in microgravity experiments, and they may be associated with particle spinning.

ACKNOWLEDGEMENTS

REFERENCES

1. Steinberg, T. A., Wilson, D. B., and Benz, F.J., *Combustion and Flame*, 88:309-320 (1992).
2. Steinberg, T.A., Wilson, D.B., and Benz, F.J., *Second International Microgravity Combustion Workshop*, 1993, pp. 273-280.
3. Dreizin, E.L., Suslov, A.V. and Trunov, M.A., *Combust. Sci. Tech.*, 87:45-58 (1992).
4. Dreizin, E.L., Suslov, A.V. and Trunov, M.A., *Combust. Sci. Tech.*, 90:79- 99 (1993).
5. Molodetsky, I.E., and Dreizin, E.L., in *Decomposition, Combustion, and Detonation Chemistry of Energetic Materials*, MRS Symp. Proceedings, Vol. 418 (T.B. Brill, Russel, T.P., Tao, W.C., and Wardle, Eds.) MRS, Pittsburgh, 1996, pp. 195-200.
6. Price, E.W., in *Fundamentals of Solid Propellant Combustion* (K.K.Kuo and M. Summerfield, Eds.), AIAA, New York, 1984, pp. 479-514.
7. Beckstead, M.W., *Twenty-Sixth JANNAF Combustion Mtg*, CPIA Publication 529, 4:255-268 (1989).
8. Nelson, L.S., Rosner, D.E., Kurzius, S.C., and Levine, H.S., *Twelfth Symposium (Int'l) on Combustion*, The Combustion Institute, Pittsburgh, 1968, pp. 59-70.
9. Levine, H.S., *High Temperature Science* 3:237-243 (1971).
10. Molodetsky I.E., Dreizin, E.L., and Law, C.K., *Twenty-Sixth Symposium (Int'l) on Combustion*, The Combustion Institute, Pittsburgh, 1997 (in press).
11. Molodetsky, I.E., Dreizin, E.L., Vicenzi, E.P., and Law, C.K., *Combustion and Flame* (submitted).
12. Dreizin, E.L. and Trunov, M.A., *Combustion and Flame*, 101:378-382 (1995).
13. Dreizin, E.L., *Combustion and Flame*, 105:541-556 (1996).
14. Pearse, R.W.B., and Gaydon, A.G., *The identification of molecular spectra.* Halsted Press, NY, 1976.

INTERACTION OF BURNING METAL PARTICLES

EDWARD L. DREIZIN

AeroChem Research Laboratory, Titan Research and Technology, Titan Corporation
Princeton, New Jersey

INTRODUCTION

Multiple particle/droplet flames are ubiquitous in practical combustion systems, and thus the flame interaction processes are of great practical importance. This explains the strong current interest in interactive combustion phenomena. Numerous theoretical and experimental combustion studies of liquid fuel drop arrays have been conducted to determine the interaction effects. Major results in this field were recently summarized in a comprehensive review [1]. Recent experiments with two adjacent liquid droplets burning under microgravity conditions [2,3] revealed new aspects of flame interaction processes, such as positive and negative interactions, which can either increase or decrease burning rates depending on the droplet separation and the combustion stage. Interaction of solid fuel flames has been studied only for bulk samples and for relatively low temperature flames [4-6].

Although metals are widely utilized in solid propellants and in explosives where multiple interacting metal particles are involved, no direct experimental studies of the burning metal particle interactions and their effect on flame propagation have been reported. Apparently, this is due to experimental difficulties associated with studying metal aerosol combustion behavior while simultaneously analyzing the processes occurring with individual particles. Observation of individual particle behavior in a burning metal cloud is practically impossible because only very fine (1-10 μm particle size range) and relatively dense metal aerosols can be ignited and burned so that individual small particles cannot be optically resolved. Thus, only gross parameters describing cloud combustion can be recovered from normal gravity metal aerosol combustion experiments. To understand the relationship of the general cloud combustion scenario with the specific features of combustion of individual particles, larger size particles could be used in experiments, so that the direct observation of individual particle behavior would be possible simultaneously with the observation of the common cloud combustion characteristics. However, it is impossible to produce and burn a stable aerosol of large metal particles because of rapid gravitational settling. Microgravity provides a unique opportunity to create a "model aerosol" consisting of relatively large (100-300 μm diameter) particles. Combustion of such particles in a cloud can be studied using methods developed in single metal particle combustion experiments. Such an "aerosol" can be formed in a sufficiently oxygen-rich environment and be dense enough so that flame propagation will be established. In microgravity, the particles will not settle, rather their motion will be due exclusively to the forces originating during combustion. Therefore, individual flame development, particle trajectories, temperature histories, smoke transport, etc., will expose many features of an actual fine metal aerosol combustion. Clouds with different metal particle number densities can be readily created in microgravity, which allows detailed experimental investigation of the processes caused by the interaction of burning metal particles.

Our current understanding of individual metal particle combustion suggests that there are many processes which significantly affect metal aerosol combustion but do not occur in clouds of non-metal particles which burn at lower temperatures, or in liquid fuel sprays. Among such processes are efficient radiative heat transfer caused by high combustion temperatures [7,8], and changes in the reaction mechanism during combustion (from heterogeneous to vapor phase combustion, from spherically symmetric to non-uniform combustion, the occurrence of microexplosions, and temperature jumps [9-13]). Different combustion products and intermediates form during combustion, and they can participate in further reactions, including those products and subproducts which form in the nanoscale condensed phase [14]. Both the particle surface layer and the particle internal composition are modified during combustion [15]. Ionized species and electrically charged particles are efficiently produced at high metal combustion temperatures and low metal ionization potentials [16,17]. These processes affect particle interactions and can be crucial for the performance of practical devices utilizing metal combustion.

This research is aimed at the investigation of combustion parameters of microgravity model aerosols: relatively large uniform metal particles aerosolized in microgravity environment. An experiment consisting of creation and ignition of a metal multiparticle system in microgravity and high-speed video-recording of the combustion events will produce visual records of the development of individual particle flames, their interactions and the particle motion they induce simultaneously with the observation of the entire aerosol combustion process. Frame by frame analysis of the video-images taken using a high-speed movie camera will allow one to determine particle brightness temperatures and the decrease in particle diameter during combustion. Analysis of the experimental results and comparison with the results of single metal particle combustion experiments, conducted under similar microgravity conditions in the

framework of a parallel program (Ref. 18), will establish the relationship between single and multiple particle burning rates and combustion temperatures, concentrations at which the flame substructure forms rather than individual particle flames, efficiency of radiative heat transfer in metal aerosol combustion, what is the role of electrostatic forces in structuring the flame and the effect of that structure on the flame propagation rate. Although some details of fine particle aerosol clouds, such as the kinetics limited burning rate, radiative heat transfer in a system with a high specific surface, particle induced turbulence, etc., will probably not be very well simulated in the planned experiments, they are relatively well understood and can be accounted for using an adequate individual particle combustion model. On the other hand, the unknown particle interaction phenomena to be studied in this research program are generic and can be readily projected onto a cloud combustion model which would also incorporate a correction for particle size.

EXPERIMENTAL METHOD

The experimental method consists of:

a) aerosolizing 100-300 µm diameter metal particles in an oxygen-containing environment under microgravity,
b) aerosol ignition using a local high energy density heat source, and
c) simultaneous observations of both the entire aerosol combustion and the behavior of single burning particles.

The experimentally measured flame propagation rate will be correlated with the observed development of individual particle flames, individual particle temperatures, combustion rates, electric charges produced on and in the vicinity of burning particles, and particle trajectories.

1. Experimental Hardware

A simplified schematic of the experimental apparatus designed and built for microgravity experiments utilizing the NASA Lewis RC 2.2 s Drop Tower is presented in Fig. 1. The experiments are conducted in a rectangular combustion chamber with a volume of less than 1 liter. It is built of aluminum and is equipped with two lexan windows, three gas-ports, and two electrical feedthroughs. The chamber's floor is a silicone rubber membrane which aerosolizes the powder using acoustic oscillations transmitted from an acoustic exciter. The chamber is mounted on top of the acoustic exciter and connected to a gas reservoir tank (3 gal) to prevent pressure build-up upon aerosol ignition. An inert gas tank is connected to the combustion chamber through a normally-closed solenoid valve. A second solenoid valve is installed in a vent from the reservoir chamber to atmosphere. Before the end of the microgravity experiment, both solenoid valves are activated and the combustion chamber is flushed with inert gas to quench the reaction. Electronic components mounted on the experimental rig include an audio generator, an audio amplifier, a 12 V DC dry cell battery, and a regulated power supply for heating of the ignition fuse wire. In addition, the apparatus includes a high-speed movie camera, and a custom-built triggering circuit.

2. Microgravity experiment sequence

When a microgravity test starts, the acoustic exciter is turned on for a 0.4 s interval that results in aerosolizing particles in the combustion chamber. The frequency of the acoustic oscillations of the chamber floor is close to 150 Hz, therefore an interval of 0.4 s provides about 60 complete vibrations to aerosolize particles. After the acoustic exciter is turned off, a time delay is provided so that the velocities of particles decrease due to aerodynamic drag. The relaxation time for the velocity of an airborne particle, $\tau=(2\rho r^2)/(9\mu)$, where ρ is the particle density, μ is gas viscosity ($\mu=1.8\cdot10^{-5}$ kg/(m·s) for room temperature air), r is particle radius. For the parameters of the experiment $\tau\approx0.2$ s, therefore, the ignition is delayed by that time interval. After the delay, the tungsten wire is rapidly heated and the aerosol ignites. The entire aerosol combustion event is estimated to occur within 0.5-0.8 s. After a time delay of 1.9 s measured from the beginning of the test, the solenoid valves are activated to flush the combustion chamber with an inert gas and quench all post-combustion reactions.

NORMAL GRAVITY IGNITION TESTS

Preliminary experiments were conducted to define conditions needed to ignite particles and to better evaluate timing for microgravity tests. Magnesium was chosen for the first group of micro-gravity experiments since it has been shown previously that even 100-200 µm size aerosolized magnesium particles can be easily ignited [19]. Particles used in our experiments were purchased from Aldrich Chemical and size-analyzed. Their size distribution, shown in Fig. 2, was determined using digitized video-images of particles taken with a camcorder equipped with close-up lenses.
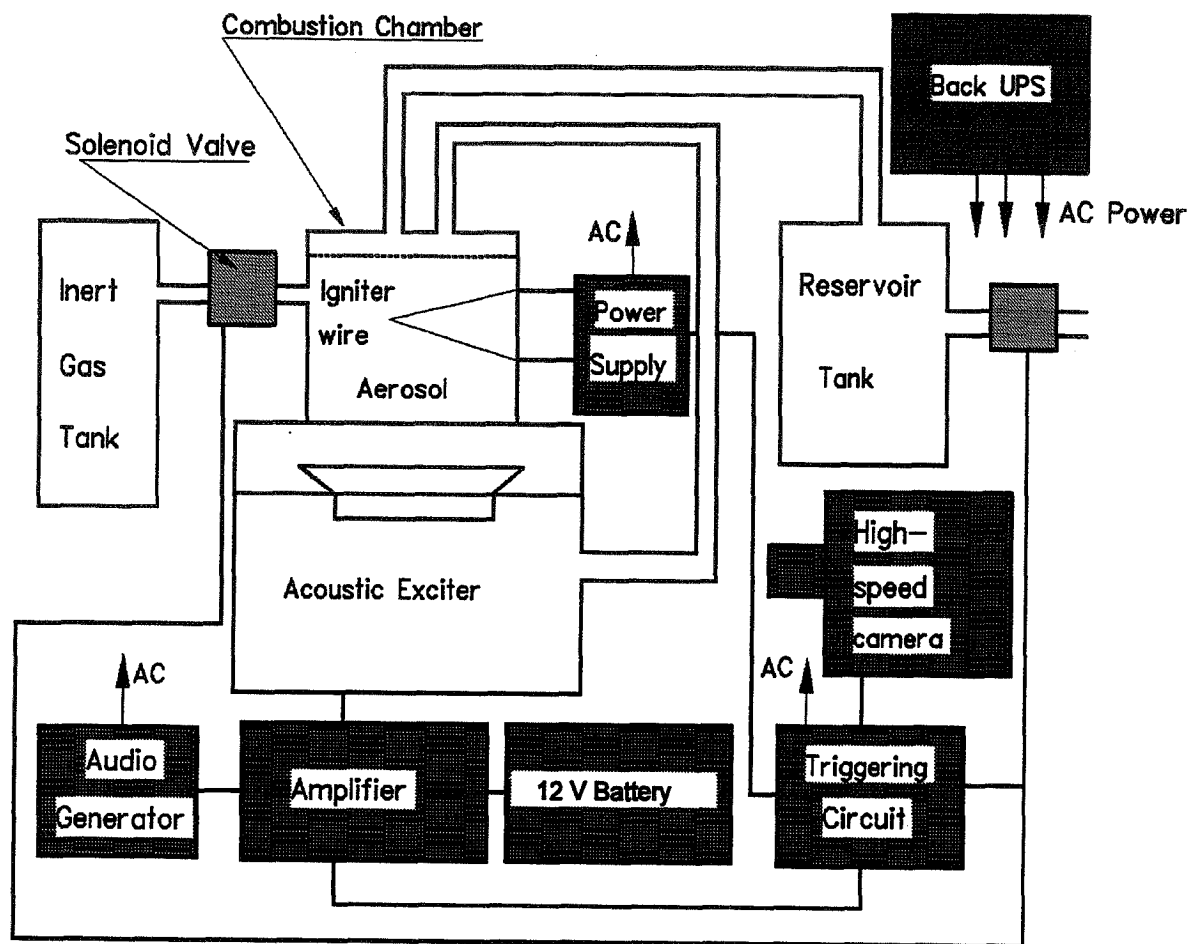
Fig. 1. General Diagram of the Experimental Apparatus

The mass of particles loaded into the combustion chamber in these normal gravity experiments was 5 g. However, in accordance with simulations [20], only about 10% of the total particle load were aerosolized above the level of 15 particle diameters (approximately 3 mm). Since the ignitor is located approximately 70 mm above the chamber floor, only a small fraction of the total particle mass load could participate in the aerosol combustion. In order to roughly evaluate the actual aerosol particle number density, an optical system measuring light absorption by aerosolized particles was used. The optical components were mounted on a linear slide and could be removed prior to ignition to obtain a clear view for the video-camera. To measure the particle concentration, a 670 nm wavelength laser beam passed through the combustion chamber to a photodiode window covered with a corresponding interference filter. The height and horizontal position of the laser diode/photodiode pair could be adjusted. The photodiode measured the baseline signal, S_0, before the acoustic exciter was turned on. Then, the aerosol was formed and a part of the light was absorbed by the aerosol particles. The signal, S, measured at that time was smaller than S_0, and the ratio, $S/S_0=1-N\cdot d\cdot\pi r^2$, where N is the particle number density, d=50 mm, is the chamber width, and r$\approx$80 μm is the average particle radius. The magnesium particle number density determined for our normal gravity experiments decreased from 0.1 g/l to 0.05 g/l as the height increased from 57 to 78 mm from the chamber floor (the chamber can be viewed through a window above the height h=40 mm). The particle number density at the level of the middle of the igniter wire, 0.075 g/l, corresponded to approximately 20 particles per cubic centimeter, or an interparticle separation of about 2.7 mm.

Several normal gravity ignition experiments were conducted in which a high-speed video camera was used to visualize flame propagation. An electrically heated 100 μm diameter tungsten wire was used as the ignition source. Examination of the video-recordings revealed that multiple particles adhered to the wire surface and ignited as the wire was heated. Then, the multiple particle flame developed and propagated in the chamber. We observed the process of multiple particle flame development, which is illustrated by images presented in Fig. 3. The flame rapidly developed in the vertical direction, which, apparently is the result of buoyancy. The flame width increased at a significantly slower rate and reached up to 35-40 mm. The duration of the flame was around 300-350
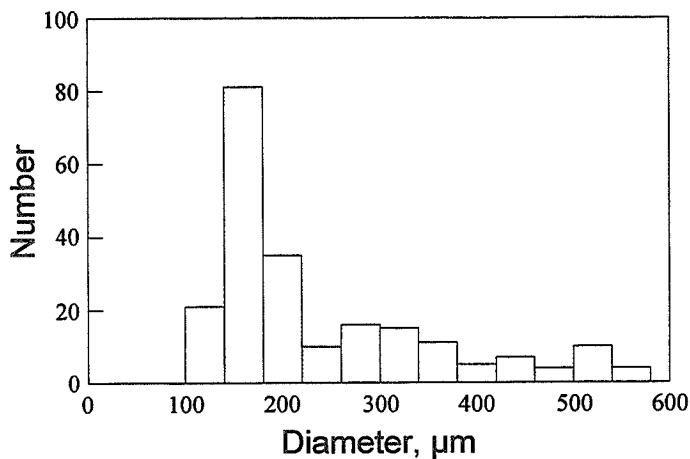
Fig. 2. Size distribution of magnesium particles used in aerosol ignition tests.

ms. The flame apparently extinguished due to oxygen deficiency in the chamber. A simple estimate shows that the oxygen contained in 1 liter of air could completely oxidize approximately 0.4 g of magnesium. Since the combustion chamber was not flushed with inert gas after the flame extinguished, in these experiments, several particles could still continue to burn, and from time to time a particle cluster could ignite. The combustion chamber was hooked up to a large vessel filled with air, so that additional oxygen could diffuse into the chamber through the connecting gas tubes. The rate of this diffusion was not sufficient to sustain an aerosol flame, but could result in re-ignition after the flame was quenched. Results of our measurements of the flame width, w, and the velocity of the flame front (in the horizontal direction) v_f, inferred from a video-record, are shown in Fig. 4. The width of a bright zone at a fixed horizontal level was used for these measurements. The flame speed is in the range reported earlier for large size particle magnesium aerosol flames [19, 21]. Oscillations observed in the flame velocity plot could be caused by a periodic additional supply of fresh particles into the combustion zone due to vibration of the chamber floor.

More measurements are needed to determine how repeatable the oscillations are and what is their correlation with the chamber floor vibrations. The total time of flame existence is about 5 times longer than that (~70 ms) reported in Ref. 22 for combustion of a single magnesium particle of 150 μm diameter, close to the average particle size in the aerosol used. Therefore, not only ignition and burn-out of a particle group adjacent to the igniter wire, but actual flame propagation into the aerosol, was observed in our experiments.
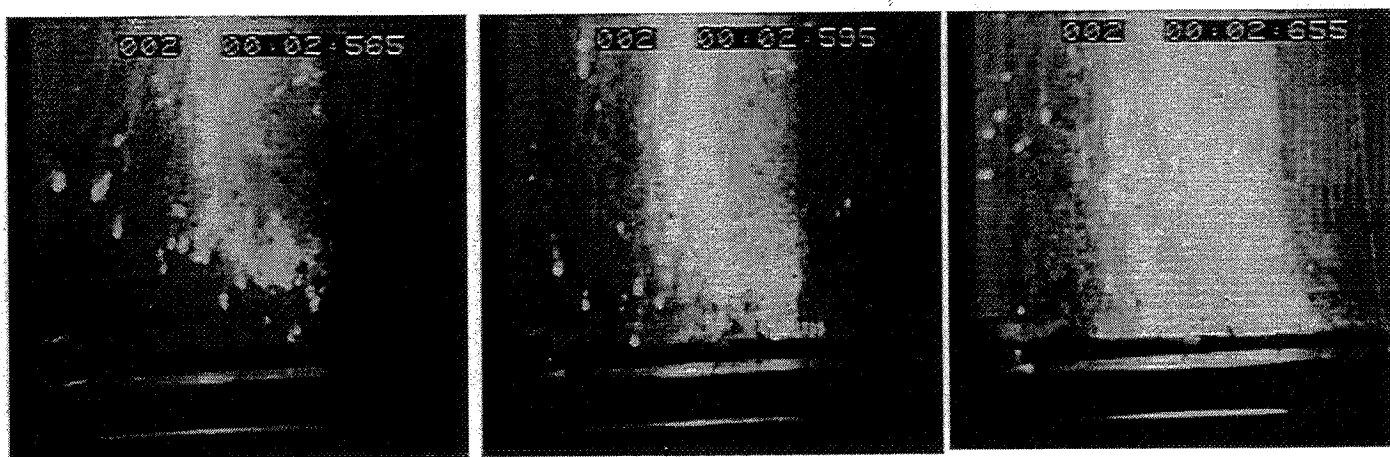
Fig. 3. Video-frame sequence showing ignition of aerosolized magnesium particles in normal gravity environment
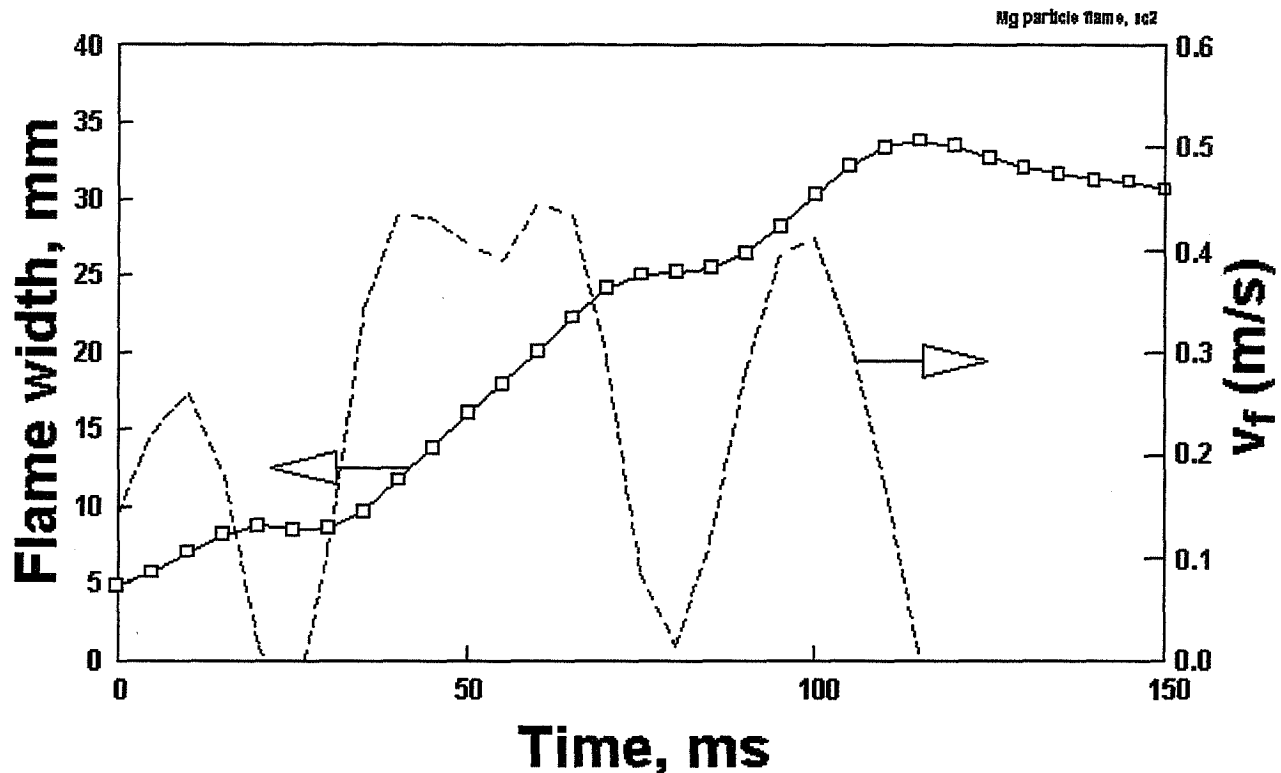
Fig. 4. Change of flame width and flame front velocity during a normal gravity
combustion experiment using aerosolized magnesium particles

SUMMARY AND PLANS

An experimental program is initiated to study the effects of the interaction of burning metal particles on ignition and combustion of metal aerosols. The idea is to use the microgravity environment to aerosolize and ignite metal particles which are large enough to observe, but would rapidly settle down at normal gravity. Using large particles makes it possible to observe development and merging of individual particle flames during aerosol combustion. An experimental apparatus has been designed and built and normal gravity ignition experiments using 150-200 μm diameter magnesium particles have been conducted. Initial microgravity tests using the 2.2 s Drop Tower of the NASA Lewis RC are scheduled for April, 1997.

ACKNOWLWDGEMENT

REFERENCES

1.   Annamalai, K., and Ryan, W., "Interactive Processes in Gasification and Combustion. Part I: Liquid Drop Arrays and Clouds," *Prog. Ener. Combus. Sci.* 18:221-295 (1992).
2.   Mikami, M., Kato, H., Sato, J., and Kono, M., "Interactive Combustion of Two Droplets in Microgravity," Twenty-Fifth Symposium (International) on Combustion, The Combustion Institute, Pittsburgh, 1994, pp. 431-438.
3.   Kono, M., "Japan's Research on Droplet and Droplet Array Combustion," Third International Microgravity Combustion Workshop, NASA CP 10174, pp. 83-88 (1995).

4.   Itoh, A. and Kurosaki, Y., "Downward Flame Spread Along Several Vertical Parallel Sheets of Paper," *Combust. Flame* 60:269-277 (1985).

5.   Tamanini, F. and Moussa, A.N., "Experiments on Turbulent Burning of Vertical Parallel Walls," *Combust. Sci. Tech.* 23:143-151 (1980).

6.   Urban, D.L., "Interactions Between Flames on Parallel Solid Surfaces," Third International Microgravity Combustion Workshop, NASA CP 10174, pp. 233-238 (1995).

7.   Leushke, G., "Beitrage zur Erforschung des Mechanismus der Flammenausbreitung in Staubwolken," *Staub* 25, pp.180-186 (1965).

8.   Eckhoff R.K., Dust Explosions in Process Industries, Butterworth-Heinemann, 1991.

9.   Friedman, R., and Macek, A. "Ignition and Combustion of Aluminum in Hot Ambient Gases," *Combust. Flame,* 6:9-19 (1962).

10. Drew, C.M., Gordon, A.S., Knipe, R.H., Kraeutle, K.J., Prentice J.L., and Price, E.W. Metal Particle Combustion Progress Report, Naval Weapons Center, China Lake, CA, *NWC TP 4435* (1968).

11. Prentice, J.L., "Combustion of Pulse-Heated Single Particles of Aluminum and Beryllium," *Combust. Sci. Tech.* 1: 358-398 (1970).

12. Nelson, L.S., Rosner, D.E., Kurzius, S.C., and Levine, H.S., "Combustion of Zirconium Droplets in Oxygen/Rare Gas Mixtures-Kinetics and Mechanism," Twelfth Symposium (International) on Combustion, The Combustion Institute, Pittsburgh, 1968, pp. 59-70.

13. Dreizin, E.L., Suslov, A.V., and Trunov, M.A., "General Trends in Metal Particle Heterogeneous Combustion," *Combust. Sci. Tech.* 90:79-99 (1993).

14. Florko, A.V. and Golovko, V.V., "Characteristics of the Radiation Emitted by and the Conditions for Nucleation of Submicron Oxide Particles During Combustion of Magnesium," *Fizika Gorerniya i Vzryva* 29:17-22 (1992) (in Russian).

15. Dreizin, E.L., Molodetsky, I.E., and Law, C.K., "Internal and Surface Phenomena in Metal Combustion," Third International Microgravity Combustion Workshop, Cleveland, OH, NASA CP 10174, pp. 129-134 (1995).

16. Florko, A.V., Kozitslii, S.V., Zolotko, A.N., and Golovko, V.V., "Mechanism of Transport of Condensed Combustion Producers to the Surface of a Burning Magnesium Particle," *Fizika Goreniya i Vzryva* 19:24-29 (1983) (in Russian).

17. Golovko, V.V., Kozitskii, S.V., and Florko, A.V., "Electric Field of a Single Burning Magnesium Particle," *Fizika Goreniya i Vzryva* 2:27-32 (1984) (in Russian).

18. Dreizin, E.L., "Internal and Surface Phenomena in Heterogeneous Metal Combustion," Fourth International Microgravity Combustion Workshop, Cleveland, OH (1997) (this volume).

19. Shevchuk, V.G., Goroshin, S.A., Klyachko, L.A., Ageyev, N.D., Kondratyev, E.N., and Zolotko, A.N., "Speed of Flame Propagation in Magnesium Particle Aerosols," *Fizika Gorenia i Vzryva* No. 1, pp. 57-63 (1980) (in Russian).

20. Lan, Y., and Rosato, A.D., "Macroscopic Behavior of Vibrating Beds of Smooth Inelastic Spheres," *Phys. Fluids* 7(8):1818-1831 (1995).

21. Ballal, D.R., "Flame Propagation Through Dust Clouds of Carbon, Coal, Aluminum, and Magnesium in an Environment of Zero Gravity," *Proc. R. Soc. Lond.* A 385, pp. 21-51 (1983).

22. Valov, A.E., Kustov, Y.A., and Shevtsov, V.I., "Spectroscopic Study of the Combustion of Solitary Magnesium Particle in Air and in Carbon Dioxide," *Combustion, Explosion, and Shock Waves* 30:431-436 (1994).

Gaseous Diffusion Flames

Page intentionally left blank

RADIATION TEMPERATURE AND EXTINCTION OF TRANSIENT GASEOUS DIFFUSION FLAMES IN MICROGRAVITY

ARVIND ATREYA, DAVID A. EVEREST, SANJAY AGRAWAL and MICHAEL K. ANDERSON
University of Michigan; Ann Arbor, MI 48109

INTRODUCTION

The absence of buoyancy-induced flows in μg and the resulting increase in the reactant residence time significantly alters the fundamentals of many combustion processes. Substantial differences between 1-g and μg flames have been reported in experiments on candle flames [1, 2], flame spread over solids [3, 4], droplet combustion [5, 6] and others. These differences are more basic than just in the visible flame shape. Longer residence times and higher concentration of combustion products in the flame zone create a thermochemical environment which changes the flame chemistry and the heat and mass transfer processes. Processes such as flame radiation (and its interaction with flame chemistry), that are often ignored under normal gravity, become very important and sometimes even controlling. This is particularly true for conditions at extinction of a μg diffusion flame.

Under 1-g, the buoyancy-generated flow, which may be characterized by a strain rate, assists the diffusion process to transport the fuel and the oxidizer to the combustion zone and remove the hot combustion products from it. These are essential functions for the survival of the flame which needs fuel and oxidizer. Numerical calculations [7] show that even flames with no heat loss become "weak" (diminished burning rate per unit flame area) in the absence of flow or zero strain rate. Thus, as the strain rate (or the flow rate) is increased, the diffusion flame which is "weak" at low strain rates is initially "strengthened" and eventually it may be "blown-out." The computed flammability boundaries show that such a reversal in flammability occurs at strain rates around 5 sec^{-1} [8]. Also, model calculations of zero strain rate transient diffusion flames show that even gas radiation is sufficient to extinguish the flame [7]. Yet, the literature substantially lacks systematic experimental confirmation of low strain rate, radiation-induced, extinction of diffusion flames. Experimentally, this can only be accomplished under microgravity conditions.

The lack of buoyant flow in μg also enhances the flame radiation due to: (i) build-up of combustion products in the flame zone which increases the gas radiation, and (ii) longer residence times make conditions appropriate for substantial amounts of soot to form which is usually responsible for most of the radiative heat loss. Thus, it is anticipated that radiative heat loss may eventually extinguish the already "weak" μg diffusion flame. While this is a convincing hypothesis, space shuttle experiments on candle flames show that in an infinite ambient atmosphere, the hemispherical candle flame in μg will burn indefinitely [1]. It is hoped that radiative extinction can be experimentally shown by the aerodynamically stabilized gaseous diffusion flames for certain conditions. Identifying these conditions (ambient atmosphere, fuel flow rate, fuel type, fuel additives, etc.) is important for spacecraft fire safety. *The objective of this research is to experimentally and theoretically investigate the radiation-induced extinction of gaseous diffusion flames and understand the interaction of flame radiation with flame chemistry.*

RESEARCH APPROACH

To experimentally investigate radiation-induced extinction, spherical geometry is being used for μg for the following reasons: (i) It reduces the complexity by making the problem one-dimensional. Thus, it is convenient for both experimental measurements and theoretical modeling. (ii) The spherical diffusion flame completely encloses the soot which is formed on the fuel rich side of the reaction zone. This increases the importance of flame radiation because now both soot and gaseous combustion products co-exist inside the high temperature spherical diffusion flame. It also increases the possibility of radiative extinction due to soot crossing the high temperature reaction zone. (iii) For small fuel injection velocities, as is usually the case for a pyrolyzing solid, the diffusion controlled flame in μg around the pyrolyzing solid naturally develops spherical symmetry. Thus, spherical diffusion flames are of interest to fires in μg.

To theoretically investigate the radiation-induced extinction limits, knowledge of the rates of production and destruction of soot and other combustion products in the thermochemical environment existing under μg conditions is essential. This requires detailed optical and gas chromatographic measurements that are not easily possible under μg conditions. Thus, supplementary 1-g experiments with detailed chemical measurements are needed. The spherical burner, however, is not suitable for these detailed 1-g experiments due to the complex buoyancy-induced flow field generated around it. Thus, a one-dimensional counterflow diffusion flame is used. At low strain rates, with the diffusion flame on the fuel side of the stagnation plane, conditions similar to the μg case are created -- soot is again forced through the high temperature reaction zone. Furthermore, high concentration of combustion products in the sooting zone can be easily obtained by adding appropriate amounts of CO_2 and H_2O to the fuel and/or the oxidizer streams. These 1-g experiments will support the development of detailed chemistry transient models for both μg and 1-g cases.

Considerable effort has been spent to ensure the success of both the μg and the 1-g experiments. It is experimentally quite difficult to obtain aerodynamically stabilized gaseous spherical diffusion flames for μg experiments and low strain rate (~ 5 sec^{-1}) counterflow diffusion flames for 1-g experiments. To obtain experimental confirmation of radiation-induced extinction and data for comparison with theoretical models, several μg experiments are being conducted as functions of the following variables: (i) ambient oxygen concentration, (ii) enhanced CO_2% & H_2O% in the atmosphere, (iii) different fuel flow rates, (iv) different fuel types and fuel additives. This data will help understand and quantify the interaction of flame radiation with flame chemistry and conditions that lead to radiative extinction. Supporting 1-g experiments with detailed chemical measurements are also being conducted for ethylene and acetylene with high concentration of combustion products in the vicinity of the reaction zone.

RESULTS

μg Theoretical Work: We first discuss a theoretical formulation for transient radiative diffusion flames to show the relationship between 1-g and μg parts and to motivate the experiments. The formulation presented here is for the simplest case of constant pressure ideal gas reactions, Le=1 and one-step chemistry. Eventually detailed chemistry and transport properties will be included to better understand the interaction between radiation and chemistry that leads to the limit phenomenon of radiative extinction. Chemistry is represented by:

$$\nu_F F + \nu_O O \rightarrow \sum_{i=1}^{N-2} \nu_i P_i \quad ; \text{with q}^\circ, \text{ the standard heat of reaction, given by: } q^\circ = h_F^o M_F \nu_F + h_O^o M_O \nu_O - \sum_{i=1}^{N-2} h_i^o M_i \nu_i \text{ and}$$

$Q = q^\circ / M_F \nu_F$ is the heat released per unit mass of fuel. Within these assumptions, we may write the following governing equations for any geometrical configuration (spherical or counterflow):

$$\textit{Mass Conservation:} \quad \frac{\partial \rho}{\partial t} + \vec{\nabla} \cdot (\rho \vec{v}) = 0 \quad ; \quad \textit{Ideal Gas:} \quad \rho T = \rho_\infty T_\infty \tag{1}$$

$$\textit{Species Conservation:} \quad \rho \frac{\partial Y_i}{\partial t} + \rho \vec{v} \cdot \vec{\nabla} Y_i - \vec{\nabla} \cdot (\rho D \vec{\nabla} Y_i) = w_i \tag{2}$$

$$\textit{Energy Conservation:} \quad \rho \frac{\partial h^s}{\partial t} + \rho \vec{v} \cdot \vec{\nabla} h^s - \vec{\nabla} \cdot (\rho D \vec{\nabla} h^s) = -\sum_i h_i^o w_i - \tag{3}$$

Here, the symbols have their usual definitions with ρ = density, T = temperature, v = velocity, Y_i = mass fraction of species i, h^s = sensible enthalpy, w_i = mass production or destruction rate per unit volume of species i and D = diffusion coefficient. The last three terms in Equ (3) respectively are: the chemical heat release rate due to gas phase combustion, the radiative heat loss rate per unit volume and the chemical heat released due to soot oxidation. The above equations, however, are insufficient because soot volume fraction must be known as a function of space and time to determine the radiative heat loss. To enable describing soot in a simple manner, we define the mass fraction of atomic constituents as follows: $\xi_j = \sum_i \left(M_j \nu_i^j / M_i \right) Y_i$ where M_i is the molecular weight of species i, M_j is the atomic weight of atom j and ν^j is the number of atoms of kind j in specie i. Assuming that the only atomic constituents present in the hydrocarbon flame are C, H, O & Inert and with $Y_{soot} \equiv \Phi \equiv \rho_s f_v / \rho$ (where: ρ_s = soot density & f_v = soot volume fraction), we obtain: $\xi_C + \xi_H + \xi_O + \xi_I + \rho_s f_v / \rho = 1$. Defining $\xi_C + \xi_H = \xi_F$ and $Z_F = \xi_F Y_{F\infty}$ we obtain $Z = \left[(\xi_F)_{F\infty} Z_F + \rho_s f_v / \rho \right]$ as the conserved scalar for a sooty flame. This yields the following soot conservation equation:

64

Soot Conservation: $\rho \dfrac{\partial \Phi}{\partial t} + \rho \vec{v} \cdot \vec{\nabla}(\Phi) - \vec{\nabla} \cdot [\rho D_s \vec{\nabla}(\Phi)] = \dot{m}_{S_p}''' - \dot{m}_{S_o}''$ (4)

The corresponding fuel equation becomes:

Fuel Conservation: $\rho \dfrac{\partial Z_F}{\partial t} + \rho \vec{v} \cdot \vec{\nabla}(Z_F) - \vec{\nabla} \cdot [\rho D \vec{\nabla}(Z_F)] = -\dfrac{1}{Y_{F\infty}} (\dot{m}_{S_p}'')$ (5)

The oxygen conservation equation for Z_O defined as $Z_O = \xi_O / Y_{O\infty}$ is obtained as:

Oxygen Conservation: $\rho \dfrac{\partial Z_O}{\partial t} + \rho \vec{v} \cdot \vec{\nabla}(Z_O) - \vec{\nabla} \cdot [\rho D \vec{\nabla}(Z_O)] = 0$ (6)

Under conditions of small soot loading, the soot terms in the energy and the fuel conservation equations (3) & (5), can be ignored. Thus, Equ.(5) may be considered homogeneous to a good approximation and becomes similar to Equ. (6). Thus, Φ calculated from the soot equation can be used to determine the radiative heat loss term in the energy equation.

The above formulation requires a description of soot formation ($\dot{m}_{S_p}''$) and oxidation ($\dot{m}_{S_o}''$) terms. To experimentally determine these terms, measurements of soot volume fraction, soot number density, temperature, velocity and species profiles are needed. These measurements along with detailed chemical measurements are being made in the l-g flames under enhanced combustion products environment (simulated μg). The most convenient l-g flame is the counterflow diffusion flame because it simplifies the above PDE's to ODE's.

μg Experimental Work: Several μg experiments under ambient pressure and oxygen concentration conditions, were performed with methane (less sooty), ethylene (sooty), and acetylene (very sooty) for flow rates ranging from 4 to 28 cm³/s. However, in all the experiments conducted to-date with different fuels and flow rates, radiative extinction was not achieved. Thus, future experiments will be conducted with larger fuel flow rates, perhaps soot promoting fuel additives and different ambient atmospheres. In these experiments, the following measurements were made: (1) *flame radius:* - measured from photographs taken by a color CCD camera. Image processing was used to determine both the flame radius and the relative image intensity. (2) *flame radiation:* - measured by three photodiodes with different spectral absorptivities. The first photodiode essentially measures the blue & green radiation, the second photodiode captures the yellow, red & near infra-red radiation, and the third photodiode is for infra-red radiation from 0.8 to 1.8 µm. (3) *flame temperature:* - measured by two S-type thermocouples and the sphere surface temperature was measured by a K-type thermocouple. In both cases 0.003" diameter wire was used. The measured temperatures were later corrected for time response and radiation.

In μg experiments it was observed that for all fuels (methane, ethylene and acetylene), initially the flame is blue (non-sooty) but becomes bright yellow (sooty) under μg conditions. Later, as the μg time progresses, the flame grows in size and becomes orange and less luminous and the soot luminosity seems to disappear. A possible explanation for this observed behavior is suggested by the theoretical calculations of Refs. [7]. It seems that at the onset of µg conditions, initially a lot of soot is formed in the vicinity of the flame front resulting in bright yellow emission. As the flame grows, several events reduce the flame luminosity: (i) The high concentration of combustion products left behind by the flame front inhibits the formation of new soot and promotes soot oxidation. (ii) The primary reaction zone, seeking oxygen, moves away from the soot region and the soot is pushed toward cooler regions by thermophoresis. Both these effects increase the distance between the soot layer and the reaction zone. (iii) The dilution and radiative heat losses caused by the increase in the concentration of the combustion products reduces the flame temperature which in turn reduces the soot formation rate and the flame luminosity.

It was further observed that, for the same fuel flow rate, methane flames eventually become blue (non-sooty) in approximately one second, ethylene flames became blue toward the end of the μg time (i.e. ~2 sec) while acetylene flames remained luminous yellow throughout the 2.2 sec μg time (although the intensity was significantly reduced). This is because of the higher sooting tendency of acetylene which enables soot formation to persist for a longer time. Thus, acetylene soot remains closer to the high temperature reaction zone for a longer time making the average soot temperature higher and the distance between the soot and the reaction layers smaller. Eventually, even the acetylene flames will become blue in μg. A detailed account of these measurements and observations is presented in Ref.[9].

μg Modeling Work: As a first step, it was of interest to see if the transient expansion of *μg* spherical diffusion flames could be predicted without including soot and flame radiation and in the limit of infinite reaction rates. This simple model was very informative and was presented in Ref.[10]. Our more recent calculatioens were done with a second order overall finite rate reaction and gas radiation. A detailed chemistry model is currently under development. The gas radiation model and other reaction rate constants used were identical to those described in Ref. [7]. Equations (1) through (4) for the 1-D spherical case were numerically solved assuming Le =1 and ρD = constant. Boundary conditions at R = R_i were:

$$at \ R=R_i: \quad T=T_\infty; \quad Y_F=1; \quad Y_O=0; \quad Y_P=0; \quad and \ Fuel \ injection \ rate = \dot{M}(t) = 4\pi R_i^2 (\rho v)_{@R_i}$$

where R_i was taken as 0.15 cm, and $as \ R \rightarrow \infty: \quad T=T_\infty; \quad Y_F=0; \quad Y_O=Y_{O\infty}; \quad Y_P=Y_{P\infty}$. Also, initial spatial distribution of temperature and species based on infinite reaction rate solution was assumed.

Model calculations for four cases are shown in Figures 1 and 2. The four cases are: (i) Case 1 - No flame radiation & fuel flow rate = 22 cm³/s of methane; (ii) Case 2 - same as case 1 but with gas radiation; (iii) Case 3 - same as case 2 but with increased ambient product concentration, $Y_{P\infty}$= 0.2 instead of zero; (iv) Case 4 - same as case 2 but with a step change in fuel flow rate from 2 cm³/s until flame radius of 1.3 cm and 22 cm³/s thereafter. Figure 1a shows several calculated flame radii for different fuel flow rates for both with and without flame radiation. Clearly, the flame radius increases with the fuel flow rate and decreases substantially due to gas radiation. Essentially, as the gas inside the spherical flame looses heat via radiation, its temperature falls and its density increases. Thus, the spherical flame collapses as is evident from Figures 1 and 2 which are time sequences of gas density and velocity. Figure 2 actually shows that there is a reversal in the gas velocities near the flame zone due to the collapsing spherical flame. However, the net flame radius still increases, albeit slowly. Figure 1b shows that for Case 3 the flame temperature falls below 1000K within 1 second. Thus, radiative extinction is possible for certain atmospheres. Also, as seen from Figure 1d, the burning rate per unit area decreases as the flame expands and radiation contributes to this decrease.

REFERENCES

1. *Dietrich, D. L., Ross, H. D. and T'ien, J. S.* "Candle Flames in Microgravity," Third Microgravity Combustion Workshop, Cleveland, Ohio, April, 1995.
2. *Ross, H. D., Sotos, R. G. and T'ien, J. S.,* Combustion Science and Technology, Vol. 75, pp. 155-160, 1991.
3. *T'ien, J. S., Sacksteder, K. R., Ferkul, P. V. and Grayson, G. D.* "Combustion of Solid Fuels in very Low Speed Oxygen Streams," Second International Microgravity Combustion Workshop," NASA Conference Publication, 1992.
4. *Ferkul, P., V.,* "A Model of Concurrent Flow Flame Spread Over a Thin Solid Fuel," NASA Contractor Report 191111, 1993.
5. *Avedisian, C., T.* "Multicomponent Droplet Combustion and Soot Formation in Microgravity," Third Microgravity Combustion Workshop, Cleveland, Ohio, April, 1995.
6. *Jackson, G., S., Avedisian, C., T. and Yang, J., C.,* Int. J. Heat Mass Transfer., Vol.35, No. 8, pp. 2017-2033, 1992.
7. *Atreya, A. and Agrawal, S.,* "Effect of Radiative Heat Loss on Diffusion Flames in Quiescent Microgravity Atmosphere," *Combustion & Flame,* (accepted for publication), 1995.
8. *T'ien, J. S.,* Combustion and Flame, Vol. 80, pp. 355-357, 1990.
9. *Pickett, K., Atreya, A., Agrawal, S., and Sacksteder, K.,* "Radiation from Unsteady Spherical Diffusion Flames in Microgravity," AIAA paper # 95-0148, January 1995.
10. *Atreya, A, Agrawal, S., Sacksteder, K., and Baum, H.,* "Observations of Methane and Ethylene Diffusion Flames Stabilized around a Blowing Porous Sphere under Microgravity Conditions," AIAA paper # 94-0572, January 1994.
11. *Law, C. K. and Faeth, G. M.,* Prog. Energy Combust. Sci., Vol. 20, 1994, pp. 65-116.
12. *Williams, F.A.,* Combustion Theory, Benjamin/Cummings Publishing Co., 2nd Ed.(1985).
13. *T'ien, J.S.,* "Diffusion Flame Extinction ... the Mechanism of Radiative Heat Loss," Comb.& Flame, 65, pp.31-34(1986).
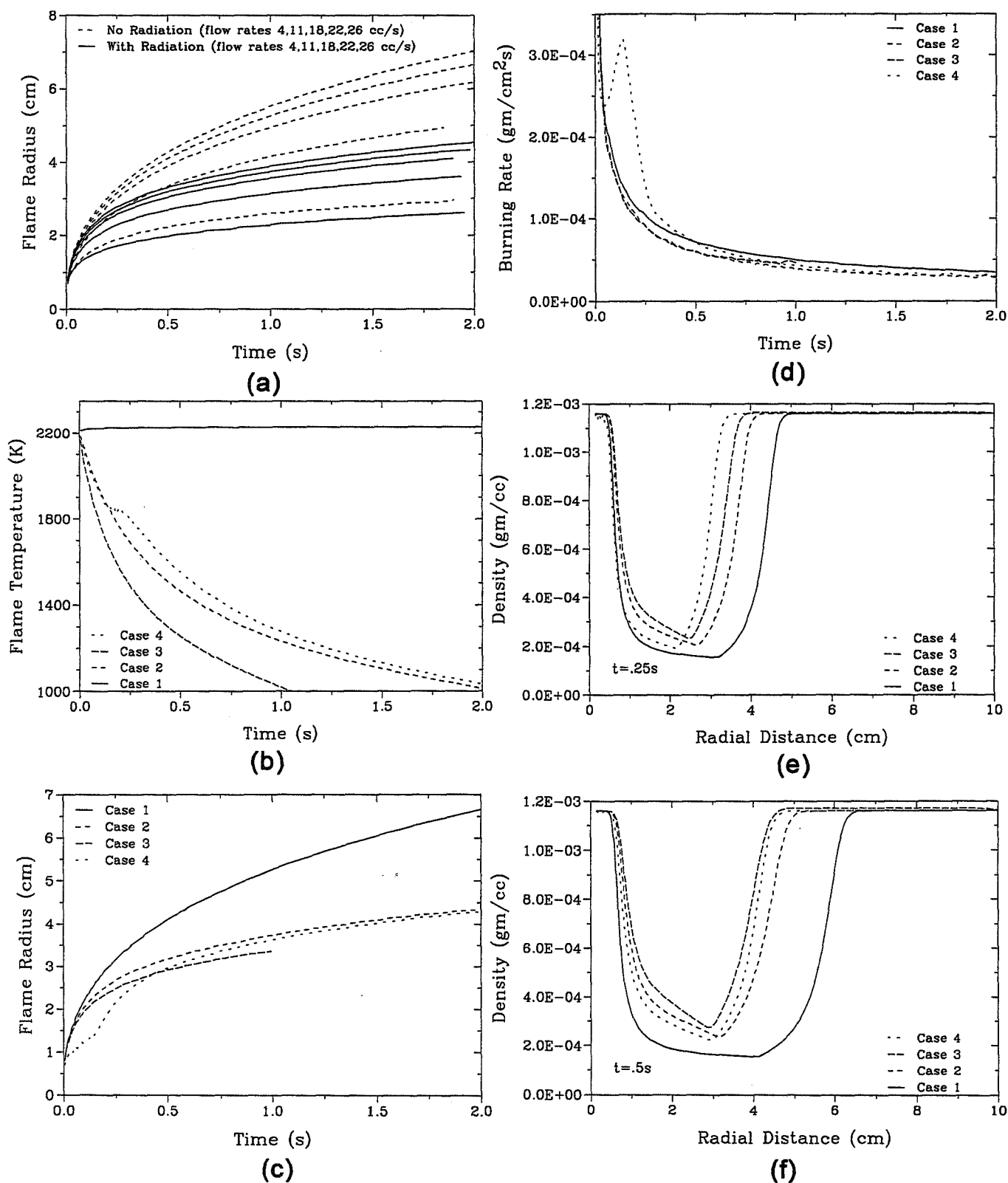
(a)

(b)

(c)

(d)

(e)

(f)

Case1: No Radiation ; Case2: With gas radiation ; Case3: With radiation
& Yip = 0.2 ; Case4: With radiation & step change in fuel flow rate.

Figure 1
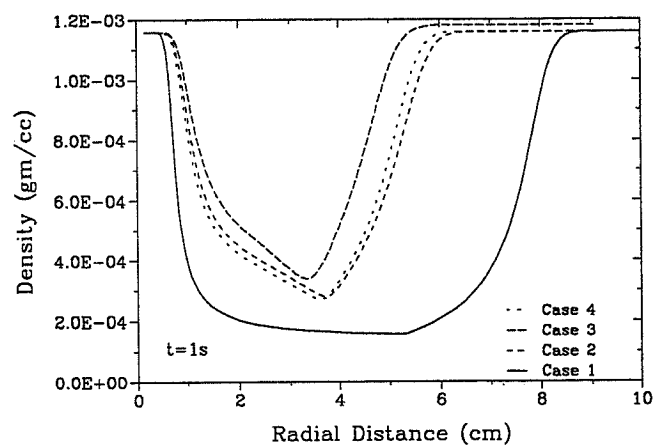
(a)
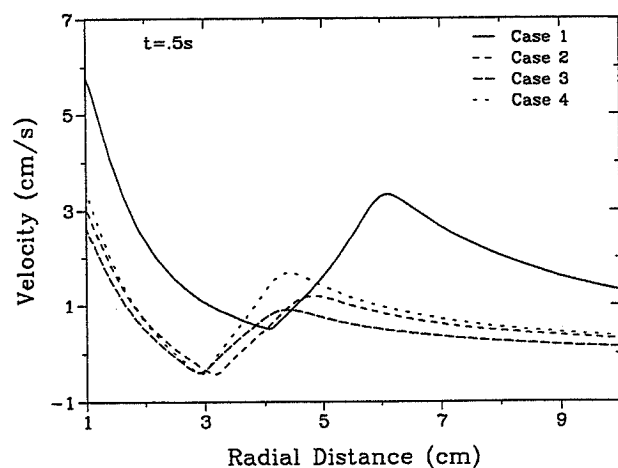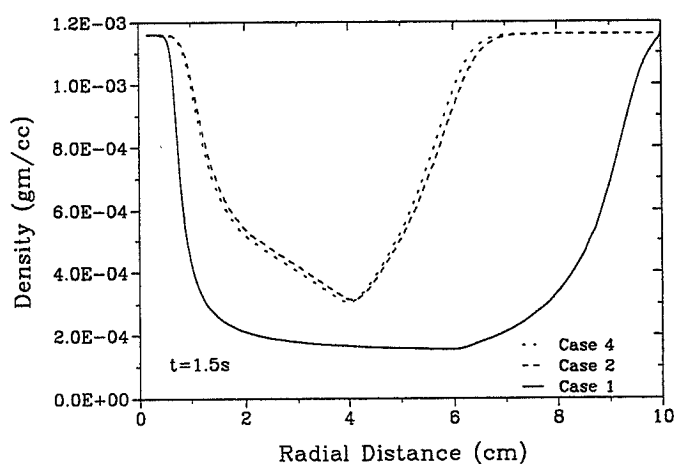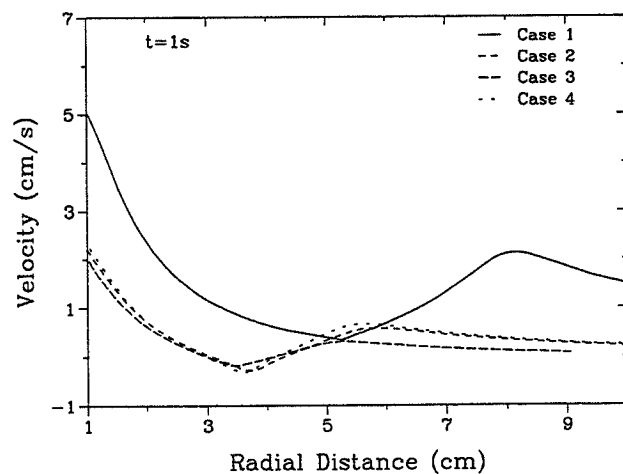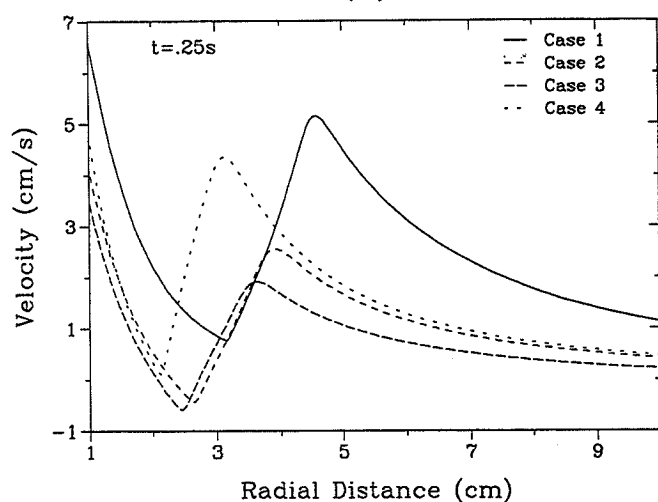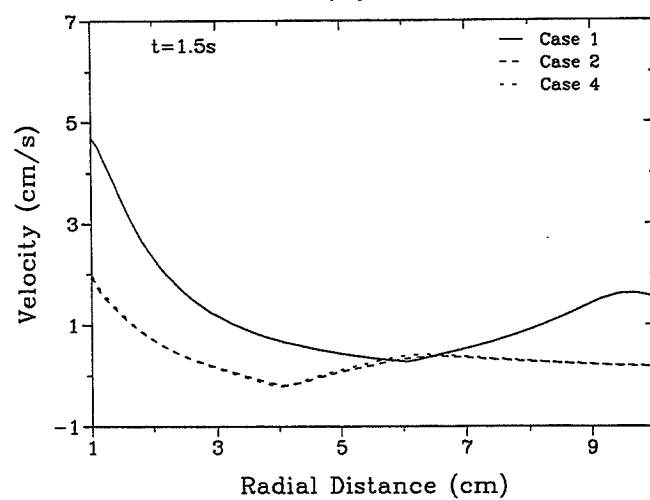
(b)

(c)

(d)

(e)

(f)

Case1: No Radiation ; Case2: With gas radiation ; Case3: With radiation & Yip = 0.2 ; Case4: With radiation & step change in fuel flow rate.

Figure 2

STUDIES OF FLAME STRUCTURE IN MICROGRAVITY*

C. K. Law, C. J. Sung, and D. L. Zhu
Department of Mechanical and Aerospace Engineering
Princeton University, Princeton, NJ 08544

Introduction

The present research endeavor is concerned with gaining fundamental understanding of the configuration, structure, and dynamics of laminar premixed and diffusion flames under conditions of negligible effects of gravity. Of particular interest is the potential to establish and hence study the properties of spherically- and cylindrically-symmetric flames [1] and their response to external forces not related to gravity. For example, in an earlier experimental study [2] of the burner-stabilized cylindrical premixed flames, the possibility of flame stabilization through flow divergence was established, while the resulting one-dimensional, adiabatic, stretchless flame also allowed an accurate means of determining the laminar flame speeds of combustible mixtures.

We have recently extended our studies of the flame structure in microgravity along the following directions: (1) Analysis of the dynamics of spherical premixed flames; (2) Analysis of the spreading of cylindrical diffusion flames; (3) Experimental observation of an interesting dual luminous zone structure of a steady-state, micro-buoyancy, spherical diffusion flame of air burning in a hydrogen/methane mixture environment, and its subsequent quantification through computational simulation with detailed chemistry and transport; (4) Experimental quantification of the unsteady growth of a spherical diffusion flame; and (5) Computational simulation of stretched, diffusionally-imbalanced premixed flames near and beyond the conventional limits of flammability, and the substantiation of the concept of extended limits of flammability. Motivation and results of these investigations are individually discussed in the following.

Results and Discussion

Response of Spherical Premixed flames under Rotation

In this investigation we are interested in understanding the influence of spinning a spherical porous burner on the response of the otherwise spherical premixed flame stabilized by the burner. Fluid mechanically such a spinning generates an inward flow toward the burner at the poles and an outward flow at the equator. The flow induces well-controlled stretch rates which vary over the flame surface. From practical considerations, the study is of relevance to the phenomena of flame-vortex interactions in turbulent flows, as well as the combustion of spinning monopropellant droplets in highly-stratified flow fields such as those downstream of the fuel injection nozzle.

Extending the previous analysis of Lozinski and Matalon [3] of a spinning fuel droplet undergoing diffusional burning to the burner-stabilized premixed flame, results were obtained [4] for all the relevant combustion responses including the burning rate and distorted flame shape. The induced nonradial flow affects the flame response in three ways: by altering heat transfer and flame curvature, and by inducing flame stretch through nonequidiffusion. Specifically, for unity Lewis number (Le), flame stretch is eliminated and the response is affected only by the flow field and heat loss. If the flame is adiabatic, rotation then causes the flame to move toward the poles and away from the equator, as shown in Fig. 1(a). However, when the ambient temperature is held at sub-adiabatic values, the flame near the poles experiences a greater downstream heat loss and consequently burns weaker and retreats from the burner. Conversely, near the equator the flame burns stronger and moves toward the burner surface. As such, the flame is distorted into an elongated, pancake shape protruding outward at the poles as shown in Fig. 1(b).

This scenario changes when non-unity Le is considered. The nonuniform flow field induced by rotation imparts a positive (negative) stretch in the vicinity of the poles (equator). The flame temperature therefore increases (decreases) near the poles (equator) when Le<1 and the converse situation occurs when Le>1. Thus as Le is increased, the distorted flame shape may change from one protruding outward at the equator to one protruding at the poles.

Spreading of Unsteady Cylindrical Diffusion Flames

It is well known that because of the wave nature of a premixed flame, it can achieve stationarity in the planar, cylindrical and spherical configurations [2, 5, 6]. On the other hand, because of the fundamentally diffusive nature of nonpremixed flames, stationarity can be achieved only in the spherical configuration. As such, the one-dimensional planar and cylindrical diffusion flames are inherently unsteady and consequently research on steady, one-dimensional diffusion flames has focused on the spherical configuration. There is, however, fundamental interest in understanding the behavior of cylindrical diffusion flames because of their intrinsic unsteadiness - a feature which is not captured by spherical diffusion flames. We have therefore analytically studied the evolution of the flame dynamics in the flame-sheet limit, with particular interest in identifying the characteristic spatial and temporal scales which govern such an evolution. Results [7] showed that the flame movement is mainly controlled by the ambient oxidizer concentration, relative to the fuel concentration, and transport diffusivity. Thus, with large ambient oxidizer concentrations, the flame behaves quasi-steadily such that its spreading rate lags that of diffusion. However, for small ambient oxidizer concentrations, the diffusion rate is smaller than the flame propagation rate, and quasi-steadiness does not exist. As the flame is far away from the burner surface, the flame temperature approaches the adiabatic diffusion flame temperature, which depends only on the ambient oxidizer concentration. For $M=1$, the ratio of the flame radius scaled by R, r_f, to the characteristic diffusion length, $r_f/\sqrt{t}$, is plotted versus time t (nondimensionalized by R^2/a) for different stoichiometrically-scaled mass fraction of the ambient oxidizer concentration $Y_{0,\infty}$ in Fig. 2, where M is the fuel burning rate per unit length scaled by $2\pi\alpha\rho$, α the thermal diffusivity, and R the burner radius. It shows that quasi-steadiness is a valid assumption for large $Y_{0,\infty}$ since $r_f/\sqrt{t}<1$. But for small $Y_{0,\infty}$, we have $r_f/\sqrt{t}>1$ and the quasi-steady assumption breaks down. Furthermore, Fig. 3 shows that the effect of $M>1$ (<1) is simply to induce the flame to move faster (slower) as more (less) fuel is convected toward the ambiance.

Micro-Buoyancy Spherical Diffusion Flames and Dual Luminous Zone Structure

Extensive µg experiments have been conducted with droplet combustion. While such experiments are of value in their own right, the small dimension and the intrinsic unsteadiness impose complications for their usefulness in flame structure studies. These difficulties are circumvented with our steady-state, burner-generated spherical diffusion flames.

As a complementary study to µg-experiments, in the present investigation we have first established a fairly buoyancy-free burner-supported spherical diffusion flame under normal gravity. The flame diameter can be as large as 4 cm or more. The sphericity, exceeding 0.9, is achieved in the following manner: (1) Reduced pressure below 1/4 atmosphere. (2) Inverse flame in that the environment is the fuel while air issues from the burner. Apparently this eliminates the influence of soot-related species which are formed on the fuel side of the flame to distort the flame shape if the fuel were on the interior side of the flame. (3) A light environment comprising fuels of low molecular weights to minimize the density stratification. Presently we use pure hydrogen or a hydrogen/methane mixture. The availability of such a long-duration, steady diffusion flame of large dimension allows detailed experimental quantification of the flame structure, which can then be compared with the computationally simulated values with detailed chemistry and transport to allow the extraction of fundamental information of the governing flame kinetics.

The spherical burner employed is made of a porous bronze material with 5 µm pore size, 1.27 cm diameter, and is supported by a 1.5 mm o.d. stainless steel capillary through which gas is fed to the burner. The burner is held in the center of a vacuum chamber, with an inside dimension of 40x40x40 cm^3. The gas composition within the chamber is kept constant with continuous ventilation. Ignition is achieved by a high voltage spark ignition. A translatable K-type thermocouple measures the flame temperature profile in the radial direction. The flame image is photographed by both regular camera and video recorder.

Figure 4 shows a flame formed by issuing a 10%O_2/90%N_2 oxidizer of mass flow rate m=0.08 g/s into a pure hydrogen environment (99.997% purity) at a pressure of 0.2 atm. The flame is viewed from the end of the burner in the direction of the oxidizer-supply tube. The weak luminosity is perhaps due to a minute quantity of impurity.

Interestingly, with a small amount of methane addition, we found that the diffusion flame consisted of two luminous "sheets" separated by a dark zone. That is, an additional "flame", or rather a luminous zone, was established external to the original, pure hydrogen flame. Subsequent investigation with counterflow flames also revealed such a structure which, however, was very hard to detect. Thus were it not for the availability of the present micro-buoyancy, large-scale diffusion flame, this important flame structure would not have been discovered.

To be more specific, the flame in Fig. 5 has a small amount of methane addition (1.6%) with the mass flow rate of oxidizer kept constant, and shows the presence of an additional flame external to the original flame.

Furthermore, the external flame appears to be green, while the inner luminosity is bluish. With further addition of methane (9.5%), the external flame gradually merged into the inner flame, as shown in Fig. 6.

The green radiation observed is believed to be due to excited C_2 (C_2^*). Since the maximum temperature occurs between the inner flame and the pure hydrogen flame is basically non-luminous in the visible regime of the spectrum, the blue emission is postulated to be caused by the chemiluminescence of excited CO_2. Using the measured temperatures at the burner surface and far away from it, as well as the injection mass flow of air as boundary conditions, the experimental situation was computationally simulated with detailed chemistry (GRI-Mech 1.2) and transport properties. The computed location of the maximum flame temperature agrees fairly well with the experimental value, as shown in Fig. 7. Based on the computed flame structure, the chemiluminescence intensity of excited CO_2 (I) was postprocessed following a second order dependence: $I=I_0[CO][O]$. The magnitude and temperature dependence of I_0 were taken from Baulch et al. [8], while the rate suggested by Slack and Grillo [9] is typically a factor of five smaller. Furthermore, since the formation/destruction reactions of excited C_2 in hydrocarbon flames has not been well-established, as a first step, the profiles of the excited CH (CH^*) was computed by including few reactions related to CH^* in the GRI-Mech. This is because for $premixed$ conditions, the profiles of CH and C_2, as well as CH^* and C_2^*, occur approximately at the same location in the flame. The reactions and rate parameters for CH^* were taken from Ref. 10. It is however to be noted that the only source of CH^* available is through C_2H+O_2, while the important C_2+OH reaction, which is one of the main routes for formation of CH^* [11], is not considered here. The chemiluminescence intensity of CH^* is then computed as $k[CH^*]$, where k is the rate constant of the reaction $CH^*{\rightarrow}CH+h\nu$, $[CH^*]$ the concentration of CH^*, h the Planck's constant, and ν the emission frequency.

Figures 8 and 9 compare the experimental locations of the two luminous zones and the computed I and $k[CH^*]$ for 1.6% and 9.5% methane addition, respectively, with m=0.0698 g/s and p=0.1 atm. It is seen that while the peak of I falls inside the bluish luminous zone indicating that the chemiluminescence of excited CO_2 seems to be responsible for the blue emission, the peak of $k[CH^*]$ is not located in the green luminous zone. Such a misalignment between CH^* and C_2^* signifies the difference in the flame structure for premixed and nonpremixed conditions. Furthermore, computational results show that the chemiluminescence reaction plays a negligible role in the combustion process. It is seen from Figs. 8 and 9 that the product of $[C_2H]$ and $[O_2]$, $[C_2H]\times[O_2]$, follows quite well with $k[CH^*]$ such that it allows us to treat the emission of the excited species independently from the flame calculation. Since the two major routes leading to C_2^* are C+CH and CH+CH [11], $[C]\times[CH]$ and $[CH]\times[CH]$ are used as markers of the excited C_2. Figures 8 and 9 further demonstrate that both $[C]\times[CH]$ and $[CH]\times[CH]$ are situated inside the green luminous zone. Figure 10 compares the evaluation of the experimental and computational locations of the two luminous zones. It is seen that the chemiluminescence of excited CO_2 and excited C_2 seems to be responsible for the blue and green emission, respectively. With increasing addition of methane, profiles of C_2^* shift toward the oxidizer side, thereby decreasing the dark space between the two luminous zones. The peak position of I remains almost unchanged, as observed in the experimental location of the blue luminous zone.

Micro-gravity Experimentation on Burner-Supported Spherical Flames

Micro-gravity experiments were performed on both spherical premixed and diffusion flames in the NASA-Lewis 2.2-second drop tower, although only the results of diffusion flames are reported. The experiments were conducted using a porous-bronze, spherical burner (5 μm pore diameter, 1.27 cm sphere diameter). A fuel mixture of 40%H_2, 10%CH_4, and 50%N_2 issued isotropically from the burner, ignited by a hot wire mounted on a rotary solenoid, and burned in atmospheric air. A small percentage of CH_4 is included in the mixture in order to visualize the flame, whose shape and standoff distance were recorded onto video tape with a high resolution video camera. Fuel mixture mass flow rates were metered using sonic flow nozzles at predetermined upstream stagnation pressures. The fuel mixture mass flow rate was variable during the length of the experiment, being computer controlled via solenoid valves and a combination of sonic nozzles; upstream stagnation pressures were monitored by pressure transducers and recorded onto a computer. The volumetric flow rates ranged from 20 to 30mL/s. The burner was not actively cooled, due to its small size and the limited experimental duration. A thermocouple measured the burner-surface temperature, which was recorded onto a computer as a function of time.

The transient response of diffusion flames due to a step change from normal gravity to microgravity conditions was studied. A single mass flow rate of fuel issued from the porous burner for the duration of the experiment. Initially, in normal gravity, the flame shape was non-spherical, and the flame standoff distance was small due to the thinning of the boundary layer around the burner by buoyancy-induced convective flows. Upon encountering microgravity condition, the flame shape became spherical, and the flame standoff distance increased. Figure 11 plots the flame standoff distance and the burner surface temperature versus time, with t=0 representing the step change from normal gravity to microgravity.

The transient flame response due to a step change in fuel mixture mass flow rate in microgravity was also studied. Figure 12 plots the flame standoff distance and the burner surface temperature versus time (with t=0 representing the step change from normal gravity to microgravity and t=1 the step change in mass flow rate under microgravity condition). The experimental results show that the flame standoff distance increased with a step increase in fuel mixture mass flow rate, and that durations longer than 2.2 seconds are required for the diffusion flames to reach steady-state. Numerical simulation with detailed chemistry and transport is currently underway. Preliminary results demonstrate that a minimal of 10 seconds are needed for the establishment of a steady-state, spherical diffusion flame due to the nature of pure diffusive transport in microgravity.

Extended Limits of Flammability
In this investigation the response of near-flammability-limit, weakly-burning counterflow premixed flames as a function of stretch rate was computationally studied with detailed chemistry and transport properties [12]. The limit mechanisms and extinction phenomena were found to be strongly influenced by the combined effects of flame stretch, mixture nonequidiffusion, and radiative loss. For sub-unity Lewis number flames such as those of lean methane/air, the combined effects of mixture nonequidiffusion and positive stretch elevate the combustion intensity such that steady burning persists beyond the fundamental flammability limit defined for the one-dimensional planar flame (Fig. 13). Furthermore, the flame response to stretch rate variations exhibits a dual extinction turning point behavior in that flame extinction occurs not only for sufficiently large stretch rates and minimal radiative heat loss, but also for sufficiently small stretch rates and relatively substantial heat loss. Consequently, for a given mixture strength, steady combustion is possible only within a finite range of the stretch rate. This range steadily diminishes with decreasing mixture strength such that there exists a critical equivalence ratio, the extended flammability limit, beyond which steady burning for the stretch-enhanced flame also ceases to be possible. For lean propane/air flames (Fig. 14), however, the mixture Lewis numbers are greater than unity such that the combined stretch and nonequidiffusion effects always diminish the burning intensity. Consequently the transition from stretch-dominated extinction to loss-dominated extinction is monotonic in terms of the equivalence ratio and the fundamental flammability limit is the proper flammability limit. The present results agree well with the recent experimental observations [13] of near-limit lean methane/air and propane/air flames, obtained under microgravity conditions needed to eliminate the influence of buoyancy which could severely affect the response of these weakly-burning flames.

References

1. Law, C. K., and Faeth, G. M., *Prog. Energy Combust. Sci.* **20**:65-113 (1994).
2. Eng, J. A, Law, C. K., and Zhu, D. L., *Twenty-Fifth Symposium (International) on Combustion*, The Combustion Institute, Pittsburg, 1994, pp. 1711-1718.
3. Lozinski, D., and Matalon, M., *Combust. Sci. and Tech.* **96**:345-367 (1994).
4. Qian, J., Bechtold, J. K., and Law, C. K., *Combust. Flame*, in press.
5. Eng, J. A., Zhu, D. L., and Law, C. K., *Combust. Flame* **100**:645-652 (1995).
6. Buckmaster, J. D., and Ludford, G. S., *Theory of Laminar Flames*, Cambridge Univ. Press, 1992, pp. 28-32.
7. Qian, J., and Law, C. K., *Combust. Flame*, in press.
8. Baulch, D. L., Drysdale, D. D., Duxbury, J., and Grant, S. J., *Evaluated Kinetic Data for High Temperature Reactions*, Vol. 3, Butterworths, London, 1976.
9. Slack, M., and Grillo, A., *Combust. Flame* **59**:189-196 (1985).
10. Hwang, S. M., Gardiner, W. C., Jr., Frenklach, M., and Hidaka, Y., *Combust. Flame* **67**:65-75 (1987).
11. Bowman, C. T., and Seery, D. J., *Combust. Flame* **12**:611-614 (1968).
12. Sung, C. J., and Law, C. K., *Twenty-Sixth Symposium (International) on Combustion*, in press.
13. Maruta, K., Yoshida, M., Ju, Y., and Niioka, T., *Twenty-Sixth Symposium (International) on Combustion*, in press.

Figure 1: Schematic of the deformed flame shapes due to rotation. The dashed curve corresponds to the case of no rotation (a sphere); the solid curve is the distorted flame front. (a) The distorted flame protrudes outward at the equator. (b) The distorted flame protrudes outward at the poles.
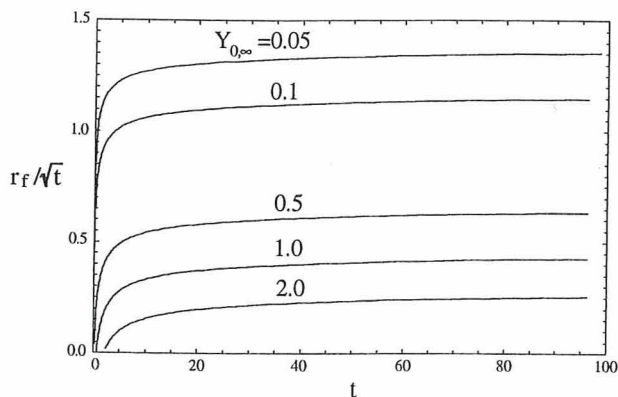
Figure 2: $r_f/\sqrt{t}$ as a function of time for different $Y_{0,\infty}$.
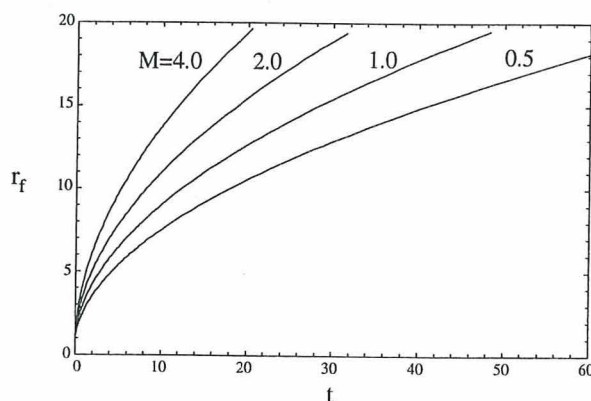
Figure 3: Flame radius r_f as a function of time with different M for $Y_{0,\infty}=0.05$.
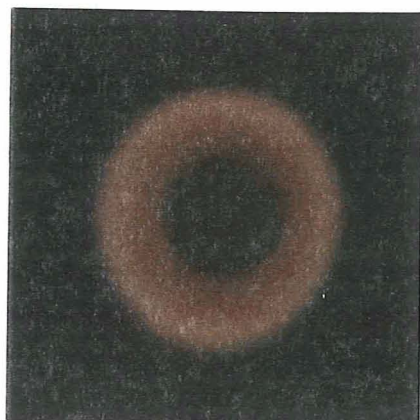
Figure 4: Flame image: pure hydrogen.

Figure 5: Flame image: 1.6% methane addition.
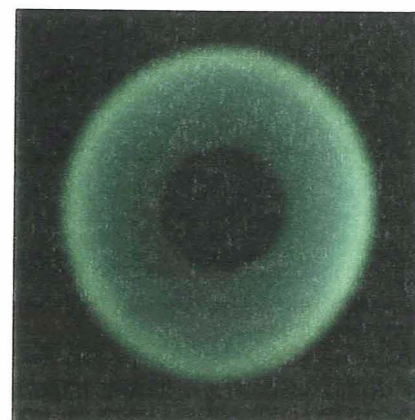
Figure 6: Flame image: 9.5% methane addition.
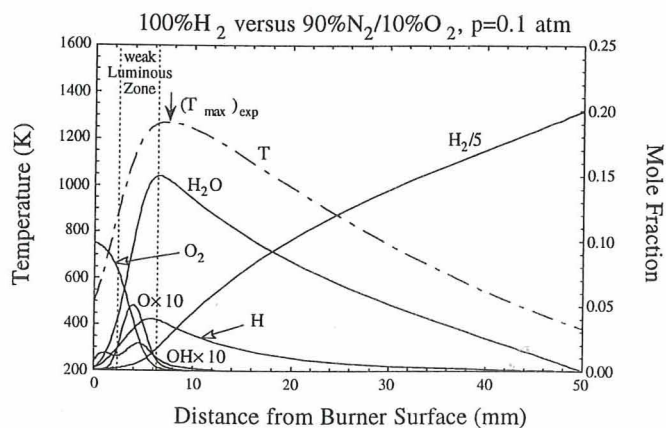
Figure 7: Computed flame structure.
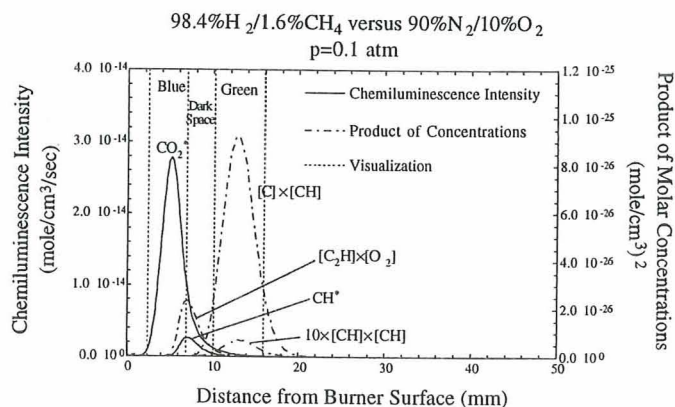
Figure 8: Determination of the source of flame emission.
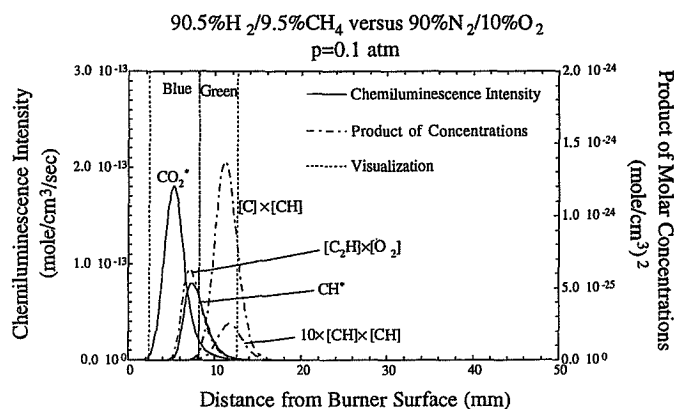
Figure 9: Determination of the source of flame emission.
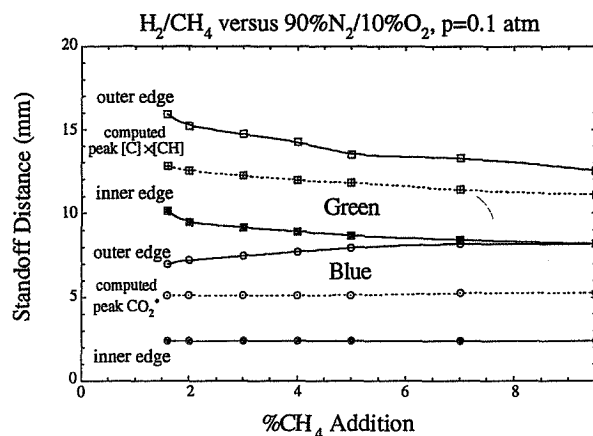
Figure 10: Evolution of the two luminous zones.
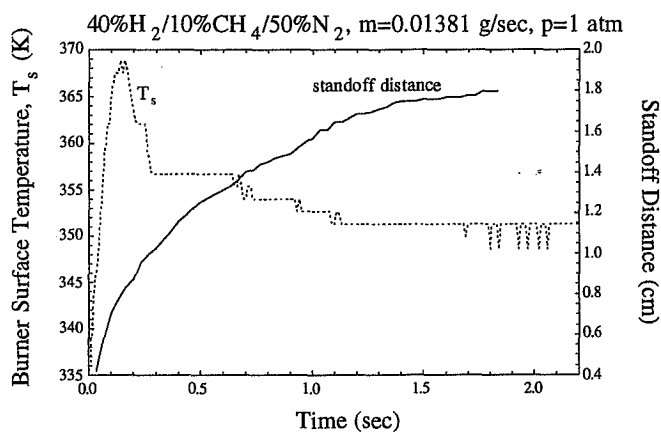
Figure 11: Temporal variation of flame location and burner surface temperature.
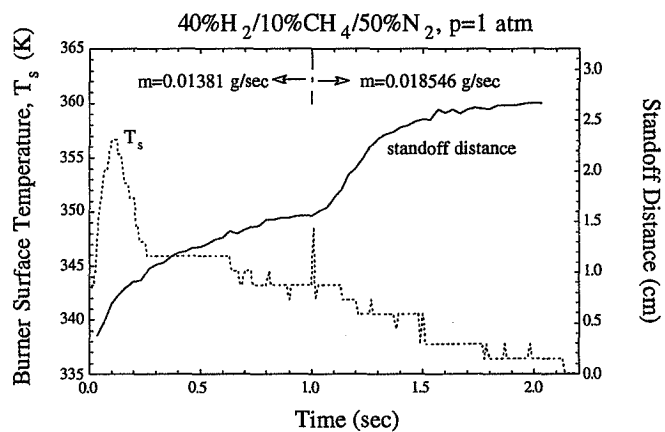
Figure 12: Temporal variation of flame location and burner surface temperature.
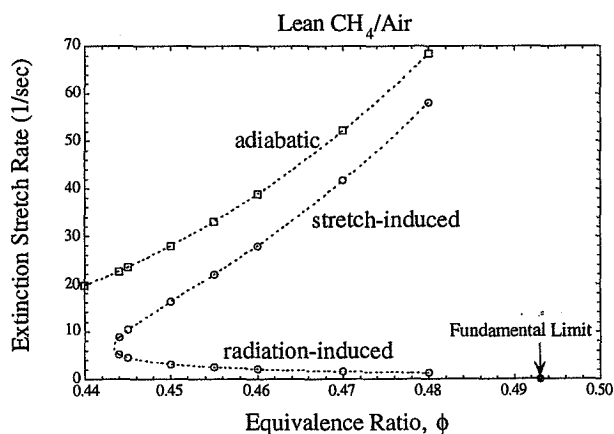
Figure 13: Extinction limits as functions of equivalence ratio, for various near-limit lean methane/air flames.
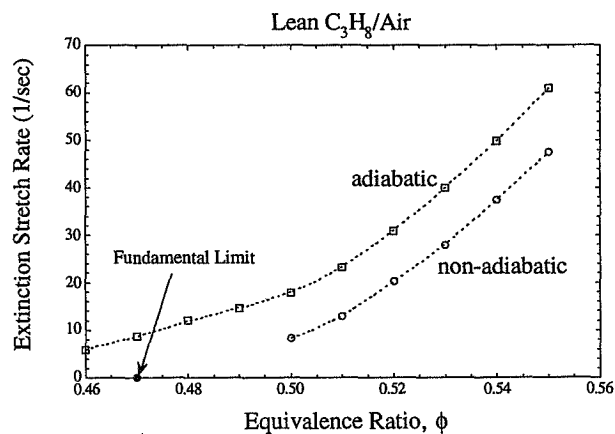
Figure 14: Extinction limits as functions of equivalence ratio, for various near-limit lean propane/air flames.

SPHERICAL DIFFUSION FLAMES: STRUCTURE AND DYNAMICS [*]

MOSHE MATALON
McCormick School of Engineering and Applied Science
Northwestern University
Evanston, Illinois

Introduction

The spherical geometry is the most suitable one to study fundamental issues concerning the structure and the dynamics of diffusion flames. From a theoretical point of view, it is the only geometry that permits the existence of a truly one-dimensional stationary diffusion flame. A stationary planar diffusion flame with the fuel supplied upstream, at $x \to -\infty$ say, and the oxidant downstream, at $x \to +\infty$ is not possible. For a steady diffusion flame to exist, one must have nonzero fluxes of fuel and oxidant towards the flame. However, in the unlimited region behind the planar flame the only bounded solutions to the reaction-free convective-diffusive operator are constants. Hence the oxidant concentration behind the flame remains constant and there is no mechanism to generate the necessary flux towards the flame. A one-dimensional problem can be formulated if the reactants are supplied at finite locations [1, 2]; but the boundary conditions in this case introduce unnecessary complications and do not appropriately model the physical reality. Indeed, a planar diffusion flame can be established in the stagnation-point flow of two opposed jets [3, 4] but the flame in this case is stretched and the flow is essentially two-dimensional. The only stationary one-dimensional diffusion flame in an unlimited environment is therefore the spherical flame.

From the experimental point of view, the spherical configuration is most suitable because measurements in this case are only required along the radial direction and sufficient information can be deduced from instantaneous photographs of the flame. Although nearly spherical flames can be produced in the laboratory on earth by ensuring that the Grashoff number is small, e.g. at low pressures, microgravity experiments are much more suitable for extensive studies under normal atmospheric conditions. Experimental studies on diffusion flames are currently carried on using either the burning of fuel drops [5] or a porous sphere burner [6].

Some of the current theoretical work carried on in this context is described below. Particular emphasis is given to extinction conditions in the presence and absence of radiative losses and to conditions leading to oscillatory combustion at low frequencies.

Burner-Generated Diffusion Flames

Spherical diffusion flames have been almost exclusively discussed in the literature in the context of a fuel drop burning in an oxidizing atmosphere. This problem, however, is inherently unsteady; the size of the droplet continually decreases as the fuel is consumed. To circumvent this difficulty the quasi-steady approximation is often invoked, but the validity of this assumption is questionable particularly during the early stages of the droplet's lifetime. An alternative way is to examine the spherically symmetric diffusion flame generated in the vicinity of a spherical burner. If gaseous fuel is internally supplied at a steady rate to a porous sphere, a stationary spherical diffusion flame may be stabilized at a certain distance from the sphere where the fuel meets the oxidant that diffuses in from the ambient gas. There is a basic difference between the quasi-steady flame surrounding a fuel drop and the steady burner-generated diffusion flame. For the droplet problem, the mass per unit time $\dot{m}$ leaving the surface of the droplet is the goal of the analysis; it is determined by the requirement that the amount of heat conducted back to the droplet must be just sufficient to vaporize the liquid fuel at the surface of the droplet. The only control parameter in this case is the Damkohler number D, which is proportional to the instantaneous surface area of the droplet and to the ambient pressure. In contrast, the mass flow rate is prescribed for the burner problem and the goal of the

analysis is to examine the response of the flame to variations in both $\dot{m}$ and D which, in an experiment, are controlled independently. The results described below are presented in terms of the dimensionless parameters

$$M = \frac{\dot{m}/4\pi\rho_\infty}{\lambda/\rho_\infty c_p a}, \qquad D = \frac{(\rho_\infty c_p/\lambda)a^2}{A^{-1}}$$

where M is a measure of the injection velocity in units of the diffusion velocity and D, the Damkohler number, is the ratio of the diffusion time to the chemical reaction time. In the above A is an appropriately defined pre-exponential factor of the chemical reaction rate, λ, c_p and ρ_∞ are the thermal conductivity, specific heat (at constant pressure) and density of the mixture and a is the radius of the porous sphere.

The burner flame is clearly affected by the heat transfer that takes place between the gas and the porous sphere. A measure of the heat loss to the burner is its conductance κ. The limit $\kappa=1$ corresponds to the adiabatic case in which all the heat conducted from the flame back to the burner is used to raise the temperature of the incoming fuel from the supply value T_0 to the local temperature of the gas just ahead of the burner. The limit $\kappa \to \infty$ corresponds to the case in which all the heat conducted back to the burner is absorbed by the sphere so that the temperature of the gas near the burner remains T_0.

A detailed description of the flame structure for arbitrary values of the fuel and oxidant Lewis numbers and for a wide range of the parameters M, D and κ is given in [7]. The analysis reveals that for large values of M a Burke-Schumann flame sheet with complete consumption of fuel and oxidant is established at a relatively large distance from the burner. For lower values of M fuel and/or oxidant leakage develop and the flame temperature drops. Excessive leakage of one of the reactants may cause extinction. In figure 1 the response of the flame to variations in M is shown for selected values of κ. The expression in the ordinate is the deviation of the flame temperature from the corresponding value for complete combustion. The turning point in the graph thus corresponds to the value of $\dot{m}$ below which a stationary flame cannot be established and is associated with extinction. Since the flame standoff distance

$$r_f = \frac{\dot{m}a\,c_p}{4\pi\lambda} \frac{L_O}{\ln\left(1+v^{-1}Y_{O_-}\right)}$$

is directly proportional to $\dot{m}$, extinction occurs when the flame is at a well defined distance from the burner; here $Y_{O\infty}$ is the mass fraction of the oxidant in the ambient gas, L_O is the Lewis number (the ratio of thermal to mass diffusivities) associated with the oxidant and v is the oxidant to fuel mass-weighted stoichiometric coefficient. For a large value of the heat loss (large κ) it is difficult to maintain a stationary flame at a sufficiently close distance to the burner; extinction occurs in this case at a larger value of $\dot{m}$ than it would in the absence of heat loss. One notes that the injection velocity at extinction is quite small; of the magnitude of the diffusion velocity. Similarly one finds that the flame is more susceptible to extinction when the fuel Lewis number or the Damkohler number are decreased; that is a larger $\dot{m}$ is needed to sustain a stationary flame when the fuel is more mobile or when the burner is smaller in size.

When the porous sphere is sufficiently large, i.e. for large values of the Damkohler number, it is possible for the flame to resist extinction and for $r_f \to a$. The flame in this case is held near the surface of the burner and remains there even when $\dot{m}$ is further reduced. The surface flame differs from the unattached diffusion flame in that it consumes only a small amount of the available oxidant. It is also susceptible to extinction when the mass flow rate through the burner becomes sufficiently low.

Radiation effects in non-premixed combustion

The results discussed earlier indicate that there is no upper limit on the prescribed mass flow rate through the burner and that the standoff distance of the diffusion flame increases indefinitely with increasing $\dot{m}$. These results could be significantly altered in the presence of volumetric heat losses. In the present discussion we shall be interested in the effects of radiation as an energy transfer mechanism, ignoring the chemical consequences. A primary source of thermal radiation in flames is from carbon particles, or soot, which start to form at temperatures near 1300K. But significant emission can also result in non-sooty flames from excited states of some intermediate species, such as OH and CH radicals, or from combustion products such as H_2O and CO_2 [8]. The results reported below assume the existence of a radiation zone within the combustion field

whose sole effect is a volumetric heat loss. Furthermore, we consider the radiation zone to exist in the region bounded between the burner and the reaction zone. It is known, for example, that the conditions most favorable for soot formation occur when fuel rich zones have strong temperature gradients. Although soot particles can be driven to the oxidant side of the flame by convection, under microgravity conditions this effect is minimized. An appropriate modification of the flame structure shows that, in the presence of radiation, extinction may occur when $\dot{m}$ exceeds a critical value. The results shown in figure 2 are expressed in terms of the heat loss parameter

$$\Omega = \frac{4\sigma a^2 T_r^4}{\lambda l_p T_\infty}.$$

Here σ is the Stefan-Boltzmann constant, l_p is the Planck mean absorption length, T_r is a reference temperature of the radiation zone and T_∞ the ambient temperature. The graphs in the figure show the drop in flame temperature from its value for complete combustion, similar to figure 1, but for several values of Ω. The solution is multi-valued with the upper branch corresponding to the stable flames. The closed curve indicates the existence of two extinction limits: a lower limit M_{min} corresponding to extinction as a result of incomplete combustion and an upper limit M_{max} corresponding to extinction as a result of excessive radiative heat loss. The results also indicate the existence of a critical value $\Omega = \Omega_c$ above which it is impossible to sustain a steady diffusion flame near the burner. The curve in figure 3 shows the flammability limits in the M - D parameter plane; steady diffusion flames will only exist for values of the Damkohler number D and the mass flow rate M within the curve.

We have also examined the effect of the thickness and location of the radiation zone on flame extinction. The thicker the zone the larger the heat loss is. This causes a reduction in M_{max} but has no effect on M_{min}. However, the radiation zone must be adjacent to the reaction zone and possibly embedded in the reaction zone to cause flame extinction; otherwise extinction is not possible for any value of Ω.

The onset of oscillations in diffusion flames

Motivated by the candle flame experiments of Ross at al. [9] and Dietrich et al. [10] we have examined the possible onset of spontaneous oscillations in diffusion flames. The candle flame experiments show that, in microgravity, the flame shape is nearly a hemisphere with a flame standoff distance (at the base of the flame) ~ 5-8 mm. The burning rate and flame temperature are considerably reduced when compared to normal gravity conditions. The hemispherical flame is nearly quasi-steady during most of the burning process but when the oxidant in the chamber is nearly consumed spontaneous oscillations develop prior to extinction. To simulate the experimental conditions we consider the simpler problem of a spherical flame surrounding a burning liquid fuel droplet [11,12]. These two problems bear some similarity in that in both cases the diffusion flame has a spherical shape and the burning depends on the heat conducted back to the condensed phase. Furthermore, we assume that the burning occurs in a reduced oxidant environment, which implies that diffusion is the dominant means of transport, and that radiative heat losses are significant as expected in microgravity conditions. Since the model problem contains the most important ingredients of the more complicated problem, it is anticipated that the dynamical properties discovered here play some role in the observed near-limit oscillations. Furthermore, the theory elucidates possible physical mechanisms that lead to flame oscillations and to the magnitude of the key parameters that trigger the instability.

For a given set of parameters, the dependence of the burning rate on the ambient oxidant concentration may be one of two shapes (see figure 4): a monotonic transition from a nearly frozen-chemistry state to an intense burning state or an S-shape response in which the lower branch corresponds to the weakly burning state and the upper branch to intense burning (the middle branch corresponds to unstable states that cannot be realized in practice). The symbols q, γ and δ in the figure represent the dimensionless heat release parameter, the scaled oxidant mass fraction $Y_{O\infty}$ and the reduced Damkohler number [12]. Note that a monotonic response turns into an S-shape when the Damkohler number δ is reduced; e.g. for smaller droplets. What characterizes the S-shaped curve is the abrupt transition from the lower to the upper branch, and vice-versa, that corresponds to ignition and extinction phenomena. Extinction will occur, for example, when the oxidant concentration is reduced below the critical value corresponding to the turning point on the upper branch of the S-curve. In contrast, when the response is monotonic, the transition from an intense to a weakly burning state occurs in a gradual way. These considerations are based solely on whether steady-state solutions exist or not. Stability considerations alter these results, as follows.

For unity Lewis numbers it is found that, in the absence of heat loss, the transitional states along the monotonic response curve are always stable. However if radiative losses are appreciable spontaneous oscillations may develop when the oxidant concentration is reduced below a critical value. For non-unity Lewis numbers oscillations may develop even in the absence of heat loss provided the effective Lewis number[#] is sufficiently large. The graphs in figure 5 illustrate this development for selected values of δ and two distinct values of L_O; the darker segments of the response curves identify the unstable oscillatory states. It should be noted that for large δ the flame is always stable; the Burke-Schumann flame sheet is therefore absolutely stable. It is found that, while at the onset the amplitude of oscillations is moderate, it increases by further decreasing the oxidant concentration and may lead to extinction that is not predicted otherwise. The graph in figure 6 identifies the region in the parameter plane, consisting of the heat loss parameter h and the Lewis number L_O, where oscillations are possible. Here the heat loss parameter $h=4\Omega(E/RT_\infty)^2$ with the reference temperature in Ω taken to be T_∞.

Similarly, for the S-shaped response it is found that oscillations may develop on the upper branch near the turning point normally associated with extinction. Again, oscillations may develop when the Lewis number is sufficiently large and the flame is more susceptible to the instability in the presence of heat loss. Since flame oscillations may lead to premature extinction, the extinction condition normally associated with the turning point on the S-curve must be modified and possibly identified with the points of exchange of stability. Finally we point out that our stability calculations were carried out allowing for spatial disturbances. It was found that, in most cases, the preferred mode at the onset of the instability was in the form of spherically symmetric oscillations.

The frequency of oscillations, at the onset of instability, is given by

$$\omega = \frac{\lambda}{\rho_\infty c_p a^2} \left(\frac{RT_\infty}{E} \right)^2 \Im(\varpi)$$

where a here is the radius of the droplet, R the gas constant, E is the activation energy of the chemical reaction and $\Im$ is the imaginary part of the eigenvalue ϖ associated with the linear stability problem (the real part of ϖ vanishes at the onset). The mean flame position is approximately given by

$$r_f = \frac{aL_O}{v^{-1}Y_{O_-}} \ln(1+B)$$

where B is the transfer number. For a flame standoff distance ~ 0.5 cm, similar to the standoff distance of the candle flame, and mass diffusivity (based on the oxidant) ~ 2 cm^2/s we find that $\omega \sim 0.7 - 1.4$ Hz. The predicted frequency of oscillations are therefore of the same order of magnitude as the ones observed in the candle flame experiments. The theory also shows that ϖ depends on the Lewis number L_O; in particular the frequency of oscillations increases with an increasing L_O. Hence spontaneous oscillations similar to the ones observed may result when the ambient oxidant becomes sufficiently low provided the Lewis number is sufficiently large and/or heat losses are appreciable. It should be pointed out however that, although the present theory matches the experimental results in terms of the frequency of oscillations, the mode of oscillations in both cases is quite different; the additional heat transfer at the base of the hemispherical flame to the candle prevents a radial motion of the flame front there and thus forces the direction of oscillations.

Recent experiments by Levy and Bulzan [13] in spray flames suggest that, under certain operating conditions, a nonstationary oscillating flame is observed rather than the more common steady laminar spray diffusion flame. These oscillations are different in nature than the well known flame flicker phenomenon of gaseous diffusion flames, having relatively small frequencies $\sim 1 - 5$ Hz. It was also noted that the same identical phenomenon is observed for a purely gaseous diffusion flame if water droplets are added to the supply of gaseous fuel. This seems to imply that the underlying mechanism inducing the oscillations is one involving heat and mass transfer. Based on a simple model [14] devised to analyze this case we found that an oscillating diffusion flame results when the loading parameter (fraction of liquid fuel contained in the droplets from the total fuel in the feed stream) is sufficiently large, so that the heat loss from the flame required for droplet vaporization is appreciable. The onset of oscillations is also found to depend on the Lewis number L_O. This phenomenon clearly bears similarity to the oscillations of the spherical flame described above; in both cases the same physical mechanisms are responsible for the flame oscillations.

[#] Here the fuel and oxidant Lewis numbers are assumed equal, for simplicity.

78

References

1. Spalding D.B and Jain V.K. 1962, *Combustion & Flame* **6**, 265.
2. Matalon M., Ludford, G.S.S. and Buckmaster J.D. 1979, *Acta Astronautica* **6**, 943.
3. Pandya T.P. and Weinberg F.J. 1963, *9th Symposium (Int.) on Combustion*, 587.
4. Linan, A. 1974, *Acta Astronautica* **1**, 1007.
5. Choi M.Y., Dryer F.L., Card J.M., Williams F.A., Haggard J.B. and Brorowski B.A. 1992, *AIAA Paper #92-242*.
6. Eng J.A., Law C.K. and Zhu D.L. 1994, *25th Symposium (Int.) on Combustion*, 1711.
7. Fromm K. and Matalon M. 1997, *AIAA Paper # 97-0239*.
8. Daguse T., Croonenbroek J.C., Rolon N., Darabiha N. and Soufiani A. 1996, *Combustion & Flame*, **106**, 27.
9. Ross H.D., Sotos R.G. and Tien J.S. 1991, *Combustion Science & Technology*, **75**, 151.
10. Dietrich D., Ross H.D and Tien J.S. 1994 *AIAA Paper #94-0429*.
11. Cheatham S. and Matalon M. 1996, *AIAA Journal* **34**(7), 1403.
12. Cheatham S. and Matalon M. 1997, *26th Symposium (Int.) on Combustion*, in press.
13. Levy Y. and Bulzan D.L. 1995, *Combustion & Flame* **100**, 543.
14. Greenberg J.B. and Matalon M. 1997, *Proceedings of the 37th Israel Annual Conference on Aerospace Sciences*, 355.
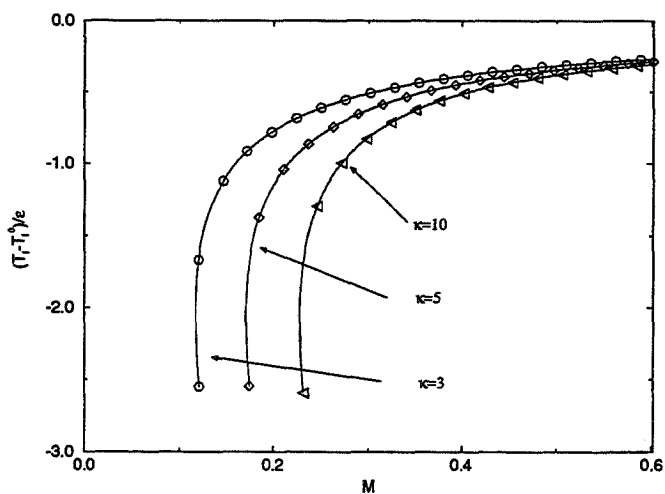
Figure 1. Variations in flame temperature as a function of the mass flow rate M and the burner's conductance κ.
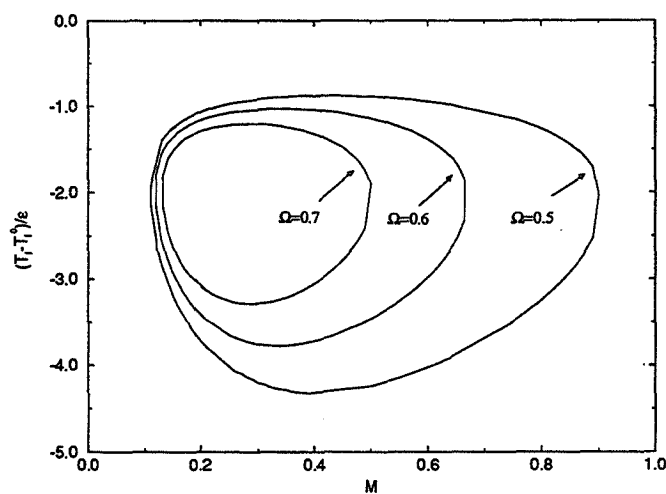
Figure 2. Variation in flame temperature as a function of the mass flow rate M and the radiative heat loss parameter Ω; calculated for the case $\kappa=1$ (no heat loss to the burner).
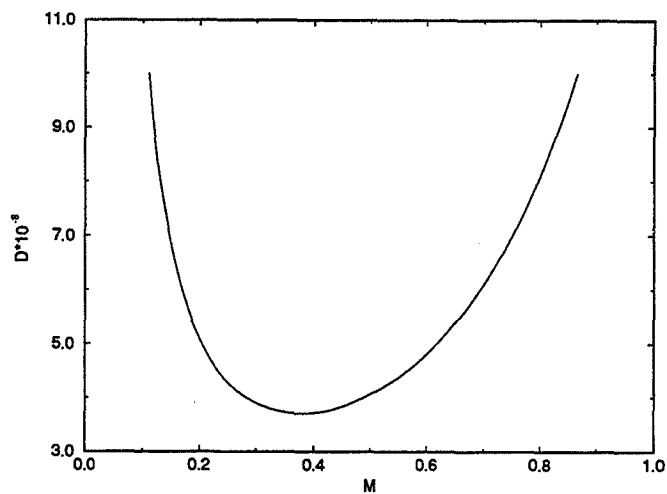
Figure 3. Flammability limits in the M - D plane
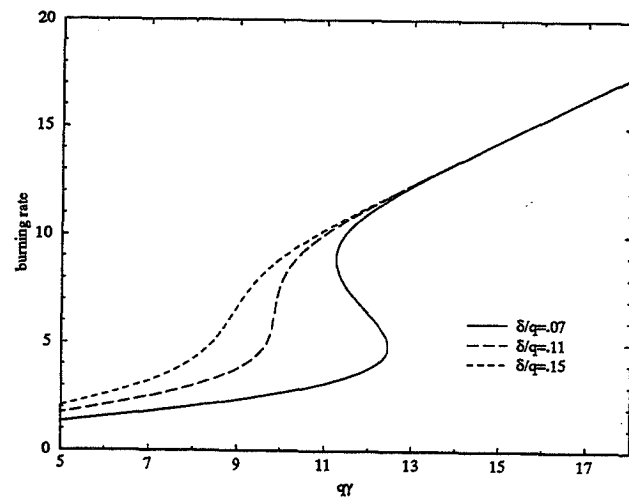
Figure 4. Response Curves - the burning rate as a function of the ambient oxidant concentration
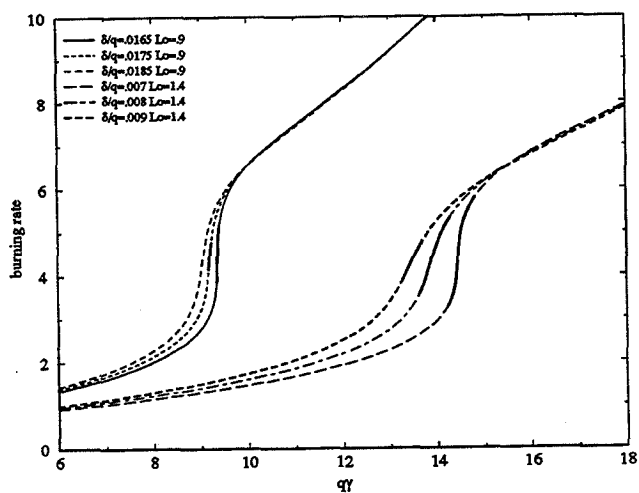
Figure 5. The onset of oscillations. The dark segments represent unstable states.
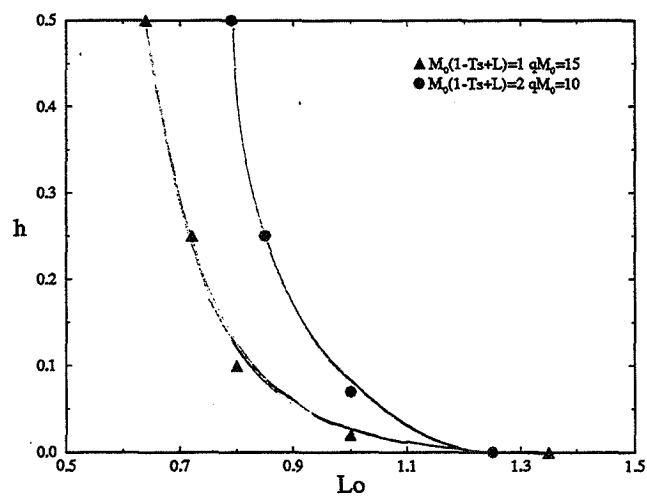
Figure 6. Stability curves in the heat loss - Lewis number parameter plane for two sets of parameters; see [11].

REACTIVE HYDRODYNAMICS IN ROTATING SPHERICAL AND CYLINDRICAL GEOMETRY

SIAVASH H. SOHRAB
Robert R. McCormick School of Engineering and Applied Science
Department of Mechanical Engineering
Northwestern University, Evanston, Illinois 60208

Introduction

In turbulent spray combustion among many complex interactions between local flow structures called turbulent eddies and droplets [1-4] are those associated with rotation of droplets. In general, for a complete statistical description of turbulent sprays, consideration of at least four degrees of freedom respectively associated with translational, rotational, vibrational (pulsational), and internal motions of the droplet are needed. Clearly the interactions between all degrees of freedom of the droplets and those for the gaseous background field will be exceedingly complex. For example, one type of interaction between the translational and the rotational velocity of droplets results in droplet helicity, $\mathcal{H}_d = \omega_d \cdot v_d$, the significance of which in turbulent spray combustion is yet to be recognized. The role of droplet rotation in turbulent spray combustion modeling and its impact on the evaporation of liquid fuel droplets was recently investigated [5-8]. Also, the impact of rotation on combustion of solid particles such as is encountered in pulverized coal combustion has been emphasized [9].

The problem of viscous flow around a rotating sphere discussed above also occurs in other areas of physical sciences such as astrophysics and geophysics. Consequently, the subject has been addressed in many classical [10-23] as well as more recent investigations [24-28]. According to these investigations, the rotation of a rigid sphere in an otherwise quiescent, unconfined environment results in the motion of the fluid towards the poles. The polar flows from the northern and southern hemispheres move along helical trajectories towards the equatorial plane. Eventually, the polar flows collide at the equatorial plane, thus producing a sheet of rotating fluid that is radially ejected outward on this plane. Therefore, a droplet induces a *strained* flow field as a result of its rotation. Since the spatial extent of equatorial jets could easily exceed many droplet diameters [5], interactions between neighboring droplets are enhanced as a result of their rotation. Also, the equatorial jet substantially alters the spherical geometry of the diffusion flame surface that surrounds a rotating droplet. The objective of the research is to gain more knowledge about the hydrodynamics within and around rotating spherical and cylindrical body of fluid, and the behavior of diffusion or premixed flame surfaces that could surround such symmetric body of rotating fluid.

EXTERNAL AND INTERNAL HYDRODYNAMICS AROUND ROTATING SPHERES

The hydrodynamics of viscous reactive and non-reactive flow around porous sphere with surface blowing was investigated [8]. The nature of extinction of diffusion flame surrounding a rotating porous sphere was determined. It was found that as the rotation velocity increased, the diffusion flame first extinguished at the poles. The polar extinction regions then grow towards the equator until finally a ring-flame configuration was achieved. As w was further increased, this ring flame also abruptly extinguished. It was found that the critical value of the Rossby number at extinction is constant, $Ro_c = 7$. Also, the influence of rotation on the torque experienced by an evaporating droplet was determined. It was shown that increasing surface blowing results in decrease of torque, suggesting that rotating droplets have longer spin relaxation times. Also, a global correspondence between the internal secondary flow recirculation zones within counterflow-counter-rotating, finite jets [29-

38], on the one hand, and the flow within rotating, stationary droplets in otherwise stagnant atmospheres, on the other, was identified [8]. The geometry of the spherical diffusion flame using the eikonal equation [39, 40] was investigated and the influence of Lewis number [41-42] on the flame extinction near the poles and the equator was discussed [8].

Following the classical study of Hill [43-44] , a new stream function is introduced to describe the hydrodynamics within a stationary, spherical body of fluid that is located at the stagnation-point of two, axi-symmetric, counterflow jets, given by

$$\Psi = r^3 (1 - r^2) \sin^2\theta \cos\theta = R^2 Z (1 - R^2 - Z^2) \tag{1}$$

when $R = r\sin\theta$ and $Z = r\cos\theta$, and the calculated streamlines in R-Z plane are shown in Fig1a. The above stream function results in the azimuthal component of vorticity $\omega_\phi = 14\ RZ$, that satisfies the viscous part of the Helmholtz vorticity equation

$$\frac{v}{r^2}\frac{\partial}{\partial r}\left(r^2\frac{\partial \omega_\phi}{\partial r}\right) + \frac{v}{r^2}\frac{\partial}{\partial \theta}\left(\frac{1}{\sin\theta}\frac{\partial}{\partial \theta}(\sin\theta\,\omega_\phi)\right) = 0 \tag{2}$$

Using the above stream function, a cascade of concentric spherical flows, when each sphere is composed of two toroidal vortices, was identified [8], as schematically shown in Fig.2a.

If one considers higher multiplicity of the angle θ in Eq.(1), one arrives at the more general form of stream function

$$\Psi = r^3 (1 - r^2) \sin^2(n\theta) \cos(n\theta) \tag{3}$$

resulting in the multi-cell flow fields shown in Figs.1b and 1c corresponding to n = 2, and 3, respectively. The 4-cell flow shown in Fig.1a is formed by two-toroidal vortices induced by two axi-symmetric counterflow jets as was discussed earlier [8]. In a similar fashion, one notes that the 8- and 12-cell flows shown in Figs. 1b and 1c, are generated by 4 and 6 toroidal vortices forming a spherical body of fluid within an external flow composed of 4, and 6 axi-symmetric counterflow jets, respectively. The counterflow jets are symmetrically positioned around the central spherical body of liquid in accordance with Figs.1b-1c. Parallel to Fig.2a, one can also construct a cascade of concentric spherical flows when each sphere within the cascade is composed of 8- or 12-cell flow. Such complex flow configurations are of both fundamental as well as practical interest.

The flow fields discussed above appear similar to those corresponding to the motion of fluid within spherical geometry induced by thermocapillary effects [45-50]. For example, the multi-cell flow fields shown in Fig.1b and 1c are similar to those obtained for thermocapillary flows [46], that are driven by gradients of surface tension that is induced by temperature gradients. It is important to note however, that the internal hydrodynamics that are shown in Figs.1a-1c, and are being discussed herein, have all together a different origin, since they are in fact induced by the rotation of the droplet. That is, as the droplet rotates, it induces two external polar flows as was discussed above. The rotating polar flows over the upper and the lower hemispheres in turn induce the internal toroidal vortex flows within the droplet, because of the action of viscosity. Under steady conditions, the toroidal vortices will also possess rigid-body azimuthal rotation. Clearly, the internal toroidal vortices within a rotating droplets will have a significant influence on its stability of the associated bifurcation problem [51-56]. On the other hand, when a non-rotating droplet is located within non-rotating counterflows, while the internal toroidal vortices do form, they will not possess any azimuthal rigid-body rotation.

It is interesting to compare the cascade of spherical flows [8, 57, 58] that are similar to those shown in Fig.2a, but are generated by the multi-cell flows of Figs.1b and 1c, with that in Fig.2b showing the *"quantized arrangement of vortices"* according to Weizsäcker [59], in his theory of the origins of the Solar system. According to this theory, such stable vortex

flows could be generated within the body of a rotating spherical "primeval" gas. By a simple analysis of the geometry of cascade of concentric spheres, it is possible to show that the successive radii of the spheres within the cascade are related to each other by the recursive relation

$$R_n = R_{n-1} [(1 + \sin \pi/\beta)/(1 - \sin \pi/\beta)] = R_o [(1 + \sin \pi/\beta)/(1 - \sin \pi/\beta)]^n \qquad (4)$$

where β is the number of cells. According to the preceding equation, for 4-cell spherical or cylindrical objects, $\beta = 4$, one obtains the equation

$$R_n = R_{n-1} (3 + 2\sqrt{2}) = R_o (3 + 2\sqrt{2})^n \qquad (5)$$

that has the same form as the Bode's law discussed by Chandrasekhar [60]

$$R_n = R_o \, \varepsilon^n \qquad (6)$$

when R_o and ε are constants. The flow fields shown in Figs.1, 2, are relevant to the modeling of droplet dynamics in strained flow fields, such as are encountered in turbulent sprays.

EXTERNAL AND INTERNAL HYDRODYNAMICS AROUND ROTATING CYLINDERS

Following the above procedures for spherical flows, a new stream function is introduced that describes the hydrodynamics within a cylindrical body of liquid situated with its axis along the stagnation-line of counterflow two-dimensional streams, given by

$$\Psi = r^2 (1 - r^2) \sin \theta \cos \theta = RZ \ (1 - R^2 - Z^2) \qquad (7)$$

that results in the calculated streamlines shown in Fig.3a. The streamlines in Fig.1a are different from those in Fig.3a, since the former is composed of two *toroidal vortices*, while the latter is formed by four *line-vortices* with axes perpendicular to the plane of the figure. The axial component of vorticity $\omega_z = 24 \, RZ$, corresponding to Eq.(7), satisfies the viscous part of the Helmholtz vorticity equation in cylindrical coordinates

$$\frac{\nu}{r} \frac{\partial}{\partial r} \left(\frac{1}{r} \frac{\partial r \, \omega_z}{\partial r} \right) + \nu \frac{\partial^2 \omega_z}{\partial \theta^2} = 0 \qquad (8)$$

If one considers higher multiplicity of the polar angle in Eq.(7), one arrives at the stream function

$$\Psi = r^2 (1 - r^2) \sin(n\theta) \cos(n\theta) \qquad (9)$$

that results in the calculated stream lines shown in Fig.3b and 3c, respectively corresponding to n = 2, and 3. Such multi-cell internal flows could be produced within a cylindrical body of liquid that is impinged upon by either four or six two-dimensional counterflow jets. It is also possible to use the flow field in Eq.(7) to construct a cascade of concentric cylindrical flows when each cylinder within the cascade is composed of four line-vortices, instead of two toroidal vortices in the spherical geometry discussed above. The experimental investigation of the predicted flow fields shown in Fig.3a-3c, are best performed in micro-gravity environment. This is because in such environments, stabilization of a cylindrical body of liquid within a counterflow two-dimensional jets will become more feasible.

CONCLUDING REMARKS

Chemically reactive and non-reactive hydrodynamics around rotating porous spheres with surface blowing in an otherwise stagnant environment, as well as that of a stationary droplet in counterflow counter-rotating jets was theoretically and experimentally investigated. New stream functions were presented to describe spherical flows formed from two, four, and six toroidal vortices. Such flow fields were identified as solutions of the viscous vorticity equation. In addition, the nature of

hydrodynamics within a cylindrical body of liquid that is located along the stagnation line of opposing two-dimensional jets was discussed. Following Hill's solution for a spherical vortex, a new stream functions was introduced to describe internal cylindirical flows formed by four line vortices. Such stream functions were also used to describe cascades of concentric spherical and cylindrical flows. The importance of such flow fields to the modelling of local hydrodynamics and dissipative processes within turbulent sprays was emphasized.. Such flows in both reactive and non-reactive systems are presently being further investigated in preparation for the future studies under microgravity conditions.

ACKNOWLEDGMENTS

REFERENCES

1. Faeth, G. M., *Prog. Energy Combust. Sci.* 9:1-76 (1983).

2. Williams, F. A., *Combustion Theory*, 2nd Ed., Addison Wesley, New York, 1985, pp.446-484.

3. Sirignano, W. A., *Prog. Energy Combust. Sci.* 9:21 (1985).

4. Chen, Z. H., Lin, T. H., and Sohrab, S. H., *Combust. Sci. Technol.* 60:63-77 (1988).

5. Pearlman, H. G., and Sohrab, S. H., *Combust. Sci. Technol.* 76:321-334 (1991).

6. Lozinski, D., and Matalon, M., *Twenty-Fourth Symposium (International) on Combustion*, The Combustion Institute, Pittsburgh, 1992, p.1483.

7. Pearlman, H. G., and Sohrab, S . H., *Combust. Flame* 92:469-474 (1993).

8. Pearlman, H. G., and Sohrab, S. H., *Combust. Flame* 108:419-441 (1997).

9. Beer, J. M., Chomiak, J., and Smoot, L. D., *Prog. Energy Combust. Sci.* 10:177-208 (1984).

10. Newton, I. *Phil. Trans.* 6:3078-3079 (1672).

11. Robins, B., *New Principles of Gunnery*, ed. Hutton, 1805.

12. Stokes, G. G., *Trans. Camb. Phil. Soc.* 8:287 (1845).

13. Thomson, J. J., *Nature* 85:251-257 (1910).

14. Davies, J. M., *J. Appl. Phys.* 20:821-828 (1949).

15. Howarth, L., *Phil. Mag.* Series 7, 42:1308-1315 (1951).

16. Nigam, S. D., *Z. Angew. Math. Phys.* 5:151-155 (1954).

17. Kobashi, Y., *J. Sci. Hiroshima Univ.* A20:149 (1957).

18. Singh, S. N., *Appl. Sci. Res.*, Sec. A 9:197-205 (1960).

19. Bowden, F. P., and Lord, R. G., *Proc. Roy. Soc.* A271:143-153 (1963).

20. Kreith, F. R., L. G., Sullivan, J. A., and Sinha, S. N., *Int. J. Heat Mass Trans.* 6:881-895 (1963).

21. Fox, J., NASA TN D-2491 (1964).

22. Banks, H. H., *Quart. J. Mech. Appl. Math.* 18:443-454 (1965).

23. Banks, H. H., *Acta Mechanica* 24:273-287 (1976).

24. Dennis, S. C., Singh, S. N., and Ingam, D. B., *J. Fluid Mech.* 101: 257-279 (1980).

25. Marcus, P. S., and Tuckerman, L. S., *J. Fluid Mech.* 185:31-65 (1987).

26. Wimmer, M., *Prog. Aerospace Sci.* 25:43-103 (1988).

27. Bühler, K., *Acta Mechanica.* 81:3-38 (1990).

28. Bühler, K., *Eur. J. Mech., B /Fluids.* 11:143-160 (1992).

29. von Karman, T., *ZAMM* 1:233 (1921).

30. Schlichting, H., *Boundary Layer Theory*, McGraw Hill, New York, 1978, pp.102-105.

31. Batchelor, G. K., *Quart. Mech. Appl. Math.* 4:29-41 (1951).

32. Chen, Z. H., Liu, G. E., and Sohrab, S. H., *Combust. Sci. Technol.* 51:39-50 (1987).

33. Lin, T. H., and Sohrab, S. H., *Combust. Sci. Technol.* 52:75-90 (1987).

34. Sivashinsky, G. I., and Sohrab, S. H., *Combust. Sci. Technol.* 53:67-74 (1987).

35. Goddard, J. D., Melville, J. B., and Zhang, K., *J. Fluid Mech.* 182:427-446 (1987).

36. Libby, P. A., Williams, F. A., and Sivashinsky, G. I., *Phys. Fluids* A2:1213-1223 (1990).

37. Kim, J. S., Libby, P. A., and Williams, F. A., *Phys. Fluids* A 4:391-408 (1992).

38. Sheu, J. W., Sohrab, S. H., and Sivashinsky, G. I., *J. Propul. and Power* 8:836-842 (1992).

39. Markstein, G. H., *Nonsteady Flame Propagation*, Pergamon, London, 1964.

40. Williams, F. A., in *The Mathematics of Combustion*, J. D. Buckmaster, Ed.., Vol.2 of Frontiers in Applied Mathemtics, Philadelphia, : SIAM, 1985, pp.97-131.

41. Sivashinsky, G. I., *Acta Astronautica* 3:889-918 (1976).

42. Buckmaster, J. D., *Seventeenth Symposium (International) on Combustion*, The Combustion Institute, Pittsburgh, 1979, p.835.

43. Panton, R. L., *Incompressible Flow*, Wiley, New York, 1984, p.332.

44. Lara-Urbaneja, P., and Sirignano, W. A., *18th Symposium (International) on Combustion*, The Combustion Institute, Pittsburgh, 1981, p.1365.

45. Young, N. O., Goldstein, J. S., and Block, M. J., *J. Fluid Mech.* 6:350 (1959).

46. Jayaraj, K., Cole, R., and Subramanian, S., *J. Colloid Interface Sci.* 85:66-77 (1982)

47. Shankar, N., and Subramanian, S. R., *J. Colloid Interface Sci.* 123:512-522 (1988)

48. Merritt, R. M., Morton, S. D., and Subramanian, S. R., *J. Colloid Interface Sci.* 155:200-209 (1993)

49. Lozinski, D., and Matalon, M., *Phys. Fluids* A 5:1596-1601 (1993).

50. Treuner, M., Galindo, V., Gerbeth, G., Langbein, D., and Rath, H. J., *J. Colloid Interface Sci.* 179:114-127 (1996)

51. Plateau, J. A. F., *Annual Report of the Board of Regents of the Smithsonian Institution*, Washington, DC, pp. 270-285, 1863.

52. Chandrasekhar, S., *Proc. R. Soc. Lond.* A 286:1-26 (1965).

53. Brown, R. A., and Scriven, L. E., *Proc. R. Soc. Lond.* A 371:331-357 (1980)

54. Luyten, P.., *Proc. R. Soc. Lond.* A 414:59-82 (1987)

55. Wang, T. G., Trinh, E. H., Croonquist, A. P., and Elleman, D. D., *Phys. Rev. Lett.* 56:452-455 (1986)

56. Wang, T. G., Anilkumar, A. V., Lee, C. P., and Lin, K. C., *J. Fluid Mech.* 276:389-403 (1994)

57. Lee, H., and Sohrab, S. H., *Combust. Flame* 101:441-451 (1995).

58. Thomas, R. H., and Walters, K., *Quart. Mech. Appl. Math.* 27:39-53 (1964).

59. Weizsäcker C. F. , *Zeits. f. Astrophys.* 22:319 (1944).

60. Chandrasekhar, S., *Rev. Modern Phys.* 18:94-102 (1946).
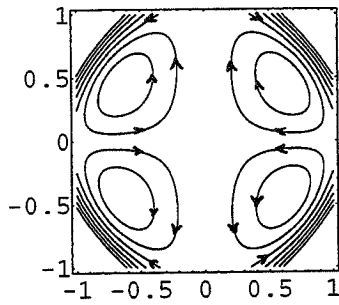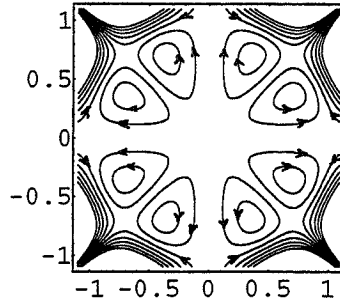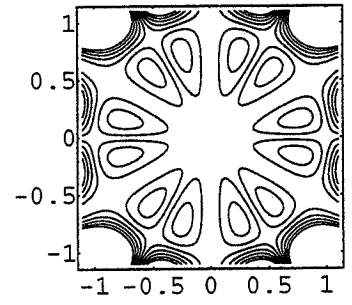
(a)   (b)   (c)

Fig.1 Calculated streamlines for multi-cell spherical flows according to Eq.(3) for n = (a) 1 (b) 2 (c) 3.

(a)
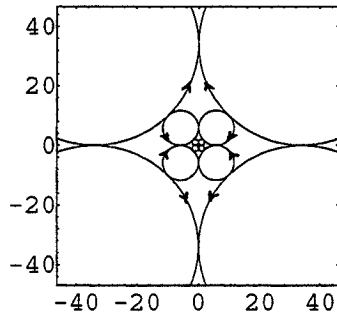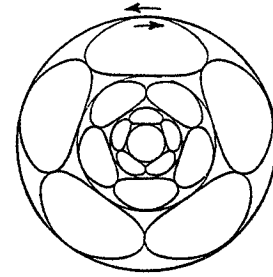
Fig.2a Cascade of concentric spherical flows [8].

(b)

Fig.2b Cascade of quantized arrangement of vortices according to Weizsäcker 's theory [59]
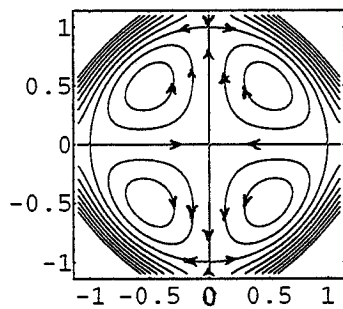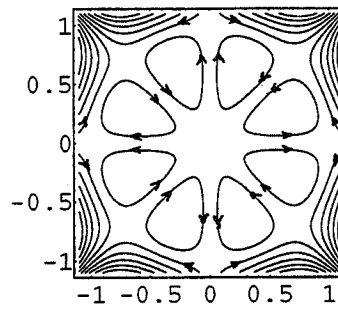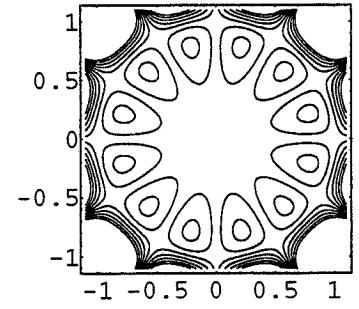
(a)   (b)   (c)

Fig.3 Calculated streamlines for multi-cell cylindrical flows according to Eq.(9) for n = (a) 1 (b) 2 (c) 3.

DIFFUSION FLAME EXTINCTION IN A LOW STRAIN FLOW

JASON SUTULA, JOSHUA JONES, JOSE L. TORERO
Department of Fire Protection Engineering
University of Maryland
College Park, MD20742-3031

and

JEFFREY BORLIK, OFODIKE A. EZEKOYE
Department of Mechanical Engineering
University of Texas at Austin
Austin, TX 78712

Introduction

Diffusion flames are of great interest in fire safety and many industrial processes. Many parameters significantly affect the flame structure, shape and stability, of particular importance are the constraints imposed by geometrical boundaries. Physical boundaries determine the characteristics of the flow, affect heat, fuel and oxidizer transport from and towards the flame and can act as heat sinks or heat sources. As a result, the existence of a flame, its shape and nature are intimately related to the geometrical characteristics of the environment that surrounds it. The counter-flow configuration provides a constant strain flow, therefore, is ideal to study the structure of diffusion flames. Most studies have concentrated on the high velocity, high strain limit, since buoyantly induced instabilities will disintegrate the planar flame as the velocity decreases [1,2]. Only recently, experimental studies in micro-gravity conditions have begun to explore the low strain regimes [3,4,5]. The main objective of these on-going studies is to determine the effect of radiative heat losses and variable strain on the structure and radiation-induced extinction of diffusion flames. For these programs, size, geometry and experimental conditions have been chosen to keep the flame unaffected by the physical boundaries.

Whether is the burning of condensed or gaseous fuels, for most real situations the boundaries impose a significant effect on the nature of the flame. There is, therefore, a need to better understand the effect that geometrical constraints (i.e. flow non-perpendicular to a fuel surface, heat losses to the boundaries, etc.) might have on the final characteristics of a diffusion flame. Preliminary experiments have shown that, in the absence of gravity [6,7], and depending on the distance from the flame to the boundary, three characteristically different regimes can be observed. Close to the boundary, the flame is parabolic, very thin and blue, almost soot-less. Diffusion is the main mechanism controlling fuel transport to the reaction zone, conduction towards the inlets is the main source of heat losses. As the distance increases the flame becomes linear and thickens, remaining blue at the oxidizer side and turning yellow at the fuel side. Here, convection brings fuel and oxidizer together and the reaction occurs in the viscous layer formed between the fuel and oxidizer streams. This region corresponds to the characteristic counter-flow flame where conduction and convection become negligible forms of heat losses and radiation becomes dominant. The flame in the third (mixed) region, between the two others, results from the combination of the scenarios presented above.

Objectives

An experimental study will be conducted using two opposing porous burners through which fuel and oxidizer will be introduced. The orientation of both burners can be changed so that an angle can be created between the inlet surfaces. The maximum attainable angle is 180° for which the resultant configuration will be that of a Wolfhard-Parker burner. If the angle is 90° the structure of the flow will be that of a boundary layer with injection. The lower limit will be 0° in which case, the counter-flow configuration is attained. Experiments in normal gravity will focus on the effect of buoyancy on the flow structure, heat and mass transport mechanisms. Orientation and flow velocities will be varied to determine when the effect of buoyancy becomes overwhelming. Experiments in partial and micro-gravity will concentrate on the low strain limit with the main goal of determining the relative importance of diffusion, natural and forced convection. Radiation heat losses will be evaluated to quantify the total energy transferred to the boundaries and also as a complement to other on-going research programs.

This experiment is specially suitable for parabolic flights since it consists of a crossed fuel and oxidizer flow. Fuel and oxidizer velocities can be regulated to make inertia dominant over all perturbations in the gravity level allowing for the use of low quality micro-gravity facilities (parabolic flights). Partial-gravity tests are envisioned to better observe the importance of natural convection in comparison to diffusion and forced convection. Time scales can be adjusted by changing fuel and oxygen velocities so that short term high quality micro gravity facilities (2.2 s. drop-tower) can be used.

Extensive theoretical work has been conducted on the counter-flow diffusion flame since the simplifying assumptions regarding the flow permit the development of analytical solutions. Reasonably accurate conditions for extinction can be obtained by using asymptotic analysis for high activation energies, therefore, an extension to the methodology first used by Linan [9] is under development and the progress achieved in this area will be presented as follows.

Experimental Study

The experimental hardware consists of two porous burners which can placed at variable opposing angles to each other (figure 1). The burners are placed inside a combustion chamber. The porosity of the burner surface is such that seeding particles can be introduced into the test section through them. Fuel and oxidizer flows are regulated by controlled mass flow meters and ignition is accomplished by an electric spark. A combustion chamber is under construction and will have five windows to guarantee optical access and to introduce a light sheet. Video recordings will be obtained by means of two CCD cameras. A micro-processor, a red diode laser (2 W) and the required optics are also be part of the hardware.

To minimize the effect of buoyancy the oxidizer burner will be placed horizontally for normal gravity tests. The fuel burner can pivot around the supporting element to modify the angle between both burner surfaces from 0° to 180° (figure 1). The burner dimensions are 120 mm long and 80 mm wide, the first dimension guarantees observation of all previously described zones, for the velocity range of interest, and the second guarantees two dimensionality at the symmetry plane. The combustion chamber will be dimensioned to minimize the effect of confinement on the flame.

Velocity Measurements
It is of great importance for these experiments to be able to accurately measure the flow velocity distribution. A light sheet particle tracking system is under development. It consists of a 2W red diode laser (SDL-820) which is used to create a light sheet by means of two cylindrical lenses. These optical elements produce a light sheet of thickness of the order of 0.5 mm and 20 mm wide. The light sheet is placed at the axis of symmetry of the burner and particles, introduced into the flow through the burners, are traced by post-processing of video recordings obtained from a CCD camera. An EPIX frame grabber will be used for this purpose. The low velocities and laminar nature of the flow allow to obtain significantly accurate velocity distributions. All elements of this system are very simple and specially tailored for the constraints of micro-gravity facilities. Accomplishing a correct flow seeding in micro-gravity represents one of the major tasks, but again the nature of the flow allows for seeding of both fuel and oxidizer before they enter the combustion chamber. So far incense has been used to seed inert flow, for calibration purposes, but further improvement of this technique is a main goal of this research program.

Temperature Measurements
Estimation of the temperature distribution will be obtained by a combination of thermocouple measurements and image processing of video recordings. A data acquisition system together with an array of 32 "type K" thermocouples serves to trace the temperature evolution. Thermocouple measurements have proven to be, so far, the most accurate means to determine temperatures in micro-gravity. Their primary (non-correctable) disadvantage involve the perturbations introduced in the flow by the probe. For these experiments a thermocouple array is placed downstream from the region of interest to provide reference temperature measurements to be correlated with luminous intensity measurements obtained from video images. This arrangement provides an simple way of obtaining accurate temperature profiles with minimum perturbation of the flow field.

Heat Transfer to the Walls
The heat transfer rates to the wall will be made using standard Schmidt-Boelter type thermopiles. The thermopiles provide linear millivolt output directly proportional to the heat flux through the gage. A particularly reliable (for combustion problems) thermopile system is produced by Medtherm Corp. These gages have relatively fast response times (order .3 seconds) and are small in size (3.13 mm in diameter). They can operate in relatively hot environments (calibrated to over 473 K) and can be subjected to heat fluxes as large as 0.3 MW/m^2. Recall that the porous plates are to be water cooled such that excessive temperatures should not prove to be an issue.

Modeling

Introduction

Techniques for modeling and characterization of turbulent flame propagation are still relatively immature and various candidate options are reported in the literature. A promising method for characterizing turbulent diffusion flames is the laminar flamelet method. In this method a turbulent flame is assumed to be composed of locally laminar flame elements. The mixing field as specified by the local mixture fraction and the strain field as specified by the scalar dissipation have generally been considered to be adequate independent variables from which a range of flame properties could be determined. Fendell [8] and Linan [9] developed the theoretical underpinnings by which examination of finite rate processes within nonpremixed could be analyzed. Linan analytically specified the conditions under which the flame extinction as a result of strain effects would occur as well as the conditions under which ignition of an initially premixed system would occur [9]. The well known S curve for ignition and extinction displays these processes. While a representation of flame sheet properties as a function of the reduced Damkohler number is useful, a more representative picture should also include flame properties away from the flame sheet. In this study we use the Linan formalism for a general hydrocarbon-air flame and create a general functional relationship which specifies flame properties in terms of two parameters: the local scalar dissipation rate and the local mixture fraction. Next, we examine a canonical flow field, a strained vortex flow, and embed the finite rate chemistry model into the flow to characterize the flame extinction process.

The flamelet method enables simple flow fields to be examined, so that full turbulent flow-field solutions do not need to be immediately found. Following Marble's [10] original investigation into the structure of diffusion flames in vortical flows, a number of investigations have described flame structure in vortical streams. The vortical flow represents a characteristic of turbulent eddying flows and has been used to infer the effects of turbulent mixing on flame dynamics. Other studies using a vortical flame element include work by Cetegen and Sirignano [11] and Baum and coworkers [12,13].

Another canonical flow which has clarified the effects of fluid mechanics on combustion dynamics is the counterflow flame. In counterflow flames the strain rate for a given flame element is well specified and controlled. Many experimental, numerical, and analytical studies have been performed in the counterflow geometry. Law and coworkers [14] have used this well specified strain field to characterize many aspects of flame-strain interaction.

In this study we focus on analytical descriptions of the flame dynamics. Without being pedantic, we note that analytic work in sufficiently complex scientific disciplines such as combustion often strengthen the theoretical basis of the science. Thus, our goals in this study are to devise a flow field which contains the essential features of turbulence as exemplified by a controlled strain field and large scale mixing. Several studies have analytically detailed finite rate chemistry induced extinction processes in nonpremixed flames. Finite-rate chemical reactions are important in the practical application of any turbulent combustion model. Small-scale flow variations in turbulence may produce enough strain to bring about local extinguishment. As previously noted, Fendell [8] and Linan [9] developed the theoretical underpinnings by which examination of finite rate processes within nonpremixed flames could be analyzed. The well-known S curve for ignition and extinction displays these processes. The major departure in this work from those previous studies is in the coupling of the flame temperature dependence on mixture fraction and scalar dissipation rate with a well characterized vortically mixing strain field.

Methodology

The methodology for the flamelet based models relies on Linan's Activation Energy Asymptotics approach. We have applied this methodology to describing the extinction process and have incorporated the extinction flamelet model into a strained vortex flow to simulate the action of turbulence. The analytic foundations for the radiation-free, one-step chemistry problem have been demonstrated by Williams [15]. The equations that govern the flame are the conservation of energy and species are:

$$\frac{\partial T}{\partial t} + u\frac{\partial T}{\partial x} + v\frac{\partial T}{\partial y} = \frac{\lambda}{\rho C_p}\left(\frac{\partial^2 T}{\partial x^2} + \frac{\partial^2 T}{\partial y^2}\right) - \frac{Q}{C_p}\dot{\omega}Y_F \tag{1}$$

$$\frac{\partial Y_F}{\partial t} + u\frac{\partial Y_F}{\partial x} + v\frac{\partial Y_F}{\partial y} = \frac{\lambda}{\rho C_p Le_F}\left(\frac{\partial^2 Y_F}{\partial x^2} + \frac{\partial^2 Y_F}{\partial y^2}\right) + \dot{\omega}Y_F \tag{2}$$

$$\frac{\partial Y_O}{\partial t} + u\frac{\partial Y_O}{\partial x} + v\frac{\partial Y_O}{\partial y} = \frac{\lambda}{\rho C_p Le_O}\left(\frac{\partial^2 Y_O}{\partial x^2} + \frac{\partial^2 Y_O}{\partial y^2}\right) + \phi\dot{\omega}Y_F \tag{3}$$

where T is the temperature, Y_F is the fuel mass fraction, and Y_O is the oxidizer mass fraction. By assuming the system is steady-state and that the Lewis numbers are unity, these equations can be simplified. Furthermore, a recent paper by Cuniot and Ponsiot [16] showed that the following analysis could be applied to non-unity Lewis number calculations with some modifications.

If there are assumed to be no sources or sinks other than the chemical reaction, then a change of variables into a mixture fraction space can separate the problem into a flow-specific part and a flow-independent part. The flow-specific part is

$$u\frac{\partial z}{\partial x}+v\frac{\partial z}{\partial y}=\frac{\lambda}{\rho C_p}\left(\frac{\partial^2 z}{\partial x^2}+\frac{\partial^2 z}{\partial y^2}\right) \tag{4}$$

in which z is the mixture fraction. The problem is then closed by specifying the relationship between the temperature and the mixture fraction. This is accomplished by changing the independent variable of equation (1) to z.

$$-\lambda\left[\left(\frac{\partial z}{\partial x}\right)^2+\left(\frac{\partial z}{\partial y}\right)^2\right]\frac{\partial^2 T}{\partial z^2}=Q\dot{\omega}Y_F \tag{5}$$

Note the importance of the gradients of z. The term in the brackets is know as the scalar dissipation, χ, and it can be found from the solution of equation (4). The chemical source term is assumed to follow the Arrhenius theory. Liñán re-scaled equation (4) such that

$$T_{Ad}-T=(\varphi+\gamma\eta)\frac{T_{Ad}^2}{T_{act}} \tag{6}$$

and

$$z=\varepsilon\eta+z_{st} \tag{7}$$

where the other variables are parameters. This led to the classic equation

$$\frac{\partial^2\varphi}{\partial\eta^2}=\delta(\varphi+\eta)^{Y_F}(\varphi-\eta)^{Y_O}\exp\left[-(\varphi+\gamma\eta)\right] \tag{8}$$

This problem is numerically solved, and we plot the temperature variation with the mixture fraction and the reduced Damkohler number δ (easily related to the scalar dissipation) in figure 2. A surface has been fit to the solution in order to make computation easier. Equation (8) yields no solution below a critical Damkohler number, which is assumed to be the extinction value. This extinction value is also tabulated.

For our purposes, this theory has been applied to a time-independent strained vortex flow. In this flow, a vortex exists within a stagnation-point flow. Compressibility effects can and will be handled, but they are not important to the development of the technique at this point. The flow field for this situation was found to be

$$u=2Ux-\frac{\Gamma}{2\pi}\frac{(y-y_0)}{(x-x_0)^2+(y-y_0)^2} \tag{9a}$$

$$v=2Uy-\frac{\Gamma}{2\pi}\frac{(x-x_0)}{(x-x_0)^2+(y-y_0)^2} \tag{9b}$$

Appropriate non-dimensional variables for this problem are

$$\theta=\frac{x}{\sqrt{\lambda/(\rho C_p U)}} \qquad \text{and} \qquad \psi=\frac{y}{\sqrt{\lambda/(\rho C_p U)}}$$

Then, equation (4) becomes:

$$\left[2\theta-\frac{\Gamma\rho C_p}{2\pi\lambda}\frac{(\psi-\psi_0)}{(\theta-\theta_0)^2+(\psi-\psi_0)^2}\right]\frac{\partial z}{\partial\theta}+\left[-2\psi-\frac{\Gamma\rho C_p}{2\pi\lambda}\frac{(\theta-\theta_0)}{(\theta-\theta_0)^2+(\psi-\psi_0)^2}\right]\frac{\partial z}{\partial\psi}=\frac{\partial^2 z}{\partial\theta^2}+\frac{\partial^2 z}{\partial\psi^2}$$

which yields a result for any strain rate.

The scalar dissipation, χ, is then

$$\chi = U\left[\left(\frac{\partial z}{\partial \theta}\right)^2 + \left(\frac{\partial z}{\partial \psi}\right)^2\right]$$

Equation (4), thus modified, was solved for this flow field, by means of a control volume finite-difference code [17]. A representative mixture fraction and scalar dissipation field are shown in figure 3. For a point of reference, a flame would sit along a line of constant mixture fraction, as defined by the chemistry. Furthermore, the flame would extinguish above a critical value of the scalar dissipation, also as defined by the chemistry. The problem was closed with the results of the flow-independent theory. Figure 4 shows the temperature field for a representative flame.

Conclusions and Future Work

Two sintered bronze burners are used to study the structure of a laminar diffusion flame and the effects that physical boundaries have on the characteristics of the flow and, therefore, on heat, fuel and oxidizer transport from and towards the flame. Extinction and flame geometry in the low velocity (strain) regime are the main areas of interest. Instabilities, due to buoyancy, constrain the range of velocities that can be studied in normal gravity, thus, the need for micro-gravity experiments. An extension of the methodology proposed by Linan and Fendell is used to model the flame. So far the modeling effort has concentrated in coupling the flame temperature dependence on mixture fraction and scalar dissipation rate with a well characterized vortically mixing strain field. A vortex exists within a stagnation-point flow, therefore, this theory has been applied to a time-independent strained vortex flow.

Acknowledgments

References

1. Puri, I.K. and Seshadri, K., *Combustion and Flame*, 65, 137-150, 1986.
2. Law, C.K., *Twenty-Second Symposium (International) on Combustion*, The Combustion Institute, 1381-1402, 1988.
3. Egolfopoulos, F.N., *Twenty-Fifth Symposium (International) on Combustion*, The Combustion Institute, 1375-1381, 1994.
4. Egolfopoulos, F.N., *Third International Micro-Gravity Combustion Workshop*, NASA LeRC, Cleveland, OH, 1995.
5. Atreya, A., Agrawal, S., Shamim, T., Pickett, K., Sacksteder, K. and Baum, H., *Third International Micro-Gravity Combustion Workshop*, NASA LeRC, Cleveland, OH, 1995.
6. Torero, J.L., Bonneau,L., Most, J. M. and Joulain, P., *Advances in Space Research*, 16, 7, 149-152, 1995.
7. Torero, J.L., Bonneau, L., Most, J.M. and Joulain, P., *Twenty-fifth Symposium (International) on Combustion, The Combustion Institute*, 1701-1709, 1994.
8. Fendell, F.F., "Ignition and Extinction in Combustion of Initially Unmixed Reactants," J. Fluid Mechanics, 21:281-303, 1965
9. Linan, A., "The Asymptotic Structure of Counterflow Diffusion Flames for Large Activation Energies," Acta Astronautica, 1:1007-1039,
10. Marble, F.E., "Growth of a Diffusion Flame in the Field of a Vortex," Recent Advances in Aerospace Sciences (C. Cassci, Ed.) 315, 1985
11. Cetegen, B.M. and Sirignano, W.A., "Study of Molecular Mixing and Finite Rate Chemical Reaction in a Mixing Layer," Twenty-Second Symposium (International) on Combustion/ The Combustion Institute 1988
12. Baum, H.R., Rehm, R.G., and Gore, J.P., "Transient Combustion in a Turbulent Eddy," Twenty-Third Symposium (International) on Combustion/ The Combustion Institute 1990
13. Baum, H.R., Corley, D.M., and Rehm, R.G., "Time-Dependent Simulation of Small Scale-Turbulent Mixing and Reaction," Twenty-First Symposium (International) on Combustion/ The Combustion Institute 1986
14. Birkan, M.A. and Law, C.K., "Asymptotic Structure and Extinction of Diffusion Flames with Chain Mechanism," Combustion and Flame, 73:127-146 1988
15. Williams, F.A., Combustion Theory, Benjamin Cummings, New York 1985
16. Cuenot, B. and Poinsot, T., "Asymptotic and Numerical Study of Diffusion Flames with Variable Lewis Number and Finite Rate Chemistry," Combustion and Flame, 104:111-137, 1996
17. Patrankar, S.V., Numerical Heat Transfer and Fluid Flow, Taylor and Francis, New York, 1980.
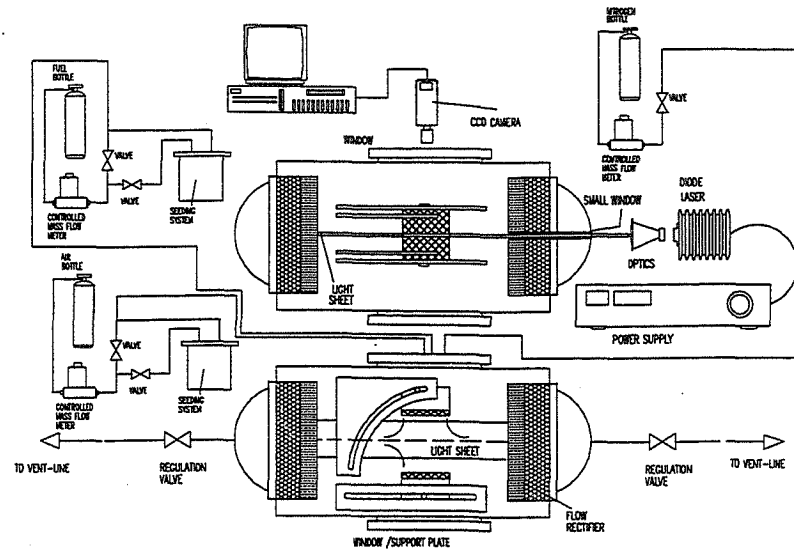
Figure 1.- Schematic of the experimental apparatus
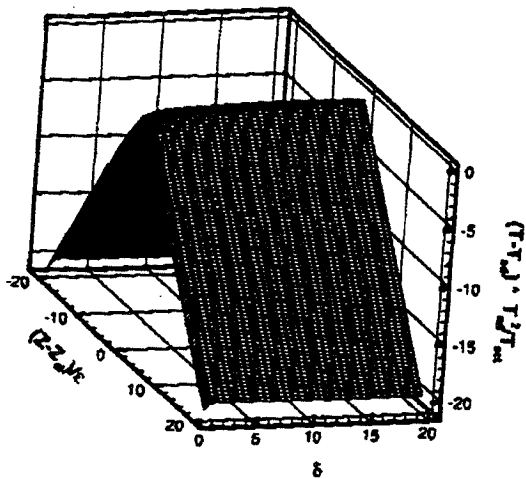
Figure2.- Temperature variation with the mixture fraction and the reduced Damkohler number δ.
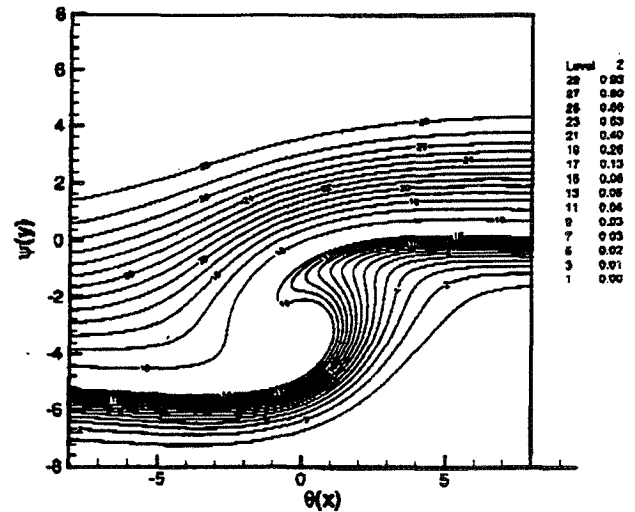
Figure 3. - A representative mixture fraction and scalar dissipation field.
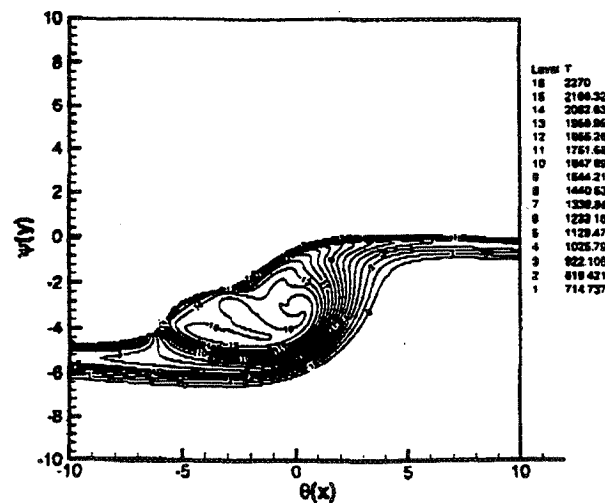
Figure 4.- Temperature field for a representative flame

STRAIN-RATE-FREE DIFFUSION FLAMES: INITIATION, PROPERTIES, AND QUENCHING[*]

FRANCIS FENDELL and Harald Rungaldier
TRW Space and Electronic Group
Redondo Beach, California

and

Suleyman Gokoglu and Donald Schultz
NASA Lewis Research Center
Cleveland, Ohio

<u>Introduction</u>

For about a half century, the stabilization of a steady *planar* deflagration on a heat-sink-type flat-flame burner has been of extraordinary service for the theoretical modeling and diagnostic probing of combusting gaseous mixtures (ref. 1). However, most engineering devices and most unwanted fire involve the burning of initially unmixed reactants. The most vigorous burning of initially separated gaseous fuel and oxidizer is the diffusion flame. In this useful idealization (limiting case), the reactants are converted to product at a mathematically thin interface, so no interpenetration of fuel and oxidizer occurs. This limit is of practical importance because it often characterizes the condition of optimal performance (and sometimes environmentally objectionable operation) of a combustor. A steady *planar* diffusion flame is most closely approached in the laboratory in the counterflow apparatus (ref. 2). The utility of this simple-strain-rate flow for the modeling and probing of diffusion flames was noted by Pandya and Weinberg 35 years ago (ref. 3), though only in the last decade or so has its use become internationally commonplace. However, typically, as the strain rate a is reduced below about 20 cm^{-1}, and the diffusion-flame limit (reaction rate *much* faster than the flow rate) is approached, the burning is observed to become unstable in earth gravity. The advantageous steady planar flow is not available in the diffusion-flame limit in earth gravity. This is unfortunate because the typical spatial scale in a counterflow is $(\kappa/a)^{1/2}$, where κ denotes a characteristic diffusion coefficient; thus, the length scale becomes large, and the reacting flow is particularly amenable to diagnostic probing, as the diffusion-flame limit is approached. The disruption of *planar* symmetry is owing the fact that, as the strain rate a decreases, the residence time $(1/a)$ of the throughput in the counterflow burner increases. Observationally, when the residence time exceeds about 50 msec, the inevitably present convective (Rayleigh-Benard) instabilities, associated with hot-under-cold (flame-under-fresh-reactant) stratification of fluid in a gravitational field (refs. 4 and 5), have time to grow to finite amplitude during transit of the burner.

Can we, with access to microgravity testing, more closely achieve the vigorous, strain-rate-free diffusion-flame limit in the burning of initially separated gaseous fuel and oxidizer? In microgravity, it is not convenient to try to "turn down" a counterflow. Rather, we decide to start with static gaseous fuel occupying one half-volume, and static gaseous oxidizer the other half-volume, of an impervious noncatalytic isothermal squat rectangular-solid container, with height significantly smaller than the length of a side of the horizontal square cross section (Fig. 1a). Typically, the chamber is 25 cm x 25 cm x 9 cm, with 1.25-3.27-cm-thick stainless-steel walls. The oxidizer is separated from the fuel by a thin (but rigid) impervious planar interface. For specificity, we take the upper half-volume to be filled uniformly with oxygen diluted with helium, and the lower half-volume to be filled uniformly with hydrogen diluted with argon, such that the two half-volumes have equal pressure, temperature, density, and (hence) "average molecular weight". At time zero, with minimal disturbance and with minimal elapse of time, we seek: (1) to remove the separator, by translation at nearly uniform speed in its own plane, through a tightly fitting slit in one side wall (Fig. 1b), and (2) to create a diffusion flame at the *planar* interface between the nonhypergolic (not spontaneously reactive) constituents of the two half-volumes (Fig. 1c). Demonstration, in a ground-based microgravity testing facility, of an experimental design for achieving a planar diffusion flame at the centerplane of the container is the primary near-term goal of this project. Straightforward analysis (refs. 6-9) of a moving-boundary problem (ref. 10) indicates that, in microgravity, the flame thenceforth travels so that it is situated at an interface at which the hydrogen and oxygen meet in stoichiometric proportion. If

---

(as we intend) the initial amount of hydrogen is deficient relative to the initial amount of oxygen, then eventually (if not immediately) the planar flame travels further and further into the half-volume initially containing hydrogen (Fig. 1d), until the hydrogen is (virtually) fully depleted. Of course, when the amount of residual hydrogen becomes small, and/or the diffusion flame approaches the cold end wall, the situation is inconsistent with a vigorous, thin diffusion flame. The burning is extinguished before the hydrogen is fully depleted, owing to the finite rate of the actual chemical-kinetic mechanism. However, there is an interval during which the travel of a virtually strain-rate-free, planar diffusion flame may be tracked; within the container in microgravity, we expect to achieve what is inaccessible in earth gravity, the only compromise being the introduction of time, as well as a Cartesian coordinate, as an independent variable (ref. 11). The rate of travel of the hydrogen-air diffusion flame is much slower than the rate of laminar flame propagation through a hydrogen-air mixture. This relatively slow travel facilitates diagnostic detection of the flame position as a function of time, but the slow travel also means that the time to burnout (extinction) probably exceeds the testing time (typically, a few seconds) available in earth-sited facilities for microgravity-environment conditions.

We have undertaken analyses (ref. 7) to predict: (1) the position and temperature of the diffusion flame as a function of time; (2) the time at which extinction of the diffusion flame occurs; and (3) the thickness of quench layers formed on side walls (i.e., on lateral boundaries, with normal vectors parallel to the diffusion-flame plane), and whether, prior to extinction, water vapor formed by burning condenses on these cold walls. We regard our (*generalized* Shvab-Zeldovich/Burke-Schumann) model as semi-empirical. We hope that empirical assignment of optimal values for dimensionless groups arising in simplistic statements of the transport and kinetic processes will permit us to fit some of the microgravity data (explicitly, the position and temperature at the thin flame in some of the experiments). We further hope that the guidance from that experience will permit us to assign values to these dimensionless groups to predict the corresponding observations in the remainder of the experiments. If so, the viability of the modeling to quantify, to a practically useful accuracy, key properties in a difficult-to-analyze diffusion flame, *with appreciably differing diffusivities*, will have been demonstrated.

Initiation of the Diffusion Flame

The design for the initiation of the diffusion flame between initially separated, not-spontaneously-reactive fuel vapor and oxidizer in microgravity has features in common with the evolution of burning of a stratified gaseous mixture in a gallery of a coal mine in earth gravity (refs. 12-14). For the ensuing description, we envision vertical end planes for the gallery. In such a gallery, the relatively light gas methane is concentrated near the ceiling of the gallery, and the relatively heavy air near the floor; mixture with combustible composition lies between an upper (horizontal) plane at the fuel-rich flammability limit, and a lower (horizontal) plane at the fuel-lean flammability limit. After ignition along a line near one end wall, the line ignitor being parallel to the floor and to the nearby end wall, a two-dimensional deflagration propagates, within the combustible mixture, from the nearby end wall toward the opposite end wall. In fact, the propagation speed is more rapid for near-stoichiometric strata than for strata with mixture near a limiting composition for combustion; thus, the horizontally propagating deflagration has a curved configuration, with the leading "nose" of the deflagration lying in a plane (the "centerplane") parallel to the floor, at a height roughly midway between the fuel-rich-limit plane and the fuel-lean-limit plane; the retarded end points of the propagating "deflagration arc" lie in the fuel-rich-limit and fuel-lean-limit planes. Behind the deflagration but above the centerplane, excess fuel vapor (but virtually no residual oxidizer) persists, there being less and less excess fuel vapor as the centerplane is approached from above. Behind the deflagration but below the centerplane, excess oxidizer (but virtually no residual fuel) persists, there being less and less excess oxidizer as the centerplane is approached from below. At the centerplane, where no excess fuel vapor or oxidizer persists, and where the temperature is approximately the highest of any strata, a planar (horizontal) diffusion flame persists; the residual fuel vapor and oxidizer diffuse toward this planar flame to continue the burning. The horizontal-anchor-resembling configuration formed by the curved deflagration and the planar diffusion flame is a "three-branched flame". However, the diffusion flame does not remain planar at much distance behind the propagating deflagration, owing to the previously discussed Rayleigh-Benard instability in earth gravity.

In microgravity, no stratification arises within the H_2/Ar and O_2/He contents of the half-volumes of our container. Prolonged interpenetration of the contents of the two half-volumes would result in a homogeneous mixture (in our case, fuel-lean). However, (Fig. 1b) a significant H_2/Ar and O_2/He stratification persists for a limited time after separator removal; ignition along a line in the centerplane, near to and parallel to one side wall, would result in the just-described "three-branch flame". Moreover, in microgravity, for not too tall a chamber, no Rayleigh-Benard instability would arise to disrupt the planarity of the diffusion flame engendered at the centerplane. We set off the line ignitor as soon as diffusive interpenetration of the fuel vapor and oxidizer gives a combustible layer sufficiently thick to sustain flame propagation.

One feature of the chamber in microgravity with no counterpart in the coal-mine gallery on earth is the translation of the flat separator, at moderate speed (~ 125 cm/s) in its own plane until its trailing edge clears the side wall. The moving separator entrains a laminar flow by viscous forces, both in boundary layers formed on the separator, along the portion of its top and bottom surfaces still within the chamber, and in the wake of its trailing edge (Fig. 2) (ref. 15). The flow in the narrow boundary layers and wake does induce a broad weak recirculatory "cell" in each half-volume; this organized motion could augment the

otherwise almost purely diffusional transport of fresh reactant toward the planar flame, but the organized (counterflow-like) flow decays under viscous diffusion in about a quarter second. Planar Fickian diffusion remains the mode of reactant transport throughout the overwhelming preponderance of the test duration. However, if, during the brief interval for which the flow in the wake of the trailing edge of the translating separator exists, the premixed flame is able to propagate into the wake, then the deflagration advances across the centerplane at a speed that is the sum of the wake-flow speed and the propagation speed. In such a case, the diffusion flame is entirely in place (i.e., fills the entire square centerplane of the container -- except in the immediate vicinity of the cold side walls) almost as fast as the trailing edge of the separator exits the chamber.

Separator Withdrawal and Flame Spread across the Centerplane

If a thin flat plate in the plane $z = 0$ is abruptly set in motion, at time $t = 0$, at constant speed u_o in the x direction, then there is associated motion of a viscous incompressible fluid in the half space $z > 0$ above the plate and in the half space $z < 0$ below the plate, with the velocity profile expressible in terms of the selfsimilar independent variable $\left[z^2/(vt)\right]$, where v denotes the (constant) kinematic viscosity of the gas. The trailing edge of the flat plate is taken to lie at $x = u_o t$. Behind the plate $\left(x < u_o t\right)$, there is no longer any skin friction, but, in the approximation adopted here, fluid in the region behind the trailing edge is instantaneously set in motion by the movement of the plate. In the domain $x < u_o t$, if u denotes the velocity in the x direction and w in the z direction, then in the boundary-layer approximation for the Eulerian formulation of the conservation of momentum in the x direction,

$$u_t + u\, u_x + w\, u_z = v\, u_{zz}. \tag{1}$$

In the "modified-Oseen" approximation, in which the nonlinear convective-transport term is linearized for tractability,

$$u_t + \frac{u_o}{3}\, u_x - v\, u_{zz} \approx 0, \tag{2}$$

where the choice of the appropriate "average coefficient" as $(u_o/3)$ is anticipated to be a good approximation on the basis of past experience. Henceforth, we adopt the notation $a \equiv u_o/3$. A solution to Eq. 2 that joins, to satisfactory approximation, to the solution holding for $x > u_o t$ is given by

$$u(x,z,t) = \begin{cases} \dfrac{2}{\pi}\, u_o \left(\dfrac{x - a\,t}{2\,a\,t}\right)^{1/2} \exp\!\left[-z^2/(4\,v\,t)\right], & a\,t < x < 3\,a\,t \\ 0, & 0 < x < a\,t. \end{cases} \tag{3}$$

Thus, when the plate has moved a distance $u_o t$, the length of the disturbed region behind the plate is $(2/3)\, u_o t$; the precise, finite length of the disturbed region is a consequence of the adoption of the Oseen approximation.

The net delivery of fluid at the "far" side wall $x = 2W$ (i.e., the volume delivered, per unit depth in the y direction, for a standard Cartesian coordinate system) is equal to $4\left[v(2W)^3/u_o\right]^{1/2}/\pi^{1/2}$. Since the net delivery of fluid at $x = 2W$ varies as $u_o^{-1/2}$, the delivery is minimized by increasing the speed of separator withdrawal, u_o. However, the velocity profile is Gaussian in the transverse coordinate z, and the flow is subject to the growth of instabilities. Transition to turbulence may occur if the Reynolds number becomes sufficiently large (i.e., if the speed u_o becomes sufficiently large) (ref. 15). For $u_o = 125$ cm/s, $2W = 25$ cm, and $v = 0.1$ cm^2/s, the delivery is 10-12 cm^2, with the duration of the interval of delivery, $t_f[= 3\,(2W)/u_o] \approx 0.6$ s; the peak delivery rate is $2\left[v(2W)u_o/\pi\right]^{1/2} \approx 20$ cm^2/s. The peak return-flow speed is 20 cm^2/s divided by the height of the return-flow domain, i.e., the half-height of the container L. If $L = 4.5$ cm, then the transversely averaged peak return speed is on the order of 4-5 cm/s. If the delivery is 10-12 cm^2, and the height over which this delivery is distributed in a return flow is 4.5 cm, then the fluid displacement by the piston-like return flow is 2-3 cm.

At least part of the fluid entrained during withdrawal of the separator may form counterrotating corner vortices, one above the midplane in the vicinity of the side wall at $x = 2W$ and a comparable one below the midplane in the vicinity of the side wall.

We estimate that the vortices might be turbulent, with radius R at the time of separator withdrawal $t_1 (= 2W/u_o)$ of 1.25 cm (ref. 16). The inviscid interaction of the two vortices with one another and with the side wall at $x = 2W$ is such that each vortex would move toward the side wall and toward the end wall of its half-volume. The entrained fluid not entering the vortex seems likely to support the translation of each vortex toward the end wall in its half-volume, but to transport the vortex away from $x = 2W$ and into the interior of the half-volume. If each vortex at its periphery interacted strongly with a nonrotating wall, the e-folding time for viscous decay would be $R^2/(\pi^2 v)$, or about 1.7 s for adopted parameter values. In the absence of such a peripheral constraint, the vortex could persist longer. We conjecture that the vortex continues to grow for a brief time beyond t_1, owing to the flow entrained in the wake of the trailing edge; if so, then the vortex radius increases from $R \approx L/4$ to $R \approx L/2$, interaction with the fixed container walls increases, and the vortex decays on the order of 3.2 s.

At time $t_o (> 0)$, line ignition occurs at $x = X_o (\geq 0)$ in the centerplane $z = 0$, where the length of the square cross section $2W \gg X_o$. Specifically, ten electrode pairs, located on the line $(x = X_o, z = 0)$ and approximately evenly distributed over the distance $2W > y > 0$, are simultaneously sparked at time $t = t_o$. We here track the flame position $X_f(z,t)$, only in the centerplane $z = 0$, and henceforth denote $X_f(0,t)$ as $X_f(t)$, for brevity of notation. If we adopt a fixed value v_f for the laminar flame propagation speed through the combustible mixture formed by diffusional interpenetration aft of the trailing edge of the translating splitter plate, then, in view of the flow field just examined,

$$\dot{X}_f(t) = \begin{cases} v_f + \dfrac{2}{\pi} u_o \left(\dfrac{X_f(t) - a\,t}{2\,a\,t} \right)^{1/2}, & a\,t \leq X_f(t) < 3\,a(t - t^*) \\ v_f, & X_o \leq X_f(t) < a\,t, \end{cases} \tag{4}$$

where $X_f(t_o) = X_o$. Ignition occurs at $t_o (> 0)$ because it takes a finite time t^* for a combustible mixture to form at position x, once the splitter plate clears position x. Thus, the time t_{spread}, defined by $X_f(t_{spread}) = 2W$, is a function of the given positive parameters X_o, t_o, v_f, t^*, u_o, and $2W$. By inspection, for rapid flamespread, we seek to initiate the flame in the wake, or, if the flame is initiated behind the wake, we seek to have the flame catch up to the wake, so that convection enhances propagation for the spread of the flame across the centerplane. We have not included expansion of burned gas in the x direction as an aid to flamespread, because, from geometric considerations, the burned gas expands primarily in the z direction, and because a conservative (upper-bound) estimate on t_{spread} is sought.

To ensure the one-dimensionality of the subsequent travel of the resulting diffusion flame, we seek as rapid a propagation across the centerplane as is consistent with physical constraints (e.g., avoiding transition to turbulence in the flow induced by separator withdrawal), and with experimental procedure (e.g., limitations of pull mechanisms for separator withdrawal, in view of the size, weight, reliability, and cost constraints for microgravity testing). Otherwise, events in portions of the centerplane from which the separator is withdrawn earlier get a headstart on events in portions of the centerplane from which the separator is withdrawn later -- an anomaly for a test with purportedly planar symmetry.

Test Rigs

Three apparati have been designed, constructed, instrumented, and used for ground-based testing in earth gravity.

First, an ignition rig, of virtually the same geometric configuration as the above-described chamber (25 cm x 25 cm x 11 cm), has been used to determine the margin against detonation. The chamber dimensions exceed the critical cell size for hydrogen-oxygen detonation; this observation raises concern if a seal or other failure inadvertently allowed the fuel and oxidizer to mix prior to ignition. Thus, testing was undertaken to determine: (1) the maximum pressure to be expected in the apparatus; and (2) the minimum voltage required by the ignitor box to initiate burning of the mixed gaseous reactants -- information needed to design the power supply for the ignitor box. Testing included trials with ten stainless-steel electrode pairs, each of 0.46-mm gap, evenly spaced over a 19-cm span. Accordingly, intended combinations of hydrogen/argon and oxygen/helium, to be carefully initially segregated in the experiment, were intentionally mixed homogeneously prior to sparking in the test rig; the equivalence ratio ϕ extended from 0.15 to 1.0; the initial pressures tested were both atmospheric and subatmospheric. Two of three 13.5-MPa acoustic transducers, all specially potted against heat, were mounted in opposite corners of a square cross-section, the third being located at the center of one of the 25 x 25 cm walls. Three distinct pressure-vs.-time profiles were recorded during the series of tests. One was the smooth rapid pressure rise and fall that is characteristic of deflagration. The second was a smooth pressure rise, followed by the onset of a short period of high frequency fluctuations (similar to pressure oscillations indicative of

end-gas knock in cylinders of spark-ignition engines) at the start of pressure tail-off. The third was a smooth pressure rise for a short period, followed by a pressure spike and brief fluctuations. The corner-mounted probes often recorded the last two phenomena, while the side-wall-centered probe recorded only the first two. Some of the pressure spikes observed were sufficient to cause failure of the corner-mounted transducers, which were rated not to fail mechanically below a static pressure of 6.8 MPa. No pressure spikes or "knock" occurred for $\phi \leq 0.4$ with the ten-gap multispark ignitor, although an alternative two-spark ignitor did give a pressure spike at $\phi = 0.4$; use of the multispark ignitor significantly reduced the propensity to spike or "knock". Typical pressure rise was about four-fifths of the theoretical adiabatic pressure rise, the difference being attributable to heat loss to the walls. An input of $75 \ V$ to the ignitor box ensured ignition (of the tested mixtures) by the multispark ignitor.

Second, a pull rig (with dimensions similar to those of the planar-flame chamber) has been constructed to determine the force required to achieve splitter-plate (separator) withdrawal at a fairly uniform speed of about 125 cm/sec. The top periphery of the portion of the splitter plate in the test chamber is in contact with an O-ring; the bottom periphery is in contact with an inflatable seal, maintained at partial inflation during withdrawal to minimize leakage of contents from the chamber. Silicon-based vacuum grease, used as a chemically inert solid lubricant for the seal-separator interface, permitted more repeatable and more uniform speed (of the separator during withdrawal) than did the alternative lubricants graphite and molybdenum disulfide. Measurement of the seal leakage has not been completed.

Third, flat flames of H_2/air, H_2/O_2, CH_4/O_2, and other mixtures are stabilized on a water-cooled sintered-porous-disc burner to calibrate the "readings" of relatively inexpensive infrared cameras, to be used for nonintrusive temperature measurements in the experiments. The ratio of the emission intensity on the 1.45-μm and 1.94-μm lines, effectively unique to the product gas H_2O, is to be used to infer the temperature; the particular ratio indicative of a specific temperature is established by recording the ratio for each of four specific temperatures, known by a proprietary technique and well distributed over the range of 2000 K-2800 K.

Plans

A combined test chamber and auxiliary chamber (for receipt and storage of the withdrawn rigid separator) have been machined, and 2.5-cm-thick fused-quartz windows for the optical access of diagnostic instrumentation are to be installed, along with the ignition subsystem and separator-withdrawal subsystem. Space allocation on a drop rig for testing the diffusion-flame-initiation design in the 5-seconds-microgravity facility is under way. Near-term testing is limited to hydrogen-fueled diffusion flames.

However, the long residence time accessible in a strain-rate-free diffusion flame makes the apparatus highly suitable for experiments for collecting sooting-rate data over a range of pressure, for hydrocarbon-vapor-fueled burning.

Acknowledgments

References

[1]Carrier, G. F., Fendell, F. E., and Bush, W. B., "Stoichiometry and Flame-Holder Effects on a One-Dimensional Flame," *Combustion Science and Technology*, Vol. 18, April 1978, pp. 33-46.

[2]Fendell, F., "Ignition and Extinction in Combustion of Initially Unmixed Reactants," *Journal of Fluid Mechanics*, Vol. 21, February 1965, pp. 281-303.

[3]Pandya, T. P., and Weinberg, F. J., "The Study of the Structure of Laminar Diffusion Flames by Optical Methods," *Ninth Symposium (International) on Combustion*, Academic Press, New York, NY, 1963, pp. 587-596.

[4]Leal, L. G., *Laminar Flow and Convective Transport Process -- Scaling Principles and Asymptotic Analysis*, 1st ed., Butterworth-Heinemann, Boston, MA, 1992, pp. 718-732.

[5]Goldstein, R. J., and Volino, R. J., "Onset and Development of Natural Convection above a Suddenly Heated Horizontal Surface," *Journal of Heat Transfer*, Vol. 117, November 1995, pp. 808-821.

[6]Fendell, F. E., Bush, W. B., Mitchell, J. A., and Fink IV, S. F., "Diffusion-Flame Burning of Fuel-Vapor Pockets in Air," *Combustion and Flame*, Vol. 98, August 1994, pp. 180-186.

[7]Fendell, F., and Wu, F., "Unsteady Planar Diffusion Flames: Ignition, Travel, Burnout," *Combustion Science and Technology*, Vol. 107, July 1995, pp. 93-126.

[8]Fendell, F., and Wu, F., "Diffusion-Flame Burning of Fuel-Vapor Pockets in Oxidizer for General Lewis Numbers," *Combustion and Flame*, Vol. 105, April 1996, pp. 1-14.

[9]Fendell, F. E., and Mitchell, J. A., "Feasibility of Planar, Unidirectional-Flow Diffusion Flames in Earth Gravity," *Combustion Science and Technology*, Vol. 120, 1997, pp. 83-118.

[10]Crank, J., *Free and Moving Boundary Problems,* 1st ed., Clarendon, Oxford, England, 1984, pp. 1-29, 187-192.

[11]Carrier, G. F., Fendell, F. E., and Marble, F. E., "The Effect of Strain Rate on Diffusion Flames," *SIAM Journal on Applied Mathematics*, Vol. 28, March 1975, pp. 463-500.

[12]Phillips, H., "Flame in a Buoyant Methane Layer," *Tenth Symposium (International) on Combustion*, Combustion Institute, Pittsburgh, PA, pp. 1277-1283.

[13]Liebman, I., Corry, J., and Perlee, H. E., "Flame Propagation in Layered Methane-Air Systems," *Combustion Science and Technology*, Vol. 1, February 1970, pp. 257-267.

[14]Feng, C. C., Lam, S. H., and Glassman, I., "Flame Propagation through Layered Fuel-Air Mixtures," *Combustion Science and Technology*, Vol. 10, January/February 1975, pp. 59-71.

[15]Sato, H., and Kuriki, K., "The Mechanics of Transition in the Wake of a Thin Plate Placed Parallel to a Uniform Flow," *Journal of Fluid Mechanics*, Vol. 11, November 1961, pp. 321-352.

[16]Tabaczynski, R. J., Hoult, D. P., and Keck, J. C., "High Reynolds Number Flow in a Moving Corner," *Journal of Fluid Mechanics*, Vol. 42, June 1970, pp. 249-255.
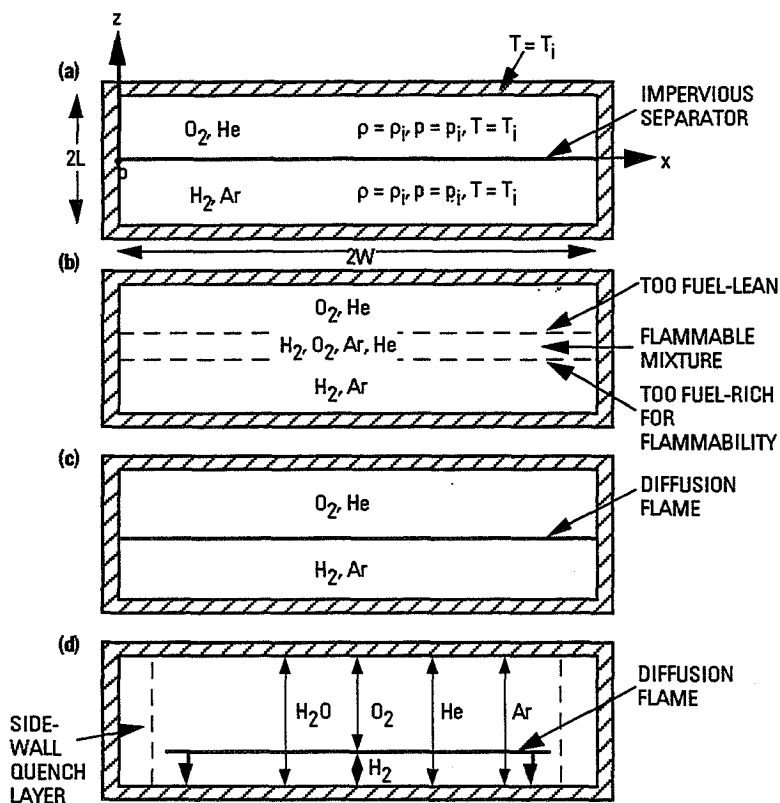
Figure 1.–A planar translating diffusion flame.
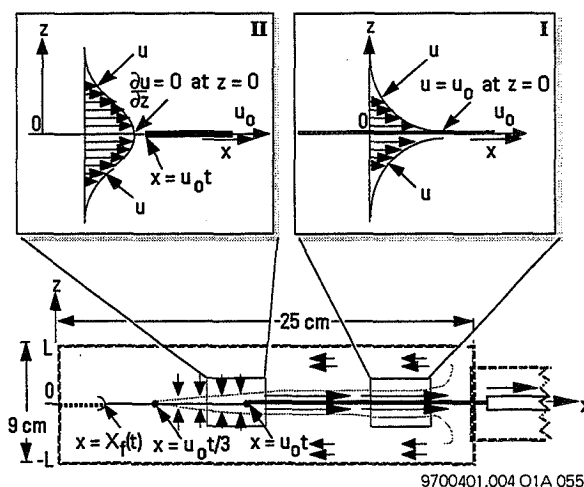
Figure 2.–Triple flame behind a moving splitter plate.

EXPERIMENTAL STUDY ON THE STABILITY OF A DIFFUSION FLAME ESTABLISHED IN A LAMINAR BOUNDARY LAYER

LYNDA BRAHMI, THOMAS VIETORIS, PIERRE JOULAIN
Laboratoire de Combustion et de Detonique
UPR9028 au CNRS, 86960 Futuroscope Cedex
FRANCE

and

JOSE L. TORERO
Department of Fire Protection Engineering
University of Maryland, College Park, MD20742-3031
USA

Introduction

Clearly defined aspects of fire safety are flame propagation and mass burning. When a heat source is in contact with a combustible material ignition may occur. Once the fuel is ignited, the flame propagates across its surface and establishes a diffusion flame over the fuel. The flame transfers heat to the surface, the combustible material vaporizes, and this vapor provides the gaseous fuel necessary to sustain the flame. This process is called mass burning. In normal gravity, temperature gradients generated by the chemical reaction, cause natural convective flows. These flows are initially laminar and transition to turbulence as the area of the burning surface increases. In spacecraft, where buoyancy is negligible, no convective flow develops and flow is limited to that induced by the ventilation system. Since characteristic ventilation velocities are of the order of 0.1 m/s, the flow can be expected to remain laminar and parallel to the surface of the fuel. The complex, often turbulent, mixed flow scenario observed in normal gravity turns into a classical combustion problem generally referred to in the literature as "The Emmons Problem" [1]. The main assumptions behind this theory are of great relevance to spacecraft fire safety and since the solution neglects gravity, have yet to be verified.

The theoretical basis for the study of a reacting laminar boundary layer was given by Emmons [1] who showed that the evaporation rate of a fuel could be expressed as a function of the mass transfer number only. The theoretical work that followed this pioneering study is reviewed by Williams [2] and experimental studies have been conducted with solid and liquid fuels [3]. When focusing on the aerodynamics of the flame, porous burners have been commonly used as a means to de-couple heat and fuel transport mechanisms [3,4]. This type of simulation allows for fuel and oxidizer to be varied independently and for unlimited experimentation time.

The role of buoyancy on a horizontal cross-flow diffusion flame has been studied theoretically by Lavid and Berlad [5] and Mao et al. [6]. Both works propose scaling parameters that when introduced in the conservation equations result in a self-similar solution of the Emmons type. Lavid and Berlad [5] propose to scale the x (horizontal) coordinate by $\xi_x = Gr_x/Re_x^2$ and the z (vertical) coordinate by $\xi_z = Gr_x/Re_x^{5/2}$. This scaling described accurately the increasing effect of buoyancy with "x". The scaling proposed by Lavid and Berlad fails for a purely buoyant regime so Mao et al. [6] proposed a mixed flow parameter, ξ_z, to scale the z coordinate ($\xi_z = (Re_x^5 + Gr_x^2)^{1/10}$) and mixed convection ratio, ξ_x, to scale the distance from the leading edge ($\xi_x = Gr_x/Re_x^{5/2}$). The mixed convection ratio ($\xi = Gr_x/Re_x^{5/2}$) was used by Torero et al. [7] to characterize the downstream evolution of the flow surrounding a horizontal diffusion flame. It was noted that $\xi < 1$ indicates predominantly forced convection perturbed by buoyancy and $\xi > 1$ suggests a predominantly free convection flow perturbed by forced convection. All these analyses were derived for [5,6] small scale laminar diffusion flames but have been only experimentally validated [7] with a gas burner.

The study of mass burning can be divided in two characteristic elements, the gas phase and the condensed phase. In the gas phase, flow structure, flame geometry, reaction chemistry and heat and mass transport mechanisms are the dominant issues. However, the condensed phase is the limiting part of the problem. The rate of fuel gasification is determined by heat feedback to the surface, pyrolysis mechanisms and kinetics. A two part study has been under development at the Laboratoire de Combustion et de Detonique to further understand the role of buoyancy on mass burning and to verify the assumptions imposed by Emmons [1] in the problem's analytical solution. The first part (1992-1997) [7, 8, 9, 10] has concentrated on the

gas phase and experiments have been conducted using a sintered bronze porous burner to simulate the condensed fuel. The experimental work has concentrated on quantifying the role of buoyancy on the flame geometry, blow-off limits and heat transfer from the flame to the burner surface. By using a porous burner, pyrolysis is not coupled to the fuel supply which allows for the gas phase to be studied independently. The aspects of this study related to flame extinction will be the main subject of the present report. The second part of this program (1997-) emphasizes the mechanisms of heat feedback to the fuel surface and the different stages leading to pyrolysis and gasification of the fuel. The effects of the fuel supply being coupled to the heat transfer from the flame will be studied by comparing the previously described simulations with experiments conducted with condensed fuels. A brief description of the ongoing and future work on this area will be also presented.

Experimental Configuration

The experiments are conducted in a test facility that involves a small scale, horizontally oriented, combustion tunnel along with the supporting instrumentation. The wind tunnel test section is 450 mm long and has a circular cross section 350 mm in diameter. Two quartz windows (diameter 200 mm) enable visual observation from the sides and two other openings (diameter 100 mm) are used to support the burner and for optical access from top or bottom. A plate is placed at the center of the chamber (figure 1) attached from either the top (ceiling configuration) or the bottom opening (floor configuration). Ethane, 99.4% pure, is uniformly injected through a porous burner, 50 mm long and 50 mm wide, mounted on the center of the plate. Compressed oxidizer flows through a settling chamber before entering the test section. The air and fuel velocities are governed with controlled mass flow meters. Information on the flame is obtained from two CCD video cameras, eleven Chromel-Alumel thermocouples and an infra red camera. The video cameras provide a top and a side view of the flame. Eight thermocouples are placed on a vertical line with their junction located on the plane of symmetry and three on the plate, close to the leading edge of the burner. The vertical thermocouples generate significant perturbations on the flow, therefore, they are placed far away from the leading edge (60 mm). The combined use of the thermocouples and the infra-red camera will be described later.

Experiments under reduced gravity conditions were conducted at the drop tower of the Instituto Nacional de Tecnica Aeroespacial (INTA-Madrid, Spain) and by using the NASA KC-135 aircraft. At the drop tower facility a free fall provided micro-gravity periods of up to 2.2 sec. (gravity levels of $10^{-5}g_0$) and, following a parabolic trajectory, up to 25 sec. of reduced gravity were obtained with the KC-135 aircraft (gravity levels of $10^{-5} g_0$).

Infrared Thermometry

The THERMOVISION 900 developed by AGEMA was used to obtain temperature distributions of a diffusion flame by means of infra-red thermometry. The potential application is to develop a diagnostic technique that will provide precise temperature measurements on flames under micro-gravity conditions. For the particular experimental configuration temperatures are of the order of 1000-1500 K, therefore, it was considered appropriate to use a CO_2 filter with the camera. The CO_2 filter allows a temperature range of 273-1800 K and works on a specific wavelength of 10.6 μm. Under these conditions the specified accuracy of the camera should be of the order of 0.1 K .

Infra-red thermography has become a major diagnostic tool for nondestructive testing an evaluation in buildings, aerospace, microelectronics and medical research [11]. The use of IR thermography in combustion related situations has been so far very limited. Measurements of flame spread velocities in microgravity conditions have been conducted by processing infra-red-images of the preheat zone of solid and liquid fuels [12], a summary of the results and procedures is given by Wieland [13]. Flame temperature distributions have been obtained with infra-red thermography for large scale kerosene pool fires [14] and for corner wall fires [15]. In both cases the main limitations to the technique were found to be the unknown emissivity of the flame, the impossibility of accurately estimating the surface area of the flame and the large heat fluxes imposed by the flames that forced to increase significantly the distance between the flame and the camera.

The magnitude of the emitted radiation, a measure of the body temperature, depends on the surface property known as emissivity (ε). The emissivity of an object is a function of its temperature, wavelength and the direction of measurement relative to the surface but an overall total emissivity can be used if the target is Labertian and the measured radiation corresponds to a specific wavelength. A common way of determining the spectral emissivity of a surface is by using a calibrated thermometer such as a thermocouple. The emissivity setting on the radiation instrument is adjusted to derive a temperature reading that matches that of the thermocouple.

An important consideration of potential error in IR thermography involves attenuation of irradiance that occurs due to the intervening environment between the object and the sensor. The attenuation of IR energy emitted from a material surface causes a systematic error in the measurement. The perturbation is due to absorption of radiation by the atmospheric gases and scattering by the particles in the air. Atmospheric absorption of radiant energy due to gases as CO_2, O_2 and H_2O is, however, minimal for certain spectral windows. Most commercial IR instruments are designed to operate in the 3-5 μm and 8-14 μm spectral region for least atmospheric attenuation [11].

For this specific case, the flame is going to be treated as a solid surface and IR thermography will only be able to provide the temperatures at the flame surface. A top view of the flame obtained with the IR camera will determine the temperature distribution at the flame surface and a side view, obtained from a CCD camera) combined with a vertical array of thermocouples (placed far downstream of the leading edge) will determine the location of the flame surface. The accuracy of this methodology will be determined by the correct determination of a correspondence law between luminous intensity, color and temperature. The surface area of the flame has to be accurately determined to obtain good results, the laminar and stable (non-pulsating) nature of the micro-gravity flames [7,8] allow for an easy and exact determination of the flame surface area. When obtaining temperature measurements of solid surfaces opaqueness of the material can represent a significant problem. If the material is not opaque radiation from the whole depth of the material will integrated before reaching the sensor. The flames to be studied are very thin and temperatures decrease radically away from the flame zone, thus, opaqueness of the flame is not of great concern.

The flame emissivity is an unknown but can be determined by calibrating the system to match the thermocouple readings down stream. Laminar diffusion flames of this type are very homogeneous in nature, therefore the assumption of constant emissivity is expected to be reasonably accurate. The only zone where this assumption might break down is close to the leading edge, where extinction and premixing might result in a different chemical structure that might affect the emissivity of the flame. A thermocouple is embedded at of the fuel leading edge, this will compensate for the lack of accuracy of the measurements and provide a second calibration element for the leading edge zone.

Radiation attenuation by absorption and scattering by the ambient gas has been minimized by choosing the 10,6 μm wave length. The small size of the chamber further reduces this problem making it of no concern. The temperature difference between the flame zone and the gases immediately surrounding it is of the order of 500 K, therefore, emission from gases other than the region close to the flame can be neglected.

Experimental Results

Ground Base Temperature Measurements

A series of experiments have been conducted to attempt an evaluation of the accuracy of the temperature measurements inferred from the irradiation measured by the infra-red camera. The burner was placed both at the ceiling and floor of the chamber and images were taken from the top and side of the burner. To obtain a characteristic temperature, the 8 thermocouple array is used. The thermocouples are spaced 15 mm from each other with the first one starting at 2 mm from the burner surface. The thermocouples provide the temperature distribution of a specific line perpendicular to the burner and located at the plane of symmetry. This temperature distribution can be used to determine, by comparison, the accuracy of the temperatures derived from the infra-red camera. as well as the emissivity of the flame.

Experimental conditions have been varied to encompass a wide range of conditions. Increasing the fuel flow results in yellow, sooty and very unstable flames, blue, non-sooting stable flames are observed for low fuel flows. The intensity of the flame can varied by changing the air flow velocity, the flame is weak for low and high air flow velocities reaching a maximum at some intermediate air flow. For all this conditions the precision of the thermographic technique was evaluated. High confidence on the thermocouple measurements was the main decision parameter when choosing all experimental conditions.

Ground based experiments where mostly conducted on the ceiling configuration. When the burner was placed on the floor, the geometry and lack of stability of the flame was inadequate for the use of this technique. It was observed that under a wide range of conditions a constant "global emissivity" was obtained. The changes in flame color and temperature had little effect on the calculated emissivity. It is important to note that this "global emissivity" is by no means the real flame emissivity, it is just a useful way to calibrate the infra-red camera to provide adequate temperature distributions. Slight changes in the emissivity were only observed when the flame was blue.

101

Ground Based Extinction Experiments

To study on the effect of gravity on the extinction limits, the flame was established and then the air flow velocity was increased until extinction occurred. For low air flow velocities, the fuel injection velocity was varied until the flame extinguished. The results are presented in figure 2, for floor burning, and figure 3, for ceiling burner, the data points represent the values of air and fuel velocities at which extinction occurred. Test were conducted for different oxygen concentrations, oxidizer (U_∞) and fuel (V_F) velocities. Oxygen concentration was varied between 11% and 70% (by volume), all flames extinguished at 11% therefore the data is not presented.

No minimum air velocity was found to be necessary for flame stability, showing that the previous results reported by Torero et al. [7] were, as expressed by the authors, dependent on the chamber geometry. For floor burning, 0.0 m/s < U_∞ < 0.15 m/s flames extinguished at an almost constant value of V_F. For U_∞ > 0.15 m/s the extinction limit depends on both fuel and oxidizer velocity, with the dependence on the former becoming less significant as U_∞ increases. It was observed, that as the oxygen concentration decreased the flame detached from the burner and blow-off occurred earlier. Increasing the oxygen concentration made the flame brighter and apparently more stable. The flame was established closer to the burner and the flame temperature increased more than 200 K (for 70% O_2). The proximity of the flame to the burner increased the heat losses resulting in earlier blow-off for oxygen concentrations above 22%. For ceiling burning, the flame is established close to the burner and its geometry is almost unaffected by the oxidizer flow (U_∞). In contrast, the injection velocity (V_F) separates the flame from the burner and is the source of significant instabilities in the flow. It can be observed from figure 3 that the extinction limits are virtually unaffected by the oxidizer flow and blow-off occurs at similar fuel injection velocities as for the floor burning. For oxygen concentrations of 12% and lower, blow-off was observed to be an almost random event (figure 3).

A phenomenological explanation of the extinction process in terms of a critical Damköhler number is provided in the work of Kodama et al. [16] and can be used to describe the characteristics of blow-off in the floor configuration. The Damköhler number is defined as the ratio between the flow (residence) time to the chemical time for the reaction. For a fixed oxygen concentration (fixed chemical time) as the flow velocity increases, the flow time decreases, and consequently so does the Damköhler number. If the injection velocity increases the stand-off distance increases, heat losses from the flame to the burner decrease and therefore the flame temperature increases [17]. Higher flame temperatures imply shorter chemical times and thus, larger Damköhler numbers. It can be concluded that increasing U_∞ or decreasing V_F will favor extinction. An increase in oxygen concentration will affect the chemical time in two opposite ways, by providing more oxygen, the reaction rate is enhanced resulting in a higher Damköhler number. By bringing the flame closer to the burner heat losses increase and the Damköhler number decreases. The dominant effect will determine the ultimate blow-off limits. This phenomenological explanation is also valid for ceiling burning but the complexity of the flow does not allow for a clear interpretation of the results.

Micro-Gravity Results

Blow-off experiments were conducted at the INTA 2.2 sec. drop tower and preliminary testing of the infra-red camera on board of the KC-135. While conducting blow-off tests in micro-gravity (INTA drop tower) flames were observed to be stable for oxygen concentration below 5% (by volume). Since ignition had to be conducted during the micro-gravity period, the 2.2 sec. drop did not allow to observe if the flames were stable or if they were entering a transient process towards extinction. Concentration was given to low oxidizer flow velocities (U_∞ < 0.02 m/s).

Four different flame regimes were observed. For oxidizer flow velocity of the order of 1 mm/s and fuel injection velocity of the order of 1 mm/s the flame propagates away from the burner in a transient manner, it is elliptical in shape and leading edge and trailing edges remain very close to the surface while moving horizontally away from the burner. For oxidizer flow velocities between 1 and 10 mm/s and similar fuel flow velocities, the flame attains a stationary position and is linear in shape. The leading edge remains very close to the surface and stationary at the fuel edge, in contrast, the trailing edge is detached from the surface. This regime corresponds well to that observed by Torero et al. [7], where diffusion could be neglected and fuel and oxidizer are mostly transported by convection towards the flame. If the oxidizer flow velocity is increased between 10 and 100 mm/s and the fuel flow velocity remains between 1 and 10 mm/s, the flame remains stationary is parabolic in shape and the leading edge remains attached to the surface. The trailing edge is detached from the surface. In this regime fuel transport is controlled by diffusion and oxidizer transport by convection which represents the classical boundary layer regime [1]. Further increase in the oxidizer velocity will lead to a blow-off regime. The leading edge

becomes unstable and depending on the oxygen concentration the flame geometry can be linear or parabolic. For low oxygen concentrations (i.e. 10%) the flame will be linear and for high oxygen concentrations (i.e. 36%) parabolic. After ignition occurs, the diffusion flame regresses till it attains a maximum downstream position (this occurs approximately 0.5 sec. into the micro-gravity period). Ahead of the flame tip a mixture of fuel/oxidizer is formed. The pre-mixed zone is then ignited by the diffusion flame tip and a premixed flame propagates towards the leading edge the propagation trajectory can be either linear or parabolic, depending on the oxygen concentration. Due to the concentration gradients (partially premixed zone) the flame is observed to propagate as a "triple flame" . When the triple flame reaches the leading edge the regression cycle starts once more.

A series of micro-gravity experiments has been conducted using the infra-red thermographic technique described above. Temperatures from the thermocouples have been used to obtain a "global emissivity" of the flame for a wide range of conditions. The oxygen concentration was varied between 12% and 50%, the fuel concentration (adding nitrogen) between 50% and 100% and the forced flow and fuel injection velocities in the ranges shown on figures 2 and 3. The results are still being evaluated but so far, it can be concluded that the "global emissivity" of the flames in micro-gravity remains almost constant for all conditions studied.

Conclusions and Future Work

A series of normal gravity and micro-gravity experiments have been conducted to study the blow-off limits of a laminar diffusion flame. The effect of gravity was evaluated by placing the fuel surface above and below the oxidizer stream. It was observed that blow-off limits in ceiling and floor configuration differ in a qualitative way but blow-off occurs at very similar oxidizer and fuel velocities. In micro gravity, the flame is significantly more stable and although no clear blow-off limits could be determined, four characteristic flame regimes were identified. The use of IR thermography to obtain flame temperatures has been proven to be feasible. Future work on this program will relate to further analysis of the gas burner data. Experiments on PMMA will start in 1997 with the goal of conducting a sounding rocket experiment in 1998. Further work on IR thermography is also envisioned.

Acknowledgments

REFERENCES

1. Emmons, H., Z. *Agnew. Math. Mech.* **36**, 60-71, 1956.
2. Williams, F.A., *Combustion Theory*, 2nd Edition, The Benjamin Cummings Publishing Company Inc., Menlo Park, CA, 485-519, 1985.
3. Hirano, T., Iwai, K. & Kanno, Y., *Astronautica Acta*, **17**, 811-818, 1972.
4. Ramachandra, A. & Raghunandan, B. N., *Combustion Science and Technology*, **36**, 109-121, 1984.
5. Lavid, M. & Berlad, A.L. *Sixteenth Symposium (International) on Combustion*, The Combustion Institute, 1557-1568, 1977.
6. Mao, C. P., Fernandez-Pello, A.C. & Pagni, P.J., *Transactions of the ASME-Heat Transfer Journal*, **106**, 304-309, 1984.
7. Torero, J.L., Bonneau, L., Most, J. M. & Joulain, P., *Twenty-Fifth Symposium (International) on Combustion*, The Combustion Institute, 1701-1709, 1994.
8. Torero, J.L., Bonneau, L., Most, J-M. and Joulain, P., *Advances in Space Research*, **16**, 7, pp. 149-152, 1995.
9. Torero, J.L., Wang, H. Y., Joulain, P. and Most, J-M., *Lecture Notes in Physics*, vol.464, 401-408, 1996.
10. Wang, H.Y., Torero, J.L., Bonneau, L. and Joulain, P., *Transport Phenomena in Combustion*, S.H. Chan Editor, 1996.
11. Gandhi, S., Spivak, S.M. and Pourdeyhimi, B., SFPE Journal of Fire Protection Engineering (in press), 1996.
12. Bundy, M., West, J., Thomas, P., Battacharjee, S., Tang, L., Altenkirch, R.A. Third International Micro-gravity Combustion Workshop, Cleveland, Ohio, April, 1995, p.11.
13. Weiland, K., Third International Micro-gravity Combustion Workshop, Cleveland, Ohio, April, 1995, p. 291.
14. Hayasaka, H., Koseki, H. and Tashiro Y., Fire Technology, 28, 2, 1992, p.110.
15. Arakawa, A., Saito, K. and Gruver, W.A., NIST-GCR-93-628, 1993, p.1.
16. Kodama, H., Miyasaka, K. and Fernandez-Pello, A.C., *Combustion Science and Technology*, 53:37-50 (1987).
17. Ramachandra, A. and Raghunandan, B.N., *Combustion Science and Technology*, 36:109-121 (1984).
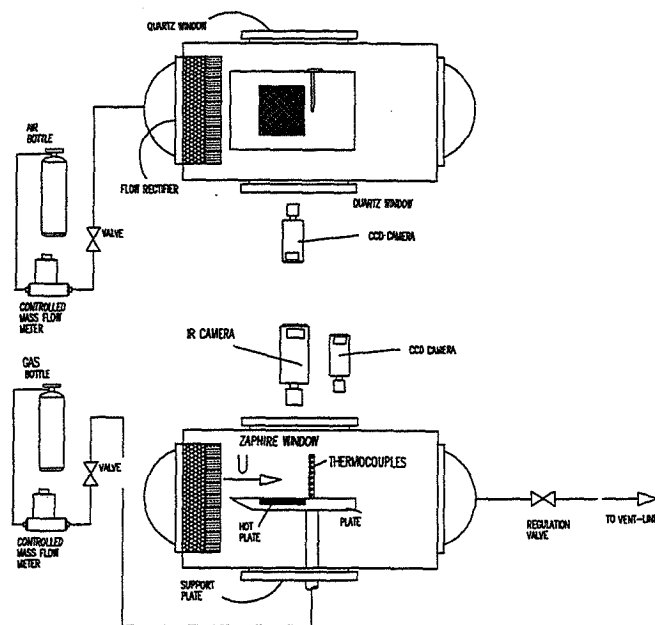
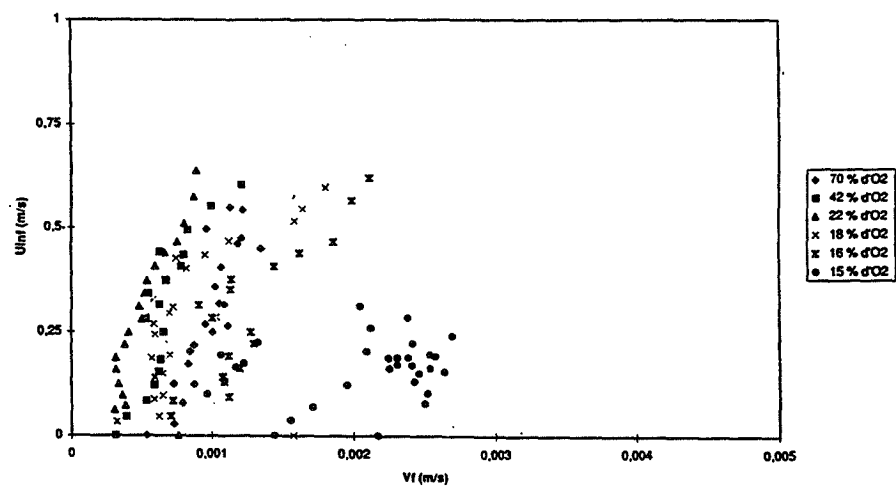Figure 1.- Schematic of the Experimental Apparatus

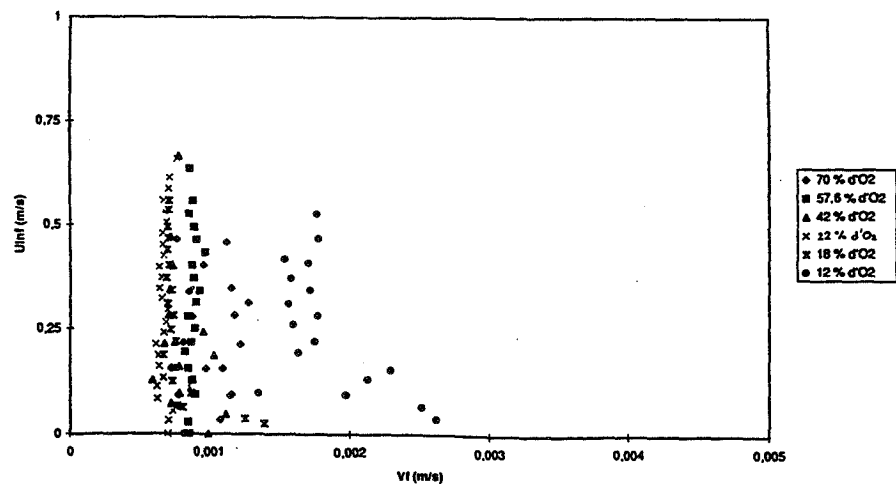Figure 2.- Blow-off limits for floor burning (normal-gravity)

Figure 3.- Blow-off limits for ceiling burning (normal gravity)

RADIATIVE EXTINCTION OF COUNTERFLOW PREMIXED FLAMES

Kaoru Maruta, *Yiguang Ju, Hongsheng Guo and Takashi Niioka(PI)

Institute of Fluid Science, Tohoku University,
Katahira, Aoba-ku, Sendai 980−77, Japan

*Department of Aeronautics and Space Engineering, Tohoku University
Aramaki Aoba, Aoba−ku, Sendai 980, Japan

ABSTRACT

This report presents experiments on counterflow premixed flames at small stretch rates and relevant numerical calculation involving radiation loss from the flame zone. Extinction experiments on counterflow methane/air and propane/air premixed flames at small stretch rates are conducted under microgravity to observe extinction characteristics of near-limit premixed twin flames. The results show two kinds of flame response, that is, C-shaped extinction curve due to radiative loss for methane/air mixture and ordinal monotonous extinction curve for propane/air mixture.

To analyze these experiments, numerical investigation addressing extinction and flammable regions of radiative counterflow premixed flames for Lewis numbers from unity to 1.82 are conducted to clarify the mechanism of these two kinds of flame response. The computation exhibited flame bifurcation resulting in a G-shaped extinction curve showing the extended limit of flammability for Lewis number near unity and a K-shaped extinction curve showing the composition flammability limit being equal to that of one-dimensional flame for Lewis number of 1.82. G- and K-shaped extinction curves respectively explain the experimental C-curve for methane/air and monotonous curve for propane/air mixtures. Furthermore, the relationship between the composition flammability limit of one-dimensional propagating flame and that of stretched flames is clarified.

INTRODUCTION

Theoretically, adiabatic flame has no flammability limit. Then, what will happen on extremely small stretched premixed flames? This was the primary motivation of this study.

Although the linear extrapolation method [1,2] to measure the flammability limit of 1-D flames by using the counterflow technique provided the reasonable values, neither the limit phenomena of counterflow premixed flames at small stretch region nor the relationship between composition flammability limit of a mixture (a *lower limit*) and that of 1-D premixed flame (a *standard limit*) has been clarified. It is extensively known that radiation loss plays a dominant role on the flammability limit of 1-D propagating flame and defines an intrinsic limit [3,4], however, some studies addressing the stretch-induced extinction limits conclude that radiation does not have a significant effect [5] on such extinction limits. On the other hand, temperature dip between twin flame was observed [6] and the existence of radiative extinction of counterflow premixed flames was predicted theoretically [7].

To explain these various findings and to understand the extinction characteristics of counterflow premixed flames thoroughly, microgravity experiments on counterflow methane/air and propane/air premixed flames and relevant numerical calculation were conducted. The experimental methodology herein presented entails the use of low-speed counterflow flames and 10 seconds of microgravity, which enables us to avoid buoyancy, conductive heat loss to the burner, and the effect of flame curvature simultaneously. By this method, excellent conditions can be realized and the behavior of near-limit flame in an extremely small stretch region can be observed.

EXPERIMENT

Figure 1 shows the apparatus consisting of a counterflow burner, an igniter, a mixture supply system, an video system, and a sequencer, all mounted in a steel framework. Methane/air and propane/air mixtures are employed to examine the effects of Lewis number on extinction characteristics of counterflow premixed flames at small stretch rates. To obtain an extinction limit at small stretch rate region within 10 seconds, fuel gas concentration of the mixture was gradually decreased until extinction, maintaining a constant flow velocity at the burner exit. Since the flow rate is very small, the burner volume should be so small as to be sensitive to fine control of mixture concentrations, hence the burner is made of a circular pipe with a porous plate instead of a nozzle burner, as shown

in Fig. 2. It is noted that conventional nozzle could not be used here because its settling region is too large to control the mixture composition in a short time. To control the flow rate accurately, electric mass flow controllers, a D/A converter, and a notebook computer were employed for the mixture supply system. Instantaneous flow rates are measured by flow-meters in the controllers, A/D converters and the notebook computer. As the fuel concentration of the mixture decreases during the drop test, twin flames gradually approach each other. Finally, they appear to merge with each other, and then extinction occurs abruptly at a certain value of the fuel concentration of the mixture. To determine the fuel concentration of the mixture at the moment of extinction exactly, delay time from the controllers to the burner exits was measured in advance and accounted when the extinction concentrations were determined. The response of the whole system, including the response of the counterflow flame itself, is estimated to confirm the whole system is under quasi-steady conditions. An arbitrary fluctuation of the mixture composition is given and the variation of the flame standoff distance with time is measured. The flame standoff distance completely obeys the control of the fuel gas concentration. This indicates that the present experiments were conducted under quasi-steady conditions. Surface temperature of the porous plate was measured and heat loss to the burner was confirmed to be negligible. Details of the treatment of these possible sources of errors have been described in our previous publication [8]. To make twin flames as flat as possible with the present burner, length of the settling region, that is, position of the porous plate was regulated according to the flow velocity at the burner exits. Microgravity of 10^{-4} to 10^{-5} G was obtained during 10 seconds of free-fall in a drop tower at the JAMIC in Hokkaido, Japan.

RESULTS OF MICROGRAVITY EXPERIMENTS

Since it is difficult to measure the stretch rate in drop-shaft experiments, the conventional stagnation velocity gradient, 2U/L, is employed. Where U and L are the flow velocity of the mixture at the burner exit and the spacing between the two pipes, respectively. Figure 3 shows the relationship between the stagnation velocity gradient and the equivalence ratio of the mixture at extinction. This figure shows that the C-shaped extinction curve for methane/air flame [8,9] and the ordinal monotonous extinction curve for propane/air flame [9]. In the case of methane/air, on the upper half of the curve, the equivalence ratio at extinction increases with the increase of 2U/L. However, on the lower half of the curve, the tendency is reversed. On the other hand, in the case of propane/air flame, stagnation velocity gradient at extinction decreases monotonously with decreasing fuel concentrations. The symbols "m" and "p" in Fig. 3 respectively denote the flammability limits of methane/air and propane/air mixtures measured by constant-volume combustion vessel by Ronney [4]. It should be noted that the present flammability limit of methane/air counterflow premixed flame was smaller than the standard limit, although the limit of propane/air counterflow flame appears to be equal to its standard limit.

C-shaped extinction curve was predicted numerically by T'ien in his pioneering work [7]. However, to the authors knowledge, our results are the first experimental data in which the C-shaped curve is obtained [8,9]. Subsequent to the experiments, Guo et al. clarified the mechanism of the C-shaped extinction curve for methane/air counterflow premixed flames by using the detailed chemistry [10]. Furthermore, Ju et al. [11,12] found the two stable flame branch phenomenon and showed a G-shaped curve for stretched methane/air premixed flame by using the detailed chemistry. This two stable flame branch phenomenon was also found by Buckmaster [13] using simple asymptotic theory. However, the flame bifurcation, flammable regions and relationship between the lower and the standard limit for general Lewis numbers have not yet been understood.

NUMERICAL CALCULATIONS

A numerical investigation was conducted to provide the deeper insight into the issue and to clarify the relationship between the lower limit and the standard limit for general Lewis numbers. The axisymmetrical counterflow configuration is used and the distance between two burners' exits is 20 cm for all calculations. The governing equations and boundary conditions are shown in our previous publications [10−12]. To discuss the combined effects of the radiation and Lewis number, one-step overall reaction is used here for simplification although the detailed chemistry has been used in our previous publications [10−12]. The activation energy is 200 KJ/mol, and the frequency factor is 1.0×10^{11} m^3/mol/s which is obtained by matching the predicted burning velocity with the experimental datum. The Lewis number is defined by the ratio of the thermal diffusivity of the mixture to the mass diffusivity of the deficient species. The Lewis numbers used here** are unity, 1.43 and 1.82. For radiation calculation, the optically thin model is employed because the optical thickness of all mixtures herein used are sufficiently small.

**More detailed calculation for general Lewis numbers has submitted to the Combustion and Flame [16].

CO2 and H2O are assumed as the emitting species. The Planck mean absorption coefficients of CO2 and H2O are solved by the modified damped Newton method in conjunction with an improved arclength continue method[11,14,15].

Flame Bifurcation Near Unity Lewis Number

Figure 4 shows the variation of flame temperature with stretch rate for typical fuel volumetric concentration Ω (percentage) at Lewis number unity which approximately corresponds to methane/air mixture. In this case, the standard limit is nearly equal to Ω =5.6. Below the standard limit, that is, Ω =5.2, 5.3 and 5.5, two limits at low and high stretch rates forming a flame isola are clearly shown resulting in the C-shaped curve. Above the standard limit, $\Omega \geq 5.7$, another flame branch (weakly stretched flame) emerges from lower stretch region of this isola. This flame stands far away from the stagnation plane and reduces to the planar propagating flame. On the other hand, with the increase of stretch rate, extinction occurs due to the combined effect of stretch and radiation heat loss (g). Moreover, as the fuel concentration increases, the flame strength increases. Thus, stretch extinction limits (d) of flames in isola move to large stretch rate and the radiation extinction limits (c) of the flame isola move to low stretch rate. At Ω =5.8, these two branches merge with each other. That is, the upper branch (fe) of the weakly stretched flame connects with the right hand side part (de) of the upper branch of the isola forming a new stable flame branch def. Meanwhile, the left hand side part (bc) of the upper branch of the isola connects with the unstable branch of the weakly stretched flame through a turning point b. Therefore, def and bc correspond to high temperature and low temperature flame branch, respectively. The high temperature flame has only a stretch extinction limit while the low temperature flame has a radiation extinction limit (c) and a jump limit (b). The opening up of the flame at unity Lewis number occurs as a result of the merging of the weakly stretched flame and the isola.

The curve indicating the extinction and jump limits at various equivalence ratios for Le=1.0 is shown in Fig. 5. AB denotes the stretch extinction limit (points d in Fig. 4.). BC represents the radiation extinction limit (points c for $\Omega \leq 5.5$) and B is the lower flammability limit of counterflow flame. CF denotes the radiation extinction limits of the low temperature flames (points c for $\Omega \geq 5.75$) and DG is a curve showing its jump limit (points b). DE denotes the jump limit of weakly stretched flames (points g). Finally, the region on the right hand side of the curve ABCDE is the flammable region of high temperature flames. Meanwhile, the region within curve GDCF is the flammable region of low temperature flame. This means that flames in this region can be either high temperature flame or low temperature flame. The standard limit should be the extrapolation of weakly stretched flame limit (DE) to zero stretch rate. It is noted that neither the linear extrapolation of the stretch extinction limit nor the radiation extinction limit of weak flame (CF) to zero stretch rate can predict the standard flammability limit. Because radiation loss in the counterflow configuration is small when flame is sustained near the stagnation plane, the lower limit is becomes leaner than the standard limit for Le=1. A comparison of Fig. 5 with Fig. 6 which is obtained by the detailed chemistry [13], shows that the one-step overall reaction is a good simplification, although there are some quantitative discrepancies on the predicted lower limit and the standard limit between these two models. It should be noted that the one-step overall reaction model makes it possible to calculate the weakly stretched flames established far away from the stagnation plane, while it is difficult to calculate by using the detailed chemistry.

Flame Bifurcation For Large Lewis Number

To examine the extinction phenomena and to bring out a reasonable explanation to the experimental data of propane/air flame, flame bifurcation at Le=1.43 and 1.82 is investigated. Le=1.82 corresponds to propane/air mixture case.

Figure 7 shows the variation of flame temperature with stretch rate for typical fuel concentrations at Lewis number of 1.43. In this case, the standard limit is a bit smaller than Ω =5.8. This figure shows there exists no flame isola for fuel concentrations lower than the standard limit, being different from the result at unity Lewis number. This is because the reduction of radiation heat loss due to the geometry effect can not compensate for the energy loss caused by the Lewis number effect. Thus, flame cannot exist for fuel concentration below the standard limit.

Figure 8 shows the extinction curve for Le=1.43. Unlike the G-shaped curve shown in Fig. 5, this curve looks a K-shaped curve, which is a reduced form of the G-shaped curve for large Lewis number. It is noted that the extrapolation of the extinction limits of high temperature flame ABE in K-shaped curve to zero stretch rate gives the standard limit, while the extrapolation of curve AB in G-shaped curve does not. This difference gives a good explanation to the present experimental data.

Figure 9 shows the extinction curve for Lewis number of 1.82, corresponding the case of propane/air mixture. The extinction curve has completely changed into a K-shaped curve. An increase of Lewis number dramatically reduces the extinction limit region at large equivalence ratios. Also, flammable region of low temperature flame

becomes narrow and shifts to large equivalence ratio with the increase of Lewis number. The variation of the flame bifurcation with the increase of Lewis numbers is a result of the competition between the radiation and Lewis number effect. At the same radiation intensity, an increase of Lewis number results in a transition of the extinction curve from the G-shaped curve to the K-shaped curve.

CONCLUSIONS

Extinction experiments on counterflow premixed methane/air and propane/air flames at small stretch rates were conducted under microgravity. C-shaped extinction curve and ordinal monotonous extinction curve were respectively obtained for methane/air and propane/air mixtures. Numerical investigation on radiative counterflow premixed flames provided clear explanations of the flame response as follows:

At unity Lewis number, which approximately corresponds to methane/air mixture, there is a flame isola with two distinct extinction limits at low and high stretch rates for the equivalence ratio lower than the standard limit. For equivalence ratio larger than the standard limit, a new flame branch with flame standing far from the stagnation plane emerges on the low stretch side of this isola. This flame branch is reduced to the standard limit with the decrease of fuel concentrations. It was found that the C-shaped curve obtained experimentally was exactly the G-curve, definitely explaining the relationship between the lower limit of counterflow premixed flame and the standard limit.

At large Lewis numbers, for equivalence ratio near the standard limit, only the weakly stretched flame branch with a single stretch extinction limit exists. The resulting extinction curve is a K-shaped and the lower limit equals to the standard limit. The G-curve has changed into the K-curve with the increase of Lewis number.

This G-K transition with the increase of Lewis number provide a physical insight into the combined effects of the radiation and Lewis number. It follows that the relation between the standard limit of one-dimensional flame and counterflow premixed flames have been clarified.

Reference
1. Law, C. K., Zhu, D. L. and Yu, G., Twenty-first Symp. (Int.) on Combust., 1986, pp.1419−1426.
2. Law, C. K. and Egolfopoulos, F. N., Twenty-third Symp. (Int.) on Combust., 1990, pp.413−421.
3. Lakshmisha, K. N., Paul, P. J. and Mukunda, H. S., Twenty-third Symp. (Int.) on Combust., 1990, pp.433−440.
4. Ronney, P. D., Twenty-second Symp. (Int.) on Combust., 1988, pp.1615−1623.
5. Sohrab, S. H. and Law, C. K. , J. Heat Mass Transfer 27−2 : 291−300 (1984).
6. Liu, G. E., Ye, Z. Y. and Sohrab, S. H., Combust. Flame 64 :193−201 (1986).
7. Platt, J. A. and T'ien, J. S., Chemical and Physical Progress in Combustion, 1990 Fall Technical Meeting, Eastern Section of the Combustion Institute, 1990.
8. Maruta, K., Yoshida, M., Ju, Y. and Niioka, T., Twenty-sixth Symp. (Int.) on Combust., 1996, to appear.
9. Maruta, K., Yoshida, M., Kobayashi, H. and Niioka, T., 33rd Symp. (Japanese) on Combust., 1995, pp. 414−416.
10. Guo, H., Ju, Y., Maruta, K., Niioka, T. and Liu, F. Combust. Flame, to appear.
11. Ju, Y., Guo, H., Maruta, K. and Liu, F., J. Fluid Mech., to appear.
12. Ju, Y., Guo, H. and Maruta, K., Trans. of JSME 63-606B : 343−348 (1997).
13. Buckmaster, J., 35th Aerospace Sciences Meet. and Exhibit., AIAA 97-0238 (1997).
14. Giovangigli, V. and Smooke, M. D., Combust. Sci. Tech. 53 : 23−49 (1987).
15. Kee, R. J. et al., Sandia Report, SAND86-8246(1986).
16. Ju, Y., Guo, H., Maruta, K. and Niioka, T., submitted to Combust. Flame, (1997).
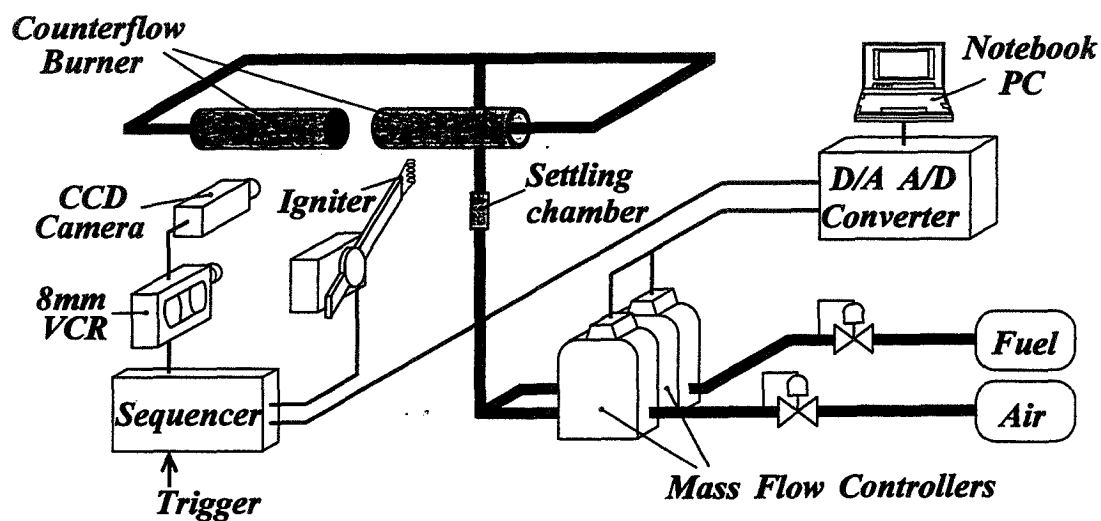
Fig. 1 Schematic of experimental apparatus.
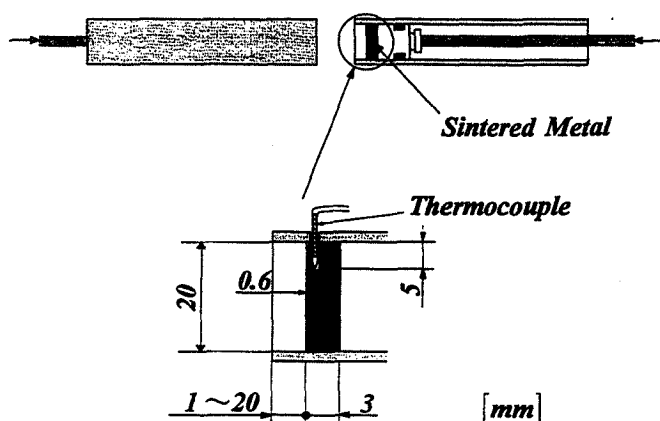
Fig. 2 The structure of the counterflow burner.
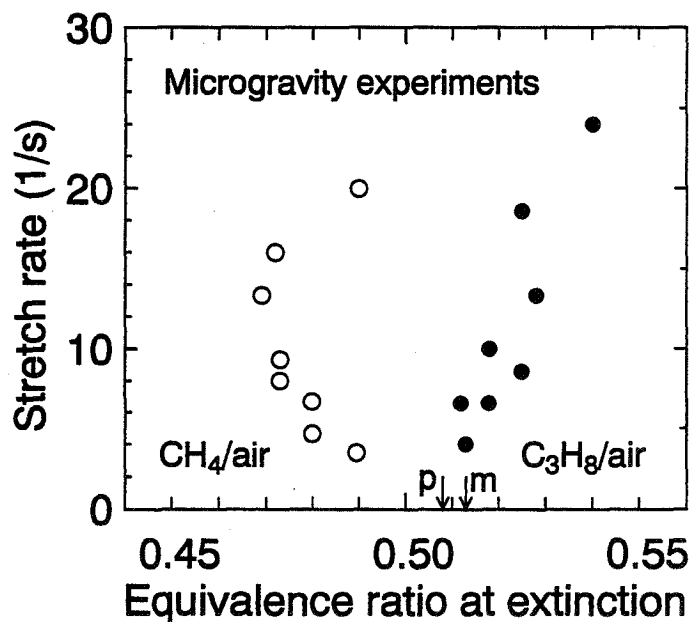
Fig. 3 The experimental extinction curve
obtained under microgravity.
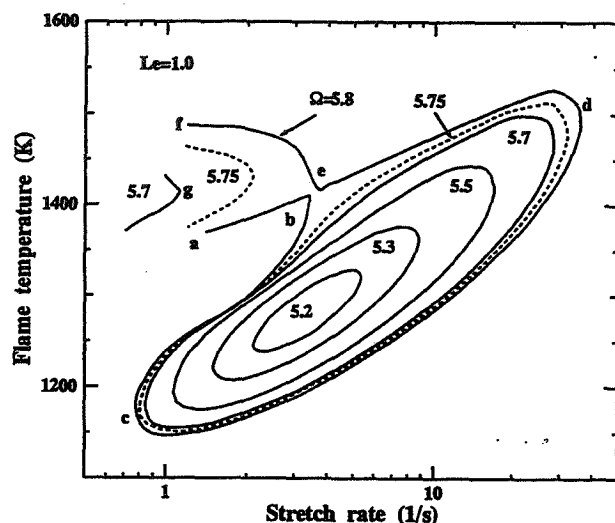
Fig. 4 Flame temperature profiles plotted
as a function of stretch rate for Le=1.0.
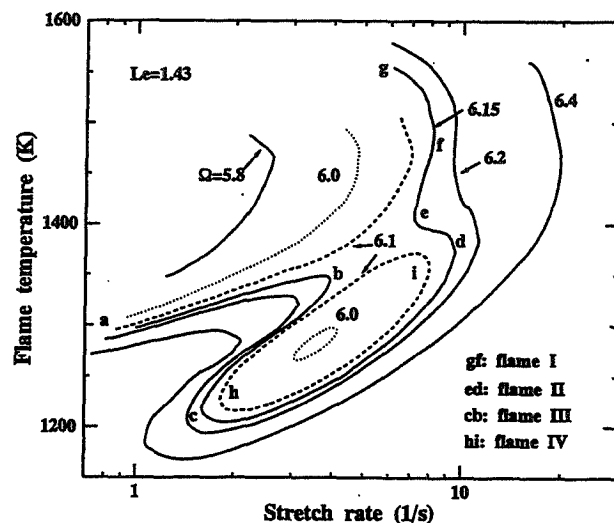
Fig. 7 Flame temperature profiles plotted
as a function of stretch rate for Le=1.43.
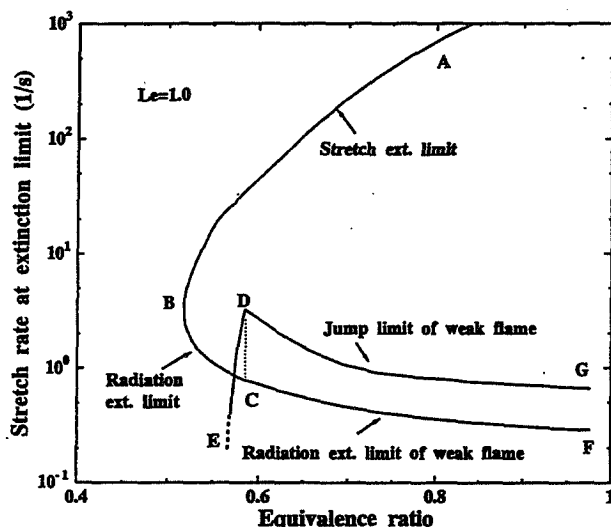
Fig. 5 The extinction curve showing the extinction limits,
the jump limits and the flammable regions at Le=1.0.
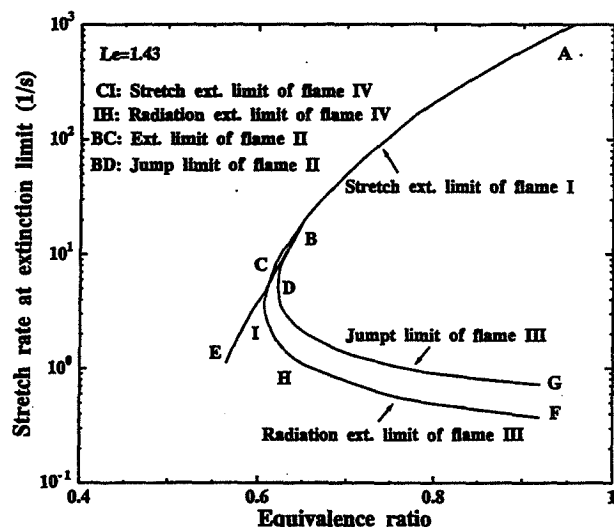
Fig. 8 The extinction curve showing the extinction limits,
the jump limits and the flammable regions at Le=1.43.
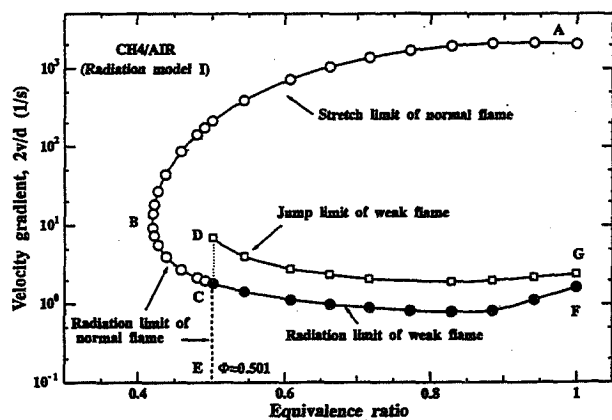
Fig. 6 The G-shaped curve calculated
by the detailed chemistry [11]
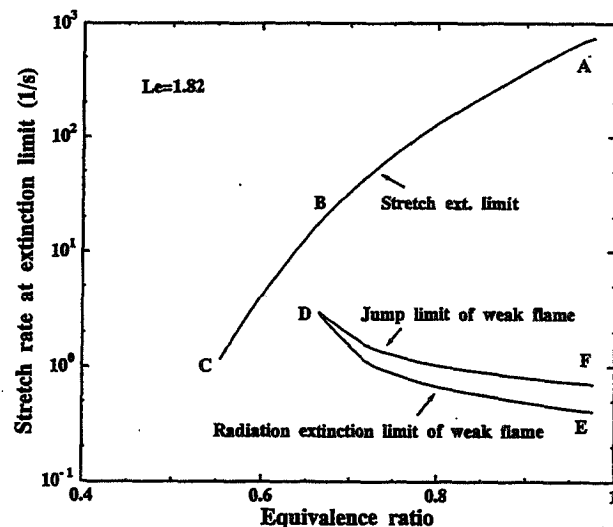
Fig. 9 The extinction curve showing the extinction limits,
the jump limits and the flammable regions at Le=1.82.

110

STRUCTURE AND STABILITY OF
BURKE-SCHUMANN DIFFUSION FLAMES*

Yong G. Lee and LEA-DER CHEN
Department of Mechanical Engineering
The University of Iowa
Iowa City, IA 52242

and

John E. Brooker and DENNIS P. STOCKER
NASA Lewis Research Center
Microgravity Science Division
Mail Stop 500-115
21000 Brookpark Road
Cleveland, OH 44135

Introduction

The general goal of this NASA Grant, NAG3-1592, is twofold: to improve our understanding of (1) the influence of buoyancy on the stability and structure of Burke-Schumann type diffusion flames, and (2) the effects of buoyancy on vortex-flame interactions in co-flow diffusion flames. A numerical code with a higher order accuracy for spatial discretization is developed in this project for simulation of time-dependent diffusion flames by Sheu (ref. 1) and Sheu and Chen (ref. 2), and an extended reduced mechanism is incorporated for prediction of methane oxidation and NOx (NO, NO_2, and N_2O) formation and emission from methane Burke-Schumann diffusion flame (BSDF) as reported in Sheu (ref. 1), and Sheu and Chen (ref. 3). Initial investigation of vortex and flame interaction within the context of fast chemistry is reported in (ref. 2). Experiments are conducted in reduced pressure to study the lift-off and stabilization of methane-fueled BSDF in reduced buoyancy environments due to reduced pressure (ref. 4). Measurements of temperature and species concentrations are made in normal and reduced pressure environments to study the effects of buoyancy on the structure of BSDF, and will be reported in this paper. To study the buoyancy effects on the lift-off and stabilization of methane-fueled jet diffusion flames in coflowing air, a glovebox investigation, Enclosed Laminar Flames (ELF), has been proposed and approved for space-based testing on the fourth United States Microgravity Payload (USMP-4) mission, scheduled for October 1997. A brief description of the ELF investigation is also presented.

Reduced Pressure Experiments

The reduced-pressure experiments are conducted in a vacuum chamber (Vacuum Atmospheres Model HE-133-5) as illustrated by Fig. 1. This vacuum chamber has an interior volume of 0.43 m^3 (inside diameter of 0.76 m and horizontal length 0.91 m) and an antechamber of 0.044 m^3. The chamber is rated to hold pressure down to 1.3×10^{-3} Pa, and has been used in an earlier experiment of Li and SF_6 wick combustion by Hsu and Chen (ref. 5). The vacuum chamber is fitted with (three) optical windows. A rectangular window of 0.46 x 0.23 m is used for photographic and video recording of the flame. The chamber is also fitted with sixteen service ports, including four electrical terminals. The service ports provide access for fuel and air supply, exhaust, gas sampling, and electrical channels for device control and data acquisition. A two-stage chemical vacuum pump (Alcatel model 2020CP) with a capacity of 7.6×10^{-3} m^3/s is used for evacuation of the test chamber. A ballast chamber attached to the main vacuum chamber is used to help to keep the pressure constant during the experiments. The chamber pressure (the main, as well as, the ante-chambers) is monitored by a differential pressure transducer (Pennwalt Model 66-100), and two pressure gages (Wika, gauge pressure range of -100 to 200 kPa).

A concentric burner similar to that used by Stocker (e.g., ref. 6) is placed vertically upward inside the vacuum chamber for measurements in reduced pressure environments. The technical grade methane (purity better than 97 %) is used as the fuel and room air as the oxidizer. The burner consists of two concentric tubes, a fuel tube and a surrounding Pyrex chimney shown by the expanded view of the burner in Fig. 1. The fuel tube is made of stainless steel tubing with an inside diameter of 2.4 or 4.8 mm, and length of 140 mm. The length-to-diameter ratio is 58 for the 2.4 mm tubing and 29 for the 4.8 mm, designed to provide a fully developed flow at the tube exit. The Pyrex chimney has an inside diameter of 44.5 mm and length of 203 mm, providing a ducted, co-flowing air surrounding the fuel jet. Air enters the burner from four radially positioned inlets near the base of the burner assembly, and passes through layers of fine glass beads (nominal diameter of 3 mm) and steel wool for flow conditioning. The fuel and air flow rates are regulated by pressure regulators and needle valves. In-line particle filters (Matheson, specified valve coefficient of 0.15) are installed immediately downstream of the pressure regulators. The fuel and air flowrates are measured by two mass flowmeters (Aalborg, Models AFM2600 and AFM4600). The mass flowmeters are calibrated using N_2 over the flow range 0 to 1.7×10^{-6} m^3/s (0-100 ml/min) and 0 to 8.3×10^{-6} m^3/s (0-500 ml/min). The specified accuracy is ±2 percent of the full scale reading for temperature in the range 278 to 323 K and pressure 35 to 1030 kPa. A constant-temperature hot wire anemometer is used to cross check the velocities at the burner inlet.

Uncoated S-type (Pt-Pt/10%Rh) fine-wire thermocouples (wire diameter of 76 μm) are used for temperature measurements. The thermocouple probe is mounted on a (stepping motor and computer controlled) micro-translational device with a specified resolution 320 μm. The automated micro-translational device and data acquisition facilitate the usage of a scanning thermocouple probe in this study. Species concentrations are determined using a microprobe. The microprobe has a tapered sampling tip of 12±5 mm in length, and an orifice diameter of 210±20 μm. This in-house made microprobe (by YGL) is carefully verified for choked flow condition before its usage in the flame measurements. The choked flow condition (probe pressure set in the range of 0.08 to 0.09 bar) is necessary for aerodynamic quenching to occur in the probe. The microprobe is mounted on the same micro-translational device for temperature measurements. Several gas analyzers are used to determine the species concentrations, for example, gas chromatography (Varian Model 3400 with TCD) for CH_4, CO_2, CO, N_2, O_2, Ar and H_2, chemiluminescence (Thermo Electron Model 10) for NO, NO_2 and NOx, and infrared (ir) (Infrared Industries, Inc.) for H_2O. The gas-sampling line (continuous flow) upstream of the ir analyzer is heated to prevent condensation of water vapor. An in-line water trap is used to prevent water vapor to enter the chemiluminescence NOx analyzer.

Detailed measurements of temperature and concentrations are made of a methane-fueled BSDF with equal fuel-jet and co-flowing air velocities set at 0.14 m/s. Two pressure conditions are considered, normal pressure (1 bar) and reduced pressure (0.3 bar). The reduced pressure condition has an equivalent buoyancy effect of that at 0.1 g, where g denotes the standard gravitational acceleration; recall that the buoyant effects are inversely proportional to pressure squared when the fuel-jet Reynolds number, or the mass flowrate, is kept constant in the experiments (ref. 7). The fuel and air mass flowrates in reduced pressure testing are kept unchanged from the normal pressure. The flame remains laminar and stabilizes at the burner exit for both normal and reduced pressure conditions.

ELF Glovebox Investigation

The lift-off, reattachment, and blow-out of enclosed jet diffusion flames will be investigated in the Enclosed Laminar Flames (ELF) investigation that will be conducted in the glovebox facility on the USMP-4 mission, scheduled in October 1997. A 50/50 mixture (volume basis) of methane and nitrogen will be used for the fuel. A co-flow of air will be produced in a miniature fan-driven wind tunnel. This investigation will be manually performed by an astronaut, and the operational parameters include the both the fuel flow and air velocity (i.e., fan speed). Astronaut training is in progress.

The hardware consists of an experiment module, a control box, 3 electrical cables, and sets of exchangeable fuel bottles and ignitors. A 1.5-mm diameter nozzle is located on the duct's flow axis. The air velocity is measured by a hot-element anemometer, and the fuel flow is set with a mass flow controller. The nozzle is instrumented with a surface thermocouple, and another thermocouple at the outlet is used to indicate extinction of the flame. The duct is also equipped with an astronaut-positionable temperature rake, instrumented with 5 thermocouples and 26 silicon carbine fibers. When exposed to the flame, the fibers will thermally radiate giving a qualitative indication of the near-flame temperature profile. The rake can be positioned at 6 discrete radial positions. The digital data will be displayed on the module for astronaut viewing and recorded with the glovebox video system. The flame will be imaged with 2 color video cameras. The flight hardware is currently being assembled.

Results And Discussion

The flame appearance in reduced pressure is qualitatively similar to that report by Yuan et al. (ref. 8). The flame luminosity greatly decreases in reduced pressure environments; a faint-blue contour is seen, consistent with μg experiments . The fine spatial resolution of thermocouple measurements allows for construction of the isotherms shown in Fig. 2. The isotherms show that the maximum temperature contour in reduced is wider, consistent with the visible flame appearance. The flame length defined by the maximum temperature in reduced pressure is also longer (by around 3 mm), although the visible flame length is shorter. This observation is different from that observed in microgravity (μg) environments by Stocker (e.g., ref. 6). The μg flame shows a longer visible length than the corresponding normal gravity flame. The temperature data show a maximum in the shoulder region for the methane fueled BSDF, cf. Fig. 2, consistent with earlier observations in the literature. The maximum temperature is higher in reduced pressure than that in normal pressure, for example, by 40 K at $z = 6$ mm, where z denotes the axial height above the burner exit. This observation is interesting because one expects a lower maximum temperature in reduced pressure environments due to the effects of (a) higher coefficients of species diffusion and (b) higher decomposition (e.g., based on the La Chatlier principles) of CO_2 to CO and O_2, and H_2O to H_2 and O_2. The measured species concentrations, indeed, indicate higher mole fractions of CO and H_2 in reduced pressure flames, cf. Fig. 3. This level of difference in measured maximum temperatures appears to be beyond the uncertainty of temperature measurements. Sources of uncertainty in data acquisition of temperature measurements include (a) catalytic effects resulting from the presence of Pt-Pt/10%Rh thermocouple wires, and (b) soot build-up on the thermocouple junction. We have found that the soot build-up on the thermocouple can substantially reduce the temperature. As an example, we observed a temperature decrease of 200 K at $z = 18$ mm (near the tip of the visible flame in normal pressure) and slightly off the centerline (by mm) within 3 s from setting the probe to this location. The temperature difference of 40 K reported at $z = 6$ mm is near the maximum width of the visible flame, and no obvious soot build-up is detected for measurements in both normal and reduced pressure environments. To ascertain the catalytic effects, a silica coated thermocouple is being used to determine the temperature-time history at locations near the flame-tip.

Measured mole fractions of eight major species, CH_4, O_2, N_2, CO_2, H_2O, H_2, CO and Ar, at $z = 6$ mm are summarized in Fig. 3. where r denotes the radial distance from the centerline. Similar to that exhibited by the isotherms, the flame in reduced pressure shows a slightly wider width. The main reaction zone of methane oxidation appears to be located in the region $5 < r$ (mm) < 6 for pressure of 0.3 bar, and $4 < r$ (mm) < 5 for pressure of 1 bar. The species concentration measured by using the micro-probe, in conjunction with the micro-translational device, has fine spatial resolutions, providing physical insight into the reaction zone structure. The N_2 concentration shows a drastic decrease entering the high temperature zone from the fuel-lean side. The O_2 concentration first decreases entering the high temperature zone, and increases to reach a local maximum, for example, around $r = 5.3$ mm, and continues to decrease and 'leak' into the fuel-rich region. This increase of O_2 in the high temperature zone coincides with the sharp decrease of CO_2 concentration and sharp increase of CO measured for the reduced-pressure flame. The leakage of O_2 into the fuel-rich region is consistent with that predicted by the rate-ratio asymptotics of Linan and Williams (ref. 9) and numerical simulation, for example, by Sheu (ref. 1) and Sheu and Chen (ref. 1-3) using a four-step reduced mechanism. We have obtained preliminary data of NO and N_2 (i.e., NOx) in the flame, and are working on data reduction to quantify the emission index from the measurements.

Conclusions

The flame in reduced pressure becomes less luminous, and shows a faint-blue visible spontaneous emission. The temperature measurements show that the methane fueled Burke-Schumann diffusion flame (BSDF) has a wider flame width and slightly longer flame length in reduced pressure (0.3 bar in this study). The maximum temperatures in the BSDF studied show a maximum temperature in the shoulder region of the flame. A by-product of this research is the illustration of the microprobe usage for species measurements can provide physical insight into the reaction zone structure of a laminar diffusion flame.

Acknowledgment

References

1. Sheu, J.-C., 1996, "Numerical Simulation of Burke-Schumann Diffusion Flames Using Finite-Rate Chemical Kinetics," Ph.D. Dissertation, The University of Iowa, Iowa City, Iowa, 1996.

2. Sheu, J.-C. and Chen, L.-D., 1996, "Higher-Order Numerical Model for Simulation of Time-Dependent Variable-Density Flow," *AIAA J.*, Vol. 34, No. 10, 1996, pp. 2090-2098.

3. Sheu, J.-C and Chen, L.-D., 1996., "A Numerical Investigation of the Effects of Radiative Heat Transfer on the Structure of a Gaseous Diffusion Flame," Paper No. 96-3091, the 1996 AIAA/ASME/ASEE/SAE Joint Propulsion Conference, Lake Buena Vista, FL, 1-3 July, 1996.

4. Lee, Y.G., and Chen, L.-D., 1997, "An Experimental Investigation of the Lifted Methane-Fueled Burke-Schumann Diffusion Flames in Reduced Pressure" in Proceedings of the Spring 1997 Technical Meeting of the Central States Section of The Combustion Institute (to appear).

5. Hsu, K.-Y. and Chen, L.-D. 1995. "An Experimental Investigation of Li and SF6 Wick Combustion," *Combustion and Flame*, Vol. 102, 1995, pp. 73-86

6. Stocker, D. P., 1991, "The Effect of Reduced-Gravity on the Shape of Laminar Burke-Schumann Diffusion Flames," Paper 15, Spring Meeting of the Central States Section of The Combustion Institute, Nashville, TN, 22-24 April, 1991.

7. Davis, R. W., Moore, E. F., Santoro, R. J., and Ness, J. R., 1990, "Isolation of Buoyancy Effects in Jet Diffusion Flame Experiments," *Combust. Sci. and Tech.*, Vol. 73, pp. 625-635.

8. Yuan, T., Durox, D., and Villermaux, E., 1993, "The Effects of Ambient Pressure Upon Global Shape and Hydrodynamic Behavior of Buoyant Laminar Jet Diffusion Flames," *Combust. Sci. and Tech.*, Vol. 92, pp. 69-86.

9. Linan, A. and Williams, F.A., 1993, *Fundamental Aspects of Combustion*, Oxford, p. 67.
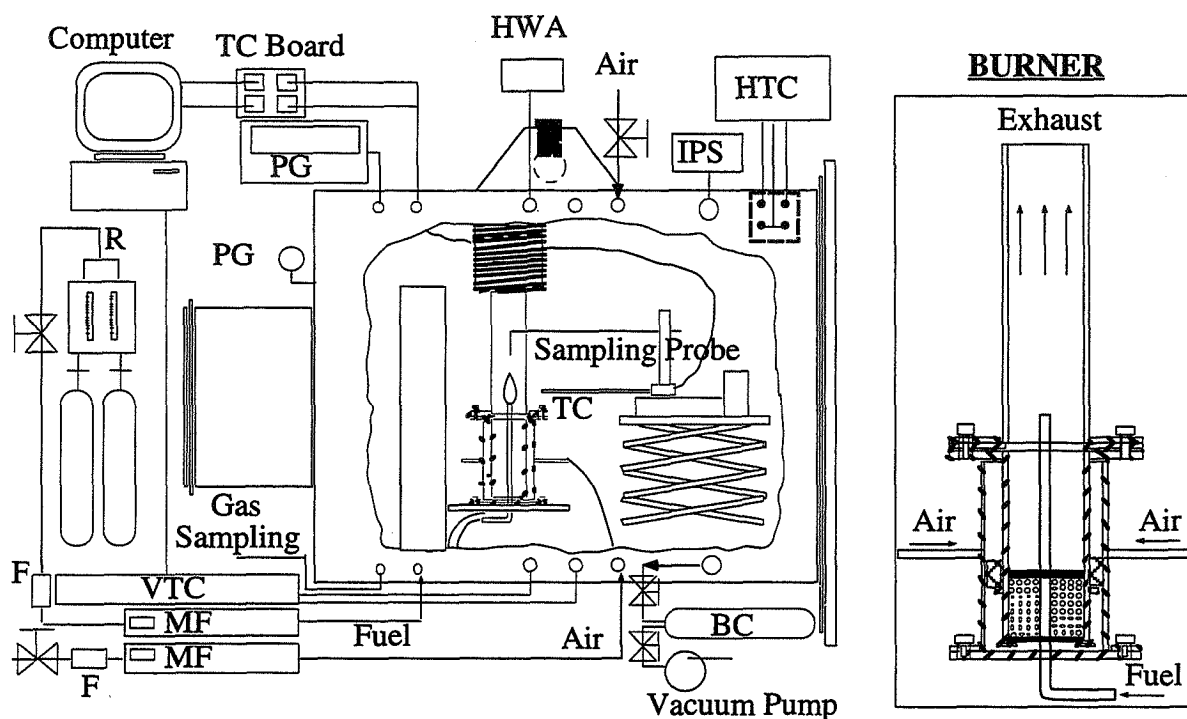
Figure 1. Experimental sepup; BC denotes the ballast chamber, F the filter, HWA the hot wire anemometer, IPS the ignitor power supply, MF the mass flowmeter, PG the pressure gage, R the rotameter, TC the thermocouple, HTC the horizontal translation controller and VTC the vertical translation controller.
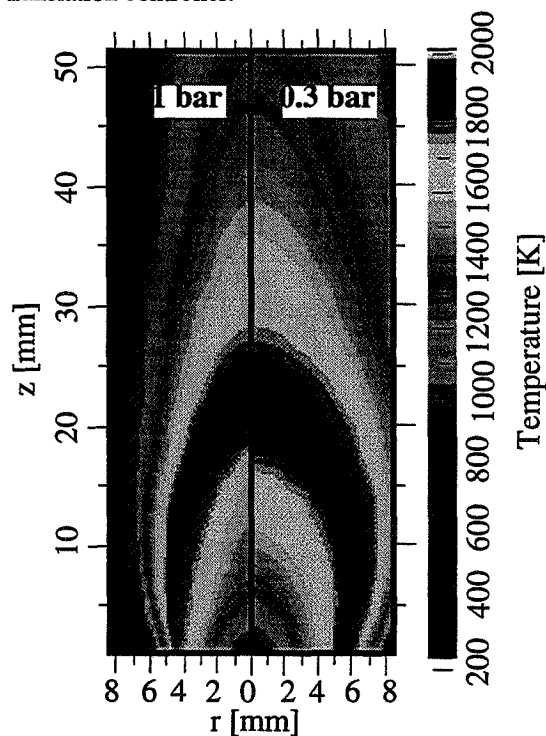
Figure 2. Comparison of measured isotherms of methane-fueled BSDF (at 0.14 m/s in normal condition) in normal pressure and reduced pressure (0.3 bar, or 0.1-g equivalent).
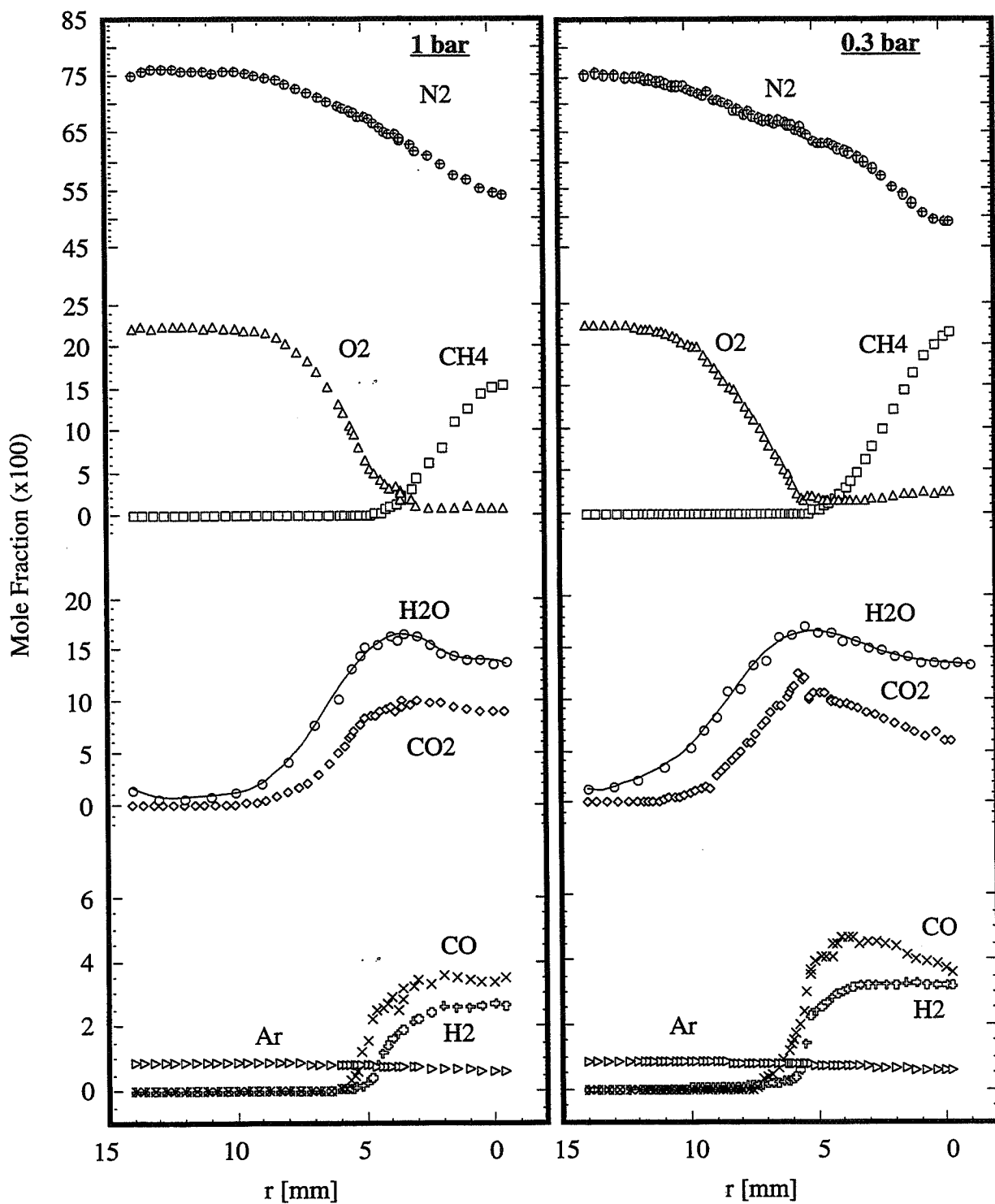
Figure 3. Comparison of measured species concentration of methane-fueled BSDF (at 0.14 m/s in normal condition) in normal pressure and reduced pressure (0.3 bar, or 0.1-g equivalent).

STUDY OF BUOYANCY EFFECTS IN DIFFUSION FLAMES USING RAINBOW SCHLIEREN DEFLECTOMETRY[*]

AJAY K. AGRAWAL and Subramanyam R. Gollahalli
School of Aerospace and Mechanical Engineering
University of Oklahoma, Norman, OK 73019

and

DeVon Griffin
NASA Lewis Research Center
Cleveland, OH 44135

Introduction

Diffusion flames are extensively encountered in many domestic and industrial processes. Even after many decades of research, a complete understanding of the diffusion flame structure is not available. The structure and properties of the flames are governed by the mixing (laminar or turbulent), chemical kinetics, radiation and soot processes. Another important phenomenon that affects flame structure in normal gravity is buoyancy. The presence of buoyancy has long hindered the rational understanding of many combustion processes. In gas jet diffusion flames, buoyancy affects the structure of the shear layer, the development of fluid instabilities, and formation of the coherent structures in the near nozzle region of the gas jets. The buoyancy driven instabilities generate vorticial structures outside the flame resulting in flame flicker. The vortices also strongly interact with the small-scale structures in the jet shear layer. This affects the transitional and turbulence characteristics of the flame. For a fundamental understanding of diffusion flames it is essential to isolate the effects of buoyancy. This is the primary goal of the experiments conducted in microgravity. Previous investigations, have shown dramatic differences between the jet flames in microgravity and normal gravity[1]. It has been observed that flames in microgravity are taller and more sooty than in normal gravity. The fuels used in these experiments were primarily hydrocarbons. In the absence of buoyancy the soot resides near the flame region, which adversely affects the entrainment of reactants. It is very important to eliminate the interference of soot on flame characteristics in microgravity. The present work, therefore, focuses on the changes in the flame structure due to buoyancy without the added complexities of heterogeneous reactions. Clean burning hydrogen is used as the fuel to avoid soot formation and minimize radiative losses. Because of the low luminosity of hydrogen flames, we use rainbow schlieren deflectometry for visualization. The visualized images are digitized for quantification.

The work reported here is divided into three sections; rainbow schlieren deflectometry (RSD), microgravity experiments and sub-atmospheric pressure experiments. The first section demonstrates the application of RSD for quantitative measurements in non-reacting and reacting flow systems. A computational effort to complement the experimental work is also included. In the second section, the experiments conducted at the 2.2s NASA Lewis Drop tower facility are described. The experiments were conducted to study the behavior of laminar, transitional and turbulent hydrogen flames in microgravity. The ability of RSD technique to provide quantitative data is highlighted. The final section deals with the sub-atmospheric pressure tests, which demonstrate that buoyancy in hydrogen diffusion flames can be scaled with pressure at normal gravity.

Rainbow Schlieren Deflectometry

The schlieren technique has been extensively used for qualitative flow visualization. Recently, Greenberg et. al. [2] developed the RSD technique for quantitative measurements. In the RSD technique, the knife edge used in the conventional schlieren apparatus is replaced by a continuously graded color filter. Quantitative measurements are made by the RSD technique utilizing computer imaging approach to create the color filter and to acquire/analyze color schlieren images. The color filters are calibrated to obtain the hue variation along the filter. The rainbow filter transmits a color uniquely represented by hue, according to the hue-saturation-intensity(HSI) model, from a given position on the filter plane. Thus, a color image of the test

section revealing the ray displacements caused by refractive index gradients in the medium is formed on the CCD array. The camera output in the RGB format is digitized by a personal computer with 24-bit color frame grabber. The digitized schlieren image together with filter calibration curve, is used to obtain the angular deflections of the light rays by the medium. The refractive index distribution is obtained from the angular deflections using Abel inversion. The refractive index is then related to density and/ or other scalar properties of the medium.

Three test cases were chosen to demonstrate the RSD technique, namely, temperature measurement in a heated air jet, oxygen concentration in an isothermal jet of helium, and temperature and oxygen concentration measurements in a hydrogen diffusion flame. In all the above cases the flow was laminar and axisymmetric and the jet issued into quiescent air. The heated jet issued from a 7.1mm nozzle with an exit Reynolds number of 400. In a heated jet, the refractive index is a function of only the temperature. The refractive index from RSD can be used to obtain the temperature distribution. The temperature measurements obtained from schlieren method were compared with thermocouple measurements (Fig. 1). The results agree well. In the second test case, oxygen concentration measurements were made in a helium jet issuing from a 7.1mm nozzle at a Reynolds number of 125. It was assumed that helium and air together behave as a binary mixture, with a fixed air composition. Hence, the gas properties are unique functions of the helium mass fraction. Thus the refractive index obtained by RSD could be directly related to oxygen concentration. The oxygen concentration was also measured using a diffusion based oxygen analyzer. The results (Fig. 2) indicate that the schlieren measurements show excellent agreement with the probe data. In the third test case measurements of temperature and oxygen concentration were made in a hydrogen flame. Laminar hydrogen flames have a large Damkohler number; hence it was assumed that the reactions reach chemical equilibrium instantly. This equilibrium chemistry model with unity Lewis number assumption was used to obtain the relation between refractive index and the scalar variables. The temperature and oxygen concentration were also independently obtained by probe measurement. The thermocouple measurements were not corrected for radiation losses. The temperature and oxygen concentration are compared in Figs. 3 and 4. The results in fuel rich region are not shown due to large uncertainties in that region, primarily attributed to instrument sensitivity, validity of the chemistry model, and unity Lewis number assumption. The schlieren measurements in the fuel lean region show good agreement with probe measurements.

RSD was used as a tool to evaluate CFD results. Numerical simulations of the hydrogen flames were performed with a mixture fraction approach and assuming equilibrium chemistry. Two diffusion models were used for the mixture fraction equation. The first model (Model 1) uses the thermal diffusivity and the second model (Model 2) uses the mass diffusivity in the mixture fraction equation. In Model 2, a two zone diffusion model [3] was used to account for non-unity Lewis number effects. The computed results of temperature and species concentration were used to generate a rainbow schlieren image which was then compared with the experimental image (Fig. 5). The computed images agree well with the experimental images near the nozzle. The computed image indicates higher upstream diffusion. The comparison of the computed temperature distribution with schlieren measurements is shown in Fig. 6. The figure shows that computations obtained from Model 2 agree well with the experiments in the fuel lean region. The discrepancy in the fuel rich region is due to reasons explained above.

Microgravity Experiments

Experiments were conducted in microgravity to study the behavior of hydrogen flames without buoyancy. The drop rig used was provided by NASA LeRC diagnostics group. While easily reconfigurable, this hardware was designed for use with rainbow schlieren optical systems. The flame data were collected during the 2.2 second drop using a Super-VHS tape recorder. The images from the video were digitized using a frame grabber. The study involved the visualization of laminar, flickering and transitional laminar flames. The schlieren image of a laminar flame obtained in microgravity is compared with that in normal gravity (Fig. 7). The jet issued from a tube of 0.3mm ID at an exit Reynolds number of 582. The figure indicates flame in microgravity with higher upstream diffusion. The images were used to obtain the refractive index distribution and temperature profiles at two axial locations, namely at 3.8D and 7.8D from the tube exit. The temperature distribution is shown in Fig. 8. The results in the fuel rich region are omitted, due to inaccuracies in recording and filter calibration. Reasonable values of the flame boundary location and the data in the fuel lean region were obtained. From the figure we observe that there is an increase in the flame width. Sharper temperature gradients near the flame at normal gravity were observed. This is caused by the convective motion of the heated gases from the flame surface. In normal gravity flickering of the flames is observed, which is induced by the outer vortices caused by buoyancy. The flames were observed in normal gravity (Figs. 9a-e); flickering frequency was ~13 Hz. In microgravity, the flickering disappears (Figs. 9f-j) as the flame grows. The flame was nearly at steady state, undergoing minor changes at the end of the drop. The transitional flames were studied to observe the effect of buoyancy on the structure of turbulence and mode of transition. The test were done using hydrogen jet issuing from a tube of 0.3mm ID and an exit Reynolds number of 1078 . The images obtained in microgravity were compared with that in normal gravity (Fig. 10). The flames show a break point at both normal and microgravity. This indicates that microgravity and normal gravity

118

flames, have similar transition behavior, unlike the observation by Hegde et. al [4], whose results indicate that the entire flame becomes turbulent in microgravity without a break point.

Sub-atmospheric Pressure Experiments

Experiments were conducted in a subatmospheric pressure combustion chamber, to simulate low buoyancy conditions. By reducing the pressure in the combustion chamber the effect of buoyancy can be reduced. The primary aim was to verify that buoyancy can be scaled with pressure[5]. Previous experiments with hydrocarbon fuels faced problems at low pressure due to chemical kinetics and heterogeneous reactions in sooting flame. The present system with non-sooting, fast reacting hydrogen fuel significantly relaxes the scaling requirements. It was observed that by using hydrogen, the buoyancy effects may be scaled at sub-atmospheric pressures. The combustion chamber is shown in Fig. 11. The combustion chamber was constructed to provide sub-atmospheric pressure and to obtain continuous combustion with the chamber oriented at any desired inclination to the gravitational field. The images of hydrogen the flame were obtained using the rainbow schlieren technique. The experiments were performed with laminar and flickering laminar flames in a Reynolds number range of 100-500. The images of the hydrogen flame (D = 0.58mm, Re= 300) obtained at different pressure levels for zero inclination of the chamber are shown in Fig. 12. The images were compared with those obtained in microgravity. The characteristic schlieren width, defined as the peak-to-peak hue width divided by the jet diameter, for different pressures in normal gravity and at one atmosphere in microgravity is plotted versus the Froude number (The ratio of the Froude number to the Froude number at normal gravity and one atmosphere pressure) (Fig. 13). The figure indicates that the low atmospheric results tend asymptotically towards the microgravity results. The images of the flame were obtained with the chamber inclined at 60^0 (D = 0.84mm, Re= 100) for different pressures (Fig. 14). It can be observed that the flame becomes straighter with reduced pressure; further indicating that the buoyancy effects diminish with pressure. The amplitude of the flickering flames is affected by the buoyancy levels (Fig. 15). With reduced pressure the amplitude of the oscillations progressively diminishes, as seen in microgravity. From the above study, it was concluded that the buoyancy can be scaled with pressure.

Future Work

Currently, work is progressing on the development of a new drop tower rig with on board digital data acquisition, modified fuel and calibration system and precise imaging. The optimization of the schlieren setup is in progress for improved sensitivity. A parallel effort is in progress for the numerical simulation of hydrogen flames with non-unity Lewis number assumption and multi-component diffusion model.

Acknowledgment

References

1.   Bahadori, M. Y., Stocker, D. P., Vaughan, D. F., Zhou, L., and Edelman, R. B., 1992, " Effects of Buoyancy on Laminar, Transitional and Turbulent Gas Jet Diffusion Flames, " *Proc. of the 2nd Int. Microgravity Combustion Workshop*, pp.   91-106, NASA CP-10113.

2.   Greenberg, P. S., Klimek, R. B., and Buchele, D. R. 1995 , "Quantitative Rainbow Schlieren Deflectometry," *Applied Optics,* Vol. 34, no. 19, pp. 3810-3822.

3.   Katta, V. R., Goss, L. P., and Roquemore, W. M., 1994, " Numerical Investigation of Transitional H2/N2 Jet Diffusion Flames," *AIAA Journal*, vol. 32, pp. 84-94.

4.   Hegde, U., Zhou, L., Bahadori, M. Y., 1994,"The Transition to Turbulence of Microgravity Gas Jet Diffusion Flames," *Combustion Science and Technology,*. 102, pp. 95-113.

5.   Mortazavi, S. M., Sunderland, P. B., Jung, J., Faeth, G. M.,1992 ," Structure and Soot Properties of Buoyant and Non-Buoyant Laminar Round Jet-Diffusion Flames," *Proc. of the 2nd Int. Microgravity Combustion Workshop*, pp. 101-114, NASA CP-10113.
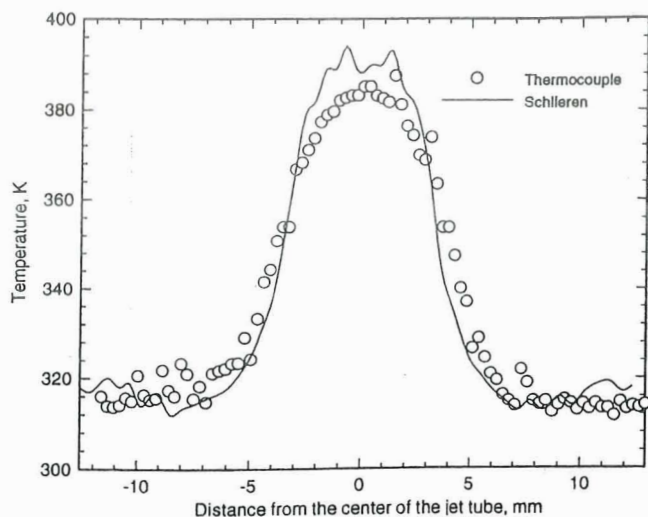
Figure 1.- Temperature in a heated air jet
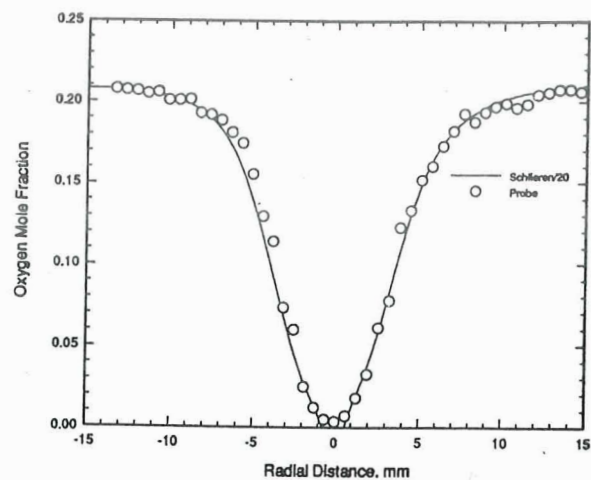
Figure 2.- Oxygen concentration in a helium jet
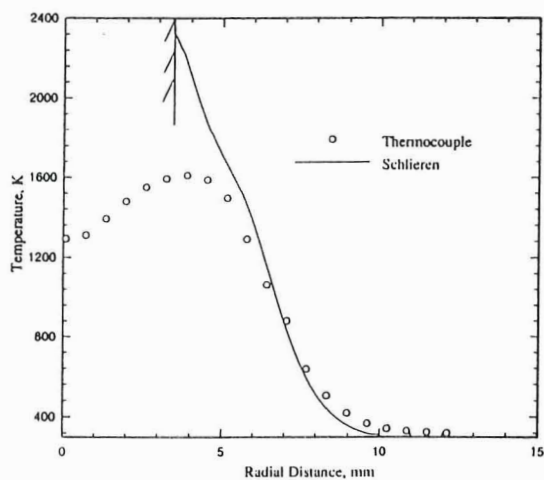
Figure 3.- Temperature in a hydrogen flame
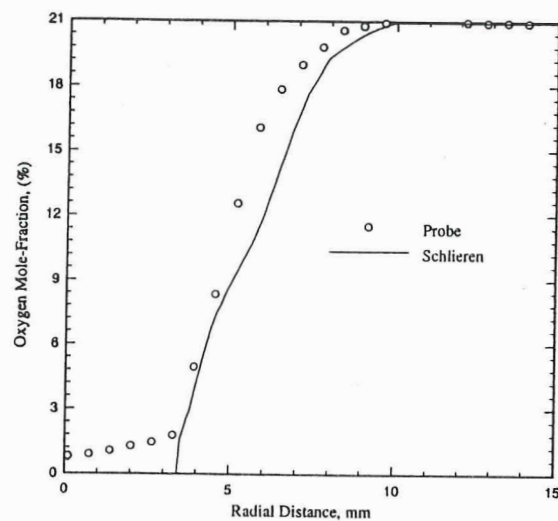
Figure 4.- Oxygen concentration in a hydrogen flame
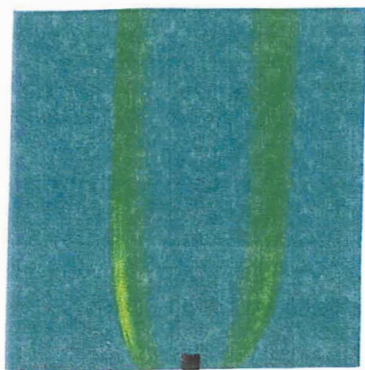
Figure 5.- Computed and experimental schlieren image of hydrogen flame
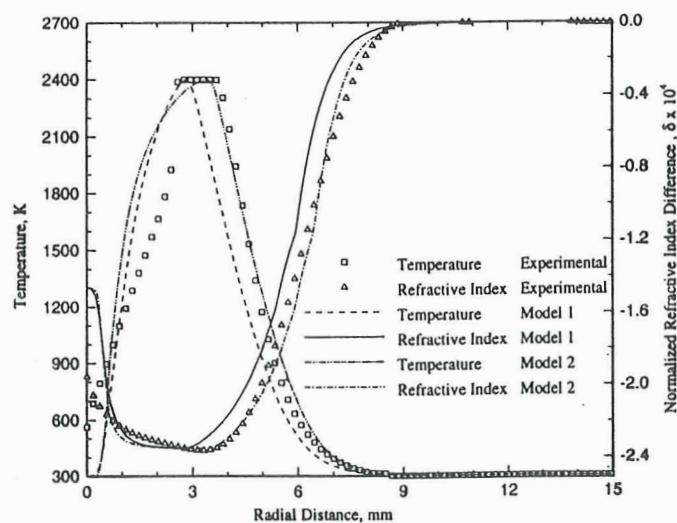
Figure 6.- Computed and RSD temperature distribution of hydrogen flame

120
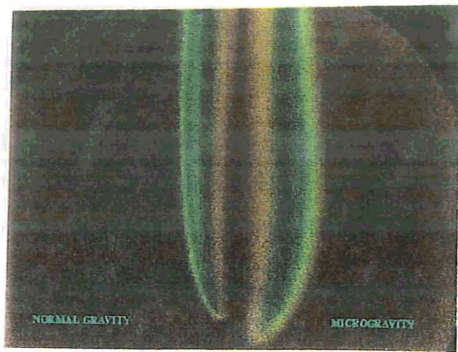
Figure 7.- Schlieren image of laminar hydrogen flame
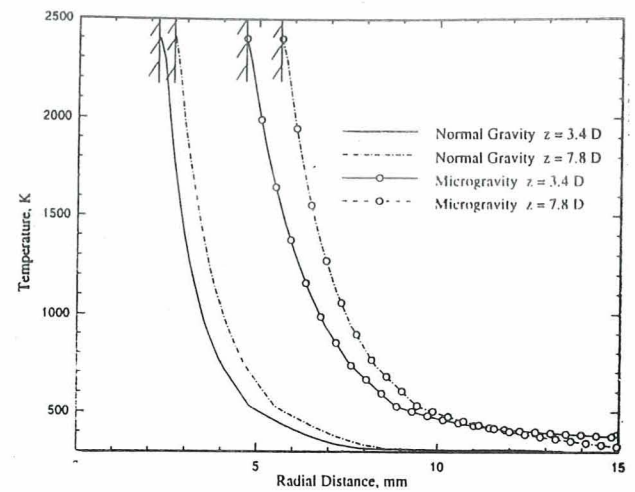
Figure 8.-RSD temperature distribution of hydrogen flame
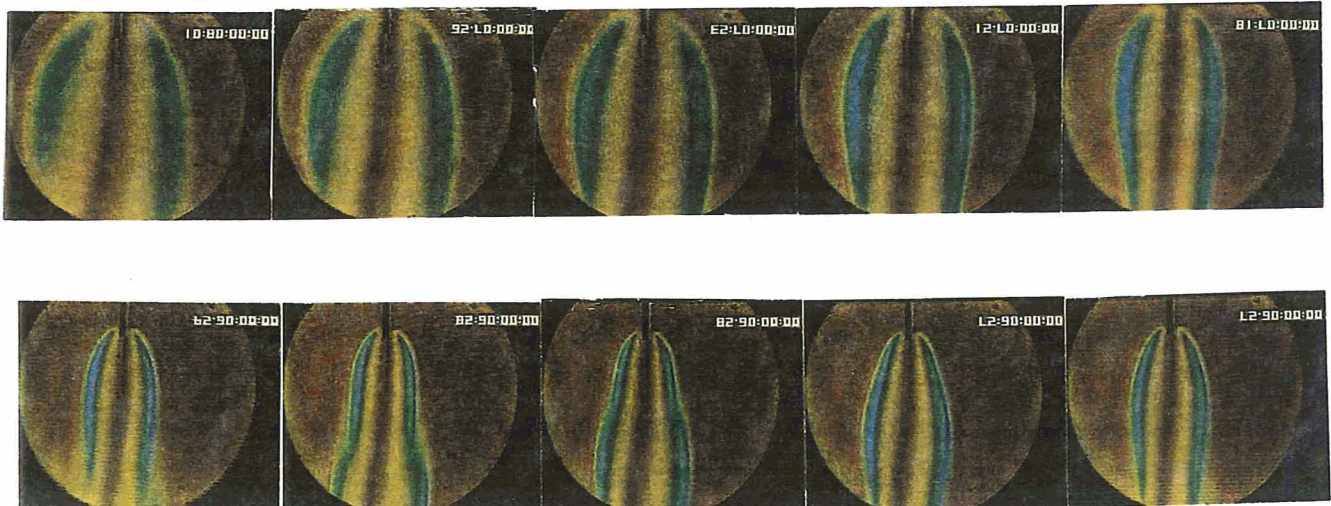
Figure 9.-Sequence of schlieren images of flickering hydrogen flames
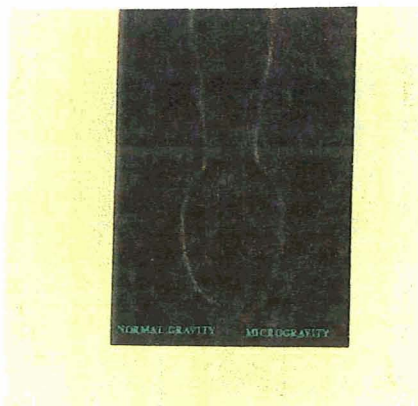
Figure 10.- Schlieren image of transitional hydrogen flame
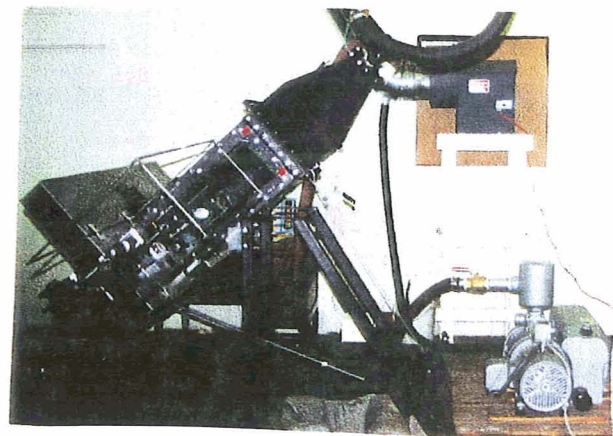
Figure 11.-Sub-atmospheric pressure setup

121

a: p = 1 atm.　　b: p = 0.8 atm.　　c: p = 0.6 atm.　　d: p = 0.2 atm.
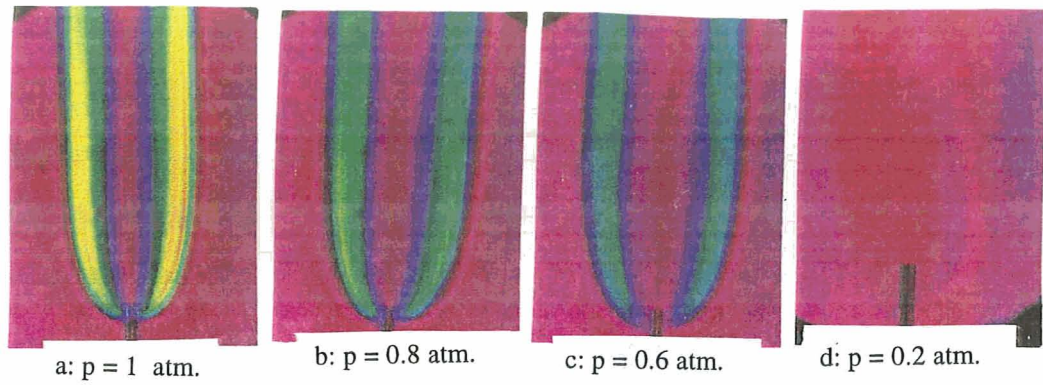
Figure 12.-Schliren images of hydrogen flames at zero inclination to gravity vector
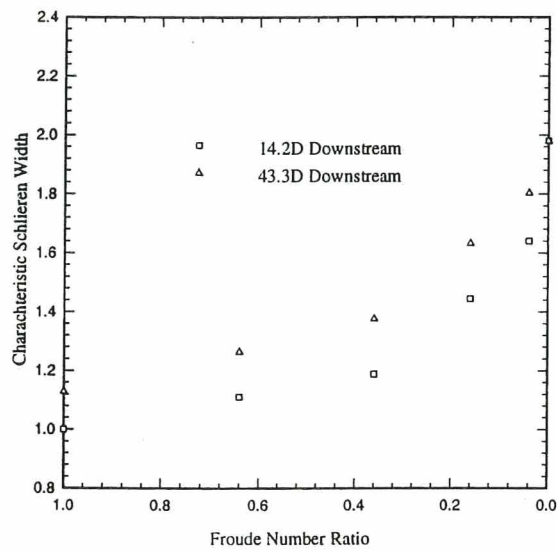
Figure 13.-Scaling of schlieren width with froude number ratio
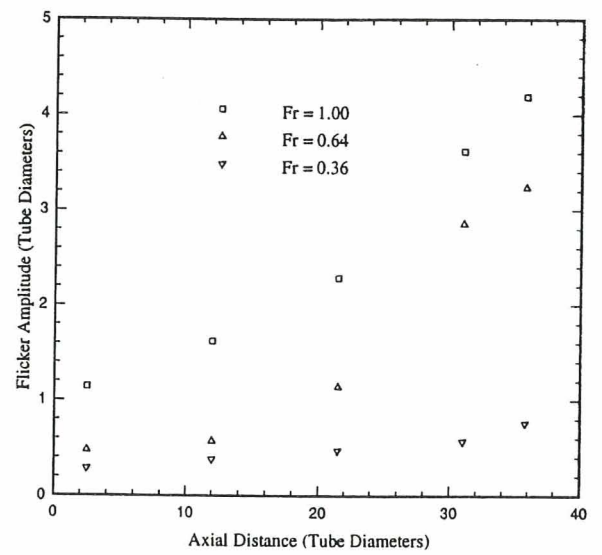
Figure 15.-Flicker amplitude variation with froude number

a: p = 1 atm.　　b: p = 0.8 atm.　　c: p = 0.6 atm.
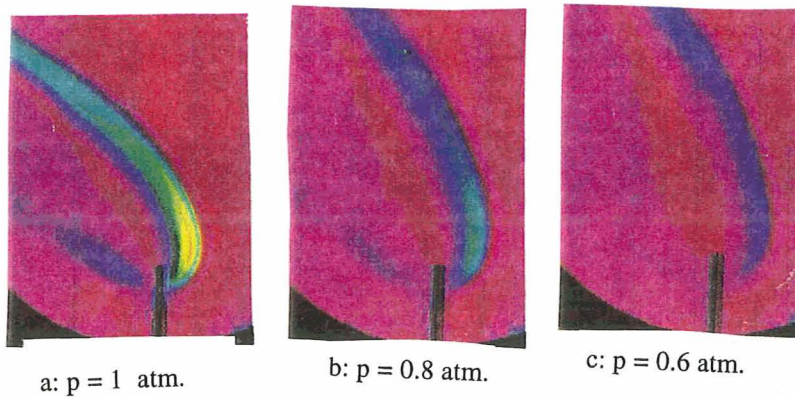
Figure 14.-Schliren images of hydrogen flames at 60^0 inclination to gravity vector

122

COMPUTATIONAL AND EXPERIMENTAL STUDY OF LAMINAR DIFFUSION FLAMES IN A MICROGRAVITY ENVIRONMENT

MARSHALL LONG, Kevin Walsh, and Mitchell Smooke

Yale University
Department of Mechanical Engineering
and Center for Laser Diagnostics
New Haven, Connecticut 06520-8284

Introduction

A detailed computational and experimental study of coflow diffusion flames in a microgravity environment has been initiated. The overall goal of the program is to apply adaptive computational algorithms and advanced imaging techniques to a simple, well-characterized burner. The results will provide new information on the formation of NOx, soot, and the interaction of convection, diffusion, and chemistry in a nonbuoyant environment. In previous work on this flame at normal gravity, quantitative two-dimensional species concentration profiles were modeled computationally and were measured using spontaneous Raman scattering and laser-induced fluorescence (LIF) [1,2]. In extending the study to microgravity conditions, improvements to the computational model have been made and new calculations performed for a range of gravity conditions. In addition, modifications to the experimental approach have been necessitated by the constraints imposed by existing microgravity facilities. Initial results from the computations and experiments are presented in the following sections.

Computational Approach

The computational model employs GRI Mech 2.11 [3] to compute the temperature field, velocities, and species concentrations. Our model of an axisymmetric laminar diffusion flame considers an unconfined laminar flame in which a cylindrical fuel stream is surrounded by a coflowing oxidizer jet. The full set of elliptic two-dimensional governing equations for mass, momentum, species, and energy are discretized on a two-dimensional mesh. The resulting nonlinear equations are then solved by a combination of time integration and Newton's method. The Newton equations are solved by a preconditioned BiCGSTAB iteration. Grid points of the two dimensional mesh are determined by equidistributing positive weight functions over mesh intervals in both the r and z directions. The complete formulation of the mathematical model is described in detail [4] elsewhere, and will not be repeated here. The chemical production rates, binary diffusion coefficients, thermal diffusion coefficients, mixture viscosity and thermal conductivity as well as thermodynamic quantities, are evaluated using vectorized and highly optimized transport and chemistry libraries [5]. In order to determine the flame structure under microgravity conditions, the results of a computed solution at normal gravity were used as a starting point. In subsequent calculations, the value of the gravitational acceleration (g) was reduced by 10 cm/sec^2 and a new solution calculated using Newton's method.

Computations performed with different values for the gravitational constant indicate that buoyancy plays an important role in both the size and shape of the laminar diffusion flame. Specifically, in Figure 1 we illustrate the temperature isotherms for flames computed with g = 982.0, 491.0 and 0.0 cm/sec^2. It is clear from the figures that, as the gravitational constant is lowered, the flames tend to become shorter and broader in appearance. This is also illustrated in Figure 2 where the corresponding CH isopleths are plotted.

While large variations in g are important in illustrating the differences between ground based and microgravity flame structure, small variations in g are important in determining whether the flame will be amenable for study in the NASA DC-9 or the Lewis drop towers. During the microgravity portion of the DC-9's parabolic trajectory, the value of the gravitational constant can vary by as much as ±1% of g. If the computed structure of the diffusion flame varies significantly under such conditions, then drop tower experiments would be the preferred experimental venue. Numerical studies indicate that the flame structure is insensitive to one percent changes in g for this coflowing geometry.

123

Emission Measurements

Laser imaging techniques such as Raman scattering and LIF present difficulties for microgravity facilities in terms of the size and power requirements of the apparatus. A challenge for the experimental work, then, is to adopt different techniques that can still provide quantitative results for comparison with the computations. Initially, these techniques must be evaluated in a ground-based environment. One promising approach applicable to our laminar flame is to do emission tomography of a selected flame radical. For example, CH is an excellent choice, as the chemiluminescence of excited state CH (denoted CH*) is a source of easily measured light at 431 nm. In addition, the structure of the CH profile is a sensitive measure of the overall flame shape. The emission measurements result in an intensity distribution proportional to number density of CH*. A quantitative CH* number density profile can be obtained by calibrating the optical system with Rayleigh scattering and applying the appropriate quenching estimate.

The emission signal is given by [6]

$$S_{em} = \eta \varepsilon A \tau V_{em} \frac{\Omega}{4\pi} N^*$$

where η is the detector efficiency in counts per photon, ε is a calibration constant of the optics, A is the Einstein A coefficient, τ is the integration time, V_{em} is the emission pixel volume, Ω is the solid angle, and N^* is the number density of emitting molecules. In order to provide a calibration for the optical system, the same apparatus is used to detect laser Rayleigh scattering from a gas of known temperature, pressure, and composition. The Rayleigh signal from a single laser pulse is [7]

$$S_R = NP_L \frac{\partial \sigma}{\partial \Omega} \Omega \varepsilon \eta V_R / h\nu$$

where N is the known number density of the gas, P_L is the laser energy per cross-sectional area, $\partial \sigma / \partial \Omega$ is the Rayleigh cross section, V_R is the Rayleigh volume over which the Rayleigh signal is integrated, and $h\nu$ is the laser photon energy. By combining these two expressions, the emission number density can be expressed as

$$N^* = \frac{4\pi S_{em} \frac{\partial \sigma}{\partial \Omega} NP_L V_R}{A\tau V_{em} S_R h\nu}$$

The effect of collisional quenching is later estimated to convert this emission number density into an absolute CH* number density.

Experimental System

The burner system used in this experiment contained a central fuel jet (4 mm diameter) surrounded by coflowing air. The fuel was 65% methane and 35% nitrogen by volume, and the exit velocity of both fuel and coflow was 35 cm/s. Complete burner specifications are given elsewhere [1]. Imaging for both emission and Rayleigh scattering was done with a cooled charge-coupled device (CCD) camera (STAR I, Photometrics) at f/16 collection efficiency. The lens to flame distance was 20 cm, and the depth of focus was measured to be 5 mm. The camera was connected to a microcomputer where the images were stored and processed. An interference filter centered at 431 nm, 10 nm full width at half maximum, was used to pick up the $A^2\Delta \rightarrow X^2\Pi$ transition in CH at 431.4 nm. The steady, laminar nature of the flame allows long (90 s) exposure times and good signal levels for the emission signal. For the Rayleigh calibration, a neodymium : yttrium aluminum garnet laser was used to pump a dye laser tuned to 431 nm. The beam passed 2 cm over the burner surface and into a power meter where the energy per pulse was measured. Typical energies per pulse were between 5 and 15 mJ. Rayleigh scattering was done on a flow of air, with N constant. The energy per pulse was varied by changing the Q-switch delay on the pump laser. In a given Rayleigh exposure, laser energy was stored and averaged by interfacing the computer and power meter. The experimental setup is shown in Figure 3.

Image Processing and Quenching Estimates

The resultant digitized images of flame emission provide an integration along a line of sight. An Abel inversion was then performed to obtain an in-plane spatial profile of CH* emission signal. The values used for the different signals and volumes are of considerable importance in determining number density. The emission signal was considered to be the number of counts above the background at a given pixel after the Abel inversion was performed. For the emission volume, the in-plane resolution was easily determined. The depth was calculated to be identical to the other two dimensions, giving us a volume of L^3, where

124

L = 74 μm. The signals were also corrected for the optical throughput of the interference filter, since the emitted light is more broad band than the scattered laser light.

A full calculation of quenching requires a quenching cross section for CH*, which in general varies with pressure, temperature, and collisional partner. Although these dependencies aren't well known, there is experimental data [8] that suggests only a weak dependence of CH* quenching on collision partner. In light of this, a conclusion similar to that of Nguyen and Paul [9] may now be drawn: since CH* is found over a narrow spatial extent and temperature range, it is reasonable to expect the quenching in CH* to be relatively constant. Accordingly, the effective quenching cross section of CH* is taken to be 6 Å^2 (as found in CH by Cattolica [10] at low pressure) and is assumed constant for all collisional partners. Temperature is obtained from the computational data and was a constant 1900 K in the region where CH (hence CH*) was present. The resulting quenching factor Q was found to be 5×10^8 s^{-1}. The fraction of CH* that emits a photon is given by A/(A+Q), which is roughly 1/250 in our system.

Results and Discussion

The measured emission signal is processed using an Abel inversion, and a quenching correction is performed to obtain a spatial profile of CH* number density. This is shown in Figure 4. The peak in-plane number density of CH* is of the order 10^{10} cm^{-3}. Also shown in Figure 4 is the computed CH profile. Peak concentrations in these profiles differ by roughly a factor of 1000. Joklik and Daily [11] found a similar ratio between ground and excited state populations in CH. Both radicals are distributed in a similar way, with maximum concentration occurring at the onset of the flame, and continuing downstream in a thin sheet along the flame edge. If the fraction of excited radicals is spatially uniform, then the features predicted by the model are in agreement with the measured CH* number density profile. Despite the coarseness of the quenching estimate and uncertainties in the absolute calibration of the optical system, the emission measurements are being made as quantitative as possible and are seen to be a sensitive check for the computed flame structure.

References

1. Smooke, M. D., Xu, Y., Zurn, R. M., Lin, P., Frank, J. H., and Long, M. B.,: *Twenty-fourth Symposium (Int'l) on Combustion,* The Combustion Institute, p. 813, (1992).
2. Smooke, M. D., Lin, P., Lam, J., and Long, M. B.,: *Twenty-third Symposium (Int'l) on Combustion,* The Combustion Institute, p. 575, (1991).
3. Bowman, C. T., Hanson, R. K., Davidson, D. F., Gardiner Jr., W. C., Lissianski, V., Smith, G. P., Golden, D. M., Frenklach, M., Wang, H., and Goldenberg, M.,: *GRI-Mech version 2.11,* http://www.gri.org, (1995).
4. Ern, A., Douglas, C. C., Smooke, M. D., *The International Journal of Supercomputer Applications,* Volume 9, No. 3, p. 167-186, (1995).
5. Giovangigli, V. and Darabiha, N.,: *Proceedings of the Conference on Mathematical Modeling in Combustion,* Vector Computers and Complex Chemistry Combustion, Lyon, France, NATO ASI Series, (1987).
6. Hertz, H. M. and Faris, G. W.,: *Opt. Lett.,* **13**, p 351, (1988).
7. Luque, J., Smith, G. P. and Crosley, D. R.,: *Twenty-sixth Symposium (Int'l) on Combustion,* in press.
8. Garland, N. L. And Crosley, D. R.,: *Twenty-first Symposium (Int'l) on Combustion,* The Combustion Institute, p. 1693, (1986).
9. Nguyen, Q. V., and Paul, P. H.,: *Twenty-sixth Symposium (Int'l) on Combustion,* in press.
10.Cattolica, R. J., Stepowski, D., Puechberty, D., and Cottereau, M.,: *J. Quant. Spectro. Rad. Transfer,* **32**, p. 363, (1984).
11. Joklik, R. G., Daily, J. W. and Pitz, W. J.,: *Twenty-first Symposium (Int'l) on Combustion,* The Combustion Institute, p. 895, (1986).
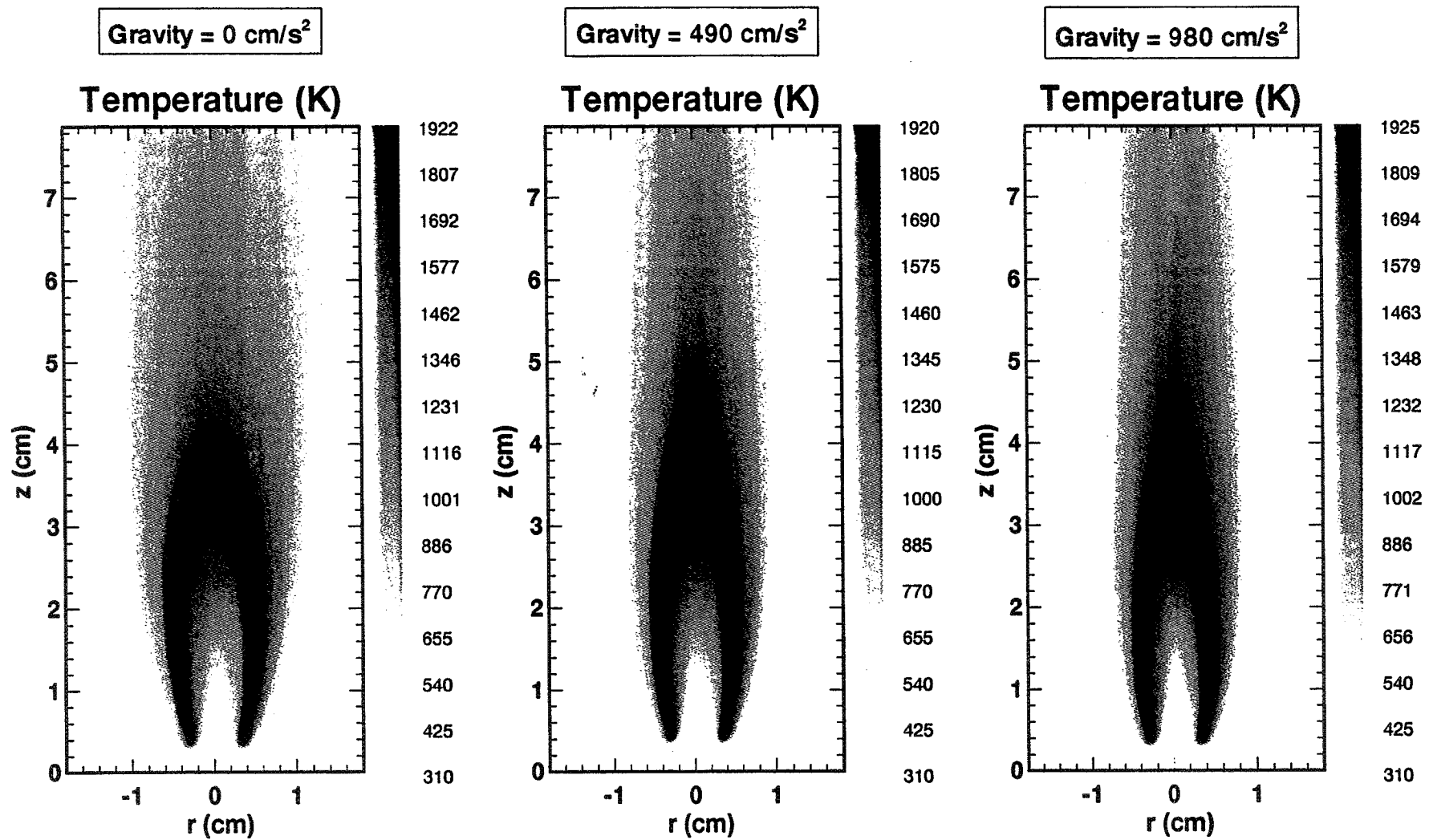
Figure 1: Computed temperature isotherms for gravity of
0, 490, and 980 cm/s²
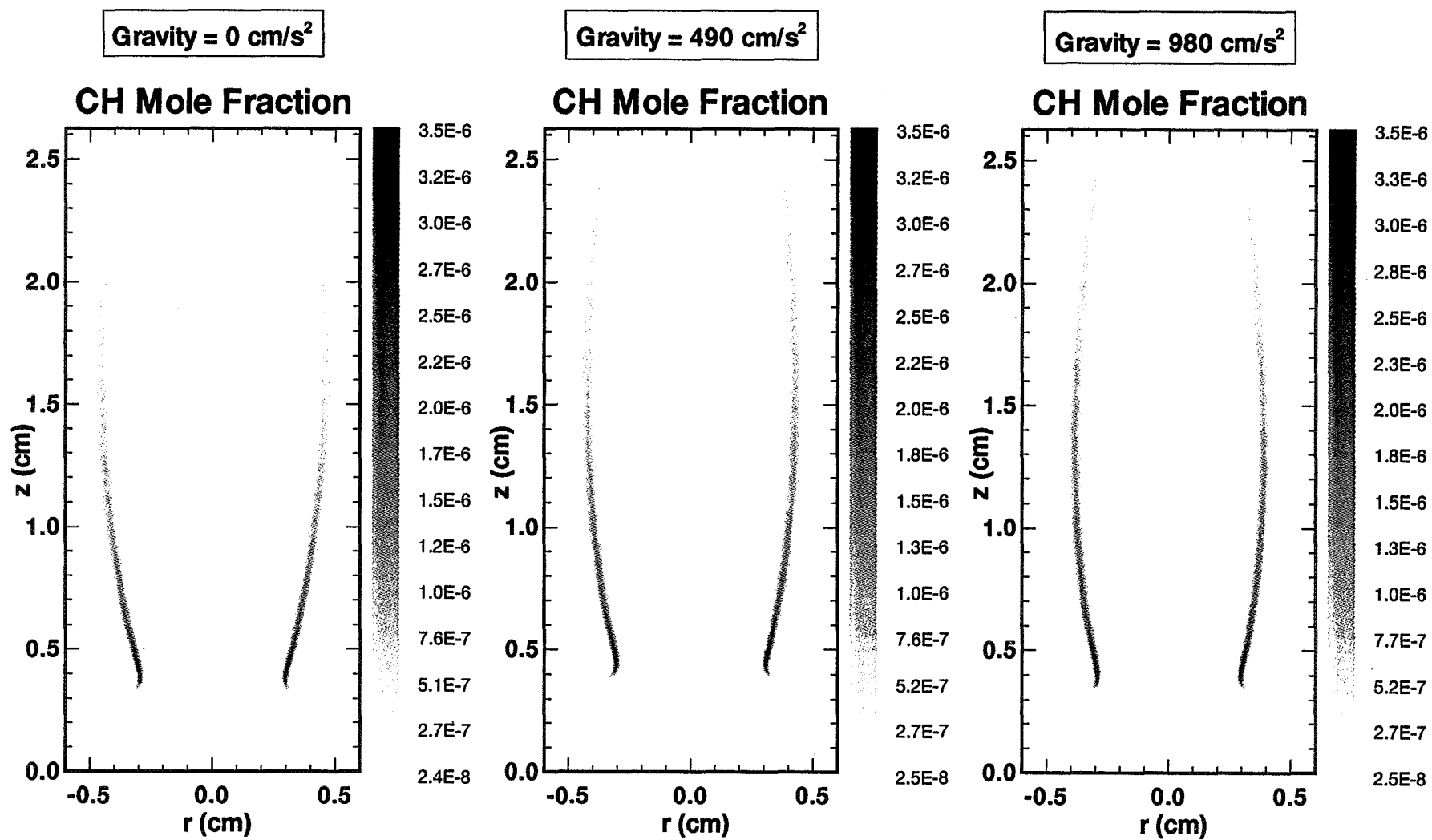
Figure 2: Computed CH isopleths for gravity of
0, 490, and 980 cm/s^2
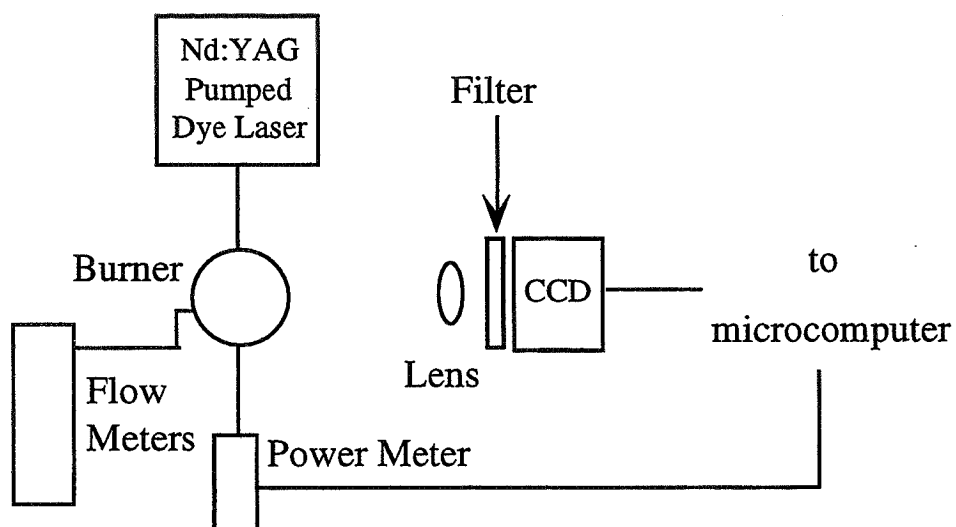
Figure 3. Experimental configuration for emission tomography.
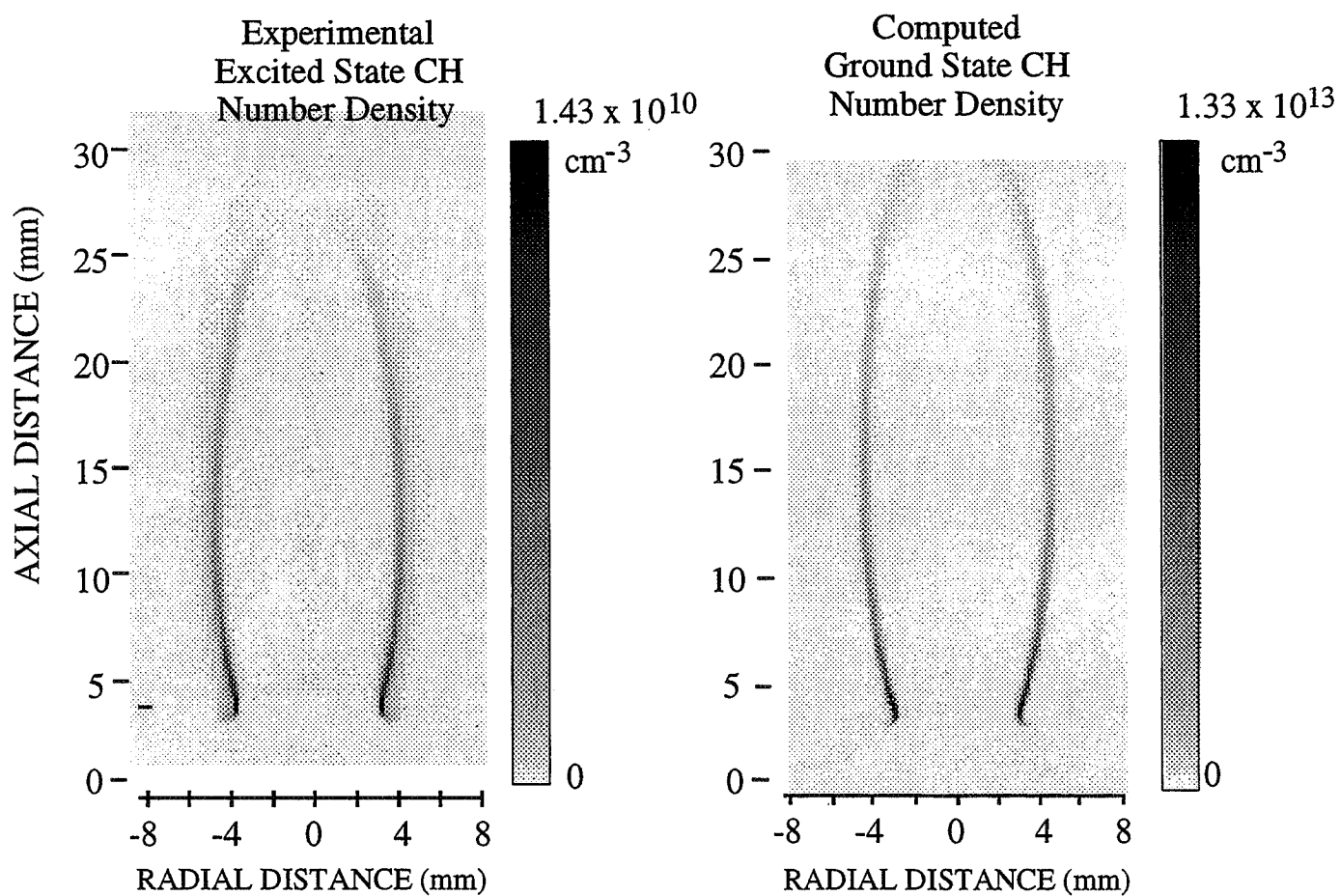
Figure 4. Spatial number density profiles of CH* (experimental) and CH (computed).

SHAPES OF BUOYANT AND NONBUOYANT
METHANE LAMINAR JET DIFFUSION FLAMES[*]

PETER B. SUNDERLAND[†], Zeng-guang Yuan[‡] and David L. Urban
NASA Lewis Research Center
Cleveland, Ohio

Introduction

Laminar gas jet diffusion flames represent a fundamental combustion configuration. Their study has contributed to numerous advances in combustion, including the development of analytical and computational combustion tools. Laminar jet flames are pertinent also to turbulent flames by use of the laminar flamelet concept.

Investigations into the shapes of noncoflowing microgravity laminar jet diffusion flames have primarily been pursued in the NASA Lewis 2.2-second drop tower, by Cochran and coworkers [1, 2] and by Bahadori and coworkers [3-6]. These studies were generally conducted at atmospheric pressure; they involved soot-containing flames and reported luminosity lengths and widths instead of the flame-sheet dimensions which are of greater value to theory evaluation and development.

The seminal model of laminar diffusion flames is that of Burke and Schumann [7], who solved the conservation of momentum equation for a jet flame in a coflowing ambient by assuming the velocity of fuel, oxidizer and products to be constant throughout. Roper and coworkers [8, 9] improved upon this model by allowing for axial variations of velocity and found flame shape to be independent of coflow velocity. Roper's suggestion that flame height should be independent of gravity level is not supported by past or present observations. Other models have been presented by Klajn and Oppenheim [10], Markstein and De Ris [11], Villermaux and Durox [12] and Li et al. [13]. The common result of all these models (except [12] in the buoyant regime) is that flame height is proportional to fuel mass flowrate, with flame width proving much more difficult to predict. Most existing flame models [7, 9, 10, 12, 13] have been compared with shapes of flames containing soot, which is known to obscure the weak blue emission of flame sheets.

The present work involves measurements of laminar gas jet diffusion flame shapes. Flame images have been obtained for buoyant and nonbuoyant methane flames burning in quiescent air at various fuel flowrates, burner diameters and ambient pressures. Soot concentrations were minimized by selecting conditions at low flowrates and low ambient pressures; this allows identification of actual flame sheets associated with blue emissions of CH and CO_2. The present modeling effort follows that of Roper [8] and is useful in explaining many of the trends observed.

Experimental Methods

The experiments were conducted in a general-purpose combustion rig, consisting of a windowed pressure vessel, a fuel delivery system, an ignitor, a color CCD camera, a microprocessor controller and lead-acid batteries. The fuel jet issued vertically upward on the axis of the cylindrical chamber, whose diameter, length and volume were 25 cm, 53 cm and 27 l, respectively. The burners were straight stainless steel tubes with beveled outside edges and inside diameters of 0.42, 0.85, 1.70, 3.25 and 5.54 mm. The burners had length-to-diameter ratios of at least 40, which ensured fully-developed laminar discharge. The flames were ignited using spring-loaded retracting hot wires (Kanthal A, 0.36 mm) mounted in tension 3 mm above the burners. These wires were 12 mm long and were energized with 28 VDC, causing them to glow and rupture within 30 ms. Following ignition, the ruptured wires retracted symmetrically with minimal flow disturbance.

On-board methane (purity 99.99%) was stored in a 75 ml bottle and delivered to the burner via, in order, a pressure regulator, a solenoid valve, an orifice, a mass-flow meter, and a second solenoid valve. Orifice diameters were varied from 0.03-0.07 mm to ensure choked flow. Fuel flowrates were determined using the in-line mass flow meter (Omega FMA-5606-ST), which was calibrated for each fuel using a bubble meter. The pair of solenoid valves minimized diffusion of air into the fuel delivery plumbing prior to release into microgravity and allowed for optimization of the timing and volume of the initial fuel

129

flow. Room air was used as the ambient for conditions at or below 1 atm; a mixture of 21.1% O_2, balance N_2 was used for the 2 atm flames.

The flames were imaged using a color CCD camera (Panasonic WV-CL352) mounted 27 mm from and perpendicular to the chamber axis. Fixed-iris lenses were used, with focal lengths (16-50 mm) chosen according to flame size, and f-numbers (1.4-6) chosen according to illumination levels. For flames containing soot, an additional camera was utilized behind a CH-line filter. Signals from the cameras were carried via fiber-optic cable to a stationary SVHS video recorder.

The conditions for the present flames are summarized in Table 1. Nomenclature is as follows: p is ambient pressure, d is burner diameter, L is the distance from the burner lip to the flame sheet intersection with the axis and w is the maximum flame width. Reynolds number is defined as $Re = \rho_0 v_0 d/\mu_0 = 4\dot{m}/\mu_0 d$, where ρ is density, v is average velocity, μ is dynamic viscosity, $\dot{m}$ is fuel mass flowrate and subscript 0 refers to fuel-inlet conditions. The normal-gravity flames were restricted to steady-state, nonflickering conditions. The microgravity flames were ignited immediately following release into microgravity. Uncertainties in the measurements are estimated to be 5% for fuel flow rate and for dimensions of the small or low-pressure flames and 20% for the dimensions of the other flames, which contained soot and required judicious estimation of flame sheet locations.

Analytical Model

The Roper model [8] was selected here because of its unique attributes, specifically its pertinence to noncoflowing conditions, its lack of assumptions regarding buoyancy levels and its ability (demonstrated here for the first time) to predict full shapes. Seeking generality, Roper used Cartesian coordinates. We briefly present the derivation in cylindrical coordinates since the present flames are axisymmetric. Roper [8] invokes several assumptions, including: axial diffusion may be neglected, temperature, velocity and mass diffusivity (T, v and D) may vary with height but are uniform at any given height, and combustion causes no change in number of molecules. Conservation of species then yields:

$$v_r(r,z)\frac{\partial C(r,z)}{\partial r} + v_z(z)\frac{\partial C}{\partial z} - \frac{D}{r}\frac{\partial}{\partial r}\left(r\frac{\partial C}{\partial r}\right) = 0 \tag{1}$$

where r, z, v_r and v_z are the radial and axial coordinates and velocities, D is mass diffusivity, $C = (f - f_a)/(f_0 - f_a)$, $f = n X_F - X_{O2}$, subscripts a and 0 indicate ambient and initial fuel conditions, X is mole fraction, and n moles of O_2 react stoichiometrically with one mole of fuel (F). The boundary conditions on Eq. 1 are $C(r,0)=1$ for $r<d/2$, where d is the burner diameter, $C(r,0)=0$ for $r>d/2$, and $C\rightarrow 0$ in the far field. The following transformation is now introduced to convert r and z to the new coordinates η and θ:

$$t(z) = \int_0^z \frac{dz}{v_z}; \quad \eta(r,z) = \frac{r}{r_D(z)}; \quad \frac{d\ln r_D}{dt} = \frac{v_r}{r}; \quad \theta(t) = D\int_0^t \frac{dt}{r_D^2} \tag{2}$$

Variables t and r_D are the elapsed residence time on the flame axis and the characteristic scale of diffusion. Eq. 1 becomes:

$$\frac{\partial C(\eta,\theta)}{\partial \theta} = \frac{1}{\eta}\frac{\partial}{\partial \eta}\left(\eta \frac{\partial C}{\partial \eta}\right) \tag{3}$$

subject to boundary conditions $C(\eta,0)=1$ for $\eta<1$ and $C\rightarrow 0$ in the far field. The solution to Eq. (3) is:

$$C(\eta,\theta) = \frac{e^{-\frac{\eta^2}{4\theta}}}{4\theta}\int_0^1 e^{-\frac{\eta_1}{4\theta}} I_0\left(\frac{\eta\sqrt{\eta_1}}{2\theta}\right) d\eta_1 \tag{4}$$

where I_0 is the modified Bessel function of first kind of order 0. This equation is called the P-function [13, 14]. Note that buoyancy, fuel flowrate, pressure and burner diameter do not appear in Eq. 4, thus permitting integration prior to specification of these quantities. We have solved Eq. 4 numerically using Romberg integration and Newton-Raphson root-finding, and contours for $C=0.095, 0.056$ and 0.040 (corresponding to CH_4, C_2H_6 and C_3H_8 stoichiometric locations) are shown in Fig. 1. Although these curves bear resemblance to laminar jet diffusion flame shapes, determination of true shapes requires converting η and θ to real-world coordinates using the relations [8]:

$$r_D = \frac{d}{2}\left(\frac{v_0 T_f}{v_z T_0}\right)^{1/2} = \left(\frac{\dot{m}T_f}{\pi\rho_0 v_z T_0}\right)^{1/2}; \quad \theta = \frac{4DT_0}{d^2 v_0 T_f}z \tag{5}$$

where T_f is the temperature at which diffusion is assumed to occur. This conversion requires knowledge of flame temperatures and axial velocity profiles. The above relations for r_D lend valuable insight into flame width behavior, as discussed below.

130

Results and Discussion

Figs. 2a and 2c show one buoyant and one nonbuoyant methane flame at otherwise identical conditions. The normal-gravity flame is a nonflickering flame shown in steady state; the microgravity flame, typical of those in this study, is nearly steady at the end of its 2.2-second duration. The color video from which these images was produced reveals a familiar appearance in the buoyant flame; it has a bright blue flame sheet, a dim blue interior and a small yellow tongue of soot just inside the flame tip. The nonbuoyant flame in Fig. 2c is longer, broader and dimmer than its buoyant counterpart. A faint blue flame sheet is barely visible on its periphery, but the flame is generally violet. This violet coloration is attributed to combined blue emissions from CH and CO_2 and dim orange emissions from low concentrations of soot at low temperatures.

Lengths of the present buoyant and nonbuoyant flames are normalized by burner diameter and plotted versus Re in Fig. 3. The buoyant and present nonbuoyant flames exhibit best-fit slopes of 1.06 and 0.86, respectively, but are fit here with unit-slope lines in accordance with theory [8, 10, 11, 13]. This unit slope reflects the observation that for both buoyant and nonbuoyant flames, $L \sim \dot{m}$ with a negligible dependence upon pressure and diameter. The nonbuoyant flames are generally longer than corresponding buoyant flames, but the two regimes converge at the large Re because nonbuoyant flame development time increases with Re and thus the present high-Re microgravity flames are smaller than their steady-state shapes.

The shown fit of present nonbuoyant flames is 64% higher than the normal-gravity fit, and the Roper model is useful in explaining this. Although the model predicts length to be independent of axial velocity for fixed $\dot{m}$ (leading Roper to question the model's ability to explain the observed difference in lengths) it also predicts that lengths scale with $T_f^{-0.67}$. Thus the considerably lower temperatures of nonbuoyant flames [6] reduce diffusion rates and are responsible for the increased lengths. The fits shown in Fig. 3 correspond to the Roper prediction using T_f values for the buoyant and nonbuoyant flames of 2690 K and 1370 K (in contrast to the 1500 K initially used in Ref. 9). Here we have invoked the relation $D \sim T_f^{1.67}/p$, where $D=20\ mm^2/s$ at 1 atm and 300 K [9]. Although these derived temperatures are a crude representation of actual flame temperatures, they are reasonable in light of the assumptions in the model.

Also shown in Fig. 3 are previous measurements [2, 4, 5] of microgravity methane flames. Reynolds numbers for these data have been corrected to the d length scale considered here. Note that these flames are at relatively high pressure and Re and thus contain significant amounts of soot; this, and the fact that only luminosity lengths were reported, explains why the unit-slope fit through these data lies 25% above the fit of present nonbuoyant lengths.

Widths of the present flames are shown in Fig. 4, including least-squares fits (with slopes of 0.52 and 0.22) of the present buoyant and nonbuoyant flames. The previous data shown [2, 5] agrees with present nonbuoyant observations because even in sooty flames, maximum luminous widths nearly coincide with maximum flame-sheet widths. Widths of both buoyant and nonbuoyant flames increase with Re, in contrast to past predictions of constant widths [10] and of widths that decrease with Re [3]. The fit of the buoyant flames yields $L/w \sim Re^{0.5}$, which is Blasius boundary-layer behavior. The slope of the nonbuoyant-flame fit is lower, possibly another indication of underdeveloped shapes at the highest Re. The relation in Fig. 4 of $w/d \sim Re^n$, where n is between 0 and 1, captures the increase in w with $\dot{m}$ and d that is observed for both buoyant and nonbuoyant flames. However, additional correlations are being sought because this relation fails to reflect the decrease of widths with pressure in buoyant flames that has been observed here and elsewhere [15].

The major phenomenological findings of present flame widths are: nonbuoyant flames are wider than their buoyant counterparts; widths increase with $\dot{m}$ and d; and buoyant flame widths decrease with pressure whereas nonbuoyant flame widths show no statistically significant variation with pressure. The analysis of Roper [8] is of assistance in interpreting many of these observations, referring to Eq. 5. Note that width is proportional to r_D and that these quantities are referred to interchangeably in this discussion. For changes in buoyancy, $r_D^2 \sim T_f/v_z$; the reduced velocities in microgravity flames more than compensate for the reduced temperatures to yield flames which are wider than in normal gravity. For pressure variations, $r_D^2 \sim v_0/v_z$, which explains observed width behavior; for buoyant flames this ratio increases as pressure decreases, and it is feasible that for nonbuoyant flames v_0/v_z is nearly independent of pressure. For changes in burner diameter, $r_D^2 \sim 1/v_z$; increasing burner size increases width via a decrease in v_z for both buoyant and nonbuoyant flames. An explanation for the increase of width with fuel flowrate is not as readily provided by Eq. 5. This issue, and quantitative explanation of the other width observations, may be possible following implementation of axial velocity profiles into the Roper model.

As mentioned earlier, we have used the Roper model to predict entire flame shapes, and predictions corresponding to the buoyant and nonbuoyant flames of Figs. 2a and 2c are shown in Fig. 2b. These contours were obtained using the same D as

131

before and T_f of 2690 K and 1370 K for the buoyant and nonbuoyant flames. These temperatures were obtained in the above discussion of Fig. 3 and ensured that the predicted buoyant and nonbuoyant heights would roughly agree with observations. For the normal-gravity prediction, it was assumed $v_z=v_0$ at all locations in the flame. This is a reasonable approximation of axial velocities in low-pressure flames that first decrease and later increase via buoyancy [16]. For the microgravity prediction, it was assumed that $v_z=v_0/8$ since this best matched the observed flame width. It is expected that $v_z<v_0$ in microgravity flames but no measurements are available to validate the ad hoc divisor of 8 adopted here. Unrestrained variation of T_f and v_z allows the Roper model to match any observed flame shape; although the choices made here are reasonable, an improved determination of values for these parameters is being sought.

Acknowledgments

References

1. Haggard, J. B. and Cochran, T. H., *Combust. Sci. Technol.* 5:291 (1972).
2. Cochran, T. H., "Experimental Investigation of Laminar Gas Jet Diffusion Flames in Zero Gravity," NASA TN D-6523, (1972).
3. Edelman, R. B. and Bahadori, M. Y., *Acta Astronautica* 13:681, (1986).
4. Bahadori, M. Y. and Stocker, D. P., "Oxygen-Concentration Effects on Microgravity Laminar Methane and Propane Diffusion Flames," Combustion Institute Eastern States Meeting, 1989.
5. Bahadori, M. Y., Edelman, R. B., Stocker, D. P. and Olson, S. L., *AIAA J.* 28:236 (1990).
6. Bahadori, M. Y., Stocker, D. P., Vaughan, D. F., Zhou, L. and Edelman, R. B., in *Modern Developments in Energy, Combustion and Spectroscopy*, (F. A. Williams et al., eds.), Pergamon Press, 1993, p. 49.
7. Burke, S. P. and Schumann, T. E. W., *Ind. Eng. Chem.* 20:998 (1928).
8. Roper, F. G., *Combust. Flame* 29:219 (1977).
9. Roper, F. G., Smith, C. and Cunningham, A. C., *Combust. Flame* 29:227 (1977).
10. Klajn, M. and Oppenheim, A. K., *Nineteenth Symposium (International) on Combustion*, The Combustion Institute, Pittsburgh, 1982, p. 223.
11. Markstein, G. H. and De Ris, J., *Twentieth Symposium (International) on Combustion*, The Combustion Institute, Pittsburgh, 1984, p. 1637.
12. Villermaux, E. and Durox, D., *Combust. Sci. Technol.* 84:279, (1992).
13. Li, S. C., Gordon, A. S. and Williams, F. A., *Combust. Sci. Technol.* 104:75 (1995).
14. Masters, J. I., *J. Chem. Phys.* 23:1865 (1955).
15. Yuan, T., Durox, D. and Villermaux, E., *Combust. Sci. Technol.* 92:69, (1993).
16. Sunderland, P. B. and Faeth, G. M., *Combust. Flame* 105:132 (1996).

TABLE 1

Summary of Test Flames

Buoyancy	p, bar	d, mm	Re	L, mm	w, mm	# Flames
	0.25	1.7	28-116	9-45	14-25	3
Nonbuoyant	0.49	0.85-1.7	28-123	11-53	10-23	5
	0.98	0.42-3.3	15-601	9-51	5-20	18
	0.25	1.7-5.5	8-233	6-60	7-15	11
Buoyant	0.49	0.85-5.5	5-152	3-27	4-12	19
	0.98	0.42-5.5	3-358	1-36	2-8	24
	1.97	0.42-5.5	2-472	1-30	1-5	19

Fig. 1. C contours from Eq. 4.

(a) buoyant   (b) model   (c) nonbuoyant
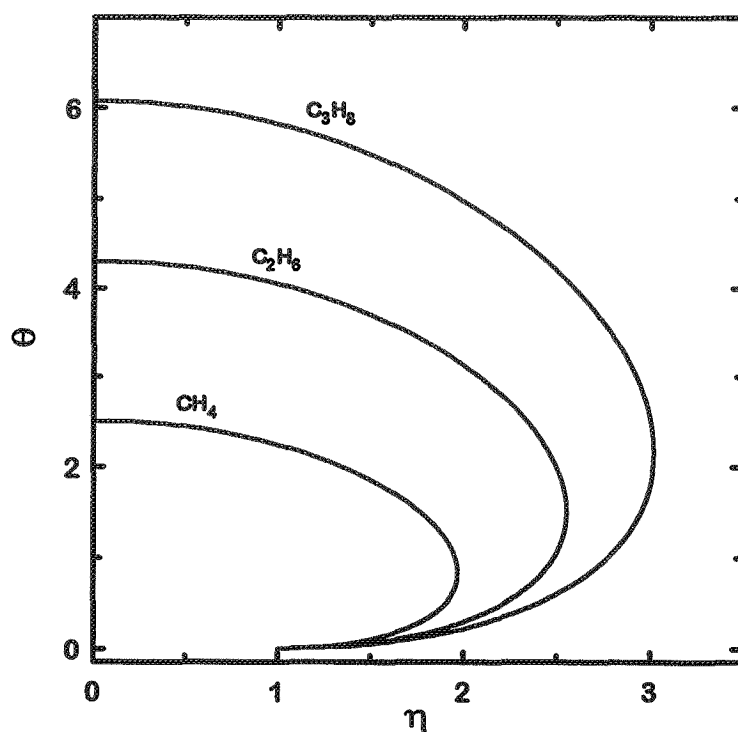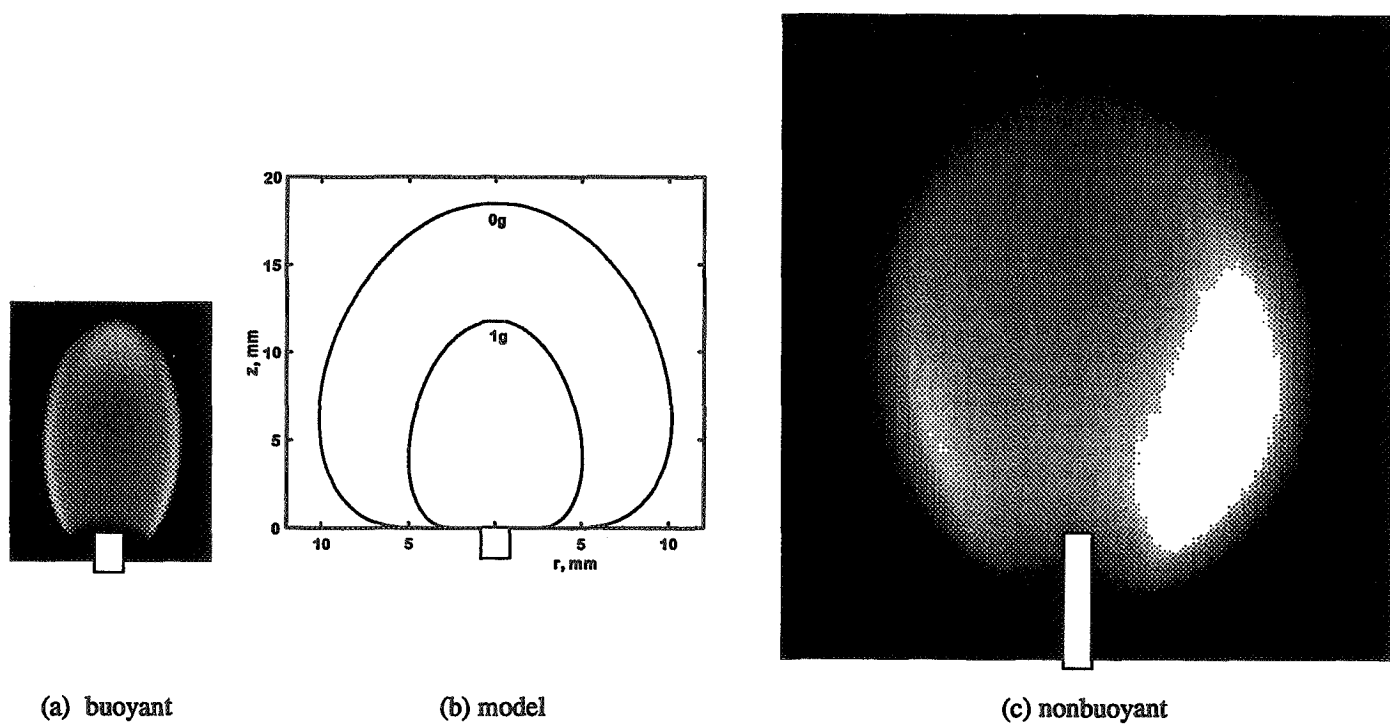
Fig. 2. Images of buoyant and nonbuoyant flames and model results. All images are at the same scale, with burner locations shown. Conditions are methane fuel, $\dot{m}$ =0.83 mg/s, d=1.7 mm, p=0.25 atm and Re=56.
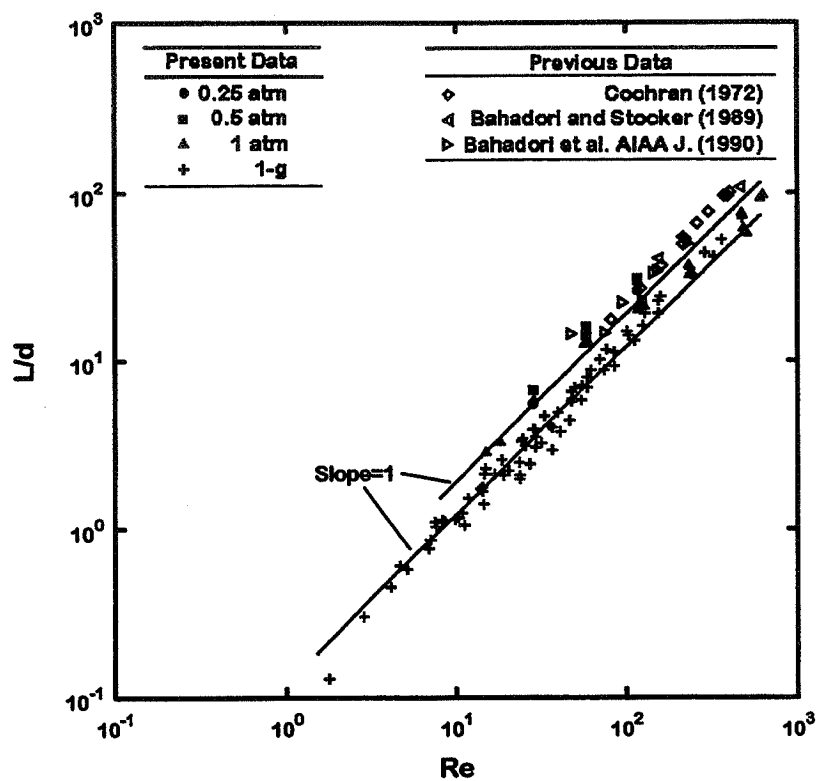
Fig. 3. Methane flame lengths.
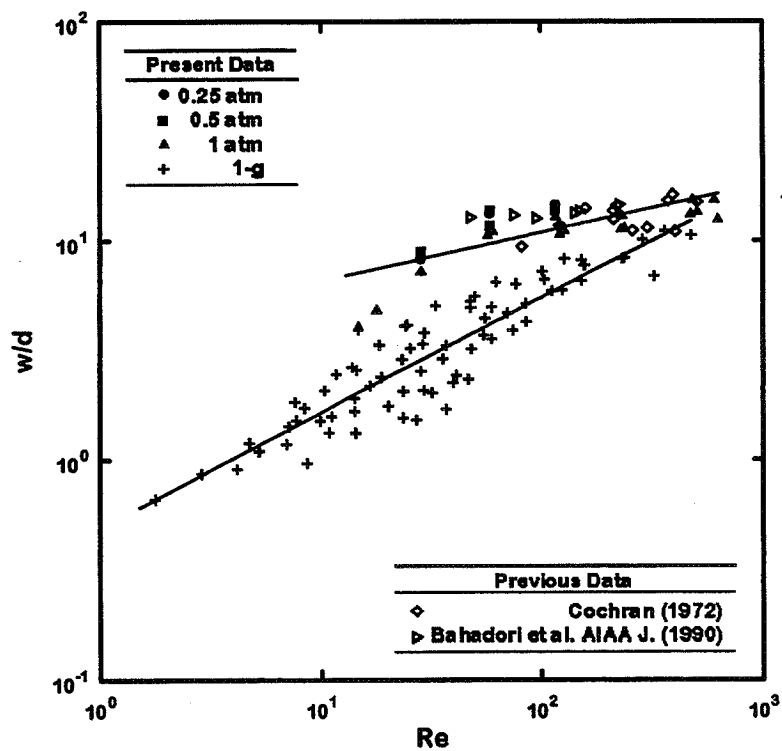
Fig. 4. Methane flame widths.

134

SPLITTING OF FORCED ELLIPTIC JETS AND FLAMES[*]

J. HERTZBERG, J. Carlton, M. Schwieterman, E. Davis, E. Bradley
Center for Combustion Research
University of Colorado
Boulder, Colorado, USA

and

M. Linne
Division of Engineering
Colorado School of Mines
Golden, Colorado, USA

Introduction

The objective of this work is to understand the fluid dynamics in the interaction of large scale, three-dimensional vortex structures and transitional diffusion flames in a microgravity environment. The vortex structures are used to provide a known perturbation of the type used in passive and active shear layer control techniques. 'Passive techniques' refers to manipulation of the system geometry to influence the three dimensional dynamics of vortex structures, and 'active' refers to any technique which adds energy (acoustic or kinetic) to the flow to influence the shear layer vortex dynamics. In this work the passive forcing is provided by an elliptic jet cross-section, and the active forcing is incorporated by perturbing the jet velocity using a loudspeaker in the plenum section.

The study of transitional diffusion flames in a microgravity environment is important for several applications: fire safety in spacecraft environments, possible practical applications of flames in low earth orbit, but most importantly for better understanding and control of all turbulent diffusion flames. Study of transitional flow allows clearer determination of the effect of shear layer controls at a Reynolds number where mechanisms of the transition to turbulence can be traced. The major drawback to this approach is that buoyancy effects dominate the flow field under these conditions. In fully turbulent flames, buoyancy plays a much smaller role. In order to examine the transitional flow in the absence of buoyancy effects, the flame must be studied in a microgravity environment.

Recent fundamental investigations of transitional, forced axisymmetric diffusion flames have led to increased understanding of the role of shear layer dynamics in the transition to turbulence of these flames. (refs. 1, 2) Experimental studies of the stabilization process of fully turbulent lifted jet flames (ref. 3) have illustrated the importance of large scale shear layer structures and their three-dimensional evolution in time. These results have important consequences for the control of efficiency and pollutant formation in turbulent jet flames via passive and active shear layer control techniques. However, while entrainment and mixing in isothermal jets are easily controlled by such forcing techniques, jet diffusion flames are more difficult to control for several reasons: both hydrogen and hydrocarbon flames form on the outer edges of the shear layer region (ref. 4), and the effects of heat release (with the exception of buoyancy) act to stabilize the flow. In fact, Hosangadi et. al. (ref. 5) state that the forcing of fuel jets offers little prospect for controlling a diffusion flame.

Nevertheless, high amplitude active forcing has been found to have a profound effect on a jet diffusion flame. Over a range of excitation frequencies the flame can be driven to split into a central jet and one or two side jets as shown in Figure 1. The split is accompanied by a partial detachment of the flame from the nozzle exit, a shortening of the flame by a factor of two, and a change from the common yellow color of soot radiation to a predominantly clear blue flame. Yellow flame tips were sometimes observed. Under some conditions, the flame bifurcated between a split state and a classic transitional diffusion flame, suggesting that a dynamical systems approach may be fruitful. Similar behavior has been observed in two separate combustor arrangements. Conditions for creating a split flame in a fully axisymmetric combustor are described in Hertzberg (ref. 6). The present paper describes experimental results from a rectangular plenum with an elliptic nozzle configuration, and includes results from normal, inverted and microgravity conditions. Laser sheet visualization of vertical and horizontal cross sections is used to examine the development of side jets in reacting and non-reacting flow.

Experimental Description

The combustor schematic is shown in Figure 2. The combustor plenum is made up of two chambers connected by a loudspeaker. For the results presented here, the 16.5 cm diameter loudspeaker is used to produce sinusoidal acoustic forcing at 540 Hz and 9.5 Vrms, a frequency and amplitude that correspond to the split jet behavior. The 2:1 aspect ratio elliptic cross sectioned (2.5 X 5.0 mm) methane jet issues from a flat plate; no co-flow is used. Thus the inlet boundary condition for the inverted and microgravity studies is well defined. The bulk velocity is 5.6 m/s for all results presented here. The Reynolds number based on the diameter of a circle of equivalent area (d = 3.54 mm) and bulk velocity is 1225. Microgravity tests were carried out in the NASA Lewis 2.2 second drop tower.

The flow visualization light source is provided by a frequency doubled (532 nm), pulsed Nd:YAG laser operating at 10 Hz. The laser power is approximately 20 mJ per pulse. A combination of cylindrical and spherical lenses is used to produce either a vertical or horizontal laser sheet. The green light scatters off micron sized canola oil droplets which have been seeded into the methane gas. Flow visualization images are recorded using a COHU model 6315 black and white CCD camera with a 50 mm lens. During the horizontal sheet measurements, the camera was positioned at a slight angle away from the axis of the jet to ensure that the flow did not impinge on the lens. Sequences of images are obtained by forcing the flow at 541 Hz. This results in a small phase difference between subsequent images, which are from different cycles. The video images are digitized and the contrast enhanced using OPTIMAS software.

Results

Since flow visualization shows that the split flame phenomenon is due to a split fuel jet, the nonreacting methane jet was studied under the same conditions that caused splitting of the flame. Vertical cross sections of the split non-reacting jet in normal gravity were taken in the major and minor axis planes. Figure 3a shows the single primary toroidal vortex ring, or 'roller', that is formed with each forcing cycle. The vortex cores are seen at 0.8 D downstream. In this plane a side jet is seen splitting off to the left at 0.9 D downstream, illustrating the tremendous jet spreading that this instability causes. The minor axis is seen in Figure 3b. A single side jet can be observed exiting towards the left of the primary jet core at approximately 5.4 D downstream of the nozzle exit, however the horizontal cross sections discussed below show multiple side jets which are not visible in any single vertical cut. Coherent toroidal structures remain in the primary jet downstream of this location, however they have been severely distorted, and the right side is more coherent than the left. The plane of the ring inclines to the right. While this may suggest development of a helical instability, no evidence of a coherent helical structure is seen in the horizontal images, presented below. This figure also indicates that the elliptic jet geometry was successful at stabilizing the azimuthal position of the side jet. Recent experiments with an annular flow of air around the nozzle have shown that a co-flow velocity of 3 to 4% of the jet velocity can also stabilize the position of the side jets, while a co-flow of more than 5% suppresses the formation of side jets.

Further information on the topography of the non-reacting jet was sought with horizontal cross sections of the non-reacting jet. The images are oriented with the minor axis pointing left to right. Phase angle is defined in each image plane relative to when the center of the roller passes through the plane. Figure 4a shows the jet at 0.9 D downstream of the nozzle exit when the phase angle $\phi = 36$ degrees. The center of the primary toroidal structure has just passed through the plane defined by the light sheet. Self induction has distorted the roller so that the portions along the minor axis are the last to pass through the image plane. Note that the formation of side jets along the major axis has begun less than one diameter downstream of the nozzle exit. There is evidence of pairs of streamwise vortex structures outside of the roller , with the structures at the top end of the major axis slightly more developed than those at the lower end. Figure 4b is at $\phi = 216$ degrees, when the 'braid' region, the region between the rollers, is passing through the image plane. There is very little jet fluid left in the core of the jet, with significant fluid concentrated in the side jet at the top of the major axis, or in the streamwise structures at the bottom. This is supported by the vertical images in Figure 3.

Figures 5a-d show one cycle of the active forcing at 1.8 D downstream. Two side jets, oriented along the major axis, have formed, ejecting fluid a significant distance from the central jet. Figure 5a, at $\phi = 0$ degrees, shows that the primary vortex structure has switched axes, and the major axis is now perpendicular to the orientation of the nozzle's major axis. Pairs of streamwise vortex structures are clearly seen in the side jets adjacent to the roller, and these structures are visible at approximately the same location in images b-d, taken at subsequent phase angles. Additional structure is seen in the side jets further from the roller, suggesting that fluid there was ejected in streamwise structures in previous cycles. In Figure 5c, taken in

the braid region, no jet fluid remains on the centerline, and the streamwise structures are indistinct. They reappear in Figure 5d, taken just before the roller enters the image plane.

Explanations for the formation of side jets (refs. 7, 8) focus on an interaction between rollers and streamwise braid structures. However, this picture of vortex structure does not differ significantly from accepted descriptions of shear layers which do not exhibit the perpendicular ejection of fluid. We propose that side jets are the result of a reconnection event involving pairs of streamwise braid structures. Such an event would create elongated vortex loops, which can then convect fluid away from the central jet by the self induction mechanism. This hypothesis is supported by the evidence of streamwise vortex structures in the side jets, and by certain features observed in the vertical cut images. An additional vortex structure of the same sign as the roller is consistently observed near the top of the roller, just prior to formation of the side jet, as seen in Figure 3b.

The reacting jet (flame) was then examined to determine the effects of heat release on the side jet formation. Vertical cross sections of the flame in the minor axis plane were taken and two samples are shown in Figure 6. The rapeseed droplets evaporate and are consumed in the high temperature region of the flame. The flame front is highlighted with a dotted line in the figure. The figure shows that the flame associated with the left side jet is attached at the nozzle while the primary jet core moves off to the right where the flame forms at approximately 6 D from the nozzle exit.

There are several differences in structure between the reacting and non-reacting jet. The flame sheet generally shows a central jet and a single side jet, as opposed to the symmetric side jets seen in the nonreacting jet, although other configurations are observed depending on details of the forcing (ref. 6). The split would often form in the minor axis plane, suggesting that heat release may be suppressing the formation of side jets further upstream in the major axis plane. However, horizontal cuts are required to confirm this. The flame is capable of suppressing the formation of side jets entirely, as evidenced by the narrow range of conditions for split flame formation compared to the broad range of conditions for nonreacting split jets. Note the structure at the top of the first primary ring in Figure 6a. This structure is similar to one observed in the non-reacting jets as well, and appears consistently at this phase.

Nonreacting and reacting jets were also observed in inverted and microgravity conditions. Neither the reacting nor nonreacting jets were observed to split or form side jets in inverted gravity, as shown in Figure 7. This suggests that negative buoyancy acts to suppress the instability responsible for the side jets. The responsible instability has been described as an 'absolute' type (ref. 7), as opposed to a convective instability. As such the instability will be governed by the density profile, with jets of densities less than 70% of the surroundings exhibiting self-excitation. The nonreacting methane jet meets this criterion, as does the flame. However, this instability theory neglects buoyancy, based on the assumption of a small Richardson number, so it is interesting to note that the orientation of the jet has a strong effect. The apparent wavelength of the primary roller structure is shorter in the nonreacting jet, seen in Figure 7a. Close examination reveals that fluid from the outer, slower moving portions of the jet are most affected by buoyancy, resulting in the apparent shortening of the wavelength. In the reacting jet, Figure 7b, the outer, slower moving jet fluid is consumed in the flame, and the apparent wavelength is now longer than the normal gravity case. This may be due to the effect of high temperature fluid surrounding the fuel jet and stabilizing the shear layer. In microgravity , however, the flame has been observed to split, as shown in Figure 8. This suggests that an additional perturbation to the shear layer in inverted gravity, caused by the recirculation of jet fluid back to the nozzle exit, may be responsible for the suppression of the absolute instability.

Conclusions

Laser sheet visualization of an axially forced jet diffusion flame and the corresponding non-reacting jet has been performed. Visualization in inverted gravity has also been performed, and a split flame in microgravity has been observed. The flame splits under a narrower range of conditions than the non-reacting flow, indicating that the flame can suppress the instability responsible for the side jets. Based on the flow visualization results, a new mechanism for the formation of side jets has been proposed which involves a reconnection of streamwise braid structures to form vortex loops which convect away from the central jet. The flame can be induced to split in microgravity, but not in inverted gravity. Overall the results suggest that a measure of global control of jet diffusion flames using high level active forcing is possible.

Immediate future work includes Particle Imaging Velocimetry (PIV) to quantify the velocity and vorticity fields in the jet under normal gravity and inverted experiments. Particle tracking will be used at the 2.2 second drop tower to quantify the velocity and vorticity fields under microgravity. However, since the flame did not reach steady state in 2.2 seconds, tests under extended microgravity will be proposed. In addition, a dynamical systems analysis is underway to determine if splitting is a chaotic phenomenon. An analysis of the split flame's combustion products is also planned.

References

1 Mahalingam, S., Cantwell, B.J., Freezer, J.H., 'Full numerical simulation of coflowing, axisymmetric jet diffusion flames', *Physics of Fluids* A 2(5) 1990, pp. 720-728.

2 Katta, V.R., and Roquemore, W.M., 'Role of inner and outer structures in transitional jet diffusion flame,' *Combustion and Flame* 92,1993, pp.274-282.

3 Schemer, R. W., Namibian, M., Filtopoulos, E.E.J., Kelly, J., 'Temporal evolution of turbulence/chemistry interactions in lifted turbulent jet flames,' *25th Symp. (Int'l) on Combustion,* In press, Combustion Institute, 1994.

4 Clemens, N.T., and Paul, P.H., Effects of heat release on the near field flow structure of hydrogen jet diffusion flames, *Combustion and Flame* 102: 271-284 (1995).

5 Hosangadi, A., Merkle, C.L., and Turns, S.R., Analysis of forced combustion jets, *AIAA Journal*, 28(8):1473-1480 (1990).

6 Hertzberg, J., Conditions for a Split Diffusion Flame, *Combustion and Flame*, in press.

7 Monkewitz, P.A., and Pfizenmaier, E., Mixing by "side jets" in strongly forced and self-excited jets, *Physics of Fluids* A, 3(5):1356-1361 (1991).

8 Brancher, P., Chomaz, J.M., and Huerre, P., Direct numerical simulations of round jets: Vortex induction and side jets, *Physics of Fluids*, 6 (5): 1768-1774 (1994)
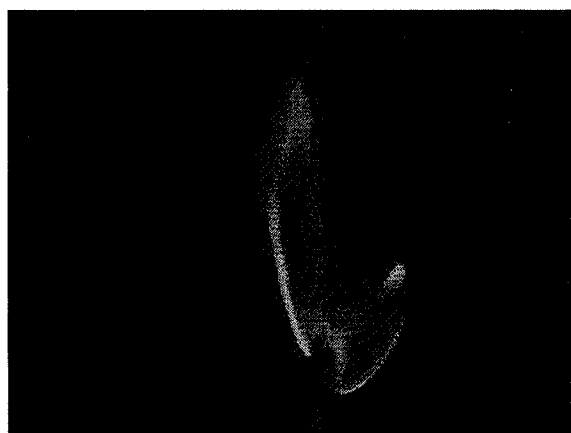
FIGURE 1: SPLIT FLAME
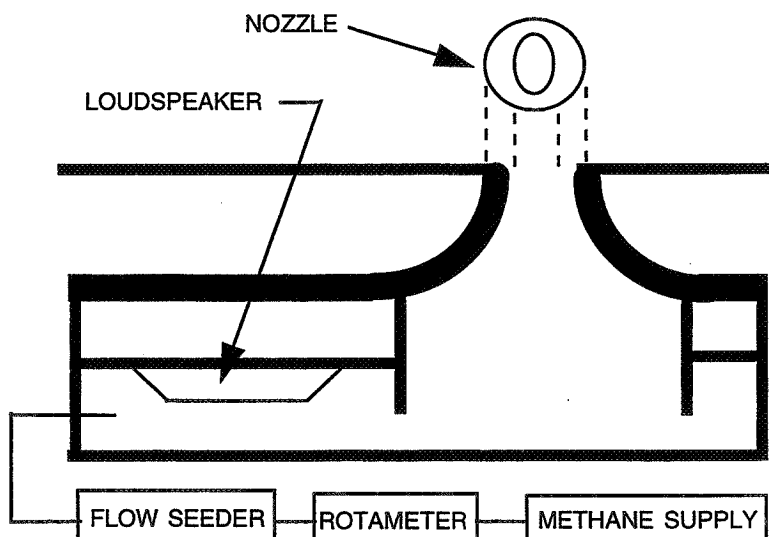
FIGURE 2: EXPERIMENTAL SCHEMATIC
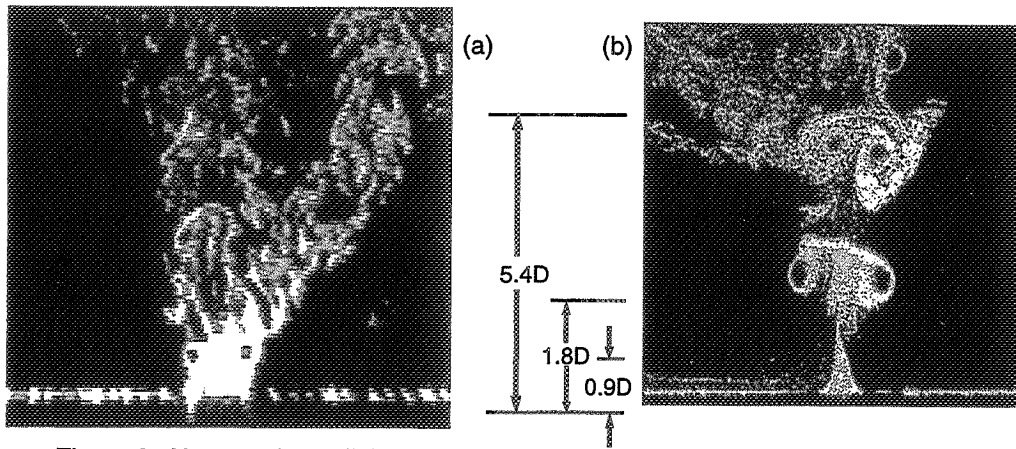
Figure 3: Nonreacting split jet in normal gravity. Major axis (a) and minor axis (b).
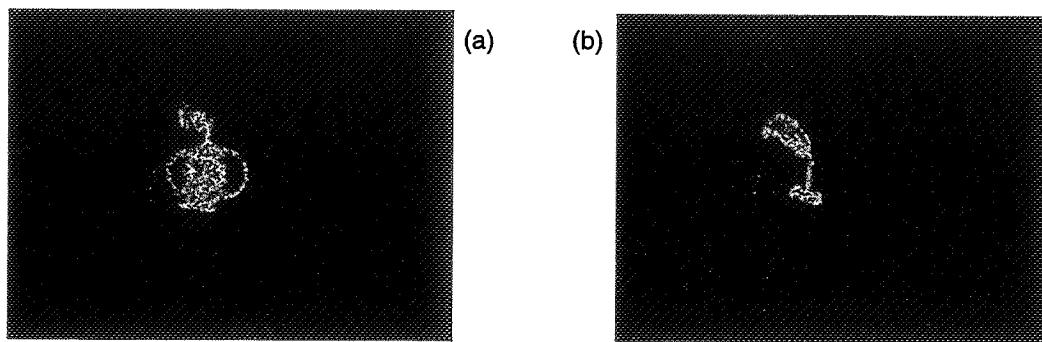
Figure 4: Horizontal cut of nonreacting, normal gravity, split jet at 0.9D downstream. Phase difference of 180 degrees between (a) and (b).

a) $\phi = 0$

b) $\phi = 36$

c) $\phi = 108$

d) $\phi = 216$
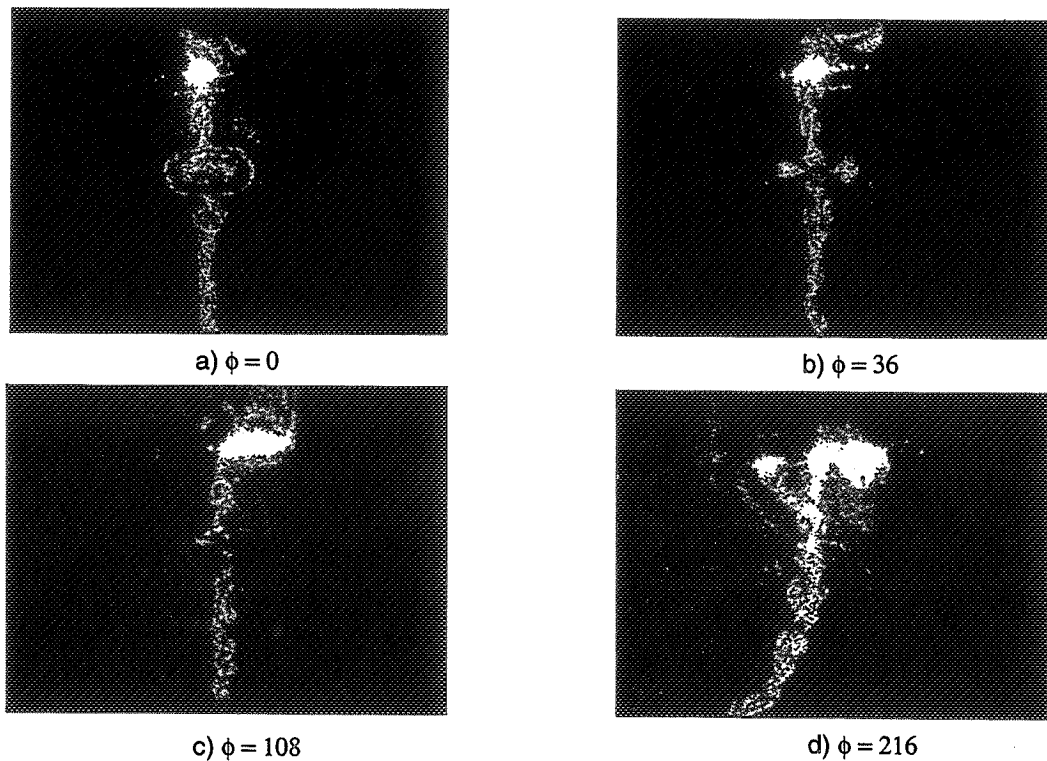
Figure 5: Horizontal cut of nonreacting, normal gravity, split jet at 1.8D downstream.
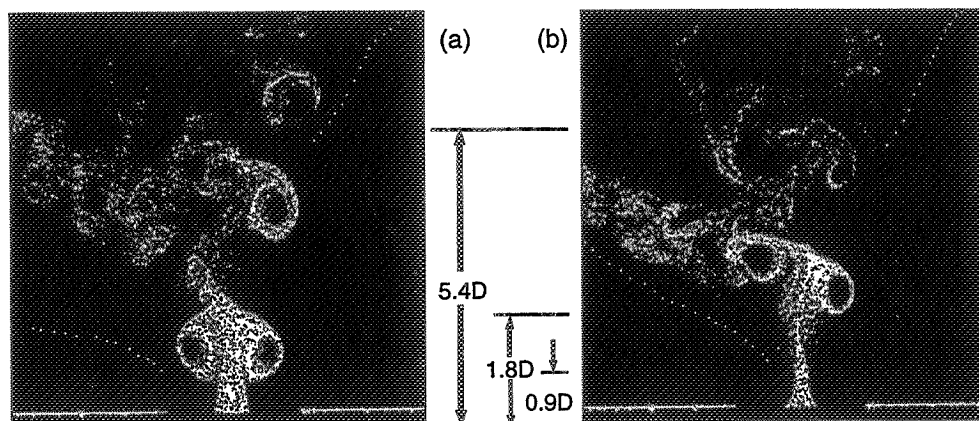
Figure 6: Reacting split jet , minor axis view, in normal gravity. Phase difference of 180 degrees between (a) and (b).
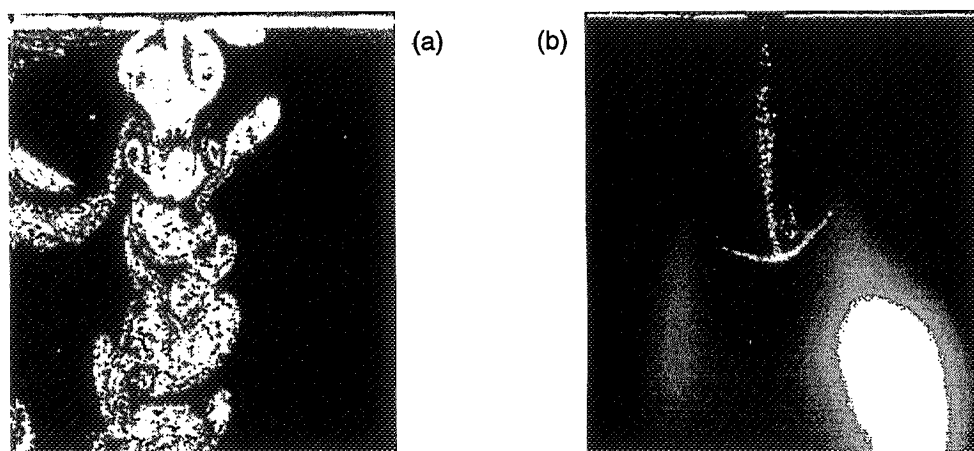
Figure 7: Inverted jet along minor axis. Nonreacting jet (a) and reacting jet (b).
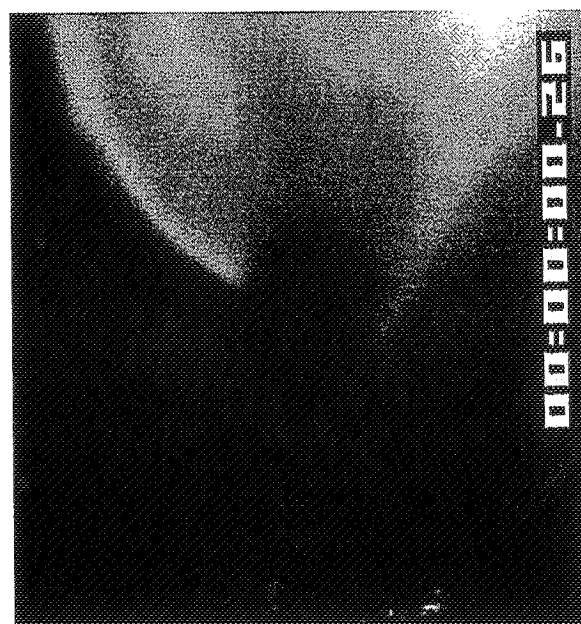
Figure 8: Reacting split jet, minor axis view, in microgravity

140

APPLICATION OF SHEAR PLATE INTERFEROMETRY TO JET DIFFUSION FLAME TEMPERATURE MEASUREMENTS[‡]

Brad A. VanDerWege, Chris J. O'Brien, and SIMONE HOCHGREB
Massachusetts Institute of Technology
Cambridge, Massachusetts

Introduction

The recent ban on the production of bromotrifluoromethane (CF_3Br) because of its high stratospheric ozone depletion potential has led to interest in finding alternative agents for fire extinguishing applications. Some of the promising alternatives are fluorinated hydrocarbons (ref. 1). A clear understanding of the effects of CF_3Br and alternative chemical suppressants on diffusion flames is therefore necessary in the selection of alternative suppressants for use in normal and microgravity.

The flame inhibition effects of halogen compounds have been studied extensively in premixed systems (ref. 2). The effect of addition of halocarbons (carbon-halogen compounds) to diffusion flames has been studied experimentally in coflow configurations (refs. 3,4) and in counterflow gaseous and liquid-pool flames (refs. 5,6). Halogenated compounds are believed to inhibit combustion by scavenging hydrogen radicals to form the relatively unreactive compound HF, or through a catalytic recombination cycle involving HBr to form H_2 (ref. 7). Comparisons between halogens show that bromine inhibition is significantly more effective than chlorine or fluorine (refs. 6,8). Although fluorinated compounds are only slightly more effective inhibitors on a mass basis than nitrogen (ref. 6), they are more effective on a volume basis and are easily stored in liquid form.

The objectives of this study are (a) to determine the stability limits of laminar jet diffusion flames with respect to inhibitor concentration in both normal and microgravity, and (b) to investigate the structure of halocarbon-inhibited flames. In the initial phase of this project, visual diagnostics were used to observe the structure and behavior of normal and microgravity flames. The initial observations showed significant changes in the structure of the flames with the addition of halocarbons to the surrounding environment, as discussed below. Furthermore, the study established that the flames are more stable relative to the addition of halocarbons in microgravity than in normal gravity. Visual diagnostics of flames are, however, necessarily limited to detection of radiative emission in the visible range, and offer only qualitative information about the nature of the processes in the flame. In particular, the study sought to understand the structure of the inhibitor-perturbed flames with regard to temperature and species concentration in the outer region of the flame. Whereas thermocouple measurements can be used in ground based studies, their implementation in drop-tower rigs is limited. A possible approach to determine the temperature field around the flame is to use interferometric techniques. The implementation and testing of a shear-plate interferometry technique is described below.

Visual Observations

Figure 1 shows the effect of inhibitor addition to the environment surrounding the jet diffusion flame in microgravity. Figure 1(a) shows the baseline uninhibited flame. The addition of 6% CF_3H to the oxidizer produces a flame with no visible soot luminosity and apparently no reaction at the tip (Fig. 1(b)). The flame with 1% CF_3Br is very sooty, with an open tip, and a reddish outer reaction zone (Fig. 1(c)). The inhibited flame in Figure 1(d) is shown during transition to extinction. Competing effect of dilution, reaction and entrainment make direct interpretation of results difficult. In each of these cases, knowledge of the gas temperature in the various regions of interest would be a vital first step to understanding the behavior of these flames.

Temperature Measurement

Diagnostics used in the NASA-Lewis 2.2-second drop tower the drop tower modules are subject to limitations in the acceptable volume, weight, power, tolerance to mechanical shock, and the short time available. In this particular case, one would like to obtain temperature information over the whole axisymmetric field, within the short time window during and after flame development. Clearly, an optical diagnostic would be recommended. For the drop tower, the entire apparatus must fit in an approximately 40 cm x 90 cm x 100 cm frame and weigh less than 140 kg. In addition, the apparatus must be powered by onboard batteries, which limits the use of high-powered lasers. The optics of the system must also be very stable, since there is

141

some vibration introduced by the release of the package, and the entire system experiences 20-50 g of deceleration. The diagnostic being considered here is a shear plate interferometer. Interferometric systems only require a low-power laser, and the two interfering beams are produced from reflections off the two faces of a glass plate, the optics are very stable. Such a diagnostic has been used by Liu and Ronney for drop tower experiments relating to radiation-driven hydrodynamic flow (ref. 9).

Interferometric Diagnostic

Figure 2 shows a schematic of the shear plate interferometer. The beam from a 2-mW helium-neon laser (Melles Griot 05-LHR-121) driven by a 12-volt power supply (Melles Griot 05-LPM-830-065) is expanded and directed through the flame chamber. The beam passes through the low-density gas of the flame and then obliquely through an uncoated glass plate. The reflections off the front and back surfaces of the plate interfere on a diffuser to form a fringe pattern. A black and white CCD (Panasonic WV-BP312) video camera records an image of the fringe pattern while a color CCD camera (Panasonic WV-CL352) records a visual image of the flame, both of which are stored in SVHS video systems. Since the path length difference between the two interfering beams is determined by the thickness of the glass plate, the interference pattern is very stable. The components of this system are also readily available and relatively inexpensive.

Index of Refraction Temperature Measurement

The shear plate interferometer described above belongs to the group of optical temperature diagnostics that measure the index of refraction of the gas to determine its temperature. The differential refraction index (δ) is nearly proportional to gas density, so that for ideal gases at a given pressure, the temperature is inversely proportional to δ (ref. 10).

$$\delta = (n-1) \propto \frac{1}{T} \qquad\qquad \delta = \delta_o \frac{T_o}{T} \qquad\qquad (1)$$

The method by which this decrease in index of refraction is captured in a fringe pattern is shown schematically in Figure 3. The laser beam passes through the gases, and is reflected at the front and back surfaces of the uncoated glass plate. A background interference spatial frequency is created by using a slightly diverging laser beam: the pathlength difference between the reflected beams increases with the angle of incidence β, creating a phase lag. This effect is shown in Figure 3 as the slope applied to the back surface reflection. The beam divergence and corresponding background frequency can be easily adjusted by moving the collimating lens (shown in Fig. 2). Since the phase of the fringe pattern at a given point is determined by the difference of the phases of the two reflections at that point, the spatial separation of the reflections is vital for producing a strong signal in the fringe pattern. The amount of spatial separation achieved is determined by the thickness of the glass plate and the angle of incidence of the beam. In general, a larger spatial separation leads to a stronger signal, but the increase is limited by the resultant decrease in the available field of view.

As the beam travels through higher temperature gases, light travels faster (lower δ), with a resultant phase lead relative to a colder region. The change in δ at a particular spatial location is therefore related to the change in phase lead (or fringe spacing) in the interference pattern. The deconvolution of the fringe pattern in a two dimensional field of uniform composition into temperature is relatively straightforward. In the present case, several characteristics complicate the analysis: (a) The axisymmetry of the field makes it necessary to use an inverse Abel transform to obtain δ at a given location, and a high sensitivity to noise close to the centerline. (b) The deconvolution of δ into temperature is complicated by the fact that the mixture composition must be estimated. Fortunately, the products of hydrocarbon combustion have an index of refraction similar to air (3.5% higher in the case of methane combustion products). For the gas composition measured in the luminous zone of a methane flame, δ is 2% higher than in air (ref. 11). For methane fuel, however, δ is 1.5 times that of air, so the change in composition would be responsible for a large fraction of the phase change within the flame zone. (c) The decreasing sensitivity of the temperature to the phase difference at higher temperature, which makes it difficult to accurately resolve temperatures around the maximum temperature.

Fringe Pattern Analysis

Individual frames of the video recorded during the experiment were digitized for analysis. A reference frame is also digitized as background signal for each experiment at a time when the flame is not present. Each horizontal line (in the direction of the spatial separation) is analyzed separately. Analysis of a fringe pattern begins with the fast Fourier-transform (FFT) based method described by Takeda et. al. (ref. 12). The algorithm for processing the images is described below. The first four steps are performed on the signal and the background in parallel.

1. An FFT of the fringe pattern is performed, which produces a spatial frequency distribution symmetric about zero, with a large peak at a low frequency and side peaks corresponding to the carrier frequency. The desired information is contained in the distribution in the side peaks around the carrier frequency.
2. One of the side peaks is isolated and shifted to remove the carrier frequency. Accurate estimation of the carrier frequency is not necessary, as long as both the signal and background are shifted by the same amount, since the subtraction of the background will result in the same net phase profile.
3. An inverse FFT of the shifted frequency distribution is taken.
4. The phase angle is obtained from the complex angle of the inverse FFT from step 3. The analysis in these first four steps will fail if the slope of the fringe pattern phase profile goes through zero, because the present analysis cannot differentiate between positive and negative frequencies and therefore assumes that all fringe frequencies correspond to positive phase slopes. This can typically be accommodated by using a higher background fringe spatial frequency.
5. The background phase profile is subtracted from the signal to obtain the differential phase profile as a function of distance.
6. The differential phase profile obtained in step 5 consists of the difference in phase between the two spatially offset reflections of the phase lead profile produced by the flame. Deconvolution of this differential phase profile requires making an assumption about the behavior of the phase lead profile at one of the edges as a starting point. This is easily accomplished by selecting a region at the edge of the frame with zero gradient. When this is not possible, an estimation of the slope of the phase profile at the edge must be made, the accuracy of which will affect the entire profile. The following equation describes the deconvolution of the differential phase profile as a function of position $\gamma(x)$.

$$\gamma(x) = \phi(x) - \phi(x+L) \qquad \text{therefore,} \qquad \phi(x) = \gamma(x) + \phi(x+L) \qquad (2)$$

   where L is the spatial separation of the images (obtained by the spacing of the reflection of the jet tube image).
7. The phase profile obtained in step 6 is the phase lead integrated through a chord of the axisymmetric flame. In order to obtain the phase lead as a function of radius, an Abel transform is taken of the integrated phase profile. The resulting value is the relative phase lead over a distance corresponding to the separation between data points. The Abel transform requires knowledge of the centerline of the symmetry and that the data points are equally spaced. The centerline can be obtained from the shadow of the nozzle or a shadow on a reference frame.
8. The final step is to convert the phase lead value at each point to temperature. The phase lead corresponds to a spatial lead proportional to the laser wavelength, which corresponds to the difference in the speed of light, and therefore in index of refraction. Once the phase profile has been shifted to have a value of zero at the location of the reference temperature, the following equation gives the combined relationship between phase lead ϕ, and the local temperature:

$$\frac{T}{T_o} = \delta_o \left(\frac{\delta_{ro}}{\delta_o} \right) \frac{(1+\alpha\phi)}{n_o - (1+\alpha\phi)} \qquad ,\text{where} \qquad \alpha = \frac{\lambda}{2\pi\ell} \qquad (3)$$

In this equation, δ_o is the differential refraction index for the reference temperature T_o, the ratio (δ_{ro}/δ_o) is the correction factor for variation in gas composition in which δ_{ro} is the differential refraction index for the local gas composition at the reference temperature, n_o is the index of refraction corresponding to a phase (ϕ) of zero, λ is the wavelength of the laser light, and ℓ is the spatial separation of the pixels.

The digitized images of the fringe patterns were typically quite noisy, so three different filtering methods were used. First, since gradients were fairly small along the axis of the flame, up to fifteen adjacent rows of the image were averaged before a single row was chosen for analysis. Second, while the center peak and second side peak are being removed in step 2, high frequencies can also be eliminated to reduce noise, with care not to remove frequencies too close to the signal. Third, since the Abel transform tends to amplify noise, filtering immediately before this step is particularly effective. Filtering before step 7 is also effective, since the signal is relatively smooth, allowing for more aggressive filtering for noise. Since the integrated phase profile should have zero slope at the centerline (due to symmetry) and decay to zero at increasing radius (assuming the reference value is taken at infinity), fitting the phase profile to a four or six-parameter Gaussian-type curve, ($y = a \ exp(bx^2) + c \ exp(dx^4)$) was found to be quite effective. Row averaging and pre-Abel fitting were found to be quite effective, but filtering while removing the low frequency and mirror peaks was found to be best used for removing high-frequency noise only.

<u>Verification and Sensitivity</u>

Verification of this method was performed in two steps. In the first step, the local index of refraction was measured across a vertical laminar jet of helium, whose index of refraction at room temperature is similar to that of air heated to flame temperatures. The expected values of the reference δ of air and helium are of course unambiguous, deviations resulting from mixing or measurement error. The measured concentration of helium (as obtained by weighting the index of refraction) as a

function of radius is shown in Fig. 4 for three different heights above the tube exit. The results are as expected, except near the centerline, where the measured concentration decreases. Misbehavior near the centerline such as this is attributed to the high sensitivity of the Abel transform near the centerline. Planar systems using this diagnostic would not suffer from this problem.

In the second verification step, temperatures measured in the product gas region of a methane Bunsen flame measured by the shear plate interferometer were compared to thermocouple measurements. The latter were made with two uncoated Pt/Pt-13%Rh (type R) thermocouples of 0.025 and 0.127 mm wire diameters. The gas temperature was estimated by fitting a convection correlation for a cylinder to the two thermocouple readings in order to correct for radiation losses. The temperature profile from the interferometer is compared to the thermocouple reading in Fig. 5, using ambient temperature as the reference value. The interferometer measurement matches the thermocouple measurements well for temperatures below 1000 K, but does a poor job above that. This is largely a result of the high sensitivity of the estimated temperature to noise in the measured phase when measuring high temperatures using a low temperature reference, as shown below.

The relative sensitivity of the calculated temperature $(\partial \ln T)/(\partial \ln \xi)$ has been determined for various parameters ξ such as local phase ϕ, local δ, the reference index of refraction n_o, laser wavelength λ, and length scale ℓ (spatial resolution of pixels). The sensitivities can be easily obtained by differentiating Eq. (3). The sensitivity of temperature to the measured phase ϕ, δ_o, and the length scale ℓ can be simplified to linear relationships with respect to temperature (in the case of $\alpha \ll 1$ and $n \sim 1$):

$$\frac{\partial T/T}{\partial \phi/\phi} \approx -\frac{\partial T/T}{\partial \ell/\ell} \approx \left(\frac{1}{T_o}\right)T - 1 \qquad\qquad \frac{\partial T/T}{\partial \delta_o/\delta_o} \approx -\left(\frac{1}{T_o}\right)T \qquad (4)$$

The relative sensitivity of the temperature measurement to ϕ and ℓ is small around the reference temperature (T_o). Since the slope in these relationships varies with the inverse of the reference temperature (T_o), the use of a higher reference temperatures decreases the sensitivity. Therefore, in order to achieve low sensitivity to uncertainties in the phase measurement, while keeping a reasonable measurement sensitivity, the reference temperature should be kept near the temperatures of interest. For example, Fig. 6 shows the sensitivity of a 2000 K temperature measurement as a function of the reference temperature. The sensitivity of temperature to the local value of the reference differential refraction index (δ_o) is one, which implies that there is a unity sensitivity of temperature to the estimations of the local species concentrations. The sensitivity of temperature is nearly independent of laser wavelength and pixel resolution. This analysis suggests that the most significant factor determining the accuracy of this diagnostic is the temperature (and therefore density) of the reference point relative to the temperatures measured. In the present case, if an ambient temperature reference is taken, the diagnostic is limited in accuracy to temperatures of about 1000 K before the sensitivity due to the combined effects of the Abel transform and phase noise becomes too large to interpret.

Microgravity Results

The interferometer was set up on a drop rig to measure temperature profiles of microgravity flames. Since no *a priori* experience existed with the diagnostic and type of flame, difficulties arose in obtaining a field of view wide enough to span the large zone of hot gases around the flame. Consequently, many of the images did not have a region of zero slope at the outer edge, making it nearly impossible to deconvolute the differential phase profile accurately. The data that could be deconvoluted often suffered from only having a reference point at low temperature. Figure 7 shows temperature profiles of a microgravity methane jet diffusion flame at three heights above the jet exit (1.5, 12.4, 23.3 mm). These profiles were produced by assuming (a) that the phase gradient at the edge of the image continued indefinitely, (b) that the peak temperature is close to adiabatic, and (c) that the gas composition is air. Although the radius of the flame is somewhat overestimated by these results (visual data indicates about 4.5 mm), the overall behavior is as expected. Since the flame is about 16 mm tall, the mid-height temperature profile should be the widest. Clearly, the ambiguity in the results must now be resolved by widening the field of view to obtain a zero-slope reference, as well as obtaining a reference temperature measurement near the peak at a given location.

Summary

The shear plate interferometry technique has been implemented and tested for applications in axisymmetric diffusion flames. The appropriate algorithms have been developed for deconvoluting the data to temperature. The following conclusions can be drawn regarding the applicability of the technique:

- The shear plate interferometer is resistant to vibration and shock and can be constructed with readily-available, relatively inexpensive components.
- The spatial frequency of the background fringes and therefore the sensitivity to the phase lead produced by the flame can be easily changed by modifying the divergence of the beam.

- The magnitude of the signal can be increased by increasing the spatial separation of the two reflections, which can be accomplished by increasing the thickness of the glass plate or the angle of incidence of the beam on it.
- Analysis of the signal requires that the slope of the integrated phase profile be known at some point in the field of view, a zero slope at one of the endpoints being the most straightforward. Knowledge of the pixel spacing, spatial separation of the two images, the laser wavelength, and position of the centerline for axisymmetric systems is also necessary.
- The index of refraction of air is similar to that of combustion products but very different to that of methane. Therefore, temperature measurements are not very sensitive to the local species concentration in the burned gas zone, but measurements inside the diffusion flame would be difficult to interpret.
- The final temperature measurement is critically dependent on the reference temperature; best measurements are obtained close to the reference temperature

References

1. Pitts, W. M., Nyden, M. R., Gann, R. G., Mallard, W. G. and Tsang, W. National Institute of Standards and Technology, Gaithersburg MD, 1990, NIST SP 1279.
2. Linteris, G.T. and Truett, L.F. *Combust. Flame*, 105:15-27 (1996).
3. Simmons, R.F. and Wolfhard, H.G,*Trans. Far. Soc.* 52, pp. 53-59 (1956).
4. Creitz, E.C. *J. Res. Nat. Bur. Stand.—A. Physics and Chemistry*, 65A, No. 4, pp. 389-396 (1961).
5. Seshadri, K. and Williams, F.A., ACS Symposium 16, Am. Chem. Soc., Washington D.C., 1975, pp. 149-179.
6. Hamins, A., Trees, D., Seshadri, K., and Chelliah, H.K, *Combust. Flame* 99:221-230 (1994).
7. Day, M.J., Stamp, D.V., Thompson, K., and Dixon-Lewis, G. *Thirteenth Symposium (Int'l) on Combustion.* The Combustion Institute, Pittsburgh, pp. 705 (1971).
8. DaCruz, F. N., Vandooren, J. and vanTiggelen, P., *Bull. Soc. Chim. Belg.*, 97(11-12):1011-1029 (1988).
9. Liu, J., and Ronney, P. Summary of oral presentation (unpublished, 1995).
10. Weinberg, F. J. Optics of Flames. Butterworth & Co. Ltd. (1963).
11. Tsuji, H. *Prog. Energy Combust. Sci.* 8:93-119 (1982).
12. Takeda, M., Ina, H., and Kobayashi, S. J. Opt. Soc. Am. Vol. 72 No. 1 pp. 156-160 (1982).

Figures

(a)   (b)   (c)   (d)
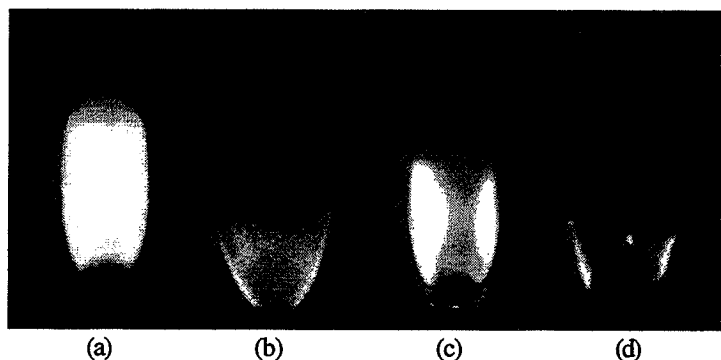
Figure 1: Sample microgravity jet diffusion flames (methane fuel, tube diameter $D = 1.7$ mm, $Re_D = 120$). (a) Uninhibited (b) 8% CF_3H added to oxidizer. (c) 1% CF_3Br added to oxidizer. (d) Transient to extinction; 1% CF_3Br, 18% O_2.
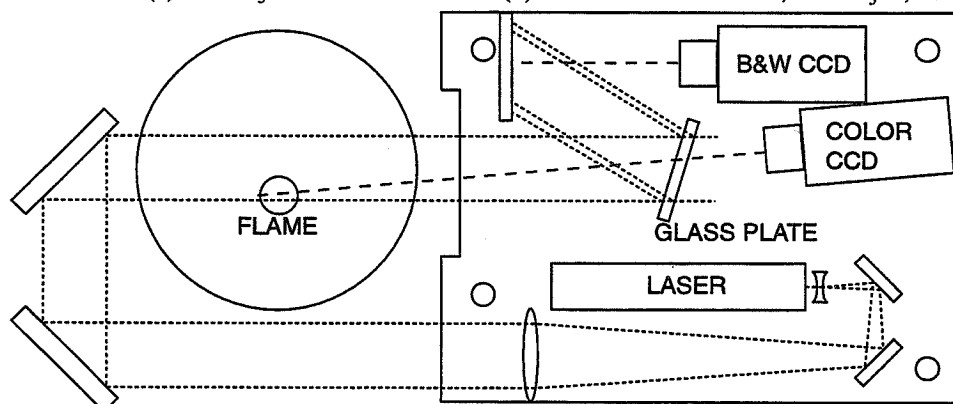
Figure 2: Schematic of interferometric temperature diagnostic for drop tower experiments.
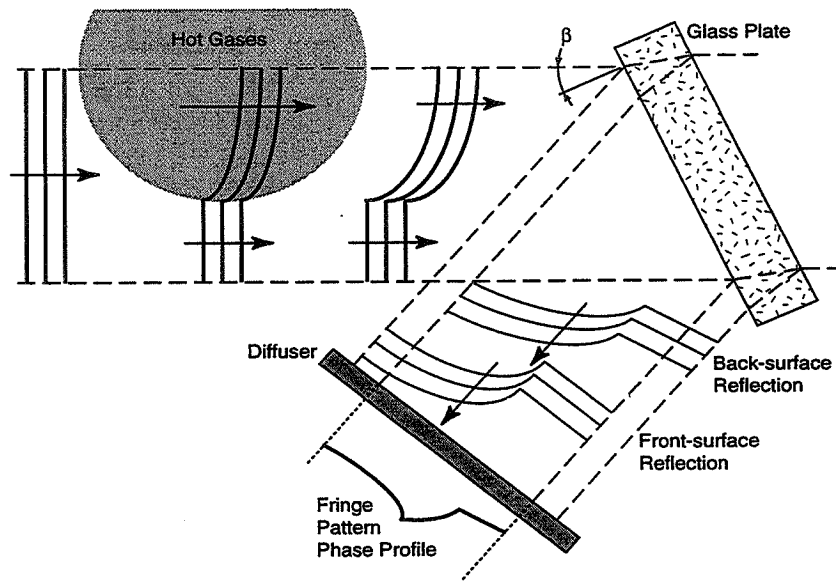
Figure 3: Diagram of the development of the laser wavefronts through the interferometric system.
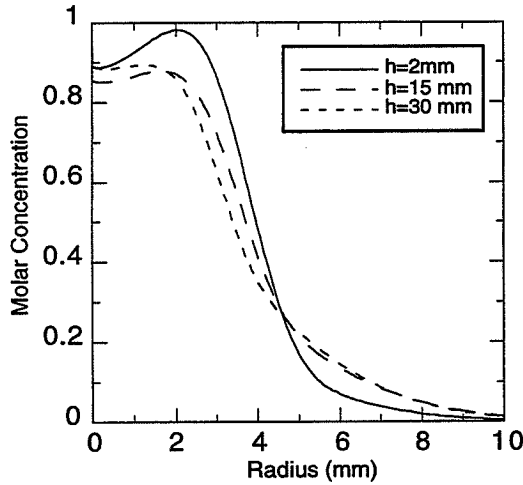
Figure 4: Measured molar concentration profiles for a 3.4 mm diameter helium jet, at different heights from the tube exit.
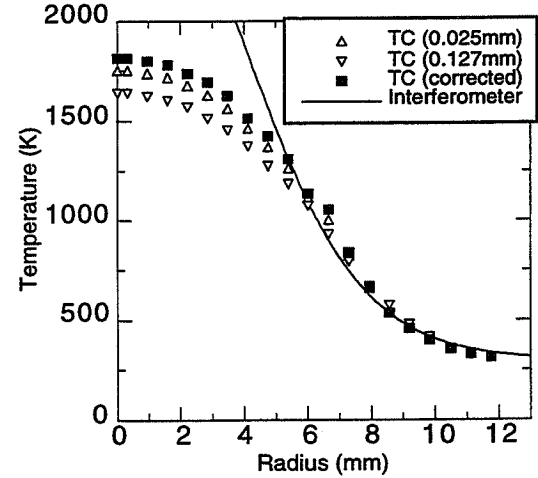
Figure 5: Temperature profiles above a methane Bunsen burner flame (h=25 mm, D=13.5 mm).
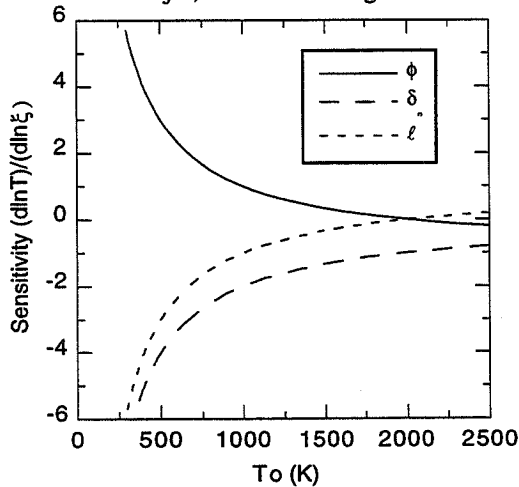
Figure 6: Sensitivity of a 2000 K temperature measurement as a function of the temperature of the reference point.
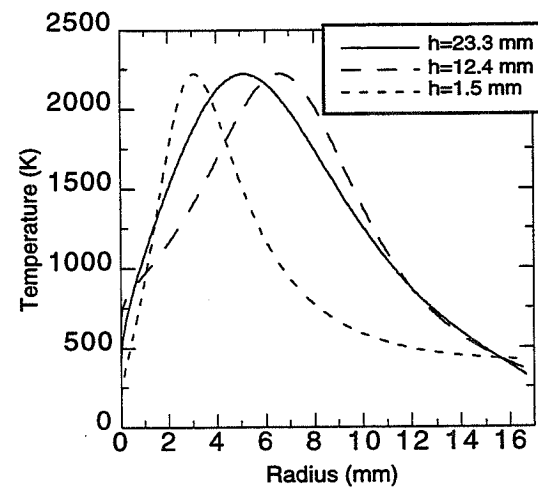
Figure 7: Temperature profiles of a μg methane diffusion flame at three heights above the nozzle ($\ell = 18$ μm/pixel, $\delta_o = 2.926 \times 10^{-3}$, $\lambda = 632.8$ nm, To=2222 K (assumed).

146

Turbulent Combustion

Page intentionally left blank

EFFECTS OF BUOYANCY ON
LAMINAR AND TURBULENT PREMIXED V-FLAMES

ROBERT K. CHENG and Benoit Bédat
Combustion Group
Energy Environmental Technologies Division
Ernest Orlando Lawrence National Berkeley Laboratory
Berkeley, CA 94720

Introduction

Turbulent combustion occurs naturally in almost all combustion systems and involves complex dynamic coupling of chemical and fluid mechanical processes. It is considered as one of the most challenging combustion research problems today. Though buoyancy has little effect on power generating systems operating under high pressures (e.g., IC engines and turbines), flames in atmospheric burners and the operation of small to medium furnaces and boilers are profoundly affected by buoyancy. Changes in burner orientation impacts on their blow-off, flash-back and extinction limits, and their range of operation, burning rate, heat transfer and emissions. Theoretically, buoyancy is often neglected in turbulent combustion models, e.g. [1]. Yet the modeling results are routinely compared with experiments of open laboratory flames that are obviously affected by buoyancy. This inconsistency is an obstacle to reconciling experiments and theories. Consequently, a fundamental understanding of the coupling between turbulent flames and buoyancy is significant to both turbulent combustion science and applications.

The overall effect of buoyancy relates to the dynamic interaction between the flame and its surrounding, i.e., the so-called elliptical problem. The overall flame shape, its flowfield, stability, and mean and local burning rates are dictated by both upstream and downstream boundary conditions. In steady propagating premixed flames, buoyancy affects the products region downstream of the flame zone. These effects are manifested upstream through the mean and fluctuating pressure fields to influence flame stretch and flame wrinkling. Intuitively, the effects buoyancy should diminish with increasing flow momentum. This is the justification for excluding buoyancy in turbulent combustion models that treats high Reynolds number flows.

The objectives of our experimental research program is to elucidate flame-buoyancy coupling processes in laminar and turbulent premixed flames, and to characterize microgravity (μg) premixed flames. The results are used to derive appropriate scaling parameters for guiding the development of theoretical models to include the effects of buoyancy. Knowledge gain from the analysis will also contribute to further understanding of the elliptical nature of premixed flames. Our current emphasis is to examine the momentum limit above which the effects of buoyancy would become insignificant. This is accomplished by comparing the flowfields and the mean properties of normal gravity flames (+g), and reversed gravity flames (-g, up-side-down flames) at different flow velocities and turbulence intensities. Microgravity (μg) flames experiments provide the key reference data to reconcile the differences between flames in +g and -g.

As flame configuration has significant impact on premixed flames characteristics [2] we have studied axi-symmetric conical flames [3,4] and plane-symmetric rod-stabilized v-flames [5]. The two configurations produce distinct features that dictates how the flames couple with buoyancy. In a conical flame, the hot products plume completely envelops the flame cone and shields the flame from direct interaction with the ambient air. The plume originates at the burner rim and generates a divergent flowfield. In comparison, the products region of v-flames forms between the twin flame sheets and it is convergent towards the center-plane. Interaction with ambient air is limited to the two end regions of the stabilized rod and beyond the flame sheets.

Diagnostics and apparatus

Laser schlieren has been the principal diagnostics for our μg experiments [3-5]. This technique requires relatively low power light source and simple optics. We use a CCD cameras with high shutter speeds (up to 1/10000 sec) to capture the changes in mean flame properties. The schlieren system is housed in a standard drop-package for the NASA Lewis Research Center (LeRC) 2.2 second drop tower. It employs a 0.5 mw He-Ne laser light source and has a field of view of 75 mm.

For laboratory studies, we use a two component laser Doppler anemometry (LDA) system to measure turbulence statistics of +g and -g flames. This computerized LDA has the capability to trace flowlines through the flame zone. As measurement of velocity statistics is crucial to our research, we have recently collaborated with Dr. Paul Greenberg of LeRC to develop a one-component LDA system for μg experiments. This set-up uses a 15 mw continuous YAG laser source and employs the standard optical layout for forward scattering. It is mounted on the optical deck of our drop-package. Placing the burner on computerized

stepping motor translation stages enables automatic traversing of the flowfield. This system has been tested successfully for measuring non-reacting turbulent flows on-board LeRC's DC9 parabolic flights. Velocity measurements in μg premixed flames is scheduled for April 1997.

We have also used Planar Laser Induced Fluorescence (PILF) to compare flame wrinkle scales of +g and -g flames. This system uses a Spectra-Physics Quanta-ray DCR-2A Nd:YAG laser. It has a pulse energy of 400 mJ/pulse (@ 532 nm with a pulse width of 8 nsec. The second harmonics of the Nd:Yag laser pumps a Spectra Physics Quanta Ray dye laser that uses Rhodamine 590 dye. A frequency doubling crystal for the dye laser output generates a ultra-violet (UV) beam that is tuned to the $P_1(2)$ absorption transition (282.58 nm) of OH (1,0) band of the $A^2 \Sigma^+ \leftarrow X^2 \Pi$ system. OH fluorescence at 306.4 nm is detected by the use of narrow band filters placed in front of an intensified Xybion CCD camera. This system is capable of producing tunable output up to 50 mJ/pulse. The laser beam is shaped into a thin (less than 200 nm) vertical sheet of 30 mm in height to obtain sufficiently high light density to optimize the signal to noise ratio. The PLIF camera has a field-of-view of 40 mm by 40 mm. This is sufficient to capture the largest relevant flame wrinkles and to span across most turbulent flame brush.

The burner has a 25 mm diameter outlet supplied by a converging nozzle mounted on a cylindrical settling chamber. The converging nozzle is designed to produced laminar flows with uniform velocity distribution. Turbulence is generated by placing a perforated plate 20 mm upstream of the exit. To generate v-flame, a rod of 2mm diameter is place across the center of the burner exit. To generate conical flames, a ring is fitted to the exit. We have been awarded a US patent for the design of this ring stabilizer for use in ultra low NOx premixed burners.

Experimental Conditions

The experimental conditions cover flow rates from 0.2 to 1.0 liter/sec (mean velocity, U, of 0.5 to 2.0 m/s), and methane/air equivalence ratio, ϕ, from 0.65 to 1.0. The Reynolds number, Re, and Richardson number, Ri, corresponding to these experiments are $600 < Re < 3000$ and $0.05 < Ri < 1.3$. The turbulent intensity is less than 1% for the laminar flame and is 8% when the perforated plate is used. These conditions produce flame that are classified as wrinkle laminar flames.

Results

Planar Laminar Flame Stabilized By Buoyancy

During the course of our investigation of -g v-flames, we discovered the existence of planar laminar flames stabilized by buoyancy (Figure 1). These flames are very stable, relatively flat, and completely detached from the burner. The basic implication is that buoyancy forces in the hot products induces the appropriate divergence to enable the flame to propagate steadily into the reactants stream.

This unique flame configuration is of fundamental importance for our study of flame/buoyancy coupling because it encapsulates the essential physics of the problem. Buoyancy is the dominant force because all other processes associated with flame geometry and means of stabilization are absent. It is an ideal configuration for investigating how buoyancy interacts with flame generated flow acceleration, what effects it has on the overall flowfield, and what are the relevant parameters to describe the interacting processes. These knowledge would be very useful for understanding the effects of buoyancy on more complex laminar and turbulent flames.

To gain better insight into this interesting flame, we investigated the conditions under which they can be generated and measured the velocity flowfield using LDA [5]. In Figure 2, the 2D velocity vectors obtained for the case of $Re = 557$, $\phi = 0.725$ show clearly that buoyancy causes the flow in the products to stagnate and form a divergent flow region below the flame zone. The curved boundary outlined by the vectors is consistent with the shape of the product/air interface seen on schlieren. Through mean pressure gradient, flow divergence in the product also induced divergence upstream in the reactants. This divergence in the reactants allows the flame to stabilize itself at the position where the mean flow velocity equals its propagating speed. This is the same stabilization principle for stagnation point flames. The stretch rate, a, for the present configuration, defined by dU/dx or dV/dy, where U and V are the mean velocity in the axial, x, and radial, y, direction, is very low. Typical values are less than 20 1/sec compared to 100 to 200 1/sec for stagnation plate stabilized flames.

Figure 3 illustrates the relevant parameters that describe the dynamics of this flame. A local Richardson number Ri can be expressed in terms of the heat release ratio, τ, velocity at the trailing edge of the flame, S_b, and the thickness of the products layer below the flame, d_b :

$$Ri = g \times \tau \times \frac{d_b}{S_b{}^2} \qquad (1)$$

Ri of unity implies a balance between the buoyant and the convective forces. The values of Ri deduced from the velocity

measurements show that most attain $Ri \approx 1$. These results suggests that d_b would be a convenient length scale for characterizing the buoyancy effects.

Laminar and Turbulent Flame Angles

The mean v-flame angle, α, provide a means to quantify the evolution of +g, -g and µg flames. To deducing α from the schlieren images, we used the composites made up of summing 120 different individual schlieren realizations. For laminar flames, an inner edge to represent each flame sheet can be deduced by using an intensity threshold. For turbulent flames, α is deduced from the centroid, i.e. the geometric mid-point, of the inner and outer edges of the broad flame brush. This definition of the turbulent flame angle is relatively insensitive to the choice of threshold values and approximates the flame angle based on using the loci of progress variable, $\bar{c}$, equals to 0.5.

The results show that the laminar +g and -g flame angles are indistinguishable beyond Re > 2000 or Ri < 0.2. This implies that the momentum limit has been reached. The mean turbulent flame angles, however, indicate quite different trends. Shown in Figure 4 are three sets of turbulent flame angles for ϕ = 0.7, 0.65, and 0.62. For flow conditions of $Ri < 0.2$, $Re > 2000$, significant differences still exist between the +g and -g turbulent flame angles. The discrepancies are largest for ϕ = 0.7 and all three sets of data do not show clear converging trends with decreasing Ri. For flames with ϕ = 0.7, the +g and -g turbulent flame angles diverge towards Ri = 0. More importantly, the µg turbulent flame datum falls almost exactly at where the linear fit of the -g flame angles intersects Ri = 0.0.

For premixed turbulent flames, flame wrinkling is an important process that broadens the flame brush and causes an increase in the mean turbulent flame angle. It may explain the differences in +g and -g turbulent flame angle. To investigate this further, we imaged flame wrinkles by the use of OH-PLIF technique. Top row of Figure 5 shows OH-PLIF images of a +g and a -g turbulent v-flame with U = 1.38m/s and ϕ = 0.7. The -g flame images has been rotated 180°. Fluorescence from OH radicals present in the products appear bright on these images. The wrinkled flame sheets are outlined by the boundaries between the bright and dark regions. The stabilizer rod where the two flame sheets originate can be discerned at the bottom of the +g flame image. The stabilizer rod is not visible on the -g flame image because the laser sheet was positioned farther away from the burner exit. These OH-PLIF images clearly show that the +g flame is much less wrinkled close to the stabilizer rod. This difference is shown more vividly when flame edges derived from twelve OH-PLIF images are superimposed (bottom row). The -g flame has a much broader flame brush confirming that buoyancy promotes flame wrinkling in -g and suppressing flame wrinkling in +g. This is in accord with the notion that with hot products above cold reactants, buoyancy can reduce flame wrinkling because it offers a stable configuration (i.e. hot above cold), and increases the convective velocity of the products. In -g, cold reactants over hot products is unstable and tends to promote flame wrinkling. These effects are amplified at higher equivalence ratios because the products are more buoyant. This explains the larger difference in the flame angles of ϕ = 0.7 flames compared to those of ϕ = 0.65 and 0.62.

It is, however rather surprising that the buoyancy effects exist for these turbulent flame because +g and -g laminar flames with similar mean flow velocities are virtually indistinguishable. We consider this to be an important observation that indicate a need to develop a new scaling parameters to consider the effects of buoyancy on turbulent flame wrinkling.

Velocity Measurements in +g and -g V-flames

The 2D velocity vectors measured in +g and -g laminar v-flames are compared in Figure 6. Also shown are the flame positions deduced from corresponding schlieren images. For these flames with Re = 1250, there are significant differences in the flame shapes and within the flowfields of +g and -g flame. In +g, flow acceleration is shown by the parallel velocity vectors in the products region. In contract, deceleration is observed in the products region of the -g flame. The stagnation point where velocity approaches zero is found at x = -30 mm and y = 0. At the edge of the flame sheet (x = -22 mm, y = -30 mm), flow circulation indicate a reversal in the direction of the products to be convected away by buoyancy. This circulation also causes the curved flame sheet.

Though the outline of the turbulent flame brushes indicate that the -g turbulent flame in Figure 7 is broader and shorter than the corresponding +g flame, differences in the velocity vectors are much less noticeable. Due to the high mean flow velocity, the characteristics stagnation point of -g flames is pushed further away from the flame zone and is beyond the measurement domain. Starting at x < -40 mm, there is a very slight deceleration within the products of the -g flame. The velocity vectors also show a more divergent flow compared to the +g case. In the nearfield region close to the stabilizer rod, the velocity vectors of the +g and -g turbulent flames are almost identical. Yet it is in this region where the OH-PLIF shows significant differences in the flame wrinkle structures. Therefore, analysis of the velocity statistics, in particular conditional statistics, would be very useful to determine if the changes in flame wrinkle structures has significant effects on flame generated turbulence.

Planned activities and diagnostic development

We plan to continue with velocity measurements in +g and -g v-flame. Conditional sampling of rms velocities will show if the broadening of the -g flame brush is accompanied by changes in turbulence statistics. These data will be compared with those measured in μg laminar and turbulent v-flames. The LDA μg flame campaign is scheduled for April 1997. Though this is a significant advancement, this LDA system is limited to measuring axial velocity component. Our experience on LDA application in μg suggests that a two-component LDA system should be feasible. We will collaborate with Dr. Greenberg to explore the development of a 2D-LDA system. Also planed for μg is an investigation of flame stabilization limits. We have observed that flame tends to blow-out easily in μg. A systematic investigation on board parabolic flights would be very useful for designing future μg flame experiments and for determining the effects of buoyancy on flame stabilization.

Our laboratory study using OH-PLIF has shown that 2D imaging technique is a powerful technique for characterizing turbulent flame structures. The use of a 2D imaging technique such as PLIF or Mie scattering based tomography for μg experiment will make significant contribution our research program. Adapting OH-PLIF or tomography to μg experiments, however, is non-trivial and requires elaborate planning and design. As this would be a major μg diagnostics development effort we shall explore the possibility of collaborating with other participants of the NASA Microgravity Combustion Program.

Several theoreticians have expressed interested in collaborating on developing models for the planar laminar flames stabilized by buoyancy. This is a very challenging problem because the flame stabilization mechanism is associated with the downstream boundary conditions. Though our preliminary analysis has shown that the buoyancy forces and momentum forces are equal at the trailing edge of the flame front, connect this conditions to the upstream and downstream conditions is non-trivial. This model, when develop, should provide a means to derive a non-dimensional scaling parameter for estimating the effects of buoyancy on steady premixed flames.

Acknowledgment

References

1. Bray, K. N. C., Libby, P.A., and Moss, J. B., *Combustion and Flame 61*:87-102 (1985).
2. Cheng, R. K., and Shepherd, *Combustion and Flame, 85,* 7-26 (1991).
3. Kostiuk, L. W., and Cheng, R. K., *Experiments in Fluids 18,* 59-68 (1994).
4. Kostiuk, L. W., and Cheng, R. K., *Combustion and Flame, 103,* 27-40 (1995).
5. Bedat, B., and Cheng, R. K., *Combustion and Flame 106,* 13-26 (1996).
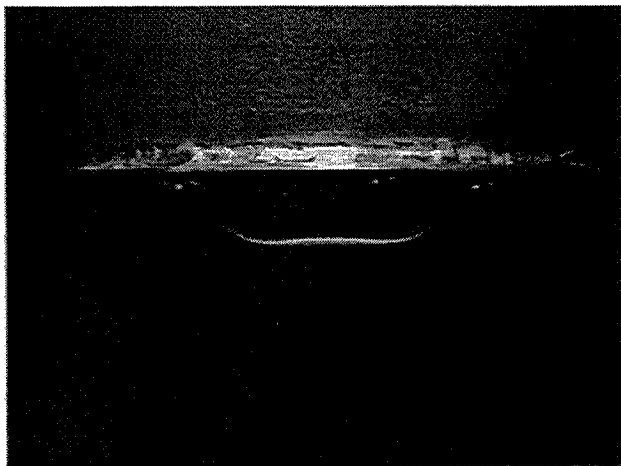
Figure 1 Premixed planar laminar flame stabilized by buoyancy
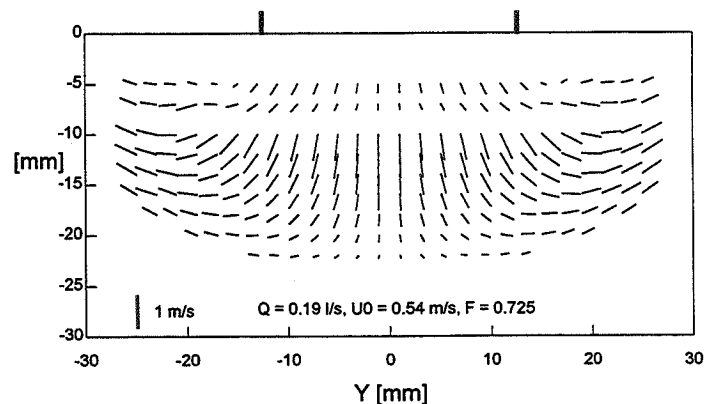
Figure 2 Velocity vectors measured in a planar laminar flame stabilized by buoyancy

152
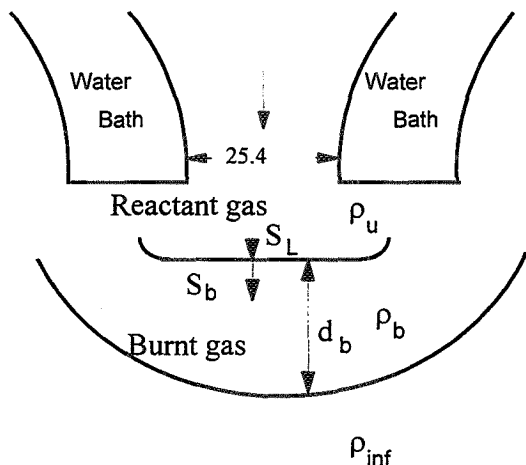
Figure 3 Schematics and relevant parameters of the laminar flame stabilized by buoyancy
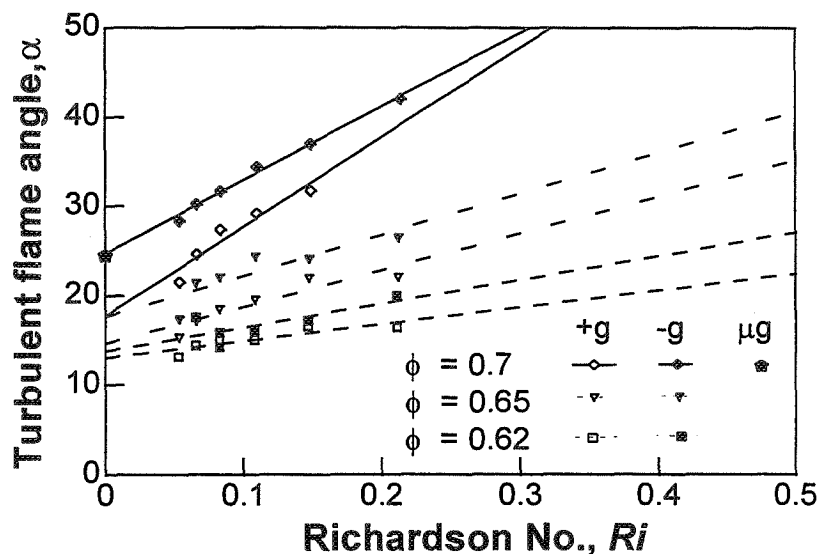
Figure 4 Comparison of +g and -g turbulent flame angles deduced from schlieren images
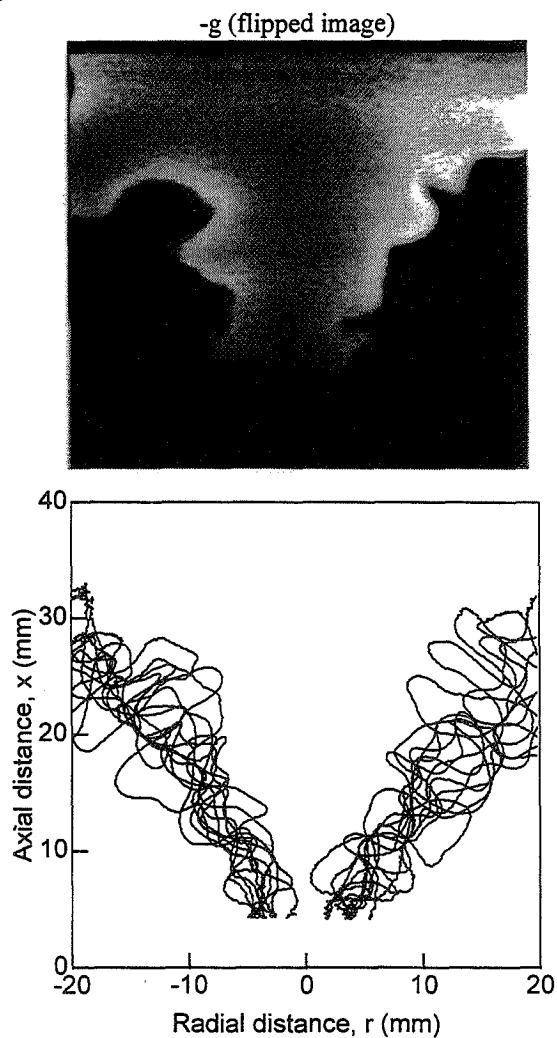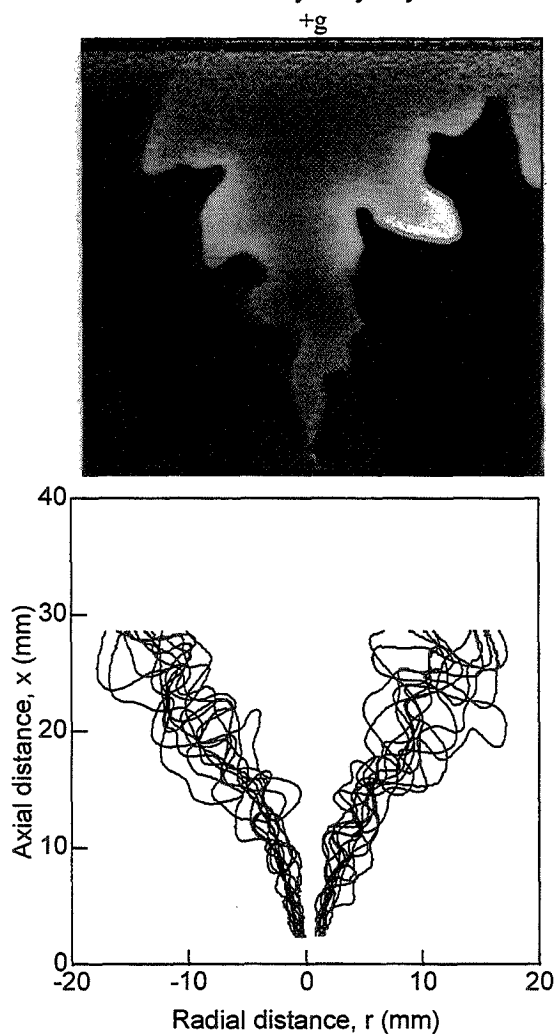
Figure 5 OH-PLIF images (top row) and superimposed flame boundaries (bottom row) of +g and -g turbulent v-flames

153

Page intentionally left blank

TURBULENT PREMIXED FLAME
PROPAGATION IN MICROGRAVITY

S. MENON[*], M. Disseau[+], V. K. Chakravarthy[+], and J. Jagoda[*]
Georgia Institute of Technology
School of Aerospace Engineering
Atlanta, Georgia

Introduction

The structure and propagation characteristics of turbulent premixed flames have been investigated for some time. For example, the turbulent flame speed has been typically estimated in terms of the laminar flame speed S_L and the local turbulence intensity u'. However, the exact form of the functional relation: $u_T/S_L = f(S_L, u')$ has not yet been determined although various models have been proposed (ref. 1). A key reason for this uncertainty is the inability to experimentally resolve all scales of motion that could contribute to the wrinkling of the premixed flame and hence, to an increase the effective burn speed. In a typical high Reynolds number flow, the small scales are impossible to resolve in an experiment (e.g., using LDV). However, turbulent fluctuations at the small scales (e.g., Kolmogorov scale) could be resolved if the Reynolds number is reduced (for example, by reducing the flow velocity). A flow field that provides sustained turbulent flow in a relatively low Reynolds number is Couette flow. It has been shown in past studies that stationary turbulent Couette flow could be achieved at Reynolds number as low as 1800. Once combustion is included, however, the large-scale turbulent stresses responsible for momentum transport can be overwhelmed by the buoyant stresses in 1g. Since this phenomenon is not present in realistic high Reynolds number devices, a microgravity environment is required to suppress the buoyancy effects while still maintaining reasonable operating pressure, temperature and observable scales at all sizes.

This paper summarizes the results obtained so far in this study. Both experimental and numerical studies are being performed to investigate turbulent premixed flames. The experiments so far have focused on characterizing the turbulent flow field in this new Couette flow facility. A major reason is that the current device has been designed to fit inside the NASA Lewis 2.2 s drop tower rig (ref. 2). As a result, this facility is much smaller than the facilities used in the past (ref. 1-3). For example, the current length to gap ratio is 14 compared to 30-158 of the earlier devices (refs. 3-7). In addition, the current device operates in a closed loop, i.e. turbulent flow is forced to reenter the test section whereas earlier devices transition the flow from laminar to turbulent. Thus, it is essential to quantify the turbulence properties of this device.

The numerical study employs large-eddy simulation (LES) technique. In this approach, all scales of motion larger than the grid resolution is captured in the simulation without modeling and only scales smaller than the grid are modeled. A localized dynamic subgrid model for the subgrid kinetic energy is used in this study to model the subgrid stresses. However, since the flame thickness is much smaller than the typical grid resolution employed in LES, conventional LES of species equations will not capture the true features of the flame. Here, a new subgrid combustion methodology has been developed to simulate the burning process within the small scales (refs. 8,9). In this approach, the local laminar burning, wrinkling due to the local subgrid turbulence and volumetric expansion due to heat release are explicitly included within the subgrid scales. This approach also predicts the local (turbulent) burn speed provided the local turbulent field is known. The experimental data on the turbulence provides the required information to (hopefully) accurately evaluate the propagation characteristics of turbulent premixed flames using this simulation approach. Thus, the present study combines the capabilities of both experimental and numerical methods to investigate premixed flames.

Experimental Facility

The experimental device shown in Fig. 1 consists of a continuos Mylar belt moving in opposite directions over a series of rollers, two of which drive the belt while four are used to adjust the spacing in the test section. It is driven by an adjustable DC motor connected to the drive roller by a set of pulleys and a v-belt. To prevent belt walking and to ease the insertion of a new

belt, a set of tensioning screws help position the far roller. Two plates are placed on the outside of the belt to reduce belt vibration. The Reynolds number for the device, Re_h, can be changed by either changing the speed of the belt, U_{belt}, or by changing the belt spacing, h. The device is surrounded by a Plexiglas box to prevent any external influence on the flow without disturbing optical access to the experiment.

The velocity flow field was mapped with a TSI 9100-7 two component laser Doppler velocimeter, which uses the 514.5 nm and 488 nm wavelengths of an 5 watt Ar^+ laser. After going through an expander and focusing using a 14 mm aperture lens, with a 750 mm focus, the probe volume was 0.13 mm in diameter and 1.3 mm long. The system was used in back scatter mode. The output signals were analyzed by a TSI IFA656 digital burst correlator, which can cope with lower signal to noise ratios than a traditional counter. One beam of each pair was frequency shifted by a Bragg cell to allow for measurement of negative velocities. Sub-micron TiO_2 particles were used to seed the flow. After passing though a fluidized bed, TiO_2 laden air is inserted into the device through a tube which produces a cloud of seed around the moving belts that is then entrained into the flow. This eliminates the possibility of biasing the data with artificial seeding velocities. FIND software, from TSI, was then used to statistically process the 50,000 samples obtained at each location. Data was velocity bias corrected according to the algorithm provided in FIND.

Numerical Method

A modified version of a subgrid model proposed earlier (refs. 8,9) is used in the present LES. The kinematic structure of premixed flames was investigated earlier (ref. 9). The model is extended here to include heat release. Within each LES cell, a representative one-dimensional domain is used to stochastically represent a local ray through the flame brush. The G-equation flame propagation model (refs. 9,10) is solved on this 1D line. The G-equation allows for propagation of the flame as a sharp front (negligible flame thickness) corresponding to a case of fast chemical kinetics (ref. 10). The effect of turbulent eddies on the species field is modeled stochastically using a scalar rearrangement process on segments chosen on the one-dimensional domain. More details is given elsewhere (refs. 9-12).

For heat release, the temperature is assumed to be a linear function of G. The obvious implication is that the transport and diffusive properties of the reactive scalar and the thermal energy are closely correlated (corresponding to a often used physical assumption of a constant Lewis number) in the subgrid domain. Transport of species and heat across LES cells is modeled using a "splicing" procedure (refs. 11,12). The thermodynamic pressure in each of the LES cells is assumed to be constant since it is well known that the second order reaction mechanisms do not cause a change in thermodynamic pressure across the flame. It is further assumed that the thermodynamic pressure is gradient free through out the physical domain. Any acoustic disturbance created by the flame is assumed at have small amplitude (zero Mach number approximation) and is communicated at infinite speed through out the domain. The LES-resolved temperature field can be obtained by filtering the local subgrid temperature fields. However, this procedure can lead to sharp discontinuity and hence, to numerical instability. Therefore, to locally smooth the LES-resolved temperature field (which is needed to close the LES equations), a diffusion equation for temperature is solved on the LES-grid at each LES time step using the subgrid-aveeraged field as an initial condition.

The numerical method is a fourth-order accurate finite-difference scheme in space and second order accurate in time. Since the thermodynamic pressure is constant, a zero Mach number version of the fractional step method (ref. 13) is used to integrate the LES equations.

Results and Discussion

Experimental Results: Figures 2a and 2b shows respectively, the mean and rms velocity distribution in the flow field. It can be seen that the profiles are not totally anti-symmetric. It was determined that this was due to an asymmetry in the end regions where the drive rollers are located and could not be avoided. However, this asymmetry did not appear to have any significant effect on the rms velocity. More importantly, the data shows a nearly constant rms fluctuations in the core which is of interest here. Figure 3 shows U^+ as a function of y^+. The data shows the expected behavior for a wall bounded shear flow. Both the viscous sublayer ($y^+ <5$) and the inertial sublayer ($30<y^+ <1000$) can be clearly observed. However, due to the noted asymmetry, the data at different Reynolds numbers do not exactly collapse as predicted by theory.

Figure 4 compares the measured streamwise fluctuations in various devices. The peak location in the present facility is in good agreement with earlier data but turbulence intensity magnitude is somewhat higher. This is probably due to the continuous nature of the flow and the compact nature of the device and is unavoidable here. Figure 5 compares the skin friction coefficient measured in this device to those in earlier devices. Deviations from the more ideal Couette flow are, once again, probably due to the recirculating nature of the flow in this compact device.

However, these results clearly establish that stationary turbulence with nearly constant turbulent fluctuations in the core of the flow exists in the present facility. Furthermore, the overall nature of the flow is in good agreement with theory and past studies in similar devices.

The experimental data can be utilized to estimate the resolved scales of motion. Using the belt spacing, $h = 2.54$ cm as the typical integral length, the Kolmogorov scale, η, is estimated in the core to be 0.23 mm for the $Re_h = 4,366$ case and 0.13 mm for the $Re_h = 10,091$ case. For the LDV system, the seed particle size is sub-micron, much smaller than η, while the LDV probe volume is of the order of η. This implies that the smallest scale can be nearly resolved. However, due to flow motion, the residence time inside the probe volume is a more accurate measure of the resolution. The velocity of the scale can be estimated by using the relation between Kolmogorov velocity scale and the magnitude of turbulent velocity: $u'/v = (Re_L)^{1/4}$. Based on the probe volume, a residence time and, therefore, a frequency 590Hz for the $Re_h = 4,366$ case and 1,030Hz for the $Re_h = 10,091$ case is estimated. This means that the data rate for the LDV should be greater than 2,060Hz to resolve Kolmogorov scales temporally. Because of the high noise levels in the system, this is difficult to achieve. Therefore, the best estimate is that the resolution is of the order of η. or larger.

These studies have clearly established the turbulent flow properties in this facility. Although hot flow studies cannot be carried out using this device (an identical hot flow facility is currently under construction), a preliminary study of buoyancy was carried out by using an excimer laser to ionize a small region of air in the flow. This produced a hot gas kernel that propagated into the flow. Using high speed Schlieren imaging, it was possible to observe the effects of shear caused by the Couette flow and the apparent distortion caused by buoyant stresses. This preliminary study suggested that buoyant effects should be observed in the actual reacting flow case. This is the focus of current study and the results will be reported in the near future.

Numerical Results: LES of non-reacting and reacting Couette flow corresponding to a Reynolds number (as defined earlier) of 10,000 have been conducted on a 49x49x33 grid. The mean velocity profile is compared with the corresponding result from the experiment in Fig 6. The LES profile is anti symmetric about the centerline whereas (as noted) there is some asymmetry in the experimental data. The rms velocity in the streamwise direction is compared to the experimental data in Fig. 7. The experiment indicates a peak in urms more closer to the wall than obtained in the LES. Assuming that the experimental results in such close vicinity of the moving belt are free of any error, one might be able to capture the peak in urms by increasing the near wall resolution. However, some uncertainty in the rms estimate is inevitable in the LES, since, the unresolved part of the turbulent kinetic energy (grid dependent) is captured only approximately as the subgrid kinetic energy. In any event, the propagation of the flame in the central core region with constant rms fluctuations is of interest in this study and this feature is captured here. Increase in the resolution in the core region captures the constant rms region more accurately, as shown earlier (ref. 9).

For reacting flows, the grid is rapidly stretched out from the wall but in the core region (mid 78%) a uniform grid is used to allow proper resolution of the propagating flame ball. The grid width is 10η in the core region and the simulation is stopped once the flame crosses this region All simulations described here are for a reference u'/S_L of 4.0. Temperature rise factors of 4 and 7 were studied. Comparison with a model simulation using Yakhot's model for the turbulent flame speed (ref. 9) were also carried out to evaluate the predictions by the new subgrid LES method. Some representative results are reported below.

Five contours corresponding to equally spaced values of G between 0 and 1 are shown for each case in Fig. 8. As can be seen, the subgrid approach tends to capture the thin premixed flame quite well (usually within 2-3 grid points) when compared to conventional LES (i.e., solving the G-equation with the LES equations). As seen earlier (ref. 9), in the conventional approach significant numerical diffusion of the scalar gradients in G occurs and overwhelms the burning rate. This error is expected in all simulations that evolve the species equations on the LES grid using finite difference or finite volume schemes. Flame surface tracking methods can be implemented for cold flames but cause problems when heat release is added. The flame generates velocities normal to the flame surface because of the expansion behind it. The vertical currents are however curtailed by the presence of the wall, so the flow velocity tends to increase greatly in the streamwise and spanwise directions leading to flattening of the flame. A iso-level of G-surface corresponding to a value of 0.5 predicted by the subgrid approach is shown in Fig. 9. This figure shows visually an approximate shape of the wrinkled flame front.

To investigate the effect of gravity, two simulations (using the subgrid model) were conducted with heat release corresponding to a temperature ratio of 7.0. The first case is run with conditions corresponding to gravity on earth, the second with zero gravity. The density gradients caused due to heat release tend to compress the flame in the upper region and diffuse the flame in the lower regions in the presence of gravity. This is not very noticeable in the present simulations because of very high burning rate causing the flame to reach the wall very quickly. In Fig. 10, ten equally spaced contours of G at the same cross plane location are plotted for the cases with and without buoyancy. The whole flame tries to lift up in the presence of gravity due to buoyancy, although it is not very noticeable in the figure. However, it can be seen that the two simulations diverge in time indicating an observable buoyancy effect on premixed flames.

There are many structural and propagation properties of premixed flames that can be analyzed to characterize the flame structure. Figure 11 shows the pdf of the stretch in the plane of the flame (caused by flame curvature and rate-of-strain effects) for the two cases. Clearly, the flame structure under 1g exhibits increased positive stretch compared to the 0g case. Further study using finite-rate kinetics model is underway to understand the effect of buoyancy on such low Re turbulent premixed flames.

Conclusions

A facility in which turbulent Couette flow could be generated in a microgravity environment was designed and built. To fit into the NASA Lewis drop tower the device had to be very compact. This means that edge effects and flow re-circulation were expected to affect the flow. The flow was thoroughly investigated using LDV and was found to be largely two dimensional away from the edges with constant turbulence intensities in the core. Slight flow asymmetries are introduced by the non symmetric re-circulation of the fluid outside the test region. Belt flutter problems were remedied by adding a pair of guide plates to the belt. In general, the flow field was found to be quite similar to previously investigated Couette flows. However, turbulence levels and associated shear stresses were higher. This is probably due to the confined re-circulation zone reintroducing turbulence into the test section. An estimate of the length scales in the flow showed that the measurements were able to resolve nearly all the length scales of interest.

Using a new LES method for subgrid combustion it has been demonstrated that the new procedure is computational feasible even on workstation type environment. It is found that this model is capable of capturing the propagation of the premixed flames by resolving the flame in the LES grid within 2-3 grid points. In contrast, conventional LES results in numerical smearing of the flame and completely inaccurate estimate of the turbulent propagation speed. Preliminary study suggests that there is observable effect of buoyancy in the 1g environment suggesting the need for microgravity experiments of the upcoming experimental combustion studies.

With the cold flow properties characterized, an identical hot flow facility is under construction. It is assumed that the turbulence properties ahead of the flame in this new device will closely match the results obtained here. This is required since the hot facility will not enable LDV measurements. The reacting flow facility is also being constructed with planned drop tower experiments in mind. Therefore, issues related to safety and structural integrity are being take into account. Further development of the numerical model will also be carried out to include finite-rate kinetics for representative premixed cases. More detail analysis of the flame structure and propagation nature will be investigated. Simulations will also be compared to the flame properties observed in the experiments.

References
1. Williams, F. A., *Combustion Theory*, Second Edition., Addison-Wesley, New York, 1985.
2. Lekan, J., Gotti, D. J., Jenkins, A. J., Owens, J. C., Johnston, M. R., "User Guide for the 2.2 Second Drop Tower of the NASA Lewis Research Center," *NASA Technical Memorandum 107090*, 1996.
3. Aydin, E. M., and Leutheusser, H. J., "Plane-Couette flow between smooth and rough walls," *Experiments in Fluids*, Vol. 11, pp. 302-312, 1991.
4. Bech, K. H., Tillmark, N., Alfredsson, P. H., Andersson, H. I., " An Investigation of Turbulent Plane Couette Flow at low Reynolds Numbers," *Journal of Fluid Mechanics*, Vol. 285, pp. 291-325, 1995.
5. El Telbany, M. M. M., Reynolds, A. J., "The Structure of Turbulent Plane Couette Flow," *Journal of Fluids Engineering*, Vol. 104, pp. 367-372, 1982.
6. Robertson, J. M., and Johnson, H. F., "Turbulence Structure in Plane Couette Flow," *J. Eng. Mech.*, Proc. of Am. Soc. of Civil Engg., Vol. 6, pp. 1171-1182, 1970.
7. Clark, J. A., "A Study of Incompressible Turbulent Boundary Layers in Channel Flow," ASME *Journal of Basic Engineering*, Vol. 90, pp. 455-468, 1968.
8. Menon, S., McMurtry, P. A., and Kerstein, A. R., "A Linear Eddy Mixing Model for LES of Turbulent Combustion," in *LES of Complex Engineering and Geophysical Flows*, Galperin, B. and Orszag, S., eds., Cambridge University Press, pp. 287-314, 1993.
9. Menon, S. and Chakravarthy, V. K., Large-Eddy Simulations of Premixed Flames in Couette Flow, AIAA Paper No. 96-3077, 32nd AIAA/ASME/SAE/ASEE Joint Propulsion Conference, Lake Buena Vista, FL, July 1996.
10. Smith, T. and Menon, S., "Model Simulations of Freely Propagating Turbulent Premixed Flames", *Symposium (International) on Combustion*, 26, 1996 (to appear).
11. Menon, S and Calhoon, W., "Subgrid Mixing and Molecular Transport Modeling for Large-Eddy Simulations of Turbulent Reacting Flows", *Symposium (International) on Combustion*, 26, 1996 (to appear).
12. Calhoon, W. H. and Menon, S., "Linear Eddy Subgrid Modeling for Reacting Large-Eddy Simulations: Heat Release Effects," AIAA-97-0368, 35th Aerospace Sciences Meeting, Reno, NV, January 6-9, 1997.
13. Chakravarthy, K. and Menon, S., "On Large-Eddy Simulations of Non-Homogeneous Flows," AIAA 97-0652, 35th Aerospace Sciences Meeting Reno, NV, January 6-9, 1997.
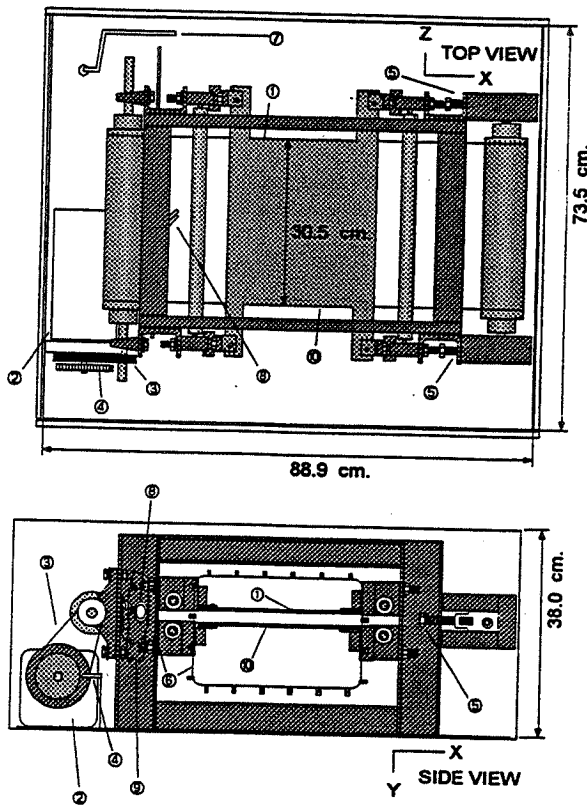
Figure 1. Setup of the experimental facility.
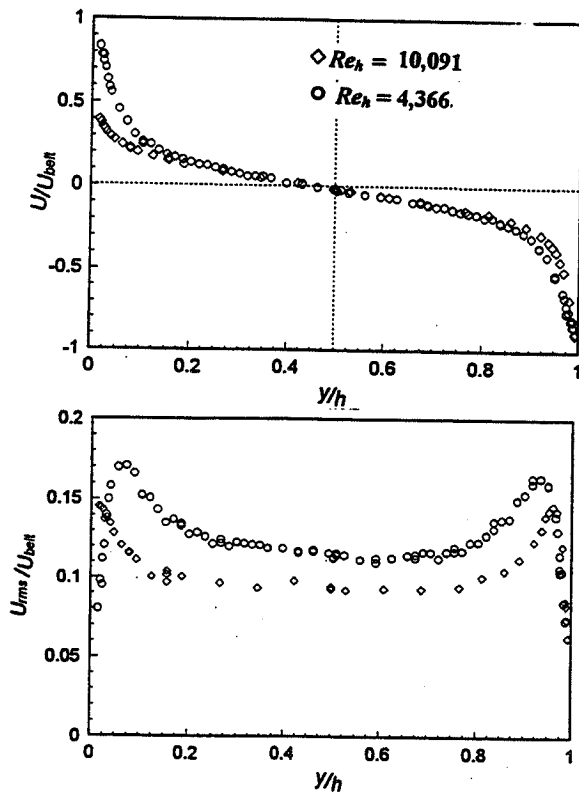
Figure 2. Mean (a) and rms (b) velocity fluctuations.
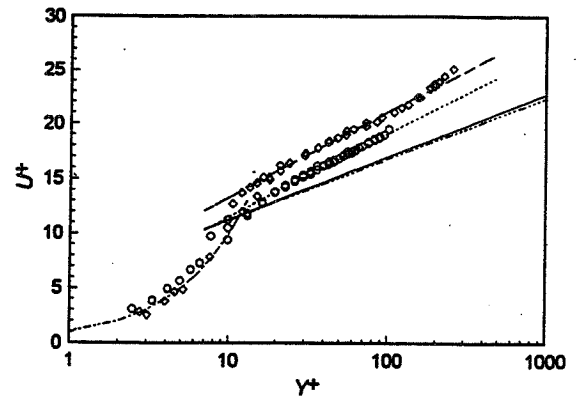
Figure 3. Non-dimensionalized near-wall velocity profile. Solid and dotted lines indicate curve fit to earlier data (refs. 3-7).
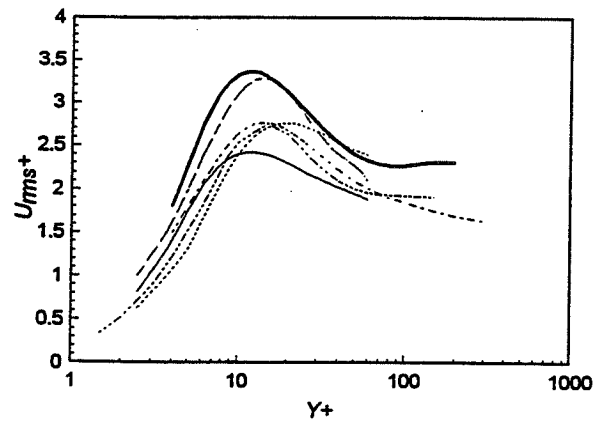
Figure 4. Comparison of present turbulence velocity fluctuation (shown as a bold line) with earlier experimental data (refs. 3-7).
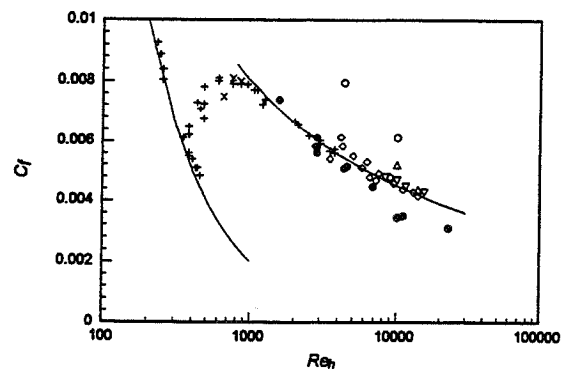
Figure 5. Skin friction coefficient comparison with earlier data. Solid circle: present study near wall; open circle: present study in the core. Other symbols correspond to data in refs. 3-7.
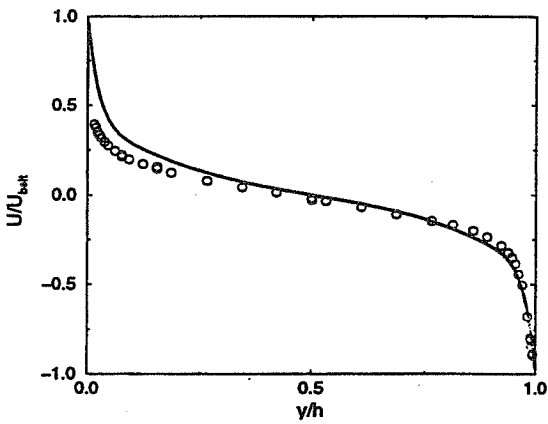
Fig.6:Mean velocity profiles
solidline:LES,symbols:expt.
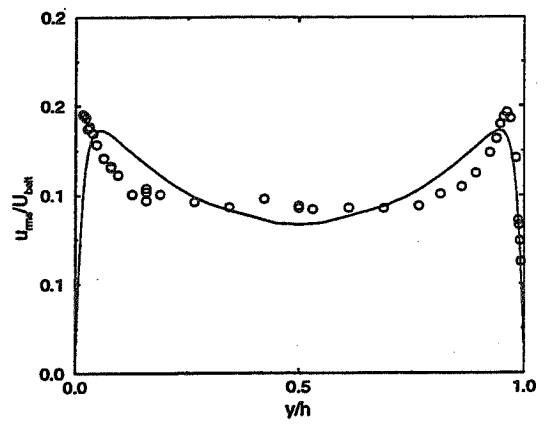
Fig.7:urms profiles
solidline:LES,symbols:expt.
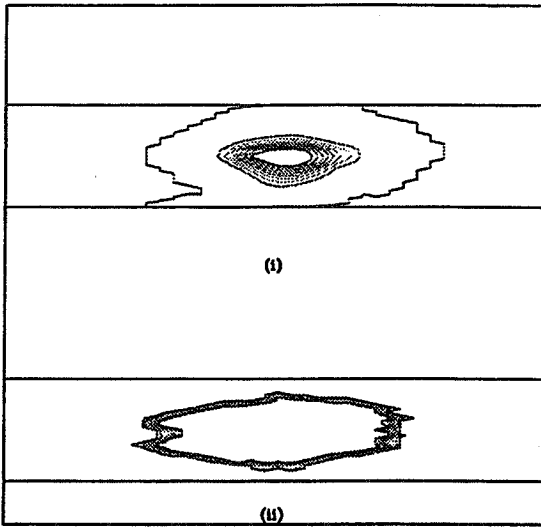
Fig.8:G-contours of equal spaced values
(i) Yakhot's model, (ii) LEM
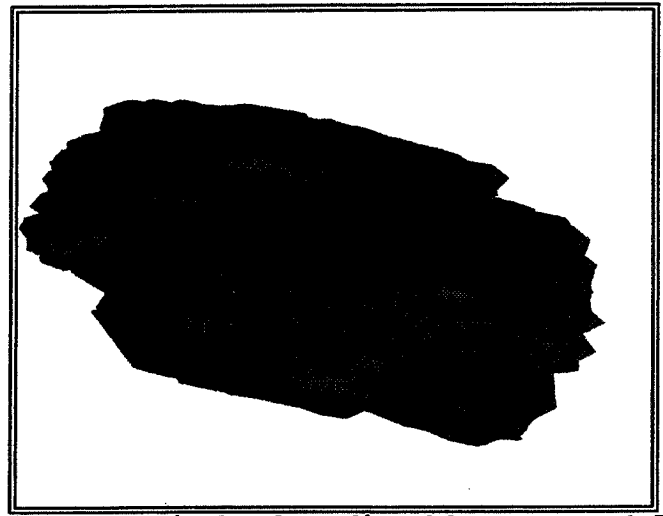
Fig.9:G=0.5 isolevel predicted by LEM at t=1.5
(t non-dimensionalized U_W and h)
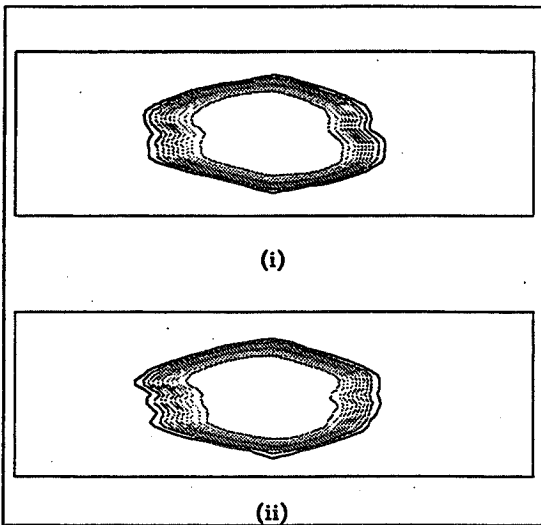
Fig.10:G-contours of equal spaced values
(i) zero gravity, (ii) gravity on earth
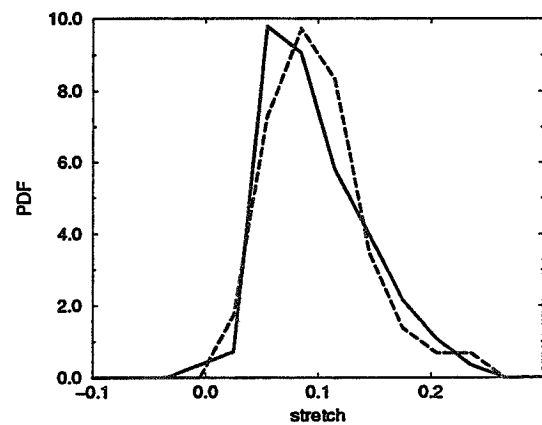
Fig.11:PDF of flame stretch
solid line: no gravity, dashed line:with gravity

UNSTEADY MULTIDIMENSIONAL SIMULATIONS OF THE STRUCTURE AND DYNAMICS OF FLAMES

K. KAILASANATH, G. Patnaik and E.S. Oran
Laboratory for Computational Physics & Fluid Dynamics
Naval Research Laboratory
Washington, DC 20375

Introduction

The primary objective of our research is to develop an understanding of the differences in the structure, stability, dynamics and extinction of flames in earth gravity and in microgravity environments. Numerical simulations, in which the various physical and chemical processes can be independently controlled, can significantly advance our understanding of these differences. Therefore, our approach is to use detailed time-dependent, multidimensional, multispecies numerical models to perform carefully designed computational experiments. Some of these computational experiments are also complementary to physical experiments performed under the Microgravity Combustion Science Program. In this report, we provide a brief summary of our research since the last microgravity combustion workshop[1].

The two major projects we have been working on are 1) the development and application of a three-dimensional, time-dependent flame model and 2) a study of the effects of gravity on flame-vortex interactions. A state-of-the-art parallel flame code, FLAME3D, has been developed and used to simulate the three-dimensional cellular structure of lean hydrogen flames [2]. The results from the simulations have been compared to our previous two-dimensional simulations to understand the role of three-dimensionality. This is discussed below in some detail after a brief discussion of the flame code. The second project deals with flame-vortex interactions under different gravitational environments such as zero, upward and downward Earth gravity. These numerical experiments are complementary to the physical experiments of Driscoll et al [3] reported elsewhere in these proceedings.

FLAME3D - A Detailed, Time-dependent, Three-dimensional Flame Model

There are a rich variety of unsteady flame phenomena that require a three-dimensional flame model for its investigation. In order to obtain definitive information about these flames, a number of physical processes need to be included and modeled to a sufficient level of detail. These processes include elementary chemical reactions, multi-species diffusion among many chemical species, thermal conduction, viscosity, radiation, and fluid convection. Body forces due to gravity are important for low speed flames and could result in Rayleigh-Taylor instabilities. Both buoyancy and fluid expansion will drive flow in the fluid, so an accurate model of compressible fluid flow is needed. Therefore, the three-dimensional, time-dependent, reactive-flow conservation equations are solved for density, momentum, energy, and the number densities of individual species. In addition to the terms that arise in the compressible Navier-Stokes equations, terms are included that represent production of species by chemical reaction, multi-species diffusion, and buoyancy. The numerical simulations of flames presented here include a detailed set of elementary reactions involving the eight reactive species, H_2, O_2, H, O, OH, HO_2, H_2O_2, H_2O, and N_2 as a diluent. All of the chemical and physical processes are solved sequentially and are then coupled asymptotically by time-step splitting. Space restrictions do not allow the elaboration of the equations solved or the numerical model, but details can be found in previous reports [4,5].

Flame Computations on Massively Parallel Processors

This three-dimensional flame model includes essentially the same physics and numerical approaches used in our two-dimensional flame models. However, this model was directly developed for massively parallel computers since it was felt that the unsteady, two-dimensional simulations were already taxing the capabilities of conventional vector supercomputers. Several issues related to the parallel computation of flames are discussed next.

The numerical models used in the NRL flame code are predominantly based on structured finite volume methods. However, the chemistry is modeled by a system of ordinary differential equations which is solved independently at each grid point. Thus, the workload at each grid point can vary considerably. It is this feature that requires the use of both structured and unstructured methods in the same code.

Certain processes, e.g. heat conduction, are represented by partial differential equations which are discretized by a finite volume technique. In these methods, the solution procedure requires substantial communications between neighboring points, but the amount of computation at each point is nearly the same. The Multiblock PARTI runtime support library [6] has been used in the NRL flame code for all structured processes. This library allows programmers to lay out distributed arrays in a flexible way, give high level descriptions for performing data movement, and distribute computation across processors.

For other processes, e.g. chemistry, the computation at each grid point can be carried out independently without requiring any communication between neighboring points. The solution procedure may require vastly different amounts of computation at each grid point and the distribution of work load can change from time step to time step as the flame evolves. To efficiently balance the work load of the chemistry process, the block-partitioned data must be redistributed across processors, and then returned to the original locations before carrying out the next structured process. This approach inherently requires a substantial amount of communication at every time step. Two new algorithms, Binpack and Binsort [6], which perform this redistribution of work load and reduce communication volume at low cost have been implemented using the CHAOS library [6]. The Binpack algorithm determines the amount of work that must be moved from heavily loaded processors to lightly loaded processors, and then generates a load balancing plan. Binsort improves the performance of Binpack by reducing the communications required for redistributing the work load.

The 3-D parallel flame code was developed on the Intel iPSC/860 at NRL but has been run in production mode on the Intel Paragon and the IBM SP-2. Simulations were carried out for a 9.5% hydrogen-air flame on a mesh of size 192 X 80 X 80 in order to study the performance of the code as a function of the number of processors. The results from this timing study on the Intel Paragon are shown in Fig. 1. By comparing the slopes of the ideal scaling curve (dotted line) to the total time (solid line) the code is shown to scale quite well up to 256 processors. The process that scales least effectively is convection, which accounts for the largest fraction of the total time and thus dominates the overall scaling. The scaling of other processes is close to ideal. The overall parallel efficiency is about 83%. The timing results for the same problem on the IBM SP-2 are very similar to those obtained on the Intel Paragon, but with a reduction by a factor of four in the overall time.

Three-dimensional Cellular Flames

Lean hydrogen-air mixtures were chosen for the initial study of the three-dimensional structure of cellular flames because earlier two-dimensional simulations are available and the chemistry is quite well established for these mixtures. The effects of gravity on flames in a 9.5% hydrogen-air mixture was studied by performing and comparing simulations of zero-gravity, upward- and downward-propagating flames.

In zero-gravity, the effect of perturbing a planar flame, is the initial formation of a single, axisymmetric cellular structure. With time, this structure grows and deforms in a three dimensional manner and splits into several distinct cells which in turn grow and split further. In an upward propagating flame in Earth gravity, the Rayleigh-Taylor instability is present in addition to the thermo-diffusive instability. This leads to the increased growth of cellular structures when compared to the zero gravity flame. The higher growth rate of the cellular structures in the upward propagating flame leads to the loss of cylindrical symmetry earlier than in the zero-gravity case. In a downward propagating flame, the light burnt gases are above the denser reactants. In this configuration gravity is a stabilizing influence on the flame. In the mixture studied here, the flame is stabilized by gravity. The initial perturbation, first grows briefly, contains OH concentrations higher than the peak found in the planar flame. Later, the OH concentration at the site of the disturbance decreases below the plane flame peak value. Still later, the OH concentration at this site once again increases above the plane flame peak value. After this time, the flame slowly reverts to its planar form. This damped oscillatory behavior has been predicted by theory [7] and has been observed in our earlier 2-D simulations [8].

The role of three-dimensionality can be clearly seen in Fig. 2 where the time evolution of the OH concentration from a 2-D simulation is compared to that from a 3-D simulation. Initially, the cellular structures appear quite similar. However, the growth rate in the 3-D calculation is much higher, leading to a larger structure. The peak OH concentration is higher by a factor of two, indicating a more vigorous reaction in the 3-D structure. By 200 ms, the cellular structure is fully 3-D with cylindrical symmetry being lost and multiple cells present. The 2-D calculation shows no sign of cell splitting even up to 500 ms. This comparison highlights the need to perform three-dimensional simulations of these cellular flames, especially if quantitative comparisons with experiments are desired.

<u>Flame-Vortex Interactions</u>

The second topic that we are investigating is the effect of gravity on flame-vortex interactions. Many studies have been carried out on flame-vortex interactions as a means to improve our understanding of turbulent flames and for the development of better models. However, the flame-vortex interaction observed in experiments performed in Earth gravity may be complicated by buoyancy effects. Recently, Sinibaldi et al [9] have reported the results of drop-tower experiments on lean propane flames that show that for some vortex strengths, the reduction in gravity can alter the structure of the flame produced by the flame-vortex interaction. Systematic numerical experiments can help in furthering our understanding of the effects of gravity and with this objective, a computational study has been initiated.

The numerical code used for these studies is essentially the same as that discussed earlier except that the geometry of the problem is assumed to be axisymmetric. A 200 x 400 grid is used to discretize a 3 cm x 12 cm computational domain. The calculations are initiated with a one-dimensional flame propagating upward, downward or in a zero-gravity environment in a premixed methane-air mixture. In all cases, a vortex ring with a gaussian distribution of vorticity in its core was superimposed on the flow field in the unburnt reactants upstream of the flame. The vortex core diameter was 0.4 cm and the ring diameter was 1.2 cm. The vortex travels toward the flame due to its self-induced velocity. The vortex quickly attains a shape similar to the one observed in the experiments. A lean methane-air mixture (0.54 equivalence ratio) was chosen because a satisfactory reaction mechanism is not yet available for propane combustion. Hence, a one-to-one comparison with the experiments of Sinibaldi et al [9] will not be attempted. However, as in the experiments, three different vortex strengths, "weak", "intermediate", and "strong" were used to vary the Froude number.

"Weak" Vortex

As the weak vortex approaches the flame, the flame is pushed back, with the greatest effect being seen on the axis, where the fluid velocity induced by vortex is highest. As the flame gets curved, vorticity of the opposite sign is generated. This vorticity is large enough that it eventually overwhelms the weak vortex. In zero gravity, the flame remains wrinkled and has sharp cusps (Fig. 3). In a downward propagating flame, buoyancy provides a stabilizing effect. The flame is less wrinkled by the vortex, and after the vortex has been destroyed by the flame, these wrinkles are damped out. Eventually, a planar flame is re-established. In an upward-propagating flame, buoyancy has the opposite effect and is destabilizing. The disturbance caused by the vortex is amplified by buoyancy, and a large finger of cold reactants falls into the products.

The effect of gravity is strongest in this case. Buoyancy clearly controls the flame shape after the flame-vortex interaction. During the flame-vortex interaction itself, the effect of gravity, though noticeable is weak

"Intermediate" Vortex

The impinging vortex in this case is stronger. The flame is more distorted and is extended further along the axis. The vortex gets past the initial location of the flame intact, and begins to entrain the hot products. This leads to the formation of a neck of flame along the axis. This neck eventually burns through, leaving a pocket of reactants with a flame around it (Fig. 3). This pocket eventually burns away.

Gravity does not alter the pocket formation significantly. The time at which a pocket is formed is essentially the same in zero gravity, upward- or downward- propagation. At late times, the downward-propagating flame becomes planar, while both the zero gravity and upward propagating flames remain wrinkled. In this case, gravity plays an even smaller role during the flame-vortex interaction, but as before, controls the final flame shape.

"Strong" Vortex

In this case, a very strong vortex impinges on the flame. The fast moving vortex drags the flame with it, extending it greatly along the axis. The strong vortex causes sufficient strain at the axis that the flame is extinguished locally (Fig. 3). It is important to note that some time is required for this to happen and that the flame does not extinguish immediately on contact with the vortex. The vortex carries some unburned pockets of reactants into the burnt products but the mixture is not hot enough, due to radiative cooling, to react. The vortex passes through the computational domain intact.

For this case, the flame-vortex interaction behavior in zero gravity and downward propagation is virtually indistinguishable, indicating that gravity plays no part in the flame-vortex interaction. However, after the vortex has passed by and the neck of the flame burns through, the final shape of the flame is affected by gravity, with the downward propagating flame becoming planar.

Importance of Radiative Heat Losses

One of the advantages of numerical simulations is the ability to turn processes on and off. For example, the simulation of the

strong vortex interaction with the flame in zero-gravity was repeated but with the radiation process turned off. In this case, the flame did not extinguish, indicating the essential role played by radiative losses in extinguishing this flame. Further analysis of the results from the simulations show that the actual extinguishment occurs when the flame is stretched into the lower temperature region. The importance of burnt gas temperature in flame extinguishment has also been highlighted in the asymptotic analysis [10] and numerical studies [11] of flames with Lewis number < 1.

Summary and Conclusions

The development and application of a detailed code for the simulation of unsteady three-dimensional flames has been discussed. Excellent scaling of the performance of this code on parallel processing computers has been demonstrated. A comparison of cellular flame structures predicted by this code with earlier two-dimensional simulations shows that the flames grow faster and split in lower concentration mixtures in three dimensions than in two. This finding clearly indicates the need for performing three-dimensional simulations of such phenomena. The successful development of this code has also opened up the possibility of studying the detailed dynamics of more complicated flame structures such as flame balls and flame strings.

The second problem reported was that of flame-vortex interactions under different gravitational environments. Phenomena such as flame extinguishment and the formation of pockets of unburned gases in the burnt region have been observed under conditions similar to those in drop-tower experiments. In all the cases studied, gravity is very important in determining the final shape of the flame. In downward propagation, buoyancy stabilizes the flame and a planar flame is restored. In zero gravity, a wrinkled flame is left behind. In upward propagation, the destabilizing effect of gravity can lead to some highly distorted flame shapes. The flame-vortex interaction itself is also influenced by gravity though not very strongly for the flames studied. In order to bring out the effects of gravity, flames with small Froude numbers and moderate Damkohler numbers must be studied. The relative role of radiative losses and stretch in the extinguishment of flames is also an issue that needs further investigation.

Acknowledgments

References

1. Kailasanath, K., Patnaik, G., and Oran, E.S., Third International Microgravity Combustion Workshop, NASA Conference Publication 10174, pp. 409-414, 1995.

2. Patnaik, G., Kailasanath, K., and Sinkovits, R.S., Proceedings of the 26th Symposium (International) on Combustion, The Combustion Institute, Pittsburg, PA., 1997.

3. Driscoll, J.F., Sinibaldi, J., and Sichel, M., Fourth International Microgravity Combustion Workshop, 1997.

4. Patnaik, G., Laskey, K.J., Kailasanath, K., Oran, E.S. and Brun, T.A., NRL Memorandum Report 6555, Naval Research Laboratory, Washington, D.C., 1989.

5. Kailasanath, K., Oran, E.S., and Boris, J.P., NRL Memorandum Report No. 4910, Naval Research Laboratory, Washington, D.C., 1982.

6. Moon, B., Patnaik, G., Bennett, R., Fyfe, D., Sussman, A., Douglas, C., Saltz, J., and Kailasanath, K., *Seventh SIAM Conference on Parallel Processing*, SIAM, New York, 1995.

7. Clavin, P., *Prog. Energy Combust. Sci.* 11:1-59 (1985).

8. Patnaik, G. and Kailasanath, K., *Twenty Third Symposium (International) on Combustion*, The Combustion Institute, Pittsburgh, PA, 1991, pp. 1641-1647.

9. Sinibaldi, J.O., Driscoll, J.F., Mueller, C.J., and Tulkki, A.E., AIAA Paper 97-0669, AIAA, Reston, VA, 1997.

10. Libby, P., Linan, A., and F. Williams, *Combust. Sci. Tech.*, Vol. 34, pp. 257-293, 1983.

11. Poinsot,T., Veynante, D., and Candel, S., *J. Fluid Mech.*, Vol. 228, pp. 561-606, 1991.
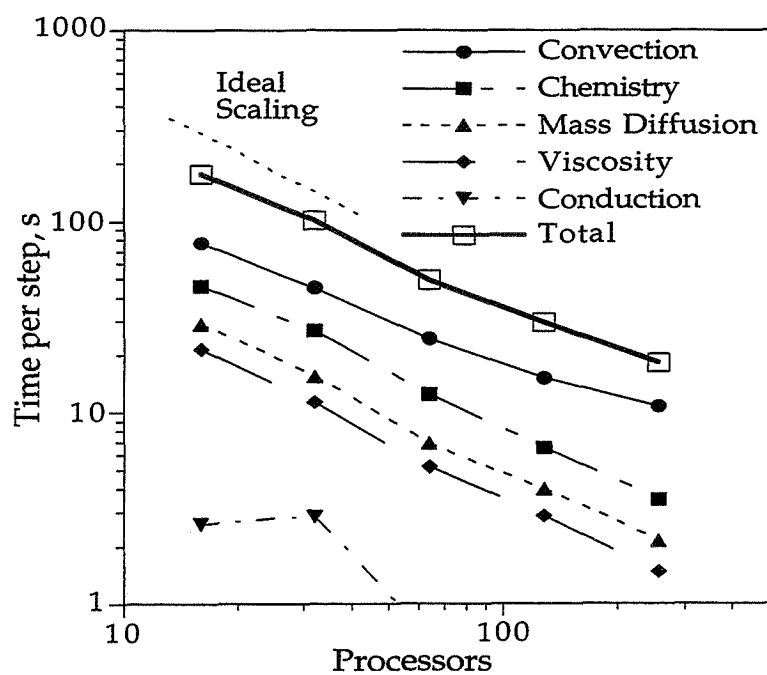
Fig. 1. Computation times on Intel Paragon with a 192 x 80 x 80 grid.
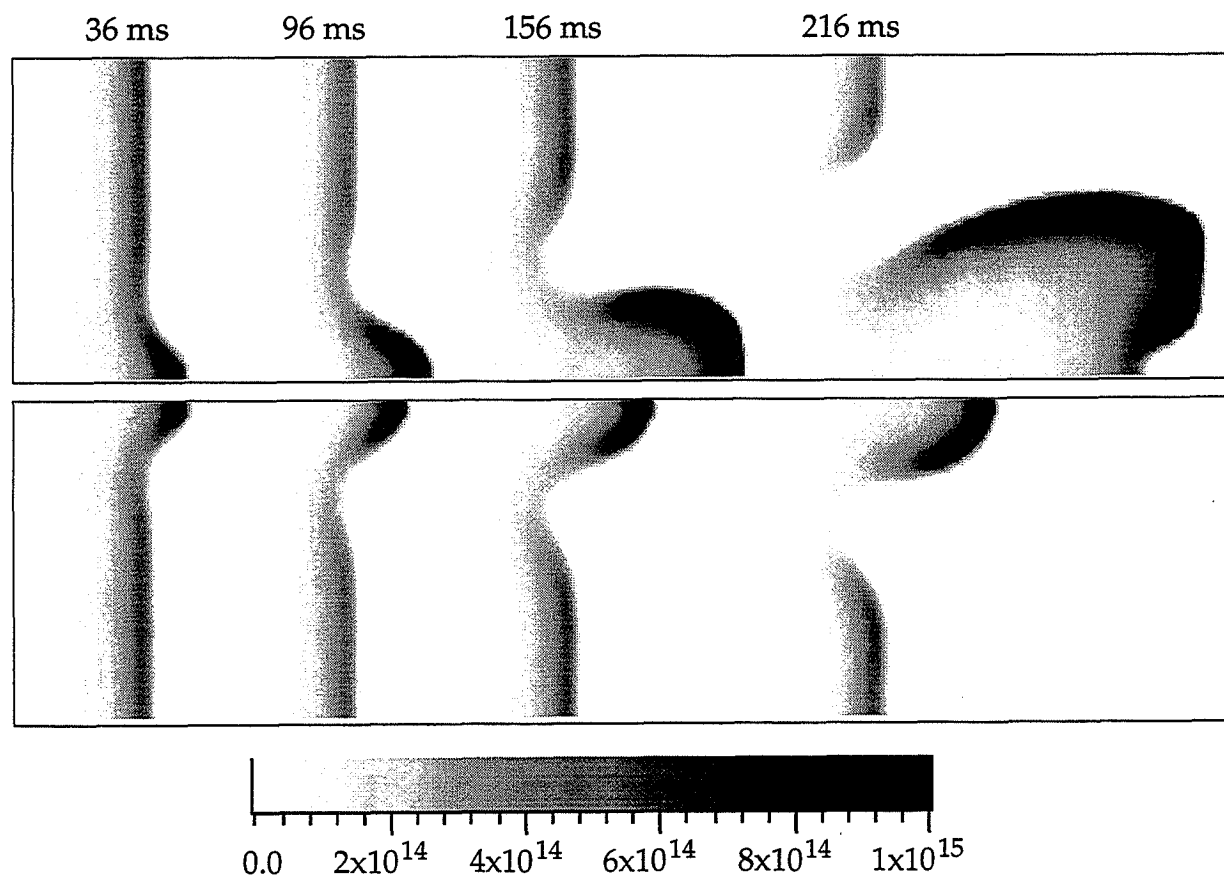
Fig. 2. Comparison of Cellular structures in slice through center of 3-D simulation (above) and 2-D simulation (below).
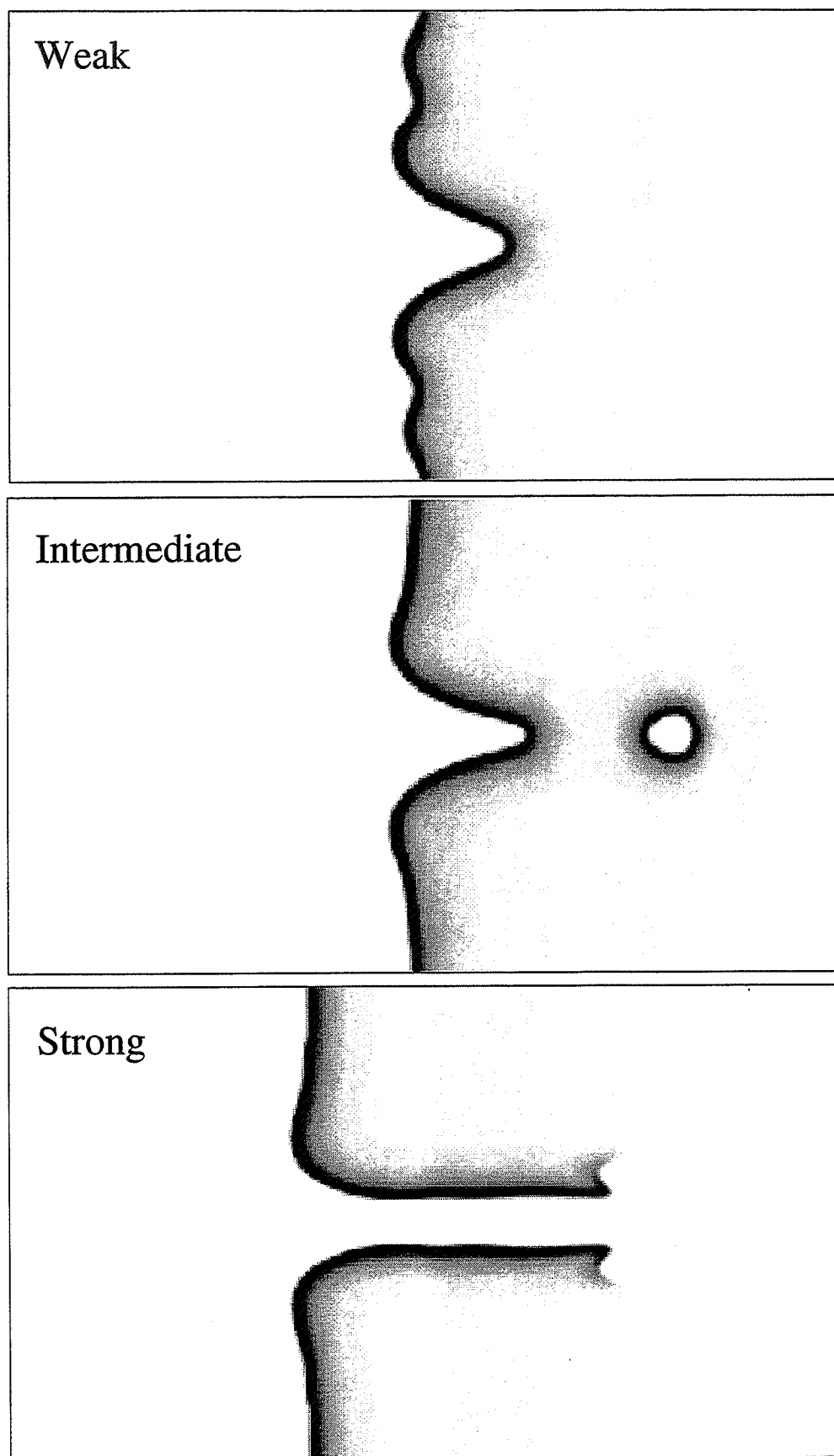
Fig. 3 OH mole fraction depicting the flame structure during interactions with vortices of different strengths.

PREMIXED FLAME -VORTEX INTERACTIONS IMAGED IN MICROGRAVITY

J. F. DRISCOLL, M. Sichel, J. O. Sinibaldi

Department of Aerospace Engineering, The University of Michigan, Ann Arbor, MI 48109

A unique experiment makes it now possible to obtain detailed images in microgravity showing how an individual vortex causes the wrinkling, stretching, area increase, and eventual extinction of a premixed flame. The repeatable, controllable flame-vortex interaction represents the fundamental building block of turbulent combustion concepts. New information is provided that is central to turbulent flame models, including measurements of all components of flame stretch, strain, and vorticity. Simultaneous measurements of all components of these quantities are not possible in fully turbulent flames but are possible in the present axisymmetric, repeatable experiment. Advanced PIV diagnostics have been used at one-g and have been developed for microgravity. Numerical simulations of the interaction are being performed by Dr. K. Kailasanath at NRL.

It is found that microgravity conditions greatly augment the flame wrinkling process. Flame area and the amplitude of wrinkles at zero-g are typically twice that observed at one-g. It is inferred that turbulent flames in microgravity could have larger surface area and thus propagate significantly faster than those in one-g, which is a potential safety hazard.

A new mechanism is identified by PIV images that shows how buoyancy retards flame wrinkling at one-g; buoyancy produces new vorticity (due to baroclinic torques) that oppose the wrinkling and the stretch imposed by the original vortex. Microgravity conditions remove this stabilizing mechanism and the amplitude of flame wrinkling typically is found to double. Microgravity also increases the flame speed by a factor of 1.8 to 2.2. Both methane and propane-air flames were studied at the NASA Lewis drop tower. Results indicate that it is important to add buoyancy to models of turbulent flames to simulate the correct flame wrinkling, stretch and burning velocity.

Microgravity Drop Tower Experiment and PIV Velocity Field Imaging

Results of the present NASA contract are summarized in three journal papers [1-3] that report local flame stretch rates, as well as Refs. 4 and 5 that report OH images and extinction limits. The experiment that was dropped at the NASA Lewis 2.2 Second Drop Tower is shown in Fig. 1. A chamber is filled with a lean propane-air or methane-air mixture (ϕ= 0.55) which is ignited such a flat laminar flame propagates downward at 10 cm/s. A loudspeaker is pulsed, forming a laminar toroidal vortex ring that moves upward. The microgravity flame is visualized using video camera images of flame emission; on other runs $SiO2$ solid particles are illuminated by a white light sheet formed using a pulsed Xenon arc lamp that provides 0.5 joule pulses at 60 pulses/sec with a 10 μs pulse duration that is short enough to freeze the fluid motion. Three vortex strengths were used, corresponding to the regimes of: wrinkled thin flames, corregated flames having pockets of unreacted gas, and local flame extinction.

Numerous PIV images have been obtained for the one-g tests, and a white light PIV system has been developed that will be used for the zero-g cases for which the flame shape already has been imaged. The one-g PIV measurements were made with exceptional spatial resolution (0.5 mm) such that vorticity and strain rate could be measured. The one-g PIV system consists of two YAG lasers used to produce two 100 mJ pulsed light sheets at 532 nm. Each photographic negative (70 mm Kodak Tech-Pan, 300 lines per mm) was scanned with a TSI Model 6000

Analyzer. A cross correlation method substantially increases the signal-to-noise over the standard autocorrelation method. There were 20 particle pairs in each interrogation spot and 50 particles/mm^3. The microgravity PIV system consists of two 10 μs pulsed Xenon white light sources (0.5 joule/pulse) that produce light sheets 2 mm thick.

Results: Flame Area and Wrinkle Amplitude - Microgravity Flames Compared to One-g Flames

Figure 2 shows PIV images obtained at one-g, while Fig. 3 compares microgravity flames and the one-g flames. For clarity, only every ninth velocity vector is plotted in Fig. 2. During flame crossing, the vorticity (shown on the right) decays to zero, but new "flame-generated vorticity" is measured for the first time in this study. The "flame-generated vorticity" is seen as the contours above the flame on the right side of Fig. 2; notice that the flow rotation above the flame is in the direction opposite to the initial vortex. The flame-generated vorticity is caused by buoyancy; baroclinic torques result from the pressure field due to gravity. A new mechanism has been identified which represents an additional way that buoyancy can stabilize a flame. That is, the buoyancy-induced "flame-generated vorticity reduces the amplitude of flame wrinkling because the velocity induced in the products in Fig. 2 creates a downward motion on the centerline above the flame. This motion significantly supresses the flame wrinkling, which occurs in the opposite direction.

Figure 3 shows that microgravity increases the flame area and wrinkling amplitude (by a factor of 1.5 to 2). Flame wrinkles on the right (microgravity conditions) are twice as large as on the left (one-g). Figure 4 quantifies the increase in flame wrinkling due to microgravity. Without buoyancy-induced stabilizing mechanisms, the flame area increases significantly. This increase in flame surface area is expected to result in larger turbulent burning velocities in microgravity. The microgravity flames are more severely thickened than the one-g flames, because buoyancy-induced "flame-generated' vorticity alters the extensive and compressive strain regions.

Measured Flame Stretch Rates

For the first time in a freely propagating flame, the local flame stretch rate has been measured. This parameter is important in all new theories of laminar and turbulent flames. Also measured is the velocity divergence (grad u) which quantifies the overall heat release rate. Figure 5 shows that a very large extensive stretch rate of 200 s^{-1} is exerted by the vortex on the flame on centerline; in addition, a strong compressive stretch rate of -200 s^{-1} is exerted near the neck of the wrinkled flame. For this lean propane-air condition (Ma = 8) theory predicts that chemistry is suppressed near centerline and is enhanced where the stretch is negative. The flame strength measurements (i.e., velocity divergence) in Fig. 4 are maximum in negative strain regions, showing that the theory is correct. The flame does not respond immediately to the imposed stretch rate on centerline (220 s^{-1}), which is five times the value of 42 s^{-1} that extinguishes a steady state counterflow flame. The flame does not immediately extinguish but requires 21 ms for extinction, which is several times the chemical time (α/S_L^2). Unsteady effects are important and a corresponding turbulent flame should be modeled as an unsteady counterflow flame which does not respond immediately to stretch.

Conclusions

1. The present experiment provides a very repeatable, controllable way to study how individual vortices interact with a flame. All components of stretch rates and vorticity have been measured at one-g and will be measured at zero-g, which is not possible in fully turbulent flames. Flame stretch was measured for the first time in a freely-propagating flame; this allows new theories of flame stretch effects to be assessed. The synchronization required to overlap the flame, vortex and light sheet during the NASA drop tests were successful.

2. Microgravity causes a significant increase in the amplitude of flame wrinkling and increase in the flame area as a vortex interacts with a premixed flame. This increase in flame area (by a factor of 1.5 to 2.0) occurs because microgravity removes the stabilizing effects of buoyancy.

3. A new mechanism is identified using PIV by which buoyancy creates "flame-generated vorticity" in the products which then induces fluid motions that supresses flame wrinkles. In microgravity, turbulent flames thus are

expected to have larger surface area, and propagate faster than at one-g. Microgravity also increases the laminar flame speed (S_L), which is consistent with previous studies in tubes.

4. The present experiment, along with the measured values of flame stretch rate, vorticity, OH concentrations, velocity profiles and flame strength, represent an ideal benchmark data set that is being compared to Direct Numerical Simulations. Solutions to the unsteady Navier Stokes equations with complex chemistry for the present conditions are being obtained by Dr. K. Kailasanath in another study in this microgravity program.

References

1. Sinibaldi, J.O., Driscoll, J.F., Mueller, C.J., Tulkki, A. "Flame-Vortex Interactions-Effects of Buoyancy Deduced from Microgravity Imaging Studies", submitted to AIAA Journal, 1997.
2. Mueller, C., Driscoll, J.F., Reuss, D., Drake, M., "Generation and Attenuation of Vorticity by Flames" to appear, Combustion and Flame, 1997.
3. Mueller, C., Driscoll, J. F., Reuss, D. and Drake, M. "Effect of Unsteady Stretch on the Strength of a Freely Propagating Flame Wrinkled by a Vortex", Proc. of the Twenty-Sixth Symp. on Combustion, 1996.
4. Mueller, C., Driscoll, J.F., Roberts, W.L., Drake, M.C., and Smooke, M.D., "Effect of Stretch Rate on Flame Chemistry To Assess Flamelet Models", Combustion and Flame 100, 323-331, 1995.
5. Roberts, W., Driscoll, J.F. "A Laminar Vortex Interacting With a Premixed Flame", Comb.Flame 87:245, 1991.

Figure 1. University of Michigan Flame-Vortex Interaction Drop Tower Experiment

1) Combustion Chamber
2) Power Supply (28 VDC)
3) Power Distribution Syst
4) TTL403 Computer
5) Xenon-Arc Lamp Elect
6) Xenon-Arc Lamp
7) Light Sheet Optics
8) CCD Camera
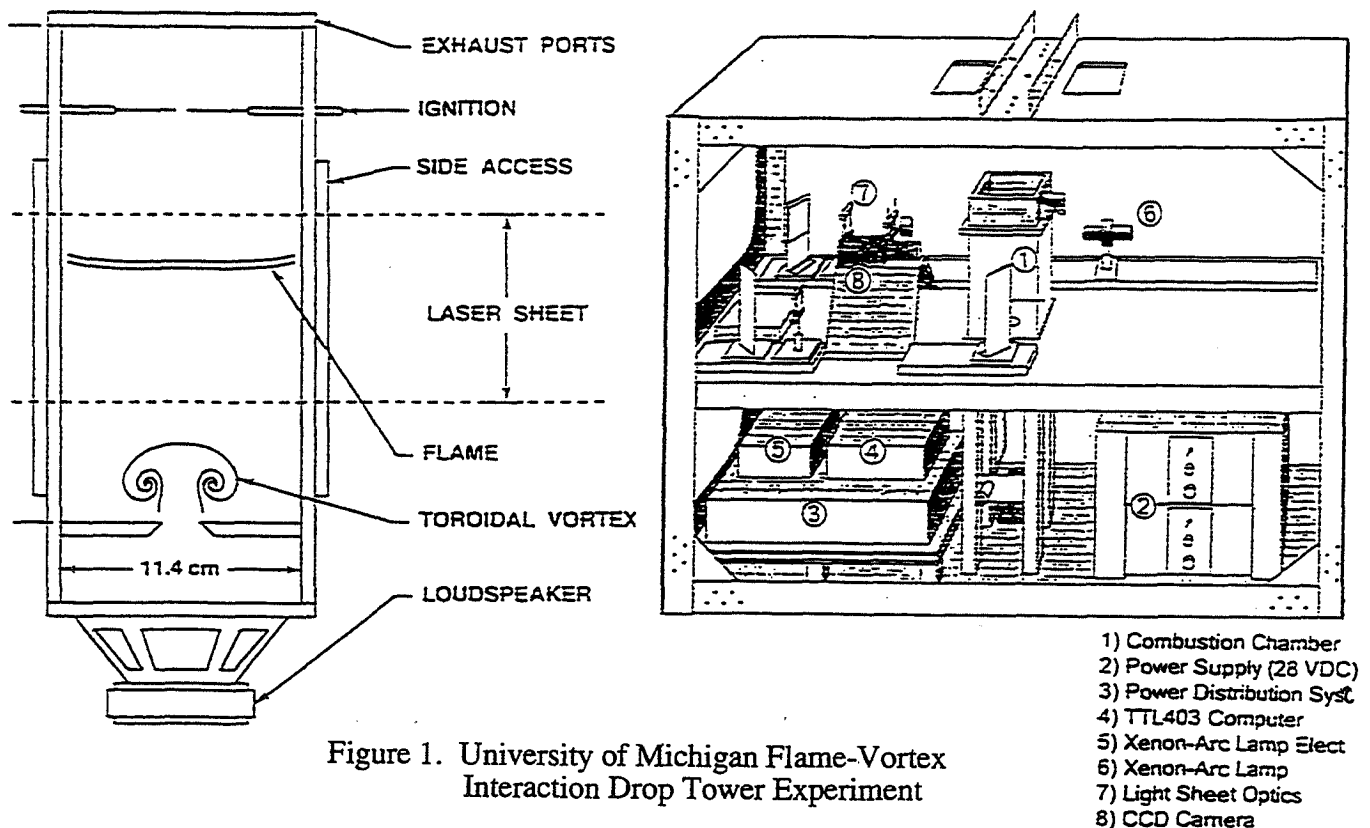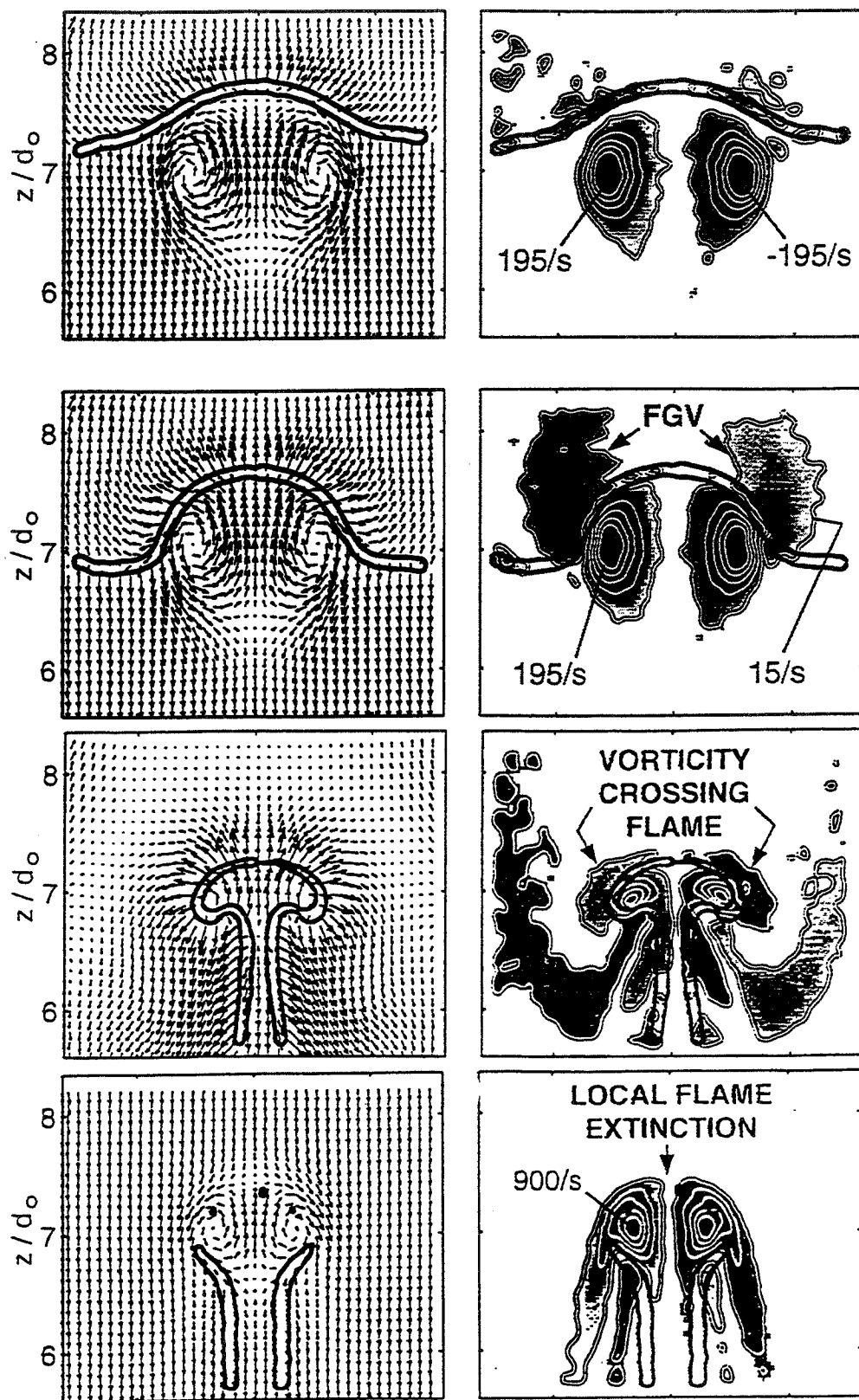
Figure 2. Vortex Passing Upward Over Flame at One-G. Left: Measured PIV velocity field; Right: Measured vorticity contours showing "flame-generated vorticity due to buoyancy above the flame; last image shows a local flame extinction case.
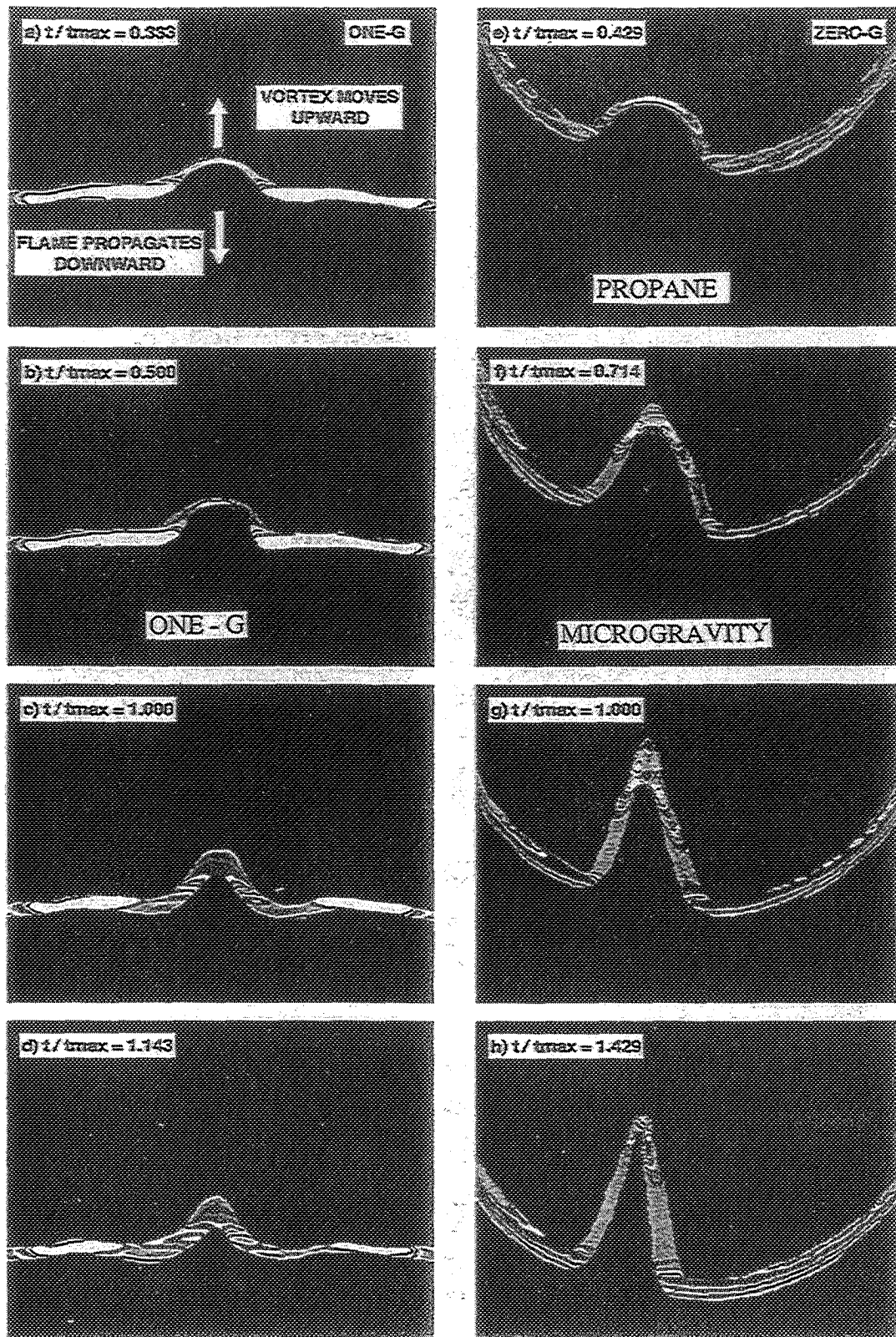
Figure 3: Increase In Flame Wrinkling Due To Microgravity For The Weak Vortex Interaction (Case A). Microgravity images appear on the right. Vortex moves upwards. tmax = time of maximum wrinkling = 100 ms (one-g), 167 ms (zero-g).
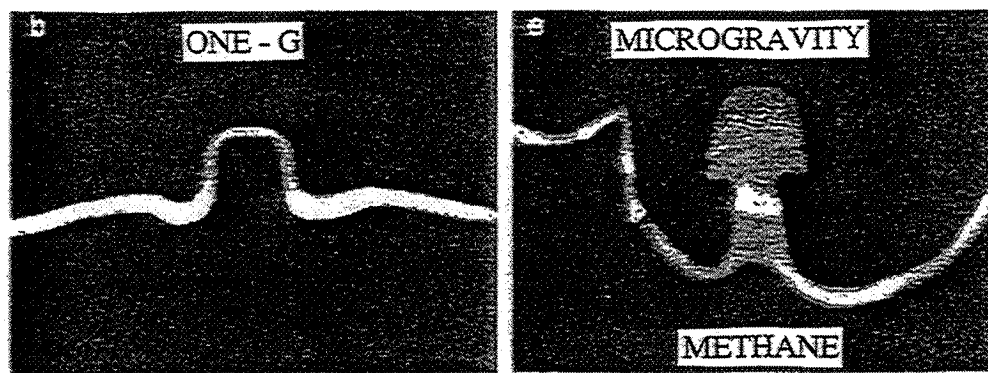
Figure 3. (continued)
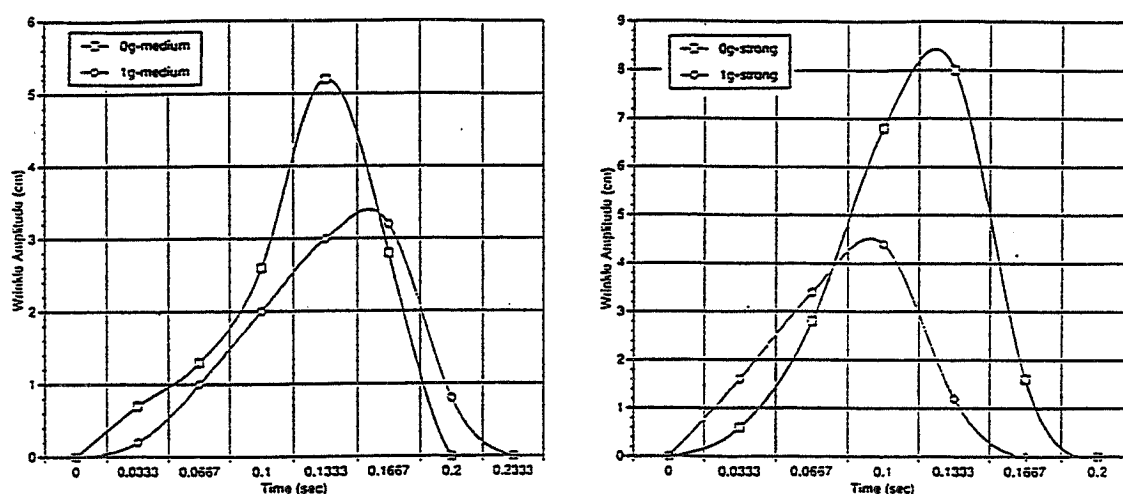
Figure 4. Measured Increase in Flame Wrinkle Amplitude and Flame Area Due to Microgravity.

a.

b.
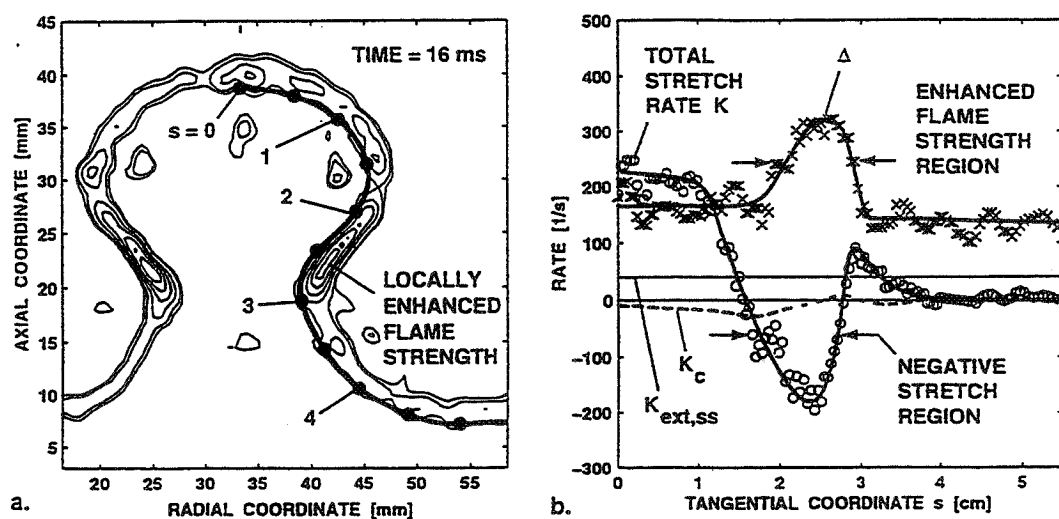
Figure 5. Measured Local Flame Stretch Rate and Its Effect on Flame Strength (Div u). Flame does not weaken where extensive strain is applied, contrary to steady state theory, but is enhanced where compressive strain is applied, in agreement with theory.

EFFECTS OF GRAVITY ON SHEARED AND NONSHEARED TURBULENT NONPREMIXED FLAMES[1]

SAID ELGHOBASHI, Oluş Boratav and Rongbin Zhong

Mechanical and Aerospace Engineering Department
University of California, Irvine, California 92697

Introduction

The present numerical study is concerned with the fundamental physics of the multi-way interaction between turbulence, chemical reaction and buoyancy in a nonpremixed flame. The method of direct numerical simulation (DNS) is used to solve the instantaneous three-dimensional governing equations (continuity, Navier-Stokes, species mass fractions and energy) under the zero-Mach number assumption. Because of the present supercomputer limitations, we consider two *simple* flow geometries, namely an initially uniform flow without shear (equivalent to grid-generated turbulence) and an initially uniform shear flow. In each flow, the fuel and oxidant initially exist as two separate streams. As the reactants mix, chemical reaction takes place and exothermic energy is released causing variations in density. In the presence of a gravity field, the spatial and temporal distributions of the induced buoyancy forces depend on the local density gradients and the direction of the gravitational acceleration.

Our **objective** is to gain an understanding of the complex interactions between the physical phenomena involved, with particular attention to the effects of buoyancy on the turbulence structure, flame behavior and factors influencing flame extinction.

We focus our attention to a location in the vicinity of the interface between two initially homogeneous gaseous reactant streams in an unbounded domain. The three-dimensional flow field is initially homogeneous isotropic or sheared turbulence with subsequent development due to density variation arising from chemical energy release and gravitational effects. We consider a simple one-step irreversible chemical reaction in which two nonpremixed reactants (fuel and oxidant) react to form product. Both finite and infinite reaction rates are considered. In the case of an infinite reaction rate, a conserved scalar formulation is employed. Whereas the fluid density is a function of space and time, the transport properties such as the kinematic viscosity, thermal conductivity, and mass diffusion coefficient are assumed constant. The dependence of these properties on temperature and concentration will be considered later in the study.

In our paper presented at the Third Microgravity Combustion Conference (ref.1) we presented the governing equations and the numerical procedure and discussed the effects of buoyancy on the vorticity field and the spectra of turbulence energy. In the present paper, we discuss the effects of buoyancy on the enstrophy, the topology and stretching of the flame surface and the reaction rate. In addition, we examine the alignment between the vorticity vector and the eigen-directions of the strain rate tensor in zero- and finite-gravity.

Results

Table I lists the conditions of the fifteen test cases which we completed during the past 18 months. The Froude number is defined as $U_o^2/(L_o g)$ where U_o and L_o are reference velocity and length scales respectively and g is the magnitude of gravitational acceleration. The time, t, throughout the manuscript is the non-dimensional time where the reference time used in the non-dimensionalization is L_o/U_o.

We initialize the flow field with a prescribed turbulence energy spectrum, $E(k) \sim ke^{-k}$, where k is the wave number. The initial Reynolds number based on the Taylor microscale $R_\lambda = 25$ for all cases except for those with the highest resolution, 128^3 mesh points, where R_λ equals 35. We allow the flow to develop until the velocity derivative skewness reaches a value $\approx$ -0.5 (the nearly asymptotic value for decaying isotropic turbulence), at which time we start the chemical reaction between two horizontal nonpremixed streams, fuel on the upper side and oxidant on the lower side. The gravity vector is in the vertical direction, i.e. perpendicular to the initial interface between the two streams. We define the resulting flame as the instantaneous three-dimensional surface coinciding with the stoichiometric mixture fraction, F_{st}, surface. We terminate the simulation before the expanding flow starts to invalidate the imposed boundary conditions.

Effects of Gravity on the Enstrophy

In this section, we summarize the results of our detailed analysis of the vorticity field and the enstrophy budget in the buoyant and nonbuoyant flames. Comparison of the vorticity distributions in the two cases, shows that (Figures are not presented due to space limitation): i) The vorticity vanishes in the reaction zone in the zero gravity case whereas it is augmented considerably in the buoyant flame. ii) The vortices of the buoyant flame are located in dipolar form: two oppositely-signed vortices saddle the F_{st} surface. iii) For the buoyant flame, the fuel side of the F_{st} surface ($F > F_{st}$) has stronger vorticity compared to the oxidant side ($F < F_{st}$). iv) The mixture fraction F contours for the buoyant flame are more convoluted than those of the nonbuoyant flame.

The effects of gravity on the vorticity, ω, field can be understood by examining the dimensionless transport equation of the enstrophy, $\Omega \equiv \frac{1}{2}\omega \cdot \omega$, for variable density flows :

$$\frac{\partial \Omega}{\partial t} + u \cdot \nabla \Omega = \underbrace{-\frac{1}{\rho^2}[\omega \cdot (\nabla P \times \nabla \rho)]}_{Baroclinic} \underbrace{-2\Omega(\nabla \cdot u)}_{Divergence} \underbrace{+\omega \cdot S \cdot \omega}_{Stretching}$$
$$\underbrace{+\frac{1}{\rho Re}\omega \cdot \nabla^2 \omega - \omega \cdot \frac{1}{\rho^2 Re}\nabla \rho \times [\nabla^2 u + \frac{1}{3}\nabla(\nabla \cdot u)]}_{Viscous} , \qquad (1)$$

where S is the rate of strain tensor and Re is the Reynolds number.

We examined the contribution of each term in Eq. (1) to the overall budget of Ω in nonbuoyant and buoyant flames, in different mixture fraction F bands. Detailed analysis of the divergence of the velocity field, $\nabla \cdot u$, the angle between the gradients of the pressure and density, and the correlation between the strain and vorticity show that, in zero gravity: i) In the vicinity of F_{st}, all the terms have negligible contribution. ii) Almost in all F bands, the magnitude of the baroclinic term is larger than that of the vortex stretching term. iii) The divergence term is negative almost everywhere and is of the same order of magnitude as the baroclinic term. iv) The pdf's of the terms in the enstrophy equation are symmetrical with respect to F_{st}.

The results for the buoyant flame show that: i) The baroclinic term is positive everywhere and its magnitude is higher than that of all the other terms. Also, its magnitude is much larger in the bands $F > F_{st}$ than in the $F < F_{st}$ bands. ii) The vortex stretching term is positive and large for $F \geq F_{st}$ bands and attains negative values for $F < F_{st}$ bands. iii) The velocity divergence term is negative for $F < F_{st}$ bands and positive for $F > F_{st}$ bands. iv) None of the pdf's is symmetrical with respect to F_{st}.

The above results provide an explanation for the increased reaction rate in buoyant flames. *First*, the flow field produced by the counter-rotating vortices generate a strain field that is responsible for forming *crests* and *troughs* and increased flame surface area-as will be discussed in the next section. *Second*, the vorticity/strain characteristics of the buoyant flame govern the alignment between the scalar gradient and the strain rate tensor eigendirections. This alignment is essential for predicting the spatial distribution of the reaction rate.

Effects of Gravity on Flame Surface Topology and Stretching

An important role of the strong counter-rotating vortices formed in the buoyant flow is to wrinkle the flame surface. In zero gravity, on the other hand, the velocity divergence due to the energy release acts as a sink of vorticity (see Eq. (1)), and hence the relatively smooth flame surface. The absence of wrinkling in this case allows $\nabla \rho$ to be nearly aligned with ∇P and hence a diminished baroclinic torque and vorticity production. Buoyancy also increases the total consumption rate of reactants as shown in Figure (1a). The time evolution of the reaction rates shows that the reactant consumption rate in the buoyant flame becomes 5 times larger than that in the nonbuoyant flame at the end of the simulation ($t = 7.5$).

It is clear from Fig. (1a) that buoyancy increases both the total flame surface area and the local reaction rate per unit surface area. In order to study the mechanism by which the reaction rate per unit surface area increases, we examine the equations governing the behavior of the F_{st} isosurface, and use DNS results to evaluate the individual terms in these equations. We have studied the topology of the flame surface (via the distribution of the mean curvature and shape parameter). However, due to space limitations, we will present a summary of our results. The details are available in (ref. 2).

We denote the region with positive mean curvature (i.e. $\nabla \cdot n > 0$) as *crest*, and the region with negative mean curvature (i.e. $\nabla \cdot n < 0$) as *trough* (see Fig. (1b)), where n is the normal to the iso-scalar surface.

In order to understand the different mechanisms which contribute to the rate of change of the area of the F_{st} isosurface, we computed each term in the equation governing the flame surface stretch rate of a surface, ϕ_s given by (ref.3):

$$\phi_s \equiv \frac{1}{\delta A} \frac{d \delta A}{dt} = S_T + u_n \nabla \cdot n \tag{2}$$

The term $S_T (\equiv -nn : \nabla u + \nabla \cdot u)$ is the rate of strain acting in the tangential plane of the iso-scalar surface. The term, $(u_n \nabla \cdot n)$, describes the effect of the flame curvature on the stretch rate ϕ_s, where u_n is the propagation velocity of the isosurface (normal to the isosurface and relative to the local fluid). The variation of the two terms on the RHS of Eq. (2) with the mean curvature is presented in Figs. (2a) and (2b). For the nonbuoyant flame, Fig. (2a) shows that the two terms and their sum are not sensitive to whether the mean curvature is positive or negative. Also, the magnitude of the tangential strain S_T is much less than that of the *surface propagation term due to curvature* $(u_n \nabla \cdot n)$. Fig. (2a) also shows that $(u_n \nabla \cdot n)$ is negative everywhere, both in positive and negative mean curvature regions. This indicates that u_n and $\nabla \cdot n$ have opposite signs, and thus u_n is always directed toward the center of curvature.

The results are quite different for the buoyant flame as seen in Fig. (2b). *First*, the strain rate values are much larger than those of the nonbuoyant flame. For example, for the large positive curvature regions, the average ϕ_s values are about seven times larger than those for the nonbuoyant flame. *Second*, ϕ_s is negative at the crests and positive at the troughs. This implies that the crests are being compressed while the troughs are being extended. *Third*, the amount of compression in the crests is much larger than the amount of extension in the troughs. The average ϕ_s value in regions of large negative curvature is about four times that in the regions of positive curvature. *Fourth*, since the amount of space occupied by the crests is much smaller than that by the troughs, the contribution to the overall ϕ_s PDF is mostly from the positive stretch region i.e. the troughs. *Finally*, our analysis indicates that (figure is not shown here) unlike the nonbuoyant case, there are large negative curvature regions where the tangential strain is as large in magnitude as the *surface propagation strain*. These regions correspond to troughs where the positive S_T values slightly exceed the negative $(u_n \nabla \cdot n)$ values on the average, resulting in a positive average, or extension of the troughs.

The higher consumption rate of reactants in the buoyant flame depend on the topology. Our analysis shows that *both* the flame wrinkling and the increased local reaction rate contribute to the higher consumption rate observed in buoyant flames. The main mechanism responsible for the flame wrinkling is the buoyancy-generated dipolar vortices (formed mainly by baroclinic effects) which produce a particular strain field manifesting itself in the *crest/trough* type topology formation.

175

The main mechanism responsible for the increased local reaction rate is again the dipolar vortices which increase the magnitude of the local strain compared to that in the nonbuoyant flame. The dipolar vortices in the vicinity of F_{st} produce a strain-dominated field which enhances the alignment of the vorticity vector with the α (extensional) eigenvector of the strain rate tensor and thus enhancing the alignment of ∇F with γ (compressive) strain direction. This alignment of ∇F and γ directly augments the production rate of the scalar dissipation rate, ϵ_F, and thus enhances the local reaction rate.

Effects of gravity on the Alignment of Vorticity and Eigenvectors of Strain Rate

In order to understand the rate of change of vorticity in any flow, one has to examine the vorticity-strain correlations and particularly the evolution equations for the (cosine of) angle between the vorticity vector and the eigen-directions of the strain rate tensor. For example, the vorticity will be augmented if the vorticity vector is aligned with the extensional strain direction. In order to to understand the effects of buoyancy on the alignment, we derived the evolution equations, in a rotating frame, for the cosine of the angle between the vorticity vector and the α, β and γ eigen-directions of the strain rate tensor. The resulting equation is (ref.4):

$$\frac{d}{dt}\hat{\Omega} = \begin{pmatrix} \alpha - D & 0 & 0 \\ 0 & \beta - D & 0 \\ 0 & 0 & \gamma - D \end{pmatrix} \hat{\Omega} - \zeta_{vorticity}\hat{\Omega} - \vec{\Omega}' \times \hat{\Omega} + \hat{B} \quad , \tag{3}$$

where $\hat{\Omega}$ is the cosine of the angle, α, β, γ are the eigenvalues of the strain tensor S_{ij} (which is *not* deviatoric), D is simply the sum of the eigenvalues ($D = \alpha + \beta + \gamma$). $\zeta_{vorticity}$ is the vorticity stretching rate and is equal to $\left(s_i\hat{\Omega}_i^2 - D\right)$, summation convention used, where s_i's are the eigenvalues α, β, and γ. The *'perfect alignment'* for the vorticity elements corresponds to $\hat{\Omega} = (\pm 1, 0, 0)$ since for this case, the vorticity element is parallel to the direction of the most extensional strain, α (i.e. $\hat{\omega} = \hat{\zeta}_1$, where $\hat{\zeta}_1$ is the direction of the most extensional strain). This perfect alignment occurs at an exponential rate and only when the last three terms on the RHS of Eq. (3) vanish. Note that the divergence D appearing in both the prefactor matrix of $\hat{\Omega}$ and $\zeta_{vorticity}$ cancel each other implying that the velocity divergence term has no contribution to the alignment. $\hat{B}$ in Eq. (3) is the baroclinic term projected on the strain coordinates. Even though the magnitude and the direction of the baroclinic term do *not* change significantly throughout our simulations, $\hat{B}$ produces a coriolis effect due to the rotation of the coordinate system. This coriolis effect can be expressed as:

$$(\nabla P \times \nabla \rho) \times \vec{\Omega}' = -[(\vec{\Omega}' \cdot \nabla \rho)\nabla P - (\vec{\Omega}' \cdot \nabla P)\nabla \rho] \quad , \tag{4}$$

where the direction cosines of projection can be ignored without loss of generality.

Equation (4) shows that the resulting vector has components along ∇P as well as along $\nabla \rho$ direction. Now, in the absence of all terms except the first two on the right-hand-side of Eq. (3), the vorticity will align along the α-strain. However, the coriolis effect of the baroclinic term (Eq. (4)) diverts the vorticity vector away from the α direction since ∇P direction is perpendicular to the vorticity direction. Thus, we conclude that when the strain term dominates over the rotation and baroclinic terms, the vorticity vector is expected to align with the α direction. We examined in detail the correlation between the strain-dominated regions and the vorticity/α-eigendirection alignment, and conclude that: i) Wherever there is strain-dominance in the field, there is a stronger tendency of vorticity/α-strain direction alignment. ii) When the rotational effects become strong, the vorticity/α-strain alignment diminishes, and the vorticity/β-strain alignment increases (figure is not shown).

These results have direct consequences on the alignment between ∇F and the vorticity, since the rate of change of ∇F vector is along the perpendicular to the vorticity vector (as can be shown by the ∇F transport equation). Hence, in regions where there is mostly α and some β alignment between vorticity and strain eigendirections, there is strong $\nabla F/\gamma$ alignment which yields high scalar dissipation and high reaction rate zones.

Conclusions

Our main objective in this study is to understand how the buoyancy modifies the structure of turbulent nonpremixed flames and why the resulting reaction rates are higher than in zero gravity flames.

First, we examined the vorticity structure and enstrophy budget in the vicinity of the F_{st} isosurface. The results can be summarized in the following flowchart:

Finite gravity $\implies$ Strong baroclinic production of vorticity $\implies$ Dipolar vortex generation $\implies$ Dipolar vortices wrinkle the flame surface and generate crests & troughs $\implies$ Vortices increase the flame stretch near troughs $\implies$ Surface area increases near troughs $\implies$ Highest reaction rate near troughs.

Second, we examined the alignment of the vorticity and strain rate eigenvectors. The results can be summarized as follows:

Strong strain-dominance near F_{st} $\implies$ Strong vorticity/α alignment near F_{st} $\implies$ Strong $\nabla F/\gamma$ alignment near F_{st} $\implies$ Large ϵ_F near F_{st} $\implies$ Highest reaction rate near F_{st}

Future Work

We are currently focusing on: i) The interaction between homogeneous shear, chemical reaction and buoyancy; ii) The effect of varying the direction of the gravity vector relative to the F/O interface plane (from normal or parallel).

References

[1] S. Elghobashi, Y. Y. Lee and R. Zhong, "Effects of Gravity on Sheared and Nonsheared Turbulent Nonpremixed Flames", Third International Microgravity Combustion Conference. (1995)

[2] R. Zhong, O. N. Boratav, and S. E. Elghobashi, "Flame Surface Topology in Turbulent Nonpremixed Reacting Flow under Buoyancy, preprint. To be submitted to Phys. Fluids.

[3] S. M. Candel, T. J. Poinsot, "Flame stretch and the balance equation for the flame area", Combust. Sci. and Tech., **70**, 1-15, (1990).

[4] O. N. Boratav, S. E. Elghobashi and R. Zhong, "On the Alignment of α-strain and Vorticity in Turbulent Nonpremixed Flames", Phys. Fluids. **8(8)**, 1-3 (1996).

Table 1: Test Cases

Gravity Magnitude	Froude Number	Damköhler Number	Mesh Points	Initial R_λ	Maximum Time
zero	Incompressible	No reaction	96^3	25	6
zero	∞	∞	64^3, 96^3	25	6
zero	∞	∞	64^3, 96^3	25	6
zero	∞	7500	64^3, 96^3	25	6
zero	∞	5000	96^3	25	6
zero	∞	5000	128^3	35	7.5
zero	∞	2500	96^3	25	6
zero	∞	1000	96^3	25	6
finite	7	∞	64^3, 96^3	25	6
finite	10	∞	64^3, 96^3	25	6
finite	17	∞	96^3	25	6
finite	10	5000	128^3	35	7.5
finite	10	7500	96^3	25	6
finite	10	5000	96^3	25	6
finite	10	2500	96^3	25	6
finite	10	1000	96^3	25	6
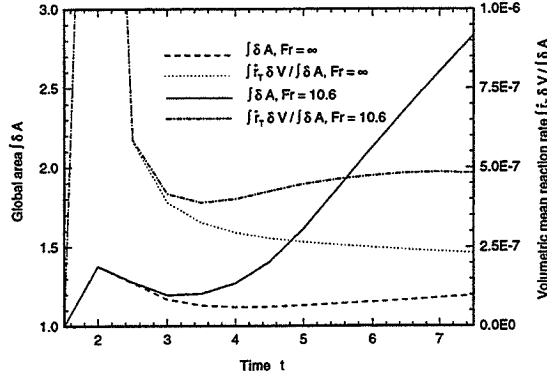
(a)
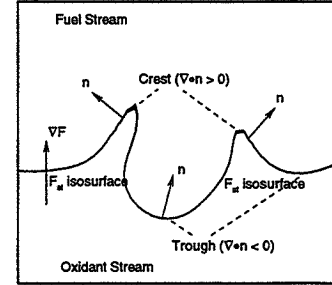
(b)

Figure 1: (a) Evolution of flame surface area and volumetric reaction rate in nonbuoyant (dotted and dashed) and buoyant (solid and dotted-dashed) runs. (b) Nomenclature and selected sign convention for the curvature ($\nabla \cdot n$) and surface normal (n). *Crests* and *Troughs* correspond to regions of positive and negative curvature respectively.
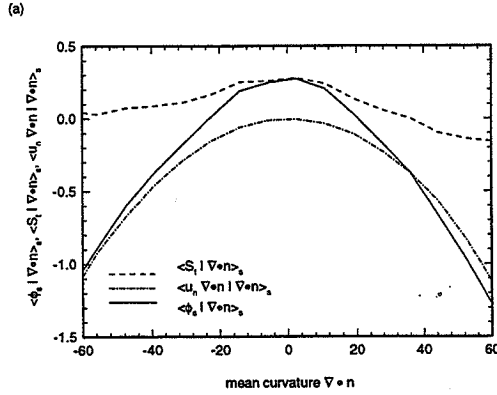
(a)
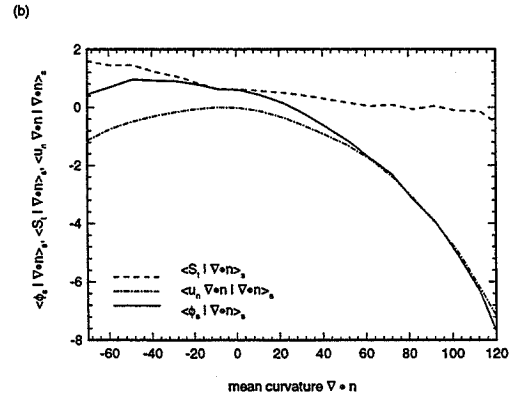
(b)

Figure 2: (a, b) Surface mean stretch rate ϕ_s (solid lines) tangential strain rate S_t (dashed) and the propagation term $u_n \nabla \cdot n$ (dashed-dotted) for (a) nonbuoyant flame ($Fr = \infty$) (b) buoyant flame ($Fr = 10.6$)

178

STRUCTURE OF MICROGRAVITY TRANSITIONAL AND PULSED JET DIFFUSION FLAMES[*]

M. YOUSEF BAHADORI
Science Applications International Corporation
Torrance, California

Uday Hegde
NYMA, Inc.
Brook Park, Ohio

and

Dennis P. Stocker
NASA Lewis Research Center
Cleveland, Ohio

Introduction

This paper describes results obtained in a study of pulsed gas jet diffusion flames to better characterize the recently observed vortex/flame interactions in microgravity transitional and turbulent diffusion flames (refs. 1 and 2), and to improve the understanding of large-scale structures in corresponding normal-gravity flames. In preparation for a space experiment, tests were conducted in the 5.18-Second Zero-Gravity Facility of the NASA Lewis Research Center. Both unpulsed and pulsed laminar flames were studied and numerical modeling of these flames was carried out for data comparison and model validation. In addition, complimentary tests for a series of unpulsed flames were conducted on-board the NASA KC-135 research aircraft.

The microgravity transitional and turbulent gas-jet diffusion flames have been observed to be dominated by large-scale disturbances, or structures. These structures first appear intermittently in the flame at Reynolds numbers (based on the cold jet injection properties) of about 2100 (ref. 1). With increase in injection Reynolds number, the rate of intermittent disturbances increases until the generation becomes continuous at Reynolds numbers of 3000 and higher. The behavior of these structures depends upon the velocity and temperature characteristics of the jet/flame shear layer. These characteristics are different in normal gravity and microgravity (ref. 2).

Large-scale structures are an integral part of turbulent flames in normal gravity as well, but these evolve and interact with the flame in a different manner compared to the microgravity case. In normal gravity, the two primary mechanisms for large-scale vortex generation are the instability of the central fuel jet and the instability of the buoyancy induced natural convection layer on the outside of the flame. Vortices generated by these mechanisms then evolve by interaction with the flame and each other. One of the results of this interaction is flame flicker (e.g., ref. 3). In microgravity, the buoyancy induced convection layer does not occur, and interactions between buoyancy-generated structures and other vortices are absent. Consequently, flame flicker is also absent. Previous normal-gravity investigations (e.g., ref. 4) have studied the interaction of well-defined and controlled vortices with the flame. It is found that enhanced entrainment may occur, and that vortex/flame coupling has an important influence on time-dependent flame behavior. These studies also show that coupling between buoyancy-generated and jet-instability generated vortices may dominate the behavior of the flame, particularly in the downstream regions. It is then of fundamental interest to investigate the behavior of pulsed diffusion flames in microgravity where buoyancy-induced structures are absent.

In the present study, large-scale, controlled disturbances are imposed on a well-defined microgravity laminar diffusion flame to better understand the effects of the structure parameters (e.g., frequency) responsible for the observed characteristics of transitional and turbulent gas jet diffusion flames. A novel technique, utilizing a sinusoidally driven iris is used to provide harmonic axisymmetric disturbances for interaction with the flame. In the following sections, the experimental method, the modeling approach, and comparisons between data and predictions are presented.

Experimental

The microgravity experiments were conducted at the 5.18-Second Zero-Gravity Facility of the NASA Lewis Research Center. The cylindrical experiment chamber was approximately 87 liters in volume with a length of about 50 cm. Propane was injected into quiescent air at atmospheric pressure through a 1.65-mm diameter nozzle made of stainless steel tubing. The nozzle tip was located 5 cm above a base plate which held the nozzle and igniter assembly. The volume flow rate of fuel was 2 scc/sec, corresponding to a cold jet Reynolds number of approximately 400. Ignition occurred shortly after the drop commenced, and was initiated by a hot wire mounted on a rotary actuator which retracted the igniter out of the flow field after ignition. Both unpulsed and pulsed flames were studied, and imposed pulsations commenced approximately two seconds after start of the drop and continued until the end of the drop.

The disturbance mechanism utilized an iris mounted approximately 5 mm above the exit plane of the nozzle. The iris opening was changed by a rotary movement of the iris leaves about pivot points, actuated by a stepper motor. The open diameter varied in a sinusoidal fashion at the selected frequency. The amount of angular movement of each leaf was limited to less than 10 degrees, so that points on the leaf moved predominantly in a radial direction giving rise to an axisymmetric excitation of the flame. The open diameter of the iris was varied sinusoidally between 1.5 cm and 2.5 cm. This range was selected based upon considerations of flame diameter and forcing disturbance strength, and ensured that the iris leaves would not physically cut into the flame and act as a heat sink. Also, this variation in iris diameter provided a disturbance of sufficient strength that could be measured by the thermocouples and radiometers. The pulsation frequencies were in the range of 0-10 Hz. There were two main reasons for selecting this range. First, this range is consistent with the frequencies of occurrence of large-scale structures that have previously been observed in microgravity transitional flames. Second, this range yields structures that have been found to interact with the buoyancy-generated structures in normal-gravity flames. It is of fundamental interest to ascertain the behavior of the structures in microgravity where such interactions are absent.

Orthogonal side views of the flame were imaged by video cameras at 30 frames per second. Type K thermocouples with bead sizes in the range of 150-200 microns were used at various axial and radial locations above the nozzle exit plane. Thermopile radiometers were mounted at a radial distance of 10 cm from the flame centerline. Both global radiation and radiation from a wedge-shaped slice of the flame (using a lens assembly mounted to the face of the radiometer) were measured. The height and width of the wedge at the flame centerline were approximately 6 mm and 18 mm, respectively. The slice radiometer was equipped with a bandpass filter centered at 1865 nm with a halfwidth of 105 nm. This wavelength corresponds to water vapor radiation. The slice radiometer enabled obtaining local oscillations of flame radiation, and was located at 4 cm above the nozzle tip. The thermocouple and radiometer data were sampled in excess of 500 Hz. Since the oscillatory response of the flame was of interest, the measured signals from the thermocouples and the radiometer have to be compensated for their time response. Measured time constants of thermocouples were in the range of 120-250 milliseconds depending upon thermocouple location, with the lower thermocouple registering the smaller time constants. The obtained time constant for the radiometer was of the order of 30 milliseconds.

In addition to tests conducted for pulsed flames in the Zero-Gravity Facility, flames were studied on-board the KC-135 research aircraft to better understand the behavior of jet diffusion flames under reduced-gravity conditions. These tests provided data such as flame radiation and flicker frequency as a function of gravitational level. Flame visualization (using video cameras at 30 frames per second) and radiation measurements (using a thermopile detector) were obtained. These tests provided better insight into the characteristics of flames under partial-gravity level, and helped in the model validation, as discussed later.

Theoretical

Two numerical models, a steady state model and a transient model, are being developed in this study. The steady, two-dimensional model which is constructed for studying axisymmetric laminar diffusion flames, incorporates the effects of inertia, viscosity, diffusion, gravity, and combustion in the boundary layer form of the partial differential equations for mass, momentum, energy, and species (ref. 5). These governing equations and their associated boundary conditions are transformed into the von Mises plane, and then solved numerically using an explicit finite-difference scheme. Radiation from water vapor and carbon dioxide is accounted for through the assumption of optically thin medium. Soot is not accounted for in this model, although it contributes to radiation. However, previous measurements suggest that most of the radiative loss in the investigated microgravity flames is from carbon dioxide and water vapor (ref. 1). The combustion model is that of a shifting equilibrium. Details of the flow field such as velocity, temperature, radiative loss, and flame shape have been predicted, and some of the results are presented later.

The numerical model of the pulsed laminar flame provides the capability of calculating transient-flame behavior under imposed disturbances. This comprehensive transient, Navier-Stokes model is utilized to predict the characteristics of the flame under the influence of imposed oscillations. The model can be one-, two-, or three-dimensional, and Cartesian, cylindrical, or curvilinear systems with non-orthogonal coordinates can be selected. The model provides velocity, pressure, temperature, and species fields in the presence of convective, conductive, and radiative heat transfer. Both diffusion-controlled and kinetic-controlled combustion models can be used. Radiation models, e.g., flux model, are structured in the code. Predictions such as oscillatory flame shapes, oscillatory temperature field, and oscillatory velocity field in the flame can be obtained, as discussed in the next section.

Results and Discussion

The measured and predicted centerline temperatures for a laminar, unpulsed microgravity propane flame are shown in Fig. 1. Predictions indicate that the temperature increases initially, and then (unlike temperature in normal-gravity flame) decays monotonically, except in a small region around $x = 12$ cm. This location corresponds to the theoretical flame tip. Beyond the flame tip, the temperature is predicted to drop again. The measurements are in good agreement with predictions considering the insufficient microgravity time available in the drop test. Estimates based upon radial diffusion suggest a quasi-steady state after about 15 seconds of burning. It must be noted that, on the other hand, the corresponding normal-gravity flame establishes in a fraction of a second following ignition, due to the presence of buoyant force and associated entrainment. The predicted and measured radial distribution of temperature at the axial location of 5 cm are shown in Fig. 2 for the microgravity flame. The trend of the data is in good agreement with the predicted radial distributions.

Different investigations (e.g., ref. 3) have shown that the frequency of oscillation of a normal-gravity laminar diffusion flame burning in quiescent oxidizing environments is in the 10-18 Hz range. These flames flicker due to hydrodynamic instability. Data on flame oscillation as a function of gravity (except for the normal-gravity case) are difficult to obtain. To date, no data on flame flicker has been available for partial gravity. The aircraft tests of a methane flame (2.5 scc/sec flow rate) provided the required data. Figure 3 shows the relationship between flicker frequency and gravitational level (see ref. 6). This relationship is in satisfactory agreement with that obtained in a separate study for high gravity levels (ref. 7).

Gravitational level was also shown to have a significant effect on global radiation from the flame. Figure 4 shows the radiation level for the range microgravity to 1.5g. The tests were conducted in the KC-135 aircraft for methane flames. With the aid of the steady state numerical model, it is shown that the predicted radiation level agrees with the data. Note that radiation from a microgravity flame can be up to an order of magnitude higher than that of a normal-gravity (or higher-g) flame due to the strong influence of buoyant effects and the resulting differences in the temperature, velocity, and species (especially the radiating water vapor and carbon dioxide) fields of the flames under buoyant and non-buoyant conditions.

Although the velocity field in the microgravity flames has not been measured to date, convection velocities of the imposed disturbances have been obtained from flame images as well as by cross correlation of the temperature oscillations. Instability theory shows that the convection velocity is usually some fraction of the local centerline velocity and can be used to infer the trend of the axial velocity. Figure 5 shows that indeed the convection velocity of the imposed disturbance decays with downstream distance. The convection velocity of large-scale structures observed in transitional and turbulent microgravity flames (ref. 2) has also been observed to decay axially suggesting that in the microgravity turbulent case both the amplitude and frequency range of the turbulent fluctuations will also decay with downstream distance.

The phases of the temperature and radiation oscillations with respect to the iris phase provide significant insight into the behavior of pulsed flames in microgravity. Figure 6 shows the time-constant corrected thermocouple signals at the flame centerline for $x = 1$ cm and $x = 4$ cm for the 3-Hz pulse case. Note that the amplitude of the temperature oscillation at $x = 4$ cm is smaller than that further upstream at $x = 1$ cm. The oscillations in the temperature signals are better depicted in Fig. 7, which shows an overlay of two (normalized) temperature signals and the time corresponding to maximum iris opening. The temperature oscillations are shown for approximately one second toward the end of the drop. Based on the phase difference between the two signals, the convection velocity for the temperature oscillations between the two axial locations is approximately 30 cm/sec. This is very close to the average centerline velocity between these locations as computed from the steady-state numerical model described earlier. The maximum centerline temperature at $x = 1$ cm coincides approximately with the minimum iris open position (i.e., maximum inward displacement of the iris).

181

The phase relationship between the radiation and iris opening for a pulse frequency of 3 Hz is shown in Fig. 8. The radiation at x = 4 cm peaks when the iris is near the minimum open position. Assuming that the convection speed of the local radiation is the same as that of the centerline temperature, the phase of the radiation at x = 1 cm can be obtained. It is estimated that the local radiation at x = 1 cm will be a maximum approximately a quarter cycle after the phase of maximum iris opening. This corresponds to the phase of maximum inward velocity of the iris.

The measured radiation, Q, is proportional to YT^4, where Y is the concentration of water vapor and T is the temperature. The maximum contribution to the radiation is therefore expected from the flame surface where both the temperature and the water vapor concentration peak. Thus, the oscillatory components of the radiation, concentration, and temperature (Q', Y', and T', respectively) are related as $(Q'/Q) \propto (Y'/Y) + 4(T'/T)$, where both Y and T are measured at the flame surface. At the low frequencies of interest in this paper, both Y' and T' at the flame are expected to be in phase with the reaction rate, and therefore, with each other. Thus, the increase in radiation level during a cycle is expected to be caused by an increase in both the temperature and water vapor concentration at the flame.

The increase in reaction rate as the iris moves in is believed to be related to enhanced air entrainment. Physically, from the no-slip condition at the iris surface, the air next to the iris must follow the motion of the iris. This behavior is also consistent with the smoke trace visualization tests conducted in this study, which indicated entrainment of the vortex during the inward movement of the iris. Numerical computations also confirm this behavior. Figure 9 shows the flow field generated by the iris movement in the presence of a cold jet, where the instantaneous field at 1/2 cycle (iris fully open) and 3/4 cycle (iris closing) are shown. It is seen that as the iris moves toward the jet (closing), air is pushed inward and more entrainment occurs.

The transient model has also been successful in predicting the oscillatory nature of the temperature and velocity in the presence of iris pulsing. Examples of predicted oscillatory temperature and centerline velocity (T' and U') are shown in Figs. 10 and 11, respectively. The predicted amplitude of temperature oscillations (Fig. 10) is of similar order as the experiment (see Fig. 6). Also, Fig. 11 shows that the mean velocity at x/L = 0.3 (where L is the predicted flame length) is approximately 20% of the injection velocity, which is in agreement with prediction from the steady-state model (see Fig. 5).

Conclusions

The tests conducted for unpulsed laminar diffusion flames show the significant effects of low gravity on these flames. Temperature distribution, flame radiation, and flame flicker data are obtained. Predictions from a steady state numerical model developed in this program are in satisfactory agreement with the data. New data on pulsed microgravity laminar diffusion flames have provided insight into the characteristics of vortex/flame interactions. These data are generated in preparation for a space experiment on pulsed flames in microgravity. With the aid of a transient numerical model of jet diffusion flames, the effects of imposed disturbances on flame structure are investigated. These results help to develop a better understanding of the behavior of transitional and turbulent jet diffusion flames in microgravity as well as in normal gravity.

References

1. Bahadori M.Y., Stocker D.P., Vaughan D.F., Zhou L., and Edelman R.B. (1993), *Modern Developments in Energy, Combustion, and Spectroscopy*, pp. 49-66, (F.A. Williams, A.K. Oppenheim, D.B. Olfe, and M. Lapp, Eds.), Pergamon Press, New York.
2. Hegde U., Zhou L., and Bahadori M.Y. (1994), *Combustion Science and Technology*, vol. 102, pp. 95-113.
3. Buckmaster J. and Peters N. (1986), *21st Symposium (International) on Combustion*, The Combustion Institute, Pittsburgh, PA, p. 1829.
4. Lovett J.A. and Turns S.R. (1993), *Combustion Science and Technology*, vol. 94, pp. 193-217.
5. Edelman R.B. and Bahadori M.Y. (1986), *Acta Astronautica*, vol. 13, pp. 681-688.
6. Bahadori M.Y., Zhou L., Stocker D.P., and Hegde U. (1996), "Measurement of Flame Flicker Under Different Gravitational Levels," Fall Eastern States Meeting of The Combustion Institute, Hilton Head, SC.
7. Katta V.R., Goss L.P., and Roquemore W.M. (1992), Paper AIAA-92-0335, AIAA 30th Aerospace Sciences Meeting, Reno, NV.
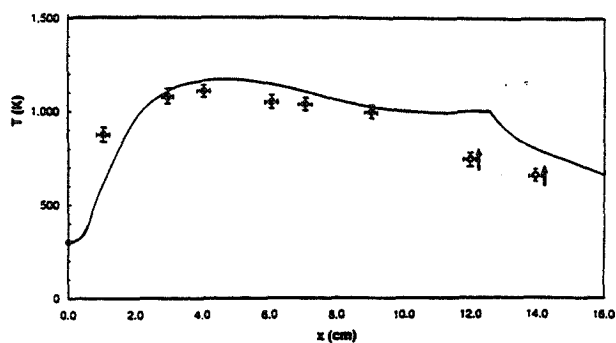
Fig. 1. Predicted and measured flame centerline temperature vs. axial distance. The temperature data at 12 and 14 cm have not reached steady state in the available microgravity period; 2 scc/sec propane flame.
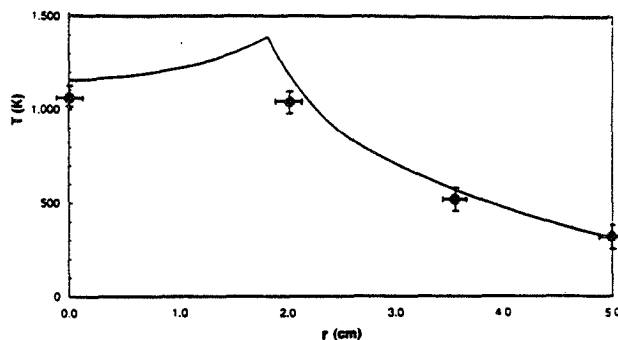
Fig. 2. Measured and predicted radial distribution of temperature for an axial location of 5 cm. The data are averages over a number of tests; 2 scc/sec propane flame.
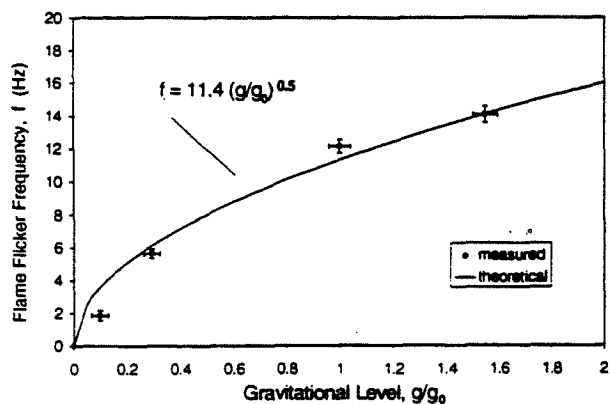
Fig. 3. Flame flicker frequency as a function of relative gravitational level; 2.5 scc/sec methane flame.
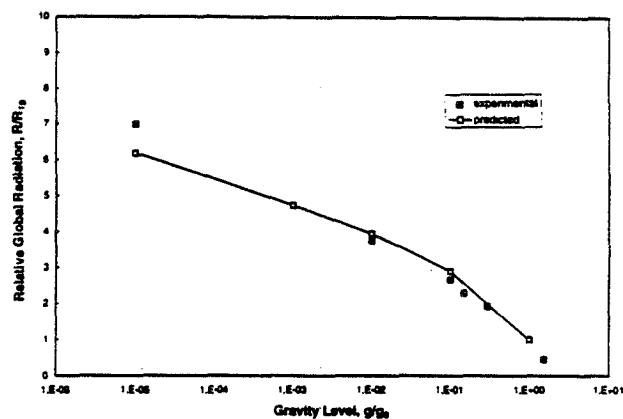
Fig. 4. Predicted and measured radiation as a function of gravitational level; 2.5 scc/sec methane flame.
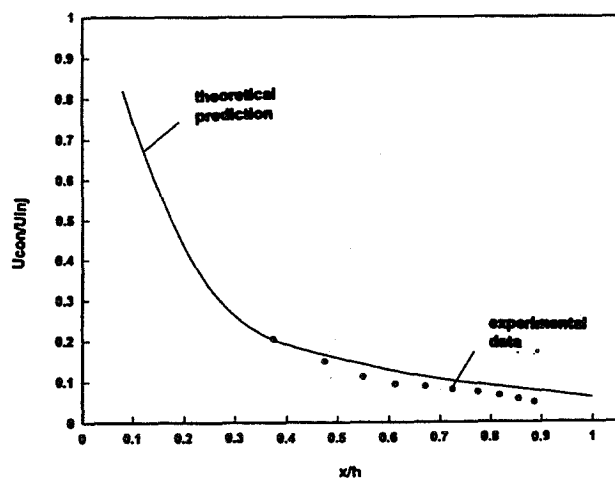
Fig. 5. Normalized predicted (solid line) and measured convection velocity for a microgravity propane flame.
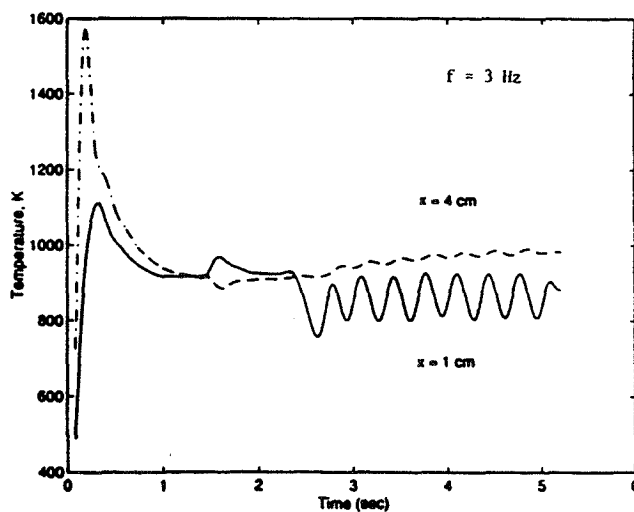
Fig. 6. Temporal evolution of the centerline temperature at x = 1 cm and x = 4 cm during a microgravity test of a 2 scc/sec propane flame; pulse frequency = 3 Hz.

183
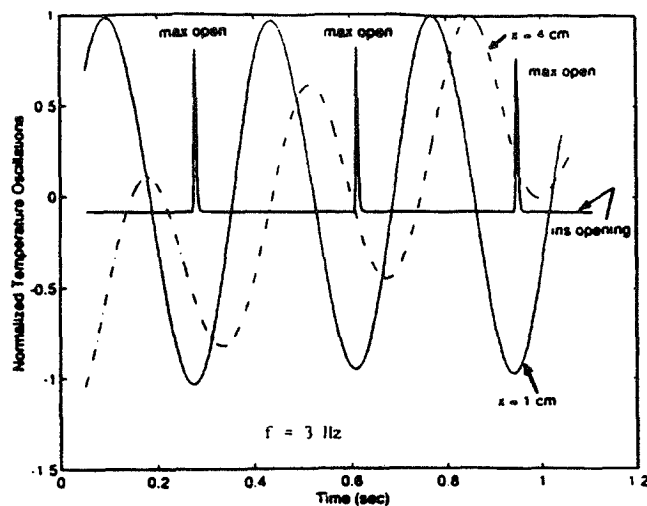
Fig. 7. Behavior of normalized temperature oscillations and iris opening; pulse frequency = 3 Hz.
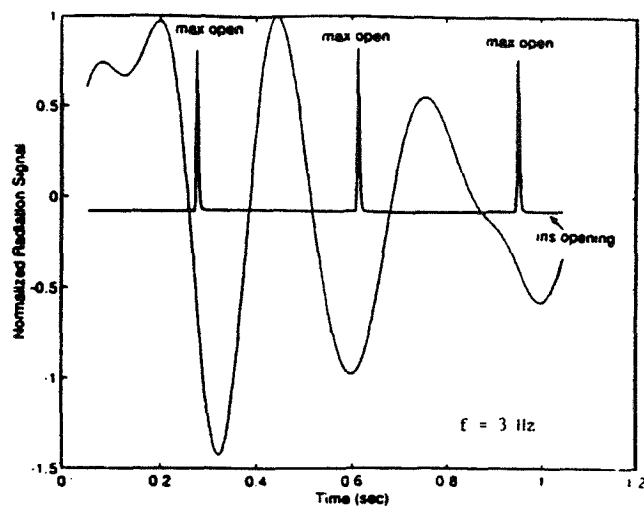
Fig. 8. Behavior of normalized radiation oscillations and iris opening; pulse frequency = 3 Hz.

(a) Iris open at 1/2 cycle

(b) Iris closing at 3/4 cycle
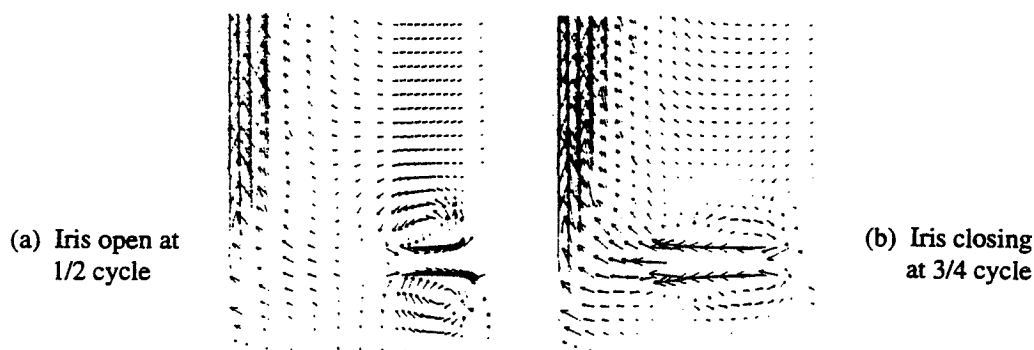
Fig. 9. Predicted instantaneous map of the velocity field of a jet under the influence of iris pulsations at 5 Hz; (a) iris open at 1/2 cycle, and (b) iris closing at 3/4 cycle.
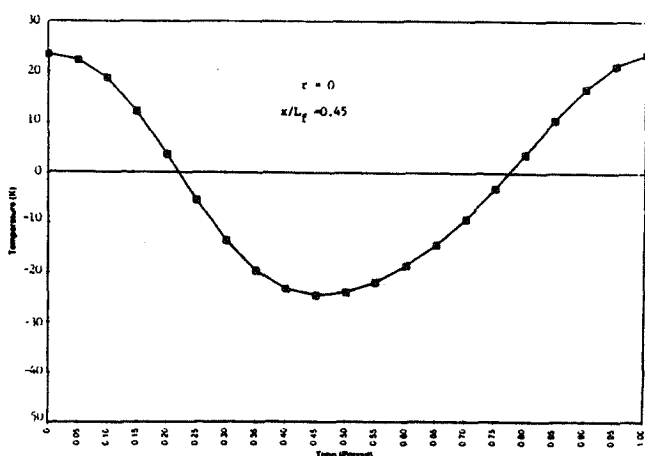
Fig. 10. Predicted oscillatory centerline temperature of a microgravity propane flame at a nondimensional height (w.r.t. flame height) of 0.45 during one cycle; pulse frequency of 5 Hz.
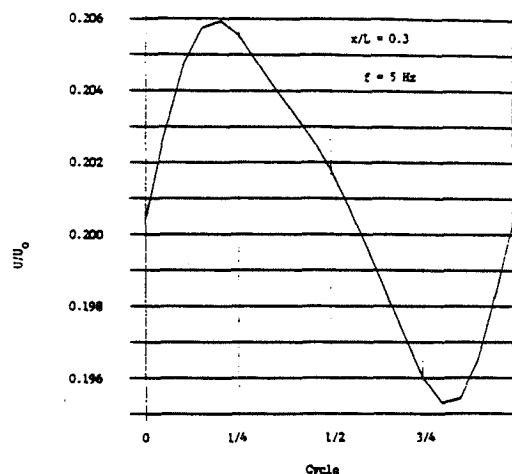
Fig. 11. Predicted nondimensional cenreline velocity (w.r.t. jet exit velocity) of the microgravity flame during one cycle at an axial location of 0.3 (nondimensionalized w.r.t. flame height); iris frequency = 5 Hz.

184

CHARACTERISTICS OF NON-PREMIXED TURBULENT FLAMES IN MICROGRAVITY

UDAY HEGDE and Zeng-guang Yuan
NYMA, Inc
Brook Park, Ohio

Dennis Stocker, NASA Lewis Research Center
Cleveland, Ohio

and

M. Yousef Bahadori, Science Applications International Corporation
Torrance, California

Introduction

The overall objectives of this research are (i) to obtain and analyze experimental data on flame images, and the spatial and temporal distributions of temperature, radiation, velocity and gas-phase species in microgravity turbulent gas-jet diffusion flames and (ii) to utilize these data to validate and refine the existing predictive capabilities. Work on this project commenced in June 1996.

The first investigations on turbulent gas-jet diffusion flames in microgravity were initiated by Bahadori and co-workers in 1991. These studies have shown that significant differences exist in the transition processes in normal-gravity and microgravity flames, and that the turbulent flames in microgravity behave very differently as compared to their buoyancy-dominated normal-gravity counterparts (Hegde 1994, ref. 1). For example, in the transition regime while the visible flame height, for given fuel and nozzle size, in normal gravity decreases, the height of the microgravity flame increases as shown in Fig. 1. In the fully developed turbulent regime, the normal-gravity flame height is independent of injection velocity, whereas the microgravity flame height continues to increase, although at a lower rate than in the laminar and transitional regimes. Other differences between the normal-gravity and microgravity flames arise in the jet shear-layer instability characteristics, extent of the transitional regime and blow-off limit characteristics (Zhou et al 1993, ref. 2, see also Fig. 1).

The parameter useful in assessing buoyant effects on gas-jet diffusion flames is the Froude number, Fr, (Glassman 1996, ref. 3) which denotes the ratio of forced convection and buoyant convection and is given by

$$Fr = u_0^2/gL$$

where u_0 is the jet injection velocity, g is the gravitational acceleration and L is the length of the flame. Note that the Richardson number, $Fr^{-1}\Delta\rho/\rho$, where ρ is a representative flame density and $\Delta\rho$ is the density difference between flame and ambient, may also be considered for estimating the influence of buoyancy. For a diffusion flame , however, $\Delta\rho/\rho$ is of unit order so that the Richardson number is essentially the inverse of the Froude number. Previous results have shown that significant differences exist between the normal-gravity and microgravity flames even when the normal-gravity flames have Froude numbers in excess of 10^3. This indicates that to obtain momentum-dominated flames under normal-gravity conditions requires extremely high jet velocities of the order of tens of meters/second. This leads to extremely large Reynolds number for typical nozzle sizes used in the laboratory which leads to problems in resolving the turbulent flow field both experimentally and computationally.

In microgravity, momentum-dominated turbulent flames are obtained at much smaller velocities than in normal gravity. Thus, significantly larger length and time microscales of the turbulent flow field under momentum-dominated conditions are obtained. Hence, studying and making measurements in turbulent gas-jet diffusion flames in microgravity offers the potential to capture the details of the turbulent flow field under momentum-dominated conditions. This understanding has a wide range

of practical applications such as diffusion flames in industrial combustors and engines where, because of high velocities, buoyancy effects are small and in the turbulence decay process in large-scale fires.

Experimental Apparatus and Approach

The experimental phase of the program has commenced and testing is planned at NASA Lewis in the 2.2-Second Drop Tower, the 5.18-Second Zero-Gravity Facility and the DC-9 aircraft. The tests are designed to take advantage of the different individual nature of these facilities.

The 2.2-Second Drop Tower provides a high-quality microgravity environment and quick turnaround times. While 2.2 seconds is not sufficient time to make statistically stationary flow field measurements, previous experience suggests that it is sufficient to provide good estimates for overall flame dimensions. Hence, tests in this facility will be conducted primarily to select the candidate flames for the detailed measurements. This is important since typical microgravity flame heights for the injection Reynolds numbers of interest (3000-10,000) for hydrocarbon fuels such as propane and methane are of the order of 50 cm for nozzle diameters to be utilized (around 1mm). It is desirable to reduce both the flame height and the heat release rate to conduct flow field measurements. One way to do this is to dilute the fuel with an inert gas, for example, nitrogen and these tests will quantify the effect of fuel dilution. The drop rig has been designed and is currently under construction.

The 5.18-Second Zero-Gravity Facility provides a high-quality microgravity environment and significantly greater time for quantitative measurements than the Drop Tower. These tests will utilize the Gas Jet Diffusion Flame hardware (Fig. 2) with selected candidate flames with the objective of making detailed measurements of temperature and flame radiation. Fine-wire thermocouples will be utilized to obtain temperatures at different axial and radial locations. Time constants of the utilized thermocouples will also be measured in order to correct the fluctuating components of the measured signals. Flame radiation will be measured using thermopile detectors both from the entire flame (i.e., global radiation) and from narrow wedge-shaped regions of the flame. At this time, a thermocouple rake with eight thermocouples has been constructed and installed in the rig. Also, the radiometer assemblies have been constructed.

The DC-9 aircraft provides more reduced-gravity time than the Drop Tower and the Zero-Gravity Facility; however, the g-levels are not as low and there can also be g-jitter effects. Tests are planned in the Gas Jet Diffusion Flame rig for aircraft experiments with selected candidate flames with the objective of visualizing the turbulent structures and for making LDV measurements. An IR camera, if available, will be used to obtain the infrared signatures of specific species by incorporating optical filters. A 16-bit data acquisition system with high sampling rate capability will be incorporated into the aircraft rig for the LDV measurements. The rig upgrade will commence this year.

Modeling

The obtained experimental data will be useful for assessing both direct numerical simulations as well as standard turbulent flame models. The primary modeling objective in this project is to assess the validity of turbulent flame models since the obtained data will provide a benchmark case for momentum-dominated gas-jet flames.

The numerical model is under development and utilizes standard turbulent models in conjunction with state relationships for chemistry for predicting the time-averaged flow field and correlations. Thus, the set of governing equations utilized are of the form

$$\text{div}(\rho u \phi - \Gamma_\phi \text{grad} \phi) = S_\phi$$

where

$\phi = u, v, w$: Momentum $\quad \Gamma_\phi = \rho (v_t + v_l)$

$S_\phi = -\text{grad}(p) + \text{gravity} + \text{viscous}$

$\phi = h$:   Enthalpy $\Gamma_\phi = \rho (v_t + v_l)/a_h$
                                 $S_\phi = -Dp/Dt + \text{heat sources}$

$\phi = 1$:   Continuity $\Gamma_\phi = 0$
                                    $S_\phi = 0 + \text{boundary sources}$

In the above equations, u, v, and w are the three components of the velocity, ρ is density, p is pressure, h is enthalpy, and v_t and v_l are the turbulent and laminar kinematic viscosities, respectively. These equations are supplemented by equations for the turbulent kinetic energy, k, and the dissipation rate , ε. The model solves for pressure, velocity, temperature, species concentrations, and turbulent kinetic energy and dissipation rate. Radiative transport, utilizing models such as the six-flux model, for major gas species (e.g., CO_2 and H_2O) will be included in the code.

Results and Discussion

In general, gas-jet diffusion flames may be classified as momentum-dominated, buoyancy-dominated or flames that are influenced by both momentum and buoyancy. Similitude and scaling arguments have been presented in the literature (e.g., Blake and McDonald 1995, ref. 4) to distinguish these regimes based upon weighted Froude and Richardson numbers. However, for the purpose of retaining clarity in the discussion herein, attention is focused only on momentum-dominated and buoyancy-dominated flames.

The fundamental difference between momentum-dominated and buoyancy-dominated gas-jet flames is illustrated in Fig.3 which plots the flame centerline velocity (normalized by injection velocity) as a function of axial distance (normalized by flame length) downstream of the nozzle for three different cases: (i) laminar 1-g (ii) laminar 0-g and (iii) turbulent flame. The laminar flame calculations are from a laminar flame model (Edelman and Bahadori 1986, ref. 5) and the turbulent flame calculations utilized a preliminary fast-chemistry version of the model described above using a k-ε formalism which does not include the gravitational acceleration term. Some success for the mean flow quantities has been reported in the literature using similar models for a high-velocity hydrogen jet flame with air co-flow where buoyant effects were reported to be small (e.g., Kent and Bilger 1976, ref. 6).

Considering the laminar case it is clear that for the buoyancy-dominated flame the axial velocity increases with distance downstream of the nozzle whereas for the momentum-dominated (0-g) case it decreases. The difference is due to buoyant acceleration in the 1-g case which yields an axial velocity dependence on the square root of the axial distance (Bahadori et al 1996, ref. 7). For the turbulent case, which represents a momentum-dominated flame because of the neglect of the gravitational acceleration term, the axial velocity exhibits a decay over the flame length although the predicted decay is not as dramatic as for the laminar 0-g case. While computations of a buoyancy-dominated turbulent flame are not presented here, there is evidence in the literature that the axial velocity increases with downstream distance in this case (e.g., Durao and Whitelaw 1974, ref. 8).

This difference in the velocity field for momentum-dominated and buoyancy-dominated flames leads to striking differences in their behavior. For example, for the laminar and transitional flames, the instability characteristics of the flame and associated shear layers are completely different. Application of parallel shear-layer instability theory showed that for the axisymmetric mode, the microgravity, momentum-dominated flame has a single critical layer which originates at the nozzle rim and crosses the flame near the tip. The normal-gravity buoyancy-influenced flame, however, has three critical layers associated with the axisymmetric mode. The innermost layer originates at the nozzle rim and is associated with the instability of the fuel jet issuing into the atmosphere. A pair of critical layers is formed on the oxidizer side of the flame sheet and , being buoyancy driven, are believed to be responsible for flame flicker which is absent in the microgravity case.

In the turbulent regime, the significance of the difference in the velocity fields may be understood in terms of the variation of the local Reynolds number based upon the local centerline velocity and local flame width. The magnitude of the local Reynolds number increases with axial distance for the normal gravity buoyancy-dominated flame and decreases with axial distance for the microgravity flame. If it is assumed that the local turbulent velocity magnitude scales with the local centerline velocity, and that the local integral length scale is proportional to the local flame width (which is relatively invariant over the flame length) then it is clear that the local turbulent Reynolds number, Re_T, follows the same trend as the local mean flow Reynolds number.

The smallest scale of turbulence, that is the Kolmogorov length scale, varies as $Re_T^{-0.75}$ indicating that for the buoyancy-dominated flame, the size of the smallest scales decreases with increasing distance along the flame (since Re_T increases) whereas for the microgravity flame, the opposite occurs (since Re_T decreases). This is consistent with turbulence dissipation behavior. The turbulence dissipation is of order u'/l where u' is the turbulent velocity fluctuation magnitude and l is the integral length scale. This is a measure of the highest frequencies (i.e., the smallest scales) in the turbulent spectrum. The integral length scale is expected to be relatively invariant over the flame length whereas u' will scale with the mean velocity. Thus, u'/l is expected to decrease downstream for the microgravity case indicating a decrease in the highest frequencies and an increase in the size of the smallest scales.

Experimental evidence supporting the above discussion is provided by Fig. 1 which shows that the microgravity turbulent flame heights are larger than the normal gravity buoyancy-dominated flame heights. Following Glassman (ref. 3), it may be argued that flame height, L, is proportional to the fuel volume flow rate, Q, and is inversely proportional to the effective diffusivity, D_{eff}; that is

$$L \propto Q/D_{eff}$$

In the laminar regime D_{eff} represents the molecular diffusivity whereas in the turbulent regime it represents an eddy diffusivity. From Fig. 1, it may be inferred that D_{eff} for the normal gravity turbulent flame is between two to three times the value of D_{eff} for the corresponding microgravity flame. D_{eff} in the turbulent regime scales as the product of a turbulent velocity scale (u') and an integral length scale. Since the integral length scale is the same for both cases, it is expected that u' is smaller for the microgravity flame as was suggested earlier.

Pending the completion of the 2.2 Second Drop Tower rig, preliminary work in the Zero-G Facility has commenced with the Gas Jet Diffusion Flame apparatus. The objectives of this initial testing are to establish the feasibility of reducing flame height in microgravity by adding a diluent to the fuel and also to assess changes in the flame behavior because of the added diluent. The initial testing has been with moderate Reynolds number flames (Re = 1000) with a propane (60%) - nitrogen (40%) injection mixture utilizing a 1.6 mm diameter nozzle. At this Reynolds number, the flame is in the laminar regime (ref. 1) which facilitates comparison with laminar flames of undiluted propane in microgravity for which a substantial data base exists. For the undiluted propane case the (luminous) flame height for the corresponding flow rate as extrapolated from available data would be approximately 40 cm. The addition of the nitrogen reduces the visible flame height to approximately 25 cm. The flame luminosity appears to be considerably reduced however compared to the undiluted case consistent with decreased amount of soot in the flame compared to the undiluted propane flame during the corresponding period of its development. This behavior is similar to the normal gravity behavior (Axelbaum and Law 1990, ref. 8) where it is attributed to a combination of reduction in fuel concentration (which is expected to be the primary effect at the investigated dilution) and flame temperature.

Temperature measurements on the centerline of the nitrogen-diluted flame are compared with corresponding measurements in the undiluted propane case in Fig. 4. The undiluted case is at a lower Reynolds number (Re = 400) but this is compensated by normalizing the axial distance by the flame length. This figure shows that the temperature distribution is similar in the two cases. It must be cautioned that the temperatures do not reach a steady state at the end of the microgravity period for the laminar flames. This is shown in Fig. 5 which plots a representative temperature development for the nitrogen-diluted flame (Re = 1000). It is unclear at present whether the temperatures will reach steady state during the available time for the moderately turbulent flames that are to be studied. The ratio of the times to reach steady state for the laminar and turbulent cases is inversely related to their effective diffusivities. From Fig. 1 and earlier discussion, the effective diffusivity for the moderately turbulent flames is approximately 30% more than for the laminar flames which indicates that the turbulent flames will reach steady state only 30% faster than the laminar flames.

Acknowledgments

References

1. Hegde, U., Zhou, L., and Bahadori, M. Y., "The Transition to Turbulence of Microgravity Gas Jet Diffusion Flames". *Combust. Sci. and Tech.*, vol. 102, pp. 95-113, 1994.
2. Zhou, L., Hegde, U. and Bahadori, M. Y., "Experimental Observation of Turbulent Gas Jet Diffusion Flames in Microgravity". Joint Central and Eastern States Section Meeting of the Combustion Institute, New Orleans, LA, 1993.
3. Glassman, I. *Combustion*. Third Edition, Academic Press, New York , 1996.
4. Blake, T. R., and McDonald, M., "Similitude and the Interpretation of Turbulent Diffusion Flames". *Combustion and Flame*, vol. 101, pp. 175-184, 1995.
5. Edelman, R. B., and Bahadori, M. Y., "Effects of Buoyancy on Gas-Jet Diffusion Flames: Experiment and Theory". *Acta Astronautica*, vol. 13, no. 11/12, pp. 681-688, 1986.
6. Kent, J. H. and Bilger, R. W., "The Prediction of Turbulent Diffusion Flame Fields and Nitric Oxide Formation". *Sixteenth Symposium (International) on Combustion*, pp. 1643-1656, The Combustion Institute, 1976.
7. Bahadori, M.Y., Zhou, L., Hegde, U., and Stocker, D. P., "Measurements of Flame Flicker Under Different Gravitational Levels". Eastern States Section Meeting of the Combustion Institute, Hilton Head, SC, 1996.
8. Axelbaum, R. L., and Law, C. K., "Soot Formation and Inert Addition in Diffusion Flames". *Twenty Third Symposium (International) on Combustion*, pp. 1517-1523, The Combustion Institute, 1990.
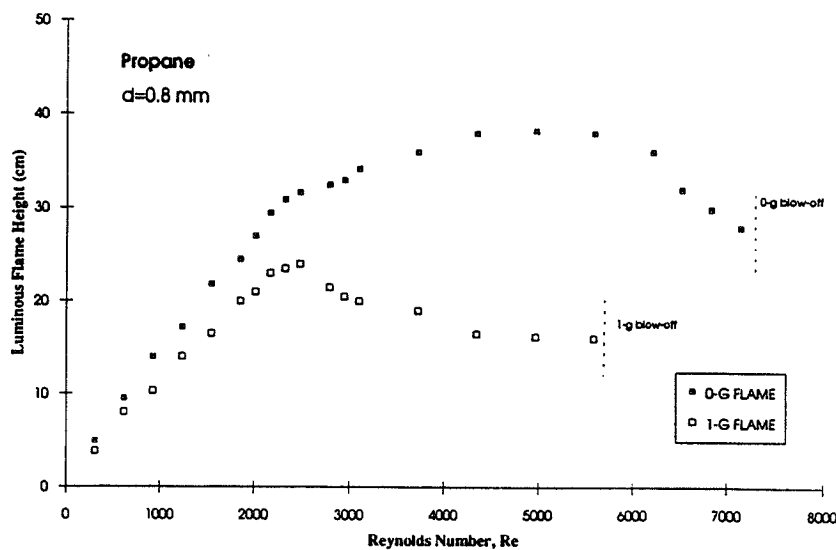
Fig. 1 Measured height of the luminous flame zone as a function of Reynolds number for propane-air flames in microgravity and normal gravity (nozzle diameter = 0.8 mm).

Fig. 2 Gas-Jet Diffusion Flame hardware for the Zero-Gravity Facility.
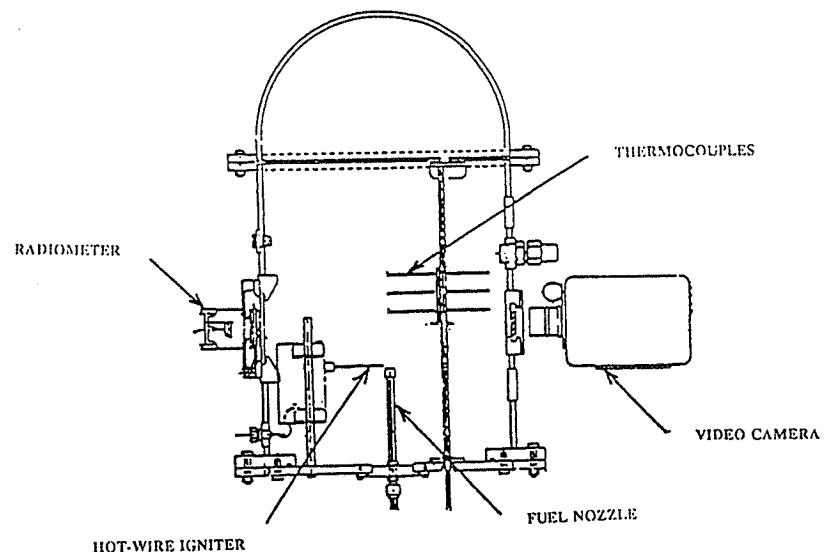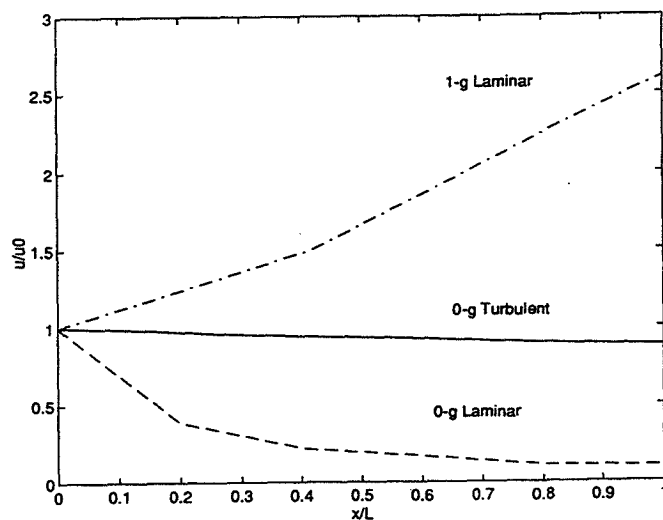
Fig. 3 Predicted normalized centerline velocity as a function of normalized axial distance. The Reynolds number for the laminar flame computations is 400 and for the turbulent flame computations is 5000.

Fig. 4 Centerline temperature measurements for propane and nitrogen-diluted propane flames in microgravity.
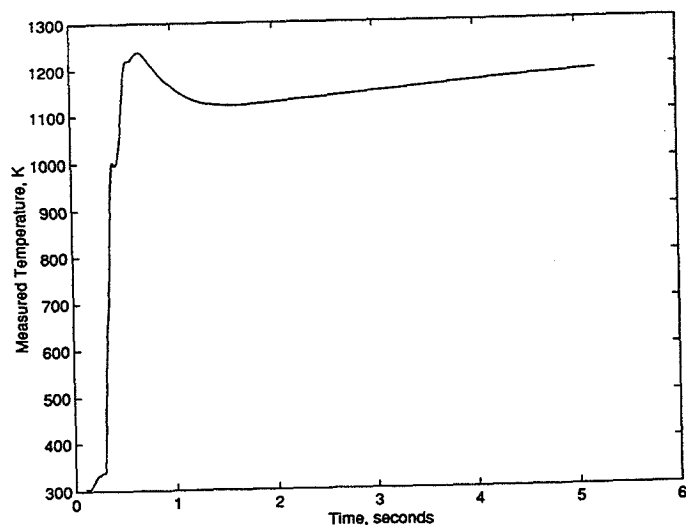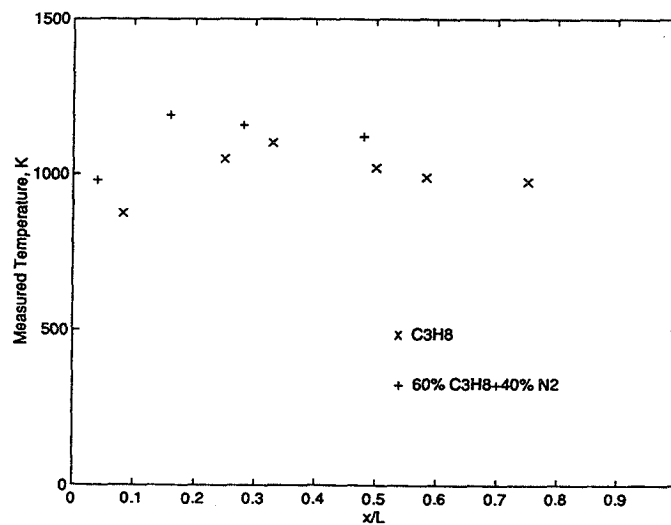
Fig. 5 Temperature development of the nitrogen-diluted propane flame on the centerline at a height of 4 cm above the nozzle. The drop commenced at time = 0 seconds. (Re = 1000).

VORTEX RING / DIFFUSION FLAME INTERACTIONS IN MICROGRAVITY CONDITIONS

Shin-Juh Chen and WERNER J.A. DAHM

Laboratory for Turbulence and Combustion (LTC)
Department of Aerospace Engineering
The University of Michigan
Ann Arbor, Michigan

INTRODUCTION

Turbulent diffusion flames involve mixing and reaction between initially non-premixed or partially premixed fuel and oxidizer streams, and represent by far the largest class of combustion problems, with applications spanning an enormous range of critical technologies ranging from aerospace propulsion systems, to industrial combustion processes, to utility power generation systems. Certain aspects of such combustion in turbulent shear flows have been accessible to experimental study under controlled conditions, often by isolating the particular phenomenon or interaction of interest in an idealized canonical configuration. There remain, however, many fundamental issues that are essential to the subject, but which have eluded study to date owing to the dominating influence of buoyancy under normal-gravity conditions.

The vortex ring / diffusion flame interaction is among such problems, and is arguably the simplest of all configurations that contain the fundamental elements of flow, transport, and combustion phenomena present in turbulent diffusion flames. These include concentrated vorticity, entrainment and mixing, strain and nonequilibrium phenomena, diffusion and differential-diffusion, partial premixing and diluent effects, and heat release effects. All of these phenomena combine in this comparatively simple canonical configuration to permit study of their interactions under carefully controllable conditions. However despite its importance in combustion science, this configuration has not previously been studied owing to the fact that it can be brought within experimental reach only under microgravity conditions; Chen & Dahm (1996).

The present paper reports the first experimental examination of this important problem in combustion science, where we examine hydrocarbon combustion in a vortex ring burning in air. Previous theoretical studies have been conducted under somewhat idealized conditions for the related case of a chemically reacting vortex pair by Karagozian & Manda (1986) and Manda & Karagozian (1989), as well as an experimental study of aqueous acid-base reaction in a vortex pair by Karagozian et al (1988). These share many features with the present problem, but differ in important ways from gaseous hydrocarbon combustion in a vortex ring, for which a broad range of nonequilibrium interactions between flow, diffusion, and reaction occur over the range of conditions examined here. The present problem is also the subject of an ongoing direct numerical simulation (DNS) study by Hewett & Madnia (1996), though owing to the scale of the calculations the range of conditions that can be examined is limited.

EXPERIMENT DESCRIPTION

Experiments are conducted in the NASA LeRC 2.2-sec drop tower with the test package shown in Fig. 1. An iris in the exit plane of an axisymmetric nozzle initially separates the fuel (propane) from air in the test section. The iris opens electronically and a diffusion layer forms at the fuel-air interface. A partial vacuum then gradually draws this diffusion layer into the nozzle throat until it reaches the position of a spark igniter, which ignites the layer. The layer stabilizes briefly and the test package is dropped, at which time a solenoid opens to a pressurized propane cylinder and thereby impulsively pushes fuel from a plenum through the nozzle into the test section. A micrometer-controlled metering valve normally held at sonic conditions controls the fuel flow rate, which together with the duration Δt of the solenoid pulse and the fuel cylinder pressure p determines the exit velocity $U(t)$ and thus the circulation density $\gamma(t)$ of the resulting vortex sheet issuing from the nozzle. The cylindrical vortex sheet rolls up to form a vortex ring, which wraps the diffusion-reaction layer around itself (Southerland et al 1991) and produces a complex interaction of the resulting flow with the diffusion and combustion process in the layer. Detailed dynamical modeling of the fuel discharge, accounting for all pressure drops and valve characteristics, allows the resulting total discharge volume V and the total circulation Γ to be determined, which are the primary variables that determine the nature of the interaction that occurs. In addition, the relative separation between the layer and the vortex sheet can be controlled by adding inert or oxidizer diluents to
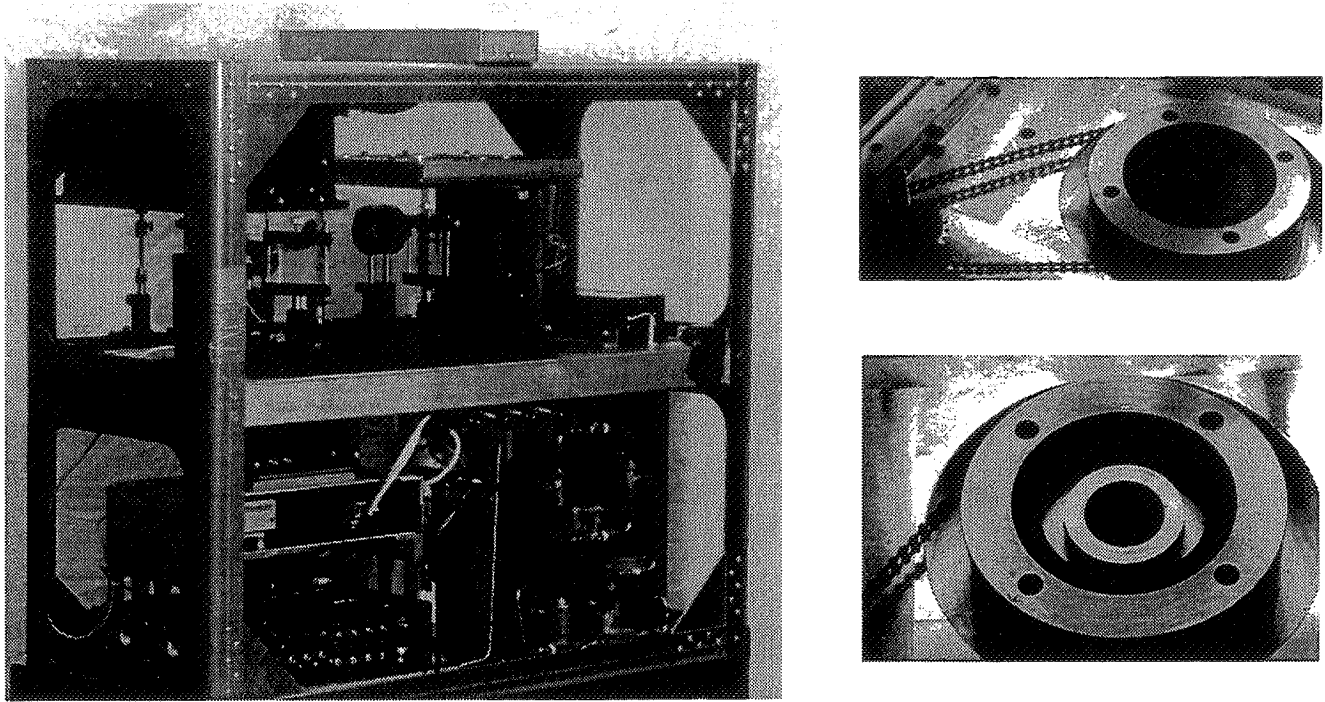
Fig. 1. Experimental drop package used for the present study of vortex ring / diffusion flame interaction in microgravity conditions. The view at left shows the (clear) test section and optics on the top shelf, with electronics and gas distribution system on bottom shelf. Shown at top right is the iris in closed position prior to drop, and at bottom right in open position showing the fuel nozzle and spark igniter in the nozzle throat. After ignition of the initial fuel-air diffusion layer, fuel issues from the nozzle to form the vortex ring.
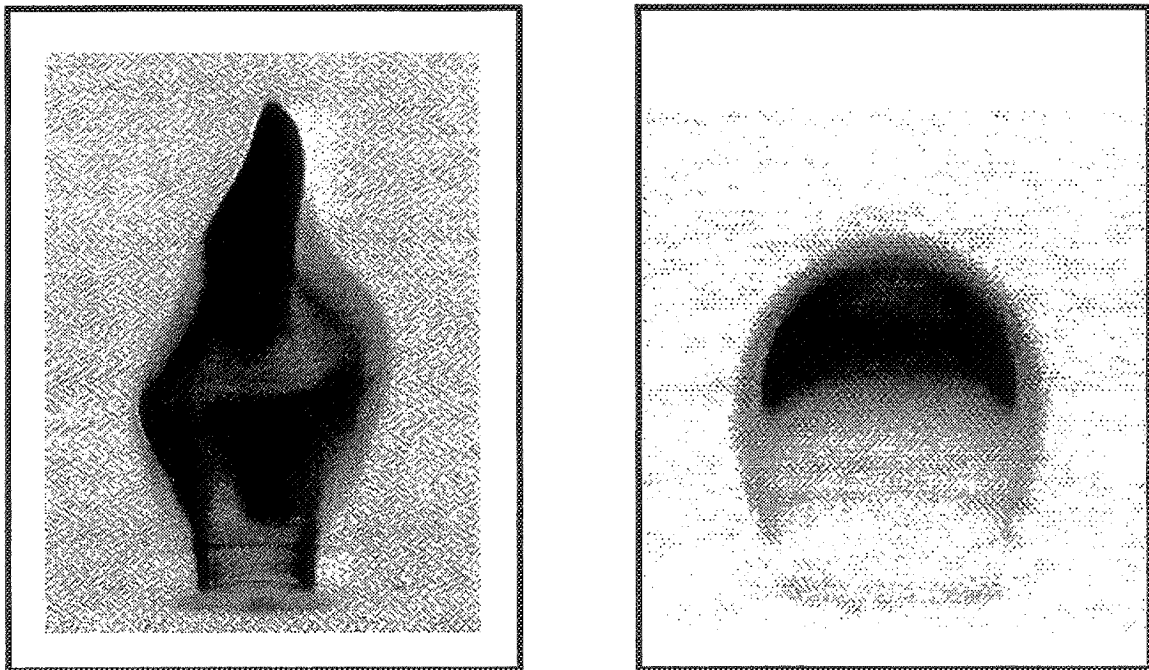
Fig. 2. Comparison of results obtained in the facility shown in Fig. 1 under normal-gravity conditions (left) and under microgravity conditions (right). Under normal gravity, the contribution of the hydrostatic pressure gradient to the baroclinically generated vorticity is very large and leads to loss of axisymmetry in the resulting interaction. Under microgravity conditions, only the hydrodynamic contribution to the baroclinic generation remains and axisymmetry is preserved, leading to highly repeatable results as demonstrated in Fig. 3. Experimental study of the vortex ring / diffusion flame interaction over the range of conditions examined in the present study cannot be done in normal gravity, and requires microgravity conditions.

192

the fuel, which also controls the heat release characteristics of the resulting combustion process, however all cases for which results are presented here used pure propane as the fuel. A CCD camera records the visible luminosity from the interaction, which are shown here in inverse gray scale form.

EXPERIMENTAL OBSERVATIONS

The experimental facility and procedure above leads to highly symmetric results for the interaction between the reaction layer and the vortex ring under microgravity conditions, as shown in Fig. 2. In contrast, buoyancy effects under normal gravity conditions effectively preclude any detailed study of the resulting interaction dynamics in a traditional laboratory setting. Furthermore, as indicated in Fig. 3, the present experimental facility leads to highly repeatable results under microgravity conditions over a very wide range of parameter values. The results presented in this section document the vortex ring / diffusion flame interaction over as much of the parameter space as is currently accessible with this facility.

The three cases shown in Fig. 3 give an indication of the very different interaction dynamics that can be seen at the relatively early times shown. An example of the long time evolution of the interaction is shown in Fig. 4, where a ring with an intermediate circulation is show from its inception through the completion of fuel burnout. Especially noteworthy is the relatively sudden formation of a bright cap on the forward half of the ring, presumably due to soot formation. This luminous cap burns out rapidly and leaves a comparatively luminous ring structure that is eventually consumed.

It must be noted clearly that the details of the interaction, while highly repeatable from one realization to another, depend strongly on the ring parameters. Of primary importance among these are the ring circulation Γ and the total fuel volume V discharged in the ring formation process. These two can in principle be set independently, since one measures the total impulse and the other the total mass of the injection process. Thus, for instance, a ring with any desired Γ could potentially be generated with asymptotically vanishing V. Any ring can thus be identified in a diagram of the type shown in Figs. 5, where contours of V are shown in a plot of the ring circulation Γ against solenoid pulse duration Δt. There is a maximum fuel volume that the ring can accommodate, and beyond this the ring "overfills" as shown in Fig. 6. By comparing results in this manner, it can be
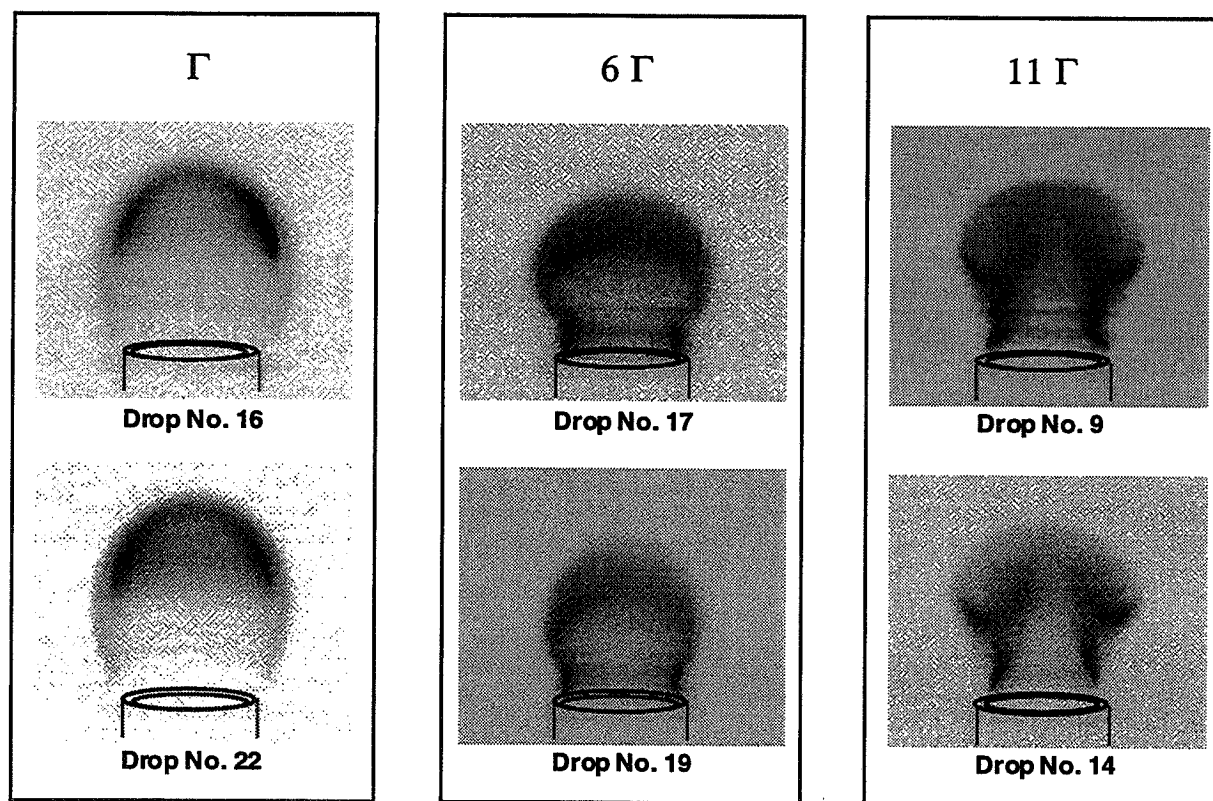
Fig. 3. Typical results obtained for two separate drops at each of three different ring circulations Γ, demonstrating the repeatability achievable in the present experiment. Relative times have been matched as closely as possible from the video frames available. The leftmost column corresponds to a ring of intermediate strength, while the middle and right columns corresponds to rings with circulations respectively 6 and 11 times higher. Note that the interaction is very different among the three Γ values shown, but that the results obtained from different drops at the same Γ are essentially identical within the accuracy with which video frames can be matched.
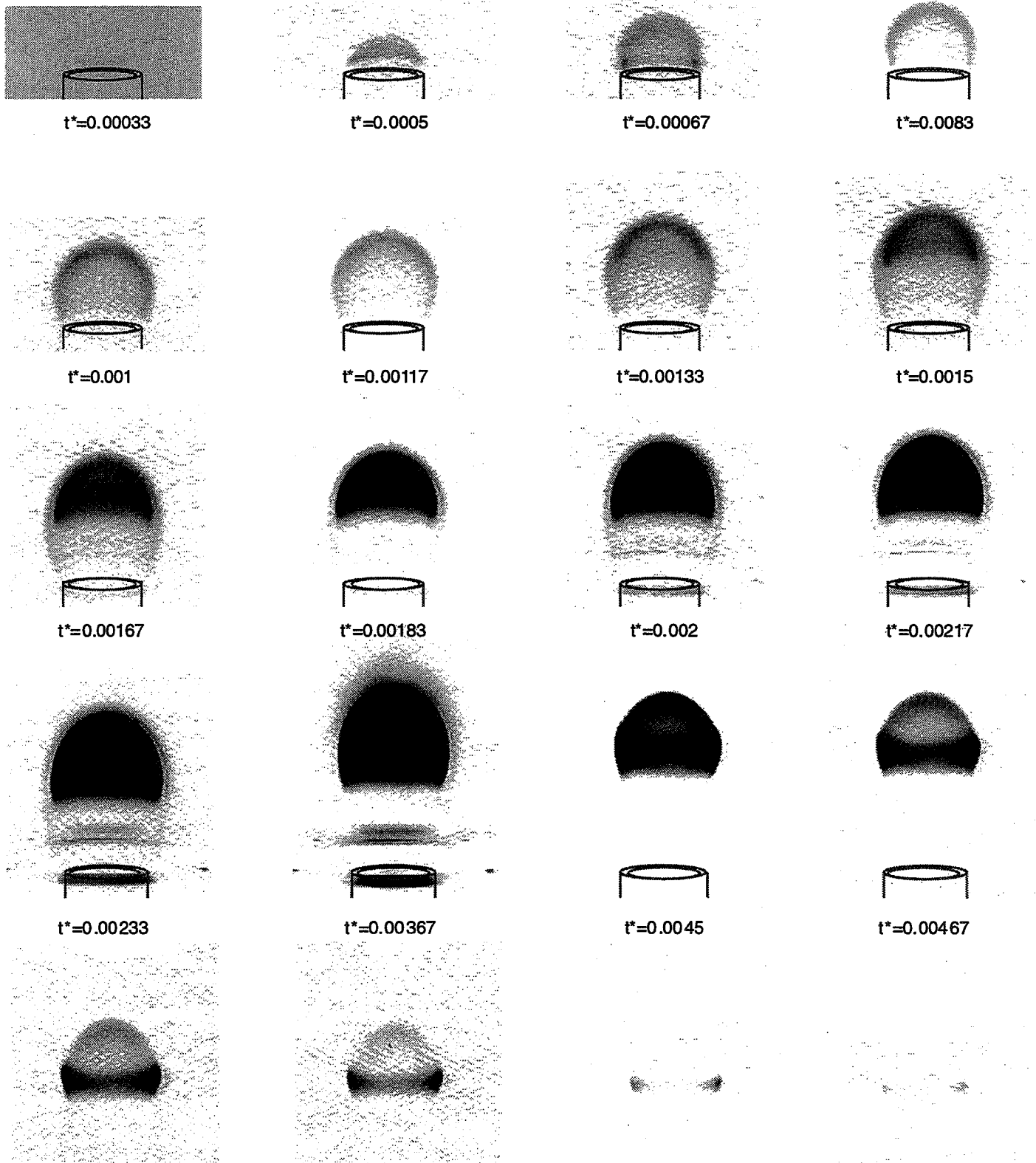
Fig. 4. Typical result for the complete time-evolution of the vortex ring / diffusion flame interaction seen under conditions corresponding to an intermediate ring circulation Γ. Time advances from left to right and then from top to bottom. Note the early stages of evolution of the ring, leading to the comparatively sudden formation of a highly luminous cap on the forward half of the ring. The luminous cap, which is presumably due to soot, burns out rapidly and a concentrated ring structure that eventually burns out.
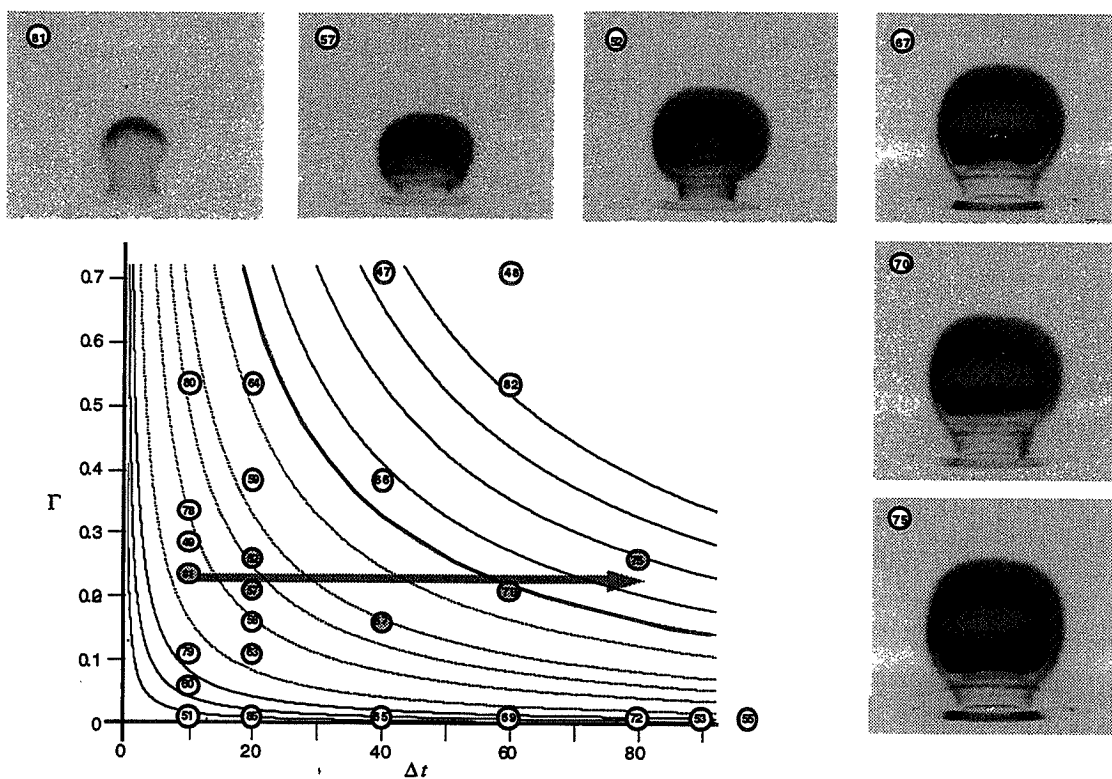
Fig. 5. Comparisons of vortex ring / diffusion flame interactions for essentially the same Γ at fixed time (100 msec) after onset of ring formation, for rings having widely differing fuel volumes as indicated by contours on which V is constant, with V increasing across contours from left to right. Note the very different structure of the interaction depending on the fuel volume discharged.
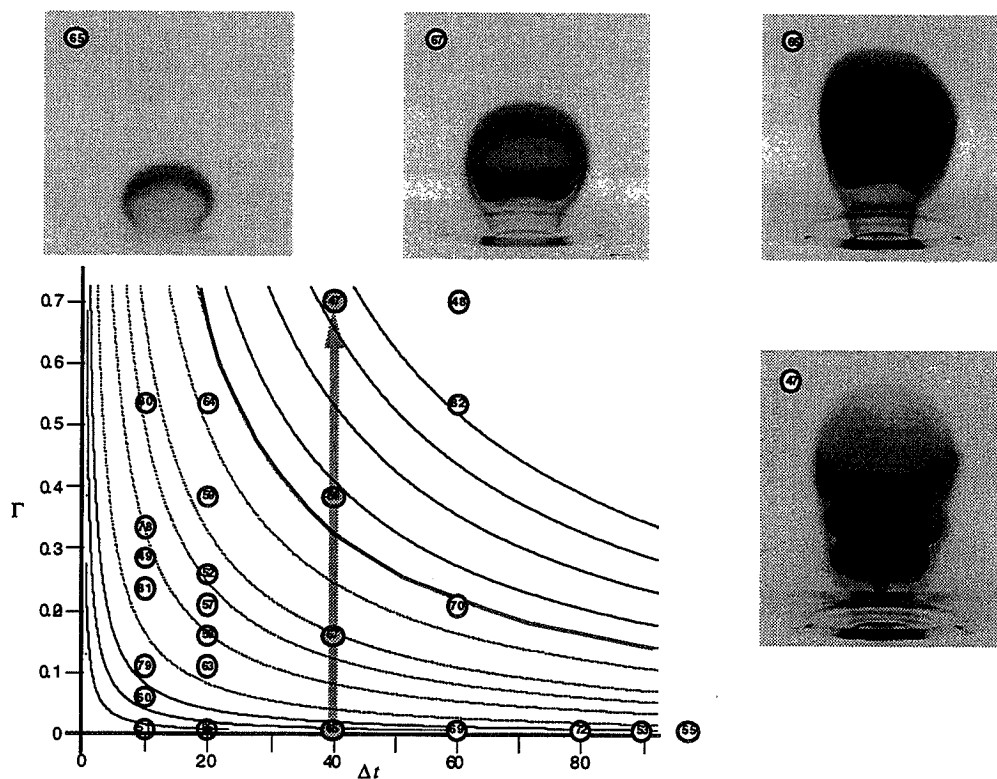
Fig. 6. Similar to Fig. 5, but showing results for fixed solenoid pulse duration Δt and increasing metering valve setting, so that both Γ and V increase along the path indicated. Note that the ring reaches an overfill limit at which the total fuel volume discharged exceeds the capacity of the ring, leading to formation of successive rings as seen in Drop 47 at lower right.
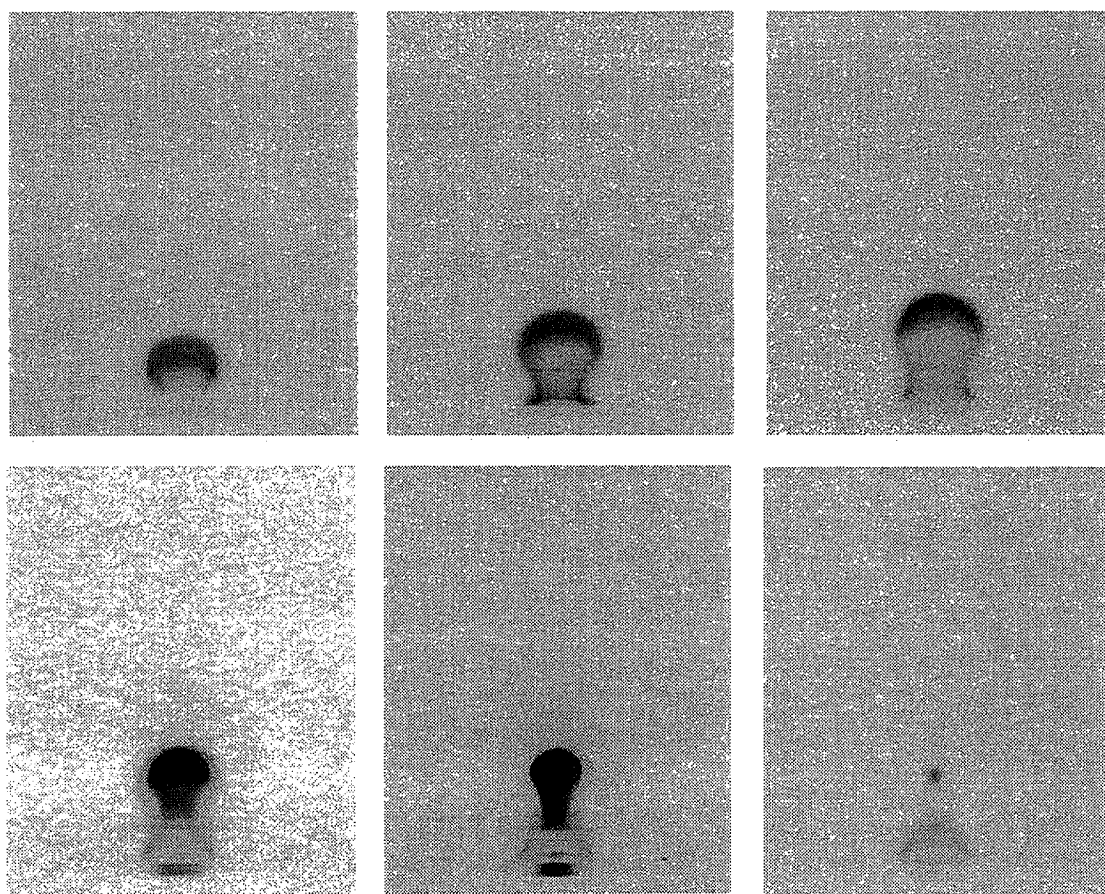
Fig. 7. Long time interaction dynamics for Drop 81, shown in upper left panel of Fig. 5, corresponding to a ring with intermediate strength but low volume. This interaction can be contrasted to that in Fig. 4, which has a much larger fuel volume. Accordingly the fuel is consumed much more quickly, though a bright luminous cap still forms on the forward part of the ring, but the burnout phase appears very different from that seen for stronger rings.

seen that a very wide range of interaction dynamics are found over the parameter range accessible in these experiments. These span from relatively strong rings with large fuel volumes, such as in Fig. 6, to relatively weak rings with small volumes as seen in Fig. 7. Those cases where detailed DNS results are available show good agreement with the simulations, but the experiments permit a far wider range of interactions to be examined, and account for detailed soot kinetics and other phenomena that are currently inaccessible to simulations. Subsequent work in these experiments is examining key cases with detailed diagnostics to permit investigation of critical aspects of flame-vortex interaction relevant to turbulent diffusion flames.

Chen, S.-J. & Dahm, W.J.A. (1996) Diffusion flame structure of a vortex ring under microgravity conditions. *Bull. Am. Phys. Soc.* **41**, 1726 (abstract only).

Dahm, W.J.A., Scheil, C.M. & Tryggvason, G. (1989) Dynamics of vortex interaction with a density interface. *J. Fluid Mech.* **205**, 1-43.

Hewett, J.S. & Madnia, C.K. (1996) Flame evolution in reacting vortex rings. *Bull. Am. Phys. Soc.* **41**, 1726 (abstract only).

Karagozian, A.R., Suganuma, Y. & Strom, B.D. (1988) Experimental studies in vortex pair motion coincident with a liquid reaction. *Phys. Fluids* **31**, 1862-1871.

Karagozian, A.R. & Manda, B.V.S. (1986) Flame structure and fuel consumption in the field of a vortex pair. *Comb. Sci. Tech.* **49**, 185-200.

Manda, B.V.S. & Karagozian, A.R. (1989) Effects of heat release on diffusion flame-vortex pair interactions. *Comb. Sci. Tech.* **61**, 101-119.

Southerland, K.B., Porter, J.R., Dahm, W.J.A. & Buch, K.A. (1991) An experimental study of the molecular mixing process in an axisymmetric laminar vortex ring. *Phys. Fluids A* **3**, 1385-1392.

Soot Processes

Page intentionally left blank

LAMINAR SOOT PROCESSES[*]

F. Xu, P.B. Sunderland,[†] K.-C. Lin and G.M. FAETH
The University of Michigan
Ann Arbor, Michigan

Introduction

Soot processes within hydrocarbon-fueled flames affect particle emissions from combustion processes, thermal loads of combustor components, hazards of unwanted fires, and capabilities for computational combustion. Thus, soot processes within laminar nonpremixed (diffusion) and premixed flames are being studied, using both space-based (flight) experiments at microgravity (mg) and supporting ground-based experiments at normal gravity (ng). The study is limited to laminar flames due to their experimental and computational tractability, noting the relevance of these results to practical turbulent flames based on laminar flamelet concepts (ref. 1). Unfortunately, buoyancy affects soot processes in laminar diffusion flames while effects of buoyancy are small for most practical flames (ref. 1); therefore, present observations of laminar diffusion flames involve either particular flame conditions where effects of buoyancy are small during ground-based experiments at ng or truly nonbuoyant flames during planned flight experiments at mg. Laminar premixed flames are also being considered during ground-based experiments at ng because soot processes are easier to interpret and less affected by buoyancy in laminar premixed flames than in laminar diffusion flames.

Experimental results from the flight experiment are not yet available; therefore, the following discussion will be limited to the ground-based experiments, considering results for laminar diffusion and premixed flames, in turn. The present description of the investigation is brief, see refs. 2-22 for more details.

Laminar Diffusion Flames

Introduction. The first phase of the ground-based study emphasized the structure and optical properties of soot in order to establish nonintrusive measurements of soot concentrations (refs. 1-11). The structure of soot is similar in all flame environments; a typical example is illustrated by the transmission electron microscope (TEM) photograph appearing in Fig. 1. In general, soot consists of roughly spherical primary particles having nearly constant diameters at a given condition, collected into mass fractal aggregates having widely-varying numbers of primary particles per aggregate (refs. 2 and 7). Fortunately, soot aggregates satisfy the Rayleigh-Debye-Gans scattering approximation while the fractal and refractive index properties of soot are nearly universal (refs. 3-6 and 11). These findings then yielded methods for measuring soot concentrations and temperatures that are being exploited for experiments at both mg and ng (refs. 3-6).

The next phases of the work involved establishing methods for predicting flame structure and estimating laminar smoke point properties of nonbuoyant laminar jet diffusion flames. This information is needed for the flight experiment where limited measurements must be supplemented by predictions in order to interpret the observations while soot emissions must be avoided in order to maintain the optical quality of windows. Reasonably effective predictions of the structure of soot-containing laminar jet diffusion flames were demonstrated based on the conserved-scalar formalism in conjunction with state relationships measured in soot-containing laminar diffusion flames (refs. 12-15). Laminar smoke point properties were measured using the NASA KC-35 mg test facility; these results provided information needed to plan flight experiments and also demonstrated substantial effects of buoyancy on laminar smoke point properties (ref. 16).

The third phase of the study of soot processes in laminar jet diffusion flames consisted of an extensive suite of measurements to find both soot and flame properties, and to exploit this information to study soot growth and nucleation, in diffusion flames. An overview of these studies is presented in the following, see refs. 19-21 for more details.

Experimental Methods. Measurements were completed along the axis of round laminar coflowing jet diffusion flames at pressures of 15-100 kPa. The following measurements were made: soot volume fractions using laser extinction, gas temperatures using either thermocouples or multiline emission, soot structure by thermophoretic sampling and analysis by TEM, gas compositions by sampling and analysis using gas chromatography and gas velocities by laser velocimetry.

Results and Discussion. Soot and flame properties along the axis of an acetylene/air round laminar coflowing jet diffusion flame at 19 kPa, with the ratio of initial ambient air to burner exit velocities, $u_a/u_f = 1.3$, are illustrated in Fig. 2. Properties shown include the streamwise velocity, u, the primary particle diameter, d_p, the soot volume fraction, f_s, the number of primary particles per unit volume, n_p, the temperature, T, the mixture fraction, f, and the mole fractions of gaseous species, X_i, as a function of distance from the burner exit, z. These results are typical of diffusion flames (refs. 19-21): major gas species satisfy universal state relationships for a given fuel and pressure, soot formation begins once temperatures exceed roughly 1200 K, soot formation ceases when hydrocarbons disappear at fuel-equivalence ratios of 1.1-1.2, n_p increases monotonically with z, but d_p and f_s exhibit maxima (the former due to interactions between soot nucleation and growth rates, the latter due to interactions between soot formation and oxidation rates).

These measurements were used to study soot growth and nucleation rates. Effective correlations of soot growth rates were based on collision efficiencies of light hydrocarbons, particularly acetylene which dominates hydrocarbon concentrations in the soot formation region, see Fig. 2. An example of a collision efficiency correlation appears in Fig. 3, where the net soot growth rate, corrected for oxidation, w_g, normalized by the mean molecular velocity of acetylene, $\bar{v}_{C_2H_2}$, is plotted as a function of acetylene concentration, $[C_2H_2]$, for acetylene-fueled diffusion flames (refs. 19 and 20) and for several premixed laminar flames (refs. 23-28). The order of the soot growth rate with respect to acetylene concentration is unity for the diffusion flames supporting soot growth by acetylene reaction at the soot surface with a collision efficiency of 0.30%. In contrast, soot growth rates in premixed flames exhibit a large vertical span, with only new soot at the highest temperatures in the premixed flames having growth rates similar to soot in diffusion flames. This behavior has been attributed to an effect of soot reactivity changes due to age in premixed flames (refs. 23-28), however, subsequent studies of premixed flames during the present investigation suggest an alternative explanation that will be discussed next.

Laminar Premixed Flames

Introduction. Laminar premixed hydrocarbon-fueled flames were studied to simplify the interpretation of measurements and to enhance computational tractability compared to laminar jet diffusion flames. In addition, earlier studies of soot growth processes in laminar premixed flames, e.g., refs. (23-28) involved approximations of soot optical and structure properties that have not proven to be very effective during recent evaluations (refs. 2-11), as well as questionable estimates of flow residence times. Present methods developed for studies of laminar diffusion flames (refs. 16-21) avoid these difficulties; therefore, the objective of this phase of the investigation was to apply these methods to studies of soot growth and nucleation in laminar premixed flames. An overview of the study is presented in the following, see ref. 22 for more details.

Experimental Methods. The measurements were completed along the axis of a 60 mm diameter water-cooled porous-plug premixed flat flame burner operating at 100 kPa. The burner flow was surrounded by a nitrogen shroud flow in order to avoid combustion of the fuel-rich soot-containing mixture with ambient air. The measurement techniques were the same as for the laminar diffusion flames (refs. 16-21). Finally, experimental conditions were similar to the ethylene/air flames of Harris and Weiner (refs. 25-27) and the methane/oxygen flames of Ramer et al. (ref. 28).

Results and Discussion. Measurements of soot and flame properties along the axis of a typical laminar premixed ethylene/air flame are illustrated in Fig. 4. These results are for a carbon/oxygen mole ratio, C/O = 0.90, but results at other conditions are qualitatively similar. Increased distance from the burner causes increased u due to buoyancy, increased f_s due to soot nucleation and growth, increased d_p due to soot growth and decreased T due to radiative heat losses, however, gas compositions remain essentially constant over the soot formation region. Thus, unlike diffusion flames where soot growth ends when hydrocarbons disappear, see Fig. 2, variations of soot growth in premixed flames are not particularly correlated with hydrocarbon concentrations, see Fig. 4.

Measured and predicted major gas species concentrations are plotted as a function of C/O ratio for the premixed ethylene/air flames in Fig. 5. The predicted concentrations are based on the detailed chemical mechanisms of Frenklach and coworkers (refs. 29-31) and Leung and Lindstedt (ref. 32), and were computed using the premixed flame code of Kee et al. (ref. 34). This code allows for multicomponent mass diffusion, thermal diffusion, variable thermophysical and transport properties and detailed chemical kinetics. Both measurements and predictions are for z = 20 mm, although effects of z are small. The agreement between predictions and measurements is excellent.

The predictions of Frenklach and coworkers (refs. 29-31) and Leung and Lindstedt (ref. 32) were then exploited to estimate concentrations of H, which is thought to be important via the hydrogen-abstraction/carbon-addition (HACA) soot growth mechanism (refs. 29-31,35). These estimates of H concentrations are illustrated in Fig. 6 and indicate that the detailed mechanisms yield very similar predictions which also agree with estimates based on the assumption of local thermodynamic equilibrium for this radical species.

The close correlation between temperature, H concentrations and soot growth rates, combined with nearly constant hydrocarbon concentrations, support the HACA mechanism of soot growth in laminar premixed flames (refs. 29-31,35). An initial evaluation of this hypothesis is illustrated in Fig. 7, where the soot growth rate normalized by C_2H_2 concentrations is plotted as a function of H concentrations for the three ethylene/air flames. The correlation of the measurements is seen to be excellent with H concentrations mainly controlling soot growth in the premixed flames. This suggests that the soot growth behavior seen in Fig. 3 represents two branches of the HACA mechanism: a vertical branch controlled by H concentrations in premixed flames and a branch controlled by C_2H_2 concentrations in diffusion flames.

Consideration of soot growth has been extended to specifically consider the HACA mechanisms of Frenklach and coworkers and Colket and Hall (refs. 29-31 and 35). These results for the HACA mechanism of Frenklach and coworkers (refs. 29-30) are illustrated in Fig. 8, where w_g is plotted as a function of their HACA reaction rate expression, R_{FW}, for premixed ethylene/air flames. The original proposal of Kazakov et al. (ref. 31) illustrated at the top of the figure was based on early data and does not exactly fit the present measurements; nevertheless, a trivial adjustment of a stearic factor in the model yields the excellent estimates of soot growth rates plotted at the bottom of the figure. Notably, similar results were obtained using the HACA soot growth model of Colket and Hall (ref. 35) after refitting one pre-exponential factor using the present measurements (ref. 22).

Current work involves similar measurements of premixed methane/oxygen flames in order to evaluate the HACA mechanism for a large H:C molar ratio. The fundamental properties of soot nucleation and oxidation are also being addressed so that improved models of soot processes can be developed for use in connection with measurements of the properties of soot-containing nonbuoyant laminar jet diffusion flames at mg.

References

1.   Law, C.K. and Faeth, G.M., Prog. Energy Combust. Sci. 20:65 (1994).

2.   Köylü, Ü.Ö. and Faeth, G.M., Combust. Flame 89:140 (1992).

3.   Köylü, Ü.Ö. and Faeth, G.M., J. Heat Trans. 115:409 (1993).

4.   Köylü, Ü.Ö. and Faeth, G.M., J. Heat Trans. 116:152 (1994).

5.   Köylü, Ü.Ö. and Faeth, G.M. J. Heat Trans. 116:971 (1994).

6.   Farias, T.L., Carvalho, M.G., Köylü, Ü.Ö. and Faeth, G.M., J. Heat Trans. 117:152 (1995).

7.   Köylü, Ü.Ö., Faeth, G.M., Farias, T.L. and Carvalho, M.G., Combust. Flame 100:621 (1995).

8.   Faeth, G.M. and Köylü, Ü.Ö., Combust. Sci. Tech. 108:207 (1995).

9.   Köylü, Ü.Ö. and Faeth, G.M., J. Heat Trans. 118:415 (1996).

10.   Farias, T.L., Carvalho, M.G., Köylü, Ü.Ö. and Faeth, G.M., Int. J. Heat and Technology 13:27 (1995).

11.   Wu, J.-S., Krishnan, S.K., and Faeth, G.M., J. Heat Trans., in press.

12.   Mortazavi, S., Sunderland, P.B., Jurng, J.J., Köylü, Ü.Ö. and Faeth, G.M., AIAA Paper No. 93- 0708, 1993.

13.   Köylü, Ü.Ö., Sunderland, P.B., Mortazavi, S. and Faeth, G.M., AIAA Paper No. 94-0428, 1994.

14. Sunderland, P.B. and Faeth, G.M., AIAA Paper No. 95-0149, 1995.

15. Sivathanu, Y.R. and Faeth, G.M., Combust. Flame 82:211 (1990).

16. Sunderland, P.B., Mortazavi, S., Faeth, G.M. and Urban, D.L., Combust. Flame 96:97 (1994).

17. Lin, K.-C. and Faeth, G.M., J. Prop. Power 12:10 (1996).

18. Lin, K.-C. and Faeth, G.M., J. Prop. Power 12:691 (1996).

19. Sunderland, P.B., Köylü, Ü.Ö. and Faeth, G.M., Combust. Flame 100:310 (1995).

20. Lin, K.-C., Sunderland, P.B. and Faeth, G.M., Combust. Flame 104:369 (1996).

21. Sunderland, P.B. and Faeth, G.M., Combust. Flame 105:132 (1996).

22. Xu, F., Sunderland, P.B. and Faeth, G.M., Combust. Flame, in press.

23. Bockhorn, H., Fetting, F., Wannemacher, G., and Wentz, H.W., *Nineteenth Symposium (International) on Combustion*, The Combustion Institute, Pittsburgh, 1982, p. 1413.

24. Bockhorn, H., Fetting, F., Heddrich, A. and Wannemacher, G.,*Twentieth Symposium (International) on Combustion*, The Combustion Institute, Pittsburgh, 1984, p. 979.

25. Harris, S.J. and Weiner, A.M. , Combust. Sci. Tech. 31:155 (1983).

26. Harris, S.J. and Weiner, A.M., Combust. Sci. Tech. 32:267 (1983).

27. Harris, S.J. and Weiner, A.M., Combust. Sci. Tech. 38:75 (1984).

28. Ramer, E.R., Merklin, J.F., Sorensen, C.M. and Taylor, T.W., Combust. Sci. Tech. 48 :241 (1986).

29. Frenklach, M. and Wang, H., *Twenty-Third Symposium (International) on Combustion*, The Combustion Institute, Pittsburgh, 1990, p.1559.

30. Frenklach, M. and Wang, H.,*Soot Formation in Combustion* (H. Bockhorn, ed.), Springer-Verlag, Berlin, 1994, p. 165.

31. Kazakov, A., Wang, H. and Frenklach, M., Combust. Flame 100:111 (1995).

32. Leung, K.M. and Lindstedt, R.P., Combust. Flame 102:129 (1995).

33. Leung, K.M., Lindstedt, R.P. and Jones, W.P., Combust. Flame 87:289 (1991).

34. Kee, R.J., Grcar, J.F., Smooke, M.D. and Miller, J.A., Report No. SAND85-8240, Sandia National Laboratories, Albuquerque, 1985.

35. Colket, M.B. and Hall, R.J., *Soot Formation in Combustion* (H. Bockhorn, ed.), Springer-Verlag, Berlin, 1994, p. 442.

Fig. 1 TEM photograph of soot aggregates within a premixed methane/oxygen flame at 100 kPa.
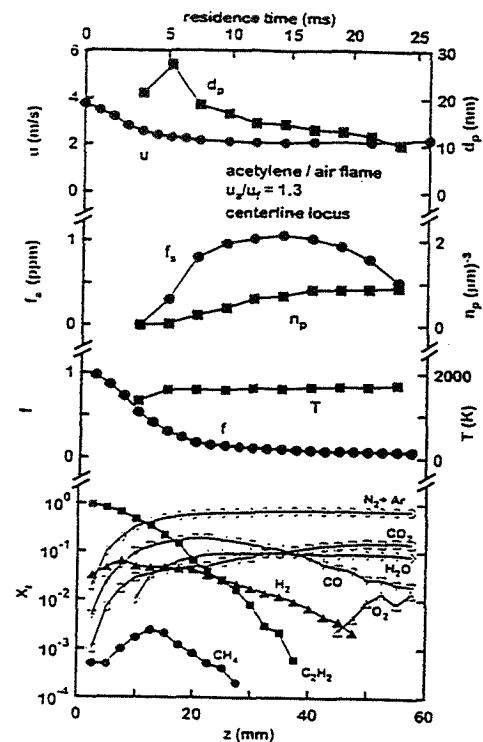
Fig. 2 Soot and flame properties along the axis of an acetylene/air laminar coflowing jet diffusion flame at 19 kPa with $u_a/u_f = 1.3$. From ref. 20.
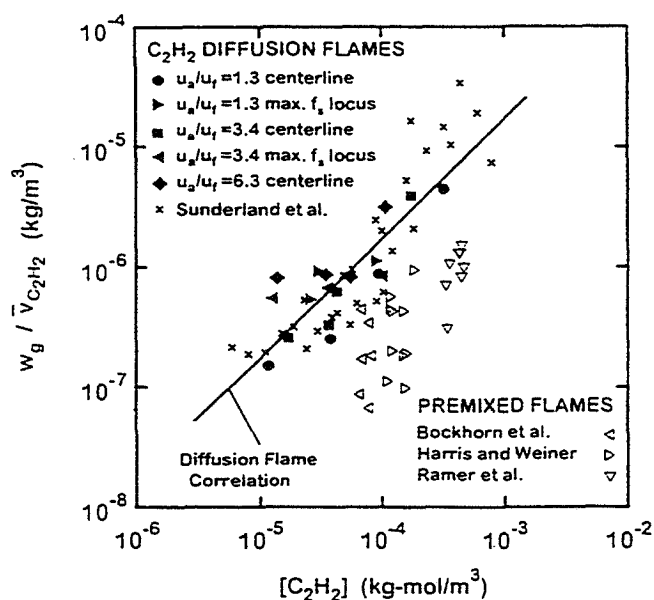
Fig. 3 Net soot growth rates in laminar acetylene/air diffusion flames from refs. 18 and 19, and in laminar premixed flames from refs. 23-28, all as a function of acetylene concentration. From ref. 20.
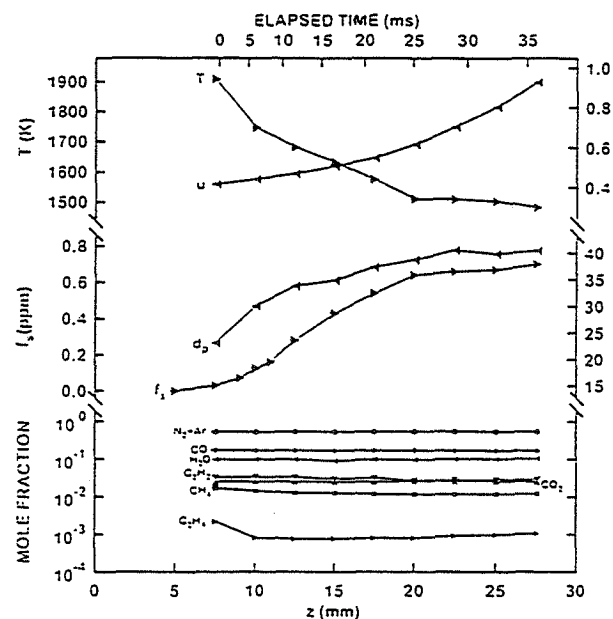
Fig. 4 Soot and flame properties along the axis of an ethylene/air laminar premixed flame with C/O = 0.98 at 100 kPa. From ref. 22.

203
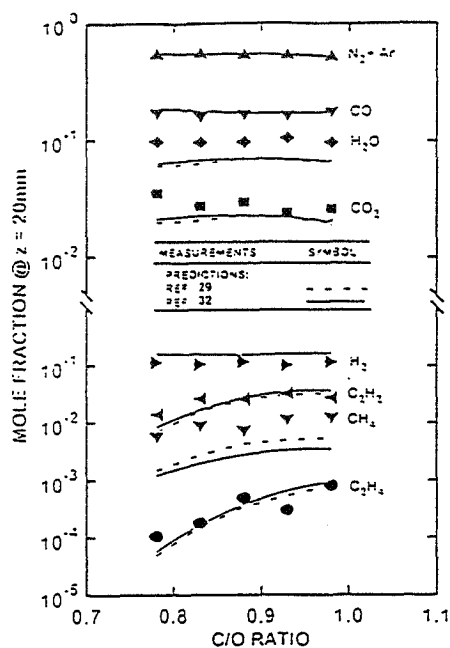
Fig. 5 Measured and predicted concentrations of major gas species at the axis of ethylene/air laminar premixed flames at z = 20 mm and 100 kPa as a function of C/O ratio. From ref. 22.
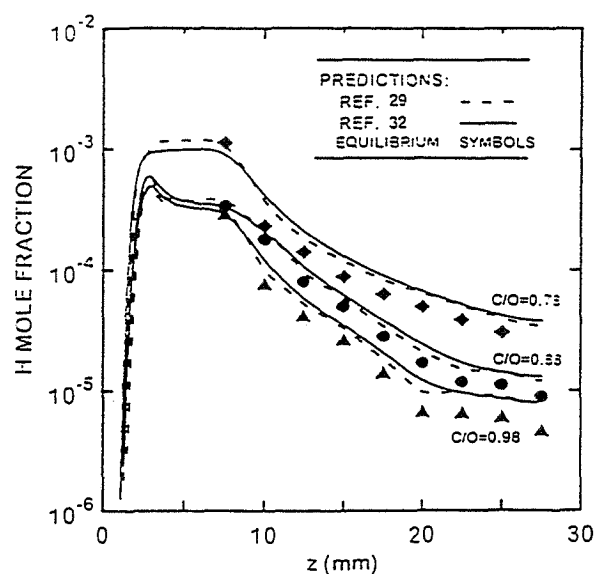
Fig. 6 Predicted H atom concentrations along the axis of laminar premixed ethylene/air flames at 100 kPa. Predictions based on detailed mechanisms of refs. 30 and 33, and the assumption of local thermodynamic equilibrium. From ref. 22.
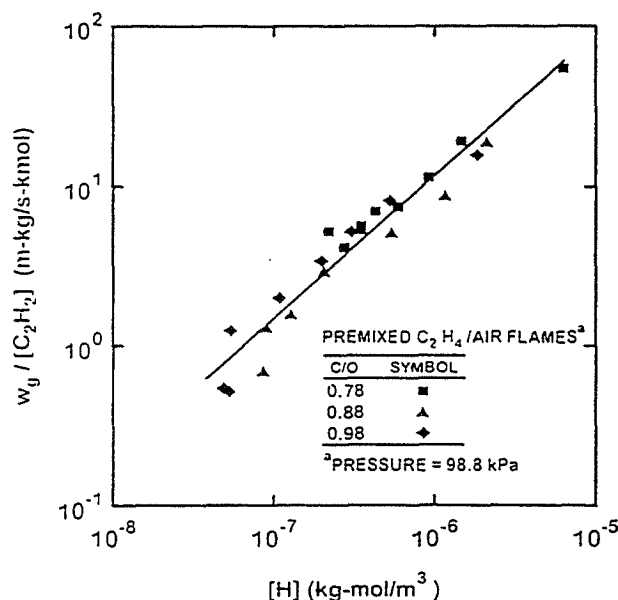
Fig. 7 Measured soot surface growth rates as a function of acetylene and H concentrations for laminar premixed ethylene/air flames at 100 kPa. From ref. 22.
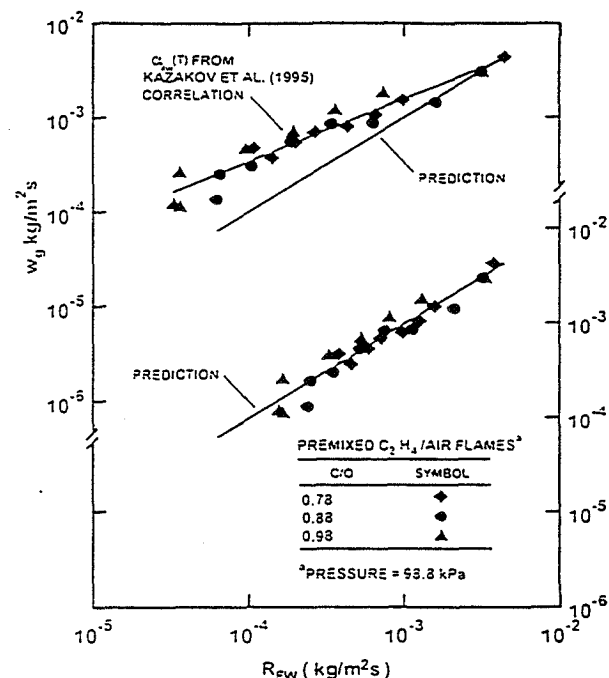
Fig. 8 Predicted and measured soot surface growth rates in premixed ethylene/air flames at 100 kPa. Predictions based on HACA mechanism of Kazakov et al. (ref. 31). From ref. 22.

204

COMPARATIVE SOOT DIAGNOSTICS: PRELIMINARY RESULTS

DAVID L. URBAN

DeVon W. Griffin
Microgravity Science Division
NASA Lewis Research Center

Melissa Y. Gard
NASA Marshall Space Flight Center

Introduction

The motivation for the CSD experiment lies in the broad practical importance of understanding combustion generated particulate. Depending upon the circumstances, particulate matter can affect the durability and performance of combustion equipment, can be a pollutant, can be used to detect fires and, in the form of soot, can be the dominant source of radiant energy from flames. The non-buoyant structure of most flames of practical interest makes understanding of soot processes in low gravity flames important to our ability to predict fire behavior on earth. These studies also have direct applications to fire safety in human-crew spacecraft, since smoke is the indicator used for automated detection in current spacecraft [1].

In the earliest missions (Mercury, Gemini and Apollo), the crew quarters were so cramped that it was considered reasonable that the astronauts would rapidly detect any fire. The Skylab module, however, included approximately 20 UV-sensing fire detectors. The Space Shuttle has 9 particle-ionization smoke detectors in the mid-deck and flight deck and Spacelab has six additional particle-ionization smoke detectors. The designated detectors for the ISS are laser-diode, forward-scattering, smoke or particulate detectors. Current plans for the ISS call for two detectors in the open area of the module, and detectors in racks that have both cooling air flow and electrical power. Due to the complete absence of data concerning the nature of particulate and radiant emission from incipient and fully developed low-g fires, all three of these detector systems were designed based upon 1-g test data and experience. As planned mission durations and complexity increase and the volume of spacecraft increases, the need for and importance of effective, crew-independent, fire detection grows significantly. To provide this level of protection, more knowledge is needed concerning low-gravity fire phenomena and, in particular, how they might be detected and suppressed.

Prior to CSD, no combustion-generated particulate samples had been collected near the flame zone for well-developed microgravity flames. All of the extant data either came from drop tower tests [2,3] and therefore only corresponded to the early stages of a fire or were collected far from the flame zone[4]. The fuel sources in the drop tower tests were restricted to laminar gas-jet diffusion flames and very rapidly overheated wire insulation [2, 3]. The gas-jet tests indicated, through thermophoretic sampling, [2] that soot primaries and aggregates (groups of primary particles) in low-gravity may be significantly larger than those in normal gravity (1-g). This raises new scientific questions about soot processes as well as practical issues for particulate size sensitivity and detection/alarm threshold levels used in on-orbit smoke detectors. Preliminary tests in the 2.2 second drop tower suggest that particulate generated by overheated wire insulation may be larger in low-g than in 1-g [3]. Transmission Electron Microscope (TEM) grids downstream of the fire region in the Wire Insulation Flammability experiment [4] as well as visual observation of long string-like aggregates, further confirm this suggestion. The combined impact of these limited results and theoretical predictions is that, as opposed to extrapolation from 1-g data, direct knowledge of low-g combustion particulate is needed for more confident design of smoke detectors for spacecraft.

This paper describes the operation and preliminary results of the CSD, a project conceived and developed at NASA Lewis Research Center. The CSD flight experiment was conducted in the Middeck Glovebox Facility (MGBX) on USMP-3. The project is supported by NASA Headquarters Microgravity Science and Applications Division and Code Q. The results presented here are from the microgravity portion of the experiment, including the temporal response of the detectors and average sizes of the primary and aggregate particles captured on the thermophoretic probes. Complete assessment of the microgravity data and its combination with the normal-gravity data are still in process and will be reported later.

Background/Previous Work

Well-established normal-gravity fires emit small particulate in the size range to which ionization detectors are more sensitive than optical detectors [5]. Less well-established or smoldering fires will produce larger particulate, owing to the large amount of condensed, unoxidized fuel pyrolysis products and the incomplete soot oxidation. For this type of fire, light scattering/obscuration detectors are more appropriate. However, for materials heated slowly as in the very early stages of some fires, the particulate can be very small, and therefore more easily sensed by ionization detectors [6]. This analysis was used by Brunswick Defense in their decision to pursue an ionization detector for the STS. The design consists of a dual-chamber ionization detector that is in the flow path created by a vane pump. This vane pump provides some active sampling capability and also the flow for an inertial separation system which is designed to make the detector insensitive to particulate larger than 1 to 2 microns, depending upon the particle

mass. These advantages are offset by a fairly large power consumption (9 Watts), fan noise, and limited life due to the moving parts. The detector produces a discrete alarm signal and two analog signals related to the detected smoke density. For the tests reported here, the analog voltage was measured. This voltage has a baseline of 11.4 for the detector used here and decreases in the presence of smoke. The alarm value is set at the factory using a fixed offset from the internal detector baseline and consequently the analog output voltage at alarm is different for each detector. The analog voltage at alarm for the detector used in this work was 10.6 volts.

The design developed for the ISS by Allied Signal consists of a 2 pass laser diode obscuration system that also has a photo-diode positioned to sense forward scattered light (30 degrees) on the return path. The system is designed to alarm based on the magnitude of the scattered light signal. Dust discrimination is based on frequency analysis of the scattered light signal. The system is less sensitive to particles smaller than the wavelength of the laser (near IR) than it is to larger particles. The minimum reported sensitivity is 0.3 microns [7]. It draws relatively little power (1.5 W) and it has a long operational life. The current planned alarm value is 2 volts or 1% obscuration per foot.

The performance of these two detectors has been compared in normal gravity [7, 8]. Consistent with expectations, for cases where large particles were expected (punk smoke) the initial response of both detectors was about the same but the ISS detector reached the alarm threshold more rapidly. For sources of smaller particle-size smoke (over heated wire) the STS detector was quicker both in initial response and in time to alarm. The implementation (alarm threshold selection) of both of these systems in microgravity is hampered by the lack of knowledge of their performance against low-gravity combustion generated particulate.

Objectives

The objectives of CSD are to examine the particulate formation from a variety of particulate-generating sources and to quantify the performance of several particulate-sensing diagnostic techniques. The sources include: a candle tested at three coflow air velocities and four overheated materials (paper, silicone rubber, and teflon and kapton coated wires) each tested at three heating rates. The paper, silicone rubber and wire insulations are materials found in spacecraft crew cabins and candles produce hydrocarbon soot typical of many practical 1-g flames. Four diagnostic techniques were employed: thermophoretic sampling to provide samples of the particulate for size analysis, laser-light extinction measurements near the source to provide total smoke production data, and laser light scattering and ionization detector measurements to provide data concerning the performance of the detectors for these particulate sources.

Hardware Description

The CSD experimental hardware consists of two modules named the Near-Field Module and Far-Field Box as shown in figure 1.The Near-Field Module is installed inside the Glovebox and contains the sample and the near field diagnostics. The Far-Field Box is external to the Glovebox and contains two spacecraft smoke detectors. Products from the near field tests are transported to the Far-Field Box and subsequently back into the Glovebox via teflon hoses which enter the Glovebox through ports in the airlock door. All of the combustion products are contained in either the Glovebox or the Far Field Box; by the time the experiment is completed, all of the products are returned to the Glovebox.

The Near-Field Module consists of a small test chamber fitted with a sample carrier that holds the sample being tested. A small fan blows air from the glovebox into the right side of the chamber past the sample and out the left side where it enters the hose to the Far-Field Module. The sample is ignited or overheated by a resistively heated Kanthal wire. The smoke particulate is sampled by a rake of thermophoretic probes and smoke production is detected by a laser light extinction system.

The Far Field Box contains a duct and a fan to transport the smoke from the Near Field Module to two spacecraft smoke detectors, one matching the STS detector and the other identical to the ISS detector except that its signal is amplified by a factor of 6.6 over the ISS standard. This amplification was added because the engineering model of the ISS detector that was used for developing the test matrix displayed very low signal levels. Since the tests were intended more as a test of each technology rather than specific designs or alarm levels, the signal was amplified in the model used in the flight tests. Post flight calibration of both units by Allied Signal revealed that the engineering model was operating below specification by a factor of 5, voiding the reason for the amplification. However, despite the amplification, sufficient dynamic range exists on the measurement that it is possible to predict when an unamplified unit would show significant detection. The analog signals from the various instruments are displayed by digital readouts on the Far Field Box where they are recorded by a video camera for later transcription.

Procedure and Operational Sequence and Data Reduction

The crew installed the near field hardware in the Glovebox, attached the Far Field Box to the Glovebox, and positioned the video cameras. The operator then ran the self diagnostic procedures on the two smoke detectors and activated the video cameras, turned on the ignitor for a predefined period of time (15 to 60 seconds), and initiated the thermophoretic soot samplers to sample the smoke. The actual duration of each combustion event was typically 2 minutes. After the experiment, the operator stowed and reloaded the soot samplers, the test sample, and the filters at the end of the return line from the Far Field Box. At this point the operator either stowed the modules or initiated another run. The tests ran very efficiently and after the first two sessions, typically ran ahead

of schedule. The sessions consisted of 2 to 7 runs each. The majority of the tests were run with predefined igniter power levels, however, to examine the response threshold, some of the tests in the final session were conducted repeatedly on the same samples at small increases of power level for each retest. After flight, the particulate collected on the thermophoretic probes were analyzed using a Transmission Electron microscope (TEM) to determine primary and aggregate particle dimensions. The remains of the samples were weighed to determine their mass loss. The digital data was transcribed from the video record and analyzed to determine the response of the detectors. Once the flight mass loss rates were determined, 1-g operation conditions to produce the same loss were determined. These conditions are being used to produce a 1-g comparison data set.

Results

In all, 25 tests were performed and the data from the runs are summarized in table 1, which lists the mass loss rate of the sample, the time it took for the signal to reach a value of 20% of the operating range of the detector and the time and value of the peak signal for both detectors. Since these tests were designed to function as a test of the detection technologies rather than the detectors themselves (or their alarm setpoints) 20% of the dynamic range was selected to tabulate as a consistent detection point for both detection technologies. The selection of the actual alarm level for each detector is more complex than mere detection as false alarm rejection and other issues must be considered. The bulk of the tests were overheated material tests in which the heating level was established to produce a target weight loss rate without causing the sample to develop a sustaining combustion reaction. The intent of these tests was to produce smoke typical of an incipient fire where much of the material is being heated but has not yet ignited. The candle tests and one of the paper tests were combustion tests where the samples were ignited so the combustion products could be observed. Figures 2-5 contain the signal data from two typical candle, one Kapton and one silicone rubber tests respectively. The response of the smoke detectors, the ignitor voltage and the signal for the lasers in the near field module are plotted with respect to time. As plotted, the data for the ISS detector overstates the sensitivity of the flight unit since the unit used here is 6.6 times more sensitive than the flight model. These tests were neither designed nor expected to reach specific alarm levels. Instead the tests were planned to provide a measure of the relative sensitivity of the two detector types to low gravity smoke particulate by providing sufficient particulate to achieve adequate signal levels on the detectors. To explore the effect of heating rate on particle size, the power level was different for each test with each material. The results of the tests are discussed below by sample type.

Candle Tests:
In all tests the detector's signals showed an immediate peak that is attributed to the wax vapor released by the ignition process. This peak was detected more quickly by the ISS detector. Once the candle was ignited, the STS detector showed strong signals for all tests while the ISS detector showed strong signals for tests 1 and 16 (e.g. Fig. 2) and very weak signals (if unamplified) for tests 6 and 11 (e.g. Fig. 3). The cause of this is still under investigation.

Paper Tests:
Runs 5g, 10 and 25e were pyrolysis runs i.e. they did not produce a flame but instead allowed the paper to degrade into pre-combustion or pyrolysis products. Of these, run 10 showed appreciable mass loss and was readily detected by the ISS detector while the STS detector produced marginal signal. In contrast, 1-g comparison tests show strong signals on both detectors. Runs 5g and 25e were the last runs in a series of tests aimed at finding the threshold detection level for the sample. These tests showed slightly higher signals for the ISS detector, however, if scaled to real detector performance (i.e. unamplified) neither detector showed distinct signal. Test 20 was a flaming test of a small paper sample and showed a marginal advantage for the STS detector. Test 15 was intended to be a pyrolysis test but self-heating caused the sample to develop a self-sustaining smolder reaction late in the test. The ISS detector detected both the pyrolysis and flaming intervals while the STS detector only detected the smoldering interval.

Teflon Wire Tests:
Both detectors showed strong signals for tests 3, 13, and 18. On test 8, however, the STS detector showed minimal signal and the ISS had a weak signal (unamplified). For Test 21 the STS detector showed a weak signal compared to no signal (even amplified) for the ISS detector. Test 23b showed no signal for either detector.

Silicone Rubber Tests:
For all of the tests with silicone rubber, the ISS detector showed very strong signals while the STS detector showed at most a weak signal (Fig. 4). This is contrary to 1-g comparison test results where this material also shows a strong signal on the STS detector.

Kapton Wire Tests:
Both detectors showed strong signals for 4, 9, 14 and 19 with both producing low signals (STS slightly higher) for test 24 which was a low mass loss test

TEM Results:
Thermophoretic sampling has been used previously in the drop tower for gas jet diffusion flames and for overheated wires [2,3]. For the overheated but not burning materials, a weak thermal gradient was expected and consequently the probe was left in place for 45 seconds while in the case of the much hotter candle flame the probe was left in for less than a second. When the probes were returned to earth, the grids were removed and analyzed in a TEM to determine the primary particle and aggregate size distribution.

Timing of the deployment of the soot sampler required rapid subjective decisions by the crew member. Based upon our video record, they did an excellent job. We encountered less stable flow of the smoke plume than we anticipated and had a high rate of loss of TEM grids due to failure of the adhesive. Consequently particulate samples were not obtained on all tests.

Figures 6 a-c contain TEM images of typical particulate from Teflon, Kapton and Candle tests. The three images are at the same magnification and show the significant variation in the particulate morphology for the three materials. Table 2 summarizes the results for the tests for which good sampling was achieved. Significantly, despite strong smoke levels visible in the video record, no particulate material was found on the TEM grids for overheated paper and silicone rubber tests. The suspected cause of this is that the particulate for these materials is actually liquid droplets which later evaporate or spread out on the grids' surface, rendering them undetectable by the TEM. The primary particle dimensions range from 30 to 40 nm for soot to 60-100 nm for Kapton and 130 to 200 nm for Teflon. The aggregate soot dimensions grow with distance from the candle from 400 nm at 15 mm from the wick to 1200 nm at 35 mm from the wick. The Kapton aggregates range from 220 - 250 nm and the Teflon aggregates range from 600-1100 nm. The dimensions reported in Table 2 are geometric averages (averages based upon a log-normal size distribution). The probe centerlines were 10 mm apart along the flow axis and are numbered sequentially beginning with the probe nearest to the sample. Each probe assembly inserted the 4 probes simultaneously. The rejection criteria for the inertial separation in the STS detector is based upon a 1 to 2 micron particle mass. Since the soot from the candle tests was still very successfully detected, either 1.2 micron soot particles have not reached the rejection mass level or enough particles were below the rejection level to deliver a strong signal. The Teflon and Kapton samples produced large primaries with the largest occurring in Teflon test 13 (195 nm) the resultant aggregates were 1.1 microns.

Discussion

Data analysis and interpretation are well underway but have not yet been completed. The companion 1-g test program is also underway but incomplete. However, the smoke produced in the low-g silicone rubber and paper tests was thick and clearly visible while in comparable 1-g tests, it was only marginally visible for the same mass loss rate. This can be explained by the absence of buoyant flows which (in 1-g) dramatically accelerate the gas velocities in the vicinity of the source, reducing the residence time of the particulate in regions of high concentration. Since particulate sizes for the smoke from these two materials could not be obtained with TEM analysis, the reasons for the lower signal levels from the STS detector can only be inferred. It is likely that these droplets had more opportunities to coalesce into droplets whose size exceeded the maximum size for which the STS detector is sensitive (1-2 microns). For very low mass loss tests for wire insulation materials, the STS detector showed more signal than the ISS model. Once the 1-g comparison tests are complete, further analysis of the results will be possible.

Conclusions

The CSD experiment successfully produced controlled quantities of smoke particulate from a variety of sources. The response of the STS and ISS detectors to these smoke sources was measured and samples of the smoke particulate were successfully obtained from many of the tests. The assembled data provide the first examination of the response of spacecraft smoke detectors to microgravity smoke particulate.

The most significant conclusion to be drawn, so far, from this work is that sensitivity to the smoke from an individual material in 1-g does not indicate strong sensitivity to the smoke from the same material in low-g. Despite the presence of a forced flow (provided by a fan) in the low-g tests the absence of buoyant flows apparently changed the particle size distribution. We have not yet determined if the change is sufficiently systematic that correlations can be obtained. Both detectors showed responsiveness for the majority of materials; the STS detector showed limited sensitivity to pyrolyzing materials that produce liquid particulate. The particle dimensions covered a wide range from 30 to 200 nm for primary particles and from 220 to 1200 nm for aggregates.

Acknowledgments

References

1) Friedman, R., 1992. Journal of Applied Fire Science, 2:243-259.
2) Ku, J.C., D.W. Griffin, Greenberg, P. S., and J. Roma. 1995: Combustion and Flame, 102:216-218.
3) Paul, M., F. Issacci, G. E. Apostalakis and I. Catton. 1993. ASME-HTD Vol. 235:59-66.
4) Greenberg, P. S., K. R. Sacksteder and T. Kashiwagi. 1995. Wire Insulation Flammability Experiment, NASA CP 3272 V II.

5) Bukowski, R.W. and G.W. Mulholland. 1978. Smoke Detector Design and Smoke Properties. NBS Technical Note 973.
6) Chuan, R. L. and H. D. Chen. 1986. Aerosol Characterization in an Incipient Fire. Second Int.l Aerosol Conf., Berlin, Sept.
7) Steisslinger, H. R., D. M. Hoy, J. A. McLin and E. C. Thomas. 1993. SAE Paper 932291.
8) McLin, J. 1993. Smoke Comparison Test Report Doc. # 93-05902, Allied Signal Aerospace.

Table 1 Detector Signals from CSD Flight tests (ISS values are scaled to flight)

Test Point	ISS Detector Time to 20% (s)	Time to Maximum (s)	Voltage at maximum	% FS at Maximum	STS Detector Time to 20% (s)	Time to Maximum (s)	Voltage at Maximum	% FS at Maximum	mass loss rate (micro-gm/s)
Paper									
10	31	33	7.22	29.6	—	---	---	—	43.4
15	20	21	7.21	29.5	54	61	9.2	91.7	consumed
20	—	24	1.56	6.1	—	18	11.27	5.8	consumed
25e	—	73	0.75	0.2	—	89	11.34	4.1	multiple tests
5g	—	71	0.74	2.1	—	70	11.37	1.3	multiple tests
Candle									
1	61	62	7.2	29.6	—	82	9.65	73.4	consumed
6	—	70	2.3	9.2	—	67	10.55	36.0	consumed
11	69	69	6.88	28.3	35	75	9.9	9.9	consumed
16	45	49	7.21	29.2	47	108	9.53	9.5	consumed
Silicon Rubber									
2	20	20	7.22	30.1	—	82	11.14	11.6	107
7	18	19	7.22	30.1	—	44	11.24	7.4	58.7
12	21	23	7.23	30.1	—	31	11.39	1.2	130
17	16	17	7.22	30.1	—	39	11.21	8.7	128
22	32	34	7.24	30.2	—	52	11.28	6.9	15.2
Teflon									
3	55	62	7.23	34.5	72	76	10.88	22.6	86.2
8	—	61	4.18	16.9	—	67	11.27	6.6	141
13	27	27	7.21	29.6	—	35	11.17	10.0	155
18	31	32	7.22	29.6	39	42	10.92	20.3	143
21	—	78	0.29	0.8	—	81	11.29	6.5	47.9
23a	—	46	0.51	1.7	—	59	11.36	2.5	multiple tests
Kapton									
4	14	15	7.21	29.6	25	37	10.1	54.4	37.5
9	14	23	7.23	29.7	28	37	10.64	32.5	56.5
14	13	14	7.21	29.6	24	33	10.19	50.8	106
19	10	10	7.21	29.6	25	30	10.36	43.6	99.4
24	—	28	0.88	3.3	—	74	11.09	14.3	4.29

Table 2 TEM results

Test Point	Probe Number	Primary Diameter (nm)	Aggregate diameter (nm)
1 (Candle)	1	44	417
	2	33	742
	3	39	1185
16(Candle)	2	38	710
	4	32	1252
8(Teflon)	1	136	608
	4	134	------
13(Teflon)	1	195	1084
	2	154	669
9 (Kapton)	1	79	234
	4	95	253
19(Kapton)	3	74	119
	4	85	184
20(Flaming Paper)	1	29	406
	2	26	425
	3	24	301

CSD System Schematic
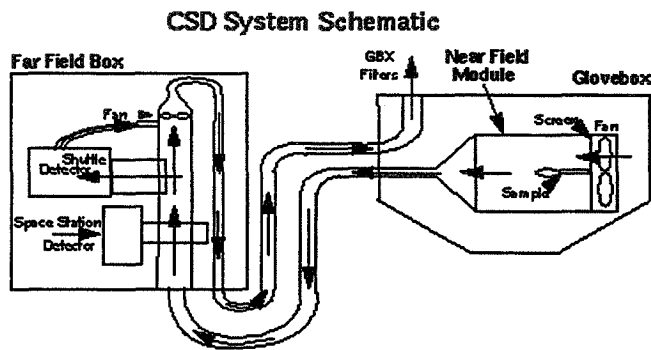
Figure 1. Schematic showing installation of the CSD Near Field Module inside the Glovebox and Far Field Module outside of the Glovebox
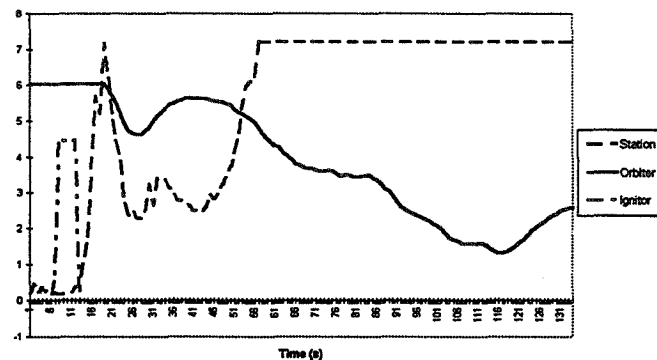
Figure 2: Traces of smoke detector signals as a function of time for a candle test (#16). Initial peak on both detectors is wax vapor released by the ignition process. The units on the vertical axis are arbitrary, the smoke detector data have been scaled so their dynamic ranges have similar vertical extent.
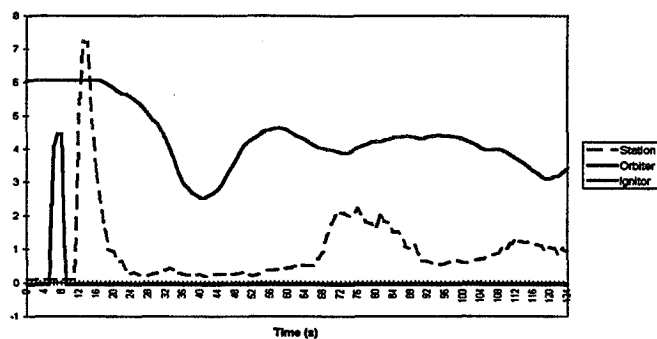
Figure 3: Traces of smoke detector signals as a function of time for a candle test (#6). Initial peak on both detectors is wax vapor released by the ignition process. The units on the vertical axis are arbitrary, the smoke detector data have been scaled so their dynamic ranges have similar vertical extent.
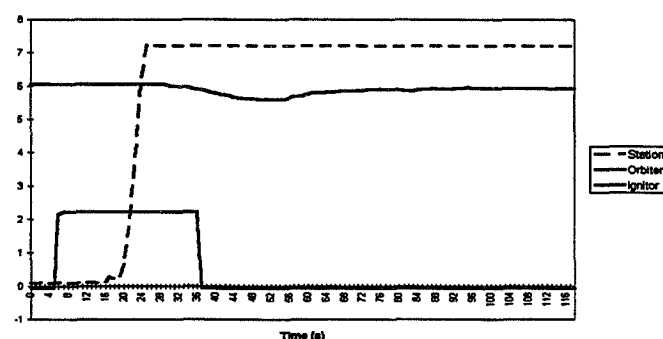
Figure 4: Traces of smoke detector signals as a function of time for a silicone rubber test (#7). The units on the vertical axis are arbitrary, the smoke detector data have been scaled so their dynamic ranges have similar vertical extent.
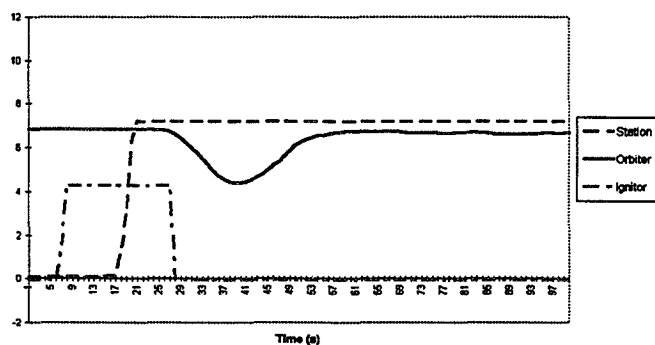
Figure 5: Traces of smoke detector signals as a function of time for a Kapton test (#14). The units on the vertical axis are arbitrary, the smoke detector data have been scaled so their dynamic ranges have similar vertical extent.
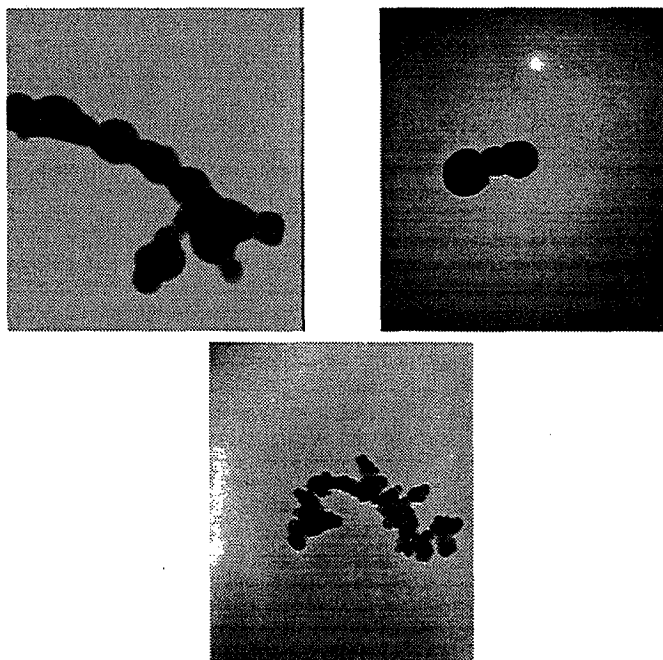
Figure 6: From top left, images of microgravity particulate from overheated Teflon and Kapton and Candle soot.

210

TEMPERATURE AND RADIATIVE HEAT FLUX MEASUREMENTS IN MICROGRAVITY JET DIFFUSION FLAMES*

JERRY C. KU
Mechanical Engineering Department
Wayne State University
Detroit, MI 48202

and

Paul S. Greenberg
Microgravity Combustion Branch
NASA Lewis Research Center
Cleveland, OH 44135

Introduction

The objective of this project is to provide detailed measurements and modeling analyses of local soot concentration, temperature and radiation heat flux distributions in laminar and turbulent jet diffusion flames under normal (1-g) and reduced gravity (0-g) conditions. Results published to date by these co-PI's and their co-workers include:
1. thermophoretic sampling and size and morphological analyses of soot aggregates in laminar flames under normal and reduced gravity conditions (ref. 1);
2. full-field absorption imaging for soot volume fraction maps in laminar (ref. 2) and turbulent flames under normal and reduced gravity conditions; details for the technique, its validation and comparisons to published point-by-point results can be found in Refs. 3 and 4, and a paper to appear in Applied Optics;
3. an accurate solver module for detailed radiation heat transfer in nongray nonhomogeneous media (refs. 5 and 6);
4. a complete model to include flame structure, soot formation and an energy equation to couple with radiation solver (ref. 7).

In this paper, we will report flame temperature measurements using fine-wire thermocouples and a full-field imaging absorption-emission technique. We will also report some spectral radiative flux measurements. Most of the results will be from turbulent jet flames. Since the acquisition of final data started only two months ago in January 1997, we have only begun to sort through and analyze some of the data we obtained, while a lot more data will be collected and analyzed before the workshop in May.

Temperature Measurements by Rapid-Insertion Fine-Wire Thermocouples

Despite their intrusive nature, thermocouples have been used by many researchers to measure temperature in flames (refs. 8-11). Major complicating factors in thermocouple flame temperature measurements are long response time (few hundred milliseconds even for 50 micron bead size), soot deposition and correction for radiation heat loss. Nonetheless, due to its simplicity, it still is a very viable technique for microgravity combustion studies. As will be discussed later, thermocouples are needed for measuring temperatures in soot-lean regions and for local instantaneous temperature in turbulent flames, since line-of-sight pyrometry type of measurements are not applicable. There have been studies of time-resolved temperature measurements in turbulent flames using thermocouples (refs. 12 and 13).

K-type thermocouple, which has a temperature range of 300 to 1750K, was used for this study. Wires of 25 micron diameter are spot-welded in-house to form a bead of the size of 50 micron or so. Rather than mounting and leaving thermocouples stationary in the flame, as has been done by most researchers, we decided to rapidly insert and retract them so flame perturbation and soot deposition are reduced to a minimum. The wires are thus attached to the same blade which has been used

211

for thermophoretic soot sampling, and the same pneumatic-actuating device was used. A piloted jet burner, with a fuel tube diameter of 0.508 mm and a pilot tube diameter of 1.283 mm, was used to produce all the turbulent flames in this study. The same fuel is used for the pilot at 1 (most cases) to 2% volumetric flow rate. After being recorded on an oscilloscope, thermocouple electrical signals are plotted and stored in a PC using the LabView package. A linear voltage-to-temperature relation is assumed for now, which can be easily modified.

Figure 1 shows the resulting transient response when the thermocouple was inserted to measure temperature along the axis at a height of $150D$ (D = nozzle diameter) in a 10 cc/s turbulent acetylene flame. 5 consecutive runs were then made at the longest residence time of about 240 millisecond. Substantial differences in these 5 temperature profiles are observed. However, this may be explained by the fact that these measurements were taken with a clean thermocouple, and factory contamination on the bead and the onset of soot deposition may be the reasons for the observed fluctuation. Subsequent measurements using the same thermocouple show very good consistency.

To obtain an equilibrium temperature, a part of the profile was fitted to a transient response function of the from (ref. 14)

$$\frac{T(t) - T(t_0)}{T_f - T(t_0)} = 1 - \exp\left[-\left(\frac{hA}{mc}\right)(t - t_0)\right], \tag{1}$$

where T_f is the equilibrium bead temperature, h is the convective heat transfer coefficient, t_0 is an arbitrary reference starting time, and A, m and c are surface area, mass and specific heat, respectively, of the bead. In fitting $T(t)$ data to the equation above, (hA/mc) is the parameter to be optimized, and temperature profiles over 150 to 300 ms were used. The results are also shown in Figure 1. Figure 2 shows the results at $100D$ heights. One point pretty clear from these plots is the fact that although profiles vary from run to run, sometimes may be substantial, but they pretty much stabilize toward a narrow range of equilibrium temperature. As mentioned earlier, measurements at $150D$ height were taken with a clean thermocouple, which may explain the inconsistency among the first 2 runs. The last 3 runs at $150D$ height and all 5 runs at $100D$ height are very consistent.

Correction for radiation heat loss are significant for thermocouple measurements in high temperature environments, and can be easily accomplished by performing an energy balance between radiation and convection given as

$$\varepsilon\sigma(T_f^4 - T_\infty^4) = h(T_g - T_f), \tag{2}$$

where T_g is the gas temperature, ε is the emissivity and σ is the Stefan-Boltzmann constant. It is not simple to estimate ε and h. The emissivity ε of the bead surface may vary between around 0.5, a value typical for oxidized metals (as for clean beads), to around 0.9, a value for carbon and graphite (as for soot-coated beads). A medium value of $\varepsilon = 0.7$ is adopted here. To estimate h, we assume that the flame has the properties of air at 1400K, which has a conductivity of $k = 9.1 \times 10^{-3}$ W/mK, a kinematic viscosity of $\nu = 2.13 \times 10^{-4}$ m^2/s and a Prandtl number of $Pr = 0.703$, and that the bead has a diameter of $d = 50$ micron. h can then be calculated from (ref. 15)

$$h = \frac{k}{d}\left[2 + \left(0.4Re_d^{1/2} + 0.06Re_d^{2/3}\right)Pr^{0.4}\right]. \tag{3}$$

Table 1 lists the values for those relevant parameters at $100D$ and $150D$ heights. The magnitude of temperature correction, 153.6 and 135.5K, respectively, are very comparable with the reported range (ref. 12). However, the resulted gas temperatures of 1313.6 and 1250.5K at $100D$ and $150D$ height, respectively, are 325.4 and 282.5K lower than the imaging pyrometry results to be discussed later. The voltage-to-temperature conversion (assumed linear here) will be among the factors to be investigated.

Full-Field Temperature Measurements Using Emission/Absorption Imaging Pyrometry

Another temperature measurement technique that was investigated is the emission/absorption tomography applied by Hall and Bonczyk (ref. 16), originally as point-by-point measurements. Since the ability in obtaining instantaneous full-field property maps (rather than point-by-point) is a tremendous advantage in microgravity experiments, we simply expanded our absorption imaging technique (ref. 2-4) to include emission imaging. The basic concepts are quite simple. The absorption coefficient ($\approx$ extinction coefficient) is first obtained from tomographic reconstruction of the line-of-sight absorbance. If the medium is optically-thin, the local emissive power (i.e., product of emissivity and Planck's function) can also be reconstructed similarly. By applying the Kirchhoff's law which equates the spectral emissivity and spectral absorptivity, the local temperature can be deduced from the Planck's function obtained as the ratio of emission and absorption measurements.

212

The advantages of this technique include using the same setup for both absorption and emission measurements with 1 CCD camera only and eliminating the uncertainties involved in estimating the spectral emissivity, which is equal to the measured absorptivity. To switch the setup from absorption to emission mode, the laser is turned off and additional neutral density filters are added as necessary. The disadvantages of the technique are its limitation in applying to laminar flame only and its inability in providing reliable results in regions where soot volume fraction is relative low and hence can not be accurately determined (as discussed in ref. 16). The former is true of all optical techniques involving line-of-sight measurement, since it is practically impossible to reconstruct instantaneous property maps due to their high fluctuation nature. However, when enough images are taken and averaged, the technique can be used to provide a good estimate for turbulent mean temperature. For turbulent flames and soot-lean regions in the flame, thermocouple seems to be the natural choice for temperature measurements.

The data analysis starts with the smoothing of line-of-sight absorbance and emission maps, then the reconstruction of local soot volume fraction and emissive power maps and from their ratio a temperature map is calculated, and finally a second smoothing on temperature profiles. The intent of this last step is to obtain reliable temperature data for soot-lean regions in the flame. However, based on limited attempts, the resulting overcome is not as satisfactory as expected.

Figure 3 shows the resulting soot volume fraction and temperature profiles for a 3.85 cc/s laminar co-flow ethylene flame, and comparisons to data obtained by Santoro et al. (ref. 9). Generally, the agreements are good, keeping in mind that temperatures were measured using thermocouples in Santoro et al. The inability of the emission/absorption technique in providing reliable temperature data in soot-lean regions both between and outside the soot peaks is clearly seen. Figure 4 shows the results for a 10 cc/s turbulent acetylene flame.

Spectral Radiation and Laser-Induced Incandescence (LII) Measurements

Both spectral radiation and laser-induced incandescence measurements provided interesting 1-g and 0-g comparisons for line-of-sight spectral intensity and instantaneous soot volume fraction along the axis of turbulent jet flames. The data are so recent that we can not analyze and include the results in this paper, but we will present them in May at the Workshop.

Summary

In summary, both thermocouple and emission/absorption imaging pyrometry technique provide reasonably satisfactory results for temperature measurement. The two techniques seem to compliment each other to cover most of the needs for temperature measurements in microgravity. Both spectral radiation and LII measurements are very significant addition to microgravity combustion diagnostics. Spectral radiation measurements providing critical wavelength-dependent radiation intensity data, and LII being the only technique capable of instantaneous turbulent soot volume fraction measurement, both are desperately needed for the understanding of physical fundamentals as well as model validations for microgravity jet diffusion flames.

Acknowledgment

References

1. Ku, J. C., Griffin, D. W., Greenberg, P. S., and Roma, J., "Buoyancy-Induced Differences in Soot Morphology," Comb. Flame, 102, 216-218 (1995).

2. Greenberg, P. S., and Ku, J. C., "Soot Volume Fraction Maps for Normal and Reduced Gravity Laminar Acetylene/Air Jet Diffusion Flames," Comb. Flame, 108, 227-230 (1997).

3. Greenberg, P. S., "Laser Doppler Velocimetry and Full-Field Soot Volume Fraction Measurements in Microgravity," 247-252, Proc. 3rd Int'l. Microgravity Comb. Workshop, Cleveland, Ohio, April 11-13 (1995).

4. Weiland, K. S., "Qualitative and Quantitative Imaging in Microgravity Combustion," 291-196, Proc. 3rd Int'l. Microgravity Comb. Workshop, Cleveland, Ohio, April 11-13 (1995).

5. Hsu, P.-F., and Ku, J. C., "Radiative Heat Transfer in Finite Cylindrical Enclosures with Nonhomogeneous Participating Media," J. Thermophys. Heat Transfer, 8, 434-440 (1994).

6. Hsu, P.-F., and Ku, J. C., "Detailed Spectral Radiation Calculations for Nonhomogeneous Soot/Gas Mixtures Based on a Simulated Ethylene Jet Diffusion Flame," 372-386, Radiative Transfer - I, Proc. 1st Int'l Symp. Radiative Transfer [ICHMT, Kusadasi, Turkey, Aug. 14-18, 1995], M. P. Menguc, ed. (1996).

7. Ku, J. C, L. Tong, and Greenberg, P. S., "Measurements and Modeling of Soot Formation and Radiation in Microgravity Jet Diffusion Flames," HTD-Vol. 335, Proc. ASME Heat Transfer Division, Vol. 4, 261-270 (1996).

8. Heitor, M. V., and Moreira, A. L. N., "Thermocouples and Sample Probes for Combustion Studies," Prog. Energy Combust. Sci., U19U, 259-278 (1993).

9. Santoro, R. J., Yeh, T. T., Horvath, J. J., and Semerjian, H. G., "The Transport and Growth of Soot Particles in Laminar Diffusion Flames," Comb. Sci. Tech, 53, 89-115 (1987).

10. Eisner, A. D., and Rosner, D. E., "Experimental Studies of Soot Particle Thermophoresis in Nonisothermal Combustion Gases Using Thermocouple Response Techniques," Comb. Flame, 61, 153-166 (1985).

11. Kent, J. H., and Wagner, H. Gg., "Why Do Diffusion Flames Emit Smoke?" Comb. Sci. Tech., 41, 245-269 (1984).

12. Cannon, S. M., "An Experimental and Numerical Study of an Elliptic Cross-Section, Turbulent, Diffusion Jet Flame," M. S. Thesis, Mechanical Engineering Department, Brigham Young University (1994).

13. Strahle, W. C., and Muthukrishnan, M., "Thermocouple Time Constant Measurement by Cross Power Spectra," AIAA J., 14, 1642-1644 (1976).

14. Eckert, E. G., and Goldstein, R. J., Measurements in Heat Transfer, 2nd ed., p. 15, Hemisphere Pub. Co. (1976).

15. Incropera, F. P.. and DeWitt, D. P., Fundamentals of Heat and Mass Transfer, 4th ed., John Wiley & Sons (1996).

16. Hall, R. J., and Bonczyk, P. A., "Sooting Flame Thermometry using Emission/Absorption Tomography," Applied Optics, 31, 4590-4598 (1990).

17. Vander Wal, R. L., Dietrich, D. L., Zhou, Z., and Choi, M. Y., "Development and Applications of Laser-Induced Incandescence," 247-252, Proc. 3rd Int'l. Microgravity Comb. Workshop, Cleveland, Ohio, April 11-13 (1995).

Table 1. Values for parameters related to thermocouple radiation heat loss correction.

Height, x	100D	150D
Axial velocity, u (m/s)*	8.1	5.9
Reynolds Number, $Re = ud/v$	1.901	1.385
Nusselt Number, $Nu = hd/k$	2.5590	2.4736
Convection Coef., h (W/m^2·K)	465.7	450.2
T_f (K), from Fig. 2	1160	1115
Correction, $T_g - T_f$ (K)	153.6	135.5
Gas Temperature, T_g (K)	1313.6	1250.5
From Pyrometry, T_g' (K)	1639 (+325.4[#])	1533 (+282.5)

* Values obtained from model predictions (ref. 7)
# Difference between thermocouple and imaging pyrometry results.

214
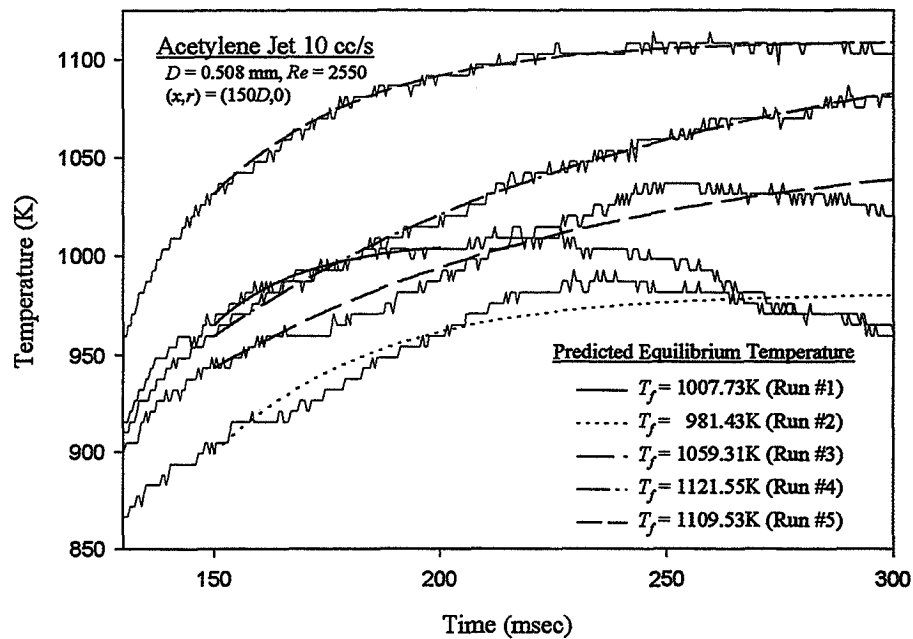
Figure 1. Thermocouple response at $x = 150D$ and curve-fits to Eq. (1) in a turbulent acetylene jet diffusion flame.
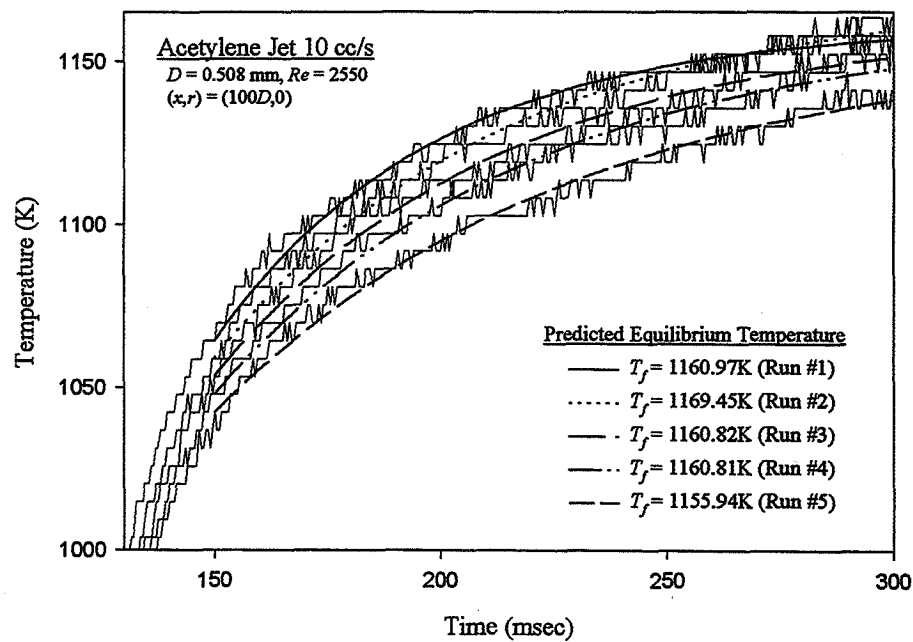
Figure 2. Thermocouple response at $x = 100D$ and curve-fits to Eq. (1) in a turbulent acetylene jet diffusion flame.
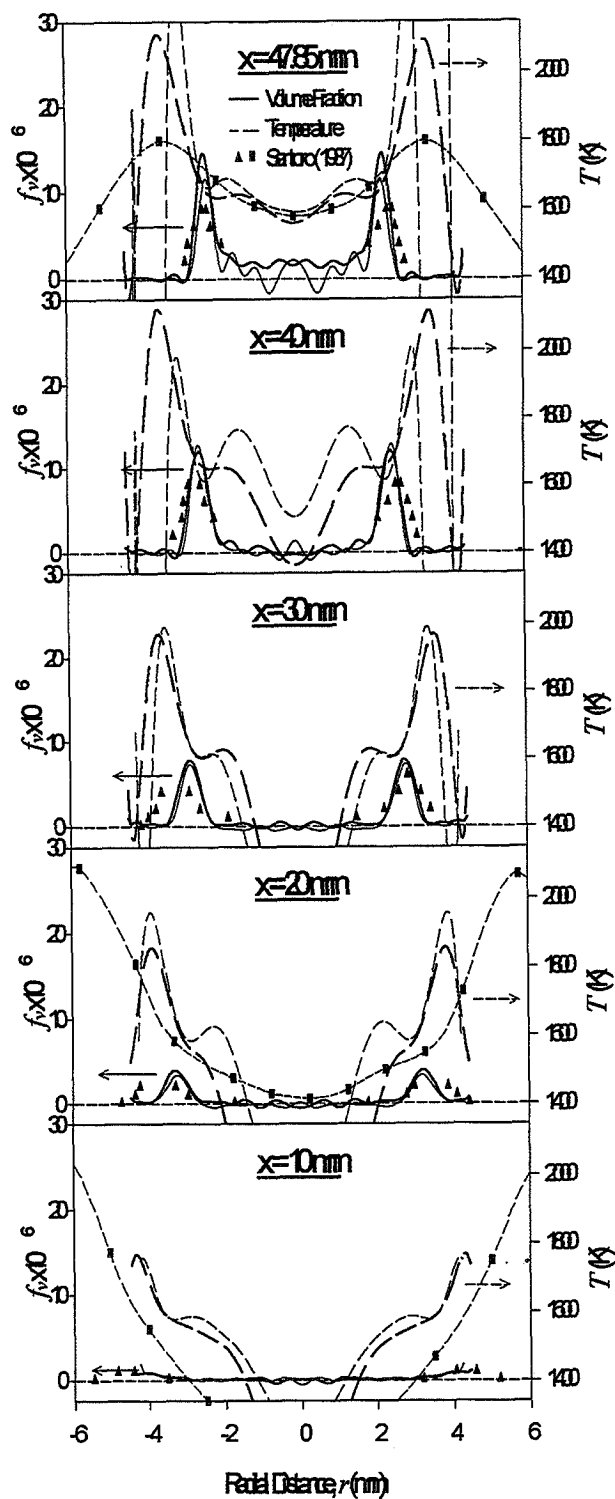
Figure 3. Soot volume fraction and temperature profiles for a 3.85 cc/s laminar co-flow ethylene flame.
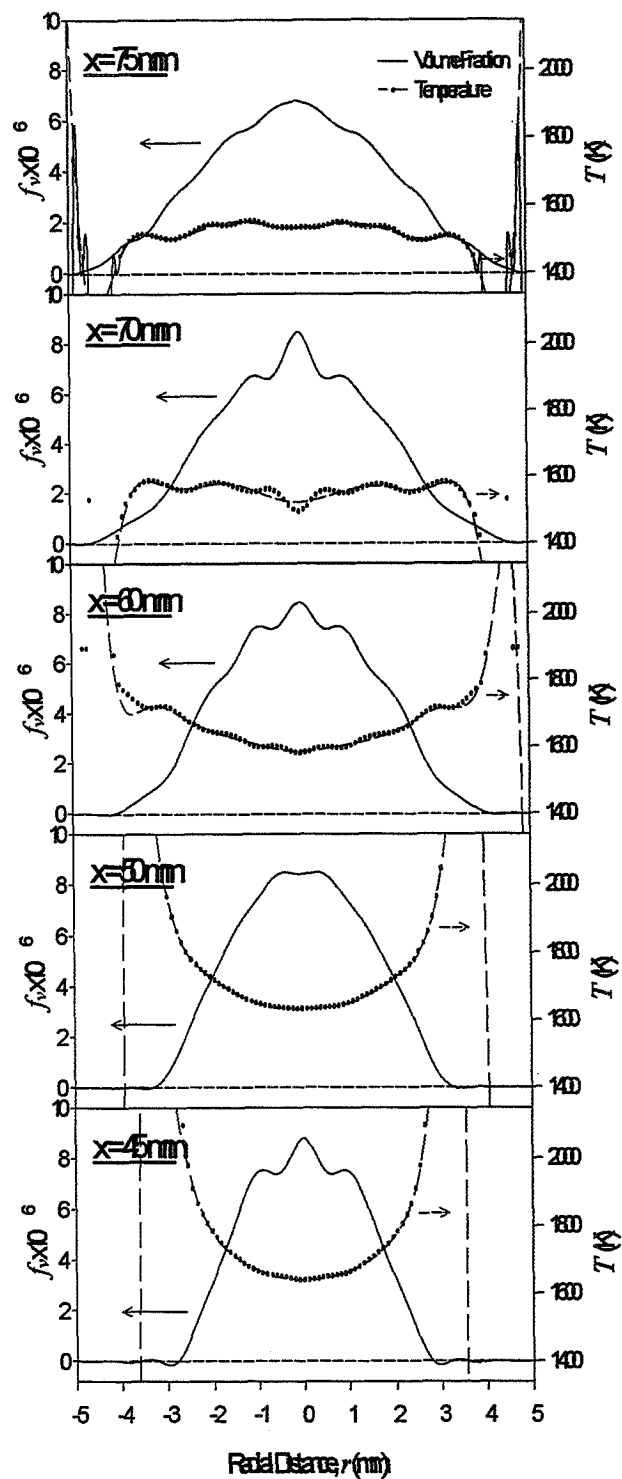
Figure 4. Soot volume fraction and temperature profiles for a 10 cc/s turbulent acetylene jet diffusion flame.

216

EFFECT OF THERMOPHORETIC FORCE ON SOOT AGGLOMERATION PROCESS IN DIFFUSION FLAMES UNDER MICROGRAVITY

Osamu FUJITA, Kenichi ITO
Department of Mechanical Science, Hokkaido University
Sapporo, Japan

Hiroyuki ITO
Toshiba Co. Ltd., Tokyo, Japan

Yasuhiro Takeshita
JSUP, Tokyo, Japan

Introduction

In the previous research the authors reported that soot agglomeration phenomenon in diffusion flames under microgravity are quite different from those under normal gravity[1,2]. Soot particles in a diffusion flame adhere each other to form very large visible agglomerates. The size of formed agglomerates were more than 100 μ m, or more than 500 times usual soot particles formed in normal gravity. Photos of the phenomenon was shown and the conditions where the large soot agglomerates appear were experimentally investigated. The large soot agglomerates formation is a phenomenon occurring under microgravity and the mechanism of the formation in microgravity has not been clarified yet.

In the present work the combustion field of a butane diffusion flame, the same as the one used in the previous paper, is investigated to elucidate the mechanism of large soot agglomerates formation under microgravity. The discussion considers the effect of thermophoretic force[3,4] and it is concluded that the large soot agglomerates formation is due to a the combination of thermophoretic forces and long residence time in a microgravity environment.

Soot particle behavior in microgravity has been studied by other researchers [5,6]. However, the phenomenon of that large soot particle formation has not been reported for a gas get diffusion flame. In the droplet combustion research Avedisian[7] has shown a picture with the large soot agglomerates emission. Some reports have found that soot particles or agglomerates tend to be larger with increases in residence time and then reach to a certain size in a gas jet diffusion flame in normal gravity[8,9]. However, that large agglomerate large as those observed in microgravity environment have never seen irrespective the flame length.

Papers noting thermophoretic effects on combustion matter were published by Dobins[10] and others [11]. They pointed out the importance of thermophoretic forces when a TEM grid was used to sample soot particles. They found that a steep temperature gradient close to the solid surface attracts soot particles to the grid surface. Some researches[12,13] reported that the effect of thermophoretic forces on fine seeded particles, such as used for LDV measurements, is not negligible. Hirano [14] has measured the drift speed of fine SiO2 and MgO particles due to thermophoretic force under constant temperature gradient.

Experimental

The experimental setup in this research is described in detail in the previous research[1]. The butane

diffusion flame stabilized on a circular tube burner was set in the combustion chamber having the volume of about 50L. The combustion behavior of the flame have recorded by a video camera and 35mm still camera. The motion of the soot agglomerate to appear in the flame was analyzed based on those images.

The microgravity experiments were performed at the Japan Microgravity Center, JAMIC, Hokkaido, Japan which provides 10−s of microgravity in a 490 m free fall shaft. The microgravity quality is less than 10^{-4} g.

Results and Discussion

Observation of large soot agglomerates

Photographs of the butane diffusion flame studied in this research are shown in Fig.1: (a) is in normal gravity and (b) is in microgravity. The inner burner diameter is 6mm, and the fuel flow rate is 0.6mL/s which results in a mean velocity of 21.2 mm/s in the burner tube. The surrounding oxygen concentration, O2, and pressure, P, are 50% and 1atm, and all discussion in the following is for this condition. The flames under normal gravity have the familiar shape, vertically longitudinal luminous flames with the flame length somewhat shorter than common because of the high oxygen concentration. In microgravity, the flame has a spherical shape of larger volume, and the luminosity is low even at 50% O2. The flame in Fig.1(b) shows a continuous release of luminous bright spots at the right and left top of the flame. According to the motion pictures, these bright spots appear around the middle of the flame and flow almost straight downstream. This phenomena is new as mentioned in the introduction and is the main subject discussed in the present paper.

The bright spot in Fig.1 was sampled with a TEM grid sampler, and the TEM image was taken. As a result, the bright spots were identified to be the large soot particle agglomerates. The soot particles composing the agglomerates are fine primary particle having 0.01−0.07 μ m [1], almost the same as particles formed in normal gravity. The typical size of the soot agglomerates was about 100 μ m, around 500 times of agglomerates formed in normal gravity.

Relation between combustion field and soot agglomeration process

Measurements of the combustion fields in microgravity have been carried out to discuss the formation mechanism of the large soot agglomerates. Figure 2 shows the radial temperature distribution at various height from the burner rim. In this figure radial position where soot formation is observed is pointed out based on the direct picture. The experimental condition is completely same as Fig.1. Temperature shows a peak value at a certain radial distance except H=20mm. At H=10−15mm where the soot particle formation appears the maximum temperature is located at r=10−12mm, a few mm outside of the soot particles formation. Maximum temperature is about 1200 °C even with O2=50%. This means the temperature of diffusion flame in microgravity is much lower than in normal gravity.

Chemical component and flow field of the objective flame is numerically estimated because their experimental data in microgravity are not available yet at this moment. Simple numerical model were adopted. Flow is assumed to be laminar flow and to be able to simulate with boundary layer approximation. Initial flow distribution at the burner tip is assumed to be a well developed circular tube flow with parabolic velocity distribution. In cylindrical coordinate system simultaneous equations of continuous equation, momentum

equation and chemical species conservation equations were numerically solved. Temperature distribution necessary for the calculation is given by the multi–term approximation of the experimental data shown in Fig.3. Finite differential method was used as a numerical technique. One step overall reaction is assumed for butane combustion. Thus, chemical species considered are fuel (butane), mentioned as M_{fu} in mass fraction, N_2 as M_{N2}, O_2 as M_{O2}, and products (sum of CO_2 and H_2O) as M_{pro}.

Figure 3 shows the calculation results of mass fractional radial distributions of each species at height from burner rim H=5, 10 and 15mm. In this figure fuel spreads outward and combustion products at the center increases, with increase in the height. The visible soot particles appears around 7.5mm from the centerline at h=10 and 15 mm. This position is a few mm inside of the most actively reacting zone. Oxygen concentration at this position is very low while fuel is still existing.

Flow field is also estimated. Figure 4 shows the horizontal velocity distribution at h=10 and 15mm as a function of radial distance from the centerline r. In this figure positive value means outward motion. At any position of r shown in this figure, horizontal flow velocity v shows a positive value, which means the flow field of this flame in microgravity is moving outward. At the position of visible soot particles appearance, v is about 4mm/s at h=10mm and about 6mm at h=15mm.

Discussion on soot agglomeration process

If soot agglomerates move along the motion of combustion gas, it should have a horizontal velocity component moving outward. However, the visible soot particles shown in Fig.1 is apparently moving straight upward or slightly drawing to the center rather than outward motion. This motion is more clear with motion picture taken with video, steadily continuing for microgravity duration. Figure 5 shows the example of soot agglomerates motion obtained from image processing technique. Though this figure is taken in the different condition, that is, fuel is propane, the qualitative tendency of the agglomerates motion is similar independent of a fuel. Near the visible flame edge soot agglomerates move toward the centerline. After passing through the flame zone soot agglomerates have a outward motion. From this result it is understood that the motion of the agglomerates does not follow the average combustion gas motion.

Takeno et al.[12] showed an experimental results that the fine TiO2 particle which is often used for a tracer particle for LDV moved to lower temperature direction in flat flame burner. He also pointed out that the motion was caused by the thermophoretic effect which gives the drift velocity towards temperature decreasing direction.

In the objective flame of this work the same effect, thermophoretic effect, must affect the motion of the soot agglomerates. The visible soot agglomerates is formed at around 7.5mm from the centerline. At this position the temperature gradient (see Fig.2) is of about 100 ℃ /mm. By using the following equation [12], the drift velocity vp of a particle in a flame is estimated.

$$ v_p = \frac{- \alpha_t D_p}{T} \nabla T \qquad -------(1) $$

where $-\alpha_t$:Temperature diffusion factor

D_p :Brown motion diffusion factor

T :Temperature

To get the value of $\alpha_t D_p$, the results by Rosner[11] was adopted. The product of particle Lewis number, $L_p = \rho C_p D_p / \lambda$, and α_t is constantly 0.42, where ρ is gas density and λ is thermal

conductivity of the gas. To calculate the value of v_p , measured gas is assumed to be air.

The estimated drift velocity at the visible soot appearing region can be more than 5mm/s or more which is almost identical to the motion velocity of combustion gas as shown in Fig.4. Sometimes the drift velocity becomes larger than the horizontal outward gas motion.

The idea discussed above is conceptually described in Fig.6. Though gas flow vector direct outward, the particles move upward straight or toward the center with reception of thermophoretic force.

Figure 7 shows the concept of soot agglomeration process occurring in the objective flame. Fine soot particles are formed at the middle or the lower area of the flame where the flame looks luminous in the picture of Fig.1(b). The fine particle moves upward with gas flow, agglomerating with other particles. Then, the thermophoretic force affects the particles motion. The soot particles close to the flame zone moves toward center of the burner because of high temperature gradient. However, thermophoretic force becomes smaller with approaching to the center because of the smaller temperature gradient. Consequently, there must be the pathline balancing between average flow and drift velocity attributed to the thermophoretic force. The particle locating in outer region tends to move toward center and, on the other hand, the particles locating in inner region tends to move outward. Then all of them tend to be gathered to an soot pathline shown in Fig.7 by an thick arrow. It makes the soot particles density fairly high and results in remarkable soot agglomeration formation as seen in Fig.1.

Concluding Remarks

To investigate the reasons for the large soot agglomerates formation in microgravity, the temperature, chemical species, and flow velocity distribution of the butane diffusion flame were investigated by experimental or computational methods. From motion of the soot agglomerate, the importance of thermophoretic force was pointed out. The drift velocity caused by the thermophoretic effect is almost identical or slightly larger than the outward motion of average gas flow. It results in the motion of soot particle moving straight upward or toward inside. Furthermore, the existence of soot path line toward which soot particles in the sooting region is drawn to form high soot concentration region was suggested. The combination of this phenomena and a long residence time of soot particles because of microgravity makes to form that large soot agglomerates reported in the previous research.

References
1.Ito,H. Fujita,O., Ito,K., Combust. Flame, 99:363−370(1994).
2.Ito,K.,Fujita,O., Ito,H., Proc.of 9th Space Utilization Symposium(In Japanese), 1992, p.30, Tokyo.
3.Derjaguin,B.V. and Yalamov,Y., J.Colloid Sci.,20, 555,(1965).
4.Talbot,L., Cheng,R.K., Schefer,R.W. and Willis,D.R., J.Fluid Mech.,101,737(1980).
5.Koylu,U.O., Faeth,G.M., Combust. Flame 89:140−156,(1992).
6.Ku,J.C., Tong.L.,Sun,J., Greenberg,P.S., and Grifin,D., Proc.of 2nd Int.Microgravity Combustion Workshop,1992, p.1.
7.Avedisian,C.T., Multicomponent Droplet combustion and soot formation in Microgravity, Proc.Third Int.Microgravity Combustion Worlshop, April 11−13,1995, Cleveland,pp.47−51.
8.Hinisch,S.,Jander,Th.Pape, and H.Gg.Wagner, 25th Symp. (Int.) on Comb., The combustion Institute, 1994, p.577. Irvin.

9. Honnery,D.R., and Kent,J.H.,Combust. Flame, 82:426–434(1990).
10. Dobbins,R.A.,and Megaridis,C.M., Langmuir, 3:254–259,(1987).
11. Rosner,D.E. and Kim,S.S., The Chemical Engrg.J.29, 147,(1984).
12. Uchida,N., Nishioka,M., and Takeno,T. Proc. of 28th Symp. on Comb. (Japanese Section), pp.37–39, 1990, Tokyo.
13. Sung,J. and Law,C.K., Combust.Sci and Tech,99,119, (1994).
14. Toda,A., Hirano,T., Dobashi,R. and Sakuraya,T. Proc. of 33th Symp. on Comb. (Japanese Section), p.405, 1995, Tokyo.

(a)　　　　　　　　(b)
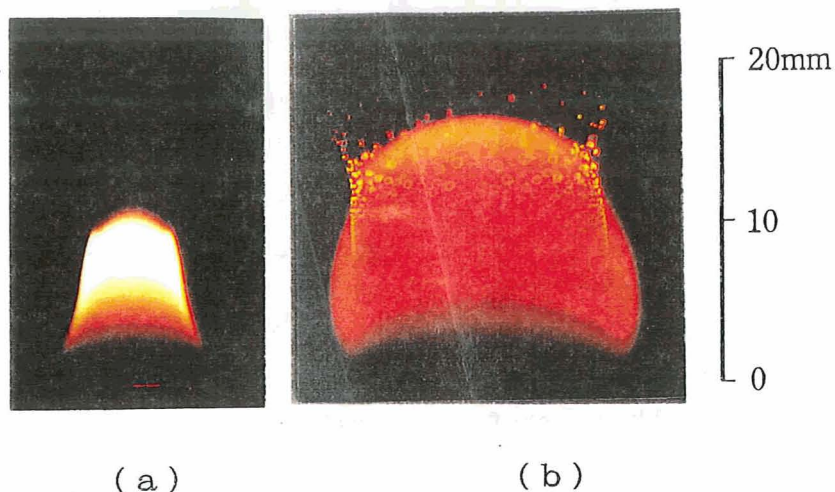
Fig.1 Objective butane gas jet diffusion flame (a) in normal gravity and (b) in microgravity. Surrounding O2=50%. The inner diameter of the burner is 6mm (the outer diameter is 8mm). The fuel flow rate is 0.6mL/s.
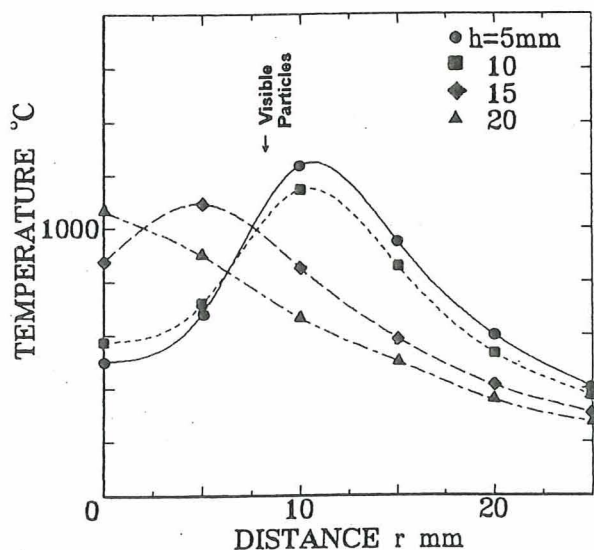
Fig.2 Radial temperature distribution at the height of 5, 10 15 and 200mm. Visible particle generation region is also pointed.
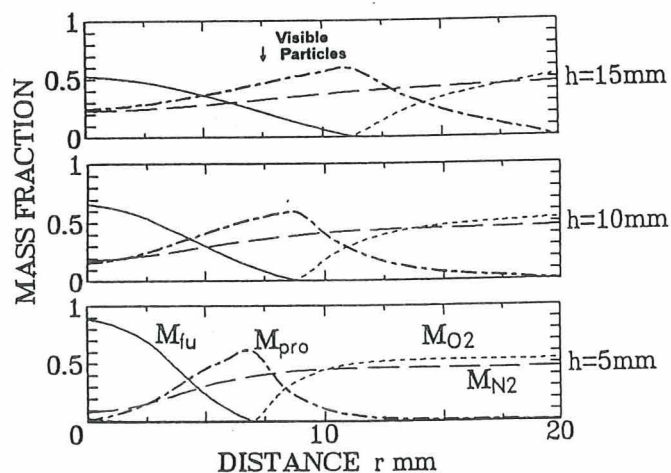
Fig.3 Radial chemical species distribution at the height of 5, 10, 15 estimated by numerical calculation. Mass fractions of fuel, oxygen, nitrogen, combustion products (CO_2+H_2O) denoted as Mfu, MO2, MN2, and Mpro, respectively.
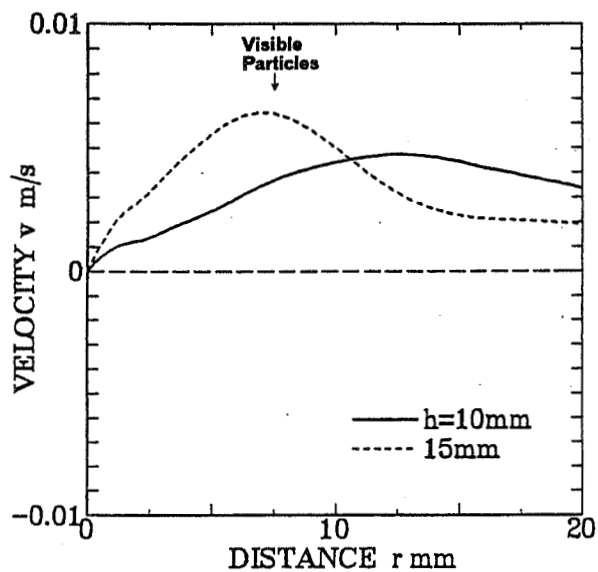
Fig.4 Radial distribution of horizontal velocity component at the height of 5 and 10mm. Positive value means the outward motion.
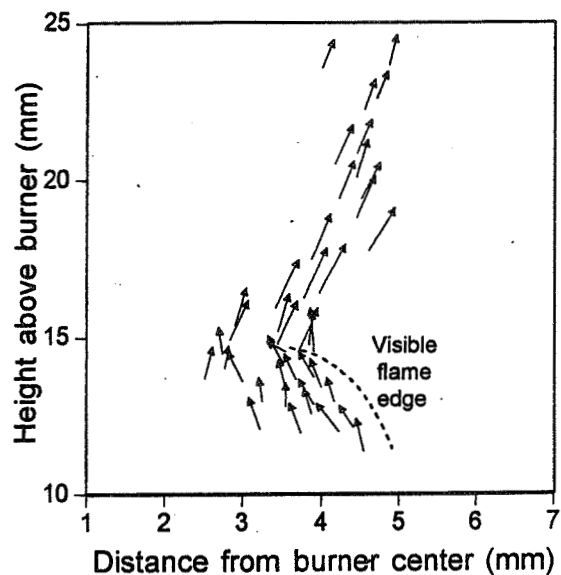
Fig.5 Soot agglomerates motion vector obtained by a image processing.
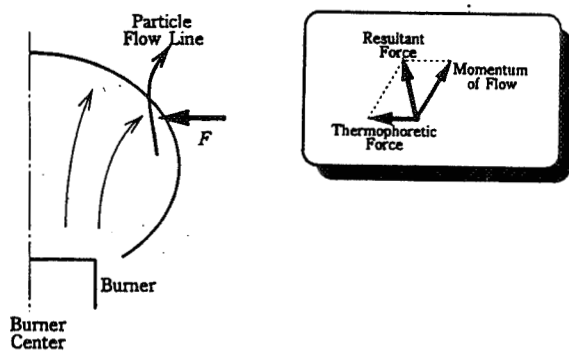
Fig.6 Conceptual description of soot agglomerates motion when the thermophoretic effect is taken into account.
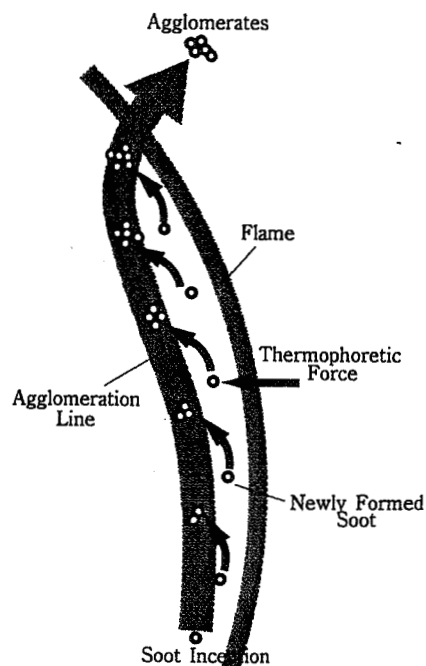
Fig.7 Conceptual description of soot particle agglomeration under the effect of thermophoretic force.

222

SOOT FORMATION IN FREELY-PROPAGATING
LAMINAR PREMIXED FLAMES*

K.-C. Lin, M.I. Hassan and G.M. Faeth
Department of Aerospace Engineering
The University of Michigan
Ann Arbor, Michigan

Introduction

Soot formation within hydrocarbon-fueled flames is an important unresolved problem of combustion science. Thus, the present study is considering soot formation in freely-propagating laminar premixed flames, exploiting the microgravity environment to simplify measurements at the high-pressure conditions of interest for many practical applications. The findings of the investigation are relevant to reducing emissions of soot and continuum radiation from combustion processes, to improving terrestrial and spacecraft fire safety, and to developing methods of computational combustion, among others.

Laminar premixed flames are attractive for studying soot formation because they are simple one-dimensional flows that are computationally tractable for detailed numerical simulations. Nevertheless, studying soot-containing burner-stabilized laminar premixed flames is problematical: spatial resolution and residence times are limited at the pressures of interest for practical applications, flame structure is sensitive to minor burner construction details so that experimental reproducibility is not very good, consistent burner behavior over the lengthy test programs needed to measure soot formation properties is hard to achieve, and burners have poor durability. Fortunately, many of these problems are mitigated for soot-containing, freely-propagating laminar premixed flames. The present investigation seeks to extend work in this laboratory for various soot processes in flames (refs. 1-17) by observing soot formation in freely-propagating laminar premixed flames. Measurements are being made at both normal gravity (ng) and microgravity (mg), using a short-drop free-fall facility to provide mg conditions.

Discussion of past studies of soot formation will be brief, see Refs. 11-17, and references cited therein, for more detailed reviews. Most experimental studies of soot formation in premixed flames are limited to burner flames (refs. 18-26). This work is valuable but it also involves significant problems. First of all, these studies adopted the Mie scattering approximations for equivalent spheres to find soot properties which recent work has shown to be incorrect (refs. 1-10). For example, actual soot particles involve polydisperse aggregates of spherical primary soot particles, see the transmission electron microscope photograph of Fig. 1 for a typical example. Thus, the assumption that each soot aggregate is an equivalent spherical particle causes significant errors of estimates of soot particle number densities and surface areas. In addition, flow velocities were found using one-dimensional flow approximations and flow cross-sectional area estimates that are questionable, which implies significant uncertainties about determination of flow residence times. Thus, new measurements of soot formation rates in premixed laminar flames that avoid these problems are needed.

Recent studies of soot processes in laminar flames in this laboratory have developed experimental techniques capable of obtaining the soot and flow properties needed to characterize soot formation rates, finding various properties, as follows (refs. 11-17): soot volume fraction, by both deconvoluting laser extinction measurements and gravimetric methods, flow temperatures by deconvoluting multiline emission measurements, soot structure by thermophoretic sampling and analysis by TEM, the compositions of major gas species by sampling and analysis using gas chromatography, gas velocities by laser velocimetry, and concentrations of heavy hydrocarbons by sampling and gravimetric methods. Subsequently, Xu et al. (ref. 17) applied these methods to measure the structure and soot properties of laminar premixed ethylene/air burner flames at atmospheric pressure. The new measurements were also used to evaluate detailed models of gas-phase chemistry and soot growth processes within premixed flames based on numerical simulations of the flames using methods developed by Kee et al. (ref. 33). It was found that the chemical reaction mechanisms of Lindstedt and coworkers (refs. 27 and 28) and Frenklach and coworkers (refs. 29-31) provide good predictions of major gas species concentrations while the hydrogen-abstraction/carbon-addition soot growth

223

mechanisms of Kazakov et al. (ref. 31) and Colket and Hall (ref. 32) provide excellent correlations of measured soot growth rates. Xu et al. (ref. 17), however, also encountered the problems of burner measurements of soot-containing laminar premixed flames mentioned earlier.

In view of the demonstrated capabilities of the measurement techniques of refs. 11-17 for studies of soot processes in laminar premixed flames, the advantages of laminar premixed flames for both measuring and simulating soot formation rates, and the potential of freely-propagating laminar premixed flames for providing observations of soot processes at pressures of interest for practical applications, the objectives of the present investigation are as follows: (1) to complete measurements of flame and soot properties in freely-propagating laminar premixed flames, considering various reactant mixtures and pressures, (2) to reduce the measurements to find soot formation rates (nucleation, growth and aggregation rates), and (3) to exploit the measurements to develop and evaluate models of these processes, emphasizing methods used in current detailed numerical simulations of laminar soot-containing flames.

Work thus far has been limited to the development of experimental methods, study of interactions between the propagation and soot formation properties of freely-propagating flames, and measurements of soot formation conditions in freely-propagating flames. These topics will be addressed, in turn, in the following.

Experimental Methods

The experimental methods were developed during past work in this laboratory (refs. 1-17 and 34-38). The apparatus consists of a spherical windowed chamber where the flames are observed, combined with a short drop free-fall facility to control effects of buoyancy, as illustrated in Fig. 2. The windowed chamber is quasi-spherical with a 356 mm cross-sectional diameter. The test mixtures are prepared in separate tanks which are then stored to assure uniform compositions. The mixtures are spark-ignited at the center of the chamber using near minimum ignition energies in order to control ignition disturbances. Only conditions with flame diameters less than 100 mm (comprising roughly 2.2% of the chamber volume) are considered so that pressure increases are less than 3.1%. Measurements include dark field still and motion pictures for flame observations, shadowgraph motion pictures for measurements of flame propagation, and the other measurements of flame and soot properties from refs. 11-17, mentioned earlier.

Correlation of Flame Propagation Properties

Selecting test conditions and interpreting test results are influenced by effects of preferential diffusion and hydrodynamic instability that can modify combustion product compositions and create disturbed flame surfaces. This involves variations of laminar burning velocities, S_L, as a function of flame stretch, K, that can be characterized using an early proposal of Markstein (ref. 34):

$$S_L = S_{L\infty} - LK \tag{1}$$

where $S_{L\infty}$ is the laminar burning velocity of an unstretched (plane) flame and L is an empirical function called the Markstein length. Representing characteristic flame length and time scales by the local values of stretched flames, Eq. 1 can be placed in dimensionless form as follows:

$$S_{L\infty}/S_L = 1 + MaKa \tag{2}$$

where $Ka = KD_u/S_L^2$ is the Karlovitz number, $Ma = L/\delta_D$ is the Markstein number, $\delta_D = D_u/S_L$ is the characteristic flame thickness, and D_u is the mass diffusivity of fuel in the unburned gas mixture. A convenient feature of this approach is that Ma tends to be independent of Ka which simplifies reporting interactions between S_L and K. Measurements of S_L are based on measurements of flame radius, r_f, as a function of time, t, when $D_u/r_f \leq 2\%$ so that effects of flame curvature and unsteadiness are small. Effects of radiative heat loss within the premixed flame sheet are ignored while adopting the *convention* of ignoring effects of K on the ratio of burned, ρ_b, and unburned, ρ_u, gas densities. Under these assumptions, S_L and K can be found as follows:

$$S_L = (\rho_b/\rho_u)d\,r_f/dt, \quad K = (2/r_f)d\,r_f/dt \tag{3}$$

where ρ_b/ρ_u is found for an unstretched adiabatic flame in the reactant mixture at initial chamber conditions assuming chemical equilibrium in the combustion product mixture (refs. 37 and 38). From Eq. 3, it is clear that freely-propagating premixed laminar flames involve progressively decreasing K as the flame radius increases.

Observations of Flame Propagation Properties

Effects of variations of K with r_f on S_L are illustrated in Fig. 3 for soot-free propane/air flames at 1 atm and various fuel-equivalence ratios, ϕ. These significant changes of S_L with r_f (or K) are caused by preferential diffusion effects which modify the gas composition within the reaction zone and the combustion products from the unburned gas mixture. Such effects must either be considered or avoided when interpreting soot formation processes in the post-flame gas mixture.

Measurements of the properties of ethylene/air flames are of particular interest due to past studies of soot formation (refs. 17 and 20-23). Observations of S_L as a function of Ka for such flames at atmospheric pressure are illustrated in Fig. 4 taken from ref. 36. The linear correlation between $S_{L\infty}/S_L$ and Ka is quite evident, implying constant Ma as mentioned earlier. As ϕ increases toward soot-containing flames, $\phi > 1.8$, flame sensitivity to stretch decreases which is very helpful because combustion product properties then become relatively insensitive of Ka, and thus r_f. Corresponding measurements of Markstein numbers from refs. 35 and 39 are illustrated in Fig. 5; these results also indicate relatively small values of Ma for ϕ in the range 1.8-2.2.

Values of $S_{L\infty}$ for ethylene/air flames at atmospheric pressure are plotted as a function of ϕ in Fig. 6. These results include stretch-corrected findings of refs. 35 and 39 as well as earlier measurements of Scholte and Vaags (ref. 40) that are not corrected for stretch. The various measurements are in good agreement at the fuel-rich conditions of interest for soot studies. Laminar burning velocities approach 100 mm/s as soot-forming conditions are approached.

Finally, effects of stable and unstable preferential diffusion conditions on the properties of freely-propagating laminar premixed flames are illustrated in Fig. 7. Stable conditions (Ma $\geq$ 0) yield relatively smooth flame surfaces except at relatively large flame diameters (typically > 100 mm) where surface irregularities caused by hydrodynamic instabilities are observed (refs. 34-38). In contrast, unstable conditions (Ma < 0) yield early transition to irregular flame surfaces that must be avoided for studies of soot formation in the post-flame region.

Observations of Flame Soot-Formation Properties

Effects of flame stretch and heat losses on soot formation in premixed flames imply that conditions for soot production in burner and freely-propagating laminar premixed flames are not the same. Thus, measurements currently are concentrating on defining both preferential diffusion/stretch interactions (already discussed) as well as soot production conditions (sooting limits).

Initial measurements of sooting conditions have involved dark-field color photographs of ethylene/air flames at various pressures. A time exposure is obtained during the period of propagation while using the transition from blue to yellow-luminosity as an indication of sooting conditions.

Examples of dark-field color photographs of flame luminosity are illustrated in Fig. 8 for ethylene/air flames at atmospheric pressure. At $\phi = 1.6$ the flame remains blue throughout the period of propagation; in contrast, strongly luminous yellow flames are observed at $\phi = 2.2$. Such results crudely bracket known sooting limits of these flames near $\phi = 1.8$, but the present results are not definitive because increased pressures toward the end of flame propagation modify sooting conditions. Thus, present work involves laser extinction and dark-field motion picture observations to find sooting conditions for a variety of hydrocarbon fuels and pressures, in conjunction with flame propagation measurements similar to those discussed in connection with Figs. 3-7, in order to determine flame conditions suitable for detailed measurements of soot formation properties.

Acknowledgments

References

1.   Köylü, Ü.Ö. and Faeth, G.M., Combust. Flame 89:140 (1992).

2.   Köylü, Ü.Ö. and Faeth, G.M., J. Heat Trans. 115:409 (1993).

3.   Köylü, Ü.Ö. and Faeth, G.M., J. Heat Trans. 116:152 (1994).

4.   Köylü, Ü.Ö. and Faeth, G.M. J. Heat Trans. 116:971 (1994).

5.   Farias, T.L., Carvalho, M.G., Köylü, Ü.Ö. and Faeth, G.M., J. Heat Trans. 117:152 (1995).

6.   Köylü, Ü.Ö., Faeth, G.M., Farias, T.L. and Carvalho, M.G., Combust. Flame 100:621 (1995).

7.   Faeth, G.M. and Köylü, Ü.Ö., Combust. Sci. Tech. 108:207 (1995).

8.   Köylü, Ü.Ö. and Faeth, G.M., J. Heat Trans. 118:415 (1996).

9.   Farias, T.L., Carvalho, M.G., Köylü, Ü.Ö. and Faeth, G.M., Int. J. Heat and Technology 13:27 (1995).

10.   Wu, J.-S., Krishnan, S.K. and Faeth, G.M., J. Heat Trans., in press.

11.   Sunderland, P.B., Mortazavi, S., Faeth, G.M. and Urban, D.L., Combust. Flame 96:97 (1994).

12.   Lin, K.-C. and Faeth, G.M., J. Prop. Power 12:10 (1996).

13.   Lin, K.-C. and Faeth, G.M., J. Prop. Power 12:691 (1996).

14.   Sunderland, P.B., Köylü, Ü.Ö. and Faeth, G.M., Combust. Flame 100:310 (1995).

15.   Lin, K.-C., Sunderland, P.B. and Faeth, G.M., Combust. Flame 104:369 (1996).

16.   Sunderland, P.B. and Faeth, G.M., Combust. Flame 105:132 (1996).

17.   Xu, F., Sunderland, P.B. and Faeth, G.M., Combust. Flame, in press.

18.   Bockhorn, H., Fetting, F., Wannemacher, G. and Wentz, H.W., Nineteenth Symposium (International) on Combustion, The Combustion Institute, Pittsburgh, 1982, p. 1413.

19.   Bockhorn, H., Fetting, F., Heddrich, A. and Wannemacher, G.,Twentieth Symposium (International) on Combustion, The Combustion Institute, Pittsburgh, 1984, p. 979.

20.   Harris, S.J. and Weiner, A.M. , Combust. Sci. Tech. 31:155 (1983).

21.   Harris, S.J. and Weiner, A.M., Combust. Sci. Tech. 32:267 (1983).

22.   Harris, S.J. and Weiner, A.M., Combust. Sci. Tech. 38:75 (1984).

23.   Ramer, E.R., Merklin, J.F., Sorensen, C.M. and Taylor, T.W., Combust. Sci. Tech. 48 :241 (1986).

24.   Bauerle, Ste., Karasevich, Y., Slavov, St., Tanke, D., Tappe, M., Thienel, Th. and Wagner, H. Gg., Twenty-Fifth Symposium (International) on Combustion, The Combustion Institute, Pittsburgh, 1994, p. 627.

25.   Hanisch, S., Jander, H., Pape, Th. and Wagner, H. Gg., Twenty-Fifth Symposium (International) on Combustion, The Combustion Institute, Pittsburgh, 1994, pp. 577.

26.   Boehn, H., Felderman, Chr., Heidermann, Th., Jander, H., Luers, B. and Wagner, H.Gg., Twenty-Fourth Symposium (International) on Combustion, The Combustion Institute, Pittsburgh, 1992, p. 991.

27.   Leung, K.M. and Lindstedt, R.P., Combust. Flame 102:129 (1995).

28.   Leung, K.M., Lindstedt, R.P. and Jones, W.P., Combust. Flame 87:289 (1991).

29.   Frenklach, M. and Wang, H., Twenty-Third Symposium (International) on Combustion, The Combustion Institute, Pittsburgh, 1990, p.1559.

30.   Frenklach, M. and Wang, H., Soot Formation in Combustion (H. Bockhorn, ed.), Springer-Verlag, Berlin, 1994, p. 165.

31.   Kazakov, A., Wang, H. and Frenklach, M., Combust. Flame 100:111 (1995).

32.   Colket, M.B. and Hall, R.J., Soot Formation in Combustion (H. Bockhorn, ed.), Springer-Verlag, Berlin, 1994, p. 442.

33.   Kee, R.J., Grcar, J.F., Smooke, M.D. and Miller, J.A., Report No. SAND85-8240, Sandia National Laboratories, Albuquerque, 1995.

34.   Kwon, S., Tseng, L.-K. and Faeth, G.M., Combust. Flame 90:230 (1992).

35.   Tseng, L.-K., Ismail, M.A. and Faeth, G.M., Combust. Flame 95:410 (1993).

36.   Aung, K.T., Tseng, L.-K., Ismail, M.A. and Faeth, G.M., Combust. Flame 102:526 (1995).

37.   Aung, K.T., Hassan, M.I. and Faeth, G.M., Combust. Flame, in press.

38.   Hassan, M.I. Aung, K.T. and Faeth, G.M., J. Prop. Power, in press.

39.   Taylor, S.C., Ph.D. Thesis, University of Leeds, 1991.

40.   Scholte, T.G. and Vaags, P.B., Combust. Flame 3:495 (1959).
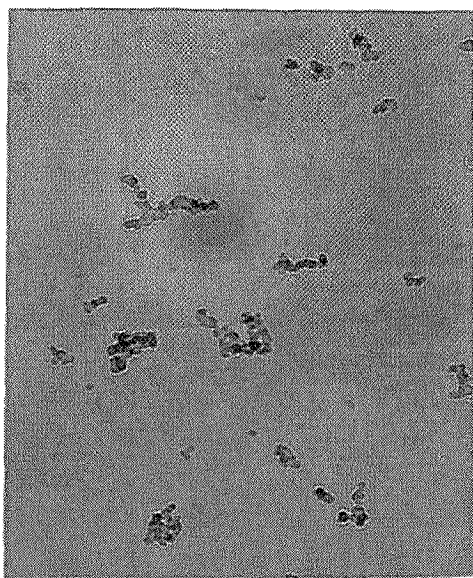
Fig. 1 TEM photographs of soot aggregates within a premixed ethylene/air flame at atmospheric pressure. From ref. 17.
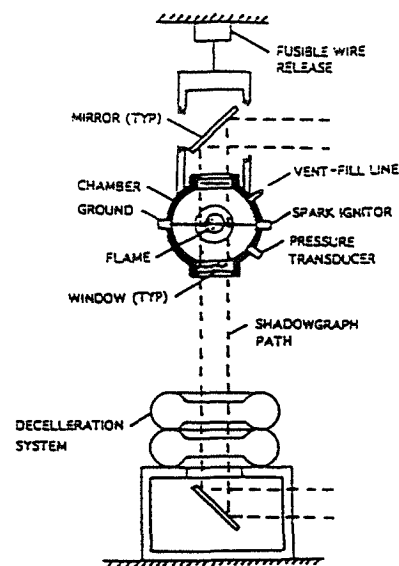
Fig. 2 Sketch of the short-drop free-fall facility for studies of freely-propagating spherical laminar premixed flames at low gravity.
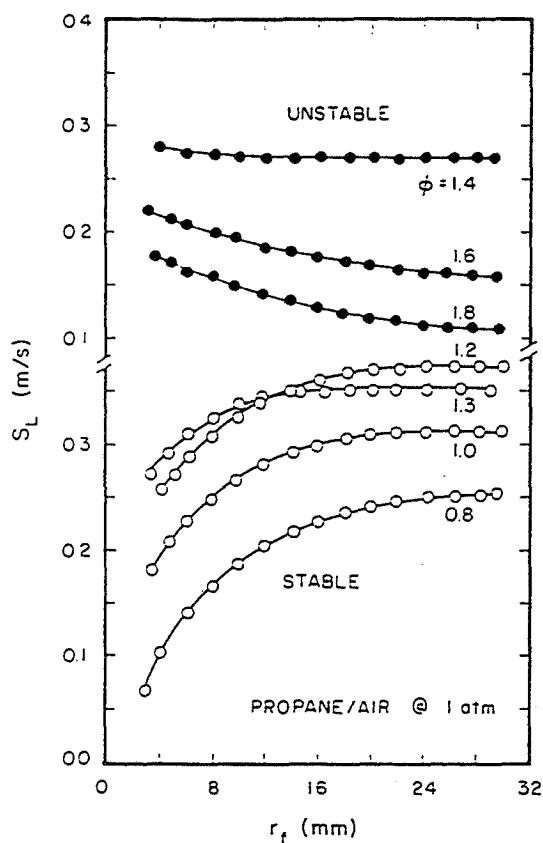
Fig. 3 Laminar burning velocity as a function of flame radius for freely-propagating spherical laminar premixed propane/air flames at 100 kPa. From ref. 35.
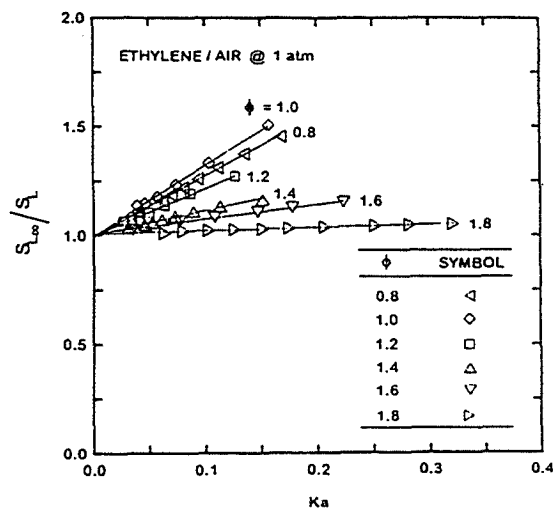
Fig. 4 Laminar burning velocity as a function of flame Karlovitz number for freely-propagating spherical laminar premixed ethylene/air flames at 100 kPa. From ref. 36.
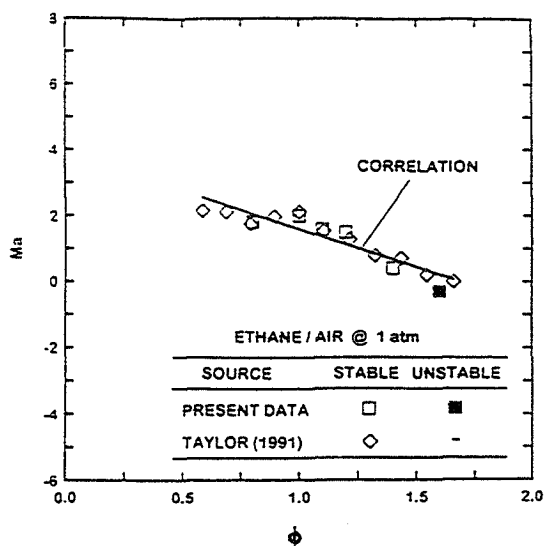
Fig. 5 Markstein numbers as a function of fuel-equivalence ratio for freely-propagating spherical laminar premixed ethylene/air flames at 100 kPa. From ref. 36.
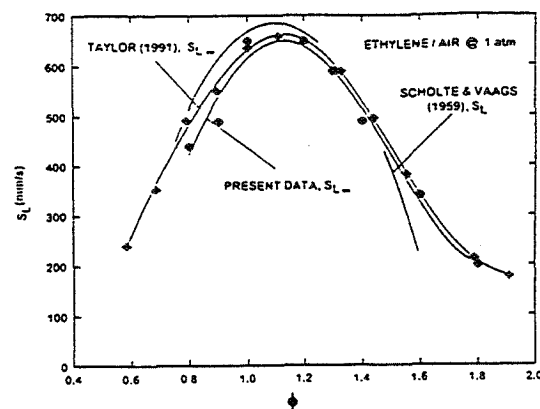
Fig. 6 Laminar burning velocity as a function of fuel-equivalence ratio for ethylene/air mixtures at 100 kPa. Results of Taylor (ref. 39) and Tseng et al. (ref. 35) corrected for stretch while results of Scholte and Vaags (Ref. 40) are not. From Ref. 36.
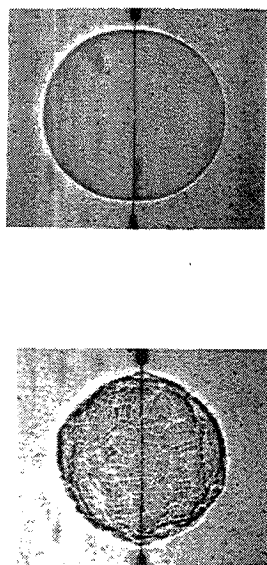
Fig. 7 Typical shadowgraph of a freely-propagating spherical laminar premixed flames at stable (top) and unstable (bottom) at preferential-diffusion mixtures.
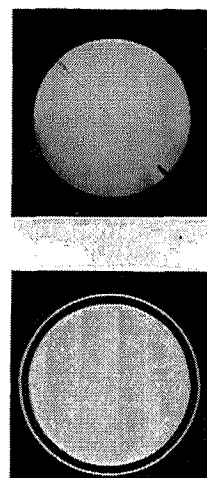
Fig. 8 Dark-field photographs of luminosity during propagation of laminar premixed ethylene/air flames at an initial pressure of 100 kPa: soot-free flame for ϕ = 1.6 (top), and soot-containing flame for ϕ = 2.2 (bottom).

EFFECTS OF FUEL PREHEAT ON SOOT FORMATION IN MICROGRAVITY LAMINAR DIFFUSION FLAMES[1]

Bogdan Konsur, CONSTANTINE M. MEGARIDIS
Department of Mechanical Engineering
University of Illinois at Chicago
Chicago, Illinois

and

DeVon W. Griffin
Microgravity Combustion Branch
NASA Lewis Research Center
Cleveland, Ohio

Introduction

Nonbuoyant flames offer themselves as an attractive and promising platform to gain a better understanding of soot mechanisms [1]. The effects of buoyancy can be eliminated temporarily in drop towers which sustain brief intervals of reduced gravity –typically lower than $10^{-3}g$– extending up to several seconds at a time. Microgravity facilities have been employed [2, 3] to show that nonbuoyant flames are longer, wider and sootier than their normal-gravity counterparts.

Sunderland et al. [4] recently verified the existence of smoke point in laminar nonbuoyant flames. As reported in [3] and [4], microgravity flames operating above their smoke point displayed a blunt tip and much broader soot-containing regimes in comparison to their buoyant counterparts. Mortazavi et al. [5] established that residence times in microgravity laminar jet diffusion flames with Re=O(100) tend to be proportional to burner diameter and inversely proportional to burner exit velocity. This offers the capability to alter residence times in nonbuoyant laminar jet diffusion flames when varying the burner exit diameters and velocities [1].

Megaridis et al. [6] presented a quantitative definition of the soot-field structure within laminar microgravity jet diffusion flames which operated well above their smoke point. The experimental methodology involved a full-field laser-light extinction technique [7] and jet diffusion flames of nitrogen-diluted (50% vol.) acetylene fuel burning in quiescent air at atmospheric pressure. The work was conducted at the 2.2s drop tower of the NASA Lewis Research Center (NASA-LeRC). Parallel work on 1-g flames was also presented in [6] to facilitate comparisons on the effect of gravity on the soot fields. As reported in [6], the soot spatial distributions in 0-g flames did not change in a detectable manner after 1s within a typical 2.2s experiment. During that period, the soot field was shown to sustain a pronounced annular structure throughout the luminous nonbuoyant-flame zone. The maximum soot volume fraction measured at 0-g was nearly a factor of two higher than that at 1-g, thus confirming the enhanced sooting tendency of nonbuoyant flames [1].

Greenberg and Ku [8] presented a similar study and reported trends that matched those of [6] for the 50% (vol.) nitrogen-diluted acetylene fuel. Furthermore, they examined pure acetylene flames and reported similar trends with respect to the influence of gravity on maximum soot volume fractions and flame cross-section-averaged soot loadings. Both studies [6, 8] clearly demonstrated the improved spatial resolution of microgravity flames compared to their normal-gravity counterparts.

The current study evaluates the influence of moderate fuel preheat on soot formation within 0-g laminar gas jet diffusion flames. While fuel temperature variations have little influence on residence times in 1-g, they have a much more significant effect in 0-g [1]. The primary objective of this program is to quantify this effect and its consequences on sooting by comparing soot volume fraction distributions under preheated and unpreheated-fuel conditions. Furthermore, the current work aims at expanding the limited soot database available for nonbuoyant flames. Soot fields in such flames can be used to perform additional tests of recently developed soot sub-models which have the potential to become powerful predicting tools in combustion design.

Experimental Setup and Conditions

The laminar gas jet diffusion flames studied herein were operated at atmospheric pressure and were based on a

---

1.6mm inner diameter stainless-steel burner which was positioned vertically in the experimental apparatus. The fuel mixture consisted of 50% (volume) C_2H_2 – 50% N_2 and was issued into quiescent air contained in a rectangular chamber with dimensions 30cm $\times$ 21cm $\times$ 43cm. The base fuel flow rate of 2.2 mg/s was selected because it defined flame sizes which provided adequate resolution of the soot fields both in 1-g and 0-g [6]; the flame luminosity lengths were between 25mm and 30mm. The mass flow rate of 2.2 mg/s corresponds to a volume flow rate of 2 cm^3/s at room temperature. A second set of experiments was conducted at a lower fuel flow rate of 1.6 mg/s. Two fuel preheat levels were studied for the base mass flow rate of 2.2 mg/s; 120°C and 160°C. These preheat levels correspond to an increase in adiabatic flame temperature by 7K and 10K, respectively, compared to the unpreheated-fuel case. Therefore, the effect of the current fuel preheat levels on fuel pyrolysis rates – and thus on soot inception rates – should be negligible. Table I lists four burner exit conditions for the flames studied in this work. Two conditions (I and II) involved unpreheated fuel, while the other two (III and IV) featured fuel preheat temperatures of 120°C and 160°C, respectively. All burner exit flow conditions listed in Table I produced non-flickering flames in normal gravity as well as within the short time period available for measurements in the drop tower. All 1-g flames corresponding to the conditions listed in Table I emitted no soot from their closed conical tip, while their nonbuoyant counterparts released soot from their open tip. The smoke point of the diluted unpreheated acetylene fuel at 0-g was determined to be in the range from 0.77 – 1.1 mg/s (0.7 to 1 cm^3/s at room temperature).

The experimental rig is the same one used in [6]. Each microgravity experiment lasts for 2.2 seconds, during which data are collected continuously. Diagnostic instrumentation includes laser-light extinction for determination of soot volume fraction distributions and direct imaging of the flame. The flame luminosity throughout each drop test is recorded and can be subsequently analyzed to determine luminous flame dimensions. Experiments are fully automated and are controlled via an onboard computer. Fuel preheat is achieved by thermocouple sensors, temperature controllers and heating tapes wrapped around the fuel feed lines. The rig design allows operation in either unpreheated or preheated mode by activating appropriate elements of the experimental setup. Soot volume fraction distributions within the flames were determined via a full-field laser-light extinction technique [7]. The instrumentation for these measurements has been described in detail in [6]. From each horizontal intensity profile (Z = constant), the radial distribution of soot volume fraction is determined using a three-point Abel deconvolution algorithm [9], and Rayleigh scattering theory with a specific value of the refractive index of soot (1.57 - 0.56i).

Results and Discussion

Detailed observations of luminous zone development after ignition in 0-g showed the initial transients to be complete before the half-way temporal point of a drop experiment (~1s). Figures 1a, b, c present the luminous images of Flames II, III and IV, respectively, as captured from the side after the brief initial transients in 0-g. The soot-emitting character of all 0-g flames examined in this work made the determination of a visible height impossible; notice the gradual darkening of flame tip with height in Fig. 1. The vertical scale in Fig. 1a corresponds to a length of 25mm. It is clear that fuel preheat has a visible effect on the structure of the soot field; see differences of shapes in Fig. 1. More specifically, the base and the tip of Flames III and IV (Fig. 1b, c; preheated fuel) are considerably narrower than those of Flame II (base flame seen in Fig. 1a; unpreheated fuel).

Soot fields in 0-g laminar jet diffusion flames anchored on the same burner (1.6mm diameter, Reynolds of the order of 100) were analyzed in [6] as a function of time to evaluate their transient post-ignition character. Figure 2 displays two instantaneous shadow-like images of the soot field as viewed by the CCD camera of the extinction setup during a drop experiment at 0.5s and 1.2s after the release of the package. Fuel ignition occurred 0.3s after the onset of microgravity. The flame conditions corresponding to these images are those of Case II in Table I. The burner mouth is located directly below the middle of the bottom edge of each image seen in Fig. 2. The apparent differences of the soot shadow at the upper half of the images of Fig. 2 confirm the changing character of the soot field after ignition in 0-g (0.3s). As reported in [6], the establishment of the soot field in these flames is completed within one second after the onset of microgravity. This was also verified in the current study for all flame conditions listed in Table I.

A series of images similar to those depicted in Fig. 2 were utilized to produce radial distributions of soot volume fraction (f_v) at distinct axial stations above the burner tip of each flame. The specific heights examined in this work are Z =10mm, 15mm, 20mm and 25mm. The spatial soot distribution at each height Z was obtained by averaging the respective distributions acquired in two to three drop experiments which were conducted using identical operating conditions. Figure 3 displays the radial variations of f_v throughout the four microgravity flames (I to IV; see Table I). Each frame in this figure corresponds to a fixed height Z (10mm, 15mm, 20mm and 25mm). Figure 3 shows clearly – as also reported in [6] – that the soot distributions maintain a noticeable annular structure throughout the entire luminous flame zone. Even though the soot volume fraction is always higher on the annulus, the soot concentrations in the vicinity of the flame axis become significantly higher when the fuel is preheated (compare curves II and III or IV at Z=25mm, for example).

The radial distributions in Fig. 3 also show that the lower exit momentum of the fuel jet in Flame I causes a widening of the soot field compared to the rest of the flames. This trend is maintained at all heights and emphasizes the importance of jet momentum in flame structure in 0-g. As the fuel exit velocity increases from Flame I to IV, the soot annulus moves closer to the flame axis. It is also seen in Fig. 3 that the radial location of the soot annulus is nearly the same for the two flames with preheated fuel (III and IV).

Figure 4 compares the streamwise variation of (a) maximum and (b) on-axis soot volume fraction at each height Z for all 0-g flames. As the radial distributions in Fig. 3 indicate, the maximum values of f_v at a fixed height always correspond to the soot annulus in the 0-g flames examined in this work. Figure 4a also includes the values of f_v on the soot annulus of a flame identical to Flame II as reported in Ref. [6], and shows good repeatability of the measurements. Figure 4a shows that the overall maximum value of f_v is ~14ppm and is achieved near Z=20mm of Flame II (unpreheated fuel). In all preheated-fuel flames the soot volume fractions peak at Z=15mm and decline thereafter. Some important conclusions can be inferred from the curves of Fig. 4 when taking into account residence time considerations. Estimates of flow residence times were produced for the base case flame (II) using the soot cloud as a flow tracer during a typical drop experiment, and taking advantage of the transient character of the extinction field after ignition in 0-g (see Fig. 2). The flow residence time through the luminous zone of Flame II was approximately 0.3s. A similar procedure for the lower flow rate (1.6mg/s) produced a residence time of about 0.4s in Flame I. These residence times scale approximately with inverse flow rate, in agreement with the analysis of Mortazavi et al. [5]. The above simplified measurements also confirm that in 0-g laminar jet diffusion flames with Re=O(100) residence times are inversely proportional to burner exit velocity for a fixed burner size [5]. The fuel exit velocities listed in Table I agree with the estimate that Flame I features a residence time that is by ~33% longer compared to Flame II. The gradually increasing fuel exit velocities from Flame II to IV (see Table I) cause reductions in residence times by 25% and ~32% in Flames III and IV, with respect to Flame II. It is established that longer residence times have a soot enhancing effect, while lower fuel flow rates have a comparative soot-inhibiting influence. The values of maximum f_v shown in Fig. 4a for Flames I and III or IV are very similar near the upper end of these flames. It appears that the soot-reducing effect of the lower flow rate of Flame I is neutralized by the soot-enhancing influence of the longer residence time in this flame compared to Flames III or IV. Thus, the two competing effects result in ultimate values of $f_v|_{max}$ that are nearly identical in Flames I, III and IV. On the other hand, the combined effect of these two factors in Flame II results in soot volume fractions that are consistently higher than those in all other flames (see Fig. 4a). An exception to this trend is seen at Z =10mm, where the preheated-fuel flames display slightly higher soot concentrations. Finally, the soot volume fractions along the flame axes, as plotted in Fig. 4b, clearly show that soot concentrations in the core of the flame are promoted by fuel preheat. The significant scatter of the data plotted in Fig. 4b is attributed to the increased error in the tomographic inversion procedure towards the flame centerline [9]. However, the overall trends shown in this figure are believed to be accurate. The strong soot-enhancing influence of fuel preheat on the flame centerline cannot be attributed to increased fuel pyrolysis rates, as the current fuel preheat levels correspond to an increase in adiabatic flame temperature of less than 10K. Neither this trend can be attributed to a residence time effect, because Flames III and IV feature shorter residence times compared to Flame II. Consequently, the higher soot volume fractions at the centerline of the preheated flames are probably caused by more efficient particle transport from the soot annulus to the axis of these flames. It is acknowledged that in Flames III and IV the soot particles need to traverse shorter distances to approach the centerline (Fig. 3), but they have less time available to achieve this because of the reduced residence times in these flames. The soot transport characteristics in a gaseous medium depend on local gas velocities and temperatures, temperature gradients along the cross-stream coordinate which, in turn, affect thermophoretic forces towards the cooler inner regions of the flame [10], air entrainment rates, or a combination of all or some of the above. Unfortunately, neither velocity nor temperature measurements are available in the 0-g flames examined herein, thus allowing no definitive statement regarding the origin of the higher soot concentrations on the centerline of the preheated-fuel flames.

Figure 5 depicts schematically the relative positioning of a typical soot aggregate with respect to the flame sheet and the burner centerline in 1-g and 0-g. In both cases, the thermophoretic velocity V_T carries the particles away from the high-temperature flame sheet and towards the symmetry axis. A simple estimate revealed that thermophoretic velocities in 0-g are significantly weaker than those encountered in 1-g (primarily due to lower temperature gradients present in 0-g [11]). The radial gas velocity V_r in the vicinity of the soot particles is also drawn in Fig. 5, and shows that strong air entrainment in 1-g amplifies the already strong effect of thermophoresis in pushing the soot towards the flame centerline. In 0-g, the expanding/decelerating jet flow pushes the particles away from the axis, thus opposing the weaker thermophoretic force, and, in turn, preventing the soot aggregates from reaching the centerline. It is noted that the longer residence times in 0-g would tend to facilitate transport of soot to the flame centerline. However, the soot particles on the annular region in 0-g need to traverse nearly twice as big a radial distance to reach the centerline compared to their 1-g counterparts [6]. In that respect, the larger radial extent of the 0-g flames inhibits

soot transport to the centerline.

<u>Conclusions</u>

An experimental investigation has been presented to quantify the influence of moderate fuel preheat (up to 160°C) on soot formation within 0-g laminar gas jet diffusion flames. The work was performed at the 2.2s drop tower of the NASA Lewis Research Center. The experimental methodology implemented jet diffusion flames of nitrogen-diluted acetylene fuel burning in quiescent air at atmospheric pressure. The study utilized a full-field laser-light extinction technique capable of determining transient soot spatial distributions in laminar axisymmetric flames. The 50% (vol.) C_2H_2/N_2 fuel mixture was injected through a 1.6mm-diameter burner with a Reynolds number O(100). All 0-g flames examined released soot from their blunt tip. Moderate fuel preheat in the 0-g laminar jet diffusion flames was found to reduce soot loadings on the annular region but caused an increase in soot volume fractions on the centerline. In addition, fuel preheat reduced the spatial extent of the soot field in 0-g. Another effect of fuel preheat on soot fields was the shift of the peak soot volume fraction to lower heights (or likewise earlier residence times). This shift suggests that the soot growth stage is shortened in 0-g when elevated fuel temperatures are used in conjunction with a fixed fuel mass flow rate. Finally, a tentative explanation was sought for the sustained annular structure of the 0-g soot fields. Estimates of the soot thermophoretic velocities in the flames revealed that the component of this quantity along the radial coordinate is significantly weaker in 0-g than in 1-g. In addition, the larger radial extent of the 0-g flames delayed soot transport to the centerline. These two factors appear to dominate in shaping the pronounced annular character of the soot field in 0-g.

References

[1] Law, C. K. and Faeth, G. M. *Prog. Energy Comb. Sci.* 20, 65 (1994).

[2] Edelman, R. B., and Bahadori, M. Y., *Acta Astronautica* 13:681 (1986).

[3] Bahadori, M. Y., Edelman, R. B., Stocker, D. P., and Olson, S. L., *AIAA J.* 28:236 (1990).

[4] Sunderland, P. B., Mortazavi, S., Faeth, G. M., and Urban, D. L., *Combust. Flame* 96:97 (1994).

[5] Mortazavi, S., Sunderland, P. B., Jurng, J., Köylü, Ü. Ö., and Faeth, G. M., AIAA Paper 93-0708 (1993).

[6] Megaridis, C. M., Konsur, B., and Griffin, D. W., *Twenty-Sixth Symposium (International) on Combustion*, The Combustion Institute, Pittsburgh, 1996, in press.

[7] Greenberg, P. S., and Ku, J. C., "Soot Imaging," *Applied Optics*, accepted, (1997).

[8] Greenberg, P. S., and Ku, J. C., *Combust. Flame* 108: 227 (1997).

[9] Dasch, C. J., *Applied Optics* 31:1146 (1992).

[10] Santoro, R. J., Yeh, T. T., Horvath, J. J., and Semerjian, H. G., *Combust. Sci. and Tech.* 53:89 (1987).

[11] Bahadori, M. Y., Stocker, D. P., Vaughan, D. F., Zhou, L., and Edelman, R. B., in *Modern Developments in Energy, Combustion and Spectroscopy* (F. A. Williams, A. K. Oppenheim, D. B. Olfe, and M. Lapp, Eds.), Pergamon Press, 1993, p. 49.

Table I: Flame Conditions

Case	Fuel Exit Temp. (°C)	Fuel Flowrate (mg/s)	Fuel Flowrate (cm³/s)	Exit Velocity (cm/s)	Exit Reynolds
I	23	1.6	1.5	74.6	96
II*	23	2.2	2	99.5	128
III	120	2.2	2.7	132.1	105
IV	160	2.2	2.9	145.5	98

* Base case
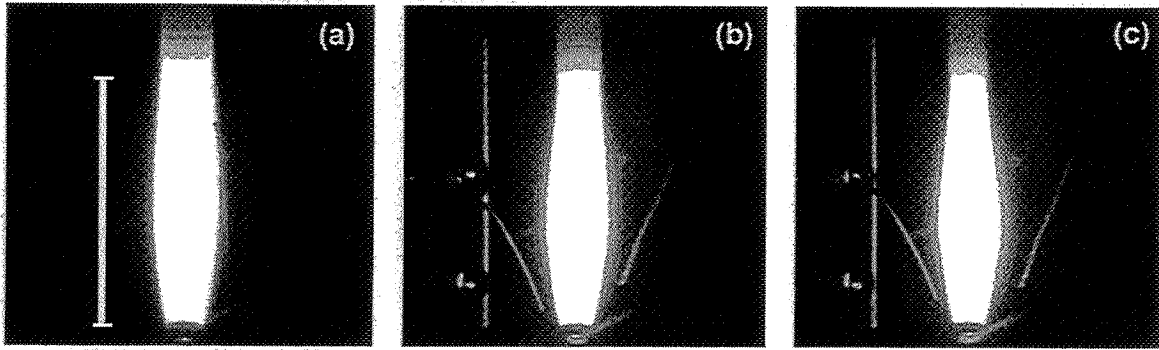
Fig. 1: Luminous flame images in 0-g: a) unpreheated fuel, b) fuel preheated to 120°C, and c) fuel preheated to 160°C. The vertical scale drawn in (a) corresponds to a length of 25mm.
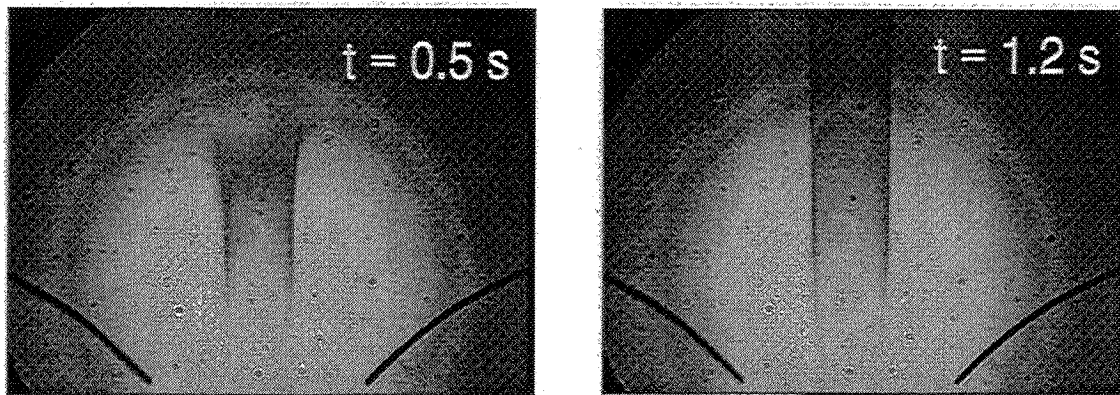
Fig. 2: Instantaneous shadow-like images of the soot field as viewed by the CCD camera of the extinction setup during a drop experiment at 0.5s and 1.2s after the onset of microgravity. Illumination is provided by the expanded laser beam. The burner mouth is located directly below the middle of the bottom edge of each image.
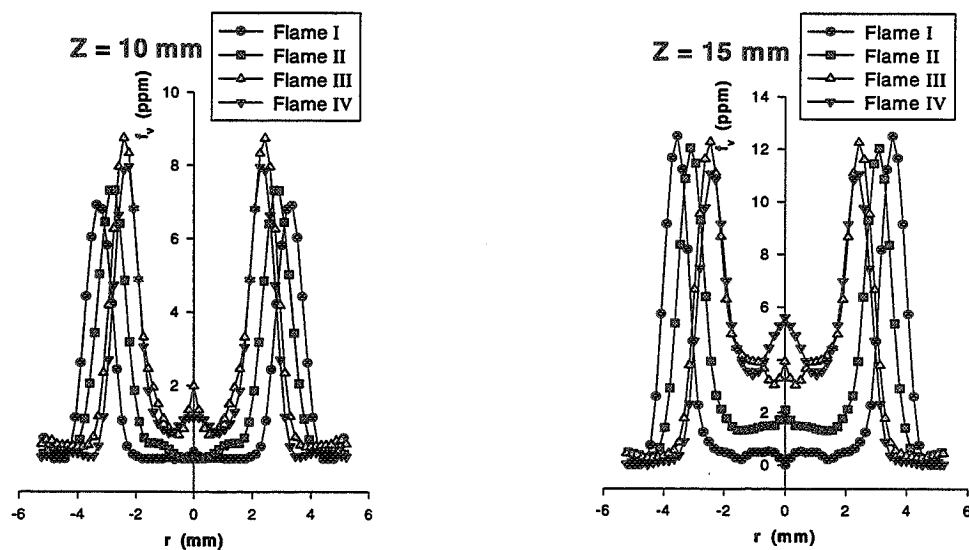
Fig. 3: Radial distributions of soot volume fraction at Z=10mm and 15mm above the burner tip of the four microgravity flames examined (I to IV; see Table I).
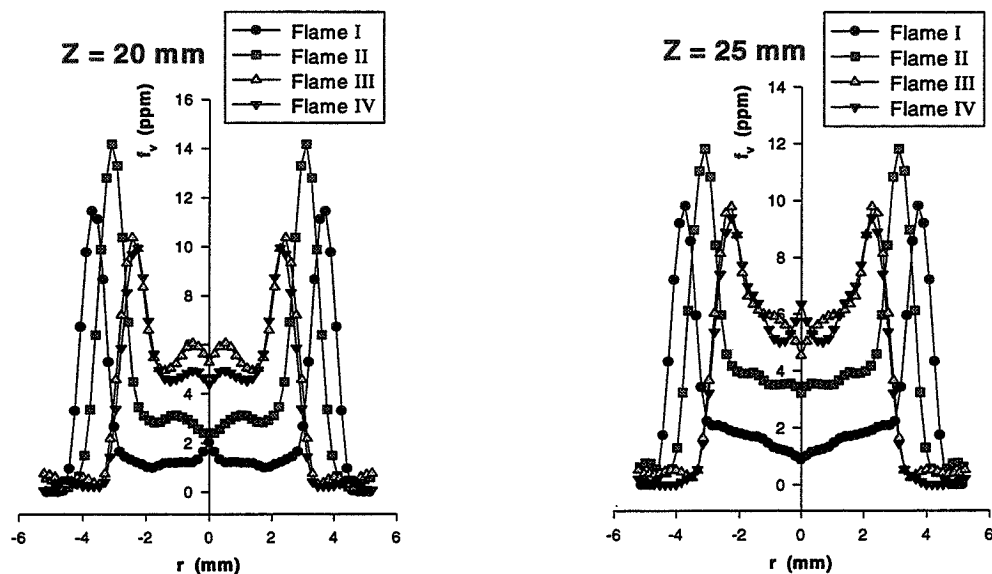
Fig. 3 (continued): Radial distributions of soot volume fraction at Z=20mm and 25mm above the burner tip of the four microgravity flames examined (I to IV; see Table I).
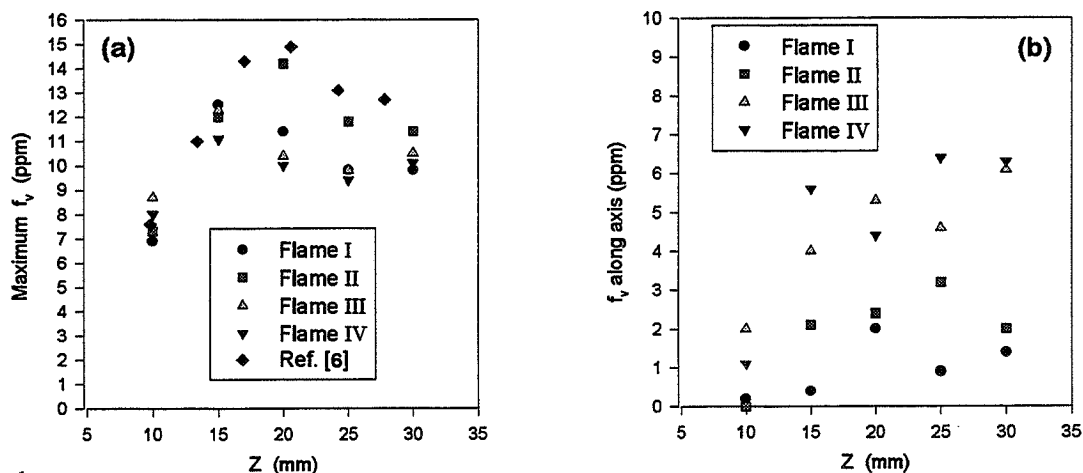
Fig. 4: Comparison of the streamwise variation of (a) maximum and (b) on-axis soot volume fraction at each height Z for all 0-g flames.
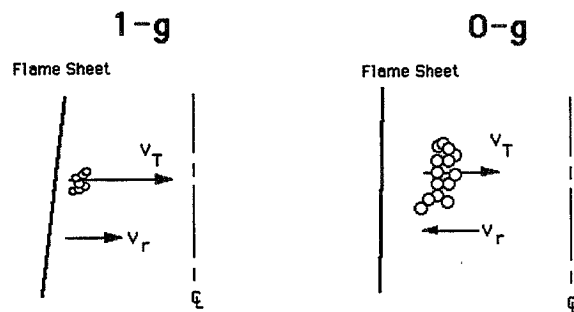
Fig. 5: Schematic illustrating the action of gas convective (v_r) and soot thermophoretic (v_T) radial velocities in typical 1-g and 0-g gas jet diffusion flames.

234

Heterogeneous Diffusion Flames

Page intentionally left blank

CANDLE FLAMES IN MICROGRAVITY

DANIEL L. DIETRICH, Howard D. Ross, David T. Frate
NASA Lewis Research Center
Cleveland, Ohio

James S. T'ien and Yong Shu
Case Western Reserve University
Cleveland, Ohio

Introduction
This work is a study of a candle flame in a microgravity environment. The purpose of the work is to determine if a steady (or quasi-steady) flame can exist in a microgravity environment, study the characteristics of the steady flame, investigate the pre-extinction flame oscillations observed in a previous experiment in more detail, and finally, determine the nature of the interactions between two closely spaced candle flames. The candle flame is used as a model combustion system, in that in microgravity it is one of the only examples of a non-propagating, steady-state, pure diffusion flame. Others have used the candle to study a number of combustion phenomena including flame flicker[1], flame oscillations[2-4], electric field effects[5] and enhanced[6] and reduced[7] gravitational effects in flames.

The present work is a continuation of a small-scale Shuttle experiment on candle flames[8,9]. That study showed that the candle flame lifetimes were on the order of 40 seconds, the flames were dim blue after a transient ignition period, and that just prior to extinction the flames oscillated spontaneously for about five seconds at a frequency of 1 Hz. The authors postulated that the gas phase in the immediate vicinity of the flame was quasi-steady. Further away from the flame, however, the assertion of a quasi-steady flame was less certain, thus the authors did not prove that a steady flame could exist. They also speculated that the short lifetime of the candle flame was due to the presence of the small, weakly perforated box that surrounded the candle.

The Candle Flames in Microgravity (CFM) experiment, with revised hardware, was recently flown aboard the Mir orbiting station, and conducted inside the glovebox facility by Dr. Shannon Lucid. In addition to the purposes described above, the experiments were NASA's first ability to ascertain the merits of the Mir environment for combustion science studies. In this article, we present the results of that experiment. We are also in the process of developing a numerical model of the microgravity candle flame. The status and results of the modeling efforts to date are also presented.

Experimental Apparatus
The design of the experiment is based on the USML-1 CFM experiment described elsewhere[8,9]. The experiments are conducted inside a glovebox facility that provided power, video and photographic capabilities and provided a level of containment. The main module of the experiment was a 20 cm cube-shaped wire mesh screen as opposed to the 12.5 cm perforated Lexan box used on USML-1. More importantly, the screen provided more than 50% free area (as opposed to less than 15% on USML-1) yielding less resistance for oxygen to diffuse to the flame and combustion products to diffuse away from the flame. The ignition system was a coiled 250 μm aluminum alloy wire heated with a current of approximately 3 amperes. For all of the experiments, the igniter was on for a preset time of 4 or 5 seconds. This was sufficient to ignite the candle in almost all of the tests.

On USML-1, 7 identical candles (2.5 mm wick diameter, 5 mm candle diameter, 12 mm candle length, and 3 mm initial exposed wick length were tested. In the Mir experiments, a variety of candle types were flown. There were 79 total candles supplied with the hardware with three different wick diameters (approximately 1, 2 and 3 mm), two different candle diameters (5 and 10 mm) and two different lengths of initially exposed wick (3 and 6 mm). All candles were 2 cm in length

The glovebox facility is in the Priroda module of the Mir orbiting station. All of the candles were burned over an approximately 3 week period. The Mir operates at nominally atmospheric pressure with an oxygen concentration that is higher than air. For the candle tests, the oxygen mole fraction in the ambient was between 0.22 and 0.25. The value is that measured and down-linked by the Russian oxygen sensors and pressure transducers on-board Mir. The Russian cosmonauts calibrate the oxygen sensor every two weeks as a regular maintenance procedure.

The data consisted of video and still photography, crew audio commentary, thermocouple measurements, and radiometric measurements and a single point oxygen measurement. The radiometer and oxygen sensor were interchangeable and located approximately 10 cm from the tip of the flame. The primary purpose of the oxygen sensor was to ensure that the ambient oxygen concentration was below 30% (safety mandate). We also hoped to determine the oxygen concentration at the sensor location (10 cm from the candle wick) as the candle burned. The still photographs were from a 35 mm SLR camera with ASA 200 film. A higher speed film would have been better, but could not be used because of anticipated film-fogging problems from prolonged exposure to cosmic radiation. The pictures indeed show a small degree of fogging due to radiation. The camera's shutter remained open until sufficient light was collected, based on central-spot metering of the candle flame; often this meant that the pictures were integrated averages of the behavior of the candle flame over 10 second intervals. The flames were too faint for the glovebox-supplied video cameras to record the flame shape when it was entirely blue.

Experimental Observations

Qualitatively, all of the candles burned similarly in the following ways. Immediately after ignition, the flames were very luminous and hemispherical, resembling the flames on USML-1. The yellow luminosity, presumably from soot, lasted well into the flame lifetime, however, unlike on USML-1 As the burning progressed, heat feedback from the flame rapidly melted the wax. For the 5 mm diameter candles, all of the exposed wax melted within 2 minutes of ignition. The shape of the candle and wax then looked as in Figure 1(b). After some time, this molten ball of wax became unstable and 'collapsed' suddenly as it moved back along the candle holder as shown in Figure 1(c). After the collapse, the yellow luminosity disappeared and the flame became dim blue, similar to the USML-1 candle flames. The flames then remained dim blue until extinction

All of the candles burned substantially longer than the longest candle flame lifetime on USML-1. The Mir experimental flame lifetimes varied from slightly over 100 seconds to over 45 minutes. The candles with the largest wicks had the shortest flame lifetimes and the candles with the smallest wicks had the largest flame lifetimes. The actual flame lifetime for seemingly identical candles varied significantly in some cases. The pre-extinction flame oscillations observed on USML-1 also occurred with the Mir flames. The oscillations also correlated with the type of wick. Specifically, no oscillations occurred in any of the experiments with the smallest wick diameter. Oscillations did occur in the other two wick diameters . The flames oscillated at a frequency similar to that on USML-1 only for a much longer time, for as long as 90 seconds in some cases. Also, although the flames on the smallest wicks did not *spontaneously* oscillate near extinction, they did oscillate when a thermocouple (and tube supporting the thermocouples) was moved close to the flame. The oscillations stopped immediately after the thermocouple was moved away from the flame.

Analysis of the 35 mm photographs yielded both the flame diameter, D , and flame height, H (both shown in Figure 1(a)) as functions of time. Additionally, the ratio H/D was also determined. The latter quantity yielded consistent behavior in the USML-1 candle tests[9]. For the USML-1 tests, H/D was initially 0.9 and decreased to approximately 0.7 at extinction (just before the oscillations). Figure 2 shows H, D, and H/D as a function of time for a Mir candle flame with a relatively long lifetime. The flame size increases for the first 75 sec of the flame lifetime, after which the flame size remains relatively constant (D remains constant, but H decreases slowly). This change in behavior at 75 seconds corresponds to the time of the collapse of the liquid wax. H/D is nearly steady until the collapse occurs after which it continuously decreases until extinction.

In general, the results (that have been analyzed to date) show that the flames were more reproducible than on USML-1. The flames typically increased in size initially and then remained at constant size or increased in size slowly as a function of time. H/D either decreased or remained constant as a function of time. The values of the flame size are consistent with USML-1, although the value of H/D is somewhat higher than on USML-1. This later observation could be due to the increased ambient oxygen concentration in the Mir tests. Our data reduction efforts are still underway. We do not yet report on the radiometric data nor the local oxygen sensor data because the former has not yet been examined in detail and the latter lacked sufficient resolution to draw satisfactory conclusions.

The purpose of using different wick sizes was to change the flame size. Figure 3 shows the flame diameter (D) as a function of time for the three different wick sizes. As expected, the larger the wick size, the larger the quasi-steady flame size. The mass burning rate of the candle flame should also be a function of the candle wick diameter. The three different wick sizes give burning rates that varied from 0.9 to 1.4 mg/s in normal gravity. The reduced gravity burning rates (based on the candle mass before and after the experiments) varied from approximately 0.2 mg/s for the smallest wick sizes to approximately 0.6 mg/s for the largest wick size.

During several of the tests, the lights were on and the glovebox cameras recorded the behavior of the liquid wax. As mentioned before, the liquid wax fully melted within 2 minutes of ignition. During and after melting, there was very significant motion in the liquid phase. The motion was apparent from seeing small bubbles that initiated near the wick. These bubbles were drawn towards the tip of the candle where they moved close to the surface and then moved quickly back towards the candle holder. This motion is consistent with surface-tension-driven flow that originates because of the lower temperature liquid that is present near the candle holder relative to that liquid closer to the flame.

One surprise was the amount of wax vapor that rapidly condensed into an aerosol that moved away from the candle flame. With the lights on, it could be seen that there was a significant amount of aerosol produced at the base of the flame near the candle holder. Throughout the lifetime of the flame, aerosol streamed out from the base of the candle and formed a ring around the inside of the candle box. This last observation was not evident on the video camera, but described in detail by the crew. The aerosol is in all likelihood condensed paraffin that is produced from the flame vaporizing the wax, and then moves along the candle (perhaps carried in the boundary layer produced by the liquid wax flow) and condenses as gets far enough away from the flame. After flame extinction, there was also a large, spherical vapor cloud that surrounds the candle and is centered at the wick.

Theoretical Model

We divide the modeling of the candle flame into two tasks. The first part treats in detail the gas phase, but with a simplified liquid phase. This is presented below. The second part will treat the liquid phase in more detail, considering the wick as a porous media through the liquid wax flows. This second phase will be completed and coupled with the gas-phase treatment in the future.

The gas-phase model assumes that the fuel is evaporated from a small porous sphere maintained at a constant radius, R, that is coated with liquid fuel. This sphere is connected to a thin rod with a prescribed temperature distribution. This thin rod is inert and acts as a heat sink to simulate the flame quenching aspect of the candle wick. Figure 1(a) shows a schematic of the problem.

Assuming axisymmetry, the mathematical formulation utilizes a two-dimensional spherical coordinate system also shown in Figure 1(a). The model assumes: one-step second-order overall Arrhenius reaction, constant specific heats and thermal conductivity, constant Lewis number for each species(although different species can have different, constant Lewis numbers), ideal gas behavior and no buoyant force. The last assumption allows us to adopt a simplified treatment of the momentum equation[10]. This includes the assumption of potential flow and the product $(\bar{\rho}\,\bar{T})$ to be constant. In addition, flame radiative losses from CO_2 and H_2O are present but a gray gas treatment is used. Finally, the liquid fuel is prescribed to be at the boiling point, T_b. The following non-dimensional variables are defined as (bars indicate dimensional quantities):

$$T = \frac{\bar{T}C_p}{\bar{q}}; \quad r = \frac{\bar{r}}{\bar{R}}; \quad \rho = \frac{\bar{\rho}}{\bar{\rho}_\infty}; \quad t = \frac{\bar{t}\bar{D}_\infty}{\bar{R}^2}; \quad u_r = \frac{\bar{R}\,\bar{u}_r}{\bar{D}_\infty}; \quad u_\theta = \frac{\bar{R}\,\bar{u}_\theta}{\bar{D}_\infty}; \quad \phi = \frac{\bar{\phi}}{\bar{D}_\infty}; \quad \Phi = \frac{\bar{\Phi}}{\bar{D}_\infty}; \quad \omega_F = \frac{\bar{C}_p\bar{R}^2}{\bar{\lambda}}\bar{\omega}_F; \quad L = \frac{\bar{L}}{\bar{q}};$$

$$E = \frac{\bar{E}C_p}{\bar{R}^u\bar{q}}; \quad Da = \frac{\bar{\rho}_\infty^2\,\bar{C}_p\bar{R}^2}{\bar{\lambda}}\bar{A}; \quad q_r = \frac{\bar{R}^2\bar{C}_p}{\bar{\lambda}\,\bar{q}}\bar{q}_r.$$

The *non-dimensional equations* are:

$$\frac{1}{r^2}\frac{\partial}{\partial r}(r^2\frac{\partial \Phi}{\partial r}) + \frac{1}{r\sin\theta}\frac{\partial}{\partial\theta}(\frac{\sin\theta}{r}(\frac{\partial\Phi}{\partial\theta})) = \frac{\omega_F + q_r}{T_\infty}$$

$$\rho\frac{\partial Y_i}{\partial t} + \rho\,u_r\frac{\partial Y_i}{\partial r} + \frac{\rho\,u_\theta}{r}\frac{\partial Y_i}{\partial\theta} - \frac{1}{Le_i r^2}\frac{\partial}{\partial r}(r^2(\frac{\partial Y_i}{\partial r})) - \frac{1}{Le_i r\sin\theta}\frac{\partial}{\partial\theta}(\frac{\sin\theta}{r}(\frac{\partial Y_i}{\partial\theta})) = v_i\omega_F$$

$$\rho\frac{\partial T}{\partial t} + \rho\,u_r\frac{\partial T}{\partial r} + \frac{\rho\,u_\theta}{r}\frac{\partial T}{\partial\theta} - \frac{1}{r^2}\frac{\partial}{\partial r}(r^2\frac{\partial T}{\partial r}) - \frac{1}{r\sin\theta}\frac{\partial}{\partial\theta}(\frac{\sin\theta}{r}(\frac{\partial T}{\partial\theta})) = \omega_F + q_r$$

$$\omega_F = Da\,\rho^2 Y_O Y_F \exp(-\frac{E}{T})$$

where Φ is a coupling variable given by $\Phi = \phi - \frac{T}{T_\infty}$ and ϕ is the velocity potential. The *boundary conditions* are:

239

@ r=1

$T = T_b$

$-\partial Y_F/\partial r = \rho\, u_r(1-Y_F)$

$\partial Y_i/\partial r = \rho\, u_r Y_i$ (i = O_2, CO_2, H_2O)

$\partial\Phi/\partial r = (1/\rho L - 1/T_\infty)*\partial T/\partial r$

@ r = ∞

$T = T_e;\ Yo = Y_e;\ Yi=0$ (i = F, CO_2, H_2O)

$\partial\Phi/\partial r = -(1/T_\infty)*\partial T/\partial r$

@ θ = π

$T(r) = Tc + (r_c-r)/(r_c-1)*(T_b - T_c)$ at $1 < r < r_c$

$T(r)=Tc$ at $rc < r < \infty$

$\partial Yi/\partial\theta = 0$ (i = F, O_2, CO_2, H_2O)

$\partial\Phi/\partial\theta = -(1/T_\infty)*\partial T/\partial\theta$

@ θ = 0

$\partial T/\partial\theta = \partial\Phi/\partial\theta = \partial Yi/\partial\theta = 0$ (i = F, O_2, CO_2, H_2O)

This set of equations is solved numerically by a time-marching scheme started with prescribed initial profiles of temperature, velocity and species.

Figure 4(a) shows the temperature distribution in 0.23 mole fraction O_2 ambient. Only one-half of the picture is shown because of symmetry. The computed peak temperature is around 1710 K and a cool zone exists near the wick (or cold rod). Figure 4(b) shows the fuel-vapor mass-fraction contours. Some fuel vapor leaks out from the inside of the flame because of the quench layer near the wick. Similarly oxygen, shown in Figure 4(c), diffuses through this cool zone into the fuel-rich zone between the flame and the wick, thus creating a small partially premixed region. Figure 4(d) is a plot of the fuel vapor reaction(consumption) rate contours. These contours are the best indicator of blue visible flame in models with one-step kinetics. Grayson[11] used w_F= 0.1 g/mm^3 s to represent the edge of the blue flame (minimum visible reaction rate) in solid-fuel flame-spread modeling, and we adopt the same criterion. Figure 4(d) clearly shows a quench zone near the wick.

Comparison between the computed flame shape and the experimental photographs shows good agreement. The numerical model produces a more hooked base than is present in the experiment. This is perhaps due to the finite thickness of the candle which the model treats as infinitely thin. The flame width, D, (outside edge of the flame, or w_F= 0.1 g/mm^3) is 14 mm and height, H, is 12.5 mm which is very close to the quasi-steady experimental value (Figure 2). The computed flame dimension depends on the porous sphere diameter, in this case R= 0.6 mm which is close to radius of the small wick used in the experiment. The computed mass burning rate m= 1.46*10^{-4} g/s is close to the lower end of the measured range. Note that the computed aspect ratio H/D is equal to 0.89. This falls in the range of experimentally observed H/D ratios.

Future modeling effort may include the study of flame extinction condition, near-limit oscillations, improvement of radiation treatment and the extension to include processes occurring inside the porous wick.

<u>Conclusions and Discussion</u>

The candle flames in the Mir tests had much longer lifetimes than those on USML-1. This is due to less resistance to oxygen transport through the candle box and a higher ambient oxygen concentration. The ambient oxygen mole fraction in the Shuttle tests was 0.217. In the Mir tests the range was from 22.5 to 24.9%. This difference alone would not however extend the lifetimes by a factor of 10 or more, as was observed. Thus, the predominant reason for the observed increase in flame lifetime for the Mir tests was the re-designed candle box.

Given a flame lifetime of up to 45 minutes, we believe that the gas-phase was quasi-steady, implying that the flame was steady over a time period much longer than any reasonable characteristic gas-phase transport time. Predictions from the numerical model suggest that the time to reach quasi-steady behavior for the gas-phase region <u>inside</u> the flame is only 10 seconds. This is consistent with drop tower and previous low gravity experiments where the flame quickly established a near-constant size.

Spontaneous oscillations are inherent to the near-extinction burning of these flames. The observed frequency was consistent with those seen before in low gravity, and are much less than observed in normal gravity[8,9]. The apparent dependence on wick diameter, implying a dependence on flame size, suggests that flame radiative losses may contribute to the onset of oscillations, as hypothesized by Cheatham and Matalon[3,4].

The rapid melting of the wax is due to the conductive (and radiative) feedback to the solid wax. The liquid wax accumulates on the wick, rather than dripping as it does in normal gravity. When the wax collapses, the flame became blue as a result of reduced wax vapor supply to the flame. The result is a lower flame temperature than needed to

produce soot. The liquid flow visualization was fortuitous, and confirmed expectations that a significant flow persists throughout the flame lifetime. The source of the bubbles is likely the air captured in the wick matrix during fabrication of the candles. As the wax melted, the air bubbles were transported into the liquid, and served as flow tracers. Quite unexpected, however, was the aerosol flow that began upon ignition.

Only a few experiments were performed with two candles, so we do not report detailed results in this paper. One finding, however, was that, unlike USML-1, both candles could be lit in close proximity to each other, because they were ignited simultaneously. This verified the hypothesis that the procedure of sequential ignition was the cause of the failure to ignite both candles in the earlier tests.

References

1. Buckmaster, J. and Peters, N. (1986). The Infinite Candle and its Stability - A Paradigm for Flickering Diffusion Flames. *Twenty-First Symposium (International) on Combustion* / The Combustion Institute, Pittsburgh, Pennsylvania, 1829.
2. Buckmaster, J. (1996). Edge-Flames and their Stability. *Combust. Sci. Tech* . to appear.
3. Cheatham, S. and Matalon, M. (1996). Near Limit Oscillations of Spherical Diffusion Flames. *AIAA Journal* 34, No. 7, 1403.
4. Cheatham, S. and Matalon, M. (1996). Heat Loss and Lewis Number Effects on the Onset of Oscillations. *Twenty-Sixth Symposium (International) on Combustion* / The Combustion Institute, Pittsburgh, Pennsylvania, to appear.
5. Carleton, F. and Weinberg, F. (1989). *Nature* 330, 635.
6. Villermaux, E. and Durox, D. (1992). On the Physics of Jet Diffusion Flames. *Combust. Sci. Tech.* 84, 279.
7. Ross, H., Sotos, R. and T'ien, J.S. (1991). Observations of Candle Flames Under Various Atmospheres in Microgravity. *Combust. Sci. Tech.* 75, 155.
8. Dietrich, D.L., Ross, H.D. and T'ien, J.S. (1995). Candle Flames in Microgravity. Third International Microgravity Combustion Workshop, Cleveland, Ohio.
9. Dietrich, D.L., Ross, H.D. and T'ien, J.S. (1994). Candle Flames in Weakly-Buoyant and Non-Buoyant Atmospheres. AIAA-94-0429
10. Baum, H.R. (1994) Modeling Lwo Reynolds Number Microgravity Combustion Problems Modeling in Combustion Science, edited by J. Buckmaster and T. Takeno, Springer,118.
11. Grayson, G., Scksteder, K.R., Ferkul, P.V., and T'ien, J.S. (1994) *Microgravity Science and Technology, VII 2*: 187.
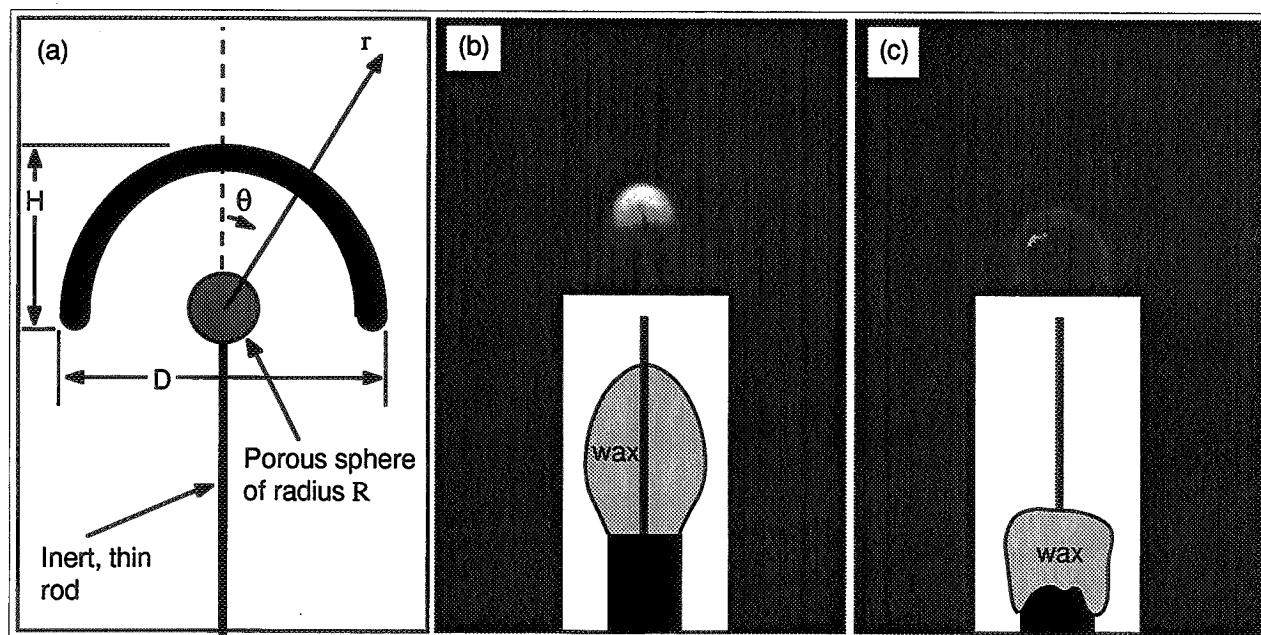
Figure 1. (a) Schematic of a microgravity candle flame with relevant dimensions and coordinate system for numerical model; (b) Candle flame before wax collapse and; (d) Candle flame after wax collapse.
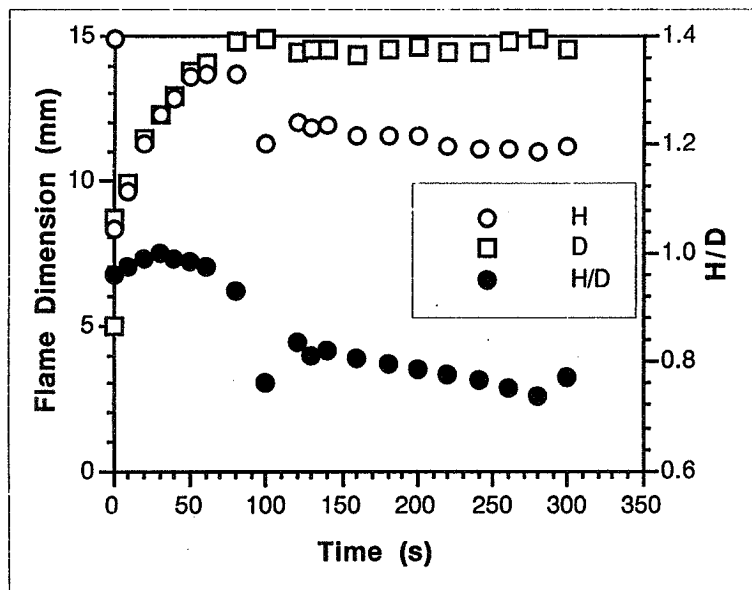
Figure 2.   Candle flame height, H, and diameter, D as a function of time for a candle with a small wick.
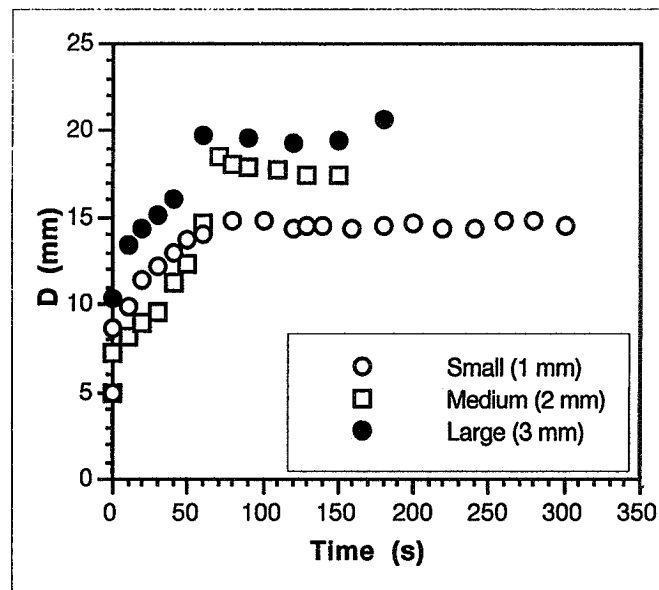
Figure 3.   Flame diameter as a function of time for three different wick diameters.
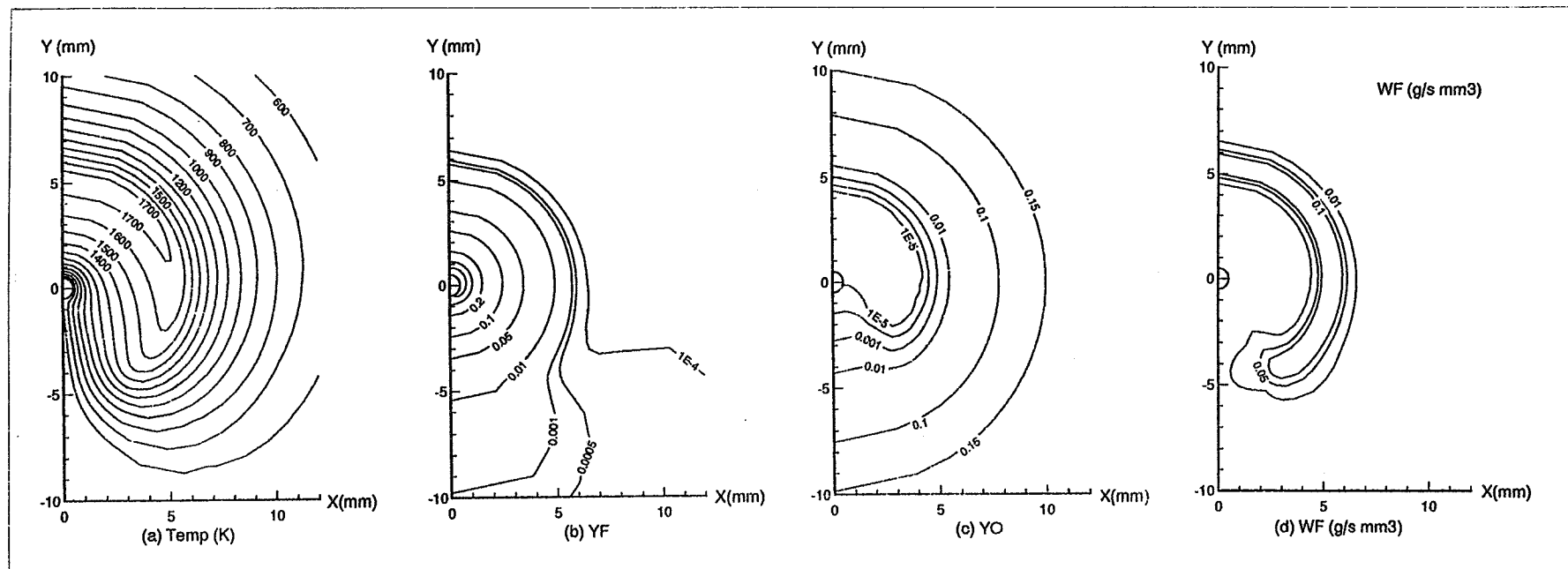
Figure 4.   Numerical modeling results for a sphere diameter of 1.2 mm in a 1 atm, 0.23 oxygen mole fraction ambient.

EXPERIMENTAL OBSERVATIONS OF PMMA SPHERES BURNING AT REDUCED GRAVITY[1]

JIANN C. YANG, ANTHONY HAMINS, MICHAEL GLOVER, and MICHELLE D. KING
Building and Fire Research Laboratory
National Institute of Standards and Technology
Gaithersburg, Maryland 20899 U.S.A.

Introduction

Polymer combustion is a very complicated process which involves the coupling of gas-phase combustion, melting, pyrolysis, and possible charring of the condensed phase. Although only a few studies on the combustion of a spherically shaped polymer have been conducted (refs. 1-3), there is renewed interest in the subject (refs. 4-7). At the Third International Microgravity Combustion Workshop (ref. 8), we presented a preliminary experimental plan and proposed an apparatus to study the combustion of a polymethylmethacrylate (PMMA) sphere at reduced gravity. In this paper, we describe the experimental hardware in detail, summarize our observations since the last workshop, and describe future studies. The main objective is to determine the burning rate of PMMA spheres at reduced gravity under different ambient oxygen concentrations and total pressures. The dependence of the burning rate on the initial sphere diameter will be examined. It is anticipated that the simple spherical geometry in conjunction with reduced gravity will facilitate an assessment of the effect of condensed phase behavior on polymer burning processes and can be used as a means to test polymer combustion models.

Research Approach

The reduced gravity environment was achieved by performing experiments aboard the NASA DC-9 Reduced Gravity Aircraft. The time available to carry out the experiments in both the 2.2 s and 5.18 s NASA drop towers is not long enough to observe the burning histories for spheres with initial diameters used in this study, although the quality of the low G environment in a drop tower (less than 10^{-4} G) is considerably superior to an aircraft flying a parabolic trajectory ($\sim 10^{-2}$ G). For all the experiments, the Grashof number was estimated to be less than 0.1.

Figure 1 is a photograph of the experimental package (shown inside the aircraft cabin). The experimental hardware is housed inside a rack (60 cm x 60 cm x 106 cm) which is mounted on the aircraft cabin floor. The hardware consists of a lap-top computer, a data acquisition and control system (for collecting thermocouple and G-level measurements during the experiments and for controlling the micro-step controllers and the ignition systems), a combustion chamber (an interior view is shown in Figure 2), DC power supplies, a pair of micro-step controllers and linear motors, two Hi8 mm CCD cameras, two ignition systems, a 120 V AC power strip, and a vacuum pump. Oxygen/nitrogen mixture cylinders are mounted separately in a gas bottle rack. The vacuum pump is used to evacuate the combustion products and facilitate the flushing and filling of the combustion chamber with the desired oxygen/nitrogen mixtures in the 1G tests. For the reduced gravity experiments, the overboard vent of the aircraft is used for operational convenience.

Although several different ignition methods have been explored (ref. 8) in the 1G experiments, two methods for igniting the PMMA spheres have been actively pursued, developed and used in the reduced gravity experiments. These two ignition techniques involve the application of (1) micro-torches and (2) heating coils.

Two opposing micro-torches were first used in the flight experiments in an attempt to symmetrically ignite the PMMA sphere. The micro-torch ignition system consists of a fuel reservoir with a refill port, a stainless steel sub-miniature solenoid valve for initiating the fuel flow, a metering valve, a spark ignition system, and a miniature nozzle. The fuel used is liquefied butane. This fuel was chosen over methane because of its low vapor pressure and ease of refilling. The fuel reservoir is a stainless steel cylinder with an outlet section packed with wicks in order to prevent the fuel from coming out as a flashing liquid. A two-phase fuel flow hinders the smooth operation of the micro-torch. The spark ignition circuit, which is used to ignite the gaseous fuel vapor at the nozzle, is battery operated. The initiation and the duration of the spark discharge can be controlled by the computer *via* a solid state relay. The micro-torch nozzle has a configuration similar to a Bunsen burner. Two identical ignition systems

---

are mounted oppositely on two linear motors which are used for moving the torches toward the sample for ignition and for retracting the torches away from the sample upon ignition.

Although the micro-torch ignition system performed satisfactory, the fuel jet perturbed the flame of the burning PMMA. Consequently, the micro-torches have been replaced by two opposing heating coils. The coils are made of metal alloys with a diameter of 250 μm. To ignite a PMMA sphere, the coils are resistively heated until they glow by using a filament transformer and are moved until they just touch the sample surface. The duration that the coil is energized is controlled by the computer *via* a solid state relay; however, the duration was fixed at 2 s for all experimental conditions.

Supported PMMA spheres were used in all the flight experiments. The technique for fabricating a supported PMMA sphere has been described in ref. 8, and a photograph of the apparatus is shown in Figure 3. The supported sample is mounted at the center of a removable holder which is placed along two parallel tracks (see Figure 2). Both K-type thermocouple wire with its junction embedded at the center of the sphere and a special Al/Cr/Fe alloy wire were used to suspend the polymer sample. The diameters of the thermocouple and the special alloy wires were both 75 μm.

The experiments are controlled by a lap-top computer, except for manual operations of valves and video cameras, chamber evacuation and filling with oxygen/nitrogen mixtures, and insertion of a sample. So far, three flight campaigns have been carried out. The first involved the use of PMMA spheres with initial diameters (D_o) of 3.18 mm, 4.76 mm, and 6.35 mm, together with the micro-torch ignition system. The ambient oxygen concentration was set at 21 % in nitrogen (by volume) at cabin temperature and 0.101 MPa. In the second and third campaigns, spheres with initial diameters of 2 mm, 2.5 mm, and 3 mm and heating coils for ignition were used. Ambient oxygen concentrations were varied from 19 %, to 21 %, 25 %, and 30 %. Experiments were conducted at cabin temperature and 0.101 MPa or 0.05 MPa.

Results to Date

Experimental observation of a suspended PMMA sphere burning at reduced gravity reveals the following characteristics. Upon ignition, the sample swells, the outermost surface layer of the burning sample bubbles, and a spherical blue flame is observed, the duration of which decreases with total ambient pressure and oxygen concentration. The spherical flame subsequently becomes more luminous (yellowish color), more bubbles nucleate, the internal bubbling intensifies, and a soot shell is formed between the flame and the sphere. Violent spluttering and ejection of molten polymer from the burning sphere are observed, followed by break-up of the soot shell. The internal bubbling and ejection of material impart impulsive motion to the suspended sphere which causes it to oscillate and slide along the supported wire. The flame loses its spherical shape largely due to the relative motion of the suspended sphere to the ambient gas and partly due to variations in G level. The movement of the sample appears to be more severe for spheres with smaller initial diameters because of smaller inertia and because of the rapid propagation of the molten front through the sphere. The ejection of molten material is more severe in reduced gravity than in 1G because gravity-induced ablation of the melt (dripping of the melt) at 1G appears to counteract the ejection process. In terms of fire safety, the ejected burning material poses a potential fire hazard to adjacent objects. In cases (D_o ≤ 3 mm) where combustion proceeds to completion during the reduced gravity period, the flame resumes its sphericity again due to a small Grashof number and smaller motion of the suspended sphere (due to surface tension).

The period of reduced gravity provided by the NASA DC-9 Reduced Gravity Aircraft is not long enough to obtain complete burning histories of spheres with initial diameters greater than 3 mm for the range of conditions tested. For spheres with D_o > 3 mm, the diameters of the bubbling spheres during combustion do not appear to change significantly (except some degree of swelling) during the entire reduced gravity period. For smaller spheres, complete combustion was observed, and soot strings were found attached to the suspending wire. Extinction was never observed in any of the experiments performed thus far.

Figure 4 is a video sequence showing a polymer sphere before ignition, at ignition, with a spherical blue flame, with a yellow flame, and with variation of the flame shape as combustion progresses. Note that the bubbling sphere moves randomly with respect to the suspending wire during combustion. The three components (Gx, Gy, and Gz) of the G vector are also shown in the bottom of each frame in the figure, and the date, time, and the parabolic trajectory number are depicted at the top of each frame. Figures 5 and 6 are snapshots of the break-up of the soot shell and the ejection of burning molten material, respectively. The formation of a soot shell is not surprising because the main polymer degradation product, methyl methacrylate, has a smoke point very similar to heptane, and a soot shell was observed during the combustion of heptane droplets at reduced gravity (ref. 9). The break-up of the soot shell in the figure is reminiscent of the phenomena associated with a toluene droplet burning at reduced gravity with a small drift velocity (ref. 10).

244

Figure 7 shows the temperature measurements obtained from suspending a thermocouple wire with the junction initially located at the center of the sphere for conditions of 25 % oxygen and 0.101 MPa. The plateau in the temperature trace for D_o = 3.18 mm is the result of the thermocouple junction being displaced to the exterior of the sphere by impulsive motion. The sharp rise in the temperature is due to the sphere being dislodged from the suspending thermocouple during the 1.8 G maneuver of the aircraft. The non-existence of the plateau in the temperature trace for larger spheres, together with the video records, reaffirms the observation of less impulsive motion for larger spheres because the location of the thermocouple junction remains relatively stationary with respect to the burning sphere and the melting front may not have propagated to the junction (*i.e.*, the junction is still embedded in solid phase polymer).

Because of the impulsive motion of the suspended bubbling PMMA spheres and the non-spherical flame shapes, it is very difficult to obtain accurate information on the transient sphere and flame diameters. However, for spheres that burn to completion over the reduced gravity period, the average burning rates can be obtained from the burning times (t_b). Given the initial mass of a sphere and assuming the mass loss due to the embedding of a supported wire to the sample is negligible, the average mass burning rate can be calculated by dividing the initial mass of a sphere (m_i) by t_b. The burning times were obtained from the video record, using frame-by-frame analysis. The uncertainty of the measurements was less than ± 30 ms.

Figures 8 and 9 summarize the burning rate results for some of the successful runs performed using the coil ignition system. The effects of total ambient pressure and oxygen concentration on the burning rate are not apparent due to the large data scatter. However, a general trend emerges, with the average burning rate increasing with the initial sphere diameter. One plausible explanation of the data scatter is that the random ejection of molten material represents a mass loss which is not accounted for in the burning rate calculations. Another reason for the scatter may be partly due to the fixed (2 s) contact ignition period. Ignition delay is expected to vary for different sphere diameters and ambient oxygen concentrations. Although the coil ignition time can be tailored to different experimental conditions, a prohibitively large number of reduced gravity experiments may be required in order to determine the optimum ignition times. Since the ignition events at reduced gravity may be different from those at 1 G, the ignition times cannot be *a priori* determined from 1 G experiments. In order to ensure ignition under various experimental conditions, a 2 s contact ignition time was used and found to be quite satisfactory. If the ignition delay time is shorter than the contact time, unnecessarily prolonged contact of the heating coils with the sample surface would undoubtedly increase the burning rate. Depending on the experimental conditions, the 2 s ignition time is approximately 10 % to 20 % of the burning time. Ignition remains one of the most challenging issues that will be continuously addressed during the course of this study.

Research Plans

We plan to continue to focus on combustion of suspended spheres. Based on the observations from the suspended burning spheres, experiments using unsupported spheres need to be re-evaluated. These experiments may prove to be not feasible with PMMA because the impulsive motion of the sphere imparted by the spluttering and ejection of molten material can cause the unsupported sphere to drift out of the field of view of the cameras, making observations impossible. We are planning to examine other polymeric materials which may exhibit distinct burning behavior. In our next flight experiments, several polypropylene spheres (3 mm) will be tested. In 1 G experiments, polypropylene does not exhibit bubbling. We are also working closely with Dr. K. Butler (of NIST), who is developing a polymer combustion model (also funded by NASA, MSAD) that incorporates the formation and growth of bubbles. Burning rate predictions from this model will be compared to our observations.

References

1. Essenhigh, R. H. and Dreier, W. L., "Combustion Behavior of Thermoplastic Polymer Spheres Burning in Quiescent Atmosphere of Air," *Fuel*, **48** (1969), pp. 330-342.
2. Waibel, R. T. and Essenhigh, R. H., "Combustion of Thermoplastic Polymer Particles in Various Oxygen Atmospheres: Comparison of Theory and Experiment," *Fourteenth Symposium (International) on Combustion*, The Combustion Institute, Pittsburgh, 1973, pp. 1413-1420.
3. Raghunandan, B. N. and Mukunda, H. S., "Combustion of Polystyrene Spheres in Air," *Fuel*, **56** (1977), pp. 271-276.
4. Chung, S.L. and Tsang, S.M., "Soot Control During the Combustion of Polystyrene," *J. Air Waste Manage. Assoc.*, **41** (1991), pp. 821-826.
5. Chung, S. L. and Lai, N. L., "Suppression of Soot by Metal Additives During the Combustion of Polystyrene," *J. Air Waste Manage. Assoc.*, **42** (1992), pp. 1082-1088.
6. Panagiotou, T. and Levendis, Y., "A Study of Combustion Characteristics of PVC, Poly(styrene), Poly(ethylene), and Poly(propylene) Particles under High Heating Rates," *Comb. & Flame*, **99** (1994), pp. 53-74.
7. Okajima, S., Kawakami, T., and Raghunandan, B. N., "Extinction of Fuel Particles Burning Under Microgravity," Work-in-Progress Poster Session, *Twenty-sixth Symposium (International) on Combustion*, The Combustion Institute, Pittsburgh,

1996.

8. Yang, J. C., and Hamins, A., "Combustion of a Polymer (PMMA) Sphere in Microgravity," *Third International Microgravity Combustion Workshop*, pp. 115-120, April 11-13, 1995.

9. Hara, H., and Kumagai, S., "Experimental Investigation of Free Droplet Combustion Under Microgravity," *Twenty-third Symposium (International) on Combustion*, The Combustion Institute, Pittsburgh, 1990, pp. 1605-1610.

10. Avedisian C. T., Yang, J. C., and Wang, C. H., "On Low Gravity Droplet Combustion," *Proc. Roy. Soc. London*, A 420 (1988), pp. 183-200.
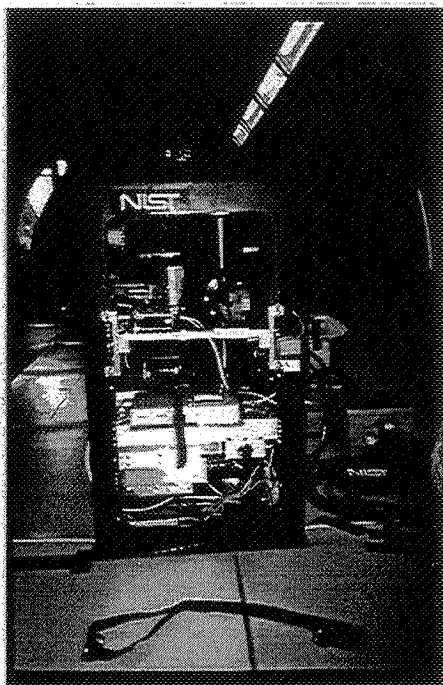
Figure 1. Experimental package.
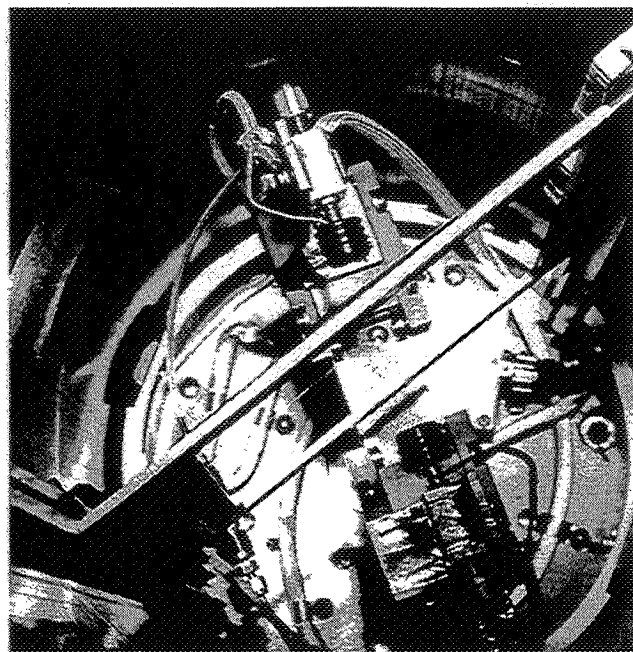
Figure 2. View of interior of combustion chamber.
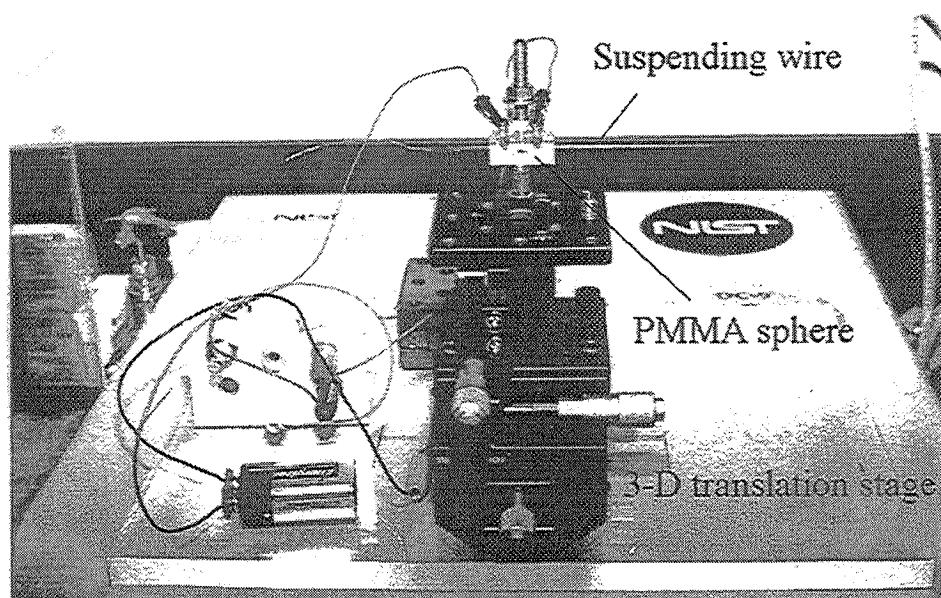
Figure 3. Apparatus used to embed a suspending wire inside a PMMA sphere.

246
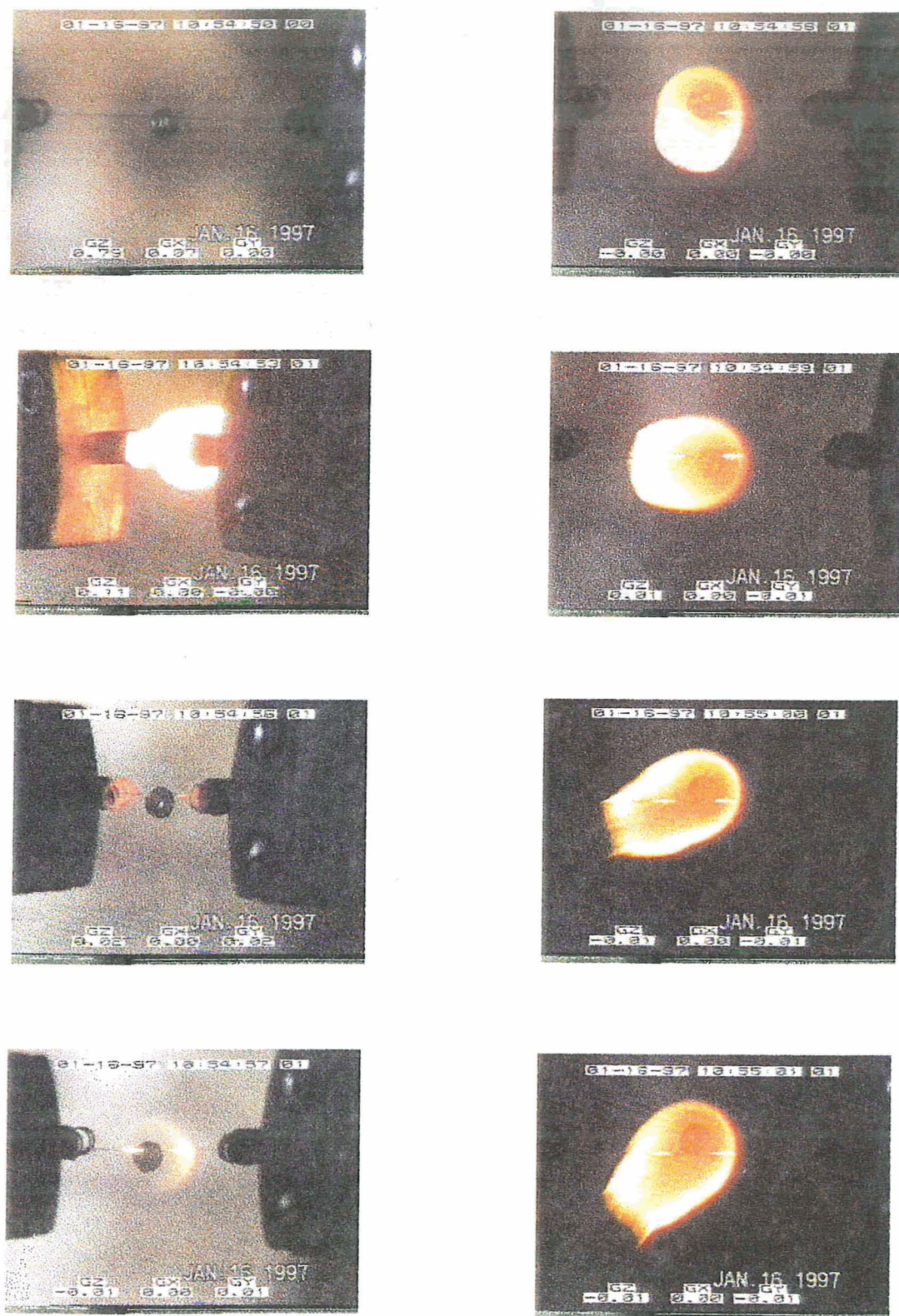
Figure 4. A video sequence showing a burning PMMA sphere (D_o = 3 mm at 19.9 % O_2 and 0.101 MPa).
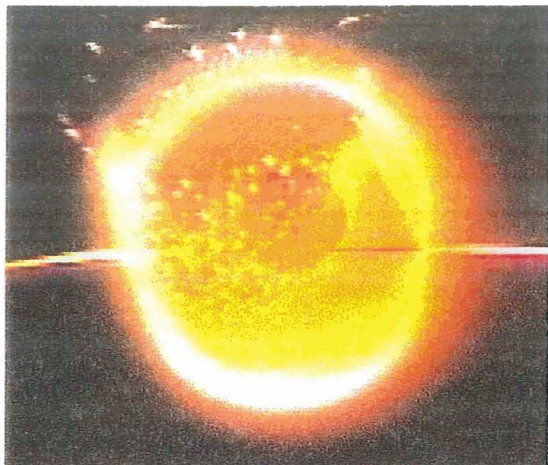
Figure 5. Break-up of a soot shell.

Figure 6. Ejection of molten material.
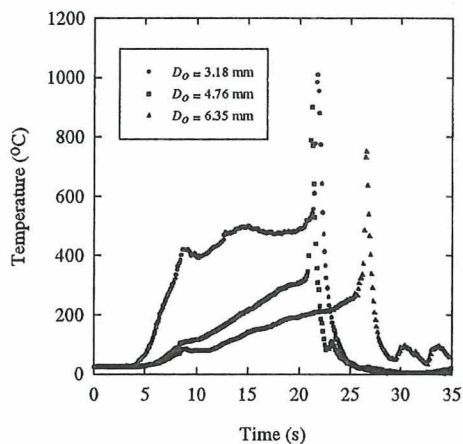
Figure 7. Temperature trace with thermocouple junction
initially at the center of a burning sphere with different D_o.
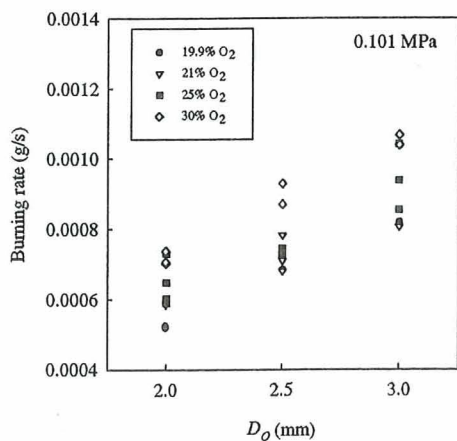
Figure 8. Burning rate as a function of D_o at different O_2
levels at 0.101 MPa.
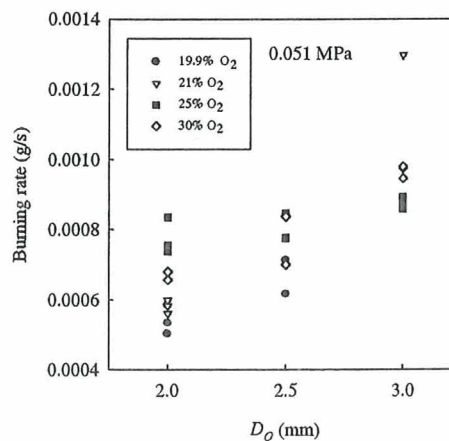
Figure 9. Burning rate as a function of D_o at different O_2
levels and 0.051 MPa.

248

NUMERICAL MODELING FOR COMBUSTION OF
THERMOPLASTIC MATERIALS
IN MICROGRAVITY*

KATHRYN M. BUTLER
Building and Fire Research Laboratory
National Institute of Standards and Technology
Gaithersburg, Maryland

Objectives

A time-dependent, three-dimensional numerical model is under development to predict the temperature field, burning rate, and bubble bursting characteristics of burning thermoplastic materials in microgravity. Model results will be compared with experiments performed under microgravity and normal gravity conditions. The model will then be used to study the effects of variations in material properties and combustion conditions on burning rate and combustion behavior.

Relevance

A clear understanding of fire spread mechanisms in microgravity is critical to the proper assessment of fire hazards from the wide variety of materials used in spacecraft. In early studies, combustion was thought to be less hazardous at low gravity due to the decreased convection of combustion products away from the flame and of oxygen into the flame. Microgravity experiments in a quiescent environment on paraffin, neoprene, foam rubber, and other combusting solids [1] showed that the flames did not reach steady-state conditions but gradually darkened and shrank in size, with some samples self-extinguishing. Such experiments supported the assumption that fire hazards in low gravity could adequately be assessed by tests of materials at normal gravity.

More recent studies have demonstrated that certain thermoplastic materials present a fire hazard unique to microgravity. During combustion, chemical reactions within the bulk of these materials generate internal bubbles, which grow and migrate until they burst at the surface. Burning fuel vapor and occasionally molten fuel are forceably ejected, potentially spreading the fire in random directions. In experiments in normal gravity, Kashiwagi and Ohlemiller [2] observed vapor jets extending a few centimeters from the surface of a radiatively heated polymethylmethacrylate (PMMA) sample, with some molten material ejected into the gas phase. In combustion experiments on Velcro fasteners made of nylon [3], the ignition of flammable gases from a bursting bubble resulted in flamelets spurting from the flame zone. Occasionally, burning liquid droplets were expelled from the sample with velocities higher than 30 cm/sec. These droplets burned robustly until all fuel was consumed, demonstrating the potential for the spread of fire in random directions over an extended distance. The Wire Insulation Flammability Experiment (WIF) [4] studied the burning properties of polyethylene insulation covering a nichrome wire in both quiescent and flowing air. Bursting fuel vapor bubbles were observed, causing pulsations of the flame and ejection of small particles of molten polyethylene. The combustion behavior of PMMA spheres in microgravity, including the bursting bubble phenomenon, is currently being studied by Yang and Hamins [5] in a set of experiments being flown on the NASA Lewis DC-9 Reduced-Gravity Aircraft.

Besides investigating an important mechanism for fire spread in microgravity, the numerical model under development will contribute to the understanding of the role of in-depth generation of bubbles in the transport of heat and volatile gases. This is a problem of considerable interest for a variety of ground-based applications. In their study of degrading PMMA, Kashiwagi and Ohlemiller [2] observed that in addition to enhancing the transport of volatiles to the surface, bursting bubbles also leave holes that increase the depth of the surface layer affected by oxygen. A steady-state regression rate for PMMA that takes bubble nucleation, growth and convection into account was computed by Wichman [6]. The development of bubbles in a melting solid is also of importance in the field of softening coal pyrolysis. When coals that

---

exhibit plastic behavior are heated, they swell to a much larger volume until a critical final swelling temperature is reached. During the swelling, the coal behaves like a highly viscous liquid, and bubbles from gas-producing chemical reactions are generated. A mathematical model of softening coal pyrolysis to predict volatile yields, plasticity, and swelling was developed and compared with experimental results by Oh [7]. This model treats the coal particles as spherical and isothermal, with a spatially uniform bubble concentration. Bubbles grow due to chemical reactions, gas diffusion, and coalescence until they contact the particle surface, at which time they are assumed to rupture.

Intumescent fire-resistant materials protect an underlying surface through the development of a thick foam char in the presence of a high heat flux. In these materials, an endothermal gasification reaction generates bubbles in the molten thermoplastic, and the gas trapped in the final swollen char provides an insulating barrier to the transport of heat. By improving our understanding of the effects of bubble growth and migration on heat transfer, and of the conditions under which a bubble near the surface will burst, the three-dimensional model will also provide insight into intumescent behavior [10], [11].

Microgravity simplifies the combustion behavior to be modelled. Bubbles are not subject to buoyancy forces, and therefore migrate under the influence of temperature gradients only. A simple spherical geometry may be considered, and the combustion process can be modelled and compared to microgravity experiments without worrying about gross distortions of the melting sample due to gravity. Experience with this model may suggest new directions for solid combustion experiments in microgravity.

Research Approach – Burning Thermoplastics Model

A time-dependent, three-dimensional numerical model of polymeric materials that melt and bubble upon exposure to heat is under development. Both rectangular and spherical geometries are available. The behavior of burning thermoplastic materials is studied by observing the combined effects of a large number of randomly distributed bubbles as they nucleate, grow, and distort the surrounding velocity and temperature fields. Hydrodynamic, thermal, and chemical mechanisms are included, and an adjustable buoyancy term allows investigation of gravity effects from 0G to 1G. The model will eventually include condensed phase chemistry specific to PMMA, the mass transport of fuel vapor and fuel by bursting bubbles, and gas phase coupling. PMMA is a relatively simple fuel that has been well studied, and physical parameters necessary for model input are readily available from the literature.

Initially, the thermoplastic material is represented by a volume of highly viscous material with randomly distributed bubble nucleation sites. Under microgravity conditions, the initial volume is spherical for comparison with microgravity experiments on combusting PMMA spheres. The volume is represented by a grid of points in (r, θ, ϕ) space. Appropriate boundary conditions are applied to the outer surface, and the energy equation is solved to determine the temperature field throughout the volume. When the local temperature at a bubble nucleation site exceeds the degradation temperature of the polymer, bubble growth is initiated. The bubble growth rate is currently determined by a simple diffusion-controlled growth relation [8]. Another approach that includes the time-dependent production of gaseous degradation products by chemical reactions is being developed. This approach is based on cell models of bubble growth that have been developed for studying foam fabrication [9], and which incorporate several important factors, including variations in gas concentration, finite thickness walls, and properties of the melt such as viscosity, surface tension, and viscoelastic properties.

A temperature gradient in the surrounding fluid induces migration of a bubble toward the region of higher temperature. Two mechanisms are potentially responsible. Thermocapillary motion is driven by surface tension gradients along the surface of the bubble, which create a tangential stress that causes fluid motion both inside and outside the bubble. The bubble is thus propelled toward warmer regions where the surface tension is lower. This force requires a fluid free from surface-active contaminants. In the presence of contamination, which is likely in the chemically active PMMA melt, internal circulation in the bubble is eliminated and thermocapillary motion is prevented. The second mechanism derives from viscosity gradients, which will drive a growing bubble toward increasing temperature if the bubble growth rate $\dot{R}$ is much larger than the resulting translation speed U [11]. With buoyancy included, and assuming the presence of contamination, the expanding bubble migrates with terminal velocity

$$\mathbf{U} = \frac{2}{3} R \dot{R} \left(-\frac{d \ln \mu}{dT} \right) \nabla T - \frac{2}{9} \frac{\Delta \rho R^2}{\mu} \mathbf{g} \quad . \tag{1}$$

In this equation, R is the bubble radius, μ viscosity, ∇T the temperature gradient, $\Delta \rho$ the difference between melt and bubble density, and g the gravity vector. The buoyancy force is set to zero for microgravity.

The expansion and migration of each individual bubble causes movement in the surrounding fluid that is transmitted to the other bubbles in the melt. Even for a small PMMA sphere whose diameter is on the order of a centimeter, the bubbles generated in-depth during combustion number in the tens to hundreds. This makes it impossible for today's computers to solve the equations of continuity, momentum, and energy while meeting the boundary conditions on the surface of each bubble. The approach taken in this model is to first solve the problem at hand in the local region around a single bubble. If the bubbles are far apart compared with their size, the flow around one bubble induced by all other bubbles can be obtained to lowest order as the sum of the individual flow fields [10] The path of an individual bubble through the surrounding melt is therefore determined by its own expansion rate, the local temperature gradient, and the sum of the velocity fields from all of the other bubbles. A description of bubble motion that is more accurate for bubbles in close proximity will be pursued.

The flexible outer surface of the thermoplastic material feels the forces from all bubbles within the volume and swells accordingly. The points of the grid representing locations within the melt also translate according to the sum of bubble velocity fields. Bubble size and location and the locations of surface and grid points are incremented in time using a Runge-Kutta scheme.

Through migration and growth, the bubbles will eventually reach the outer surface of the volume. The model currently treats this in a simple way by allowing two options. The first option assumes that the bubble is trapped by the sample material. The position of the outer surface is set to the surface of the bubble that would otherwise escape, and the bubble is contained. The second option considers the bubble to have "burst" upon breaking the outer surface. The bubble is then eliminated from further calculations. Merging of bubbles within the volume is treated in a similar way. Overlapping bubbles may either be left alone or merged, in which case one of the bubbles is eliminated and the other assigned a radius consistent with the combined volumes of both bubbles and located at their center of mass.

The model treatment of nucleation and growth of bubbles within a spherical thermoplastic sample is illustrated in Figure 1. To demonstrate the sequence of events, two hundred bubble nucleation sites are randomly located on a plane through the center of the sphere. A steady heat flux is applied to the upper surface. As the temperature within the sphere increases with time, bubbles at increasing depths begin to grow. The bubbles move toward the hot surface where the viscosity is lower (no buoyancy has been included in this calculation), and tend to separate due to the expansion of other bubbles. The outer surface swells to contain the bubbles, and merging of bubbles has been prevented. In this set of illustrations the effect of the bubbles on heat transfer has not been taken into account. Since the ratio of the thermal conductivity of the gas contained within a bubble to the melt is about 0.1, this effect will be significant.

The solution of the energy equation for this problem poses some difficulties. As the in-depth bubbles grow, the outer surface is distorted, and the outer boundary condition no longer applies along a geometrically simple interface. The bubbles vary considerably in size and grow with time, complicating the solution in their vicinity. These difficulties are addressed by dividing the problem to be solved into two: an equation of the entire melt that satisfies the outer boundary conditions, and a separate set of problems that satisfy the local boundary conditions at each bubble. The variations in heat flux contributed by the bubble fields at the surface of the melt are subtracted from the boundary conditions of the melt problem to maintain the accuracy of the total temperature field. The summation of the melt solution with the individual bubble solutions then gives a reasonable approximation to the total temperature field, at least under the condition that the bubbles are far apart relative to their size.

A Lagrangian approach to the melt problem, which modifies the energy equation to maintain the initial simple geometry for calculations, has run into computational problems due to singularities in velocity near the growing bubbles. If the timescale for thermal diffusion is much shorter than the timescales for bubble expansion and translation, then the solution to the transient energy equation in the local neighborhood around a single bubble is well approximated by the sum of a dipole singularity plus a source:

$$T = \mathbf{r} \cdot \nabla T \left[1 - \frac{R^3}{r^3} \frac{(\alpha - 1)}{(\alpha + 2)} \right] + \frac{R^2}{kr} \dot{q}'' \quad . \tag{2}$$

In this equation, T is the melt temperature, k is the thermal conductivity of the melt, α is the ratio of the thermal conductivity of the bubble to that of the melt, and $\dot{q}''$ is a heat source that represents the heat evolved in the chemical gasification reactions. The strengths of the source and dipole singularities vary with time and the local temperature gradient. The difficulty here is in the determination of the value of the temperature gradient at the bubble site, due to the effect of its neighbors. The best approach for the determination of the temperature field is under review.

In the current model, a constant heat flux is applied to the outer surface of the thermoplastic sample, and the heat transfer is through conduction only. Although the condensed phase phenomena are of primary interest in this research project, the behavior of the gas phase must also be included to properly simulate a burning solid. Initially, a simple description consisting of the Shvab-Zel'dovich formulation [12], which assumes that heat and mass diffuse at equal rates in the gas phase, and the flame-sheet approximation will be added to the model. Finite-rate kinetics [13] and radiation heat transfer from the flame [14] will be considered for refinement of the coupling between gas phase and condensed phase.

Research Approach – Bubble Bursting Model

Of particular interest in this modeling effort is the behavior of bubbles generated within the combusting thermoplastic material as they reach the surface. The rate of bursting and the force with which burning fuel and volatile gases are expelled from the bursting bubble will determine the fire spread hazard in microgravity, as well as having a large impact on heat and mass transport.

In their experiments on burning PMMA samples, Kashiwagi and Ohlemiller [2] observed that the bubble frequency increased and bursting was less violent with increasing levels of oxygen. They hypothesized that this behavior was due to substantially lower viscosity in the near-surface region. Experiments currently being flown on the NASA Lewis DC-9 Reduced Gravity Aircraft by Yang [5] are investigating the combustion behavior of PMMA spheres in microgravity. Spheres of diameters 2, 2.5, and 3 millimeters are attached to thin wires for support and ignited by heater wires under various conditions of pressure and oxygen level. Preliminary observations show that although in-depth bubbling begins immediately upon ignition, the flame front around the PMMA spheres is roughly spherical and relatively undisturbed for the first few seconds of burning. This calm period is followed by the sudden onset of rapid spurting of flamelets in random directions, which continues until the fuel is used up. Figure 2 contains representative images from both the early and late stages of burning from this set of experiments.

To understand what drives the bursting process, a separate numerical model will be developed to investigate in detail the behavior of a single bubble as it reaches the surface of a melted thermoplastic object. This is a multiphase fluid flow problem involving complex time-dependent three-dimensional boundaries. Two potential modeling techniques have been identified for this task: the lattice Boltzmann method [15] and an interface-capturing two-phase fluid model recently developed by Nadiga and Zaleski [16] that uses finite differences. The lattice Boltzmann method is well suited to following the development of complex interfaces in multiphase fluids in three dimensions. For example, Martys and Chen [17] have successfully modeled the displacement in a porous medium of one fluid by a second fluid that is immiscible with the first. The finite difference model is also designed to model complex fluid interfaces, and additionally incorporates correct thermodynamic relationships in the model formulation. In either case, development work will be necessary to include the thermodynamic quantities for the bubble bursting problem.

Variables thought to be influential on the bursting behavior include bubble size and internal pressure, bubble growth rate and velocity, and the viscosity, surface tension, and viscoelastic properties of the melt at the surface. These factors will be incorporated into the bubble bursting model as the modeling technique allows.

The results from the bubble bursting model will be used in the burning thermoplastics model to determine whether a bubble is retained or released when it reaches the surface, based on the material properties of the surface and the characteristics of the bubble. If the bubble bursts, the vapor contained within will be released, decreasing the size of the melted thermoplastic sample.

Research Plans

In this three-dimensional, time-dependent model, the behavior of bubbling thermoplastics is studied from first principles. The basic geometry and framework for the model has been completed. The next steps in development include satisfactory treatment of heat transfer and the incorporation of a submodel of bubble growth that takes into account chemistry, diffusion, finite thickness walls, and properties of the melt. Values representing PMMA will be assigned to the input parameters, and the chemistry of decomposition of PMMA into its gaseous monomer will be incorporated into the equations for heat transfer and bubble growth rate. Calculations of gas phase mechanisms will then be added in sufficient detail to adequately represent the coupling between the flame and the surface of the burning thermoplastic sample.

A separate model of the bubble bursting process will be developed to determine the conditions under which burning fuel vapor and droplets are expelled from the surface. Results from this model will be incorporated into the burning thermoplastics model.

Once the model has been adequately developed, its predictions will be compared to experiments. The comparisons will be used to improve and validate the model. Finally, a parametric study will investigate the effects of combustion conditions and material properties on the burning behavior of thermoplastic materials.

References

[1] Kimzey, J.H., et al., "Flammability in Zero-Gravity Environment," NASA TR R-246, 1966.

[2] Kashiwagi, T. and Ohlemiller, T.J., "A Study of Oxygen Effects on Nonflaming Transient Gasification of PMMA and PE During Thermal Irradiation," 19th Symposium (International) on Combustion, The Combustion Institute, 1982.

[3] Olson, S.L. and Sotos, R.G., "Combustion of Velcro in Low Gravity," NASA TM 88970, 1987.

[4] Greenberg, P.S., Sacksteder, K.R., and Kashiwagi, T., "The USML-1 Wire Insulation Flammability Glovebox Experiment," *Third International Microgravity Combustion Workshop*, NASA Lewis Research Center, Cleveland, Ohio, April 11-13, 1995, pp. 25-30.

[5] Yang, J.C. and Hamins, A., "Combustion of a Polymer (PMMA) Sphere in Microgravity," *Third International Microgravity Combustion Workshop*, NASA Lewis Research Center, Cleveland, Ohio, April 11-13, 1995, pp. 115-120.

[6] Wichman, I.S., "A Model Describing the Steady-State Gasification of Bubble-Forming Thermoplastics in Response to an Incident Heat Flux," *Comb. and Flame* 63:217–229 (1986).

[7] Oh, M.S., Peters, W.A., and Howard, J.B., "An Experimental and Modeling Study of Softening Coal Pyrolysis," *AIChE J.* 35:775–792 (1989).

[8] Epstein, P.S. and M.S. Plesset, "On the Stability of Gas Bubbles in Liquid-Gas Solutions," *J. Chem. Phys.* 18:1505–1509 (1950).

[9] Amon, M. and Denson, C.D., "A Study of the Dynamics of Foam Growth: Analysis of the Growth of Closely Spaced Spherical Bubbles," *Polym. Eng. and Sci.* 24:1026–1034 (1984).

[10] Butler, K.M., Baum, H.R., and Kashiwagi, T., "A Three-Dimensional Kinetic Model for the Swelling of Intumescent Materials," NISTIR 5499, NIST Annual Conference on Fire Research: Book of Abstracts, October 17–20, 1994, pp. 109-110.

[11] Butler, K.M., "Physical Modeling of Intumescent Fire Retardant Polymers," Chapter 15, in *Polymeric Foams: Science and Technology*, ACS Symposium Series # 669, ACS Books, in press, to be released in May 1997.

[12] Williams, F.A., *Combustion Theory*, The Benjamin/Cummings Publishing Company, Inc., Menlo Park (1985).

[13] Law, C.K., "Recent Advances in Droplet Vaporization and Combustion," *Prog. Energy Combust. Sci* 8:171-201 (1982).

[14] Chang, K.-C. and Shieh, J.-S., "Theoretical Investigation of Transient Droplet Combustion by Considering Flame Radiation," *Int. J. Heat Mass Transfer* 38:2611–2621 (1995).

[15] Chen, S., Wang, Z., Shan, X., and Doolen, G.D., "Lattice Boltzmann Computational Fluid Dynamics in Three Dimensions," *J. Stat. Phys.* 68:379–400 (1992).

[16] Nadiga, B.T. and Zaleski, S., "Investigations of a Two-Phase Fluid Model," *Eur. J. Mech., B/Fluids* 15:885–896 (1996).

[17] Martys, N.S. and Chen, H., "Simulation of Multicomponent Fluids in Complex Three-Dimensional Geometries by the Lattice Boltzmann Method," *Phys. Rev. E* 53:743–750 (1996).

FIGURE 2: Images from combustion of a PMMA sphere in microgravity. The top image shows a sphere in the first few seconds after ignition, with a relatively undisturbed spherical flame front. Later in the burning process (after about ten seconds), sputtering occurs, with multiple flamelets shooting in random directions. One of these flamelets is captured in the bottom image.

FIGURE 1: Development of bubbles in the interior of a sphere with time as a steady heat flux is applied to the outer surface. Darker regions indicate lower temperatures.

Combustion of PTFE: The Effects of Gravity and Pigmentation on Ultrafine Particle Generation

J. THOMAS MCKINNON and Rajiv Srivastava
Department of Chemical Engineering
Colorado School of Mines, Golden, CO 80401

and

Paul Todd
Department of Chemical Engineering
University of Colorado, Boulder, CO 80309

Abstract

Ultrafine particles generated during polymer thermodegradation are a major health hazard, owing to their unique pathway of processing in the lung. This hazard in manned spacecraft is poorly understood, because the particulate products of polymer thermodegradation are generated under low gravity conditions. Particulate generated from the degradation of polytetrafluoroethylene (PTFE), insulation coating for 20 AWG copper wire (representative of spacecraft application) under intense ohmic heating were studied in terrestrial gravity and microgravity. Microgravity tests were done in a 1.2-second drop tower at the Colorado School of Mines (CSM). Thermophoretic sampling was used for particulate collection. Transmission electron microscopy (TEM) and scanning transmission electron microscopy (STEM) were used to examine the smoke particulates. Image software was used to calculate particle size distribution. In addition to gravity, the color of PTFE insulation has an overwhelming effect on size, shape and morphology of the particulate. Nanometer-sized primary particles were found in all cases, and aggregation and size distribution was dependent on both color and gravity; higher aggregation occurred in low gravity. Particulates from white, black, red and yellow colored PTFE insulations were studied. Elemental analysis of the particulates shows the presence of inorganic pigments.

Introduction

Polymer thermodegradation fumes are a known industrial hazard and a component of smoke during aircraft fires. Fires aboard spacecraft have been reported in the past. Four fires have been reported on orbit during the U.S. Shuttle program, all of which were due to overheated wires or electrical components (ref. 1). In all four of these cases, the fires were stopped by removing power to the instruments without the use of a fire extinguisher. If a Halon extinguisher is used, it is NASA policy to immediately end the mission (ref. 2). As the International Space Station is developed and space missions become longer and more involved, it is inevitable that these types of incidents will become more numerous. Thus, the ability to predict the types and severity of health hazards associated with PTFE combustion becomes more valuable. Probabilistic Safety Assessment (PSA) methods, which have been suggested in the past to provide an effective program of fire protection aboard a manned spacecraft require prediction of fire scenarios, their probability and their consequences (ref. 3). A likely fire precursor is the overheating of wire causing combustion of the insulation (ref. 4). PTFE which is widely used on board spacecraft because of its excellent mechanical, electrical, and chemical-resistance properties is the model compound for this study. Despite the many advantageous properties of PTFE, it has been shown to produce a host of hazardous substances when thermally degraded.

One oxidation product of PTFE is carbonyl fluoride, COF_2. This is the fluorinated analog to phosgene ($COCl_2$), a material used in WWI as a chemical warfare agent. Carbonyl fluoride has a threshold limit value (TLV) of 2 PPM as compared to 0.1 PPM for phosgene. Many other gas-phase materials which are produced, such as perfluoroisobutylene (C_4F_8), are even more toxic than carbonyl fluoride. However, it is the generation of particulates which is of most concern. Experiments have been done to test the effects of products of PTFE combustion on rats (ref. 5). Three milligrams of PTFE were burned in a crucible and the animals were exposed to the emitted smoke. Unexpectedly, the toxicity level of PTFE was orders of magnitude greater than the researchers had anticipated. Although carbonyl fluoride, perfluoroisobutylene, and HF were present in the smoke, their concentrations were not sufficiently high to account for the observed toxicity. The extremely toxic component of the PTFE smoke was not identified in their study, but the evidence points to submicron particles nucleated in the gas phase. More recent research has identified the role of ultrafine particles, irrespective of composition, in "fume fever" (ref. 6). The symptoms

of fume fever are highly elevated body temperatures, malaise, loss of appetite, and other influenza-like symptoms apparently related to an inflammatory response of the interstitial tissue of the lung, where abnormal masses of polymorpho nuclear leukocytes gather (ref. 7). The lung handles ultrafine particles very differently from the way it handles microparticles, and, rather than being disposed of via the macrophages, these particles find their way into interstitial spaces of the deep pulmonary tissues (ref. 8).

A number of chemical studies on the combustion of PTFE were reported in the 1960's when PTFE was becoming a popular consumer product, especially for high-temperature applications (refs. 9-12). These reports are a rich source of data on the production of gas-phase products, and from them a limited amount of kinetic information can be derived. Experiments were performed under a variety of ambient conditions, and most published results are focused on a number of specific volatile products. No studies in this category detail a mechanism of soot formation, and only recently have particulate products become of interest for their own sake (ref. 13). Due to the fact that the ultrafine particle problem has only recently come to light it is timely to re-visit PTFE thermodegradation with the production of ultrafine particles in mind. Furthermore, the possibility of studying the production of ultrafine particles in low gravity affords insight into the mechanism of their formation.

Very little work has been done to date on the effect of gravity on particle formation in sooting flames or other systems. One of the earliest low-gravity thermodegradation of polymers experiments, performed on Skylab, was a study of the overheating of an insulated wire (ref. 2). Chemical kinetic details of the pathway to ultrafine particle production in PTFE degradation in low gravity (and in unit gravity for that matter) are severely lacking. Only one preliminary study of the emission of particulate products ("soot") in low gravity exists (ref. 3). In this study, "Tefzel" (poly-ethyltetrafluorethylene) insulated wire was heated to an unspecified temperature by passing a 475 A current during the 2.2 s of free fall in the NASA Lewis Research Center drop tower. Smoke was emitted in two ways: through the trimmed ends of the insulation where the wire was attached to posts and through explosive jets caused by the vaporization of products closest to the wire. This jetting phenomenon, both in low-g and one-g, led to oval shaped particulates and stringy coagulates, owing to the momentum carried by the products as they were convected away from the wire by explosive expansion. Small numbers of particles (ca. 75) were measured by electron microscopy, and the frequency of larger particulates (>400nm) was higher in the low-gravity samples. In both cases, more than half of the particles were less than 250 nm in diameter, and the distributions were approximately log-normal on a per-particle basis.

In the context of this project, we are considering "combustion" to be the high temperature degradation of a material in an oxygen-containing environment regardless of its inherent rate of heat release or the sustainability of the process. Of specific interest to this work is the effect of gravity and pigmentation on the particle formation mechanisms. In a low-g environment the forces of buoyancy are removed. This totally changes the time-temperature-concentration history to which the nucleating and growing particles are exposed. The objective of this work is investigation of size, morphological analysis and composition of ultrafine particles from PTFE combustion and thermodegradation produced in a one-g and a low-g environment. The motivation for the project is to provide a basic foundation for policy on spacecraft health and safety with regard to fire safety and spacecraft polymers. We present our results of our terrestrial gravity and microgravity experiments on ultrafine particle formation from PTFE thermodegradation.

Materials and Methods

A drop tower facility was designed and developed at the CSM, and drop hardware designed such that easy integration into the NASA Lewis 2.2 s drop tower could take place at a later date. The practical working height is 45 feet with a catwalk access. The drop tower allows a free fall duration of about 1.2 s factoring in the 4.5 feet of foam padding on the ground used to catch the experiment. The free fall achieves a reduced gravity of the order of 10^{-2} g. The experiment assembly is hoisted to the ceiling by a 3:1 block and tackle. The frame is lifted by a thin single strand wire which is subsequently cut to initiate the free fall.

The drop frame was made to simulate the frame used by NASA LeRC as closely as possible (ref. 14) and was constructed of welded 6061-T6 aluminum. To pyrolyze the PTFE insulation, obtain images, and for smoke particle sampling and analysis, the same methodology was used for both the terrestrial gravity and microgravity experiments. Two 2-volt rechargeable lead acid batteries (Hawker 25 amp-hr) were used in the circuit. Current measurements have shown that these produce enough power to degrade the insulation, and are reliable and reproducible. A 7 cm long 20 AWG PTFE insulated wire was used as the test specimen. The conductor was stranded silver plated copper with an insulation thickness of 0.25 mm.

The PTFE insulated wire was bent in an inverted "U" shape to facilitate imaging using a sheet of laser light from an argon ion

laser. A Sony CCD-TR400 Hi8 HandyCam was used as the imager and recorder. The laser light sheet was aimed over the apex of the wire bend. The wire was housed in a clear 20 cm X 25 cm acrylic containment box. Copper ignition posts were attached to the wire and 10 AWG aluminum wire was used in the balance of the circuit.

A partial schematic of the drop apparatus is shown in Fig. 1. The PTFE insulated wire was melted via ohmic heating from the power supply. A 10 gauge aluminum wire connected the batteries to the test wire. The current to the test wire was initiated using a timing circuit which sensed the start of the drop. When the piano wire (temporary ground) holding the experiment assembly was cut, current flowed and the precision timing circuit was enabled. For imaging, an argon ion laser operating in the blue and green (460 nm to 532 nm) was used as the light source for the video camera. A standard telecommunications 100 micron core diameter fiber optic was dropped with the experiment while the laser remained at the top of the tower. The fiber coupler aimed the light into a 5X microscope objective, and that light passed through a cylindrical optic. The resulting sheet of blue light (A-A' in Fig. 1) was collimated vertically and horizontally and focused over the test wire inside the acrylic containment box. The images were transferred from the camcorder on to a VHS video tape and were later digitized. Particles were collected 800 ms into the free fall using the thermophoretic sampling technique (ref. 3). A TEM microgrid was placed on a probe held 2 cm above the tip of the "U" shaped PTFE wire and was connected to a solenoid and a timer for precise timing of the probe pull. The solenoid retracted the copper grid into a cylindrical enclosure, shielding it from further particle deposition. For the experiments, PTFE insulated copper wire (5856, 20 AWG, MIL-W-16878D) was used exclusively. Four colors of PTFE insulation viz. white, black, red and yellow were used for the study. All experiments were performed in ambient atmosphere.

The current history in the copper wire was measured using a Fluke 80i-kW current probe and is shown in Fig. 2A. A maximum current of 144 A was achieved about 1 second into the event. At 2.77 seconds, the wire reached its melting point of 1083 °C and fused. This relationship between current and time was assumed consistent between reduced gravity and the terrestrial gravity tests. The voltage drop across the test wire was also measured under terrestrial gravity and is shown in Fig. 2B. The voltage drop across the wire rose somewhat linearly with time. The voltage was measured across the terminal posts to which the wire was connected, and not the wire itself because of heat considerations. The power produced in the wire proved more than adequate to pyrolyze the PTFE insulation. Calculations based on the voltage and current measurements gave a power dissipation of 122 watts. The actual amount of heat conducted to the insulation was less than 122 watts due to losses.

Results and Discussion

The plume video image taken during the terrestrial gravity test is shown in Fig. 3A. The signal seen by the camera was due to scattering of the laser light. During pyrolysis, very little smoke was seen. This observation is consistent with the earlier studies in which it was concluded that only about 1% of the pyrolysis products were smoke (ref. 4). The images show that the plume was laminar. The microgravity plume image is shown in Fig. 3B. The circular plume is evidence that good microgravity conditions ($< 10^{-2}$ g) were achieved. There is a region around the wire, where there appears to be no light scattering. When pyrolysis first occurs, there is a zone of chemical reaction near the surface of the insulation. In this region of molecular interaction which results in molecular weight growth, scattering of light is below the detection limit of the camera. If the particles are extremely small so that their diameter is an order of magnitude less than the wavelength of the incident light, then Rayleigh scattering takes place, but a highly sensitive instrument would be needed to see the signal. Only when the diameter and number density of particles is favorable will the signal be recorded by the camera.

Transmission electron micrographs of the particles from PTFE degradation in both terrestrial gravity and microgravity are shown in Fig. 4 for the yellow, red, black and white colored PTFE insulation. There was a marked difference between the particles produced under microgravity and those produced under terrestrial gravity. The particles produced under microgravity are mostly clustered (black, red and yellow) as compared to the particles produced under terrestrial gravity which are separated and show no agglomeration. Particles from white colored PTFE insulation are not agglomerated or clustered under microgravity conditions. A working hypothesis is that the laminar shear force causes the particles to separate under terrestrial gravity whereas the absence of such a force under microgravity causes the particles to stay together. The particles under terrestrial gravity have no set shape, and they vary from spherical to flakes and even squares. The salient features of the particles are summarized in Table I. It is evident that pigmentation plays an important role in determining the structure and morphology of the particulates generated from the thermal degradation of the fluorinated polymer in microgravity. STEM analysis from the red colored insulation revealed trace quantities of cadmium in the particulates which is an important finding from the of health and safety viewpoint. Particulate clusters generated in microgravity are 5-1000 times bigger (depending on aggregation) than the ones generated in the terrestrial gravity, and hence they can be processed with greater efficiency by macrophages in the pulmonary alveoli and thus represent a decreased health risk. On the other hand, presence of inorganic

257

pigments such as Cd in the red pigmented insulation may increase the toxicity of these particles manifold. To our knowledge the toxicity of pigmented fluoropolymer fumes have not been studied.

Conclusions

From this study the following new conclusions can be drawn:
- Ultrafine particles are produced during PTFE thermodegradation both in terrestrial gravity and microgravity.
- Ultrafine particles produced in microgravity are more likely to be aggregated.
- Pigments play the dominant role in determining the morphology of the particulate products of colored-polymer thermodegradation.

The health and safety implications of the above findings are:
- Polymer fume effects should be a concern on spacecraft just as they are on aircraft and in terrestrial environments.
- Aggregates of ultrafine particles could be processed more like microparticles in the pulmonary alveoli; that is, it is possible that they would be processed by macrophages.
- Ultrafine particles in microgravity may carry inorganic components of polymer colorants to the lung, with the accompanying cytotoxic effects of each component. Considering the significance of additives revealed in this study, consideration might be given to formulating PTFE wire insulation so as to promote ultrafine particle aggregation and/or reduce the amount or toxicity of colored components.

Future studies will be directed at clarifying the role of colorants in ultrafine particle generation and in modeling the forces or conditions that enhance fine-particle aggregation. Furthermore, mechanisms of particle growth in general will be sought and applied to insulating polymers other than PTFE.

Acknowledgments

References

1. Ross, H. D., Second International Microgravity Workshop, September 15-17, 1992, NASA CP-10113.
2. Friedman, R. in *Environmental Health Issues in Space*, Ed. T. Clarkson, University of Rochester, NY, pp. 55-67, 1992.
3. Paul, M. R., et al., National Heat Transfer Conference, Atlanta, 9 August, 1993.
4. Paxton, K. R., et al., ASME Winter Annual Meeting, November, 1993.
5. Baker, B. B. and Kaiser, M. A., *Analytical Chemistry* 63, pp. 79A-83A, 1991.
6. Oberdoerster, G., et al., *Environmental Health Perspectives* 92, 193, 1992.
7. Oberdoerster, G., et al., *J. Aerosol Sci.* 21, 384-387, 1990.
8. Oberdoerster, G., et al., *Acta Aeronautica* 27, 251-256, 1992.
9. Kupel, R. D., et al., *Analytical Chemistry* 36, 386-389, 1964.
10. Scheel, L. D., et al., *Amer. Indus. Hyg. Assoc. J.* 29, 41-48, 1968.
11. Arito, H. and Soda, R., *Ann. Occup. Hyg.* 20, 247-255, 1977.
12. Madorsky, S. L. in *Thermal Degradation of Organic Polymers*, Eds. H. F. Mark and E. H. Immergut, John Wiley and Sons, 1964.
13. Dobbins, R. A. and Megaridis, C. M., *Langmuir* 3, 254-259, 1987.
14. Lekan, J., et al., NASA Technical Memorandum 107090, NASA Lewis Research Center, April 1996.

Table I. Salient features of particles from PTFE degradation in ambient air at ambient humidity.

Color of PTFE insulation	Environment	Form	Size Range	Features
Yellow	Terrestrial gravity	Single particles.	69 nm - 1500 nm.	No fixed shape, usually flaky.
Yellow	Microgravity	Agglomerated.	250 - 15500 nm.	Individual particles range from 250 nm
Red	Terrestrial gravity	Agglomeration, usually 4-10 particles.	Smallest size 100 nm, cluster lengths upto 1200 nm.	Particle shape close to spherical.
Red	Microgravity	Agglomeration, globules joined with filaments.	Globules as small as 70 nm. Cluster chains as long as 12000 nm.	Single particles also occur, as small as 140 nm.
Black	Terrestrial gravity	Single particles, no aggregation.	215 nm - 2500 nm	No fixed shape, usually flaky.
Black	Microgravity	Clustered and agglomerated.	Smallest size 190 nm, cluster lengths upto 4000 nm.	Spherical in shape, some show a nucleus in center.
White	Terrestrial gravity	Single particles, no agglomeration.	145 nm - 500 nm	Both flaky and spherical particles
White	Microgravity	Single particles, no agglomeration.	250 nm - 300 nm	Spherical particles with nucleus in center.
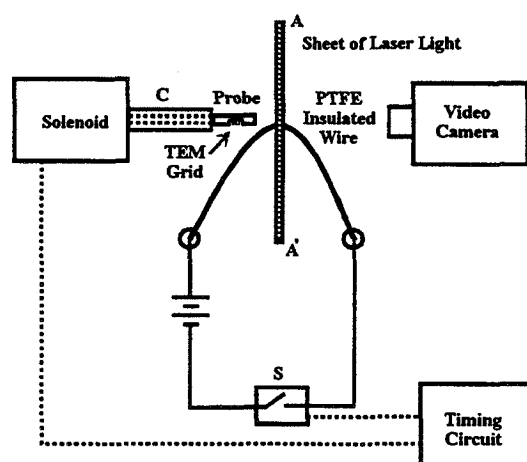
Figure 1. Experiment Setup. At onset of low-g, switch S closes. The timing circuit retracts Probe into Cylinder C via the Solenoid at the specified sampling time (typically 800 ms). Sheet of Laser Light AA' perpendicular to the plane of the page, illuminates the particulate plume which is recorded by the Video Camera.
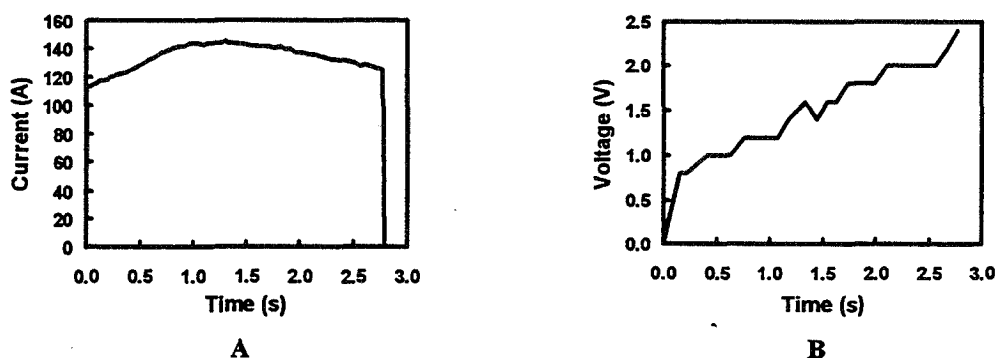
Figure 2. A. Current history of the PTFE insulated wire. B. Voltage drop across the PTFE insulated wire.
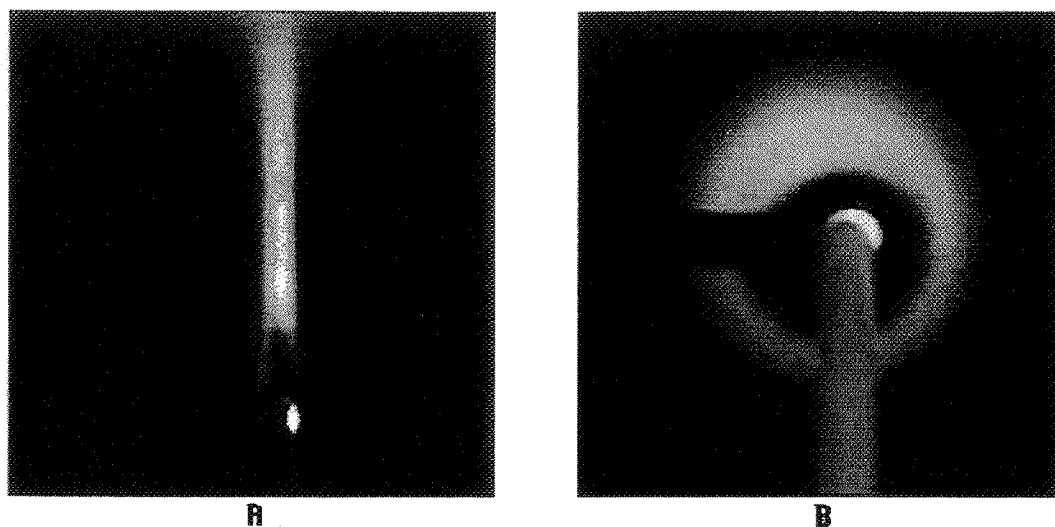
Figure 3. A. Laminar buoyant plume image under terrestrial gravity. B. Cylindrical plume image under microgravity.
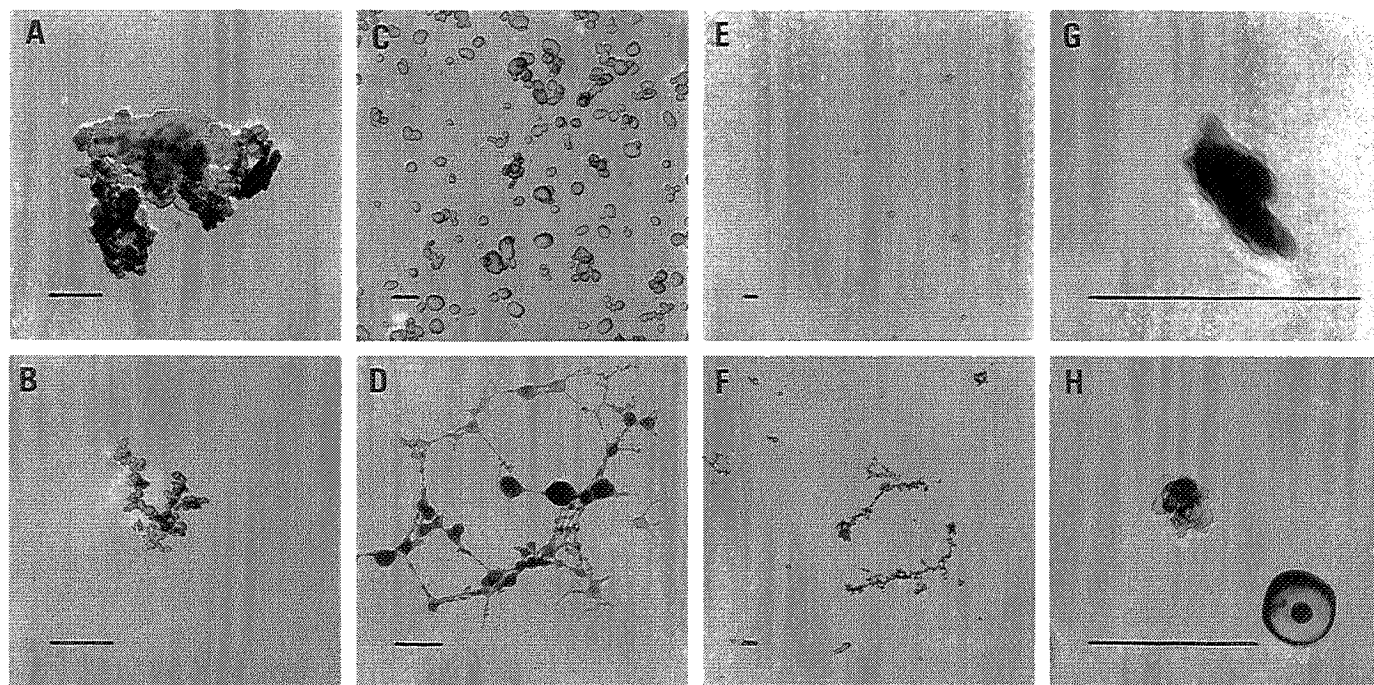
Figure 4. Particles from thermodegradation of PTFE: A. Yellow insulation, terrestrial gravity. B. Yellow insulation, microgravity. C. Red insulation, terrestrial gravity. D. Red insulation, microgravity. E. Black insulation, terrestrial gravity. F. Black insulation, microgravity. G. White insulation, terrestrial gravity. H. White insulation, microgravity. Each bar represents 500 nm.

260

ANALYSIS OF HYDRODYNAMIC (LANDAU) INSTABILITY IN LIQUID-PROPELLANT COMBUSTION AT NORMAL AND REDUCED GRAVITY

STEPHEN B. MARGOLIS
Combustion Research Facility, MS 9052
Sandia National Laboratories, Livermore, California 94551-0969

Introduction

The burning of liquid propellants is a fundamental combustion problem that is applicable to various types of propulsion and energetic systems. The deflagration process is often rather complex, with vaporization and pyrolysis occurring at the liquid/gas interface and distributed combustion occurring either in the gas phase[1] or in a spray.[2] Nonetheless, there are realistic limiting cases in which combustion may be approximated by an overall reaction at the liquid/gas interface. In one such limit, the gas flame occurs under near-breakaway conditions, exerting little thermal or hydrodynamic influence on the burning propellant. In another such limit, distributed combustion occurs in an intrusive regime, the reaction zone lying closer to the liquid/gas interface than the length scale of any disturbance of interest. Finally, the liquid propellant may simply undergo exothermic decomposition at the surface without any significant distributed combustion, such as appears to occur in some types of hydroxylammonium nitrate (HAN)-based liquid propellants at low pressures.[3] Such limiting models have recently been formulated,[4,5] thereby significantly generalizing earlier classical models[6,7] that were originally introduced to study the hydrodynamic stability of a reactive liquid/gas interface. In all of these investigations, gravity appears explicitly and plays a significant role, along with surface tension, viscosity, and, in the more recent models, certain reaction-rate parameters associated with the pressure and temperature sensitivities of the reaction itself. In particular, these parameters determine the stability of the deflagration with respect to not only classical hydrodynamic disturbances, but also with respect to reactive/diffusive influences as well. Indeed, the inverse Froude number, representing the ratio of buoyant to inertial forces, appears explicitly in all of these models, and consequently, in the dispersion relation that determines the neutral stability boundaries beyond which steady, planar burning is unstable to nonsteady, and/or nonplanar (cellular) modes of burning.[8,9]. These instabilities thus lead to a number of interesting phenomena, such as the sloshing type of waves that have been observed in mixtures of HAN and triethanolammonium nitrate (TEAN) with water.[3] Although the Froude number was treated as an O(1) quantity in these studies, the limit of small inverse Froude number corresponding to the microgravity regime is increasingly of interest and can be treated explicitly, leading to various limiting forms of the models, the neutral stability boundaries, and, ultimately, the evolution equations that govern the nonlinear dynamics of the propagating reaction front. In the present work, we formally exploit this limiting parameter regime to compare some of the features of hydrodynamic instability of liquid-propellant combustion at reduced gravity with the same phenomenon at normal gravity.

Mathematical Formulation

The starting point for the present work is our recent model[4,5] that generalizes classical models[6,7] of a reactive liquid/gas interface by replacing the simple assumption of a fixed normal propagation speed with a reaction/pyrolysis rate that is a function of the local pressure and temperature. This introduces important new sensitivity parameters that couple the local burning rate with the pressure and temperature fields. Thus, it is assumed, as in the classical models, that there is no distributed reaction in either the liquid or gas phases, but that there exists either a pyrolysis reaction or an exothermic decomposition at the liquid/gas interface that depends on local conditions there. In its most general form, the model includes full heat and momentum transport, allowing for viscous effects in both the liquid and gas phases, as well as effects due to gravity and surface tension. For additional simplicity, however, it is assumed that within the liquid and gas phases separately, the density, heat capacity, kinematic viscosity and thermal diffusivity are constants, with appropriate jumps in these quantities across the phase boundary.

The nondimensional location of this interface as a function of space and time is denoted by $x_3 = \Phi_s(x_1, x_2, t)$, where the adopted coordinate system is fixed with respect to the stationary liquid at $x_3 = -\infty$ (Figure 1). Then, in the moving coordinate system $x = x_1$, $y = x_2$, $z = x_3 - \Phi_s(x_1, x_2, t)$, in terms of which the liquid/gas interface always lies at $z = 0$, the complete formulation of the problem is given as follows. Conservation of mass, energy and momentum within each phase imply

$$\nabla \cdot \mathbf{v} = 0, \quad z \neq 0, \qquad \frac{\partial \Theta}{\partial t} - \frac{\partial \Phi_s}{\partial t}\frac{\partial \Theta}{\partial z} + \mathbf{v} \cdot \nabla\Theta = \begin{Bmatrix} 1 \\ \lambda \end{Bmatrix} \nabla^2\Theta, \quad z \lessgtr 0, \tag{1,2}$$

261

$$\frac{\partial \mathbf{v}}{\partial t} - \frac{\partial \Phi_s}{\partial t}\frac{\partial \mathbf{v}}{\partial z} + (\mathbf{v} \cdot \nabla)\mathbf{v} = (0, 0, -Fr^{-1}) - \begin{Bmatrix} 1 \\ \rho^{-1} \end{Bmatrix} \nabla p + \begin{Bmatrix} Pr_l \\ \lambda Pr_g \end{Bmatrix} \nabla^2 \mathbf{v}, \quad z \lessgtr 0, \tag{3}$$

where $\mathbf{v}$, Θ and p denote velocity, temperature and pressure, respectively, $Pr_{l,g}$ denote the liquid and gas-phase Prandtl numbers, ρ, λ and c (used below) are the gas-to-liquid density, thermal diffusivity and heat-capacity ratios, and Fr is the Froude number.

The above equations are subject to the boundary conditions $\mathbf{v} = 0$, $\Theta = 0$ at $z = -\infty$, $\Theta = 1$ at $z = +\infty$, $\Theta|_{z=0-} = \Theta|_{z=0+}$, and appropriate jump and continuity conditions at the liquid/gas interface. The latter consist of continuity of the transverse velocity components (no-slip) and conservation of (normal) mass flux,

$$\hat{\mathbf{n}}_s \times \mathbf{v}_- = \hat{\mathbf{n}}_s \times \mathbf{v}_+, \quad \hat{\mathbf{n}}_s \cdot (\mathbf{v}_- - \rho \mathbf{v}_+) = (1 - \rho)S(\Phi_s)\frac{\partial \Phi_s}{\partial t}, \tag{4,5}$$

the mass burning rate (pyrolysis) law,

$$\hat{\mathbf{n}}_s \cdot \mathbf{v}_- - S(\Phi_s)\frac{\partial \Phi_s}{\partial t} = A(\Theta|_{z=0}, p|_{z=0+}) \exp\left[\frac{N(1-\sigma_u)(\Theta|_{z=0}-1)}{\sigma_u + (1-\sigma_u)\Theta|_{z=0}}\right], \tag{6}$$

and conservation of the normal and transverse components of momentum and heat fluxes,

$$p|_{z=0-} - p|_{z=0+} = \hat{\mathbf{n}}_s \cdot [\rho \mathbf{v}_+(\hat{\mathbf{n}}_s \cdot \mathbf{v}_+) - \mathbf{v}_-(\hat{\mathbf{n}}_s \cdot \mathbf{v}_-) - \rho\lambda Pr_g \mathbf{e}_+ \cdot \hat{\mathbf{n}}_s + Pr_l \mathbf{e}_- \cdot \hat{\mathbf{n}}_s] + \hat{\mathbf{n}}_s \cdot (\mathbf{v}_- - \rho\mathbf{v}_+)S(\Phi_s)\frac{\partial \Phi_s}{\partial t}$$
$$- \gamma S^3(\Phi_s)\left\{\frac{\partial^2 \Phi_s}{\partial x^2}\left[1 + \left(\frac{\partial \Phi_s}{\partial y}\right)^2\right] + \frac{\partial^2 \Phi_s}{\partial y^2}\left[1 + \left(\frac{\partial \Phi_s}{\partial x}\right)^2\right] - 2\frac{\partial \Phi_s}{\partial x}\frac{\partial \Phi_s}{\partial y}\frac{\partial^2 \Phi_s}{\partial x \partial y}\right\}, \tag{7}$$

$$\hat{\mathbf{n}}_s \times \left[\rho \mathbf{v}_+(\hat{\mathbf{n}}_s \cdot \mathbf{v}_+) - \mathbf{v}_-(\hat{\mathbf{n}}_s \cdot \mathbf{v}_-) + (\mathbf{v}_- - \rho\mathbf{v}_+)S(\Phi_s)\frac{\partial \Phi_s}{\partial t}\right] = \hat{\mathbf{n}}_s \times (\rho\lambda Pr_g \mathbf{e}_+ \cdot \hat{\mathbf{n}}_s - Pr_l \mathbf{e}_- \cdot \hat{\mathbf{n}}_s), \tag{8}$$

$$\hat{\mathbf{n}}_s \cdot (c\rho\lambda\nabla\Theta|_{z=0+} - \nabla\Theta|_{z=0-}) = \hat{\mathbf{n}}_s \cdot [(c\rho\mathbf{v}_+ - \mathbf{v}_-)\Theta|_{z=0} + \hat{c}(\sigma_u\rho\mathbf{v}_+ - \mathbf{v}_-)] + [(1-c\rho)\Theta|_{z=0} + \hat{c}(1-\sigma_u\rho)]S(\Phi_s)\frac{\partial \Phi_s}{\partial t}, \tag{9}$$

where $\hat{c} = c/(1-\sigma_u)$, $\mathbf{e}$ is the rate-of-strain tensor, γ is the surface tension, σ_u is the unburned-to-burned temperature ratio, N is the nondimensional activation energy, A is the temperature- and pressure-dependent reaction-rate coefficient, $S(\Phi_s) \equiv [1 + (\partial\Phi_s/\partial x)^2 + (\partial\Phi_s/\partial y)^2]^{-1/2}$, and the unit normal $\hat{\mathbf{n}}_s = (-\partial\Phi_s/\partial x, -\partial\Phi_s/\partial y, 1)S(\Phi_s)$. Here, the gradient operator ∇ and the Laplacian ∇^2 are given in the moving coordinate system by

$$\nabla = \left(\frac{\partial}{\partial x} - \frac{\partial\Phi_s}{\partial x}\frac{\partial}{\partial z}, \frac{\partial}{\partial y} - \frac{\partial\Phi_s}{\partial y}\frac{\partial}{\partial z}, \frac{\partial}{\partial z}\right),$$

$$\nabla^2 = \frac{\partial^2}{\partial x^2} + \frac{\partial^2}{\partial y^2} + \frac{1}{S^2}\frac{\partial^2}{\partial z^2} - 2\frac{\partial\Phi_s}{\partial x}\frac{\partial^2}{\partial x \partial z} - 2\frac{\partial\Phi_s}{\partial y}\frac{\partial^2}{\partial y \partial z} - \left(\frac{\partial^2\Phi_s}{\partial x^2} + \frac{\partial^2\Phi_s}{\partial y^2}\right)\frac{\partial}{\partial z}.$$

However, the vector $\mathbf{v}$ still denotes the velocity with respect to the (x_1, x_2, x_3) coordinate system.

The Basic Solution and Classical Stability Results

A nontrivial basic solution to the above problem, corresponding to the special case of a steady, planar deflagration, is given by $\Phi_s^0 = -t$ and

$$\mathbf{v}^0 = (0, 0, v^0), \quad v^0 = \begin{cases} 0, & z < 0 \\ \rho^{-1} - 1, & z > 0, \end{cases} \quad \Theta^0(z) = \begin{cases} e^z, & z < 0 \\ 1 & z > 0, \end{cases} \quad p^0(z) = \begin{cases} -Fr^{-1}z + \rho^{-1} - 1, & z < 0 \\ -\rho Fr^{-1}z, & z > 0. \end{cases} \tag{10}$$

The linear stability analysis of this solution now proceeds in a standard fashion. However, owing to the significant number of parameters, a complete analysis of the resulting dispersion relation is quite complex. Realistic limits that may be exploited to facilitate the analysis include $\rho \ll 1$, $Pr_g/Pr_l \ll 1$, and in the microgravity regime, $Fr^{-1} \ll 1$.

In the study due to Landau,[6] the effects of gravity (assumed to act normal to the undisturbed planar interface in the direction of the unburned liquid) and surface tension were shown to be stabilizing, leading to a criterion for the absolute stability for steady, planar deflagration of the form (in our nondimensional notation) $4\gamma Fr^{-1}\rho^2/(1-\rho) > 1$. In the study due to Levich,[7] surface tension was neglected, but the effects due to the viscosity of the liquid were included, leading to the absolute stability criterion $Fr^{-1}Pr_l(3\rho)^{3/2} > 1$. Thus, these two studies, under the assumption of a constant

normal burning rate, demonstrated that sufficiently large values of either viscosity or surface tension, when coupled with the effects due to gravity, may render steady, planar deflagration stable to hydrodynamic disturbances. In the present work, we shall focus, using our extended model described above, primarily on hydrodynamic (Landau) instability. Thus, in the linear stability analysis, we retain only the pressure sensitivity $A_p \equiv \partial A/\partial p|_{\Theta=1,p=0}$ in the pyrolysis law (4), neglecting the temperature sensitivity $\Xi = N(1-\sigma_u) + A_\Theta$, where $A_\Theta \equiv \partial A/\partial \Theta|_{\Theta=1,p=0}$. The latter assumption thus filters out reactive/diffusive instabilities associated with the thermal coupling of the temperature field,[4,5] but facilitates the analysis of instability due to hydrodynamic effects alone. We note that the mass burning rate of many propellants has been shown empirically to correlate well with pressure.

Formal Analysis of the Zero-Viscosity Limit

In the limit of zero viscosities ($Pr_l = Pr_g = 0$), our extended model differs from the classical one due to Landau[6] only in the local pressure sensitivity of the normal burning rate. In that limit, the neutral stability boundaries with respect to infinitesimal hydrodynamic disturbances proportional to $e^{i\omega t \pm i k \cdot x}$, where k and x are the transverse wavenumber and coordinate vectors, respectively, are exhibited in Figure 2. Steady, planar burning is always unstable for positive values of A_p, but in the region $A_p \leq 0$, there exist both cellular ($\omega = 0$) and pulsating ($\omega \neq 0$) stability boundaries $A_p(k; \rho, \gamma, Fr^{-1})$ given by[5]

$$A_p = \rho \frac{\rho(1-\rho)Fr^{-1} + \rho\gamma k^2 - (1-\rho)k}{\rho^2(3-\rho)Fr^{-1} + \rho^2\gamma k^2 + (1-\rho)(2-\rho)k} \leq 0 \qquad (11)$$

and $A_p = -\rho/(1-\rho)$, respectively, where $k = |k|$. Steady, planar combustion is thus stable in the region $A_p < 0$ that lies between these two curves. The pulsating stability boundary is a straight line in the (A_p, k) plane, whereas the cellular stability boundary is a curve which lies at or above the straight line $A_p = -\rho/(2-\rho)$. The shape of the latter boundary depends on whether or not the parameters Fr^{-1} and/or γ are zero. In the limit that γFr^{-1} approaches the value $(1-\rho)/4\rho^2$ from below, the cellular stability boundary recedes from the region $A_p < 0$. For $\gamma Fr^{-1} > (1-\rho)/4\rho^2$, the stable region is the strip $-\rho/(1-\rho) < A_p < 0$. Thus, when $A_p = 0$, the classical Landau result for cellular instability is recovered. However, even a small positive value of A_p renders steady, planar burning intrinsically unstable for all disturbance wavenumbers, regardless of the stabilizing effects of gravity and surface tension. This result may be anticipated from quasi-steady physical considerations. That is, a burning velocity that increases with increasing pressure is a hydrodynamically unstable situation, since an increase in the burning velocity results in an increase in the pressure jump across the liquid/gas interface, and vice-versa. However, a sufficiently large negative value of A_p results in a pulsating hydrodynamic instability, the existence of which was a new prediction for liquid-propellant combustion. Zero and negative values of A_p over certain pressure ranges are characteristic of the so-called "plateau" and "mesa" types of solid propellants,[10] as well as for the HAN-based liquid propellants mentioned above.[3]

Of particular interest in the present work is the hydrodynamic stability of liquid-propellant combustion in the limit of small gravitational effects (i.e., microgravity). In this limit, the shape of the upper hydrodynamic stability boundary in Figure 2, corresponding to the classical Landau instability, clearly approximates the $Fr^{-1} = 0$ curve except for small wavenumbers, where, unless the inverse Froude number is identically zero, the neutral stability boundary must turn and intersect the horizontal axis. Consequently, the neutral stability boundary has a minimum for some small value of the transverse wavenumber k of the disturbance, implying loss of stability of the basic solution to long wavelength perturbations as the pressure sensitivity A_p defined above decreases in magnitude. This, in turn, suggests a small wavenumber nonlinear stability analysis in the unstable regime, which generally leads to simplified nonlinear evolution equations of the Kuramoto-Sivashinsky type for the finite amplitude perturbations.[13,14]

To establish the nature of hydrodynamic instability in the microgravity regime in a formal sense, we may realistically consider the parameter regime $\rho \ll 1$, $Fr^{-1} \ll 1$, with $Fr^{-1} \sim \rho$. For example, typical values are $\rho \sim 10^{-3} - 10^{-4}$, liquid thermal diffusivity $\tilde{\lambda}_l \sim 0.1$ m^2/sec, and the steady, planar burning rate $\tilde{U} \sim 1 - 10$ cm/sec depending on pressure.[3] Hence, from the definition $Fr^{-1} \equiv \tilde{g}\tilde{\lambda}_l/\tilde{U}^3$, we conclude that $Fr^{-1} \sim \rho$ implies that the dimensional gravitational acceleration $\tilde{g} \lesssim 10^{-5}$ m/sec^2, which marks the onset of the microgravity regime. Thus, introducing the bookkeeping parameter $\epsilon \ll 1$, we define scaled parameters g^*, ρ^* and A_p^* according to $\rho = \rho^*\epsilon$, $Fr^{-1} = g^*\epsilon$ and $A_p = A_p^*\epsilon$. In that regime, it is readily seen from Eq. (11) that there are three distinct wavenumber scales: an inner scale $k_i = k/\epsilon^2$, the outer scale k, and a far outer scale $k_f = k\epsilon$. In the thin inner and thick far outer regions, we thus obtain

$$A_p^* \sim A_p^{*(i)} \sim \frac{\rho^*(\rho^* g^* - k_i)}{2k_i} \quad \text{and} \quad A_p^* \sim A_p^{*(f)} \sim \frac{1}{2}\rho^*(\rho^*\gamma k_f - 1), \qquad (12)$$

respectively. Each of these expansions may be matched to the O(1) outer expansion $A_p^* \sim A_p^{*(o)} \sim -\rho^*/2$, and thus a

composite expansion $A_p^{*(c)}(k)$ may be constructed as

$$A_p^{*(c)} \sim A_p^{*(i)} + A_p^{*(o)} + A_p^{*(f)} - \lim_{k_i \to \infty} A_p^{*(i)} - \lim_{k_f \to 0} A_p^{*(f)} \sim -\frac{1}{2}\rho^* + \frac{1}{2}\epsilon\rho^{*2}\gamma k + \epsilon^2 \frac{\rho^{*2}g^*}{2k}, \tag{13}$$

where the definitions of k_i and k_f have been used to express the final result in terms of k (Figure 3). Thus, the hydrodynamic stability boundary in the microgravity regime considered here lies in the region $A_p^* \leq 0$, intersecting the $A_p^* = 0$ axis at $k \sim 1/(\rho^*\gamma\epsilon) \gg 1$ and at $k \sim \rho^*g^*\epsilon^2 \ll 1$, with a single local minimum at $k \sim \sqrt{\epsilon g^*/\gamma} \sim 1/\sqrt{\gamma Fr} \sim O(\sqrt{\epsilon})$. Thus, instability first occurs for long wave disturbances at the critical value $A_p^* \sim -\rho^*/2 + \rho^{*2}\sqrt{g^*\gamma}\,\epsilon^{3/2}$ (i.e., at $A_p \sim -\rho/2 + \rho^2\sqrt{\gamma/Fr}$).

Hydrodynamic Stability of the Full Model

Guided by these results for the inviscid case, the linear stability analysis may be extended to include the effects of viscosity as follows. Retaining the above scalings, we note that $\rho\lambda Pr_g = \mu Pr_l$, where $\mu = \mu_g/\mu_l$ is the gas-to-liquid viscosity ratio. Thus, it is reasonable to treat $Pr_l \equiv P$ as an O(1) parameter, and to consider the limit $\mu = \mu^*\epsilon \ll 1$. Introducing these scalings directly into the linear stability problem obtained from the linearization of the model about the basic solution (8), solutions may be sought in the form of appropriate expansions in powers of ϵ.[15] Proceeding in this fashion, we find that the hydrodynamic stability boundary in the small and intermediate wavenumber regimes is, to leading order, identical to that given above for the inviscid case, while this boundary in the large wavenumber regime, reflecting the influence of viscous effects, is given by

$$A_p^{*(f)} \sim -\rho^* + \frac{2\rho^*\mu^* P[1 + k_f(\rho^*\gamma + 2\mu^* P + 2\rho^* P)]}{4\mu^* P(1 + \rho^* P k_f) - (1 - R)(\rho^*\gamma + 2\mu^* P)}, \quad R = \left[1 + 4\mu^{*2}P^2 k_f^2\right]^{1/2}. \tag{14}$$

A composite expansion is thus constructed as in Eq. (13), giving the result

$$A_p^{*(c)} \sim \epsilon^2 \frac{\rho^{*2}g^*}{2k} - \rho^* + \frac{2\rho^*\mu^* P[1 + \epsilon k(\rho^*\gamma + 2\mu^* P + 2\rho^* P)]}{4\mu^* P(1 + \epsilon k \rho^* P) - (\rho^*\gamma + 2\mu^* P)\left[1 - (1 + 4\mu^{*2}P^2\epsilon^2 k^2)^{1/2}\right]}. \tag{15}$$

The corresponding result for normal gravity is obtained by replacing the scaled gravity ϵg^* with the O(1) parameter Fr^{-1}, and both the normal and reduced gravity boundaries are graphically exhibited in Figure 4 for various zero and representative nonzero values of μ^*, P, Fr^{-1} and γ. It is readily seen that the essential qualitative difference between the normal and reduced-gravity curves is the location of the critical wavenumber for instability. Specifically, it is readily shown from Eq. (15) that the minimum in the neutral stability boundaries occurs for O(1) values of k under normal gravity, and at $k \sim O(\epsilon^{1/2})$ in the reduced-gravity limit, as in the inviscid case described above. Indeed, it may be shown that Eq. (15) collapses to Eq. (13) in the limit of zero viscosity ($P \to 0$), but it is now seen that viscous effects in both the liquid (P) and gas ($\mu^* P$) are comparable to surface-tension effects (γ) in damping large wavenumber disturbances. The equal importance of gas-phase viscosity relative to that of the liquid phase may be shown to arise from the fact that gas-phase disturbances are larger in magnitude than those in the liquid, such that a weak damping of a larger magnitude disturbance is of equal importance as an O(1) damping of a smaller magnitude disturbance.[15] The result (15) thus synthesizes and significantly extends the classical Landau/Levich results,[6,7] not only in allowing for a dynamic dependence of the burning rate on local conditions in the vicinity of the liquid/gas interface, but also in its formal treatment of those processes (surface tension, liquid and gas-phase viscosity) that affect damping of large-wavenumber disturbances.

Other cellular and pulsating stability boundaries are obtained[5] for nonzero values of the temperature sensitivity parameter Ξ, and are thus of a reactive/diffusive nature since they arise from a coupling of the burning rate to the local temperature field. These have been analyzed in the realistic limit $\rho \ll 1$ for the inviscid case,[5] and the generalization of these results to the fully viscous problem in both the normal and reduced-gravity regimes is currently under investigation. One important result obtained from the inviscid analysis is that the effect of nonzero thermal sensitivity Ξ turns out to have little bearing on the hydrodynamic cellular stability boundaries shown in Figures 2 – 4, while O(1) values of this parameter remove the hydrodynamic pulsating boundary to large negative values of A_p. Thus, it is the upper stability boundary in Figure 2, corresponding to the onset of steady cells on the propellant surface, that is the hydrodynamic instability of interest. An analysis of nonlinear stability in the neighborhood of this boundary[8,9] not only confirms the existence of steady cellular structures above this boundary, but also demonstrates how the interaction of certain types

of cellular modes can result in secondary and tertiary transitions to time-periodic motions[11-13] that may correspond to the sloshing type of behavior observed in HAN/TEAN/water mixtures.[3]

Conclusion

The present work has described a formal treatment of hydrodynamic instability in liquid-propellant combustion in both the normal and reduced-gravity parameter regimes. Exploiting the smallness of the gas-to-liquid density ratio, an asymptotic treatment of a generalized Landau/Levich - type model that allowed for a dynamic dependence of the burning rate on local perturbations was described. It was shown that there were three distinct wavenumber regimes to be considered, with different physical process assuming dominance in each. In particular, it was shown that the gravitational acceleration (assumed to be normal to the undisturbed liquid/gas interface in the direction of the liquid) is responsible for stabilizing long-wave disturbances, whereas surface tension and viscosity are effective in stabilizing short-wave perturbations. As a consequence, reduced gravity results in a shift in the minimum of the neutral stability boundary towards smaller wavenumbers, such that the onset of hydrodynamic instability, predicted to occur for sufficiently small negative values of the pressure-sensitivity coefficient A_p, becomes a long-wave instability in that limit. An additional result is that gas-phase viscosity plays an equally large role as liquid viscosity in the large wavenumber regime. This important effect, absent from previous treatments, stems from the fact that gas-phase disturbances are larger in magnitude than those in the liquid phase. Consequently, although the gas-to-liquid viscosity ratio is small, a weak damping of a larger magnitude disturbance is of equal importance to an O(1) damping of a smaller magnitude disturbance. In addition, the inclusion of both viscous and surface-tension effects in a single analysis, which are of comparable importance for short-wave perturbations, represents an important synthesis of the classical Landau/Levich theories.

Acknowledgment

References

1. Ya. B. Zel'dovich, G. I. Barenblatt, V. B. Librovich and G. M. Makhviladze, *The Mathematical Theory of Combustion and Explosions*, Consultants Bureau, New York, 1985.
2. F. A. Williams, *Combustion Theory*, Benjamin/Cummings, Menlo Park, 1985.
3. S. R. Vosen, *The Burning Rate of Hydroxylammonium Nitrate Based Liquid Propellants*, Twenty-Second Symposium (International) on Combustion (1989), 1817–1825.
4. R. C. Armstrong and S. B. Margolis, *Hydrodynamic and Reactive/Diffusive Instabilities in a Dynamic Model of Liquid Propellant Combustion*, Twenty-Second Symposium (International) on Combustion (1989), 1807–1815.
5. R. C. Armstrong and S. B. Margolis, *Hydrodynamic and Reactive/Diffusive Instabilities in a Dynamic Model of Liquid Propellant Combustion—II. Inviscid Fluid Motions*, Combust. Flame **77** (1989), 123-138.
6. L. D. Landau, *On the Theory of Slow Combustion*, Acta Physicochimica URSS **19** (1944), 77-85; Zh. Eksp. i Teor. Fiz. **14**, 240.
7. V. G. Levich, *On the Stability of the Flame Front When a Liquid is Burning Slowly*, Dokl. Akad. Nauk SSSR **109** (1956), pp. 975–978.
8. S. B. Margolis, G. I. Sivashinsky, and J. K. Bechtold, *Secondary Infinite-Period Bifurcation of Spinning Combustion Waves Near a Hydrodynamic Cellular Stability Boundary*, Physica D **43** (1990), 181–198.
9. J. K. Bechtold and S. B. Margolis, *Nonlinear Hydrodynamic Stability and Spinning Deflagration of Liquid Propellants*, SIAM J. Appl. Math. **51** (1991), 1356–1379.
10. Y. M. Timnat, *Advanced Chemical Rocket Propulsion*, Academic Press, London, 1987.
11. T. Erneux and E. L. Reiss, *Splitting of Steady Multiple Eigenvalues may Lead to Periodic Cascading Bifurcation*, SIAM J. Appl. Math. **43** (1983), 613–624.
12. J. D. Buckmaster, *Polyhedral Flames—an Exercise in Bimodal Bifurcation Analysis*, SIAM J. Appl. Math. **44** (1984), 40–55.
13. S. B. Margolis and G. I. Sivashinsky, *On Spinning Propagation of Cellular Flames*, Combust. Sci. Tech. **69** (1990), 99–131.
14. S. B. Margolis and G. I. Sivashinsky, *Flame Propagation in Vertical Channels: Bifurcation to Bimodal Cellular Flames*, SIAM J. Appl. Math. **44** (1984), 344–368.
15. S. B. Margolis, *Hydrodynamic Instability in an Extended Landau/Levich Model of Liquid-Propellant Combustion at Normal and Reduced Gravity*, submitted for publication (1997).

gas/liquid interface:

$$\tilde{x}_3 = \tilde{\Phi}_s(\tilde{x}_1, \tilde{x}_2, \tilde{t})$$

gas

liquid

$\hat{n}_s$

$\tilde{v}_-$

$\tilde{v}_+$

$\tilde{x}_1$

$\tilde{x}_2$

$\tilde{x}_3$

Figure 1. Model geometry.
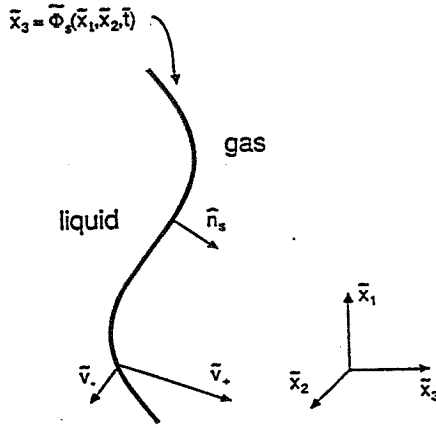
NEUTRAL STABILITY BOUNDARIES ($\Xi = 0$)
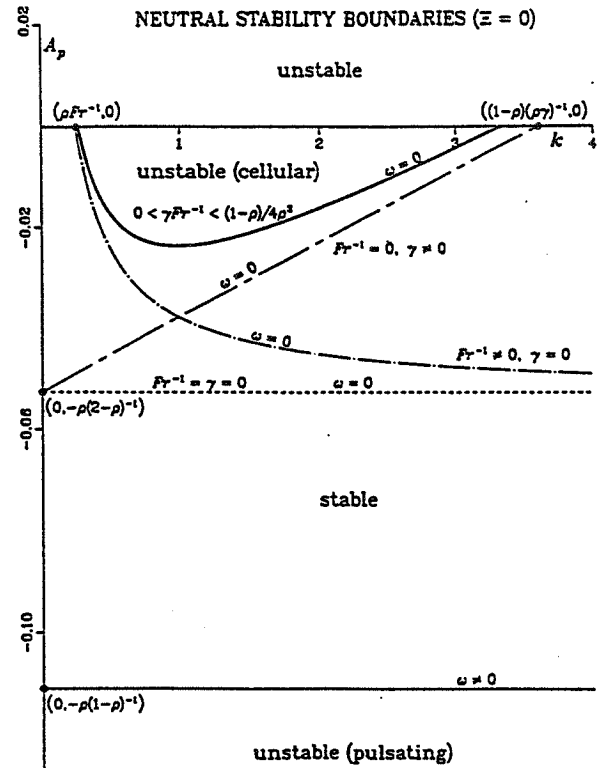
Figure 2. Inviscid hydrodynamic neutral stability boundaries, based on Eq. (11).

HYDRODYNAMIC STABILITY BOUNDARIES ($\rho \ll 1$)
Inviscid Case ($P = 0$)
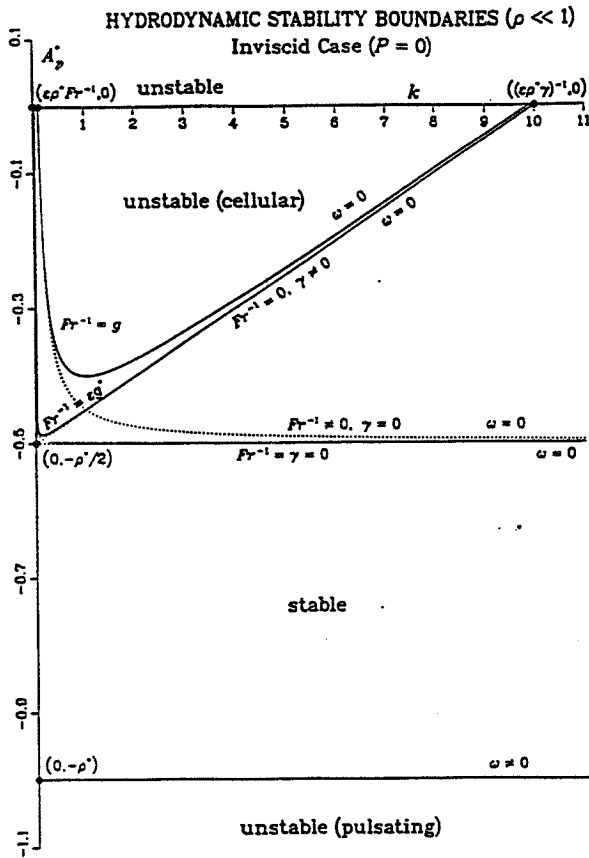
Figure 3. Asymptotic representation of the cellular hydrodynamic stability boundary for the inviscid case, based on Eq. (13).

HYDRODYNAMIC STABILITY BOUNDARIES ($\rho \ll 1$)
Viscous Case ($P > 0$)
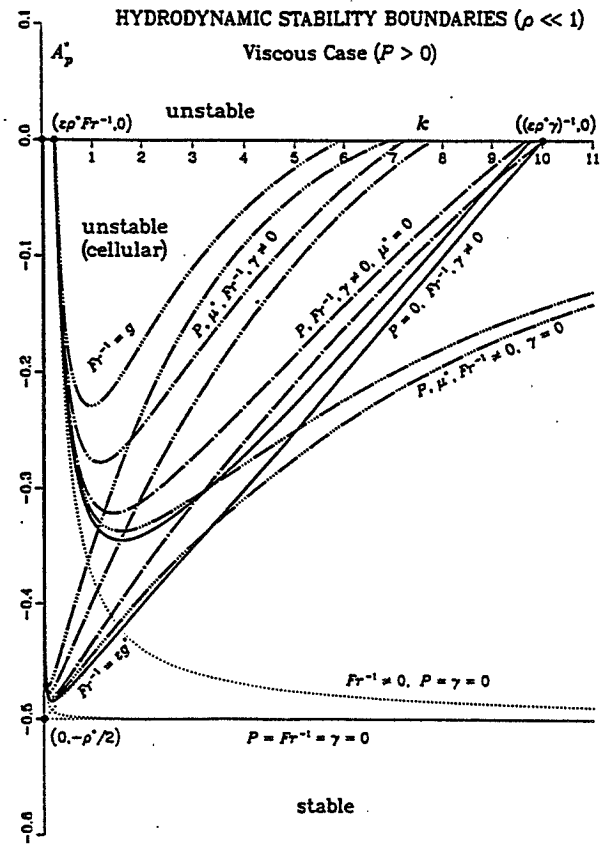
Figure 4. Asymptotic representation of the cellular hydrodynamic stability boundary for the viscous case, based on Eq. (15).

266

STRETCHED DIFFUSION FLAMES IN VON KARMAN SWIRLING FLOWS

VEDHA NAYAGAM
Analex Corporation
Brook Park, Ohio

and

Forman A. Williams
Center for Energy and Combustion Research
University of California, San Diego
La Jolla, California

Introduction

Flame stretch plays a critical role in determining the fundamental characteristics of a diffusion flame, including its extinction and burning efficiencies. The concept of 'flame stretch' to characterize the effects of straining flows on flames was first introduced by Karlovitz (1953). Following his work, this concept was further exploited to characterize flame dynamics by a number of authors including Lewis and von Elbe (1961), and Markstein (1964). The mathematical definition of flame stretch and its physical meanings can be found in the review article by Law (1988). Most of the experimental studies on stretched diffusion flames thus far have been in the high velocity, high stretch regime. Under normal gravity conditions high temperature differences encountered in a flame causes buoyancy induced flows making it difficult to obtain low flow, low stretch flames in practice. Even the experiments in the high-stretch regime employ flow configurations that are essentially two-dimensional. The three dimensionality of the swirling flow field observed in many common combustion devices are missing in these configurations. The most commonly used experimental configurations are the counter flow diffusion flames, stagnation-point boundary layers, spherically symmetric combustion such as droplet combustion or porous sphere combustion with injected fuel, cylindrical flames and flat flame burners. The nature of the influences of the swirl on the structure and extinction of diffusion flames have not been addressed in any great detail thus far in the literature.

Recent experimental studies in microgravity have shown that slow ventilation flows encountered in a spacecraft could sustain a flame that may otherwise not be able to exist in normal gravity or in a quiescent microgravity environment. Also, it has been pointed out by T'ien (1990) that the flammability ranking of materials could be reversed from normal gravity, high-stretch flames to microgravity, low-stretch flames. More recently, Holcomb and T'ien (1995) studied the combustion of spinning fuel disk in a quiescent low gravity environment and showed that both radiative extinction at low rotation and blow-off extinction at high rotation exist. Interestingly, the rotationally induced flames have higher maximum temperatures and wider range of flammability limits compared to the forced convective situation. Holcomb and T'ien also concluded that despite the qualitative similarities between the forced convective case (stagnation-point flow) and the von Karman flow, quantitatively they are different in terms of the maximum flame temperatures and burning rates, i.e., a simple common stretch rate parameter does not correlate the data. These conclusion have important implications with regard to material flammability ranking and in general to spacecraft fire safety. It is also possible that the results obtained from studies of laminar-flame extinction may be applied for predictions in turbulent situations through estimates of strain rates in turbulent fields (Williams, 1981; Peters, 1984).

In this study, which is a collaborative effort between University of California, San Diego, and the Analex Corporation, a relatively novel experimental configuration of a spinning fuel disk is used to systematically investigate the effect of stretch on laminar diffusion flames. This so-called 'von Karman-flow' configuration provides a unique opportunity to precisely control the stretch rates over a wide range experimentally (Vedha -Nayagam et al., 1990) . From the theoretical point of view the governing equations for this flow reduce to a set of ordinary differential equations under similarity transformations and permits us to include detailed models for the physical and chemical processes. In the following sections we describe the objectives of the research along with the theoretical and experimental efforts currently underway to achieve the stated objectives.

Objectives

The primary objective of this research is to experimentally map the flammability boundaries of diffusion flames supported by condensed-phase fuels under varying stretch conditions produced by swirling flows. Experimental studies will be focused on the low-stretch regime, obtainable only in a microgravity environment. Theoretical models using asymptotic techniques will also be developed as a part of this study to predict the observed results. Theoretical models will include the effects of both surface and gas-phase radiative heat loss effects on extinction. The experimental technique employed here while providing an easy and

accurate method to control the stretch rates, yields a one-dimensional theoretical problem under similarity transformations so that complex physical and chemical processes could be modeled with relative ease.

Theoretical Modeling

As a first step, an activation energy asymptotic (AEA) model is developed for the combustion of a spinning fuel disk in a quiescent microgravity environment. We follow the procedure developed by Krishnamurthy et al. (1988) who first showed that Linan's (1974) inviscid analysis for the counter-flow diffusion flame can be made applicable to predict flame extinction for condensed fuels burning in a laminar, viscous stagnation-point boundary layer by suitable transformations. Since then this procedure has been applied to predict extinction conditions, and to extract global chemical kinetic parameters when the fuel chemistry is not well understood, for spherically-symmetric droplet burning (Law, 1975), mixed convective burning of spherical particles (Wu et al., 1982), and horizontal and vertical burning of fuel surfaces in the presence of buoyancy (Puri, 1992). In these studies extinction conditions are characterized by a critical Damkohler number which is a ratio of a characteristic flow time to chemical time. When the system Damkohler number falls below this critical value, the flow times are so small that the chemistry does not have enough time to proceed and the flame dies. It should be noted that it is also possible to express this condition in terms of a critical scalar dissipation rate (Peters, 1983). The effects of gas-phase radiation and surface radiation on the laminar diffusion flame extinction has been considered by Shorab et al. (1982), and Shorab and Williams (1981).

While the previously mentioned studies were focused on extinction at large stretch rates or the 'blow-off' extinction, T'ien and his co-workers have identified a new regime at low stretch rates where the radiation loss from the fuel surface leads to flame extinction (T'ien, 1986, Foutch and T'ien 1987). T'ien using numerical calculations for condensed-fuel diffusion flame in a stagnation-point boundary layer showed that at low stretch rates the radiative heat loss decreases at much smaller rate compared to the heat release rate from the flame zone leading to extinction. This extinction was classified as radiative extinction as opposed to the 'blow-off' extinction observed at high stretch rates. More recent studies have employed asymptotic techniques to investigate the diffusion flame extinction mechanisms at low and high stretch rates (Chao et al., 1990; Chao and Law, 1993, and Oh et al., 1994). Oh et al.'s (1994) results for diffusion flames in stagnation-point flow show that the dominant mechanism for flame extinction is fuel leakage in the high-stretch regime and both fuel and oxidizer leakage in the low-stretch regime.

Before proceeding with the description of the AEA model it is worthwhile mention that for the case of premixed flames both experimental and theoretical studies have been carried out to investigate swirl effects (Chen et al., 1987; Libby and Williams, 1990; Kim et al., 1992). Also, the fluid dynamics literature for von Karman flows are extensive and they are not reviewed here. A review of this field can be found in Zandbergen and Dijksra (1987).

Activation Energy Formulation for von Karman Flows

Consider an infinite fuel disk rotating in a quiescent environment about its axis of symmetry with an angular velocity Ω. It is assumed that a steady, laminar flame exist, and the buoyancy forces are negligible. The governing equations for mass, momentum, energy, and species can be reduced to a set of ODEs using the similarity variables defined below. With the independent variable defined by

$$\eta = \int_0^{z\sqrt{v_\infty/\Omega}} (\rho/\rho_e)\, dz \qquad (1)$$

and the dependent variables,

$$F(\eta) = \frac{u}{\Omega r}, \quad G(\eta) = \frac{v}{\Omega r}, \quad H(\eta) = \frac{\rho w}{\rho_\infty \sqrt{v_\infty \Omega}}, \quad \widetilde{T} = \frac{T\, c_p}{Q}, \quad \widetilde{Y}_F = Y_F, \quad \widetilde{Y}_O = \sigma Y_O, \qquad (2)$$

the governing equations are

$$H' + 2F = 0 \qquad (3)$$

$$F'' - HF' - F^2 + G^2 = 0 \qquad (4)$$

$$G'' - HG' - 2FG = 0 \qquad (5)$$

$$\widetilde{T}'' - H\widetilde{T}' = -D\widetilde{Y}_F\widetilde{Y}_O \exp(-\widetilde{T}_a/\widetilde{T}) \qquad (6)$$

$$\widetilde{Y}_i'' - H\widetilde{Y}_i' = D\widetilde{Y}_F\widetilde{Y}_O \exp(-\widetilde{T}_a/\widetilde{T}) \qquad (7)$$

subject to the boundary conditions

$$F(0)=0,\ G(0)=1,\ H(0)=H_w=\widetilde{T}'(0)/q,\ \widetilde{T}(0)=\widetilde{T}_w,$$

$$\widetilde{Y}_F(0)=H_w\left[1-\widetilde{Y}_F(0)\right],\ \widetilde{Y}_O(0)=H_w\widetilde{Y}_O(0),$$

$$F(\infty)=G(\infty)=\widetilde{Y}_F(\infty)=0,\ \widetilde{Y}_O(\infty)=\widetilde{Y}_{O\infty},\ \widetilde{T}(\infty)=\widetilde{T}_\infty. \qquad (8)$$

In Eqs.(6) and (7) the Damkohler number D is given by

$$D = \frac{A_F \rho \sigma}{W_O \Omega} \qquad (9)$$

The chemical reaction is assumed to be one-step, second-order irreversible Arrhenius reaction between the fuel and oxidizer of the form,

$$\nu_F[\text{Fuel}] + \nu_O[\text{Oxidizer}] \rightarrow \nu_P[\text{Product}] \qquad (9)$$

The specific reaction rate is given by

$$\omega = - (B_o/W_o)\rho^2 \, Y_F Y_O \exp(-T_a/T) \qquad (10)$$

Following Krishnamurthy et al. (1976) , the energy and species conservation equations are transformed to a form originally analyzed by Linan (1974) using the transformation

$$\xi = \frac{H_w}{(1+B)} \int_\eta^\infty e^h \, d\eta, \quad \text{with } h = \int_0^\eta H(\eta) \, d\eta. \qquad (11)$$

where,

$$B = \frac{\widetilde{Y}_{O\infty} + \widetilde{T}_\infty - \widetilde{T}_w}{(q + \widetilde{Y}_{O\infty})} \qquad (12)$$

This transformation suppresses the non-essential convective term in the governing equation leaving only the diffusion term and the source term. Furthermore, the region $0 < \eta < \infty$ is mapped into a finite domain, and the dependent variables become linear functions of ξ in the limit of infinite activation energy (thin-flame limit).

The transformed governing equations are,

$$\frac{\partial^2 \widetilde{T}}{\partial \xi^2} + \frac{D}{K} \, \widetilde{Y}_F \widetilde{Y}_O \exp(-\widetilde{T}_a/\widetilde{T}) = 0 \qquad (13)$$

$$\frac{\partial^2 \widetilde{Y}_i}{\partial \xi^2} - \frac{D}{K} \, \widetilde{Y}_F \widetilde{Y}_O \exp(-\widetilde{T}_a/\widetilde{T}) = 0 \qquad (14)$$

Using Zhvab-Zeldovich formulation it is easy to show that the fuel and oxygen concentrations are given by

$$\widetilde{Y}_F = \widetilde{T}_\infty - \widetilde{T} + (1-\beta)\xi, \text{ and } \widetilde{Y}_O = \widetilde{T}_\infty - \widetilde{T} + \widetilde{Y}_{O\infty} - (\widetilde{Y}_{O\infty} + \beta)\xi, \qquad (15)$$

where,

$$\beta = q + \widetilde{T}_\infty - \widetilde{T}_w. \qquad (16)$$

Also, at the fuel surface, and at the flame-sheet locations the following expressions hold true;

$$\xi_w = \frac{B}{1+B}, \quad \widetilde{Y}_{Fw} = \frac{(\widetilde{T}_\infty - \widetilde{T}_w)}{1+B} - \frac{B(q-1)}{1+B}, \qquad (17)$$

$$\xi_f = \frac{\widetilde{Y}_{O\infty}}{1+\widetilde{Y}_{O\infty}}, \quad \widetilde{T}_f = \widetilde{T}_\infty - \frac{\widetilde{Y}_{O\infty}}{1+\widetilde{Y}_{O\infty}}.$$

In the flame sheet limit, or as $T_a \rightarrow \infty$, the temperature profiles on either side of the flame sheet is given by,

$$\widetilde{T} = \widetilde{Y}_{O\infty} + \widetilde{T}_\infty - (\widetilde{Y}_{O\infty} + \beta)\xi, \quad \xi_f \leq \xi \leq \xi_w, \qquad (18)$$

$$\widetilde{T} = \widetilde{T}_\infty + (1-\beta)\xi, \quad 0 \leq \xi \leq \xi_f.$$

Finite rate chemistry effects leading to extinction can now be determined treating T_f^2/T_a as a small parameter and expanding Equation (13), as done by Linan (1974). Since Eqn. (13) and its boundary conditions are identical to the problem analyzed by Linan, his results are directly applicable to the present analysis. The extinction Damkohler number, D_e, is then given by

$$D_e = \delta_{0E} \left[\frac{(1+\alpha)H_w e^{h_f}}{2(1+B)} \right] \varepsilon^{-3} e^{1/\varepsilon} \widetilde{T}^{-3} \qquad (19)$$

where,

$$\varepsilon = \frac{\widetilde{T}_f}{\widetilde{T}_a}, \text{ and } \alpha = \widetilde{Y}_{O\infty}. \qquad (20)$$

The reduced Damkohler number, δ_{0E}, at extinction can be expressed as function of a single parameter γ and is given by the following polynomial approximation,

$$\delta_{0E} = e\left[(1-|\gamma|) - (1-|\gamma|)^2 + 0.26(1-|\gamma|)^3 + 0.055(1-|\gamma|)^4\right]. \tag{21}$$

with

$$\gamma = \frac{\left[\alpha + 2(\widetilde{T}_\infty + q - \widetilde{T}_w) - 1\right]}{(1+\alpha)}. \tag{22}$$

Before the extinction Damkohler number, D_e, could be evaluated, the terms H_w and e^{hf}, which reflect the fluid mechanics of the rotating disk problem, need to be computed based on flame sheet theory. Combining Eqns. (6) and (7) we get the coupling function equation for $Q_0 = T + Y_0$ as,

$$\widetilde{Q}_0'' - H\widetilde{Q}_0' = 0 \tag{23}$$

with the boundary conditions

$$H(0) \equiv H_w = \widetilde{Q}_0'(0)/q, \quad \widetilde{Q}_0(0) = \widetilde{T}_w. \tag{24}$$

The flame sheet, in the similarity coordinate η, is located where $Q(\eta_f) = T_f$. The independently specifiable parameters for the problem are $Y_{0\infty}$, q, $\widetilde{T}_w$, and $\widetilde{T}_w$. Since the physical meaning of these parameters are readily apparent, the parametric results can be presented in terms of these parameters, as done by Wu et al.(1982). Flame-sheet model calculations to obtain H_w and e^{hf} are currently underway and limited results will be available during the workshop.

Experiments

Preliminary experiments on the combustion of spinning fuel disks in air were carried out by Midkiff et al. (1990). Their measured burning rates agreed with the flame-sheet model developed previously by Vedha-Nayagam et al. (1990) for large rotational speeds (> 700 rpm). Their experiments also showed the need to accurately account for the heat loss through in-depth conduction in the fuel bed as well as surface radiation in determining the burning rates. In these preliminary experiments conducted in air at one atmospheric pressure extinction was not observed because at low stretch rates buoyancy induced flows leads to a pool-burning type configuration, and the dc motor used could not reach the high speeds necessary to observe blow-off extinction. For PMMA disks burning in air at high rotational speeds the gas-phase flame was completely blue and at low speeds the flame color changed to orange, indicating soot radiation. The amount of soot deposited on the guard plate extending out of the fuel disk showed marked differences indicating soot production rates are also strongly dependent on the strain field produced in the experiment.

In order to extend the range of operational speed and ambient environmental conditions, a new experiment hardware was designed and built. The experimental rig is capable of accommodating fuel disks of varying size and producing a precisely controllable rotational speed from zero to 15,000 rpm. The rotating disk assembly is housed in a sealed, stainless steel combustion chamber so that the ambient pressure and oxygen concentrations could be varied over a wide range. The experimental apparatus is also integrated into a drop tower frame and could be used in the NASA Lewis 2 second and/or the 5 second drop tower. With some minor modifications the rig could also be flown on board an aircraft flying parabolic trajectories. Figure 1 shows the assembly diagram of the rotating disk apparatus. In the following a brief description of the various components of the experimental apparatus is provided.

The major components of the apparatus are: a) the combustion chamber, b) fuel-disk assembly and the spinning mechanism, c) ignition and extinction systems, d) data acquisition and control systems, and e) diagnostic systems. All these subsystems have been designed and fabricated to fit inside the standard drop-tower rack (and aircraft) and meet the weight restrictions. Each of these subsystems are described briefly in the following.

a) The Combustion Chamber: The combustion chamber is a cylindrical container of internal volume of 27 liters made of stainless steel and capable of operating over the pressure range of low vacuum to 3 atmospheres. The chamber is also equipped with optical quality view ports and a vacuum tight feed-through. For high-stretch, 1-g experiments a larger environmental chamber is used.

b) Fuel Disks and Spinning Mechanism: Our base-line fuel material is polymethylmethacrylate (PMMA). Cast PMMA disks of varying diameters (5 cm to 10 cm) embedded in a 9 inch diameter aluminum plate will be used. The fuel disk assembly is spun using a brushless dc servo motor (Inland Motor; Model No. RBE-01251). The speed of the dc motor is controlled by Galil motion control card (Model No: DMC-100-10) with feedback from an optical encoder (HP HEDS 9100) attached to the bottom of the motor armature (see, Fig. 3). The motor is capable of rotational speeds from zero to 15,000 rpm and are controllable to within ±1% over the full range.

c) Data Acquisition and Control Systems: The gas-phase temperature profiles and the chamber internal pressure are measured using Type B (Pt/Pt-Rd) thermocouples and a pressure transducer via a Sensoray Smart Sensor Processor (Model #7430). This processor has eight channels with 16-bit resolution. The overall control of the experiment is performed through a programmable CPU unit (Ziatech ZT 8901: Single board V53 computer).

d) Other Diagnostic Equipment: An UV-sensitive, intensified array video camera (Xybion) with a narrow-bandpass filter centered around 310 nm is used to image the OH-radical emission at this wavelength. Infrared emissions of the MMA vapor at 3.4 μm will be captured using a mutispectral PtSi detector camera (Inframetrics). The Xybion camera is capable of withstanding high-g levels expected during a drop-tower test. We anticipate using the infrared camera only in the aircraft (DC-9, or KC-135) environment. A high speed 16 mm film camera is also used to capture the flame extinction process.

Summary and Planned Activities

The experiment hardware buildup has been completed. Preliminary 1-g experiments were carried out to calibrate and verify the motor control loop accuracy. The results show that the control system is capable of maintaining the disk rotational speed within ± 1% of the specified value. We have also carried out limited 1-g tests with fuel soaked porous disk to fine-tune the temperature measurement system and the optical diagnostic systems. Further systematic 1-g tests are planned for the summer at the University of California, San Diego. The theoretical modeling effort is continuing with the inclusion of surface and gas-phase radiation effects.

References

Bray, R. (1985). Laminar flamelet modeling in turbulent combustion, in Numerical Simulation of Combustion Phenomena, R. Glowinski et al., Eds., Lecture Notes in Physics, Springer-Verlag, p.90.

Chao, B. H., Law, C. K., and T'ien, J. S. (1990). Structure and extinction of diffusion flames with flame radiation. Twenty-Third Symposium (International) on Combustion, The Combustion Institute, pp. 523-531.

Chao, B. H., and Law, C. K. (1993). Asymptotic theory of flame extinction with surface radiation. Combustion and flame, Vol. 92, pp. 1-24.

Chen, Z. H., Liu, G. E., and Shorab, S. H. (1987). Premixed flames in counterflow jets under rigid-body rotation. Combust. Sci. and Tech. Vol. 5, pp. 39-50.

Foutch, D. W., and T'ien, J. S. (1987). Extinction of a stagnation-point diffusion flame at reduced gravity. AIAA Journal, Vol. 25, No. 7, pp. 972-976.

Holcomb, J. M., and T'ien, J. M., (1994). Combustion and extinction of a stagnation-point diffusion flame in viscosity-driven rotational flow. Central States Section/The Combustion Institute, Madison, Wisconsin.

Karlovitz, B., Denniston, D. W., Knap-Schaefer, D. H., and Wells, F. E. (1953). Studies on turbulent flames: A. Flame propagation across velocity gradients; B. Turbulence measurements in flames. Fourth Symposium (International) on Combustion, The Combustion Institute, pp. 613- 620.

Kent J. H. and Williams, F. A. (1974). Extinction of Laminar Diffusion Flames for Liquid Fuels. Fifteenth Symposium (International) on Combustion, The Combustion Institute, Pittsburgh, PA, pp. 315-325.

Kim, J. S., Libby, P. A., and Williams, F. A. (1992). Influences of swirl on the structure and extinction of strained premixed flames. Part II: Strong rates of rotation. *Phy. Fluids A*, 4, 391-408.

Krishnamurthy, L., Williams, F. A., and Seshadri, K. (1976). Asymptotic theory of diffusion flame extinction in the stagnation-point boundary layer. *Combst. Flame* 26, 363-377.

Lewis, B. and von Elbe, G. (1961). Combustion, Flames and Explosion of Gases, Academic Press, NY.

Libby, P. A., Williams, F. A., and Sivashinsky, G. I. (1990). Influences of swirl on the structure and extinction of strained premixed flames. Part I: Moderrate rates of rotation. *Phy. Fluids A*, 7, 1213-1223.

Lin, T. H., and Shorab, S. H. (1987). Influence of vorticity on counterflow diffusion flames. Combust. Sci. and Tech., Vol. 52, pp. 75-90.

Linan, A. (1974). The asymptotic structure of counterflow diffusion flames for large activation energies. *Acta Astronautica.* 1, 1007-1039.

Law, C. K. (1988). Dynamics of stretched flames. Twenty-Second Symposium (International) on Combustion, The Combustion Institute, Pittsburgh, pp. 1381-1402.

Law, C. K. (1975). Asymptotic theory for ignition and extinction in droplet burning. *Combust. Flame* 24, 89-98.

Markstein, G. (1964). Nonsteady Flame Propagation, MacMillan, NY.

Midkiff, K. C., Mahalingam, B., and Vedha-Nayagam, M. (1990). Comparison of Predicted to Measured Mass Flux Rates in Flames Supported on a Rotating Fuel Surfaces. Fall Technical Meeting, Central States Section/The Combustion Institute, Orlando, Florida.

Oh, T.-K., Lee, J. S., and Chung, S. H. (1994). Effect of gas-phase and surface radiation on the structure and extinction of diffusion flames stabilized on a condensed fuel, Int. J. Heat Mass Trans., Vol. 37, No. 18, pp. 2893-2900.

Puri, I. K. (1992). Extinction Criteria for Buoyant Nonpremixed Flames. *Combst. Sci. Tech.* 84, 305-321.

Peters, N. (1983). Local quenching due to flame stretch and non-premixed turbulent combustion. Combust. Sci. and Tech., Vol. 30, pp. 1-17.

Peters, N. (1984). Laminar diffusion flamelet models in non-premixed turbulent combustion. Prog. Energy Combust. Sci., Vol. 10, No. 3, pp. 319-339.

Peters, N. and Williams, F. A. (1983). Liftoff characteristics of turbulent jet diffusion flames. *AIAA J.* **21**, 423-429.

Shorab, S. H., Linan, A., and Williams, F. A. (1982). Asymptotic theory of diffusion flame extinction with radiant loss from the flame zone. *Combst. Sci. Tech.* **27**, 143-154.

Shorab, S. H., and Williams, F. A. (1981). Extinction of diffusion flames adjacent to flat surfaces of burning polymers, J. Polym. Sci. Vol. 19, p. 2955.

T'ien, J. S. (1986). Diffusion flame extinction at small stretch rates: The mechanism of radiative loss. Combustion and Flame, Vol. 65, pp.31-34.

T'ien, J. S. (1990). The possibility of a reversal of material flammability ranking from normal gravity to microgravity. *Combustion and Flame*, **80**, 355-357.

Vedha-Nayagam, M., Midkiff, K. C., and Mahalingam, B. (1990). Laminar Forced Convective Burning of a Rotating Disk in Microgravity. Spring Technical Meeting, Central States Section/The Combustion Institute, Cincinnati, Ohio.

Williams, F. A. (1975). Recent advances in theoretical descriptions of turbulent diffusion flames, in: *Turbulent Mixing in Non-Reactive and Reactive Flows*, Plenum Press, pp. 189-208.

Williams, F. A. (1981). A review of flame extinction. Fire Safety Journal, Vol. 3, pp. 163-175.

Williams, F. A. (1991). Overview of asymptotics for methane flames (Chapter 4), in Reduced Kinetic Mechanisms and Asymptotic Approximations for Methane-Air Flames, Ed. Smooke, M. D., Springer-Verlag, New York.

WU, X., Law, C. K., and Frernandez-Pello, A. C. (1982). A unified criterion for the convective extinction of fuel particles. *Combust. Flame* **44**, 113-124.

Zandbergen, R. J., and Dijkstra, D. (1987). von Karman swirling flows. *Annu. Rev. Fluid Mech.*, **19**, 465.

Figure 1. Von Karman Swirling Flow Combustion Experiment Apparatus.
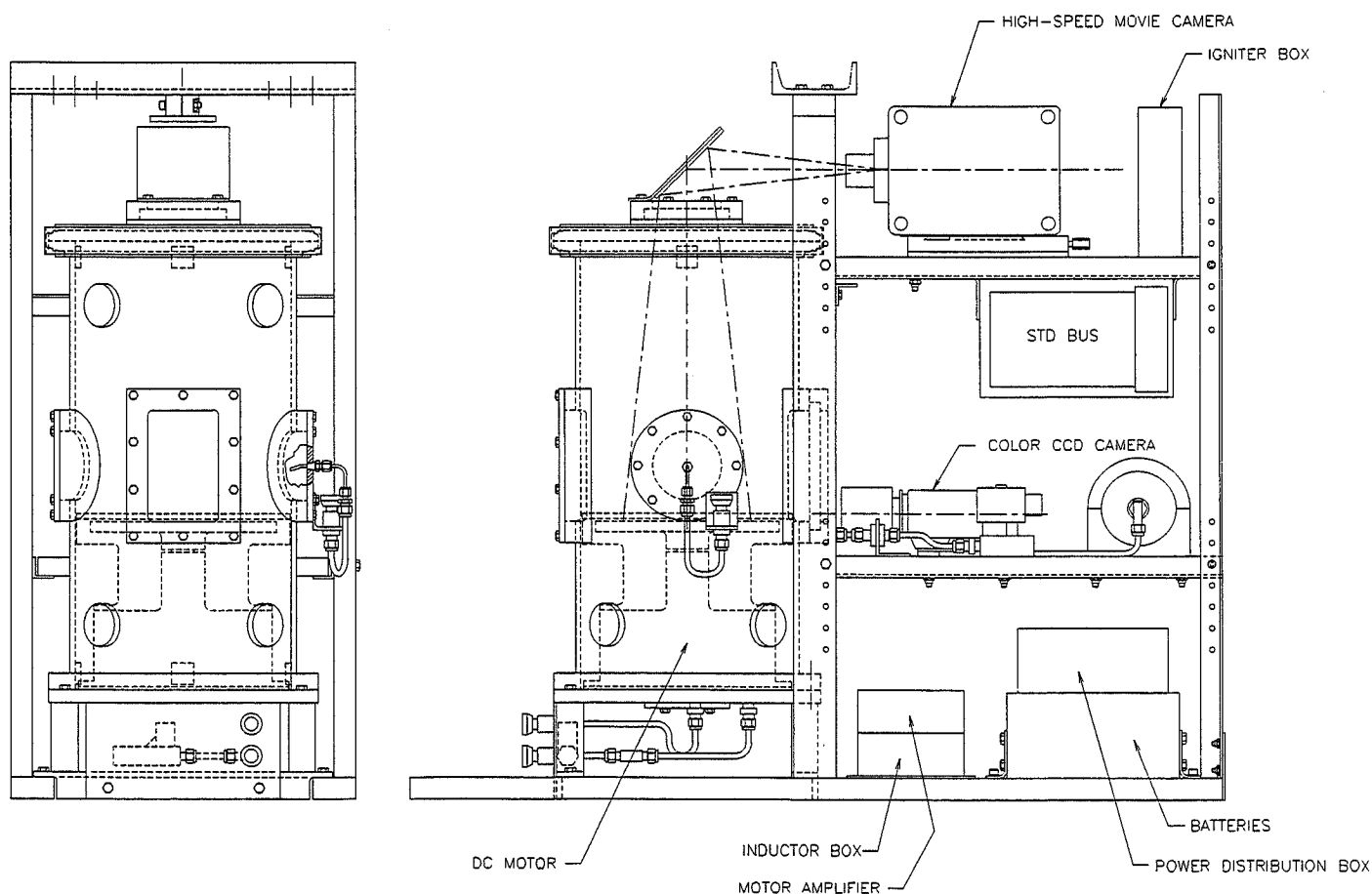
Combustion Diagnostics

Page intentionally left blank

SELECTED DIAGNOSTICS FOR MICROGRAVITY COMBUSTION SCIENCE

Paul S. Greenberg; NASA-Lewis Research Center   DeVon W. Griffin; NASA-Lewis Research Center
Karen J. Weiland; NASA-Lewis Research Center   William Yanis; NYMA; Lewis Research Center Group

Introduction

The evolution of our understanding of combustion phenomena occurring under reduced gravity conditions poses a continuing demand for diagnostic tools of increased sophistication. Existing methods have become insufficient to keep pace with emerging refinements in the underlying theories and predictive models. The coupling of physical mechanisms inherent in combustion systems mandates the simultaneous determination of numerous thermophysical quantities, principally temperature, velocity, and species concentrations. Observed differences attributable to variations in experimental configuration, fuels and diluents, and initial conditions enhance the difficulty of developing diagnostic methods suitable for the acquisition of the required data over the desired range of experimental parameters.

Efforts to provide for ongoing diagnostic development supporting microgravity combustion science experiments are conducted within the Microgravity Science Division at the NASA-Lewis Research Center. The following describes recent results from several diagnostic development efforts conducted under this project.

Laser Doppler Velocimetry

Laser doppler velocimetry (LDV) utilizes the frequency shift of scattered radiation to perform remote, non-intrusive measurements of local fluid velocities. Recent advances in both solid-state laser and detector technologies and high speed digital signal processing (DSP) architectures have permitted the construction of compact, mechanically robust systems suitable for microgravity combustion science applications.

The systems described here utilize dual-beam heterodyne detection. This configuration affords optimal performance under the broadest range of measurement applications. The intersection of the dual input beams defines the optical sample volume, which for the present systems is on the order of 70 microns ($1/e^2$ diameter). The doppler shift of light scattered from small seed particles introduced into the flow field is utilized to determine the Eulerian velocity within the sample volume. The capacity for high temporal data rates provides a valuable tool for the investigation of time dependent flows and turbulent phenomena.

Two basic optical configurations are employed, depending on the specifics of the application. A forward scattering system is utilized for applications involving large spectral bandwidths, such as highly turbulent flows. Strongly enhanced forward scattering cross sections permit the use of smaller seed particles in conjunction with relatively low power laser sources. The smaller particles are necessary to follow detailed features of the flow structure with suitable fidelity. The system reported here utilizes a 14 milliwatt diode-pumped, doubled Nd:YAG laser operating at 532 nanometers. Shorter wavelengths are generally advantageous by virtue of the k^4 dependence of the scattered signal. Further compaction of the receiving optics module is achieved via fiber optic coupling of the photodetector. The detector is composed of a low-noise avalanche photodiode (APD) with an integrated preamp and line driver. The use of APD's is favored in this application, since the high quantum efficiency dominates the excess gain provided by conventional photomultiplier tubes.

Optical systems have also been constructed in a coaxial backscatter configuration using laser diode sources emitting at 680 and 780 nanometers. In addition to simplifying alignment considerations, this configuration also provides single-ended optical access. Such an arrangement affords the possibility of rapid spatial scanning of the sample volume using computer controlled turning mirrors or diffractive optics. A system of this type has been constructed for use in the various reduced-gravity facilities. The onboard computer system generates the waveforms to achieve the desired spatial scan sequence, and simultaneously provides timing flags to synchronize with the data acquisition system.

Data is acquired and processed using a novel burst-spectral signal processor. This processor utilizes parallel DSP to achieve acquisition, processing, archiving, and real-time graphic display at rates approaching 10^4 measurements per second. The 16-bit PC plug-in card configuration facilitates integration into a variety of experimental packages. Of particular value in the context of the reduced gravity facilities is the ability to operate the processor as a transient recorder. In this fashion, the original data stream is preserved, allowing flexibility in post-processing options.

Shown in figure 1 is velocity vs. time data corresponding to non-reacting flow from a burner with Re 2100 at the exit. Turbulence is generated by impingement on a diffuser plate located 20 mm upstream of the exit. Also shown is the associated velocity probability density function (pdf). Figure 2 illustrates the mean velocity and RMS of the pdf as a function of axial height above the burner. This data was acquired on the NASA DC-9 reduced gravity aircraft using the forward scatter optical system previously described.

Particle Image Velocimetry

Measurement of velocity maps for flows by using Particle Imaging Velocimetry requires an intense light source manipulated

to form a light sheet which is an illuminated volume with a thickness of approximately 1 mm, a width of at least 50 mm and an axial extent of at least 150 mm. In 1G labs, high-energy lasers are routinely used for this purpose. Use of such a laser in the 2.2 second drop tower is more difficult since the laser head and power supply are too massive to be included internal to the drop package. Therefore, a multi-mode fiber optic cable with a core diameter of 600 micrometers was used to transmit light from the laser to the drop rig. Once on the rig, cylindrical optics were used to suitably condition the light sheet and center it over the burner exit.

Scattering particles were entrained in the fuel flow by placing them in an input plenum through which the gas flowed. The 0.1 mm diameter of the entrance orifice was designed to produce a Reynolds number of 2100 in the plenum when the mean velocity from a 0.312 cm diameter nozzle at the exit of the plenum was 8.72 cm/sec. In initial tests, the seed exited the nozzle in a continuous stream that was much too dense to resolve individual particle images as required. When a screen was placed inside the plenum over the base of the exit nozzle, the particulate stream was disrupted and individual particles could be resolved. The flow velocity was also reduced to a level where the Reynolds number in the plenum was approximately 370. A velocity field map is shown in figure 3. In this illustration, the nozzle is denoted by a square and the 0G flamefront location corresponds to the hemispherical line. The axes are labeled according to pixel number.

The same seeder concept was also applied to seeding a 1G flow from a 33 mm ID tube with a non-combusting flow. In this experiment air exited a 33 mm diameter, 600 mm long tube with a mean velocity of 5.23 mm/sec. Given the large tube diameter, a Reynolds number of 1153 was produced with an entrance diameter of 0.3 mm. The flow field is shown in figure 4 where the labels for the axes correspond to distance in inches. In all cases, quantitative velocity maps were obtained from the original raw particle image sequences using analysis tools developed at the NASA-Lewis Research Center.

Simultaneous Soot Volume Fraction and Temperature Measurements

A variety of non-intrusive optical methods have been demonstrated for the determination of soot volume and fraction and temperature. Specifically, optical extinction has been utilized for the former, and emission pyrometry for the latter. Both examples involve the tomographic inversion of integrated line-of-sight data. Recently, a method was developed to permit the rapid, two-dimensional determination of soot volume fraction fields. A system has also been developed for the Combustion Module-1 program to determine soot temperature fields via two-wavelength emission tomography.

The present effort focuses on performing simultaneous measurements of volume fraction and temperature, while also addressing issues concerning the specification of the spectrally dependent emissivity for carbonaceous soot. This work is an extension of previous efforts by Hall and Bonzcyk, essentially extending the method to multi-dimensional measurements. The method is predicated on the fact that [in the optically thin limit] Kirchoff's Law establishes the equivalence between absorptivity and emissivity. Since optical extinction in effect determines per volume absorptivity, emission measurements performed along identical optical lines of sight yield path integrated data proportional to the associated extinction values. The constant of proportionality is the Planck Function, leading directly to the determination of temperature without the need to explicitly determine appropriate values for soot emissivity.

To insure this proportional equality, it is essential that the emission and extinction measurements be specified over identical optical paths. Isotropic emissions must therefore be collected over narrow, spatially non-overlapping ray fans. When utilizing a pixel-based detector array, the permissible collection angle is determined by the quantity $d_p/2r_fM$, where d_p is the dimension of a pixel, r_f is the maximum radius of the emitting species, and M is the system magnification. Achieving a spatially invariant angular collection efficiency is accomplished through the use of a telecentric imaging system.

Line profiles from a resulting SVF and temperature map are shown in figure 5 for the case of a 3.85 cc/sec ethylene-air coflow burner. Data from previous measurements by Santoro et al are shown for comparison. As would be expected, temperature measurements derived from concomitant SVF measurements yield unphysical values in regions where the soot loading becomes negligible. This is consistent with the concept of measuring the temperature of the soot field itself. In the laminar diffusion flame, the location of the soot shell occurs at radii internal to the reaction surface, and therefore measurements of soot temperature obtained by this method would not be anticipated to accurately determine peak gas phase temperatures. Figure 6 depicts similar measurements in a Re 2550 turbulent acetylene diffusion flame. Due to significantly enhanced mixing, the occurrence of soot is less sharply confined, as observed in the preceding laminar flame data.

Rapid-Insertion Fine Wire Thermocouples

The use of rapid-insertion fine wire thermocouples provides a simple complement to emission pyrometry techniques. The latter, when implemented in the visible spectrum, are dominated by radiant contributions from soot. While isolated gas phase emissions are observed in the infrared, the output still remains a line-of-sight integrated quantity. This measurement therefore provides a useful complement for the determination of spatially localized temperature measurements in possibly non-sooting regions of combustion phenomena of arbitrary symmetry.

Minimizing the intrusive nature of a physical probe is enhanced by reductions in thermal mass, aerodynamic cross section, and residence time. These importance of these features have been confirmed by high speed imagery and high speed schlieren

photography of thermophoretic soot sampling probes. To this end, an identical pneumatic actuator assembly was used for the present thermocouple measurements. In this case, the 2 mm gap in the tip of the probe normally occupied by the transmission electron microscopy collection grid is spanned by a fine wire thermocouple. The results reported here were obtained using type K thermocouples with a wire diameter of 1 mil. The active junctions were formed by laser welding, forming a spherical bead of approximately twice the wire diameter. The raw leads are bonded to the surface of the probe blade with a thin, high temperature, electrically insulating coating.

To reduce conductive effects along the metallic leads, the thermocouple was oriented perpendicular to the blade gap, and along vertical axis of the flame. The exposed thermocouple leads are therefore exposed to minimal thermal gradients. The use of 1 mil wire places the bead 40 wire diameters away from the larger thermal mass presented by the probe blade. The apparatus is oriented so that the thermocouple bead falls on the centerline of the burner axis when the actuator is in the fully extended position.

Typical raw voltage response functions are shown in figure 7 for the case of a turbulent acetylene jet diffusion flame at Re 2550. Convective and radiative corrections have not yet been applied. The junctions were located 100 exit diameters downstream. The actual residence times of the probe were measured with a simple optical gate. The gate is formed by a laser sheet which is interrupted by the traversing probe. Following the probe, the sheet is focused onto a high-speed PIN diode, and stored on a digital sampling oscilloscope. Shot-to-shot variations in residence time are negligible. Extrapolations based on an exponential response model demonstrate good agreement between sequential measurements. The observed slight monotonic increase in response time from sequential insertions is attributed to the increase in bead diameter due to the deposition of soot.

Miniature Spectrometer Detection of Visible Flame Emissions

An important observable in microgravity flames is the color of the flame, or more specifically, the spectral distribution of the flame emissions. This may lead to conclusions about the types of species present in different flame regions, comparisons of the relative amounts of the species between microgravity and normal gravity flames, and to the results from flame models. On a practical level, the intensity distribution may guide the selection of optical bandpass filters and light sources for imaging measurements. Conventional laboratory monochromators offer high resolution, but are large and sensitive to mechanical shock. A solid-state, miniature spectrometer, the MMS 1, has been obtained from Carl Zeiss, GmbH to address this specific need.

The entire unit is 70 mm x 60 mm x 43 mm, features a glass body spectrometer, and contains an integrated grating and linear diode array. An input optical fiber bundle composed of approximately 30 single fibers couples the input to the spectrometer, and has an inner diameter of 0.5 mm. It converts the light from a circular input to a linear output of 70 micron by 2.5 mm that forms the input slit of the spectrometer. The grating is holographically blazed to have its maximum efficiency at 215 nm, and images the entrance slit onto the diode array. The same grating is used throughout the uv and visible. The spectrometer has a 256 pixel element linear diode array that simultaneously records a complete spectrum over the range of 300 to 1150 nm.

The electronics are in a separate module that interfaces between the spectrometer and the computer. An analog/digital card in the PC104 computer (described later in this paper) on the drop rig triggers data acquisition and digitizes the signal from the electronics module. A Pascal computer program controls the experiment sequence, including activation of a gas solenoid, hot wire ignitor, and data acquisition.

Prior to use in the drop tower, the MMS underwent a series of laboratory tests. Three sources were used to check the wavelength calibration: a small mercury pen lamp, a helium-neon laser, and a nitrogen laser. Each separately illuminated the fiber optic input to the spectrometer. The peaks were fit to a Gaussian to determine the pixel positions of maximum intensity. Using calibration coefficients supplied by the manufacturer, agreement of the main mercury lines at 365, 404, 435, 545, and 578 nm, and the laser lines at 632 and 337 nm to the measured wavelengths was obtained for five of the lines to within 0.3 nm, agreeing with the manufacturer's specification.

The relative spectral response calibration was done using a quartz-halogen tungsten coiled filament lamp. The system response is not flat, but exhibits a peak sensitivity at 600 nm, falling to 10% of the peak at 415 and 920 nm. The lack of response below 415 nm is due to the optical elements in the lens. A correction function was generated and applied to the subsequent flame spectra to account for the spectral response of the lens/detector system. Above 920 nm, most of the large fluctuations seen in the spectra may be attributed to the smaller detector response. The spectrometer linearity with integration time, from the minimum time of 10.5 msec up to 100 msec, was examined using an atomic spectral lamp. Linearity for different line intensities was observed up to near the bit count limit of 4095.

An initial test drop was conducted using a set of light emitting diodes in the green, red, and near infrared. A comparison of the wavelength maxima location and intensities before and during the drop shows slight changes on the order of 0.5 nm and 3% decrease in intensity.

For a demonstration of flame spectra, the MMS is mounted onto the optics plate of a 2.2 sec drop rig. A 50 mm F/2 macro lens collects the flame emissions and focuses them onto the fiber optic. The magnification is roughly 1/3, so that only a small part of the flame is imaged onto the input diameter of the fiber. A pinhole is used at a separate time to measure the position in the flame that the spectrometer views. Typical accelerations at the end of the drop are between 10-20 G as measured by a

shock accelerometer mounted near the spectrometer. A simple laminar ethylene diffusion flame was chosen as it is commonly studied and easily and reliably ignited. The nozzle inner diameter of 2.5 mm and ethylene flow rate of 0.072 sccm gives a flame 2.2 cm high. The operational sequence is collection of a background (dark) spectrum, flame ignition in 1-g by a hot wire, collection of several 1g spectra, release of the drop package, and collection of transition and 0g spectra. Video is taken of the flame during the entire sequence.

The first set of drops was conducted with the spectrometer imaging low in the flame, 5-7 mm above the nozzle. The flame has a blue color to the eye at this height. The integration time is 33 msec to obtain satisfactory signal levels. The transition to a stable 0G flame appears to take about 1 second, after which the flame spectra are nearly identical until the end of the drop. The spectra in 1G and 0G look qualitatively similar except for the magnitudes, as shown in Figure 8, and show a continuous emission as would be expected from a spectra dominated by particulate emission. Surprisingly little emission or structure is seen in the blue wavelengths above 415 nm that can be detected by the optical system. (The spectrum from a butane flame shows prominent CH emission at 431 nm and C_2 emissions at 473 and 516 nm.) The peak emission occurs in both 1G and 0G flames in the near-infrared, near 950 to 1000 nm. In general, the 0-g spectra are weaker by 2 to 5 times those in 1-g with the greatest 1-g/0-g ratio occurring at 450 nm. The greatest subtracted difference occurs at 900 nm.

Higher in the flame near the center, at 9-10 mm above the nozzle, the signals are considerably stronger. The flame has a yellow color to the eye at this height. The integration time is reduced to 15 msec to keep the signals from going off-scale. The peak wavelength in 1G is 975 nm; in 0G, the peak is not reached, as the signal is still increasing with wavelength. The differences between the magnitudes of the 1G and 0G spectra are even more dramatic than those lower in the flame as shown in Figure 8, with the 1-g/0-g ratio being over 50 times at 525 nm. The greatest subtracted difference occurs at 950 nm, similar to lower in the flame.

One preliminary test of a 1G methane diffusion flame showed that it is considerably weaker than the ethylene flame and blue-shifted in its emissions, as expected from its appearance to the eye. An integration time of 100 msec yielded signals that are roughly 50 counts, compared to over 3000 for the ethylene flame with an integration time of only 15 msec.

To date, the MMS has been subjected to 42 drops. The above results show that this spectrometer system is able to spectrally resolve flames and provide information on their radiant emissions in the visible. A uv-vis version of the MMS was recently received and will be tested for its applicability to enhance the blue and ultraviolet emissions from species such as OH.

Data Acquisition and Control for Microgravity Diagnostic Systems

Advances in diagnostic techniques utilized in the reduced gravity facilities have resulted in the requirement to upgrade the associated data acquisition and control capabilities. A PC104 system was selected for several reasons. First, it is a primary standard for embedded systems. This standard provides a platform that is virtually identical to the desk top PC; the system configuration is based on the standard 16 bit ISA bus. Numerous vendors manufacture boards that will readily mate with this bus architecture. This provides ready availability of a broad variety of capabilities, including power supply cards, CPU cards, frame grabbers, analog signal conditioning, digital I/O, etc. Another important factor is size. Basic cards have an outline of less than 100 by 100 mm. When stacked, the cards are separated by 15 mm. The minimum system can therefore be packaged into a 150 x 150 x 50 mm. An additional motivation is consistency with laboratory applications. Most bench top systems can be duplicated in the PC104 format. Programs written to run under DOS will also run with out modification on a PC104 system.

The present configuration consists of a 486 CPU, a PCMCIA interface, and a data acquisition card. The data acquisition card has 16 single ended or 8 differential analog inputs, digitized to 12 bit resolution with a maximum sampling rate of 200 kilohertz. Analog outputs are supplied through two 12 bit D/A converters. Also provided are 16 digital lines which drive the various solenoids, relays, and status indicators. As configured the system requires only a 5 volt input, and typically consumes 6 watts of power. Should the need arise to alter this configuration, a second acquisition card can be added to the stack to enhance or expand these capabilities.

Upon initialization, the system loads DOS from the solid-state disk (SSD) on the CPU card. The config.sys file and autoexec.bat files in the SSD load all of the necessary system drivers. The final command in the autoexec.bat runs a batch file on the PCMCIA flash card. The data acquisition program can then be executed from the PCMCIA card. Data taken during the experiment sequence is then stored back to the same card. Upon completion, the card is removed, and interfaced to either a laptop or desk top machine to analyze and archive the data. In this fashion, the data acquisition program can be changed without having to gain access to the system, facilitating parallel utilization by several users.
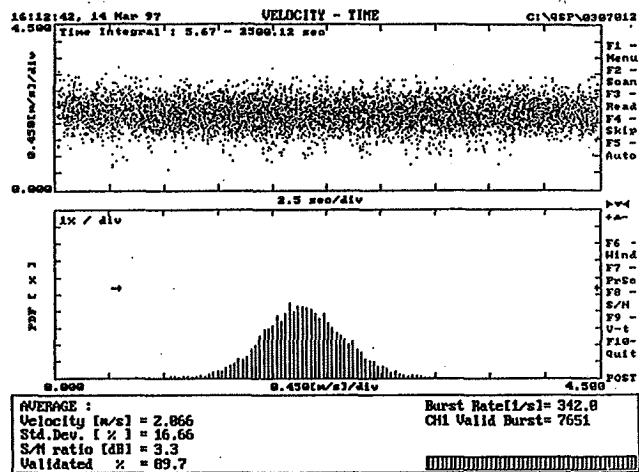
Figure 1: Velocity vs. time and pdf for turbulent non-reacting jet in 0g
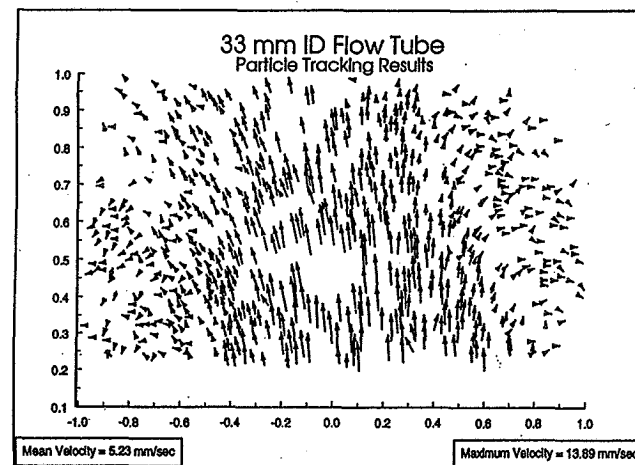
Figure 3: Velocity map for low velocity non-reacting jet in normal gravity
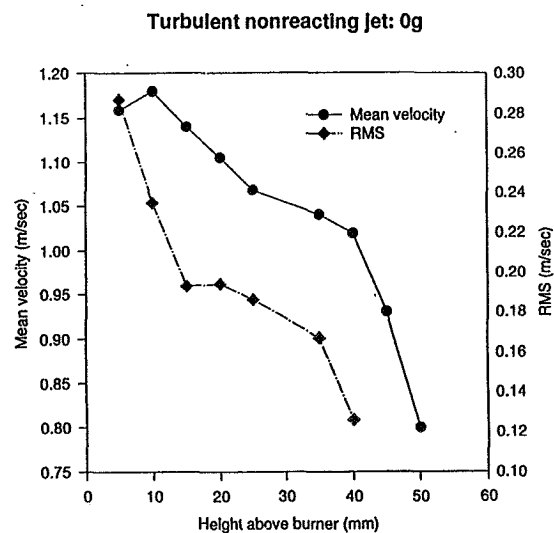
Figure 2: Mean velocity and RMS vs. height above burner for turbulent non-reacting jet in 0g
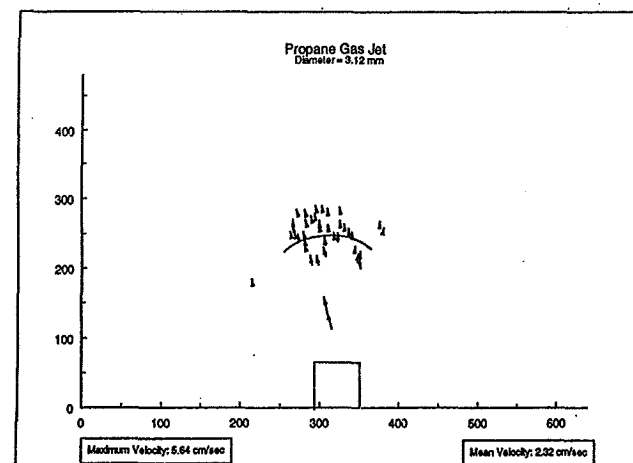
Figure 4: Velocity map for propane jet diffusion flame in 0g
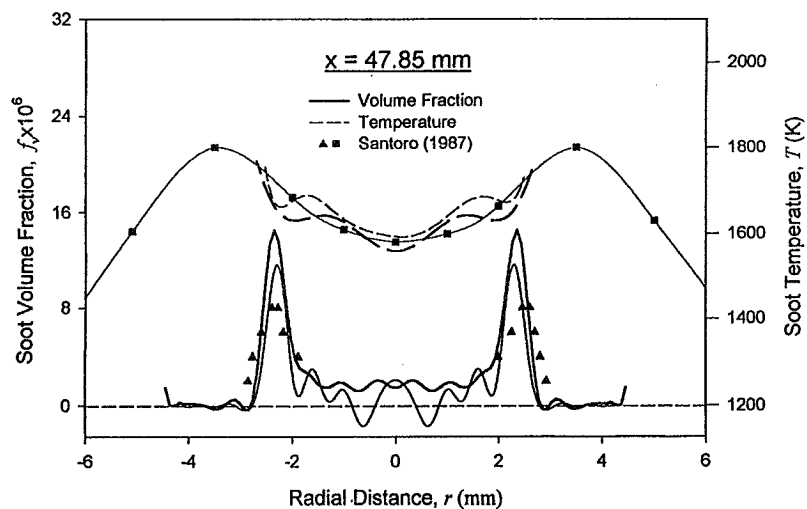
Figure 5: Soot volume fraction and temperature for 3.85 cc/sec laminar ethylene diffusion flame
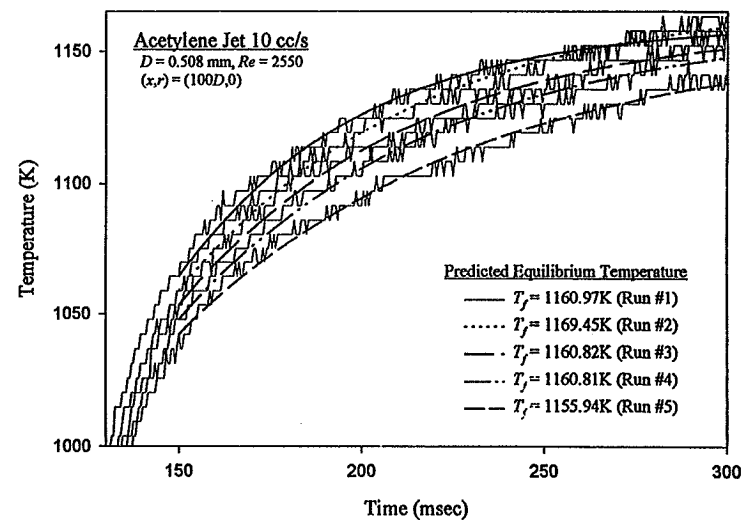
Figure 7: Transient response of 1 mil thermocouples in Re 2550 turbulent jet acetylene flame
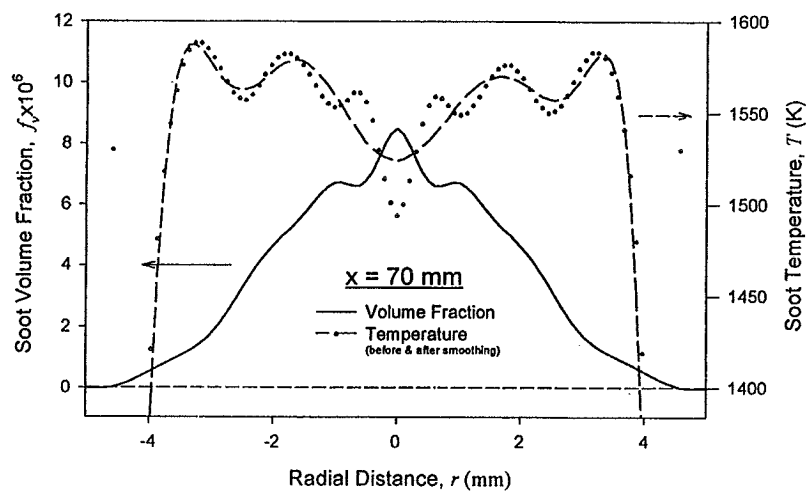
Figure 6: Soot volume fraction and temperature for Re 2550 turbulent jet acetylene flame
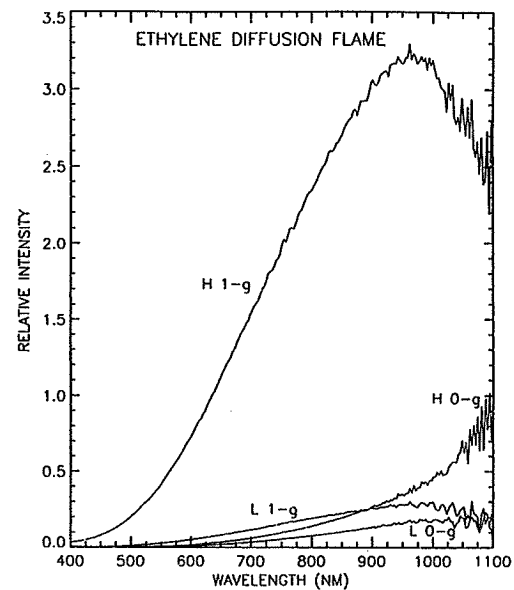
Figure 8: Spectral emission from ethylene jet diffusion flame in normal and reduced gravity
H: 9-10 mm above burner; L: 5-7 mm above burner

Real Time Quantitative 3-D Imaging of Diffusion Flame Species[*]

Daniel J. Kane and Joel A. Silver
Southwest Sciences, Inc.
Santa Fe, New Mexico

Introduction

A low-gravity environment, in space or ground-based facilities such as drop towers, provides a unique setting for study of combustion mechanisms. Understanding the physical phenomena controlling the ignition and spread of flames in microgravity has importance for space safety as well as better characterization of dynamical and chemical combustion processes which are normally masked by buoyancy and other gravity-related effects. (refs. 1,2) Even the use of so-called "limiting cases" or the construction of 1-D or 2-D models and experiments fail to make the analysis of combustion simultaneously simple and accurate.

Ideally, to bridge the gap between chemistry and fluid mechanics in microgravity combustion, species concentrations and temperature profiles are needed throughout the flame. However, restrictions associated with performing measurements in reduced gravity, especially size and weight considerations, have generally limited microgravity combustion studies to the capture of flame emissions on film or video (refs. 3-6) laser Schlieren imaging (ref. 1) and (intrusive) temperature measurements using thermocouples. Given the development of detailed theoretical models, more sophisticated studies are needed to provide the kind of quantitative data necessary to characterize the properties of microgravity combustion processes as well as provide accurate feedback to improve the predictive capabilities of the computational models.

While there have been a myriad of fluid mechanical visualization studies in microgravity combustion, little experimental work has been completed to obtain reactant and product concentrations within a microgravity flame. This is largely due to the fact that traditional sampling methods (quenching microprobes using GC and/or mass spec analysis) are too heavy, slow, and cumbersome for microgravity experiments. Non-intrusive optical spectroscopic techniques have — up until now — also required excessively bulky, power hungry equipment. However, with the advent of near-IR diode lasers, the possibility now exists to obtain reactant and product concentrations and temperatures *non-intrusively* in microgravity combustion studies.

Over the past ten years, Southwest Sciences has focused its research on the high sensitivity, quantitative detection of gas phase species using diode lasers. Our research approach combines three innovations in an experimental system resulting in a new capability for nonintrusive measurement of major combustion species. FM spectroscopy or high frequency wavelength modulation spectroscopy (WMS) have recently been applied to sensitive absorption measurements at Southwest Sciences and in other laboratories using GaAlAs or InGaAsP diode lasers in the visible or near-infrared (refs. 7-9) as well as lead-salt lasers in the mid-infrared spectral region (refs. 10-14). Because these lasers exhibit essentially no source noise at the high detection frequencies employed with this technique, the achievement of sensitivity approaching the detector shot noise limit is possible. Such high sensitivity permits the *in situ* detection of chemical species of interest such as water, methane, O_2, CO, CO_2, OH, *etc*.

Review of Relevant Research

Most of the studies of microgravity combustion research of gas diffusion flames have centered on macroscopic observables. High-speed film based and CCD cameras have been used to compare flame size under microgravity conditions with flame sizes under normal gravity (ref. 3). Flame sizes, time to steady state and extinguishment have all been examined as a function of Reynolds number (refs. 3-6). Diffusion flame temperatures have been measured using thermocouples. Rainbow Schlieren deflectometry has been developed to glean temperature profiles of flames and techniques to monitor soot production have been developed (ref. 1). Numerous theoretical studies have also been completed on gas jet flames in microgravity (refs. 1,5,6). However, little work has been

---

completed which quantitatively monitors species concentration under microgravity conditions. Especially disconcerting is the fact that even fundamental properties such as spatially resolved temperatures in microgravity flames are poorly known. Existing models are obviously sensitive to temperature, but cannot predict it well either (ref. 15).

The candle flame has long been used as an example of the prototypical combustion source. In microgravity, it becomes spherical, with little or no sooting. The flame is larger and cooler than in normal gravity, since diffusion gradients are smaller. Studies of simple candles burning in microgravity (ref. 16) especially those in the USML-1 Space Shuttle flight (where μ-g time was not a limiting factor) (ref. 17) reveal a number of interesting results. The flame diameter rapidly reaches a steady state value after ignition whereas the flame height sometimes decreases with time, increases, or remains the same. Extinction usually occurs within 60 seconds, preceded by a five second period of oscillations. According to the original expectation, these flames should last about three minutes (based on the initial amount of O_2 present). However, due to the design of the experimental enclosure (a perforated box inside of a larger chamber), calculations suggest that the flames extinguish early due to diffusional limitations of O_2 to the flame.

A second experiment has shown it impossible to sequentially ignite two nearby candles, where the second is within the flame diameter of the first. This effect could be due to a diffusion limitation of available oxygen to the second candle (where the first candle is burning at a diffusion limited rate), the expansion of hot product gases which may lower the ability of O_2 to diffuse, or a combination of the two. For both cases, the determination of localized temperature and water concentrations would be of great assistance in unraveling the effects of chemistry and diffusion.

On another USML-1 experiment (ref. 18), wire insulation flammability tests under various oxidizer flow conditions suggest that diffusion limitations were the cause of the observed results. In particular, it was suggested that vaporized insulation gases may mix with oxygen in a region near enough to the hot wire to cause a gas phase ignition, a situation which would be less likely in 1-g, where buoyancy effects might convect these gases away from its possible ignition source. Similar problems in understanding microgravity combustion of liquid pools (ref. 15), nonpremixed (refs. 19,20) and premixed (ref. 21) flames also exist.

The first quantitative measurements of species concentrations in microgravity flames focused on detection of water vapor and methane in nonpremixed diffusion jets (ref 19). A near-infrared diode laser operating at 1.341 μm was used in most of the experiments to detect water vapor in propane and methane flames. The instrument utilized fiber optics to direct the diode laser radiation into eight detection channels for simultaneous measurements along multiple lines of sight. These fiber optics pipe the laser beam (all control and acquisition electronics remained at the top of the drop tower) to the μ-g flame region through a suspended multifiber cable. A fiber optic splitter transmits eight beams across the flame (for spatial resolution) which are recaptured and focused into eight return fibers. A high speed data acquisition system allows a detection bandwidth of 10 Hz. Complete WMS absorption spectra are acquired along each line-of-sight to provide temporal-spatial maps of the water vapor concentration during the drop. The results from these experiments suggest that large amounts of water vapor occur at distances removed from the outer surface of the flame, where theoretical predictions do not expect any water vapor. These concentrations are not seen in normal gravity flames. In comparing pre- and post-ignited flames, this shell had different appearances. It is closer to the flame center in the pre-ignited case and does not extend to outer radii as rapidly. Clearly, a chemical steady state is not achieved in any of these experiments, as diffusion occurred over nearly the two seconds during which the flame (according to the videos) appeared stable.

Objective of This Research

We want to develop a better understanding of the roles of ignition, diffusion and turbulence in microgravity diffusion flames. To accomplish this goal, we will develop imaging high-frequency Wavelength Modulation Spectroscopy (WMS). With this new technique, we will be able to monitor strong absorbers such as water, methane, and possibly hydroxyl radicals. By coupling the imaging of water vapor with the imaging of methane in diffusion flames, we will be able to localize reaction zones in the flame leading to a better understanding of the roles of diffusion and buoyancy.

We will start our project by obtaining time-dependent water vapor concentration profiles of combustion in microgravity conditions using WMS and a near-infrared diode laser. The strong absorption line strengths of water make detection by optical means attractive and will allow 2-D absorption images to be obtained in real time. By taking advantage of flame symmetry, these absorption images should be readily transformable to 3-D concentration profiles. By using two closely spaced water lines with different temperature dependencies, flame temperature profiles can be determined. This technique has the advantage over other laser-based methods as being simple and inexpensive to implement, provides signals which are directly linear in concentration, and is easily calibrated to provide accurate quantitative results. First, to test the system, we will obtain water vapor concentration profiles and temperature profiles of candle flames. These studies for water will then be extended to diffusion jets of varying Reynolds number.

282

Later, we will move to methane (and/or hydroxyl radicals) which is a weaker absorber.

We will also examine the reaction zone in a methane and air diffusion flame in a Wolfhard-Parker slot burner (ref. 22). This type of burner creates a two-dimensional diffusion flame, so that we will not have to apply any transforms to obtain 3-D species and temperature profiles. Hence, we will be able to examine the reaction zone in this flame at virtually any resolution. Any changes in the reaction zone will be observed when the transition is made from 1-g to μ-g or flow rates are changed. Our previous microgravity water vapor absorption experiments of gas jet diffusion flames showed high concentrations of water at much greater radii than theoretical models predicted. We believe this to be a result of ignition. This will be another problem we will address in this project. These measurements of water vapor, temperature and methane in diffusion flames and candle flames will provide time and spatial resolutions sufficient to answer many outstanding questions concerning the relative effects of diffusion and kinetic limitations on observed combustion properties.

Finally, we will investigate the effects of different ignition sources on flame properties. Temporal water vapor concentrations and gas temperatures will be measured as a function of flame ignition source (spark, hot wire) for both pre- and post-drop situations. The transition of pre-ignited flames to microgravity will also be observed as part of this task. In this Section, we describe the technical approach and experimental details describing how these methods will be applied.

Spectroscopy in the Near-Infrared

We use the HITRAN (ref. 23) spectral database and data published by Delaye (ref. 24) to determine H_2O line positions, line strengths, linewidth parameters, and temperature dependencies. Our previous work with near-infrared diode laser detection of water vapor in combustion systems shows these strong overtone lines are free from spectral interferences by other gases.

A strong $2v_3$ band of methane near 1659 nm also exists and is now accessible with recently available lasers. Again, the HITRAN database provides useful spectroscopic information that has been confirmed by some of our previous experiments. In our recent μ-g experiments, we utilized the R(1) line in the v_3 band. The proposed experiments will use the stronger R(3) line. Finally, OH (hydroxyl radical) exhibits many absorption lines lying between 1.4 and 1.5 μm. We have used a low pressure, laboratory burner to identify several strong OH lines that are free from interference by water vapor.

Near-IR Diode Lasers for High Resolution Spectroscopy

The light sources used for this project will be distributed-feedback (DFB) InGaAsP diode lasers operating near 1393 nm for water vapor, 1659 nm for methane, and 1480 nm for OH. For spectroscopic applications, the wavelength of diode lasers may be tuned by changing the laser temperature or injection current. The InGaAsP lasers operate at room temperature, and coarse tuning of the laser wavelength can be accomplished by varying the laser temperature using a thermoelectric cooler. High resolution wavelength tuning is obtained by varying the laser injection current. The type of lasers to be used in this program have a temperature tuning rate of approximately 0.08 nm/°C, so that under normal conditions (-20 to +40°C), a tuning range of about 4.8 nm (25 cm^{-1}) is expected. This overlaps a number of suitable absorption lines for each gas of interest. Single mode output powers range from 1 to 5 mW.

High Frequency Wavelength Modulation Spectroscopy

While for abundant, strongly absorbing species such as water differential absorption is adequate, for less abundant species such as methane a more sensitive detection approach is required. High frequency laser wavelength modulation spectroscopy (WMS) is a technique used to measure the weak absorption signals or strong absorption signals very quickly. The usefulness of this method is that the WMS signals are linearly proportional to the absorber gas concentration. Unlike direct absorption, the detection sensitivity is limited by detector quantum noise and not by laser 1/f noise. This can improve the detection sensitivity by 3-4 orders of magnitude. We have described this technique in considerable detail in two recent publications, including comparisons with other high frequency diode laser detection methods (e.g. one- and two-tone frequency modulation spectroscopy) (refs. 10,11) In addition, these methods were recently applied to the measurement of water vapor in microgravity diffusion jet flames (ref. 19).

Briefly, this method, which is an extension of diode laser "derivative spectroscopy" techniques widely used at kHz frequencies (ref. 14) involves superposition of a small sinusoidal modulation at frequency f on the diode laser injection current. Typically, the

amplitude of this current modulation is characterized by the dimensionless WMS modulation index m, which reflects the magnitude of excursion in frequency space induced by the modulation. The magnitude of m is set so that the induced wavelength modulation is comparable to the width of the spectral feature under study. Normally, phase-sensitive electronics demodulate the photocurrent at the modulation frequency, f, or a harmonic, nf. In the small modulation limit, the WMS lineshape is the nth derivative of the original molecular absorption lineshape. In practice, the modulation index is set at a value to maximize the signal level and, in this regime, lineshapes are only derivative-like but can be readily calculated.

By implementing wavelength modulation at sufficiently high frequencies, laser noise is minimal and detector-limited (ideally, shot noise-limited) sensitivity can be achieved. Our studies have shown that detection frequencies as low as 100 kHz are often sufficient to achieve these objectives, although the optimum frequency is laser dependent. The distinction between WMS and FM spectroscopy (as described, for example, in Ref. 7) is mostly semantic — FM spectroscopy is defined as using modulation frequencies comparable to the absorption linewidths (~3 GHz or greater for the present experiments), whereas WMS uses modulation frequencies much smaller than the absorption linewidths. The distinction becomes important for atmospheric pressure measurements where linewidths require modulation frequencies well into the GHz regime using the FM schemes.

Data Analysis - Spectroscopic Measurement of Species Concentration and Temperature

The measurement of concentration by diode laser absorption is based on straightforward implementation of Beer's law,

$$N = \alpha/\sigma\ell, \tag{1}$$

where N is the number density with units of cm^{-3}, α is the measured absorbance, σ is the absorption cross section, and ℓ is the absorption path length. The cross section at line center, σ_0, is related to the temperature-dependent absorption line strength, S(T), by

$$\sigma_0 = S(T) \cdot \phi(\nu_0), \tag{2}$$

where $\phi(\nu)$ is the line shape function. In the Doppler-broadened limit, which is a good approximation for measurements at combustion temperatures and pressures of 1 atmosphere or less, $\phi(\nu_0)$ has a value of 0.47 $\Delta\nu_D^{-1}$, where $\Delta\nu_D$ is the Doppler half width at half maximum. In the pressure-broadened limit, $\phi(\nu_0) = (\pi\Delta\nu_L)^{-1}$, where $\Delta\nu_L$ is the pressure broadened (Lorentzian) half width. This limit is a good approximation for measurements at room temperature and atmospheric pressure. At intermediate temperature and pressure combinations, the line shape is described by a Voigt profile, which has the analytic form at line center of $\phi(\nu_0) = \phi_D$ $\cdot \exp(a^2) \cdot \text{erfc}(a)$, where ϕ_D is the Doppler line shape at line center, given above, and $a = \sqrt{ln2} \, (\Delta\nu_L / \Delta\nu_D)$.

From the above discussion, one can see that the determination of number density by the diode laser absorption technique depends on spectroscopic parameters that are functions of temperature. The temperature dependence of the line strength S(T) can be readily calculated to very high accuracy. Thus, this parameter is well known at all temperatures provided that it has been accurately measured at one temperature. We have conducted laboratory measurements of the relevant line strengths and broadening coefficients at room temperature to verify the accuracy of the HITRAN numbers used in the analysis.

Temperature

Flame temperatures can be determined by measuring the ratio of absorption signals for two nearby absorption lines. The ratio is proportional to the ratio of line strengths, which depends only on temperature and known molecular parameters. The line strength ratio for two absorption lines is

$$\frac{S_1}{S_2} = \frac{S_1(T_0)}{S_2(T_0)} \exp[\frac{-hc\Delta E_{rot}}{k}(\frac{1}{T}-\frac{1}{T_0})] \tag{3}$$

where T_0 is a reference temperature and ΔE_{rot} is the difference in lower state rotational energy for the two lines. The 1393 nm laser does overlap a group of four closely spaced water lines. If we assume an accuracy of 5% in the WMS measurements, then temperature can be measured to approximately $\pm$ 50 K.

Experimental Hardware

The experimental design must 1) increase the spatial resolution beyond that which we had accomplished in our previous μg experiments program, 2) provide a 2-D absorption profile so that the entire flame can be covered in a single drop, 3) have the optics, burner, gases, laser, camera, computer and data acquisition, and batteries fit on the drop tower rig. Since we plan to use a drop rig supplied by NASA, our system must be extremely compact. The laser and all other electronics are solid state devices so they can withstand the moderate g-levels present at impact of the drop tower rig.

The optical layout is fairly simple. The laser is collimated by an anti-reflection coated gradient index (GRIN) lens to a diameter of ~1 mm, and is pointed into an X-Y optical scanner placed at the focus of an off-axis paraboloid. This will raster the laser beam across the flame. A second off-axis paraboloid will focus the beam onto a single detector. We expect this device to have an image rate of about 200,000 pixels per second allowing 100×100 arrays to be obtained at a rate of 20 Hz. This high data rate is attainable because of the large signal-to-noise obtained when using WMS. The high bandwidth requirements of imaging will force a modulation frequency of 5 MHz and a detection frequency of 10 MHz. Raster scanning will also allow the amount and position of the scan to be controlled so that different parts of the flame may be analyzed at varying temporal and spatial resolutions. For example, in some of the experiments we plan to use a Wolfhard-Parker slot burner to provide axial symmetry. Since no (Abel) transform will be needed, we can increase the resolution to concentrate on only the portions of the flame of interest such as the reaction zone (ref. 25). Ultimately, we hope to obtain the water and methane concentration over this region along with the temperatures.

Planned Experiments

We hope to conduct the following experiments during the project:

1) Obtain water vapor profiles and temperature profiles of μg candle flames as an initial shake down of the system.

2) Obtain methane concentrations, water vapor concentrations, and temperature profiles of the reaction zone in a laminar methane-air diffusion flame using a Wolfhard-Parker slot burner (methane measurements may not require WMS in these experiments).

3) Map out 3-D methane concentrations, water vapor concentrations, and temperature profiles of gas jet diffusion flames using an Abel transform (ref. 26). We will also examine ignition effects, various flow rates, and transitions from 1-g to μ-g flames.

References

1. Proc. Second International Microgravity Combustion Workshop, NASA Conference Pub. 10113, Cleveland, OH (1992.)
2. H.D. Ross, "Neither Up Nor Down: A Perspective on Combustion Science in Microgravity," Fall Meeting of the Eastern States Section of The Combustion Institute (October, 1993), preprint.
3. M. Y. Bahadori, R. B. Edelman, D. P. Stocker, and S. L. Olsen, AIAA Journal **28**, 236 (1990).
4. T. H. Cochran and W. J. Mascia, "An Investigation of Gravity Effects on Laminar Gas-Jet Diffusion Flames," NASA TN D-5872 (1970).
5. R. B. Edelman, O. F. Fortune, G. Weilerstein, T. H. Cochran, and J. B. Haggard, "An Analytical and Experimental Investigation of Gravity Effects upon Laminar Gas Jet-Diffusion Flames," *Fourteenth Symposium on Combustion*, The Combustion Institute, Pittsburgh, PA, 399 (1973).
6. R. B. Edelman and M. Y. Bahadori, Acta Astronautica **13**, 681 (1986).
7. D.B. Oh, A.C. Stanton and J.A. Silver, J. Phys. Chem. **97**, 2246 (1993).
8. A.C. Stanton and J.A. Silver, Appl. Opt. **27**, 5009 (1988).
9. D. B. Oh, D. S. Bomse and A. C. Stanton, "Quantitative Measurement of O_2 in Laboratory Flames Using Near-IR Diode Lasers", 1991 OSA Annual Meeting, San Jose, CA, (1991).
10. J.A. Silver, Appl. Opt. **31**, 707 (1992).
11. D. S. Bomse, A. C. Stanton and J. A. Silver, Appl. Opt. **31**, 718 (1992).

12. J.A. Silver and A.C. Stanton, Appl. Opt. **27**, 4438 (1988).
13. J.A. Silver, D.S. Bomse, and A.C. Stanton, Appl. Opt. **30**, 1505 (1991).
14. J.A. Silver and A.C. Stanton, Appl. Opt. **26**, 2558 (1987).
15. D.N. Schiller, H.D. Ross and W.A. Sirignano, Comb. Sci. Technol., submitted for publication (1993).
16. D.L. Dietrich, H.D. Ross and J.S. Tien, "Candle Flames in Microgravity: Space Shuttle Results," Fall Meeting of the Eastern States Section of The Combustion Institute (October, 1993), preprint.
17. H.D. Ross, R.G. Sotos and J. S. Tien, Combust Sci. Technol.**75**, 155 (1991).
18. P.S. Greenberg, "Wire Insulation Flammability Experiment, "USML-1 90-Day Science Report, NASA Lewis Research Center (October 23, 1992).
19. J.A. Silver, D.J. Kane and P.J. Greenberg, Appl Opt. **34**, 2787 (1995).
20. M.Y. Bahadori and R.B. Edelman, SAI Corp. Final Report for Contract No. NAS3-22822, August, 1992, and references therein.
21. A. Abdul-Madrid and P.D. Ronney, Int. Symp. on Combust. **23**, 423 (1990).
22. K. C. Smyth, J. H. Miller, R. C. Dorfman, W. G. Mallard, and R. J. Santoro, Combustion and Flame **62**, 157 (1985).
23. L. S. Rothman, R. R. Gamache, R. H. Tipping, C. P. Rinsland, M. A. H. Smith, D. C. Benner, V. Malathy Devi, J.-M. Flaud, C. Camy-Peyret, A. Perrin, A. Goldman, S. T. Massie, L. R. Brown, and R. A. Toth, "The HITRAN Molecular Database: Editions of 1991 and 1992," **48**, 469 (1992).
24. C. Delaye, J. M. Hartmann, and J. Taine, Appl. Opt. **28** 5080 (1989).
25. M. Gerstein, Int'l Symp. Combust. 4, **35** (1953).
26. C. Dasch, Appl. Opt. **31**, 1146 (1992).

ELUCIDATION OF FREE RADICAL AND OPTOGALVANIC SPECTROSCOPY ASSOCIATED WITH MICROGRAVITY COMBUSTION VIA CONVENTIONAL AND NOVEL LASER PLATFORMS

PRABHAKAR MISRA*, Yong-Bo She, Xinming Zhu and Michael King
Laser Spectroscopy Laboratory
Department of Physics and Astronomy
Howard University, Washington, D.C. 20059

Introduction and Overview

Combustion studies under both normal gravity and microgravity conditions depend a great deal on the availability and quality of the diagnostic systems used for such investigations. Microgravity phenomena are specially susceptible to even small perturbations and therefore non-intrusive diagnostic techniques are of paramount importance for successful understanding of reduced-gravity combustion phenomena. Several non-intrusive diagnostic techniques are available for probing and delineating normal as well as reduced gravity combustion processes, such as Rayleigh scattering, Raman scattering, Mie scattering, velocimetry, interferometric and Schlieren techniques, emission and laser-induced fluorescence (LIF) spectroscopy. Our approach is to use the LIF technique as a non-intrusive diagnostic tool for the study of combustion-associated free radicals (refs. 1 and 2) and use the concomitant optogalvanic transitions to accomplish precise calibration of the laser wavelengths used for recording the excitation spectra of transient molecular species. In attempting to perform spectroscopic measurements on chemical intermediates, we have used conventional laser sources as well as new and novel platforms employing rare-earth doped solid-state lasers (ref. 3).

Conventional (commercially available) sources of tunable UV laser radiation are extremely cumbersome and energy-consuming devices that are not very suitable for either in-space or in-flight (or microgravity drop tower) experiments. Traditional LIF sources of tunable UV laser radiation involve in addition to a pump laser (usually a Nd:YAG laser with an attached frequency-doubling stage), a tunable dye laser. In turn, the dye laser has to be provided with a dye circulation system and a subsequent stage for frequency-doubling of the dye laser radiation, together with a servo-tuning system (termed the "Autotracker") to follow the wavelength changes and also an optical system (called the "Frequency Separator") for separation of the emanating visible and UV beams as illustrated in Figure 1. In contrast to this approach, we have devised an alternate arrangement for recording LIF excitation spectra of free radicals (following appropriate precursor fragmentation) that utilizes a tunable rare-earth doped solid state laser system with direct UV pumping.

We have designed a compact and portable tunable UV laser system incorporating features necessary for both in-space and in-flight spectroscopy experiments. For the purpose of LIF excitation, we have developed an all-solid-state tunable UV laser that employs direct pumping of the solid-state UV-active medium employing UV harmonics from a Nd:YAG laser. An optical scheme with counterpropagating photolysis and excitation beams focused by suitable lenses into a reaction vacuum chamber (as shown in Fig. 2) was employed.

Results and Discussion

Free radicals, such as hydroxyl (OH) and alkoxy (RO; R=CH_3, C_2H_5), are important chemical intermediates in many combustion processes. In particular, LIF is a powerful non-intrusive method to study the spectroscopic characterization of such free radicals and their chemical kinetics in a flame environment under both normal gravity and microgravity combustion conditions.

*Corresponding Author

287

Ethoxy (C_2H_5O), for example, is an important alkoxy radical produced in combustion and oxidation processes involving hydrocarbons. Spectroscopic studies of the ethoxy radical have received much less attention than the first member of the alkoxy family, methoxy (CH_3O). We have performed an extensive laser excitation study of the rovibrationally cold ethoxy radical. A typical laser excitation fluorescence spectrum of the B ^{2}A'-X ^{2}A" system for the C_2H_5O radical is shown in Figure 3, while Table 1 summarizes the observed bands in the excitation spectrum in the 29181-32139 cm^{-1} range. Seven molecular vibrational frequencies have been determined for the excited B ^{2}A' state and eight frequencies for the ground state X ^{2}A". In addition, vibrational and anharmonic constants for the C-O stretch mode have been determined via least-square fits for both electronic states.

We have also studied the chemical kinetics of the methoxy (CH_3O) free radical in presence of nitrogen dioxide (NO_2) employing time-resolved LIF-spectroscopy. The concentration depletion of the methoxy free radical was monitored by variations in LIF-intensity and a Stern-Volmer plot provided the reaction rate constant $k = 5.918 \times 10^{-12}$ cm^3/molecule.sec at room temperature. Measurements were also conducted at higher temperatures (upto 200° C), and the activation energy of the reaction between methoxy and nitrogen dioxide was determined to be $E_A = -4.876$ kJ/mol. Figure 4 shows the Arrhenius plot obtained for the pseudo-second order rate constant for the reaction of CH_3O with NO_2, while Figure 5 illustrates a comparison of the experimental and theoretical logarithms of the rate constants for the corresponding recombination reaction.

In connection with LIF spectroscopy experiments, precise wavelength calibration of the tunable lasers used is very important (ref. 4). There do exist some optogalvanic (OG)-spectral wavelength tables in literature. However, very few of the compilations are either available or complete enough for calibrating the tunable laser output, especially at longer visible wavelengths and in the ultra-violet (UV) optical region The laser-assisted optogalvanic (LOG) effect provides a good solution for existing wavelength calibration inadequacies in the visible and near UV regions of the electromagnetic spectrum. The LOG effect is sensitive to the species present in a gas discharge medium, and it is convenient for direct calibration of the tunable laser output in our experiments. We have conducted a detailed study of OG-transitions using a commercial Fe-Ne hollow cathode lamp, especially in the wavelength ranges 291-317 nm and 607-662 nm. More than 167 OG-spectral lines have been recorded in these two wavelength regimes, of which sixty have been successfully assigned to neon atomic transitions. Some of these LOG transitions are illustrated in Fig. 6. These OG spectral transitions (summarized in Table 2) have proved very useful in the precise and reliable calibration of LIF excitation studies of combustion-associated free radicals. It is envisioned that the laser spectroscopic and the associated optogalvanic investigations will prove of value for the elucidation of both normal gravity and microgravity combustion phenomena.

Acknowledgement

References

1. P. Misra, X. Zhu, C.-Y. Hsueh, and J.B. Halpern, "Laser excitation and emission spectroscopy of the methoxy radical in a supersonic jet," *Chem. Phys.* **178**, 377-385 (1993).
2. X. Zhu, M.M. Kamal, and P. Misra, "Laser-induced excitation and dispersed fluorescence spectra of the ethoxy radical," *Pure & Applied Optics* **5**, 1021-1029 (1996).
3. M.A. Dubinskiy, M.M. Kamal, and P. Misra, "An innovative approach to the development of a portable unit for analytical flame characterization in a microgravity environment," *Proceedings of the Third International Microgravity Combustion Workshop*, NASA Lewis Research Center, Cleveland, OH, 1995, pp. 263-268.
4. X. Zhu, A.H. Nur, and P. Misra, "Laser optogalvanic wavelength calibration with a commercial hollow cathode iron-neon discharge lamp," *J. Quant. Specrosc. Radiat. Transfer* **52**, 167-177 (1994).

288
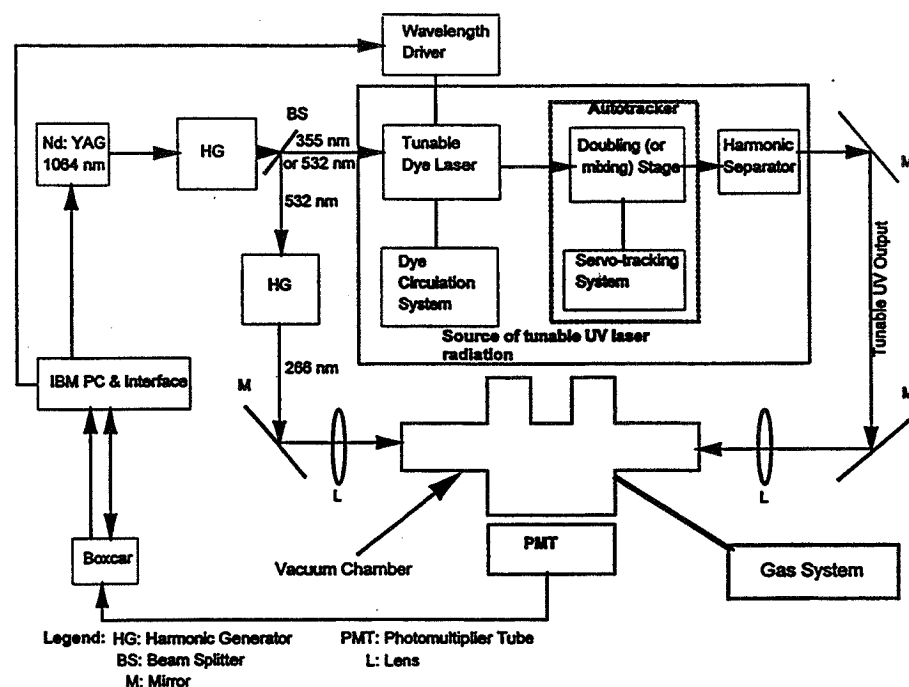
Fig. 1 Conventional arrangement for recording the Laser Induced Fluorescence (LIF) excitation spectra of free radicals (following precursor laser fragmentation) using dye laser-based multiple frequency conversion technology for obtaining tunable UV laser radiation.
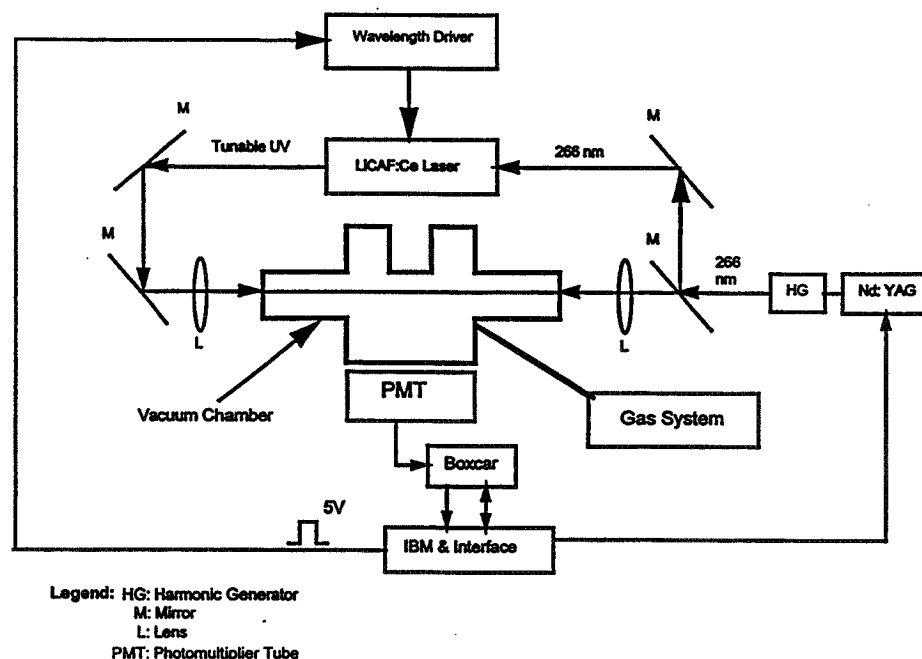
Fig. 2 Advanced arrangement for recording LIF excitation spectra of free radicals (following precursor laser fragmentation) based on a tunable LiCAF:Ce laser with direct UV pumping.
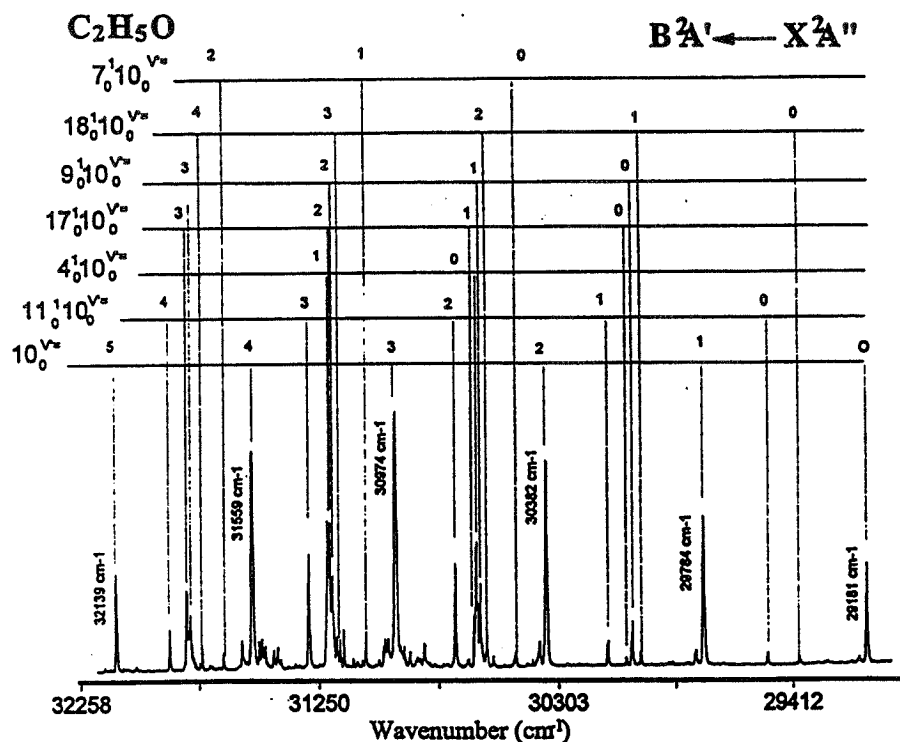
Fig. 3 Laser excitation fluorescence spectrum of the B $^2A'$ - X $^2A''$ system of the C_2H_5O radical. The time delay between the excimer laser and the dye laser was 8 μs.

Table 1 Observed bands in the C_2H_5O B $^2A'$ - X $^2A''$ excitation spectrum.

Wavenumber (cm^{-1})	Relative intensity	Rel. to 10_0^0 (cm^{-1})	Vibrational assignment	Wavenumber (cm^{-1})	Relative intensity	Rel. to 10_0^0 (cm^{-1})	Vibrational assignment
29 181	272	0	10_0^0	31 005	78	1824	$a_0^1 10_0^3$
29 210	35	29	a_0^1	31 017	77	1836	$b_0^1 10_0^3$
29 236	23	55	b_0^1	31 096	52	1915	$7_0^1 10_0^1$
29 425	38	244	18_0^1	31 109	30	1928	
29 543	47	362	11_0^1	31 133	19	1952	
29 784	321	603	10_0^1	31 147	23	1966	
29 812	40	629	$a_0^1 10_0^1$	31 170	15	1989	
29 845	22	664	$b_0^1 10_0^1$	31 187	107	2006	
30 022	50	841	$18_0^1 10_0^1$	31 202	82	2021	$18_0^1 10_0^3$
30 050	129	869	17_0^1	31 213	68	2032	
30 074	35	893	9_0^1	31 230	230	2049	$4_0^1 10_0^1$
30 146	62	965	$11_0^1 10_0^1$	31 249	381	2068	$9_0^1 10_0^2$
30 382	524	1201	10_0^2	31 241	349	2060	$17_0^1 10_0^2$
30 410	75	1229	$a_0^1 10_0^2$	31 326	226	2145	$11_0^1 10_0^3$
30 437	30	1256	$b_0^1 10_0^2$	31 559	555	2378	10_0^4
30 504	50	1323	7_0^1	31 599	80	2418	$a_0^1 10_0^4$
30 614	94	1433	$18_0^1 10_0^2$	31 679	34	2498	$a_0^1 10_0^4$
30 641	197	1460	4_0^1	31 770	59	2589	$18_0^1 10_0^4$
30 653	327	1472	$17_0^1 10_0^1$	31 819	135	2638	
30 665	142	1484	$9_0^1 10_0^1$	31 833	210	2652	$9_0^1 10_0^3$
30 740	200	1559	$11_0^1 10_0^2$	31 907	84	2726	$11_0^1 10_0^4$
30 974	628	1793	10_0^3	32 139	218	2958	10_0^5

Fig. 4   Arrhenius plot of the pseudo-second order rate constant for the reaction of CH_3O and NO_2.

Fig. 5   A comparison of the experimental and theoretical Arrhenius plots for the recombination reaction of CH_3O with NO_2.

291

Table 2 Observed optogalvanic spectral lines and their assignments using a commercial Fe-Ne hollow cathode tube.

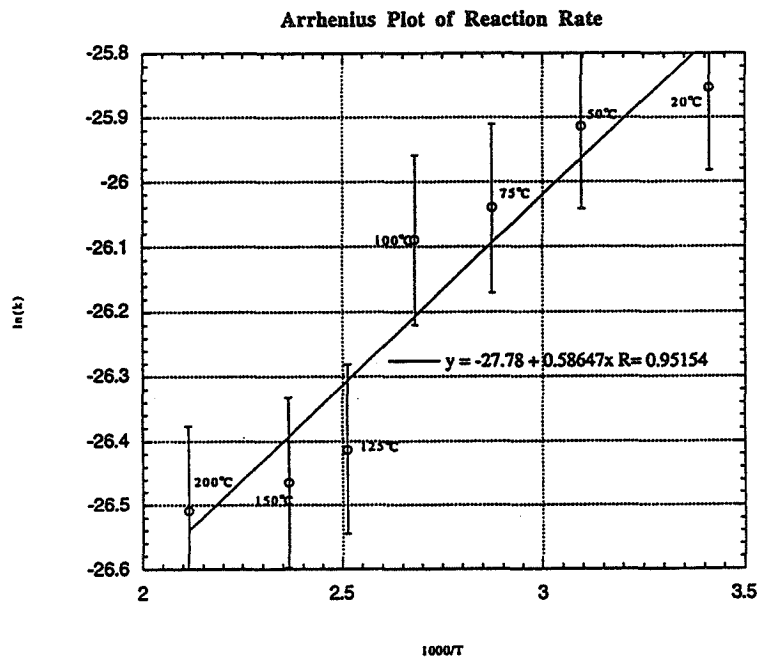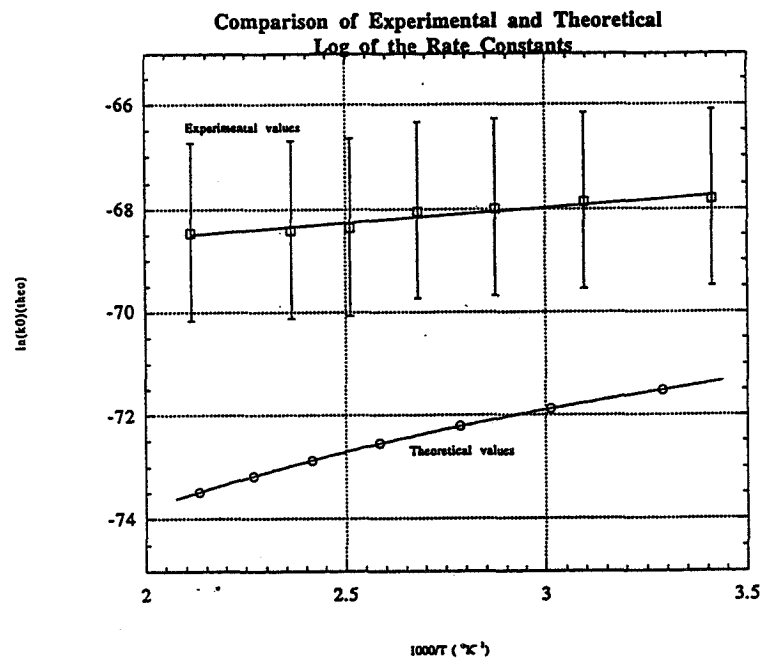| Wavelength (nm)	Ion	Assignment	Wavelength (nm)	Ion	Assignment
291.146	Ne I	$3s[3/2]^{\circ}2 - 5p'[3/2]2$	588.190	Ne I	$3s[3/2]^{\circ}2 - 3p'[1/2]1$
291.317	Ne I	$3s[3/2]^{\circ}2 - 5p'[1/2]1$	594.483	Ne I	$3s[3/2]^{\circ}2 - 3p'[3/2]2$
292.931	Ne I	$3s[3/2]^{\circ}1 - 5p'[1/2]0$	596.162	Ne I	$3p'[1/2]1 - 4d'[3/2]^{\circ}1$
293.272	Ne I	$3s'[1/2]^{\circ}1 - 6p[1/2]0$	596.547	Ne I	$3p'[1/2]1 - 4d'[3/2]^{\circ}2$
294.458	Ne I	$3s'[1/2]^{\circ}1 - 6p[3/2]1$	596.617	Ne I	$3p'[1/2]1 - 4d'[5/2]^{\circ}2$
294.673	Ne I	$3s'[1/2]^{\circ}1 - 6p[5/2]2$	597.553	Ne I	$3s[3/2]^{\circ}2 - 3p'[3/2]1$
294.730	Ne I	$3s[3/2]^{\circ}1 - 5p'[3/2]2$	607.434	Ne I	$3s[3/2]^{\circ}1 - 3p[1/2]0$
294.904	Ne I	$3s[3/2]^{\circ}1 - 5p'[1/2]1$	609.616	Ne I	$3s[3/2]^{\circ}1 - 3p'[3/2]2$
294.932	Ne I	$3s[3/2]^{\circ}1 - 5p'[3/2]1$	611.803	Ne I	$3p[3/2]2 - 5s'[1/2]^{\circ}1$
295.253	Ne I	$3s'[1/2]^{\circ}1 - 5p[1/2]1$	612.846	Ne I	$3s[3/2]^{\circ}1 - 3p'[3/2]1$
295.730	Ne I	$3s[3/2]^{\circ}2 - 4f'[5/2]3$	614.306	Ne I	$3s[3/2]^{\circ}2 - 3p[3/2]2$
297.228	Fe I	$a^5P_2 - 1^5D_3$	616.359	Ne I	$3s'[1/2]^{\circ}0 - 3p'[1/2]1$
297.471	Ne I	$3s[3/2]^{\circ}2 - 5p[3/2]2$	617.529	Ne I	$3p'[3/2]2 - 4d[5/2]^{\circ}2$
297.552	Ne I	$3s[3/2]^{\circ}2 - 5p[3/2]1$	618.215	Ne I	$3p[5/2]3 - 5s[3/2]^{\circ}2$
297.981	Ne I	$3s[3/2]^{\circ}2 - 5p[5/2]2$	612.388	Ne I	$3p[5/2]2 - 5s[3/2]^{\circ}1$
298.064	Ne I	$3s'[1/2]^{\circ}0 - 5p'[1/2]1$	621.728	Ne I	$3s[3/2]^{\circ}2 - 3p[3/2]1$
298.092	Ne I	$3s'[1/2]^{\circ}0 - 5p'[3/2]1$	624.673	Ne I	$3p[5/2]2 - 5s[3/2]^{\circ}2$
298.266	Ne I	$3s[3/2]^{\circ}2 - 5p[5/2]3$	624.959	Ne I	$3p'[1/2]0 - 6s[3/2]^{\circ}1$
301.735	Ne I	$3s[3/2]^{\circ}1 - 5p[5/2]2$	626.650	Ne I	$3s'[1/2]^{\circ}0 - 3p'[3/2]1$
303.031	Ne I	$3s[3/2]^{\circ}0 - 5p[3/2]1$	627.302	Ne I	$3p'[1/2]1 - 4d[1/2]^{\circ}1$
304.595	Ne I	$3s'[1/2]^{\circ}0 - 5p[3/2]1$	630.479	Ne I	$3s[3/2]^{\circ}1 - 3p[3/2]2$
305.739	Ne I	$3s'[1/2]^{\circ}1 - 5p'[1/2]0$	631.369	Ne I	$3p[3/2]1 - 5s'[1/2]^{\circ}0$
306.370	Ne I	$3s'[1/2]^{\circ}0 - 5p[1/2]1$	633.443	Ne I	$3s[3/2]^{\circ}2 - 3p[5/2]2$
307.697	Ne I	$3s'[1/2]^{\circ}1 - 5p'[3/2]2$	636.501	Ne I	$3p[3/2]1 - 5s[3/2]^{\circ}1$
307.888	Ne I	$3s'[1/2]^{\circ}1 - 5p'[1/2]1$	638.299	Ne I	$3p[3/2]^{\circ}1 - 3p[3/2]1$
307.918	Ne I	$3s'[1/2]^{\circ}1 - 5p'[3/2]1$	640.225	Ne I	$3s[3/2]^{\circ}2 - 3p[5/2]3$
312.620	Ne I	$3s'[1/2]^{\circ}1 - 5p[1/2]0$	650.653	Ne I	$3s[3/2]^{\circ}1 - 3p[5/2]2$
314.770	Ne I	$3s'[1/2]^{\circ}1 - 5p[3/2]2$	653.288	Ne I	$3s'[1/2]^{\circ}0 - 3p[3/2]1$
314.861	Ne I	$3s'[1/2]^{\circ}1 - 5p[3/2]1$	659.895	Ne I	$3s'[1/2]^{\circ}0 - 3p'[1/2]1$
315.341	Ne I	$3s'[1/2]^{\circ}1 - 5p[5/2]2$			
316.758	Ne I	$3s'[1/2]^{\circ}1 - 5p[1/2]1$			
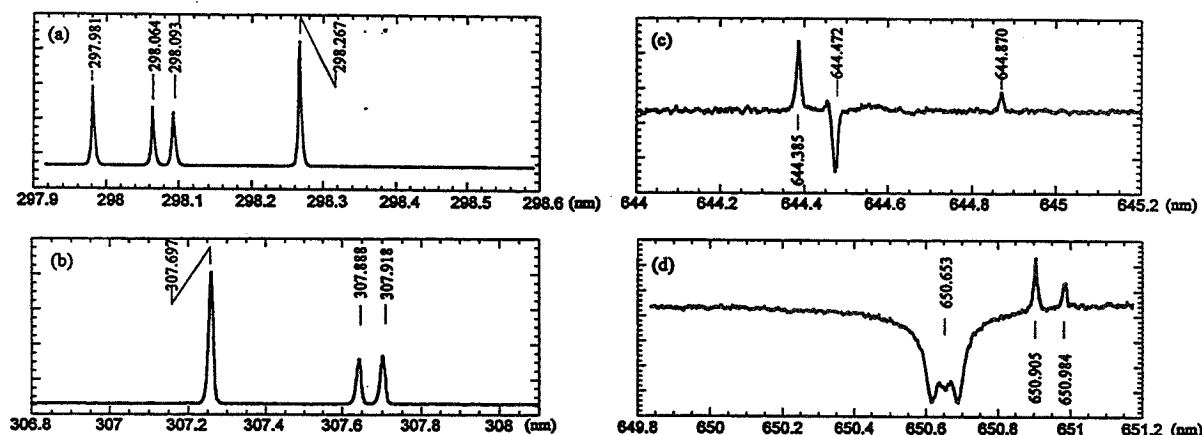
Fig. 6 Observed laser optogalvanic spectral transitions using a commercial Fe-Ne hollow cathode tube. Spectra (a) and (b) are portions of the OG-spectra of Ne I in the UV-optical region 297.9 - 298.6 nm and 306.8 - 308.2 nm, respectively. Spectra (c) and (d) are portions of the OG-spectra in the visible region 644.0 - 645.2 nm and 649.8 - 651.2 nm, respectively. A Nd:YAG-laser (Spectra-Physics GCR-11)-pumped tunable dye laser (PDL-3) that is frequency-doubled was used as the excitation light source. R610, R640, DCM and (R640+DCM) dye solutions were used in the dye laser to cover the wide optical region studied. The OG-spectra were recorded at a laser output energy of about 10 μJ in the UV, and the discharge voltage and current across the hollow cathode tube were 200 V and 1 mA. The spectra were recorded by using a boxcar averager in conjunction with a microcomputer.

QUANTITATIVE MEASUREMENT OF OXYGEN IN MICROGRAVITY COMBUSTION*

JOEL A. SILVER
Southwest Sciences, Inc.
Santa Fe, New Mexico

Introduction

A low-gravity environment, in space or in ground-based facilities such as drop towers, provides a unique setting for studying combustion mechanisms. Understanding the physical phenomena controlling the ignition and spread of flames in microgravity has importance for space safety as well as for better characterization of dynamical and chemical combustion processes which are normally masked by buoyancy and other gravity-related effects. Due to restrictions associated with performing measurements in reduced gravity, diagnostic methods which have been applied to microgravity combustion studies have generally been limited to capture of flame emissions on film or video, laser Schlieren imaging and (intrusive) temperature measurements using thermocouples. Given the development of detailed theoretical models, more sophisticated diagnostic methods are needed to provide the kind of quantitative data necessary to characterize the properties of microgravity combustion processes as well as provide accurate feedback to improve the predictive capabilities of the models. When the demands of space flight are considered, the need for improved diagnostic systems which are rugged, compact, reliable, and operate at low power becomes apparent.

The objective of this research is twofold. First, we want to develop a better understanding of the relative roles of diffusion and reaction of oxygen in microgravity combustion. As the primary oxidizer species, oxygen plays a major role in controlling the observed properties of flames, including flame front speed (in solid or liquid flames), extinguishment characteristics, flame size and flame temperature. The second objective is to develop better diagnostics based on diode laser absorption which can be of real value in both microgravity combustion research and as a sensor on-board Spacelab as either an air quality monitor or as part of a fire detection system.

In our prior microgravity work (ref. 1), an eight line-of-sight fiber optic system measured water vapor mole fractions in the NASA Lewis 2.2-sec Drop Tower. In that system, the laser and all electronics resided at the top of the drop tower and was connected via a fiber optic cable to the rig, on which a "pitch and catch" set of fiber collimating lenses were used to transmit the laser beam across a jet diffusion flame. This system required eight independent detection/demodulation units and had poor spatial resolution.

This research builds on this earlier work, resulting in an improved capability for quantitative, nonintrusive measurement of major combustion species. A vertical cavity surface-emitting diode laser (VCSEL) and a continuous spatial scanning method permit the measurement of temporal and spatial profiles of the concentrations and temperatures of molecular oxygen. High detection sensitivity is achieved with wavelength modulation spectroscopy (WMS) (refs. 2-3). One-g experiments are performed using a slot diffusion flame. Microgravity measurements on a solid fuel (cellulose sheet) system are planned for the NASA Lewis 2.2-second Drop Tower Facility.

Experimental Approach

An overview of the experimental setup is shown in Fig. 1. The output of the diode laser is focused onto an optical scanning mirror positioned at the focus of an off-axis paraboloidal (OAP) reflector. Since all light rays emanating from this point are reflected along parallel paths by the OAP, this results in a collimated laser beam (~1 mm dia.) which linearly traverses the flame region as the mirror is scanned. A second OAP refocuses the beam onto a single detector. The mirror pair is configured so that the total optical path at any transverse position is essentially constant.

This new approach has the advantage over our previous work of much higher spatial resolution with a concurrent simplification in complexity and size of the detection electronics. A single detection channel sequentially records all data avoiding earlier problems

---

associated with multiple detection channels (relative calibrations, drift, cost, etc.) A commercial state-of-the-art digital signal processing (DSP) data acquisition board is used to generate both the mirror dithering and laser ramp waveforms (16-bit digital-to-analog converters at 400 kHz), as well as acquire (250 kHz, 12-bit analog-to-digital converters), and pre-process the data using a 40 MHz DSP. This unit is controlled by a stand-alone 80486 computer board with a 40-MB solid state hard drive.

Two electronics units are used — the first comprises the computer, solid state hard drive, DSP board and scanner control. The second contains the modulation and demodulation electronics, and laser controller. This entire system mounts on the drop rig and is designed to run autonomously.

This arrangement permits a temporal map of concentration and temperature of O_2 to be obtained during the microgravity experiment. In a typical run, the mirror is swept using a sawtooth waveform at a rate of 10 Hz, so that the laser samples a selected (3-4) cm wide region encompassing the flame. As the scanner mirror is swept and the laser traverses the flame region, an absorption spectrum is recorded at each transverse position corresponding to a spatial resolution of about 1 mm. The laser wavelength sweeps across two adjacent absorption lines of O_2. From these data, the temperature and absolute concentration of O_2 can be recovered for each spatial element as a function of drop time.

The vertical cavity surface-emitting laser, unlike the Fabry-Perot GaAlAs lasers typically used in this spectral region, is a true single-mode device. In contrast to very expensive DFB lasers, which have only recently become available near 760 nm, VCSEL lasers are much less expensive and can be wavelength scanned over a range ten times that of other diode lasers. We have obtained custom VCSEL lasers at near 761 nm to access a pair of O_2 rotational lines in the $b^1\Sigma$-$X^3\Sigma$ electronic transition.

Molecular oxygen is very difficult to detect spectroscopically by absorption because its primary vibrational and electronic transitions are classically forbidden. The weak atmospheric band near 760 nm can be observed using absorption, however, if one has a sensitive enough method. Conventional absorption methods are limited by source (laser) noise. Because diode laser intensity noise power per unit frequency decreases rapidly at higher frequencies, WMS achieves much improved sensitivity by shifting the detection bandwidth to a high frequency regime (refs. 2-3). A small sinusoidal modulation is superimposed on the diode laser injection current. This current modulation produces a modulation of the laser wavelength. Typically, the amplitude of the current modulation is chosen so that the induced wavelength modulation is comparable to the width of the spectral feature under study. As the laser sweeps across a spectral feature, this frequency modulation induces an amplitude modulation on the photodetector. Phase-sensitive electronics are then used to detect the signal at the second harmonic ($2f$) of this frequency.

Fractional absorption sensitivities at the near shot-noise limit ($\sim10^{-7}$) for both near- and mid-IR diode lasers have been achieved in carefully optimized laboratory studies (ref. 3). In more practical field measurements, absorption sensitivities of 1×10^{-5} — 3×10^{-6} have been demonstrated (refs. 4-5). These numbers assume a measurement bandwidth of 1 Hz, but the actual detection bandwidth is limited only by the modulation frequency. The system used in the present experiments employs a modulation frequency of 500 kHz and uses a 35 kHz detection bandwidth.

Given the flexibility of the data acquisition system, both in-phase and quadrature components of the phase-sensitive detector output are recorded. Thus the detection phase does not have to be preset and can be optimized during data analysis. The dc photocurrent is also acquired. Since this signal is proportional to the laser intensity (I_0) all variations in alignment, beam attenuation, etc. are accounted for by normalizing the ac signal to dc.

Measurement of Oxygen Mole Fraction and Temperature

In the weak absorbance limit of Beer's Law, the absolute absorber concentration N is related to the WMS signal by

$$Signal(v) = C \cdot \alpha(v) \cdot f_{WMS} \, , \quad \text{where} \quad \alpha(v) = \sigma(v)NL, \tag{1}$$

and C is a system electronic calibration constant, f_{WMS} is a factor relating the WMS signal to the absorption cross section (approximately 0.6), α is the absorbance, σ the absorption cross section line shape function (of wavenumber v) and L is the absorption path length. Given the system temperature and pressure, the absolute concentration is linearly proportional to the measured signal and is readily obtained. The mole fraction of oxygen at each spatial and temporal point is the ratio of this measured concentration to the total gas concentration at each corresponding point.

Temperature is obtained by measuring the peak ratio of two adjacent lines. This ratio is independent of concentration. Our goal is to select two closely spaced, but not overlapping, lines where the composite numerical factor used to convert signal to mole fraction is sensitive to temperature for one of the lines and insensitive for the other over the temperature range of interest. Once temperature is determined, the mole fraction is obtained by a multi-linear regression fit of the observed spectrum to a computed spectrum. The signal level of this theoretical spectrum is referenced to a measured (pre-drop) room temperature spectrum where the concentration of oxygen is known.

There are two fundamental difficulties in any *in situ* measurement of oxygen in a flame. The first problem is the extremely weak absorption line strength of O_2. For the best pair of absorption lines we can access ($R^{13}Q^{14}$ and a blend of $R^{15}R^{15}$ and $R^{43}Q^{44}$), a signal-to-noise ratio (SNR) after numerical filtering of about 50 is achieved in room air, equivalent to an absorbance of 1.5×10^{-4} at the acquisition bandwidth of 35 kHz. While not appearing to be very good, this corresponds to a 1 Hz equivalent bandwidth detection limit of about 8×10^{-7}, an exceptionally good value. Our ability to make good quantitative measurements of oxygen in the flame depends on how well we can reduce the background noise.

The second problem is that oxygen is present along the entire optical path, not just in or near the flame. In the present experiment the total optical path length is 31 cm, while the flame region is only about four cm long. Thus we must remove the room air contribution to measurements along this path, reducing the SNR.

Results

One-g measurements are made in a Wolfhard-Parker methane-air diffusion slot burner (ref. 6) which approximates a 2-dimensional flame along it 41 mm path. The laser beam is scanned across a 32 mm region (1.3 mm resolution) of the flame at a height 9 mm above the burner surface. Full spatial scans are made at a rate of 10 Hz. The gas flow conditions are in the burner are chosen to mimic those used by Smith *et. al.* (ref. 6), where various species concentrations were made using a sampling mass spectrometer. Slight differences are expected since our measurements are made at a local atmospheric pressure of 590 torr.

Figure 2 shows experimental and theoretical $2f$ spectra of O_2 at room temperature. This plot illustrates the measured line shapes match those expected from theory using experimentally determined modulation depth and laser linewidth terms. Figure 3 is a surface plot of the O_2 spectrum as a function of position in the flame. Since this is a steady-state flame, "drop time" is not relevant here. The room air (external path) oxygen signal has been removed in this figure. The line shape on the left-hand side of the plot has a cross section that slowly decreases with temperature, while the right-hand (blended) line cross sections remain about constant. Of course, both signals decrease inversely with temperature due to the decrease in total number density at higher temperatures. As a consequence the noise levels are substantially higher than in Fig. 2. Nevertheless, the depletion of oxygen in the center of the flame is clearly evident. One can also see that the ratio of line intensities changes in moving from outside the flame into its center.

A rough approximation to the O_2 mole fraction as a function of flame position is illustrated in Fig. 4. This is obtained using our data with the temperature distribution obtained from ref. 6. Qualitative agreement is reasonably good.

Discussion

The difficulty of these measurements must be emphasized. Because we are attempting to measure full spectra at a rate of 250 Hz (70 kHz digitization rate), the SNR at each data point is relatively poor, despite the outstanding overall system performance. In the work presented here, a low pass Butterworth filter is used to smooth the data. While reasonably successful, it leaves residual noise at frequencies similar to those which comprise the $2f$ signal. We are presently exploring more robust noise reduction methods. Two approaches which show great promise are the use of wavelets (ref. 7) and multi-dimensional filtering.

Wavelet analysis permits manipulation of the various frequencies which comprise a signal, similar to Fourier analysis, but with the added ability to apply these manipulations using a windowing technique having *variable-sized regions*. This means we can selectively remove appropriate amounts of noise having the same frequency components as the signal, but without affecting any of the signal levels. Preliminary calculations on sample experimental spectra show a five-fold reduction in SNR over the low pass filter.

Another step we will use to squeeze out mole fractions and temperatures recognizes that we acquire a three dimensional map of intensity, where the dimensions are wavelength, time and position. At present we only filter along the wavelength axis. But additional filtering across all dimensions should improve our results. This effective treats the data as a 2-D or 3-D image and we

can use appropriate image recognition methods. This should be especially useful since we expect only low frequency signals as a function of time and position (i.e., the signals along these axes are not expected to have sharp features).

During this year, a series of solids combustion measurements of oxygen will be made in the 2.2-sec drop tower. We will study the effects of opposed flow velocity, pressure and O_2 content on the depletion of O_2. Measurement of spatially-resolved flame temperatures and mole fractions will provide information on the diffusion and combustion rates of oxygen and be used to validate theoretical models of these processes.

References

1. J.A. Silver, D.J. Kane and P.S. Greenberg, "Quantitative Species Measurements in Microgravity Flames With Near-IR Diode Lasers, Appl. Opt. **34,** 2787-2801 (1995).
2. J. Silver, "Frequency Modulation Spectroscopy for Trace Species Detection: Theory and Comparison Among Experimental Methods," Appl. Opt. **31,** 707-717 (1992).
3. D.S. Bomse, A.C. Stanton and J.A. Silver, "Frequency Modulation and Wavelength Modulation Spectroscopies: Comparison of Experimental Methods Using a Lead-Salt Diode Laser," Appl. Opt. **31,** 718-731 (1992).
4. J.A. Silver and D.C. Hovde, "Near-infrared Diode Laser Airborne Hygrometer," Rev. Sci. Instrum. **65,** 1691-1694 (1994).
5. D.S. Bomse, "Diode Lasers: Finding Trace Gases in the Lab and the Plant," Photonics Spectra (June, 1995) pp. 88-94.
6. K.C. Smith, J.H. Miller, R.C. Dorfman, W.G. Mallard and R.J. Santoro, "Soot Inception in a Methane/Air diffusion Flame as Characterized by Detailed Species Profiles," Comb. Flame **62,** 157-181 (1985).
7. Wavelets and Filter Banks, by G. Strung and T. Nguyen (Wellesley-Cambridge Press, 1996).

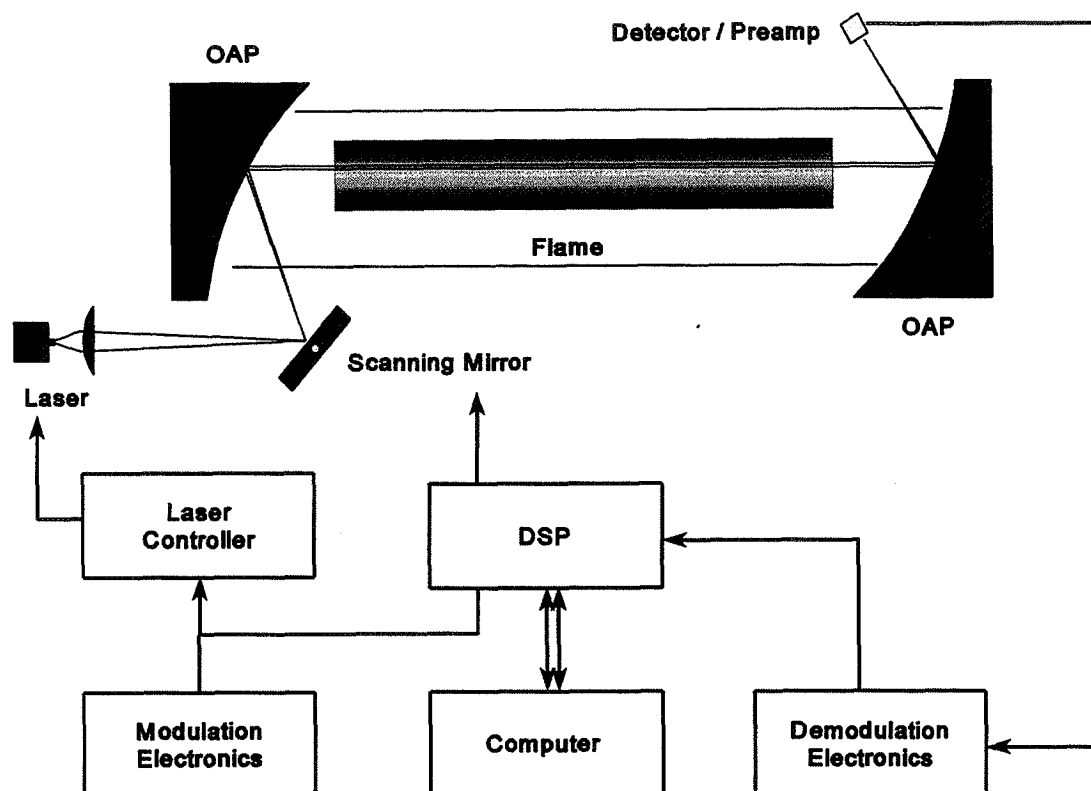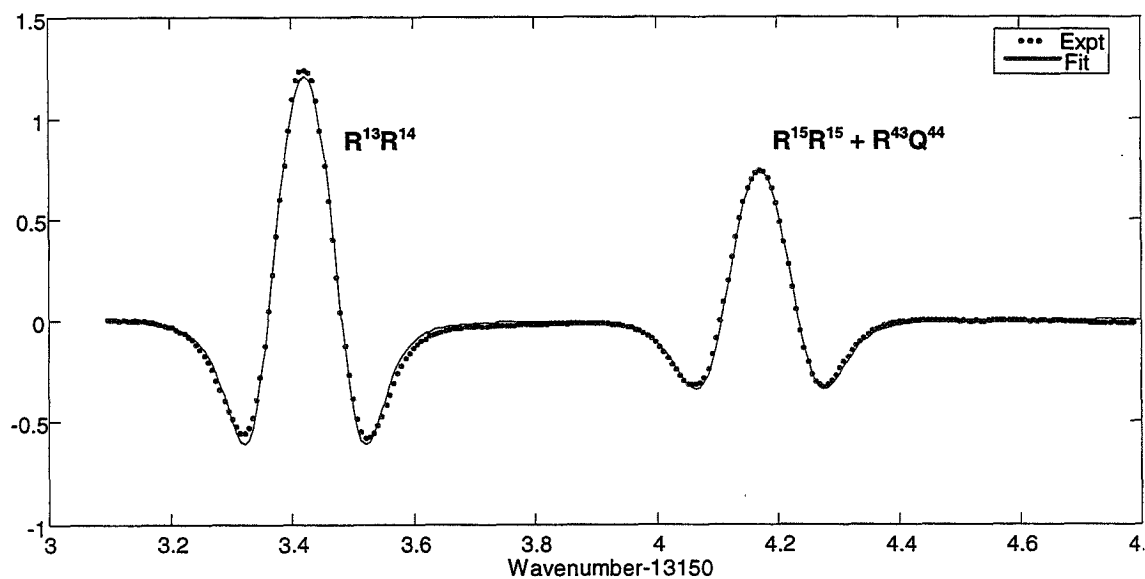Figure 1 - Schematic of experimental setup.

Figure 2 - Experimental (•) , and best fit computed (—) spectrum of O_2.
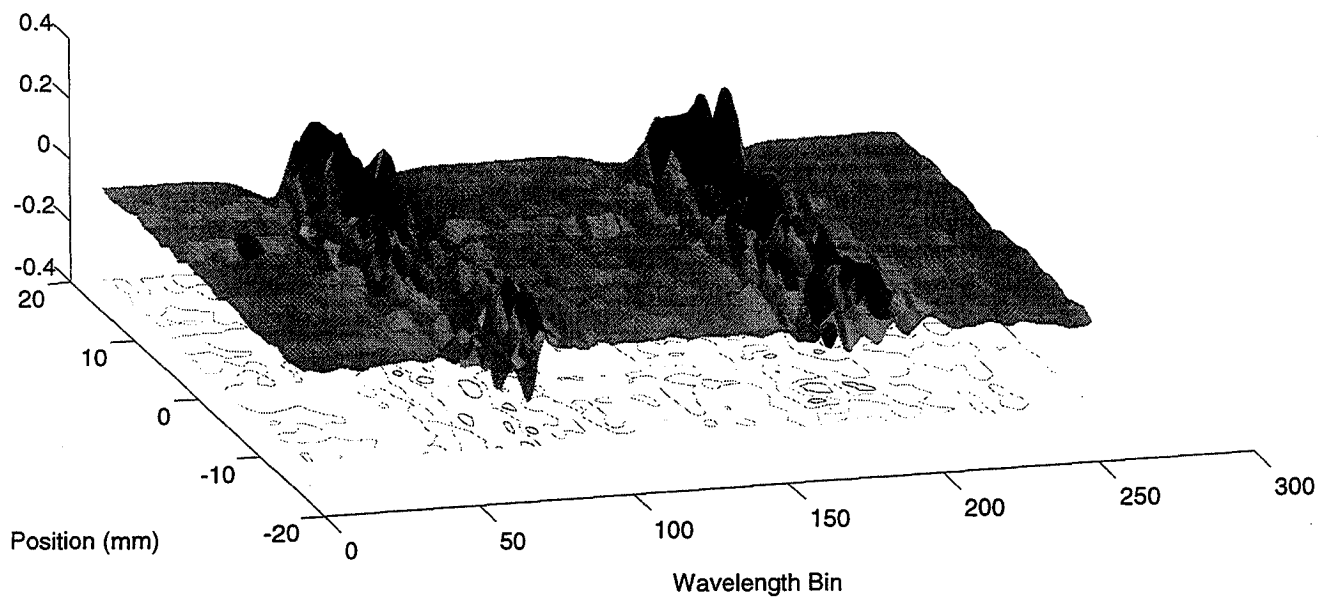
Figure 3 - Map of spectral intensity versus flame position.
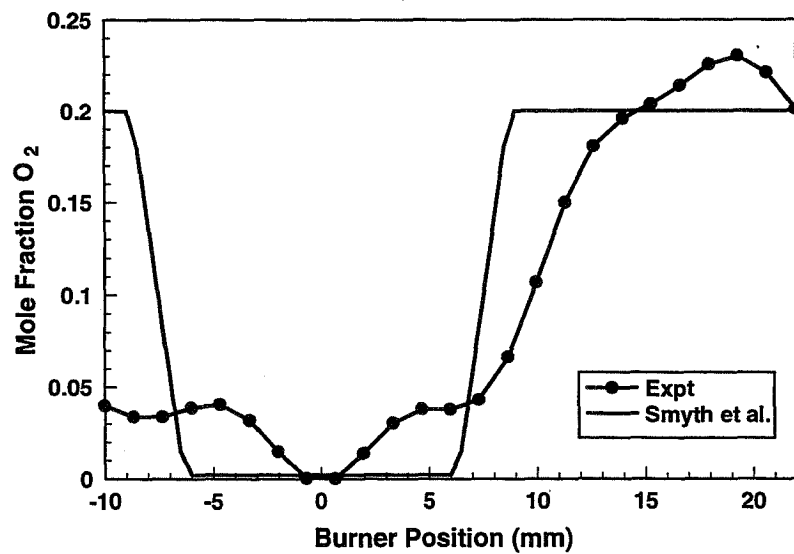

Figure 4 - Comparison of O_2 mole fractions using slot burner.

OH PLANAR LASER-INDUCED FLUORESCENCE
FROM MICROGRAVITY DROPLET COMBUSITON

MICHAEL WINTER
Jason Wegge
Kyung-Tae Kang[†]
United Technologies Research Center
East Hartford, Connecticut

Abstract

Droplet combustion under microgravity conditions has been extensively studied, but laser diagnostics have just begun to be employed in microgravity droplet experiments. This is due in part to the level of difficulty associated with laser system size, power and economic availability. Hydroxyl radical (OH) is an important product of combustion, and laser-induced fluorescence (LIF) has proved to be an adequate and sensitive tool to measure OH. In this study, a frequency doubled Nd:YAG laser and a doubled dye laser, compact and reliable enough to perform OH PLIF experiments aboard a parabolic flight-path aircraft, has been developed and successfully demonstrated in a methanol droplet flame experiment. Application to microgravity conditions is planned aboard parabolic flight-path aircraft.

Introduction

The combustion of individual droplets has been studied by many researchers using theoretical and experimental tools (ref. 1). Droplets provide an idealized geometry for investigating the interaction of the physical and chemical processes in non-premixed combustion phenomena. A significant means of simplifying droplet combustion is to approach the phenomena in a microgravity environment where the problem may be described as radially symmetric. A great deal of activity is ongoing in this area including calculations and experiments in drop towers and aboard spacecraft (refs. 2 and 3).

Droplet combustion under microgravity conditions has been extensively studied. Rapid advances have recently been possible in numerical simulation of droplet combustion under microgravity conditions, while experimental capabilities remain primitive (ref. 4). Calculations can now provide detailed information on mass and energy transport, complex gas-phase chemistry, multicomponent molecular diffusion, surface evaporation and heterogeneous reaction. However, experiments concerning these phenomena typically results in pictures of the burning droplets, and the data therefrom describe droplet surface regression along with flame and soot shell position. Recently laser diagnostics for particle scattering (ref. 5) and a system using diode laser absorption (ref. 6) have been used in the LeRC 2.2-second Drop Tower. Laser-induced fluorescence (LIF) of OH and CH radical and laser-induced incandescence (LII) for measuring soot volume fraction have been under development (ref. 3).

Optical diagnostics offer several advantages over physical probes because they permit nonintrusive, multi-point measurements. Nonintrusive measurement is of particular importance for droplet combustion in microgravity environments, where physical contact would introduce an unacceptable level of perturbation. Optical diagnostics can also resolve transport measurements to length-scales much smaller than the droplet diameter. They provide qualitative and quantitative information on the instantaneous distribution of desired scalar or vector quantities in two or three dimensions. Recently, combustion phenomena of individual droplets have been studied using laser diagnostics in microgravity conditions (ref. 4). In the research (ref. 4), sodium PLIF and radical emission imaging at 308 nm were performed. Measurements of PLIF from seed species, such as sodium, have uncertainties due to sodium distribution in the fuel and its behavior at the flame front. Images of OH emission provided integrated, line of sight data from chemical processes that create OH in the excited state occurs with spectral overlap from natural emission from CH*. The emission data was compared with direct measurements of PLIF from OH in a quantitative manner.

Hydroxyl radical (OH) is an important product of combustion and is useful for evaluating chemical models of droplet combustion calculations (ref. 7), it is considered to be a diagnostic that describes the position of the flame zone (ref. 8). LIF has proved to be an adequate and sensitive tool to measure OH. In this study, a compact and reliable dye laser pumped by a compact Nd:YAG laser is developed to enable an OH PLIF experiment aboard parabolic flight-path aircraft used to provide a microgravity environment.

[†] Postdoc

Experimental Method And Design

Flight tests to establish low gravity conditions for a variety of microgravity experiments are performed on the NASA Lewis DC-9 aircraft. This aircraft has been modified to perform parabolic trajectories, providing up to 22 seconds of g-levels as low as 10^{-2}. A cost effective laser design utilized available equipment to produce a reliable system that can operate within the constraints of the microgravity environment. Flight safety regulations impose some restrictions on the size and weight of the experimental hardware (ref. 9).

Figure 1 shows a schematic of the OH PLIF system including a Nd:YAG laser, a dye laser and an intensified CCD camera. The Nd:YAG laser, CRF400 from Big Sky Laser, provides 210 mJ at 532 nm and 5 Hz and, has been adapted for the flight apparatus.

A compact dye laser has been designed for use with the Nd:YAG laser in acquiring measurements in the flight apparatus. It is a modified commercial dye laser module which contains a grating to allow wavelength tuning over the spectral fluorescence range of the dye; in this case Rhodamine 590. The dye concentration is optimized for 5 Hz operation at 45 mg R590 per 250 ml of methanol. The cavity is a modified Littrow configuration. The output is doubled with a KDP crystal to produce a 282 nm beam. A single pass amplifier stage was added to the dye laser and the oscillator dye cell was modified to a flowing type cell. In order to minimize fluid pumping and reservoir requirements, both cells use same dye concentration. Tests showed that the dye laser will operate satisfactorily up to 10 Hz repetition rate in this configuration. A holographic grating (2400 lines/mm, 560 nm blaze angle) from Optometrics USA was installed to improve the tuning characteristics of the dye laser and the bandwidth of its visible output. The bandwidth of the dye laser affects the efficiency of frequency doubling to 282 nm with the KDP doubling crystal. Expanding the oscillator cavity length enhances the efficiency of frequency doubling by narrowing the spectral line width. The frequency doubling efficiency is further enhanced by more linearly polarizing the light inside of the oscillator cavity of the dye laser by inclusion of several Brewster-angled windows between the oscillator dye cell and the grating. The compact Nd:YAG laser and modified dye laser module easily fit within a typical hardware rack used for flight experiments. A unique facet of this system is that the entire excitation source for pumping OH PLIF occupies a footprint of 0.3 m^2. System output powers up to ~1 mj in the ultraviolet can be achieved. The ability to achieve this degree of size reduction in high power tunable laser source, will enable other portable applications of these techniques.

Two camera systems are currently used in the flight apparatus. One is an intensified CCD (Stanford computer optics model 4Quick 05) that is operated at 5 Hz to achieve synchronization with the laser pulse frequency. A second CCD camera is used to observe droplet deployment and ignition and to record the flame luminosity during a droplet combustion test. Both cameras are provided with microscopic optical lenses (Nye Lyman-Alpha II and Sony Model No. 809435) to resolve both the droplet and surrounding flow field. The images from both cameras are passed through synchronized time code generators which superimpose a time code signal on the images prior to recording on 8 mm VCR's. This allows post-processing comparison of the luminosity and the OH PLIF signals on a frame by frame basis.

A photograph of the in-flight droplet experiment module is shown in Fig. 2. The figure shows the Nd:YAG laser, tunable dye laser, intensified camera system, VCR, timing control system, an Apple Newton personal digital assistant (PDA) with experimental control software, timing electronics, and power distribution module. The experiment contains a windowed combustion vessel. Inside the combustion vessel resides a remote controlled droplet generation system along with an electrodynamic levitator. As seen in Fig. 2 the system resides in a NASA-standard aircraft double rackmount. The miniaturization of this complex experiment required several significant innovations to meet flight power, size, weight, robustness, cost and safety constraints.

Performance

Figure 3(a) shows a visible spectrum of the dye laser and Fig. 3(b) shows an ultra-violet spectrum of the frequency doubled output. Use of a high dispersion grating and a long cavity length enhances the tuning characteristics of the dye laser and reduces the bandwidth of its output to less than 0.6 nm FWHM. A narrow bandwidth at the fundamental frequency provides for increased doubling efficiency to the OH absorption at 282 nm yielding a FWHM of 0.147 nm.

Figure 4 shows an OH PLIF image of the upper side of the flame around a methanol droplet in normal gravity conditions. The droplet was suspended on a fiber with a diameter of about 610 μm and a 1mm bead on the end. The methanol droplet was expelled from a racheted syringe that deployed 0.005 ml repeatedly on the bead. The initial diameter of each droplet is about 2mm and ellipsoidal because of gravity and fiber effects. In Fig. 4, the fluorescence of the fiber interfered with the lower side of the flame image, the circular object (~ 1.5 mm) in the lower side of the image is the end of the fiber. An interference filter with FWHM of 10 nm effectively blocks luminosity and scattering. The initial methanol droplet does not emit any fluorescence;

fluorescence in the images appeared in the late stage of burning. Emission from the burning methanol droplet can be explained in two ways. The first is that the fluorescence of the burning methanol droplet is from pyrolized methanol fuel that is convected to the surface of the droplet and condenses there (ref. 10). The second might be attributable to scattering of the LIF signal by the droplet surface.

Conclusion

Reduction in the size of OH PLIF excitation sources have been achieved. This will increase the transportability of these systems for application to many diverse combustion applications. A Nd:YAG laser and a dye laser, compact and reliable enough to make an OH PLIF experiment for in-flight experiments aboard a parabolic trajectory aircraft has been developed and used to successfully demonstrate OH PLIF of a methanol droplet flame. Its size and laser intensity are suitable as a tool for microgravity droplet burning experiments. In-flight applications are planned.

Acknowledgments

References

1. Law, C.K., "Recent Advances in Droplet Vaporization and Combustion." Progress in Energy and Combustion Sciences 8, 171-201 (1982).

2. Microgravity Science and Application; Program Tasks and Biography for FY1994, NASA Office of Life and Microgravity Sciences and Applications, March 1995.

3. Microgravity Science and Application; Program Tasks and Biography for FY1995, NASA Office of Life and Microgravity Sciences and Applications, March 1996.

4. Winter, M., "In-Flight Laser Diagnostic for Microgravity Droplet Combustion," 34th Aerospace Sciences Meeting and Exhibit, January 15-18, 1996, Reno, NV.

5. Griffin, D.W., and Yanis, W., "Full Field Gas Velocity Measurements in Microgravity," Third International Microgravity Combustion Workshop, NASA Lewis Research Center, Cleveland, OH, p253 (1995).

6. Silver, J.A., "Quantitative Measurement of Oxygen in Microgravity Combustion Workshop, NASA Lewis Research Center, Cleveland, OH, p279 (1995).

7. Quagliardi, T.M., Laufer, G., Krauss, R.H., and McDaniel ,J.C., Jr., "Laser Selection Criteria for OH Fluorescence Measurements in Supersonic Combustion Test Facility," AIAA Journal 31, 520-527 (1993).

8. Johnson, A.W., Sreenivasan, K.R., and Winter M., "The Thickness Distribution of OH Regions in a Turbulent Diffusion Flame," Combustion Science Technology 89, 1-7 (1993).

9. Yaniec, J.C., "Users Guide for NASA Lewis Research Center DC-9 Reduced-Gravity Aircraft Program," NASA Technical Memorandum 106755, January 1995.

10. Zhang, B. L. and Williams, F. A., "Simplified Analyses of Methanol Droplet Combustion for Comparison with Microgravity Experimental Results," 34th Aerospace Sciences Meeting and Exhibit, Jan 15-18, 1996
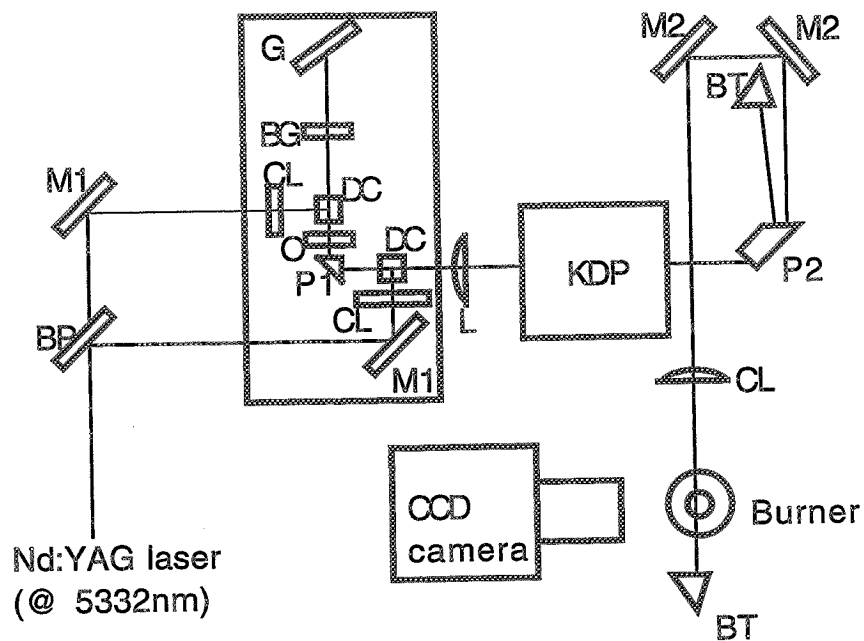
Figure 1. OH planar laser induced fluorescence system. (BS, beam splitter; M1, 532 nm mirror; CL, cylindrical lens; DC, dye cell; G, grating; BG, Brewster angled windows; PR1, prism mirror; L, focusing lens; KDP, KDP frequency doubling crystal; M2, 282 nm mirror; O, Output coupler; PR2, Pellin Broca prism; BT, beam trap)
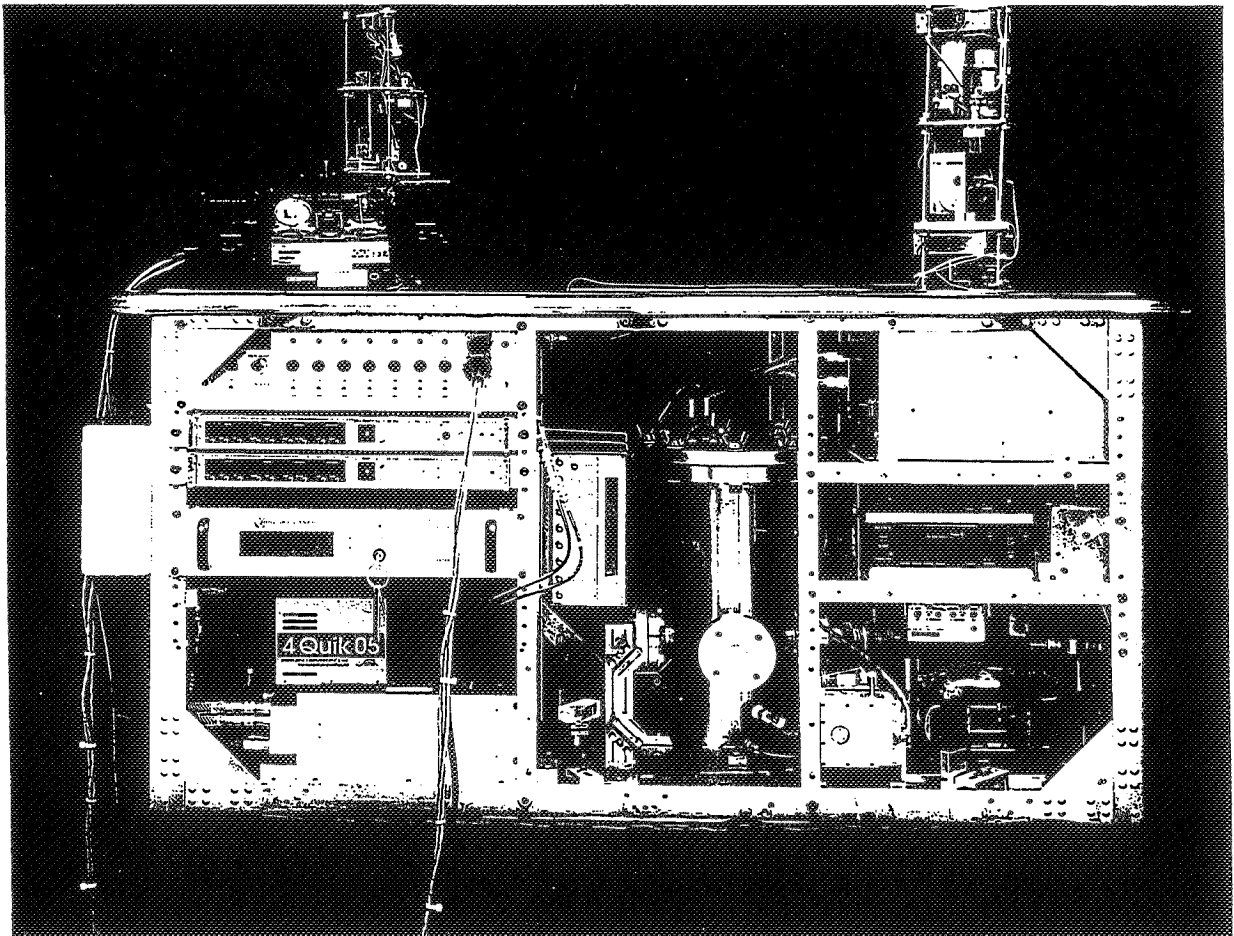
Figure 2. Laser diagnostic droplet combustion experimental flight module
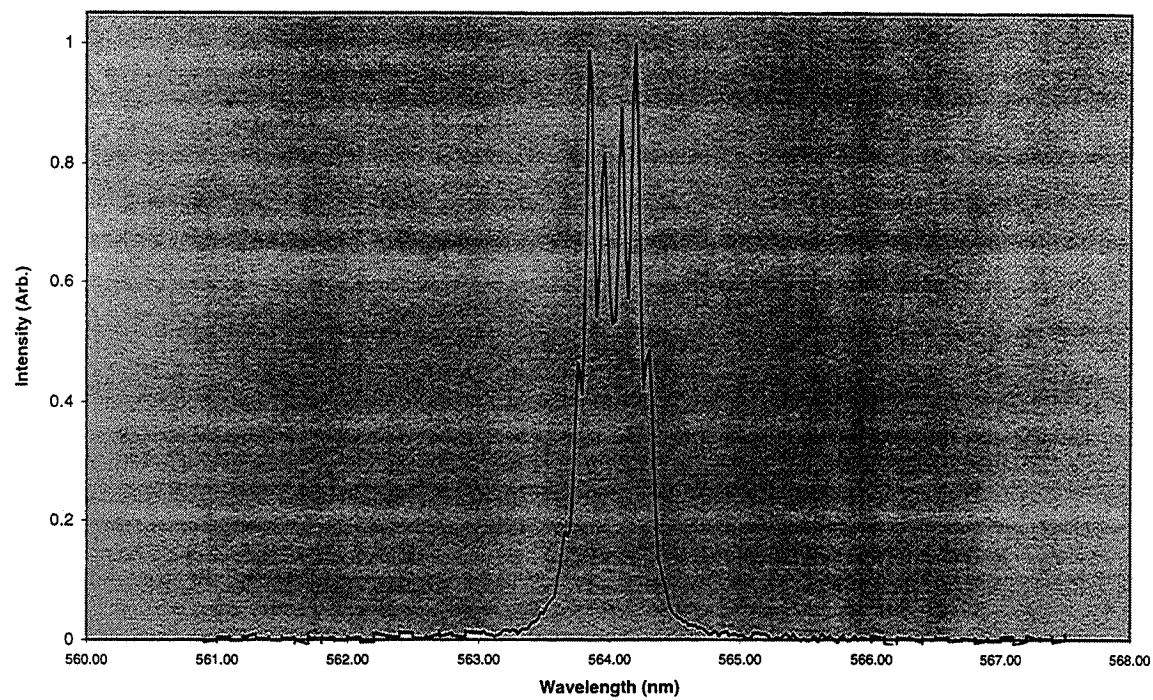
Figure 3(a). Dye laser spectrum (fundamental)

Peak = 282.46 nm
FWHM = 0.147 nm
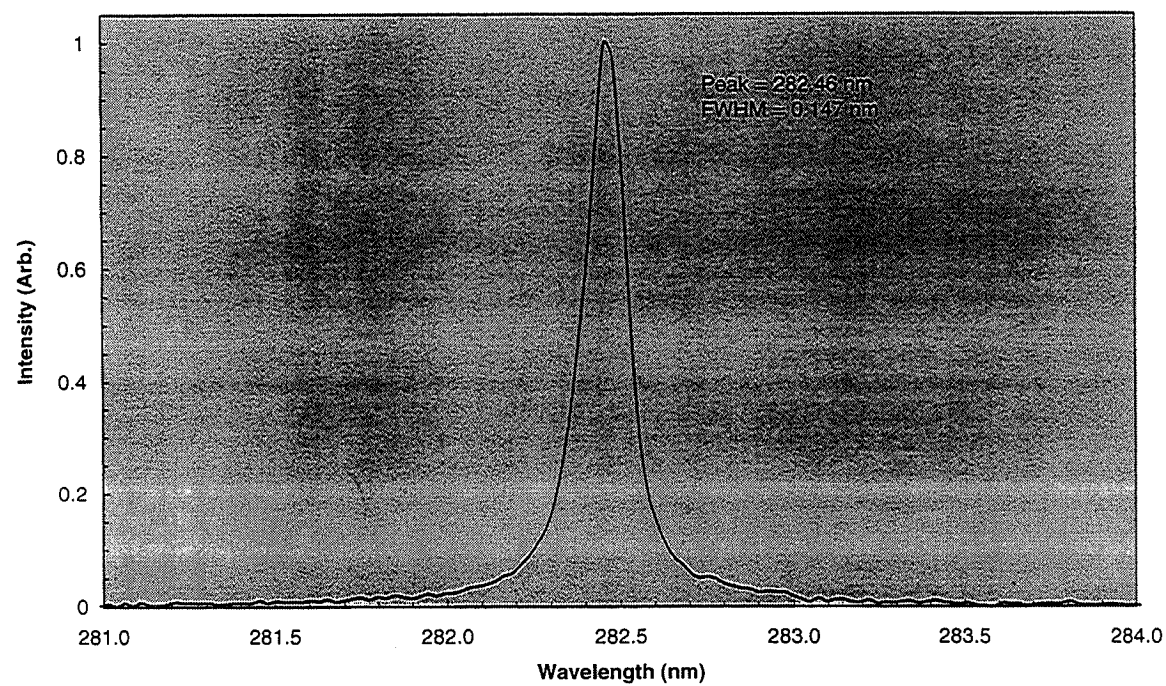
Figure 3(b). Dye Laser Spectrum (frequency doubled)

303
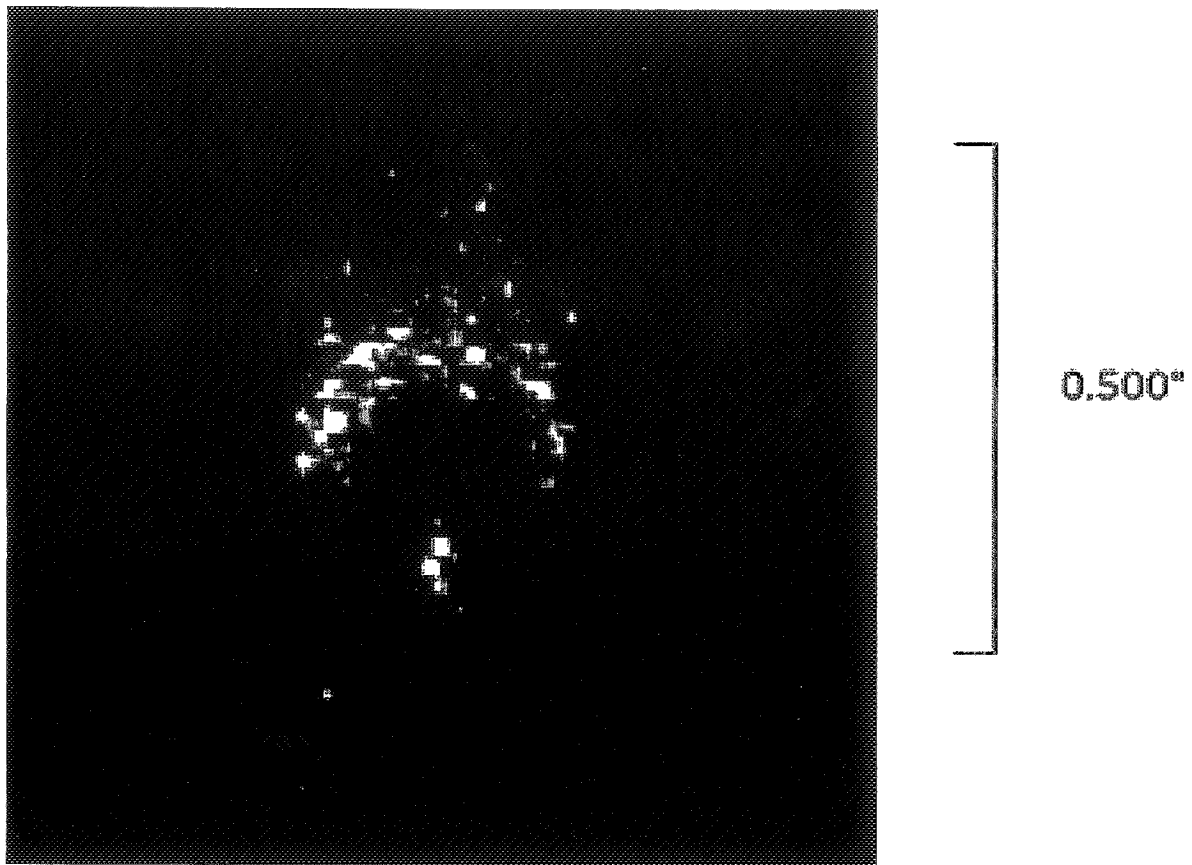
Figure 4. OH PLIF of droplet flame. Laser induced fluorescence is generated from the parabolic flight worthy systems.

LASER-INDUCED INCANDESCENCE IN MICROGRAVITY

RANDY L. VANDER WAL
NYMA @ NASA-Lewis
Cleveland, OH 44135

Introduction

Knowledge of soot concentration is important due to its presence and impact upon a wide range of combustion processes ranging from diffusion to premixed flames, laminar to turbulent processes and homogeneous to heterogeneous combustion. Measurement of soot volume fraction (f_v) is essential to discerning its formation and growth [1]. The presence of soot also affects other physical and chemical properties of combustion thereby affecting studies not directly concerned with either its formation or growth, such as radiative heat transfer, CO oxidation and fuel vaporization or pyrolysis rates [1].

Microgravity offers unique opportunities for studying both soot growth and the effect of soot radiation upon flame structure and spread [2]. Spatial scales and residence time scales are greatly extended in 0-g facilitating soot growth studies. With the varied geometries, short duration microgravity test times and time-varying processes there is a demand for measurement of f_v with high spatial and temporal resolution.

Laser-induced incandescence (LII) has advanced f_v measurements in many 1-g combustion processes. To create laser-induced incandescence, a pulsed high intensity laser heats soot to incandescence temperatures [3]. Using appropriate spectral and temporal detection conditions, the resulting incandescence can be selectively detected apart from the non-laser-heated soot and flame gases. Theoretical modelling [4] and experiments [5-7] have shown that the resulting incandescence is representative of f_v. Using an intensified array camera and a laser sheet for excitation, one- and two-dimensionally resolved LII images of f_v have been obtained in 1-g [6-10].

LII has been characterized and developed at NASA-Lewis for soot volume fraction determination in a wide range of 1-g combustion applications. Broadly grouped, the chacterization work has included studies of excitation intensity, excitation wavelength and the optimum temporal and spectral detection conditions to enable an accurate representation of soot volume fraction by LII [6,11]. Tests for special requirements imposed by different combustion processes have been performed in laminar [6,8,9] and turbulent [7,8] diffusion flames, rich sooting premixed flames [6], single droplet combustion [10], and other heterogeneous combustion. These studies demonstrated LII's high sensitivity, temporal and spatial capabilities and its geometric versatility.

In contrast to the advantages offered to combustion studies by a microgravity environment, advanced diagnostics, specifically those requiring pulsed laser diagnostics have been limited due to the size, weight and power limitations in a low-gravity environment. Reported here are the first demonstrations of LII performed in a microgravity environment. Examples are shown for laminar and turbulent gas-jet diffusion flames in 0-g.

Experimental Approach

Experiments were performed in the 2.2 sec drop tower facility at NASA-Lewis [12].

To enable LII, light from a pulsed Nd:YAG laser is delivered via a 35 m long section of high OH-content, 1000 μm core diameter (30 μm cladding thickness) optical fiber to the drop package from the laser resident on the eigth floor of the drop tower. The jacket of the optical fiber consisted of black PVC with Kevlar-strengthening fibers. A special high power SMA-905 input connector was vital to coupling of the pulsed laser light into the optical fiber. Laser light at 532 nm from a short cavity, pulsed Nd:YAG laser manufactured by Big Sky Laser Inc. was coupled into the optical fiber using a 200 mm focal length plano-convex BK-7 lens. The combined input coupling efficiency of 532 nm light into the fiber plus transmission through the 35 m optical fiber was roughly 75%.

Figure 1 illustrates the layout of the drop rig. The divergence of the laser light at 532 nm emerging from the optical fiber is reduced by a 50-mm diameter, 100-mm-focal-length, fused-silica, spherical lens placed ~40 mm after the fiber. A laser sheet was formed using a 125 mm focal length 50 mm round cylindrical lens. Only the central 30 mm of the light sheet, representing the most uniform spatial intensity, was used for creating the laser-induced incandescence. A dichroic mirror following the cylindrical lens allowed for precise placement of the light sheet through the flame centerline. A beam dump

collected the laser light after the burner thereby eliminating scattered laser light. With an incident energy of 10 mj and estimated beam sheet width of 400 um, the laser intensity was roughly 1×10^7 W/cm^2.

LII images were detected by a ruggedized Xybion ISG-250 ICCD camera through a bandpass interference filter transmitting 400-450 nm. A glass lens used at f/8 fitted with a 10 mm extension tube provided a field-of-view (FOV) of about 30 mm. A custom electonics module provided power to the camera from the rig batteries and coupled the video and related timing signals out from the ICCD camera and gate pulse into the camera intensifier. Natural flame luminosity was detected by a Sony XC-77 black and white camera or a Sony XC-999 color video camera. Video signals from both cameras were transmitted though FM (6 MHz bandwidth) video transmitters attached to the drop rig, a dual fiber-optic video cable running between the drop rig and the top floor of the drop tower and FM video receivers located on the top floor of the drop tower. The LII signal was recorded on Beta video tape while the natural flame luminosity was recorded on SVHS video tape. A frame-grabber digitized images for subsequent analysis.

Synchronization of the laser, camera intensifier gate and camera video signal was achieved using custom electronics to detect the top-of-frame pulse on each LII video frame and provide a trigger pulse to a delay generator. The delay generator in turn triggered the laser and provided an inverted TTL pulse to serve as the gate pulse for the ICCD camera intensifier. The camera gate pulse was delivered through a 35 m length of BNC (RG58) cable connected to the camera control unit aboard the drop rig.

Drops were initiated by loading a computer program into an onboard droppable data acquisition/control system. This unit also controlled solid state relays to deliver power to the spark ignitor, cameras, and gas solenoid. A preburn prior to the drop ensured fuel within the gas-jet nozzle and confirmation of all systems working. Upon package release into free-fall, an electrical circuit was opened to provide a rising edge TTL trigger to initiate fuel delivery and ignition.

Laminar gas-jet diffusion flames were established on a 1.1 mm i.d. nozzle with approximately a 30° outside edge taper. The burner for the turbulent gas-jet diffusion flame utilized a 0.51 mm i.d. Nozzle (length/diameter >20) with a co-annular pilot diffusion flame. In each case a regulator and fine control valve were adjusted against a mass flow meter to deliver a known fuel flow rate. The acetylene flow through the central gas-jet tube was 1.0 slpm giving a Reynolds number of 4250 while the acetylene flow for the laminar coannular pilot flame was roughly 10 sccm.

Results And Discussion

LII System Response

Figure 2 illustrates the measured system dependence upon LII intensity. To test this dependence, a laminar steady-state gas-jet flame of ethylene was established in 1-g supported on the same 1.1 mm i.d. burner nozzle with a fuel flow rate of 48 sccm. The signal excitation and detection were configured as if the measurements were being performed in low-gravity. Consequently, the graph represents the results of an end-to-end test of the LII signal detection, transmitting and processing equipment which includes the intensified camera, the video fiber-optic transmitter plus receiver, beta recorder and the frame-grabber used for digitization of the video signal. With a fixed camera intensifier gain typical of that needed for LII 0-g measurements, the LII intensity reaching the camera was varied by placing calibrated neutral density filters in the optical path. Within the resulting digitized LII image, a region-of-interest (ROI) was defined containing 624 pixels within the flame tip where a rather spatially uniform f_v distribution (<20% spatial intensity variation) was observed. The average pixel intensity within this region was calculated. Since the LII intensity incident upon the camera photocathode will vary as,

$$\text{Signal}_{(\text{det.})} = C * \text{LII} * 10^{(-\text{N.D.})}$$

where C is a constant, a semi-logarithmic plot of Signal$_{(\text{det.})}$ versus N.D. filter value should be linear provided all subsequent signal processing is linearly dependent upon the detected LII signal. This is observed in Fig. 2. The error bars represent one standard deviation of the ROI average intensity. Even if the curve were nonlinear, it would still provide a calibration curve for translating final digitized pixel intensities into relative LII intensities. The observed linearity allows straightforward interpretation of LII intensities as proportional to f_v.

Camera gain calibration

Lower LII signals arising from lower soot concentrations could be readily detected by adjusting the camera intensifier gain. To establish the relative detection sensitivities at different intensifier gains, calibration measurements were performed. Again, the entire LII excitation/detection system was set up as if to perform low-gravity measurements. LII images of a laminar steady-state flame of ethylene (48 sccm flow rate) were acquired using different intensifier gains. Neutral density

filters maintained the signal intensity within the dynamic range of the detection system. Analysis of a region of interest (620 pixels) near the tip of the flame provided an average LII intensity for the particular gain setting (higher gains correspond to smaller readout values). Comparison of the relative LII intensities corrected for the neutral density filter attenuation provided a relative measure of the detection sensitivity at the different gain settings. To faciliate comparison, the relative values were normalized by the LII average intensity measured with the lowest practical gain setting. These results are shown in Fig. 3. The error bars were calculated assuming Poisson statistics with the standard deviation calculated as the square root of the average LII pixel intensity. These limits were found empirically to well encompass the variation observed in the average LII intensity calculated within the ROI.

Although the semi-logarithmic plot conveniently illustrates the range of detection sensitivities, there is a physical basis for this method of plotting. Because the photon detection event is described by a Poisson distribution [13] and the intensifier amplification process is exponential [14], with a linear detection system, the detected signal intensity would be expected to scale exponentially with the intensifier gain provided no saturation of the electron multiplication process occured within the microchannel plate, coupled phosphor screen or CCD pixel well. As Fig. 3 shows, using the intensifier, more than a 1000-fold increase in detection sensitivity can be achieved relative to that at a gain setting of 4.70. Based on soot volume fractions of about 15 ppm for the laminar 50/50 (v/v) acetylene/nitrogen mixture in 1-g detected using a gain of 4.70, a detection sensitivity of nearly 0.01 ppm is predicted based on Fig. 3

Validation of LII

Figure 4 shows LII images of a laminar acetylene gas-jet diffusion flame in 1-g and 0-g with a fuel flow rate of 70 sccm. The effect of buoyancy upon the flame shape and soot processes is clear. Buoyancy induced air entrainment causes radial confinement of the gas-jet in 1-g. In 0-g, the initial fuel-jet momentum governs the flow with the divergence of the gas-jet clearly observed from the soot spatial distribution. In contrast to 1-g, flow trajectories in 0-g follow a monotonic path in mixture fraction and temperature while within the flame leading to extended spatial scales for soot inception and subsequent growth.

To verify the validity of the LII measurements as representative of f_v, LII radial intensity profiles from the acetylene gas-jet flame in 0-g are compared with those derived from a full-field extinction method that has been reported previously [15]. The axial positions were chosen to illustrate different spatial and intensity variations in f_v. Three radial pixel rows of the LII image were averaged together for better signal-to-noise thus giving a spatial resolution of 0.25 mm. Each LII profile was also corrected for attenuation by soot between the LII image plane and camera. To convert the relative LII intensities to f_v, each LII radial profile was multiplied by a scaling factor which was determined by the ratio of the summed LII intensity from all radial profiles to the radially summed f_v's at the same axial positions. As can be seen from Fig. 5, good agreement is observed between the LII measurements and those derived from extinction where both the relative spatial variations and intensities are similar. While previous tests of LII have shown it to yield accurate relative measurements in 1-g by comparison with light extinction and gravimetric sampling, these results are the first tests validating LII as a diagnostic for f_v in 0-g.

Additional Demonstrations

Laminar gas-jet flame

Figure 6 shows LII images obtained from a laminar ethane gas-jet diffusion flame in 1-g and 0-g. In each case, the fuel flow rate was 70 sccm with resulting Reynolds number of 200. Due to buoyancy-induced instabilities, the normal gravity flame frequently flickered, consequently a representative image was chosen. As clearly seen by Fig. 6, buoyant accleration overcomes the divergent cold-gas flow causing radial confinement of the flame in 1-g. With soot oxidation proceeding inward towards the flame centerline, soot on the jet centerline is oxidized last resulting in the steeple shaped soot distribution at the flame tip. With buoyant acceleration eliminated in 0-g, the initial divergence of the exiting fuel flow is largely preserved resulting in a flame spatial extent determined much more by stoichiometry requirements than in 1-g. Similar to the laminar gas-jet flame of acetylene, absence of buoyant entrainment leads to an increase in the spatial extent of soot inception and growth. Despite the fuel abundance within the central core of the flame, a combination of insufficient fuel pyrolysis products and diminished temperatures relative to 1-g likely inhibit soot formation reactions along the axial streamline resulting in the absence of soot at the flame tip.

Although the flicker observed in 1-g causes variation in peak f_v (ranging from 0.3 to 0.6 ppm in the tip of the flame), the ratio of the 0-g to 1-g f_v is roughly 3 based on a comparison of LII intensities. This example also illustrates the sensitivity of LII as the radially integrated f_v-pathlength product is 6.7×10^{-7} cm yielding a transmittance of 0.95 using Ke = 4.9 from Dazell and Sarofim [16]. Such a high transmittance is marginally detectable using unstabilized HeNe lasers, voltage biased photodetectors and 8-bit digitization. On the basis of the camera gain calibration curve, approximately a factor of 30 higher sensitivity (or a factor of 30 lower f_v) is achievable using a camera gain of 4.40 compared to 4.575 as was presently

used. Such a high transmittance is likely undetectable even using sensitive lock-in detection of absorbance which possesses a practical limit of roughly 0.1 % absorbance sensitivity with RC timeconstants on the order of 100s' of msec.

Turbulent gas-jet flame

Figure 7a, perhaps the best illustration of the temporal plus spatial capabilities of LII and its geometric versatility, shows a LII image from a turbulent gas-jet flame of acetylene with Reynolds number of 4250 in 0-g. Even using a detection gate of 500 ns to ensure capture of the of the LII signal, temporal frequencies of greater than 1 MHz can be frozen. As determined using a replica of the 1951 Air Force test pattern, the spatial resolution is approximately 5 line pairs per millimeter allowing spatial structures of 0.1 mm to be resolved. Figure 7b is a contour plot of Fig. 7a. Absolute soot volume fractions were calculated based on the LII image intensity in the turbulent flame relative to that of the reference flame system using the camera intensifier calibration curve of Fig. 3.

Vortex visualization

Figure 8 is a LII image of soot within a vortex formed by propane fuel issuing from a gas-jet nozzle. The central bulge is due to the initial jet momentum while the side recirculation regions result from air entrainment into the shear layer. Initiation of fuel flow and subsequent ignition were performed in low-gravity (after package release from the "music" wire). The nominal jet Reynold's number was 330 based on the nozzle ID of 1.1 mm and flow rate of 70 sccm. The higher f_v in the recirculation regions is sensible as fuel parcels in these regions experience extended times at elevated temperatures promoting fuel pyrolysis processes and soot growth. The transient vortex and steep spatial gradients require the temporal and spatial capabilities of LII.

Conclusions

Combustion processes exhibit rather different features in microgravity compared to normal gravity. With the elimination of buoyancy-induced convection, both flame shape and f_v differ substantially compared to the same fuel/burner system in normal gravity. The sensitivity, temporal and spatial capabilities in addition to geometric versatility enable LII to reveal the soot volume fraction regardless of these differences. Comparison of radial f_vs obtained by light extinction and LII validate LII for f_v determination in low-gravity. Application of LII to a laminar gas-jet flame of ethane illustrates the sensitivity of LII while application to a turbulent diffusion flame of acetylene and vortex formed by a transient gas-jet diffusion flame of propane demonstrate the high temporal and spatial capabilities of LII for f_v determination. Spatial and concentration differences of f_v in 1-g and 0-g environments are readily illustrated by comparison of the LII images.

Acknowledgements

Disclaimer

Manufacturer and product names are used to aid understanding and do not constitute an endorsement by the federal government.

References

1. Soot Formation in Combustion, (H. Bockhorn Ed.), Springer-Verlag, Heidelberg, (1994).
2. Proceedings of the Third International Microgravity Combustion Workshop, (NASA CP–10174), April 11-13, Cleveland, OH (1995).
3. Eckbreth, A.C., Laser Diagnostics for Combustion Temperature and Species, Gordon and Breach, Amsterdam, The Netherlands, 2nd ed. 1996. p. 254.
4. Melton, L.A., Appl. Opt. 23:2201 (1984).
5. Quay, B., Lee, T.W., Ni, T. and Santoro, R.J., Combust. and Flame 97:394 (1994).
6. Vander Wal, R.L. and Weiland, K.J., J. Appl. Phys. B59:445 (1994).
7. Vander Wal, R.L., Zhou, Z. and Choi, M.Y., Combust. And Flame 105:462 (1996).
8. Ni, T., Pinson, J.A., Gupta, S. and Santoro, R.J., Appl. Opt. 34:7083 (1995).
9. Shaddix, C.R. and Smyth, K.C. Combust. And Flame 107:418-452 (1996).
10. Vander Wal, R.L. and Dietrich, D.L. Appl. Opt. 34:1103 (1995).
11. Vander Wal, R.L., Appl. Opt. 35:6548 (1996).
12. Lekan, J., Gotti, D.J., Jenkins, A.J., Owens, J.C. and Johnston, M.R., NASA TM–107090, April, (1996).
13. Stanford Research Systems, Application Notes, 1996-1997, Note no. 4, p. 186.
14. Engstrom, R.W., RCA Photomultplier handbook, The RCA Corporation, (1980).
15. Greenberg, P.S. and Ku, J.C. Combust. And Flame 108:227-230 (1997).
16. Dalzell, W.H. and Sarofim, A.L. J. Heat Transfer 91:100-106 (1969).
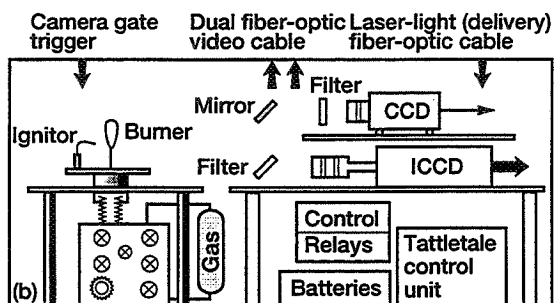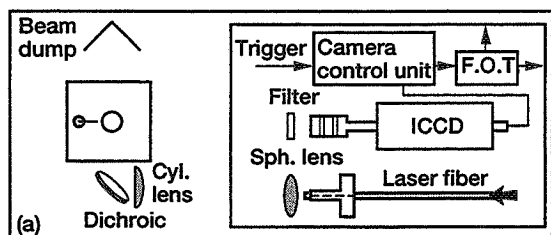
Figure 1.—(a) Top view of the hardware and optical layout of the drop rig. (b) Corresponding side view.
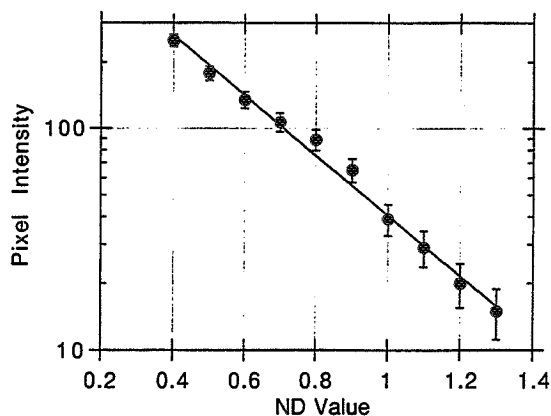
Figure 2.—Average LII pixel intensity versus neutral density filter value (ND) preceding the LII camera. See text for details.
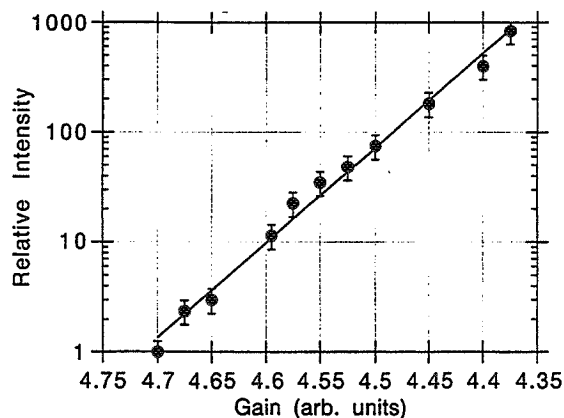
Figure 3.—Camera intensifier gain calibration curve. Note that higher intensifier gains correspond to smaller values of the gain setting. See text for details.
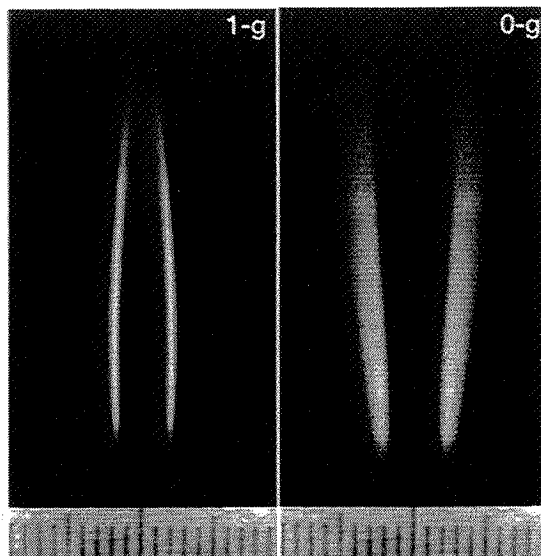
Figure 4.—LII images of a laminar acetylene gas-jet diffusion flame in 1-g and 0-g. The burner nozzle is 1 mm above the picture bottom (but is not observable in the LII images). The ruler spatial scale is in millimeters.

309
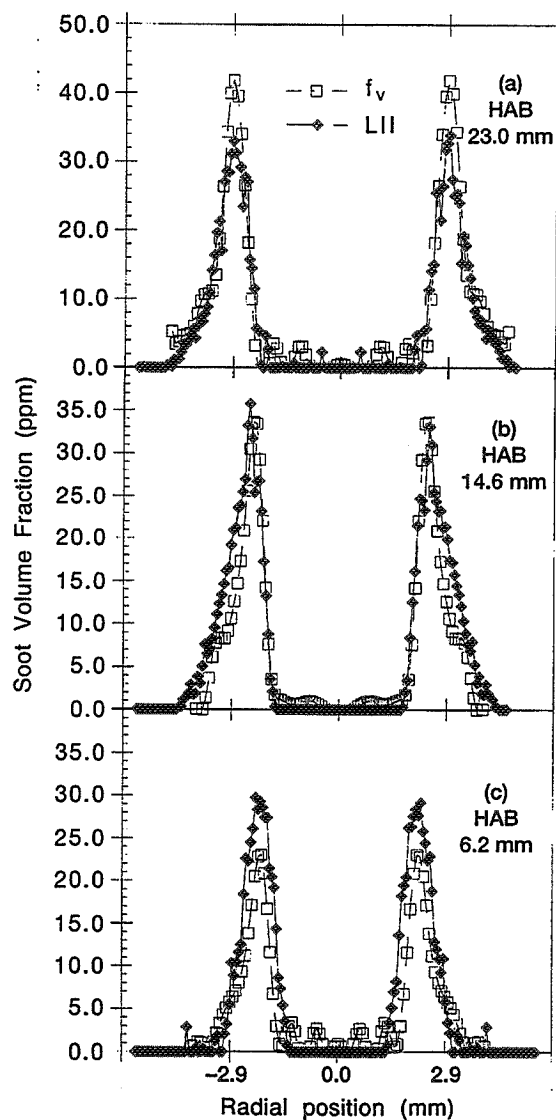
Figure 5.—Comparison of LII radial intensities with f_v determined through light extinction in the laminar gas-jet flame of acetylene in 0-g (shown in Fig. 4) at the indicated axial heights above the burner.

Figure 6.—LII images of a laminar ethane gas-jet diffusion flame in 1-g and 0-g. The burner nozzle is 11 mm below the picture bottom. The ruler spatial scale is in millimeters. See text for details.
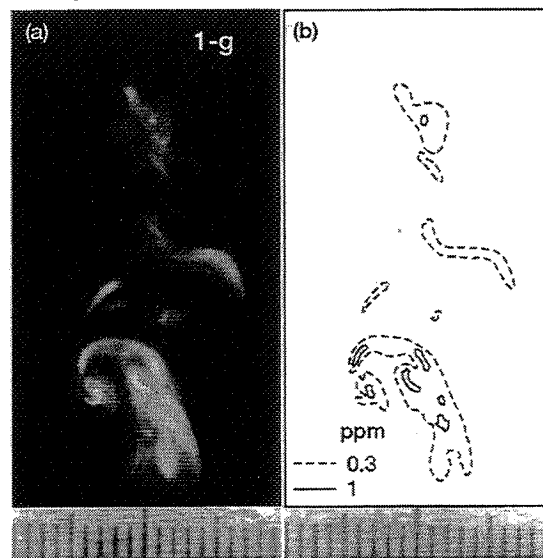
Figure 7.—(a) LII image of soot within the oxidation region of a turbulent gas-jet flame of acetylene. (b) Contour plot of (a) with f_v values given in ppm. The image bottom is 100 mm above the burner nozzle. The ruler spatial scale is in millimeters.

Figure 8.—(a) LII image of a vortex formed during initial formation of a laminar gas-jet flame of propane in 0-g. (b) Contour plot of (a) with f_v values given in ppm. Both fuel flow and ignition were initiated in 0-g. The nominal steady-state fuel flow rate was 70 sccm. The burner nozzle is 11 mm below the picture bottom. See text for details.

310

LIF THERMOMETRY OF A FUEL DROPLET BURNING UNDER MICROGRAVITY IN A DROP SHAFT

Toshikazu Kadota, Katsumasa Suzuki
Tomohiro Fujii and Daisuke Segawa
Osaka Prefecture University
Sakai, Osaka Japan
Mitsuhiro Tsue
· University of Tokyo
Tokyo, Japan

Introduction

The achievement of the combustion research under microgravity depends substantially on the availability of diagnostic systems. The non–intrusive diagnostic systems are potentially applicable for providing the accurate, realistic and detailed information on momentum, mass and energy transport, complex gas phase chemistry, and phase change in the combustion field under microgravity. The non–intrusive nature of optical instruments is essential to the measurement of combustion process under microgravity which is very nervous to any perturbation. This has resulted in the increased interest in the development of the non–intrusive diagnostic systems available for the combustion experiments under microgravity. Although extensive efforts have been directed toward this subject(1)–(3), the diagnostic system remains largely undeveloped.

The laser–based non–intrusive diagnostic systems have been successfully employed to the research of various combustion processes under the terrestrial condition. However, the application of the non–intrusive diagnostics to the combustion experiments under microgravity is accompanied by several constraints which happen to be crucial. A very limited space is only available for constructing a highly sophisticated system which is so sensitive that it is easily affected by the magnitude of gravitational force, vibration and heterogeneous field of temperature and density of the environments. Usually, the system should be properly adjusted prior to the experiment. It is quite difficult to tune the instr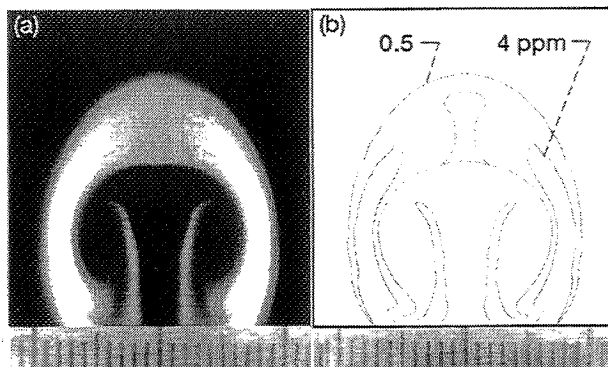uments during measurements. The programmed sequence of operation should also be provided. The flame under microgravity tends to be highly sooty. The strong black body radiation from soot in the flame often causes the hazardous noise in various optical measurements.

This paper describes a part of the recent results obtained in a series of the research program on the development of non–intrusive diagnostic systems available for combustion experiments under microgravity. An attempt has been made to solve the above problems for developing a compact non–intrusive diagnostic system to do the instantaneous measurements of the

temperature of a fuel droplet burning under microgravity in a drop shaft on the basis of the laser induced fluorescence thermometry which has been reported to be successfully applied for a single fuel droplet and a cloud of fine droplets in a fuel spray under the terrestrial condition(4)-(7).

Experimental Procedure

The principle of the LIF thermometry used in the present study consists of monitoring the temperature-dependent fluorescence emission spectra of laser excited fuel droplets doped with small amounts of appropriate organic additives. The liquid fuels tested was n-octane. This was doped with 2.5 % naphthalene and 1 % TMPD (N,N,N',N' tetramethyl-p-phenylene diamine). Preparation of test fuel was done in nitrogen environments to prevent TMPD from being oxidized.

Figure 1 illustrates schematically the experimental apparatus. A remote controlled fuel supply system was provided to suspend a fuel droplet with an initial diameter approximately 2.0 mm at the spheroidal portion of the tip of a quartz fiber of the diameter 0.7 mm in quiescent gaseous environments. The ignition of the droplet was made by an electrically heated coil which was allowed to translate. Right after the droplet ignition, the heating coil was removed and kept away from the droplet in order to prevent the droplet flame from being perturbed. An ultraviolet photodetecter was provided to determine the instance of the first appearance of the flame kernel around the droplet which is much less sensitive to the black body radiation from the heating coil. A CCD camera was provided for the photographic observation of the droplet surrounded by an envelope flame.

The excitation source for all fluorescence emission spectra was a nitrogen laser emitting monochromatic radiation at a wavelength of 337.1 nm, a pulse energy of 2.5 mJ/p, a pulse width of 5 ns and a frequency of 1-10 Hz. A cylindrical lens was used to focus the incident laser light on the optical center where a fuel droplet was allowed to burn. The optical detection system consisted of a convex lens with a 60 mm focal length and an optical multichannel analyzer (OMA) with a gated image intensifier. The electrical output signal from the OMA was recorded and processed with a personal computer on board. A pair of pulse generators were available to synchronize the excitation of laser and the gating of the image intensifier. The period of time for gating the image intensifier was set so short as to be able to neglect the black body radiation from soot in the droplet flame. The difference between the signals from the OMA with and without laser excitation gives the background noise and the fluorescence emission signal of interest.

Figure 2 shows the detailed geometry of the optics in the vicinity of the droplet flame. The axis of the optical detection system was set to pass through the center of the droplet at 80 degrees inclined to the axis of the incident laser light on the same horizontal plane. Monitored was the fluorescence emission from a minute area of the fuel droplet enclosed in a circle of diameter 0.03 mm.

Figure 3 shows the fuel supply system which consists of a hypodermic needle, a syringe and a flexible plastic tube. This was driven by two sets of a stepping motor and a rack-pinion mechanism which were actuated with the command of a remote switch outside the capsule via

a controller and an interface board. After the tip of needle approached to the fine quartz fiber, the piston of syringe was allowed to translate for squeezing the fuel inside it toward the needle. This resulted in the formation of a droplet suspended at the tip of quartz fiber followed by the withdrawal of the needle away from the quartz fiber. Thereafter, the droplet was ignited by the movable heating coil.

Figure 4 shows the apparatus installed in the rack of the capsule of the drop shaft in the MGLAB (Microgravity Laboratory of Japan). The inner diameter and the height of the cylindrical rack are 760 mm and 885 mm, respectively. The lower portion of the rack was installed with a nitrogen laser, a combustion chamber in which a fuel droplet was allowed to burn, a CCD camera, a fuel supply system and an OMA with a gated image intensifier, and a battery. The upper portion of the rack was available for the installation of the other parts of the apparatus including a personal computer with a battery for its exclusive use, a controller for the image intensifier, pulse generators for the image intensifier and the nitrogen laser. All of them were enclosed inside the capsule which was allowed to fall freely from the top of the vacuum tube in the MGLAB drop shaft. This provides 4.5 seconds of the period of time for the combustion experiments under microgravity of the level of 10–5 g.

Experimental Results

Figure 5 shows a family of instantaneous fluorescence emission spectra from an n–octane droplet which was subjected to the irradiation of a single pulse of the incident nitrogen laser at different times t elapsed after the droplet ignition. The droplet flame was observed to be spherical and fairly sooty as expected. Fortunately, only a single shot of laser excitation could cause the fluorescence of which intensity was much higher than the level of noise due to black body radiation from soot in the flame. This figure demonstrates that the fluorescence emission spectra vary with the lapse of time after ignition which corresponds to the increase of the droplet temperature. It is evident that the peak intensity decreases remarkably and the intensity at longer wavelength increases. The fluorescence at the wavelength approximately 380 nm might primarily be due to the excited TMPD fluorescence.

It is not clear whether or not the fluorescence emission spectra are derived from the thin layer near the droplet surface or at the interior of the droplet; it may be the average over the optical path length. Small amounts of naphthalene or TMPD tends to remain on the surface of the quartz fiber at the end of droplet evaporation. Because this may alter the fluorescence emission spectra in the following test run, the tip of the quartz fiber was held in a nonluminous flame after each test run. Preliminary test results showed that the quartz fiber did not have an appreciable effect on the measured fluorescence emission spectra. It was also found that the intensity of fluorescence emission from a droplet with no dopant was much weaker than one from a doped droplet.

The determination of the droplet temperature was based on the spectral band ratio. The fluorescence emission intensities were monitored at an appropriate set of two different wavelengths and the temperature was determined from the resultant intensity ratio. An alternative approach is the determination of the droplet temperature based on the spectral band contour of the fluorescence emission spectra which was not employed in the present study. The relationship between the intensity ratio and the droplet temperature measured by using a

thermocouple has been preliminarily determined. This has provided a library of the intensity ratio curve as a function of the concentrations of oxygen, water vapor and carbon dioxide in the ambient gas, the velocity of the droplet relative to the ambient gas, the concentration of TMPD and naphthalene doped in the droplet and a set of two wavelengths selected.

The library of the intensity ratio curve is available to determine the time history of the droplet temperature based on the measured results of the consecutive fluorescence emission spectra as shown in Fig. 5. Fig. 6 shows the time history of the n-octane droplet temperature under microgravity in the drop shaft. It is evident that the droplet temperature shows an abrupt increase right after the ignition, followed by the gradually increase later. The temperature curve approaches an asymptote below the saturated temperature of n-octane in the last period of combustion. Although data are a little scattered, the results are generally rational.

Conclusions

An attempt was made to develop the compact non-intrusive diagnostic system applicable for the measurement of the instantaneous temperature of the fuel droplet burning under microgravity in the capsule of the drop shaft. The thermometry was made by monitoring the temperature-dependent fluorescence emission spectra of laser excited fuel droplets doped with small amounts of appropriate organic additives.
The primary conclusions reached in the present study are as follows.
(1)The newly developed diagnostic system is successfully applicable for the instantaneous and non-intrusive thermometry of the droplet burning under microgravity in the drop shaft.
(2)The ratio of fluorescence emission intensities at an appropriate set of two different wavelengths is an appropriate criterion for the in-situ determination of droplet temperature.
(3)A single shot of nitrogen laser excitation is able to cause the fluorescence of which intensity is much higher than the level of noise due to black body radiation from soot in the flame.

This study is carried out as a part of "Space Utilization Frontiers Joint Research Projects" promoted by NASDA and Japan Space Utilization Promotion Center.

References

(1)Greenberg,P.S., "Capabilities and Constraints of Combustion Diagnostics in Microgravity", The Second International Microgravity Combustion Workshop, (1993), 61-66.
(2)Kadota,T.,"Diagnostics in Japan's Microgravity Experiments", The Third International Microgravity Combustion Workshop, (1995), 257-262.
(3)Winter,M., "Laser Diagnostics for Microgravity Droplet Studies", (1995), ibid., 291-296.
(4)Murray,A.M. and Melton,L.A., "Fluorescence Method for Determination of Temperature in Fuel Sprays", Appl. Opt., Vol.24, No.17(1985), 2783-2787.
(5)Gossage,H.E. and Melton,L.A., "Fluorescence Temperatures Using Intramolecular Exciplexes", Appl. Opt., Vol.26, No.11(1987), 2256-2259.
(6)Kadota,T., Miyoshi,K., Taniguchi,Y. and Tsue,M., "Exciplex-Based Fluorescence Method for Remote Probing of Fuel Droplet Temperature", SAE Paper 910729, (1991).
(7)Kadota,T., Tsue,M. and Miyoshi,K., "Laser-Induced Fluorescence Thermometry of Burning and Evaporating Fuel Droplets", Ed. by Kuo,K.K. and Parr,T.P., "Non-Intrusive Combustion Diagnostics", Begell House, (1994), 87-97.

1. nitrogen laser
2. lens
3. droplet
4. fuel supply system
5. heater
6. quartz fiber
7. lens
8. slit
9. OMA with I.I.
10. pulse generator
11. pulse generator
12. computer
13. controller
14. CCD camera
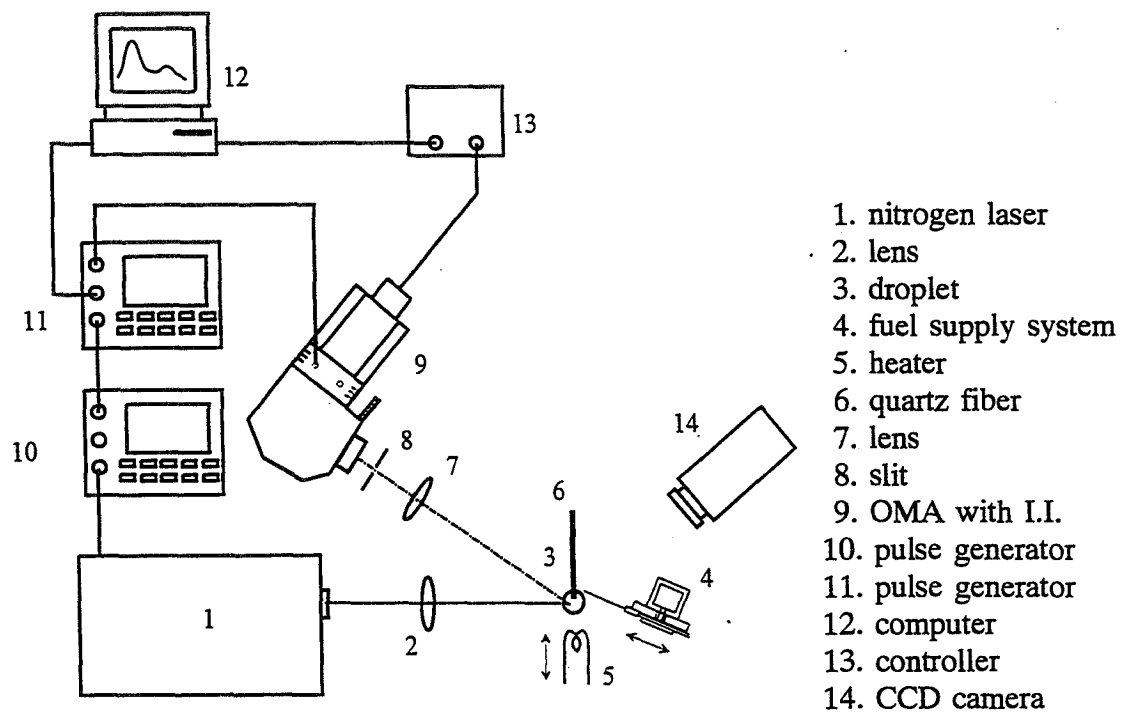
Fig.1 Schematic diagram of experimental apparatus

Fig.2 Field of View

1. Stepping motor   7. Fuel droplet
2. Rack and pinion   8. Heater
3. Needle   9. Interface board
4. Plastic tube   10. Pocket computer
5. Syringe   11. Controller
6. Quartz fiber   12. Remote switch

Fig.3 Fuel supply system

315

Top view   Front view

Fig.4 Experimental apparatus installed in the rack of capsule
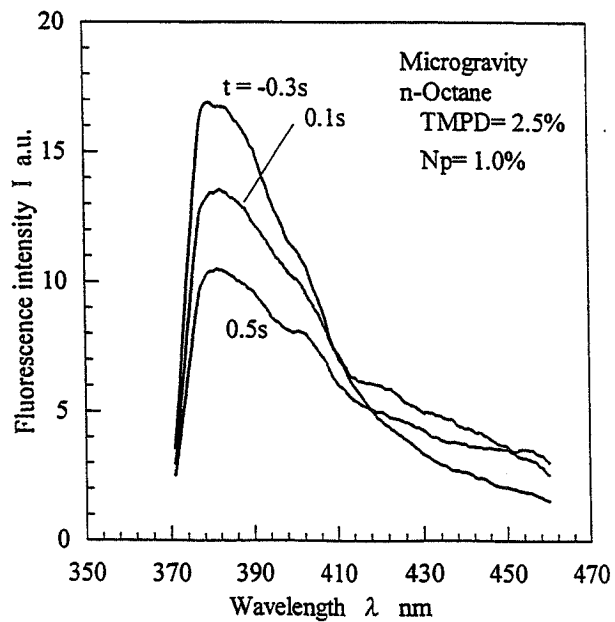
Fig.5 Fluorescence emission spectra   Fig.6 Time history of droplet temperature

RECENT DEVELOPMENTS AND APPLICATIONS
OF THE COMBUSTION DIAGNOSTICS AT BREMEN DROP TOWER

Ch. Eigenbrod*, J. König*, W. Triebel**

*Center of Applied Space Technology and Microgravity, ZARM, Bremen, Germany
**Institute for High-Technology in Physics, IPHT, Jena, Germany

ABSTRACT

The Bremen drop tower laser diagnostics for microgravity combustion research application have been further developed. These developments, that are either already implemented or in the test phase, are described in detail hereby. The developments are following guidelines given by the experimenters requirements or to improve the implementation into the drop tower operation. Besides the standard capabilities of:

- OH-LIPF (248nm) with 250 frames/s picture acquisition
- quasi-on-line data transmission via internet,
- high-speed video image processing,
- image data storage on compact disc coming along to the experimenter including the video image processing software,

the developments are concerning:

- remote calibration prior to each drop to OH, O_2 or NO resonance lines,
- two-line LIPF thermography (OH-OH) with 125 Hz pulse/frame repetition rate for each line,
- two species LIPF (e.g. OH - hot O_2),
- on-off resonance LIPF (e.g. for OH detection in a broadband absorbing chemical environment) with 125 Hz pulse/frame repetition rate for each line,
- in-capsule Raman-shift to e.g. aldehyde resonance lines.

The application section of the paper describes recent results from applying the laser diagnostics to fuel droplet- and PMMA combustion.

INTRODUCTION

The drop tower located in Bremen, Germany, a groundbased short term microgravity facility provides three "flights" of 4.75s duration each a day. To reduce the aerodynamical drag of the free falling capsule and thus achieve a residual gravity level of better than $10^{-5}g_o$ the complete drop tube is evacuated down to 10Pa. A UV-excimer laser, that can be operated at up to 250 Hz is attached a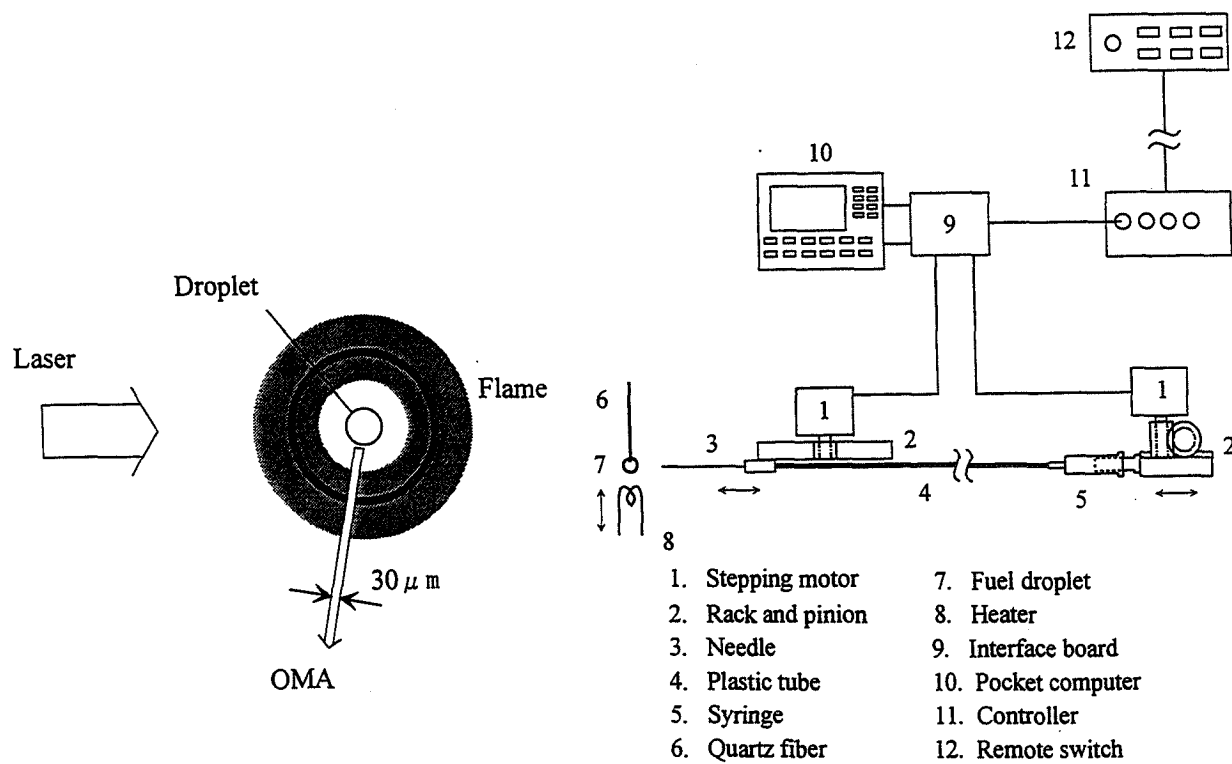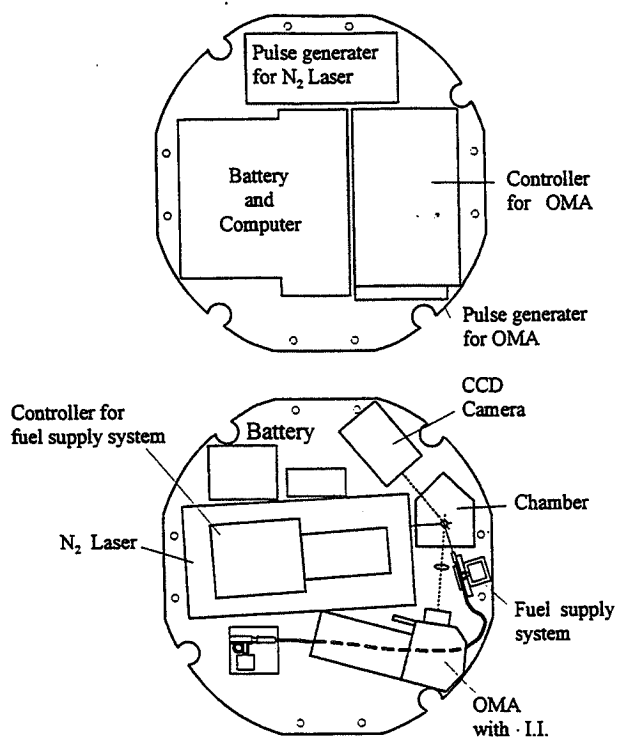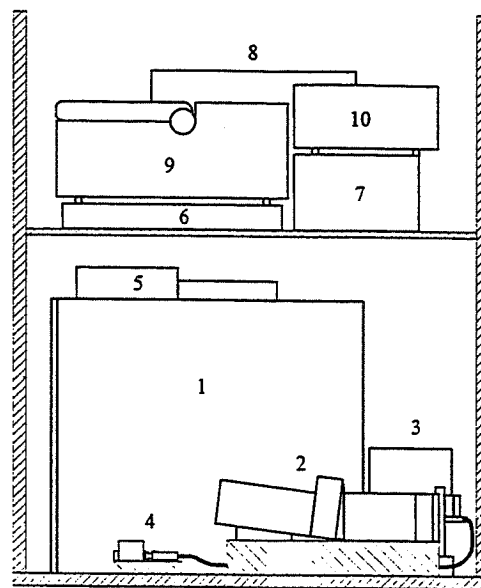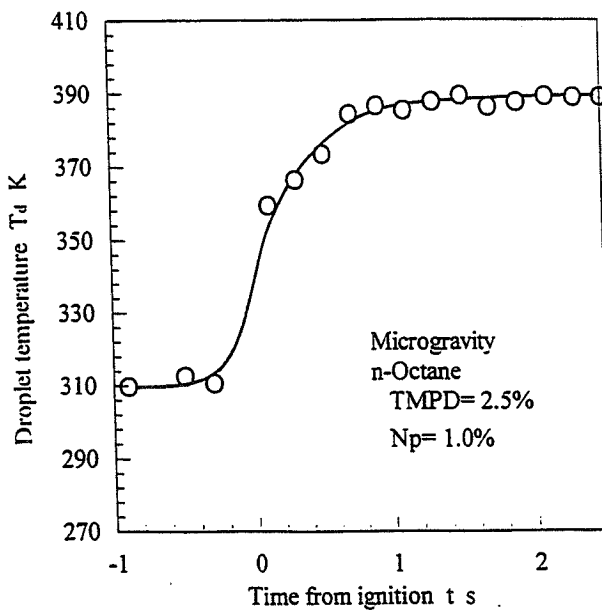t the top of the tower. The light beam is mirrored into the free falling capsule and is shaped to a light sheet before entering the test section for two dimensional measurements. The fully modular outline of the capsule allows a rapid change of the experimental setups mounted on plattforms in a rack. Thus the UV-laser system, as well as the intensified high speed camera and the digital storage, can be adopted for various types of experiments. Even though there is an extremely wide scope of experiments in the field of fluid mechanic-, material science or microbiological research that could benefit from that equippment, it is primarily designed to investigate on reacting flows.

Microgravity droplet combustion research gained numerous important information on the fundamental processes about the transportation mechanisms during evaporation, ignition, quasi steady burning and extinction [1]. Burning a single isolated fuel droplet or groups of fuel droplets under conditions of a quiescent surrounding gas atmosphere and quasi weightlessness, the diffusion controlled mechanisms become unveilled. Characteristic properties like ignition delay, burning lifetime, flame radius, light emission spectra and the formation of soot could easily be determined by employing nonintrusive photo-optical means [2,3].

Non-intrusive UV-laser diagnostics are well established in terrestrial combustion laboratories [4,5]. Deep insight was provided especially in the structure of the reaction zone in laminar and turbulent diffusion flames. By using narrowbanded lasers, which are recently available in a wide range of wavelengths, numerous species like OH, NO, NCO, NH_2 and molecules like O_2, H_2O can distinctly be detected by laser-induced-fluorescence. For special experimental conditions, the number of molecules like OH-radicals can be detected even quantitatively [6]. However, due to the strong light scattering of particles, overlapping the light yield of comparatively weak induced fluorescence, these tools are very difficult to apply to flows containing a liquid and gaseous phase. The presence of non-resonant absorbing matter often restricts the maximum pulse repetition rate allowed for the diagnostics to be still non-intrusive [7]. Moreover, the utilization of those techniques to microgravity facilities was restricted due to restrictions in mass, size and power consumption, and shock resistance, the setup has to meet [8].

SYSTEM DESCRIPTION

To achieve a fixed position of the UV laser beam relative to the drop capsule at the beginning of the drop experiment, the laser system is attached to the top of the vaccum tube of the drop tower. The laser beam is then expanded and reflected towards the falling capsule, entering the drop bus through a window at the top of the capsule. An active control system guides the beam through a light sheet optic to the experiment (Fig.1).
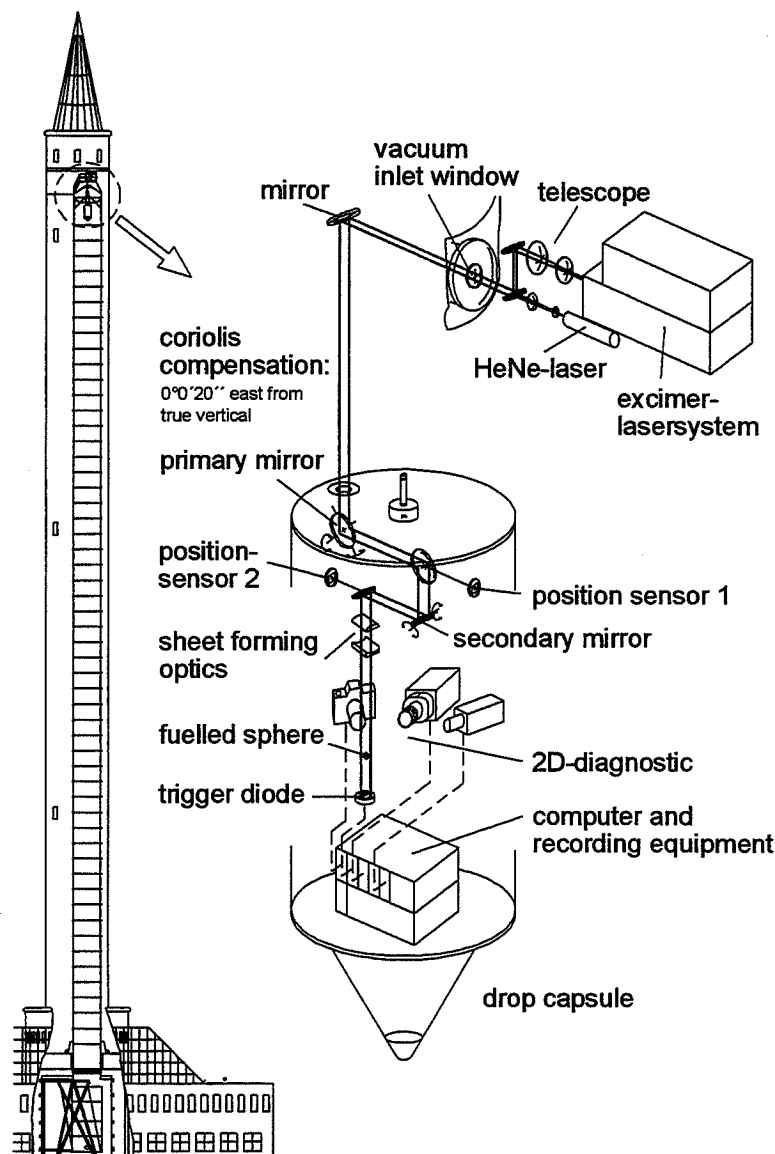
Fig. 1: Drop tower with drop capsule and beam guide of UV-lasersystem

Two UV-excimer lasers (*Lambda Physik LPX 120i, LPX 220i*) are used in an oscillator-amplifier configuration. The oscillator is equipped with an external narrowband unit using a tunable Littrow grating. Currently the lasers are used at 248nm (KrF⁺) emitting light pulses of 20ns duration with up to 400mJ per puls at 250 Hz pulse repetition rate. To obtain induced fluorescence from the OH concentration field that is almost independant of quenching effects and gas temperature, the laser becomes tuned to the $P_2(8)$ line of the $A^2\Sigma \rightarrow X^2\Pi$ transition of the OH. To ensure a proper wavelength tuning, the system is calibrated by a computer controlled reference fluorescence scan of hot oxygen directly prior to the drop experiment. Therefore a special tube furnace, equipped with a UV-photomultiplier is permanently mounted at the laser beam path. The grabbed O_2 spectrum and its grid position is then transformed to the OH spectrum. The NO resonance can be calibrated the same way. All functions to calibrate and operate the system are driven remotely from the control room of the tower.

In order to minimize the divergence of the laser beam over the operation distance range of 5 to 120m, the beam is expanded to 28 x 28 mm^2 by means of a telescope at the laser exit and formed to a thin sheet inside the drop capsule later [8].

Due to the mechanical deformations of the drop tube during evacuation, the wind forces acting to the tower and approximately 10:1 coupled into the tube and the coriolis force dependend deviation of the drop capsule (approximately 12mm) over the free-fall distance of 110m, the capsule does not follow the laser beam perfectly. To realign the laser light to the light sheet optic and finally to the experimental section, a hence called "pointing assembly" (PA) is mounted at the top end of the drop bus. By means of two positioning sensors (PSD) and two motorized gimbal mirrors, angular and lateral shifts are corrected by a computer controller in closed loop configuration. Since the energy distribution of the UV excimer laser varies from puls to puls and does not generate an appropriate signal on the position sensors, a continuous HeNe laser beam (633nm wavelength) is feeded to the UV-beam coaxially, before the expanded UV-laser beam is mirrored into the vaccum tube.
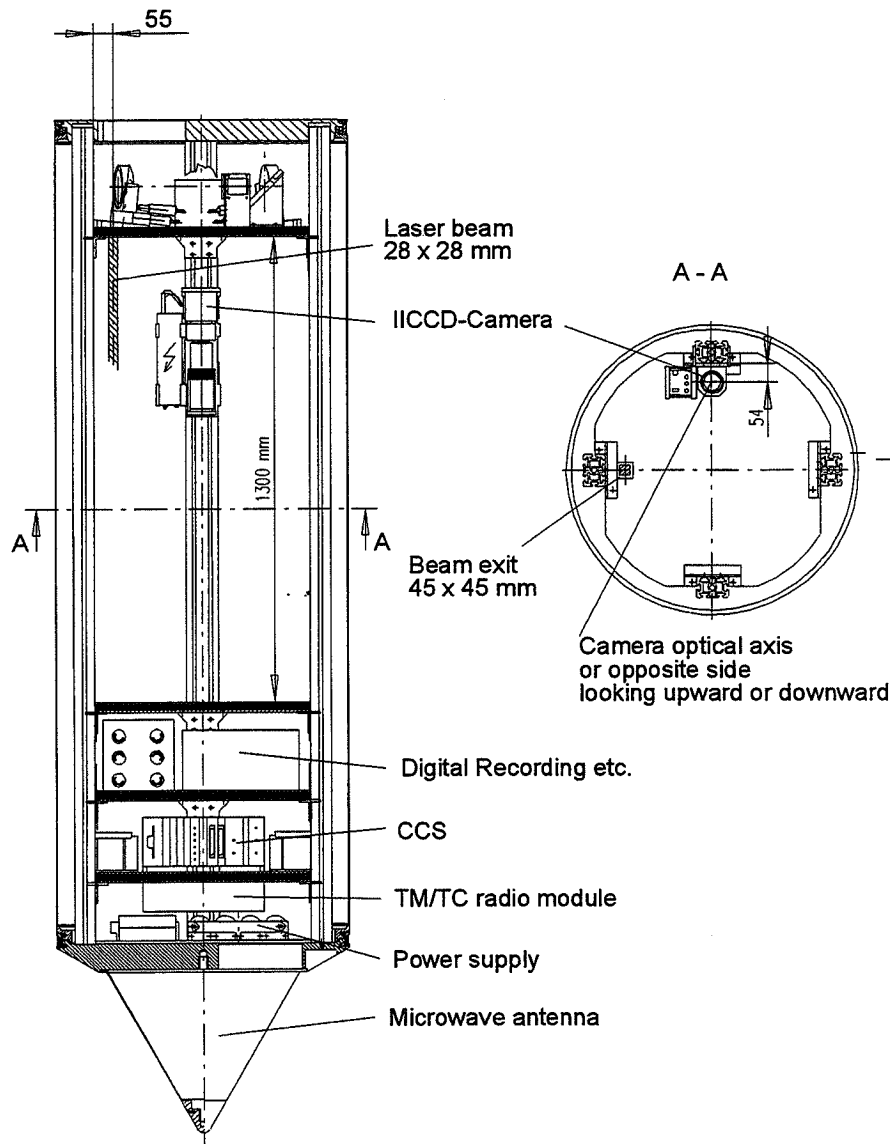
Fig. 2: Drop capsule including all housekeeping infrastructure for experiment control and combustion diagnostics

The Littrow grid tuning the laser to a certain wavelenght is equipped with a piezoelectric driver and can thus oscillate between to predetermined lines. These lines being of the same specie (two states) or of different species can so alternately be excited. For the acurate position and amplitude as well as exact triggering of the laser a function generator is an integral part of the top end hardware. All laser parts are thermally controled to prevent from temperature dependend drift of the preadjusted parameters.

Fig. 2 depicts the laser diagnostic drop bus containing from top:

* the pointing assembly,
* the payload volume of 1.3m height and a platform diameter of 700mm (600mm between the stringers) containing the two stage intensified high-speed camera of 256 x 256 pixels. The camera can look upward or downward mounted to the depicted stringer or the oppsite one. Assumed, the light sheet is passing the combustion section horizotally, the orthogonally grabbed image must also be mirrored. The camera is equipped with the appropriate filter and a *NIKKON* UV-lens,
* the delay generator and digital recorder platform. The delay generator serves for accurate synchronization of the camera gate to the laser pulse. This is been accomplished by detecting the incoming pulse through a UV-photodetector and triggering the camera to the next pulse 4ms later at 250 Hz pulse repetition rate. The digital video recorder consists of a frame grabber and a 96 MByte video RAM. After braking of the capsule the data can be tranferred into the computer network via a microwave antenna mounted in the nose-cone.
* the capsule computer system (CCS) described elsewhere [9] serves for experiment control and housekeeping data acquisition.
* the experiment power supply described in [9].

The Raman cell for excitation wavelenght shift to e.g. aldhyde lines is under ground testing and thus not implemented in the picture. To avoid the cell to reduce the payload volume it is planned to implement it into the stringer along the entrance beam. The cell operated at 248nm input waveleght will deliver the following output data:

Line	Wavelenght [nm]	opt. H_2-pressure [bar]	Efficiency [%]
AS 1	225	3	3.5
S 1	277	2	31
S 2	313	3	16
S 3	360	9	15
S 4	423	7	3

Tab. 1: Test data of the Raman-cell

Fig. 3: Image data acquisition, -handling and processing

Fig. 3 depicts the schematic of the video data handling. The specially developed PC-based video image processing softare is designed to handle the vast amount of video data applying standard algorithms as well as calculations spezialized for combustion analysis such as spatial filtering, intensity following plot, histogram development etc. not only to single frames but also to a predetermined number of f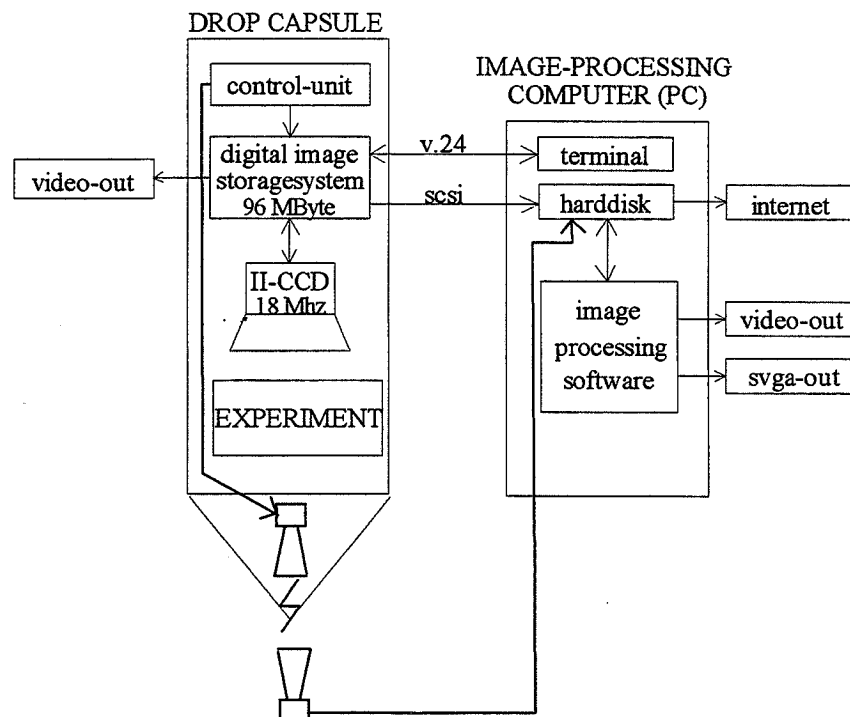rames of the video. The output can be either data (sent or stored on CD) or VCR format. A *WINDOWS* compatible version instead of a *DOS* version will soon be finished.

APPLICATIONS

Droplet diffusion flames are being observed by OH-LIPF under microgravity utilizing the porous sphere technique [8]: A sphere made of a fine silica fibre matrix (80% vol. porosity) with a diameter of 6.75mm was placed in the center of the UV-laser light sheet. An aperture was used to shield the sphere from direct impact of the laser light and to prevent the camera from high intensity scattering. Before dropping the capsule the sphere is completely drenched with pure hydrocarbon fuel (n-heptane) so as to achieve properties very close to an all fuel droplet. The ambient gas was air at atmospheric pressure and 293K temperature. The fuel was ignited 1s after the release of the drop capsule. Fig. 4a and 4b show selected laser induced fluorescence images of an n-heptane drenched sphere 240ms after the assisted ignition. The first picture (4a) shows the complete fluorescence field with the excimer laser beeing narrowbanded tuned to the electronic transition of the OH $(P_2(8))$. Fig. 4b is the result of subtracting a picture obtained at the same instant (at another drop experiment) with the laser tuned "off" that OH-transition, thus exciting barely broad band fluorescing species and no OH-radicals, from figure 4a. As can be concluded by the aid of pictures from the visual spectra and the measurements done by Aldred et al [10], the inner zone of high fluorescence intensity accounts for broadband fluorescence of hydrocarbon intermediates equal or larger than C_2. In the contrary the outer ring does only account for the fluorescence of OH radicals. The slight inflection of the fluorescence intensity next to the zone of high OH-concentration towards the porous sphere shows, that most larger hydrcarbons are consumed before the vaporized fuel reaches the reaction zone.
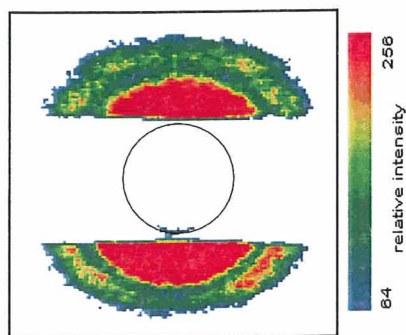
Fig.4a: LIPF image of an n-heptane drenched sphere burning under microgravity condition; OH plus broadband fluorescence
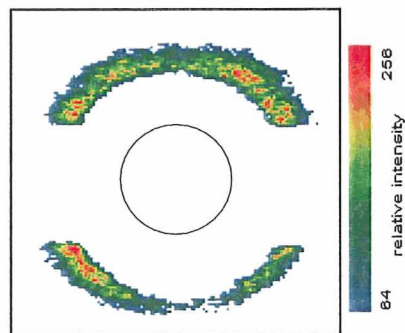
Fig.4b: LIPF image of an n-heptane drenched sphere burning under microgravity condition; OH fluorescence

Experiments on methanol drenched spheres did not show signals of non-resonant reacting molecules and thus is much easier to investigate on [8]. The effects showed above were one important reason for the development of the oscillating grid technique because data from different drop experiments rarely fit as well as in the case shown. Strongly broadband absorbing zones do also collect some laser energy leading to a measurable effect below a repetition rate of 250 Hz. Ground based experiments have to help determine the fuel dependent maximum repetition rate (and flame position dependent because of the 1g character) to keep this technique low intrusive at least.

The evaluation of a drop experiment on n-heptane, comparing the OH-LIPF signal with the visual appearance collected through videography and photography during the same experiment showed, that the position of the maximum OH-concentration coincides almost perfectly with the thin blue layer of CH luminosity and thus the reaction zone. Due to the size of the sphere, the flame stand-off ratio is slowly growing and quasi steady burning cannot be reached within the duration of microgravity availible during one drop experiment.

To prepare the application of the OH-laser diagnostic to PMMA flames it could recently be shown under terrestrial conditions, that the broadband absorption of the vaporized solid is much lower than expected. The minimum distance of the UV light sheet to the probe could be as small as 1mm. The sooting plume of a fully developed flame, as apparent under 1g conditions, is of course highly broadband absorbing and thus impossible to investigat on. But under microgravity conditions the burning rate is expected to be much lower and the flame less sooty.

CONCLUSION

A UV-excimer laser based laserdiagnostic system has been established at the drop tower of Bremen. For the first time, non intrusive diagnostics like LIF and LIPF, can be used for experiments under microgravity condition. A powerful digital high speed camera is capable to record images in the visible spectrum, as well as intensified and gated two dimensional spectroscopic data. Both systems are designed to operate simultaneously up to a repetition rate of 250Hz (full frame mode), furnishing observations of fast or transient processes.

OH-LIPF was used to observe the gas phase reactions of burning hydrocarbon fuel-drenched porous spheres under microgravity condition. Qualitative OH-concentration images could be recorded for methanol and n-heptane under microgravity- and PMMA flames under terrestrial conditions.

By controlling the energy distribution in each individual laser shot quantitative LIPF will be available in the near future. By changing the excitation wavelength, access will be given to measure minor and major species like NO, O_2 and H_2O and aldehydes. A narrow band unit, that is capable to intermittently change the excitation wavelengh of the UV-laser from shot to shot with 125Hz is currently under development. Thus non-intrusive two dimensional temperature measurements in reacting gas phases are supposed to be available soon.

ACKNOWLEDGEMENT

REFERENCES

[1]   C.K. Law, G.M. Faeth: "Opportunities and challanges of combustion in microgravity", *prog. energy and comb. sci.*, 20, 65, London (1994)

[2]   M. Tanabe, M. Kono, M. Sato, J. König, C. Eigenbrod, H. J. Rath: ''Effects of natural convection on two stage ignition of an n-dodecane droplet'', *25th (int.) symp. on combustion*, the combustion institute, Pittsburgh, pp 455-461 (1994).

[3]   M.Y.Choi, F.L. Dryer, J.B. Haggard jr.: "Observation on a slow burning regime for hydrocarbon droplets: n-heptane/air results", *23rd (int.) symp. on comb*, 1597, Pittsburgh (1990)

[4]   G.Kychakow, R.D. Howe, R.K. Hanson: "Use of planar laser-induced fluorescence for the study of combustion flowfields, *AIAA No.83-1361*, Seattle (1983)

[5]   K. Kohse-Höinghaus: "Laser techniques for the quantitative detection of reactive intermediates in combustion systems", *prog. energy comb. sci.*, 20, 203, London (1994)

[6]   R.K. Hanson: "Quantitative absorbtion and fluorescence diagnostics in combustion systems", *3rd int. symp. on speial topics in chem. prop.*, Scheveningen (1993)

[7]   J. König, C. Eigenbrod, M. Tanabe, H. Renken, H. J. Rath: ''Characterization of spherical hydrocarbon fuel flames: Laser diagnosis of the chemical structure through the OH-radical, *26th int. symposium on combustion*, Neapel (1996).

[8]   C. Eigenbrod, J. König, T. Bolik, T. Behrens, F. Dinkelacker, H. J. Rath, H. Albrecht, D. Müller, T. Schröder, W. Triebel: ''Development of an UV-laser diagnostic system for combustion research under zero-gravity at drop tower Bremen'', *7th int. symposium on application of laser techniques to fluid mechanics*, Lisbon (1994).

[9]   Drop Tower "Bremen" User's Manual, Version 2.2 - 7/92 (under review).

[10]   J.W.Aldred, J.C. Patel, A.Williams: "The mechanism of combustion of droplets and spheres of liquid n-heptane", *Combust. flame*, 17:139, (1971)

MICROGRAVITY ENVIRONMENT
CHARACTERIZATION PROGRAM

Richard DeLombard[1], Roshanak Hakimzadeh[1], and Melissa J. B. Rogers[2]
[1]NASA Lewis Research Center, Cleveland, Ohio
[2] Tal-Cut Co., N. Olmsted, Ohio

ABSTRACT

The Microgravity Science and Applications Division (MSAD), a division within NASA's Office of Life and Microgravity Science and Applications, sponsors a broad range of space-based research in biotechnology, combustion science, fluid physics, fundamental physics, and materials science. To better understand and exploit the orbital environment, MSAD has developed methods and hardware to characterize accelerations on microgravity experiment carriers. MSAD supports research to verify analytically derived acceleration requirements for experiments and provides vibration isolation for sensitive experiments.

The Microgravity Measurement and Analysis Project (MMAP), supported by MSAD, incorporates four projects: the Space Acceleration Measurement System (SAMS), the Orbital Acceleration Research Experiment (OARE), the SAMS for International Space Station (SAMS-II), and the Principal Investigator Microgravity Services (PIMS). SAMS was developed to record microgravity accelerations and the OARE was developed to record very low-frequency microgravity accelerations on-board the NASA Orbiters. The SAMS is also used for cooperative investigations on the Russian Mir space station. The SAMS-II is being developed for the same function on-board the International Space Station (ISS). PIMS utilizes microgravity acceleration data to develop a description of each microgravity mission's acceleration environment and to support microgravity investigators in interpreting possible effects of the acceleration environment on their experiments. These elements of the MSAD program will be used to define acceleration requirements for future Orbiter and ISS payloads.

This paper describes the MMAP and summarizes the products and services available to principal investigators and other users. This paper also presents some microgravity acceleration characterization results from the last six years of Orbiter microgravity missions.

INTRODUCTION

Biotechnology, combustion science, fluid physics, fundamental physics, and materials science experiments are conducted on the NASA Space Shuttle Orbiters to take advantage of the reduced gravity environment resulting from the continuous free fall state of low earth orbit. Accelerometer systems are flown on the Orbiters to record the microgravity environment which is composed of quasi-steady accelerations and vibrations of the Orbiter, equipment, and local structures.

The purpose of the Microgravity Measurement and Analysis Project (MMAP) at NASA Lewis Research Center is to measure and characterize the microgravity environment on-board the NASA space shuttle Orbiters, the Russian Mir space station, and the International Space Station (ISS) and to provide this information to the microgravity science community. The Principal Investigator Microgravity Services (PIMS) group within MMAP works closely with the microgravity science community to identify the various effects of the environment on their experiments.

Accelerometer data from a mission are acquired and processed in response to requirements by the Principal Investigators (PIs) of science experiments. These data are then provided to the microgravity science community in the form of reports and on a file server, and special analyses are performed to support specific requests by the experiment principal investigators (PIs). More information is available in reference [1] on how to obtain the data generated by the MMAP organization. Additional information on interpreting the microgravity environment on the Orbiters is available in reference [2].

The microgravity environment needs to be considered when analyzing the results of a science experiment conducted in orbital conditions. In experiments conducted on Earth, the force of gravity dominates the effects of other smaller disturbances on an experiment. In general low-level vibrations, such

323

as seismic disturbances and refrigerator and building air conditioner operations do not disturb ground-based experiments. With the "absence" of gravity due to the free-fall condition of orbit, smaller vibrations related to equipment operations (for example) can have a predominant effect on an experiment.

This paper provides a description of the microgravity environment on the Orbiters. The measurement techniques used by the SAMS and OARE organizations are described, and a summary of the services provided by PIMS to the microgravity experiment teams is provided. Also, typical microgravity acceleration data from the past space shuttle missions are presented.

INSTRUMENTATION

Space Acceleration Measurement System (SAMS)

SAMS was developed to measure the low-gravity environment of Orbiters in support of MSAD-sponsored science payloads. The first mission for SAMS was STS-40 in June 1991 and SAMS units have flown on sixteen missions since then. One of the seven flight units was installed on the Mir space station in 1994.

A SAMS unit consists of three remote triaxial sensor heads and a data acquisition unit. SAMS data has been acquired in the Orbiter middeck, on carriers in the cargo bay, in the Spacelab module, and in the SPACEHAB module. SAMS units measure the environment with low pass bandwidths of 2.5, 5, 10, 25, 50, or 100 Hertz. More detailed descriptions of the SAMS accelerometers are available in the literature [3, 4]. In this paper the SAMS data is presented in Orbiter structural coordinates [5].

A new generation accelerometer system, called SAMS-II, is being developed to support the science experiments on-board the ISS. This unit will have many new features to cater to the operational scenarios on-board the ISS [6].

Orbital Acceleration Research Experiment (OARE)

The OARE was designed to measure low-frequency (quasi-steady) accelerations from below 10 nano-g up to 25 milli-g. OARE consists of three-axis sensor, an in-flight calibration subsystem, and a data acquisition unit [7, 8]. The sensor output acceleration signal is filtered with a Bessel filter with a cut-off frequency of 1 Hertz. The output signal is digitized at 10 samples per second and is processed and digitally filtered with an adaptive trimmean filter prior to storage on-board.

The OARE instrument is mounted to the floor of Columbia's cargo bay on a keel bridge. Utilizing OARE data and Orbiter real-time parameters, the quasi-steady acceleration levels for locations separate from the OARE instrument may be estimated in real-time. In this paper the OARE data is presented in Orbiter body coordinates [5]. OARE has acquired data on nine Orbiter missions to date.

MICROGRAVITY ENVIRONMENT

The microgravity environment on-board the Orbiter is generally separated into three classes: quasi-steady, vibratory and transient.

The quasi-steady regime is generally considered to be at those frequencies below the lowest natural structural resonance frequency of the vehicle. For the NASA Orbiters this lowest frequency is about 0.4 Hertz. Below this frequency, the Orbiter responds to disturbing forces as a rigid body. In general three additive sources of acceleration contribute to the resultant quasi-steady environment: aerodynamic drag, gravity gradient and rotational effects. The gravity gradient and rotational components are both related to the distance from the center of gravity (c.g.) of the Orbiter. Examples of other quasi-steady disturbances include Orbiter maneuvers and venting forces. Figure 1 shows the OARE data and two attitudes of the Orbiter during the STS-62 mission. This data shows the effect on the Orbiter quasi-steady environment during a maneuver. Since the atmospheric drag is reversed in the Z-axis direction, the acceleration levels for the OARE Z axis data is seen to reverse sign from before to after the attitude change.

Above the natural frequencies, the vehicle structure responds to local disturbances and transmits vibration throughout its structure. These disturbances could be oscillatory and/or transient in nature. The response at a particular location is a complex combination of disturbances from multiple sources. Typical sources of oscillatory disturbances include pumps, fans, centrifuges, crew exercise, and antenna motions. Transient accelerations are caused by sudden and irregular disturbance sources on the vehicle. The most

apparent are the thrusters which are operated to maintain the Orbiter's attitude. Figure 2 indicates the vibratory and transient nature of the microgravity environment of the Orbiter Columbia during a portion of the STS- 47 mission. The disturbance in the first half of the plot was caused by the vibrations related to a refrigerator compressor. A transient is visible following the turn-off of the compressor.

EFFECTS OF THE MICROGRAVITY ENVIRONMENT ON SCIENCE

Experiments are performed in space to take advantage of the unique advantages offered by the space environment. However, researchers may discover that their experiments are affected by microgravity disturbances on the Orbiter. The effects on science which are caused by the microgravity environment can include convective flow of gases and fluids, sedimentation of impurities, and drift of free-floating droplets.

Many microgravity experimenters have been concerned with the acceleration environment during their experiment operations. Combustion researchers quite often request inhibits for thruster firing, crew activity, and other possible disturbances during the experiment operations. Crystal growers have required that low-frequency acceleration levels be minimized to limit the convective flow in the molten material. In addition, some crystal growth experiments desire optimum values of the axial to radial ratio of the residual quasi-steady acceleration at the sample melt location.

Oscillatory and transient disturbances have had dramatic effects on experiments operating on-orbit. On STS-32, the Microgravity Disturbance Experiment (MDE) demonstrated the effects of crew exercise on a liquid bridge of indium [9]. The MDE included the Rockwell Fluids Experiment Apparatus and the Honeywell In-space Accelerometer. Oscillation of the liquid bridge was observed and filmed by a crew member while another crew member exercised on the Orbiter treadmill. In some cases, the liquid bridge oscillated so violently that it hit the side walls of the chamber.

On STS-52 and STS-75, the MEPHISTO experiment observed large changes in the concentration when the experiment was exposed to transient forces from Orbiter thrusters being fired [10]. Even though the thruster events were only about 34 seconds long, the disturbance to the diffusion field lasted 15 minutes or longer.

On STS-73, oscillations were observed on the free liquid surface in the Surface Tension Driven Convection Experiment (STDCE). One possible source of this disturbance was identified to be the fans inside the glovebox, specifically the cooling and air circulation fans. To investigate this, the decision was made during the mission to turn these fans off. The data from a SAMS sensor head with a filter cut-off frequency of 25 Hertz (sample rate was 125 samples per second) indicated that disturbances with frequency components at 20, 38, 43, 48 and 53 Hertz may be attributed to these fans. Figure 3 shows a SAMS power spectral density (PSD) plot from this sensor head. Note that the PSD is displayed out to the highest frequency possible to show the higher frequency (> 25 Hertz) disturbances. A better picture is obtained from the color spectrogram plot of the data [11]. As a result of this, during the STS-73 mission, the STDCE team requested that the fans be turned off during critical operations of the STDCE. These disturbances should be considered when experiments are operated in the glovebox.

The expected effects of the microgravity environment need to be addressed early in the experiment and mission planning process. Incorporating plans for controlling the microgravity environment while developing a mission timeline is important. Some aspects of a mission which may be manipulated to help control the microgravity environment are the crew timeline, Orbiter attitude and control, Orbiter altitude, and payload equipment operations. In addition vibration isolation systems may be considered for particularly sensitive experiments [12].

CONCLUSIONS

Consideration of the microgravity environment must start early in the planning and execution of a microgravity experiment. The MMAP group is available for assistance with understanding the microgravity environment at any stage in this process.

For each mission, the individual experiment operation times are planned carefully to minimize the effects of microgravity. Although the microgravity environment of the space shuttle Orbiters have been well characterized, the effects of this environment on the scientific experiments need to be better understood. In the past few years, the PIMS group has worked closely with the microgravity PIs to identify the microgravity disturbances and effects on science. The PIMS project has collected a database of

325

disturbances and effects on science. However, further research needs to be performed to better understand the effects of microgravity on science in order to fully utilize future microgravity laboratories, such as the ISS.

ACKNOWLEDGMENTS

The authors would like to thank Mr. Kevin M. McPherson and Mr. Tim Reckart for preparing the OARE data, and Mr. Kenneth Hrovat for preparing the SAMS data.

REFERENCES

1 Microgravity environment information available on world wide web page at URL: http://www.lerc.nasa.gov/www/mmap

2 R. DeLombard; "Compendium of Information for Interpreting the Microgravity Environment of the Orbiter Spacecraft", NASA TM-107032, 1996.

3 R. DeLombard and B.D. Finley; "Space Acceleration Measurement System Description and Operation on the First Spacelab Life Sciences Mission", NASA TM-105301, 1991.

4 R. DeLombard, B.D. Finley and C.R. Baugher; "Development of and Flight Results from the Space Acceleration Measurement System (SAMS)", AIAA 92-0354 (NASA TM-105652), January 1992.

5   R. Hakimzadeh, K. Hrovat, K.M. McPherson, M.E. Moskowitz and M.J.B. Rogers; "Summary Report of Mission Acceleration Measurements for STS- 78", NASA TM-107401, 1997 (page 2).

6 T. Sutliff; "Acceleration Measurement Capability on International Space Station Supporting Microgravity Science Payloads", AIAA 97-0349 (NASA TM-107415), January 1997.

7 R.C. Blanchard, M.K. Hendrix, J.C. Fox, D.J. Thomas and J.Y. Nicholson; "Orbital Acceleration Research Experiment", J. of Spacecraft and Rockets, Vol. 24, No. 6 (1987).

8 R.C. Blanchard, J.Y. Nicholson and J.R. Ritter; "STS-40 Orbital Acceleration Research Experiment flight Results During a Typical Sleep Period", Microgravity Science Technology, Vol. V, No. 2 (1992).

9 B.J. Dunbar, D.A. Thomas and J.N. Schoess; "The Microgravity Environment of the Space Shuttle Columbia Middeck During STS-32", NASA Technical Paper 3140, November 1991.

10 J.I.D. Alexander; "Response of Crystal Growth Experiments to Time- Dependent Residual Accelerations", Proceedings Materials and Fluids Under Low Gravity, Berlin, Germany (1995).

11 M.J.B. Rogers and R. DeLombard; "Summary Report of Mission Acceleration Measurements for STS-73", NASA TM-107269, July 1996.

12 R. DeLombard, G.S. Bushnell, D. Edberg, A. Karchmer and B. Tryggvasson; "Microgravity Environment Countermeasures Panel Discussion", AIAA 97- 0351, Reno, NV, January 1997.

Orbiter -XLV / +ZVV Attitude   Orbiter -XLV / -ZVV Attitude
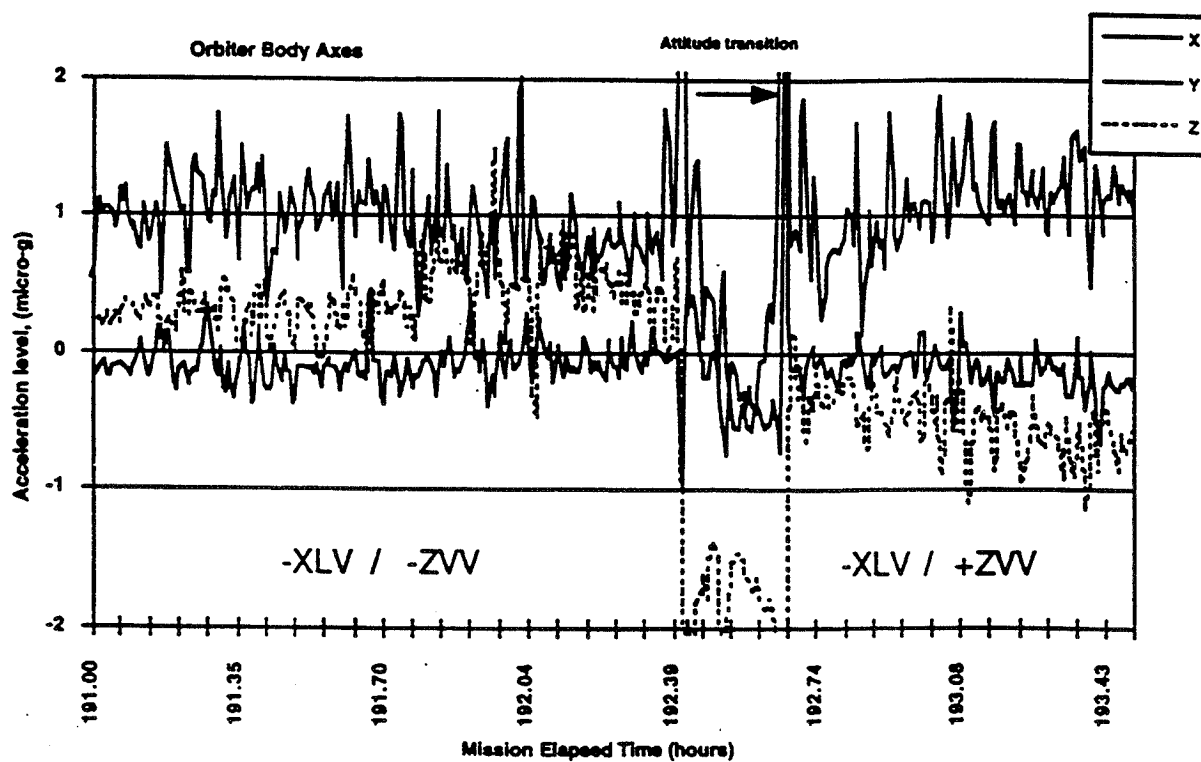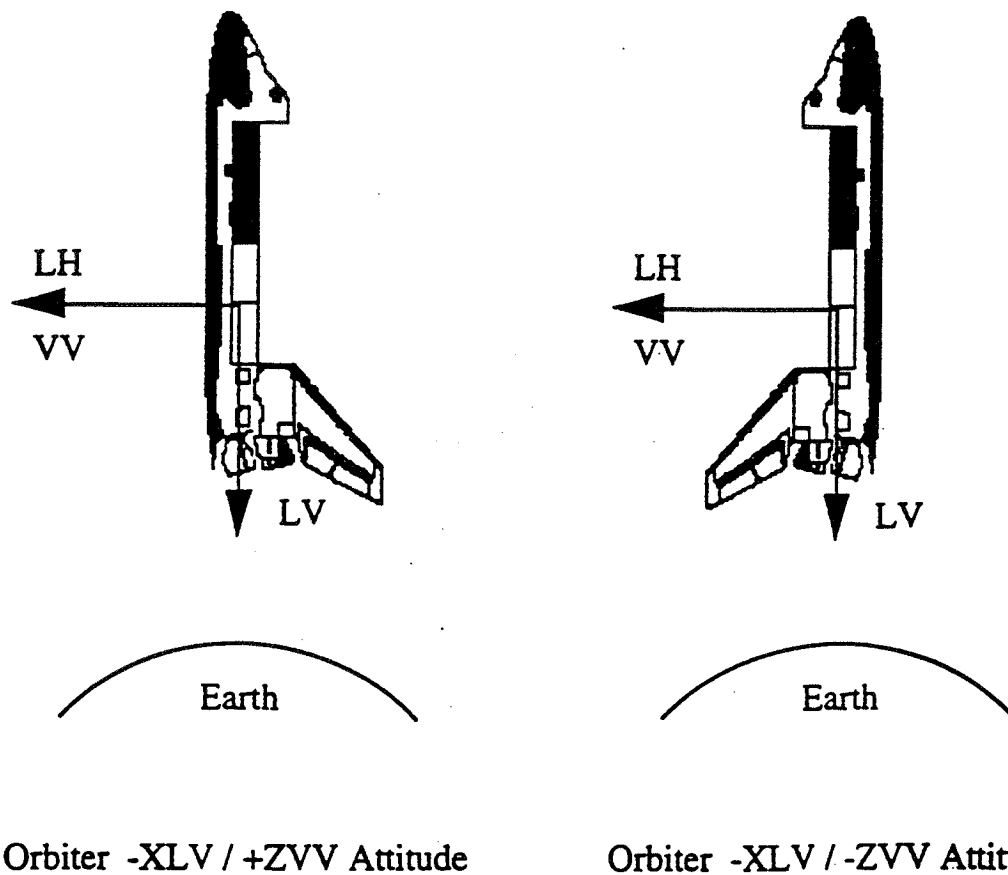
Figure 1: Attitude transition during USMP-2 operations (-XLV/-ZVV to -XLV/+ZVV)
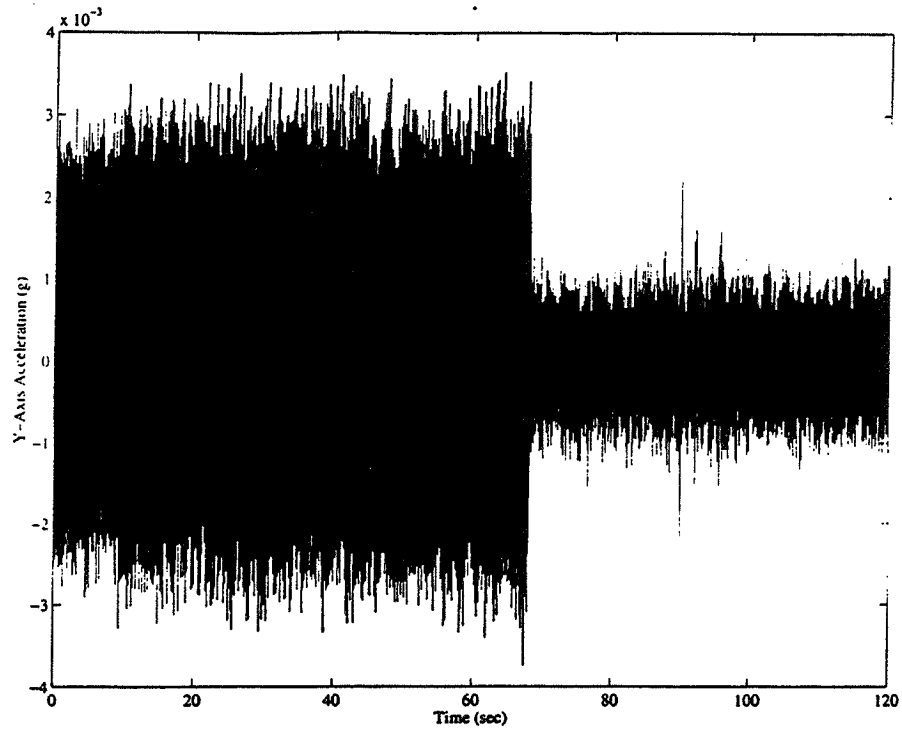
Figure 2: SAMS data showing deactivation of refrigerator compressor at about 70 seconds and a transient acceleration event at about 90 seconds.
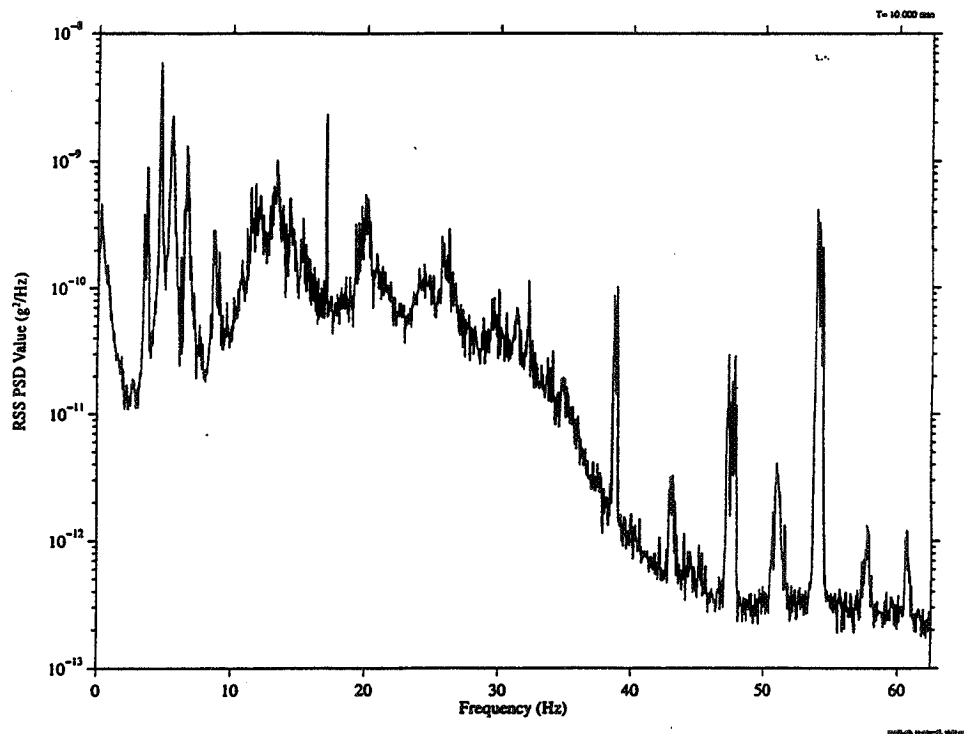

Figure 3: SAMS data showing accelerations related to glovebox facility fans at 20, 38, 43, 48, and 53 Hz.

Premixed Flames

Page intentionally left blank

STUDIES OF PREMIXED LAMINAR AND TURBULENT FLAMES AT MICROGRAVITY

PAUL D. RONNEY[*]
Department of Mechanical Engineering
University of Southern California
Los Angeles, CA

Objectives

Several topics related to the experimental and theoretical study of the combustion limits in premixed flames at reduced gravity have been investigated. The topics studied include: (1) numerical simulation of flame ball structure and stability; (2) interferometry for μg combustion experiments; (3) simulation of buoyancy effects in premixed flames using aqueous autocatalytic reactions; (4) premixed flame propagation in Hele-Shaw cells; and (5) experimental characterization of flame balls.

1. Numerical simulation of flame ball structure and stability

Despite many years of study, the mechanisms of flame extinction and stability limits in pre-mixed gases are still not well understood. Studies of these flames would lead to improved theoretical models of near-limit combustion. At μg, near-limit phenomena are quite different than at 1g, and a new near-limit flame structure call "flame balls" has been discovered by the PI. An experimental study of flame balls, called Structure Of Flame Balls At Low Lewis-number (SOFBALL), will be conducted on the MSL-1 space shuttle mission scheduled for launch on April 3, 1997. These structures are of considerable interest because they represent the simplest possible interaction between chemical and transport processes in a combusting system.

While some numerical modeling of flame balls has been performed [1, 2], these studies did not investigate the transient properties of the flame balls, therefore their stability could not be compared to theoretical predictions or experiments. Also, the effect of diluent type, one of the parameters of the SOFBALL experiment, was not investigated. The goal is to develop a detailed numerical model of flame balls, including the effects of unsteadiness and diluent type, that can be compared with the results of the SOFBALL flight experiments.

A one dimensional, time dependent flame code employing detailed chemical and transport sub-models forms the basis of this study. The governing nonsteady equations of species and energy conservation in spherical coordinates were solved until one of the three outcomes were achieved: (1) the flame extinguished; (2) an expanding, steadily propagating flame developed; or (3) a steady flame ball evolved.

The results indicate that chemical models employed affect flame ball properties substantially even though all mechanisms have been calibrated to obtain similar burning velocities for mixtures away from flammability limits (Fig. 1). Thus, results of flame ball experiments may provide a new basis for testing these models at low flame temperatures (<1200K). In addition, the far-field radiative loss is found to affect the behavior of flame balls in a manner very different from propagating planar flames. These results indicate most radiative loss occurs at $r >> r^*$, where r^* is the flame ball radius. This observation is significant because the effects of near-field and far-field loss are qualitatively different according to theory [3]. In particular, only with far-field losses are oscillatory solutions and a dynamic extinction limit predicted in addition to the static (turning-point) limit.

Figure 2 shows that at our computed lean stability limit for H_2-air mixtures ($\phi = 0.0847$, where ϕ is the equivalence ratio), $d(r^*)/d(\phi)$ is large but finite, thus a static turning-point limit has not been reached. The experimental lean stability limit is $\phi = 0.0825 \pm 0.0013$, close to but slightly lower than the prediction. However, quantitative agreement for flame radii is weak, indicating the need for improved μg conditions, e.g., on the CM-1/SOFBALL experiment on MSL-1. It was also found that the flame ball radius increases with increasing mole percent fuel, while the trend of the maximum temperature depends on the radiation and

transport properties of the diluent. This is not predicted by theory because the effects of radiating diluent and the ratio of mass diffusivity of the product (H_2O) to that of the diluent is not included in the theoretical models [1, 3].

A new feature was identified in these simulations: mixtures capable of exhibiting both stable flame balls and steadily propagating flames depending on the initial condition. For H_2-O_2 mixtures richer than the lean stability limit for the steadily propagating planar flames, either solution is possible, though only a narrow window of conditions can initiate plane flames starting from the initial conditions used in this study, namely a stable flame ball whose temperature and concentration profiles are stretched or shrunk.

An important part of the flame ball modeling is the accurate prediction of the flame ball emission intensity profile. Spatial radiation distribution is measured by intensified CCD cameras, which are sensitive only in the region of 400-900 nm. For comparing the intensified CCD camera data with numerical simulation results, emissivities of the relevant gases in visible region are needed. A model has been developed for the calculation of emissivity of gases in this 400-900 nm region. We consider the multi-band structure as an assembly of many individual lines. Compared with commonly-used Elsasser model and statistical models, which ease the computation by assuming simplified spectral band structure, this method takes account of the detail structure of spectral bands. All of the fundamental data of spectra can be found in data base HITRAN data base.

2. Interferometry for μg combustion experiments

A new interferogram processing method is developed for processing flame ball interferograms obtained in the JAMIC drop tower experiments (see below) to measure the temperature distribution. This new method is based on the Fourier Transform method, which has advantage of using all the points on the interferogram instead of using only the points on the centers of the fringes like most other methods. Furthermore, unlike conventional Fourier Transport methods, it does not require a slow variation of phase difference in the test section, and thus is applicable to flames and other systems having steep temperature gradients.

The basic idea of the method is as follows. By taking a interferogram of the background flow field and processing it with the Fourier Transform method, one can obtain the low frequency continuity distribution, the amplitude of modulation and phase distribution of the background flow field interferogram. Interferograms operate with an assumption that the flow field measured affects only the phase distribution, therefore, the phase variation caused by the flow field can be measured by subtraction and division operation between the interferogram of background and flow field measured. To test the entire interferometry procedure, a temperature distribution measurement for Bunsen flame was obtained with maximum value of 1632 K while the STANJAN code gave a maximum temperature value of 1678 K. Considering the approximations involved in the STANJAN code, especially the adiabatic assumption, a measured value with 50 K lower than the calculated value is reasonable. To make use of this new method, a shear plate interferometer has been constructed and used in more than one hundred drops both in NASA and JAMIC drop tower experiments without failure.

3. Simulation of buoyancy effects in premixed flames using aqueous autocatalytic reactions

In order to study the behavior of propagating flames at high turbulence levels, without the complications of density changes or heat losses, the PI has introduced the use of aqueous autocatalytic chemical reactions that produces propagating fronts as a paradigm for turbulent premixed combustion. Theses aqueous fronts exhibit very little density change across the front, have simple chemistry, are unaffected by heat losses since the front is nearly isothermal and have high Schmidt numbers, allowing the front to remain "flamelet-like" even in the presence of very strong flow disturbances or turbulence.

An aqueous autocatalytic chemical system (specifically the iodate-hydrosulfite reaction) was applied to a study of the effects of buoyancy on front propagation using a two dimensional Hele-Shaw apparatus. The Hele-Shaw apparatus is particularly advantageous for comparing experimental results to numerical systems because the Navier-Stokes equations reduces to Darcy's law, which is a linear equation. Also, the well-known "G-equation" can be used to simulate the front propagation process. Thus, autocatalytic reactions in Hele-Shaw

flow represent the simplest possible experimental realization of the interaction of a propagating front with buoyancy-induced convection.

The fronts were recorded and analyzed using a digital video image processing system. Analogous to the Saffman-Taylor instability, fingering-type instabilities were observed (Fig. 3). The existence of fingering is somewhat surprising since the Saffman-Taylor mechanism is not present in our case (because there is no viscosity difference or surface tension across the front). The following fingering mechanism is tentatively proposed: the heat release at the front heats up the media ($\Delta T \approx 3K$) and then cools back down to ambient due to heat loss to the cooler walls. The length of this cool-down zone is comparable to the wavelength of the fingering instability, though a definitive link between the fingering and thermal zone thickness has not yet been made.

Despite the uncertainly in the wrinkling mechanism, an expression to estimate the magnitude of the buoyancy-induced flow disturbances was derived based on the Saffman-Taylor model, resulting in the expression $U = u'/S_L = (\pi/12)g\delta w^2/\nu S_L$ where u' represents the characteristic buoyancy-induced velocity (i.e. a "turbulence intensity"), S_L is the planar propagation rate of the front, g is the gravitational acceleration, δ is the fractional density change across the front, w is the thickness of the cell and ν is the kinematic viscosity. The "turbulent burning velocity" (S_T) is plotted as a function of U in Fig. 4. These results show that the Yakhot model [4] $S_T/S_L = \exp((u'/S_L)/(S_T/S_L))^2$ fit the experimental data for this experiment as well as our previous results from several different forced-turbulence flows. These results suggest a rather simple description of the role of buoyancy on the front propagation in this simple chemical and hydrodynamic system.

To complement the Hele-Shaw experiment, a joint research program with Prof. Jerry Gollub of Haverford College has been initiated. The purpose of this experiment was to study front propagation in a two-dimensional array of vortices generated using a magnetohydrodynamic flow system. The presence of the two flame regimes (flamelet regime and distributed reaction zone regime) depends on the Damköhler number (10 to 240) indicating the ratio of a characteristic reaction rate to a mean strain rate. In this initial set of tests, several very useful data points were obtained. A new experiment setup is being constructed at Haverford and further experiments will be conducted.

A limitation on the utility of aqueous fronts is that even the small fractional density change across the aqueous front leads to significant buoyancy influences at one-g because of their very low laminar front propagation rate (S_L). Only when the turbulence intensity (u') is much greater than S_L is this limitation unimportant. However, gaseous flames quench at these high values of u'/S_L, probably due to heat loss effects that do not influence the nearly isothermal aqueous fronts. Our scaling analysis has shown that space experiments would enable us to study the aqueous fronts at values of u'/S_L accessible to gas combustion experiments and numerical simulations, enabling us to create a "bridge" between studies of fronts with and without substantial density changes. An ideal flow for studying the interaction of propagating fronts with flow disturbances is the Taylor-Couette flow in the annulus between two rotating concentric cylinders. Consequently, the PI has proposed the Front Interaction with Vortex Experiment (FIVE) as a Space Shuttle Glovebox experiment.

4. Premixed Flame Propagation in Hele-Shaw cells

The Hele-Shaw cell is a widely-used apparatus for studying buoyancy effects in non-reactive fluids in a highly simplified two-dimensional geometry, however, it has never been employed to study gaseous flame fronts. It is widely known that buoyancy effects induce "fingering" instabilities in Hele-Shaw cells. Therefore the motivation for this research task is to determine if the same effects will occur in gaseous flame fronts as is seen in non-reacting fluids and in the aqueous fronts described above, and relate any observed flame instabilities to those observed in three-dimensional flows.

Joulin and Sivashinsky [5] extended the classical analysis of fingering instability by Saffman and Taylor (1958) to consider a propagating flame front. Their analysis predicts that fingering may occur due to viscosity and density changes across the front, however, their analysis does not provide a means to predict the observed fingering wavelength because flame quenching via heat losses and other phenomena such as diffusive effects that would suppress short wave-length instability is not included due to mathematical difficulties. Hence, the

333

goal of this study is to compare experimental results at long wavelengths to Joulin and Sivashinsky's analysis and to assess experimentally the behavior of the front in the short wavelength limit.

The apparatus is designed to meet certain restrictions due to the need to avoid flame quenching and turbulent conditions within the cell. The equipment used consists of two clear rectangular Plexiglas plates of dimension 21 x 29 inches sandwiching an aluminum plate with the same outer dimensions as the Plexiglas but having a rectangular cutout of dimension 15.5 x 23.5 inches and a thickness of 0.5 inches. The cutout acts as the combustion chamber for the experiment.

Experiments have been conducted with CH_4-air and C_3H_8-air mixtures of varying strength for upward, downward and horizontal propagation. Unlike the aqueous reactions, where fingering was found only for upward propagating flames (indicating buoyancy-driven instabilities), for the gaseous case wrinkling is found for all propagation directions. An example is shown in Fig. 5. This indicates that the thermal expansion (Darrieus-Landau) and/or viscous fingering instabilities, which are not present in the aqueous system, are important in the gaseous system. This is consistent with Joulin and Sivashinsky's predictions. Future work will focus on determining the mechanisms responsible for the observed wavelength selection and its influence on the propagation rate (S_T).

5. Experimental characterization of flame balls

5.1. KC-135 and DC-9 experiments

In support of several unresolved engineering issues concerning the CM-1/SOFBALL space flight experiment, eight weeks of low-gravity flight tests have been performed in the past two years on NASA's KC-135 and DC-9 research aircraft. A SOFBALL-like experiment configuration was employed to test various schemes for false coloring of video images for on-orbit real-time determination of the optimal gain setting for the intensified video cameras, and to assess whether the intensification of the video cameras is sufficient to image the flame balls under flight-like conditions. The false coloring is needed because it has been found in previous KC-135 tests that most cases the experiment conductor tends to set the gain too high, resulting in saturated (i.e. overexposed) images. Also, from these aircraft tests the PI has determined the final flight test mixtures, the test point ordering, the optimal Xybion camera settings, the initial radiometer gain settings and the spark parameters (voltage, capacitance and gap) to be used for each space flight test.

5.2. JAMIC experiments

A set of μg experiments were performed in the JAMIC drop tower using weakly combustible gas mixtures having low Lewis number. These mixtures were chosen because prior drop-tower and aircraft experiments have shown that these mixtures exhibit "flame balls." The JAMIC facility provides much a longer μg duration than other drop-tower facilities and much higher quality μg than aircraft experiments. The data obtained can thereby be used to extend prior ground-based experiments and augment space flight experiments to be performed in April 1997 on Spacelab mission MSL-1.

Preliminary data indicate that the test results are very consistent with prior aircraft μg results despite the much poorer quality of μg in the aircraft experiments (Figures 6&7). This result is somewhat surprising considering that our estimates suggest that in the aircraft experiments the gravity levels are still large enough that transport of heat and mass to and from the flame balls are likely to be dominated by buoyant convection rather than diffusion and radiation.

Both JAMIC and earlier aircraft μg experimental data show larger flame balls and weaker radiant emission than theoretical predictions. This result is also somewhat surprising because radiant emission should increase with increasing flame ball size, thus the directions of the discrepancies seem contradictory. The simplest explanation would be that the radiative model employed in the calculations overpredicts the actual loss. Since the same conclusion has recently been reached independently by other research groups, we are re-evaluating the proper use of C. L. Tien's data for combustion modelling.

References

1. Buckmaster, J. D., Smooke, M. D. and Giovangigli, V., *Combust. Flame* 94, 113-124 (1993).
2. Smooke, M. D. and Ern, A. NASA Conference Publication 10174, 445-450 (1995).
3. Buckmaster, J. D., Joulin, G. and Ronney, P. D., *Combust. Flame* 84, 411-422 (1991).
4. Yakhot, V., *Combust. Sci. Tech.* 60, 191 (1988).
5. Joulin, G. and Sivashinsky, G. I., *Combust. Sci. Tech.* 77, 329 (1991).

Figures
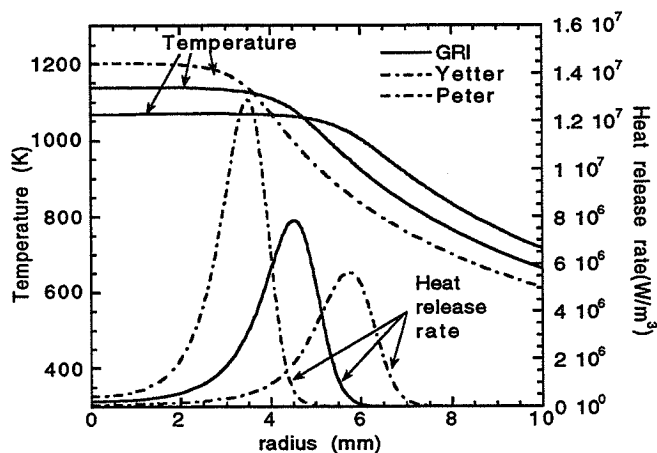
Figure 1. Structure of a flame ball at steady state in a 4% H_2-air mixture for 3 different H_2-O_2 chemical mechanisms.
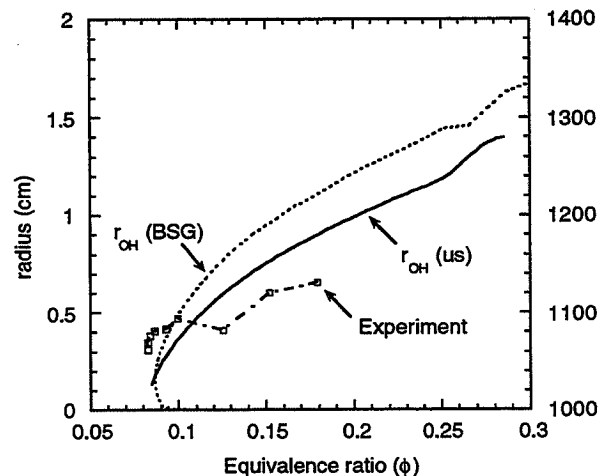
Figure 2. Radius at peak OH concentration (r_{OH}) for steady flames computed by us compared to experimentally observed radius as a function of ϕ for flame balls in H_2-air mixtures.
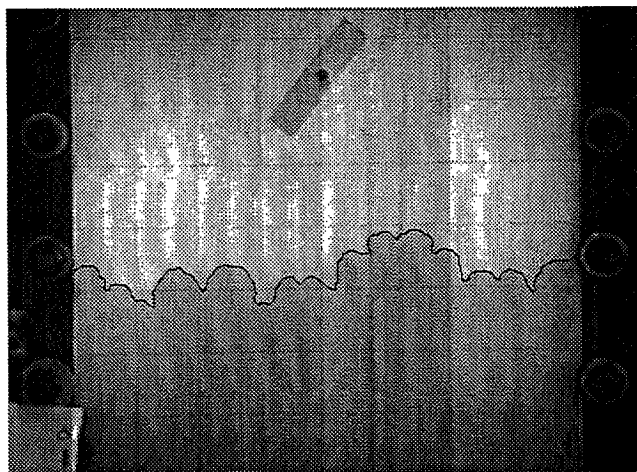
Figure 3. The autocatalytic upward propagating front in a two dimensional Hele-Shaw apparatus. Fingering-type instabilities were observed. Field of view is 25cm by 19cm.
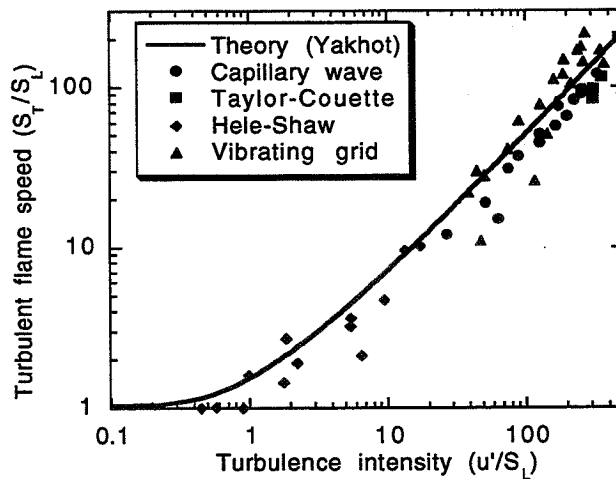
Figure 4. Comparison of measured values of turbulent front propagation rate (s_T) normalized by the laminar, undisturbed propagation rate (s_L) to the values of s_T/s_L predicted by Yakhot's renormalization group mode [4], for several different turbulent flows.
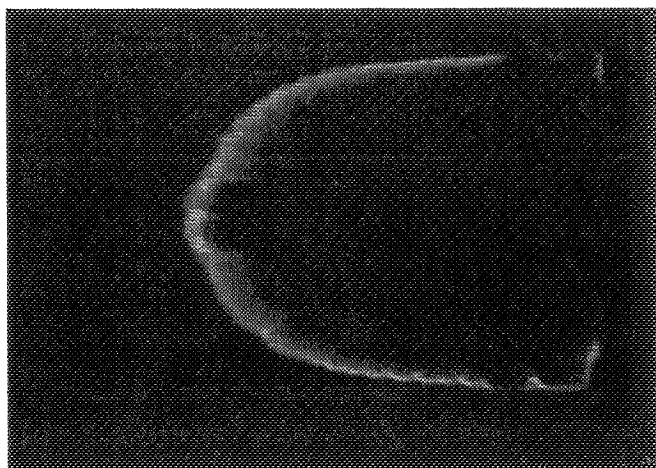
Figure 5. Image for a propagating flame travelling upward(toward left) in a 7.1% CH_4-air mixture in a two dimensional Hele-Shaw apparatus. Field of view is 39.4cm by 30cm.

Figure 6. Flame ball image from JAMIC experiment for mixture with 6.75% H_2, 13.5% O_2 and diluent SF_6 at 3 atm. Field of view is 25cm by 20cm.
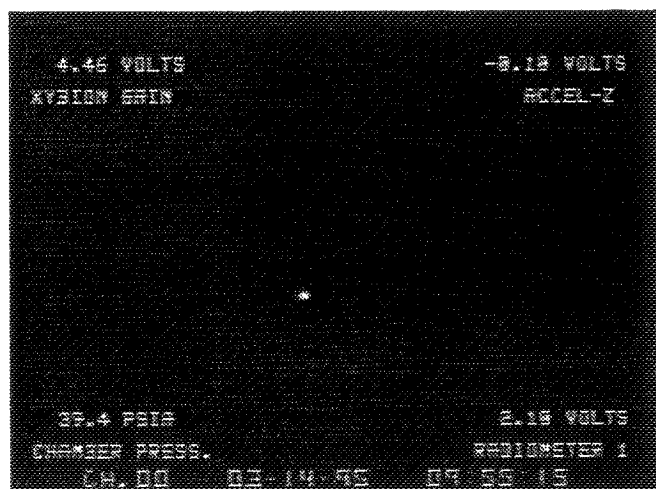
Figure 7. Flame ball image from KC-135 flight experiment for mixture with 6.7 % H_2, 13.33% O_2 and diluent SF_6 at 3 atm. Field of view is 32cm by 24cm.

PREMIXED GAS COMBUSTION:
AN EXCITABLE SYSTEM

HOWARD PEARLMAN
Research Assistant Professor
University of Southern California
resident at NASA LeRC
Cleveland, OH 44135

Abstract

Rotating spiral and target patterns have been observed experimentally on freely-propagating premixed gas flames in large diameter tubes at normal gravity (1g). These modes of propagation occur in near-limit mixtures which have a Lewis number (Le, defined as the ratio of the thermal diffusivity of the cold mixture to the mass diffusivity of the scarce component into the mixture) sufficiently greater than one. However, at 1g, buoyant flows strongly distort the flame curvature, hydrodynamics (thus stretch) and convective transport of species and heat. In turn, these alter the critical Le required for onset of instability.

To isolate and better understand the mechanisms which drive the observed patterns and their dynamics, 1g and microgravity (μg) experiments are being conducted to determine: (1) the structure and dynamics of the patterns, (2) a map of the critical Le and heat loss for their occurrence, (3) the relative significance of the chemical kinetics and (4) the effect of curvature (local wave and global flame front) on wave propagation. With this in hand, we will be better prepared to discuss an additional mode, a state of "chemical turbulence," which seems to be the ultimate fate of many of these near-limit flames prior to extinction.

Background

"Excitable" behavior can and does occur in premixed gas combustion where a system is considered "excitable" if a small, but finite, disturbance is capable of triggering a large excursion away from the systems steady state only to return at a later time. If the system waits for a stimulus to trigger the next excursion, it is called an hourglass whereas if the system spontaneously goes into consecutive excursions, it is called a clock. Oscillatory, clock-type behavior has long been observed in many combustion processes such as thermokinetically-driven oscillations in low-temperature reactions and cool flames [1,2]. Similarly, hourglass-behavior can occur in any partially-combusted mixture whose products are also flammable. For example, near-limit, low-Le mixtures which support "flameballs" at μg can often be ignited multiple times since only a small percentage of the initial reactants are consumed (at least within the experimental time alotted) [3].

Likewise, many combustion processes also satisfy the two essential criteria for self-organization: the systems (1) are often far-from-equilibrium and (2) have a feedback mechanism (chemical and/or thermal) [4].

While self-organizing and oscillatory behavior are not new, until recently, "excitability" has not been associated with gas-phase combustion. Perhaps, this is because the typical wave patterns (expanding target patterns and rotating spiral waves) common to most oscillatory reactive-diffusive systems have only recently been observed in combustion [5,6]. In these studies, 1g downwardly-propagating and μg flames in tubes were considered in a high-Le premixture of n-butane and 21.0% oxygen diluted with helium (Le≈4.0). Both radial oscillations and spinning waves were observed on the surface of these flames which insinuated that premixed gas flames may share many of the features typically attributed to excitable, reactive-diffusive systems. In hindsight, evidence of such patterns is believed to have been observed in: spinning propagation in freely-propagating acetylene decomposition flames in tubes [7] and (2) oscillatory, spinning and chaotic dynamics in burner-stabilized flames [8-11].

In recent 1g tests, both rotating spiral waves and expanding target patterns have also been found in several lean mixtures which contain a heavy alkane (propane, butane, heptane, octane, or nonane) or ketone (acetone) and 21.0% oxygen diluted with helium [12,13]. Like the modes in the butane-oxygen-helium flames [5,6], the spiral and target patterns occur in near-limit mixtures. Specifically, as the fuel concentration is decreased toward the lean flammability limit, steadily-propagating, uniform flames first transition to flames with target patterns then to flames which support both rotating spiral waves and target patterns. As the limit

is further approached, the patterns become spatially disordered and temporally chaotic: a state reminiscent of "chemical turbulence."

This paper aims to introduce the concept of "excitability" to premixed gas combustion by way of experimental observation. It begins with a description of the 1g experimental apparatus together with a brief summary of each mode. A description of the μg-work-in-progress is then presented.

1g Experimental Apparatus

The 1g apparatus consists of a vertically-oriented 28.5cm internal diameter plexiglas tube, approximately 50cm long. The tube is permanently closed at the bottom and initially sealed at the top with a 3 micron thick polyester membrane. The membrane is used to contain the mixture prior to ignition and is simply supported to the top of the tube with two rubberbands. Two high-speed, intensified, 1000 frame per second, video cameras view the flame; one camera images the flame through a mirror mounted on the top at a 45 degree angle with respect to the vertical and the other camera views the flame axially through the side-wall of the tube (Fig.1).

For the butane tests, a gaseous mixture of lean n-butane-21.0% oxygen-balance helium is flushed through the tube. After approximately 9 tube volumes are circulated through, the 10th volume is captured by closing both wall-mounted ball valves.

In contrast, the heptane, octane, nonane and acetone tests are performed by first filling the tube with a 1atm, 21.0% oxygen-balance helium mixture and then injecting, with a hypodermic syringe, the liquid-phase fuel into a small beaker fastened to the base of the tube. The fuel is weighed accurately, prior to injection, to the hundredth of a gram and quickly (within approximately one minute) injected into the beaker to minimize mass loss due to vaporization. This error is not believed to exceed ±0.005g (equivalent to ±0.003% volumetric fuel concentration error). The beaker is then heated to enhance vaporization while at the same time a mixing fan is turned on to ensure homogeneity of the mixture. After the fuel is completely vaporized, the heater is turned off while the fan remains on for an additional 15 minutes (each minute the fan circulates the entire volume about 10 times). Then, the fan is turned off and the mixture is allowed approximately 10 minutes to quiesce before ignition with a propane lighter.

Single Target Patterns

Downwardly-propagating flames in all of the above-mentioned mixtures support radially-propagating, concentric-ring waves immediately following a centrally-located ignition. A radial view of a typical target pattern is shown in Fig.2. These waves appear to emanate from a pacemaker-site and expand radially outward toward the tube walls.

The characteristic radial speeds are on the order of 2-3m/s and the characteristic separation distance between consecutive radial waves is typically 3-4cm for flames in the butane and acetone mixtures and 2-3cm for those in heptane and octane mixtures. The decrease in radial wave spacing may be due to the smaller mass diffusivity of the heavier fuels (scales as inverse of the square root of the molecular weight) and thus smaller diffusive lengths. Perhaps, at higher pressure, the wave separation distance will also decrease since the characteristic length may scale as a diffusivity divided by a flame speed where diffusivity scales as inverse pressure.

Preliminary tests have also been performed to see how the patterns evolve after contact with a barrier. This is done by inserting a vertical divider into the lower half of the tube and observing visually how the flame reacts to such an obstacle. While the conductive heat loss to the divider is sufficient to locally quench the flames, the patterns develop in a seemingly independent manner on either side of the divider, albeit nonaxisymmetrically. Since the waves appear to be blocked by impermeable barriers, they may, in fact, be trigger waves, as opposed to phase waves, where their speeds are proportional to the inverse of their local phase gradients.

Multiple Target Patterns

Often, in these near-limit flames, multiple pacemakers sites develop spontaneously. If one of the pacemaker frequencies is faster than the others, its surrounding waves slowly encroach on the waves surrounding the slower pacemakers. In this way, the slower pacemakers and their target patterns are gradually consumed by the faster waves. Eventually, after several cycles, the fastest pacemaker determines the pattern.

338

In many cases, however, the pacemaker frequencies are close to each other such that one sight does not gain control of the system by annihilating the slower ones. A state is then established where the multiple sites and their target patterns coexist and continuously interact at their boundaries. Once again, the waves annihilate each other in their regions of interaction (perhaps due to local depletion of the scarce reactant) and combine at their free-ends. An example is shown in Fig.3.

Spiral Waves

In still leaner mixtures, rotating spiral waves develop. They usually occur when a ring of an existing target extinguishes locally on its circumference. Presumably, this is due to an azimuthally-disturbance or perhaps, a local element along the ring fails to get spontaneously triggered by the adjacent volume and tends towards its "equilibrium" state, a state of inflammability, similar to hourglass-type behavior.

Once formed, the two free-ends of the broken ring then form two counter-propagating spiral waves. These spirals compete for the same intermediate reactants, annihilate each other in their region of intersection and then repeat the above sequence until one of the rotating spirals curls inward in advance of the other. A typical sequence of spiral wave development and subsequent rotation is shown in Fig.4.

It would be interesting in future studies to determine whether or not the spiral can form a scroll wave or fancy ring in 3-dimensions similar to the scrolls and twisted rolls observed in other excitable systems like the Belousov-Zhabotinsky reaction.

Chemical Turbulence

As the flammability limit is asymptotically approached (to within the experimental accuracy of the gas mixing system), the patterns often appear spatially disordered and temporally chaotic; a mode suggestive of "chemical" or "diffusion-induced" turbulence. This is believed to occur when the synchronization (entrainment) between the local volume elements breaks down [14] and has many parallels in chemical and biological systems such as the onset of atrial fibrillation [15].

Admittedly, much work remains to be done, yet the potential existence of chemical turbulence in premixed combustion is a tantalizing prospect and, as such, raises a host of questions. What are the important degrees of freedom? what are their characteristic times? under what conditions might we expect such behavior?

μg-Work-In-Progress

The elimination of buoyant convection will allow unobstructed study of the reactive-diffusive structure and dynamics of these flames. This will allow us to focus on the physics with unimpaired vision.

To date, preliminary tests have been performed in the 2.2 Second Drop Tower at NASA Lewis Research Center and show that target, spinning and mixed mode patterns also exist at μg.

Conclusions

Expanding target and rotating spiral waves have been observed on the surface of downward, freely-propagating, near-limit, premixed gas flames in lean mixtures of butane, heptane, octane, nonane and acetone (whose molecular weight, and thus diffusive properties, are nearly identical to those of the butane mixtures, yet has different chemistry) diluted with oxygen and helium at 1g. These waves are believed to be trigger waves, since they do not penetrate impermeable barriers. In addition, the characteristic spacing between adjacent waves is generally observed to decrease as the molecular weight of the scarce reactant (fuel) increases.

Some of key properties of the patterns are:

(1)   Propagating, radially-concentric rings, a target pattern, may form centered around a pacemaker site,
(2)   Multiple pacemaker sites may exist simultaneously. If the frequencies vary considerably such that the waves surrounding the faster site annihilate those which surround the slower site(s) through successive collisions, one site, the fastest site, will ultimately prevail,

(3)   Counter-rotating spirals occur when a ring on a target pattern breaks. After successive collisions, one of the spirals typically tends to wind inward in advance of the other. Further interaction annihilates the core of the delayed spiral leaving behind the spiral wave which wound inward first,

(4)   "Chemical turbulence" is believed to occur very close to the lean flammability limit, characterized by spatial disorder and apparent temporal chaos.

References

1. Gray, P. and Scott, S.K. *Chemical Oscillations and Instabilities: Non-linear Chemical Kinetics,* Clarendon Press, Oxford, 1994, pp. 408-447.
2. Lewis, B. and von Elbe, G. *Combustion, Flames and Explosions of Gases,* Third Ed., Academic Press, Inc., New York, 1987.
3. Ronney, P., Whaling, K.N., Abbud-Madrid, A., Gatto, J.L., Pisowicz, V.L. *AIAA,* 32 (3): 569 (1994).
4. Nicolis, G. and Progogine, I. *Self-Organization in Nonequilibrium Systems: From Dissipative Structures to Order through Fluctuations,* John Wiley and Sons, New York, 1977.
5. Pearlman, H. and Ronney, P. *J. Chem. Phys.* 101 (3): 2632 (1994).
6. Pearlman, H. and Ronney, P. *Physics of Fluids* 6 (12): 4009 (1994).
7. I.M. Gololobov, Granovskii, E.A., and Gostintsev, Yu. A. *Combust. Explos. Sh.Waves* 17:22 (1981).
8. El-Hamdi, M., Gorman, M., Mapp, J.W., Blackshear, J.I., Jr. *Combustion Science and Technology* 55:33 (1987).
9. Matkowsky, B.J. and Olagunju, D.O. *SIAM J. Appl. Math.* 40:551 (1980).
10. Margolis, S.B. *Combustion Science and Technology* 22:143 (1980).
11. Buckmaster, J.D. *SIAM J. Appl. Math.* 43:1335 (1982).
12. Pearlman, H. "Target and Spiral Wave Patterns in Premixed Gas Combustion," The Western States Section of The Combustion Institute, USC, October 26-28, 1996.
13. Pearlman, H. "Excitability in Near-Limit, Premixed Gas Combustion," The Eastern States Section of The Combustion Institute, Hilton Head, SC, December 9-11, 1996
14. Kuramoto, Y. *Chemical Oscillations, Waves and Turbulence,* Springer-Verlag, New York, 1984.
15. Winfree, A.T. *The Geometry of Biological Time,* Springer-Verlag, New York, 1990.
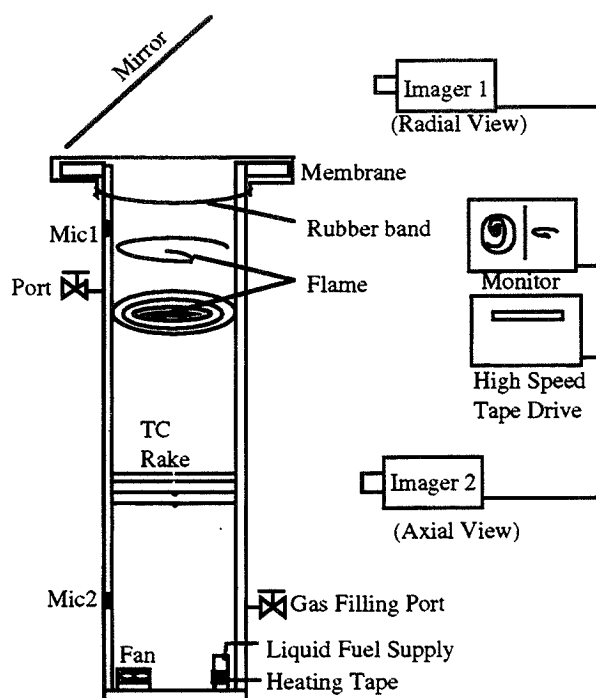
Fig.1: Freely-propagating flame tube apparatus
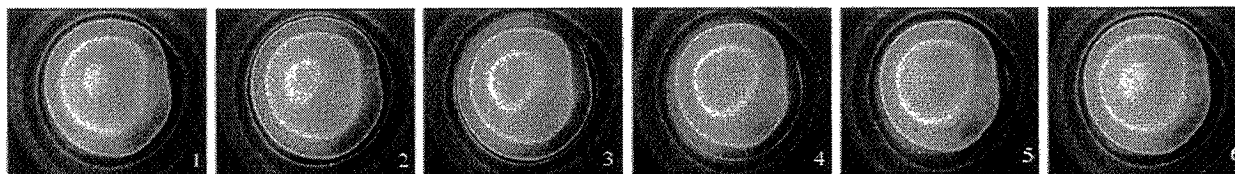
Fig.2: Target pattern surrounding a pacemaker site in a mixture containing $1.46\%C_4H_{10}$-$21.0\%O_2$-He. Radial view. Time between images is 1/500sec. Oscillation frequency $\approx 93Hz$. Tube diameter = 28.5cm.
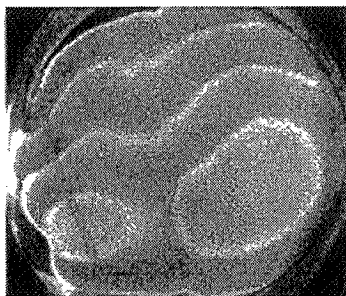
Fig.3: Multiple target patterns on the surface of a downwardly-propagating flame in a mixture of $1.46\%C_4H_{10}$-$21.0\%O_2$-He.

341
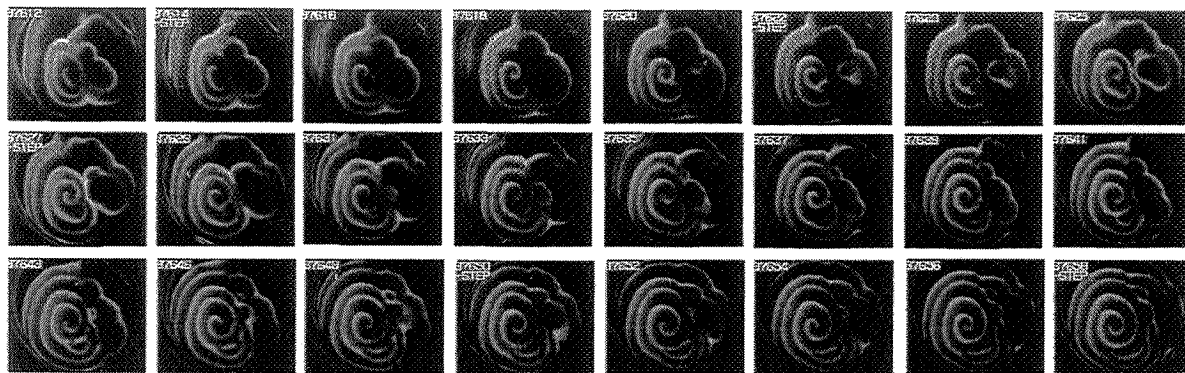
Fig.4: Development of a rotating spiral wave from an azimuthally-disturbed, closed, ring in a mixture containing 0.80%C_8H_{18}-21.0%O_2-He. Radial view. Time between consecutive images is 1/500sec. Ordered from left to right in consecutive rows.
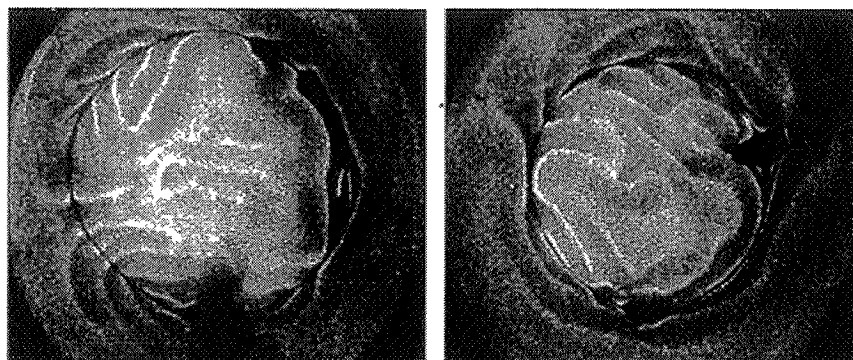
Fig.5: Complex pattern formation produced by the interaction of multiple "flamelets" reminiscent of "chemical turbulence." These frames are not consecutive images, but randomly chosen at different axial locations during the same experiment (same initial parameters) to illustrate the lack of spatial and temporal order.

GRAVITATIONAL INFLUENCES ON FLAME PROPAGATION THROUGH NON-UNIFORM PREMIXED GAS SYSTEMS[‡]

FLETCHER J. MILLER
&
Ed White
Case Western Reserve University

Howard D. Ross
NASA Lewis Research Center

Introduction

Flame spread through *uniformly* premixed gas systems, while not completely understood, is nevertheless a well-studied problem in combustion science. In contrast, flame propagation through *non-uniform* premixed gas systems (also called "layered systems") has been the subject of relatively few previous studies. In a recent theoretical paper Talley [1] lists sprays, flame spread over liquids, and the leading edge of lifted turbulent diffusion flames as applications where flame behavior in layers is important, and goes on to note that, "Compared with the two better known limiting cases [pure diffusion and pure premixed flames] these intermediate mixtures have so far received relatively little attention." Layered mixtures, however, are ubiquitous in terrestrial fire hazards such as chemical spills, underground mining operations, and automobile and aircraft crashes. The flames in such systems have been shown to carry over fences, and to propagate past the ends of the fuel spill, thus representing a hazardous area beyond that associated with the original fuel location. They also represent a likely fire hazard aboard long-duration spacecraft such as the International Space Station -- perhaps second in probability only to electrical wire /insulation breakdowns – because flammable gases may accumulate near waste storage, laboratory fluids, fuel cells, lasers, etc.

In addition, it is known that gravitational effects, while only of minor importance for stoichiometric mixtures, are strong for lean-limit, *homogeneous* gas mixtures [2]. While not specifically mentioning layered systems, Law and Faeth in their review on microgravity combustion call for more research on near-limit phenomena [3]. Flammability limits have been found by some investigators to be not only different in μg, but also outside (lower than) the normal range of upward vs. downward spread limits at 1-g [4]. This, coupled with the finding cited below by Liebman et al [5] that in layered systems the flame can propagate in regions *outside the accepted lean flammability limit even at normal gravity*, makes it especially difficult to assess fire hazards in μg based on 1-g data. Indeed, Law and Faeth state that "... any notion that flammability limits for [homogeneous, premixed] gases at normal gravity are applicable to conditions at μg is erroneous." Since gaseous fire hazards aboard spacecraft would likely involve propagation through a mixture spanning a range of concentrations and fuel layers, experiments in such systems are critical to understand the phenomena.

A review of the existing literature, as described below, suggests gravity may influence the flame propagation rate of layered premixed systems by up to 50% in a wide range of circumstances. Thus, observations of flame propagation rates in normal gravity and in microgravity should readily establish this effect; such experiments would validate at a global level existing models which include gravitational influence. In this paper we present the beginning of a project to experimentally determine flame spread rates in layered systems in normal and microgravity. In particular, we focus on the case where there is nowhere a stoichiometric concentration of fuel vapor (i.e., the system is always fuel lean). Research on layered systems in which the mixture is everywhere below stoichiometric proportions has been scarcely reported for normal gravity, and not at all for microgravity conditions. See Fig. 1 for a schematic of the layered system under consideration in this work.

Gravity can influence the rate of flame propagation in a layered system in at least three ways: through a hydrostatic pressure gradient, through buoyantly induced flows during spread, or by affecting the initial distribution of fuel vapor. The first effect has been professed as important for all equivalence ratios since agreement between predicted and observed flame spread rates in normal gravity tests is improved by the inclusion of the hydrostatic pressure term in models (see below) [6]. Without this term, underpredictions by 50% compared to experiments were observed. This improvement, however, only proves correlation, not cause, and needs to be experimentally verified.

The second way in which gravity may influence the flame propagation in a stratified layer is in how it affects the flows responsible for the redistribution of the fuel vapor, oxygen, and combustion products once a propagating flame is established. Previous research indicates that convective or aerodynamic effects can induce flows ahead of the flame that alter the fuel vapor concentration distribution and assist the flame spread. The high propagation speeds in layers that maintain at some height in the layer a stoichiometric concentration suggest buoyant flow might not develop rapidly enough to affect spread; however, in the sub-stoichiometric regime this may not be the case. These flows and their causes have not been measured in either normal gravity or microgravity.

Effects of gravity on the initial distribution of fuel from a point source and how that affects flame spread are essentially unexplored in the literature. In normal gravity a leaking buoyant fuel (e.g., hydrogen) will rise from its source dispersing somewhat as it goes until it encounters a ceiling where it may collect and form a flammable layer. In microgravity the fuel would not be buoyant and instead will collect around its source or be redistributed by the slow (5-10 cm/s) flows due to ventilation systems and crew movements. Just the opposite may occur with point sources of heavier-than-air fuels. These differences in fuel vapor distribution can lead to very different flame propagation behavior and thus different fire hazards.

Previous Experimental Research with Liquids

For flames spreading over a liquid above its flash point, the main parameters governing the flame spread rate are the height of the flammable layer, the fuel-air mixture concentration, and the mixture's concentration gradient within the layer. Behavior of the flame also depends on whether T_o is high enough to create a stoichiometric concentration of fuel vapor and air. For $T_o < T_{st}$ the presence of the pool affects the flame spread rate even though a flammable gas-phase mixture exists prior to ignition (T_{st} is the temperature at which a stoichiometric mixture exists). Ishida [7] showed this convincingly in experiments with glass beads in a pool of n-octane; without the beads the flame spread almost an order of magnitude faster than with the beads for the same temperature above the flash point. Further experiments showed that for $T_o < T_{st}$ the fuel bed orientation relative to the gravity vector also affected V_f, [7].

If $T_o > T_{st}$, the flame appearance and V_f are similar to a system comprised of layered gases without a liquid surface, indicating that the liquid phase is uninvolved in propagation. In this range V_f is two to five times greater than the laminar burning velocity, S_f, for a stoichiometric, homogeneous mixture. In order to exceed S_f to this degree, the flame front must be curved which causes a significant pressure gradient across the front; flame spread is then enhanced by gas-phase motion ahead of and in the same direction as spread [8]. From aerodynamic and mass continuity considerations, the motion can be driven by the expansion of the low-density products which displaces and redistributes the unburned gas layers ahead of the flame into a broader, curved area [8]. The reported upstream distance covered by this disturbance ranges from a few centimeters [9] to 10-15 cm [6].

The redistribution of flammable layers preceding the flame has significant safety implications. Flames may jump over fences or barriers or propagate past the end of the fuel spill. A redistribution of flammable gases preceding a spreading flame can enable a flame to jump over an endwall and continue propagating for some axial distance. As long as the height of the endwall is less than about 10 times the height of the flammable layers experiments show that the flame will make this jump [10]. A similar experiment was conducted with a fence spanning the width and extending above a pool of flammable liquid [11]. In this way flammable gases were available to promote the flame spread if the initial flame could jump over the fence, which it did for some the initial conditions.

Previous Experimental Research on Gas-Phase Systems

Phillips conducted foundational experiments in a gallery by diffusing methane through a porous surface that formed the top of a gallery [12]. He employed a color schlieren technique to measure the concentration profiles perpendicular to the diffusing surface before ignition, but apparently did not record schlieren data during the flame propagation [13]. For the conditions he tested, Phillips found a constant flame speed regardless of the quantity of methane or the concentration gradient. However, except for a few experiments with coal gas which were not quantified, all of the tests were conducted with methane layers that were above unity equivalence ratio.

Feng et al employed a separator plate in a gallery so a two-layer system could be formed, the flammable layer of methane (or methane/air) being on top [8]. In particular they explored the effect of gallery height and found that the flame spread steadily for tall galleries, but was unsteady and accelerating for shorter ones. They employed a multiple exposure camera to get the spread rate, but had no way to visualize the flow or concentration distribution. These tests again always included a layer at

stoichiometric concentration.

Researchers at the Bureau of Mines also have investigated this problem both for heavy gases sitting on floors [5] and for lighter gases trapped under ceilings [9]. As with their predecessors, all the mixtures tested had concentrations above the stoichiometric level. They reported that the flame speed was dependent on the flammable zone thickness and the concentration gradients (in contrast to Phillips [12]), and interestingly, that the flame propagated through regions that were *below* the lean flammability limit for homogeneous mixtures. They attribute this to a stabilizing influence of combustion in nearby richer zones, but this finding further suggests that fire hazards of this type may extend outside their initial boundaries.

Previous Modeling Efforts

In their data analysis Liebman et al [9] found that inclusion of gravitational effects through the Richardson number (which they defined as the ratio of buoyant forces tending to stabilize a layer to shear forces tending to mix it) was useful for the closed gallery case. However, extension of their correlation to 0-g predicts infinitely fast spread, which is obviously wrong.

Feng et al [8] treated both the open and bounded gallery configurations through a streamtube approach. In its simplest form, the infinite flow field is divided into three regions: a layer of combustible gas of *uniform concentration*, a burned gas layer, and a pure air layer. For the infinite open gallery, V_f/S_f is predicted to be equal to the square root of the ratio of the unburned to the burned gas density [8]. When the gallery is also a finite length with open ends, they showed that V_f is never steady, but increases along the gallery length. The model of Feng et al, however, overpredicted by about 50% the V_f observed in Kaptein and Hermance's experiments [6]. The latter authors demonstrated that agreement with their experimental results was improved by modifying the Feng model to include a *gravitational* potential energy term accounting for the different heights of the combustible and burned gas layers.

Objectives of This Work

The following are objectives of our 4-year study: (a) to determine experimentally if there is a gravitational influence on the flame spread rate in layered fuel mixtures, (b) to determine what factors influence the gravitational dependence ; (c) to measure the flame spread rates, the fuel vapor concentration levels, and the hypothesized redistribution of flammable gases ahead of the spreading flame in both normal gravity and in microgravity; and (d) to extend an existing numerical model for sub-flash flame spread over liquid pools to the case of layered mixtures and use it to explore gravitational effects as well as to compare to experimental findings.

Experimental Apparatus and Procedure

A schematic of our experimental apparatus is shown in Fig. 2. It consists of an aluminum fuel tray 76 cm long by 10 cm wide by 3.2 mm deep with a wall thickness of 4 mm. The tray is inlaid flush to the tops of the side walls with porous bronze with an average pore size of 110 μm and a porosity of 40%. An aluminum panel, through which water from a temperature bath flows, is bolted to the bottom of the tray and is used to control the tray temperature. The tray is surrounded on one long side as well as on the top by Lexan panels, and on the other long side by an aluminum panel, forming a duct around the tray with dimensions 108 mm wide by 112 mm high. The end walls of the duct have openings 80 mm by 90 mm (to allow gas expansion out each end) which are covered with perforated plates to reduce the chance of room air currents entering the duct. A hot wire at one end of the duct ignites the mixture.

Two color CCD cameras are used to record the flame spread process. A top view of the entire tray length is used to determine the flame spread velocity by recording the flame on S-VHS video and using previously developed software [14] to track its progress. The shape of the flame front is also noted in the top view. The side view camera has a horizontal field of view of 70 mm and is centered on a point about 25 cm from the ignitor. It is operated with a shutter speed of 1/250 sec per video field to better capture the flame as it passes. The signals from the cameras are mixed and recorded on one tape.

A sheathed, type T thermocouple is glued into a small slot flush with the top of the porous bronze at the end of the tray opposite the ignitor and recorded manually. Prior to conducting any experiments (and with the duct lid removed) the fuel tray surface temperature was recorded with an infrared camera which showed it to be uniform within 0.75 °C. Upon reaching temperature, methanol is poured over the bronze until it wets the entire top surface. A stainless steel lid with a rubber gasket around the edge is slid over the tray by lifting up the duct aluminum wall which slide in slots in the duct end walls (cf fig. 2). This prevents evaporation and an accumulation of fuel vapor above the tray. After waiting for the methanol to equilibrate in the

345

tray, the lid is pulled out, the side wall lowered, and after a specified time for fuel evaporation and diffusion, the fuel-air mixture is ignited.

In order to measure the fuel vapor concentration ahead of the flame we have been experimenting with a rainbow schlieren deflectometry system capable of detecting the fuel concentration gradient. The test system presently consists of a collimating lens of 550 mm focal length and a decollimating lens of 1550 mm focal length with the light supplied by a fiber-coupled arc lamp passing through a 75 µm wide slit. A small test pool 15 cm long was placed in the test section. At the secondary focus we placed a standard 2 mm Cartesian rainbow filter [15] oriented to detect vertical concentration gradients and recorded the images with a color CCD camera as the tray lid was removed. No flame spread tests have been done in this system. Currently we are building a 4 m focal length system which will give increased sensitivity to better record any changes that occur during flame spread.

Results and Discussion

Figure 3 contains the result of using the rainbow schlieren system to measure the fuel vapor layer 1.0 sec. after removing the test tray lid. Knowing the initial pool temperature, and using the procedure described in [15] we integrated the hue variation in the schlieren image to obtain the fuel concentration as a function of height above the pool. Figure 3 shows a calculated profile based on the 1-D diffusion equation along with our experimentally determined profile. As can be seen, the agreement is good except that the measured profile dips below zero. Unfortunately, the apparatus at the time did not have schlieren quality windows, so the side walls were removed for the measurement. This allowed fuel vapor to diffuse outside the test region (changing the path length) and skew the measurement, a condition that will be remedied in the future. As part of this project, we plan to develop an independent experimental measurement technique based on laser light absorption to provide a second check of this measurement. The schlieren system will then be used for real-time measurements of the layer thickness ahead of the flame during spread.

Flame spread tests have been conducted in normal gravity as described above for methanol at temperatures between 21 °C and 11 °C. (For reference, the for methanol T_{flash} = 11 °C and T_{st} = 21 °C). Representative flame position vs. time data as determined by flame tracking are shown in Fig. 4. Initially we had some problems achieving a flat flame front during spread (i.e. flame front perpendicular to spread direction), but those were overcome by more care in removing the lid, so that all of the data shown are from flames that propagated with flat fronts (except for a small amount of curvature near the wall due to heat loss). The ignition delay (the time between removing the lid and igniting) was approximately 3.5 sec for these cases. As can be seen, the flame spread is very uniform (i.e., no pulsations) with the higher temperature cases spreading faster.

In Figure 5 we present a compilation of all of the runs showing the effect of the initial temperature on spread rate. At least three runs are represented at each temperature. The data as shown in Fig. 4 are fit with a straight line to get the flame velocity. Points that did not track well due to ignitor interference or tray end effects were first eliminated. This graph shows the spread rate for substoichiometric conditions has an exponential dependence on temperature when the diffusion time is held constant. Once T_{st} is reached, the flame speed increases only slowly, if at all with temperature. The data agree well with that taken previously by Hirano for spread over pure liquids [16], who also found that at higher temperatures the flame spread at rates well above the laminar burning velocity for stoichiometric, homogeneous mixtures. In contrast to Hirano we were unable to achieve ignition below 11 °C, presumably due to heat loss to the bronze which is higher than the pure liquid fuel he used, and which also may account for somewhat lower spread rates at the lower temperatures.

Since some previous flame spread studies were conducted in ducts with either one of the ends closed, we performed a few preliminary tests to determine what effect the duct might be having on the flame spread. For a temperature of 15 °C and short diffusion times (a few sec.) the flame spread rate was unchanged; for diffusion times of ~ 20 sec. we were unable to get straight flame fronts; for long times (~ 1 min.) the flame spread very rapidly (estimated from a few video frames to be 3.5 m/s). In the latter case, hot gas expansion behind the flame front drives it forward at a faster rate than would otherwise be expected. This effect also explains the high propagation rates seen by Hirano [17] for uniform mixtures, since he ignited in the center of an axisymmetric chamber and the hot gases had no escape path

The side view of the flame is shown in Figure 6. This is representative of the flames we saw. It appears to be a triple flame with the lower leg quenched. We believe the upper leg of the flame - which is much higher than the height of the lean layer limit prior to the flame arrival - to be burning at or near the lean flammability limit, and the middle or horizontal leg behind the flame to be burning closer to stoichiometric conditions as heat from the flame passage evaporates more fuel behind it and excess air due to the fuel lean condition above diffuse together. The overall height of the flame was found to increase as the diffusion

346

time increased for a given temperature.

Conclusions and Future Plans

We have built an apparatus for measuring flame spread rates through non-homogeneous fuel-air mixtures as a function of layer thickness and concentration. The layer thickness is adjusted by controlling the diffusion time above a fuel-saturated porous media, while the concentration is controlled by the fuel temperature. Normal gravity tests with methanol have so far explored largely the effect of temperature, as well as the effects of various aspects of the apparatus. Good agreement with previous research has been obtained. We have also demonstrated the ability of a rainbow schlieren system to quantitatively measure fuel vapor concentrations in the static case. As the next step, we plan to implement this diagnostic into the flame spread tests, as well as the laser absorption method mentioned above. Though not described in the paper, we completed the design of a 2.2 sec drop tower rig for conducting experiments in microgravity, after establishment of the flammable layer profile in 1g. The rig design includes the rainbow schlieren measurement system, and a capability for high-speed cinematography, but not the line absorption technique. In addition, we plan to use diffusing gases in place of evaporating liquids for some tests in both normal and microgravity so that we can explore roof layers. For some tests, we hope to investigate the effect of oxygen concentration on the flame behavior in microgravity, since this has direct applicability to fire hazards aboard the International Space Station, and diluent type, since previous work has shown a dramatic effect on liquid flash point, for example. Finally, in the later years of this project, we will utilize a numerical model developed by Schiller et al [18] and apply it to the case for layered mixtures.

References

[1]   D. G. Talley, "Some Properties of Nearly Premixed Laminar Flame Propagation Along Weakly Stratified Layers in Combustible Gas Mixtures," *Combustion and Flame*, vol. 79, pp. 141-150, 1990.

[2]   P. D. Ronney and H. Y. Wachman, "Effects of Gravity on Laminar Premixed Gas Combustion: 1. Flammability Limits and Burning Velocities," *Combustion and Flame*, vol. 62, pp. 107-119, 1985.

[3]   C. K. Law and G. M. Faeth, "Opportunities and Challenges of Combustion in Microgravity," *Prog. Energy Combust. Sci.*, vol. 20, pp. 65-113, 1994.

[4]   R. A. Strehlow, K. A. Noe, and B. L. Wherley, *21st Symposium (Int'l) on Combustion*, pp. 1479-1494, 1986.

[5]   I. Liebman, H. Perlee, and J. Corry, "Investigation of Flame Propagation Characteristics in Layered Gas Mixtures," U.S. Bureau of Mines 7078, 1968.

[6]   M. Kaptein and C. E. Hermance, "Horizontal Propagation of Laminar Flames Through Vertically Diffusing Mixtures Above a Ground Plane," presented at 16th Symposium (Int'l) on Combustion, 1976.

[7]   H. Ishida, "Flame Spread over Ground Soaked with Highly Volatile Liquid Fuel," *Fire Safety Journal*, vol. 13, pp. 115, 1988.

[8]   C. C. Feng, S. H. Lam, and I. Glassman, "Flame Propagation Through Layered Fuel-Air Mixtures," *Combustion Science and Technology*, vol. 10, pp. 59-71, 1975.

[9]   I. Leibman, J. Corry, and H. E. Perlee, "Flame Propagation in Layered Methane-Air Systems," *Combustion Science and Technology*, vol. 1, pp. 257-267, 1970.

[10]   T. Hirano, T. Suzuki, and I. Mashiko, "Flame Behavior Near Steps Bounding Layered Flammable Mixtures," *Eighteenth Symposium (Int'l) on Combustion*, pp. 647-655, 1981.

[11]   T. Suzuki, I. Mashiko, N. Tanabe, and T. Hirano, "Flame Jumping over obstacles on the surface of a flammable liquid at superflash temperatures," in *Combustion in Reactive Systems*, J. Bowen, Ed., 1981.

[12]   H. Phillips, "Flame in a Buoyant Methane Layer," presented at Tenth Symposium (International) on Combustion, 1965.

[13]   H. Phillips, "A three-colour quantitative schlieren system," *Journal of Scientific Instruments*, vol. 1, pp. 413-416, 1968.

[14]   F. J. Miller and H. D. Ross, "Further Observations of Flame Spread over Laboratory-Scale Alcohol Pools," *24th Symposium (International) on Combustion*, pp. 1703-1711, 1993.

[15]   P. Greenberg and R. Klimek, "Quantitative Rainbow Schlieren Deflectometry," *Applied Optics*, 1995.

[16]   T. Hirano, T. Suzuki, I. Mashiko, and N. Tanabe, "Gas Movements in Front of Flames Propagating Across Methanol," *Combustion Science and Technology*, vol. 22, pp. 83-91, 1980.

[17]   T. Hirano, T. Suzuki, I. Mashiko, and K. Iwai, "Flame Propagation Through Mixtures with Concentration Gradient," *Sixteenth Symposium (International) on Combustion*, pp. 1307-1315, 1976.

[18]   D. N. Schiller, H. D. Ross, and W. A. Sirignano, "Computational Analysis of Flame Spread Across Alcohol Pools," *Combust. Sci. Technol.*, vol. 118, pp. 205, 1996.
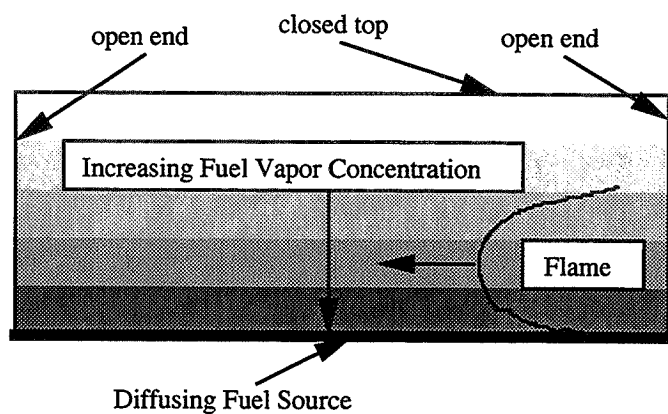
Figure 1. Schematic showing fuel vapor layers that develop above a fuel source. Flame leading edge spreads along a line near stoichiometric.
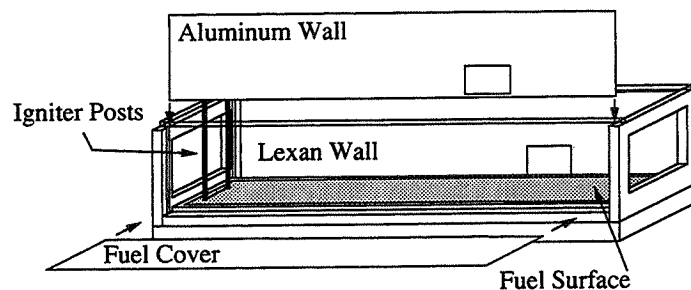
Figure 2. Experimental Apparatus.
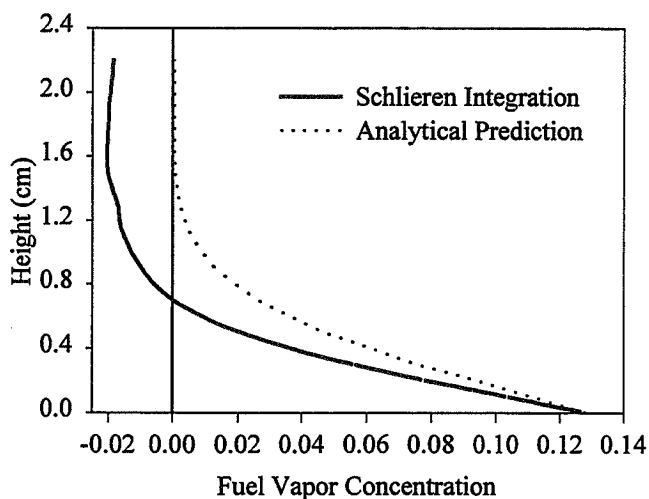
Figure 3. Fuel vapor concentration above the fuel bed as measured by Rainbow Schlieren compared to calculated distribution.
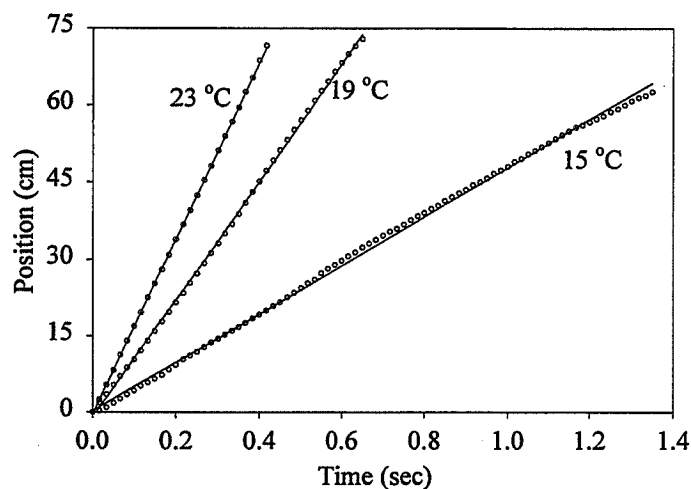
Figure 4. Flame postion vs. time for several sub-stoichio-metric tempertures.
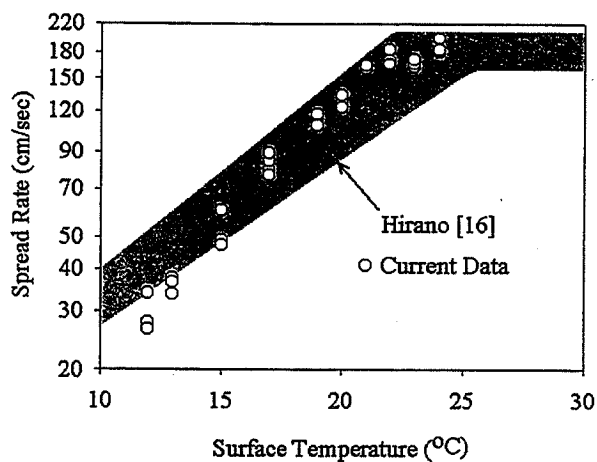
Figure 5. Flame velocity over methanol-soaked porous bronze vs. temperature compared to data for pure methanol [16].
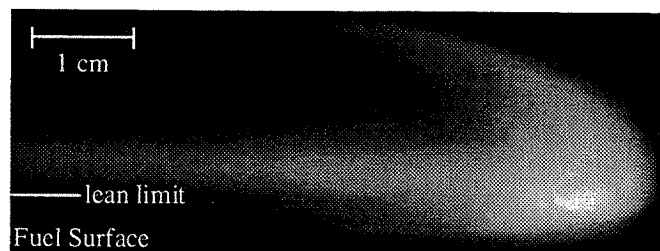
Figure 6. Side View of 1g flame for T_o = 21 °C and a diffusion time of 3.1 sec.. Flame is all blue (no soot).

348

Dynamics and Structure of Weakly-Strained Flames at Normal and Microgravity

CHRISTINE M. VAGELOPOULOS,*·FOKION N. EGOLFOPOULOS,* AND FLETCHER J. MILLER+
* Department of Mechanical Engineering
University of Southern California
Los Angeles, California

+ Case Western Reserve University
Cleveland, Ohio

Introduction

Strained laminar flames have been the subject of extensive studies the last thirty years or so, typically in opposed-jet, stagnation-flow configurations. The motivation behind such extensive efforts emerges from the relevance of such flames to a number of combustion phenomena and issues. First, it is believed that such flames are of relevance to turbulent combustion, given that under certain conditions, turbulent flames can be viewed as an assembly of strained laminar flamelets [1-3]. Second, the opposed-jet, stagnation-flow configuration is a particularly meritorious configuration, in which the details of the physico-chemical processes can be probed and understood. More specifically, the stagnation-flow configuration allows for the accurate determination of fundamental flame properties [3, 4] and can be modeled conveniently with the use of detailed description of chemical kinetics and molecular transport. Thus, on one hand the interaction between fluid mechanics and chemical kinetics can be investigated from first principles and on the other, existing kinetic and/or transport models can be (partially) validated with confidence. The response and phenomena of interest of laminar flames are quite different, depending on whether the strain rate is low or high.

At high strain rates, the fluid mechanics have a strong influence on the flame structure, affecting thus the flame temperature, burning rate, and species concentrations, and for high enough values the strain rate can cause flame extinction. The quantification of extinction strain rates from laminar flame studies, is a very important contribution to the modeling of turbulent combustion.

At low strain rates, flames have the tendency to closely resemble the ideal model of a one-dimensional, steady, adiabatic flame. This model, however, can not be experimentally reproduced. Thus, substantial efforts have been made to use information from low strain rate flames for the determination of fundamental flame properties, which are then only functions of the mixture and independent of external parameters such as fluid mechanics and/or heat loss. A profound example is the counterflow technique for the determination of laminar flame speeds, as proposed by Law and coworkers [3-6]. Low strain rate flames are of relevance and interest to many combustion phenomena including turbulent combustion, flammability limits, and flame stabilization. Furthermore, weakly-strained, weakly-burning non-premixed flames can be of relevance to flame spread. Our previous studies [7, 8] have shown that weakly-burning flames (premixed and non-premixed) are particularly sensitive to chain mechanisms competitions, thermal radiation, and flow field unsteadiness and that such effects can readily couple leading to phenomena of significant fundamental and practical interest.

Weakly-strained flames on the other hand, are particularly difficult to stabilize in the laboratory. This has been indirectly indicated in our previous studies [9], in which the goal was to measure flame speeds at very low strain rates so that the experimentally determined laminar flame speed through extrapolations to zero strain rate, is closer to its true value. In these experiments, flame unsteadiness, severe distortions of the flame surface and eventual flash-back would make any measurements highly unreliable and/or impossible as the strain rate is reduced to very low values. Furthermore, the stabilization of stable, measurable, near-limit premixed flames has also been found to be impossible, because of the severe distortion of the flame assembly and various forms of flame motion. Similar observations have been made in our laboratory for weakly-strained non-premixed flames. Such phenomena find their origin to the buoyancy-induced natural convection and instabilities as higher density fluid finds itself on top of a lower density fluid. Thus, the use of microgravity becomes essential in order to provide meaningful insight into this important and challenging combustion regime.

Objectives

In view of the foregoing considerations, we have undertaken the task to conduct a combined experimental and numerical study on the details of weakly-strained laminar premixed and non-premixed flames, and to assess systematically the effects of kinetics, heat loss, unsteadiness, and gravity. More specifically the main objectives of the program are to:

1. Experimentally determine the *true laminar flame speed* at near-zero strain rates at 1- and 0-g
2. Experimentally determine the *true flammability limits* using particle image velocimetry at 0-g
3. Quantify the onset of *thermo-diffusional instabilities* at ultra-low strain rates
4. Experimentally determine the *extinction limits* of weakly-burning, non-premixed flames at 0-g
5. Experimentally determine the *response to unsteadiness* of weakly-burning flames at 1- and 0-g

6. Numerically simulate the experiments by developing and using quasi-one-dimensional and axisymmetric codes with the use of detailed description of chemical kinetics, molecular transport, and thermal radiation

7. Provide physical insight into the important and frequently controversial issues including laminar flame speeds, flammability limits, radiation and gravity effects, by identifying the controlling mechanisms.

Experimental Approach

The counterflow configuration includes the use of two opposed nozzles from which the reactant streams emerge and impinge on each other. Alternatively, strained flames can be established by impinging one jet on a flat plate, which can be of variable temperature; the jet-plate configuration is used for the study of the effect of downstream heat losses on the propagation and extinction of premixed flames. Nozzles with diameters of 20, 30, and 40 mm are used and they are surrounded by nitrogen coflow. The implementation of the stagnation flow technique in microgravity required the use of several and involved modifications compared to the normal-gravity configuration. Given that the duration of the experiments is 2.2 sec in the drop tower, the system has been automated by using a tattletale-based electronic circuit, which provides all necessary commands.

The partial pressure mixing technique is used in order to create the test mixtures of air and fuel in a high pressure tank. An adaptive mass flow control system (PID) is used to set, monitor, and vary the flow rate of the combustible gas mixture sent to the burner(s). By varying the flow rate, the imposed strain rate in the flow field is controlled and varied. Ignition is obtained by using retractable electrodes and a powerful ignition circuit. Weakly-burning flames are difficult to ignite, and the ignition process had to be enhanced. More specifically, an ordinary liquid fuel lighter was modified and is being used to generate a pilot flame. The nozzle of the pilot flame is located between the existing spark electrodes and it is mounted on the same retractable arm which can be put into the ignition zone, and its operation is controlled by a solenoid switch.

Upon ignition, the flow rate to the burners is controlled by the PID unit, which is programmed to increase or decrease the mixture flow rate to the burners by any desirable amount and rate. Thus, low and high strain rates can be obtained. Given the limited available microgravity time, it was decided that the fluid mechanics would be quantified by using the particle image velocimetry (PIV) technique, which allows for the instantaneous measurement of the velocity field, and which can result to an accurate determination of local strain rates and flame speeds, something that has not been previously done at 0-g. Development and establishment of PIV in both 1-g and in the 2.2 sec drop tower facilities has been a challenge and has occupied much of our experimental efforts.

Initially, a 100 mW laser diode was placed on the rig along with the appropriate optics designed to generate the light sheet necessary for PIV purposes. The observations during the experiments that followed at the drop tower led to the conclusion that a more powerful light source is needed. Subsequently, a CW Argon-ion laser has been used at 1-g with higher power in the range of 500 to 800 mW and the data are recorded on a 30 frame/sec CCD camera. Given the low framing rate for the video images and the high velocities in the flow field (10 to 100 cm/s) a chopper has been added to the system for the particle tracking and this has resulted to very satisfactory images for the first time. At present, we are in the process of implementing a more powerful CW light source in the drop tower so that the 0-g measurements can be taken. An auxiliary purpose of this project is to develop and integrate an accurate PIV technique in our 1-g stagnation-flow experiment, which has a number of advantages over the conventional laser Doppler velocimetry (LDV) technique. First, it provides instantaneous flow field information which can be very useful in capturing multi-dimensional and unsteady effects. Second, it can reduce the experimental data acquisition times by 1 to 2 orders of magnitude.

Numerical Approach

The numerical simulations of the experiments are conducted by using existing one-dimensional codes, and by developing appropriate forms of axisymmetric and two-dimensional codes. In all simulations detailed descriptions of chemical kinetics, molecular transport, and thermal radiation are included.

A modified version of the Sandia one-dimensional premix code [10] is being used for the determination of laminar flame speeds. Our stagnation-flow code [11] is being used for the description of the steady and unsteady chemistry-fluid mechanics interactions in the vicinity of the centerline of the stagnation-flow configuration. In both codes, two types of radiation heat transfer have been used. The first includes the use of the Planck mean absorption coefficient at the optically thin limit similarly to our previous studies [7, 8]. The second includes the use of the detailed narrow-band radiation model, RADCAL, developed by Grosshandler [12]. This model can predict the spectral structure of various combustion products over a wide range of temperature, pressure, and pathlength. It also computes the spectral intensity, from a non-isothermal mixture of combustion gases and soot incident upon a volume element within or external to the environment. The program solves the equation of transfer for an absorbing and emitting medium (no scattering) by breaking the line-of-sight into a number of uniform elements and by using molecular models and tabulated data for spectral absorption coefficients. The goal of this second approach is to examine the validity of the Planck mean absorption coefficient approach as well as the effect of optical thickness on various near-limit phenomena.

The multi-dimensional modeling efforts of this study includes the development of both axisymmetric and two-dimensional unsteady codes. Finite difference, and Newton-type iteration schemes are being used similarly to the Sandia codes. These codes are currently in their development stage. The eventual use of such codes is expected to provide significant insight into the physics of the stagnation-type reacting flow, which are still not well-understood under realistic conditions, as will be further discussed later.

Summary of Research

A number of issues have been addressed under this program. More specifically, studies have been done on the effect of downstream heat loss on the dynamics of strained premixed flames, the effect of strain rate and buoyancy on flame stability, the direct determination of laminar flame speeds at the limit of near-zero strain rate, and the effect of unsteadiness on the response of strained diffusion flames. Given the space limitations, results and discussion on unsteady diffusion flames will not be presented.

Downstream Heat Loss Effects on Strained Premixed Flames

This study included experimental and numerical investigations of strained, laminar, premixed flames stabilized by one jet impinging on a variable-temperature, chemically-inert wall [13]. The wall material was stainless steel and its temperature was controlled by using electrical heaters. Both experiments and numerical simulations demonstrated that the extent of interaction between the wall and the gas phase closely depends on the magnitude of the strain rate. At high strain rates, the flame approaches the non-adiabatic wall, its flame speed is reduced, and the extinction strain rate is substantially reduced compared to the opposed-jet, adiabatic experiments. It was also found that the wall temperature had only a moderate effect on extinction, which is chiefly controlled by the presence of heat loss and less by its magnitude. The numerical simulations supported the experimental arguments and quantitative agreement was found between experiments and simulations which were conducted by using the GRI 2.1 C_2 kinetic mechanism [14].

At low strain rates, on the other hand, the flame is stabilized at several flames thicknesses away from the wall and the effect of downstream heat loss was found by both the experiments and simulations to be minimal. The important implication of this behavior is that the single jet-wall configuration can be used for the determination of laminar flame speeds as an alternative means to the conventional opposed-jet configuration of Law and coworkers [3-6]. Figure 1 depicts representative experimental results of the reference, strained, flame speed, $S_{u,ref}$, as function of the imposed strain rate for various wall temperatures for a fuel-lean methane/air flame; L stands for the nozzle-stagnation plane distance and ϕ for the fuel/air equivalence ratio. In the same figure, the results obtained by using the opposed-jet configuration are also shown. It can be seen that the data are nearly-indistinguishable, and that any scatter is well within the experimental uncertainty of the LDV. It should also be noted that measurements could not be obtained at very low strain rates, similarly to all our past 1-g measurements. This constitutes a significant constraint in our efforts to probe the ultra-low strain rate regime, which apparently is essential for the determination of laminar flame speeds. Furthermore, the phenomena and underlying mechanisms controlling this strain rate regime have not been previously assessed adequately, and it is one of the main goals of this program to provide sufficient insight, and examine whether alternative means exist for probing this ultra-low strain rate regime.

Strain Rate and Buoyancy Effects on Flame Stability

The assumption that flat flames are stabilized in a stagnation-flow configuration is valid only when the flames are experiencing a substantial amount of straining. To further investigate this issue, systematic experiments were conducted, with various separation distances, L, and nozzle exit velocities, u_{exit}, and it was found that the flame shape depends on both L and u_{exit}. More specifically, by keeping the L fixed and equal to about one nozzle diameter, the flame is nearly-flat for large u_{exit}'s, while as the u_{exit} decreases, the flame approaches the burner, and develops a non-uniform curvature with the convex pointing towards upstream around the centerline and towards downstream away from the centerline, as it can be schematically seen in Fig. 2. For any further reduction of u_{exit}, the flame shape becomes more convex around its centerline, it enters the nozzle and flashback initiates at the center of the jet; under such extreme conditions, measurements are not possible. For the conditions of Fig. 2, it can be seen that at the vicinity of the nozzle exit, the axial velocity increases initially with the radius, and then it decreases as the nozzle wall is approached and boundary layer effects become important. Experiments at higher u_{exit}'s result to more uniform axial velocity profiles in the radial direction and the flame shape becomes considerably flatter.

In our first attempts to correct this non-uniform behavior, the design of the aerodynamically contoured nozzles was optimized. Thus, the nozzles were designed by deriving a contraction contour based on a 5th order polynomial which results, mathematically and experimentally, to very flat u_{exit} profiles for free-jets. However, this optimization still did not solve the problem. Subsequently, it was realized that any optimized nozzle design is based on the assumption that the radial pressure gradient at the nozzle exit is zero, given that such designs are typically derived for free-jets. However, this is not the case for a stagnation flow configuration, in which radial pressure gradients are needed for the motion of fluid elements outwardly in the radial direction. These radial pressure gradients can affect the radial distribution of u_{exit}. This was numerically shown by considering the steady axisymmetric momentum conservation equations in both the axial (-x) and radial (-r) directions. First, numerical solutions were obtained for the ideal stagnation flow by using various u_{exit}'s. Then by using these solutions, numerical integrations of the momentum equations were performed in order to determine the pressure distributions along the

centerline of the domain. The pressure at the center of the nozzle exit was used as a reference pressure, P_{ref}, and the distribution of the pressure differential $\Delta P = P - P_{ref}$ was determined. Results showed that indeed pressure gradients develop in both x- and r-directions. In the r-direction, the P is reduced quadratically, as the radius increases. Physically, the pressure variations can be better presented through a non-dimensional pressure coefficient, C_p, which results from the scaling of ΔP with the reference inertia forces at the nozzle exit, i.e. $C_p = \Delta P/(2\rho_{exit}u_{exit}^2)$. The radial distribution of C_p is shown in Fig. 3 for a $\phi = 0.75$ CH_4/air flame with L=20 mm and for $u_{exit}=50$, 100, and 200 cm/s, at a distance 1 mm above the burner. It is apparent that the C_p values are larger in magnitude for the low u_{exit}. A direct consequence of this observation is that the very low strain rates may not be obtained for flames which are also flat, by simply lowering u_{exit}. Any attempt to resolve this problem by increasing L, which reduces the magnitude of C_p, would fail because as u_{exit} is reduced, conical Bunsen flames will be stabilized, and pertinent discussion on this phenomenon follows.

The presence of gravity further complicates experiments at low strain rates when the opposed-jet configuration is used. For low u_{exit}'s, an upward displacement of the twin-flame assembly is observed. Thus, substantial deviation from the symmetry is established to the point that measurements can be conducted only after flow adjustments have been done in both feed nozzles. This displacement was found from our numerical simulations to depend on the asymmetric C_p distribution between the two nozzles. At low strain rates, buoyancy also results in flame distortion and motion.

In view of the importance of the low strain-rate flames for the experimental determination of laminar flame speeds, an alternative approach was assessed.

Direct Experimental Determination of Laminar Flame Speeds
Given the aforementioned limitations, a simple observation led us to an alternative approach, which we propose as a viable one for the determination of the *true laminar flame speed*. The establishment of a flat, strained flame requires the existence of radial pressure gradients the magnitudes of which depend on the values of u_{exit} and L. However, a flat strained flame can become a conical Bunsen flame as the u_{exit} is reduced and L increases. This physically occurs because by reducing u_{exit} and increasing L, the stagnation flow starts resembling a free-jet flow in which the Bunsen flame stabilization mechanism is the prevailing one. It is also known, that while the stagnation-flow flames are positively strained, the Bunsen flames are negatively strained. Thus, if a smooth, quasi-steady transition is obtained from the stagnation to Bunsen flame, the ideal model of one-dimensional, unstrained, planar, steady, adiabatic, laminar flame can be approximately obtained within a specific spatial length, and its flame speed will be the true laminar flame speed; the schematic of the transition is shown in Fig. 4.

This concept was successfully tested for different mixtures by obtaining LDV data through the use of a QSP processor. For each equivalence ratio the following process was followed. First, the transition was smoothly obtained by using the PID unit to reduce the flow rate, and the area of transition was approximately identified through the use of a telescope equipped with appropriate length scale. Subsequently, the beam crossing point was positioned at various locations within this area as well as (intentionally) slightly below and above of it; all measurements were done on the centerline. Representative real-time velocity measurements at a fixed spatial point are shown in Fig. 5. It can be seen that indeed a minimum velocity value is obtained, which is defined as the reference upstream flame speed, $S_{u,ref}$. Such values of $S_{u,ref}$ were obtained for various spatial locations and the results are shown in Fig. 6. It can be seen that a minimum plateau region is achieved. The higher values of $S_{u,ref}$ to the left of the plateau are caused by the presence of finite steady strain rate, which is higher at flame locations closer to the stagnation plane. The location at which the $S_{u,ref}$ starts increasing at the right of the plateau, coincides with the location at which the flame starts moving by itself towards the nozzle in order to eventually be stabilized as a conical Bunsen flame. This flame motion is observed even when the flow rate is fixed. The observed increase of $S_{u,ref}$ during that motion, is mainly an artifact of the LDV measurements, which are biased towards higher values, given that these are transient measurements and as the flame moves towards the nozzle, the thermal expansion region will affect the measurements at a fixed spatial location. Additional factors affecting the flame during this transition, are the finite strain rate as it is induced by flame motion and curvature, as well as the Bunsen tip-like behavior as the flame becomes gradually more curved. It should be noted in Fig. 5, that the time scales of flow rate reduction are quite large to induce any transient effects to the flames. Independent flame visualization was conducted with a CCD camera, and results indicate that the induced downward flame displacement velocity during the reduction of the flow rate is of the order of few mm/s. It should be also noted, that the state corresponding to the right end of the plateau of Fig. 6 is naturally a condition beyond which a flat strained flame can not be stabilized. Thus, this state must be characterized by an infinitesimally small strain rate, given that a finite strain rate would not allow the flame to undergo the transition to Bunsen flame. Therefore, we propose that the value of the minimum plateau of Fig. 6 just before the transition starts, is a representative value of the *true laminar flame speed*, S_u^o. Results were obtained for methane/air, ethane/air, and propane/air flames at 1 atm. The results for methane/air and ethane/air are shown in Figs. 7 and 8 along with our previous data. The present data are generally lower compared to our previous data, which were obtained through linear extrapolations to zero strain rate.

It should be noted that measurements were not possible for rich flames with the existing apparatus, because of the interference which the outer diffusion flame causes during the transition. This problem will be resolved by conducting the

experiments in an enclosed, inert environment. Furthermore, the proposed technique could not be applied to very lean flames because of buoyancy induced instabilities and such measurements will be conducted at 0-g with the use of PIV.

Conclusions

Experimental and numerical studies were conducted for weakly-strained, laminar premixed flames. The dynamic response and stability of such flames was assessed for a large number of mixtures. A new technique is proposed for the direct experimental determination of laminar flame speeds at the limit of near-zero strain rate.

Acknowledgments

References
1. LIBBY, P. A. AND WILLIAMS, F. A.: *Combust. and Flame* 44, pp. 287-303 (1982).
2. PETERS, N.: *Prog. Energy Combust. Sci.* 10, pp. 221-252 (1984).
3. LAW, C.K.: *Twenty-Second Symposium (International) on Combustion*, The Combustion Institute, Pittsburgh, 1988, pp. 1381-1402.
4. LAW, C. K., ZHU, D. L., AND YU, G: *Twenty-First Symposium (International) on Combustion*, The Combustion Institute, Pittsburgh, 1986, pp. 1419-1426.
5. WU, C. K. AND LAW, C. K.: *Twentieth Symposium (International) on Combustion*, The Combustion Institute, Pittsburgh, 1984, pp. 1941-1949.
6. EGOLFOPOULOS, F. N., CHO, P., AND LAW, C. K.: *Combust. Flame* 76, pp. 375-391 (1989).
7. LAW, C.K. AND EGOLFOPOULOS, F.N.: *Twenty-Fourth Symposium (International) on Combustion*, Combustion Institute, Pittsburgh, 1992, pp. 137-144.
8. EGOLFOPOULOS, F.N.: *Twenty-Fifth Symposium (International) on Combustion*, Combustion Institute, Pittsburgh, 1994, pp. 1375-1381.
9. VAGELOPOULOS, C.M., EGOLFOPOULOS, F.N., AND LAW, C.K., Twenty-Fifth Symposium (International) on Combustion, The Combustion Institute, Pittsburgh, 1994, pp. 1341-1347.
10. KEE, R. J., GRCAR, J. F., SMOOKE, M. D., AND MILLER J. A.: A Fortran Program for Modeling Steady Laminar One-Dimensional Premixed Flames. Sandia Report SAND85-8240., 1985.
11. EGOLFOPOULOS, F.N. AND CAMPBELL, C.S.: *J. Fluid Mech.* 318, pp 1-29 (1996).
12. GROSSHANDLER, W. L.: RADCAL: A Narrow-Band Model for Radiation Calculations in a Combustion Environment. NIST Technical Note 1402 (1993).
13. EGOLFOPOULOS, F.N., ZHANG, H., AND ZHANG, Z.: Wall Effects on the Propagation and Extinction of Strained, Laminar, Premixed Flames. To appear in *Combustion and Flame*.
14. BOWMAN, C.T., FRENKLACK, M., GARDINER, W., AND SMITH, G.: The GRI 2.1 mechanism. Personal communications (1995).
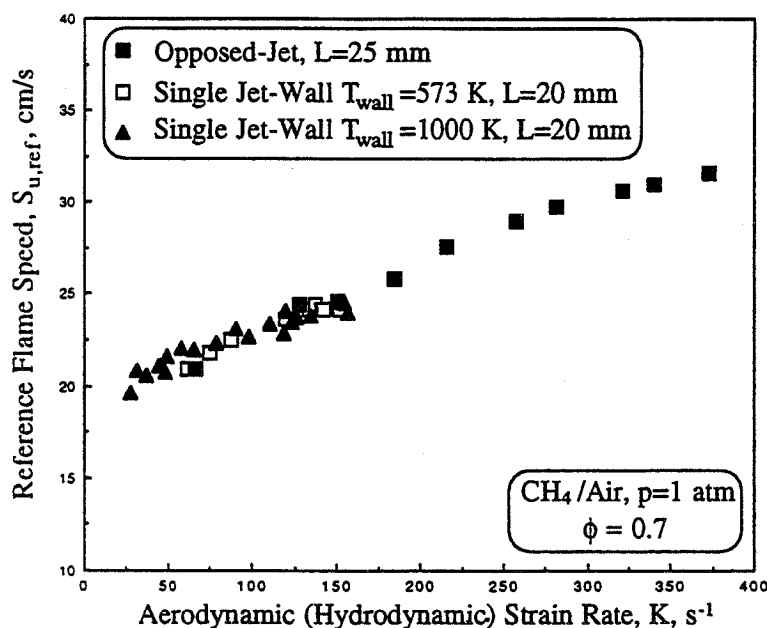
Figure 1. Wall effect on reference flame speed
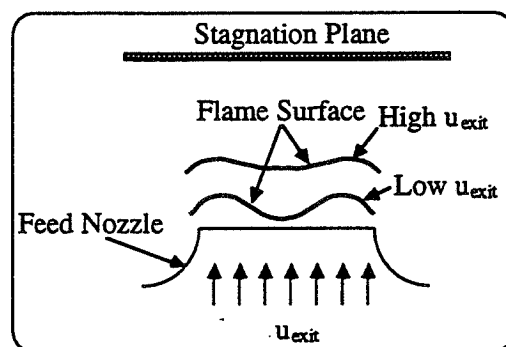
Figure 2. Strain rate effect on flame shape
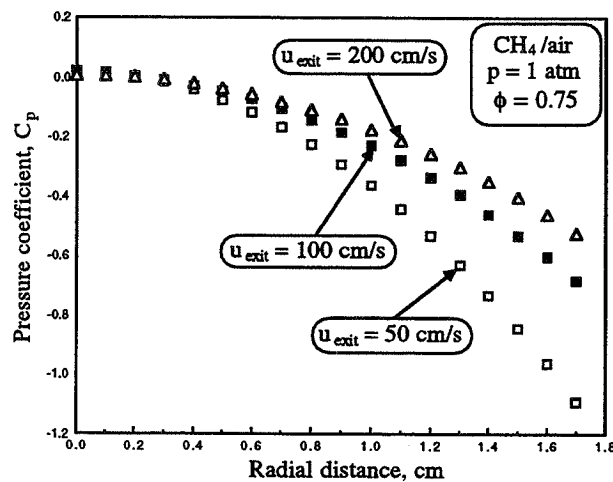
Figure 3. Strain rate effect on radial pressure distribution
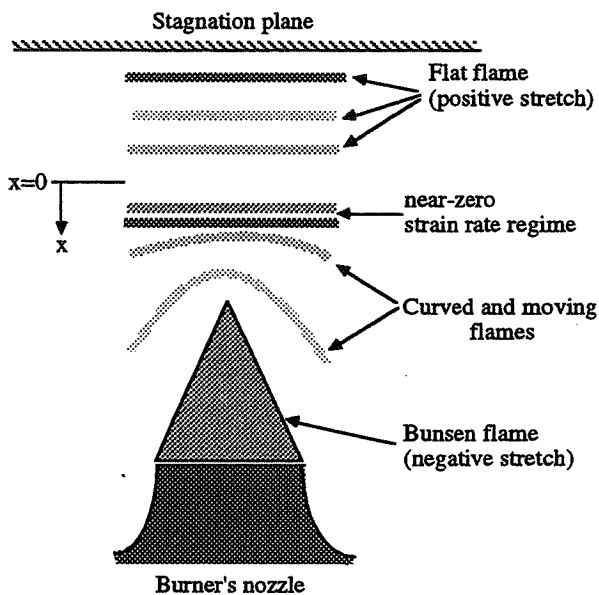
Figure 4. Schematic of transition
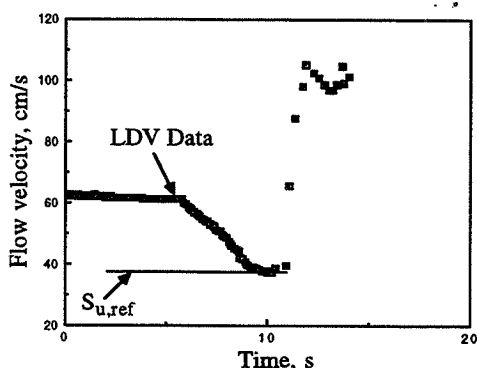
Figure 5. Real-time variation of flow velocity at a fixed spatial location during transition
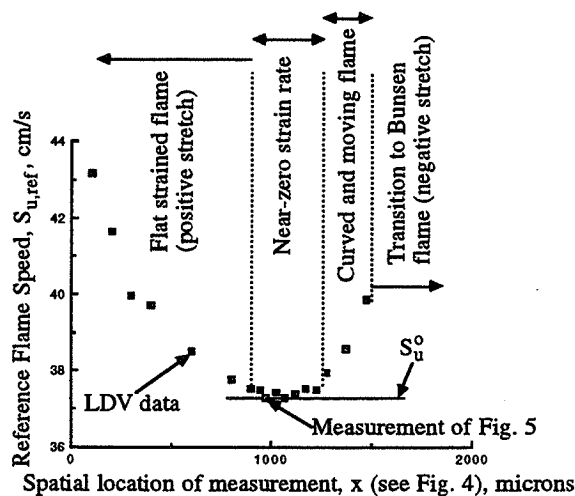
Figure 6. Effect of measuring location on reference flame speed
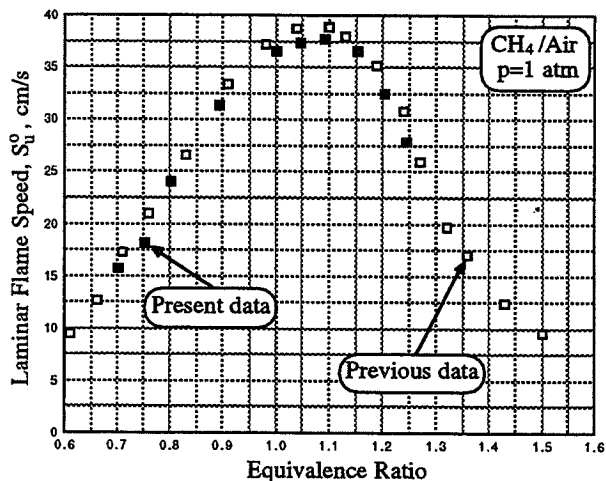
Figure 7. Comparisons between previously determined and present laminar flame speeds for methane/air mixtures
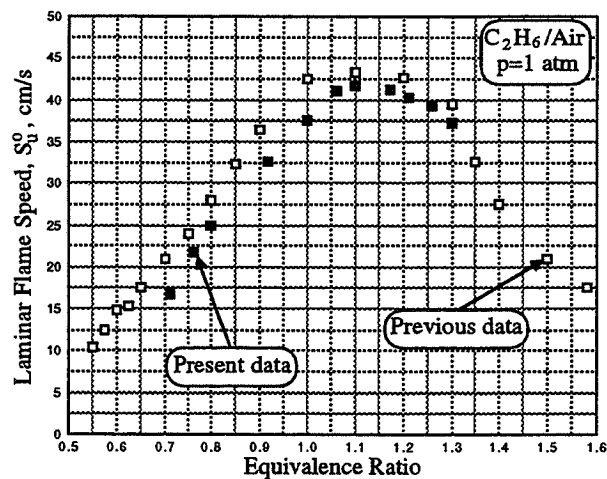
Figure 8. Comparisons between previously determined and present laminar flame speeds for ethane/air mixtures

MODELING OF MICROGRAVITY COMBUSTION EXPERIMENTS

J. BUCKMASTER
Department of Aeronautical and Astronautical Engineering
University of Illinois, Urbana, IL

Introduction

This program started in February 1991, and is designed to improve our understanding of basic combustion phenomena by the modeling of various configurations undergoing experimental study by others. Results through 1994 were reported in the Third Workshop (ref.1) and incomplete citations therein are listed below in complete form, refs.2-9. Work done since that time has concentrated on edge flames and radiation effects in premixed combustion, with some minor work on flame-balls.

Flame-balls

Flame-balls are stationary, premixed spherical flames observed in certain near-limit mixtures and are the focus of SOFBALL, Paul Ronney's experimental program (ref.1, p. 439) which, by the time this document appears, should have reached its apotheosis in the flight of STS-83. Radiation losses play an important role in flame-ball physics, defining inflammability limits and stability boundaries. In the asymptotic context which has been the foundation of all the analytical work, near-field losses on the scale $r/r_* = O(1)$ play a distinct role from far-field losses on the scale $r/r_* = O(\varepsilon^{-1})$. Here r is the radial distance, r_* is the flame-ball radius, and $\varepsilon (<< 1)$ is the inverse activation energy. Previous discussions (e.g. refs.10,11) have treated the near- and far-field problems in a disjoint fashion, and have established stability results specific to each.

In practice, of course, there is a continuum of losses, a seamless distribution covering both the near-field and the far-field, and what is needed is a seamless model. Unpublished results, a preliminary report of which is presented in ref.12, deal with some aspects of this issue. A very simple model in which chemical reaction is modeled by a δ-function (in a familiar fashion), and radiation losses are proportional to $(T - T_\infty)[H_2O]$ permits exact solutions in which the relative magnitude of far-field and near-field losses can be varied by varying the concentration of water-vapor in the far atmosphere. What we would like to do is incorporate a more accurate radiation model with a proper accounting of the temperature dependence of the Planck length and, at first blush, an asymptotic strategy $(\varepsilon \to 0)$ permits this. Unfortunately, when the near-field losses are significant, the asymptotic results are of no value for realistic values of the activation energy (the inflammability limit is lost), and all that emerges from this strategy that is useful is a solution for when the far-field losses dominate. Nontheless this puts the analysis of ref.11 in a clear physical context, relating the magnitude of the far-field losses to the concentration of H_2O at $r \to \infty$.

Edge-flames

Edge-flames are defined, roughly speaking, as flame-sheets with edges, and arise most commonly in non-premixed gases, or in non-uniform mixtures. They have their most striking manifestation in the microgravity program in the candle-flame experiments of Dietrich, Ross, and T'ien, particularly in the experiment carried aboard USML-1 (ref.1, p.31). In a mugen[1], a candle-flame adopts a hemispherical shape with a clearly defined circular edge. Extinction occurs via asphyxiation in the small-volume glovebox, and is preceded by large amplitude oscillations of the edge, which retreats and advances several times. The dynamics of this process does not involve any significant movement of the flame-sheet in the direction normal to the sheet. Of course, edge-flames arise in other contexts: flame-spread over fuel beds; flames attached to tube-burners; turbulent diffusion flames; etc.

In an effort to understand better the physics of edge-flames, we have developed a one-dimensional model (refs.13,14,15), which incorporates the physics indicated in the cartoon shown in Figure 1. The key ingredients are transverse flows of heat, oxidizer and fuel between the flame and the boundaries, and the model, which describes quantities averaged over the y-direction, describes the evolution of the flame structure in the s-direction. A key property of the model is that the averaged reaction rate is chosen to mimic diffusion-limiting in the limit of infinite Damköhler number.

---

[1] An acronym the author has proposed to denote a "micro-gravity environment". Apparently it means "without end" in Japanese, and so is doubly appropriate when the environment is created in space.

For an unbounded edge-flame with both Lewis numbers equal to 1, the model, in non-dimensional form is:

$$V\frac{d\vartheta}{ds} - \frac{d^2\vartheta}{ds^2} = -(\vartheta - \vartheta_w) + D(1-\vartheta)^2 e^{1/\varepsilon.(1-1/\vartheta)} \equiv f(\vartheta, D),\tag{1}$$

where ϑ is the average temperature, V is the speed with which the edge moves, ϑ_w is the temperature of the fuel and oxygen boundaries, D is a Damköhler number, and ε is an inverse activation energy. In the limit $D \to \infty$, when the underlying two-dimensional problem contains a Burke-Schuman flame sheet, $\vartheta \to 1$. The term $(\vartheta - \vartheta_w)$ models the transverse fluxes identified above.

Equilibrium is defined by setting $f \equiv 0$, and this defines an S-shaped response in the (ϑ, D) plane, a familiar characteristic of diffusion flames (Figure 2). For a range of Damköhler numbers between the extinction value (upper turning point) D_e and the ignition value (lower turning point) D_i there is stable biequilibrium, and a solution can be constructed, sans cold-boundary difficulty, in which state {1} characterizes the solution as $s \to -\infty$, and state {2} characterizes the solution as $s \to \infty$. This solution can be constructed using asymptotic tools when $\varepsilon \to 0$ and yields, amongst other things, an explicit formula for the edge speed,

$$V = \chi - 1/\chi, \quad \chi \propto \sqrt{D}.\tag{2}$$

In the limit $\chi \to \infty$ (D$_i$ is suitably large) $V \sim \sqrt{D}$, as for a premixed flame, but for $\chi = 1$ the edge is stationary, and for $\chi < 1$ (but $D > D_e$) the edge speed is negative. The formula (2) is not valid when D is close to D_e, and what has to be done then is discussed in ref.15. Attached flames for which the evolution is from $s = 0$ to $s \to \infty$ are discussed in ref.14. And ref.13 discusses stability calculations carried out for $Le_X = 1$, $Le_Y = 1 + O(\varepsilon)$ (cf. NEF analyses, ref.16).

Of particular interest insofar as the candle-flame experiment is concerned are the stability results when $Le_Y > 1$, for these reveal the possibility of a one-dimensional pulsating instability (advancing and retreating edge) at realistic values of the Lewis number, Figure 3. Of course, the cartoon on which the model is based (Fig. 1) has ingredients that are different from the candle configuration, so that the results can only be suggestive. But it would be of great interest to carry out the candle experiment in an atmosphere in which N$_2$ is replaced (or partly replaced) by a heavy inert such as SF$_6$, so that Le_Y is less than 1. This also raises the possibility that oscillations seen in flame-spread over liquid fuels (ref.1, p. 37) are a Lewis-number effort, a speculation that could be tested quite easily.

A 'spin-off' problem that does not appear to be directly related to any current activity within the microgravity experimental program is that of edge-flames in homogeneous mixtures. These novel structures can arise in strained-flow configurations relevant to near-limit flames rising in tubes, and a preliminary report describing numerical simulations of such flames is presented in refs.17,18.

Radiation effects on stretched flames

It was, perhaps, C.K. Law (ref.19) who first suggested that inflammability limits could be measured by examining premixed flames in a twin counterflow of fresh mixture in the limit of vanishing strain rate. A mugen provides the proper context in which this should be done, and experiments are described in ref.20 that were carried out in the Hokkaido drop tower. For methane/air mixtures these experiments yield a C-shaped quenching boundary of the type shown in Figure 4 (a theoretical curve from ref.21). For equivalence ratios greater than a minimum value there is a strong-strain limit and a weak-strain limit. The minimum equivalence ratio is smaller than the classical inflammability limit defined by a one dimensional flame subject only to radiation losses, and so defines an *inferior* limit. Clearly the data corresponding to Figure 4 does not yield the classical limit and this gives rise to the question: where is it hidden?

The theoretical analysis of ref.21 provides the answer in a straightforward fashion[2]. It examines the model equations (constant density, one-step kinetics)

$$-\rho C_p \alpha x \frac{dT}{dx} = \lambda \frac{d^2 T}{dx^2} - q(T - T_\infty) + QBY_\infty e^{-E/2RT*} \delta(x - x_*),$$

$$-\rho \alpha x \frac{dY}{dx} = \rho D \frac{d^2 Y}{dx^2} - BY_\infty e^{-E/2RT*} \delta(x - x_*),\tag{3}$$

---

[2] T'ien (private communication) examined the problem numerically in unpublished work presented at the Eastern States meeting some years ago, but his results are not as complete as those of ref.21 See also the related work in refs.22,23.

where α is the rate of strain and the term in q accounts for radiation losses. Parameters are chosen to correspond, in a rough fashion, to lean methane/air mixtures, and this includes the choice $Le = 0.9$. Then the classical inflammability limit is $Y_\infty = 0.024987...$, where Y_∞ is the mass fraction of methane.

Figure 5 shows variations of the flame position with α when $Y_\infty = 0.022$; these are sublimit solutions and the movement of the bottom end points of the isola with Y_∞ defines the C-shaped response of Figure 4. Figure 6 shows its variations when $Y_\infty = 0.025$; since it is a superlimit value, there are two solutions as $\alpha \to 0$ (the upper branch is stable). And Figure 7 shows the variations when $Y_\infty = 0.02493$. The classical inflammability limit is defined by the transition between Figures 6 and 7 when the open curve of Figure 6 pinches off at $\alpha = 0$; it is in no way related to the values defined by the lower isola, the origins of Figure 4.

The sequence of events is different for different Lewis numbers. A modest increase in Le (with all the other parameters fixed) to 1.2 eliminates the response of Figure 7 and the classical limit is defined by the transition between Figures 5 and 6, when the open upper curve first appears. And for even larger values of Lewis number (1.52, for example), sublimit solutions and the lower isola do not exist, and only the upper curve of Figure 6 exists for values of Y_∞ in a neighborhood of the classical limit.

References

[1] NASA Conference Publication 10174, Proceedings of the Third International Microgravity Combustion Workshop. Cleveland, Ohio, April 11-13, 1995.
[2] M. D. Cicco, J. Buckmaster. " The role of slip in the generation of acoustic instabilities in gas turbines". J. of Propulsion and Power, 12, 34-40, 1996.
[3] J. Buckmaster, T. Jackson. "The effects of radiation on the thermal-diffusive stability boundaries of premixed flames". Combustion Science and Technology, 103, 299-313, 1995.
[4] J. Buckmaster, A. Agarwal. "Unsteady spherical flames in dusty gases". Combustion Science and Technology, 103, 191-206, 1995.
[5] D. Lozinski, J. Buckmaster. "Quenching of reverse smolder". Combustion and Flame, 102, 87-100, 1995.
[6] J. Buckmaster, D. Lozinski. "Some topics in reverse smolder," article in Modeling in Combustion Science, LNP 449, Springer-Verlag, pp. 308-314, 1995.
[7] J. Buckmaster, D. Lozinski. "An elementary discussion of foward smoldering". Combustion and Flame 104, 300-310, 1996.
[8] J. Buckmaster. "A theory of shallow smolder waves". IMA Journal of Applied Mathematics, 56, 87-102, 1996.
[9] I. Fisher, J. Buckmaster, D. Lozinski, M. Matalon. "Vapor diffusiom flames, their stability, and annular pool fires", article in Modeling in Combustion Science, LNP 449, Springer-Verlag, pp. 249-257, 1995.
[10] J. Buckmaster, G. Joulin, P. Ronney. "The structure and stability of nonadiabatic flame-balls". Combustion and Flame, 79, 381-392, 1990.
[11] J. Buckmaster, G. Joulin, P. Ronney. "The structure and stability of nonadiabatic flame-balls, II. Effects of far-field losses". Combustion and Flame, 84, 411-422, 1991.
[12] J. Buckmaster. "Radiation losses in hydrogen-air flame-balls," presented at the Technical Meeting of the Central States Section of the Combustion Institute, May 5-7, 1996, pp. 316-321 (no ISBN number).
[13] J. Buckmaster. "Edge-flames and their stability," Combustion Science and Technology. 115, 41-68, 1996.
[14] J. Buckmaster, R. Weber. "Edge-flame holding," 26th Symposium, in press.
[15] J. Buckmaster. "Edge-flames," J. of Engineering Mathematics, in press.
[16] J. Buckmaster, G.S.S. Ludford. Lectures on Mathematical Combustion. SIAM Press, Philadelphia, 1983.
[17],[18] T. G. Vedarajan, J. Buckmaster. "Premixed Flames with edges - failure waves and ignition waves," Central States Sectional Meeting, April 1997, Western States Sectional Meeting, April 1997.
[19] C. K. Law, F.N. Egolfopoulos. "A kinetic criterion of flammability limits: the C-H-O-inert system," 23rd Symposium on Combustion, pp.413-421, 1991.
[20] K. Marata, M. Yoshida, Y. Ju, T. Niioka. 26th Symposium, to appear.
[21] J. Buckmaster. "The effects of radiation on stretched flames," Combustion Theory and Modeling, 1, 1-11, 1997.
[22] C.J. Song, C.K. Law. 26th Symposium, to appear.
[23] H. Guo, Y. Ju, K. Maruta, T. Niioka. Combustion and Flame, to appear.
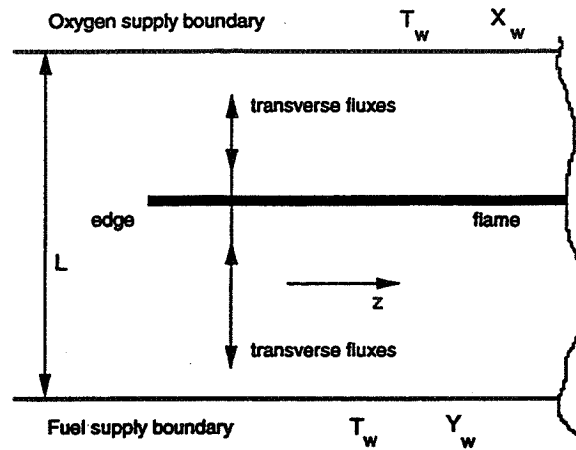
Fig.1. A cartoon showing the physical ingredients of edge-flames. z is equivalent to s (Eq. 1), and y is measured vertically.
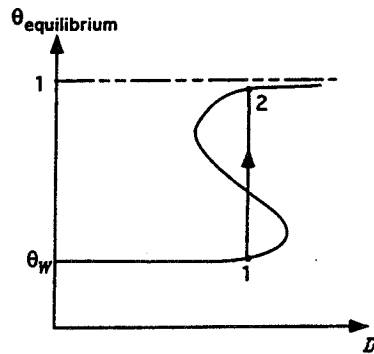
Fig.2. Equilibrium, $f \equiv 0$.
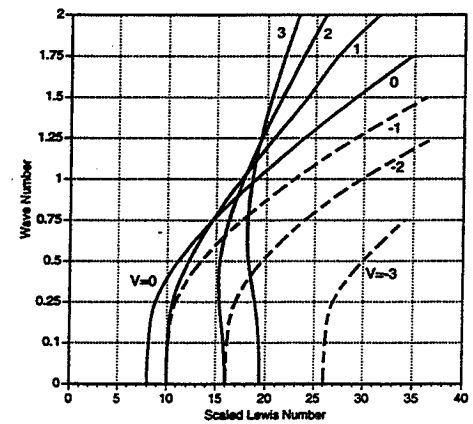
Fig.3. Stability boundary for an edge-flame, $Le_Y > 1$. A scaled Lewis number of 8 corresponds to a Lewis number of roughly 1.5, and there is instability to the right of these boundaries, each of which corresponds to a different edge speed V.
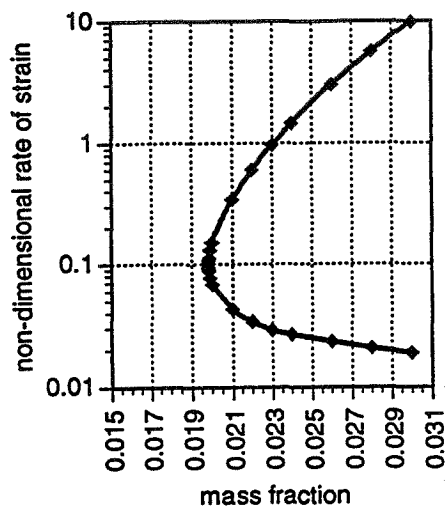
Fig.4. Quenching boundary. Flames only exist within the C.
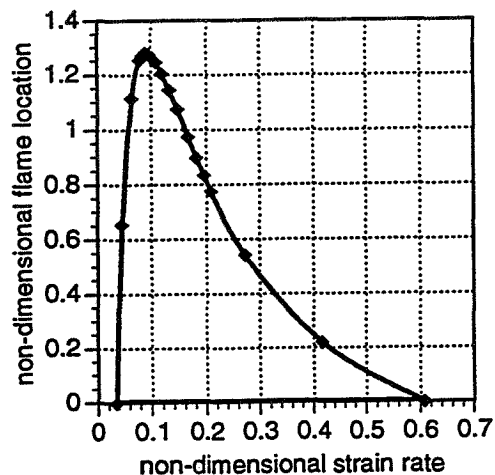
Fig.5. Flame response when $Y_\infty = 0.022$.
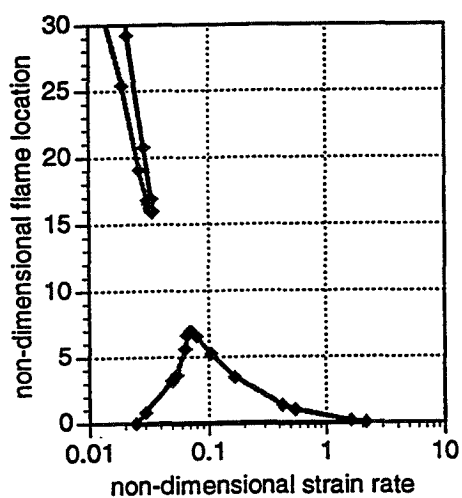
Fig.6. Flame response when $Y_\infty = 0.025$.
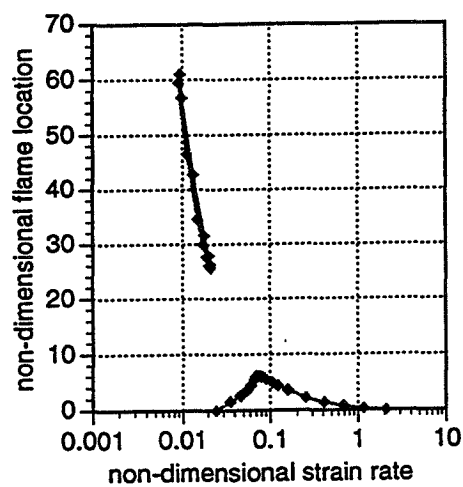
Fig.7. Flame response when $Y_\infty = 0.02493$.

Page intentionally left blank

COMPUTATIONAL MODELING OF THE STRUCTURE AND EXTINCTION OF FLAME BALLS IN A MICROGRAVITY ENVIRONMENT

M. D. Smooke
Department of Mechanical Engineering
Yale University
New Haven, CT

Introduction

Combustion models that simulate pollutant formation and study chemically controlled extinction limits in flames often combine detailed chemical kinetics with complicated transport phenomena. One of the simplest models in which these processes are studied is the plane premixed laminar flame. This problem is appealing due to its simple flow geometry and it has been used by kineticists in understanding elementary reaction mechanisms in the oxidation of fuels. Although premixed flames have been studied extensively (experimentally and numerically) in a normal Earth based gravity environment, there is relatively little experimental and virtually no numerical investigations of these systems in a microgravity environment. To this end, we have begun a program designed to study computationally the effects of radiation losses on spherically symmetric premixed hydrogen-air flames in a microgravity environment in which there are no convective flows (see also, [1-2]). We are considering a detailed transport and finite rate multistep kinetics model. To be able to compute soltuions (both stable and unstable) in the neighborhood of the lean and rich extinction limits, we must modify the basic solution algorithm to include an arclength continuation procedure. In this way a parameter such as the equivalence ratio can be varied while still having a computationally stable algorithm.

Problem Formulation

Our goal is to predict theoretically the mass fractions of the species and the temperature as functions of the independent coordinate r.

The equations governing the structure of a steady, spherically symmetric, isobaric flame-ball are

$$-\frac{1}{r^2}\frac{d}{dr}(r^2\rho Y_k V_k) + \dot{\omega}_k W_k = 0, \qquad k = 1, 2, \ldots, K, \tag{1}$$

$$\frac{1}{r^2}\frac{d}{dr}\left(r^2\lambda\frac{dT}{dr}\right) - \sum_{k=1}^{K}\rho Y_k V_k c_{p_k}\frac{dT}{dr} - \sum_{k=1}^{K}\dot{\omega}_k h_k W_k - \frac{1}{r^2}\frac{d}{dr}(r^2 q_R) = 0, \tag{2}$$

$$\rho = \frac{p\overline{W}}{RT}. \tag{3}$$

In these equations r denotes the independent spatial coordinate; T, the temperature; Y_k, the mass fraction of the kth species; p, the pressure; ρ, the mass density; W_k, the molecular weight of the kth species; $\overline{W}$, the mean molecular weight of the mixture; R, the universal gas constant; λ, the thermal conductivity of the mixture; c_p, the constant pressure heat capacity of the mixture; c_{pk}, the constant pressure heat capacity of the kth species; $\dot{\omega}_k$, the molar rate of production of the kth species per unit volume; h_k, the specific enthalpy of the kth species; q_R the radiative heat flux and V_k, the diffusion velocity of the kth species.

Utilizing the kinetic theory of dilute gas mixtures, we can write the following expression for the species diffusion velocities

$$V_k = -\sum_{l=1}^{K} D_{kl} \nabla X_l - \theta_k \nabla \log(T), \qquad (4)$$

where D_{kl}, $1 \le k, l \le K$, are the species diffusion coefficients and θ_k, $1 \le k \le K$, are the thermal diffusion coefficients. The species diffusion coefficients are symmetric and satisfy the important relations

$$\sum_{k=1}^{K} Y_k D_{kl} = 0, \ 1 \le l \le K, \qquad \sum_{k=1}^{K} Y_k \theta_k = 0, \qquad (5)$$

which guarantee the mass conservation constraint

$$\sum_{k=1}^{K} Y_k V_k = 0. \qquad (6)$$

Using the recent theory of iterative transport algorithms [3], rigorous kinetic theory expressions can be derived for all of the transport coefficients. In particular, the thermal conductivity, the diffusion coefficients and the thermal diffusion coefficients are obtained by solving constrained singular linear systems. These approximate expressions are accurate and computationally much more cost-effective than a direct numerical inversion of the associated linear systems. Moreover, the approximate species diffusion coefficients and thermal diffusion coefficients automatically satisfy the mass conservation constraint (6).

Since radiation plays a key role in defining the structure and stability of flame-balls, it is necessary to construct a careful estimate of the radiation term q_R. We assume that for hydrogen-air mixtures the only significant radiating species is H_2O (For methane-air systems additional terms from CO and CO_2 will be included). By utilizing an optically thin limit in which self absorption of radiation is neglected, the divergence of the net radiative flux is given by

$$\frac{1}{r^2} \frac{d}{dr}(r^2 q_R) = 4\pi \sum_i \alpha_i B_i(T) \qquad (7)$$

where $B_i(T)$ is the Planck function evaluated at the band centers of the contributing vibration-rotation or pure rotational bands whose integrated intensities are given by α_i [4,5].

362

To complete the specificiation of the problem, boundary conditions are needed at both ends of the computational domain. The boundary conditions in the fresh mixture are given by

$$T(\infty) = T_f, \quad Y_k(\infty) = Y_{k_f}, \quad k = 1, 2, \ldots, K. \tag{8}$$

Symmetry conditions at the origin are given by

$$\frac{dT}{dr}(0) = 0, \quad \frac{dY_k}{dr}(0) = 0, \quad k = 1, 2, \ldots, K. \tag{9}$$

Finally, we point out that the chemical production rates and transport coefficients are evaluated with optimized and highly efficient libraries [3,6].

Method of Solution

The equations in (1-4,7-9) form a nonlinear two-point boundary value problem. The solution method for a single solution has been discussed in detail elsewhere and we outline only the essential features here [7,8]. Our goal is to obtain a discrete solution of the governing equations on the finite difference mesh $\mathcal{M}$. By replacing the continuous differential operators by finite difference expressions, the problem of finding an analytic solution of the governing equations is converted into one of finding an approximation to this solution at each point of the mesh $\mathcal{M}$. We seek the solution U^* of the nonlinear system of difference equations

$$F(U) = 0. \tag{10}$$

Assuming we can obtain an initial solution estimate U^0 that is sufficiently "close" to U^*, the system of equations in (10) can be solved by Newton's method. We write

$$J(U^k)\left(U^{k+1} - U^k\right) = -\lambda_k F(U^k), \quad k = 0, 1, \ldots, \tag{11}$$

where U^k denotes the kth solution iterate, λ_k the kth damping parameter $(0 < \lambda \leq 1)$ and $J(U^k) = \partial F(U^k)/\partial U$ the Jacobian matrix. A system of linear block tridiagonal equations must be solved at each iteration for corrections to the previous solution vector. As we found in the solution of burner-stabilized and freely propagating premixed laminar flames, the cost of forming (we use a numerical Jacobian) and factoring the Jacobian matrix can be a significant part of the cost of the total calculation. In such problems we apply a modified Newton method in which the Jacobian is re-evaluated periodically.

The solution of combustion problems, such as the flame-ball system, requires that the computational mesh be determined adaptively. We equidistribute the mesh $\mathcal{M}$ on the interval $[0, \infty]$ with respect to the non-negative function W and the constant C. Specifically, we form the mesh by employing a weight function that equidistributes the difference in the components of the discrete solution and its gradient between adjacent mesh points.

In addition to the generation of a single solution for these systems, we have studied the dependence of these flames (the flammability limits) on the equivalence ratio ϕ. While the solution method discussed above can be utilized to generate a single solution, it is not effective for the computation of solutions as one approaches turning points of the

system. To be able to study flames in the neighborhood of extinction, we must apply a phase-space, pseudo-arclength continuation method with Newton-like iterations and global adaptive gridding [9-11]. The set of governing equations for the flame-ball configuration reduces to a system of the form

$$\mathcal{F}(\mathcal{X}, \phi) = 0, \tag{12}$$

where $\mathcal{X} = (T, Y_1, \ldots, Y_K)$ is the solution vector. The solutions $(\mathcal{X}, \phi)$ in (12) form a one-dimensional manifold which, as a result of the presence of turning points, cannot be parameterized in the form $(\mathcal{X}(\phi), \phi)$. The upper part of the manifold denotes the stable solutions and the lower part the unstable ones assuming there are no Hopf bifurcations.

To generate this solution set, $(\mathcal{X}, \phi)$ is reparameterized into $(\mathcal{X}(s), \phi(s))$ where s is a new independent parameter and ϕ becomes an eigenvalue. The system in (12) can now be written

$$\mathcal{F}(\mathcal{X}(s), \phi(s)) = 0, \tag{13}$$

and the dependence of s on the augmented solution vector $(\mathcal{X}, \phi)$ is specified by an extra scalar equation

$$\mathcal{N}(\mathcal{X}(s), \phi(s), s) = 0, \tag{14}$$

which is chosen such that s approximates the arclength of the solution branch in a given phase space. Rather than solving the coupled system in (13) and (14), we replace ϕ by a function ϕ of z and we let the unknown $\mathcal{Z} = (\mathcal{X}^T, \phi)^T$ be the solution of a three-point limit value problem

$$\mathcal{H}(\mathcal{Z}, s) = \begin{bmatrix} \mathcal{F}(\mathcal{X}, \phi) \\ \dfrac{d\phi}{dz} \\ \mathcal{N}(\mathcal{X}(\hat{z}), \phi(\hat{z}), s) \end{bmatrix} = 0, \tag{15}$$

where $\hat{z}$ is a given point in $[0, \infty]$. The system in (15) is solved by combining a first-order Euler predictor and a corrector step involving Newton-like iterations and adaptive gridding.

Numerical Results

During the first three years of the project our goals have included verifying the sensitivity of the flame ball radius and the value of the lean and rich flammability limits to 1) the hydrogen-air chemistry, 2) the transport model, 3) the radiation approximation, 4) the length of the computational domain and 5) the far field radiation losses. Utilizing a modified hydrogen-air reaction mechanism [12] with the transport model employed in [3], we continued our studies from last year in which flame balls were computed as a function of the equivalence ratio ϕ [13]. Specifically, we examined the effect of far field radiative losses due to water vapor. By including various percentages (mole fraction) of water vapor in the far field mixture, we have been able to predict modest changes in the lean flammability limit of the flame balls. Work in this area is continuing in collaboration with John Buckmaster. Future work will examine the structure of hydrogen-carbon monoxide flame balls and the effects of a radiation model in which self absorption is included.

References

1. Lewis, B. and von Elbe, G., *Combustion, Flames and Explosions of Gases*, Academic, New York, (1961).

2. Ronney, P., *Comb. and Flame*, **82**, (1990).

3. Ern, A. and Giovangigli, V., *Multicomponent Transport Algorithms*. New Series Monographs, Volume m 24 of Lecture Notes in Physics, Springer-Verlag, Heidelberg, (1994).

4. Hall, R. J., *J. Quant. Spec. Rad. Tran.*, **49**, (1993).

5. Hall, R. J., *J. Quant. Spec. Rad. Tran.*, **51**, (1994).

6. Giovangigli, V., and Darabiha, N.: Vector Computers and Complex Chemistry Combustion, in Proceedings of the Conference on Mathematical Modeling in Combustion, Lyon, France, NATO ASI Series, (1987).

7. Smooke, M. D., *J. Comp. Phys.*, **48**, (1982).

8. Smooke, M. D., Miller, J. A. and Kee, R. J.,"Solution of Premixed and Counterflow Diffusion Flame Problems by Adaptive Boundary Value Methods," in Numerical Boundary Value ODEs, U. M. Ascher and R. D. Russell, Eds., Birkhauser, Basel, (1985).

9. Keller, H. B.: Numerical Solution of Bifurcation and Nonlinear Eigenvalue Problems, in Applications of Bifurcation Theory, P. Rabinowitz, Ed., Academic Press, New York, (1977).

10. Giovangigli, V. and Smooke, M. D.: *Comb. Sci. and Tech.*, **53**, (1987).

11. Giovangigli, V. and Smooke, M. D.: *Applied Numerical Mathematics*, **5**, (1989).

12. Trees, D., Brown, T. M., Seshadri, K., Smooke, M. D., Balakrishnan, G., Pitz, R. W., Giovangigli, V. and Nandula, S. P., "The Structure of Nonpremixed Hydrogen-Air Flames," to be published *Comb. Sci. and Tech.*, (1995).

13. Buckmaster, J., Smooke, M. D. and Giovangigli, V., *Comb. and Flame*, **94**, (1993).

Page intentionally left blank

Flammability, Smoldering, Ignition, and Flame Spread

Page intentionally left blank

SMOLDERING COMBUSTION EXPERIMENTS IN MICROGRAVITY[*]

David C. Walther and A. CARLOS FERNANDEZ-PELLO
University of California, Berkeley
Berkeley, California

and

David L. Urban
NASA Lewis Research Center
Cleveland, Ohio

ABSTRACT

The Microgravity Smoldering Combustion (MSC) experiment is part of a study of the smolder characteristics of porous combustible materials in a microgravity environment. Smoldering is a non-flaming form of combustion that takes place in the interior of porous materials and takes place in a number of processes ranging from smoldering of porous insulation materials to high temperature synthesis of metals. The objective of the study is to provide a better understanding of the controlling mechanisms of smolder, both in microgravity and normal-gravity. As with many forms of combustion, gravity affects the availability of oxidizer and transport of heat, and therefore the rate of combustion.

Microgravity smolder experiments, in both a quiescent oxidizing environment, and in a forced oxidizing flow have been conducted aboard the NASA Space Shuttle (STS-69 and STS-77 missions) to determine the effect of the ambient oxygen concentration and oxidizer forced flow velocity on smolder combustion in microgravity. The experimental apparatus is contained within the NASA Get Away Special Canister (GAS-CAN) Payload. These two sets of experiments investigate the propagation of smolder along the polyurethane foam sample under both diffusion driven and forced flow driven smoldering.

The results of the microgravity experiments are compared with identical ones carried out in normal gravity, and are used to verify present theories of smolder combustion. The results of this study will provide new insights into the smoldering combustion process. Thermocouple histories show that the microgravity smolder reaction temperatures (T_s) and propagation velocities (U_s) lie between those of identical normal-gravity upward and downward tests. These observations indicate the effect of buoyancy on the transport of oxidizer to the reaction front.

INTRODUCTION

Smoldering is a basic combustion problem that encompasses a number of fundamental processes, including: heat and mass transfer in a porous media, endothermic pyrolysis of the combustible, ignition, propagation and extinction of heterogeneous exothermic reactions at the solid/gas pore interface, and the onset of gas phase reactions (flaming) from the existing surface reactions [1,2]. Smoldering presents a serious fire risk because the reaction can propagate slowly in the material interior and go undetected for long periods of time. It typically yields a substantially higher conversion of fuel to toxic compounds than does flaming (though more slowly), and may undergo a sudden transition to flaming [3-5]. Smolder of cable insulation, another common fire hazard, is of particular concern in the space program; to date there have been a few minor incidents of overheated and charred cables and electrical components reported on Space Shuttle flights [6,7]. Recently, the planned establishment of the International Space Station and other space facilities has increased interest in the study of smoldering in microgravity because of the need to preempt the possibility, and/or to minimize the effect of a smolder initiated fire during the operation of these facilities [8,9].

Smoldering is defined as a non-flaming, self-sustaining, propagating, exothermic, surface reaction, deriving its principal heat from heterogeneous oxidation of the fuel (*i.e.* direct attack of oxygen on the surface of a solid-phase fuel) [1,2]. If the material is sufficiently permeable, smoldering is not confined to its outer surface and can propagate as a reaction wave through the interior of the material. Smoldering may occur in a variety of processes ranging from smolder of porous insulating materials [10-12] to underground coal combustion [13]. Many materials can sustain smoldering, from wood to charcoal. There are two distinct classifications for the one-dimensional propagation of a smolder reaction: opposed and forward [14]. These are defined

according to the direction in which the fuel and oxidizer enter the reaction zone. In opposed (or reverse) smolder, the configuration examined here, the reaction front propagates in a direction opposite to the oxidizer flow. This configuration is also referred to as co-current, or premixed-flame-like smolder, because with the coordinate system anchored at the reaction zone, fuel and oxidizer enter the reaction zone from the same direction, albeit with different velocities. In opposed smolder propagation, the heat released by the heterogeneous oxidation (smolder) reaction is transferred ahead of the reaction by conduction and radiation, heating the unreacted fuel and the incoming oxidizer. The resulting increase of the virgin fuel temperature leads to the onset of the smolder reaction, and consequently gives way to its propagation through the fuel. The combustion process is generally oxygen deficient, and the propagating reaction leaves behind a char that contains a significant amount of unburned fuel. The rate of smolder propagation is basically dictated by a balance between the rate of heat released by the reaction and the energy required to heat the solid fuel and gaseous oxidizer to the smolder reaction temperature. Increasing the oxidizer flow rate increases the rates of fuel oxidation and heat release, and consequently the rate of smolder propagation, until it reaches a point at which the rate of heat losses to the incoming oxidizer overwhelm the heat released by the reaction and extinction occurs [15]. In the presence of gravity, buoyancy interferes with both forced convection and diffusion, and consequently with the transport processes controlling smoldering. In the absence of gravity, the transport processes lead to a secondary classification of smoldering into forced convection driven and diffusion driven smolder. In reality, with multidimensional geometries, smolder propagation is always a combination of opposed and forward modes with one mode usually dominating. The propagation of the smolder reaction is, therefore, a complexly coupled phenomenon involving processes related to the transport of heat and mass in a porous media, together with surface pyrolysis and combustion reactions [1,2].

The MSC experiments are aimed at providing a better fundamental understanding of the controlling mechanisms of smoldering. This in turn will aid the prevention and control of smolder-originated fires, both in normal-gravity and in a space-based environment. The project objectives are the understanding and prediction of smoldering combustion under normal- and microgravity conditions; accomplished by conducting smolder experiments on the ground and in a space-based laboratory, and developing theoretical models of the process. Space-based experiments are necessary because smoldering is a very slow process and consequently its study in a microgravity environment requires extended periods of time that can only be achieved in space.

HARDWARE DESCRIPTION

MSC is conducted in a 20 liter, hermetically sealed, aluminum combustion chamber that incorporates into the NASA GAS-CAN assembly, Figure 1. An unretarded polyurethane foam cylinder 120 mm diameter by 140 mm long (void fraction 97.5%) is housed within a quartz cylinder assembly that permits video imaging of the smolder process while maintaining a one-dimensional forced flow. The igniter (an electrically heated wire, sandwiched between two porous ceramic discs) is placed in contact with the one end of the foam cylinder. A vessel housing a char sample (120 mm by 52 mm long) is placed at the other side of the igniter for insulation purposes. For forced flow smolder tests, a cap with the oxidizer flow inlet is fitted at the end of the quartz cylinder opposite the igniter, such that the oxidizer flows oppose the direction of smolder propagation. The oxidizer supply system provides a constant mass flow through the sample via a regulated upstream pressure and choked flow orifice. The sample is instrumented with an array of 10 thermocouples which provide an axial as well as radial temperature history of the propagation. The temperature data are later used to determine the rate of smolder propagation and the characteristics of the reaction.

The overall MSC flight assembly consists of two shelves; one that holds the two combustion chambers and one which contains the experimental electronics. The electronics shelf contains an 800 W.hr. capacity silver-zinc battery, a power control unit (PCU), an ignition power unit (IPU), a data acquisition and control assembly (DACS), two video camera controllers, and two 8 mm video tape recorders. The components of the electronic

The MSC Sample Holder (bottom right) is contained within the 21.7 liter combustion chamber. This chamber is incorporated into the GAS canister apparatus (right).

Igniter
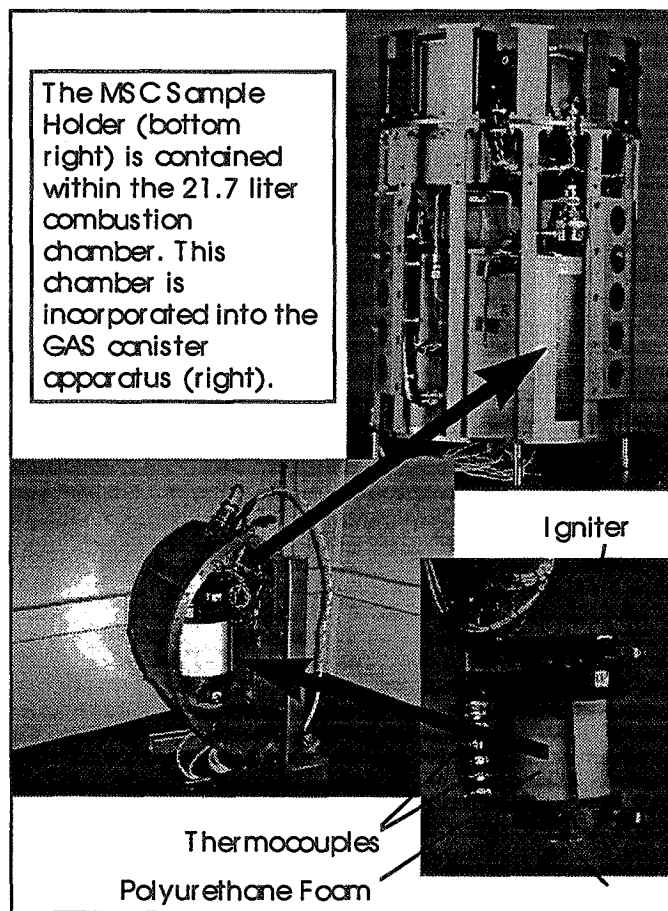
Thermocouples

Polyurethane Foam

Figure 1. MSC Test Apparatus

shelf provide the power and control the data recording for the experiment. The two shelves are tied together by support stingers. The entire apparatus integrates into the Get Away Special Canister (GAS-CAN) which is flown in the Shuttle cargo bay.

EXPERIMENTAL MATRIX

Two sets of experiments have been conducted in the Space Shuttle (missions STS-69 and STS-77). The experiments investigate the propagation of smolder along the polyurethane foam sample under both diffusion driven and forced flow driven smoldering. The conditions for the first set (STS-69) of experiments are; 1A) quiescent 35% O_2 / 65% N_2 environment, and 1B) forced opposed air flow of 1 mm/sec. velocity. The conditions for the second set (STS-77) of experiments are; 2A) quiescent 40% O_2 / 60% N_2 environment, and 2B) forced opposed air flow of 2 mm/sec. velocity. Polyurethane foam was selected as fuel because it is representative of materials commonly used on both earth and space based facilities and it maintains its structural integrity upon smoldering. The environmental conditions are part of a matrix of planned experiments that represent a non-convective environment of oxygen concentration above that of air, and a convective environment with velocities similar to those that can be expected from ventilation systems in space facilities.

RESULTS

The microgravity smolder experiment results are presented in Table I. Normal-gravity tests conducted in the same combustion chamber as the MSC tests with identical igniter power profiles are also presented for comparison. These experiments show that forced flow smolder combustion in the absence of gravity is weaker than in normal-gravity downward smolder and more vigorous than upward smolder. The microgravity quiescent environment tests do not propagate beyond the influence of the igniter, in contrast to normal-gravity smolder tests where propagation throughout the entire sample was observed. This illustrates the effect of reduced oxidizer supply to the reaction zone. The flows induced by buoyancy in normal-gravity enhance oxidizer supply to the reaction zone in downward smolder, while, in upward smolder the buoyant flow and the downward forced flow (1 and 2 mm/sec) are in opposition and partially cancel one another. This results in a reduced oxidizer supply, thereby weakening the reaction. The coupled effect of reduced oxygen supply and heat losses may also affect the relative concentrations of the combustion products. Post combustion gas analysis will give further information in this regard as well as provide answers about the effect of gravity on combustion product toxicity. The results from the MSC experiments can also be used for the verification of models, both numerical and analytical, that incorporate the effect of gravity on smoldering combustion.

Table I. MSC Experimental Results Summary.

Mission Flight	Flow Conditions	Orientation	O_2 Concentration (%)	Ignition of Self-Sustaining Smolder	Smolder Velocity (mm/s)	Smolder Temperature (°C)
STS-69	Forced, 1 mm/sec.	0-g	21	Yes	0.10	385
Sim.	Forced, 1 mm/sec.	1-g, Downward	21	Yes	0.12	395
Sim.	Forced, 1 mm/sec.	1-g, Upward	21	No	-	-
STS-77	Forced, 2 mm/sec.	0-g	21	Yes	0.16	410
Sim.	Forced, 2 mm/sec.	1-g, Downward	21	Yes	0.18	420*
Sim.	Forced, 2 mm/sec.	1-g, Upward	21	Yes	0.11	390
STS-69	Quiescent	0-g	35	No	-	-
Sim.	Quiescent	1-g, Downward	35	Yes	0.07	380
Sim.	Quiescent	1-g, Upward	35	No	-	-
STS-77	Quiescent	0-g	40	No	-	-
Sim.	Quiescent	1-g Downward	40	Yes	0.10	400
Sim.	Quiescent	1-g Upward	40	Yes	0.04	350

*Noisy Signal Output

Forced Flow Tests

The flow cases showed strong smolder propagation along the entire sample length for both tests. Temperature profiles along the foam centerline for the 1 mm/sec forced air flow case are presented in Figure 2 for the microgravity test and in Figure 3 for the 1-g (downward) simulation. The temperature profiles from the last three thermocouples, not affected by the igniter, are used to calculate the smolder velocity. The microgravity smolder average spread rate lies between the corresponding upward and downward normal-gravity smolder. This to be expected since, at these flow conditions, smolder propagation is strongly dependent on the availability of oxygen, and in normal-gravity, upward propagation, the buoyant flow opposes (and partially

cancels) the forced flow; while in the downward case, the buoyant flow adds to the forced flow. In the case of the low air flow velocity (1 mm/sec) the smolder velocity in microgravity is approximately 20% lower than the corresponding normal-gravity downward smolder velocity (0.10 mm/sec vs. 0.12 mm/sec). In an upward propagation test, the smolder front actually extinguished as a result of the opposition of the forced flow and the buoyant flow. In the case of 2 mm/sec forced flow, the smolder propagation velocity in microgravity is approximately 12% smaller than in normal-gravity, downward smolder (0.16 mm/sec vs. 0.18 mm/sec) and 31% larger than normal-gravity, upward smolder and (0.16 mm/sec vs. 0.11 mm/sec). The reaction front smolder temperature in microgravity is seen to also fall between those encountered in normal-gravity upward and downward tests. The difference between the normal- and microgravity reaction temperatures is on the order of 10 $^\circ$C.

In normal-gravity, transient smolder propagation (acceleration) at the end of the sample is often observed. This effect, however, is not observed in microgravity. This verifies that transient smolder is due to increased buoyancy effects as the smolder front approaches the sample end due to reduction in pressure losses through the foam. Also, the characteristics of the secondary, forward propagating, char reactions that occur once the opposed smolder front has reached the sample end differ in normal- and microgravity due to the effect of buoyancy on the forced air flow.
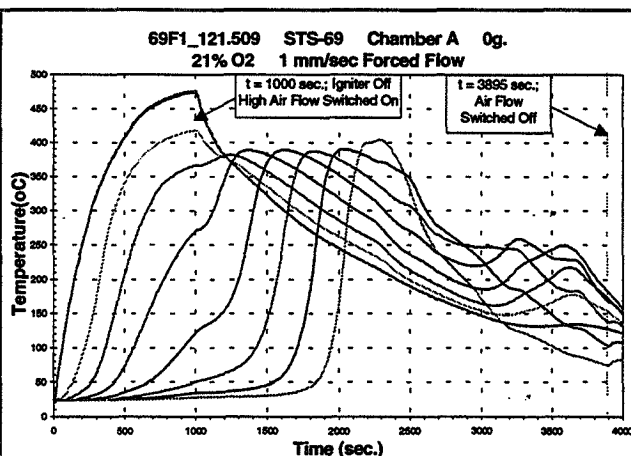
Figure 2. Temperature History STS-69;
0-g, 1mm/sec Forced Air.
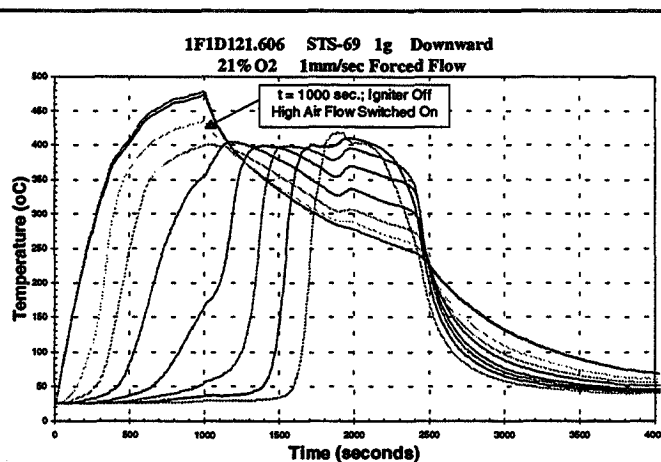
Figure 3. Temperature History STS-69 Simulation;
1-g Downward, 1mm/sec Forced Air.
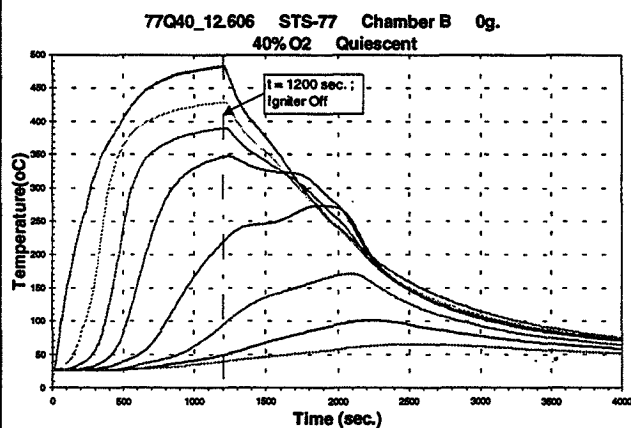
Figure 4. Temperature History STS-77;
0-g, 40% O_2 Quiescent.
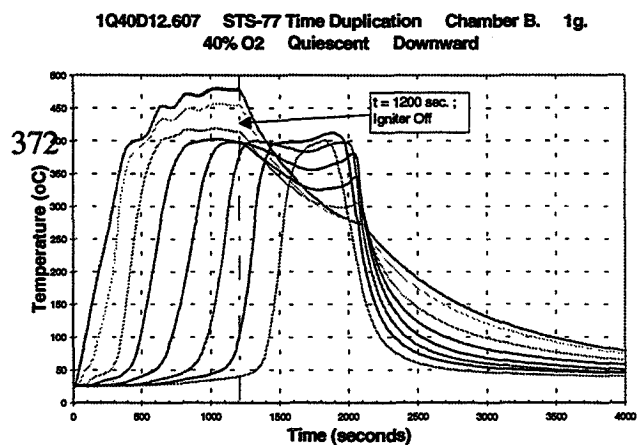
Figure 5. Temperature History STS-77 Simulation;
1-g Downward, 40% O_2 Quiescent.

Quiescent Tests

In these tests, the oxygen concentration is the variable experimental parameter. Temperature profiles along the foam centerline for the 40% O_2 case are presented in Figure 4 for the microgravity test and in Figure 5 for the 1-g (downward) simulation. It was found that while neither of the quiescent microgravity cases propagated, both of the normal-gravity, downward cases (35 and 40%) and only the 40% O_2 normal-gravity, upward case propagated. In 35% O_2 environments, the normal-gravity,

downward configuration was the only test condition to establish a self-sustaining smolder. In 40% O_2 environments, the smolder propagation velocity in normal-gravity, downward smolder was 60% larger than normal-gravity upward smolder (0.10 mm/sec vs. 0.04 mm/sec). These results indicate the influence of increased oxygen supply due to buoyancy to the smolder reaction.

In the 35% O_2 test case, noise in the temperature readings apparently due to condensation of combustion products on the thermocouple compensation electronics caused the computer to shut down the igniter prematurely at 650 seconds (compared to an expected time of 1000 seconds). This malfunction caused concern that lack of a self-propagating smolder may have been caused by the early shut down of the igniter. Despite the more aggressive conditions of the second test (40% O_2, igniter time 1200 seconds), the smolder front did not propagate either. This is a dramatic difference from the normal-gravity smolder, where under these conditions the smolder reaction propagates vigorously along the whole sample length. These results seem to confirm the model predictions of Aldushin, et. al. [16], which conclude that smoldering cannot self-propagate in the absence of gravity. One should be cautious, however, to extend the present results to other geometries (different width and length samples), void fractions and fuels.

MODEL VERIFICATION AND DATA CORRELATION

Present models of forced flow opposed smolder combustion [17,18] are basically pure forced flow analyses, consequently the microgravity data set of this work is, in principle, the only one suited for their verification. A simplified version of the opposed flow smolder model of Dosanjh, et. al. [15] has been used to derive an explicit expression for the smolder propagation velocity and to correlate the MSC microgravity smolder velocity data obtained to date. In the model, smoldering is assumed to be one-dimensional and steady in a frame of reference anchored at the reaction zone. Note that in this frame of reference the fuel and oxidizer enter the reaction in the same direction in opposed smolder (premixed-like reaction). The gas and solid are assumed to be in local thermal equilibrium, and the solid phase is considered continuous with a constant void fraction. Energy transport due to concentration gradients, dissipation by viscosity, work done by body forces, and kinetic-energy of the gas phase are neglected. Since smolder velocities are generally smaller than oxidizer flow velocities, gas velocities are taken as known quantities at each location in the sample. Furthermore, it is assumed that the smolder process occurs under oxygen limited conditions, consequently the heat released is given by the product of the oxidizer mass flux at the reaction zone, and smolder heat of combustion (energy per unit mass of oxidizer), which is assumed constant and known. Radiation is incorporated in the analysis using a diffusion approximation. With these assumptions, and neglecting heat losses to the surrounding environment, the smolder propagation problem is simply described by the following form of the energy equation:

$$\left[\dot{m}_F'' C_{PF} + \dot{m}_A'' C_{PA}\right]\frac{dT}{dx} = \left[\lambda_{eff} + \lambda_{rad}\right]\frac{d^2T}{dx^2} + Q\frac{d\dot{m}_O''}{dx}$$ (Eq. 1)

where the mass fluxes of fuel, air, and oxygen entering the reaction zone are given by:

$$\dot{m}_F'' = (1 - \phi)\rho_F U_S$$ (Eq. 2)

$$\dot{m}_A'' = \rho_A u_g$$ (Eq. 3)

$$\dot{m}_O'' = Y_O \dot{m}_A'' - \phi \rho_A D \frac{\partial Y_O}{\partial x}$$ (Eq. 4)

and λ_{eff} is an effective thermal conductivity of the foam and D is the diffusivity:

$$\lambda_{eff} = \phi \lambda_A + (1 - \phi)\lambda_F$$ (Eq. 5)

The boundary conditions that complete the problem are , at $x = x_s$, $T = T_S$, $\dot{m}_O'' = 0$. $\frac{\partial T}{\partial x} = 0$. At $x \to \infty$, $T = T_i$, $\dot{m}_O'' = \dot{m}_{O,i}''$,

$\frac{\partial T}{\partial x} = 0$. Integrating with respect to x from x_s to ∞, the following expression is obtained for the opposed flow smolder propagation velocity:

$$U_S = \frac{\rho_A\left[QY_{O,i} - C_{PA}(T_S - T_i)\right]}{\rho_F C_{PF}(1 - \phi)(T_S - T_i)} u_g$$ (Eq. 6)

where U_S is the smolder velocity, ρ_A and ρ_F are the densities of the air and foam, C_{PA} and C_{PF} are the specific heats of the air and foam, ϕ is the porosity, Q is the smolder heat of combustion, Y_O is the inlet oxygen mass fraction, u_g is the inlet gas (Darcy) velocity, and T_S and T_i are the smolder and inlet air temperatures. The experimentally measured smolder reaction temperature is used in Eq. (6) to correlate the experimental data. The smolder heat of combustion is not well determined for smolder combustion [2] and depends strongly on the thermo-chemistry of the smolder process. In this work, the optimization of the data
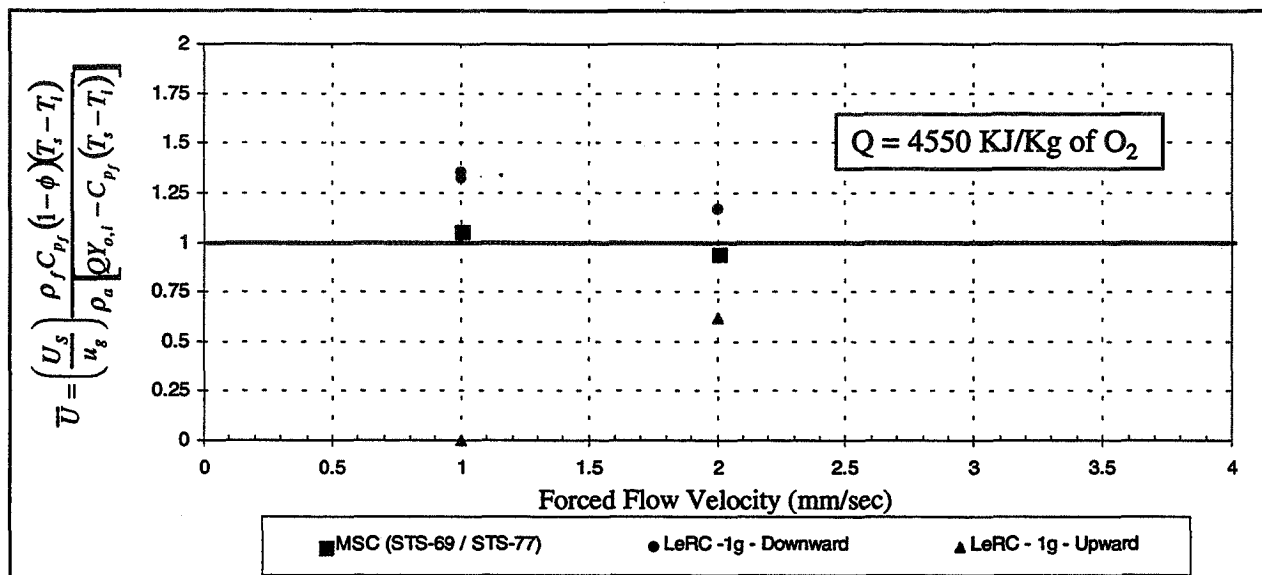
The chart contains the y-axis label:

$$\bar{U} = \left(\dfrac{U_s}{u_g}\right) \dfrac{\rho_f C_{p_f}(1-\phi)(T_s-T_i)}{\rho_a [QY_{o,l} - C_{p_f}(T_s-T_i)]}$$

Q = 4550 KJ/Kg of O$_2$

x-axis: Forced Flow Velocity (mm/sec)

Legend: ■ MSC (STS-69 / STS-77)   ● LeRC -1g - Downward   ▲ LeRC - 1g - Upward

Figure 6. MSC Data Correlation.

correlation is actually used to empirically deduce its value (4,550 kJ/kg of O$_2$). Also, the oxidizer flow velocity is known if there is only a pure forced flow of oxidizer (no buoyancy). The results are presented in Figure 6, together with the normal-gravity results for the two flow conditions tested. Based on the two data points presently available, the model of Dosanjh, et. al [29] correlates well the experimental data. Noteworthy in the correlation is the effect of gravity on the smolder process.

CONCLUSIONS

Gravity induces a buoyant flow that enhances oxidizer flow to the reaction front in downward forced-flow opposed smolder and creates a mixed flow situation that deters oxidizer flow to the reaction front in an upward configuration. The effect of this buoyant flow can be seen upon examination of the smolder velocities and reaction temperatures from the MSC experiment in microgravity and in normal-gravity upward and downward smolder. These experiments demonstrate the difficulty of decoupling the effects on smolder propagation of oxidizer flow to and heat losses from the reaction front and the errors that may arise in trying to quantify these buoyant flows. The MSC data can be used to better determine the characteristics of smolder when free from buoyant effects and therefore provide verification for smolder models.

REFERENCES

1. Williams, F.A., *Combustion Theory*, Second Edition, The Benjamin/Cummings Publishing Company, Inc., 1985.
2. Ohlemiller, T.J., *Prog. Eng. & Comb. Sci*, 11, pp.277-310, 1986.
3. Interagency Committee on Cigarette and Little Cigar Fire Safety, "Toward a Less Fire Prone Cigarette," Report Submitted to United States Congress, October 29, 1987.
4. Ortiz-Molina, M.G., Toong, T.Y., Moussa, N.A., and Tesero, G.C., *Seventeenth Symposium (International) on Combustion*, The Combustion Institute, pp.1191-1200, 1979.
5. Williams, F.A., *Sixteenth Symposium (International) on Combustion*, The Combustion Institute, pp.1191-1200, 1979.
6. Damant, G.H., *J. Textile Institute*, 85, pp.505-525, 1994.
7. Ross, H.D., "Invited Lecture," *National Fire Protection Association Annual Meeting*, May, 1996.
8. Friedman, R., NASA Technical Memorandum 106403, 1994.
9. Palmer, H., "Closing Address," *International Microgravity Workshop*, NASA LeRC, Cleveland, OH, January 25, 1989.

10. Rogers, F.E. and Ohlemiller, T.J., *Comb. Sci. Tech.*, 24, pp.129-137, 1980.
11. McCarter, R.J, *J. of Consumer Prod. Flam.*, 3, pp.128-140, 1976.
12. McCarter, R.J., *J. of Fire and Flammability*, 9, pp.119-126, 1978.
13. Winslow, A.M., *Sixteenth Symposium (International) on Combustion*, The Combustion Institute, pp.503-414, 1976.
14. Ohlemiller, T.J. and Lucca, D.A., *Combustion and Flame*, 54, pp.131-147, 1983.
15. Dosanjh, S. Pagni, P.J. and Fernandez-Pello, A.C., *Combustion and Flame*, 68, pp.131-147, 1987.
16. Aldushin, A.P., Matkowsky, B.J., and Schult, D.A., *Combustion and Flame*, 107, pp.151-175, 1996.
17. Schult, D.A., Matkowsky, B.J., Volpert, V.A., and Fernandez-Pello, A.C., *Combustion and Flame*, 101, pp.471-490, 1995.
18. Lozinski, D. and Buckmaster, J., "Some Topics in Reverse Smolder," *Combustion and Flame* (in press), 1996.

FLAME SPREAD ACROSS LIQUIDS

HOWARD D. ROSS
NASA Lewis Research Center

Fletcher J. Miller
Case Western Reserve University

William A. Sirignano
&
David Schiller
University of California at Irvine

Introduction

The principal goal of our recent research on flame spread across liquid pools is the detailed identification of the mechanisms that control the rate and nature of flame spread when the liquid pool is initially at an isothermal bulk temperature that is below the fuel's flash point temperature. In our project, we specialize the subject to highlight the roles of buoyancy-related processes regarding the mechanisms of flame spread, an area of research cited recently by Linan and Williams [1] as one that needs further attention and which microgravity (μg) experiments could help to resolve. Toward resolving the effects of buoyancy on this flame spread problem, comparisons – between 1g and μg experimental observations, and between model predictions and experimental data at each of these gravitational levels – are extensively utilized. The following describes the present experimental and computational foundation supporting identification of the mechanisms that control flame spread in the pulsating flame spread regime for which long-duration, μg flame spread experiments have been conducted aboard a sounding rocket. See [2] for further details of the experimental hardware.

Results

Normal Gravity Experiments

A series of 1g experiments was recently performed examining low-speed, forced air flow effects on pulsating flame spread [3]. These experiments used top and side-viewing flame imaging systems, liquid-phase Rainbow Schlieren Deflectometry (RSD), two liquid-phase Particle Image Velocimetry (PIV) systems, and Infrared (IR) thermography for surface temperature determination. A 30 cm long x 2 cm wide x 2.5 cm deep fuel tray was located inside a 10 cm x 10 cm cross-sectional area flow duct to provide a laminar, forced-air flow, ranging from 5 cm/s to 30 cm/s in the freestream over the fuel tray. The values of opposed, forced-air flow velocity were selected to be on the same order or less than that which occurs due to buoyancy in 1g experiments of this scale [4]. The experiments were conducted with dry air at 1 atm and the temperature of the butanol fuel was between 20 and 21 C (depending on the test) at the time of ignition; the dry air was utilized to avoid potential complications from water absorption in the fuel prior to the test.

The 1g flame shape near the leading edge is unaffected by the very low, opposed, forced air speeds (<10 cm/s), as it is overwhelmed by the effects of naturally induced buoyant air flow. As the forced air speed is increased, the trailing portion of the flame is pinned closer to the surface; the trailing plume that develops is filled with soot and the plume itself is sporadically blown downstream horizontally, in the opposite direction to the spreading flame, by the forced air flow. The 1g pulsating flame frequency is affected by the forced opposed air flow. Figure 1 shows the pulsation frequency increases as the forced, opposed air flow decreases from 30 cm/s to 5 cm/s.

The thermal gradients in the RSD image indicate that the depth to which the liquid is heated is not affected systematically by the air speed. The near-surface behavior cannot be analyzed because the RSD images were all off-scale in this region. The PIV systems showed vortical motion consistent with the RSD, but showed motion a couple cm ahead of the flame, that was not apparent in the RSD since the flow is not heated sufficiently at that point. Detailed tests of the quiescent case are currently being performed.

In all of the 1g opposed air flow tests, the IR images show that a pair of thermal vortices form on the pool surface 1-2 cm ahead of the flame during the crawling phase of the flame pulsation cycle [5]– see Fig. 2. These indicate sideflow processes which are not apparent from the top view of the flame shape or from the side-view PIV. The IR images also verify the existence of a surface temperature valley [6] if one scans axially along a line at constant distance from the edge of the fuel tray. These are further confirmed by thermocouple measurements along the surface, as shown in fig. 5.

Given the predicted importance of the gas-phase recirculation cell to flame pulsation mechanism [7], it is surprising how little experimental measurement has been done to verify its existence. Initial LDV and PIV experiments were not able to resolve the detailed, near-surface phenomena[4, 8]. Smoke-wire visualization of a recirculation cell was successful in the very slow flame spread across fuel-soaked beds and even across solids [9]; it is not clear that this is the same phenomena as predicted for flame spread across pure liquid fuels. Smoke-wire visualization was applied recently, to this problem and verified, for the first time, more of the details of the recirculation cell, as shown in fig. 3. Quoting from [10]: "The flame is spreading from right to left (against the freestream air), while the smoke is moving off the wire initially from left to right because of the forced air flow. As the smoke and flame close on each other, the smoke front begins to curl downward because, as predicted, the surface flow just ahead of the flame is moving from right to left, and the no-slip condition is fulfilled. The smoke front then begins to move upward and defines the extent of the cell. .... At the time of the smoke release, the flame was nearing the end of the crawl (slow) phase of the cycle when it entered the Field Of View. According to the numerical model, this is the moment when the recirculation cell should be largest, and in fact that is what we saw from this test and many others. However, when the flame entered the FOV during or right after the jump phase of the pulsation cycle, we saw no cell, or a very poorly formed one, which again agrees with the model since it predicts the cell is destroyed during a jump."

Using the apparatus described above, we also performed some 1g tests with concurrent air flow. Few experiments – either in 1g or µg -- with concurrent air flow have been conducted in the pulsating regime , and those have focused primarily on the effects of wind velocities, typically above 1 m/s, on the flame shape and average flame spread rate [11, 12].

As can be seen in figure 8, the flame front is much higher than in the opposed flow case (see [2] for a comparison figure) and even takes on a "C" shape for the highest flow rates. This near-vertical front is due to the forced flow offsetting the induced buoyant flow. The flame position vs. time is shown in fig. 1 for four values of the concurrent flow rate. At very low concurrent air speeds, the pulsation frequency continues to increase (relative to the opposed air flow results) in accordance with increases in the concurrent air speed. The fact that the flame characteristic is still one of pulsation indicates that, despite the concurrent air flow, buoyancy remained the most influential force in the gas-phase flow field (consistent with the flame shape results); its dominance however is progressively reduced as the magnitude of the forced, concurrent air flow increases. At the highest concurrent air speeds (20 - 30 cm/s), the forced air flow dominates over buoyancy, and the flame loses its pulsating spread behavior; instead it gradually, and then rapidly, accelerates across the surface of the pool.

Unlike the opposed flow tests, a liquid-phase thermal vortex with a well-defined center under the flame is seen only at the lowest concurrent air flow speeds. Over most of the range of concurrent air flow speeds, the liquid phase is, instead, without a well-formed thermal vortex. There is movement of the thermal gradients in the liquid phase which accompanies the flame but this movement is erratic in direction and without a well-defined vortex center.

At the lowest speeds in the concurrent air flow tests, the IR images do not show twin thermal vortices but indicate a long preheat length (a maximum of about 3 - 4 cm) with asymmetric curls much closer to the flame during the crawling phase of pulsating spread. The front of the preheat region farthest from the flame is parabolic and symmetric. As the speed of the concurrent air flow increased, there is an absence of the asymmetric curls, the preheat distance increases to several centimeters, and the shape at the front of the preheat zone remains parabolic and symmetric (see Fig. 2).

Microgravity Experiments:

Our earlier work showed that flames do not spread across shallow, alcohol pools in air at 1 atm in microgravity unless a forced air flow is provided in a direction opposing the flame [13]. These early experiments lacked detailed diagnostics and did not elucidate the effects of pool depth where buoyancy might be important. Low-speed air flow, at levels comparable to and below those associated with buoyantly induced air flow, were shown to have a major effect on flammability and flame spread across solid fuels in µg. This motivated an examination of the effects of air flow speed and direction for the case of liquid pools.

At the previous workshop we reported on the results of the first of a set of three µg experiments – with forced opposed air speeds of 5 to 30 cm/s -- in the same heavily instrumented apparatus described above and in [2] – that were conducted in a sounding rocket, rather than a drop tower, because of the µg test time required to fill the tray with fuel, to reach quiescence in the liquid, and for the flame to spread, and finally because of the volume required by the diagnostic instrumentation. The results of the full set are now presented.

In every case, the µg flame appears entirely blue and therefore soot-free (in contrast to the soot-filled flames in 1g). This occurs despite a forced air speed up to 30 cm/s - the same order as naturally induced by buoyancy. A reason for this difference is offered below. The intensity of the µg flame, especially far from the leading edge, is also less than comparable blue portions of the 1g flame. These findings are consistent with lower flame temperatures in µg. In µg, only one large thermal vortical structure appears in the liquid phase, as imaged by RSD, moving steadily with the flame in a manner again analogous to the crawling phase in the 1g pulsation cycle. The RSD also shows heating extends deeper into the fuel depth, and both the IR and RSD show surface preheating farther ahead of the flame in µg.

The experimental results regarding spread and extinction are as follows (fig. 4):

- at 30 cm/s opposed air flow, the flame spreads slowly and near-steadily.
- at 20 cm/s, the same occurs but the flame spreads much more slowly.
- at 10 cm/s, the flame initially spreads slowly, weakens as it spreads, and then flashes in a near-extinction behavior.
- at 5 cm/s, the flame begins to spread, then flashes partially across the pool and extinguishes. (This last test was actually a second burn of the same fuel following the 20 cm/s burn.)

As the forced air flow speed is reduced, the spread rate diminishes and the thermal effects ahead of and beneath the flame are felt farther from the flame front. With further reductions in the forced air speed, the flame weakens to the point that flame spread cannot be sustained. This is consistent with the drop tower observations in both axisymmetric and rectangular trays of smaller dimension for quiescent spread. In distinct contrast, the flame is always sustained in 1g at these forced air speeds and indeed with no forced air flow.

The μg flames also showed a different liquid surface temperature structure comprised of larger, asymmetrical curls ahead of the flame[2]. Nonetheless, the μg test results provide further confirmation of the surface temperature valley and for the need for high spatial and temporal resolution in experiments. As shown in fig. 5, when the leading edge of the visible, μg flame is only 2 mm in front of the thermocouple junction, the surface temperature is 36.2 C (very near the flash point of butanol). When the leading edge of the μg flame is 2 mm past this junction, the temperature is 51.7 C, and continues a sharp rise until the main body of the trailing flame is sufficiently far off the surface to cause the surface temperature to dip briefly. Then as the trailing flame establishes over the surface, the pool surface temperature again rises toward the fuel's boiling point.

In μg, because the flame spread is slow (cf. fig. 4) , liquid motion is observed by the PIV systems much farther ahead of the flame than in 1g, and the velocity under the flame leading edge is faster, being at least 10 mm/s in the 30 cm/s test [5]. It is certainly higher than 10 mm/s, because very near the leading edge, the motion was so fast the particles streaked and were difficult to track. The center of the vortex preceding the flame is deeper in μg, but the overall pattern looks relatively similar [5].

The slow μg flame velocity, observed at all forced air speeds, is an order of magnitude less than that which occurs on Earth in the uniform spread regime [11]. This behavior, supported by the RSD and PIV measurements, suggests the flame spread character is unrelated to classically defined uniform spread. Instead, it is similar in magnitude and character to the slow spread velocity associated with the crawling phase of the pulsation cycle or the pseudo-uniform spread regime.

Definitive tests with concurrent air flow in microgravity have yet to take place. Using a 15 cm long x 2 cm wide x 1 cm deep tray inside a 4 cm square cross section flow duct we have performed a few preliminary tests in the 5.2 sec. Zero-Gravity Facility at NASA Lewis. The concurrent air flow rates tested were 20 cm/s and 30 cm/s with 1-butanol as the fuel at temperatures ranging from 21 to 24 °C. The flame spread readily at in the 30 cm/s cases, with a distinctively different shape than the opposed flow cases. Instead of being flat across the front, it was steeply parabolic as seen from above. From the side, it had a stand-off distance of several mm, in contrast to the near zero stand-off distance in opposed flow. There were no flame pulsations, and the spread rate was higher than the opposed case. In contrast, at 20 cm/s the flame ignited, spread a couple of cm, and then extinguished. In only one case did we witness flame spread at 20 cm/s, and that was at the highest temperature of 24.3 °C in which case it appeared similar to the 30 cm/s case.

Comparison With Models:

The numerical model of [7] predicts that the mean flame spread rate and pulsation frequency increase with opposed air velocity in 1g. This is because the pulsation frequency is predicted to be inversely proportional to the maximum length of the gas-phase recirculation cell (the longer the cell, the more time is required to accumulate a flammable mixture). The opposed flow is predicted to reduce the length of this cell. Unfortunately, this trend appears to be different from the experimental observations for unknown reasons. The model also predicts that the mechanism causing pulsating flame spread is independent of gravity as long as a sufficient, opposed air flow in the freestream occurs (in 1g this is induced by buoyancy, in μg this is provided by the mechanical fan). Thus, the model predicts that pulsating spread can and will occur in μg; however, as noted above, the μg experiments to date show a slow, near-steady spread.

To try to explain this disagreement, dimensional effects were examined [5]. The model is two-dimensional and cannot account for the effects of a finite flame width or the sidewall losses associated with the tray. One consequence of this difference is that hot gas expansion in the model is inherently constrained to the vertical and longitudinal directions. In general, however, hot gas expansion can occur in these directions and in the transverse direction. Hence gas expansion toward the sides – a mechanism available in the experiments but not in the model – could decrease the extent of hot gas expansion ahead of the flame.

This effect has not yet been verified in μg experiments, but successful laser sheet smoke-flow visualization of the lateral hot gas expansion was recently achieved for the first time in 1g experiments [10]. As can be seen in this top view (fig. 6), all but the central streakline are laterally displaced as the flame approaches providing the first clear evidence of lateral hot gas thermal

377

expansion. The central streakline is not laterally displaced, but instead forms the gas-phase recirculation cell shown in figure 3. The other streaklines show that the oncoming air flow is perturbed at least 2 cm ahead of the flame front, and the lateral expansion at the front location is of the order of 5 mm. The maximum streakline displacement occurs where the flame meets the side wall, which is a few mm behind the near-flat flame front due to curvature. After passing the flame front, the flow begins to turn back toward the flame again as it is caught in the buoyantly-driven flow; at some point it is no longer visible, probably because it is carried upward and out of the light sheet. The flow toward the trailing flame serves to raise the reaction rate and elevate the flame temperature to the point that soot is formed. The absence of this side flow phenomenon likely suppresses soot formation in the µg experiments described above, resulting in the all-blue, µg flames even at the relatively high forced air speeds. Because there is no lateral air inflow driven by buoyancy that would tend to cancel the lateral expansion, the effects of hot gas expansion might be more appreciable in these µg experiments (and other µg flame spread studies presently underway). To try to estimate the importance of this mechanism, the model was run with the hot gas expansion artificially set to zero [5]. Figure 7 shows excellent agreement is found between the model and experiment in terms of spread rate and the spread character.

Modeling of concurrent flow effects on flame spread in 1g is in its early stages and is presently restricted to shallow pools of n-propanol [14]. As the concurrent air speed increases from zero, the pulsations become more frequent. This is consistent with the experimental observations. When the air speed reaches 30 cm/s, the predicted spread becomes very erratic, failing to progress on a time-averaged basis very far forward. Instead it appears to oscillate irregularly forward and backward with large amplitude. This is in contrast to the experimental results obtained to date; again the differences in the dimensionality between model and experiment may contribute to the disagreement.

The model's predictions for flame spread behavior with concurrent flow in µg are much better behaved. For these same initial temperatures at µg, the model predicts that, at speeds less than 20 cm/s: (a) consistent with predictions for quiescent air, extinction occurs if only a small amount of vaporization occurs prior to ignition; and (b) flame spread is uniform when the fuel vapor distribution is fully developed prior to ignition.

As discussed above, preliminary tests in the 5.2 sec Zero-Gravity Facility confirm point (b) where uniform spread was found; the limited test time, however, did not enable spread across the entire fuel tray. Longer duration experimental examination for these flow conditions is planned in both narrow and wide trays [5];the latter should mitigate the effects of lateral transport and hot gas expansion. Pulsating spread is not predicted in µg with forced, concurrent air flow because no opposed gas-phase flow exists to form the gas-phase recirculation cell ahead of the flame. This generic characteristic is quite consistent between experiment and model, regardless of gravitational level: pulsating spread occurs only when there is a gas-phase recirculation cell. A recirculation cell exists when there is: (1) surface convection moving with the flame at speeds higher than the flame spread rate and (2) gas-phase convection in the freestream air moving opposite to the flame spread direction.

Conclusions

The above description provides many of the detailed findings from recent experiments and modeling of flame spread across liquid fuel pools. This area of research is gaining renewed interest by groups around the world. Among the more important observations so far, of all of our research to date, are the following, drawn from [15]:

Pulsating spread is affected both by liquid-phase transport (as seen by the requirement for liquid-phase convection preceding the flame and by the pulsation dependence on tray depth) and by gas-phase transport (as seen by the effects of oxygen concentration, diluent type, air-flow direction and speed). A key insight is suggested by the model: the existence of pulsating spread correlates with the existence of a gas-phase recirculation cell. Smoke flow visualization in 1g, forced-flow, pulsating spread experiments has now verified the predicted development and destruction of this gas-phase recirculation cell.

Even with forced, opposed air velocities of the same order of magnitude as that induced naturally by buoyancy in normal gravity, the µg flame behavior is completely different. The preheat length, the depth of the thermal vortex, the surface flow (distance, character, and magnitude) ahead of the flame, the rate of fluid rotation in the vortex, the flammability, the flame intensity, soot formation (none in µg), and the flame spread rate and character are all affected by the magnitude of forced air flow in µg.

Pulsating spread under forced opposed-air flow conditions in µg is predicted, however it remains unobserved experimentally. The difference is presently attributed to the effects of lateral hot gas expansion that can not be directly included in the model nor completely eliminated from the experiments. Recent experiments verify that hot gas expansion affects the approaching flow up to 2 cm ahead of the flame and causes a displacement of streaklines in normal gravity; the effect is speculated to be greater in µg.

Low-speed concurrent air flow, at a magnitude similar to that induced by buoyancy in the opposite direction, affects the existence and nature of pulsating spread in 1g. As the concurrent air speed increases to a magnitude of 30 cm/s, pulsating spread disappears. The model and experiments presently disagree, for unknown reasons, on the flame spread character at this air speed.

The recent application of detailed diagnostics to the problem of flame spread across liquid pools exposed inherent three dimensional effects. Measurement of the liquid surface temperature with an infrared camera revealed twin vortices in 1g, and large, asymmetric swirls in μg [5], and smoke flow visualization in 1g shows strong lateral displacement of the incoming stream [10]. This indicates a need to extend the existing numerical model to three dimensions.

References

[1]   A. Linan and F. A. Williams, *Fundamental Aspects of Combustion*. New York: Oxford University Press, 1993.
[2]   H. D. Ross, F. J. Miller, D. N. Schiller, and W. A. Sirignano, "Flame Spread Across Liquids," presented at 3rd International Microgravity Combustion Workshop, NASA Lewis Research Center, Cleveland, OH, 1995.
[3]   H. D. Ross and F. J. Miller, "Flame Spread Processes Across Liquid Pools With a Low-Speed Opposed or Concurrent Air Flow," presented at Eastern States Section of the Combustion Institute Fall Meeting, Hilton Head, SC, 1996.
[4]   J. S. Newman, "Laser Doppler Velocimeter Measurements of the Gas and Liquid Flow Fields Induced by Flame Propagation over a Liquid Fuel Surface," : MS Thesis, Princeton University, 1979.
[5]   H. D. Ross and F. J. Miller, "Detailed Experiments of Flame Spread Across Deep Butanol Pools," *26th International Symposium on Combustion*, 1996.
[6]   I. Glassman and F. Dryer, "Flame Spreading Across Liquid Fuels," *Fire Safety Journal*, vol. 3, pp. 123-138, 1981.
[7]   D. N. Schiller and W. A. Sirignano, "Opposed-Flow Flame Spread Across Alcohol Pools," presented at 34th AIAA Aerospace Sciences Meeting, Reno, NV, 1996.
[8]   R. J. Santoro, A. C. Fernandez-Pello, F. L. Dryer, and I. Glassman, "Application of a two-component LDV to the measurement of flows induced by flames propagating over condensed fuels," *Applied Optics*, vol. 17, pp. 3843-3850, 1978.
[9]   T. Suzuki, M. Kawamata, K. Matsumoto, and T. Hirano, "Aerodynamic and Thermal Structures of the Leading Flame Edge Spreading Over Fuel Soaked Sand in an Opposed Air Stream," presented at ASME/JSME Thermal Engineering Proceedings, 1991.
[10]   F. J. Miller, A. Mielke, J. Roncace, and H. D. Ross, "Smoke Visualization of the Gas-Phase Flow During Flame Spread over a Liquid Pool in the Pulsating Spread Regime," presented at Fall Meeting of the Eastern States Section of The Combustion Institute, Hilton Head, SC, 1996.
[11]   J. H. Burgoyne and A. F. Roberts, "The spread of flame across a liquid surface II. Steady-state conditions," *Proc. Roy. Soc. A.*, vol. 308, pp. 55-68, 1968.
[12]   T. Suzuki and T. Hirano, "Flame Propagation Across a Liquid Fuel in an Air Stream," *Nineteenth Symposium (Int'l) on Combustion*, pp. 877- 884, 1982.
[13]   F. J. Miller and H. D. Ross, "Further Observations of Flame Spread over Laboratory-Scale Alcohol Pools," *24th Symposium (International) on Combustion*, pp. 1703-1711, 1993.
[14]   D. N. Schiller and W. A. Sirignano, "Flame Spread With Concurrent Air Flow Across n-Propanol Pools," presented at Fall Meeting of the Western States Section of the Combustion Institute, 1995.
[15]   H. D. Ross and F. J. Miller, "Gravitational and Low-Speed Convective Effects on Flame Spread Across Liquid Fuel Pools: A Comparative Analysis," presented at 5th International Symposium on Fire Safety Science, Melbourne, Australia, 1997.
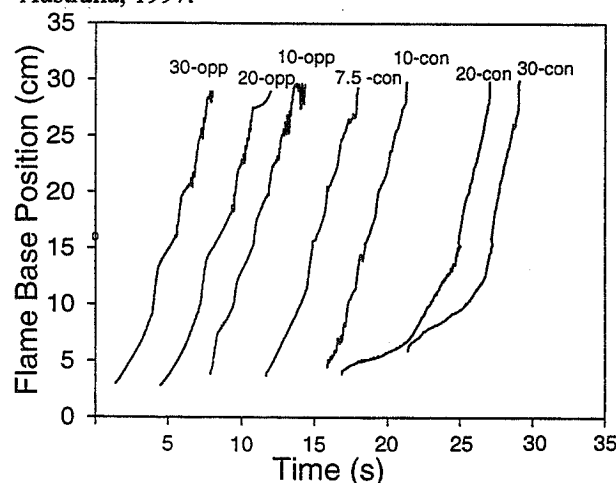
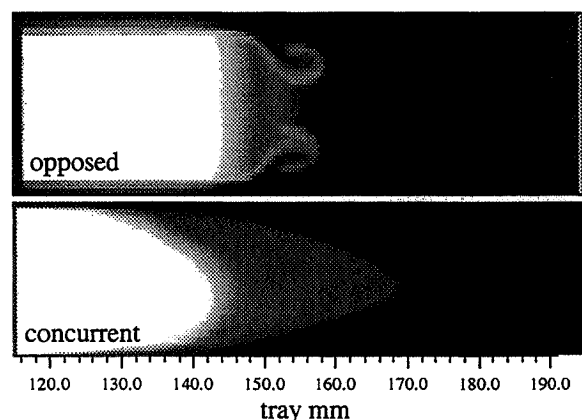Figure 1. Flame position vs. time for several forced air flow velocities, both opposed and concurrent.

Figure 2. Infrared top view of the liquid surface temperature ahead of a spreading flame for two air flow directions at 30 cm/s
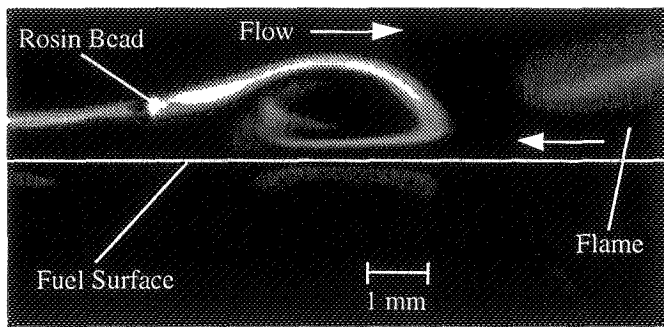
379

Figure 3. Smoke flow visualization of the recirculation cell in front of a pulsating flame. 30 cm/s opposed flow.

Figure 4. Flame postition vs. time for four opposed air flow rates in microgravity, and one typical normal gravity case.
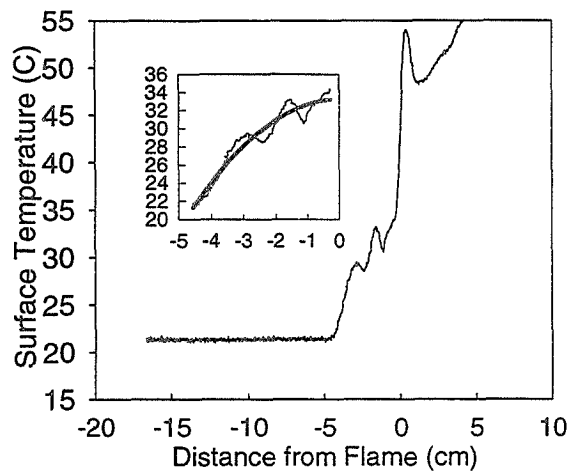

Figure 5. Liquid surface temperature ahead of a spreading flame in microgravity for an opposed flow rate of 30 cm/s. Inset shows square root fit.
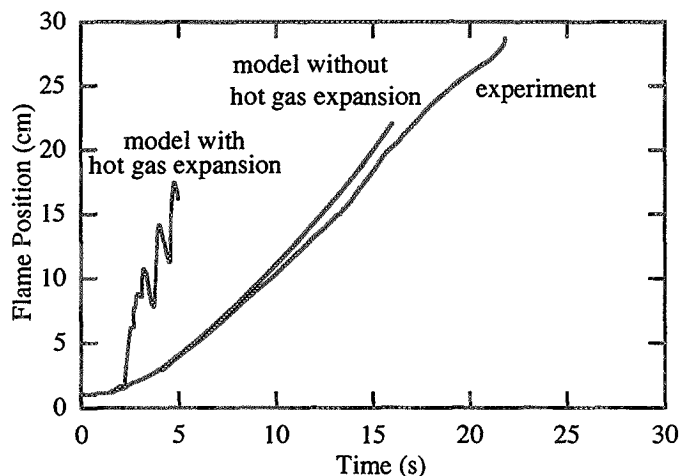

Figure 6. Top view of flame spread showing divergence of smoke streaklines due to hot gas expansion at the flame front. Opposed flow of 30 cm/s..

Figure 7. Flame position vs. time with a 30 cm/s opposed flow in microgravity showing effect of eliminating hot gas expansion from model.
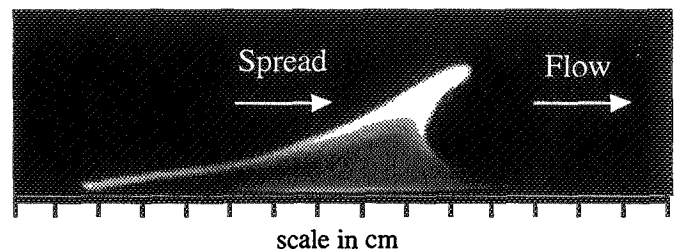
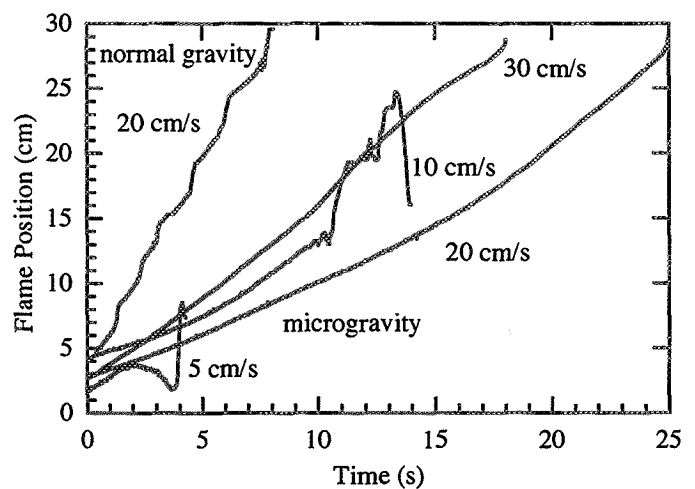Figure 8. Side view flame shape with a 30 cm/s concurrent flow in normal gravity. Refer to [2] for opposed flow shapes in both normal and microgravity. Next round of sounding rocket flights will measure flame spread in concurrent flow

SOLID SURFACE COMBUSTION EXPERIMENT: THICK FUEL RESULTS[1]

ROBERT A. ALTENKIRCH
Washington State University
Pullman, Washington

and

Subrata Bhattacharjee[1], Jeff West[1]/Lin Tang[2]/Kurt Sacksteder[3]/Michael A. Delichatsios[4]
[1]San Diego State University, San Diego, California/ [2]Washington State University, Pullman, Washington
[3]NASA Lewis Research Center, Cleveland, Ohio/ [4]Factory Mutual Research, Norwood, Massachusetts

Introduction

In the Solid Surface Combustion Experiment (SSCE), a series of five experiments for flame spread over a thin cellulosic fuel and thick polymethylmethacrylate in a quiescent O_2/N_2 oxidizing environment was conducted. Results from the five cellulosic experiments, and the supporting modeling and ground-based effort, are reported elsewhere (refs. 1-7). For the thin fuels, the spread rate, following ignition, rapidly adjusts to a steady value. Radiation heat transfer is a dominant phenomenon in the spread process at microgravity. While classical theory based on conduction arguments alone predicts the spread rate to be independent of pressure for spread over thin fuels (ref. 8), the spread rate in microgravity increases with increasing pressure. The increase is due to a decrease in the diffusion length scale with increasing pressure and a concomitant decrease in the optical depth of the flame and hence a decrease in the radiative heat loss from the flame as well. The result is an increase in flame temperature, and spread rate, with pressure. In the absence of radiation, classical theory for infinitely-fast, gas-phase kinetics predicts that the spread rate is independent of opposing flow velocity, but in the low flow environment the flame encounters in an initially quiescent, microgravity environment in which the opposing flow is eventually equivalent to the spread rate, the spread rate decreases with a decrease in opposing flow speed, due to the enhancement of radiative heat losses at the low flows.

It is well known that the propagation speed of a flame spreading over a thick fuel bed in an opposing flow environment depends on the strength and character of the opposing flow (refs. 9-11). Building on the understanding of the spread of a flame over a thin fuel, in which forward heat transfer through the solid is suppressed, we report here results from the SSCE for the more practical thick fuel configuration for quiescent flame spread in microgravity (ref. 12). This configuration has not been investigated to any great extent, experimentally, because the slow spread rates, much slower than those for a thin fuel, result in a need for substantial experimental time, time that is difficult to obtain in Earth-bound facilities such as drop towers.

Here we describe the results of experiments for spread over polymethylmethacrylate, PMMA, samples in the microgravity environment of the Space Shuttle. The results are coupled with modelling in an effort to describe the physics of the spread process for thick fuels in a quiescent, microgravity environment and uncover differences between thin and thick fuels. A quenching phenomenon not present for thin fuels is delineated, namely the fact that for thick fuels the possibility exists that, absent an opposing flow of sufficient strength to press the flame close enough to the fuel surface to allow the heated layer in the solid to develop, the heated layer fails to become "fully developed." The result is that the flame slows, which in turn causes an increase in the relative radiative loss from the flame, leading eventually to extinction. This potential inability of a thick fuel to develop a steady spread rate is not present for a thin fuel because the heated layer is the fuel thickness, which reaches a uniform temperature across the thickness relatively rapidly.

Experiment

The experiment apparatus was largely the same used for cellulosic sample experiments (ref. 12): a 39 liter chamber filled before flight with the test atmosphere, two cine cameras providing top and side perspectives of the PMMA samples, and a data acquisition and control computer. Three Shuttle missions were conducted with quiescent test atmospheres consisting of mixtures

381

of O_2/N_2 at 70% O_2/1 atm pressure (STS-54), 50% O_2/1 atm (STS-63), and 50% O_2/2 atm (STS-64). In each flight two PMMA samples, 25.4 mm long x 6.35 mm wide x 3.18 mm thick were imbedded in an aluminum structure, with one large face exposed to the chamber atmosphere in the plane of the structure surface. The bottom and side faces of the samples were insulated from the structure. A resistively-heated Kanthol wire for ignition was imbedded 1.6 mm from one end. Three type R thermocouples were installed for each sample: one each in the gas-phase, at the fuel surface, and imbedded in the fuel. The thermocouples above and below the surface were at different distances from the surface of the two samples to provide a reconstructed five-point temperature profile. In 70% O_2, 0.127 mm diameter thermocouple wire was used throughout. For the 50% O_2 tests, 0.076 mm wire was used for the surface and imbedded thermocouples and 0.025 mm wire in the gas phase.
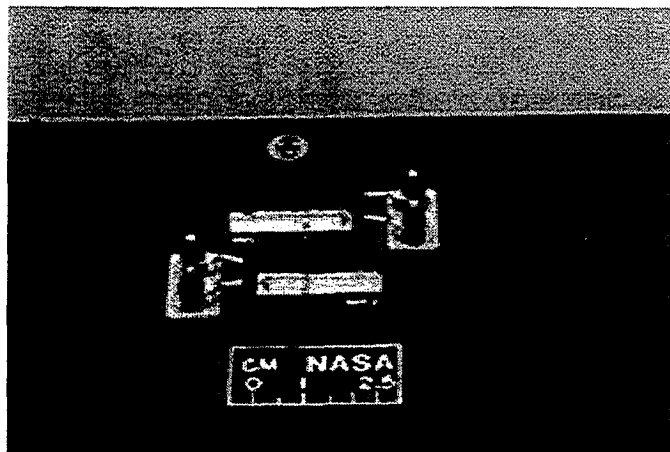

Figure 1 Samples and sample holder for PMMA samples.

A sliding-plate mechanism for flame quenching was deployed under computer control to preserve the fuel surface shape after flame spreading was complete. In STS-54, the flame arrival time at the sample end was estimated by the rise time to a threshold temperature at the thermocouple locations. In STS-64, the first sample quench time was computed using a higher threshold temperature, and the second sample was allowed to burn until the cine film was consumed. In STS-63, both samples were allowed to burn until the cine film was consumed, but the cameras were started 60 seconds after ignition in the second sample.

Experimental Results

For brevity, only flame position as a function of time data are presented here. These data allow a description of the phenomena involved to be developed. In Fig. 2, position of the spreading flames, measured using image analysis software (ref. 5), with time are shown. The flattened portions of these plots are associated with the flames encountering the gas-phase thermocouples, which glow brightly and partly obscure the dim flame images. The size of the gas-phase thermocouples was initially chosen to match that of earlier experiments with thin, cellulosic fuels (ref. 6). Following the first experiment at 70% O_2, when it was found that thermocouples of that size influence the spread process for a portion of the experiment, presumably because of the low flame temperatures due to substantial radiative heat loss from the flame, computed to be as much as 60% of the heat released, Earth-bound near extinction experiments were conducted to determine if the use of smaller thermocouples would be less intrusive, which it was found to be. As a result, for subsequent flight experiments, the smallest thermocouples that could be physically installed were used. Once the flames pass the thermocouple, they resume a trajectory of gradually decreasing slope, i.e., a decreasing spread rate. The flame in 70% O_2, 1 atm was beginning to escape the thermocouple when it was quenched by the experiment's computer.

Modelling

The mathematical model employed has been reported elsewhere (refs. 2,6,7,13), so only a brief description is presented here. Unsteady, dimensionless, two-dimensional conservation equations in the gas for energy, momentum, fuel, oxygen, and nitrogen are expressed in a generic format. An ignition source term is applied to a portion of the solid and gas near the interface and at the location of the experimental igniter. A Planck mean absorption coefficient, $a_{P,GB}$, calculated from the method of Global Energy Balance (refs. 2,7), considering CO_2, H_2O, methylmethacrylate vapor, and the temperature distribution in the flame accounts for reabsorption of radiation. Typical values of $a_{P,GB}$ range from 2 to 4 m^{-1}. Feedback of gas radiation to the fuel surface, surface reradiation, and three-dimensional radiation effects due to the finite width of the sample are included.

In addition to the conservation equations, the equation of state for density, a square-root dependence of viscosity and thermal conductivity in the gas on temperature, and a pyrolysis formula based on negligible surface regression, constant solid density, and first-order kinetics (ref. 14) are used to complete the formulation. Property values are listed elsewhere (ref. 15).

The set of equations and suitable boundary conditions are solved numerically using the SIMPLER algorithm (ref. 16). A 25.4 mm long sample of PMMA, with the same width and half-thickness dimensions as the experiment, is embedded flush with an inert surface, with the exception of the 70% O_2 environment for which the computational sample was 10 mm longer, for reasons that will be apparent below. The inert surface is used to direct the gas flow toward the reaction zone and to provide suitable boundary conditions for analysis. The downstream inert surface, behind the ignition end, is 4 cm long, and the upstream inert

surface, toward which the flame is spreading, is 23.46 cm long (22.46 cm for 70% O_2). The computation is performed over a 30 cm long x 20 cm high domain. The ignition power input per unit volume is 2.2×10^8 W/m^3, which when multiplied by the ignition volume results in 2.4 W of ignition power, approximately the experimental input. This power input is continued until flame ignition occurs, which is usually at approximately 1.8 s, at which time it is shut off.

Computations on several grids were performed to establish the level of refinement required for essentially grid-independent results, the grid chosen being 140 (x-nodes) x 52 (y-nodes), x being along the solid, y normal to the solid, with 8 y-direction nodes in the solid. Along the y-direction, the grid step size is 0.625 mm from the fuel surface into the gas to y=10 mm. After 10 mm a power-law variation for grid distribution to the top of the domain is used. The grid distribution along the x-direction consists of a step size of 1.74 mm from x=0 to x=4 cm (downstream inert surface), followed by a step size of 0.283 mm to x=6.54 cm (fuel sample), and then followed by a power-law variation to the right-hand-side of the domain (upstream inert surface). The time step ranged from 0.05 to 0.5 s, and the relative convergence criterion for all field variables was 0.005.

In Fig. 3, the experimental results are presented again for comparison to the computational results. The computations track the flame progression relatively well as the flame spreads from time zero and captures the fact that the spread rate decreases with time. As the computations are extended beyond the experimental time, the flame continues to spread at a decreasing rate until it reaches a maximum distance of progression, at which time the leading edge retreats as the flame shrinks in size and then extinguishes. This behavior was found for all three environments considered. For 70% O_2, the progression was beyond the 25.4 mm experimental sample length, and so computationally the sample was extended 10 mm as mentioned above.

Discussion

Previous results for thin cellulosic fuels in a quiescent, microgravity environment showed that the flame spread rate following ignition quickly adjusted to a fixed value (ref. 6,7). Here we find, however, that for the thick fuels, the spread rate continually decreases with time until eventually, computationally, the flame extinguishes. This behavior is somewhat understandable as described below.

Consider a region near the leading edge of the flame in which the thermal diffusion length is $L_g = \alpha_g / V_f$, V_f, the spread rate, being the velocity scale. Actually, the length over which heat is transferred is less than α_g / V_f because of radiation (ref. 3), the consequences of which will be evident later, but initially in the spread process radiation is unimportant until the flame evolves to sufficient size. Within the solid, there is a y-direction thermal scale for the heated layer depth of $\delta_y = \sqrt{\alpha_s \alpha_g / V_f^2}$, α_g / V_f^2 being the time the solid is heated from T_∞ to the vaporization temperature T_v and an x-direction scale of $\delta_x = \alpha_s / V_f$.

At the flame leading edge, an approximate steady-state energy balance on the solid gives
$\rho_s c_s (T_v - T_\infty) V_f \delta_y \approx \lambda_g (B - r) \Delta h_v^o / c_g - \varepsilon_s \sigma (T_v^4 - T_\infty^4) \delta_x$ where the first term on the right-hand-side is the heat conduction from the flame to the fuel upstream through the gas and solid (refs. 17,18), and the second is the radiative loss from the surface in which the x-direction length in the solid has been taken to be larger than that in the gas for now. B is the transfer number, and r is the stoichiometric fuel-air ratio. For a thin fuel, in which δ_y is τ, δ_y / δ_x is small such that upstream conduction in the solid is negligible, and δ_x is L_g because the heat conduction is through the gas, we get a steady solution for V_f as long as the heat conducted from the gas exceeds the heat lost by radiation, i.e.,

$$2V_f \approx \frac{\lambda_g (B-r)\Delta h_v^o}{c_g \rho_s c_s (T_v - T_\infty)\tau} + \sqrt{\left(\frac{\lambda_g (B-r)\Delta h_v^o}{c_g \rho_s c_s (T_v - T_\infty)\tau}\right)^2 - \frac{4\varepsilon_s \sigma (T_v^4 - T_\infty^4)\alpha_g}{\rho_s c_s (T_v - T_\infty)\tau}} \qquad (1)$$

When radiation is neglected, Eq. (1) gives the de Ris-Delichatsios formula (refs. 8,17,18) except for a factor of $\pi / 4$. As mentioned above, experiments for thin cellulosic samples in a quiescent, microgravity environment yield a steady spread rate for those environments in which the flame spreads.

Assuming slow variations from one steady state to another, the unsteady counterpart of the above energy balance is obtained by

adding the term $\frac{d}{dt}\rho_s c_s(T_v - T_\infty)\delta_y\delta_x$ to the left-hand-side in which we use the same steady-state length scales as an approximation. For the thin fuel again, with $\delta_x = L_g$ and $\delta_y = \tau$, the unsteady term divided by the convective term gives $(1/V_f)\frac{d}{dt}\frac{\alpha_g}{V_f}$ so that the time scale becomes α_g/V_f^2, which is of the order of 1 to 10 s for the spread rates measured (ref. 6).

For the thick fuel, with $\delta_x = \alpha_s/V_f$, the time scale is α_s/V_f^2. With $\alpha_s \cong 10^{-3}\alpha_g$ and the spread rate approximately two orders of magnitude, or more, smaller than for the thin fuel, the time scale can be more than an order of magnitude larger than that for a thin fuel, large to the extent that the flame is unable to adjust to a steady state as the in-depth heated layer in the solid near the leading edge continues to grow with time. From the approximate energy balance for the thick fuel, neglecting the radiative loss, we get, early in the spread process, that $V_f \propto 1/\sqrt{t}$ where the proportionality factor is inversely proportional to B. That is, for higher oxygen concentrations, V_f decreases initially more rapidly. Once this decrease takes place, the flame seeks to adjust to a steady state such that the V_f dependence on t changes and is a function of the environment.

Steady spread over PMMA in a quiescent, microgravity environment should exist if the fuel, or heated layer in the solid, is thin enough as it exists for thin cellulosic samples. Steady-state computations, in which the unsteady term in the computational model is dropped, and the steady computations carried out in flame-fixed coordinates as described elsewhere (refs. 6,7), except that the above solid-phase model for PMMA used here is employed, show that for thicknesses of and below 0.05 mm for 50% O_2/1 atm and 0.2 mm for 100% O_2/2 atm, steady spread for PMMA of the same width as the experimental samples is obtained. For these computations, a domain approximately 111 cm long and 89 cm high with a 90x50 non-uniform grid in the gas and 10 grid lines in the solid was used. The relatively large domain is needed to allow the oxygen field to develop. The computed spread rates for these limiting thicknesses are approximately 2 and 1 mm/s, respectively. These thicknesses are comparable to the thickness of 0.083 mm for which cellulosic samples gave steady spread rates in an O_2 percentage as low as 35% at 1 atm (ref. 6).

The mechanism causing the unsteady spread and eventual extinction for the thick fuel can be explained by comparing computed temperature and oxygen contours at several times during the unsteady spread process as shown from computations in Fig. 4. The thermal diffusion scale in the gas is α_g/V_f, as mentioned above, and for unit Lewis number this is the mass diffusion scale as well. However, the actual thermal length scale in the gas over which temperature changes occur is reduced because of the effects of radiation (ref. 3). The reduction increases as the spread rate decreases, and the effects of radiation become more pronounced while the mass diffusion scale increases. As a result, as the flame evolves over time for the thick fuel, the spread rate decreases with time, and the mismatch between the thermal length scale and the mass diffusion scale grows. Eventually, the diffusion rate of oxygen to the high temperature flame, proportional to $y_{ox,\infty}/L_g$, is too small to sustain the flame, and the flame extinguishes. This behavior is evident in Fig. 4. While there are oxygen concentrations below which thin fuels are unable to support spreading flames, and this inability has been identified with the effects of radiation on the gas-phase chemical kinetics (ref. 2), and oxygen diffusion (ref. 19), apparently the spread rate for thin fuels is high enough that the flame spreads at a steady rate.

Conclusions

Experiments for flame spread over flat surfaces of thick fuels in microgravity show that the flame spread rate slowly decreases with time. Because the fuel is thick, the heated layer in the solid evolves in time. Spread rates are low enough that radiative effects are important, and they cause the distance over which temperature changes occur in the gas to be reduced over what it would be in the absence of radiation when the conduction and mass diffusion scales are comparable. In contrast, the distance over which oxygen must diffuse to reach the flame is unaffected by radiation. As a result, this distance grows in time as the flame slows, which results in a reduction of the diffusion rate to the flame to lead eventually to flame extinction. There appears to be a critical thickness below which steady spreading is obtained in microgravity. Below this thickness, the fuel is heated rapidly, and the spread rate remains high enough that any difference in the distance over which temperature changes and mass diffusion occur is unimportant in comparison to the thick fuels.

References

1. Bhattacharjee, S., Altenkirch, R.A., Srikantaiah, N., and Vedha-Nayagam, M. (1990). *Combustion Science and Technology* 69, 1-15.
2. Bhattacharjee, S. and Altenkirch, R.A. (1991). *Twenty-Third Symposium (International) on Combustion*, The Combustion Institute, Pittsburgh, pp. 1627-1633.

3. Bhattacharjee, S., Altenkirch, R.A., Olson, S.L., and Sotos, R.G. (1991). *Journal of Heat Transfer* 113, 670-676.
4. Bhattacharjee, S. and Altenkirch, R.A. (1992). *Twenty-Fourth Symposium (International) on Combustion*, The Combustion Institute, Pittsburgh, pp. 1669-1676.
5. Bhattacharjee, S., Altenkirch, R.A., and Sacksteder, K. (1993). *Combustion Science and Technology* 91, 225-242 .
6. Ramachandra, P.A., Altenkirch, R.A., Bhattacharjee, S., Tang, L., Sacksteder, K., and Wolverton, M.K. (1995). *Combustion and Flame* 100, pp. 71-84.
7. Bhattacharjee, S., Altenkirch, R.A., and Sacksteder, K. (1996). *Journal of Heat Transfer* 118, pp. 181-190.
8. de Ris, J.N. (1969). *Twelfth Symposium (International) on Combustion*, The Combustion Institute, Pittsburgh, pp. 241-252.
9. Wichman, I. S., Williams, F., A., and Glassman, I. (1982). *Nineteenth Symposium (International) on Combustion*, The Combustion Institute, Pittsburgh, pp. 835-845.
10. Fernandez-Pello, A.C., Ray, S.R., and Glassman, I. (1981). *Eighteenth Symposium (International) on Combustion*, The Combustion Institute, Pittsburgh, pp. 579-587.
11. Williams, F.A. (1977). *Sixteenth Symposium (International) on Combustion*, The Combustion Institute, Pittsburgh, pp. 1281-1294.
12. Vento, D., Zavesky, R., Sacksteder, K., and Altenkirch, R.A. (1989). *The Solid Surface Combustion Space Shuttle Experiment Hardware Description and Ground-Based Test Results*, NASA TM 101963.
13. Bullard, D.B., Tang., L, Altenkirch, R.A., and Bhattacharjee, S. (1993). *Adv. Space Res.* 13-7: 171-184.
14. Lengelle, G. (1970). *AIAA J.* 8: 1989-1986.
15. West, J., Tang, L., Altenkirch, R.A., Bhattacharjee, S., Sacksteder, K., and Delichatsios, M.A. (1997). Quiescent Flame Spread Over Thick Fuels in Microgravity, *Twenty-Sixth Symposium (International) on Combustion*, The Combustion Institute, in press.
16. Patankar, S.V. (1980). *Numerical Heat Transfer and Fluid Flow*, Hemisphere, New York.
17. Delichatsios, M.A. (1993). *Comb. Flame* 95: 336-339.
18. Delichatsios, M.A. (1994). *Comb. Flame* 99: 601-609.
19. Olson, S.L. (1990). *Comb. Sci. Technol.* 76: 233-249.

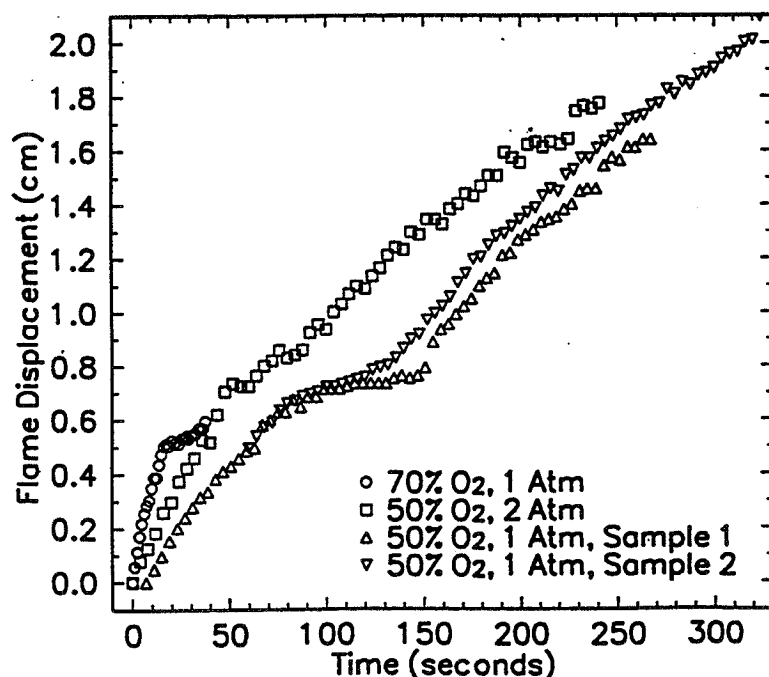## SSCE PMMA Flame Postition Composite
STS−54, STS−63, STS−64

Figure 2 The progress of spreading-flame position over burning PMMA samples. The flame in 70% O_2, 1 atm (circles) appears retarded by the thermocouples (0.127 mm wire). The position of the 50% O_2, 2 atm flame (squares) is obscured by the glowing thermocouple at about 50 s after ignition (0.025 mm wire), but flame progress is unaffected. Data from the other 50% O_2, 2 atm flame (not shown) is indistinguishable from the first until it is quenched by the computer at about 70 s after ignition. Two flames in 50% O_2, 1 atm (triangles) show distinguishable thermocouple influence: the flame encountering the thermocouple 3 mm above the fuel surface (sample 1) follows a delayed trajectory similar to its companion encountering the thermocouple 1 mm above the surface.
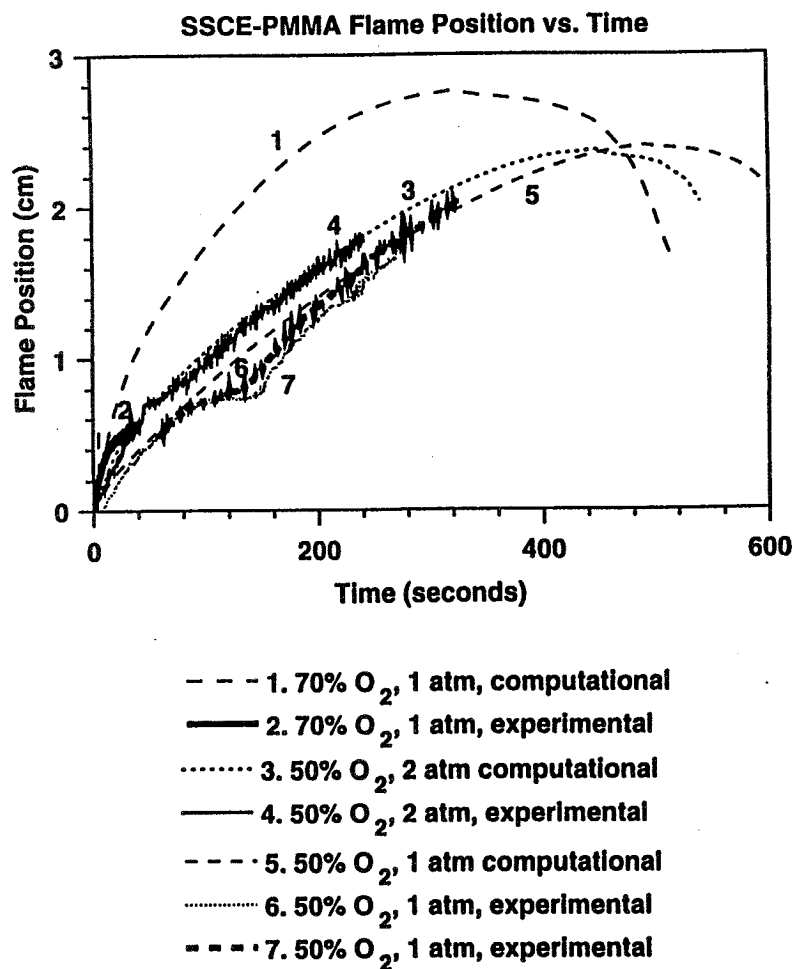
SSCE-PMMA Flame Position vs. Time

- – – 1. 70% O_2, 1 atm, computational
- —— 2. 70% O_2, 1 atm, experimental
- ········ 3. 50% O_2, 2 atm computational
- —— 4. 50% O_2, 2 atm, experimental
- – – · 5. 50% O_2, 1 atm computational
- ············ 6. 50% O_2, 1 atm, experimental
- ▬ ▬ ▬ · 7. 50% O_2, 1 atm, experimental

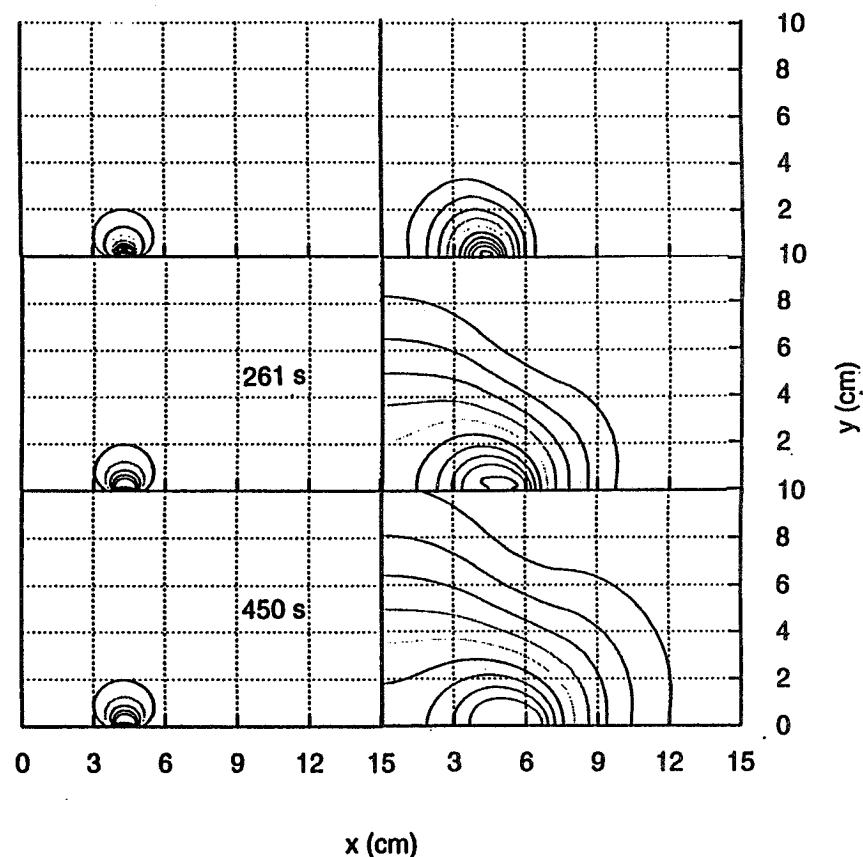Figure 3 Computed and experimental (from Fig. 2) flame position as a function of time.

x (cm)

Figure 4 Computed temperature (left-hand-side) and oxygen (right-hand-side) contours for 50% O_2/2 atm ($y_{o\infty}$ =0.533) for three different times during the spread process. The outermost oxygen contour is for $y_{o\infty}$ =0.45, and the temperature contours are from 450 K to 1350 K for 48 s to 1050 K at 261 and 450 s. The thickness of the region over which oxygen diffuses grows with time such that the high temperature contours find themselves in a region in which the flux of oxygen is decreasing with time.

REFLIGHT OF THE SOLID SURFACE COMBUSTION EXPERIMENT: OPPOSED-FLOW FLAME SPREAD OVER CYLINDRICAL FUELS[1]

SUBRATA BHATTACHARJEE
San Diego State University
San Diego, California

and

Robert A. Altenkirch[1] /Regis Worley[2] /Lin Tang[1], Matt Bundy[1] /Kurt Sacksteder[3] /Michael A. Delichatsios[4]
[1]Washington State University, Pullman, Washington/ [2]San Diego State University, San Diego, California/
[3]NASA Lewis Research Center, Cleveland, Ohio/ [4]Factory Mutual Research, Norwood, Massachusetts

Introduction

Although much has been learned about flame spreading at low gravity from recent experimental and theoretical efforts (see, e.g., refs. 1-3) understanding of the role of radiation heat transfer is limited. The difficulty lies in the fact that the modelling that must be done in concert with a limited number of low-gravity experiments to assist in interpretation of experimental results is complicated by several factors when radiation is involved. Although the process of radiative heat transfer is well described by the radiative transfer equation (RTE), the solution of the RTE itself is cumbersome, and almost always approximate due to, among other things, the three-dimensional nature of the radiative field, spectral and temperature dependence of properties, soot formation, turbulence-radiation interaction, and inhomogeneity of the medium.

The effort described here is a reflight of the Solid Surface Combustion Experiment (SSCE) (ref. 4), with extension of the flight matrix first and then experiment modification. The objectives of the reflight are to extend the understanding of the interplay of the radiative processes that affect the flame spread mechanisms.

Two experiments are scheduled for flight aboard the Space Shuttle using the existing SSCE chamber and electronics. In each experiment, thick PMMA is the fuel, the thick fuel being used for reflight because most "real fuels" are thick. One experiment is an extension of the SSCE PMMA experiment using exactly the same flat surface configuration used in previous SSCE flights but exchanging the dual sample configuration of the earlier experiments for a single long sample. The "long sample" configuration is chosen to allow observation of the predicted phenomena following ignition and flame spread, which for flat, thick fuel surfaces appears to be unsteady, leading eventually to flame extinction because of the influence of radiative processes (ref. 3).

The second experiment, and the one on which we concentrate here, is to utilize a cylindrical geometry, which provides a unique environment whereby the effects of finite flame width inherent in the flat surface experiments on the radiative field is eliminated. The problem is inherently two dimensional, not only from a hydrodynamic point of view but also the radiative field, and so approximations of dimensionality in applying radiation models are not needed.

Considerable work has been done over the past three decades on flame spread over a flat fuel bed placed in an opposing flow. Although the influence of parameters such as ambient oxygen level, pressure, fuel thickness, etc. are well understood, there are relatively few studies on the effects of fuel geometry, e.g., the cylindrical geometry considered here compared to the flat-surface geometry, an important parameter for practical applications.

Kosdon et al. (ref. 5) developed a similarity solution for flames over cylindrical fuels and compared the mass burning rate with experiments performed on cellulosic and birchwood samples. Fernandez-Pello and Santoro (ref. 6) studied downward flame propagation over PMMA cylinders with an emphasis on the determination of the mechanism of flame spread. They concluded that the dominant mode of heat transfer is a function of the fuel thickness, with the solid conduction playing a more dominant role for thicker fuels. Tewarson and Khan (ref. 7) studied the effects of flame spread rates for electrical cables, but in a concurrent flow configuration.

Here we discuss the experiments to be conducted with cylindrical fuel samples in a quiescent, microgravity environment on future Space Shuttle flights, and the supporting modelling effort, which includes scaling, analytical, and numerical work. Some of the modelling results are compared among themselves and to available experimental results.

Reflight Experiments

The reflight experiments, as mentioned above, consist of two experiments using the existing SSCE chamber (ref. 4) and electronics. In each experiment, PMMA is the fuel. The first experiment is to exchange the dual sample configuration of the earlier experiments for the single long sample, 6.2 mm wide, 2.9 mm thick, and 59.9 mm long, to be burned in a test atmosphere of 50% O_2/ 50% N_2 at 1 atm. The sample will be exposed to the atmosphere on one 6.2 mm x 59.9 mm surface; the other surfaces will be insulated from the surroundings. Because the sample is expected to extinguish during the test (ref. 3), there are no provisions for quenching the sample. The sample will be ignited using the same resistively heated Kanthol wire energized for 5 seconds at 3.75 amps. Six thermocouples will be suspended above the sample at a height of 10 mm from the sample surface, spaced along the sample centerline. These thermocouples will provide a redundant measure of the flame spread progress and the change in the temperature field away from the flame leading edge, while avoiding the possible interference with the quenching process. The flame will be imaged using a video camera from one perspective and a cine camera from an orthogonal perspective.

The second experiment takes advantage of the reduction in dimensionality of the radiation environment provided by a cylindrical sample. Two samples will be burned in this test, both in 50% O_2/ 50% N_2 (see Figure 1). The first sample will be 44 mm long and 6.4 mm in diameter. The first half of the sample length will be hollow with a 1.0 mm wall thickness, the other half length solid. This single sample provides examples of both a "large diameter," thin fuel and a large diameter, thick fuel. The second sample is 40 mm long and 2.0 mm in diameter, and solid, to provide a "small diameter," thin fuel. Both samples will be ignited using the same Kanthol wire ignitor. The thin wall, large diameter sample section is expected to burn at a steady rate in the 50% O_2 test atmosphere, while the thick sample section is expected to spread to extinction. The small diameter sample is also expected to burn at a steady rate.
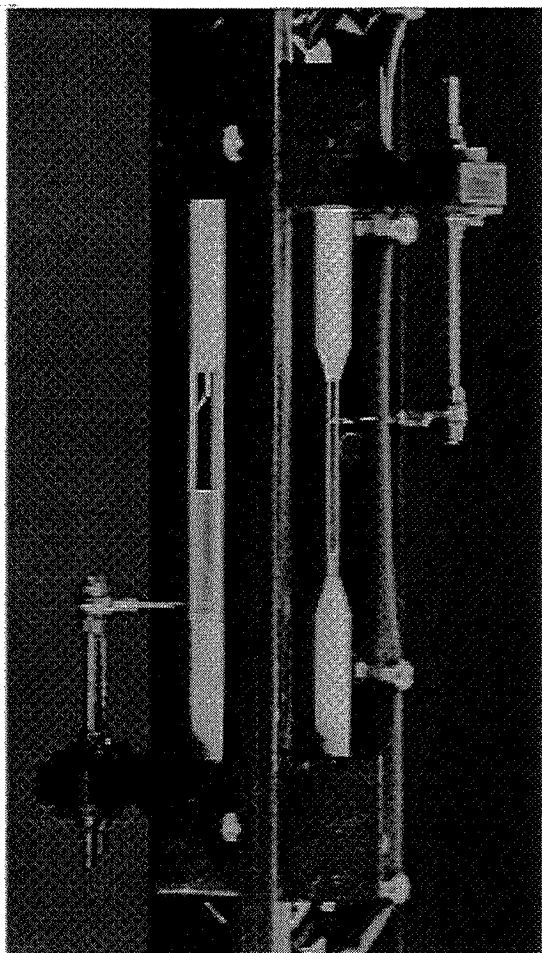

Figure 1 Cylindrical PMMA samples. Upper sample is 2.0 mm in diameter. Lower sample is 6.4 mm in diameter; right side is hollow, left side solid.

Modelling Formulation

The mathematical formulation is patterned after the flat surface formulation (refs. 2,3) except for the global-balance radiation model, which is reformulated for the cylindrical geometry. The numerical solution employs the finite-volume formulation of Patankar (ref. 8) for the hydrodynamic calculations and the TTNH formulation of Grosshandler (ref. 9) for line-of-sight radiation calculations with the species, CO_2, H_2O, and MMA vapor. The computational code has been validated by comparing the numerical result with analytical solutions available for simpler models.

Scaling

Consider the control volume near the leading edge of the flame shown in Figure 2 in flame-fixed coordinates with the oxidizer approaching the flame at a velocity $V_r = V_g + V_f$ and the fuel at V_f, where V_g is a known opposing flow velocity, and V_f is the desired spread rate. Assuming negligible blowing in the preheat

region, V_r is the only velocity scale leading to the following gas-phase diffusion/conduction length scales.

$$L_{gx} \approx \frac{\alpha_g}{V_r}, \qquad L_{gy} \approx \sqrt{\alpha_g \frac{L_{gx}}{V_r}} = \frac{\alpha_g}{V_r}, \qquad \text{Thus: } L_{gx} \approx L_{gy} \approx L_g = \frac{\alpha_g}{V_r}. \qquad (1)$$

For flat surfaces in the thermal regime the solid is preheated primarily through gas phase conduction (refs. 10,11). Assuming the same mechanism for the cylindrical geometry, the solid-phase length scales can be expressed as follows, where R is the solid cylinder radius.

$$L_{sx} \approx L_{gx} = \frac{\alpha_g}{V_r} \qquad L_{sy} \approx \min\left(R, \sqrt{\alpha_s \frac{L_{sx}}{V_f}}\right) = \min\left(R, \sqrt{\frac{\alpha_s \alpha_g}{V_f V_r}}\right) \qquad (2)$$

Taking into account the radial variation of surface area, the conduction heat flux from the gas to the solid phase at the fuel surface can be scaled as:

$$\dot{q}''_{gsc} = \gamma\, \dot{q}''_{gsc,cart}, \quad \text{where,} \qquad \dot{q}''_{cart} = \lambda_g \frac{T_f - T_v}{L_g}, \qquad \gamma = \frac{L_g/R}{\ell n\left(1 + \frac{L_g}{R}\right)} \qquad (3)$$

The total heat flow from the gas phase to the preheating zone of the solid phase is expended in the sensible heating of the solid from T_∞ to T_v as it approaches the flame with a velocity V_f in the flame-fixed coordinates.

$$\rho_s c_s V_f (T_v - T_\infty) \cdot \left[\pi R^2 - \pi (R - L_{sy})^2\right] \approx 2\pi R \dot{q}''_{gsc} \qquad (4)$$

Therefore, $\qquad V_f \approx \dfrac{\gamma}{\left(1 - \dfrac{L_{sy}}{2R}\right)} \dfrac{\lambda_g}{\rho_s c_s L_{sy}} \dfrac{(T_f - T_v)}{(T_v - T_\infty)} \qquad (5)$

The thermally thin and thick limits are obtained by combining Eqs. (5) and (2).

$$V_{f,thin} \approx 2\gamma \frac{\lambda_g}{\rho_s c_s R} \frac{(T_f - T_v)}{(T_v - T_\infty)}, \quad V_{f,thick} \approx \frac{\gamma^2}{\left(1 - \dfrac{1}{2R}\sqrt{\dfrac{\alpha_s \alpha_g}{V_{f,thick} V_r}}\right)^2} \frac{V_r \lambda_g \rho_g c_g}{\lambda_s \rho_s c_s} \left(\frac{T_f - T_v}{T_v - T_\infty}\right)^2 \qquad (6)$$

Note that while the thick formula is a transcendental equation, the thin formula, when compared to the corresponding flat surface formula (ref. 12), indicates that the spread rate is at least twice as fast for thin cylindrical fuels compared to flat surface fuels in the thermal regime.

Results and Discussion

Spread rates, computed for cylindrical fuels of different radii in a downward spread configuration under atmospheric conditions, are compared with experimental results (ref. 6,13) and prediction from Eq. (5) in Figure 3. The computational predictions agree reasonably well with the experimental spread rates. Finite-rate kinetics are known (ref. 14) to have a significant effect at 21% O_2. The scaling formula, built with the assumption of infinite-rate kinetics, understandably overpredicts the spread rate. However, it captures the nature of the variation of V_f with the fuel radius. In calculating V_f from Eq. (5), a recently developed (ref. 14) expression for an equivalent opposing flow velocity has been used for V_r.

Computational spread rates in a thermal regime configuration, V_g =40 cm/s, O_2 level 50%, for both flat and cylindrical fuels are presented in Figure 4. Corresponding predictions from Eq. (5) are plotted in Figure 5. The radius of the cylindrical fuel and the half-thickness of the flat fuel are both referred to as τ. The cylindrical spread rate in the thin regime is at least twice as fast as the corresponding flat case as anticipated. For the cylindrical thin fuel, however, the computational results to date are not grid-independent.

Computational results for which the radiation computation was frozen at one particular condition are presented for a quiescent microgravity environment in Figure 6. Because the radiative field in Figure 6 was not computed for each configuration

separately, the results are qualitative. Results for hollow cylinders are included. The thickness of the cylindrical shell and the half-thickness of the flat fuel are both referred to as τ. For a given radius, spread rate over a hollow cylinder (with the interior cavity filled with insulation) decreases with increasing thickness and merges with the results from $\tau = R$ for cylinders, i.e., solid cylinders with no cavity. For both flat surfaces and solid cylindrical surfaces the spread rate continues to decrease as the fuel thickness increases until no steady-state solution can be found indicating the possibility of extinction after a critical fuel thickness. This is understandable in that in the absence of any imposed flow, the thickness of the heated layer in the solid is approximately,

from Eq. (2), $L_{sy} = \dfrac{\sqrt{\alpha_s \alpha_g}}{V_f}$. As the spread rate decreases, a progressively thicker layer of fuel is heated by the flame, which

in turn reduces the spread rate further as evident from Eq. (5). As this layer is developing, the mass diffusional scale in the gas grows while radiation losses keep the flame from growing in size such that eventually, oxygen diffusion into the flame is insufficient to sustain it and extinction occurs (ref. 3). Unsteady numerical computation for spread over a PMMA cylinder of 5 cm radius and 2 mm wall thickness in a quiescent microgravity environment is shown in Figure 7 in which flame position as a function of time is presented. The spread rate continually decreases until the flame reaches a location at which it continues to burn for a substantial amount of time without forward progress while radiation losses depress the flame temperature over time. Eventually, the flame leading edge, actually the peak heat flux from the gas to the solid, retreats, and the flame extinguishes.

Summary

The cylindrical geometry provides an attractive geometry for investigating the influence of radiation on flame spread in a quiescent microgravity environment because it eliminates the three dimensional effects inherent in the flat surface geometry of finite width. Simple analyses based on energy balances along with numerical modelling of the spread process indicate that spread rates over the cylindrical surface are faster than for the flat surface for the same sample thickness, i.e., radius. The unsteady behavior observed for thick, flat surface fuels is anticipated in the cylindrical geometry as well. Space Shuttle experiments are planned to delineate the unsteady effects observed in earlier SSCE experiments for both flat and cylindrical surfaces.

References

1. McGrattan, K.B., Kashiwagi, T., Baum, H.R., and Olson, S.L. (1996). *Combustion and Flame* 106, 377-391.
2. Bhattacharjee, S. and Altenkirch, R.A. (1991). *Twenty-Third Symposium (International) on Combustion*, The Combustion Institute, Pittsburgh, pp. 1627-1633.
3. West, J., Tang, L., Altenkirch, R.A., Bhattacharjee, S., Sacksteder, K., and Delichatsios, M.A. (1997). Quiescent Flame Spread Over Thick Fuels in Microgravity, *Twenty-Sixth Symposium (International) on Combustion*, The Combustion Institute, in press.
4. Vento, D., Zavesky, R., Sacksteder, K., and Altenkirch, R.A. (1989). *The Solid Surface Combustion Space Shuttle Experiment Hardware Description and Ground-Based Test Results*, NASA TM 101963.
5. Kosdon, F.J., Williams, F.A., and Buman, C. (1969). *Twelfth Symposium (International) on Combustion*, The Combustion Institute, Pittsburgh, p. 1151.
6. Fernandez-Pello, A.C., and Santoro, R.J. (1978). *Seventeenth Symposium (International) on Combustion*, The Combustion Institute, Pittsburgh, p. 1201.
7. Tewarson, A., and Khan, M.M. (1988). *Twenty-Second Symposium (International) on Combustion*, The Combustion Institute, Pittsburgh, p. 1231.
8. Patankar, S.V. (1980). *Numerical Heat Transfer and Fluid Flow*, McGraw Hill, New York.
9. Grosshandler, W.L. (1980). *International Journal of Heat and Mass Transfer* 23, 1447-1459.
10. West, J., King, M., Bhattacharjee, S., and Altenkirch, R.A. (1997). "Comprehensive Determination of Forward Heat Transfer in Flame Spread Over Thermally Thick Solid Fuels in an Opposing Flow in the Thermal, Microgravity, and Kinetic Regimes," *Combustion Science and Technology*, submitted.
11. Ito, A. and Kashiwagi, T. (1986). *Twenty-First Symposium (International) on Combustion*, The Combustion Institute, Pittsburgh, pp. 65-74.
12. de Ris, J. N. (1969). *Twelfth Symposium (International) on Combustion*, The Combustion Institute, Pittsburgh, pp. 241-252.
13. Bundy, M. (1995). *Experimental Investigation of Downward Spreading Flame over Thick and Thin Fuel*, MS Thesis, San Diego State University.
14. King, M. (1996). *Numerical Investigation of Downward Spreading Flame over Thick and Thin Fuel*, MS Thesis, San Diego State University.
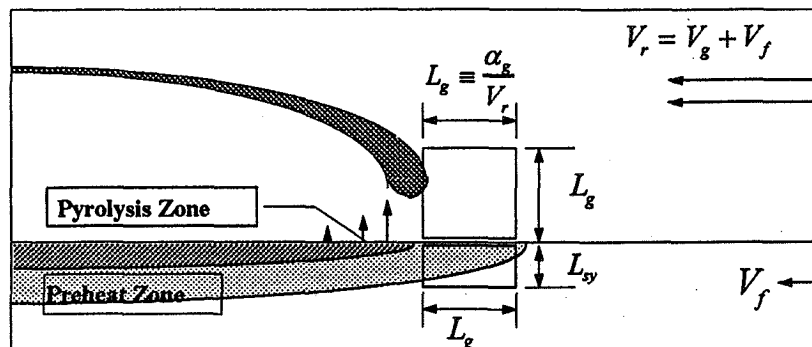
Figure 2 Schematic of the flame with a control volume at the leading edge showing various length scales.
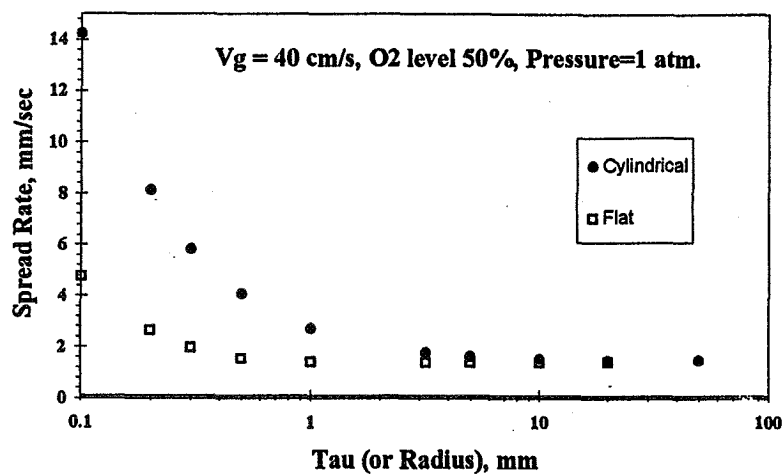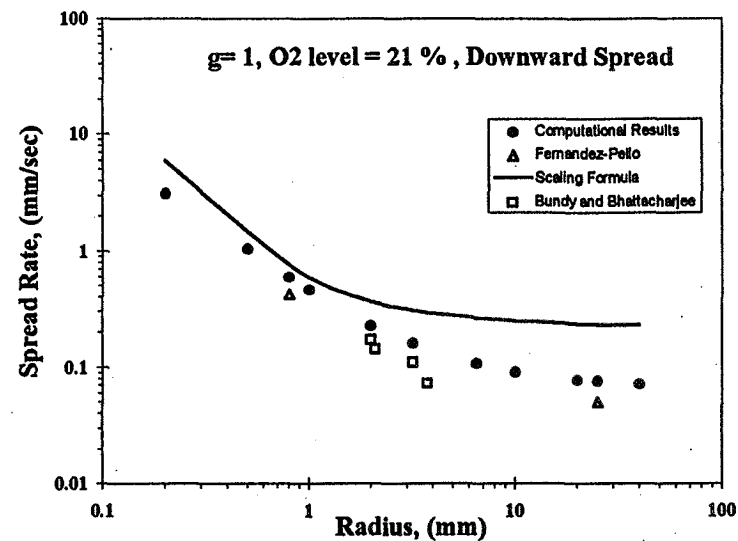

Figure 3 Comparison of computational, experimental, and scaling results for downward spread over cylindrical fuels under atmospheric conditions.

Figure 4 Computational spread rates for spread over flat and cylindrical fuels in the thermal regime.

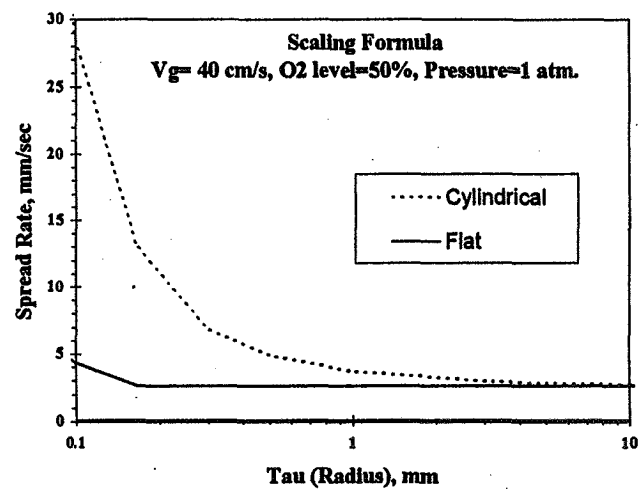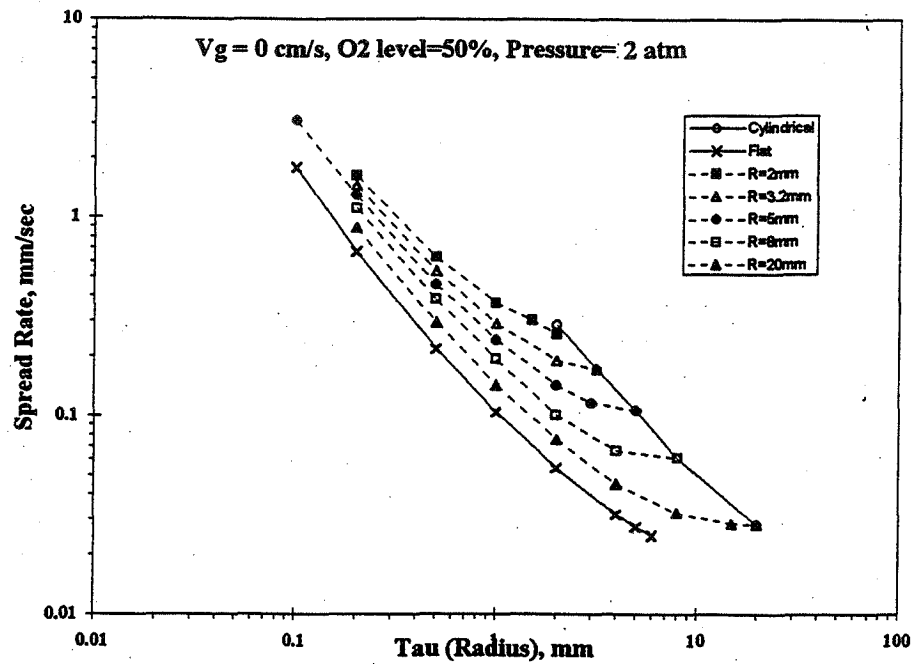Figure 5 Spread rates predicted from scaling in the thermal regime.

Figure 6 Computed spread rtes over cylindrical and flat surfaces in a quiescent microgravity environment. For "large" thickness no steady-state solutions are found. Radiation is not computed for each configuration but is frozen for one and impressed on the others.
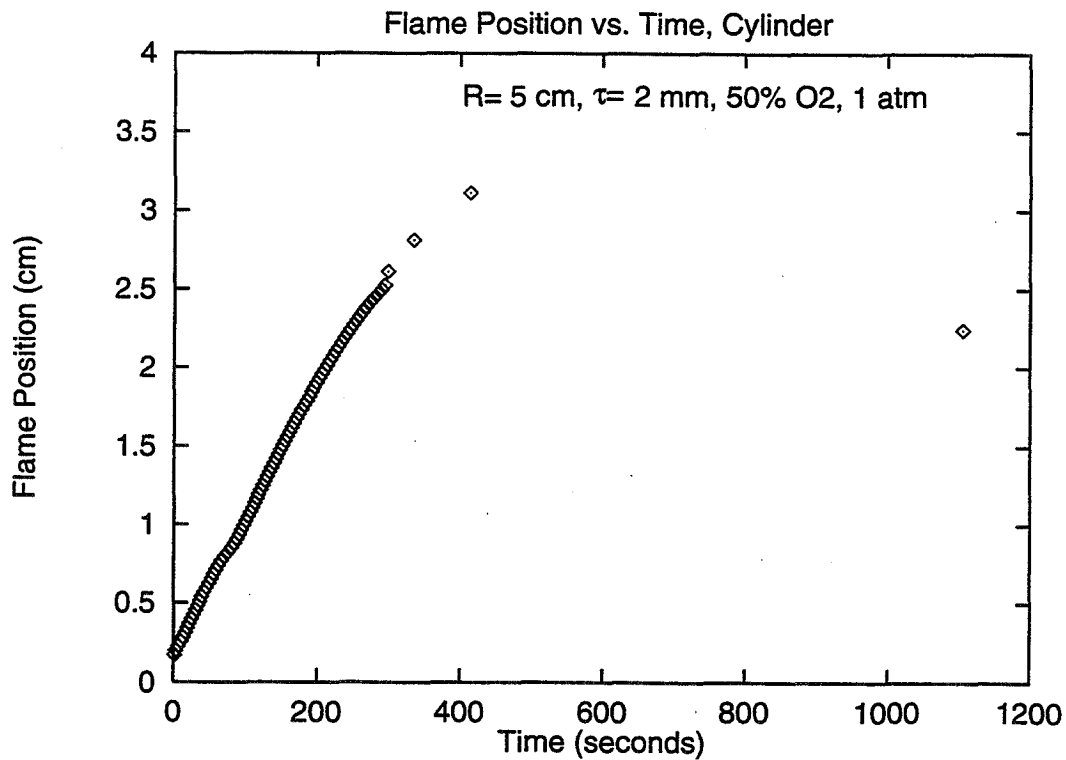

Figure 7 Computed flame position as a function of time for a "thick" cylinder with radiation computed as part of the solution as opposed to being impressed on the conditions as are the frozen radiation computations of Figure 6.

Diffusive and Radiative Transport in Fires Experiment: DARTFire[1]

SANDRA L. OLSON
NASA Lewis Research Center
Cleveland, Ohio

Robert A. Altenkirch[1] /Subrata Bhattacharjee[2] /Lin Tang[1] /Uday Hegde[3]
[1]Washington State University, Pullman, Washington/ [2]San Diego State University, San Diego, California
[3]NASA Lewis Research Center, Cleveland, Ohio

Introduction

The physics of opposed-flow flame spread over solid fuels is reasonably well understood for the situation in which the incoming flow speed is much grater than the flame spread rate. The propagation process is dominated by forward conduction heat transfer, either through the gas or solid, and the gas-phase kinetics (ref. 1-3). The characteristics of the spread process can generally be divided into a thermal regime, i.e., a regime in which gas-phase kinetics can be considered infinitely-fast, the spread rate being dictated by conduction hear transfer, and a kinetic regime in which gas-phase chemical kinetics is important. For thin fuels in the thermal regime, the spread rate is independent of flow speed while for thick fuels it is proportional to the flow speed (ref. 1). In the kinetic regime, increases in flow speed cause a reduction in spread rate that eventually leads to flame extinction through flame blowoff (ref. 1-4).

Reductions of flow velocity in the thermal regime are limited by the flow induced by the Earth's buoyancy, on the order of several 10's of cm/s. In a microgravity environment, however, slower flows may be obtained, and the spread process enters into a new regime, the microgravity regime (ref. 5). The diffusional length scale in the gas, L_g, is approximately the thermal diffusivity of the gas divided by the incoming flow speed. Reductions in flow speed tend to increase the this diffusional length, which increases the size of the flame and hence increases the importance of radiation. Qualitatively, the ratios of radiation loss from the flame, R_g, and radiation loss from the fuel surface, R_s, to conduction from the gas to the solid are (ref. 6):

$$R_g = \frac{4a_p\sigma}{\lambda_g}\left(\frac{T_f^4 - T_{env}^4}{T_f - T_v}\right)L_g^2 \; ; \; R_s = \frac{\varepsilon\sigma}{\lambda_g}\left(\frac{T_v^4 - T_{env}^4}{T_f - T_v}\right)L_g \tag{1}$$

and so the increase in L_g with a reduction in opposing flow speed results in an increase of the above ratios. For the speeds that may be encountered in a microgravity environment, the ratios are such that radiative phenomena are important. In Eq. (1), a_p is a Planck mean absorption coefficient, λ_g is the thermal conductivity of the gas, T_f and T_v are the flame and vaporization temperature, and T_{env} is a radiative environment temperature.

Recent results from the Solid Surface Combustion Experiment indicate that while for thin fuels radiation in a quiescent environment is important, and it causes a reduction in steady flame spread rates compared to the Earth-bound environment, for thick fuels, there appears to be no steady-state spread process in a quiescent environment (refs. 5,6). For thick fuels the possibility exists that, absent an opposing flow of sufficient strength to press the flame close enough to the fuel surface to allow the heated layer in the solid to develop, the heated layer fails to become "fully developed." The result is that the flame slows, and, because the incoming flow speed to the flame is the spread rate, there is an increase in the relative radiative loss from the flame, leading eventually to extinction. This potential inability of a thick fuel to develop a steady spread rate is not present for a thin fuel because the heated layer is the fuel thickness, which reaches a uniform temperature across the thickness relatively rapidly.

The objectives of the DARTFire experiment are to investigate the transition from ignition to either flame propagation or extinction in order to determine the characteristics of those environments that lead to flame evolution. In addition, flame shapes and measured gas-phase field variables, spread rates, radiative characteristics, and solid-phase regression rates are compared with model prediction. Thick PMMA is the fuel, which is subjected to a low speed forced flow in the microgravity environment of a sounding rocket flight while certain of the fuel samples are subjected to a laser flux in order to control the radiative environment of the flames. It is the interplay of the radiative and diffusional processes that determine if the flames spread at a steady rate or if they evolve to extinction in low velocity flows. The low speed threshold below which steady spread would appear not to be possible may be delineated in the course of the experiments.

Experimental

DARTFire sounding rocket hardware is shown in Figure 1. The flow supply system accounts for the first (left) third of the 10 foot overall length. The twin flow tunnels and diagnostics take up the middle third, and the electronics the last (right) third. Two experiments are conducted simultaneously during the approximately 6 minute experiment.

The mirror twin flow tunnels support from 1-20 cm/s flow through each tunnel with 10 cm x 10 cm flow crossection. Black PMMA samples, 2 cm long x 2 cm thick x 0.635 cm wide, are mounted in the floor of the duct 4 cm from the inlet flow straighteners.
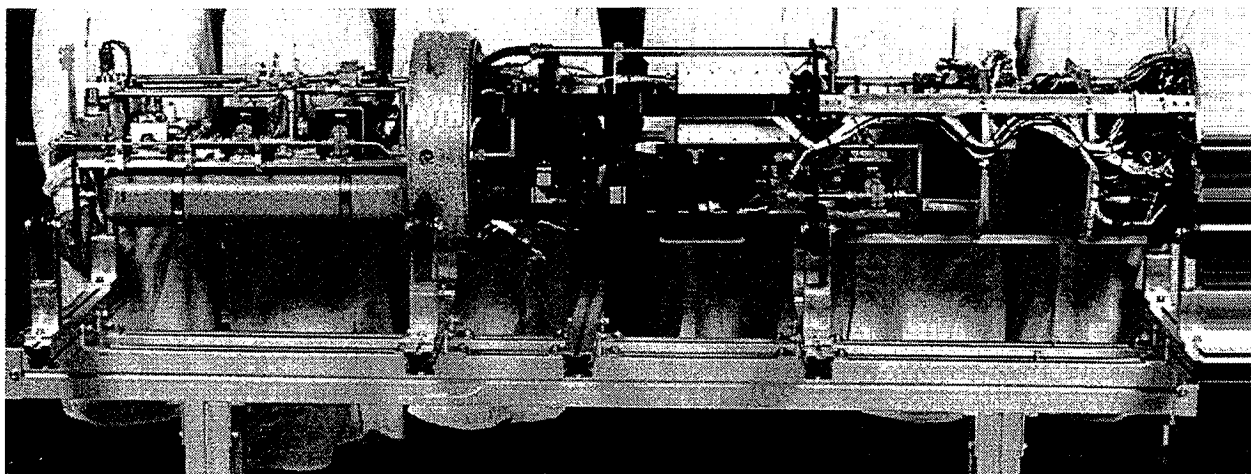

Figure 1. DARTFire sounding rocket hardware mounted on support rack. During launch, thick metal skins cover the payload.

A laser diode and associated lenses are mounted in the ceiling of one of the two ducts to provide an external radiant flux of up to 2 W/cm^2 onto the sample surface. The controlled external radiant flux allows the surface energy balance to be adjusted to compensate for radiant loss from the surface and gaseous species. The walls of the tunnels have windows for ultraviolet-visible and infrared imaging of the flame. These two primary diagnostic cameras are discussed below.

Other diagnostics include spot radiometers with a 6 mm diameter field of view to image the surface and gas-phase emissions over the spectral wavelength range of 8-14 μm. A total of 6 gas-phase type R and solid-phase type K thermocouples are used to record flame temperatures, surface pyrolysis temperatures, and in-depth temperatures from each sample during the experiment.

The test matrix is shown in Table 1. For those experiments in which there was a laser flux, the sample was ignited with the laser on, the laser was turned off following spread to the middle of the sample, and then the laser was turned back on toward the end of the spread process. Measured spread rates, and spread rates computed from the modelling effort described below, are also shown. Three flights have been conducted to date. A fourth flight is being requested for later this year with the conditions of 70% O_2, either 1 or 5 cm/s flow, with no laser flux, and 50% O_2 at 1 cm/s with a laser flux of 1 W/cm^2 but with the ordering of when the flame is subjected to the laser irradiation reversed from previous flights, i.e., the flame will initially spread with the laser off, and when the flame is approximately half-way along the sample, the laser would then be turned on.

UV-Visible Imaging

A multispectral intensified array video camera is used to image the flame. This has increased sensitivity over film and therefore can enable direct visualization of radical species by incorporating appropriate filters. Color images are obtained by combining red, green, and blue filtered images to obtain a 24-bit color composite image of the flame as part of the post-mission image

Table 1

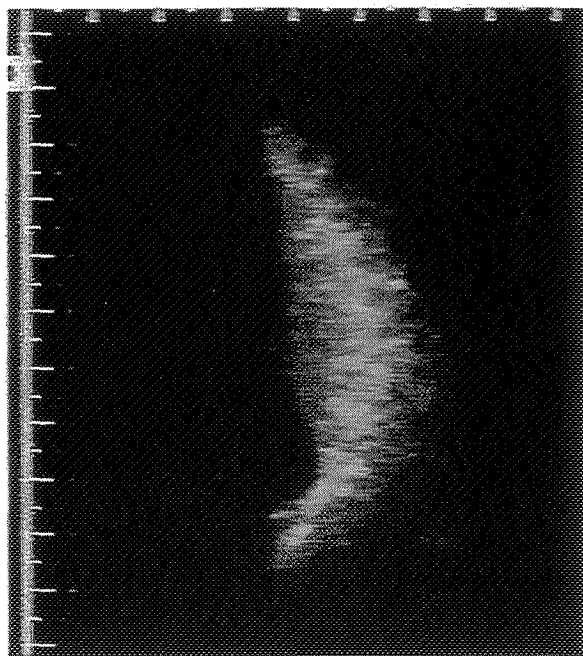| Flight Tunnel	Molar Oxygen Concentration, %	Bulk Flow Velocity, cm/s	Imposed Radiant Flux, W/cm^2	Meas V_f, mm/s Laser on/off	Model V_f, mm/s Laser on/off
1A	35	1	1	no ignition	
1B	50	1	0	- / 0.20	- / 0.10
2A	50	1	1	0.19/ 0.10	0.27/ 0.10
2B	50	5	0	- / 0.32	- / 0.31
3A	50	1	2	0.33/ 0.20	0.48/ 0.12
3B	50	10	0	- / 0.45	- / 0.47
4A (proposed)	50	1	1		
4B (proposed)	70	1 or 5	0		

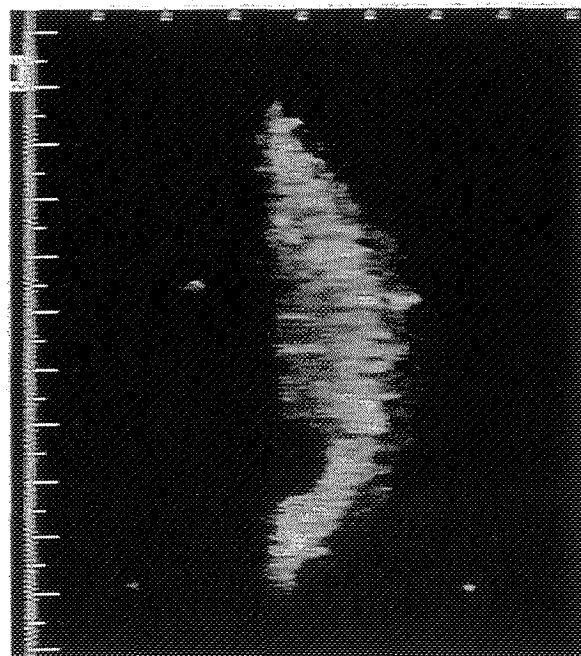Figure 2a: Reconstructed color image of flame from test 2A. Ticks are 0.5 mm.

Figure 2b: OH chemiluminescent image from same time as color image. Ticks are 0.5 mm.

processing. An example of this is shown in Figure 2a. The chemiluminescence of OH and CH radicals in the reaction zone is imaged through 20 nm bandwidth OH and CH filters at 310 nm and 430 nm, as shown in Figure 2b. The camera utilizes peak mode to avoid saturation of the bright flames against the dark background, and it optimizes exposure time for each filter image independently.

Infrared Imaging

Infrared emission from the gaseous combustion products is also monitored during the DARTFire experiment. A multispectral PtSi detector camera (Inframetrics, Inc. Model Infra-Cam PtSi FPA (256x256 pixel array)) was modified to include a 6-filter internal wheel. Filters include 1.87μm (H_2O), 2.7 and 4.3 μm (CO_2), 3.4 μm (MMA vapor), 4.8 μm (CO), and soot at 1.6 μm where the gas is "clear." Infrared imaging has provided an immense quantity of data regarding the species fields in the experiment. CO_2 and H_2O images are shown in Figure 4. Blackbody calibration of each filter provides an effective blackbody temperature for each video grey level.

Data Treatment

The side-view of the flame as it spreads across the fuel is captured by the infrared video camera. The rotating filter wheel with six filters having different bandwidths (two for CO_2 bands, one for H_2O band, one for MMA band, one for soot and one for total radiation) in front of the camera lens produces alternating frames of six different kinds. The video data are digitized frame by frame, and the frames are sorted and reassembled according to the filter numbers resulting in six separate digital video images of the flame.

Now consider two images at two different bands, l_1 and l_2, taken within one rotation of the filter wheel. The maximum time gap between these frames can be about 0.01 s (the wheel rotates at 60 Hz). The flame spread rate being on the order of 0.1 to 1.0 mm/s, the maximum displacement is about 0.01 mm between two images, which is insignificant. Suppose the signal recorded at a particular point in the flame is s_1 and s_2 corresponding to the bands l_1 and l_2 of CO_2. Using the calibration curve of the camera and filter transmittance, the ratio of the band intensities i_1 / i_2 can be obtained from s_1 and s_2.

In terms of bandwidth A_1 and A_2 (ref. 7), $i_{b1} / i_{b2} = A_2 i_1 / A_1 i_2$, which can be solved for temperature if A_1 and A_2 are known. From a representative theoretical flame, A_1 and A_2 can be obtained using a narrow-band radiation program such as s RADCAL (ref. 8). The temperature calculated from the blackbody intensity ratio can be used to refine the calculation of A_1 and A_2. The final temperature though will be a function of CO_2 concentration of the theoretical flame.

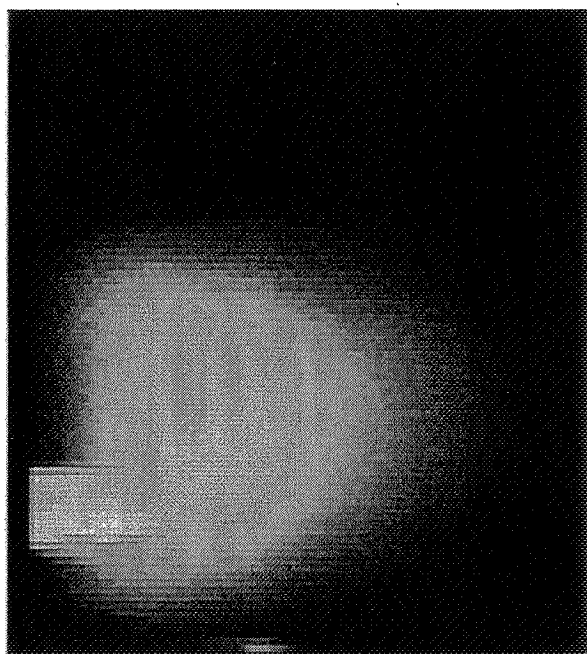Figure 3a: 1.87 μm band H_2O image from test 2A. Approximately same time and scale as Fig. 3.

Figure 3b: 4.3 μm band CO_2 image from test 2A. Approximately same time and scale as Fig. 3.

A check on the theoretical prediction of the CO_2 concentration can be made by utilizing the surface temperature measurements. At a point on the fuel surface, A_2 / A_1 can be evaluated experimentally from the blackbody intensity ratio, because the temperature and the intensity ratios are both known. For a given temperature RADCAL can accurately predict the concentration of CO_2 from the value of A_2 / A_1.

Image data for OH and CH from the Xybion camera may be used to infer relative OH distributions and flame location (ref. 9). Ultimate comparison to computed flame position and structure requires a more detailed model of the gas-phase combustion chemistry in which intermediates such as OH are computationally tracked (refs. 9,10).

Modelling

The mathematical formulation for the forced, opposing flow configuration is patterned after earlier formulations (refs. 5,11). The numerical solution employs the finite-volume formulation of Patankar (ref. 12) for the hydrodynamic calculations and the TTNH formulation of Grosshandler (ref. 8) for line-of-sight radiation calculations with the species, CO_2, H_2O, and MMA vapor. The computational code has been validated by comparing the numerical result with analytical solutions available for simpler models. Both steady and unsteady versions of the numerical code are available, but for the results reported here, only the unsteady version was used.

Spread Rate Results

Spread rates increase with increasing flow speed, both experimentally and computationally, and the modelling predicts relatively well the dependence of spread rate on incoming oxidizer flow velocity. The laser flux increases the spread rate, consistent with previous observations for downward spread at normal gravity (ref. 13). For the fuel that is preheated with the laser prior to flame arrival, when the laser is turned off, the spread rate decreases, but to a value higher than what it is under identical flow conditions without preheating. The effect of the laser preheating appears to be to increase the fuel temperature near the surface in the solid, which results in the increased spread rate (ref. 13). The experimental spread rate reported for experiment 1B appears to be higher than expected, i.e., it is equivalent to the spread rate for the same flow conditions but with a laser flux of 1 W/cm^2 from experiment 2A, although it might be expected to be slightly less than the result from experiment 2A with the laser off consistent with modelling results. The proposed flight matrix point was selected in part to investigate the repeatability of the experiments, particularly at the 1 cm/s flow speed, so as to determine the veracity of the spread rate measurement in experiment 1B.

In previous opposed-flow results for spread over PMMA (ref. 3) in an Earth-bound apparatus, three flame spread regimes were identified, one at "low flow velocities" in which the spread rate is independent of opposing flow, low velocity here being approximately below 90 cm/s for 50% O_2, a regime in which the spread rate is proportional to the flow speed to a power, the thermal regime, and one in which the spread rate decreases with increasing flow speed until blowoff occurs. The low velocity regime occurs because of the influence of buoyancy induced flow, absent in the DARTFire experiment so that the thermal regime may be extended to lower flow velocities. In the thermal regime, the dependence of spread rate on incoming flow speed, U_∞, is, from ref. 3, approximately $V_f \propto U_\infty^{0.43}$, above about 90 cm/s up to where the kinetic regime appears at about 450 cm/s. This dependence from the experimental and computational results in Table 1, excluding experiment 1B, persists down to an opposing flow speed of about 5 cm/s, at which point the dependence of V_f on U_∞ increases to about $V_f \propto U_\infty^{0.62}$. The change in the dependence signals the onset of radiative processes, which as the flow speed is reduced further, eventually lead to the unsteady spread behavior that leads to extinction observed in quiescent, microgravity flame spread experiments.

The unsteadiness and ultimate spread to extinction is, as mentioned above, due to the effects of radiation. Increased radiation causes the flame to shrink in size, the flame finds itself in a region of decreasing presence of oxygen, and the distance through which oxygen must diffuse to reach the flame, being unaffected by radiation, grows in time until eventually the oxygen supply to the flame is insufficient to sustain it, and the flame extinguishes. Transition from the classical thermal regime of flame spread over thick PMMA for 50% O_2 to the microgravity regime in which radiation is important and will lead to extinction in a quiescent environment appears to occur for flows on the order of 5 cm/s. This threshold opposing flow should be a function of oxygen concentration.

Summary

A low velocity, opposed-flow, flame spread experiment designed for execution on a sounding rocket has been described. Early results of infrared and ultraviolet-visible imaging using video cameras and narrow band filters have been described along with planned digital image data reduction. Measured and computed spread rates show that the classical thermal regime for flame spread over thick PMMA persists, for 50% O_2, down to about 5 cm/s, at which point a transition to a microgravity regime in which radiation eventually leads to extinction in at least a quiescent environment. The microgravity regime of flame spread is then distinct from the thermal and kinetic regimes previously identified.

References

1. de Ris, J.N. (1969). *Twelfth Symposium (International) on Combustion*, The Combustion Institute, Pittsburgh, pp. 241-252.
2. Altenkirch, R.A., Eichhorn, R., and Shang, P.C. (1980). *Combustion and Flame* 37, 71-83.
3. Fernandez-Pello, A.C., Ray, S.R., and Glassman, I. (1981). *Eighteenth Symposium (International) on Combustion*, The Combustion Institute, Pittsburgh, pp. 579-587.
4. Altenkirch, R.A., Eichhorn, R., and Rizvi, A.R. (1983). *Combustion Science and Technology* 32, 49-66.
5. West, J., Tang, L., Altenkirch, R.A., Bhattacharjee, S., Sacksteder, K., and Delichatsios, M.A. (1997). Quiescent Flame Spread Over Thick Fuels in Microgravity, *Twenty-Sixth Symposium (International) on Combustion*, The Combustion Institute, in press.
6. Bhattacharjee, S., Altenkirch, R.A., and Sacksteder, K. (1996). *Journal of Heat Transfer* 118, pp. 181-190.
7. Siegel, R. and Howell, J.R. (1981). *Thermal Radiation Heat Transfer*, Hemisphere Publishing Corporation, McGraw-Hill Book Company, New York.
8. Grosshandler, W.L. (1980). *International Journal of Heat and Mass Transfer* 23, 1447-1459.
9. Marchese, A.J., Dryer, F.L., Nayagam, V., and Colotonio, R.O. (1997). Hydroxyl Radical Chemiluminescence Imaging and the Structure of Microgravity Droplet Flames, *Twenty-Sixth Symposium (International) on Combustion*, The Combustion Institute, in press.
10. Wolverton, M.K., Altenkirch, R.A., and Tang, L. (1997). A Comparison of Single and Multi-Step Chemical Kinetics Models in Opposed-Flow Flame Spread over Cellulosic Fuels, *Central States Section of the Combustion Institute*, to appear.
11. Bhattacharjee, S. and Altenkirch, R.A. (1991). *Twenty-Third Symposium (International) on Combustion*, The Combustion Institute, Pittsburgh, pp. 1627-1633.
12. Patankar, S.V. (1980). *Numerical Heat Transfer and Fluid Flow*, McGraw Hill, New York.
13. Fernandez-Pello, A.C. (1977). Combustion Science and Technology 17, 1-9.

SOLID INFLAMMABILITY BOUNDARY AT LOW SPEED (SIBAL)*

JAMES S. T'IEN[†], Kurt R. Sacksteder[‡], Paul V. Ferkul[#], Hasan Bedir[†], Hsin-Yi Shih[†],
Paul S. Greenberg[‡], Richard D. Pettegrew[†], Nancy Piltch[‡], and David Frate[‡]

Introduction

This research program is concerned with the effect of low speed flow on the spreading and extinction processes of flames over solid fuels. We are particularly interested in the flammability boundary and the near-limit flame behavior in a microgravity environment. Primary attention is given to flame propagation in concurrent flow -- the more hazardous situation from the point of view of fire safety. Both theoretical modeling and experimental research are in progress.

This project passed the Science Concept Review (SCR) in 1996. As a result, the experiment continues on the flight definition path, and is currently scheduled to be performed in the Space Station Fluids and Combustion Facility (FCF).

Flame Spread Model

Modeling efforts on low-speed concurrent-flow flame spread over solids have advanced significantly. First, the model with only surface radiation [1] was extended to include gas radiation from CO_2 and H_2O for forced flow using a discrete-ordinate method assuming gray, participating media [2]. More recently, this model was modified to study purely buoyant upward flame spread in reduced gravity [3]. In this investigation, it is found that
  (1) For thin solids, steady upward flame spread is possible (at least for the low-gravity levels investigated).
  (2) The flame·lengths and spread rates are approximately proportional to gravity level.
  (3) A low-gravity flame quenching limit, attributed to radiative loss, is predicted.
  (4) Flame radiative feedback constitutes an important part of the solid surface energy balance.
  (5) The quantitative prediction of the flame spread rate alone does not give a good indication as to the whether the theoretical model is complete.

The model in [2] was also extended to flame spread inside a flow tunnel [4]. Because of both the restrictions on the size of the hardware and the rate of supply of fresh gases in a flight experiment in space, a flow tunnel of finite cross-sectional area and limited length has to be used. However, a finite tunnel height can cause substantial influence on the flame through gas dynamic interaction. In addition, the radiative interaction between the flame, the burning solid, and the tunnel wall can alter the energy balance in the system.

The model predictions shown in fig. 1 compare flammability boundaries with and without tunnel walls present. In the tunnel case, the half-height is 5.5 cm, a uniform flow starts 8 cm upstream from the solid burnout point (fixed in space by a feedback system, see fig. 3), and the tunnel wall is assumed to have no radiation reflection. Both of these two flammability boundaries are U-shaped. However, the case with the tunnel is shifted to the left, i.e., extinction occurs at lower inflow velocities.

To understand the reason for this shift of extinction boundary, we computed the flow velocity vectors and the flame shapes as a function of tunnel wall height (fig. 2). When the tunnel height, D_h, is decreased from 10 cm to 2 cm, the flame lengths increase dramatically. This is the result of the flow field change. At large channel height, thermal expansion of hot combustion products can have a velocity component in the vertical direction (perpendicular to solid surface). But at small channel height, this is forbidden. Consequently, the longitudinal velocities are greatly increased as can be seen for $D_h = 2$ cm in fig. 2. These larger velocities parallel to the solid surface increase the rate of flame conductive heat transfer to the solid which produces more fuel vapor and a longer flame. We refer to this as the flow channeling effect.

From $D_h = 2$ cm to 1 cm, fig. 2 shows a decreasing flame length because of two effects. First, the flames are very close to the tunnel wall which is maintained at 300 K in the computation. The conductive loss cools the flame and the combustion products, reduces the thermal expansion effect, and shortens the flame. Second, there is less oxygen available in the narrower channel since the flow area is reduced.

The effect of thermal radiation reflected from the tunnel wall was also studied in [4]. Increasing wall reflectivity was found to lengthen the flame and increase the spread rate, which is expected due to the lessening of heat loss from the system. The study in [4] demonstrates that the influence of the experimental setup on the flame can be substantial. Furthermore, a detailed modeling study is needed both to identify the experimental design parameters and for meaningful comparison to experimental results.

Flame Radiation Studies

Since thermal radiation is a key factor affecting the flame behavior in low-speed flows, considerable effort has been spent in the last couple of years on improving the computational scheme for flame radiation. Using a one-dimensional stagnation-point solid-fuel diffusion flame as a test case and CO_2 and H_2O as the radiation participating gases, various gray and non-gray models were evaluated for accuracy and computational time [5]. This study shows that
(1) Low-stretch diffusion flames are in general not optically-thin.
(2) The use of a Planck-mean absorption coefficient under-predicts absorption and over-predicts emission.
(3) The three non-gray models (narrow band, wide band, and sum of gray gases) give comparable predictions, but the computational times can be quite different.

In [5] and [6], we further show that if only the heat flux to the solid surface is important and a gray gas model is preferred (e.g., for computational efficiency), it is possible to multiply the Planck-mean absorption coefficient by a correction factor to obtain reasonably accurate results. For one-dimensional and quasi one-dimensional flames, an empirical relation to determine this correction coefficient is suggested in [6]. A review article on radiative extinction of diffusion flames summarizes this and other aspects [7].

Experimental Work

The ground-based experiments done to date consist of two series of drop tower tests using a sample translation carriage, and aircraft tests using a fuel positioning device. In addition, two series of glovebox tests were recently performed on the Space Shuttle and Mir Space Station as a preliminary for the proposed full-scale experiment.

In the drop tower tests [8, 9], the relative flow between the gas and solid fuel was generated by moving the sample through a quiescent atmosphere (This approach is well-suited to studying low-speed flows given the time and space limitations of the drop tower). The effect of varying flow speed, oxygen percentage, and ignition technique was examined. In summary, these tests provided an indication of the general flame appearance and behavior, and agreed qualitatively with model predictions. However, the flames did not quite reach steady state, restricting direct comparison to the model results.

A theoretical expression of the time needed to reach steady state was derived based on pyrolysis length and spread rate. Using the thinnest "practical" fuel[1], we can use the computed results to evaluate the expression: the time needed to reach steady state turns out to be about 16 seconds. Clearly, available drop tower experiment time is inadequate.

Besides this, in the time it takes a flame to reach steady state, it will have spread some distance. This makes sizing the chamber and positioning any viewing windows difficult or impossible. Therefore, to permit the flame to reach steady state in a reasonably sized volume, a fuel positioning device, called the Solid Fuel Delivery System (SFDS), was built. The central idea of this experimental concept is maintaining the flame fixed in space as the solid fuel is consumed by feeding fuel into the flame at the necessary rate (fig. 3).

Reduced gravity aircraft tests with this hardware were performed. The main purpose was to examine the engineering concepts in microgravity, and the results were very encouraging. Ignition was attained reliably using a retractable, hot-wire. The fuel remained flat, and the flame was held stationary during combustion. Fuel fed smoothly into the flame zone, effectively providing an unlimited supply, while allowing long duration burns [11].

The parabolic trajectories provided reduced-gravity durations of up to 25 seconds, which would seem long enough to reach steady state. However, both experimental results and model predictions demonstrated that the residual g-level (10^{-2} g/g_E) disturbed the flame to such a degree that the objectives of the project were not achievable using airplanes.

Ultimately, the only way to conduct long-duration experiments in microgravity is by going to space, and in fact, hardware for this project is currently being developed to that end. Since typical flight project development time is several years, we took

---

[1]The flame will quench if the fuel becomes too thin [10].

advantage of an opportunity to conduct a preliminary, small-scale space experiment. This was called the Forced Flow Flame Spreading Test (FFFT), and was able to be developed and flown quickly because it was small and simple. The FFFT utilized the Microgravity Glovebox which provided containment, power, and viewing access.

The FFFT hardware consisted of a low-speed wind tunnel within which fuel samples could be burned. The edge view of the flame was photographed using a 35 mm camera, and the top view was recorded on videotape. Up to six thermocouple displays provided flame and fuel temperature data. Gas sample bottles were used to collect products of combustion from selected tests.

The first series, conducted in the STS-75 (USMP-3) mission in March 1996, consisted of two solid fuel configurations: 1) thin, flat samples of ashless filter paper (cellulose) and 2) cylindrical samples of cast cellulose formed around a cylindrical cartridge heater. In this series, concurrent flow velocities were varied from 1-8 cm/sec [12]. The second series, conducted aboard the Russian Mir Space Station in August 1996 consisted of flat samples of cast cellulose of different thicknesses, and cylinders of polyethylene (conventional wire insulation). In this series, the flow velocity was fixed at 3 cm/sec. Below we will briefly describe and summarize some of the observations for the thin, flat samples.

Flame and Fuel Behavior

In fig. 4, the edge view of a flame in 1 cm/s flow (from left to right) is shown. The flame appears dim blue and diffuse, typical for microgravity. The model prediction of the same case is shown also. We assume that the predicted fuel consumption rate distribution correlates with the visible flame. The flame shape agrees qualitatively with the model prediction, in that the contours follow the flame outline. However, the quantitative comparison depends on which particular fuel consumption contour coincides with the minimum flame luminosity. In earlier work, the fuel consumption rate of 10^{-4} g/cm^3/s was found to give a good indication of the visible flame, based on drop tower results [1].

Even for the thinnest fuel, the time it takes for the flame to consume the sample is around 15 seconds. In fig. 5, two temperature traces are shown for such a sample burning in an airflow of 3 cm/s. Looking at the thermocouple initially mounted in the solid fuel, we can see that it is first heated to approximately 400 C, at which point the temperature levels off due to pyrolysis. Then as the fuel is burned out, the flame moves past the thermocouple yielding a temperature peak. The gas-phase thermocouple, located about 1 cm above the fuel, indicates a maximum temperature of around 1100 C. The temperature traces observed agree qualitatively with the steady model predictions, but because the sample size is limited, the flames have not yet reached steady state.

Despite the limitations of this small and simple experiment, there are several findings which are helpful to the development of the full-scale space experiment. The most valuable is the behavior of the ashless filter paper in concurrent-flow flame spreading that we had not seen in our earlier ground-based testing. In the longer tests, fuel under the lengthier flames fractured (cracked) in the pyrolysis zone, propagating the flame in a highly three-dimensional manner. The cracks also permitted fuel curling, further complicating the flow field. Since making these observations we have begun a program to screen various types of thin solid fuel candidates using low-pressure upward flame spread tests. In addition, the development of the glovebox experiment provided an opportunity to design an ultra-low-speed flow tunnel that is needed in the proposed space experiment. The control and measurement of flow magnitude and uniformity in this regime is a real challenge since conventional and advanced flow measurement techniques fail at low velocities or interfere in some way with the weak flames there.

Summary

This project will attempt to validate the theoretical prediction of the flammability boundary for a thin combustible solid in low-speed, forced-concurrent flow. So far, we have utilized the available ground-based facilities (drop towers and aircraft) as much as possible, and have gone as far as we can here. The extensive experiments we conducted show that the time required to determine the solid flammability limit and for the flame to reach steady state is not sufficient in ground-based facilities. Further, the g-jitter in an airplane flying a parabolic trajectory was shown to introduce too high a flow disturbance or too short a test time during free float. The small-scale glovebox experiment yielded useful but incomplete information. The only way we can obtain complete and meaningful experimental results to validate the theory adequately is by performing an extended microgravity experiment using advanced diagnostic techniques.

In light of the volume and stowage limitations of spacecraft, we have developed a novel flammability test device which facilitates the proposed experiment. The proto-type version of this device was tested successfully in low-gravity aircraft trials. This concept will permit a systematic investigation of the model-predicted flammability boundary and critical low-oxygen limit. The existence of this limit for materials is not only of scientific interest, but has significant implications for spacecraft fire safety.

References
1   Ferkul, P. V. and T'ien, J. S.: A Model of Low-Speed Concurrent Flow Flame Spread Over a Thin Fuel, Combustion Science and Technology, Vol. 99, No. 4-6, pp. 345-370 (1994).
2   Jiang, C.-B.: A Model of Flame Spread Over a Thin Solid in Concurrent Flow with Flame Radiation, Ph.D. Thesis, Department of Mechanical and Aerospace Engineering, Case Western Reserve University (1995).
3   Jiang, C.-B., T'ien, J. S., and Shih, H.-Y.: Model Calculation of Steady Upward Flame Spread Over a Thin Solid in Reduced Gravity, Twenty-Sixth Symposium (International) on Combustion. In press.
4   Shih, H.-Y. and T'ien, J. S.: Modeling Wall Influence on Solid-Fuel Flame Spread in a Flow Tunnel, AIAA Paper 97-0236 (1997).
5   Bedir, H., T'ien, J. S., and Lee, H. S.: Comparison of Different Radiation Treatments for One Dimensional Diffusion Flame, Fall Technical Meeting of the Eastern States Section of the Combustion Institute (1996).
6   Rhatigan, J., Bedir, H., and T'ien, J. S.: Gas Phase Radiative Effect on the Burning and Extinction of a Solid Fuel. Submitted to Combustion and Flame.
7   T'ien, J. S. And Bedir, H.: Radiative Extinction of Diffusion Flames: A Review, Asia-Pacific Conference on Combustion, Osaka, Japan, May 12-15 (1997).
8   Grayson, G. D.: An Experimental Study of Low-Speed Concurrent Flow Flame Spread Over a Thin Fuel, M.S. Thesis, Department of Mechanical and Aerospace Engineering, Case Western Reserve University (1991).
9   Pettegrew, R. D.: An Experimental Study of Ignition Effect and Flame Growth Over a Thin Solid Fuel in Low-Speed Concurrent Flow Using Drop-Tower Facilities, M.S. Thesis, Department of Mechanical and Aerospace Engineering, Case Western Reserve University (1995).
10 DiBlasi, C.: Process of Flames Spreading Over the Surface of Charring Fuels: Effects of the Solid Thickness, Combustion and Flame, Vol. 97, pp. 225-239 (1994).
11 Ferkul, P. V., T'ien, J. S., Pettegrew, R. D., and Sacksteder, K. R.: A Novel Device for Studying Flame Spread Over Thin Solid Fuel, Fall Technical Meeting of the Eastern States Section of the Combustion Institute (1996).
12 Sacksteder, K.R., T'ien, J.S., Greenberg, P.S., Ferkul, P.V., Pettegrew, R.D., and Shih, H.-Y.: Forced Flow Flame Spreading Test: Preliminary Findings from the USMP-3 Shuttle Mission, Joint Launch Plus One Year Review of USML-2 and USMP-3, NASA Conference Publication (1997).
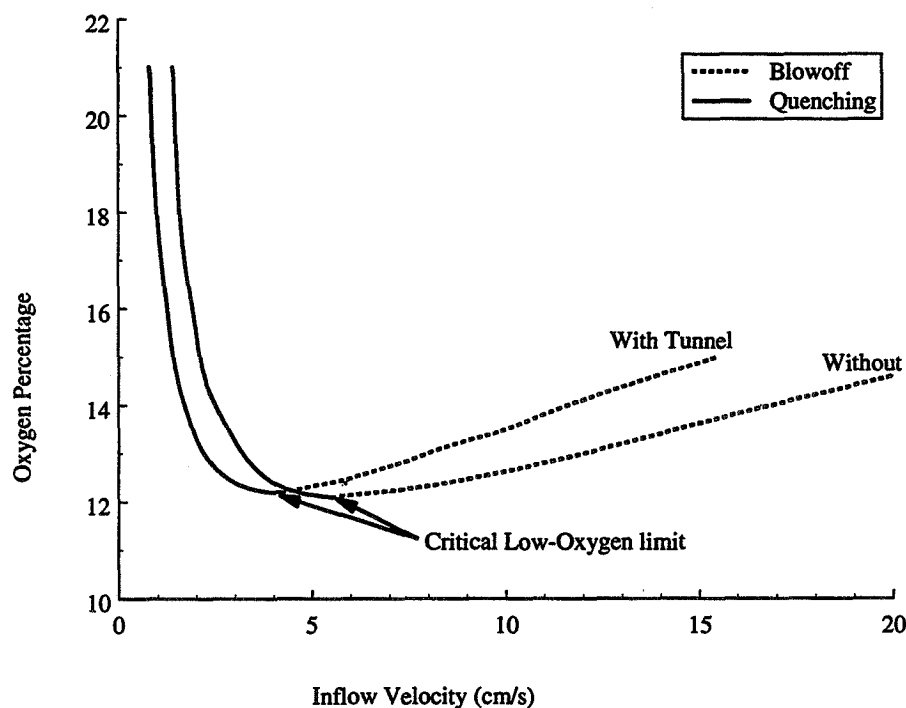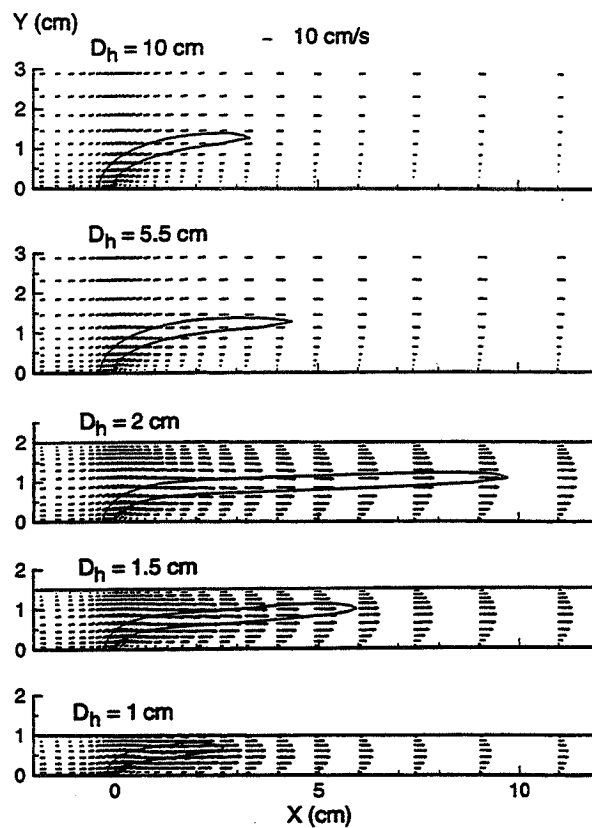
Figure 1. Flammability Boundary.

Figure 2. Flame Shape and Flow Structure (Velocity Vectors) for Different Tunnel Heights.
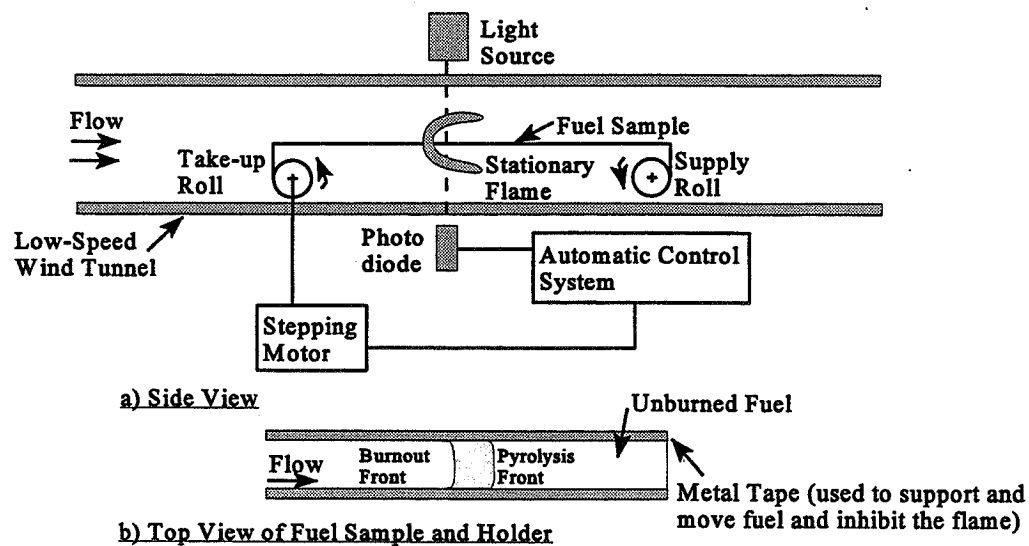

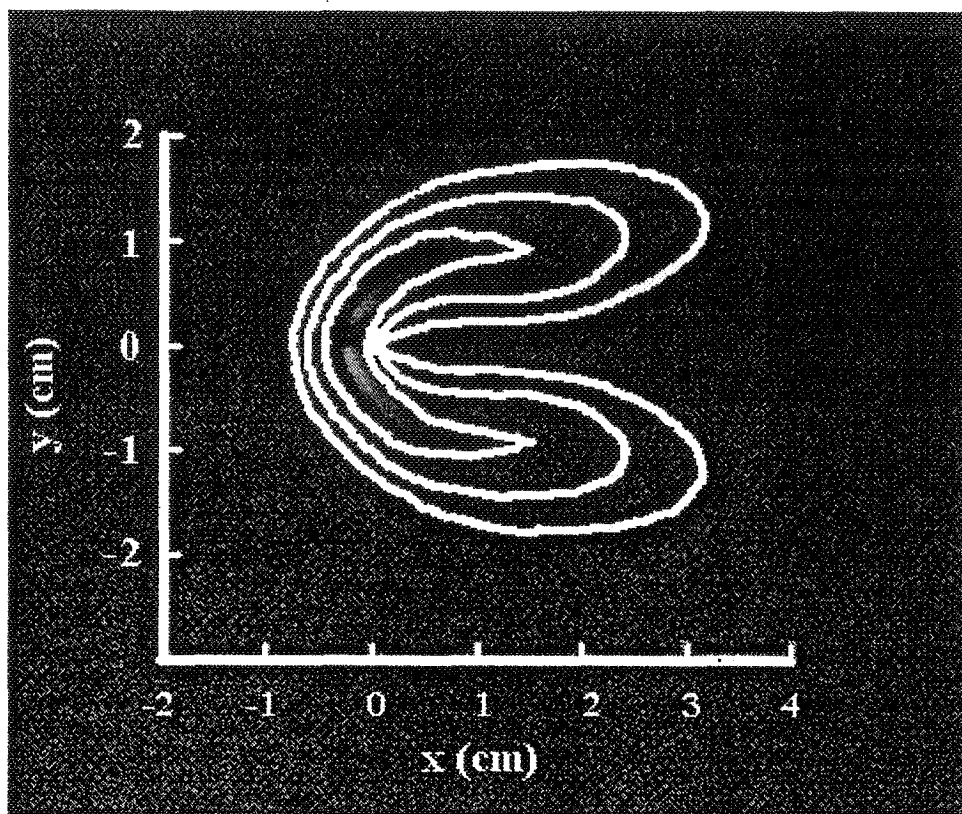Figure 3. Schematic of Solid Fuel Delivery System.

Figure 4. Comparison of Visible Flame and Computed Fuel Consumption Rate Contours. The dim flame essentially fills the innermost contour, 10^{-4} g/cm^3/s. A factor of ten separates contours.
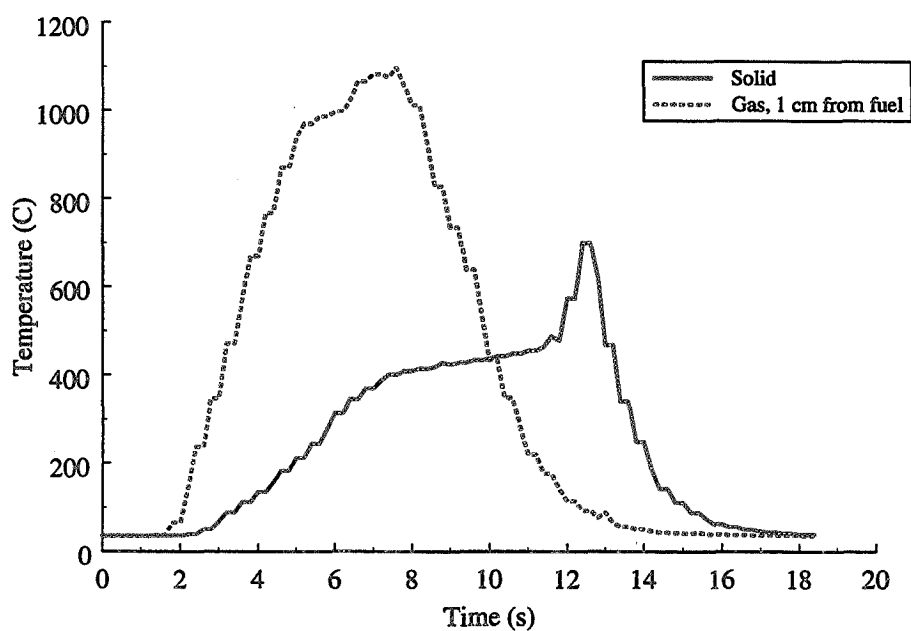

Figure 5. Temperature Traces for Thinnest Fuel in 3 cm/s Airflow, from FFFT Glovebox Experiment.

FLOW EFFECTS ON THE FLAMMABILITY DIAGRAMS OF SOLID FUELS

J. L. Cordova, J. Ceamanos, A. C. FERNANDEZ-PELLO
Department of Mechanical Engineering
University of California at Berkeley
Berkeley, CA 94720-1740

and

R. T. Long, J. L. Torero, J. G. Quintiere
Department of Fire Protection Engineering
University of Maryland
College Park, MD 20742-3031

ABSTRACT

A research program is currently underway with the final objective of developing a fundamental understanding of the controlling mechanisms underlying the flammability diagrams of solid combustible materials and their derived fire properties. Given that there is a high possibility of an accidental fire occurring in a space-based facility, understanding the fire properties of materials that will be used in such facilities is of critical importance. With this purpose, the flammability diagrams of the materials, as those produced by the Lateral Ignition and Flame Spread Test (LIFT) apparatus and by a new forced flow device, the Forced Flow Ignition and Flame Spread Test (FIST) apparatus, will be obtained. The specific objective of the program is to apply the new flammability apparatus, which will more accurately reflect the potential ambient conditions of space-based environments, to the characterization of the materials for space applications. This paper presents a parametric study of oxidizer flow effects on the ignition curve of the flammability diagrams of PMMA. The dependence of the ignition delay time on the external radiant flux and either the sample width (LIFT) or the flow velocity (FIST) has been studied. Although preliminary, the results indicate that natural and forced convection flow changes, affect the characteristics of the ignition curves of the flammability diagrams. The major effect on the ignition time appears to be due to convective transfer variations at the fuel surface. At high radiant fluxes or high flow velocities, however, it appears that gas phase processes become increasingly important, affecting the overall ignition delay time. A numerical analysis of the solid fuel heating and pyrolysis has also been developed. The theoretical predictions approximate the experiments well for conditions in which the gas phase induction time is negligible.

INTRODUCTION

The possibility of an accidental fire in a space-based facility is a primary safety concern. It is, therefore, of critical importance to characterize the fire properties of materials that will be used in such facilities. At present, however, no testing methodology exists that specifically addresses the fire properties of materials subjected to conditions expected in space installations. Current tests are based on the common theory that materials in reduced-gravity burn less readily than in normal-gravity conditions. Although this is probably true in a quiescent microgravity environment (where diffusion is the primary transport mechanism), spacecraft environments generally have low velocity air currents that are produced by their ventilation and heating systems (of the order of 0.1 m/s). Recent experiments of flame spread in microgravity [1] show that at these low velocities, ignition is vigorous, flame spread is faster, and the limiting oxygen concentration for flame spread is lower than in normal-gravity. Furthermore, CO removal and oxygen replenishing systems in the space facilities cause oxygen concentration fluctuations which also have an effect on the burning of materials. It is, therefore, critical to establish a test for fire conditions that will properly represent the fire hazards that are expected to be encountered in a space installation.

The Lateral Ignition and Flame Spread Test (LIFT) apparatus [2], although not considered a general fire test method, can provide important information about the ignition and flame spread characteristics of a material, including such fire properties as critical radiant flux for ignition, ignition delay, ignition temperature, flame spread rate constants, and extinction limit. These fire properties are extracted from the flammability diagrams of the material, which are constructed from the data obtained by means of the LIFT apparatus, and consist of curves of ignition delay and flame spread rate as a function of the value of an externally applied radiant flux. The LIFT apparatus, however, relies on the effect of buoyancy for the transport of heat and mass, and

405

consequently, cannot be used in microgravity. Despite this, the fundamental concepts underlying its operation can be used to develop a similar test that reflects more accurately the specific conditions expected in a space based facility.

The overall objective of the present work is to study the effects of gravity on the flammability diagrams of solid combustible materials and the fire properties derived from such diagrams. The specific objectives are: 1) to develop a new flammability apparatus that will better reflect the potential ambient conditions of space-based environments, *i.e.*, microgravity, low velocity flow, oxygen concentrations slightly above and below that of air, and 2) to use the apparatus to obtain more appropriate flammability diagrams for common materials used in space facilities, such as plastics, cable jacketing, electronic boards, etc. The new test apparatus, FIST, for Forced-flow Ignition and Flame Spread Test, will be based on forced flow transport of heat and mass, but will still provide information about the ignition delay and flame spread rate (opposed and co-current) of combustible materials as a function of the external radiant flux for a range of oxidizer flow velocities and oxygen concentrations.

Since the theoretical background of ignition and flame spread in forced and natural convective conditions is fundamentally the same, the LIFT and FIST flammability diagrams are expected to be similar, although some of the fire properties obtained with the latter will be dependent on the velocity and oxygen concentration of the flow. Comparison of the flammability diagrams of a few well known materials obtained in the LIFT and FIST apparatuses in normal-gravity, and in the FIST apparatus in microgravity, will provide information about the effects of gravity on the fire properties of the materials tested. This information will be used to develop a conceptual design for a test of the flammability of materials in microgravity. It is envisioned that the knowledge gained could result in a standard testing procedure to determine fire hazard characteristics of materials in a space based environment.

BUOYANCY EFFECTS ON THE LIFT IGNITION DIAGRAMS

LIFT is an ASTM standard for determination of material ignition and flame spread properties; details on the dimensions and geometrical characteristics of this device can be found in Ref. 2. The theory behind this test and the methodology of application have been previously established, and may be found in Refs. 3,4. LIFT consists of two independent tests, namely a piloted ignition test and a lateral flame spread test. For both tests, the fuel sample is placed in front of a radiant panel that forms an angle of 15° with the fuel surface with the minimum distance between fuel and panel being 125 mm (Fig. 1). The radiant panel provides a heat flux distribution over the fuel surface which is nearly uniform in the zone where sample and heater panel are closest to each other, and decays as the distance between the sample and the panel increases. The ignition sample (155 mm x 155 mm) is placed in the region of nearly uniform heat flux while a larger sample (155 mm x 806 mm) is used to study the effect of external radiation on lateral flame spread.

To study the effect of scale on the fire properties obtained by the LIFT, the sample dimensions will be systematically reduced, and ignition and flame spread tests will be conducted to construct the flammability diagrams. Variation of the characteristic length scale of the experiment may be approached in two ways: changing the fuel size or changing the characteristic length scale that controls natural convection, and consequently the magnitude of the flow that will bring the pyrolyzate towards the pilot flame. The objective is to determine a minimum sample size, independent of the flow, that will provide consistent fire properties in order to asses the effect that natural convection might have on test results.

A simple scaling analysis shows that two important parameters controlling the ignition phenomenon are the Nusselt and the Sherwood numbers. For a vertical hot plate subjected to natural convective transport, these non-dimensional numbers are respectively:

$$Nu \approx Ra_L^{1/4} \quad \text{and} \quad Sh \approx Le^{1/3} Ra_L^{1/4} .$$

Here, Le is the Lewis number, and Ra, the Rayleigh number given by $Ra_L = (v_B L)^2 / (\alpha v)$, where the characteristic buoyancy induced velocity, v_B, behaves like $v_B \propto \sqrt{\beta g_0 L \Delta T}$. Here, $\beta = 1/T_\infty$ is the thermal expansion coefficient for the gas, T_∞ is the ambient temperature, g_0 is the acceleration of gravity, ΔT is the temperature difference between the hot wall and the ambient, α is the thermal diffusivity, v the kinematic viscosity, and L the characteristic length scale of the problem. A change in the length scale, L, will result in an associated change of the induced velocity, which will in turn affect the rate of heat and mass transfer from the fuel surface to the air stream through its impact on the Rayleigh number. Given the dependence of the Nusselt and the Sherwood numbers on the value of the Rayleigh number, it is clear that their values may be changed by the aforementioned manipulation of the characteristic length scale of the problem. The primary objective of this stage of the project is to explore the

combined effects that variations in the Nusselt and Sherwood numbers have on the ignition delay time ($t_{(ig)}$), the critical external flux for ignition ($\dot{q}''_{0,ig}$) and other fire properties of materials due to variations of the Rayleigh number.
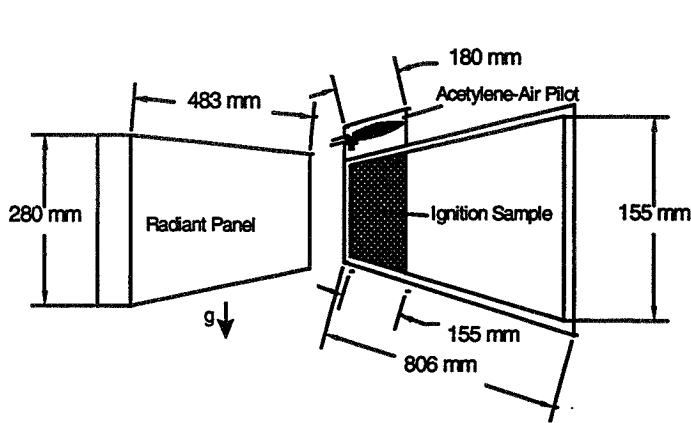

Figure 1: Schematic of LIFT apparatus with ignition specifications (perspective view).
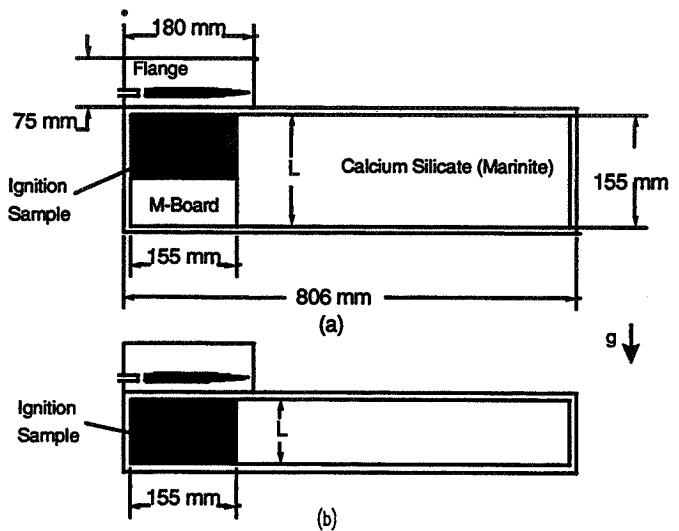

Figure 2: Sample holder configurations: a) preserves the characteristic length scale, b) decreases the characteristic length scale with the sample size.

A data acquisition system, together with an array of 32 K-type thermocouples records the fuel temperature evolution, and a 2 W red diode laser is used to create a light sheet for visualization of the natural boundary layer. The pyrolyzate has been used to visualize the stream lines near the fuel surface. To date, results have been qualitative in nature.

Ignition tests have been performed using PMMA as fuel for different sample sizes, and in two distinct configurations, one that preserves the characteristic length scale of the flow (Fig. 2a), and the other that varies L with sample size (Fig. 2b). It has been observed that changing the sample size has no effect on the ignition delay time or the critical heat flux for ignition if the characteristic length scale L remains unchanged. The sample size has been systematically decreased down to a width of 65 mm. A typical series of ignition delay times for different sample sizes is presented in Fig. 3. It is important to note that these results present good agreement with values for PMMA reported in Refs. 3,4. Results for the tests conducted with the flange are labeled (f) in Fig. 3, and for those without it (nf); for the larger samples, no significant effect on the ignition delay times can be observed.
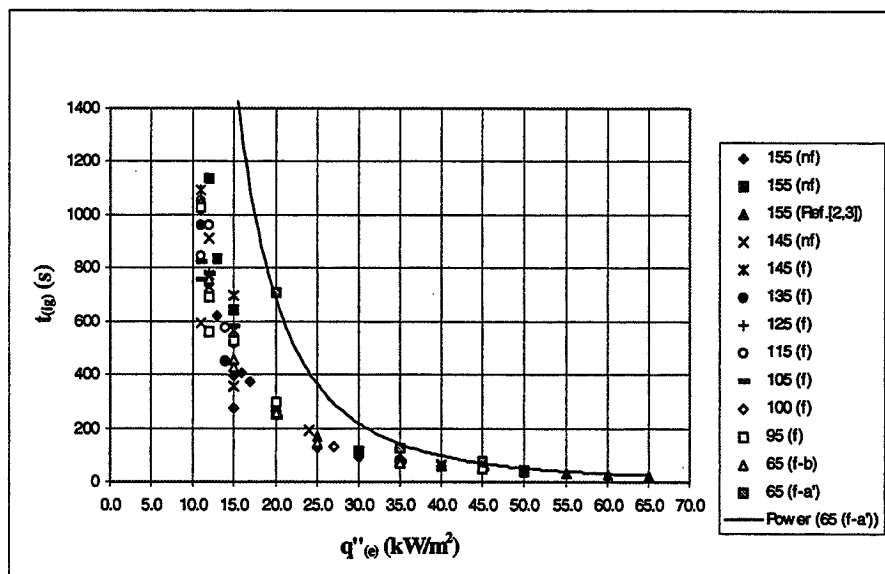

Figure 3 Ignition delay time, $t_{(ig)}$, as a function of external heat flux intensity, $\dot{q}''_{(e)}$.

A series of preliminary experiments has been conducted varying the fuel sample position in both the holder shown in Fig. 2a, and that in Fig. 2b. The ignition delay time, for a specific heat flux, has been found to vary significantly with L. For the sample holder shown in Fig. 2b, however, the ignition delay time remained unchanged for $L>65$ mm, showing a significant decrease for smaller samples exposed to heat fluxes smaller than 20 kW/m^2. Placing the sample at the bottom of the holder increased the ignition delay time for low heat fluxes, but the difference became insignificant as the external radiation increased (65 (f-a') in Fig. 3). A significant difference on the critical heat flux for ignition was only observed under these conditions. These preliminary results are not yet conclusive, and the effect of variations of L on this critical heat flux is still to be determined.

Sample size will continue to be reduced until the ignition delay time is only affected by the characteristic length of the fuel sample, and not by the characteristic length of the flow. A similar procedure will be followed when conducting the flame spread tests. The structure of the buoyantly induced convective flow will be studied in the context of its effects on the fire properties of the material. These tests will be extended to different materials in order to validate the conclusions drawn for conditions not as ideal as those provided by PMMA.

FLOW EFFECTS ON THE FIST IGNITION DIAGRAMS

The procedure and theory behind the FIST apparatus is similar to that of the LIFT, but replacing the buoyant flow with a forced flow induced along the sample length, and parallel to its surface. It also consists of two independent tests, a piloted ignition test, and an opposed (or co-current) flame spread test. For both tests, the fuel sample is placed in the test section of a combustion wind tunnel, and it is exposed to an external heat flux provided by a radiant panel placed parallel to the sample surface. The radiant panel output is designed so that it provides a heat flux distribution to the fuel surface which, for ignition tests, is nearly uniform over one section of the sample, and for flame spread tests, gradually decays over the rest of the sample length.

As with the LIFT apparatus, two relevant non-dimensional parameters control the time to ignition. These are the Nusselt and the Sherwood numbers, which for the case of a flat plate subjected to laminar, forced convective transport, are defined as:

$$Nu_L = 0.664 \, Re_L^{1/2} \, Pr^{1/3} \quad \text{and} \quad Sh_L = 0.664 \, Re_L^{1/2} \, Sc^{1/3}.$$

Here, Pr is the Prandtl number, Sc is the Schmidt number, and Re_L is the Reynolds number given by $Re_L = U_\infty L/v$. From this, it becomes apparent that variations in the flow velocity, U_∞, have a direct effect on the transport parameters. Thus, as in the LIFT experiments where variation of the characteristic length produces a variation of the Rayleigh number, the variation of the flow velocity in the FIST experiments induces a variation of the Reynolds number. Control over the Nusselt and the Sherwood numbers, and therefore over the rates of heat and mass transfer of the problem, is thereby attained.

Experiment

The experiments are conducted in the experimental apparatus shown schematically in Fig. 4. It consists of a small scale combustion wind tunnel and supporting instrumentation. The wind tunnel is composed of two main sections vertically mounted on a three-axis moving table. The inlet section constitutes a settling chamber and converging nozzle that directs oxidizer gas to the test section. The test section, of rectangular cross sectional area, has one of its walls lined with a thick Marinite sheet, where the fuel sample is mounted flush with the Marinite surface. The side walls of the test section are made of 0.6 mm Pyrex windows for optical access. The wall opposite to the fuel specimen is fitted with a panel containing an array of independently controlled radiant heaters. The radiant heaters are initially located outside the test
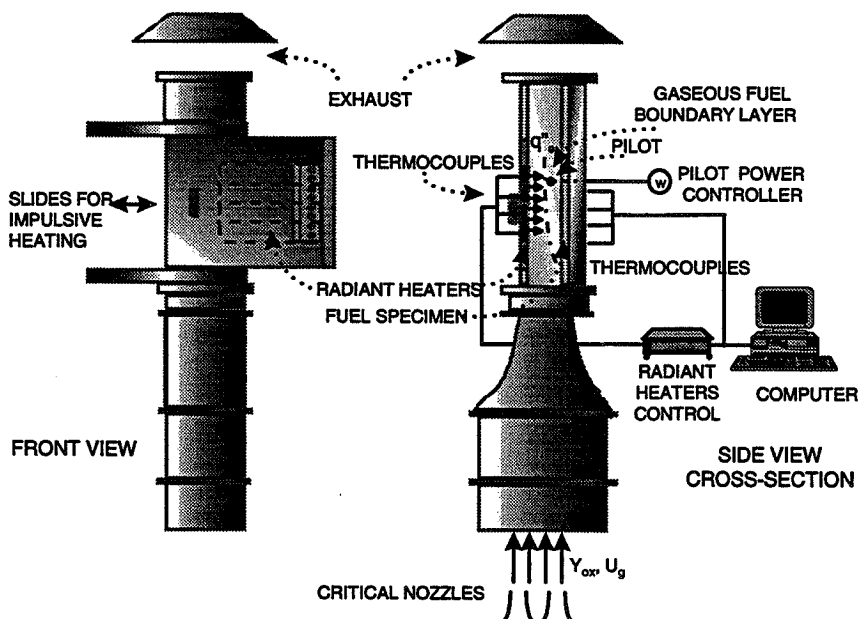

Figure 4: Schematic of FIST apparatus

section until they reach steady state conditions, at which point the panel is rapidly slid into the test section, impulsively irradiating the fuel with a prescribed heat flux distribution. The outlet of the test section discharges into a fume hood for elimination of combustion gases.

The fuel sample is heated by the radiant flux until it begins to pyrolyze. The pyrolyzed fuel mixes with the oxidizer flow, and the resulting combustible mixture, if within the flammability limits, is ignited by a Nichrome wire that is located off the trailing edge of the fuel sample at a fixed distance from its surface. The oxidizer gas supplied is house compressed air, bottled oxygen, and bottled nitrogen, independently metered with critical nozzles, and mixed in the settling chamber. The flow velocity is measured with a LDV system. A data acquisition computer records, at regular time intervals, temperature readings gathered with K-type thermocouples, embedded in the fuel sample at different depths and locations.

A set of preliminary experiments to obtain the ignition delay time, $t_{(ig)}$, as a function of radiant heat flux intensity, $\dot{q}''_{(e)}$, has been carried out for PMMA samples (85 mm x 50 mm x 12.7 mm) for two different air flow velocities. Results are presented in Fig. 5. As would be expected, higher radiant fluxes and lower flow velocities result in shorter ignition times.
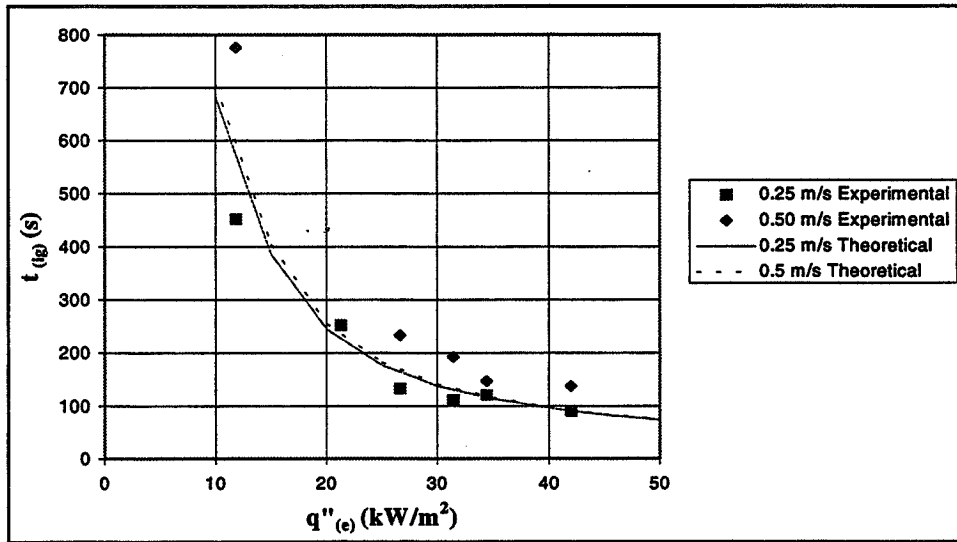

Figure 5 Experimental and theoretical ignition delay times, $t_{(ig)}$, as a function of external heat flux intensity, $\dot{q}''_{(e)}$ and flow velocity.

Theory

A numerical solution of a simplified model for the heating and thermal pyrolysis of a fuel sample, held subject to a constant radiant flux and to a forced flow of oxidizer parallel to its surface has been obtained as a first approximation to modeling the ignition phenomenon. The problem is approximated by the following transient, two-dimensional, form of the energy equation with its corresponding initial and boundary conditions:

$$\rho c \frac{\partial T}{\partial t} = \left(\frac{\partial^2 T}{\partial x^2} + \frac{\partial^2 T}{\partial y^2} \right) - \rho H_v A exp\left(-\frac{E_a}{R_u T} \right)$$

$$T(t = 0, x, y) = T_0$$

$$\left. \frac{\partial T}{\partial x} \right|_{x=0} = 0; \quad \left. \frac{\partial T}{\partial x} \right|_{x=L} = 0; \quad \left. \frac{\partial T}{\partial x} \right|_{y=-H} = 0$$

$$-\lambda \left. \frac{\partial T}{\partial y} \right|_{y=0} = h_\infty(t,x,y)(T_{y=0} - T_\infty) + \varepsilon\sigma(T^4_{y=0} - T^4_\infty) + \dot{q}''_e$$

The Arrhenius, one step, endothermic reaction term simulates the pyrolysis process, as described in Ref. 5; here, $L = 85$ mm and $H = 12.7$ mm are the length and thickness of the fuel sample, $h_\infty(t,x,y)$ the convective coefficient, T_0 and T_∞ the initial

temperature of the fuel slab and the temperature of the air flow, respectively, and σ the Boltzmann coefficient. The values of the thermophysical properties used in the numerical calculation are shown in Table I, and are taken from Refs. 5,6. The finite difference representation of this non-linear form of the energy equation is solved using an Alternating Direction Implicit method, in particular an iterative version of the Peaceman-Rachford Method as described in Ref. 7.

Table I

Property	Value Used
Density, ρ	1170 kg m^{-3}
Thermal conductivity, λ	$0.185 \text{ W m}^{-1} \text{ K}^{-1}$
Heat capacity, c	$1220 \text{ J kg}^{-1} \text{ K}^{-1}$
Emissivity, ε	0.92
Heat of pyrolysis, H_v	1.007 MJ kg^{-1}
Pre-exp. Factor, A	$3.2 \ 10^9 \text{ s}^{-1}$
Activation energy, E_a	142 kJ mole^{-1}

The time for the solid to start the pyrolysis process, or pyrolysis time, may be obtained from the solution of the equation for the temperature field. It may be assumed, as a first approximation, that the time for gas phase mixing and ignition, or induction time, is small compared to the pyrolysis time; in this manner, the pyrolysis time can be considered to be approximately equal to the ignition delay time. The ignition time predictions for the radiant flux and flow velocities used in the experiments are presented in Fig. 5 for comparison with the experiments. It is seen that the model predicts the experiments well. The difference between the theoretical predictions and experimental measurements is most likely due to the influence of the induction process.

CONCLUSIONS AND FUTURE WORK

An experimental and theoretical program is in progress to develop a fundamental understanding of the controlling mechanisms underlying the flammability diagrams of combustible materials produced by the LIFT and FIST apparatuses. Although preliminary, the results for the dependence of the ignition delay time on the external radiant flux and either the sample width (LIFT) or the flow velocity (FIST) indicate that natural and forced convection flow changes, respectively, affect the characteristics of the ignition curves of the flammability diagrams. The major effect on the ignition time seems to be due to convective transfer variations at the fuel surface. At high radiant fluxes or high flow velocities, however, it appears that gas phase processes become increasingly important, affecting the overall ignition delay time. The theoretical predictions agree well with the experiments, at least for conditions in which the gas phase induction time is negligible.

The present parametric study of the oxidizer flow effects on the flammability diagrams of combustible materials will be continued. The information obtained will be used to define an experiment that is adequate for the conditions of reduced-gravity and low convective currents found in space based environments.

ACKNOWLEDGMENTS

REFERENCES

[1] Olson, S. O., "Mechanisms of microgravity flame spread over a thin solid fuel: Oxygen and opposed flow effects", *Combustion Science and Technology*, 76, 223-249, 1991.

[2] Annual Book of ASTM Standards, Vol. 04-07, 1055-1077, 1993.

[3] Quintiere, J. G., "A Simplified Theory for Generalizing Results from a Radiant Panel Rate of Flame Spread Apparatus," *Fire and Materials*, 5, 2, 52-60, 1981.

[4] Quintiere, J. G. and Harkleroad, M., "New Concepts for Measuring Flame Spread Properties", NBSIR 84-2943, 1984.

[5] Vovelle, C., Delfau, J. L., Reullion, M., Bransier, J., Laraqui, N., Experimental and Numerical Study of the Thermal Degradation of PMMA, Combustion Science and Technology, 53, 187-201, 1987.

[6] Fernandez-Pello, A. C., Ray, S. R., Glassman, I., Flame Spread in an Opposed Forced Flow: the Effect of Ambient Oxygen Concentration, *Eighteenth Symposium (International) on Combustion*, The Combustion Institute, 579-589, 1981.

[7] Thomas, J. W., *Numerical Partial Differential Equations: Finite Difference Methods*, Springer-Verlag, NY, 1995.

IGNITION, TRANSITION, FLAME SPREAD IN MULTIDIMENSIONAL CONFIGURATIONS IN MICROGRAVITY

TAKASHI KASHIWAGI, William E. Mell, Kevin B. McGrattan, Howard R. Baum
National Institute of Standards and Technology, Gaithersburg, Maryland

Sandra L. Olson
NASA Lewis Research Center, Cleveland, Ohio

and

Osamu Fujita, Masao Kikuchi, Kenichi Ito
Hokkaido University, Sapporo, Japan

Introduction

Ignition of solid fuels by external thermal radiation and subsequent transition to flame spread are processes that not only are of considerable scientific interest but which also have fire safety applications. A material which undergoes a momentary ignition might be tolerable but a material which permits a transition to subsequent flame spread would significantly increase the fire hazard in a spacecraft. Therefore, the limiting condition under which flame cannot spread should be calculated from a model of the transition from ignition instead of by the traditional approach based on limits to a steady flame spread model. However, although the fundamental processes involved in ignition have been suggested [1,2] there have been no definitive experimental or modeling studies due to the flow motion generated by buoyancy near the heated sample surface.

Almost all previous works have studied ignition and flame spreading separately [3,4,5]. In previous flame spread studies, time-dependent flame spread models are limited to upward flame spread over a vertically oriented material surface in normal gravity which is generally assumed to be two-dimensional. Almost all detailed flame spread models [6,7,8] were based on a steady-state flame spread rate and, as far as we are aware, there are no previous studies of three-dimensional time-dependent flame spread which is initiated from a small, localized ignited area. This scenario is most common in real fires. Thus, the study of localized ignition and the subsequent transition to flame spread in multidimensional configurations in a microgravity environment is needed to obtain new information for understanding transition and flame growth mechanisms.

Smoldering (non-flaming glowing combustion) is one of the common modes of initiation of fires; it might provide potentially hazardous conditions due to its high CO yield, but there are only a limited number of studies available in microgravity, in particular for surface smoldering phenomena. Although the heat release rate from smoldering is smaller than that from flaming, the temperature of the smoldering front is as high as 800 °C or more and the induced buoyant flow velocity from the high temperature smoldering front is roughly 20 cm/s in normal gravity. Since the supply of oxygen to the smoldering front is one of the critical parameters which control smoldering spread rate, it is expected that surface smoldering growth behavior at slow external flow of up to 5 cm/s in microgravity could be significantly different from that in normal gravity.

In this study, microgravity experiments which required longer test times such as in air and surface smoldering experiments were conducted in the space shuttle STS-75 flight; shorter experimental tests such as in 35% and 50% oxygen were conducted in the droptower in the Japan Microgravity Center, JAMIC. Their experimental data along with theoretically calculated results from solving numerically the time-dependent Navier-Stokes equations are summarized in this paper.

Experimental Description and Results

The experimental module, shown schematically in Figure 1, uses a small fan to generate a low flow velocity of up to 6.5 cm/s through the test section. The test section is 85 mm wide x 95 mm high x 171 mm long. A near-infrared tungsten/halogen radiant heater is used to ignite a circular area in the center part of a sample in the three-dimensional configuration. The power to the lamp was measured during each test and it was turned off after ignition at a preset time. The emission spectrum of the lamp was measured from

2 to 20 μm using a FTIR. A 10 cm x 8.7 cm sheet of Whatman 44[1] ashless filter paper was used as the sample. The center part of the sheet over the irradiated area was blackened to increase absorption of the incident beam from the lamp. The samples were ignited at a central location either by the focused beam from the lamp (three-dimensional configuration) or along a line by a heated wire to observe planar flame growth (two-dimensional configuration). A few samples were doped with a smolder promoting agent, potassium acetate, to study smolder propagation from a central ignition point. Six 0.05 mm diameter type K thermocouples and an ignitor wire (30 gauge Kanthal wire) were pre-installed across the sample on each sample holder. Four thermocouples were installed in the sample at the center, 2 cm and 4 cm downstream from the center and at 2 cm upstream. Two thermocouples were installed at 2 mm above the sample surface at 2 cm upstream and also at 2 cm downstream locations from the center. Color video pictures were taken in the direction normal to the sample surface to view changes in the flame shape and char pattern. Red diodes were used to illuminate the sample surface. Still color photographs were taken at an oblique angle to the sample by a motor-driven 35 mm camera.

Ignition was achieved in all tests using either a heated wire or a lamp. Radiative ignition by the lamp was quite reproducible and the results show that the ignition delay time was not significantly affected (within 10%) by the external flow velocities used in this study. The ignition delay time was 4.4 ± 0.4s in air, 4.2 ±0.3s in 35% oxygen, and 3.8 ± 0.2s in 50% oxygen. These ignition delay times included about 2.2s from power on to a point where the output of the lamp reached the designated flux. Ignition by a heated wire was less reproducible than that by the lamp due to changes in wire contact with the sample caused by the expansion of the wire as it heated. Ignition tended to occur at one face of the sample surface at first followed by the second ignition on the other face of the sample. The second ignition occurred very quickly in 50% oxygen but it took several seconds in air.

The transition from ignition to flame spread occurred in quiescent 35% and 50% oxygen but it did not occur in quiescent air. In the two-dimensional configuration, the transition from ignition to downstream flame spread never occurred; only the transition to upstream spread took place. This is clearly seen for the case in air at the external flow velocity of 5 cm/s as shown in Fig.2. In air, the color of the flame was blue and it became somewhat orange in 35% and 50% oxygen. The brightness and the length of the flame increased with an increase in oxygen concentration and also in external flow velocity. The tail of the flame extended further downstream and char was even formed downstream near the initially ignited region. However, downstream sample temperatures measured by thermocouples did not exceed over about 330 °C compared to about 500 °C for upstream sample temperatures beneath the traveling upstream flame front. In the three-dimensional configuration, the flame spread pattern was strongly affected by oxygen concentration and flow velocity. In air, at 0.5 cm/s, a small flame spread only upstream maintaining the initial flame shape from shortly after ignition. The flame never grew laterally from its initial width and this is also clearly seen in the growth pattern of char in Fig. 3a. However, the flame and char growth patterns did grow laterally outward with an increase in the external velocity, as shown in Figs 3b and 3c. At 2 cm/s, the flame had a crescent shape and the char growth pattern was initially an elongated circle pointing upstream; at later times, it became fan-shaped. At 6.5 cm/s, the shape of the flame became like a horseshoe with the tails of the horseshoe flame extending downstream. The char pattern became a circle elongated in the upstream direction with a relatively flat downstream side. A similar shape was also observed in 35% and 50% oxygen concentrations at 5 cm/s external flow velocity. A major difference in flame shape between air in this study and 50% oxygen concentration is that a spreading spherical flame was observed in a quiescent condition in 50% oxygen concentration compared with no transition to flame spread in the air case. Therefore, at low external velocities, the char patterns were more or less spherical in 50% oxygen concentration instead of the narrow strip char pattern observed in the air case. The observed trend of opening the angle of the char pattern in the upstream direction with an increase in external flow velocity of air in microgravity is quite different from the narrowing angle trend of the down stream flame with an increase in external flow velocity in normal gravity. However, it is expected that further increase in external velocity in microgravity would eventually reduce the upstream flame spread rate and be sufficient to promote downstream flame spread. Thus, this observed trend of the char pattern is unique and should occur only at low external flow velocities and low oxygen concentrations, such as in air, in microgravity.

The histories of the location of the char front spreading upstream along the centerline could be fit reasonably well by linear equations with time. Thus, apparently steady-state-like upstream char front spread rates along the centerline were obtained for each experiment. The results are shown in Fig.4. Some caution is needed in comparing the results between the two-dimensional configuration and the three-dimensional configuration due to the transient nature of the three-dimensional flame and there are not sufficient data for the case in air in the two-dimensional configuration. The results show that the upstream char spread rate appears

to reach a plateau in the flow velocity range of about 5 - 10 cm/s, where the spread rate becomes independent of the external flow velocity [9]. Although the difference between the two-dimensional configuration and the three-dimensional configuration in 50% oxygen is within the scatter of the data, the results in 35% oxygen indicate that the spread rate in the three-dimensional configuration is faster than in the two-dimensional configuration due possibly to a larger oxygen supply at the curved flame front. In the regime where oxygen supply is the critical rate-controlling process, a curved flame front has a larger area for incoming oxygen to reach. This could be more clearly seen in air but unfortunately there were not enough data in the two-dimensional configuration. Some care is needed to make sure to generate a planar flame in the two-dimensional configuration. If a planar flame is not generated, the result is instead a three-dimensional configuration.

Four smoldering experiments were conducted in the space shuttle STS-75 with ignition initiated at the center of the sample by the lamp. The sample was doped with potassium ions to enhance char formation and char oxidation (4.2 weight % ±5% in spatial non-uniformity). Although a ring-shaped smoldering front was initially observed in normal gravity (the ring-shaped front gradually deformed due to induced buoyant flow from the hot smoldering surface), unexpected, very complex finger-shaped char patterns with localized smoldering fronts at the finger tips were observed in microgravity; such patterns are seen in Fig.5. In these pictures, the white spots are the localized smoldering fronts. The direction of growth of the char pattern was mainly upstream; higher external flow velocity tends to increase the number of localized smoldering fronts, the number of fingers, and also the frequency of bifurcations from each finger. At present it is not clear what caused this complex pattern.

The flame spread behavior along the open edges of the paper sample was studied at external flow velocities of 2, 3, and 5 cm/s in air using a narrow sample, 4 cm in width, in the same sample holder. Ignition was achieved by the lamp illuminating the center of the sample; initially, the flame spread radially upstream. Once the flame reached the open edges of the sample, the flame at each edge spread much more rapidly than the flame along the center line. At the open edges of the sample, oxygen supply to the flame (almost 360°) and energy feedback from the flame to the sample (from three sides) are much larger than that for the flame along the center of the sample (about 180° for oxygen supply and only two sides for energy feedback).

Theoretical Calculation

A complete description of the mathematical model has been given in Ref. [10]. The gas phase is governed by the conservation equations of mass, momentum, energy and species (fuel gases and oxygen) under low Mach number combustion and heat transfer conditions. In past work (two-dimensional configuration), it was assumed that the velocity field was approximated by a potential flow [10,11]. Now, the full Navier-Stokes form of the momentum conservation equation (in three-dimensional configuration) is solved. However, the potential flow approximation is used to apply boundary conditions since the rapid expansion at ignition cannot be treated properly with conventional zero gradient boundary conditions. The uniform inlet flow condition is specified at the upstream edge of a paper sample and a boundary layer along the sample surface is calculated. The gas phase oxidation reaction is represented by a global one step reaction characterized by a second order Arrhenius rate equation. The pre-exponential factor is 5.0×10^9 cm^3/(g·s) and the activation energy is 67 kJ/mol. The heat of combustion is 35 kJ/g, and the stoichiometric constant is 3.57. These values are the same as those used in the two-dimensional study [10]. It has been observed that the ignition and transition to flame spread are very sensitive to the choice of the gas phase reaction constants. The present choice is guided by a desire to roughly match flame spread rates with the experiments of Olson [5]. However, the objective of the study is not necessarily to duplicate experimental results exactly by manipulating the model parameters, but rather to deduce trends of the transient phenomena.

The sample used in the experiments is more thermally stable than the paper used in our previous study [10,11]. Its thickness is 0.13 mm, area density 5.7 mg/cm^2 and specific heat 0.96 J/(g·K). It is assumed that this value of specific heat applies to the char and ash, as well, and that it increases linearly with temperature. It is assumed that the sheet is thermally-thin and also of uniform composition through its depth. Radiative loss from the sample surface is included but radiation from the flame is not included in the model, and the emissivity of the sample is estimated to be 0.6. The pyrolysis of the cellulosic sheet is described by a slightly exothermic global pyrolysis reaction, an exothermic global thermal oxidative degradation reaction, and an exothermic global char oxidation reaction. The kinetic constants for each degradation reaction were derived with the same type of thermogravimetric analysis used in our previous study [12].

The equations for the continuity, momentum, gas phase temperature and two species concentrations are written in finite difference form and solved with a simple time splitting scheme in which it is assumed that the oxidative reaction occurs over a small part of the overall time step, and the convective and diffusive terms are differenced and updated with an ADI (Alternating Direction Implicit) scheme. The momentum equation is solved with a simple projection method which relies on the prescription of the velocity field at the boundary of the computational domain. This boundary velocity is provided by the potential flow approximation. A Poisson

equation for pressure is solved with a direct solver. For the simulations described below, the computational domain was 10 cm in the windward direction, 5 cm spanning half of the lateral direction and 5 cm in the normal direction. Symmetry is assumed about the plane which is spanned by vectors normal to the paper surface and parallel to the wind direction. Also, the paper itself is assumed to be a plane of symmetry. A typical grid contains about 260,000 cells (128x64x32), and the calculations require about 48 hours of CPU time on a current generation workstation for a 5 second simulation of the events.

A typical result of flame spread behavior in a 33% oxygen atmosphere in the two-dimensional configuration is shown in Fig.6. The sample is ignited at the center part of the sample by a prescribed external radiant flux distribution (similar to the experimentally used lamp in the three-dimensional configuration) across the sample. At a quiescent condition and 1 cm/s flow, no transition from ignition to flame is achieved in the calculation. From 2 cm/s to 12 cm/s flow, the transition is achieved and steady flame spread is calculated only toward upstream which is the same trend as that observed in the experiment as shown in Fig.2. The char pattern shown in Fig.2 is very similar to that shown in Fig.6. The calculated upstream char spread rate with respect to external flow velocity is shown in Fig.7. From about 5 cm/s to 12 cm/s flow, the char spread rate is nearly independent of external flow velocity and this trend is consistent with the data shown in Fig.4 and previous experimental results [5]. In a atmosphere of quiescent 50% oxygen in the three-dimensional configuration, the results show a flame of initially hemispherical dome shape. The top part of the flame eventually opens as it propagates far from the ignited area in the outward direction[13]. Although this behavior of the flame appears to be reasonable, the opening of the top part of the flame was not observed due to lack of available test time, 10s, in the droptower. At 5 cm/s flow, the initial shape of the flame is similar to the quiescent case since the flow field is dominated by the rapid thermal expansion of the flaming ignition. However, after ignition the external flow begins to reshape the flame into a horseshoe pointed into the imposed flow as shown in Fig.8. The calculated char pattern for this case is similar to that shown in Fig. 3c but the flame in 50% oxygen is much brighter than that in air. The history of the upstream char front in 33% and 50% oxygen concentration in the three-dimensional configuration shows nearly linear growth with time after the transition from ignition. The relationship between the calculated upstream char spread rate and external flow velocity is shown in Fig.7. The symbols with a x mark indicate that ignition and some transition occurred but the flame died before spreading beyond the irradiated area. A comparison of the upstream char spread rate between the two-dimensional configuration and the three-dimensional configuration indicates a trend in which, at low external flow velocities, only the three-dimensional configuration appears to favor the transition and subsequent flame spread. This trend is similar to the case for 35% oxygen shown in Fig.4. However, the difference in the char spread rate between the two-dimensional configuration and the three-dimensional configuration is very small with the values of the gas phase kinetic constants used in this study. This difference tends to become less at higher oxygen concentration such as in 50% oxygen as shown in Figs. 4 and 7. In order to confirm this trend further, calculation at lower oxygen concentration is planned. Also, a proposal was written to conduct more experiments in the two-dimensional configuration in air.

Acknowledgments

References

1. Kashiwagi, T. *Fire Safety J.* 3: 185-200(1981).

2. Muto, N., Hirano, T. and Akita, K. *Seventeenth Symposium (International) on Combustion*, The Combustion Institute, Pittsburgh, 1183-1190(1978).

3. Bhattacharjee, S and Altenkirch, R.A. *Twenty-Third Symposium (International) on Combustion*, TheCombustion Institute, Pittsburgh, 1627-1633(1990).

4.Frey, A.E. and Tien, J.S., *Combust. Flame*, 36: 263 -289(1979).

5. Olson, S.L. *Combust. Sci. Tech.* 76:233-249 (1991).

6. Di Blasi, C., Crescitelli, S. and Russo, G. *Fire Safety Science- Proceedings of the Second International Symposium*, p119-128(1989).

7. Bhattacharjee, S., Altenkirch, A., Srikantaiah, N., and Vedhanayagam, M. *Combust. Sci. Tech.* 69:1-15(1990).

8. Ferkul, P.V. and Tien, J.S. *Combust. Sci. Tech.* 99:345-370(1994).

9. de Ris, J.N. , *Twefth Symposium (International) on Combustion*, The Combustion Institute, Pittsburgh, pp.241-252(1969)

10. Nakabe, K., McGrattan, K.B., Kashiwagi, T., Baum, H.R., Yamashita, H., and Kushida, G., *Combust. Flame*, 98:361-374(1994)

11. McGrattan, K.B., Kashiwagi, T., Baum, H.R., and Olson, S.L., *Combust. Flame*, 106:377-391(1996).

12. Kashiwagi, T. and Nambu, H., *Combust. Flame*, 88:345-368(1992).

13.Kashiwagi, T., McGrattan, K.B., Olson, S.L., Fujita, O., Kikuchi, M., and Ito, K.,"Effects of Slow Wind on Localized Radiative Ignition and Transition to Flame Spread in Microgravity" to be published in *Twenty-sixth Symposium (International) on Combustion*, The Combustion Institute, Pittsburgh, (1997).
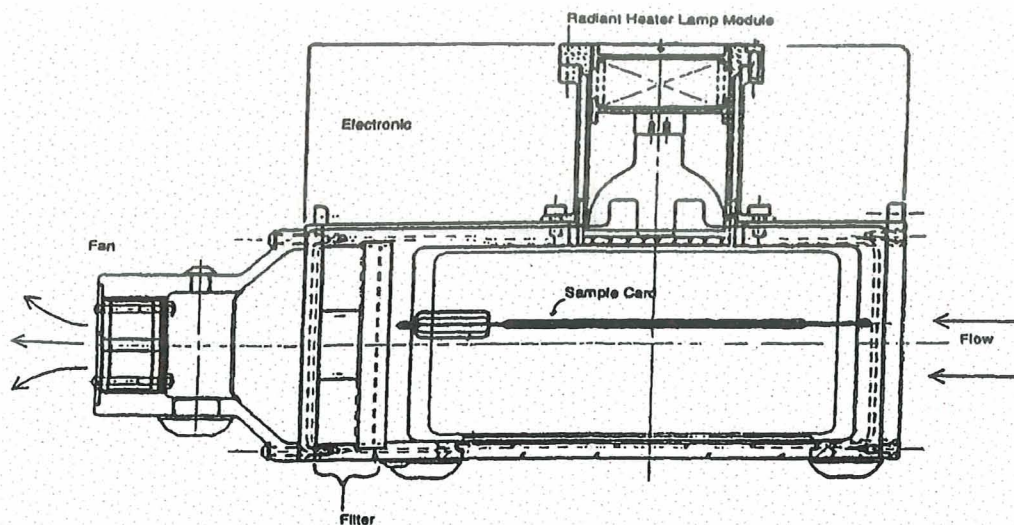
Figure 1 Schematic cross section view of hardware

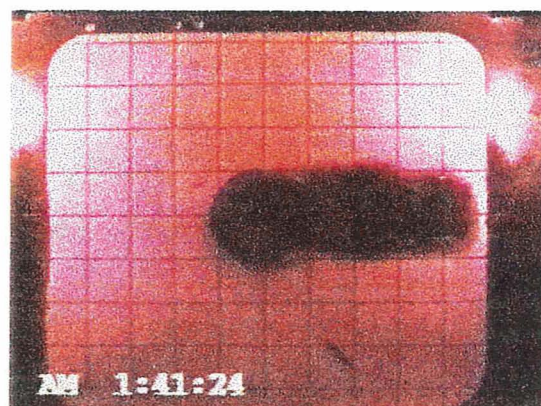Fig. 2: Experimental 2D spread in air, 5 cm/s flow from right

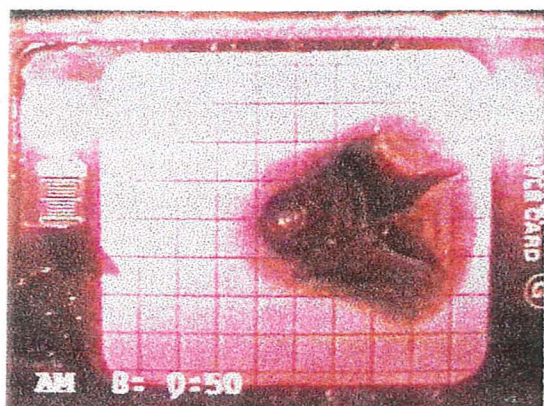Fig. 3a: Experimental 3D spread in air, 0.5 cm/s flow from right

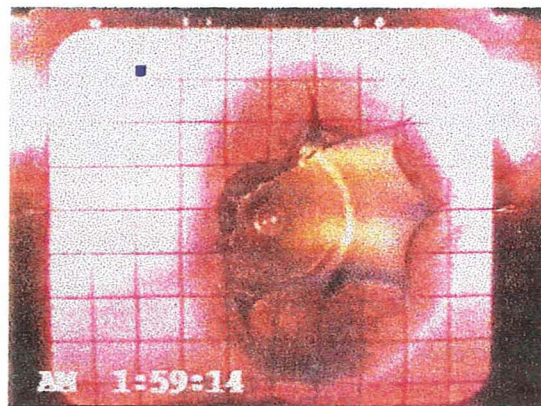Fig. 3b: Experimental 3D spread in air, 2 cm/s flow from right

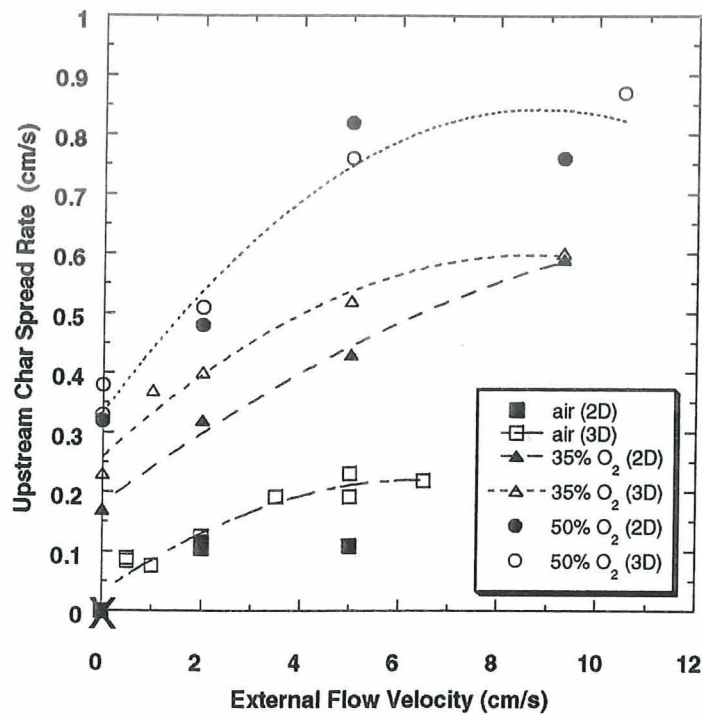Fig. 3ci: Experimental 3D spread in air, 6.5 cm/s flow from right

Fig.4 Experimental upstream char spread rate vs flow velocity

Fig.5: Smoldering char pattern with smoldering fronts in air, 2 cm/s flow from right

Char Mass Fraction
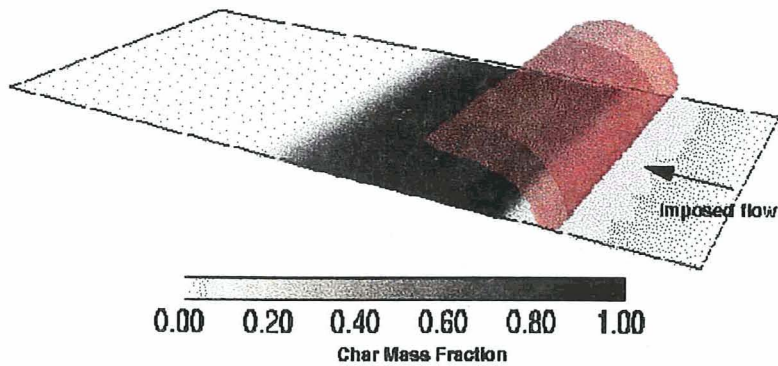
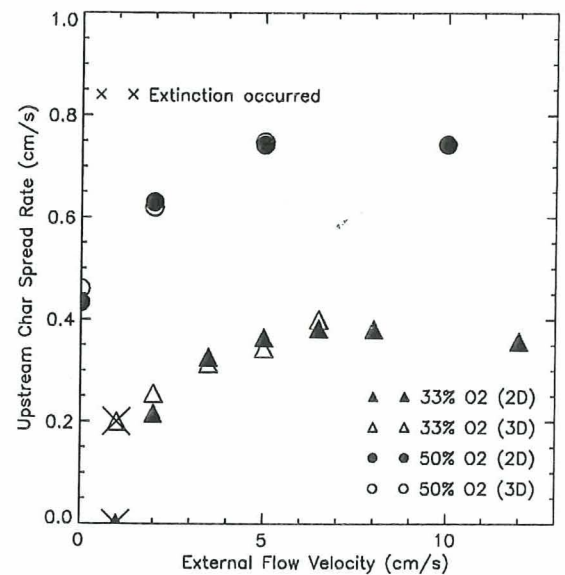Fig. 6: 2D 5 cm/s (Calculation)

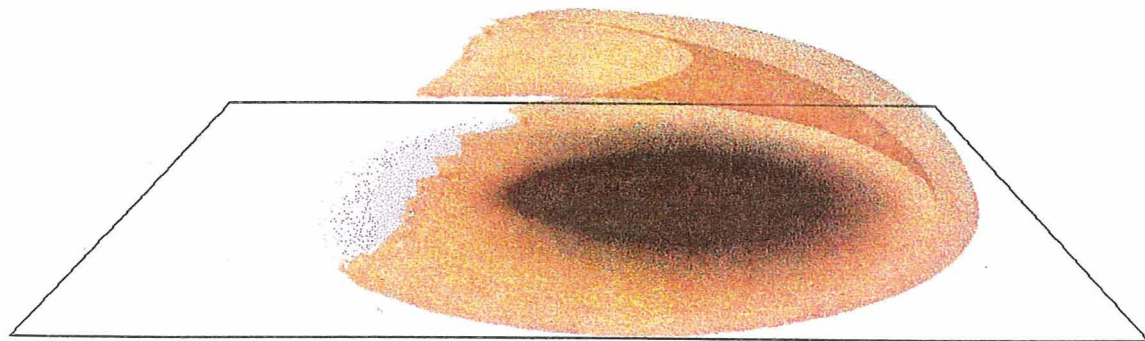Fig.7 Calculated upstream char spread rate vs external flow velocity

Fig. 8: Calculated flame and char pattern in 3D configuration, 5 cm/s in 50% oxygen

PREMIXED ATMOSPHERE AND CONVECTION INFLUENCES ON FLAME INHIBITION AND COMBUSTION (PACIFIC)[*]

Linton K. Honda and PAUL D. RONNEY
Department of Mechanical Engineering
University of Southern California, Los Angeles, CA 90089-1453

Introduction

Flame spread over flat solid fuel beds is a useful paradigm for studying the behavior of more complex two-phase nonpremixed flames. For practical applications, two of the most important elements of flame spreading are the effects of (1) the ambient atmosphere (e.g. pressure and composition) and (2) the flow environment on the spread rate and extinction conditions. Concerning (1), studies of flame spread in vitiated air and non-standard atmospheres such as those found in undersea vessels and spacecraft are particularly important for the assessment of fire hazards in these environments as well as determination of the effectiveness of fire suppressants. Concerning (2), the flow environment may vary widely even when no forced flow is present because of buoyancy effects. Consequently, the goal of this work is to employ microgravity (μg) experiments to extend previous studies of the effects of ambient atmosphere and the flow environment on flame spread through the use of microgravity (μg) experiments. Because of the considerable differences between upward (concurrent-flow) and downward (opposed-flow) flame spread at one-g (Williams, 1976, Fernandez-Pello, 1984), in this work both upward and downward one-g spread are tested.

Two types of changes to the oxidizing atmosphere are considered in this work. One is the addition of sub-flammability-limit concentrations of a gaseous fuel ("partially premixed" atmospheres). This is of interest because in fires in enclosures, combustion may occur under poorly ventilated conditions, so that oxygen is partially depleted from the air and is replaced by combustible gases such as fuel vapors, H_2 or CO. Subsequent fire spread over the solid fuel could occur under conditions of varying oxygen and gaseous fuel content. The potential significance of flame spread under vitiated or partially premixed conditions has been noted previously (Beyler, 1984). The second change is the diluent type, which affects the radiative properties of the mixture as well as the Lewis number (Le) of the reactants in the atmosphere, which for oxygen is defined as the thermal diffusivity of the bulk mixture divided by the mass diffusivity of oxygen into the bulk mixture. Understanding the effect of diluent type is desirable because in some undersea and spaceborne habitations, it is desirable to use diluent gases other than nitrogen. Prior experiments have shown that both radiation (Bhattacharjee and Altenkirch, 1993) and Lewis number (Zhang et al, 1992) effects are important in flame spreading problems.

Approach

Figure 1 shows a block diagram of the flame spread apparatus employed for both one-g and μg tests. The experiments were conducted in a 20 liter combustion chamber which was filled with the desired atmosphere by a computer-controlled partial pressure gas mixing system. The chamber was large enough that under all conditions less than 2% of the oxygen initially in the chamber was consumed during the test. For tests of diluent effects, the inert gases He, Ar, N_2, CO_2 and SF_6 were used since they provide a variety of radiative properties and Lewis numbers from about 0.3 to 1.4.. CO and CH_4 were used for the gaseous fuels in the partially-premixed tests. 5 cm wide Kimwipe samples with a length of 15 cm or longer were used and were held by aluminum quenching plates on both sides. The samples were ignited by an electrically-heated Kanthal wire. For some upward flame spreading tests at one-g, a special 2 meter tall chamber (not shown) was constructed because this distance was often required to reach steady state spread rates. The flame spread process was imaged via three CCD video cameras. One camera was located with its viewing axis orthogonal to the plane of the fuel sample to image the pyrolysis front. A second CCD camera was positioned with its viewing axis in the plane of the fuel sample to image the flame front. A third CCD camera imaged laser shearing interferograms of the flames, again from a side view. The interferometer arrangement is also shown in Fig. 1.

Results

a. Flame spread dynamics at μg

It was found that steady flame spread at μg was generally achieved within about 1 sec of free-fall due to the fact that the fuel samples were relatively thin and consequently the spread rate (S_f) was relatively high. Similar behavior was found by Olson et al (1988) and Olson (1991). Two cases of the transition from steady spread at 1g to steady spread at μg are shown in Fig. 2, with each having the same 1g spread rate but one having a lower S_f at μg than 1g and the other having a higher S_f at μg than 1g. Additionally, Figs. 3 and 4 show that the spread rates determined by all three imaging systems mentioned above were practically indistinguishable and therefore will be discussed interchangeably.

b. Partially premixed flame spread

It was found that the effect of adding gaseous fuel to the ambient atmosphere was qualitatively similar at 1g and μg in that S_f could be increased significantly by adding gaseous fuel (Fig. 3). Note that the μg spread rate is compared to the one-g downward (opposed buoyant flow) spread rate, because at μg flame spread without forced flow is always of the opposed-flow variety. The effect of adding gaseous fuel is stronger at μg than 1g, and in fact S_f is actually higher at μg than one-g at high fuel concentrations. Also, the effect of added gaseous fuel was found to be more substantial at higher oxygen concentration and with CO fuel.

All of these results are consistent with an extension of the simple theoretical model proposed by Ronney et al (1995) for one-g downward flame spread with added gaseous fuel by substituting the flame spread rate (S_f) itself for the opposed flow velocity (V) at μg. It must be emphasized that the only change made to the model was to set $V = S_f$ for the μg predictions, whereas as in the prior study $V \sim (g\alpha_g)^{1/3}$ was employed at one-g. The predictions seen in Fig. 3 show only fair agreement with experiment in terms of the actual values of S_f, but very good agreement in terms of the relative values of S_f at 1g and μg. For example, with 18% O_2 in N_2 with added CO fuel at $\phi = 0.35$, the ratio of the μg to 1g spread rates is 1.29 for the experiments and 1.35 for the predictions.

c. Diluent type

Figures 4a - e show a surprising effect of the diluent type. For He and N_2 and Ar diluents, the μg flame spread rate is always lower than the 1g spread rate and the minimum oxygen concentrations that would support flame spread were lower at 1g than at μg for these diluents. These results are entirely consistent with prior studies using O_2 - N_2 mixtures (e.g. Olson, 1991; Bhattacharjee and Altenkirch, 1993). The reason for the higher spread rates and wider flammable range at 1g is widely thought to be due to radiative heat losses. These losses are larger at μg because the opposed flow velocity V is lower and thus the transport zone thickness δ is larger, consequently the total volume over which heat losses are active increases at μg, with a resulting decrease in S_f and the flammable range of mixtures. The increase in δ at μg was confirmed by comparison of interferometer images of flames at 1g and μg. In contrast to He and N_2, for CO_2 diluent, there is very little difference between S_f at 1g and μg. The minimum O_2 concentration is slightly lower at μg than at 1g. Finally, for SF_6 diluent, S_f is substantially higher at μg than at 1g for all oxygen concentrations and the minimum O_2 concentration is significantly lower at μg than 1g.

Two possible mechanisms for this unusual behavior of CO_2 and SF_6 are hypothesized here. The first is an oxygen Lewis number effect, since the trend of these data is consistent with Le, which is highest for He diluent and lowest for SF_6. Le effects on flame spread at one-g have been studied experimentally by Zhang et al (1992) and theoretically by Greenberg and Ronney (1993). It was found that to a first approximation, the effect of Le on S_f was due solely to its effect on flame temperature (T_f) so that the classical expressions for S_f based on the creeping flow assumption can be retained if T_f are modified to account for Lewis number effects. Law and Chung's (1982) analysis predicts that T_f is higher for lower Le and that the effect of Lewis number on T_f decreases as the strength of convection increases; when convection is sufficiently strong, Le does not affect T_f. Therefore, if convection effects were significant at 1g, T_f and thus probably for atmospheres having varying Le, S_f would be more similar at 1g than μg, and furthermore T_f and S_f would be higher at low Le. This is entirely consistent with the experimental observations, however, there is no evidence that convection has a significant effect on S_f even at one-g because Zhang et al (1992) showed that Greenberg

418

and Ronney's (1993) model of Le effects on flame spread accurately predicted the experimental results at one-g without having to consider flame spread in a mode other than creeping flow.

A second possible mechanism for the observed diluent effects is radiative heat transfer to and from the gases. Neither He nor N_2 emit thermal radiation at flame temperatures and thus only the H_2O and CO_2 combustion products produce significant thermal radiation. At the conditions tested in this study, the Planck mean absorption length (L_p) for the combustion products in He and N_2 diluents are typically 1 m and thus much larger than the characteristic size of the flame, consequently, the radiation processed can be considered optically thin and therefore mainly a loss process. However, for CO_2 and especially SF_6 diluents, L_p may be comparable to δ. For example, at 300K and 1 atm, L_p for pure SF_6 is about 0.3 cm. Under such conditions, reabsorption of emitted radiation cannot readily be neglected. With reabsorption, radiation emitted near the zones of peak temperature may not be lost to the surroundings; in fact under such conditions reabsorption of emitted radiation may augment conventional thermal conduction and increase the spread rate above that without radiative transfer. This effect has been demonstrated for premixed gas flames at μg by Abbud-Madrid and Ronney (1993) by seeding the combustible gases with inert, radiating particles.

To test the radiation hypothesis, a set of tests were performed for each diluent at varying pressure for one value of the O_2 mole fraction which is well above both the one-g and μg flammability limits for that diluent. As the pressure increases, L_p decreases and thus if the hypothesis is correct, the effects of diluent type seen at 1 atm should be stronger (weaker) at higher (lower) pressures. Results are shown in Fig. 5. For all diluents except He, S_f at 1g is mostly unaffected by pressure, which is consistent with prior data by Zhang *et al* (1992) as well as the deRis (1969) prediction. At μg, for all diluents S_f increases with pressure, except for CO_2 where S_f is essentially unaffected by pressure. These results (except CO_2) are consistent with prior μg experiments in O_2-N_2 mixtures (Bhattacharjee and Altenkirch, 1993), and lends some support to the radiation hypothesis. Numerical modeling, particularly with detailed diffusion and radiation emission-absorption sub-models, could be very useful to determine if the effects proposed her based on physical arguments can be verified and if other factors not addressed here may be relevant.

d. Upward flame spread at one-g

Buoyancy-controlled flame spread at one-g may be in the downward or upward direction. In the latter case buoyant convection and diffusive transport are in the same direction and as a result the fuel surface area exposed to the hot combustion products increases with time, often leading to accelerating rather than steady fire growth (Williams, 1976). For this reason the theory of concurrent-flow flame spread is not as well developed as downward spread. However, current models assume adiabatic burning across an infinitely wide sample. Honda and Ronney (1995) have proposed that heat and momentum losses, not considered in prior theories, could limit flame spread acceleration. Because of these losses, it seems unlikely that, for a sample of finite width, the boundary layer thickness could grow to a value larger than the sample width. Also, it seems unlikely that the flame length could grow indefinitely, because the radiative loss from the fuel surface would eventually grow to the point where it would exceed the heat generation rate. Hence, the following hypotheses have been proposed: (1) for narrow fuel surfaces, the flame length will grow until the boundary-layer thickness is comparable to the width (W) of the sample, at which point the transverse heat and momentum losses will prevent further growth in the flame length (convective stabilization) and (2) for wider fuel surfaces, the flame length will grow until the rate of heat loss per unit area due to surface radiation is comparable to the heat flux per unit area to the fuel surface at which point these radiative losses will prevent further growth in the flame length (radiative stabilization). Using these hypotheses along with boundary-layer analyses leads to predictions of the form $S_{f,upward}/S_{f,downward} \sim Gr_w{}^n Pl_w{}^m$, where $Gr_w \equiv gW^3/v_g{}^2$ is the Grashof number based on sample width, g is the gravitational acceleration, v_g is the kinematic viscosity, $Pl_w \equiv \lambda_g(T_f - T_v)/[W\epsilon\sigma(T_v{}^4 - T_\infty{}^4)]$ is a *Planck number* (ratio of conduction to radiation transport rates), λ_g is the thermal conductivity, T_v is the vaporization temperature, ϵ the emissivity, σ the Stefan-Boltzman constant, and T_∞ the ambient temperature.

These predictions were tested using the aforementioned apparatus. It was found that the upward flame spread rate was indeed steady after a transient length, however in many cases the 2 meter tall chamber was required to reach this steady state condition. Figure 6 shows the measured correlation between $S_{f,con}/S_{f,opp}$ and Gr_w for an 8-decade range of Gr_w. At low Gr_w, the proposed relation $S_{f,upward}/S_{f,downward} \sim Gr_w{}^1$ (and thus $S_{f,upward} \sim W^3$) fits each family of data taken in a fixed atmosphere very well, which supports the predicted scaling analysis for convective stabilization with laminar flow, although between different atmospheres there is some variation in the value of $S_{f,upward}/S_{f,downward}$ at the same Gr_w.

At intermediate Gr_w, each family of data at the higher pressures follows the trend $S_{f,upward}/S_{f,downward} \sim Gr_w^{4/7}$ predicted for convective stabilization with turbulent reasonably well. At still higher Gr_w, all data bend towards horizontal, indicating $S_{f,con}/S_{f,opp} \sim Gr_w^0$. This is consistent with the radiative stabilization hypothesis. Thus, the effects of convective and radiative losses provide a means for limiting the rate of concurrent-flow flame spread and furthermore a means for estimating the steady spread rate.

References

Abbud-Madrid, A. and Ronney (1993). "Premixed Flame Propagation in an Optically Thick gas," AIAA Journal, 31-11, pp. 2179-2181.

Bhattacharjee, S. (1993). "A Comparison of Numerical and Analytical Solution of the Creeping Flame Spread Over Thermally Thin Material," *Combust. Flame* 93, 434

deRis, J. N. (1969). "Spread of a Laminar Diffusion Flame," *Twelfth Symposium (International) on Combustion*, The Combustion Institute, Pittsburgh, 1969, p. 241

Fernandez-Pello, A. C. (1984). "Flame Spread Modeling," *Combust. Sci. Tech.* 39, 119.

Greenberg J.B., Ronney, P. D. (1993). "Analysis of Lewis Number Effects in Flame Spread," *International Journal of Heat and Mass Transfer*, Vol. 36, pp. 315-323.

Honda, L. K., and Ronney, P. D. (1995) "Mechanisms of Concurrent-Flow Flame Spread Over Thin Solid Fuels". *Western States Section of the Combustion Institute*, Stanford University, Palo Alto, CA, October 30-31.

Law, C. K., and Chung, S. H. (1982). "Steady State Diffusion flame Structure with Lewis Number Variations". *Combustion Science and Technology*, 29, pp. 129 -145.

Olson, S. (1991). Combust. Sci. Tech. 76, 160.

Olson, S., Ferkul, P. V., Tien, J. S. (1988). Twenty-Second Symposium (International) on Combustion, Combustion Institute, p. 1213.

Ronney, P. D., Greenberg, J. B., Zhang, Y., Roegner, E. V. (1995) "Flame Spread Over Thin Solid Fuels in Partially Premixed Atmospheres," Combustion and Flame, Vol. 100, pp 474-484.

Williams, F.A. (1976). "Mechanisms of Fire Spread," *Sixteenth Symposium (International) on Combustion*, The Combustion Institute, p.1281.

Zhang, Y., Ronney, P. D., Roegner, E., Greenberg, J. B. (1992). "Lewis Number Effects on Flame Spreading Over Thin Solid Fuels," *Combustion and Flame* 90, 71.
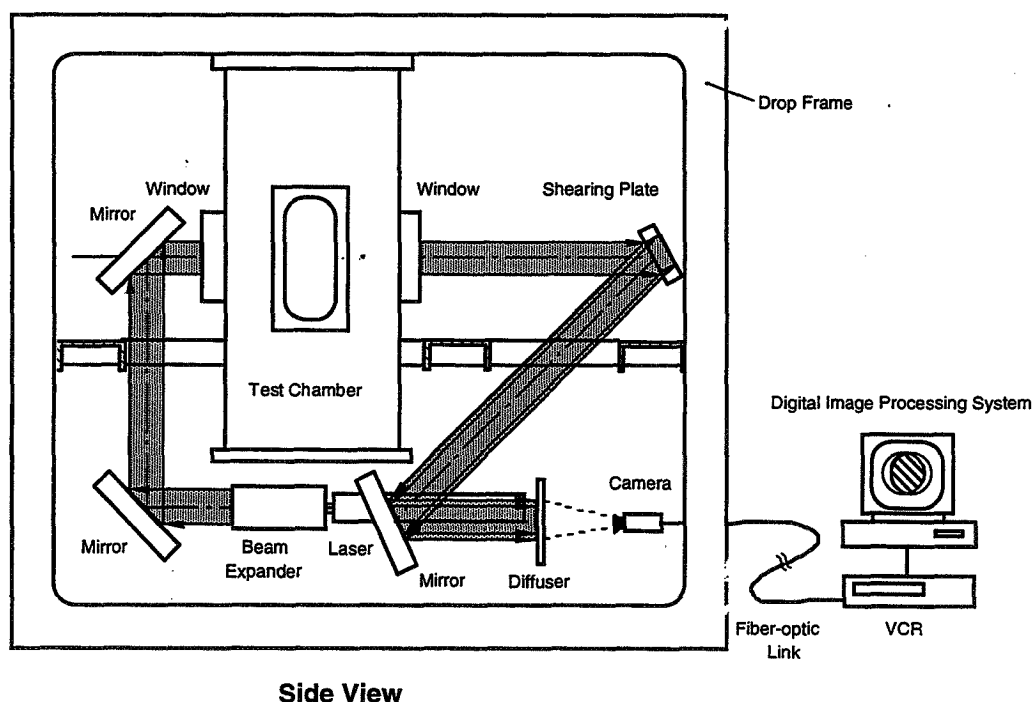
Figures

Side View

Figure 1. Schematic of drop frame and interferometer apparatus.
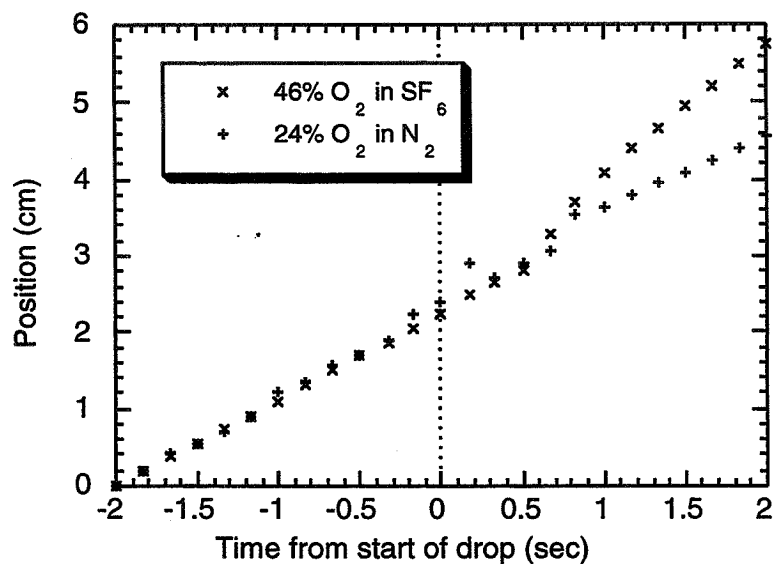
Figure 2. Example of transition to from steady flame spread at 1g to steady flame spread at µg for 24% O_2 in N_2 at 1 atm (S_f (1g) > S_f (µg)) and 46% O_2 in SF_6 at 1 atm (S_f (1g) < S_f (µg)).
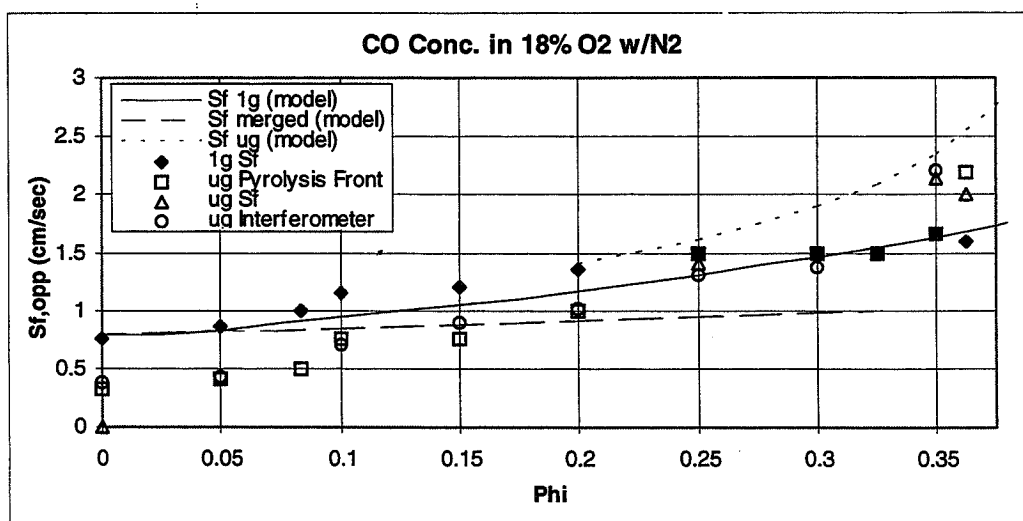
Figure 3. Flame spread rates vs. equivalence ratio (f). Atmosphere: 18% O_2 in N_2 at 1 atm with CO as added gaseous fuel.
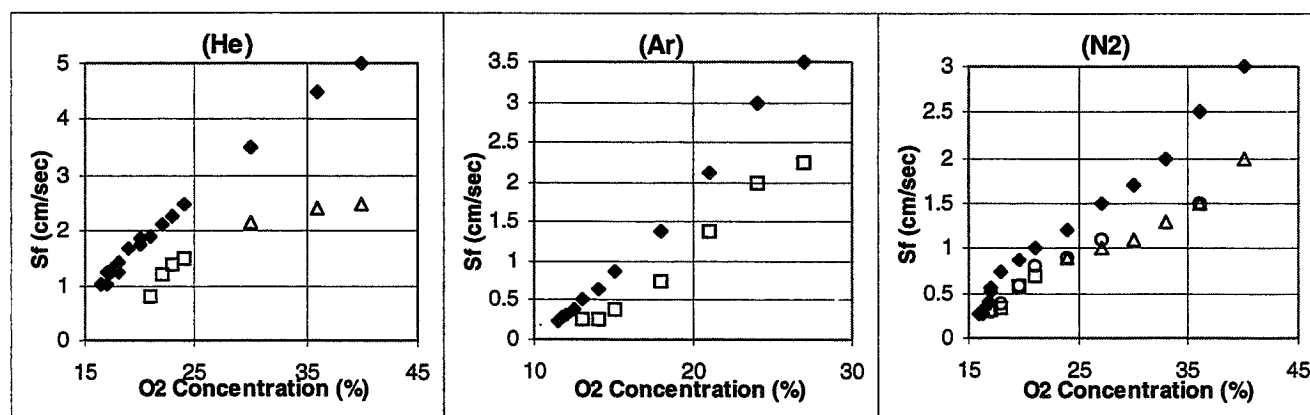
Figure 4a, b, & c. Flame spread rates vs. O_2 mole fraction. Atmosphere: O_2 in He Ar, and N_2 at 1 atm, respectively..

421

Figure 4d and e. Flame spread rates vs. O_2 mole fraction at 1 atm. Atmosphere: O_2 in CO_2 and SF_6 respectively.

Figure 5. Flame spread rates vs. pressure at µg and one-g (downward) for several diluent gases.

Figure 6. Steady upward flame spread rates (referenced to the downward spread rate) vs. Grashof number for various sample widths, diluents and pressures.

FLAME ATTACHMENT IN FLAME SPREAD
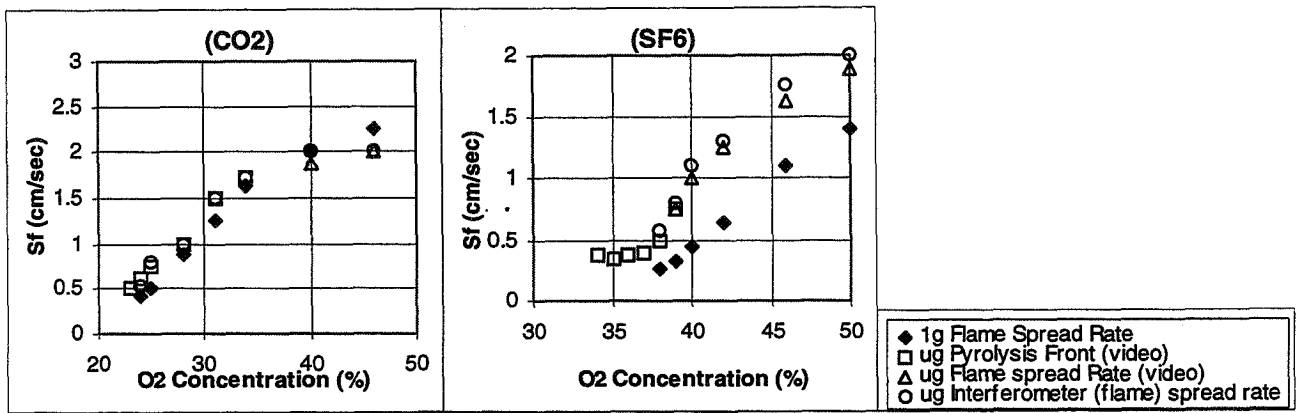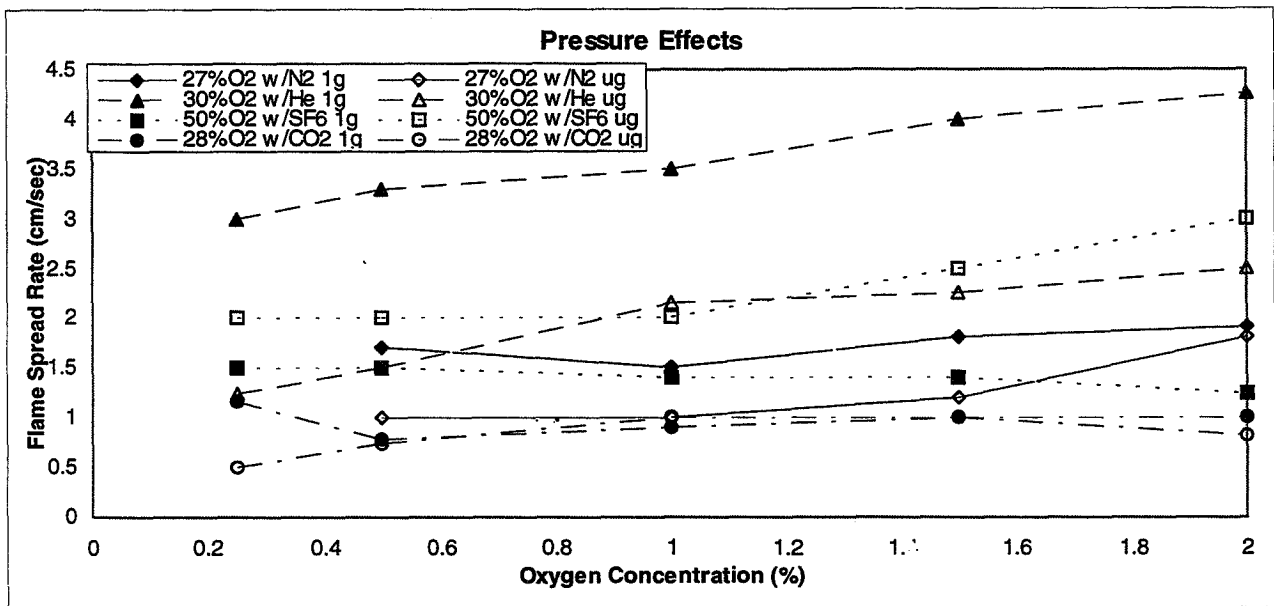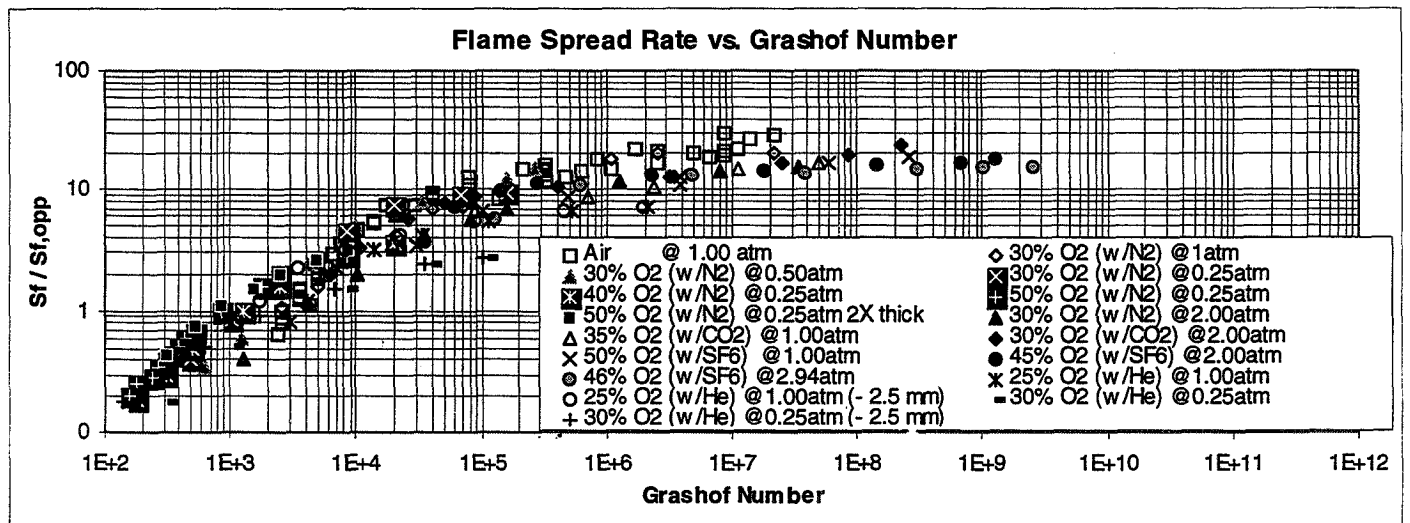
INDREK S. WICHMAN
Michigan State University
East Lansing, Michigan

and

Bassem Ramadan
Michigan State University
East Lansing, Michigan

Introduction:

Flame attachment is a subject that can be studied in many contexts and which has a relatively long history. All diffusion flames are ultimately attached somewhere along their length to one or more surfaces. Depending on the type of particular application, the attachment region may be important to the behavior of the entire flame. Flame spread over solid fuels is one area in which flame attachment is apparently of central importance. It is widely believed, through it has not yet been conclusively demonstrated, that the attachment region—alternately called the "flame tip," "flame foot," "attachment point," & etc.—controls the entire spread process.

Flame spread is an important problem for both practical and academic reasons. On the practical level, one wishes to prevent or, at worst, control unwanted flame spread over combustible materials; to know what levels of heat flux are necessary to sustain flame spreading once it has begun; to design materials that are as minimally hazardous as possible; and to devise extinguishment methods that are both sound and useful. Academically, flame spread is one of the most difficult problems of combustion theory, combining a fully interacting multidimensional transient gas and solid phase problem with chemistry, heat transfer, radiation and material properties that may change during spreading. For this reason, it has been a challenge for scores of combustion researchers.

Previous work has pointed toward a means for solving the long-standing flame spread problem by formally dividing it into zones in which simplified versions of the equations may be solved [1]. A representational or qualitative division of the problem was suggested [1], but no formal program of asymptotic subdivision into separate zones was actually carried out. Instead, a model problem that contained the essential features of the flame tip region was formulated [2-4]. This model problem, which is discussed in detail later in this section and article, has recently been closely examined for many of the features it has in common with the original flame spread problem. Our examination has been greatly aided by the appearance of two recent works on the subject of flame spread [5,6]. In [5], a doctrinaire division of the problem of flame spread into zones of influence is discussed in some detail. Adherence to formal methods of order of magnitude analysis is maintained, based on previous successes with similar approaches in non-combusting fluid flows. Such considerations lead ultimately to partitionings such as the famous triple deck theory [7], and lead to a definition of the flame tip zone as a "Navier-Stokes region," where the equations are inherently multidimensionally diffusive, surrounded by regions of successively lower complexity, until the free stream flow, which is inviscid. The essential features of such a division were suggested in a less formal way by the classical work of Carrier and Lin [8], who also showed the existence of an inner Navier-Stokes region, where a boundary layer approximation became impossible to justify. A somewhat less rigorous approach to the flame spread problem is presented in [6], where the slug flow configuration of deRis [9] is exploited to develop an elliptic (2-D) formulation for the mixture fraction variable. The mixture fraction variable is then weaved into an essentially simplified analysis of the remaining parabolic problem. Although there are many gaps in the analysis, and there are some weak points that need reworking, this study [6] points the way for making the connection between formal boundary-layer types of analysis [5] and the real essence or quiddity of the problem of flame spread. Our belief is that this essence derives from the strict examination of the "Navier-Stokes" region through a solvable model problem, which can be reconnected to the flame spread problem without the artificial strictures of the rigorous triple deck theory (which requires enormous free-stream Reynolds numbers, for instance). To summarize [5,6], they both suggest in very different ways that the key to understanding and describing flame spread in the finite-chemistry limit lies in the consideration of the elliptic flame tip vicinity, called the Navier-Stokes region in the one [5], and modeled using elliptic equations for the mixture fraction in terms of a simplified model problem in the other [6].

Our approach has been to thoroughly examine difficult but solvable component problems. These involve: a study of the flame structure, to determine the role of the triple-flame nature of the flame tip on its behavior near the surface [3,4]; a detailed examination of the flame quench zone, where the equations are elliptic and their solution becomes extremely sensitive to the boundary conditions used [4]; a flame quenching calculation, to obtain formulae for the quenching distance and the conductive heat flux distribution under the quenched flame tip [4]; a scaling analysis of the processes of flame attachment and liftoff [10]; a detailed study of the nature of the field variable (temperature, species mass fractions, enthalpy) near the flame tip, including an examination of the differences between attached and fully lifted flames; and the development of correlations of the heat flux from the flame tip in terms of the Damköhler number, the global stoichiometry, and the Zeldovich number. We shall now describe each of these studies in turn.

Flame Structure Near Flame Tip:

In [3] we developed a simplified description of the triple-flame structure in a convective flow near a cold wall. The focus was on the flame shape, most easily seen in plots of gas phase reactivity contours, and generally resembling a slightly backswept "hammerhead" configuration. A transformation of coordinates is employed that enables the energy equation to be integrated across the premixed flame (PF) arc, subject to an upstream matching condition obtained by solving a simplified version of the outer, quench-zone problem. An approximate matching condition is thereby deduced which enables a differential equation to be derived for the PF arc shape. The solution of this equation produces flame shape contours that are in good agreement with the numerically-generated "hammerhead" profiles. The principal value of this work arises from the composite validity of the numerous simplifying assumptions used. We have determined that: (i) for moderate flow rates, the zero-flow mixture fraction field near the flame tip is accurate for deciding the species variables; (ii) the simplified outer (quench) problem produces flame shapes in good agreement with numerics; (iii) a mathematical normalization condition produces a flame shape equation that generates physically meaningful results; (iv) triple flames lose their "triple character very near the cold surface and when the global stoichiometry approaches extreme values.

More important than the actual agreement between the theory and the numerical computations are the implications of the agreement. Firstly, in the theory we have used the zero-flow mixture fraction (Z) field; however, comparisons made to cases with significant flow rates showed good agreement. We infer that the differences between the zero flow ($\varepsilon = 0$) Z-fields are not important near the triple flame structure. Our direct comparison of the Z fields shows that they are similar near the origin and far downstream. They differ only slightly in between. Since the triple flame structure is usually quite close to the surface, the use of the far-simpler, analytically-calculable zero flow Z-field is a useful simplification. Secondly, in our simplified theory we employed a self-consistent but truncated variant of the quench zone problem. The use of the normalization condition renders the flame shape calculation realistic by producing a zero slope at the tip of the PF arc. The agreement with the numerical calculations demonstrates that a rationally simplified quench zone model produces satisfactory results, and that our normalization criterion is correct: the PF arc slopes near the triple point (TP) are in fact smooth and continuous, as predicted from our theory. Thirdly, and perhaps most importantly, our scaling of the various zones is, in view of our results, entirely justified. The scaling was traditional, with $O(\beta^{-1})$ PF and DF arcs and an $O(\beta^{-2})$ region around TP. This is an interesting result, especially since recent work on simplified triple flame models has suggested some unique and previously unseen scalings of the various zones [11]. A detailed examination of the TP region, which we have not presented here, produces results that are much more complicated. As suggested by the examinations of [4] there is an inner elliptic region that is of order $\beta^{-1}x\beta^{-1}$ area that joins the two PF arcs, the DF arc and the upstream quench zone. When this is included in the flame arc analysis, it makes the examination more difficult but also more accurate. We have circumvented this difficult examination by imposing the normalization criterion in the TP vicinity, which preserves the continuity of the flame arc solution while smoothing over the nuances of the small inner zone.

Flame Quenching:

In [4] we examine the flame attachment problem in detail. This study is-in part - a detailed examination of the nature of flame tips. In contrast to alternative formulations [11] the elliptic character of the problem has not been eliminated. We have shown in [4] that a model problem can be formulated to describe the quenching of diffusion flames near cold surfaces. Under some conditions such as constant density, no convective flow, etc., we are able to derive a quench-distance formula that can be compared to numerical solutions. Extensions or generalizations of this formula are developed, and cases for which no solutions are possible are elucidated. The general comparison between the theoretical and numerical solutions is very good, especially for high Damköhler number. The comparison is improved over the entire range of Damköhler number by employing a sophisticated matching procedure leading to a nonlinear boundary-value problem. The sole requirement in this boundary-value

problem is the adequate definition of a "quenching temperature", τ_q, which we specified in two ways: (i) asymptotic τ_q; and (ii) fixed τ_q. Both procedures produced reasonable agreement with the numerical results, indicating that the detailed τ_q choice is insensitive. The simple and detailed models are described at length. Insofar as the rigor of these models can be increased, we are confident that their predictions of actual quenching will be significantly improved. We showed, however, that our correlations appeared to work well even with convection. We are therefore led to believe that the parametric content of the quenching formula is greater than expected for the restricted circumstances allowing its derivation. This study essentially completes our previous work [3], in which the only undetermined parameter was the quenching distance (which we specified from a complementary numerical solution). Here, we have produced a model for calculating that quenching distance. An important practical consequence of these quenching calculations is the ability to calculate the heat fluxes to the cold wall beneath the flame. This is the first time, to the knowledge of the authors, that the detailed nature of the flux distribution at the cold wall under (something resembling a) spreading flame has been determined. Formulae are produced for the heat flux in terms of global stoichiometry and gas-phase chemical parameters, and their anticipated use in are improved theory of flame spread is discussed.

Scaling Analysis of Flame Attachment and Liftoff:

Here the problem of flame attachment and liftoff is examined through scaling methods [10], leading to three distinct regimes of practical and theoretical interest: (1) a very slow flow regime; (2) a slow flow regime; (3) a moderate to fast flow regime. Correlations are developed for regimes (2), (3), whereas (1), which is independent of the flowrate, is describable by methods already outlined in the section previous. These correlations are not obtained through arbitrary means, but by the careful examination of the integral versions of the conservation equations, whose main terms are balanced through the use of characteristic nondimensional parameters. The theoretically deduced correlation formulae are carefully tested against numerical solutions, wherein we determine that correlations utilizing physically straightforward parameters such as the quench distance are much more useable than correlations containing derived parameters having no direct physical significance. We determine that for moderate to large flow rates, the flow itself dictates changes of flame structure relative to liftoff height, whereas with low flow rates the sensitivity to the reaction rate through the Zeldovich number dominates. The following correlations were deduced: (1) for moderate to high flow rates, the quenching distance is proportional to the 7/4 power of the flow rate; (2) for low flow rates, the quenching distance is proportional to the first power of the flow rate. The characteristic reaction layer width, which we said was a derived parameter, may have the significance of indicating the magnitude of the flame-tip width. It remains to determine whether or not this is true by examining the heat fluxes imparted by the flame tip to the surface. Comparisons of our results are made with four different groups of experiments; these comparisons range from favorable to excellent.

The Mixing Layer; Enthalpy Loss to Surfaces:

We have previously analyzed the generic structure of the species, temperature and enthalpy fields near the tip of the quenched flame [12]. A great variety of flame shapes was shown to be possible, although some have not yet been experimentally observed. Constraints are imposed on the conclusions for our generic case by features that have been neglected, such as the detailed flow field or the chemical reaction rate. These constraints narrow the actual set of possibilities, as demonstrated in [3,4]. For instance, it is possible, under some circumstances, that one of the two PF branches cannot exist [3]. As an example, for flame spread over solid fuels the observations suggest a vigorous lean PF and a practically nonexistent fuel-side PF. We have established the following facts in [12]. First, the orthogonal system of coordinates (Z,N) is not well suited to quenched flame tip analysis. A natural system of coordinates, with axes intersecting at the triple point and lying along the DF and PF arc, is more suitable. Such a coordinate system requires an interactive transformation of coordinates whose functional form is deduced along with the solution for the dependent variables. Second, in the non-isenthalpic case, a region of negative H exists downstream of the divider when $Le_o=Le_F=1$. This weakens the two PFs, producing a sharper or narrower flame structure. Third, a flame-shape analysis yields many interesting possibilities. Many of these flame shapes may not be realized in practice, however, because of finite chemistry and heat losses which weaken the flame. We have recently performed some numerical examinations of the mathematical features described in [12]. One of these is a detailed study of the enthalpy defect region, where the influence of the cold divider is most acutely felt. This region has a complicated structure that must be clearly understood before practical results can be properly interpreted. Another feature we have studied is the dynamic phenomenon of flame tip propagation speed. The tip of the flame has been postulated to move at the stoichiometric PF speed [13]. We have tested this hypothesis, and have determined that there are two distinct regimes of flame propagation. In one, the stoichiometric PF speed correlates with the local flow speed, and the hypotheses of [13] is justified. In the other, the PF speed is uncorrelated with the local flow speed, and the hypothesis of [13] is untenable. Here, the flame tip is dominated by losses, which entirely

alter the freely-propagating flame model that leads to correlations such as [13]. It remains for us to determine the physical dimensions of the region of breakdown, and its correlation with the enthalpy-defect zone. This work is now in progress.

Heat Flux to Bounding Surfaces:

As already mentioned at the end of the "Flame Quenching" section, an important practical consequence of our flame quenching calculation is the new-found ability to calculate heat fluxes to the surfaces beneath the quenched flame tip. Some background on this important practical calculation is necessary. In the field of flame spread, it has been the rule, rather than the exception, that practical, useful correlations are generally developed from integral theories utilizing the common methods of intuitive argument, physical insight and simplified global mathematics involving little more than the operations of arithmetic [1]. In these models, there is one crucial caveat: if the heat flux to the surface is only approximately or improperly known, the resulting correlations become unwieldy and unappealing for use. Thus, more than a few such practical correlation formulae have been rendered obsolete (note: they often perform the function of correlating data quite well). The opposite of this unwieldy complexity is the spare model of deRis [9], which is still the most commonly used theoretical correlation. The difficulty with the deRis model (and others like it) is that the heat flux details are oversimplified, with unphysical values in certain locations. Underneath the (attached) flame tip, the flux is infinite. Subsequent attempts to remove these infinites have resorted to ad-hoc methods. The recent, and most successful attempt [6] has used a more realistic flux distribution, but still employs the unappealing device of formulating a far downstream parabolic model and extrapolating upstream into a location where parabolicity breaks down. Thus, the resulting flux correlation loses much of its credibility. We believe that the resolution of this difficulty is to perform a detailed examination of the heat fluxes generated by a quenched flame to its nearby surroundings. In this way, we squarely address the "materials" question: the designer/user of a certain material is most interested in the level of thermal insult it will be subjected to, not the detailed nature of the gas-phase flame (interesting though it may be to a combustion scientist). We also open the door to the development of correlations that meld the austere elegance of the deRis model away from the flame tip to a detail-rich but physically realistic model near the flame tip. As shown in [6], such a combination can produce a much deeper understanding of - and predictive capability for - the heretofore intractable flame spread problem. Our approach is to employ the quenched flame tip model to derive a formula for the heat flux received by the cold wall beneath the flame. This formula is expressed as the product of a function of global stoichiometry with a function of reduced Damköhler number. Although this result may have been "anticipated" by persons of superior physical insight, the function of stoichiometry cannot be derived by mere physico-inuitive considerations: a mathematical model is necessary. We are presently comparing the model predictions to numerical results for the same problem. One of our goals in this research is to develop means for characterizing the heat flux distribution in terms of quantities with physical relevance. One such quantity is the maximum heat flux, $q*$. Another is its location, $x*$. Yet another is the total flux received, Q. A parameter that may also be useful is a measure of the region in which most of the heat flux (say the fraction $1-e^{-1}$) is received. In a physical sense, such boundaries would provide a practical measure of the size of the region directly affected by the flame tip. Such formation is of direct relevance for the "materials" question.

Numerical Computations:

We have developed various computational models corresponding to the theoretical models. The simplest models examine only the heat transfer and species transformation features, with the fluid dynamics accounted for by the assumption of inviscid, constant density slug flow. Here, complexities such as vorticity, flow separation and reattachment, local flow expansion due to heating, etc., are not included. Consequently, these models focus on the quantities described above: flame-tip structure; attachment and liftoff; details of mixing layers; enthalpy loss; heat fluxes to boundaries. Whenever possible, direct comparisons are made to theoretical calculations. The most complex model, however, is far more detailed. It includes the full Navier-Stokes equations with variable properties, plus the energy and species equations (also with variable properties). All boundary conditions are physically realistic (no slip, etc.). Certain very surprising similarities with the slug flow model are found. Slightly downstream of the divider, we find that the flame tip essentially eliminates the local gas-phase velocity gradients. Therefore, the flow into the flame tip (TP) is very similar qualitatively to that employed in the slug flow model are found. Slightly downstream of the divider, we find that the flame tip essentially eliminates the local gas-phase velocity gradients. Therefore, the flow into the flame tip (TP) is very similar qualitatively to that employed in the slug flow model. For laminar flow, we have also determined that the thermal expansion eliminates the recirculation zones that appear without chemical reaction. Consequently, the fluid dynamics are greatly influenced by the state of the combustion (flame). Because the flow is laminar and steady, there is an upper bound $Re \sim O(10^3)$ which we cannot exceed. We are investigating the various attachment (quenching) and lifting behaviors in light of previous developments for the reduced models. There appear to be three regimes of flame attachment. In the lowest, heat losses dominate and the flow details are unimportant. In the next, the flow details are important and the flame quenching follows, essentially, the predicted model behavior. In the final stage,

chemistry is no longer important. The reaction is so fast that the flame is essentially buoyancy dominated. For this reason, the flame tip cannot approach any closer to the surface since the thermal expansion at the flame tip prevents additional downward movement. It would be interesting to develop this model without buoyancy (gravity "turned off"). We are presently pursuing such an examination. We shall also examine the case when the model is turned sideways, and gravity is made orthogonal to the flow direction.

Flame Spread:

Here we follow the approach described below. First, we recognize the formal validity of the Higuera [5] approach in mathematically delineating various zones across the viscous and thermal boundary layers in opposed-flow flame spread. The opposed velocity in the Navier-Stokes region encompassing the flame tip has the characteristic value u_g, which may be written as the product of the square root of a velocity gradient (a) with a diffusivity α. This limit, however, need not be strictly valid (since it requires an enormous free-stream Reynolds number), but for purposes of developing our analysis, we may consider it qualitatively valid. In the Navier-Stokes region, the steady-flow equations are elliptic. A qualitative understanding of this region can be obtained by replacing the variable velocity coefficient, ay, with the slug-flow value u_g, which renders the equations in constant coefficient form. Then, established methods of analysis may be employed to solve for the mixture fraction Z and for the normal temperature gradient along the surface. From the former, we calculate the mixture fraction gradient, which we employ in a subsequent asymptotic analysis of the energy equation near the flame tip. From the latter, we obtain expressions for the heat flux into the surface everywhere except near the flame tip. The asymptotic analysis of the equations near the flame tip produces, as in the section "Flame Quenching", expressions for the heat flux into the surface, which we join to the expressions upstream and downstream of the flame tip. This heat flux formula will then be used in a manner analogous to Rybanin [6], leading to a flame spread formula that includes all processes occurring over the length of the heated solid surface, over which spreading occurs. This formula should be capable of predicting the dependence of the flame spread rate on chemical parameters, as in [6] but with greater accuracy. We are presently developing the Navier-Stokes region model, from which the fluxes to the surface will be evaluated.

1. Wichman, I.S., "Theory of Opposed-Flow Flame Spread," Prog. Energy and Combustion Science, 18, 553-593 (1992).

2. Wichman, I.S., "On the Quenching of a Diffusion Flame Near a Cold Wall" Combustion Science and Technology, 64, 295-313 (1989),

3. Wichman, I.S., Lakkaraju, N., and Ramadan, B., "The Structure of Quenched Triple Flames Near Cold Walls in Convective Flows," MSU CRL #07-30-96. Also submitted to Comb. Sci Tech. (1996).

4. Wichman, I.S., Pavlova, Z., and Ramadan B., "Attachment of Diffusion Flames Near Cold, Chemically Inert Surfaces With and Without Reactant Flow," MSU CRL #09-24-96 (1996). Also, to be submitted (1997).

5. Higuera, F.J., Liñán, A., and Iglesias, I., "Effects of Boundary Layer Displacement and Separation on Opposed-Flow Flame Spread," to appear in Combustion Theory and Modeling (1997).

6. Rybanin, S.S., "The Dependence of the Flame Spread Rate Over Solid Fuel on Damkohler Number and Heat Loss," to appear in 26th symposium (International) on Combustion, the Combustion Institute, Pittsburgh (1997).

7. Van Dyke, M., Perturbation Methods in Fluid Mechanics, Parabolic Press, Stanford, CA (1975).

8. Carrier, G.F., and Lin., "On the Nature of the Boundary Layer Near the Leading Edge of a Flat Plate", Quart. Appl. Math, 6, pp. 63-68 (1948).

9. deRis, J.N., "Spread of a Laminar Diffusion Flame," Twelfth Symposium (International) on Combustion, the Combustion Institute, Pittsburgh, pp. 241-252 (1969).

10. Wichman, I.S., and Ramadan, B., "Scaling Analysis of Diffusion Flame Attachment and Liftoff," to appear in 2nd International Symposium on Scale Modeling, Lexington, KY (1997).

11. Buckmaster, J., and Weber, R., "Edge-Flame Holding," to appear in 26th Symposium (International) on Combustion, The Combustion Institute, Pittsburgh (1997).

12. Wichman, I.S., "Basic Features of Triple Flames in Combustion Theory", in <u>Transport Phenomena in Combustion</u> (ed. S.,H. Chan), Taylor and Francis, pp. 456-466, 1996.

13. Takahaski, F. et al., Twentieth Symposium (International) on Combustion, The Combustion Institute, Pittsburgh, pp. 295-302 (1985).

INTERACTIONS BETWEEN FLAMES ON PARALLEL SOLID SURFACES

DAVID L. URBAN
Microgravity Science Division

Jeffrey S. Goldmeer
National Research Council

Zeng-guang Yuan
NYMA Inc.

NASA Lewis Research Center

Introduction

The interactions between flames spreading over parallel solid sheets of paper are being studied in normal gravity and in microgravity. This geometry provides interesting opportunities to study the interaction of radiative and diffusive transport mechanisms on the spread process. Radiative losses from flames are recognized as an important component of flame spread [1, 2]. These loss mechanisms are changed when the flame interacts with other flames. Most practical heterogeneous combustion processes involve interacting discrete burning fuel elements, consequently, the study of these interactions is of practical significance. Owing largely to this practical importance, flame interactions have been an area of active research, however microgravity research has been largely limited to droplets, [3, 4]. Consideration of parallel solid surfaces has been limited to 1-g studies [5, 6, 7, 8, 9, 10]. Of these works, [5, 7, 8] considered flame spread.

Emmons and Shen [5] studied horizontal flame spread over an array of vertically oriented paper sheets. The flame spread rate was found to be proportional to the fuel sheet aspect ratio (height/separation) for small and large values of the aspect ratio. However, the proportionality was different in these two cases and, at intermediate values, the correlation broke down. Using a simple model for the energy transport ahead of the flame and a value for the burning zone width, estimated from the data, acceptable agreement was obtained with the experimental data.

Kim, De Ris and Kroesser [6] performed a theoretical and experimental analysis of the burning rate between two parallel fuel surfaces. Assumptions similar to those in the work of De Ris [11] were made (unity Lewis number, infinite gas phase reaction rate and insignificant radiative transport). Burning rate was found to be controlled by the product of the Grashof number and the channel aspect ratio (b/l (channel half width/length)). Good agreement was found between the theoretical formulation and the burning rate for methanol-soaked slabs. The selection of methanol as the test fuel increased the suitability of the assumption that radiation could be neglected since methanol flames produce little soot and consequently the radiative transport from the flames can be expected to be small. Three burning regimes were found depending upon the ratio l/b^4. For small values of l/b^4, the burning rate was independent of b; for larger values, the burning rate is independent of l but proportional to the b^3. At intermediate values a simple parameter dependence was not observed.

Ohlemiller and Villa [12] and Ohlemiller [13] suggest the importance of considering the radiant interaction between two surfaces in NASA's flammability assessment of materials. The current flammability standard for materials to be used on spacecraft [14] is an upward burning test with a single sheet of material. As Ohlemiller [13] suggests, this is a geometry that is not necessarily the worst case it is intended to be. Without radiant preheating of the unburned material, the flammability hazard is lower than with modest radiative feedback. This issue is also being addressed in another program [15] where the influence of radiant preheating on ignitability and spread is addressed. The radiant interaction between surfaces is also very important in terrestrial fire safety; the classic example is wood, which is nearly nonflammable as a single large sheet but very flammable if multiple pieces are arranged to allow radiant interaction.

The parallel spread geometry offers several distinct differences from single sheet spread, the appearance of the internal flame, instabilities of the internal flame, pressure dependence of spread rate and spread rate variation with separation distance. These issues are being studied as part of this program and are discussed below.

Experiment Description

The tests were conducted for downward flame spread over parallel sheets of paper. The fuel was stored in a desiccator and the chamber filling process exposed the fuel to vacuum or dry air for at least two hours. The low gravity tests were conducted in the NASA LeRC 2.2 second drop tower. The majority of the tests were conducted in a 27 liter chamber although a some of the early tests were in a 45 liter chamber. The fuel was Kimwipe laboratory wipes, selected because of their uniform thickness and low mass/area (1.9 mg/cm^2) The sample frame opening was 5 or 7.5 cm wide and the flame spread rate and flame structure were observed using a color video camera on the edge view. The oxidant was either mixed in the chamber using partial pressures or supplied directly from a gas bottle, in either case the mixture error was less than 0.5 mole%. The bulk of the low gravity tests were conducted at 30% oxygen because a value within the quiescent microgravity flammability range for Kimwipe was desired, while the normal gravity tests were conducted at 21% oxygen. The diluent was either helium or nitrogen. Test pressures ranged from 0.13 to 2 atmospheres, and separation distances between the fuel sheets varied from 6.4 to 76 mm. Unlike single sheet tests, it was learned that the ignition process must be carefully controlled to prevent the ignition products from filling the gap between the fuels, thereby preventing development of internal flame(s).

The experiment imaging was recorded in S-VHS video format. After the tests, the video frames were digitized using a frame grabber and the flame spread rate was determined using object tracking software which stepped through the video images and determined the position of the leading edge of the flame. The spread rates were very stable throughout the tests with correlation coefficients greater than 0.99. Where there was a flame between the sheets of paper (internal flame), the reported spread rates are the average of the spread rates of the internal and external flames on at least one of the sheets. The camera was centered on the edge of one of the sheets to provide optimum imaging of one pair of flames. At large separation distances, the flames on the second sheet were sufficiently distorted that they could not be tracked; for these cases the spread was determined from only the sheet aligned with the camera. The overall spread rate measurement accuracy was greater than the repeatability which was of the order of 0.15cm/s.

A limited number of tests were conducted in flowing air on the NASA DC-9 aircraft using the Spacecraft Fire Safety Facility. This facility provides a flow through a chamber that is similar to the one used in the drop tower tests. Experimental timing and video recording were similar to the drop tower tests. The details of the experimental facility are described elsewhere [16].

Interferometer Development

To study the conductive transport in these flames, an interferometer system is under development for use in the drop tower. The system takes advantage of a single beam interferometer: Point Diffraction Interferometry (PDI) [17] which uses a portion of the light through the test section to provide the reference beam. This provides considerable resistance to vibration effects seen with traditional interferometers. Like other interferometric and Schlieren systems, it is fundamentally a line of sight measurement and is subject to the usual edge and concentration effects. The advantage over Schlieren and shearing interferometry systems is that the fringes are lines of constant index of refraction rather than of the gradient so the images are more readily interpreted. The disadvantage is that it is less adjustable to accommodate a range of temperature gradients. The implementation of the system took advantage of an imaging soot volume fraction system which was already configured for use in the 2.2 second drop tower. Results from a breadboard system are shown in figure 1 which contains the interferogram of a vertical flat plate at 300 C and figure 2 which contains a comparison of temperature profiles from the vertical flat plate obtained with a thermocouple and the interferometer. Figure 3 is an interferogram of flames spreading over parallel sheets in normal gravity. The system offers significant promise as a diagnostic for visualizing the interactions between these flames in drop tower applications.

Results and Discussion

It was found that although the flame interactions in microgravity display trends similar to those seen in normal gravity, the microgravity flames exhibit greater interaction for a given separation distance, the difference being attributed to the absence of the buoyant flow. The interaction displays four phases as separation distance is increased (Fig. 4): 1. no flame between the sheets of paper (internal flame), 2. an unstable internal flame, 3. a single internal flame which becomes more deeply notched with separation distance, and 4. individual internal flames on each surface which in the limit of large separation become independent of each other. These results are similar to those reported for normal gravity flames by Kurosaki, Ito and Chiba [7] who reported, as separation distance was reduced, a progression from independent flames through increasing flame interaction to ultimate extinguishment of the internal flame. The range of separation distances over which the interaction was apparent was much greater than that seen in normal gravity tests (Fig. 5) where separate flames are observed at 10 mm separation while the low-g flames were still connected at 40 mm separation.

430

Figure 6 contains the spread rates for parallel sheets at various separation distances with helium and nitrogen diluents. A separation distance of infinity was used to represent the single sheet case. As is evident on the plot, the spread rate reduction at close separation extended to greater separation distances for helium than for nitrogen. For nitrogen diluent, once the inner flame was completely established, the spread rate approximated the single sheet value. For helium, an actual maximum is present, similar to the 1-g results of Kurosaki et al. [7]. The greater dependence on separation distance for the helium case is consistent with helium's larger thermal diffusivity, which was also evident in the fact that the helium flames were much larger than the corresponding nitrogen flames, and interacted over greater separation distances. The tendency of the internal flame to extinguish at larger separations for helium can be attributed to increased conductive losses to the paper. Assuming the inner flame to be an oxygen limited process a simple dimensional comparison of the heat loss to the fuel surface suggests that as the separation distance is reduced, the heat loss to the surface becomes greater than the energy available from reaction. The limited change in the spread rate with separation for the nitrogen diluent is less extensive than that reported for 1-g interactions [7] particularly given the evident interaction in the video record.

The change in the non-dimensional spread rate as a function of pressure is presented in figure 7. The rates are non-dimensionalized using the thin fuel spread model of De Ris [11]. Using this relation the non-dimensional spread rate is:

$$\overline{V}_f = V_f / \left(\frac{\sqrt{2}\lambda}{\rho_w c_{pw} \tau} \frac{(T_f - T_v)}{(T_v - T_\infty)} \right)$$

Where the flame temperature is calculated using the adiabatic flame temperature [18] and the vaporization temperature was taken to be 618 K. The product of the solid thickness and density is 0.0011 gm/cm^2 for the half-thickness and the specific heat is 1.26 kJ/kg/K. The mixture thermal conductivity was calculated using the Sandia Transport Package [19]. The De Ris model predicts that spread for a thin sheet is independent of pressure. However for sets of parallel sheets in microgravity, there is a clear pressure dependence, whereas the 1-g data show very limited dependence once the inner flame is established at approximately 0.15 Atm. This pressure dependence, in microgravity is consistent with the results of Bhattacharjee et al. [2] who observed similar pressure dependence for the Solid Surface Combustion Experiment (single sheets). Their modeling suggests that the difference between the measured spread rate and the De Ris [11] prediction is due to radiative losses from the flame while the spread rate increase with pressure is also due to radiation, in this case, radiative heating of the preheat zone. Figure 8 is a logarithmic plot of the same data with associated linear fits which show the spread rate dependence on pressure is well predicted by a power between 0.75 and 1.

Conclusions

The current work has shown the importance of detailed understanding of the transport processes that contribute to the flame spread. The planned implementation of an interferometer in the drop rig combined with radiometric measurements of flame radiation will help determine the extent to which radiation from the flame to the surface participates in the spread. The flame spread as a function of separation distance shows stronger interaction effects for helium than for the nitrogen case. This is attributed to the difference in the thermal diffusivity.

References
1) Sacksteder, K.R. and J.S. T'ien. 1994. Buoyant Downward Diffusion Flame Spread and Extinction in Partial Gravity Accelerations. Twenty-fifth Symposium (International) on Combustion, 1685-1692.
2) Bhattacharjee, S., R.A. Altenkirch, and K. Sacksteder. 1996. The Effect of Ambient Pressure on Flame Spread over Thin Cellulosic Fuel in a Quiescent, Microgravity Environment. Journal of Heat Transfer, V 118, 181-190.
3) Dietrich, D.L. and J.B. Haggard. 1992. Combustion of Interacting Droplet Arrays in a Microgravity Environment. Second International Microgravity Combustion Workshop, NASA CP 10113, 317-323.
4) Mikami, M., H. Kato, J. Sato, and M. Kono. 1994. Interactive Combustion of Two Droplets in Microgravity. Presented at 25 Symposium (International) on Combustion, Irvine CA.
5) Emmons, H.W., and T. Shen. 1971. Fire Spread in Paper Arrays, Thirteenth Symposium (International) on Combustion 917-926.
6) Kim, J.S., J. De Ris, and F.W. Kroesser. 1974. Laminar Burning Between Parallel Fuel Surfaces. International Journal of Heat and Mass Transfer 17:439-451.
7) Kurosaki, Y., A. Ito and M. Chiba. 1979. Downward Flame Spread Along Two Vertical, Parallel Sheets of Thin Combustible Solid. Seventeenth Symposium (International) on Combustion 1211-1220.
8) Itoh, A., and Y. Kurosaki. 1985. Downward Flame Spread along Several Vertical, Parallel Sheets of Paper. Combustion and Flame 60:269-277.
9) Tamanini, F. and A.N. Moussa. 1980. Experiments on the Turbulent Burning of Vertical Parallel Walls. Combustion Science

and Technology 23:143-151.

10) Toong, T.Y. 1961. A Theoretical Study of Interactions Between Two Parallel Burning Fuel Plates. Combustion and Flame 5:221-227.

11) De Ris, J.N. 1969. Spread of a Laminar Diffusion Flame. Twelfth Symposium (International) on Combustion 241-252.

12) Ohlemiller, T.J., and K.M. Villa. 1991. Material Flammability Test Assessment for Space Station Freedom. NISTIR 4591, NASA CR-187115, NIST, Gaithersburg, MD.

13) Ohlemiller, T.J. 1992. An Assessment of the NASA Flammability Screening Test and Related Aspects of Material Flammability. NISTIR 4882, NASA CR-189226, NIST, Gaithersburg, MD.

14) NHB 8060.1C. 1991. Flammability, Odor, Offgassing, and Compatibility Requirements for Material in Environments the Support Combustion. NASA OSMQ.

15) Cordova, J.L, J. Ceamanos, A.C. Fernandez-Pello, R.T. Long, J.L. Torero and J.G. Quintiere. 1997. Flow Effects on the Flammability Diagrams of Solid Fuels. Fourth International Microgravity Combustion Workshop, Cleveland OH.

16) Goldmeer, J.S. Extinction of a Diffusion Flame over a PMMA Cylinder by Depressurization in Reduced-Gravity. 1996. NASA CR-198550.

17) Smartt, R.N. 1979. Special Applications of the Point-Diffraction Interferometer, SPIE Vol 192, 35-40.

18) Pratt, B.S. and D.T. Pratt. 1984. An Interactive Code for Calculation of Gas-phase Chemical Equilibrium: EQLBRM, NASA CR-168337.

19) Kee, R.J., J. Warnatz, and J.A. Miller. 1983. A Fortran Computer Code Package for the Evaluation of Gas-Phase Viscosities, Conductivities and Diffusion Coefficients. SAND83-8209.
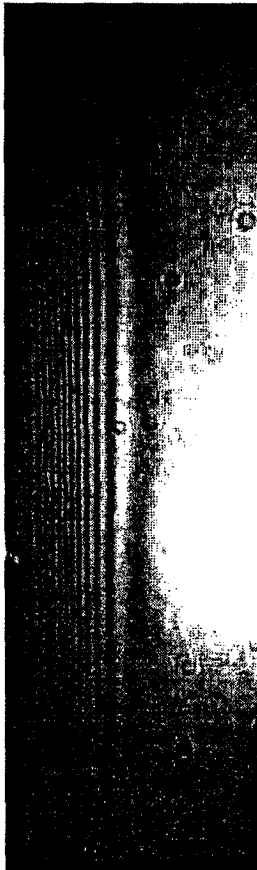
Figure 1. Interferogram of the edge view of a vertical heated flat plate at 300 C. The surface of the heated plate is on the left of the image
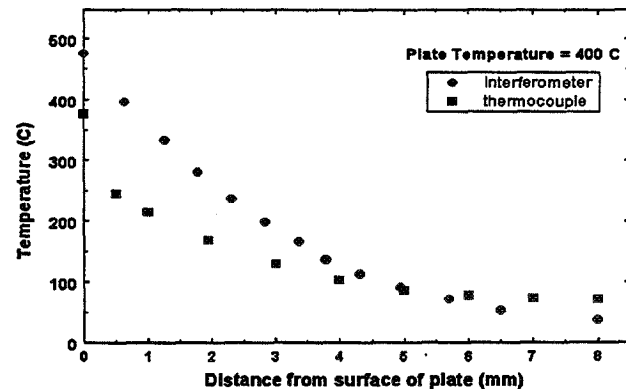

Figure 2. Temperature versus distance from a 400 C vertical flat-plate determined using the Point Diffraction Interferometer versus thermocouple measurements.
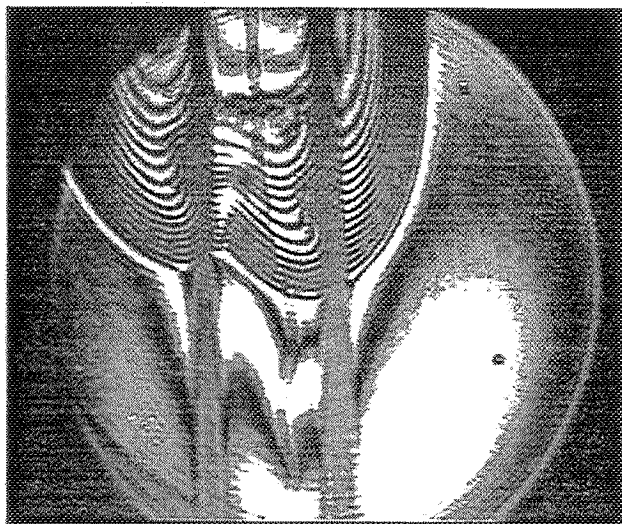
Figure 3 Interferogram of edge view of flames spreading downward (1-g) over parallel sheets in ambient air. The separation distance is 6.5 mm. The line visible between the fuel sheets is the ignitor wire.
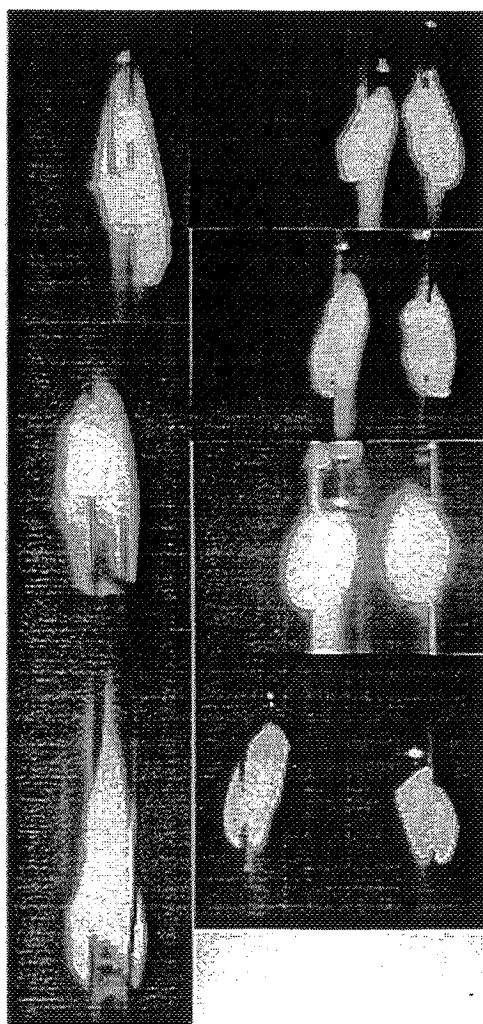

Figure 4. Edge view of flames propagating in microgravity over parallel sheets of Kimwipe at different separation distances in 30% oxygen, balance nitrogen, at 1 Atm. Separation distances in order (top to bottom, left to right) are 6.4, 10, 20, 30, 40 and 50 mm. Glowing material at top of each flame is the ignitor wire.

Figure 5. Edge view of flames propagating in normal gravity over parallel sheets of Kimwipe at different separation distances in dry air at 1 Atm. Separation distances in order (top to bottom, left to right) are 3 mm, 4.7, 6.4, 10, 15, 20, and 30 mm.
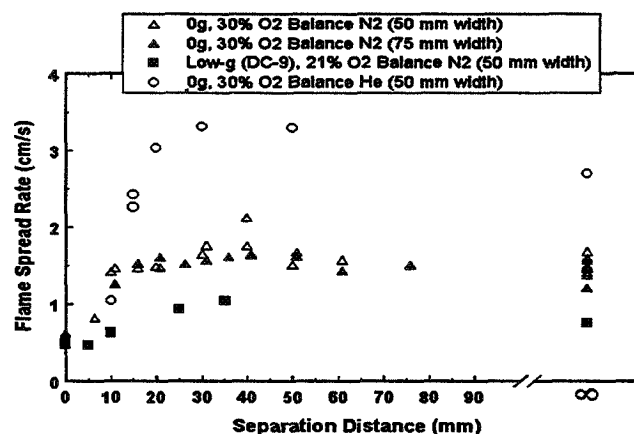
433

Figure 6. Spread rate versus separation distance for parallel sheets in microgravity at 1 atmosphere. The DC-9 tests were in air with a forced flow velocity of 10 cm/s. The other tests were in quiescent mixtures of 30% oxygen with nitrogen or helium.
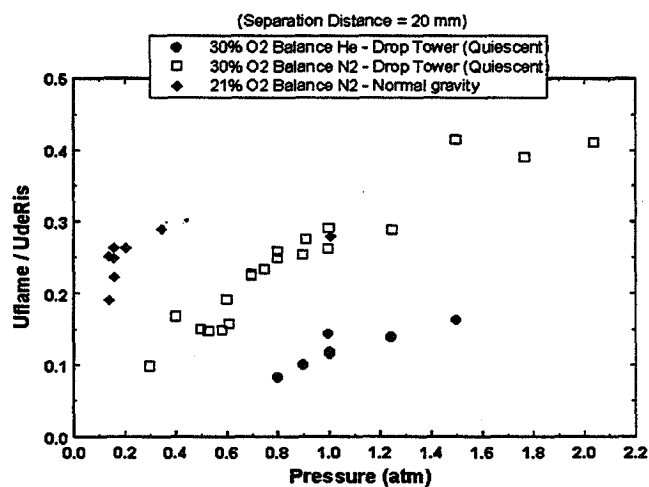

Figure 7 Non-dimensional spread rate versus pressure in 1-g and in low-g.
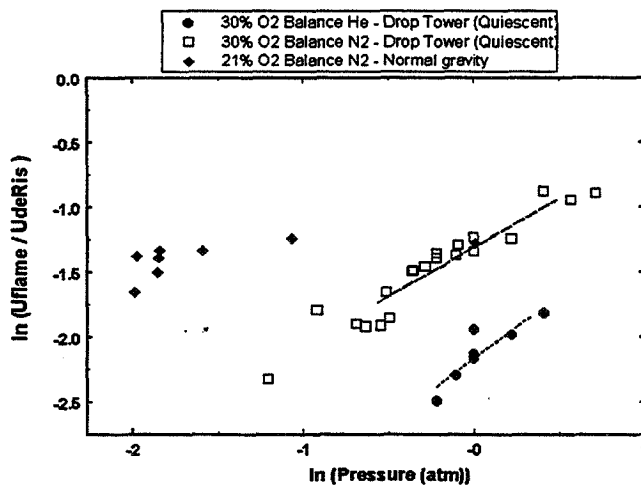

Figure 8 Non-dimensional spread versus pressure. The slope of the nitrogen diluent case is 0.76 and the helium diluent case is 0.98.

EXTINGUISHMENT OF A DIFFUSION FLAME OVER A PMMA CYLINDER BY DEPRESSURIZATION IN LOW-GRAVITY

JEFFREY S. GOLDMEER[*] and James S. T'ien
Case Western Reserve University
Cleveland, Ohio

and

David L. Urban
NASA Lewis Research Center
Cleveland, Ohio

Introduction

The behavior of flames in low-speed flows in low-gravity is relevant to spacecraft fire safety [1]. Previous work [2-5] has shown that flames in the presence of low-speed forced flows in low-gravity may be more flammable than in a forced flow of the same magnitude in normal gravity. Additionally, fire suppression plans for the International Space Station include the use of venting (depressurization) as an emergency option for extinguishing fires [6]. This procedure would induce flows in the affected compartment that could temporarily intensify the fire, as was observed in flammability tests of solids conducted on board Skylab [7]. Despite a general understanding, current knowledge of the combined effects of reduced pressure and forced flow on a burning solid in low-gravity is inadequate for the design of a venting extinguishment system.

Previous studies in low-g have examined flammability limits for thermally thin solids [3-5]. However, there are differences when burning thick materials because the interior solid-phase temperature continuously changes, which affects the percentage of gas-phase heat feedback to the solid-phase. Changes in the heat feedback to the solid-phase can affect the flammability characteristics of the material [2]. In the current work, the extinction of a diffusion flame burning over PMMA (polymethyl methacrylate) cylinders during depressurization with a low-speed cross flow was examined experimentally and via numerical simulations.

Experimental Hardware & Procedures

Solid PMMA cylinders that were placed perpendicular to the forced flow were selected as the sample geometry as two distinct flow regions exist when a cylinder is placed in a cross-flow: a forward stagnation region and a wake region. The PMMA cylinders were 1.9 cm in diameter and 2.5 cm in length and steel washers were placed at the ends of the samples to limit burning along the ends of the cylinders. The experiments were conducted on board the NASA Lewis Research Center's reduced-gravity aircraft that provides twenty second periods of low-gravity (±0.01 g's) [8]. The samples were ignited by a resistively heated wire before entering low-g at one atmosphere; the chamber pressure was reduced to the test condition during low-g. The samples were ignited during the normal-gravity portion of the flight trajectory because the time required to establish the flame was longer than the entire low-g period. To determine the low-pressure extinction limit the chamber pressure was reduced at a rate of 0.24 atm/minute from the initial low-g test pressure until the flame extinguished. During each experiment the acceleration levels, chamber pressure, solid-phase centerline temperature, and video images of the flame (both radial and axial views) were recorded.

Experimental Results

The experiments examined the low-pressure extinction limit in air as a function of pressure and solid-phase centerline temperature at a constant velocity of ten cm/s. The low-pressure limit could not be reached with flow velocities larger than ten cm/s due to limitations of the vacuum system. Limited extinction data was collected at five cm/s due to the effects of g-jitter, which is a perturbation of the acceleration level. In the cases in which extinction occurred, the acceleration data was examined to determine if extinction was caused by g-jitter or the reduction in pressure. In cases in which there was no g-jitter and the flame extinguished, extinction occurred by one of two modes: quench or blow-off. Quenching extinction was observed when the flame tips receded toward the forward stagnation point (FSP) and the flame continued to shrink until it extinguished. Quenching extinction occurred in tests with a centerline temperature less than 320 K. Blow-off extinction was attributed to cases in which the flame was carried downstream by the forced flow as illustrated by the time sequence of images shown in Figure 1. The white streaks at the bottom of each image are the ignitor wire heated by the flame.

A flammability map was created using the experimental extinction pressure and solid-phase centerline temperature data at extinction (Figure 2). Experimentally, the cylinders supported a flame to the right of the boundary. No flames were observed at conditions to the left of the extinction data. As expected, the experimental results indicate that a hotter material requires a lower pressure to

* Jeffrey Goldmeer is currently a National Research Council Research Associate at the NASA Lewis Research Center.

extinguish. As the solid-phase centerline temperature increases, the extinction pressure decreases, and with a centerline temperature of 525 K, the flame is sustained to a pressure of 0.1 atm before extinguishing. At pressures above 0.3 atm the flame did not extinguish. The error bar on the boundary represents the scatter in the data that could have been caused by variations in the magnitude and duration of the high-gravity portion of the trajectory, or the transition from normal-gravity to low-gravity. One of the limitations of the experiments was the small size of the PMMA cylinders. The sample length and diameter were nearly equal, and because of this, the experimental configuration was not completely two-dimensional; there were axial heat losses from the samples and the flame shape exhibited some three-dimensional effects.

Numerical Model & Simulations Procedures

The numerical simulation used in this research iteratively couples a two-dimensional quasi-steady gas-phase model [2] with a two-dimensional transient solid-phase model [9]. The gas-phase model includes Navier-Stokes, continuity, energy and species equations with a one-step second order overall chemical reaction and Arrhenius kinetics. This model does not include gas-phase radiation, it assumes an infinite cylinder, and the computational domain has a streamwise symmetry boundary condition two diameters from the centerline. The solid-phase model includes conductive heat transfer within the solid and surface regression due to vaporization. The energy balance at the gas/solid phase interface is given by:

$$\lambda_G \frac{\partial T}{\partial n}\Big|_G = \lambda_S \frac{\partial T}{\partial n}\Big|_S + \dot{m}L + Q_{RAD} \qquad (1)$$

in which λ_S and λ_G are the solid-phase and the gas-phase thermal conductivities, n is the surface normal, $\dot{m}$ is the vaporization rate, L is the heat of vaporization, and Q_{RAD} is surface radiation. The ratio of the solid-phase and gas-phase conduction terms in the energy balance is defined as Φ, which can be written as:

$$\Phi = \frac{\lambda_S (\partial T / \partial n)_S}{\lambda_G (\partial T / \partial n)_G} = 1 - \frac{\dot{m}L + Q_{RAD}}{\lambda_G (\partial T / \partial n)_G} \qquad (2)$$

This ratio varies in time and along the circumference of the cylinder. Experimentally, the status of the flame at the forward stagnation point (FSP) was critical to sustained combustion. In quenching extinction the flame at the FSP was the last to extinguish; if the flame at the FSP was locally extinguished, the remaining portions of the flame followed quickly (blow-off). No wake flames were observed in the present low-g experiments. Thus, the value of Φ at the forward stagnation point (Φ_{FSP}) is used in evaluating the simulation results. The computed Φ_{FSP} and the centerline temperature as a function of time are shown in Figure 3 together with the experimentally measured centerline temperatures. (The different symbols for the experimental centerline temperature represent different cases with different final pressures.) Since there is a one-to-one correspondence between Φ_{FSP} and the centerline temperature, the measured centerline temperature can be used to infer Φ_{FSP}, which is an important parameter in the quasi-steady gas flame model. High values of Φ_{FSP} (near 0.9) occur at ignition and Φ_{FSP} decreases as the gas-phase heats the solid-phase (Figure 3). The small discrepancy between the experimental temperature data and the model's predictions may be due to experimental axial heat losses that are not included in the model.

The simulations start with the solid-phase model mimicking the transient heat-up process during ignition and flame spread [9]. Using the experimental data as a guide, the solid-phase simulation generates the surface boundary condition needed to couple with the gas-phase flame equations. The coupled system of unsteady solid equations and quasi-steady gas-phase equations are then used to model the flame behavior as the pressure is reduced. Two sets of simulations have been made; in the first set, the simulation parameters are selected to mimic the experimental conditions. In the second set, parameter values that could not be examined experimentally were simulated. The coupled model is run until the flame extinguishes.

Numerical Results

Initial simulations examined conditions similar to the present low-gravity experiments. The predicted flame behavior during depressurization and extinction, which is similar to the experimental flame behavior, can be visualized with fuel reaction rate contours from a single case (Figures 4 and 5). The images in Figure 4 are predicted quasi-steady flames during depressurization. The stand-off distance, which is defined as the distance from the surface of the cylinder to the middle of the maximum fuel reaction rate contour, is predicted to increase as the pressure decreases; this effect was also observed in the low-g experiments. The predicted blow-off extinction process for this case is shown in Figure 5; image (A) is at the identical conditions as image (F) in Figure 4 and images (B) - (E) are at the next step in the model's coupling process that occurs with a lower pressure and a decrease in Φ_{FSP}. Images (A) and (E) in Figure 5 are quasi-steady predictions while images (B) - (D) are intermediate gas-phase steps. The ability to use the intermediate steps from the gas-phase model as representations of a transient process is possible because the convergence routine uses a fictitious time marching term [9]. During the extinction process, the predicted reaction rate contours behave similarly to the experimental flame extinction process (Figure 1); the experimental flame and the predicted contours detach from the forward stagnation point and are carried downstream by the forced flow. Table 1 summarizes model parameters and outputs for the simulation case illustrated in Figures 4 and 5.

The simulation predicts low-pressure extinction limits consistent with the experimental limits (Figure 6). In this figure, the extinction pressure is expressed as a function of Φ_{FSP}. The experimental value of Φ_{FSP} is deduced from the centerline temperature data (Figure 3). The error bars in Figure 6 represent the possible range of Φ_{FSP} due to the difference between the predicted centerline temperature and the experimental data.

Additional simulations examine conditions that could not be investigated experimentally due to limitations of the hardware and test facilities. These simulations examine the effects of flow velocities, ranging from one to twenty cm/s, which is important as the induced velocity in the space station module would be a function of location relative to the vent valve. These additional simulations also examine the effects of increases in the solid-phase temperatures (decreases in Φ) before depressurization, which is relevant to the space station procedure as the elapsed time between the detection of a fire and the start of depressurization cannot be predetermined. Thirdly, the additional simulations examine depressurization rates lower than the present experimental rate (slower depressurization), which includes the proposed space station venting scenario, which is an order of magnitude slower than that of the present experiments.

The effect of velocity on the extinction limit is not monotonic. At values of constant Φ_{FSP}, flames are sustained to lower pressures at ten cm/s than at one or twenty cm/s (Figure 7); the region above each constant velocity curve is the flammable domain. At constant velocity, flames are sustained as the pressure decreases if Φ_{FSP} decreases, which is equivalent to increases in the solid-phase temperature (Figure 8). A negative value of Φ_{FSP} indicates that the temperature gradient within the solid is reversed; the hot solid conducts heat to the surface to compensate for the decrease in heat feedback from the flame that occurs because the reaction rate decreases with pressure [9]. This reversal in Φ_{FSP} occurs in simulations in with a long depressurization time, or a long period of burning before depressurization.

Increasing the solid-phase temperature (decreasing Φ) by either a longer period of burning before depressurization, or an increase in the depressurization time, decreases the extinction pressure. The model predicts blow-off extinction at velocities greater than fifteen cm/s and quenching at velocities less than eight cm/s. Additionally, the simulations predict that the path taken to the extinction boundary is not critical; extinction will occur at the boundary whatever the path taken (assuming a quasi-steady gas-phase process).

Conclusions
The degree of heat up in a thick solid material affects the low-pressure extinction limits in low-gravity. The relevant solid-phase parameter is Φ, which is the ratio of solid-phase to gas-phase conduction at the gas-solid interface. The solid-phase temperature increases during combustion, Φ decreases and the extinction pressure decreases. The low-pressure limit is also affected by the presence of a forced flow; a condition of increased flammability occurs at velocities of eight to ten cm/s. This is also the critical velocity dividing two different extinction modes: quenching extinction occurs at lower velocities and blow-off at higher velocities.

The results of this research could be used to refine the International Space Station's venting specifications, which state that the affected module would be depressurized from 1.0 atm to 0.3 atm within a period of ten minutes [4]. This research suggests that an effective venting procedure would be to quickly depressurize the module to a pressure of 0.1 atm, which would probably extinguish the fire. Rapid venting to the final pressure would limit additional heating of the solid-phase that would otherwise cause a decrease in the extinction pressure. The disadvantage to rapid venting is that it could cause the flame to intensify, as documented in the Skylab experiments [7]. The current simulations indicate that the flame might temporarily intensify if there was an increase in the forced flow, but the increases in the gas-phase temperatures and reaction rates quickly disappear as the pressure decreases.

References
1.   Friedman, R., and Sacksteder, K., 1988, "Fire Behavior and Risk Analysis in Spacecraft", NASA TM-100944.
2.   Yang, C.T., and T'ien, J.S., Submitted to the 1997 ASME Heat Transfer Conference.
3.   Ferkul, P., and Tien, J., 1994, Combustion Science and Technology, Vol. 99, pp. 345-370
4.   Olson et al., 1988, Twenty-Second Symposium (International) on Combustion, pp. 1213-1227.
5.   Sacksteder, K., and T'ien, J., 1994,, Twenty-Fifth Symposium (International) on Combustion, pp. 1685-1692.
6.   System Specification for the International Space Station, 1994, Boeing Defense and Space Group, Specification #41000A.
7.   Kimzey, J., 1986, "Skylab Experiment M-479: Zero-Gravity Flammability", NASA JSC 22293.
8.   Lekan, J., Neumann, E., and Sotos, R., 1992, Second International Microgravity Combustion Workshop, NASA CP-10113.
9.   Goldmeer, J.,1996, "Extinguishment of a Diffusion Flame over a PMMA Cylinder During Depressurization in Reduced-Gravity", NASA CR 198550.

Time (sec)	Caption legend	Pressure (atm)	Re$_D$	Φ_{FSP}	Maximum T$_{GAS}$ (K)	Solid-phase Centerline Temperature (K)	Stand-off distance (cm)
6	Fig 4 - (A)	0.880	3.84	0.290	2194	406	0.61
24	Fig 4 - (B)	0.610	2.68	0.256	2194	431	0.73
42	Fig 4 - (C)	0.430	1.87	0.238	2155	453	0.95
60	Fig 4 - (D)	0.300	1.30	0.221	2161	474	1.14
78	Fig 4 - (E)	0.210	0.20	0.204	2114	494	1.24
102	Fig 4 - (F) Fig 5 - (A)	0.130	0.56	0.175	1981	517	1.32
108	Fig 5 - (E)	0.115	0.50	0.150	513	522	No Flame

Table 1
Summary of predicted flame behavior during depressurization (U$_{FORCED}$ = 10 cm/s)
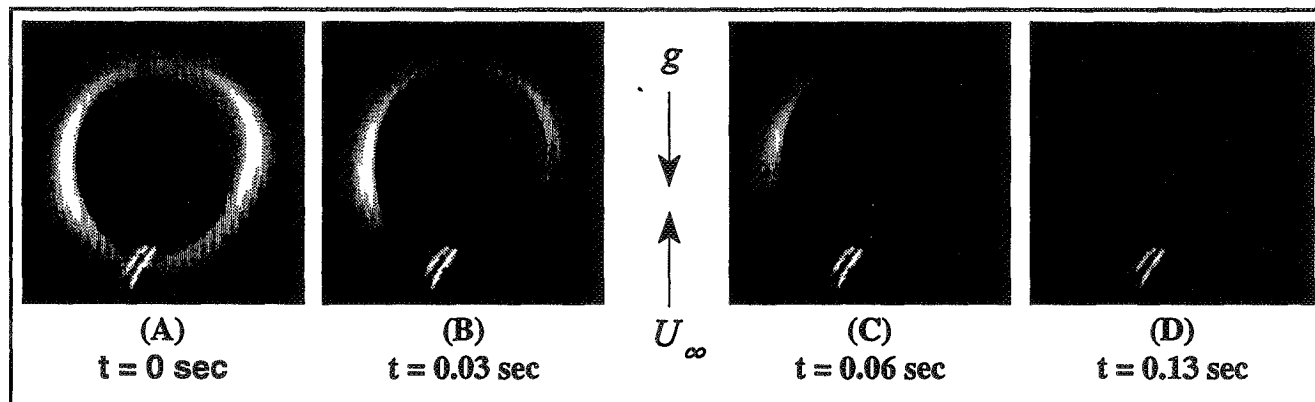
Figure 1
Blow-off extinction in low-gravity
(P = 0.242 Atm; U$_{FORCED}$ = 10 cm/sec; T(r=0)= 326K)
Z-Axis acceleration was approximately zero-g (±5 milli-g's)
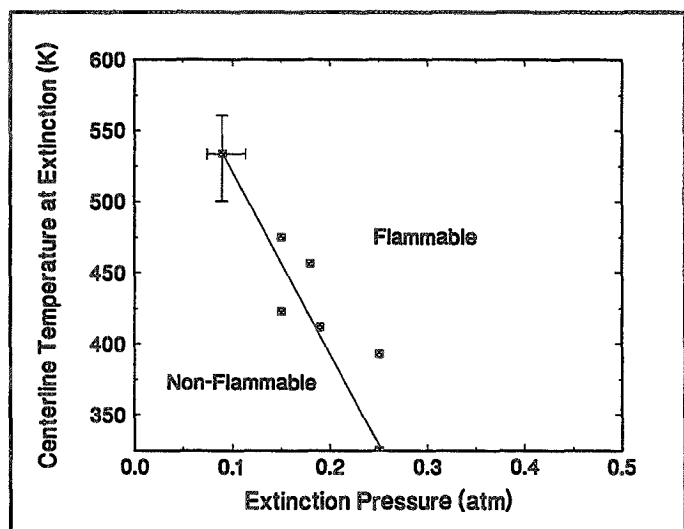
Figure 2
Experimental extinction boundary at constant velocity
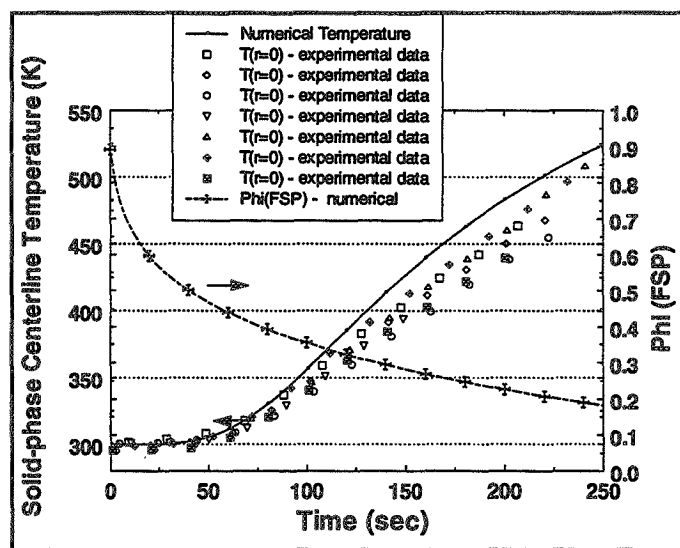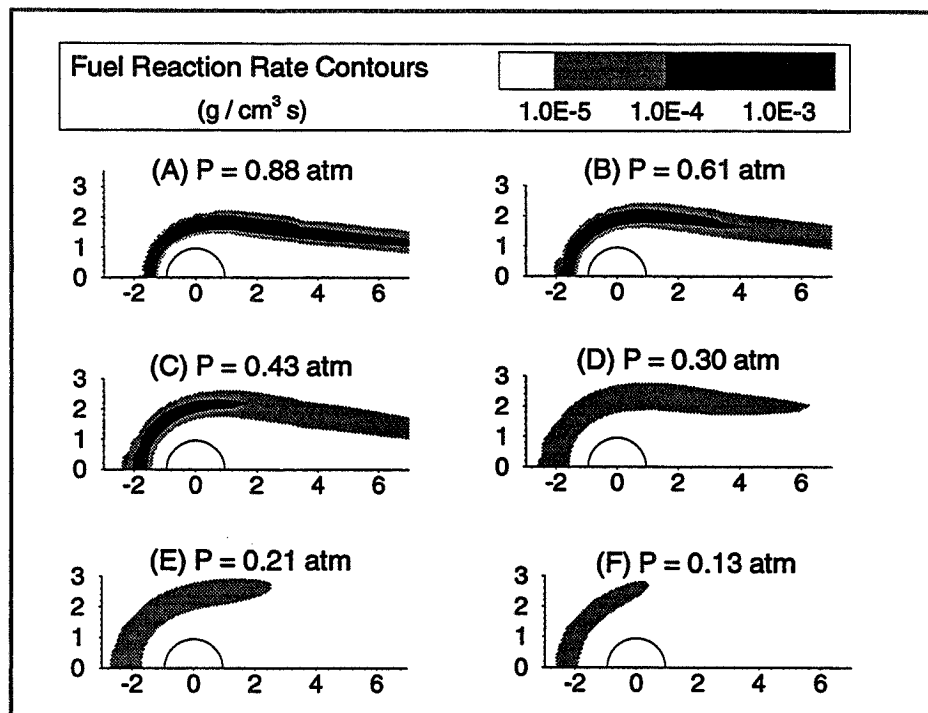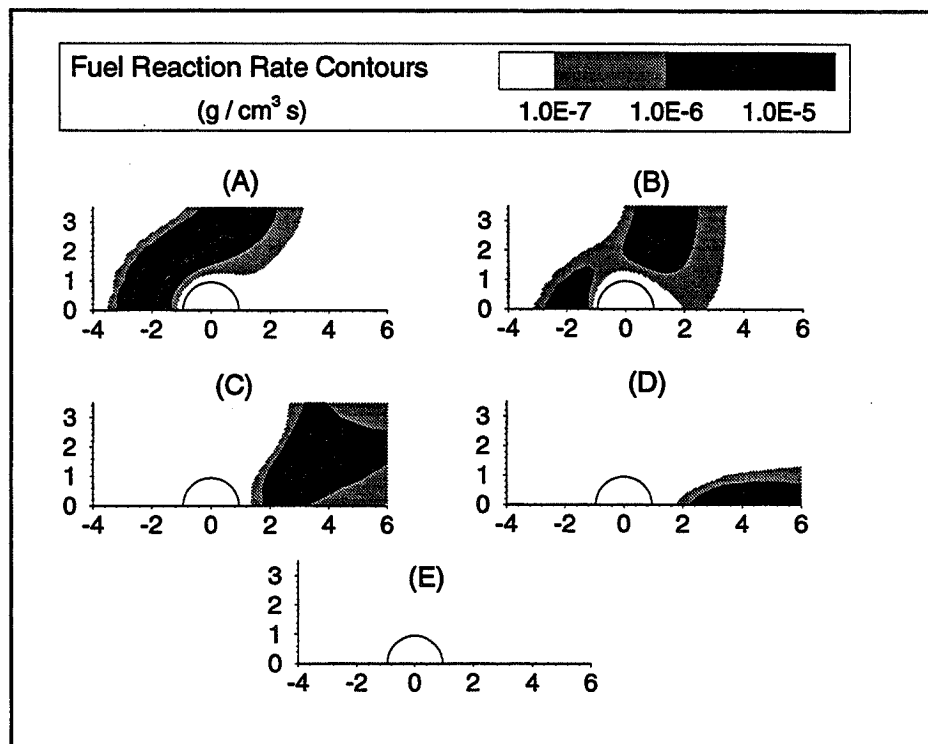(U$_{FORCED}$ = 10 cm/s)

Figure 3
Comparison of experimental and numerical solid-phase
centerline temperature and computed values of Φ_{FSP}

438

Figure 4

Predicted fuel reaction rate contours during depressurization with $U_\infty = 10$ cm/s
(dimensions in cm)

Figure 5

Predicted reaction rate contours during blow-off extinction with $U_\infty = 10$ cm/s
(A): $P = 0.13$ atm, and $\Phi_{FSP} = 0.175$
(B) - (E): $P = 0.115$ atm, and $\Phi_{FSP} = 0.15$
Images (A) and (E) are quasi-steady solutions to the gas-phase model
Images (B) - (D) are intermediate gas-phase steps
(all dimensions in cm)

439
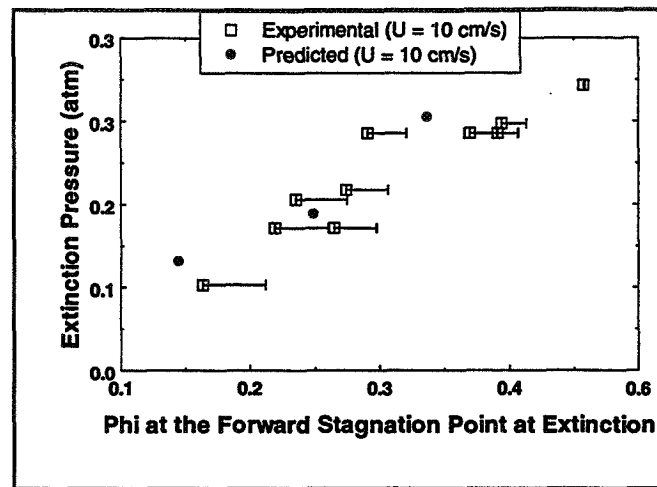
Figure 6
Comparison of experimental and predicted extinction
boundaries at 10 cm/s
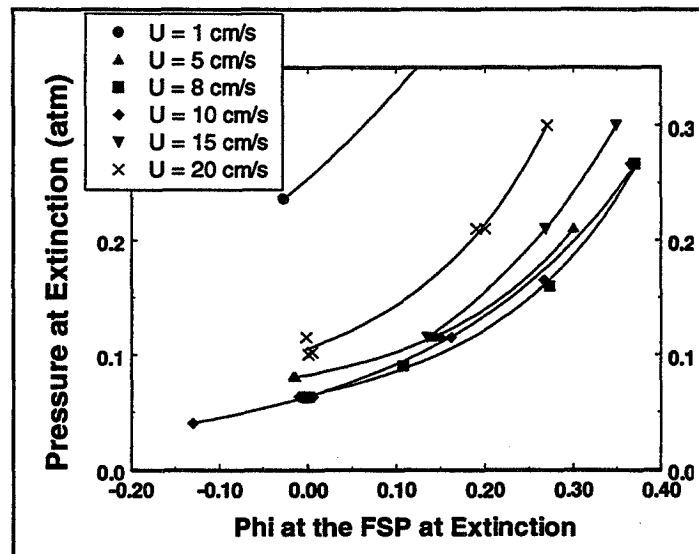
Figure 7
Predicted extinction boundaries at constant velocity
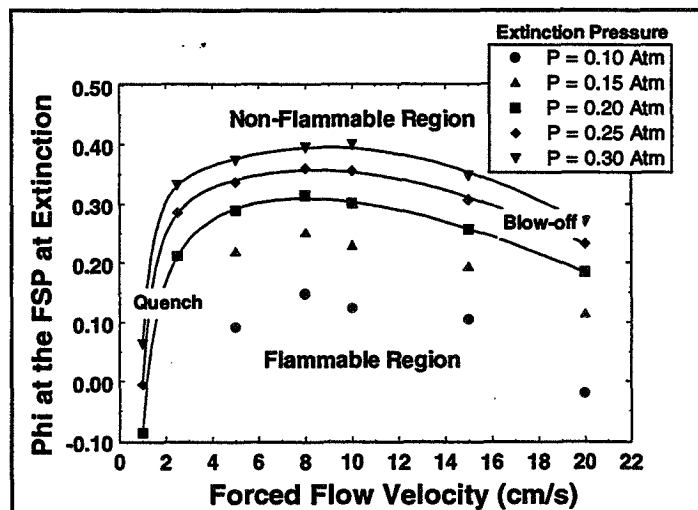
Figure 8
Predicted extinction boundaries at constant pressure

A NOVEL APPLICATION OF ULTRASONIC IMAGING TO STUDY SMOLDERING COMBUSTION[*]

S. D. Tse, R. A. Anthenien, and A. CARLOS. FERNANDEZ-PELLO
University of California at Berkeley
Berkeley, CA

and

K. Miyasaka
Fukui University
Fukui, Japan

ABSTRACT

An ultrasonic imaging technique has been developed to examine the propagation of a smolder reaction within a porous combustible material. The technique provides information about the location of a propagating smolder front, as well as line-of-sight average permeability variations of the smoldering material. The method utilizes the observation that transmission of an ultrasonic signal through a porous material increases with permeability. Since a propagating smolder reaction leaves behind char with a higher permeability than the original material, ultrasound transmission can be employed to monitor smolder progress. The technique can also be used to track the char evolution as it continues to react. Experiments are presented where the technique is applied to smoldering combustion in a two-dimensional geometry. The results have furthered the understanding of two-dimensional smolder, especially in identifying the controlling mechanisms leading to the transition from smoldering to flaming. The applicability of ultrasonic tomography to smoldering combustion has also been investigated.

NOMENCLATURE.

A	Proportionality constant	Greek Symbols	
c_0	Sound speed	α	Attenuation coefficient
d_p	Pore diameter	γ	Ratio of specific heats
ds	Differential path length element	Λ	Viscous characteristic length
f	Frequency (Hz)	Λ'	Thermal characteristic length
f_c	Characteristic frequency (Hz)	δ	Viscous skin depth
$f(r)$	Radial distribution function	ϕ	Porosity
$I(x)$	Intesity of sound wave as function of x	κ	Permeability
l	Metric across sample	μ	Dynamic viscosity
L	Sample thickness	ν	Kinematic viscosity
$p(l)$	Projection function	σ	Shape factor for viscous characteristic length
$P(x)$	Pressure of sound wave as fcn. of distance		
Pr	Prandtl number	σ'	Shape factor for thermal characteristic length
Q	Attenuation of sound wave per cycle		
r	Radius	τ	Tortuosity
T	Temperature		
u	Average flow (Darcy) velocity		
V	RMS voltage		
V_0	Unattenuated signal RMS voltage		
V_φ	Phase velocity of sound wave		

INTRODUCTION

Combustion in porous materials has been investigated for several decades. The subject encompasses an extensive area, ranging from fire development in permeable solid combustibles to high-temperature synthesis of materials. The type of combustion of interest here is smoldering, which is defined as a non-flaming, self-propagating, exothermic, surface reaction, deriving its principal heat from heterogeneous oxidation of the fuel [1]. Many materials can sustain smoldering, including coal, cotton, paper, plastics, wood, tobacco products, thermal and electrical insulation, and various dusts. If the material is sufficiently permeable, smoldering is not confined to its outer surface and can propagate as a reaction wave through the material. From a practical point of view, smoldering presents a serious fire risk, especially since it can propagate within the interior of a material and go undetected for long periods of time. Smoldering is of particular interest to the space program since a few minor incidents of charred cables and electrical components have been reported on Space Shuttle flights. Smoldering also typically yields a substantially higher conversion of fuel to toxic products than flaming (albeit more slowly) and may undergo a sudden transition to flaming. The transition to flaming has recently been shown to be connected with the formation of large voids in the resultant char formed behind the propagating smolder reaction [2].

An ultrasonic imaging technique has been developed to determine the progress of the smolder wave and the evolution of char permeability within smoldering, flexible, polyurethane foam. Images obtained with the technique have helped to verify the important role of secondary reactions within the char which provide the increased permeability conditions necessary for the transition from smoldering to flaming [2]. The technique represents a novel and important step forward in the study of smoldering combustion. It is currently under consideration for incorporation in the Microgravity Smoldering Combustion (MSC) program to monitor the smolder front propagation corroborated by thermocouple readings, and determine the effect of gravity on the secondary reactions in the char.

THEORY OF SOUND PROPAGATION IN POROUS MEDIA

The propagation characteristics (e.g. attenuation) of sound waves through a material medium are determined by the nature and structure of that medium. Biot's theory [3,4,5] shows that acoustic propagation in a fluid-saturated, porous-solid medium depends on several macroscopic parameters (i.e. porosity, elastic constants, densities of the phases, fluid viscosity, tortuosity and permeability). In the present setup, the medium is a solid fuel matrix (polyurethane) with an interconnected void that is saturated with gaseous fluids (air and combustion products).

For a plane harmonic sound wave, absorption is characterized by an exponential decrease in intensity of the wave with traveling distance[6]:

$$I(x) = I_0 e^{-2\int_0^x \alpha ds} \qquad (1)$$

where all symbols used in this work are defined in the nomenclature. The attenuation coefficient, α, of a porous medium depends on the properties of the medium and the sound frequency, f.

In a viscous fluid, shear surface oscillations decay over the viscous skin depth, $\delta = (2 \cdot v/f)^{1/2}$ [7,8,9]. Solving for the frequency when δ is of the same order as the typical pore diameter, $d_p \sim (\kappa/\phi)^{1/2}$, the characteristic frequency of the fluid-saturated, porous-solid medium [7] can be obtained:

$$f_c = \frac{v \cdot \phi}{\kappa} \qquad (2)$$

For frequencies below f_c, δ is larger than the typical pore size and the whole fluid is involved in the solid oscillation; for frequencies above f_c, only the fluid over δ is involved [10]. Furthermore, above the characteristic frequency, the shape of the pores must be taken into consideration as well; whereas below it, the porosity and permeability of the medium adequately describe the geometry.

In our experiments, f_c = 5 kHz for the virgin polyurethane foam; and f_c = 20 Hz for the char. The operating frequency of 40 kHz, selected in the present application (see below), ensures that we are always in the high frequency limit. Thus only theory relative to this limit will be discussed.

The viscous skin depth, has been related to the attenuation per cycle by Johnson *et al.* [11]:

442

$$\lim_{f \to \infty} \frac{1}{Q} = \delta \left(\frac{1}{\Lambda} + \frac{\gamma - 1}{\sqrt{Pr} \cdot \Lambda'} \right) \tag{3}$$

with the attenuation per cycle given by [7]:

$$Q = \frac{1}{2} \frac{f}{\alpha \cdot V_\varphi} \tag{4}$$

The viscous and thermal characteristic lengths are given, respectively, by [11]:

$$\Lambda = \frac{1}{\sigma} \left(\frac{8 \cdot \tau \cdot \kappa}{\phi} \right)^{\frac{1}{2}} \tag{5}$$

$$\Lambda' = \sigma \sigma' \Lambda \tag{6}$$

where the shape factors, σ and σ', for most materials, lie between 0.3 and 3 [11]. For cylindrical pores of circular cross section, $\sigma = \sigma' = 1$.

Utilizing the above equations as well as the relation for the phase velocity in the high frequency limit [7]:

$$\lim_{f \to \infty} V_\varphi = \frac{c_0}{\sqrt{\tau}} \tag{7}$$

we arrive at the following relation for the attenuation coefficient:

$$\alpha = \frac{1}{4c_0} \sqrt{\frac{f \cdot v \cdot \phi}{\kappa}} \left(\sigma + \frac{\gamma - 1}{\sigma' \cdot \sqrt{Pr}} \right) \tag{8}$$

Consequently, by measuring the attenuation coefficient, the line-of-sight average permeability of the material can be determined. Torero et al. [12] has shown that the permeability of flexible polyurethane foam can increase up to 4 orders of magnitude, due to the passage of a smolder wave. Since flexible polyurethane foams are very porous to begin with ($\phi \approx 0.975$), at most, only a 2.5% change in porosity is possible. Thus, it is reasonable to take ϕ to be constant at unity in Eq. 8. If the foam structure on the pore-level is assumed to be cylinders of circular cross-section, then the attenuation coefficient is only a function of v, κ, and c_0 for a fixed ultrasonic frequency. Both c_0 and v are functions of T; however, since v typically varies as $T^{3/2}$ and c_0 goes as $T^{1/2}$, α will vary only as $T^{1/4}$. Not only is the attenuation coefficient a very weak function of temperature, but the absolute temperature of the material merely doubles with the passage of a smolder wave, while the permeability increases more than an order of magnitude. For our purposes then, the attenuation coefficient can be well approximated as being inversely proportional to the square root of permeability, $i.e.$:

$$\alpha = \frac{A}{\sqrt{\kappa}} \tag{9}$$

$$A = \frac{\sqrt{f \cdot v \cdot \phi}}{4c_0} \left(1 + \frac{\gamma - 1}{\sqrt{Pr}} \right) \tag{10}$$

and A can be determined experimentally via calibration, in a manner to be explained subsequently. Therefore, by measuring the attenuation of a sound wave propagating through a porous medium, we can determine a line of sight average value for the permeability; and, by taking it a step further using tomographic techniques, we can obtain the value of the permeability for each point in the sample.

IMAGING METHOD AND APPARATUS

The ultrasonic imaging technique developed here is based on evidence that, for an ultrasonic frequency defined by the porous medium's properties, the degree of attenuation of an ultrasonic signal through a porous material decreases with increasing permeability. Thus, since a propagating smolder reaction leaves behind char with a higher permeability than the original material, the relative attenuation of ultrasonic transmissions can be employed to differentiate virgin material from char and to monitor any permeability variations of a smoldering material.

Operation procedures, along with design considerations, for the ultrasonic imaging technique for a single set of speaker and microphone are as follows:
1) A speaker emits a 40 kHz ultrasonic sinusoidal wave-train pulse through the porous medium. The wave-train pulse consists of a given number of cycles, (6). The duration of the wave-train pulse is experimentally determined to maximize received signal amplitude versus time spread of the transmitted wave-train pulse due to superposition of diffracted and reflected signals in the porous medium.

2) A microphone receives a wave-form which includes the transmitted wave-train pulse along with reflection and other interference signals. This wave-form is amplified and converted to an RMS signal. Based on the shortest path length through the sample, the first peak in the received wave-form identifies the desired transmitted signal through the foam/char.

3) The received RMS wave-form is digitally sampled by a computer and stored into memory. The entire received wave-form constitutes a single ultrasonic transmission data point, where the attenuation of the transmitted wave-train pulse is deduced in post-processing.

4) The next ultrasonic transmission data point is taken. The frequency of wave-train pulses is very important. The time between wave-train pulses must be longer than the time of flight for a single pulse. Enough time must also be allowed to minimize superposition effects from previously sent wave-trains that can be reflected back into the propagation path of interest. The time interval is limited by the desired rate of ultrasonic transmission data points to be taken.

In the present setup, linear arrays of speaker/microphones are employed, to reduce the time needed to scan the sample. The schematic of the ultrasonic imaging technique used in this work is shown in Fig. 1. Line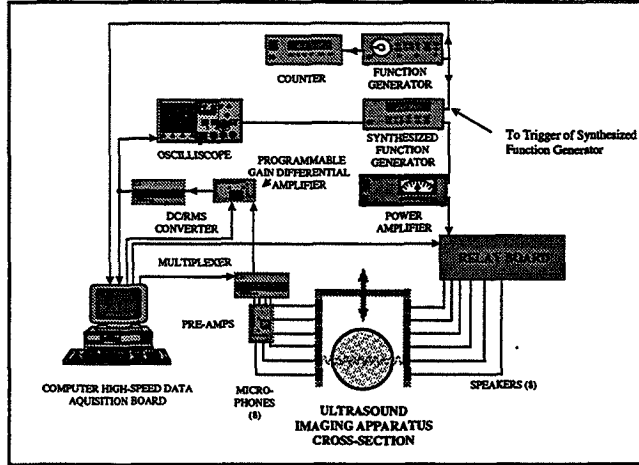-of-sight transmission projections are produced by scanning the samples with horizontal arrays of speakers and microphones, mounted to a 2-axis moving UniSlide® assembly. The pulsed ultrasound signals are amplified to 75 V peak-to-peak and are sent sequentially to the ultrasonic speakers. An array of 8 ultrasonic microphones receive the transmitted pulsed signals.

As indicated above, an entire received wave-form represents a single ultrasonic transmission data point. The negative log of the ratio of the received signal to an unattenuated signal (calibrated for attenuation due to beam expansion) gives the value of the line-of-sight integral of the attenuation coefficient, *i.e.*:

Fig. 1 Ultrasound imaging apparatus and setup

$$\int_0^L \alpha \cdot ds = -\ln\left(\frac{V}{V_0}\right) \tag{11}$$

Assuming that attenuation of a transmitted ultrasonic signal is only a function of permeability, as described in the previous section, the permeability calibration becomes straightforward. Inserting the expression for α of Eq. 9 into Eq. 12, and solving for A, we obtain for a sample of isotropic permeability:

$$A = -\frac{\sqrt{\kappa}}{L}\ln\left(\frac{V}{V_0}\right) \tag{12}$$

By measuring the ultrasonic intensity attenuation in terms of RMS voltage ratio for a virgin polyurethane foam sample of thickness, L, and isotropic permeability, κ_{foam}, the proportionality constant, A, which relates acoustic attenuation to permeability, is determined. Note: for an isotropic medium κ_{foam} can be measured by using Darcy's law:

$$u = -\frac{\kappa}{\mu}\frac{\Delta P}{L} \tag{13}$$

2-D IMAGING OF A SMOLDERING SAMPLE

The ultrasonic technique is applied to analyze the mechanisms of transition from smoldering to flaming combustion in a two-dimensional geometry. A detailed description of the two-dimensional smoldering facility and its operation may be found in Tse *et. al.* [2]

Ultrasonic images of the sample at two periods during its smolder are presented in Fig. 2. The delineation of the smolder front can clearly be identified. In addition, ultrasonic imaging shows that the permeability of the char left behind by the smolder wave increases (via the formation of voids) as smolder progresses. Producing a single image requires approximately 10 minutes due to scanning and data storage limitation rates. Figure 2a corresponds to a period prior to flaming when the smolder front is propagating at 26 cm from the igniter. Figure 2b corresponds to the sample immediately after flaming; note that combustion is extinguished immediately with a nitrogen purge upon flaming. The shades of gray-scale describe the line-of-sight value of permeability, with white corresponding to virgin foam and black to air (void). The technique provides information about the location of the smolder front and changes in permeability throughout the char region. The presence of voids is clearly observed in Fig. 2, and corroborated with visual examination of the char after completion of an experiment.
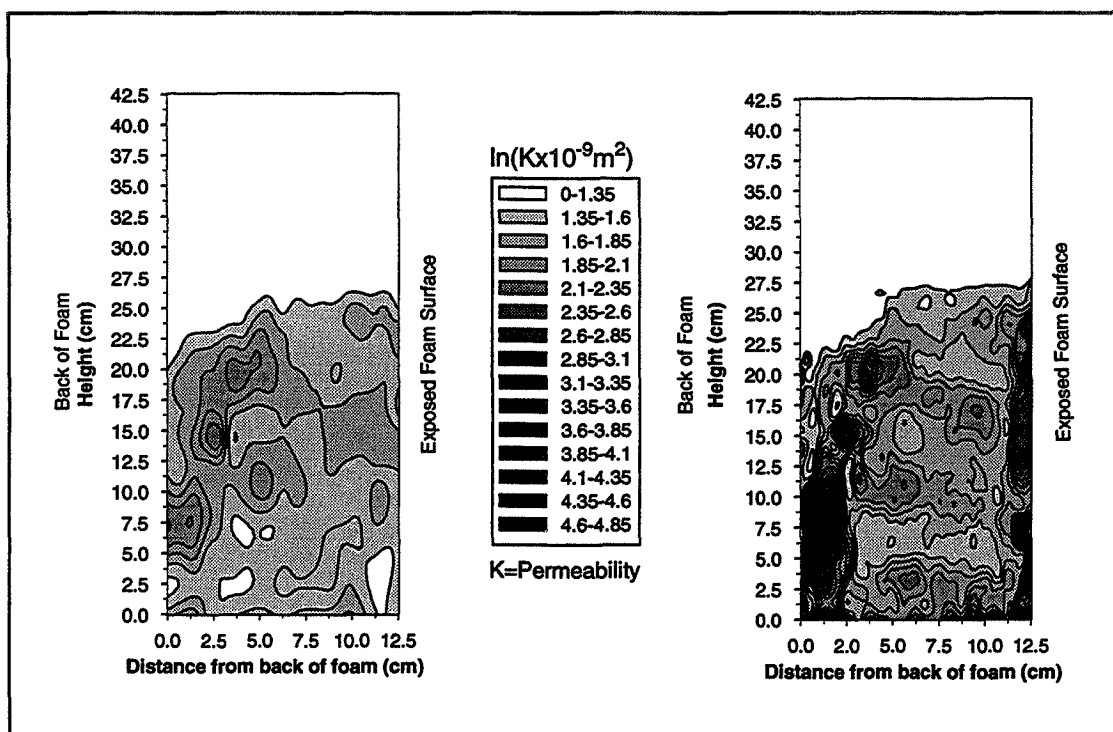
Fig. 2 Time evolution for line-of-sight average of ultrasound image of 2-dimensional smoldering

By scanning in a reduced region, the ultrasonic imaging technique can also be used to obtain the evolution of the char permeability at a particular location in the sample as can be seen in Fig. 3. The results show that the char continues to react and increase substantially in permeability long after the primary smolder front has passed, confirming that secondary char oxidation is responsible for the formation of the voids.

Ultrasonic images, as those of Fig. 2, together with thermocouple probing of the foam interior and schlieren interferometry of the gas phase at the foam/air-flow interface, reveal that transition to flaming is not the result of an accelerating smolder, but of the onset of gas-phase reactions in the void-filled, hot char region. The increasing permeability of the char, which favors the transport of oxidizer and volatiles to its interior, in conjunction with the reduced heat losses, results in the transition to flaming. Gas analyzer data of mixed-aggregate exhaust gases indicate significant increases in hydrocarbon production as the smolder nears transition to flaming. The larger pore size in the char favors gas-phase radical chain reactions; in contrast, the smaller pore size (~200 μm) near the smolder front tends to suppress gas-phase reactions by surface quenching of the free radicals, encouraging solid surface attack of oxygen [1]. By balancing the higher convective heat losses due to an increased permeability, these gas-phase reactions can then "insulate" intense heterogeneous reactions in the char region, occurring at the char surface. Nonetheless, flaming ignition is not a requisite result of elevated temperature, since temperature gradients in a reacting mixture are always accompanied by composition gradients [13]. In the immediate vicinity of the local char surface where the temperature is most favorable for a high reaction rate, the reactant concentration is least favorable: oxygen concentration will be the lowest (compounded by the fact that surface reactions are competing with gas-phase reactions for oxidizer) and fuel and product concentrations will be the highest. The proposed sudden influx of oxidizer, allowed in by increased permeability of the char, as confirmed by ultrasonic imaging, provides the impetus needed for the transition. More detailed information about the process can be found in Ref. [2].
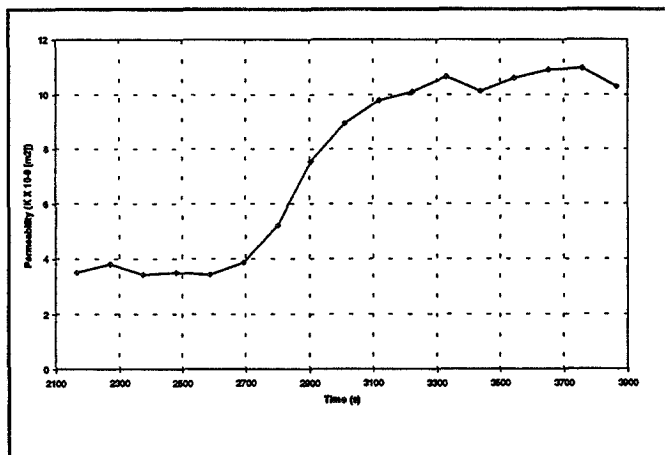

Fig. 3 Time evolution of permeability in char at one point utilizing line-of-sight average Ultrasound Imaging

AXISYMMETRIC TOMOGRAPHY

The ultrasound technique can also be used for the purpose of monitoring the smolder front, with regard to its shape and

445

propagation velocity. To verify that the application of ultrasonic tomography provides an accurate three-dimensional mapping of the foam/char interface, a phantom sample simulating an axisymmetric smolder front has been employed. A polyurethane foam cylinder, with an inner cylinder composed of char in the lower half of its length, is scanned; and the results are calibrated. Details may be found in Tse *et. al* [14].

The calibrated projections can be deconvoluted using the Abel transform to reconstruct the axisymmetric spatial field of the measured properties. A three-dimensional image of material permeability is then constructed from a vertical stack of deconvoluted two-dimensional slices. The technique provides valuable information about the shape and location of a propagating smolder front and the changes in permeability and temperature throughout the char region as a function of time.

The Abel transform is used to reconstruct the radial distribution of the line of sight projections. The Abel transform is only one of many possible methods available to reconstruct an axisymmetric field., such as the onion peeling method and the filtered back projection. It takes the form [15]:

$$f(r) = -\frac{1}{\pi} \int_r^\infty \frac{p'(l)}{\sqrt{l^2 - r^2}} dl \qquad (14)$$

Any rapid changes in the projection will cause overshoot and noise due to the derivative. Hughey and Santavicca [16] indicate that the Abel transform accumulates error at the center of the distribution unless many samples are taken. This high number of samples, however, generates high frequency noise. These effects can be minimized using the Filtered Abel Transform [15]. This method allows for the projection to be filtered of high wave number components before transformation. While filtering provides for a smoother output, it also reduces response therefore, a filter providing the best compromise of smoothness and response for the data should be chosen.

CONCLUDING REMARKS

The innovative application of ultrasonic imaging employed here brings the study of optically inaccessible heterogeneous combustion into a new perspective, where new insight into the mechanisms controlling smoldering combustion is revealed via visualization of evolving material properties. The technique is especially informative concerning char permeability evolution and propagation of the smolder front. Development of this technique into an ultrasonic tomography of non-axisymmetric material permeability and temperature fields for a smoldering fuel in real time is worth pursuing. The line-of-sight imaging method is currently under development by NASA for use in the MSC Get Away Special Canister (GAS-CAN) smolder test apparatus.

REFERENCES

1. Ohlemiller, T.J., Modeling of Smoldering Combustion Propagation, *Prog. Eng. Comb. Sci.* Vol.11, (1985), p.277.
2. Tse, S.D., Fernandez-Pello, A.C., and Miyasaka, K., Controlling Mechanisms in the Transition from Smoldering to Flaming in Flexible Polyurethane Foam, *26th Symp. (Int.) Comb., Comb. Inst.*, Pittsburgh, (1996).
3. Biot, M.A., Theory of Propagation of Elastic Waves in a Fluid-Saturated Porous Solid. I. Low-Frequency Range, *J. Acous. Soc. Amer.*, Vol.28, (1956), p.168.
4. Biot, M.A., Theory of Propagation of Elastic Waves in a Fluid-Saturated Porous Solid. II. Higher Frequency Range, *J. Acous. Soc. Amer.*, Vol.28, (1956), p.179.
5. Biot, M.A., Mechanics of Deformation and Acoustic Propagation in Porous Media, *J. App. Phys.*, Vol.33, (1962), p.1482.
6. Kuttruff, Heinrich. Ultrasonics: Fundamentals and Applications, Elsevier Science Publishing Co., Inc, New York, (1991).
7. Leclaire, P., Kelders, L., Lauriks, W., Gloriuex, C., and Thoen, J. Determination of the viscous characteristic length in air-filled porous materials by ultrasonic attenuation measurements, *J. Acous. Soc. Amer.*, Vol.99, (1996), p.1944.
8. Henry, M., Lemarinier, P., Allard, J., Bonardet, J., and Gedeon, A., Evaluation of the characteristic dimensions for porous sound-absorbing materials, *J. App. Phys.*, Vol.77, (1995), p.17.

9. Allard, J., Castagnede, B., Henry, M., and Lauriks, W. Evaluation of tortuosity in acoustic porous materials saturated by air, *Rev. Sci. Inst.*, Vol.65, (1994), p.754.
10. Bacri, J., Hoyos, M., Rakotomalala, N., Salin, D., Bourlin, M., Daccord, G., Lenormand, R., and Soucemarianadin, S., Ultrasonic Diagnostic in Porous Media and Suspensions, *J. Phys. III* France, Vol.1, (1991), p.1455.
11. Johnson, D., Koplik, J., and Dashen, R., Theory of Dynamic Permeability and Tortuosity in Fluid-Saturated Porous Media, *J. Fluid Mech.*, Vol.176, (1987), p.379.
12. Torero, J.L., Fernandez-Pello, A.C., and Kitano, M., Opposed Forced Flow Smoldering of Polyurethane Foam, *Comb. Sci. Tech.*, Vol.91, (1993), p.95.
13. Kanury, A.M., Introduction to Combustion Phenomena, Gordon and Breach Science Publishers, (1975).
14 Tse, S.D., Anthenien, R.A., Fernandez-Pello, A.C., and Miyasaka, K, A Novel Application of Ultrasonic Imaging and Tomography to Study Smoldering Combustion, *Comb. Sci. Tech.*, Submitted (1997).
15. Yuan, Z., The Filtered Abel Transform and Its Application in Combustion Diagnostics, *WSS/Comb. Inst., Fall Mtg*, (1995).
16. Hughey , B., and Santavicca, D., A Comparison of Techniques for Reconstructing Axisymmetric Reacting Flow Fields from Absorption Measurements, *Comb. Sci. Tech.*, Vol.29, (1982), p.167.

Droplet Combustion

Page intentionally left blank

INFLUENCES OF WATER ON METHANOL DROPLET BURNING AND EXTINCTION

FORMAN A. WILLIAMS

Center For Energy And Combustion Research
Department Of Applied Mechanics And Engineering Sciences
University Of California, San Diego
La Jolla, Ca 92093-0411

Introduction

Studies of droplet burning and extinction have been progressing for a number of years with support from the NASA program on microgravity combustion. Besides theoretical investigations, the research involves experiments in drop towers at the NASA Lewis Research Center and in Spacelab on the Space Shuttle. The first Spacelab experiments were performed a year and a half ago in the Glovebox, a relatively inexpensive facility, on the USML-2 mission. The next Spacelab experiments are planned for the MSL-1 mission in April, after the deadline for this report but before this scheduled meeting. Besides the Glovebox experiments (the second set of fiber-supported droplet-combination experiments, FSDC-2), this April mission has a full-scale droplet-combustion experiment (DCE-1), in which heptane droplets of 2 mm to 5 mm initial diameter are burned in various helium-oxygen atmospheres. The FSDC experiments burn various alcohols and alkanes, both pure and binary mixtures, with this same range of initial diameter, but always in Spacelab cabin air. These flight experiments are pursued jointly with the researchers at NASA Lewis Research Center and at various universities. In particular, Prof. F. L. Dryer of Princeton University is involved in all of this work.

Most of the FSDC-1 data were obtained with droplets of methanol and of methanol-water mixtures. A preliminary presentation of results from these tests has been made (ref. 1). The results for these methanol systems motivated further theoretical studies, beyond previous work (ref. 2), which are reported here. Essentially, theory had predicted droplet extinction diameters that increased nearly linearly with droplet initial diameters, and the experimental results confirmed that prediction. But the values of the experimental extinction diameters exceeded those predicted theoretically. The studies reported here address the reason for this discrepancy, with special attention paid to influences of the Lewis number of the water vapor and of absorption of water form the atmosphere into the fuel prior to ignition. This work has been submitted for publication (ref. 3).

Character of the Theory

We previously presented a theory for the combustion and extinction of methanol droplets, accounting for time-dependent absorption of water, produced in the flame, by the liquid fuel during the burning (ref. 2). Among the simplifying assumptions of the theory were the hypotheses that the Lewis numbers of all gas-phase constituents in the system were unity. Water is a particularly important gas-phase species because it is produced at the flame and diffuses away, being absorbed by the liquid fuel during the first part of the burning history, then later vaporizing with the fuel, thereby reducing the flame temperature and promoting extinction. Since the value of the diffusion coefficient of water in the gas phase may affect these transports, it is of interest to investigate how the theoretical predictions are modified when the Lewis number of water is changed. The results of such a parametric study are reported here.

The theory treats the gas phase as being quasisteady and introduces a Burke-Schumann approximation, in which all of the chemistry occurs instantaneously at a reaction sheet (a sphere concentric with the liquid drop) in a first approximation. Starting with this approximation, rate-ratio asymptotics are employed to resolve the structure of the thin reaction sheet and thereby to obtain quasisteady extinction conditions (ref. 2). Overall balances for fuel, water and energy in the liquid are introduced, under the assumption of spatial liquid-phase homogeneity, leading to a set of ordinary differential equations in time to be integrated. These differential equations employ algebraic solutions to the conservation equations for the quasisteady gas phase. To

simplify the algebraic formulas as much as possible, Lewis numbers for all species in the gas phase were taken to be unity in the transport zones outside the reaction sheet (although nonunity Lewis numbers within the reaction regions are taken into account) (ref. 2). The present contribution generalizes the theory by introducing an additional parameter L, a Lewis number defined as the ratio of the thermal diffusivity to the diffusion coefficient for water, in the analysis of the gas-phase transport zones.

Let Y denote the mass fraction of water in the liquid and ε the outward mass flux fraction of water in the gas in the transport region between the liquid and the flame, so that $1-\varepsilon$ is the mass flux fraction of methanol in that region. If M is the total mass of liquid, then the conservation equation for M is

$$dM/dt = -m , \qquad (1)$$

where m is the total mass flow rate in the gas of material leaving the liquid surface. The corresponding conservation equation for liquid water mass is

$$d(MY)/dt = - \varepsilon m , \qquad (2)$$

giving, with Eq. 1,

$$MdY/dM = \varepsilon - Y . \qquad (3)$$

These fundamental balance equations are considered below along with energy conservation for the liquid, equations for the quasisteady gas phase and interface equilibrium equations. The approximation that the temperature and composition of the liquid are spatially homogeneous is considered to be justified by sufficiently rapid liquid-phase mixing that is generated by a solutal-Marangoni instability (ref. 2).

Simplified Estimates For Large Lewis Numbers

The value of ε initially is small and negative as the water produced in the flame gradually diffuses into the liquid. The flux remains negative and nearly constant over a fraction of the burning lifetime when the liquid mixes perfectly. If $\varepsilon = - \varepsilon_o$ (where ε_o is a positive constant) during this water-accumulation phase, then the integral of Eq. 3 over this period, subject to $M = M_o$ and $Y = 0$ initially, is

$$M = M_o/(1+Y/\varepsilon_o) . \qquad (4)$$

Since, in terms of the liquid density ρ_ℓ and diameter d_ℓ ,

$$M = (\pi/6)\rho_\ell d_\ell^3 , \qquad (5)$$

when the very small variation of ρ_ℓ is neglected Eq. 4 gives, for the diameter d_ℓ,

$$d_\ell = d_o (1 +Y/\varepsilon_o)^{-1/3} , \qquad (6)$$

where d_o is the initial drop diameter.

The water mass fraction Y in Eq. 6 increases continually with time. When it reaches a sufficiently large value that the interphase equilibrium water mole fraction in the gas phase at the liquid surface approaches the water mole fraction at the flame, ε increases from $-\varepsilon_o$ to positive values that increase rapidly. That is, over a time interval there is a transition from rather slow water absorption in the liquid to relatively vigorous water vaporization along with the fuel. The combustion stoichiometry and liquid-gas phase equilibria are such that this transition occurs around a liquid water mass fraction of $Y \sim 0.3$. Since the flame-temperature reduction associated with the significant water delivery with the fuel causes the quasisteady flame-extinction condition to be reached when ε becomes appreciably positive, in a very rough approximation the value of Y at which

this sequence of events begins can be identified as a liquid-phase water mass fraction for extinction, Y_e. The extinction diameter d_e is then found from Eq. 6 to be

$$d_e = d_o (1 + Y_e/\varepsilon_o)^{-1/3} . \tag{7}$$

Since the value of Y_e varies little with initial diameter, Eq. 7 predicts near-linearity between d_e and d_o. Such a near-linearity is indeed found experimentally (ref. 1).

Explanation of effects of Lewis numbers on the basis of Eq. 7 entails reasoning how different diffusion coefficients affect average values of Y_e/ε_o. The reasoning is most straight forward if convection is neglected, that is, gas-phase transport effects are approximated as purely diffusive. Vaporization may be considered to be driven mainly by heat conduction from the flame, so that, if ℓ is an effective heat of vaporization per unit mass for the liquid, in Eq. 1

$$\ell m \approx 2\rho D c_p A (T_f - T_\ell) / (d_f - d_\ell) , \tag{8}$$

where ρ denotes gas density, D gas thermal diffusivity, c_p gas specific heat at constant pressure, A sphere area, T_f flame temperature, T_ℓ liquid temperature and d_f flame diameter. On the other hand, with water absorption dominated by water diffusion, in Eq. 2

$$-\varepsilon m \approx 2\rho (D/L) A Y_{wf} / (d_f - d_\ell) , \tag{9}$$

where Y_{wf} is the water mass fraction at the flame and L the Lewis number for water in the gas, so that D/L is the ordinary diffusion coefficient of water vapor in the gas surrounding the droplet. Equations 8 and 9 lead to

$$\varepsilon_o \approx \{(Y_{wf} \ell) / [c_p (T_f - T_\ell)]\} / L \tag{10}$$

as an estimated average value of ε_o for use in Eq. 7. The quantity in braces in Eq. 10 is on the order of 0.05 and nearly constant. If this observation is employed to write, from Eq. 10, $\varepsilon_o = c/L$, where c is a constant, then Eq. 7 becomes

$$d_e = d_o (1 + L Y_e/c)^{-1/3} , \tag{11}$$

which indicates that d_e/d_o increases with decreasing L. Since the last term in Eq. 11 typically is a little larger than the first, it is seen that d_e/d_o is estimated to be roughly proportional to $(L Y_e)^{-1/3}$.

Theory for Water Lewis Number Different From Unity

To perform a more through analysis that can test the preceding heuristic reasoning, the quasisteady conservation equations for fuel, oxygen, water and energy in the gas phase were written and solved for $L \neq 1$ (ref. 3). The analysis assumed constant specific heats and constant ρD. The results showed that, for burning in dry atmospheres

$$Y_{wf} = [\varepsilon + v_w (1-\varepsilon)] \times [1 - \{1 + Y_{0\infty}/[v (1-\varepsilon)]\}^{-L}] \tag{12}$$

where $v = 3/2$ is the stoichiometric mass ratio of oxygen to methanol, $v_w = 9/8$ is the mass of water produced per unit mass of fuel consumed, and $Y_{0\infty}$ is the mass fraction of oxygen in the ambient atmosphere. The corresponding expression for the water mass fraction is the gas at the droplet surface, Y_{ws}, is

$$(Y_{ws} - \varepsilon) (1 - \varepsilon + Y_{0\infty}/v)^L = (1 - \varepsilon - Y_{fs})^L$$
$$\times \{ v_w (1 - \varepsilon)^{1-L} (1 - \varepsilon + Y_{0\infty}/v)^L$$
$$- [\varepsilon + v_w (1-\varepsilon)]\} . \tag{13}$$

Unlike the special case $L = 1$, Eq. 13 cannot be solved explicitly for ε. Although this makes the computation procedure more complex than that of ref. 2, the calculations, through numerical integrations of two ordinary differential equations forward in time, nevertheless can be performed (ref. 3).

Results and Discussion

Equations 1 and 5 enable the square of the droplet diameter to be plotted as a function of time from the theoretical results. Figure 1 shows such a plot, obtained by taking $\rho D t /(\rho_\ell d_o^2)$ as the nondimensional time parameter. The case considered is that of an initially pure methanol drop of 5 mm initial diameter, burning in normal dry atmospheric air. Results for three different Lewis numbers are shown for comparing the effect of Lewis number of water on the burning rate. The corresponding extinction conditions are shown on the three curves as open circles. The results in Fig. 1 are independent of specific values of the transport properties because of the selected nondimensionalization. The curve for $L = 1.50$ is almost identical to that for $L = 1.0$, that is, an increase of Lewis number of water in larger range does not affect the burning rate appreciably, although the lower diffusion coefficient of water vapor at the higher Lewis number somewhat decreases the amount of water absorbed and thereby decreases the extinction diameter. For $L = 0.1$, however, there is much less curvature in the d-square plot, indicating much less water absorbed by the drop during its combustion and resulting in a much smaller extinction diameter.

The quasisteady extinction diameter d_e is obtained here as in our previous work (ref. 2). According to the previous paper (ref. 2), the value of d_e depends strongly on ε but is independent of L and d_o. It is therefore convenient to plot results as functions of ε, as shown in Fig. 2. That figure exhibits the common curve of extinction diameter as a function of ε and results of the present analysis for droplet diameter d_ℓ as a function of ε. These latter curves are presented for two different initial diameters d_o at one value of the Lewis number L and for a variety of different Lewis numbers L for one of the diameters. These results were obtained by starting the integrations with $Y = 0$ at $M = M_o$. The value of M_o is related to d_o by Eq. 5. In Fig. 2 ε is negative initially, that is, the liquid absorbs water, while later, when the d_ℓ curves cross the vertical line, water evaporates from the liquid along with the fuel. Extinction occurs when the d_ℓ curve intersects the curve of extinction diameter.

Figure 2 shows that the effect of the Lewis number of water is generally less than estimated in section 2. The extinction diameter for $L = 1.5$ is noticeably less than that for $L = 1.0$, consistent with the previous reasoning, but that for $L = 0.83$, the value recommended for water vapor (ref. 4), is just slightly larger. Figure 2 shows that, in fact, the maximum extinction diameter occurs at about $L = 0.83$, and smaller values of L give smaller extinction diameters, smaller by an order of magnitude when $L = 0.1$. The curves show that only at the higher Lewis numbers does the liquid spend most of its history absorbing water. At small Lewis numbers the period of water absorption is quite short. The qualitative considerations leading to Eq. 11 become inapplicable. A different phenomenon becomes dominant at small Lewis numbers.

Small Lewis numbers correspond to large diffusion coefficients, resulting in conditions under which diffusion of water should dominate its convection. The gas-phase conservation equations for water thus show clearly that, when L is small, changes in Y_w must scale in proportion to L. This applies even for the water concentration at the flame, since it may readily be found by expanding Eq. 12 for small values of L that Y_{wf} approaches zero in proportion to L as L approaches zero for burning in dry atmospheres. The previous qualitative reasoning addressed only the diffusion from the flame to the liquid, ignoring changes in Y_{wf}. Water also diffuses outward from the flame. This outward diffusion, for a fixed rate of production of water at the flame and a fixed flame diameter, requires the water concentration at the flame to decrease as its diffusion coefficient increases, so that the flux (the product of the diffusion coefficient and the concentration gradient) remains fixed. The decrease in Y_{wf} with decreasing L then reduces the flux of water into the liquid. In this limit of large water diffusion coefficient, the water content of the ambient atmosphere can become relevant, since diffusion can then cause water levels everywhere in the gas to approach ambient levels. Equation 11 can be used only for large L, the revised scaling discussed here being needed for small L.

Other quantities are readily calculated from the theory as described above. Figure 3 shows the predicted evolution of the liquid temperature and the water mass fraction in the liquid, for the conditions corresponding

to Fig. 2. The insensitivity to L is seen in this figure as well; for the smaller droplet, the curves for $L = 0.83$ would be indistinguishable from those for $L = 1.00$.

It is of interest to compare the theoretical prediction with experiment. Results of the present theory can be employed to calculate the extinction diameter as a function of the initial diameter. Such curves are shown in Fig. 4 for $L = 1.00$, which gives essentially the same results as for $L = 0.83$, the reported (ref. 4) Lewis number of water. The figure exhibits predictions for three different initial water mass fractions Y_o of the liquid. These predictions are obtained from the same kinds of integrations of the ordinary differential equations, starting with $Y = Y_o$ (rather than $Y = 0$) at $M = M_o$. The theoretical results for $Y_o = 0.2$ are seen to be in reasonable agreement with experiment. There are, however, many sources of experimental uncertainty, as has been discussed (ref. 1), and it may be concluded that values of Y_o lying somewhere between 0 and 0.2 are most likely for these experiments.

It may be concluded that there are two limits in which water produced in the flame is not absorbed by the liquid fuel during drop combustion. In the limit of infinite water Lewis number, the water does not diffuse but instead is merely convected away from the flame with the flow to infinity. In the limit of zero water Lewis number, the water diffuses to infinity so quickly that the water concentration at the flame becomes vanishingly small in dry ambient atmospheres, and hence the equilibrium water concentration in the liquid approached zero. Significant water absorption in burning methanol drops therefore occurs only for water Lewis numbers in the vicinity of unity. Calculations indicate that the Lewis number for water associated with methanol drops burning in air, a value slightly below unity, nearly maximizes the peak rate of water absorption by the liquid fuel during combustion. This results in the largest curvature possible for d-square plots, within the context of the theory, as well as the largest extinction diameters. The extinction diameters are predicted to be even larger if some water is present initially in the fuel prior to ignition, and comparison of predictions with experimental results suggests that this situation indeed occurs in some experiments. Further information on this is being published (ref. 5, 6).

Future Plans

The planned future research is associated mainly with the MSL-1 flight. Work is in progress on refining previous predictions (refs. 7, 8, 9) of heptane droplet burning rates and extinction, with emphasis on helium-oxygen atmospheres. These atmospheres complicate simplified analyses by making assumptions of Lewis numbers equal to unity in external transport zones become quite poor. Improved chemical-kinetic description for heptane oxidation are being used in these studies. Continuing theoretical studies of alcohol droplet combustion also are planned in connection with the Glovebox experiments on that flight, as are extension of the heptane types of studies to decane. The experiments with alcohols are intended to provide sharper tests of the theory presented here.

References

1. Dietrich, D.L., Haggard, J.B., Jr., Dryer, F.L., Nayagam, V., Shaw, B.D., and Williams, F.A., *Twenty-Sixth (International) Symposium on Combustion*, The Combustion Institute, Pittsburgh, PA, pp., 1201-1208, 1997.
2. Zhang, B. L., Card, J. M. and Williams, F. A., *Combust. Flame*, 105: 267-290 (1996).
3. Zhang, B. L. and Williams, F. A., "The Effects of the Lewis Number of Water Vapor on the Combustion and Extinction of Methanol Drops," *Combust. Flame*, to appear, 1997.
4. Smooke, M. D., ed., *Reduced Kinetic Mechanisms and Asymptotic Approximations for Methane-Air Flames*, Springer-Verlag, Berlin, p. 21, 1991.
5. Zhang, B.L. and Williams, F.A., "Alcohol Droplet Combustion," *Acta Astronautica*, to appear, 1997.
6. Zhang, B. L. and Williams, F. A., "Theoretical Studies of Methanol Droplet Combustion Based On Results From the Shuttle Spacelab During the USML-2 Mission," *Acta Astronautica*, submitted, 1997.
7. Card, J.M., and Williams, F.A., *Combust. Sci. Technol.*, 84:91-119 (1992).
8. Card, J.M., and Williams, F.A., *Combust. Flame*, 91:187-199 (1992).
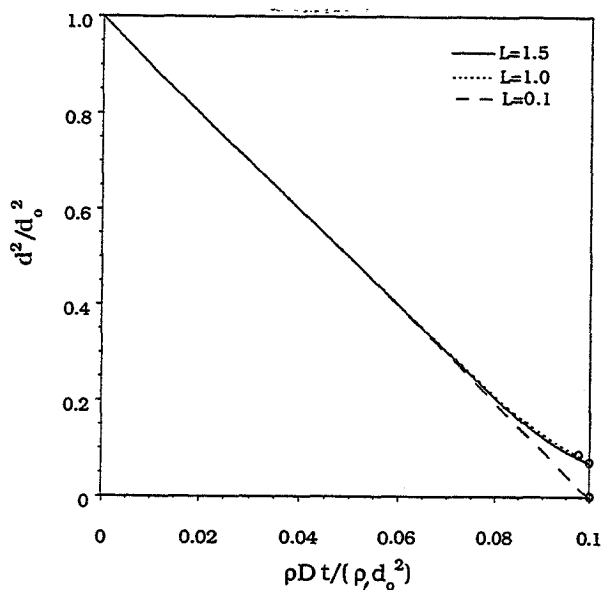9. Card, J.M., *Combust. Flame*, 93:375-390 (1993).

Figure 1 The square of the droplet diameter as a function of time for initially pure methanol burning in normal atmospheric air, with initial diameter of 5.00 mm and three different Lewis numbers of water; the o's on the curve identify extinction conditions.
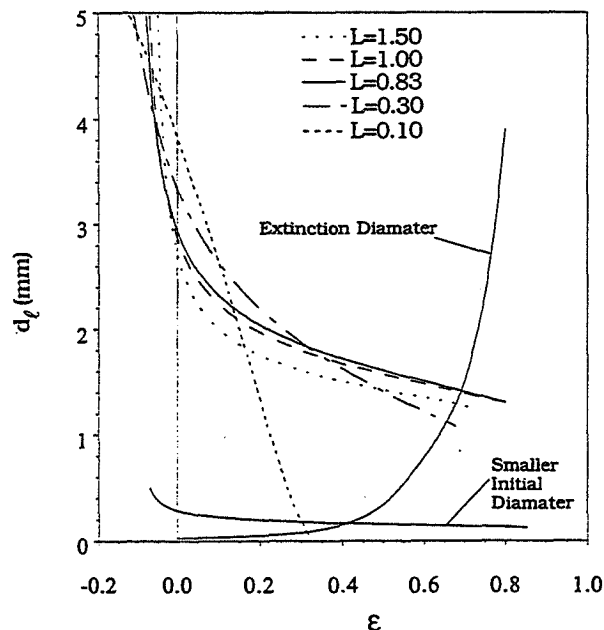

Figure 2 Theoretical dependence of the diameter d_ℓ and the extinction diameters d_e on the outward water mass flux fraction ε for different values of the Lewis number L of water, for initially pure methanol burning in normal atmospheric air, with initial drop diameters of 5.00 mm and 0.50 mm.
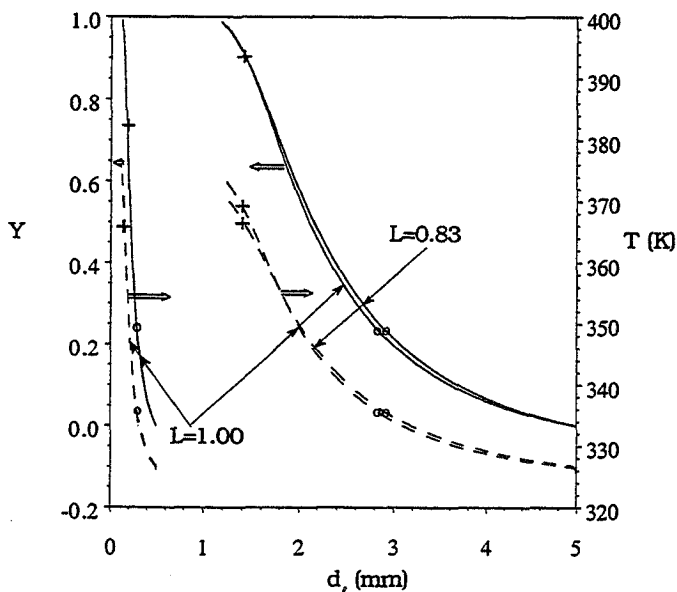
Figure 3 The water mass fraction in the liquid Y (solid curves) and the liquid temperature T_ℓ (dashed curves) as functions of the diameter d_ℓ for two different values of the Lewis number L of water, for initially pure methanol burning in normal atmospheric air, with initial diameters of 5.00 mm and 0.50 mm; the o's on the curves identify onset of water evaporation and the x's identify extinction conditions.
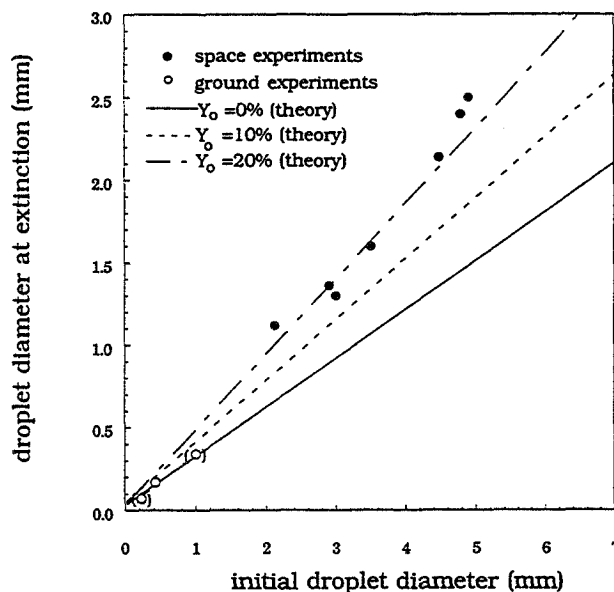
Figure 4 Comparisons of theoretical and experimental extinction diameters for methanol burning in normal atmospheric air; the lines are the results of the present theory for methanol, initially containing different percentages of water in the drop, with all gas-phase Lewis numbers unity, and the points are from experiments.

454

SCIENCE SUPPORT FOR SPACE-BASED DROPLET COMBUSTION: DROP TOWER EXPERIMENTS AND DETAILED NUMERICAL MODELING[+]

Anthony J. Marchese[*] and FREDERICK L. DRYER
Department of Mechanical and Aerospace Engineering
Princeton University, Princeton, NJ 08544
fldryer@phoenix.princeton.edu

Introduction

This program supports the engineering design, data analysis, and data interpretation requirements for the study of initially single component, spherically symmetric, isolated droplet combustion studies. Experimental emphasis is on the study of simple alcohols (methanol, ethanol) and alkanes (n-heptane, n-decane) as fuels with time dependent measurements of drop size, flame-stand-off, liquid-phase composition, and finally, extinction. Experiments have included bench-scale studies at Princeton, studies in the 2.2 and 5.18 drop towers at NASA-LeRC, and both the Fiber Supported Droplet Combustion (FSDC-1, FSDC-2) and the free Droplet Combustion Experiment (DCE) studies aboard the shuttle.

Test matrix and data interpretation are performed through spherically-symmetric, time-dependent numerical computations which embody detailed submodels for physical and chemical processes. The computed burning rate, flame stand-off, and extinction diameter are compared with the respective measurements for each individual experiment. In particular, the data from FSDC-1 and subsequent space-based experiments provide the opportunity to compare all three types of data simultaneously with the computed parameters. Recent numerical efforts are extending the computational tools to consider time dependent, axisymmetric 2-dimensional reactive flow situations. The sections below summarize recent progress.

Detailed Kinetic Modeling Of N-Alkane Droplet Combustion [1]

There is a critical need for partially-reduced, high temperature, n-alkane kinetic mechanisms which accurately reproduce a wide variety of kinetic and flame observations, which are sufficiently small for use in transient, uni-dimensional reactive flow computations, and which can serve as skeletal models for developing even smaller reduced representations for multi-dimensional, time-dependent computations and rate-ratio asymptotic studies. Such a mechanism has been developed for n-heptane [2], and the technique utilized can easily be extended to consider larger alkanes and mixtures. The mechanism considers fuel thermal decomposition reactions and realistically accounts for the site-specific abstraction of hydrogen atoms and the subsequent heptyl radical β-scission processes. Validation against kinetic data from stirred reactors, a flow reactor, shock tubes, and laminar flames were first performed. The mechanism was then incorporated in transient, spherically symmetric, isolated droplet calculations using a time-dependent, finite element, chemically reacting flow model [1,3] which also considers detailed molecular transport [4]. No kinetic or gas-phase transport parameters were modified to achieve agreement with experimental results. The only free parameter in the model is that utilized to approximate enhanced mass transfer due to internal liquid-phase motion [5]. Internal motions are inherent in experimental droplet deployment techniques and may also result from thermal and/or solutal Marangoni effects, but not from gas-phase convective motions relative to the droplet[5]. The development was motivated primarily by DCE experiments[6], first flown aboard Space Shuttle Columbia (STS-83) in April, 1997

The entire combustion history (ignition, premixed/diffusive flame transition, droplet heating, vapor accumulation, quasi-steady combustion, and extinction/burn out) were calculated. Ignition delay experiments [7] were simulated and, during quasi-steady combustion, the calculated droplet flame structures were compared with calculations using an earlier mechanism proposed by Warnatz [8]. For the combustion of small (< 1 mm) heptane droplets in air at 1 atm, the model predicts very small extinction diameters which is consistent with the results of Hara and Kumagai [9] and Yang and Avedisian [10] who observed either "burn-out" (i.e. extinction diameter too small to measure) or extinction diameters of less than 100 microns.

The DCE experiments consider large (1 - 5 mm), single component (n-heptane) droplets burned in He/O₂ oxidizing environments of various O₂ content at atmospheric and sub-atmospheric pressures. Reduced pressures and inert substitution reduce sooting propensity and increase extinction diameters [11,12], thus enabling accurate experimental measurements which are not perturbed by sooting effects.

Figure 1 compares the species and temperature calculated using the new mechanism and the semi-empirical mechanism of Warnatz and reveals a dramatic difference in the C_2 and C_3 intermediate distributions. In terms of maximum mass fraction, the new mechanism predicts an increase in C_2H_4 and C_2H_2 production by factors of 8 and 3, respectively, and a 4-fold decrease in maximum C_3H_6 mass fraction. However, both mechanisms predict a similar flame position (location of maximum flame temperature) and similar distributions of major species (O_2, CO, CO_2).
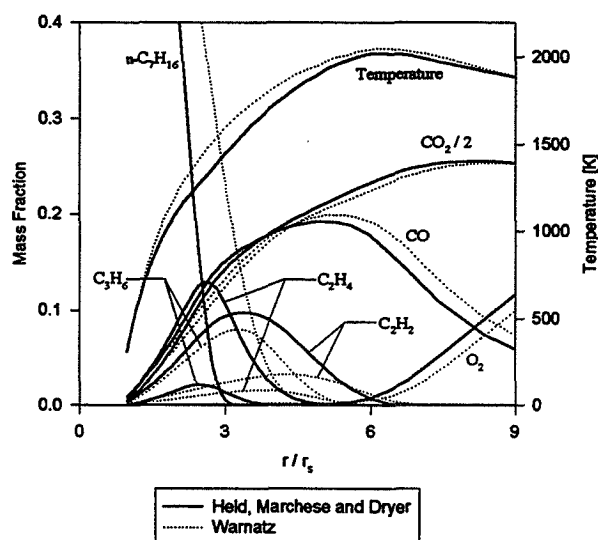
Figure 1. Calculated temperature and gas phase species C_7H_{16}, O_2, C_2H_4, C_2H_2, C_3H_6, and CO for the combustion of an n-heptane droplet at 1.0 second after ignition in an oxidizing environment of 40% O_2 / 60% He at 0.25 atm.

The latter result is consistent with the diffusion flame modeling study of Bui-Pham and Seshadri [13] where temperature and major species measurements were reasonably reproduced using the Warnatz mechanism. For the intermediate C_2 and C_3 species, the new mechanism also appears to be in better qualitative agreement with the experimental measurements of Hamins and Seshadri [14]. There, the measured ordering of these compounds was $C_2H_4 > C_2H_2 > C_3H_6$. At the conditions of Fig. 1, the reaction responsible for the largest percentage of fuel consumption (23.96%) was thermal decomposition:

$$C_7H_{16} \rightarrow C_2H_5 + 1 - C_5H_{11}.$$
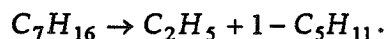
The second-leading consumption reaction (17.36%) was the H-atom abstraction via H radical attack leading to 2-heptyl:

$$C_7H_{16} + H \rightarrow 2 - C_7H_{16} + H_2.$$
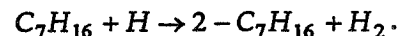
In overall terms, fuel thermal decomposition accounted for 50.2% of all the fuel consumption, while all of the fuel + H radical attack reactions accounted for an additional 46.6%. The only other class of reactions responsible for greater than 1% of the overall fuel consumption were the fuel + CH_3 radical attack reactions. These observations are important to further reduction of the mechanism and emphasize the significance of decomposition in large-hydrocarbon diffusion flames.

OH* Chemiluminescence Imaging Of Microgravity Droplet Flames [15]

In hydrocarbon flames, the following reaction is known to be a principal source of electronically-excited hydroxyl radicals, OH* [16]:

$$CH(^2\Pi_u) + O_2(^3\Sigma_g) \xrightarrow{k_1} CO(^1\Sigma^+) + OH^*(^2\Sigma^+).$$
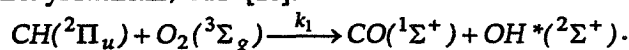
The OH* radicals are consumed through the competing reactions:

$$OH^*(^2\Sigma^+) + M \xrightarrow{k_2} OH(^2\Pi) + M$$

$$OH^*(^2\Sigma^+) \xrightarrow{k_3} OH(^2\Pi) + h\nu$$
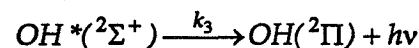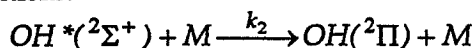
where the former reactions correspond to quenching by various collisional partners, M, and the last reaction corresponds to the electronic transition $^2\Sigma^+ - ^2\Pi$ which is observed as an ultraviolet OH emission band at 306.4 nm.

Chemiluminescence measurements, along with detailed predictions of electronically-excited hydroxyl radical concentration, have been demonstrated as a means of quantitatively comparing experimental and computed flame position and structure [15]. The procedure is applied in DCE, where an intensified array video camera is used to measure OH* chemiluminescence within the droplet diffusion flame [6]. To develop and validate the approach, isolated microgravity droplet combustion experiments were conducted in drop towers using n-heptane and methanol fuels. Hydroxyl chemiluminescence chemistry was incorporated into a detailed droplet combustion model, thus yielding OH* as one of the predicted parameters. The chemiluminescence mechanism is discussed elsewhere [1].

Tests were conducted using similar, but separate experimental rigs in the 2.2 second and 5.18 second Zero Gravity Facility (ZGF) drop towers at NASA-LeRC. The generic design of the rigs is described in detail elsewhere [1]. A high speed motion picture camera recorded black and white, back-lit droplet images at 200 frames per second. The OH* radical chemiluminescence images were acquired using a Xybion ISG-250 intensified-array CCD video camera fitted with a 50 mm,

UV lens and narrow band interference filter centered at 310 nm (full-width, half-maximum of 10 nm). The Xybion video (and high-speed camera) images were analyzed using a PC-based image analysis system.

To reconstruct the desired OH* emission-intensity distribution, F(r), given the measured line-of-site projection, P(r), the inverse Abel transform was performed:

$$F(r) = -\frac{1}{\pi} \int_r^\infty \frac{P'(\rho)}{(\rho^2 - r^2)^{1/2}} d\rho$$

where P'(r) is the derivative of P with respect to radius, r. A least-squares smoothing algorithm was first applied to the data, followed by the three-point Abel deconvolution algorithm.
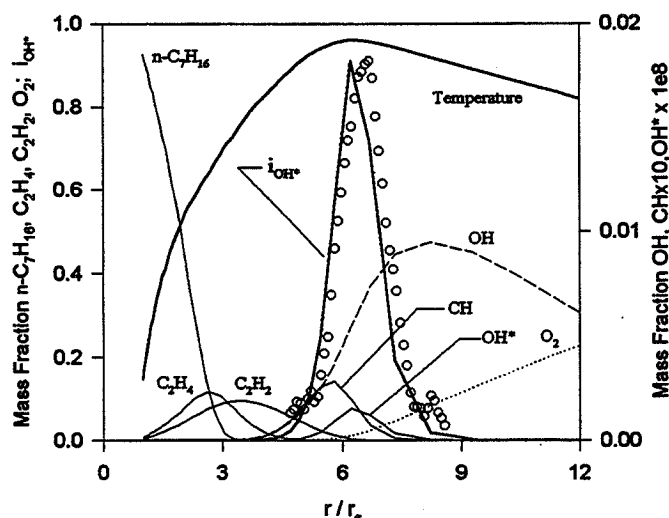
Figure 2. Comparison of computed mass fractions of species v. radial position, with the normalized experimental OH* distribution at 1 second after ignition. Fuel: n-heptane; Initial diameter: 1.9 mm; Environment: 40% O_2/60% He, 0.25 Atm.

The numerical model predicts the peak CH mass fraction to be very near the radius of maximum flame temperature, where the O_2 mass fraction also approaches zero (Fig. 2). Thus, in accordance with the $CH + O_2 \rightarrow CO + OH*$ route of OH* production, the model predicts the peak OH* mass fraction (and, consequently the peak OH* emission) to occur at a slightly greater radius than that of the maximum flame temperature. Note that the OH* and CH profiles within the flame are very narrow and better define flame features that the temperature profile, which is much less well defined in terms of peak shape.

The data analysis procedure outlined above was also applied to methanol droplet combustion, with similar modifications of an earlier developed numerical model [5, 15]. Methanol combustion produces very little CH radical, and examination of the reaction fluxes showed that the CH+O_2 reaction was not responsible for the production of OH*. Rather, OH* was produced

(in the minute quantities necessary) through thermal excitation processes.

Drop Tower Experiments: Methanol/ Water Mixtures

In order to further experimentally validate the droplet combustion model for methanol, calculations were compared with initially pure methanol and methanol/water mixture droplet combustion experiments conducted in the 2.2 second drop tower facility at NASA-LeRC [17]. Tests were performed in oxidizing environments of 18%-35%O_2/N_2 with initial liquid water contents of 0-20%. Instantaneous droplet diameter measurements were made using back-lit, high-speed photography, along with instantaneous flame position determined by monitoring chemiluminescence of electronically-excited hydroxyl radicals (OH*), as described above. Burning rates and flame stand-off ratio time histories for a wide array of methanol and methanol/water droplet combustion conditions were compared with the model results.

In Fig. 3, the experimental data have been five-point averaged and both axes have been normalized by the initial diameter-squared since initial diameter of the droplets varied between 1000 and 1500 mm. The measured burning rate increases substantially with increasing oxygen content and agreement between measured and calculated diameter history is excellent.
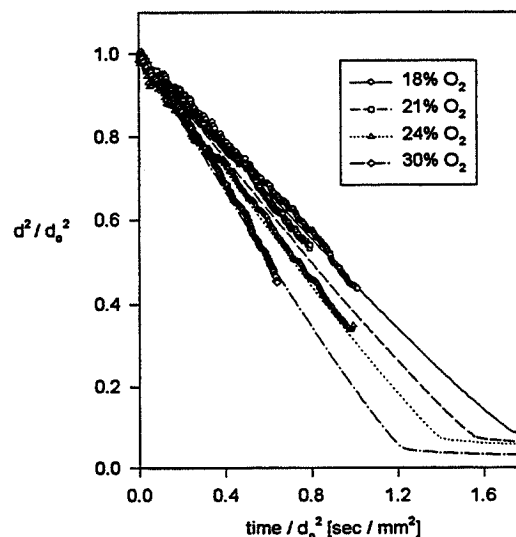

Figure 3. Experimental and numerically predicted data for initially pure methanol droplets burning in various nitrogen/oxygen environments at 1 atmosphere.

The flame position (Fig. 4) was measured using the OH* chemiluminescence method as described in the previous section. In methanol droplet combustion, the flame position is expected to decrease with time once the droplet begins to re-vaporize water which is absorbed into the liquid phase earlier in the combustion process. The increased water within the flame zone decreases the flame temperature, which in turn causes the

457

flame to move closer to the surface. In the experiments, the burn times were not sufficient to observe re-gasification of condensed water. Thus, after the initial transient period, the flame position was very nearly constant for each initial oxygen content.
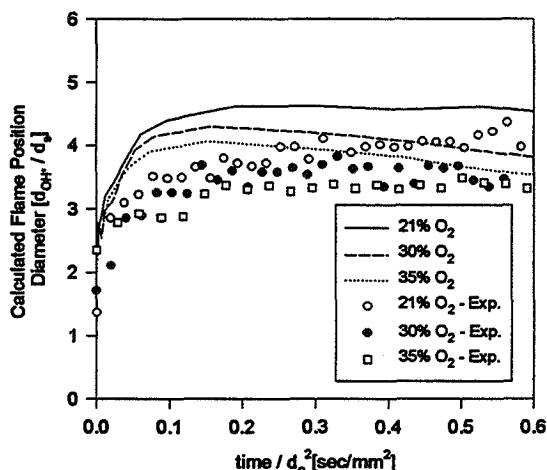

Figure 4. Measured and predicted instantaneous flame position, d_f/d_s, for methanol droplets in 21%, 30%, and 35% O_2 with N_2 inert at 1 atm. pressure.

As expected, the flame position decreased with increasing oxygen content due to stoichiometry considerations. After an initial transient period, average normalized flame positions of 4.1, 3.6, and 3.4 were measured for oxygen contents of 21%, 30% and 35%, respectively. Thus in addition to accurately predicting the burning rate, the model simultaneously predicts the flame position to within one normalized diameter at each condition.

Thermal Radiation Effects: FSDC-1 Results

In October 1995, the first ever space-based droplet combustion experiments, FSDC-1, were conducted aboard the Second United States Microgravity Laboratory (USML-2) mission, on Space Shuttle Columbia. Preliminary results for these experiments, which included methanol, methanol/water mixtures, heptane and heptane/ hexadecane mixtures as fuels, have been summarized earlier [18]. More recently, further numerical modeling for methanol and methanol/water experiments confirms that radiative effects are significant in experiments with initial diameters greater than 1 mm [19, 20]. For the first time, computed burning rate, flame stand-off, and extinction diameter are simultaneously compared with experiments.

To model the effect of non-luminous, radiative heat loss from the droplet flame, the gas phase conservation of energy was modified to include the radiative heat flux, q_R [1,19]. By considering the droplet and infinity as concentric spheres separated by a radiating medium, the formulation of Viskanta and Merriam [21,22] was

used to calculate the divergence of the net radiative flux:

$$\nabla \cdot q_R = \frac{1}{r^2}\frac{\partial}{\partial r}(r^2 q_R) = \kappa_P\left[4\sigma_B T_g^4 - G(r)\right].$$

The Planck-mean absorption coefficient, k_P, was calculated locally in space and time, from the calculated gas phase temperature and mole fractions of CO, CO_2, and H_2O. To describe the variation in Planck-mean absorption coefficient with temperature for each of these species, polynomials were fitted to the curves presented in Tien [23].

Figures 5 and 6 are plots of diameter-squared and instantaneous burning rate, respectively, vs. time for 5 millimeter initial diameter methanol/water droplets.
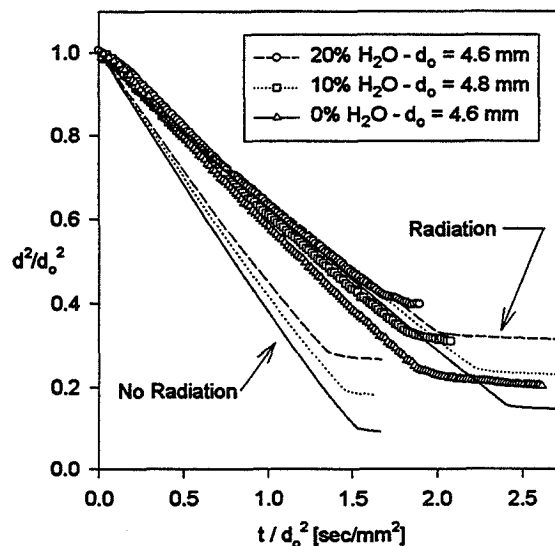

Figure 5. Measured and calculated diameter squared for 5 mm methanol/water droplets.

The results show that the extinction diameter increases and the burning rate decreases with increasing initial water content. The results also show that at initial droplet diameters of this size, the effect of radiation can no longer be ignored. In the calculations in which radiation is neglected, the numerical model greatly over-predicts the burning rate and under-predicts the extinction diameter. In the calculations that include radiative heat loss [1,19,20], the burning rate and extinction diameter show much better agreement with experiment.

It is interesting to note from Fig. 6 that radiation loss actually lessens the observed variation in burning rate with time. This result occurs since, early in the droplet lifetime when the diameter is largest, the burning rate is retarded primarily due to radiative heat loss, while later in the droplet lifetime, the burning rate is retarded by the re-vaporization of condensed phase water.

458

Figure 7 is a plot of the measured and calculated (including radiation) flame position for the experiments shown in Figs 5 and 6. Agreement between experiments and the model are quite remarkable. In each case, the quasi-steady flame position is calculated to within 0.5 normalized diameter of the experimental measurements. The calculated flame position is less sensitive to
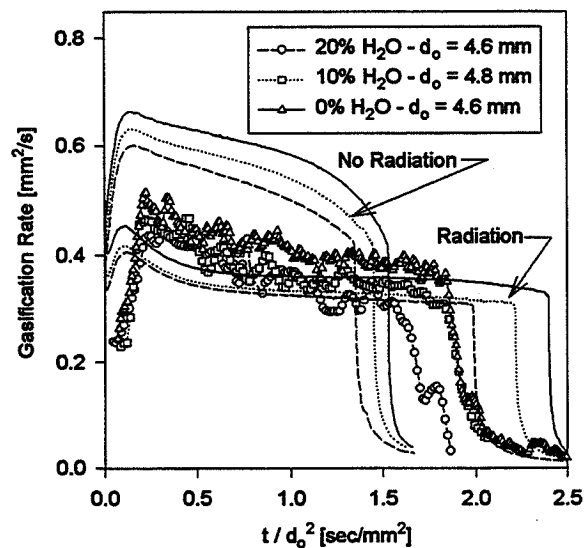

Figure 6. Measured and calculated instantaneous burning rate for 5 mm methanol/water droplets.

radiation effects than the burning rate or extinction diameter. For example, for a 5 mm methanol droplet, the quasi-steady flame position decreases by roughly 10% due to radiation loss while the burning rate decreases by 40%.

Comparison of model results with drop tower experiments [17] as well as FSDC-1 results [18] show that because of radiation, the burning rate decreases for increasing initial diameters larger than about 1.5 mm. A similar dependence of burning rate on drop size has been observed in microgravity n-heptane droplet combustion experiments in which soot was produced and soot-shells were observed [24,25]. The results presented here, as well as computations in progress, clearly show that non-luminous radiation can significantly affect the burning rate of n-heptane droplet combustion, even in the absence of sooting.

Figure 8 shows the measured extinction diameter as a function of initial diameter for pure methanol and methanol/water droplets. The experimental results show a nearly linear increase in extinction diameter with increasing initial diameter. By neglecting radiation, a linear increase in extinction diameter with increasing initial diameter has been previously predicted numerically [5] and asymptotically [26] for initially pure methanol droplets. Numerically, this result is only observed if the liquid phase internal motions are

assumed significantly enhance liquid phase mass transport.

Thus, the results shown in Fig. 8 suggest the presence of liquid phase motions within the interior of the droplet. Such motions can result from experimental methods of droplet generation and deployment and they may also be caused by thermal and/or solutal Marangoni effects [5,17,26].
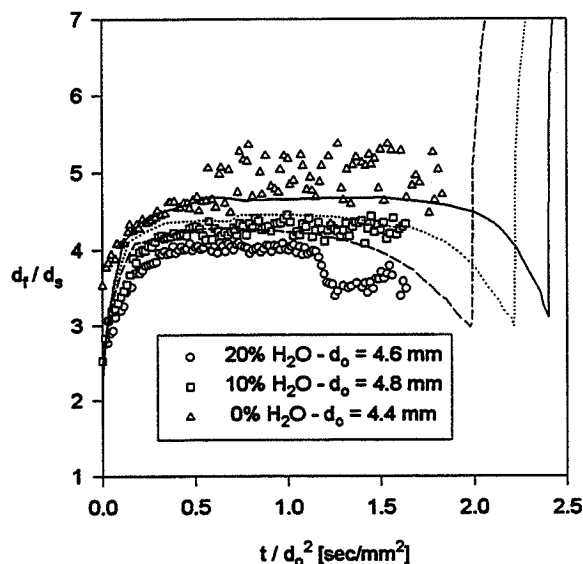

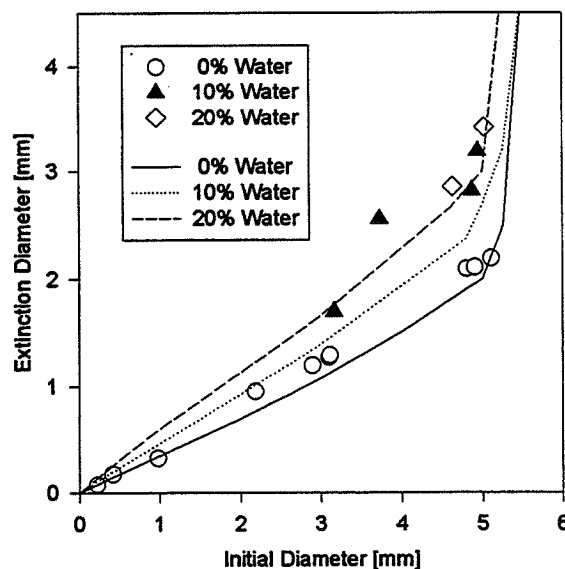**Figure 7.** Measured and calculated flame position for 5 mm methanol/water droplets.

Figure 8. Extinction diameter as a function of initial diameter for methanol/water mixtures. Symbols are experimental results; Lines are calculated results.

The calculations shown in Fig. 8 (which include the effect of radiation) show a nearly linear increase in extinction diameter with increasing initial diameter until a critical initial diameter is reached. For larger initial diameters, the extinction diameter quickly approaches the

459

initial diameter because extinction occurs before the establishment of quasi-steady burning. The radiative extinction phenomena for droplet burning was studied by Chao, et al [27] using asymptotics.

In FSDC-1 experiments on methanol and methanol/water mixtures, large droplets were exceedingly difficult to ignite and required several applications of the ignition source. It should be noted, however, that the time-dependent model employed here predicts that droplets larger than the critical diameter noted above, ignite but extinguish after very short, unsteady burning times. Transient burning may exist for varying times dependent on the ignition energy, but quasi steady burning will not occur prior to extinction.

Summary

Here, it has been shown that isolated droplet combustion problems can be utilized to develop, validate, and study the interactions of physical and chemical sub-models for chemically reacting systems. Thus, numerical modeling methodology and sub-model refinements for physical and chemical processes, along with advances in experimental diagnostics, add yet another uni-dimensional combustion venue to those previously available (i.e. gaseous, laminar premixed and diffusion flames). Simultaneous comparison of multiple parameters in such venues give increased confidence in the developed sub-models and their interactions. The resulting complex sub-models yield the bases for developing simplified representations that are compatible with the computational constraints of multidimensional models for heterogeneous combustion problems such as sprays.

References

1. Marchese, A. J., Ph. D. Dissertation, Department of M.A.E., Princeton University (1996).

2. Held, T. J., Marchese, A. J., and Dryer, F. L., Comb. Sci. Tech., In press (1996).

3. Cho, S. Y., Yetter, R. A., and Dryer, F. L., J. Comp. Phys. 102, 160-179 (1992).

4. Kee, R. J., Dixon-Lewis, J., Warnatz, J. Coltrin, J. A., and Miller, J. A.,SAND86-8246 (1986).

5. Marchese, A.J. and Dryer, F.L., Combust. Flame, 105, 104 (1996).

6. Williams, F. A., and Dryer, F. L. Science Requirements Document for the Droplet Combustion Experiment, NASA Lewis Research Center, Cleveland, OH (1994).

7. Faeth, G. M., and Olson (1968). Transactions of the ASME, 1793 (1968).

8. Warnatz, J. Twentieth Symposium (International) on Combustion, The Combustion Institute, Pittsburgh, PA, 1984, p. 845.

9. Hara, H. and Kumagai, S. Twenty-third Symposium (International) on Combustion, The Combustion Institute, Pittsburgh, PA, 1990, p. 1605.

10. Yang, J. C., and Avedisian, C. T. Twenty-second Symposium (International) on Combustion, The Combustion Institute, Pittsburgh, PA, 1988, p. 2037.

11. Chung, S. H., and Law, C. K. Combust. Flame, 64, 237 (1986).

12. Choi, M. Y., Cho, S. Y., Dryer, F. L., and Haggard, J. B., Jr. Microgravity Science and Technology, Springer-Verlag, IV/2, 134 (1991).

13. Bui-Pham, M. and Seshadri, K. Combust. Sci. and Tech. 79, 293 (1991).

14. Hamins and Seshadri, Combust. Flame 68, 295 (1987).

15. Marchese, A. J., Dryer, F. L., Nayagam, V., and Colantonio, R. Twenty-Sixth Symposium (International) on Combustion, The Combustion Institute, Pittsburgh, PA, 1996, pp. 1219.

16. Gaydon, A. G. (1974). The Spectroscopy of Flames, Chapman and Hall, London, p. 196.

17. Marchese, A. J., Dryer, F. L., Colantonio, R., Nayagam, V. (1996). Twenty-Sixth Symposium (International) on Combustion, The Combustion Institute, Pittsburgh, PA, 1996, pp. 1209.

18. Dietrich, D. L., Dryer, F. L, Haggard, J. B., Jr., Nayagam, V., Shaw, B. D., and Williams, F. A. Twenty-Sixth Symposium (International) on Combustion, The Combustion Institute, Pittsburgh, PA, 1996, pp. 1201.

19. Marchese, A.J. and Dryer, F. L., Comb. Sci. Tech. In press (1997).

20. Marchese, A.J. and Dryer, F.L., Fall Technical Meeting, ESS/CI, Hilton Head, SC, December, 1996.

21. Saitoh, T., Yamazaki, K., and Viskanta, R., Journal of Thermophysics and Heat Transfer. 7/1, 94 (1993).

22. Viskanta, R. and Merriam, R. L., Journal of Heat Transfer. 90/2, 248 (1968).

23. Tien, C. L., Thermal Radiation Properties of Gases. Advances in Heat Transfer, Vol. 5., Academic Press, New York, 1968, pp. 115-193.

24. Choi, M. Y., Dryer, F. L., and Haggard, J. B., Jr., Twenty-Third Symposium (International) on Combustion, The Combustion Institute, 1990, p. 1611.

25. Jackson, G. and Avedisian, C. T., AIAA-93-0130 (1993).

26. Zhang, B. L., Card, J., and Williams, F. A., Combust. Flame 105, 267 (1996).

27. Chao, B. H., Law, C. K., and T'ien, J. S., Twenty-Third Symposium (International) on Combustion, The Combustion Institute,1990, p. 523.

The Effects of Sooting and Radiation on Droplet Combustion[*]

Kyeong-Ook Lee, Samuel L. Manzello and MUN YOUNG CHOI
Department of Mechanical Engineering
University of Illinois at Chicago
Chicago, IL 60607

Introduction

The burning of liquid hydrocarbon fuels accounts for a significant portion of global energy production (ref. 1). With predicted future increases in demand and limited reserves of hydrocarbon fuel, it is important to maximize the efficiency of all processes that involve conversion of fuel. With the exception of unwanted fires, most applications involve introduction of liquid fuels into an oxidizing environment in the form of sprays which are comprised of groups of individual droplets. Therefore, tremendous benefits can result from a better understanding of spray combustion processes. Yet, theoretical developments and experimental measurements of spray combustion remains a daunting task due to the complex coupling of a turbulent, two-phase flow with phase change and chemical reactions (ref. 2). However, it is recognized that individual droplet behavior (including ignition, evaporation and combustion) is a necessary component for laying the foundation for a better understanding of spray processes (refs. 1 and 3).

Droplet combustion is also an ideal problem for gaining a better understanding of non-premixed flames (ref. 4). Under the idealized situation producing spherically-symmetric flames (produced under conditions of reduced natural and forced convection), it represents the simplest geometry in which to formulate and solve the governing equations of mass, species and heat transfer for a chemically reacting two-phase flow with phase change. The importance of this topic has promoted extensive theoretical investigations for more than 40 years.

In the early 1950's, the fundamental theory of droplet combustion was pioneered by Spalding (ref. 5) and Godsave (ref. 6). The classic solution known as the 'd²-law' predicts that the rate of decrease of the square of the droplet diameter [burning rate] and the ratio between the flame and droplet diameters [flame standoff ratio] remain constant during the combustion process.

Extensive experimental investigations have been conducted through the years using various methods to verify the 'd²-law' predictions. However, the most effective method of producing spherically-symmetric conditions was to perform experiments in reduced-gravity environments. Kumagai and coworkers (ref. 7) performed the first isolated droplet combustion experiments under reduced-gravity using droptower facilities. The measured burning rate of 0.78 mm²/sec for heptane has been widely accepted as a fundamental value for more than two decades and was used as a benchmark for testing the predictions of the 'd²-law' and subsequent theories.

Kumagai's experiments also clearly demonstrated the deficiencies of the 'd²-law'. For example, the burning rate predictions did not match the experimental value unless the thermophysical properties were chosen judiciously. The measured flame stand-off ratio (instantaneous flame diameter divided by the droplet diameter) was significantly smaller than the predicted value (~30 to 40). Furthermore, the simple 'd²-law' could not predict many of the important and interesting behaviors that were observed in subsequent μg droplet combustion experiments including: increasing flame standoff ratio; droplet microexplosion; droplet heat-up effects; fuel-vapor accumulation effects; droplet flame extinction; non-linear burning rates; significant soot formation and accumulation into a shell, etc. Through the years, there have been numerous improvements to droplet combustion theory to address these issues including: the effects of non-unity lewis numbers (ref. 8), departures from quasi-steady combustion (ref. 9), low volatility impurity condensation (ref. 10), transient droplet heating (ref. 11), fuel vapor accumulation (ref. 12), kinetic extinction (ref. 13-15) and condensation of liquid-phase products (ref. 14). However, the effects of sooting and radiation have not been included in droplet combustion analysis. This may be the reason for the large discrepancies between the experimental measurements and predictions of the burning parameters for n-heptane.

Objectives

In this study, we propose to perform detailed measurements of the soot concentration distribution, temperature distribution, soot morphology using proven techniques to satisfy the primary scientific objectives which include:

1.   Resolve the effects of sooting and radiation on the burning parameters including:

461

- Droplet burning rate
- Soot standoff ratio
- Flame standoff ratio, r_f/r_d
- Flame temperature
- Flame extinction

2. Use the extensive database of measurements for validation of detailed numerical models that incorporate empirical soot formation, growth, accumulation and radiation mechanisms.

3. Determine changes in the soot morphology caused by the extended exposure to high temperature and reactive environment within the sootshell.

4. Determine the causes that prevent sootshell formation for large droplets.

The proposed experiments require quiescent environments of μg to clarify mechanisms that are normally obscured under normal-g conditions. For example, modification to the burning behavior is predicated upon the formation of a sootshell surrounding the droplet. Sootshell formation can only be manifested under μg conditions. Microgravity experiments performed in ground-based facilities have only begun to reveal the importance of the effects of sooting. However, this approach inherently limits the range of initial droplet sizes that can be studied to be between 1.0 mm to 1.45 mm. The modest variation in the degree of sooting produced in such a narrow range cannot be used to satisfy the scientific objectives of the proposed study. Extended μg times beyond the capabilities of ground-based facilities are required to fully investigate the important sooting behavior and its influence on droplet combustion.

Soot Measurement Techniques

In most microgravity droplet combustion studies, the degree of sooting was only estimated by the 'darkness' of the sootshell measured from the backlit high-speed photographs. However, there are serious deficiencies in this technique. For example, the higher degree of light attenuation through the flame of a larger droplet would indicate that it is sootier than a smaller droplet flame even if the soot distributions were identical for both cases. Under such situations, the level of transmission of light (I/I_o, where I is the transmitted light intensity and I_o is the incident light intensity) through the flame will be much lower for the larger droplet due to the larger magnitude of the integrated product of the local soot volume fraction and incremental pathlength. Based on such measurements, the claim that one droplet flame is 'sootier' than the other may not be valid.

In the first microgravity droplet combustion experiments using heptane fuel (ref. 7), sootshells were only faintly visible. However in subsequent experiments using a similar range of droplet sizes (ref. 16), sootshells were made clearly visible by apparently using a lower level of backlighting. Therefore, the degree of darkness of the sootshell is also a function of the type of backlighting combined with the method in which the photographic film is developed. Thus, the 'darkness' of the sootshell provides a poor quantitative assessment of the degree of sooting even for droplets that are identical in size. In many of the previous studies, very low levels of backlighting produced 'dark' sootshells for heptane which interfered with the measurements of the droplet diameter needed for burning rate calculations. Thus, most experiments were performed by using light levels that would saturate the sootshell region in an effort to 'eliminate' the sootshell. Although brighter backlighting provided a simple solution for eliminating soot interference with droplet size measurements, the effects of sooting on the droplet burning characteristics such as burning rate, flame structure, disruptive burning, thermophoresis and kinetic extinction still persisted throughout the burning lifetime.

An alternative diagnostic approach using full-field light extinction and tomographic inversion was developed by Greenberg and coworkers (ref. 17). This method was adopted for use in measuring the soot concentration of droplet flames burning under microgravity conditions at 1 atm (ref. 18). This technique operates on the principle that the soot-containing region of the microgravity droplet flame is spherically-symmetric and that the variation of the transmission of laser intensity through planar surfaces that are normal to the radial direction can be tomographically inverted to obtain the soot volume fraction distribution. The line of sight projection data, $P_{f_v}(x)$ (which is related to the transmission of laser intensity) is dependent on the radial distribution of the soot volume fraction:

$$P_{f_v}(x) = \int_{-\infty}^{\infty} f_v(\sqrt{x^2+y^2})dy \tag{1}$$

where f_v is the soot volume fraction and $r^2 = x^2 + y^2$. The projection equation can be rearranged as:

$$P_{f_v}(x) = -\frac{\lambda}{K_e}\ln(\frac{I_\lambda}{I_{\lambda o}}) = \int_{-\infty}^{\infty} f_v \sqrt{(x^2+y^2)}dy \qquad (2)$$

where λ is the wavelength of the light source and K_e is the dimensionless extinction constant of soot. The measured projections values can be tomographically inverted by applying a 3-pt Abel transform to obtain $f_v(r)$ (ref. 19).

Experimental Description

The experiments were performed at the 2.2 second droptower at NASA-Lewis Research Center in Cleveland, OH. **Figure 1** displays the schematic of the experimental apparatus. Light from a 635 nm diode laser attached to a single-mode optical fiber was expanded and collimated to 50 mm in diameter. The expanded beam was directed through the top optical port of the combustion chamber using a 75 mm diameter mirror positioned at 45°. The transmitted beam was focused using a 200 mm plano-convex lens and redirected using a second 75 mm mirror (also positioned at 45°). The beam was then imaged through a spatial filter to a high-resolution CCD camera located on the bottom optical plate. An image quality interference filter and an absorption neutral density (o.d. 3.0) filter were placed directly in front of the camera to discriminate against flame emission or stray light. A second CCD camera was placed on the middle optical plate to capture the flame image. Two fiber optic cables were used to connect cameras attached to the rig to a Betacam recorder.

The filament was needed to prevent droplet motion during the experiment. Droplet movement caused by the deployment and/or the ignition process may prevent the observation of the entire burning process due to clipping of the sooting region by the camera field of view. Due to the small size of the filament, heat transferred from the flame to the droplet through the filament is several orders of magnitude smaller than heat transferred through the gas-phase at the droplet surface. Thus, the filament is not expected to augment or inhibit the burning process. The hypodermic syringes which were attached to separate rotary motors were rapidly retracted to deploy the droplets. After deployment, the droplet was ignited by using two sets of kanthol hotwires. After ignition, the ignitors were retracted to allow for undisturbed burning.

Results and Discussions

Figures 2a-b displays a laser-backlit image of a 1.8 mm n-heptane droplet flame at 0.7 and 1.2 seconds after free-fall. In order to obtain the projection values, P_{f_v}, the transmitted intensity distribution must be divided by the incident laser intensity distribution. In an effort to extend the observation time available to perform the experiment, the incident laser intensity distribution was obtained prior to free-fall. However, due to inevitable vibration of the optical components during the transition from normal-gravity to microgravity, the incident laser intensity distribution displayed measurable temporal variations until t = 0.6~0.7 sec which reduced the total observation time to less than 1 second.

The intensity distributions for the attenuated and unattenuated images were measured by digitizing the Betacam images with a high-resolution frame acquisition and processing board and a custom image processing algorithm. The images were filtered using a linear, 3 pixel by 3 pixel mean filter. In order to obtain the projection values, P_{f_v}, the intensity ratio distributions (I/I_0) were calculated by dividing the graylevel values for the sooting image along a vertical line through the center of the droplet by corresponding intensities measured for the background image (which was captured prior to droplet ignition and therefore unattenuated by soot). The intensity ratios were then averaged using a moving 5-pt operator. The I/I_0 distribution indicates the location of maximum light attenuation but does not directly provide information regarding the concentration of soot. The projected light extinction ratio distributions obtained as a function of time were used to determine the soot volume fraction, $f_v(r)$, using a 3-pt Abel deconvolution technique (ref. 19) with soot optical property determined using light extinction/gravimetric calibration technique (ref. 20). **Figure 3** displays the deconvoluted soot volume fraction distributions calculated as a function of time for the 1.8 mm heptane droplet. It is speculated that the combination of increased residence time due to lack of buoyancy (which enhance soot formation) and thermophoretic forces which transport the soot towards the droplet surface (preventing oxidation of the soot particles) create conditions in which significant amount of soot is accumulated into a soot-cloud within the fuel-rich region (refs. 21 and 22).

The maximum soot volume fraction is seen to increase as a function of time until quasi-steady state burning phase is achieved. This is related to the increase of flame size and the residence time which promotes soot formation. As burning progresses toward the quasi-steady state, soot concentrations within the flame is also increased by the effects of thermophoresis which prevent soot particles from

being transported toward the flame front. For these reasons, the residence time for soot formation and growth must also take into account the unique behavior observed only for droplet combustion in which the soot particles within the soot-cloud persists throughout the burning lifetime.

The concentrations of soot measured for the microgravity heptane flames are significantly higher than the nominal values of 1~2 ppm measured under normal-gravity conditions by Vander Wal and coworkers using laser-induced incandescence (refs. 23 and 24). Probable causes for this enhancement is due to differences in residence time and thermophoresis. Under microgravity conditions, the effects of gas-phase and soot radiation are of greater importance to the overall burning behavior for diffusion flames than in normal-g conditions (ref. 25). For the buoyant flame produced in normal-gravity conditions, the gas-phase velocity increases as a function of height along its trajectory above the droplet, $v_z = (\Delta \rho g z / \rho)^{1/2}$, with maximum velocity occurring near the soot production region (which corresponds to the highest temperature region). For the non-buoyant flame produced in microgravity, the gas-phase velocity is $v_r = (dm/dt)/(4\rho \pi r^2)$. For a given mass consumption rate, the gas-phase velocity is minimum near the flame front. Thus, the residence time near the reaction zone is relatively longer for microgravity conditions (due to the $1/r^2$ effect) for pyrolysis reactions leading to soot formation. Furthermore, soot particles experience even longer residence times (under microgravity conditions) due to the effects of thermophoresis which causes accumulation of the formed soot particles within the soot-cloud region. Whereas in normal-gravity conditions, the formed soot particles are transported through the flame.

Experiments were performed using a 1.0 mm and a 1.8 mm initial diameter droplet burning in atmospheric pressure air for comparisons (ref. 26). **Figure 4** displays the time-varying maximum soot volume fraction, $f_{v,max}$, and the SSR for the 1.0 mm and the 1.8 mm droplet plotted as a function of time divided by the square of the initial diameter (which is proportional to the fractional burning time). The measured soot standoff ratios for the 1.0 mm droplet are in good agreement with those reported by Jackson and Avedisian (ref. 27). For the smaller droplet, the available microgravity times are sufficient to observe that the soot volume fractions have achieved a maximum value and begin to decrease as a function of time. As the droplet size decreases due to burning, it is likely that the rate of soot formation at the flame front is also decreasing through combinations of reduced rate of mass vaporization and reductions in maximum temperature due to increased reactant leakage through the flame. Simultaneously, the Stefan flux near the droplet surface increases (assuming that the burning rate is constant) while the thermophoretic force is expected to decrease due to reductions in the temperature gradient causing soot to be transported towards the flame. These combined effects can reduce the amount of soot accumulated within the sootcloud as a function of time. Quasi-steady conditions were not attained for the larger droplet. A more relevant parameter to compare is the instantaneous soot mass within the region bounded by the droplet and the flame (which is calculated by integrating the product of the soot density and f_v distributions with respect to volume. Soot density of 1.8 g/cc was used). Since, the volume of the flame will scale as d^3, soot mass within the envelope flame is likely to be significantly larger for the 1.8 mm droplet. Comparison of the maximum instantaneous soot mass for the 1.8 mm droplet is approximately three times larger than the corresponding value for the smaller droplet. Considering that the instantaneous mass ratios between the two droplets are likely to increase with longer observation times available to analyze the larger droplet, it is evident that there is a strong size-dependent effect on the degree of sooting. Additional experiments performed using droplet size variation and ambient pressure reduction will be presented at the workshop.

References

1.   Faeth, G.M., Prog. Energy and Comb. Sci., 3, p. 191, 1977.
2.   Presser, C., Gupta, A.K., Avedisian, C.T. and Semerjian, H.G., Twenth-Third Symposium (Int'l) on Combustion, The Combustion Institute, p. 1361, 1990.
3.   Law, C.K. and Faeth, G.M., Prog. Energy Combust. Sci, 20:65, 1994.
4.   Williams, F.A. and Dryer, F.L., Science Requirements Document for Droplet Combustion
5.   Spalding, D.B., Fourth Symposium (Int'l) on Combustion, Williams and Wilkins, Baltimore, MD, 1953
6.   Godsave, G.A.E., Fourth Symposium on Combustion, p. 813, 1953.
7.   Kumagai, S., Sakai, T. and Okajima, S., Thirteenth Symposium on Combustion, p. 779, 1971.
8.   Law, C.K. and Law, H.K., Combust. Sci. Technol., 12:207, 1976.
9.   Crespo, A. and Linan, A., Combust. Sci. Technol., 11:9, 1975.
10.   Shaw, B.D. and Williams, F.A., Int. J. Heat Mass Transf. 33:301, 1990.
11.   Law, C.K., Combust. Flame, 26:17, 1976.

12. Law, C.K., Chung, S.H. and Srinivasan, N., Combust. Flame, 38:173, 1980.
13. Chung, S.H. and Law, C.K., Combust. and Flame, 1986
14. Cho, S.Y., Choi, M.Y. and Dryer, F.L.: Twenty-Third Symposium (International) On Combustion, The Combustion Institute, p. 1605, 1990.
15. Card, J.M. and Williams, F.A., Combust. Sci. Technol., 84:91, 1992.
16. Okajima, S. and Kumagai, S., Fifteenth Symposium (Int'l) on Combustion, The Combustion Institute, Pittsburgh, PA, p. 401, 1975.
17. Griffin, D.W. and Greenberg, P.S., Selected Microgravity Combustion Diagnostics Techniques, 2nd Int'l Microgravity Combustion Workshop, Cleveland, OH, 1992.
    Greenberg, P.S. and Ku, J.C.: Combustion and Flame vol. 108, p.227 (1997).
18. Lee, K.O., K. Jensen and M.Y. Choi, Investigation of Sooting in Normal-Gravity Droplet Combustion Using Light Extinction and Gravimetric Techniques, to be published in the 26th Symposium (Int'l) on Combustion, 1996.
19. Dasch, C.J., Applied Optics, 31, p. 1146, 1992.
20. Choi, M.Y., Mulholland, G.W., Hamins, A. and Kashiwagi, T., Comb. Flame, 102:161-169, 1995.
21. Choi, M.Y., Dryer, F.L. and Haggard, Jr., J.B.: Twenty-Third Symposium (International) On Combustion, The Combustion Institute, p. 1597, 1990.
22. Shaw, B.D., Dryer, F.L., Williams, F.A. and Haggard, Jr., J.B.: Sooting And Disruption In Spherically-Symmetrical Combustion Of Decane In Air, Acta Astronautica, 17, p. 1195, 1988.
23. Vander Wal, R.L., Dietrich, D.L. and Choi, M.Y., Relative Soot Volume Fractions in Droplet Combustion via Laser-Induced Incandescense, Eastern States Meeting of the Combustion Institute, Clearwater Beach, FL, 1994.
24. Vander Wal, R.L. and Dietrich, D.L, Appl. Optics, 34:1103, 1995.
25. Atreya, A., Agrawal, S., Shamin, T., Pickett, K., Sacksteder, K.R. and Baum, H.R., "Radiant Extinction of Gaseous Diffusion Flames", 3rd International Microgravity Combustion Workshop, 1995.
26. Choi, M.Y. and Lee, K.-O., "Investigation of Sooting in Microgravity Droplet Combustion", Presented at the 26th Symposium (Int'l) on Combustion, 1996.
27. Jackson, G.S. and Avedisian, C.T., Proc. R. Soc. Lond. A 446:255, 1994.
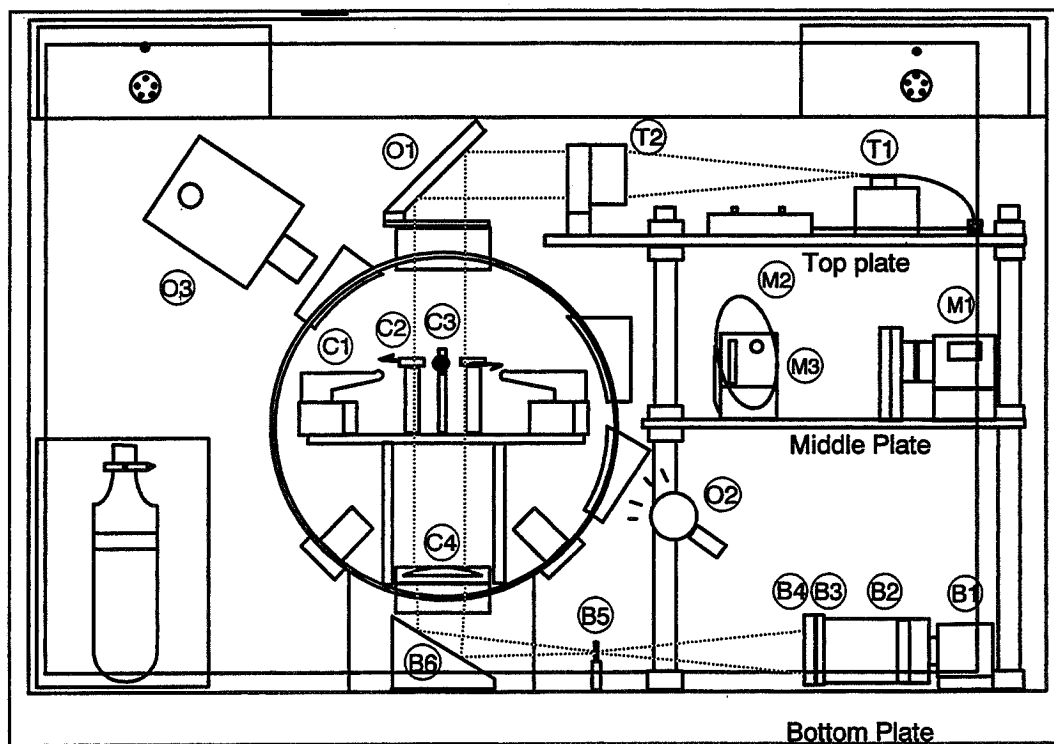
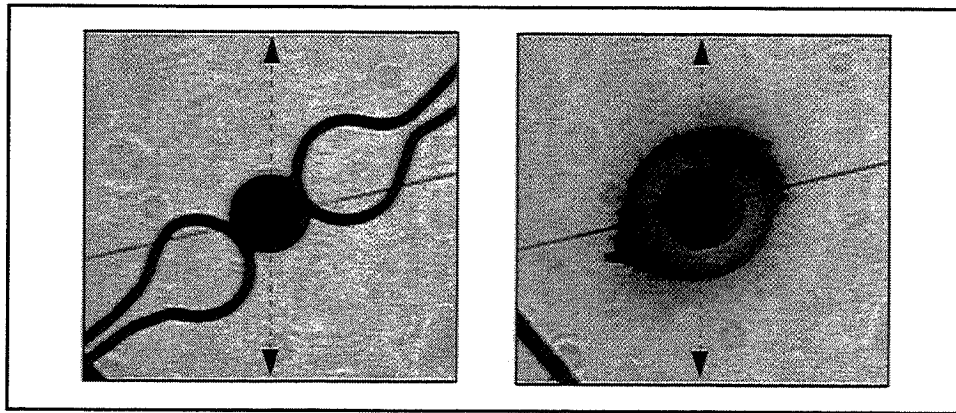Figure 1.--Schematic of Microgravity Experimental Apparatus

Figure 2a-b.--Laser backlit images of droplet and soot containing region.
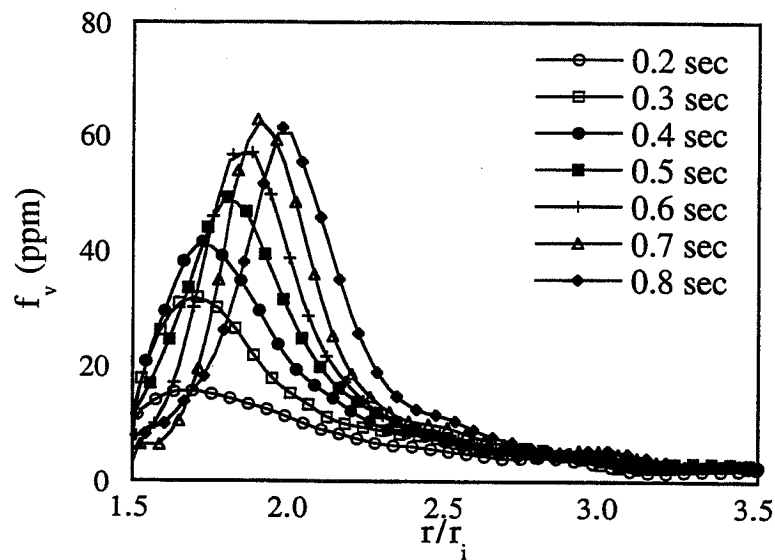

Figure 3.--Soot volume fraction distributions for 1.8 mm droplet.
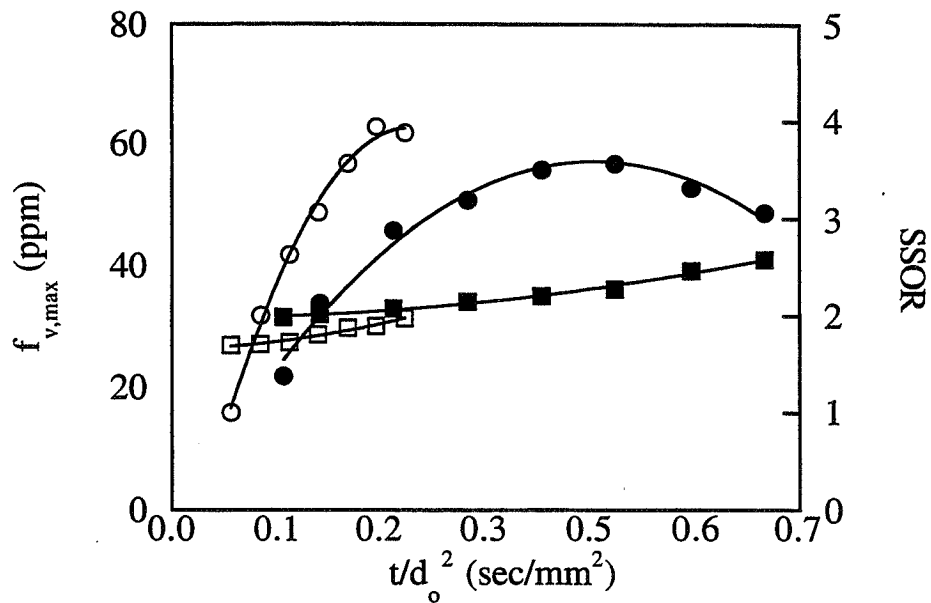

Figure 4.--Maximum soot volume fraction and soot standoff ratio (SSOR) for 1.8 mm and 1.0 mm droplets.

466

EMULSION DROPLET COMBUSTION IN MICROGRAVITY: WATER/HEPTANE EMULSIONS

C. THOMAS AVEDISIAN
Cornell University
Ithaca, New York

Introduction

This presentation reviews a series of experiments to further examine parametric effects on sooting processes of droplet flames in microgravity. The particular focus is on a fuel droplet emulsified with water, specifically emulsions of n-heptane as the fuel-phase and water as the dispersed phase. Water was selected as the additive because of its anticipated effect on soot formation, and the heptane fuel phase was chosen to theoretically reduce the likelihood of microexplosions because its boiling point is nearly the same as that of water: 100°C for water and 98°C for heptane. The water content was varied while the initial droplet diameter was kept within a small range. The experiments were carried out in microgravity to reduce the effects of buoyancy and to promote spherical symmetry in the burning process. Spherically symmetric droplet burning is a convenient starting point for analysis, but experimental data are difficult to obtain for this situation as evidenced by the fact that no quantitative data have been reported on unsupported emulsion droplet combustion in a convection-free environment. The present study improves upon past work carried out on emulsion droplet combustion in microgravity (Kimura et al. 1986; Okajima et al. 1986) which employed emulsion droplets suspended from a fiber. The fiber can be intrusive to the emulsion droplet burning process as it can promote coalescence of the dispersed water phase and heterogeneous nucleation on the fiber.

Prior work has shown that the presence of water in liquid hydrocarbons can have both beneficial and detrimental effects on the combustion process. Water is known to reduce soot formation and radiation heat transfer to combustor walls Gollahalli (1979) reduce flame temperatures and thereby NO_x emissions (Wang et al. 1984), and encourage secondary droplet atomization or microexplosion (Lasheras et al. 1979). Water also tends to retard ignition and and promote early extinction. The former effect restricted the range of water volume fractions as discussed below.

Description of the Experiment

An experiment is carried out by first starting at normal gravity and propelling a test emulsion droplet in a near vertical trajectory within a confined chamber (room temperature air in the present study) and then releasing into free-fall the combustion chamber with attached cameras and lighting when the droplet reaches the apex of its trajectory. If the release of the package is properly timed, the chamber, cameras, and downwardly moving droplet fall at almost the same rate. The ability to 'levitate' the test droplet this way is dependent on knowing the trajectory height and the time it takes the droplet to reach it. Unusual difficulties were experienced in achieving the requisite degree of repeatability for the water/heptane emulsion droplets examined using a piezoelectric droplet generator. This problem limited the number of successful observations of the burning process. The unsteadiness was believed to have been due to the presence of a surfactant and water microdroplets within the droplet, which influence both the effective viscosity of the emulsion and the surface tension . Results are presented in Section 4 for the most successful observations as determined by the clarity of the photographic image and the ability of the droplet to remain within the field of view for a significant fraction of its burning history.

Due to the difficulty of perfectly timing the package release there is usually some motion of the droplet relative to the camera. This motion is responsible for most of the observed asymmetries in the burning process as the magnitude of the effective gravity in the moving frame of reference is already low enough (less than 10^{-4} since a drag shield is used for all of the experiments discussed here) that buoyancy effects are small. Further discussion of the experimental set-up is given elsewhere (Jackson et al 1992 1994).

The initial droplet diameters examined were within a relatively narrow range that a diameter effect on burning (Jackson and Avedisian 1994) was not expected. The small droplet sizes studied challenges the ability to clearly photograph the burning process, but clear photographs were obtained for droplets of the sizes studied and the images were accurately analyzed by transport to a computer to obtain quantitative measurements of the evolution of diameter.

The primary means of data acquisition was photographic, from a high speed 16mm cine camera (LOCAM) with attached 90 mm/f2 Olympus Macro Lens. The movies provide qualitative information of flame luminosity and soot formation, as well as quantitative information on the evolution of droplet diameter and burning rates. To use the photographic image intensity for assessing sooting, all parameters (e.g., initial droplet diameter, ambient conditions, etc., including the back lighting intensity) are fixed except the water concentration. An effort was made to ensure this situation for the experiments reported here by using similar backlight intensity and keeping the parameters, except water, within a small enough range to show its primary effect on the burning process.

free-floating droplet which can push it out of the camera's field of view, a low boiling point and easily ignited fuel (heptane) is used to mitigate this problem. Asymmetries (e.g., irregular flame configuration) are observed immediately after ignition but they quickly vanish (within 2 ms for a burning process that is longer than 500ms) and give way to reasonably spherical flame shapes.

Preparation of Emulsions

The choice of emulsion mixture fractions tested was determined in part by the ability to spark-ignite the droplets, and coping with the unsteadiness of the droplet stream for the emulsions noted previously. Water volume fractions above about 40% required spark energies for ignition high enough that significant impulses were imparted to the droplet to throw them out of line and prevent their levitation by microgravity, or which would create long-lasting disturbances to the surrounding gas. For these reasons, the experimental results reported here are limited to water volume fractions under 30%.

The emulsions were prepared by combining the components in a beaker and dispersing them by agitation in an ultrasonic mixer. About 3% by volume of emulsifying agent (a mixture of Span 80 and Tween 80) was added during agitation. The composition of the emulsions discussed in this paper are the following: 87% heptane, 10% water and 3% surfactant for the emulsion labeled '10%' water; and 68% heptane, 29% water, and 3% emulsifier by volume for the emulsion labeled '30%' water.

Experimental Results

The evolution of diameter for emulsion droplets containing 10% (by volume) and 30% (by volume) water is shown in figs. 1 and 2, respectively. Data for a pure unsupported heptane droplet (0% water) previously reported (Jackson and Avedisian 1994) are included for comparison. In the figures, the ordinate 'Δ' is the droplet diameter (D) divided by the initial droplet diameter (D_0), and the abscissa is a scaled time, 'ξ' ($\equiv t/D_0^2$). The motivation for presenting the results in this way is derived from the 'D-squared' law (e.g., Glassman 1987) result,

$$\Delta^2 = 1. - K\xi \qquad\qquad\qquad 1$$

The variation of Δ^2 with ξ directly gives the so-called 'burning rate', K. Some of the results show that the burning rate is not constant throughout the combustion history. If K were unique, the burning process would be termed 'frozen' as postulated for emulsions (Law 1977) while a staged burning process is more typical of miscible mixtures. The evidence is not strongly supportive of staged burning for the 10% emulsion as shown in fig. 1, but the burning rate is uniformly lower for the emulsion droplets than heptane. For the 30% emulsion, the observation of staged burning is clear. In the early period, stage 1 ($\xi < 0.3$ mm^2/s), K for the emulsion is the same as heptane. In stage 2 (0.3mm^2/s$<\xi<$1.3mm^2/s) the burning rate is lower because of water vaporization. This type of staged burning for the water/heptane emulsion droplets burning in microgravity is similar to that observed during Leidenfrost evaporation of a water/heptane emulsion droplet at a hot surface (Avedisian and Fatehi 1988). A prediction of the emulsion droplet burning rate from a detailed chemistry model (Jackson and Avedisian 1996) assumes a frozen burning process which should be applicable to the period where both water and heptane are vaporizing, stage 2. The results show that the stage 2 burning rate for the 30% emulsion droplet is about 0.56mm^2/s as compared to an average measured value (fig. 2) of $K_2 \approx 0.53$mm^2/s. This agreement for K_2 shows that stage 2 burning has both water and heptane vaporizing in proportion to their mixture fractions as assumed in the numerical analysis.

A third period of burning appears to exist ($\xi > 1.3$s/mm^2 in figs. 1 and 2) for the emulsion droplets during which K ($\equiv K_3$) is almost zero. Though for the 30% emulsion droplets no accurate diameter measurements could be made after $\xi > 1.3$s/mm^2 because the droplets drifted slightly out of focus or partially out of the field of view, the droplets in view could still be discerned by eye from the high speed film record. The dotted line in fig. 2 is the trend that is believed to best represent the evolution of diameter during this period for this water concentration.

Stage 3 where $K \approx 0$ in figs. 1 and 2 is related to miscibility effects of the droplet components; the droplet is still burning. For the water/heptane system, the surfactant is miscible in both water and heptane and liquid diffusional processes (e.g., Wang et al. 1984) cannot often transport the volatile miscible component (heptane in this case) to the droplet surface at the same rate at which it evaporates. The droplet then surface becomes enriched by the nonvolatile component, the droplet temperature increases, and the average liquid density decreases. These competing effects result in the diameter being nearly constant for a time over which $\Delta \approx$ constant and $K \approx 0$. Once the droplet reaches a temperature at which the nonvolatile component can undergo significant vaporization, the diameter again decreases unless some other phenomena occurs such as extinction or microexplosions if the droplet temperature exceeds a threshold value to initiate bubble nucleation. This latter situation occurs for the data shown in figs. 1 and 2 which terminates the ability to record droplet diameter (the 'starred' points in figs. 1 and 2). If bubble nucleation within the droplet would not have occurred, a fourth stage of burning (not shown in figs. 1 and 2) would presumably have been dominated by surfactant vaporization.

While flame boundaries for the emulsion droplet were too faint for quantitative measurement of their diameters for the image analysis system used, close inspection of the video camera records showed luminous zone boundaries moving inward toward the droplet late in the burning process during the period where the droplet diameter was almost constant (stage 3 in figs. 1 and 2). This behavior is attributed to an increase in emulsifier concentration during this period, and to reduced vaporization as the droplet temperature rises. The phenomenon of shrinking flames which accompanies a change in the dominant vaporizing species, here from heptane and water to surfactant, is similar to that observed for miscible mixture droplets at normal gravity (Wang et al. 1984). Shrinking flames for the water/heptane emulsion droplets signify reduced vaporization and that heat from the flame is largely being used to heat the droplet surface which has become enriched in the emulsifier concentration. Eventually, either the flame will extinguish if surfactant vapors cannot sustain combustion, or the droplet may microexplode if the droplet temperature increases substantially.

Soot Formation

Soot aggregates formed when fuel droplets burn when the relative droplet/gas motion is small can be trapped between the droplet and flame in a spherical 'shell' structure surrounding the droplet. First observed by Okajima and Kumagai (1975), the soot shell for spherical droplet flames has been discussed in a review (Avedisian 1997). Soot particle entrapment during fuel droplet combustion has been analyzed in an approximate way (Jackson et al. 1992; Jackson and Avedisian 1996) and the results show that the entrapment and associated stability of capture for a soot aggregate between the droplet and flame is dependent on the aggregate size, the smaller aggregates being stably locked into position and the larger ones more prone to being moved by perturbations of the surrounding flow. Particularly large aggregates can be pushed through the flame and not remain trapped at all, which is a more prevalent experience for aggregates later in the burning history as has been experimentally observed (Jackson and Avedisian 1994) and predicted (Jackson and Avedisian 1996).

Soot aggregate entrapment was observed for emulsions in this study. Figure 3 shows three representative photographs of free-burning heptane (0% water), 10% water and 30% water emulsion droplets. The pure heptane sequence is from Jackson and Avedisian (1994) and reproduced for comparison. Motion picture movie frames from which the prints were taken had similar back-lighting and relative motion of the droplet to the camera. For illustration, the movie frames were selected to correspond to ξ $\approx .416 \ s/mm^2$ to facilitate comparison.

As shown in fig. 3, there is a reduction in flame luminosity and soot formation for the emulsion droplets in comparison to a pure heptane droplet. While the photos are not quantitative concerning sooting tendencies, they do clearly show reduced soot formation and aggregate entrapment for the emulsions compared to pure heptane. The mechanism is postulated as follows. The water which is vaporized from the emulsion surface is immediately on the fuel-rich side of the flame where also the soot forms, which can reduce the flame temperature and increase the rate of production of OH radicals through increased water dissociation in the fuel pyrolysis zone. Vaporization of water can also inhibit soot formation by pulling the flame closer to the droplet surface which reduces the residence time for fuel pyrolysis.

The reduction of sooting of the emulsion droplets relative to heptane is consistent with a complex chemistry model of quasi-steady water/heptane emulsion droplet combustion (Jackson and Avedisian 1996). The Warnatz (1984) kinetic mechanism was used though more detailed but computationally intensive kinetic mechanisms exist (Lindstedt and Maruice 1995) for heptane. Though neither the formation of soot aggregates nor radiation were specifically included in that model, considering detailed chemistry allowed tracking of the acetylene distribution that would not have been possible by a single step reaction process. Fig. 4 shows the radial distribution (r/r_d where $r_d=D_o/2$) of the computed amount of acetylene (and other species) with various water concentrations for a droplet diameter of 0.6mm. The acetylene distribution narrows and the peak reduces as the water content increases. To determine the effect of water on the C_2H_2 distribution, the proportional amount of acetylene formed between the droplet and flame per unit mass of fuel vaporized, $M \equiv \dfrac{\dot{m}_{C_2H_2}}{\dot{m}_{fuel}}$, was calculated by integrating the acetylene distributions shown in fig.4:

$$\dot{m}_{C_2H_2} = \int_{r_d}^{\infty} \left(r^2 \rho Y_{C_2H_2} W_{soot} A e^{\frac{-E_a}{RT}} \right) dr \qquad\qquad 2$$

where the upper limit to simulate a boundary at infinity was $100 r_d$. The following parameters were used in eq. 2 (Fairweather et al. 1992): $W_{soot} \approx 12000 g/mole$, $E_a \approx 172 kJ/mole$, $A \approx 10.36 \times 10^6 s^{-1}$. The variation of M with water content is shown in fig. 5. The results show that the amount of heptane converted to acetylene decreases rapidly as the water content increases. Since it is reasonable to expect that soot will track with acetylene, soot formation is predicted to decrease as the water content in the droplet increases.

The ability to observe soot aggregates is somewhat dependent on the lighting used for photography (Avedisian 1997). Soot seems to be more visible as the light intensity is reduced, while the droplet is more clearly observed with high intensity lighting. For the photos shown in fig. 3, less intense back lighting was used for the emulsion droplet than the heptane droplet which should have increased soot visibility for the emulsion droplet. But the image intensity is still less pronounced for the emulsion droplet than the heptane droplet.

The luminosity of the sooting droplet flame shows the extent of symmetry of the burning process. For perfect spherical symmetry, the soot shell and luminous zone should be concentric and spherical. It is evident from fig. 3 that this is not precisely the case for the emulsion droplets. The soot shell exhibits a tail for the emulsion droplet at some point during burning because of the small drift of the droplet compared to the pure heptane droplet. Nonspherical flames can also evidence liquid motion since the flow at the reaction zone must have a nonradial component for the flame to be nonspherical, hence also at the droplet surface which leads to liquid motion. The strength of the liquid motion set up by the gas phase tangential velocity component at the droplet surface is much less than in the gas phase owing to the large density difference among the phases for conditions far from the critical point.

Microexplosions

Because the water and heptane boiling points are almost identical, there should theoretically have been no possibility for bubble nucleation to occur within the droplet during the burning history. However, secondary atomization was observed for both the 10% and 30% emulsion droplets. Nucleation was attributed to dissolved surfactant in the fuel phase to drive up the droplet temperature to superheat the water.

Secondary atomization of the water-in-heptane emulsion droplets was characterized by fragmentation into several smaller droplets in more than one event unlike that observed for a unsupported methanol/dodecanol mixture droplet in microgravity (Yang et al. 1990). The difference between the miscible mixture and immiscible emulsion fragmentation process is due to the internal bubble nucleation process, which is at the interface between the water microdroplets and surrounding (mixture) fuel phase for the emulsions, but which is within the bulk of the fuel for a miscible mixture. Bubble nucleation on the surface of an internal water microdroplet which is near to the droplet surface can produce 'spitting' and ejection of liquid through the interface and a less intense disruptive event. Such a fragmentation process would not occur in one catastrophic event.

Summary and future work

This study has provided new measurements of the evolution of droplet diameter of unsupported water/heptane emulsion droplets burning in microgravity to reduce the effects of convection. The goal was to create spherical symmetry in the burning process. Several conclusions can be drawn from the study. Emulsification of heptane with water reduces the flame luminosity and soot formation. Soot collects in a shell-like structure for the emulsion drops similar to observations of single component fuels and miscible mixtures burning in microgravity. A staged burning process occurs for the emulsions studied. In the final stage of burning, the emulsions droplets are sometimes observed to explode. This result is attributed to dissolution of the surfactant in the fuel which increases the droplet temperature to above the boiling point of water. Finally, burning rates for the water/heptane emulsion are slightly lower than heptane in an intermediate stage of burning, and decrease as the water concentration increases.

Continuing work will consider further effects of additives on sooting processes and burning rates. The unsteadiness in the droplet stream that was a problem for these emulsion experiments should be reduced for unsupported miscible mixtures which is a current focus. Also, the experimental method will be continually upgraded to improve the data quality.

Acknowledgments

References

Avedisian, C.T. 1997 *Comb. Sci. Tech. Book Series..* vol 4, pp. 135-159 Gordon and Breach.

Avedisian, C.T. and Fatehi, M. 1988 *Int. J. Heat Mass Trans.*, **31**, 1587-1603 .

Fairweather, M., Jones, W.P. and Lindstedt, R.P. 1992 *Comb. Flame* **89**, 45.

Glassman, I. 1987 *Combustion*, 2nd Edition, p. 275, New York, Academic Press.

Gollahalli, S.R. 1979 *Comb. Sci. Tech.*, **19**, 245-250 .

Jackson, G.S. and Avedisian, C.T. 1996 *Comb. Sci. Tech.* **115**, 127-147.

Jackson, G.S, Avedisian, C.T., and Yang, J.C. 1992 *Int. J. Heat Mass Trans.*, **35**, 2017-2033.

Jackson, G.S. and Avedisian, C.T. 1994 *Proc. R. Soc. London*, A**446**, 255-276.

Law, C.K. 1977 *Comb. Sci. Tech.* **17**, 79.

Kimura, M., Ihara, H. Okajima, S., and Iwama, A., 1986 *Comb. Sci. Tech.*, **44**, 289-306.

Lasheras, J.C., Fernandez-Pello, A.C. and Dryer, F.L. 1979 *Comb. Sci. Tech.*, **21**, 1-14.

Lindstedt, R.P. and Maurice, L.Q. 1995 *Comb. Sci. Tech.* **107**, 317-353.

Okajima, S., Kanno, H., and Kumagai, S. 1985 *Acta Astronatut.*, **12**, 555-563.

Okajima, S. and Kumagai, S. 1975 *15th Symp. (Int.) Comb.*, Pittsburgh, Pa.: The Combustion Institute, Pittsburgh, pp. 401-407.

Wang, C.H., Liu, X.Q., and Law, C.K. 1984 *Comb. Flame*, **56**, 175-197.

Warnatz, J. 1984 *20h Symp. (Int.) Comb.*, Pittsburgh, Pa.: The Combustion Institute, Pittsburgh, pp. 845

Wang, C.H., Liu, X.Q., and Law, C.K. 1984 *Comb. Flame*, **56**, 175-197.

Yang, J.C., Jackson, G.S. and Avedisian, C.T. 1990 *23rd Symp. (Int.) Comb.*, Pittsburgh, Pa.: The Combustion Institute, Pittsburgh, pp. 1619-1625.
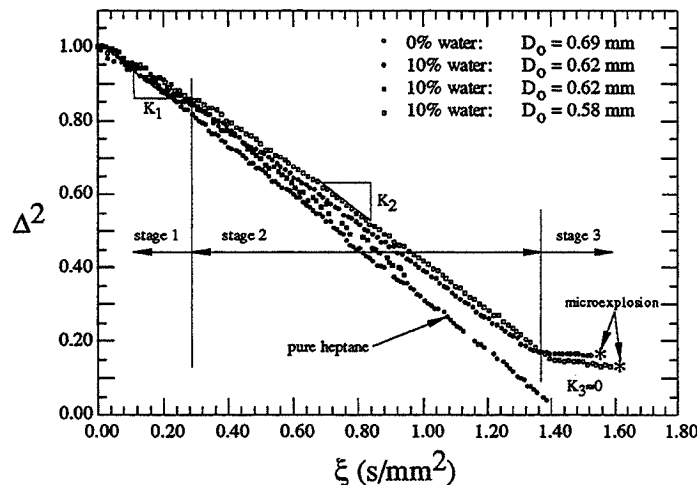
Figure 1: Evolution of diameter for unsupported 10% water/heptane emulsion droplets compared with pure heptane (0% water).
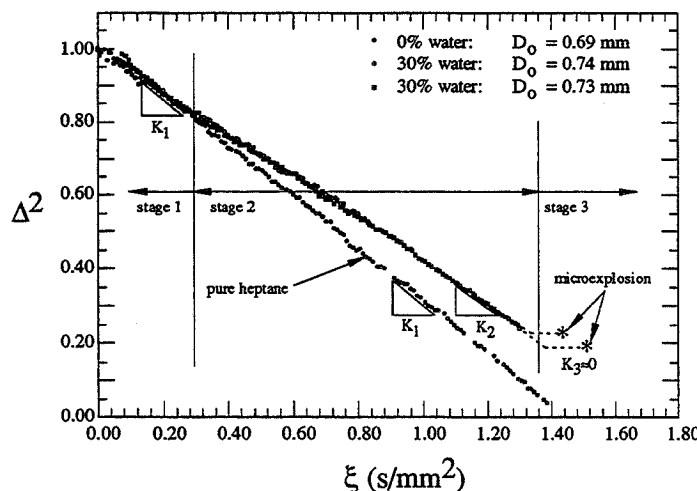

Figure 2: Evolution of diameter for unsupported 30% water/heptane emulsion droplets compared with pure heptane (0% water)
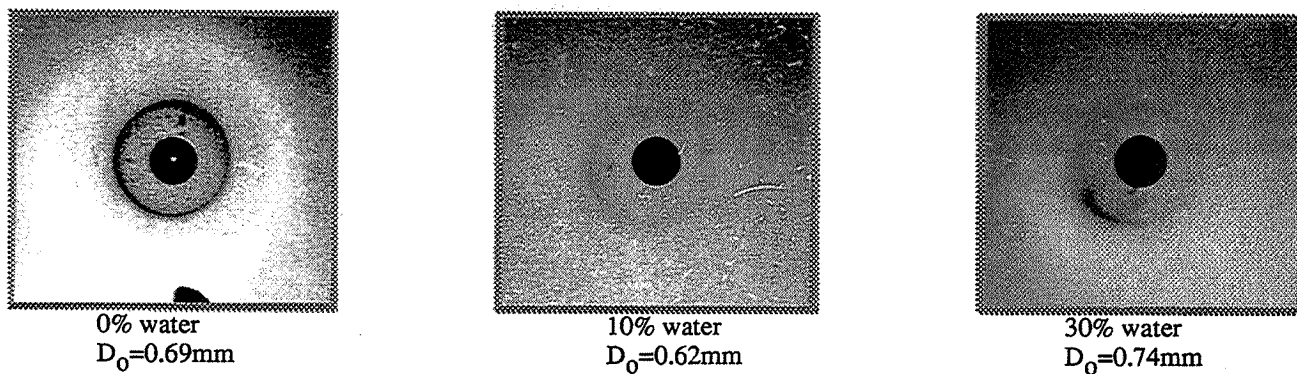
471

0% water
D_0=0.69mm

10% water
D_0=0.62mm

30% water
D_0=0.74mm

Figure 3: Representative photographs of a) heptane (0% water); b)10% emulsion ; and c) 30% emulsion. Photos are reproduced from motion picture sequences for $\xi \approx 0.416 s/mm^2$. Initial droplet diameter (D_0) is given beneath each photo. The photos show the soot shell and lowered sooting for the emulsion droplets relative to heptane.
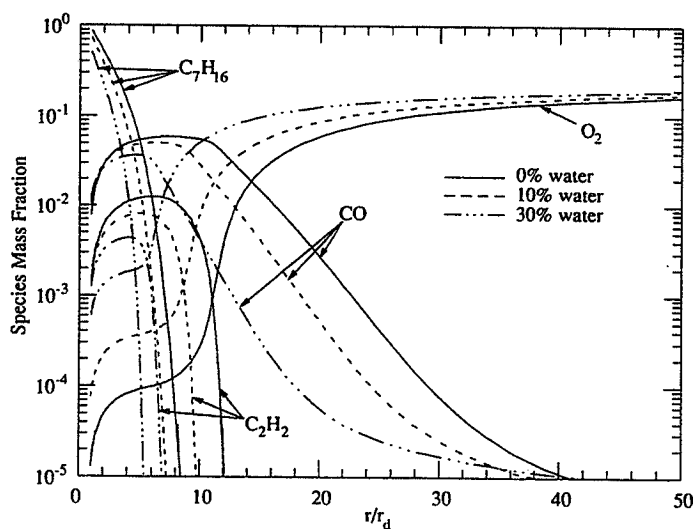

Figure 4: Distribution of various species around heptane/water emulsions, D_0=0.6mm
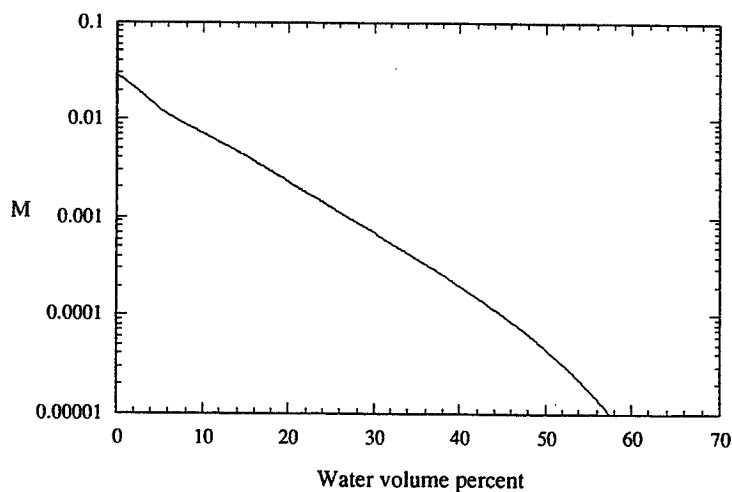
Figure 5: Effect of water concentration on fractional conversion of vaporized heptane to acetylene, D_0=0.6mm

472

COMBUSTION OF TWO-COMPONENT MISCIBLE DROPLETS
IN REDUCED GRAVITY

BENJAMIN D. SHAW
University of California, Davis

Introduction

This research focuses on reduced-gravity combustion of binary miscible droplets initially in the mm size range or larger. Combustion experiments were performed using the NASA Lewis 2.2 sec Drop Tower, as well as the Glovebox Facility during a 1995 flight of the Space Shuttle. This paper will focus on work performed over the previous two years. Results from earlier research are described elsewhere[1,2,3].

As reported previously[2], a large number of experiments was performed using the NASA Lewis 2.2 sec drop tower. Mixtures of alkanes and/or alcohols were studied. The fuel components were selected to have significantly different volatilities. Initial oxygen mole fractions from about 0.15 - 0.5 and initial pressures from 0.3 - 3 atm were employed. Different inerts were used (He, CO_2, Ar, N_2) to change burning rates and sooting behaviors. A major effort has been the analysis of results from these experiments. More recently, particle seeding was employed to allow visualization of flowfields inside droplets in microgravity. In some of these experiments, line-of-sight measurements of average soot volume fractions were made, and thermocouples were used to measure gas temperatures. All experiments (ground and Glovebox) were conducted to gain information on the following:

> Transient droplet diameters (including three-staged combustion behaviors and microexplosion).
> Transient flame behaviors (sudden flame contraction, luminosity, extinction).
> Droplet internal flowfields (i.e., whether spherical symmetry was closely approached).
> Behaviors of observable soot particles.
> Transient variations in line-of sight soot volume fraction measurements.
> Flame temperatures.

Theoretical efforts have also been conducted in parallel with the experiments. This research included:

> Studies of hydrodynamic stability of spherically-symmetrical droplet gasification (to address the question as to whether spherically-symmetrical droplet gasification may be destabilized from thermosolutal capillary effects).
> Studies to extend previous results for prediction of the onset of flame contraction.
> Studies to estimate whether flame-to-droplet diameter ratios will be unsteady or essentially constant during most of the combustion history of a droplet.
> Computational modeling of effects of capillary stresses on droplet gasification.

Significance

This research is providing fundamental data on liquid species diffusion rates in burning droplets. Information is being also generated on extinction of two-component droplets and the role of solutalthermal capillary instabilities in determining droplet internal flows. These data are useful practically (e.g., for spray modeling), as well as scientifically. Data are also generated on topics germane to fundamental droplet combustion physics (e.g., gas-phase unsteadiness, gas temperatures and sooting).

Experimental Approach

Ground experiments were performed at the NASA Lewis 2.2 sec Drop Tower using a drop rig built at UC Davis. In an experiment, a droplet was grown (in a pressure chamber) between two opposed hypodermic needles. The needles were retracted simultaneously in opposite directions. Droplets were ignited using two symmetrically-placed ignition sparks (≈ 100 mJ each). Spark electrodes were retracted after ignition, and droplet and flame behaviors were observed photographically using two ccd video cameras and two 16 mm cine cameras. Orthogonal views were taken; one backlit view was a close-up of the droplet while the other showed the flame (no backlight). In most experiments, droplets were grown around a 12 μm support fiber

which held droplets nearly motionless and even if there was drift along the fiber it was very small (≈ 0.1 mm/s). It is noted that the opposed-needle technique and small support fibers were first used by NASA researchers[4,5].

After the drop rig had been used for some time, improvements were made to allow measurements of line-of-sight soot volume fractions, gas temperatures, and droplet internal flows (using particle seeding). This work, which was done over the last two years, involved adding a laser diode, optics, photodiodes, a thermocouple, and a programmable microcontroller to the rig. In the flow visualization experiments, small amounts of 50 μm aluminum-oxide particles were seeded into the droplets prior to ignition. The particles were illuminated by a 15 mW laser diode. The light scattered from the particles was imaged by video and high-speed film cameras to allow observation of droplet internal flow patterns. In other experiments, extinction of a laser beam was used to obtain line-of-sight measurements of average soot volume fractions, and a thermocouple was also used to measure gas temperatures near burning droplets. Details on the drop rig are presented elsewhere[6,7].

The Glovebox experiments were performed using the Fiber Supported Droplet Combustion (FSDC) apparatus, which was developed at the NASA Lewis Research Center. These experiments were performed in conjunction with other PI's in the NASA Microgravity Combustion Science Program. Droplets initially as large as about 5 mm were burned in Shuttle air.

Experimental Results

Estimates of Liquid Species Diffusivities

Theory predicts that the ratio of the droplet diameter d_c at the onset of flame contraction (which occurs from sudden droplet heating as the liquid surface mass fraction of the low volatility component rapidly approaches unity) to the initial droplet diameter d_0 is a function of the initial low-volatility mass fraction y_0 in the droplet and the inverse Peclet number $\varepsilon = 8D/K_1$, where D is the liquid species diffusivity and and K_1 the burning-rate constant prior to the flame contraction. Under typical conditions, $\varepsilon \ll 1$ is expected. Asymptotic theory has been developed[8] which capitalizes on the smallness of ε. This theory was originally developed for predicting flame contraction either very early in the droplet history or for times of the order of the droplet lifetime, but not at intermediate times. This theory was extended (using matched asymptotic expansions) so that it is applicable at intermediate times as well. In addition, the theory was extended to higher order. The theoretical results predict that a flame contraction will occur when the following equation is met

$$1 + h_{0-} + \varepsilon h_{1-} + H_{0-}/\varepsilon + H_{1-} + \varepsilon H_{2-} - h_{match} = 1/y_0 \qquad (1)$$

where $h_{0-} = \phi \, [1 + erf(\phi^{1/2}/2)]/2 + erf(\phi^{1/2}/2) + (\phi/\pi)^{1/2}e^{-\phi/4}$, $h_{1-} = 4 + \phi + 3\phi^2/2 - 2e^{-\phi/4} + e^{-\phi/4} I/\pi$, $H_{0-} = (e^{3\tau} - 1)/3$, $H_{1-} = (e^{3\tau} + 2)/3$, $H_{2-} = 22/9 + (14 - 24\tau)e^{3\tau}/9$, $h_{match} = 1 + \tau/\varepsilon + \varepsilon[4 + \tau/\varepsilon + 3\tau^2/(2\varepsilon^2)]$, and $I = \pi e^{\phi/4} (2 + \phi/2 + 3\phi^2/4) [erf(\phi^{1/2}/2) - 1] + (\pi\phi)^{1/2} (3\phi/2 - 2)$. In addition, $\tau = \ln(d_0/d)$ is a dimensionless time, and $\phi = \tau/\varepsilon$ a rescaled time. Equation (1) was used to evaluate liquid species diffusivities in heptane/hexadecane droplets by utilizing experimental data for the ratio d_c/d_0, thus defining $\tau = \tau_c$ at the flame contraction onset. This τ_c value was inserted into Eq. (1), and the value of ε that satisfied Eq. (1) was then determined iteratively. Figure (1) shows plots of Eq. (1) as well as data on the droplet volume ratio ($V_c/V_0 = d_c^3/d_0^3$) at the onset of flame contraction for the present ground-based experiments, the high-pressure experiments of Mikami et al.[9], the Glovebox experiments[10], and normal-gravity experiments performed by Wang et al.[11]; all of these data are for heptane/hexadecane droplets burning in various ambients.

Using data in Fig. (1), liquid species diffusivities were evaluated using the definition $D = \varepsilon K_1/8$. Results are shown in Fig. (2), which shows that D varies significantly with pressure. This is a result of variations in liquid saturation temperatures (variations in D with ambient compositions or initial liquid compositions were not appreciable in the present experiments). The 1-atm data of Law et al., as well as the FSDC data, have D values that are significantly larger than the present ground experiments (at 1 atm). This is likely from variations in droplet internal circulation. The species diffusivities from the present experiments are in ranges that would be expected theoretically. It is noted, however, that flow visualization experiments (see below) revealed that significant droplet internal circulation was also present in these experiments. As a result, fundamental values of the liquid species diffusion rates that apply to heptane/hexadecane droplet combustion have not been as well-characterized as possible.

Flow Visualization Experiments

A series of experiments was performed where droplets were seeded with 50 μm aluminum-oxide particles, and then ignited in reduced gravity[6], though some droplets were intentionally not ignited. Alkane mixture droplets, alcohol mixture droplets, and

methanol/water mixture droplets were investigated. The particles were illuminated with a laser diode, and particle positions were recorded photographically. Data on particle positions were used to determine two-dimensional particle velocities inside droplets. In all the experiments, peak particle velocities were in the range 10 - 60 mm/s, and peak particle velocities did not decay to levels less than 10 mm/s over the observation times of 1 - 2 sec, even when droplets were not ignited. Data on sooting and gas temperatures were also generated during these experiments; these data are presently being analyzed.

Figure 3 shows data for a droplet initially composed of a mixture of heptane and hexadecane, where the initial hexadecane mass fraction was 0.05. Data are not shown for the time period 0.1 - 0.3 sec because of soot obscuration. From about 0.3 sec - 0.8 sec, peak tracer particle velocities were in the range of 10 - 15 mm/s. The data terminate at about 0.8 sec because a microexplosion shattered this droplet (i.e., the droplet shattered from rapid internal bubble growth).

Data for a droplet composed initially of a mixture of methanol and dodecanol (initial dodecanol mass fraction of 0.4) are shown in Fig. 4. As is evident in this figure, peak particle velocities as well as the spread in particle velocities were much larger in this case than for the droplet in Fig. 3. After retraction of the deployment needles, particle velocities of up to about 60 mm/s were observed. When ignition occurred at about 0.09 sec, the peak particle velocities were clearly observed to decrease to about 10 mm/s, after which time the velocities increased substantially to values that approached 60 mm/s. This temporary decrease in particle velocities is very likely related to the fact that strong radial temperature profiles would have been set up for a short time while the droplet was heating, promoting damping of liquid-phase velocities from thermal Marangoni effects. At a time of about 1 sec, the flame was observed to contract, indicating that the droplet was heating from a rapid buildup of dodecanol at the droplet surface. This rapid heating would also cause strong radial temperature gradients to temporarily exist in the droplet, which could damp interior velocity profiles from thermal Marangoni effects. At the time of the flame contraction, the particle velocities were observed to significantly decrease in value. After the flame contraction, particle velocities were observed to increase. This droplet shattered from a microexplosion at about 1.3 sec.

FSDC Experiments

The Glovebox Facility was utilized during a 1995 flight of the Space Shuttle (USML-2) to enable preliminary experiments to be performed on combustion of large heptane/hexadecane droplets (initially up to 5.2 mm in diameter); use was made of the FSDC apparatus, where droplets were burned in Shuttle air. Even though these experiments were necessarily limited in scope, they allowed the first observation of flame contraction phenomena for large droplets. They also allowed unexpected sooting and extinction phenomena to be observed. Details on these and other FSDC experiments are presented elsewhere[10].

Figure 5 shows droplet diameter data for two different droplets burned in the FSDC experiments. The smaller droplet was initially about 3.5 mm in diameter, and the larger droplet was initially about 5.2 mm in diameter. The data for the smaller droplet clearly display staged combustion, i.e., where two periods of nearly d-square law combustion are separated by a plateau region where vaporization rates are significantly decreased. In Fig. 5, the variables K_1 and K_3 are burning-rate constants (based on the droplet diameter) observed for the smaller droplet before and after the "plateau". The onset of the plateau has been observed in ground-based experiments to coincide with flame contractions associated with rapid droplet heating when the liquid surface mass fraction of hexadecane closely approaches unity. This is expected to be the case here, as well. In the present experiments, however, it was unexpectedly found that the flames of these droplets were very dim and could not be imaged by the video cameras. Unlike the alcohol droplets burned in the other FSDC experiments, glowing of support fibers also was not evident in the video images of burning alkane droplets, suggesting that flame temperatures were very low for these mixture droplets. Data on flame behaviors unfortunately could therefore not be obtained from the experiments.

The larger droplet in Fig. 5 did not display staged combustion behavior. In addition, this droplet may have extinguished about 25 sec into its burn, as evidenced by the leveling off of the plot of the square of the droplet diameter at about this time. Interestingly, the apparent extinction took place at about the time when a flame contraction was expected to occur, suggesting that the flame contraction may have induced extinction; this was never observed in any of the ground-based experiments we have performed with initially-smaller droplets, nor has this been reported by other investigators. An attempt was made to re-ignite the larger droplet about 52 sec; this attempt appeared to be unsuccessful.

The largest droplet was observed to soot significantly more than the smaller droplets, as well as for smaller droplets burned in drop towers under similar environmental conditions. Even though the heptane/hexadecane droplets in the FSDC experiments displayed significant sooting, these droplets were not observed to form soot shells which are characteristically observed during reduced-gravity combustion with smaller droplets composed of similar mixtures (as observed in drop tower experiments[7,12]). A theoretical explanation for the apparent lack of soot shells is lacking. However, the lower flame temperatures that likely were present in these experiments could have been responsible for the lack of soot shells. This is because soot shells occur as a result of soot particles being held at a particular radial location by a balance of outwardly-directed drag forces and inwardly-directed thermophoretic forces. The lower flame temperatures would have reduced the thermophoretic forces such that drag

forces could have always been sufficient to force soot particles away from the droplets. Another difference from ground-based observations is that blue flames were visually detectable during most of the combustion history. For smaller droplets burned in ground-based facilities (in air at one atm), any blue was totally obscured by brighter yellow soot radiation for most of the combustion history.

Analytical Research And Results

Stability Analyses

Stability analyses[13] have addressed the problem of hydrodynamic stability of a two-component droplet undergoing spherically-symmetrical gasification. A linear stability approach was used to predict influences of thermal and solutal Marangoni effects on hydrodynamic stability of bi-component droplets evaporating in a spherically-symmetrical manner in hot environments. It was predicted that with zeotropic mixtures and for $\partial\sigma/\partial T < 0$ and and $\partial\sigma/\partial y < 0$ (where σ is surface tension, T temperature, and y the surface mass fraction of the more volatile droplet component), the thermal and solutal Marangoni effects oppose each other in that the thermal effect is stabilizing and the concentration effect is destabilizing. The model was applied to alkane/alkane and alcohol/water mixture droplets. The alkane mixture droplets were predicted to be hydrodynamically stable. For alcohol/water mixtures, results suggest that critical radii for marginal stability exist; when a droplet has a radius larger than the critical radius, it is predicted to be unstable. For an initially-pure methanol which subsequently absorbs water from the ambient, the critical radius is predicted to depend upon the amount of water in the environment. Critical radii for the onset of instability in initially-pure methanol droplets are predicted to be small (Fig. 6).

Flame Standoff Ratio Unsteadiness

Williams[14] has observed that simplified estimates as to whether the flame standoff ratio should be steady or unsteady for most of the droplet lifetime can be made by noting that since a droplet exists for only a finite period of time (t_d, the droplet lifetime), there must be an outer zone where transient diffusion is important. The radial location R_D of this zone can estimated as $R_D \approx (D_O t_d)^{1/2}$ where D_O is a characteristic species diffusivity, taken here to the the diffusivity the oxidizer. If the quasisteady flame radius r_f is significantly smaller than R_D, then flame standoff ratios should be nearly constant over most of the lifetime of a droplet. However, if $r_f \gtrsim R_D$, then flame standoff ratio unsteadiness should be significant. Williams has presented simplified analyses based upon these ideas to estimate whether flame unsteadiness should be present. His model assumes that the gas phase has a Lewis umber of unity. This assumption is questionable, especially for He/O_2 ambients such as those investigated here. Because of this, an approximate analysis was developed to enable estimates of the effects of gas-phase unsteadiness on flame standoff ratios to be obtained. This analysis is a generalization of the approach of Williams. Because of space limitations, the development of the present theory, which is based upon solving a conservation equation for oxidizer expressed in terms of a mole fraction, is not shown here. The final result for the ratio r_f/R_D is shown below as Eq. (2), where the relation $t_d \approx 4r_d^2/K$ was used. In this equation, n is molar density, ρ_d the droplet density, W_{F_1} the molecular weight of fuel species 1, y_{F_1} the mass fraction of fuel species 1 vaporized from the droplet surface, and K the burning-rate constant based upon the droplet diameter, and v_{F_i}, v_{P_i}, and v_O are coefficients in the one-step reaction $\Sigma v_{F_i} F_i + v_O O \rightarrow \Sigma v_{P_i} P_i$ (F_i is fuel species i, O is oxidizer, and P_i product species i). In addition $x_{O,\infty}$ is the ambient oxidizer mole fraction.

$$\frac{r_f}{R_D} \approx \frac{y_{F_1}\rho_d K^{3/2}(\Sigma v_{P_i} - v_O)/v_{F_1}}{16 W_{F_1} n D_O^{3/2} \ln\left[1 + x_{O,\infty}(\Sigma v_{P_i} - v_O)/v_O\right]}. \tag{2}$$

For combustion of heptane/hexadecane droplets in air at 0.1 MPa, Eq. (2) yields $r_f/R_D \approx 0.5$, while for combustion of heptane/hexadecane droplets in an He/O_2 environment ($x_{O,\infty} = 0.3$) at 0.1 MPa, Eq. (2) yields $r_f/R_D \approx 0.06$. These estimates indicate that flame standoff ratios are approaching the limit of being quasisteady for combustion in air (while still being unsteady), and that quasisteady flame standoff ratios are to be expected for combustion in the He/O_2 mixture; these expectations are in agreement with data obtained as part of the present program. These theoretical r_f/R_D values were obtained by using experimental values for average burning rate constants for the entire burning histories following droplet heatup, and assuming the combustion products were CO_2 and H_2O. The product $nD_O^{3/2}$ was evaluated at an average temperature of 1000 K, and the diffusivity D_O was selected to be the binary diffusion coefficient of O_2 in either N_2 or He.

476

Computational Research And Results

Detailed computational modeling (in collaboration with H. A. Dwyer) has focused upon predicting the effects of capillary flows (from droplet surface temperature and/or composition gradients) on droplet vaporization. Briefly, the governing equations are cast in a finite-volume form, and solved numerically for transient liquid- and gas-phase variables. Variable properties in both the liquid and gas phases are allowed. Modeling of single-component droplet vaporization in a hot environment has clearly shown that surface-tension gradients dramatically influence droplet vaporization and internal circulation behaviors under conditions that are representative of slowly-drifting droplets in reduced-gravity experiments as well as rapidly-translating droplets in practical high-pressure sprays[15]. Modeling of methanol-water droplets has also demonstrated that solutal capillary flows can dramatically influence droplet internal flows, even for rapidly-moving droplets[16]. These results, which are important practically as well as scientifically, support the stability analyses described above.

Future Plans

Future work will involve further analysis of data from the drop tower experiments, e.g., on the effects of ambient conditions on sooting. In addition, parabolic-flight- xperiments in support of planned flight experiments will be performed. These experiments will involve generating data on droplet internal flow decay times over longer timescales that can be obtained in a drop tower. Science data on combustion of heptane/hexadecane droplets slightly larger than about 1 mm will also be pursued using the NASA Lewis 5.1 sec Drop Tower, for example, with environments that will provide a more stringent test of Eq. (2). Theoretical studies will also be pursued. It is of great interest to continue the Marangoni flow studies; this will be done computationally as well as analytically. The computational model will be extended to include combustio, while analytical modeling will involve performing a nonlinear bifurcation analysis.

Acknowledgments

References

1   Shaw, B. D. and Aharon, I., NASA CP 10113, pp. 297-302 (1993).
2   Shaw, B. D., Aharon, I., Gage, J. W., Jenkins, A. J., and Kahoe, T. K., NASA CP 10174, pp. 95-102 (1995).
3   Beitelmal, A. and Shaw, B. D., AIAA paper 95-0144.
4   Haggard, J. B. and Kropp, J. L. AIAA paper 87-0576.
5   Dietrich, D. L., and Haggard, J. B., Jr., NASA CP 10113, pp. 317-323 (1992).
6   Chen, G. and Shaw, B. D., paper WSS 96F-063 presented at the 1996 Fall Meeting of the Western States Section of the Combustion Institute, University of Southern California.
7   Aharon, I., Ph.D. Thesis, Mechanical and Aeronautical Engineering Department, University of California, Davis (1996).
8   Shaw, B. D., and Williams, F. A., Int. J. Heat Mass Transfer 33: 301 (1990).
9   Mikami, M., Kono, M., Sato, J., Dietrich, D. L., Williams, F. A., Combust. Sci. Technol. 90: 111 (1993).
10 "Droplet Combustion Experiments In Spacelab," Dietrich, D. L., Haggard, J. B., Jr., Dryer, F. L., Nayagam, V., Shaw, B. D., and Williams, F. A., presented at the 26th International Symposium on Combustion, Naples, Italy (1996).
11 Wang, C. H., Liu, X. Q., and Law, C. K., Combustion and Flame 56: pp. 175-197 (1984).
12 Aharon, I. and Shaw, B. D., paper WSS 95F-226 presented at the 1995 Fall Meeting of the Western States Section of the Combustion Institute, Stanford, CA.
13 Aharon, I. and Shaw, B. D., Physics of Fluids 8: pp. 1820-1827 (1996).
14 Williams, F. A., Acta Astronautica. 12, 7/8, 547 (1985).
15 Niazmand, H., Shaw, B. D., Dwyer, H. A., and Aharon, I., Combustion Science and Technology 103: p. 219 (1995).
16 "Surface Tension Influences on Methanol Droplet Evaporation in the Presence of Water," Dwyer, H. A., Aharon, I., Shaw, B. D., and Niazmand, H., presented at the 26th International Symposium on Combustion, Naples, Italy (1996).
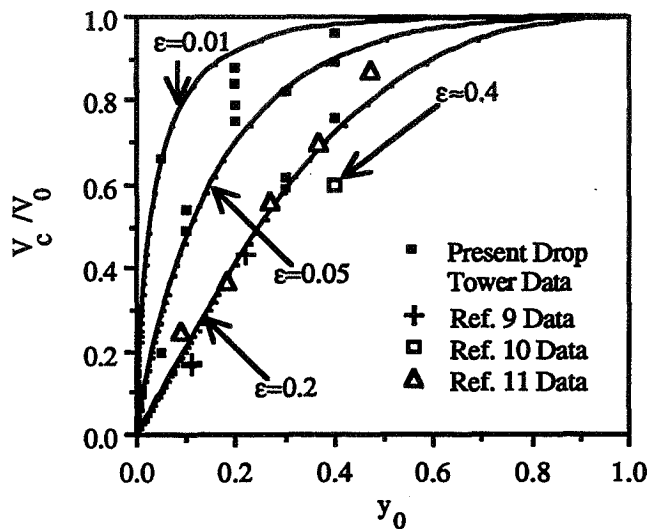
Fig. 1   Plot of V_c/V_0 vs y_0. The lines are plots of Eq. (1).
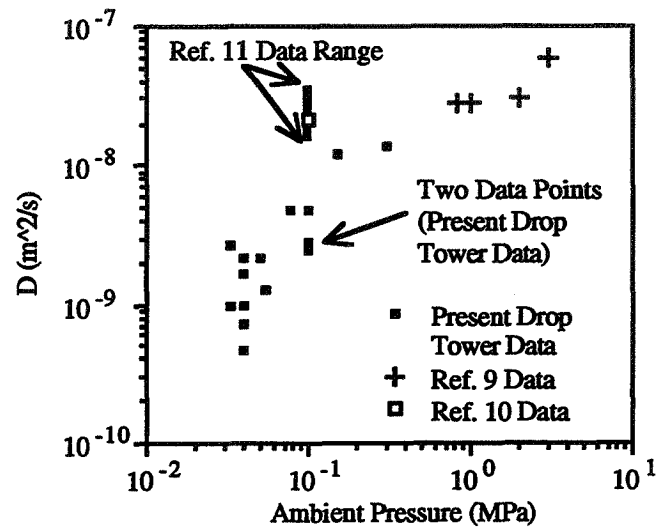

Fig. 2.   Calculated liquid species diffusivities in heptane/hexadecane droplets.
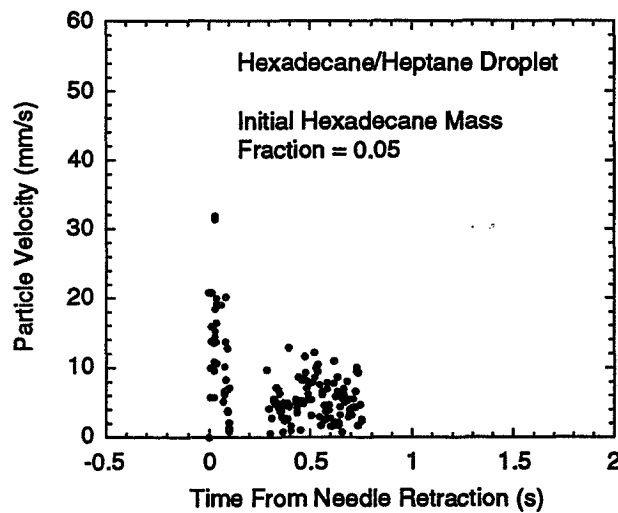

Fig. 3.   Tracer particle velocities (combustion in 1-atm air).
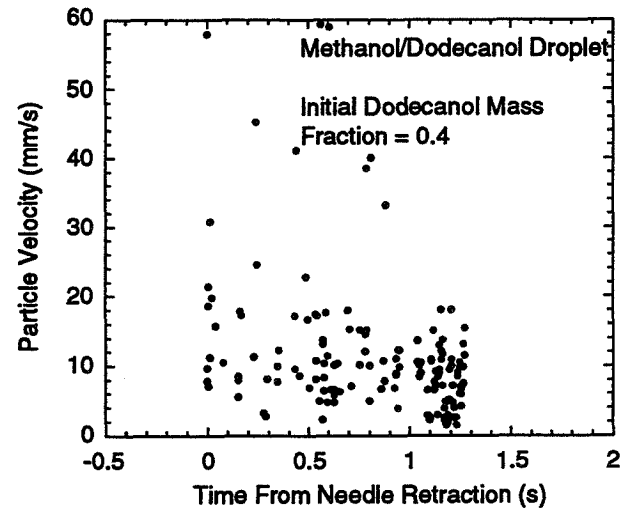

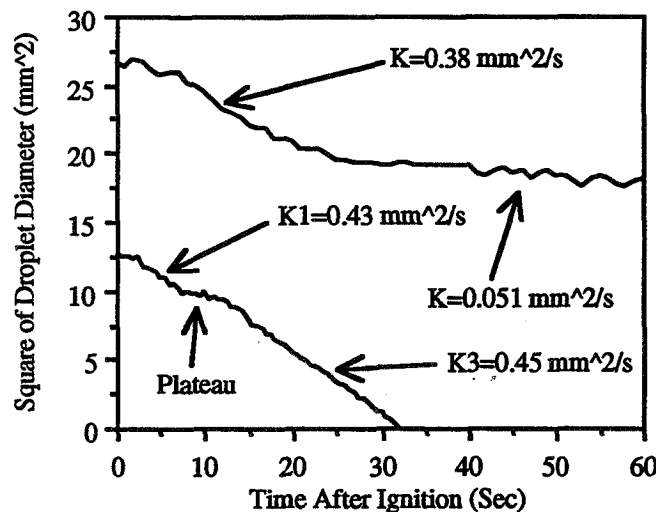Fig. 4.   Tracer particle velocities (combustion in 1-atm air).

Fig. 5.   Droplet size data for heptane/hexadecane droplets in the FSDC experiments. The initial hexadecane mass fraction was 0.4.
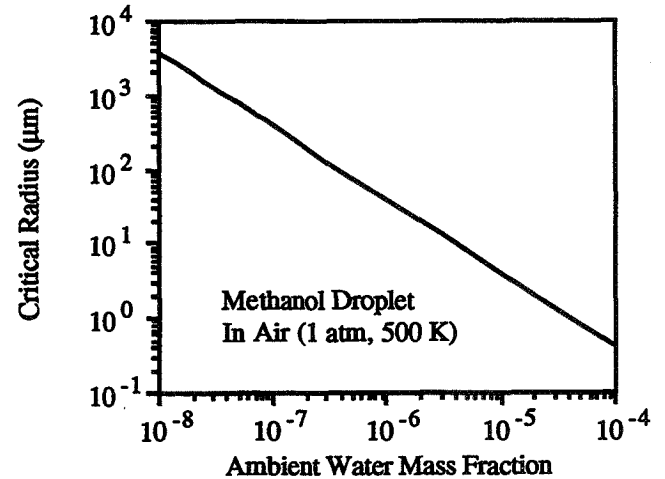

Fig. 6.   Critical radii for the onset of instability in methanol droplets gasifying in air.

478

COMBUSTION OF INTERACTING DROPLET ARRAYS IN A MICROGRAVITY ENVIRONMENT

DANIEL L. DIETRICH
NASA Lewis Research Center
Cleveland, Ohio

Peter M. Struk
Case Western Reserve University
Cleveland, Ohio

Kunihiro Kitano, Koji Ikeda and Senji Honma
Hokkaido National Industrial Institute
Hokkaido, Japan

Introduction

This research program involves the study of single droplets and linear arrays of droplets in weakly-buoyant and non-buoyant environments. The primary purpose of the single droplet work was to (1) provide a data base from which to compare droplet array results and (2) to correlate the effects of buoyancy on flame shape. Traditionally convective effects in droplet combustion are represented in terms of the Reynolds number, Re, for forced convection and the Grashof number, Gr, for natural convection. Typically, corrections to the burning rate constant for convective effects are written in terms of Re or Gr[1]. The Stefan velocity is not included in these correlations, even though from purely physical reasons, one would expect it to be important, especially at higher burning rates.

The flame distortion due to convective effects is less documented quantitatively. Kumagai and Isoda[2,3] do predict flame shape in natural and forced convective flow fields. Their focus, however, was to predict the actual flame dimensions. Law and co-workers[4-6] used reduced pressure, high oxidizer ambients to obtain spherical flames. This implies that buoyant flows were reduced at the low pressures, as indicated by a very small Grashof number. Ross et al.[7], however, using scaling arguments showed that reducing the pressure does not have a large effect on the magnitude of the buoyant velocity. Struk et al.[8] showed elongated flame shapes during simulated (porous sphere) droplet combustion. The elongation of the flames was due to residual gravity levels aboard the reduced gravity aircraft on which the experiments were conducted. These flame shapes, as well as some data from the literature[4] were interpreted based on a dimensionless grouping called the sphericity parameter, Sp. Sp is the ratio of a characteristic computed buoyant velocity to the Stefan velocity at the flame front.

The purpose of the droplet arrays work is to extend the database and theories that exist for single droplets into the regime where droplet interactions are important. The eventual goal being to use the results of this work as inputs to models on spray combustion where droplets seldom burn individually; instead the combustion history of a droplet is strongly influenced by the presence of the neighboring droplets. Recently, Annamali and Ryan[9] have summarized the current status of droplet array, cloud and spray combustion. A number of simplified theories [e.g. refs.10-14], and detailed numerical studies [e.g. ref.15] of droplet vaporization/combustion where multiple droplet effects are present are now available. These theories all neglect the effect of buoyancy. Experimentally, most studies to date suffer the effects of buoyancy. It is the dominant transport mechanism in the problem. Only the works of Law and co-workers[4,5] and more recently by Mikami et al.[16] were performed in an environment where buoyancy effects were small. Law and co-workers were limited to high oxygen index, low pressure ambient environments since there studies were conducted in normal gravity.

Experimental Apparatus

All of the experiments reported herein utilized fiber supported droplets. Typically, 125 or 140 μm fibers with small beads (< 400 μm) on the end supported the droplets, except for some experiments with 230 μm fibers (still with a 400 μm bead). Ignition was via heated electrical wires that were removed after ignition. In some of the experiments, the igniter wire was rapidly pulsed on and off at high current. This typically resulted in lower ignition times.

The data for the experiments are backlit views of the burning droplet to yield droplet size as a function of time and non-illuminated views of the flame. The flame view was either by color or black and white video cameras or 35 mm

SLR cameras. Because of the limited dynamic range of a video camera, using it to image the natural flame can yield deceiving results for flame size. For example, our results show that for a single heptane droplet, the very luminous yellow is surrounded by a thin blue flame. A typical video camera will not image both the yellow and the blue. To compensate for this, blue glass filters preceded the video cameras on many tests so that the entire flame could be adequately imaged.

The droplets are not spherical in shape, but elongated because of the presence of the supporting fiber. All of the droplet sizes reported herein are equivalent droplet sizes. The equivalent size is computed as either the cubic root of the product of the major diameter and the minor diameter squared, or the diameter of a sphere with the same projected area as that measured. The two methods yield very similar results except when the droplet becomes very close to the fiber size at the end of the burn. This period is neglected in the burning rate measurements reported herein. Flame size measurements are made from the outside edge of the visible flame.

Experiments were conducted at the NASA Lewis Research Center 2.2 second drop tower, the Japan Microgravity Center (JAMIC) 10 second drop tower and in normal gravity laboratories. The environmental conditions and gravity levels are such that the burning in the drop towers is free from buoyant effects.

<u>Single Droplet Combustion</u>
Traditionally, a Grashof number based on droplet diameter, Gr_D, as shown by equation (1) has been used to gauge the effect of buoyancy on a burning fuel droplet. Later, Struk defined a sphericity parameter, Sp, to describe the effect of buoyancy on flame shape[8]. They defined the sphericity parameter, shown in equation (2), as the ratio of buoyant velocity to blowing velocity (Stefan flow) at the flame. Besides using a much larger length scale (the flame) when compared with Gr_D, Sp incorporates the effect of mass burning rate (Stefan flow) which intuitively would have an effect on flame shape.

$$Gr_D = g\beta d_d^3 \left(\frac{P}{\bar{R}T_f\mu} \right)^2 \left[T_f - T_s \right] \quad (1); \qquad Sp = \frac{4\pi r_f^{5/2} P}{\dot{m}\bar{R}T_f} \left(g\beta \left[T_f - T_s \right] \right)^{1/2} \quad (2)$$

In these expressions, g is the acceleration due to gravity, β is the coefficient of volumetric expansion, P is the pressure, R the universal gas constant, T_f the flame temperature, μ is the viscosity, m is the burning rate of the fuel (computed from the experimental burning rate constant), and d_d and r_f are the droplet diameter and flame radius respectively. One would expect that if Sp was much less than one then spherical symmetry should prevail. Conversely, a departure from spherical symmetry would be expected as Sp approaches and becomes greater than one. The results[8] showed the expected trends, although the magnitude of Sp was somewhat larger than expected. For Sp slightly less than one ($\approx$ .6 and lower), a flame was observed to have a concentricity (radius ratio) within 25 percent of one. For values of Sp above one, the flame concentricity began diverging from unity. The aspect ratio, however, was within 10 percent of one for all Sp values computed (less than 11).

It was the purpose of this work to further test the validity and accuracy of Sp by observing near spherical flames in various ambient conditions in normal gravity. Additionally, the effect of Gr_D on flame shape was also investigated for comparison. To avoid initial transient effects and later fiber effects, Sp and Gr_D were computed for each test using the measured flame and droplet diameters near the midpoint of the burn. Only one datum was obtained for each droplet burn. Decane was the primary test fuel, with a smaller number of tests with methanol. All of the tests were at atmospheric to sub-atmospheric pressures. Ambient environments were oxygen/nitrogen and oxygen/helium systems. Oxygen mole fractions ranged from 0.18 to 0.60, with high mole fractions at very low pressures, or in helium diluted atmospheres. Figure 1 shows the burning rate constant as a function of Gr_D for this testing. The families of curves represent different pressures in the same ambient.

Except for the measured burning rate and pressure, the remaining property values were estimated[17-19]. The flame temperature for this analysis was computed using an expression[20] from classical droplet combustion theory. The droplet surface temperature was assumed to be the boiling temperature of the fuel at the appropriate pressure. Gas property values of $C_{P,G}$ and μ were evaluated at the mean value between the estimated flame temperature, T_f, and the droplet surface temperature, T_s. The specific heat at constant pressure, $C_{P,G}$, of the ambient mixture was estimated using the mass-average value of the mixture components. Finally, the Wilkes' approximation was used for estimating the dynamic viscosity, μ, of the mixture[9].

The flame shape was gauged by two parameters, radius ratio and aspect ratio[4]. The radius ratio is the ratio of the droplet center to the top edge of the flame to the droplet center to the bottom edge of the flame and describes the concentricity of the flame relative to the droplet. The aspect ratio is the ratio of visible flame height to flame width. For a spherically symmetric flame both the radius ratio and aspect ratio should tend to unity, and the deviation from unity is used as a gauge of how close the burning is to spherically symmetric.

Figure 2 shows the relationship between Sp and both radius ratio and aspect ratio. For a given fuel and ambient composition, reductions in Sp come from decreases in the ambient pressure. There are also four reduced gravity points, two from the JAMIC facility (methanol and decane) and two from DC-9 aircraft testing[8], in Figure 2. The sphericity parameter ranges through 3 orders of magnitude from roughly 0.1 to 100. As Sp increases, both the radius ratio and aspect ratio increase, which means that the departure from spherical symmetry is increasing.

Figure 2 shows only a Sp of less than 0.4 produces a radius ratio within 40% of unity. For some select cases, larger values of Sp were observed to have a similar radius ratios. Aspect ratios near unity, however, were much easier to achieve. For values of Sp less than 11, aspect ratios were within 25% of one for almost all cases tested. These observation should be noted as it demonstrates the difficulty in achieving a concentric spherical flame around a droplet in normal gravity and even some reduced gravity conditions. Additionally, the data demonstrates that many flames despite appearing quite spherical in terms of aspect ratio are in fact influenced by buoyancy in such a manner which shifts the center of the flame relative to the center of the droplet. The scatter of Figure 2 is largely attributed to uncertainty in flame temperature estimates. This estimate produces unreasonably high flame temperatures, especially for cases with high ambient oxidizer concentrations. Specifically, the classical theory neglects radiative loss, which could be significant for the high temperature flames present in high oxidizer tests.

Figure 3 shows the effect of Grashof number based on droplet diameter, Gr_D, on flame radius ratio and aspect ratio. Trends similar to those observed in Figure 2 are seen in Figure 3 although more scatter is observed especially at the larger values of Gr_D. While the figures resemble each other qualitatively, a large decrease in magnitude is observed (and expected) from Sp to Gr_D. The several order of magnitude change in Gr_D when compared to Sp is primarily due to the changing length scale (from flame to droplet dimensions) which has a cubic dependence in Gr_D.

From a physical standpoint, Grashof number based on droplet dimensions has little physical meaning in describing flame shape. The Grashof number is defined as the ratio of buoyant to viscous forces. The observed flame shape which is several times larger than the droplet suggests that an appropriate length scale in the Grashof number should be larger than the droplet diameter. Additionally, the influence of viscosity on flame shape is not entirely clear. In light of the fact that the fluid viscosity does not significantly change (perhaps a factor of 2 variation) during different test conditions, a pure interpretation of Figure 3 suggests that the large variation of Gr_D must occur due to changing buoyant strength. Examination of equation (1) above reveals that the only significantly changing parameter in Gr_D is the pressure (and gravity in the two reduced gravity cases). As mentioned in the introduction, the magnitude of the buoyant flow is not significantly changed by changes in ambient pressure. Thus, the Grashof number based on droplet dimensions captures only a small portion of the relevant physics that are necessary in describing flame shape.

If instead of the Gr_D, we consider $Sc\sqrt{Gr_F}$, where Gr_F is the Grashof number based on flame dimensions, then another interpretation can be made. This new quantity is then the ratio of buoyant to diffusion velocities at the flame front. As the flame standoff distance increases, Stefan flow rapidly decays and the importance of diffusion as the dominant transport mode increases. Diffusion is expected to become more dominant (than the Stefan flow) in cases where the flame is very far from the droplet such as those observed previously in reduced gravity where the ratio of flame to droplet diameter approached 10^8. Thus, we believe that near spherical flames can be described by Sp or $Sc\sqrt{Gr_F}$ or some combination thereof. In the limit of small flame standoff distances, buoyancy competes with Stefan flow in defining the flame shape. As the flame moves further away from the droplet, diffusion replaces Stefan flow as the mode of fuel transport to the flame. A more complete discussion of the above ideas is available in Struk et al.[13]

Droplet Array Combustion
Linear droplet arrays have been burned in both normal and microgravity environments. The microgravity combustion work included three droplet arrays of three fuels: n-heptane, n-decane and methanol. The majority of the experiments were in an air ambient at atmospheric pressure. There was some testing in higher pressure ambients. The primary variables were the inter-droplet spacing and fuel type. The data are presented in terms of a burning rate constant. For droplet array experiments, the burning behavior does not typically follow the d-square law.

481

Nevertheless, we still use a burning rate constant which is averaged over the lifetime of the droplet. In this computation, the later stages of burning are ignored since fiber effects could be important.

Figure 3 shows the droplet history for a three droplet array of n-heptane with a spacing between the droplets of 6 mm. The initial droplet size for this case was 1.1 mm yielding an L/D_o of 5.5. The center droplet of the array shows a slightly smaller burning rate (k = 0.53 mm^2/s) than the two edge droplets (k = 0.56, 0.57 mm^2/s). This trend is logical if one considers that oxygen transport to the center droplet is reduced due to the presence of the two outer droplets. All three droplets have smaller burning rates than that for a single droplet of n-heptane measured to be 0.65 mm^2/s.

Figure 4 shows the burning rate constant of the center droplet of a three droplet array as a function of initial non-dimensional separation distance (L/Do) for both n-heptane and methanol. This figure shows that for n-heptane, within experimental error, the burning lifetime decreases gradually and monotonically as a function of L/D_o. These results disagree slightly with the work of Mikami[16]. The authors in that work showed that, for a two-droplet array, that droplet lifetime was nearly independent (decreased then increased slightly) of L/D_o from infinite (single droplet combustion) to L/D_o of 6. The burn time then increased significantly with further reductions in L/D_o. We note however, that at $L/D_o \sim 4$ (the limits in both studies), the expected increase in droplet lifetime (approximately 20%) is in agreement with the value in the present study. We note that the results are not directly comparable since Mikami[16] studied a two-droplet array and the present study is of a three-droplet array. We should note that although not shown, the average burning rate constant for decane also decreases monotonically with L/D_o (L/D_o between 4 and 20).

Since methanol has a fuel bound oxygen atom, its flame standoff distance is smaller than that for pure alkane fuels. If the droplet lifetime increases as a result of competition for oxygen, then methanol should experience a smaller increase in droplet lifetime (or decrease in average burning rate constant) for a given initial separation distance. This is in fact the case as evidenced in Figure 4. At a given non-dimensional separation distance, L/D_o, the methanol experiences less of a decrease in the average burning rate constant. In addition, whereas the burning lifetime of n-heptane was monotonic with L/D_o, the lifetime of a methanol droplet reached a minimum at $L/D_o = 17$. The actual minimum lies somewhere between $L/D_o = 15$ and ∞, but there is insufficient data to identify it exactly. The magnitude of k/k_o at this peak is not that much greater than one. For reference, the value of the single droplet burning rate constant, $k_o = 0.59$ mm^2/s, is identical to that of recent work at the Lewis Research Center 2.2 second drop tower[22].

The trend observed above for methanol is not unusual for droplet arrays burning in a normal gravity environment. Figure 6 (shown out of order) shows results for n-decane burning in air at a pressure of 0.25 atm in normal gravity. Again, the normalized burning rate (by single droplet value) is shown as a function of normalized separation distance. The burning rate reaches a maximum at $L/Do \sim 5$. This is attributable to the intensification of the buoyant flow as the droplet separation distance decreases. This is consistent with the one atm. results of Mikami[16] with n-heptane.

References

1. Law, C.K. and Williams, F.A. (1972) "Kinetics and Convection in the Combustion of Alkane Droplets," *Combustion and Flame* **19**, 393.
2. Isoda, H. and Kumagai, S. "New Aspects of Droplet Combustion," (1959) *Seventh Symposium (International) on Combustion* , Butterworths Scientific Publications, 523.
3. Kumagai, S. and Isoda, H. "Combustion of Fuel Droplets in a Falling Chamber," (1957) *Sixth Symposium (International) on Combustion* , Reinhold Publishing Corp., 726 .
4. Miyasaka, K. and Law, C.K. "Combustion of Strongly-Interacting Linear Droplet Arrays," (1981) *Eighteenth Symposium (International) on Combustion / The Combustion Institute*, 283.
5. Xiong, T.Y., Law, C.K. and Miyasaka, K. (1984) "Interactive Vaporization and Combustion of Binary Droplet Systems," *Twentieth Symposium (International) on Combustion/The Combustion Institute*, 1781.
6. Chung, S.H. and Law, C.K. (1986) "An Experimental Study of Droplet Extinction in the Absence of External Convection," *Combustion and Flame* **64**, 237 .
7. Ross, H.D., Dietrich, D.L., and T'ien, J.S. (1990) "Observations of Candle Flames in Low Pressure and Low Gravity," Fall Technical Meeting of the Eastern States Section of The Combustion Institute, Orlando, Florida.
8. Struk, P.M., Dietrich, D.L., T'ien, J.S. (1996) "Large Droplet Combustion Experiment Using Porous Spheres Conducted in Reduced Gravity Aboard an Aircraft: Extinction and the Effects of G-jitter," *Microgravity Science and Technology* , in press.

9. Annamalai, K. and W. Ryan. (1992) "Interactive Processes in Gasification and Combustion. Part I: Liquid Drop Arrays and Clouds," *Progress in Energy and Combustion Science* **18**, 221.

10. Brzustowski, T.A., E.M. Twardus, S. Wojcicki and A. Sobiesiak. (1979) "Interaction of Two Burning Fuel Droplets of Arbitrary Size," *AIAA Journal* **17**, No. 11, 1234.

11. Labowsky, M. (1980) "Calculation of the Burning Rates of Interacting Fuel Droplets," *Combustion Science and Technology* **22**, 217.

12. Marberry, M., A.K. Ray and K. Leung. (1984) "Effect of Multiple Particle Interactions on Burning Droplets," *Combustion and Flame* **57**, 237.

13. Samson, R., D. Bedeaux and J.M. Deutch. (1978) "A Simple Model of Fuel Spray Burning II. Linear Droplet Streams," *Combustion and Flame* **31**, 223.

14. Umemura, A. (1994) "Interactive Droplet Vaporization and Combustion: Approach from Asymptotics," *Progress in Energy and Combustion Science* **20**, 325.

15. Dunn-Rankin, D., Sirignano, W.A., Rangel, R.H. and Orme, M.E. (1995) "Droplet Arrays and Streams," *Mechanics and Combustion of Droplets and Sprays*, edited by H.H. Chiu and N. Chigier, Begell House, New York, 1995, 74.

16. Mikami, M., Kato, H., Sato, J. and Kono, M. (1995) "Interactive Combustion of Two Droplets in Microgravity," *Twenty-Fifth Symposium (International) on Combustion / The Combustion Institute*, 423.

17. Reid, R.C., Prausnitz, J.M., and Sherwood, T.K. (1977) *The Properties of Gases & Liquids*, 3rd ed., McGraw-Hill, New York.

18. Touloukian, Y.S., Makita, T. (1970) "Specific Heat: Nonmetallic Liquids and Gasses," *Thermophysical Properties of Matter* **6**, IFI/Plenum, New York

19. Touloukian, Y.S., Liley, P.E., Saxena, S.C., (1970) "Thermal Conductivity: Nonmetallic Liquids and Gasses," *Thermophysical Properties of Matter* **3**, IFI/Plenum, New York.

20. Williams, F.A., (1985) *Combustion Theory*, 2nd ed., CA: Benjamin/Cummings, Menlo Park, California.

21. Struk, P.M., T'ien, J.S. and Dietrich, D.L., (1997) "Experimental Studies of Flame Shape Around Droplets in Different Buoyant Environments," AIAA-97-1001, 35th Aerospace Sciences Meeting, Reno, Nevada, 1987.

22. Marchese, A.J., Dryer, F.L., Colantonio, R. and Nayagam, V. (1997) "Microgravity Combustion of Methanol and Methanol/Water Droplets: Drop Tower Experiments and Model Predictions," *Twenty-Sixth Symposium (International) on Combustion / The Combustion Institute*, to appear.
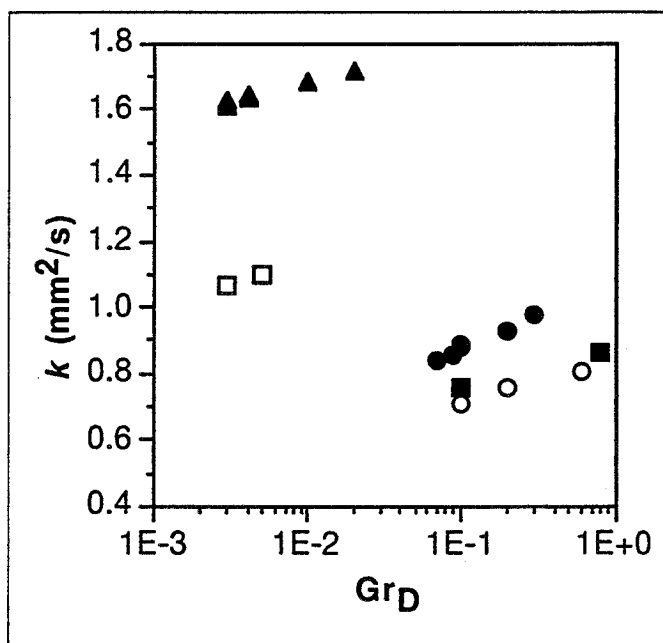
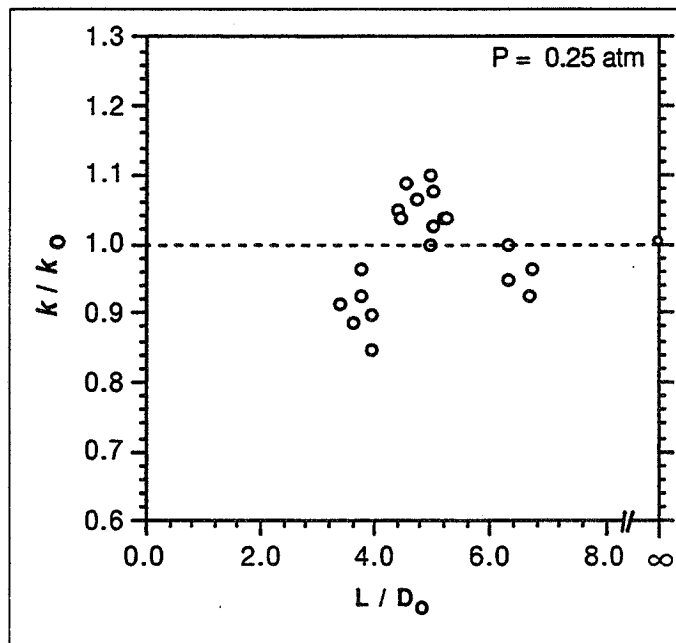Figure 1. Average burning rate constant as a function of Grashof number for normal gravity single droplet testing.

Figure 6. Normalized average burning rate constant as as a function of normalized droplet separation for n-decane in air at 0.25 atm pressure.
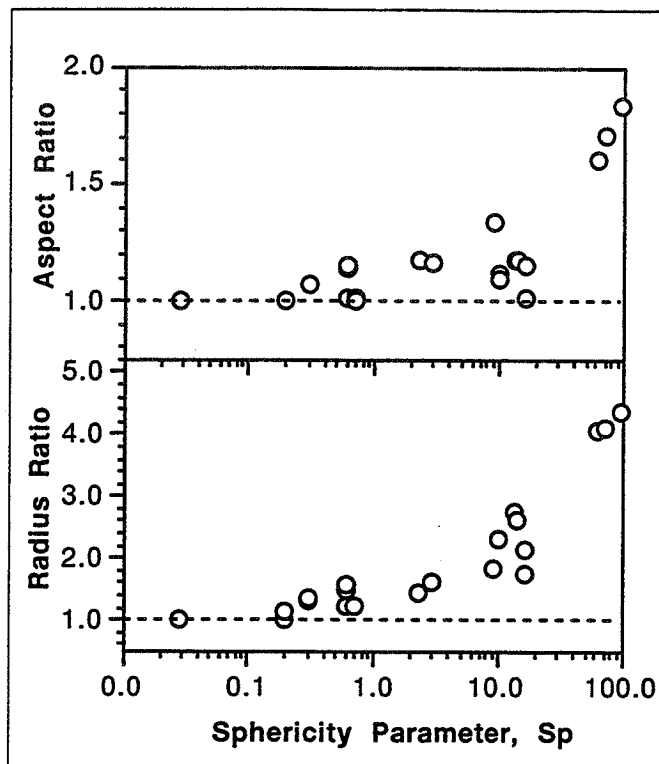
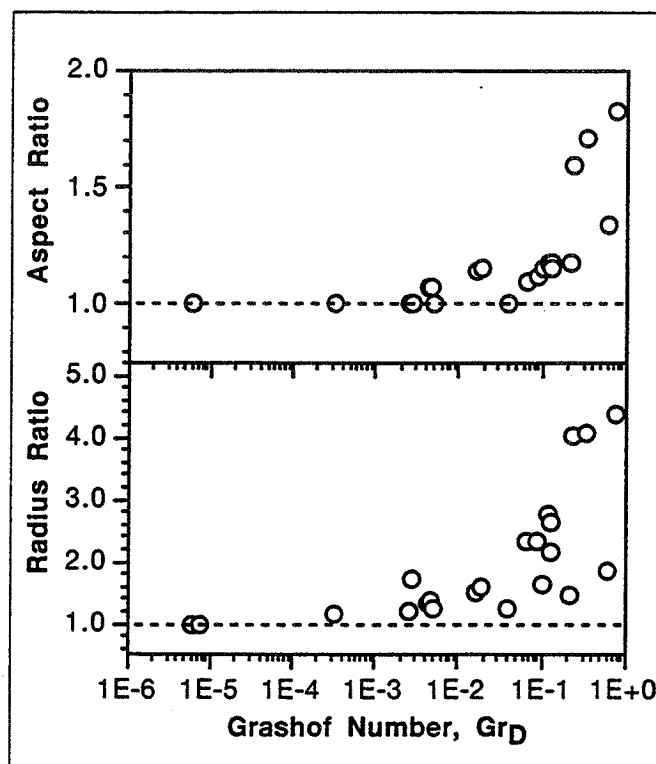Figure 2. Flame radius ratio and aspect ratio as a function of sphericity parameter.

Figure 3. Flame radius ratio and aspect ratio as a function of Grashof number (based on droplet diameter).
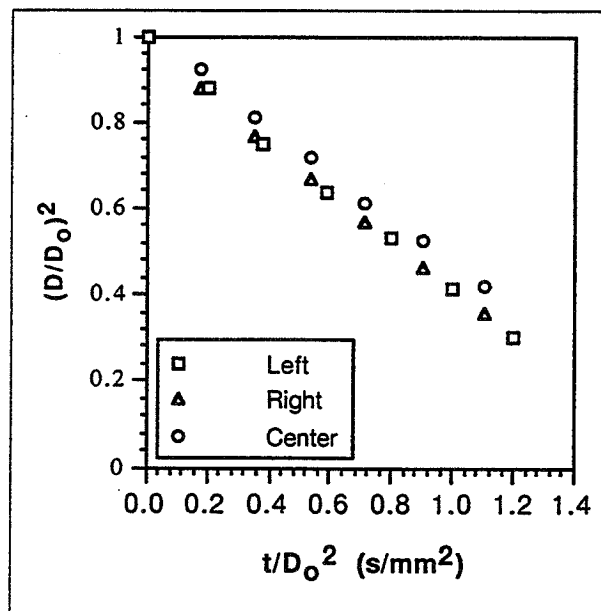

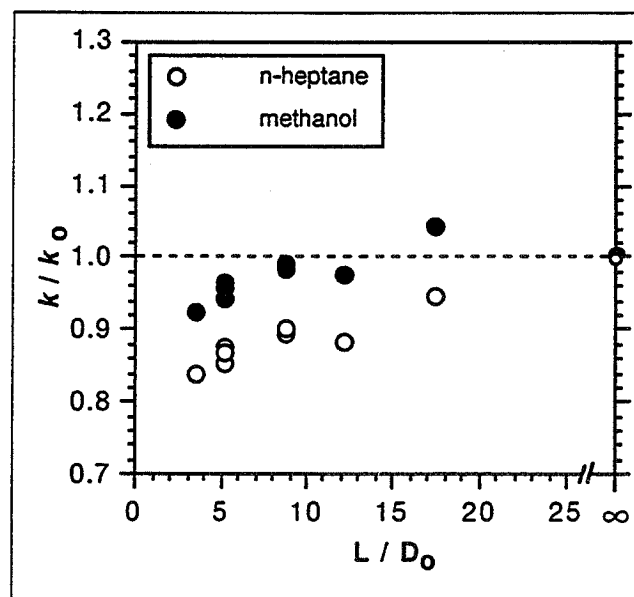Figure 4. Burning history for each droplet of a three-droplet array of n-heptane with $L/D_o = 5.5$

Figure 5. Average burning rate constant as a function that for single droplet, k_o) by non-dimensional droplet separation distance for methanol.

FORMATION AND COMBUSTION OF
UNCONFINED DROP CLUSTERS IN MICROGRAVITY*

S. Liu, G. Craig, Y. Zhang, and G. A. RUFF
Mechanical Engineering and Mechanics Department
Drexel University
Philadelphia, Pennsylvania 19104

Introduction

Motivation Single-drop and droplet array studies have become common methods to isolate and investigate the effects of many of the complexities that enter into the drop combustion process. Microgravity environments are required to allow larger drops to be studied while minimizing or eliminating the confounding effects of buoyancy.[1-6] Based on the results from current isolated drop, drop array, and spray studies funded through the Microgravity Science and Applications Division, it has become clear that even with the effects of buoyancy removed, the extrapolation of results from droplet array studies to spray flames is difficult.[5] The problem occurs because even the simplest spray systems introduce complexities of multi-disperse drop sizes and drop-drop interactions, coupled with more complicated fluid dynamics.

Not only do these features make the interpretation of experimental data difficult, they also make the problem very difficult to analyze computationally. Group combustion models, in which the interaction between droplets is treated on a statistical manner, have become a popular method to investigate the behavior of large numbers of interacting droplets, particularly through the work of Ryan et al.[7] and Bellan and co-workers.[8-12] While these models idealize the actual spray systems to a point where they can be treated computationally, the experimental analogy to these models is difficult to achieve because it requires the formation and combustion of drop clusters without the effects of buoyancy. Therefore, even though these models have provided useful and insightful information, the verification of the results by direct comparison with experimental data is still lacking.

These two observations form the motivation for this work. Direct experimental observations and measurements in well-defined droplet clusters would fill a large gap in our current understanding of droplet and spray combustion. This will provide a more direct link between droplet array studies and those performed using full combusting spray systems. It will also provide unique experimental data for the calibration, verification, and improvement of group combustion models for both liquid and solid particles. The specific objectives of this project are identified in the following section.

Objectives The overall objective of the proposed research is to study the combustion of well-characterized drop clusters. The formation of the clusters will be precisely controlled using an acoustic levitation system so that very dilute, as well as very dense clusters can be created and stabilized before combustion is begun. Therefore, this experiment will allow the complete spectrum of droplet interactions during combustion to be observed and quantified. The specific objectives of this study include:

(1)   design and fabrication of a unique droplet combustion experiment using acoustic levitation to stabilize a droplet cluster prior to combustion,
(2)   investigate the droplet combustion in the individual particle combustion, group combustion, and sheath combustion regimes by varying the number of droplets, droplet size, and cluster diameter,
(3)   investigate the effect of drop size distribution, droplet composition, and continuous-phase oxygen concentration on cluster combustion.

This data will reduce the extrapolation required to extend results of droplet array studies to those obtained spray combustion systems. The data will also provide the needed experimental verification of group combustion models currently being applied to complex flow situations.

Background

The experimental and computational tools used to study the combustion of interacting, combusting drops has been improving since the 1950's. Isolated drop studies have been extremely useful for quantifying the interactions between the complex fluid mechanics and chemical kinetics that occur in the combustion of (i) multi-component drops,[13] (ii) drops in a high pressure environment,[14,15] or (iii) drops in a high turbulent intensity environment.[16] Extrapolation of these experimental results to the more complex interactions that occur in spray flames requires knowledge of how drop-drop interactions modify isolated drop

---

behavior. Experimental investigations of these phenomena have generally utilized two-dimensional droplet arrays and parallel streams of droplets.[17,18]

Much of this past work can be summarized by stating that burning time generally increases as droplet spacing decreases because the closer the drops are to each other, the more they compete with their neighbors for oxygen. At a drop spacing of 2 diameters, the burning time has been observed to increase by approximately a factor of two[17] indicating that the D^2 burning law does not rigorously apply for interacting drops. Based on the body of experimental work in the literature and in reviews on the subject,[19,20] the inter-droplet spacings for which drop interactions first become important for vaporization and combustion generally falls in the range of 10 - 25 droplet diameters. The range is quoted because the results depend to some extent on the specific experimental configuration investigated. At larger inter-droplet spacings, it has been concluded that there should be little, if any, interaction and isolated drop combustion results should be applicable. Even though much of this research was conducted using relatively small drops, the effects of buoyancy were often significant and quickly dominated the transport process. To supplement these experimental results, detailed numerical simulations of droplet interaction and combustion[21,22] have been conducted and generally support the conclusions of the experimental results.

Mirroring the investigations conducted at 1-g, combustion research is being conducted using isolated droplets, droplet arrays, and spray flames to eliminate the effects of buoyancy. Of course, the focus of the studies listed differ and emphasize various aspects of drop combustion. In particular, Dietrich[1] recently reported on current investigations to study the combustion of interacting 1- and 2-D droplet arrays. Arrays consisting of up to three droplets have been investigated using multidirectional viewing to observe transient drop size and flame position. As stated in the motivation of the current project, even in microgravity, it has proven to be difficult to apply the results of single droplet and droplet array studies to explain spray combustion measurements and observations.[5] The objective of the current experiment is to study droplet interactions for a larger number of drops in an unconfined cluster.

Experimental Approach

The unique feature of the current work is that a well-characterized drop cluster will be formed in a resonant acoustic field prior to the start of the combustion experiment in microgravity. Figure 1 shows a sketch of the experimental apparatus being designed for tests to be conducted in the 2.2-Second Drop Tower at the NASA Lewis Research Center. It consists of an acoustic levitator assembly including piezoelectric transducers, a stepped horn, resonator, and cylindrical field tube. Two droplet-on-demand drop generators are positioned so that drops can be placed in a cluster formed at the one of the nodes in the resonant acoustic field. the Using these drop generators, the number and size of drops placed in the cluster can be accurately controlled. An electrical charge will be placed on the drops to prevent coalescence during the formation of the cluster. The size and shape of the cluster can be controlled by proper design of the acoustic resonance chamber and control of the frequency and power at which it is driven. Because the presence of the acoustic field would greatly influence drop combustion, the field will be turned off at the start of the microgravity period. The resonance chamber and drop generators will be retracted from the cluster so that they do not interfere with the combustion process, initiated using a coiled hot-wire. Progress on the design and construction of this apparatus is discussed in the next section. However, to achieve the objectives of this project, this experimental apparatus must produce an appropriate numbers of drops in a well-defined volume. Defining these conditions and designing the apparatus to obtain them is discussed in the following paragraph.

The combustion of clusters of droplets can be characterized by three general regimes: the Individual Particle Combustion (IPC) regime, where drops are relatively far apart and burn as isolated drops; the group combustion (GC) regime, where droplets compete for oxygen and droplet interaction is important; and the sheath combustion (SC) regime where the drops are very close together and burn as a single drop having the same radius as the drop cluster. These regimes are often described in terms of a group combustion number, G, defined as

$$G = \frac{\text{Mass transfer between the gas and droplets in the cloud}}{\text{Mass transfer between the ambience and the cloud surface}} \tag{1}$$

Fortunately, this can be evaluated and written in equation form as

$$G = 3 \, \sigma \, R_c^{2}/a^{2} \tag{2}$$

where σ is the fuel volume fraction, R_c is the radius of the drop cluster, and a is the radius of the drops. It is useful to interpret these G-numbers in terms of the normalized interdroplet spacing (l / d), where d is the diameter of the droplets in the cluster. The fuel volume fraction can be calculated as $\sigma = (4\pi/3) \, n \, a^3$, where n is the number density of drops. The number of drops in a cluster, N, is given by

$$N = (4\pi/3)\, n\, R_c^{\,3} \tag{3}$$

Equations (2) and (3) can be combined to yield an expression for the number of drops, N, and a function of cluster diameter and G.

$$N = \frac{G}{3}\frac{D_c}{d} \tag{4}$$

This equation is particularly relevant to this research because the diameter of the cluster will be determined by the design of the acoustic levitator. Based on a resonant frequency of 20 kHz, the diameter of the drop cluster will be approximately 8.5 mm. Figure 2 shows the number of drops as a function of drop size for this cluster diameter calculated using Eq. (4). Lines of constant group combustion number are also shown. The boundaries separating these regimes have been postulated for both liquid droplets and char particles[20] but are admittedly somewhat vague because of the lack of sufficient experimental data. For liquid drops, G < 0.1 is the IPC regime, while G > 100 is generally considered to be the SC regime. Intermediate values of G are classified as a group combustion regime. Note that the GC regime extends over several orders of magnitude of G and undoubtedly there are rather large transition regions between these regimes. Recall that previous experimental work discussed in the Background section indicated that drop-drop interactions became important for drop spacings on the order of 10 - 25 drop diameters. Lines of l/d = 10 and 25 can be drawn on Fig. 2 is a rectangular drop arrangement is assumed. (The conclusions depend little on the arrangement of the drops in the cluster but it does enter into the calculation.) If we require at least 10 drops are required to define a "cluster," values of G between 0.1 and 10 can be obtained by varying the drop size from less than 100 microns to several thousand microns. A practical limit for the maximum number of drops that can be produced and levitated at a time is approximately 50 depending, of course, on their diameter. This value is estimated from the work of Tian and Apfel[23] and Zhuyou et al.[24] who have levitated multiple drops in an acoustic field. With this limit on the maximum number of drops in the cluster, drop spacings of between 10 to 25 can be obtained by changing the drop size from approximately 100 - 400 microns. This is well within the capability of the drop generators being designed for this experiment. If two drop generators are used and each can produce drops at a rate of at least one drop every 5 sec, a cluster of 50 drops can be produced in about 2 minutes. This appears reasonable for drop tower operation. Another feature evident from this figure is that the same group combustion number can be obtained at a range of drop sizes and nondimensional spacings. Therefore, this experiment provides to opportunity to investigate the scaling of group combustion phenomena using these parameters.

Instrumentation The diagnostic capability to be incorporated into the experimental package includes multiview imaging to view the motion of the droplets and to characterize the droplet cluster before the start of the experiment. Continuous-phase temperature histories in the drop cluster will also be obtained using micro-thermocouples suspended across the cluster. Laser-induced fluoresence (LIF) will also be applied to observe the position of the flame front. As this experimental facility is developed, many of the other diagnostics being developed in the NASA Microgravity Combustion program can be applied. For example, it will be useful to measure instantaneous droplet temperature using liquid phase thermometry and concentrations of various combustion species using line absorption techniques. The optical access to be provided in the proposed facility will allow many of these to be applied as needed.

Test Conditions Initially, droplet clusters will be formed using n-decane, heptane, and methanol, as many of the droplet array and group combustion studies have done. This will allow the droplet burning rates obtained from this research to be directly compared with results of isolated droplet and droplet array studies. The position and movement of the flame front will provide some of the first experimental data for comparison with group combustion models obtained using large numbers of drops. Data will be obtained as a function of group combustion number, drop size, number of drops, drop size distribution, and ambient oxygen concentration. Several tests are also planned in which drops will be formed with binary fuels composed of heptane/methanol, heptane/ethanol, or heptane/hexadecane to experimentally investigate the effect of fuel volatility on cluster combustion and help define future research.

Results To Date

Funding for this project began in June 1996 so the work completed to date has focused on the design and construction of the drop generation and acoustic levitation systems. This section describes the status of the work in each of these areas.

Drop Generation System The drop production requirements of the current research include the ability to produce a precise number of drops having a diameter of between 100 - 1000 microns. If drop sizes become much greater than 1000 microns, they will flatten significantly in the acoustic field producing rather large oscillations when the field is turned off. It is also advantageous to produce these drops without introducing a probe into the acoustic field or the existing cluster of drops. An aerodynamic droplet-on-demand generation mechanism, similar to that used by Takahashi et al.,[25] has been designed and is undergoing testing and calibration. A small syringe pump was constructed using a 3 mm diam syringe to accurately deliver the

proper amount of liquid to the capillary tip. The pump is driven using a piezoelectric screw drive, typically used to position optics. The accuracy of this device allows movement of the plunger as small as 30 nm while delivering a force of approximately 20 N. Drop sizes between 100 and 1000 microns can be produced using capillary tubes having diameters as small as 85 microns with this apparatus. Once the required amount of fluid is delivered to the capillary tip, it is detached by opening a solenoid valve and allowing a jet of air ($\Delta p < 0.3$ psi) to flow along the capillary and detach the drop from the tip. The operation of the entire system is computer controlled so that a specific size and number of drops can be produced as rapidly as possible. Calibration of the drop generator is required so that the drop size can be accurately controlled by specifying the displacement of the syringe. It is planned to use two of these devices in the experimental package to increase the drop size range that can be produced and decrease the time required to form the cluster. To prevent coalescence and collision of the drops while the cluster is being formed, a small electrostatic charge will be placed on the droplets by subjecting them to a low intensity electric field as they detach from the capillary.

<u>Acoustic Levitator</u> Detailed calculations verifying the frequency, power, and size requirements for the acoustic levitator have been performed and the design completed. Based on operational and power limitations, the acoustic levitator will be driven at a frequency of approximately 20 kHz, although this frequency can be varied in the current design. Using an off-the-shelf acoustic driver, we have verified the operating principle of the confined acoustic field by successfully levitating small styrofoam balls inside a cylindrical chamber, similar to the configuration of our experiment. A sketch of the acoustic levitator being fabricated is shown in Fig. 1 as installed in the experimental apparatus. The levitator consists of two piezoelectric transducers in a sandwich configuration between front and rear transmitter blocks. A titanium stepped horn is attached to the transmitter to amplify the transducer displacement and minimize the power required to produce the acoustic field. The tip of the horn in 30-mm-diam and the cylindrical resonance tube has a diameter of 35 mm. These dimensions were selected to produce an acoustic pressure well (approximately 8.5 mm high by 11 mm in diameter) while exciting the (0,1) mode to be used for lateral positioning of the drops. The signal from a waveform generator, amplified up to 400 W, drives the transducers. The state of the acoustic field in the levitator will be monitored using a microphone. A computer will monitor the output from the microphone and appropriately adjust the frequency output by waveform generator to maintain a resonance condition to account for changes in temperature during the formation of the cluster.

<u>Summary</u>

The principle of operation of the acoustic levitator and drop generator has been proven in our lab and these devices are being fabricated. Detailed testing and evaluation will begin as they are completed. The next major step will be to combine the drop generator and acoustic levitator components into a single system capable of forming drop clusters in a resonant acoustic field. Combustion experiments will be performed at 1-g to establish procedures to be used during drop tower testing, verify diagnostic techniques, and obtain baseline data to compare with those data obtained at reduced gravity. The drop tower tests are currently scheduled to be conducted in the second half of year three.

<u>References</u>

1. Dietrich, D. L., "Combustion of Interacting Droplet Arrays in a Microgravity Environment," Third International Microgravity Combustion Workshop," Cleveland, Ohio, April 11-13, 1995.
2. Shaw, B. D., Aharon, I., Gage, J. W., Jenkins, A. J. and Kahoe, T. J., "Combustion of Two-Component Miscible Droplets in Reduced Gravity," Third International Microgravity Combustion Workshop," Cleveland, Ohio, April 11-13, 1995.
3. Kono, M., "Japan's Research on Droplet and Droplet Array Combustion," Third International Microgravity Combustion Workshop," Cleveland, Ohio, April 11-13, 1995.
4. Sato, J., "Japan's Research on Particle Clouds and Sprays," Third International Microgravity Combustion Workshop," Cleveland, Ohio, April 11-13, 1995.
5. Gomez, A. and Chen, G., "Spray Combustion at Normal and Reduced Gravity in Counter-flow and Co-Flow Configurations," Third International Microgravity Combustion Workshop," Cleveland, Ohio, April 11-13, 1995.
6. Chauveau, C. and Gökalp, I., "High Pressure Droplet Burning Experiments in Reduced Gravity," Third International Microgravity Combustion Workshop," Cleveland, Ohio, April 11-13, 1995.
7. Ryan, W., Annamalai, K, and Caton, J., "Relation Between Group Combustion and Drop Array Studies," *Combustion and Flame* **80**, pp. 313-321, 1990.
8. Bellan, J. and Cuffel, R., "A Theory of Nondilute Spray Evaporation Based Upon Multiple Drop Interactions," *Combustion and Flame* **51**, pp. 51-67, 1983.
9. Bellan, J. and Harstad, K. "The Details of the Convective Evaporation of Dense and Dilute Clusters of Drops," *Int. J. Heat Mass Transfer* **30**, pp. 1083-1093, 1987.
10. Bellan, J. and Harstad, K., "Turbulence Effects During Evaporation of Drops in Clusters," *Int. J. Heat Mass Transfer* **31**, No. 8, pp. 1655-1668, 1988.

11. Bellan, J. and Harstad, K., "Evaporation, Ignition, and Combustion of Nondilute Clusters of Drops," *Combustion and Flame* **79**, pp. 272-286, 1990.

12. Bellan, J. and Harstad, K., "Steady Injection of Identical Clusters of Evaporating Drops Embedded in Jet Vortices," *Atomization and Sprays* **5**, pp. 1-16, 1995.

13. Law, C. K., "Recent Advances in Multicomponent and Propellant Droplet Vaporization and Combustion," ASME Paper No. 86-WA/HT-14, presented at the Winter Annual Meeting, Anaheim, California, December 7-12, 1986.

14. Hartfield, J. P. and Farrel, P. V., "Droplet Evaporation in High Pressure Gas," *J. Heat Transfer* **115**, pp. 699-706, 1993.

15. Curtis, E. W. and Farrel, P. V., "A Numerical Study of High-Pressure Droplet Vaporization," *Combustion and Flame* **90**, pp. 85-102, 1992.

16. Gökalp, I., Chauveau, C., Simon, O., and Chesneau, X., "Mass Transfer from Liquid Fuel Droplets in Turbulent Flow," *Combustion and Flame* **89**, pp. 286-298, 1992.

17. Sangiovanni, J. J. and Labowsky, M., "Burning Times of Linear Fuel Droplets Arrays: A Comparison of Experiment and Theory," *Combustion and Flame* **47**, pp. 15-30, 1982.

18. Queiroz, M. and Yao, S. C., "Experimental Exploration of the Thermal Structure of an Array of Burning Droplet Streams," *Combustion and Flame* **82**, pp. 346-360, 1990.

19. Annamalai, K. and Ryan, W., "Interactive Processes in Gasification and Combustion. Part I: Liquid Drop Arrays and Clouds," *Progress in Energy and Combustion Science* **18**, pp. 221, 1992.

20. Annamalai, K., and Ramalingam, S., "Group Combustion of Char/Carbon Particles" *Combustion and Flame* **70**, pp. 307-332, 1987.

21. Raju, M. S. and Sirignano, W. A., "Interaction Between Two Vaporizing Droplets in an Intermediate Reynolds Number Flow," *Physics of Fluids A* **2**, pp. 1780-1796, 1990.

22. Kim, I., Elghobashi, S. E. and Sirignano, W. A., "Three-Dimensional Droplet Interactions in Dense Sprays," AIAA Paper No. AIAA-91-0073, Presented at the 29th Aerospace Sciences Meeting, January 7-10, Reno, Nevada, 1991.

23. Tian, Y. and Apfel, R. E., "A New Kind of Multiple-Droplet Levitator," Presented at the 129th Annual Meeting of the Acoustical Society of America, Washington, DC, May 30 - June 3, 1995.

24. Zhuyou, C., Shuqin, L., Zhimin, L., Mingli, G., Yulong, M., and Chenghao, W., "Development of an Acoustic Levitation reactor," *Powder Technology* **69**, pp. 125 - 131, 1992.

25. Takahashi, F., Sivo, J. and Dryer, F. L., "Development of an Aerodynamic Droplet Generator," Mechanical and Aerospace Engineering Report No. 1822, Princeton University, Princeton, New Jersey, 1988.
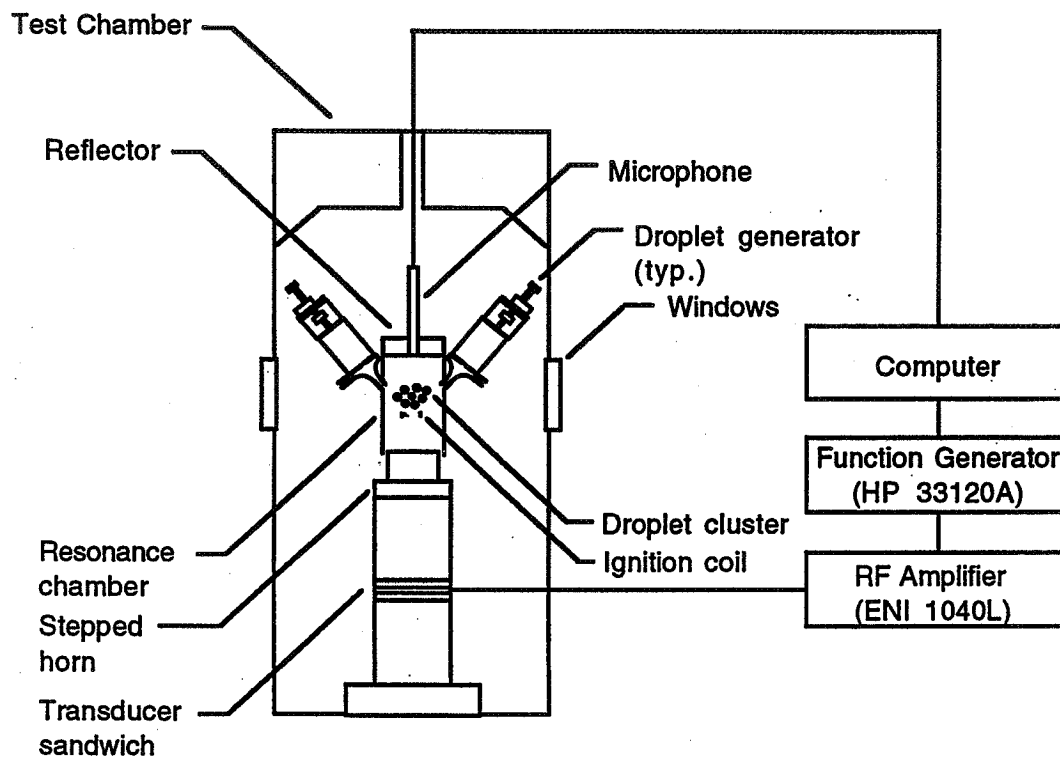
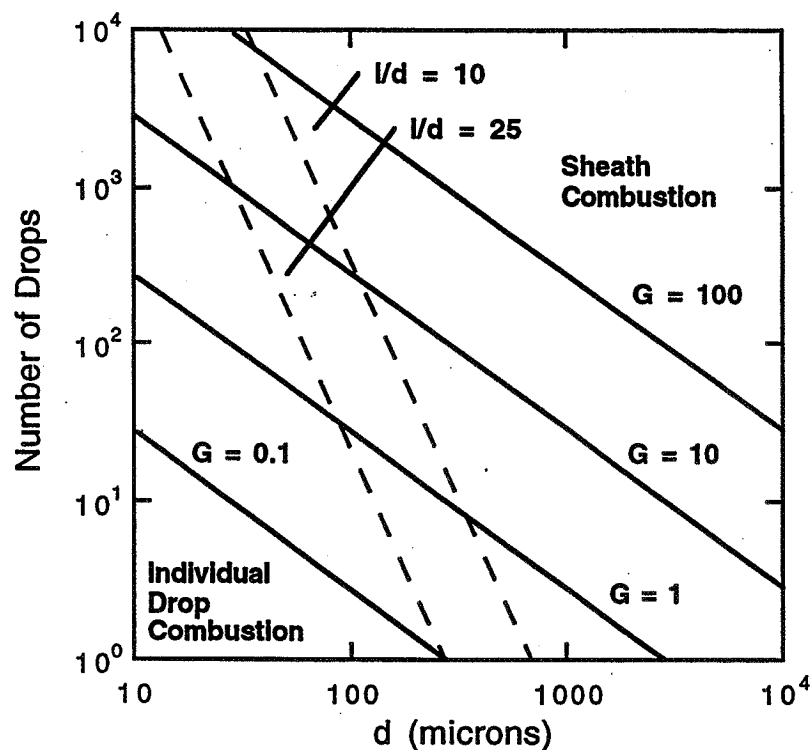Figure 1. Acoustic levitation device and test chamber

Figure 2. Group combustion regimes (cluster diameter = 8.5 mm)

MICROGRAVITY EXPERIMENT ON FLAME SPREAD
OF A FUEL DROPLET ARRAY

SHINICHIRO KATO, HIROYUKI MIZUNO,
HIDEAKI KOBAYASHI and TAKASHI NIIOKA

Institute of Fluid Science, Tohoku University, Katahira, Aoba-ku,
Sendai 980-77, Japan

ABSTRACT

Flame spread phenomena in a suspended fuel droplet array were experimentally investigated for n-decane and n-hexadecane in microgravity and normal gravity. Seven droplets of the same size were arranged horizontally at equal spacings. Flame spread rates were measured based on OH emission histories detected by a high-speed video camera with an image intensifier for droplet diameters of 0.50, 0.75, and 1.0 mm at ambient pressure from 0.1 to about 2.0 MPa.

Results show that, as droplet spacing becomes smaller, flame spread rate increases and has a maximum value at a certain spacing in both microgravity and normal gravity. A further decrease in droplet spacing causes the spread rate to decrease due to the large latent heat of vaporization. The flame spread rate in microgravity is larger than that in normal gravity. The spacing at the flame spread limit in microgravity is more than two times as large as that in normal gravity, but the spacing at the maximum flame spread rate in microgravity is only a little larger than that in normal gravity.

INTRODUCTION

Many practical combustion systems such as gas turbine combustors, diesel engines, and rocket motors use liquid fuels, and most of them are related to spray combustion at high pressures. In spray combustion, burning velocity is affected by droplet size, droplet number density, fuel volatility, ambient temperature, pressure, and so on. As a fundamental study of spray combustion, many studies have been done on vaporization [1,2], ignition [3-7], and combustion [8-12] of a single droplet in high-pressure ambience. Experimental studies on droplet combustion have shown that the burning rate constant has a maximum around the critical pressure of liquid fuel [8,10,11]. On the other hand, in the case of droplet ignition [7], it has been shown that the ignition time decreases monotonously with pressure, even over the critical pressure. Flame spread phenomena are more complicated because they have the characteristics of both combustion and ignition. In order to understand the fundamental mechanism of flame spread in fuel spray, investigations of the flame spread phenomenon in a simplified system of fuel droplets such as a droplet array are useful, particularly for less volatile fuels. The droplet combustion of less volatile fuels are interesting also from the point of view of aerospace propulsion systems using high-density fuels with high boiling points [8].

There are many excellent reviews related to spray combustion [13-17] and interactive droplet vaporization and combustion [18,19]. As for the flame spread of a fuel droplet array, Okajima et al. [20,21] experimentally investigated flame spread rates of volatile fuel droplets (n-heptane, benzene, and ethanol) and reported that the spread rates increase monotonously as the spacing between adjacent droplets becomes smaller. However, there have been very few studies on the flame spread at high-pressures around critical pressures, i.e., those at which drastic changes of transport properties such as thermal conductivity and heat capacity take place.

In the present study, characteristics of flame spread phenomenon of a fuel droplet array with very little fuel vapor were experimentally investigated at normal and high-pressures. Flame spread rates were measured for n-decane and n-hexadecane droplets with diameters of 0.50, 0.75, and 1.0 mm. The droplet spacing from center to center of droplets was changed from 1.0 to 9.0 mm at ambient pressures from 0.1 to 2.0 MPa. To remove the effects of natural convection, the microgravity experiments were performed and compared with the results obtained in normal gravity.

EXPERIMENTAL APPARATUS AND METHOD

The microgravity experiments were performed using the drop shaft facility of Japan Microgravity Laboratory (MGLAB) in Toki, Japan. The free-fall length of the facility is 100 m and the free-fall time is 4.5 sec. The size of the drop capsule is ϕ 900 mm (*diameter*) x 2280 mm (*height*) and the inner experimental space is ϕ 720 mm (*diameter*) x 885 mm (*height*).

The experimental setup is schematically shown in Fig.1. Flame spread experiments were performed in a high-pressure chamber installed in the drop capsule. The interior of the chamber is cylindrical with a inner diameter of 250 mm and a inner

height of 500 mm. The chamber has three silica windows with a diameter of 50 mm, so that flame spread phenomena at high-pressure can be observed with a high-speed video camera through the windows. Seven fuel droplets of the same size and with equal spacing were arranged horizontally. Seven silica fibers, 130 μm in diameter, were arranged horizontally at equal spacings and seven fuel droplet of the same size were arranged at the end of the fibers. In order to attach the fuel droplet to the fiber easily, the end of the silica fiber was made so that it had a spherical end with a diameter of about 300 μm. A 4-axis-stage manipulator with a microsyringe controlled automatically by a personal computer was installed in the chamber, and seven droplets with the same diameter were produced before releasing the capsule. The whole operation was observed with a CCD video camera through the silica windows.

The first droplet of the array was ignited instantaneously by an electric igniter made of a platinum wire, and then the flame spread from one droplet to another. As soon as the capsule was released, the igniter was activated and flame spread was completed in the microgravity period. The liquid fuels used were n-decane ($P_{cr} = 2.11$ MPa, where P_{cr} is the critical pressure) and n-hexadecane ($P_{cr} = 1.42$ MPa). Ambient pressures, P, were from 0.1 to 2.0 MPa for normal gravity experiments and from 0.1MPa to 0.5MPa for microgravity experiments.

The flame spread rates were measured by analyzing the history of OH emission images detected by an intensified high-speed video camera with a recording rate of 250 to 4500 frames/sec through a UV lens with an OH (0,0) band filter (the center wavelength is 307 nm and FWHM is 14 nm).

RESULTS AND DISCUSSION

Normal Gravity Experiments

Prior to the microgravity experiments, the experiments in normal gravity were performed to investigate the feature of the flame spread phenomenon and to prepare for microgravity experiments.

Figure 2 shows OH emission images of n-decane flame with a droplet diameter of 1.0 mm taken by an intensified high-speed video camera in normal gravity. In the case of the relatively large droplet spacing, S (=4.0mm), at atmospheric pressure shown in Fig. 2 (a), we can see that the first droplet has finished burning before the last droplet has been ignited. On the other hand, when the spacing is small (S=2.0mm) as shown in Fig. 2 (b), we cannot distinguish the combustion of individual droplets since the flame has spread forming a flame enveloping the whole droplet array. Because of the effect of natural convection, large wake flames are formed upward in both cases. When the ambient pressure is high (P=0.7MPa) as shown in Fig. 2(c), the flame diameter at the bottom of the droplet becomes small and the long wake flame compared to the droplet diameter flows upward because of enhanced natural convection at high pressure.

Figure 3 shows typical OH emission histories in normal gravity determined at the pointed head of the spreading flame. The ignition point is the left end of the first droplet in Fig. 2. Although the flame spread at the first and second droplets is greatly influenced by the igniter, we can see that almost steady flame spread takes place after the flame reached the third droplet. Therefore, the flame spread rate was measured by dividing droplet spacing, S, by average spread time, τ_{fs} from the third to the sixth droplet in this experiment.

Figure 4 shows variations of flame spread rate of an n-decane and an n-hexadecane with droplet spacings for three kinds of ambient pressures. This is the case of an initial droplet diameter, d_0, of 1.0 mm. We can see that there are limits of spacing beyond which the flame cannot spread. When the spacing is greater than the limit, flame spread does not occur because a burning single droplet cannot provide sufficient heat to a adjacent droplet, and so the adjacent droplet cannot be ignited. In this case, combustion of only one droplet occurred. As the spacing becomes smaller, the flame spread rate increases and then decreases after taking a maximum spread rate at a certain spacing.

As the flame of the burning droplet approaches the adjacent unburned droplet, vaporization and reaction are promoted because the droplet surface is exposed to higher temperature gases. It is supposed that when the spacing is roughly equal to flame radius of a burning droplet, the heat transfer from the flame to the unburned droplet should become maximum. When the spacing is very small, the flame front approaches the adjacent unburned droplet before the spherical flame has fully developed. As a result, when droplets are located close to each other, cooling effect due to the latent heat of vaporization of an unburned droplet is relatively large. Therefore, the reaction rate decreases, and then the spread rate decreases as spacing becomes very small. Consequently, the spread rate has a maximum at a certain spacing.

The effects of ambient pressures on the flame spread rate are also shown in Fig. 4. As ambient pressure becomes higher, the spread rate decreases. This is because flame diameters, i.e., those in the high temperature region, become smaller due to decreased mass and heat transfer with increasing pressures [7]. As a result, spacings at both the flame spread limit and the maximum spread rate become smaller. The spread rates of n-hexadecane are smaller than those of n-decane over the whole range of droplet spacings. This is basically due to the difference in volatility between n-hexadecane and n-decane. The boiling point of n-hexadecane (560 K) is higher than that of n-decane (447 K), so that n-hexadecane has a longer vaporization time than n-decane. Figure 5 shows variations of flame spread rate with droplet spacings for three kinds of initial droplet diameters at 0.1 MPa.

As droplet diameter increases, the maximum spread rate decreases and the spacing at the maximum spread rate increases because a larger droplet has a longer ignition time due to its large heat capacity. On the other hand, the spacing at the flame spread limit becomes larger with increasing droplet diameters. The decrease in the spread rate of smaller droplets for larger spacing is significant. It is because the rapid decrease in droplet diameter with time for smaller droplets.

Figure 6 shows variations of the flame spread rate with ambient pressures for a droplet diameter of 1.0 mm. The spread rate decreases monotonously as pressure rises for every spacing, and the gradient is steep at lower pressures. The droplet array with larger spacing has a flame spread limit at lower pressures. It is known that, in the case of a single droplet, ignition time decreases with increasing pressures [7]. If the flame spread is caused by continual ignition of a droplet array, the spread rate should increase with pressure. When the spacing is relatively large, flame spread becomes impossible as soon as the pressure exceeds 0.1 MPa. Therefore, the spacing has to be very small so that the flame can spread in a high-pressure ambience in normal gravity. No flame spread was observed for n-decane at supercritical pressure (2.11 MPa) in the present experiment, while the flame spread occured over supercritical pressures when the spacing is 1.5 mm for n-hexadecane.

In the case of the flame spread phenomenon, the supercritical condition of fuel is hardly attained near the spreading flame front even though the ambient pressure is at the supercritical pressure of fuel because the partial pressure of fuel near the flame front is low due to the existence of a large amount of air. Therefore, it is suggested that the aspect of supercritical phenomenon mentioned in Refs. 8, 10, and 11 does not appear.

The flame spread characteristics shown in Figs.4 and 5 are different from the experimental results for volatile fuels (n-heptane, benzene, and ethanol) reported by Okajima et al. [20,21]. In their experiments, the spread rate did not have a maximum value but increased monotonously as the spacing became smaller. We suppose that it was because the fuels were very volatile. In the case of n-heptane, the stoichiometric mixture ratio is 1.87 in vol.% (partial pressure is 0.00187 MPa at an ambient pressure of 0.1 MPa) and the vapor pressure on the droplet surface at equilibrium condition at room temperature is 0.00606 MPa. The amount of vapor of n-heptane should be much greater than the stoichiometric mixture ratio near the droplet surface, even without heat from a flame. A premixture of n-heptane and air must exist moderately around a droplet array. It seems that the flame spread rate approaches the laminar burning velocity as the spacing becomes small because vaporization time can be ignored. On the other hand, n-decane and n-hexadecane evaporate very little if there is not flame near the unburned droplet.

Microgravity Experiments

Figure 7 shows the OH emission images taken in microgravity for n-decane. The diameter of the droplets is 1.0 mm and the ambient pressure is 0.1MPa. The difference between these images and the images for normal gravity experiments shown in Fig.3 is significant. No wake flame is formed and the flame spread occurs axisymmetrically. The diameter of these axisymmetric flame is much larger than that of the flame diameter in normal gravity. It was found that intensities of OH emission was weaker than that in normal gravity. In the case of larger spacing (S=9.0mm) as shown in Fig.7(3), spherical single flame is formed at the pointed head of the spreading flame. OH emission characteristics at 0.5MPa were almost the same as those at 0.1MPa, but the diameter of the flame was much smaller that that at 0.1MPa.

Figure 8 shows variations of flame spread rate in microgravity for the n-decane droplet array. The droplet diameter is 1.0 mm and ambient pressures are 0.1MPa and 0.5MPa. The procedure to measure the flame spread rate is the same as that in normal gravity. We can see that the maximum spread rate exists even in microgravity, meaning that this phenomenon is not caused by the existence of natural convection. At both pressures, 0.1MPa and 0.5MPa, the spacing at the maximum spread rate in microgravity is only a little larger than that in normal gravity, but the spacing at the flame spread limit in microgravity is more than two times as large as that in normal gravity. This implies that flame spread might occur over the critical pressure in microgravity even for very large spacing of droplet array.

Droplet ignition and combustion are transient phenomena and flame diameter changes with time. Here, we define the maximum flame diameter as that of fully developed flame in the droplet lifetime for each droplet, which may be equal to the maximum diameter of the flame of a single droplet. It was found in the present experiment that the maximum flame diameter in microgravity was more than 9.0 mm, which is also more than two times as large as that in normal gravity. This is because there is no natural convection, and because flame spread phenomena are influenced by only diffusive heat and mass transfer. This large maximum flame diameter in microgravity produces a large flame spread rate due to the enhanced heat transfer to unburned droplets. On the other hand, the minimum flame diameter in microgravity, which is defined as the instantaneous diameter at the moment of droplet ignition, is almost the same as that in normal gravity, so that the spacing at the maximum spread rate in microgravity is only a little larger than that in normal gravity.

I seems that the flame spread phenomenon at the spacing of 0 mm is the same as that for a fuel liquid column, meaning that the spread rate of a droplet array should approach that of the liquid column as the spacing becomes extremely small. The flame spread phenomenon at pressures much higher than critical pressure is interesting. In microgravity, flame spread seems to occurs even for large droplet spacing at high-pressure as mentioned above. We are planning to investigate this phenomenon in the future experiments.

CONCLUDING REMARKS

Flame spread experiments of a fuel droplet array in microgravity and normal gravity were performed and the following findings were obtained:

1. The flame spread rate of a droplet array increases and then decreases after attaining a maximum spread rate at a certain spacing.
2. Flame spread does not occur when droplet spacing is larger than a certain value.
3. Droplet spacing at the flame spread limit and the maximum flame spread rate become smaller as droplet diameter decreases or ambient pressure increases.
4. The flame spread rate decreases monotonously with pressure, but no drastic changes of the spread rate are observed around the critical pressure, indicating the difference from the single droplet combustion [8,10,11].
5. In microgravity, the flame spread rate is faster than that in normal gravity. The spacing at the flame spread limit in microgravity is more than two times as large as that in normal gravity, but the spacing at the maximum flame spread rate in microgravity is only a little larger than that in normal gravity.

ACKNOWLEDGMENTS

REFERENCES

(1) Kadota, T., Hiroyasu, H., Chida, T. and Imamoto, Y., *Trans. Jpn. Soc. Mech. Eng. Ser. B*, 40: 3147-3154 (1974), (in Japanese).
(2) Tsue, M., Nomura, H., Niwa, M. Miyano, H., Sato, J. and Kono, M., *Trans. Jpn. Soc. Aero. Space Sci.* 37: 21-28 (1993), (in Japanese).
(3) Kadota, T., Hiroyasu, H. and Oya, H., *Trans. Jpn. Soc. Mech. Eng. Ser. B*, 41: 2475-2485 (1975), (in Japanese).
(4) Saitoh, T., Ishiguro, S. and Niioka, T., *Combust. Flame* 48: 27-32 (1982).
(5) Takei, M., Tsukamoto, T. and Niioka, T., *Combust. Flame* 93: 149-156 (1993).
(6) Mawid, M. and Aggarwal, S. K., *Combust. Sci. Tech.* 65: 137-146 (1989).
(7) Nakanishi, R., Kobayashi, H., Kato, S. and Niioka, T., *25th Symp. (Int.) on Comb.*, The Combustion Institute, 1994, pp.2475-2485.
(8) Takahashi, M., Niioka, T., Sato, J. and Yamakawa, M., Technical Report of National Aerospace Laboratory, TR-1001, 1988, (in Japanese).
(9) Niioka, T., Hasegawa, S., Tsukamoto, T. and Sato, J., *Combust. Flame* 86: 171-178 (1991).
(10) Tsukamoto, T. and Niioka, T., *Microgravity Sci. Tech.* 4: 219-222 (1993).
(11) Sato, J., Tsue, M. and Kono, M., *Combust. Flame* 82: 142-148 (1990).
(12) Hiraiwa, T., Ono, N. and Niioka, T., *24th Symp. (Int.) on Comb.*, The Combustion Institute, 1993, pp.239-245.
(13) Williams, F. A., *Combust. Flame* 21: 1-31 (1973).
(14) Faeth, G. M., *Prog. Energy Combust. Sci.* 3: 191-224 (1977).
(15) Law, C. K., *Prog. Energy Combust. Sci.* 8: 171-201 (1982).
(16) Sirignano, W. A., *Prog. Energy Combust. Sci.* 9: 291-322 (1983).
(17) Chigier, N., *Combust. Flame* 51: 127-139 (1983).
(18) Annamalai, K. and Ryan, W., *Prog. Energy Combust. Sci.* 18: 221-295 (1992).
(19) Umemura, A., *Prog. Energy Combust. Sci.* 20: 325-372 (1994).
(20) Okajima, S., Kimoto, T., Abe, K. and Yamaguchi, S., *Trans. Jpn. Soc. Mech. Eng. Ser. B*, 47: 2058-2065 (1981), (in Japanese).
(21) Yoshida, S., Hara, H. and Okajima, S., *Trans. Jpn. Soc. Mech. Eng. Ser. B*, 55: 1241-1247 (1989), (in Japanese).
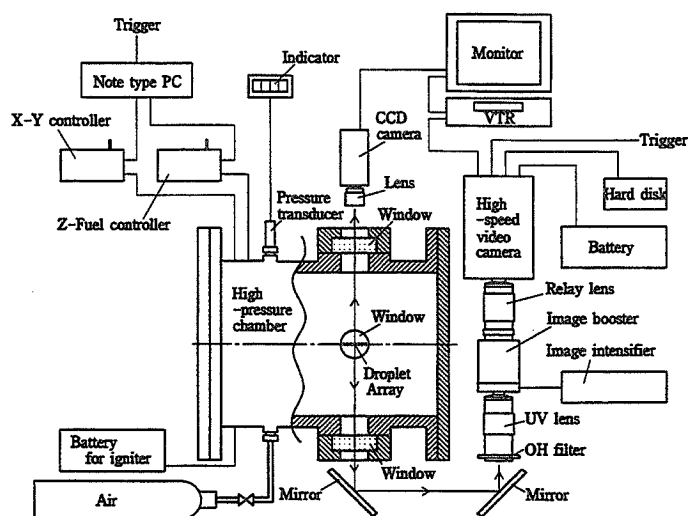
Figure 1. Schematics of the experimental setup.

Figure 2. OH emission images in normal gravity : n-decane, $d_0 = 1.0$ mm; (a) S = 4.0 mm, P=0.1MPa ; (b) S = 2.0 mm, P=0.1MPa; (c) S = 2.0 mm, P = 0.7 MPa.
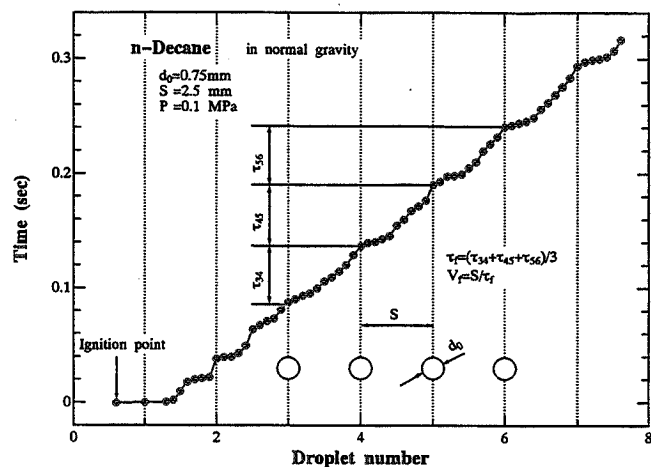
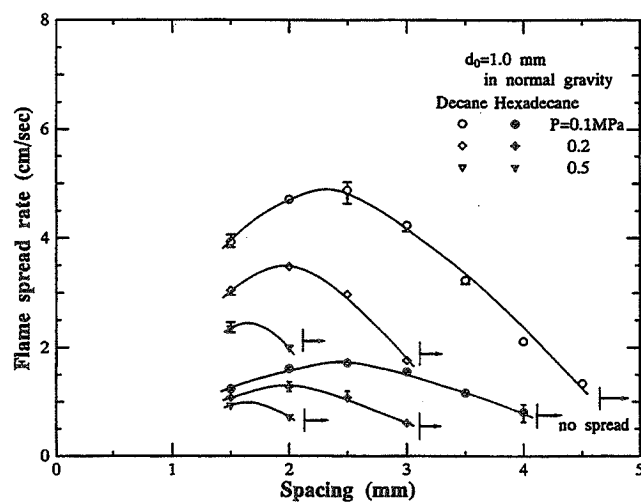Figure 3. Typical OH emission histories in normal gravity : n-decane, $d_0 = 0.75$ mm, S = 2.5 mm, P = 0.1 MPa.

Figure 4. Variations of flame spread rate with droplet spacingsfor n-decane and for n-hexadecane at various pressures in normal gravity.
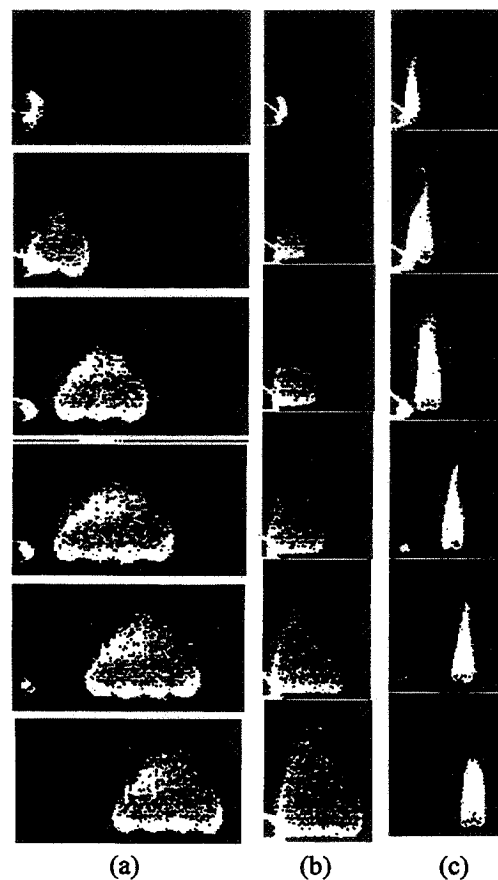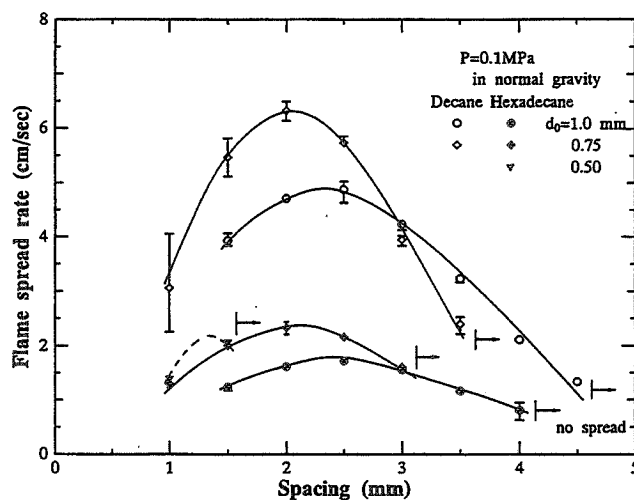

Figure 5. Variations of flame spread rate with droplet spacings for n-decane and n-hexadecane for various initial droplet diameters at 0.1 MPa in normal gravity.

495
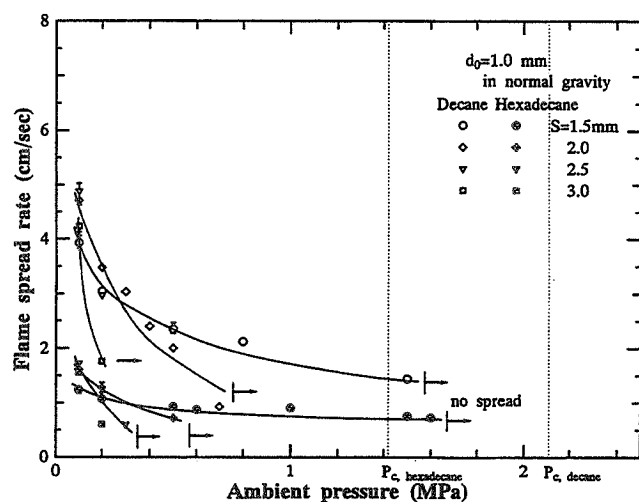
Figure 6.   Variations of flame spread rate with ambient pressures for n-decane and n-hexadecane for various droplet spacings in normal gravity.
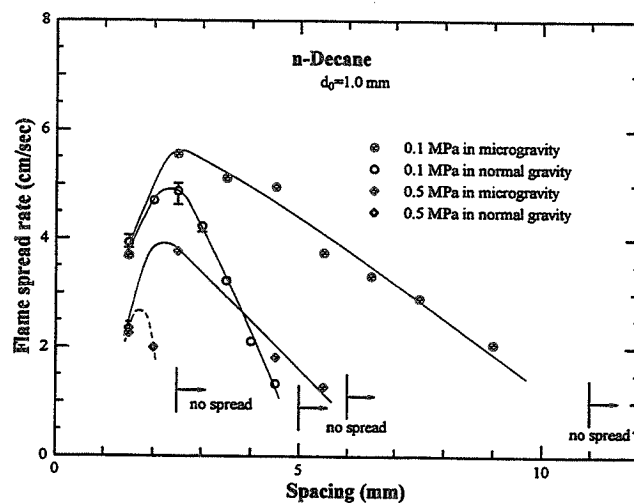
Figure 8.   Variations of flame spread rate with droplet spacings for n-decane at 0.1 MPa and 0.5MPa in microgravity and comparison with the case in normal gravity.
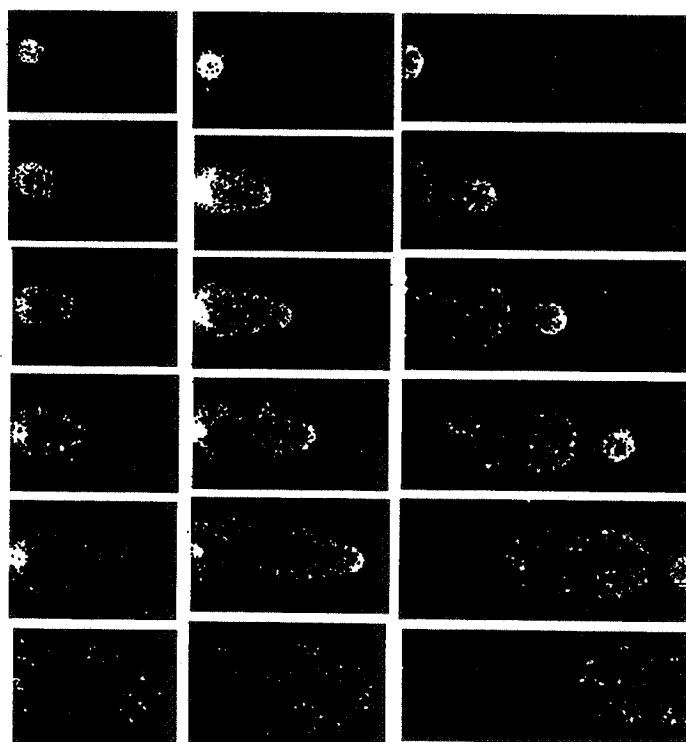
(a)   (b)   (c)

Figure 7.   OH emission images in microgravity :
n-decane, $d_0 = 1.0$ mm, P=0.1MPa ; (a) S = 2.5 mm;
(b) S = 4.5mm; (c) S = 9.0 mm.

496

PRESSURE EFFECTS IN DROPLET COMBUSTION OF MISCIBLE BINARY FUELS

MASATO MIKAMI

Yamaguchi University
Tokiwadai, Ube, Yamaguchi 755, Japan

Osamu Habara and Michikata Kono
Department of Aeronautics, University of Tokyo
Hongo, Bunkyo-ku, Tokyo 113, Japan

Jun'ichi Sato
Research Institute
Ishikawajima-Harima Heavy Industries Co., Ltd.
Toyosu, Koto-ku, Tokyo 135 Japan

Daniel L. Dietrich
NASA Lewis Research Center, Cleveland, Ohio 44135

and

Forman A. Williams
Center For Energy And Combustion Research
Department Of Applied Mechanics And Engineering Sciences
University Of California, San Diego
La Jolla, Ca 92093-0411

Introduction

The objective of this research is to improve understanding of the combustion of binary fuel mixtures in the vicinity of the critical point. Fiber-supported droplets of mixtures of n-heptane and n-hexadecane, initially 1 mm in diameter, were burned in room-temperature air at pressures from 1 MPa to 6 MPa under free-fall microgravity conditions. For most mixtures the total burning time was observed to achieve a minimum value at pressures well above the critical pressure of either of the pure fuels. This behavior is explained in terms of critical mixing conditions of a ternary system consisting of the two fuels and nitrogen. The importance of inert-gas dissolution in the liquid fuel near the critical point is thereby re-emphasized, and nonmonotonic dependence of dissolution on initial fuel composition is demonstrated. The results provide information that can be used to estimate high-pressure burning rates of fuel mixtures.

Although near-critical conditions occur in many practical applications of droplet combustion, understanding of high-pressure combustion of fuel mixtures is incomplete. For normal pressures, well below critical values, both experimental and theoretical work on the combustion of droplets of miscible binary fuels have confirmed and explained three-stage (normal -slow-normal) burning and the occurrence of disruption under suitable conditions. The few experimental studies that have been performed on binary fuel mixtures at elevated pressures (ref. 1, 2) concerned n-heptane, n-hexadecane mixtures and showed that three-stage droplet burning persists, at least up to 3 MPa, but becomes less pronounced with increasing pressure. On the other hand, a computational study of the evaporation of an n-heptane, n-octane mixture in hot nitrogen showed no staged evaporation but attainment of critical mixing above 6 MPa (ref. 3). There is considerable knowledge about the high-pressure combustion of pure-fuel droplets, including both experimental (ref. 4-9) and theoretical (ref. 5, 6, 10-16) work. This research established the subcritical decrease in burning lifetime with increasing pressure, mainly through the decreasing diffusion coefficient, leading to a minimum burning lifetime at a pressure in the vicinity of the critical value. The value of this minimum lifetime and the pressure at which it occurs are affected strongly by the high solubility of inert gases in the liquid fuel near the critical point (ref. 3, 5, 12-14, 16). Critical conditions are modified by this absorption, so that phase interfaces with latent heats can exist at pressures well above the critical pressure of the pure fuel. In a binary mixture of fuel and inert gas, at any given pressure there is a critical mixing point, at which the gaseous and liquid phases become identical, having a temperature above which the system maintains a single phase. During the burning

or evaporation of a pure fuel droplet, at successively higher pressures, the liquid-gas interface eventually reaches a critical mixing point; at and beyond this critical mixing, phase distinctions and latent heats vanish. The minimum burning lifetime occurs at a pressure near those for which critical mixing is achieved at some time during the droplet combustion history.

The present study addresses high-pressure combustion of binary-fuel droplets, necessitating consideration of ternary mixture diagrams to explain the influence of inert-gas absorption on attainment of critical mixing. Advantage is taken of microgravity facilities to enable burning lifetimes to be measured up to 6 MPa without influences of natural convection and without loss of the ability of a fiber to suspend the droplet. Minima of burning lifetimes are measured, and the pressures at which those minima occur are identified. The experimental results are explained by considerations of critical mixing. Staged burning, although weak, is not entirely inconsequential in explaining certain aspects of the minima. The behavior of the particular alkane mixture studied should be representative of that of other binary alkane mixtures and of many other binary fuel mixtures as well.

Experimental Apparatus and Procedure

The combustion experiments were performed in microgravity in a drop tower at the NASA Lewis Research Center that provides 2.2 seconds of microgravity (less than 10^{-5} times normal gravity), so that the buoyancy effects could be negligible. The suspended droplet technique was used, which is good enough to reveal pressure effects on burning lifetime of the binary fuel droplets. The experimental apparatus and procedure in the present study are basically the same as in the previous study by the authors (ref. 2). The initial droplet diameter d_0 was approximately 1 mm. All the burning times were corrected to that of the droplet with $d_0 = 1$ mm by assuming d^2-law for the burning time. The corrected burning time is called burning lifetime in the present paper. The fuels were n-heptane and n-hexadecane mixtures with initial hexadecane mass fraction Y_0 (or initial hexadecane more fraction (X_0)), ranging from 0 (pure heptane) to 1.0 (pure hexadecane). The ambient gas used was air at pressures ranging from 1.0 to 6.0 MPa, which exceeds the critical pressure of either of pure heptane (2.74 MPa) and hexadecane (1.41 MPa).

Results

Figure 1 exhibits the measured burning lifetimes t_b as functions of pressure P for five different initial hexadecane mass fractions Y_0. No experiment was performed at $P = 6$ MPa for $Y_0 = 0.63$, but a corresponding set of experiments that include this point was performed for pairs of droplets separated by 4 mm. The burning lifetimes for the droplet pairs were longer by amounts ranging from about 0.3 at 1 MPa to about 0.1 at 6 MPa (as expected from effects of droplet interactions without natural convection), but otherwise they exhibited the same trends seen in Fig. 2. The point in parentheses in Fig. 1 was obtained from the droplet-pair data by applying the 0.1 s correction for interaction.

Figure 1 shows that the minimum of t_b occurs at about $P = 3$ MPa for both pure fuels and at higher pressures for the mixtures. The dependence of the pressure P_m at which t_b is a minimum on the initial hexadecane mole fraction in the liquid phase X_0 is plotted in Fig. 2. The initial hexadecane mole fraction X_0 is used as the abscissa instead of the mass fraction Y_0 because the dependence shown in this figure is largely influenced by the phase equilibrium as will be discussed later, in which the mole fractions of the phase interface play an important role. It is seen that adding a small amount of hexadecane to pure heptane causes P_m to increase sharply. The value of P_m soon reaches a maximum, and further addition of hexadecane causes P_m to decrease gradually.

Discussion of Binary Systems

Figure 3 shows diagrams of phase equilibrium for three two-component systems, (a) n-heptane/nitrogen, (b) n-hexadecane/nitrogen and (c) n-heptane/n-hexadecane. These diagrams have been calculated by equating the fugacities of each component in each phase, by the method shown in Reid et al. (ref. 17), using the Peng-Robinson equation of state. The data needed for these calculations are available in Reid et al. (Ref. 17). Nitrogen is selected here as representative of the inerts (principally N_2, CO_2 and H_2O) present during combustion because of lack of data for other species. This seems reasonable because the polar nature of H_2O

is not likely to be very significant at the relatively high temperatures of interest here (ref. 5). The solid lines in Fig. 3 are liquid compositions and the dashed lines gas compositions; they meet at the critical mixing point.

The qualitative characteristics seen in Figs 3a and 3b are quite similar. At normal atmospheric pressure, the mole fraction of nitrogen absorbed in the liquid is very small, but it becomes appreciable near the critical pressure of the pure fuel and is responsible for the emergence of the critical mixing point above that pressure. At any given time during the combustion of a droplet of a pure fuel, the thermodynamic states will lie along a locus in Fig. 3a or 3b, going from the left-had edge and the flame temperature at the flame sheet to the right-hand edge and the droplet temperature at the center of the droplet. At normal atmospheric pressure, as the temperature decreases this locus reaches the phase equilibrium curve for the gas at the interface then jumps essentially to the right-hand edge and remains there in the liquid. In the opposite extreme, at sufficiently high-pressures, the locus avoids the boundary of the two phase region entirely and moves continuously from the left to the right edge. As the pressure is increased above the normal atmospheric value, the magnitude of the jump in the composition X that occurs at the phase boundary decreases, and that jump finally disappears when the pressure becomes high enough for the locus to meet the phase boundary a the critical mixing point. Depending on the shape of the phase boundary, the locus of states in the liquid may or may not follow that boundary over a nonzero range of temperature for pressures equal to or slightly above those for which the intersection occurs at the critical mixing point. However, eventually the locus must leave the boundary to reach the right edge, and as indicated above, at sufficiently high pressures it does not encounter the boundary at all.

The shape of the locus of states discussed above depends, of course, on values and variations of transport properties, as well as on time during the droplet burning history. For typical initial conditions, as time increases the locus intersection moves towards critical mixing, and it reaches this condition if the pressure is sufficiently high (ref. 3, 13). The pressure P_m is approximately that for which this condition occurs roughly in the middle of the burning history. The differences in the ratios P_m/P_C for heptane and hexadecane are associated with the quantitative differences between Figs. 3a and 3b. The phase boundary temperatures are much lower in Fig. 3a, but the flame and initial droplet temperatures are nearly the same for the two fuels. At 3 MPa the locus of states typically reaches a value of X greater than 0.98 at a temperature around 500 K, and this is sufficient to avoid the phase boundary for heptane. Because of the higher temperatures in Fig. 3b, that avoidance does not occur at 2 MPa but finally does begin to occur around 3 MPa, giving a much larger ratio of P_m/P_C for this fuel. The higher critical temperature for hexadecane (722 K), in comparison with heptane (540 K), is thus the main source of its larger value of P_m/P_C. Another contributing factor is the fact that the heat capacity of hexadecane is larger than that of heptane at the same ratio of temperature to critical temperature, so that more heating is required for hexadecane to reach critical mixing.

This same reasoning explains why P_m/P_C is larger for vaporization (ref. 13) or for burning in nitrogen-enriched atmospheres (ref. 2). Under such situations, the effective flame temperature is lower, and therefore, far from the droplet, the locus of states begins closer to the phase boundary. At lower driving temperatures, higher pressures are needed to reach critical mixing an avoid the two phase region.

The diagram of phase equilibrium for the binary fuel mixtures without inert, shown in fig. 3c, is different from those of Figs. 3a and 3b. A normal phase boundary occurs at atmospheric pressure. These two liquids are sufficiently similar that there are no azeotropes under any conditions. A critical mixing point appears when the pressure is raised above the critical pressure of hexadecane. Above the critical pressure of heptane, a lower critical mixing point occurs as well. The extent of the two-phase region decreases with increasing pressure and eventually disappears at a critical point of the mixture P_{C3}, above 3 MPa. At high pressures the two-phase region has a larger mole fraction of heptane than hexadecane in both phases. These characteristics are relevant to the behavior of the ternary system, as discussed below.

Discussion of the Ternary System

Figure 4 shows calculated diagrams of phase equilibrium for the ternary n-heptane/n-hexadecane/nitrogen system for four different pressure ranges, (a) $P < P_{C1}$, (b) $P_{C1} < P < P_{C2}$, (c) $P_{C2} < P < P_{C3}$ and (d) $P_{C3} < P$. the calculations were performed by equating the fugacities of both phases for all three constituents. The bases

of these three-dimensional diagrams are standard equilateral triangles with pure components at the vertices and binary mixtures along the edges. Solid curves give liquid-phase concentrations and dashed curves gas-phase concentrations. Isothermal lines are shown at successive temperature increments of 50 K, dashed in the gas, solid in the liquid and chained in excluded regions. The locus of states now goes from the nitrogen vertex at flame temperature to the fuel composition on the heptane-hexadecane face.

The low-pressure characteristics seen in Fig. 4a are clear from the low-pressure curves in Fig. 3. Figure 4 shows that, above the critical pressure of hexadecane, a critical mixing line appears, over a limited range of relative concentrations of heptane and hexadecane. As expected from Fig. 3c, Fig. 4c shows that, above the critical pressure of heptane, there are both upper and lower critical mixing lines. Finally, above the maximum critical pressure of the heptane-hexadecane system, a critical mixing line extends throughout the entire range of relative concentrations of heptane and hexadecane, as seen in Fig. 4d. Addition of small amounts of hexadecane to heptane reduces the solubility of nitrogen in the liquid, as can be seen in Fig. 4b, 4c or 4d from the existence of a plane through the nitrogen vertex for which the liquid-phase nitrogen mole fraction is a minimum. Such behavior typically is associated with the existence of both upper and lower critical mixing points in the heptane-hexadecane system, as seen in Fig. 3c.

Consider first systems having relatively large initial hexadecane mole fractions X_0 in the binary fuel mixture. Such systems lie close to the nitrogen-hexadecane face of Fig. 4c, and their behavior will be very much like that discussed for Fig 3b. As the droplet vaporizes, the ratio of hexadecane to heptane in the liquid phase increases slowly, and the surface concentration approaches that of the nitrogen-hexadecane system more closely. As the pressure is increased, attainment of critical mixing occurs when the previously discussed locus of states in Fig. 4 reaches the critical mixing line. A higher pressure is required to reach this line than is required with pure hexadecane because the solubility of the inert in the liquid mixture is less than in pure hexadecane.

Consider next systems for which the initial hexadecane mole fraction X_0 is small. This condition maximizes influences of staged burning. As combustion proceeds, the ratio of hexadecane to heptane at the droplet surface increases, slowly at first but then rapidly as the slow stage begins. In the third stage, the hexadecane fraction in the liquid at the surface is well above its initial value, and the inert solubility is correspondingly larger. This stage, however, comprises a small fraction of the burning lifetime when X_0 is small. Phenomena can influence t_b appreciably therefore only if they occur during the first stage. During this stage, the increase in the hexadecane concentration initially reduces the inert solubility and substantially increases the temperature along the critical mixing line in Fig. 4 or 4d. Both of these effects cause critical mixing to be more difficult to achieve and correspondingly give rise to the sharp increase in P_m with X_0 at small values of X_0 in Fig. 2. Since the minimum inert solubility occurs when the molar ratio of hexadecane to heptane plus hexadecane is about 0.15, the surface hexadecane buildup during the first stage implies that X_0 should be less than 0.15 at the maximum in Fig. 2. Consistent with this deduction, it is observed to be about 0.005.

Conclusions

Aspects of staged burning have been seen to have some influence on the pressure at which the minimum burning lifetime occurs in high-pressure droplet combustion of miscible binary fuels. It is necessary to consider absorption of inert gases in the liquid fuel to determine properly the pressure at which the minimum occurs. Diagrams of ternary phase equilibria are helpful for this purpose, despite the dearth of needed high-pressure phase-equilibrium data. Improved understanding of the combustion of binary fuel mixtures in the vicinity of critical conditions can be obtained by investigations of this kind.

Acknowledgment

References

1. Niioka, T. and Sato, J., *21st Symp. (Int.) Comb.*, The Combustion Institute, 1988, pp. 625-631.

2. Mikami, M., Kono, M., Sato, J., Dietrich, D.L. and Williams, F.A., *Combust. Sci. Tech.*, Vol. **90**, pp. 111-123 (1993).

3. Hsieh, K.C., Shuen, J.S. and Yang, V., *Combust. Sci. Tech.*, Vol. **76**, pp. 111-132 (1991).

4. Faeth, G.M., Dominicis, D.P., Tulpinsky, J.F. and Olson, D.R., *12th Symp. (Int.) Comb.*, The Combustion Institute, 1969, pp. 9-18.

5. Lazar, R.S. and Faeth, G.M., *13th Symp. (Int.) Comb.*, The Combustion Institute, 1971, pp. 801-811.

6. Canada, G.S. and Faeth, G.M., *14th Symp. (Int.) Comb.*, The Combustion Institute, 1973, pp. 1345-1354.

7. Kadota, T. and Hiroyasu, H., *18th Symp. (Int.) Comb.*, The Combustion Institute, 1981, pp. 275-282.

8. Takahashi, M., Niioka, t., Sato, J. and Yamakawa, M., *Burning Rate Constant of Fuel Droplet under High Pressure*, Technical Report of National Aerospace Laboratory TR-1001, (*in Japanese*) 1988.

9. Sato, J., Tsue, M., Niwa, M. and Kono, M., *Combust. Flame* **82**: 142-150 (1990).

10. Spalding, D.B., *ARS Journal* **29**: 828-835 (1959).

11. Rosner, D.E., *AIAA Journal* **5**: 163-166 (1967).

12. Rosner, D.E. and Chang, W.S., *Combust. Sci. Tech.*, Vol. **7**, pp. 145-158 (1973).

13. Umemura, A., *21st Symp. (Int.) Comb.*, The Combustion Institute, 1988, pp. 463-471.

14. Shuen, J.S., Yang, V. and Hsiao, C.C., *Combust. Flame* **89**: 299-319 (1992).

15. Tsukamoto, T. and Niioka, T., *Microgravity Sci. Tech.* **4**: 219-222 (1993).

16. Li, Y.Q. and Umemura, A., *Trans. Japan Society of Mechanical Engineers*, Vol. **59**, pp. 337-342 (in Japanese) (1993).

17. Reid, R.C., Prausnitz, J.M. and Poling, B.E., *The Properties of Gases and Liquids* (4th ed.), McGraw-Hill, New York, 1987, pp. 337-357.
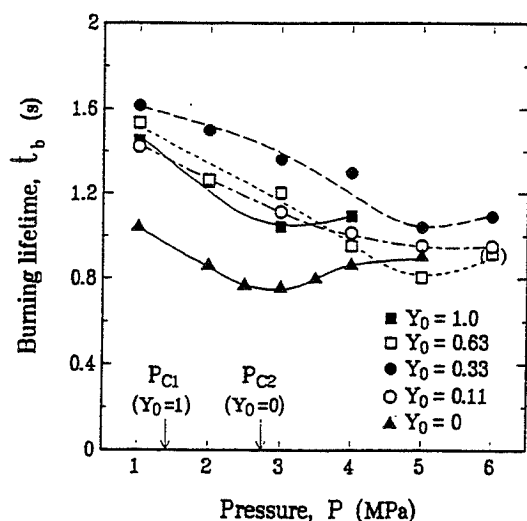
Fig. 1 Dependence of the burning lifetime t_b on pressure P for different initial hexadecane mass fraction in the liquid phase Y_0.
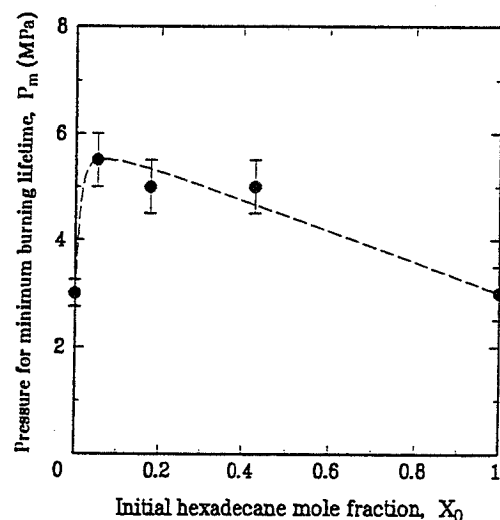
Fig. 2 Dependence of the pressure P_m at which the burning lifetime t_b is a minimum on the initial hexadecane mole fraction in the liquid phase X_0.
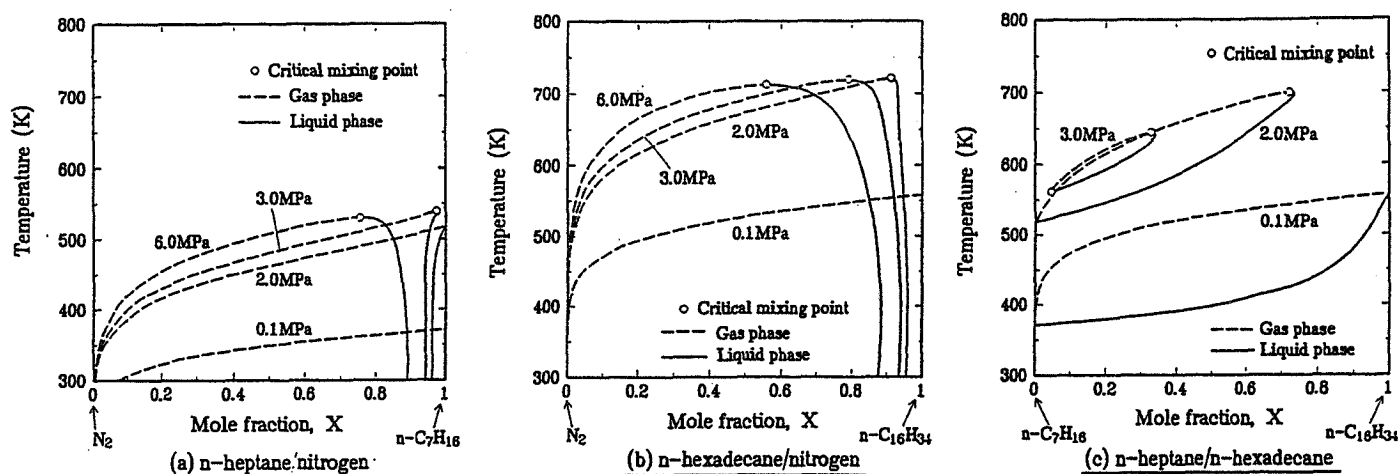
Fig. 3 Calculated diagrams of phase equilibrium for binary systems at different pressures:
(a) n-heptane/nitrogen, (b) n-hexadecane/nitrogen, (c) n-heptane/n-hexadecane.
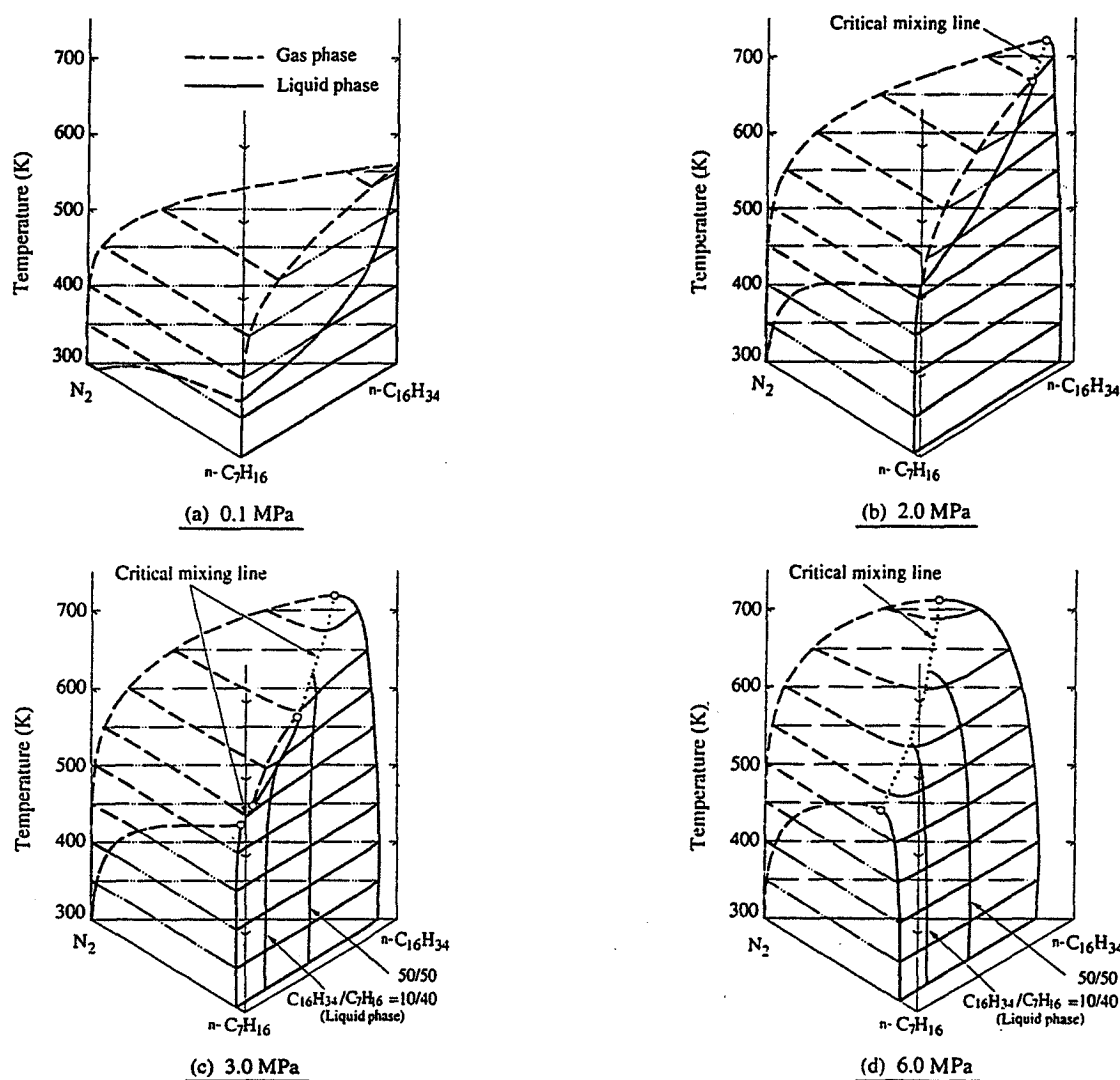
Fig. 4 Calculated diagrams of phase equilibrium for the ternary-heptane/n-hexadecane/nitrogen system;
(a) 0.1 MPa $(P < P_{C1})$, (b) 2.0 MPa $(P_{C1} < P < P_{C2})$, (c) 3.0 MPa $(P_{C2} < P < P_{C3})$, (d) 6.0 MPa $(P_{C3} < P)$.

502

HIGH PRESSURE BURNING OF METHANOL DROPLETS: A COMPARISON BETWEEN PARABOLIC FLIGHT AND DROP TOWER EXPERIMENTS

I. Gokalp, C. Chauveau, B. Vieille
Laboratoire de Combustion et Systemes Reactifs
Centre National de la Recherche Scientifique
45071 Orleans cedex 2, France

and

T. Kadota, D.Segawa
Department of Mechanical Engineering
Osaka Prefecture University
Gakuen-Cho, Sakai, Osaka 593, Japan

***Abstract** : A franco-japanese collaboration program on microgravity combustion has been initiated. Part of this program is devoted to the investigation of high pressure methanol droplet vaporization and burning. Two different facilities have been used in Japan and in France both under normal gravity and reduced gravity conditions. Each facility uses the fiber suspended droplet technique. Experiments have been conducted jointly by the two teams. Reduced gravity conditions have been generated in France by the use of parabolic flights. Several experiments have been conducted in Japan at the JAMIC drop shaft. One objective of the study is to determine the pressure effects on the burning rate and burning time of methanol droplets, under both subcritical and supercritical gaseous environments. A related issue is to obtain this information under variable residual gravity levels, in order to analyze the gravity induced buoyancy effects on droplet burning phenomena. Experiments with both facilities and under normal gravity and two residual gravity levels confirm the strong increase of the methanol droplet burning rates up to the critical pressure. Important quantitative differences have been however observed between the burning rate values obtained by using the two facilities, under normal gravity and reduced gravity. It appears therefore crucial to homogenize the experimental procedures in both facilities.*

INTRODUCTION

The operating pressures in a variety of liquid fueled combustors including gas turbines, diesel engines and launcher propulsors are continuously increasing to reach higher thermal efficiencies and higher rates of heat release. This has resulted in an increased interest in the study of the vaporization and burning of liquid fuel droplets in high pressure gaseous environments [1]. The basic questions to be addressed in these studies are several. One crucial issue is the determination of the gasification times versus the pressure. The droplet gasification times control indeed many aspects of spray combustion, including the reactive mixture formation. Another important, and obviously related, issue is the determination of the droplet gasification regimes. Depending on the thermodynamic and flow conditions surrounding the droplet, its gasification may occur either by pure vaporization or by burning. Also, under high pressure conditions, the droplet may reach supercritical conditions, which drastically changes the heat and mass transfer mechanisms between the two phases.

Experimenting high pressure droplet burning under normal gravity is not an easy task. For example, when approaching thermodynamic critical conditions, the reduction of the liquid surface tension does not allow the use of the fiber suspended droplet technique. Furthermore, buoyancy forces increase as pressure squared, so that under

503

very high pressure conditions, droplet gasification regimes are buoyancy controlled. Consequently, high pressure droplet burning experiments are generally conducted under reduced gravity conditions, in order to widen the experimental conditions where the fiber suspended droplet technique can be used, or, better, to experiment with free floating droplets, and in order to significantly reduce buoyancy effects [2-5].

In high pressure droplet burning experiments in reduced gravity, the residual gravity level becomes an important parameter. For example, recent high pressure droplet burning experiments conducted with several n-alkanes during parabolic flights (where the residual gravity level is of the order of 10^{-2} g_0) did not show a minimum burning time around the critical pressure [1], which was observed [4] during drop tower experiments (where the residual gravity level is of the order of 10^{-5} g_0), and also predicted theoretically [6]. In addition, droplet burning experiments conducted with n-alkanes under normal pressure conditions during parabolic flights did not show the soot shell formation [7] observed during drop tower experiments [8,9]. Furthermore, in order to fully understand the influence of gravity induced buoyancy on droplet burning, it is desirable to systematically vary the residual gravity level.

A part of the franco-japanese cooperative research program on microgravity combustion is devoted to understand the vaporization and combustion processes of methanol droplets in high pressure gaseous environments under normal and variable gravity through the experimental work conducted with the use of the JAMIC drop shaft in Japan and the parabolic flights of the CNES aircraft in France. Methanol has been chosen as the test fuel both for its low sooting tendency and also because it is considered to be one of the most promising candidates as alternative fuel for several applications. The experiments under normal gravity and microgravity are conducted with the methanol droplet suspended at the tip of a fiber, both in subcritical and supercritical gaseous environments. The effect of ambient pressure, temperature, oxygen concentration and humidity on the burning rate constant, the burning life time, the droplet temperature and the flame structure are planned to be studied. Also discussed will be the effect of adsorption of water vapor generated in the process of chemical reaction into methanol. Special attention will be given to the optical observation of the liquid phase near the critical point.

This paper presents recent results on the burning of methanol droplets in high pressure gaseous environments under normal gravity and microgravity conditions generated in the JAMIC drop shaft and during parabolic flights. The experiments have been jointly conducted by the two teams. Different experimental facilities have been used during experiments in France and in Japan. These preliminary experimental results are therefore compared and discussed with reference to differences in the experimental procedures and in the residual gravity levels.

EXPERIMENTAL PROCEDURES

The global concept of the Japanese and French experimental facilities is the same. Fiber suspended droplets are ignited in high pressure chambers. The droplet burning rates in normal temperature air are determined from the video observation of droplet diameter time histories for increasing chamber pressures. Differences exist however between the two facilities which are separately described below.

Experimental facility used in France

Droplet gasification experiments conducted in France under variable pressure conditions are performed in a specially designed facility: the High Pressure Droplet Gasification Facility (HP-DGF). The HP-DGF is designed to investigate the gasification regimes of suspended or free-floating droplets under variable pressure conditions, up to 12 MPa. Low pressure droplet burning experiments can also be performed. This facility can be used both on ground and during the parabolic flights of an aircraft. The apparatus has been fully described previously [1]. A droplet is formed by two symmetrically opposed injectors and suspended on a quartz fiber of diameter 0.2 mm with an

enlarged extremity of 0.4 mm. Droplet injection occurs at the beginning of the microgravity period. For high pressure droplet burning experiments, an improved version of the ignition system consisting of two symmetrical heated coils is used. The coils are located about 15 droplet diameters below and above the suspending fiber and are used to heat the air in the vicinity of the droplet after its injection. The heating current is shut down when droplet autoignition is obtained. The sequences of droplet injection and ignition operations are computer controlled. The residual gravity level is recorded during the parabolic flight experiment and synchronized with the camera acquisition signal during the microgravity period [1].

The principle diagnostic system used is based on the visualization of the droplet burning phenomena. Suspended droplets are backlighted; this provides the necessary contrast for direct threshold definition. The image recording equipment is the Kodak-Ektapro 1000 high speed video camera, which can record up to 1000 full frames per second and allows detailed analysis of droplet lifetime during combustion. The Ektapro 1000 Motion Analyzer's live, real-time viewing makes possible to follow the investigated phenomena frame per frame. A second camera has been added to the Kodak-Ektapro 1000 system, in order to observe simultaneously the droplet and the flame with appropriate magnification rates. The digitized images from the Kodak-Ektapro system are transferred to a microcomputer where the image analysis is performed. Burning droplet experiments have been conducted under both normal and reduced gravity conditions. The weakly sooting behavior of methanol droplets allows the observation of the droplet dimensions during the entire burning period. For the reduced pressure range explored here (P_r up to 1.2), the droplet projected surface area regresses quasi-linearly with time as expected from the D^2 law; this authorizes the determination of an average burning rate as $K = - d(D^2)/dt$. For all the droplet burning experiments reported here, the suspended droplet initial diameters are scattered around 1.5 mm; the ambient air temperature is 300 K.

Experimental facility used in Japan

A methanol droplet is allowed to burn in a cylindrical high pressure combustion chamber with inner diameter 80 mm and height 130 mm. A pair of opposing windows of diameter 30 mm allow to observe the droplet burning inside the combustion chamber. The combustion chamber is equipped with a quartz suspending fiber of diameter 0.5 mm with an enlarged spherical tip, a remote controlled fuel supply system, an igniter which consists of an electrically heated nichrome coil, gears and stepping motors. All the equipment except a remote switch and a video monitor is installed in a rack of the capsule of the drop shaft.

Prior to the free fall of the capsule, the remote controlled fuel supply system is actuated to suspend a droplet at the spheroidal portion of the tip of the quartz fiber. This is driven by a pair of stepping motors which are actuated with the command of the remote switch outside the capsule via a controller. The free fall of the capsule generates a signal to turn on the heating current of the nichrome coil. This is followed by the approach of the igniter to the droplet for ignition. Right after the droplet ignition, the nichrome coil is removed and kept away from the droplet in order to prevent the droplet flame from being perturbed. Back lighted images of the droplet enveloped in a spherically symmetric flame are recorded by using a high speed video camera. Real time observation of all the events occurring inside the combustion chamber is monitored with the use of a video camera on board and a video monitor provided in the control room.

RESULTS AND DISCUSSION

Results obtained with the Japanese facility are described first. Figure 1 shows the time histories of the squared methanol droplet diameter burning in microgravity in various ambient pressures. The data can be fitted with straight lines. This indicates that the D^2 law is valid for the burning of a methanol droplet in high pressure stagnant gaseous environments. The slope of the straight line gives the burning rate. Fig. 2 shows the effect of ambient pressure on

505

the burning rate both under microgravity and terrestrial conditions. The abscissa is the ambient pressure relative to the critical pressure of methanol (P_c = 7.95 MPa). It is apparent that the burning rate increases monotonously with increasing ambient pressure. This implies that the burning rate is unlikely to show a peak near the ambient pressure equal to the critical pressure of the methanol. Microgravity causes the burning rate to be lower than the one under normal gravity.

The results obtained with the French facility show similar trends. The average burning rates of methanol droplets determined under normal and reduced gravity are compared in Fig. 3 for a pressure range extending up to P_r = 1.15. As expected, the reduced gravity K values are lower than the normal gravity values; both increase however continuously with increasing pressure. The strong increase of K with pressure above P_r = 0.8 under normal gravity remains unexplained.

Results obtained both with Japanese and French facilities under normal gravity and two different residual gravity levels confirm therefore that the burning rate of methanol droplets increases with increasing pressure. This behavior is likely to be explained with the decrease of the latent heat of vaporization with increasing pressure. The reduced pressure levels attained in both studies do not allow to address properly the question of the minimum burning time (or maximum burning rate) in the vicinity of the critical pressure. It is however illuminating to discuss the differences observed in both studies. This discussion is conducted by using Fig. 4 where the French to Japan ratio of methanol droplet burning rates is plotted against reduced pressure. Several quantitative observations can be made.

Under normal gravity conditions, methanol droplet burning rates obtained with the two facilities are close up to P_r = 0.2. The burning rates obtained with the Japanese facility increase strongly for higher pressures and attain values almost twice the French values. Several factors may cause this difference. First, the dimensions of the suspending fiber used in Japanese experiments are larger; therefore larger droplets (about 2 mm in diameter) are suspended. The fiber effects are therefore larger in the Japanese case. Furthermore, larger droplets will be subject to larger Grashof numbers and larger buoyancy effects. Differences in the heating energy supplied during the ignition may also explain some of the differences.

Under reduced gravity conditions, methanol droplet burning rates obtained with the Japanese facility is lower than the French values, up to P_r = 0.3. This is expected as the residual gravity level in the JAMIC drop shaft should be about three order of magnitude lower than that obtained during parabolic flights. The ratio is however well below unity for increasing pressures. Again, differences in the experimental procedures may explain this result. With increasing pressures, as the droplet burning time decreases, the ignition heating time becomes a more important factor. Comparisons reveal that the relative times the ignition coil spends in the vicinity of the droplet after ignition are larger in the experiments conducted with the Japanese facility.

CONCLUSIONS AND FUTURE WORK

A franco-japanese collaboration program on microgravity combustion has been initiated. Part of this program is devoted to the investigation of high pressure methanol droplet vaporization and burning. Two different facilities have been used in Japan and in France both under normal gravity and reduced gravity conditions. Each facility uses the fiber suspended droplet technique. Experiments have been conducted jointly by the two teams. Reduced gravity conditions have been generated in France by the use of parabolic flights ; several campaigns have been previously conducted with the CNES Caravelle ; a joint campaign has been conducted with the NASA KC-135 aircraft. Several experiments have been conducted in Japan at the JAMIC drop shaft.

One objective of the study is to determine the pressure effects on the burning rate and burning time of methanol droplets, under both subcritical and supercritical gaseous environments. A related issue is to obtain this information under variable residual gravity levels, in order to analyze the gravity induced buoyancy effects on droplet burning

phenomena. Experiments with both facilities and under normal gravity and two residual gravity levels confirm the strong increase of the methanol droplet burning rates up to the critical pressure. Important quantitative differences have been however observed between the burning rate values obtained by using the two facilities, under normal gravity and reduced gravity. It appears therefore crucial to homogenize the experimental procedures in both facilities. In the near future, joint parabolic flight experiments will be conducted by using the CNES Airbus Zero g. This campaign is planned for May 1997. A second joint JAMIC drop shaft experiments campaign is planned for November 1997. During 1998, a dedicated experimental facility will be jointly developed and will be used both in JAMIC experiments and during the parabolic flights of the CNES Airbus. In parallel, ESA supported sounding rocket experiments will be conducted by the French team in November 1998.

ACKNOWLEDGMENTS

REFERENCES

[1] B. Vieille, C. Chauveau, X. Chesneau, A. Odeide and I. Gokalp, *Twenty-Sixth Symposium (International) on Combustion*, The Combustion Institute, 1996. To appear

[2] T. Kadota and H. Hiroyasu, *Eighteenth (International) Symposium on Combustion*, The Combustion Institute, Pittsburgh, pp. 275-282, 1981

[3] C. Chauveau, X. Chesneau, X., and I. Gokalp, *Adv. Space Res.* 16 : 157-160, 1995

[4] J. Sato, M. Tsue, M. Niwa, and M. Kono, *Combust. Flame* 82 : 142-150, 1990

[5] X. Chesneau, C. Chauveau and I. Gokalp, *AIAA Paper No. 94-0688,* 1994

[6] D.B. Spalding, *ARS J.* 29 : 828-835, 1959

[7] C. Chauveau, X. Chesneau, and I. Gokalp, *AIAA Paper No. 93-0824,* 1993

[8] M.Y. Choi, *PhD thesis*, Princeton University, Princeton N.J., 1992

[9] G.S. Jackson and C.T. Avedisian, *Proc. R. Soc. Lond,* A446, 255-276, 1994
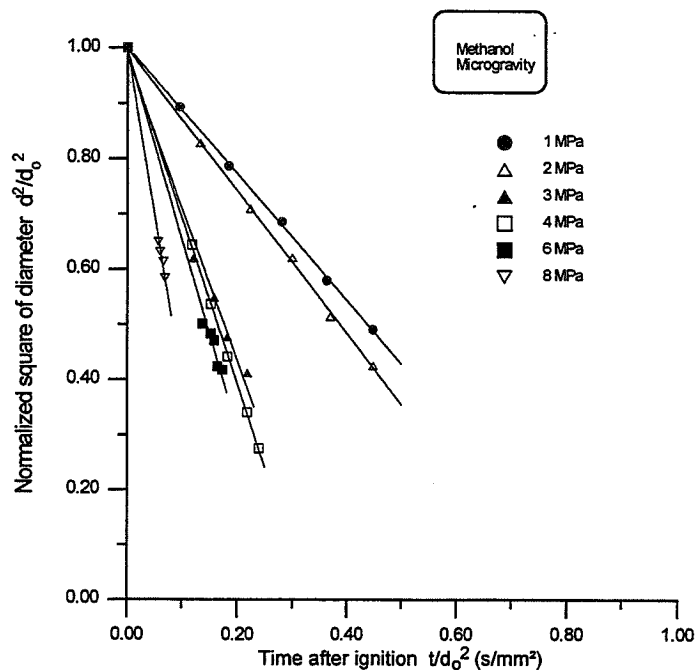
Fig.1 Time histories of the normalize squared droplet diameter versus pressure. JAMIC experiments.
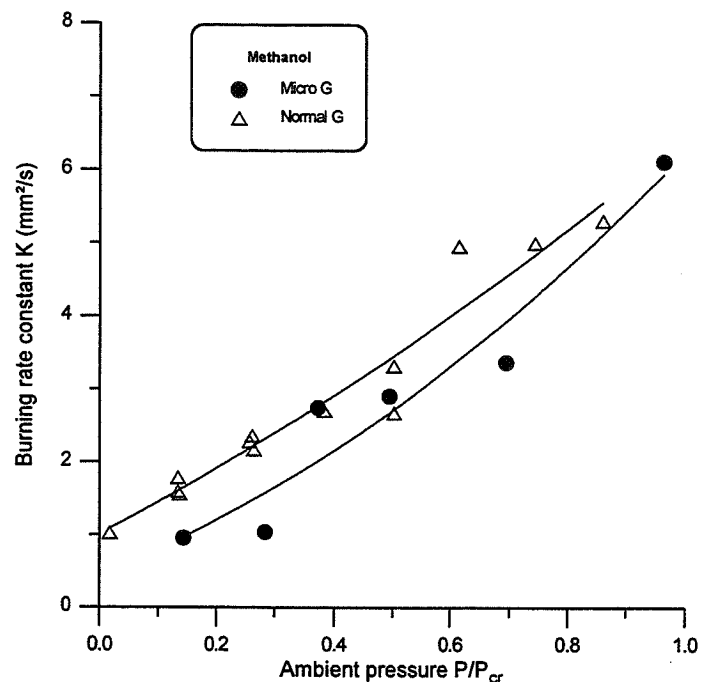
Fig.2 Variation of the average burning rate versus reduced pressure. Comparison between the normal gravity and JAMIC experiments with the Japanese facility.
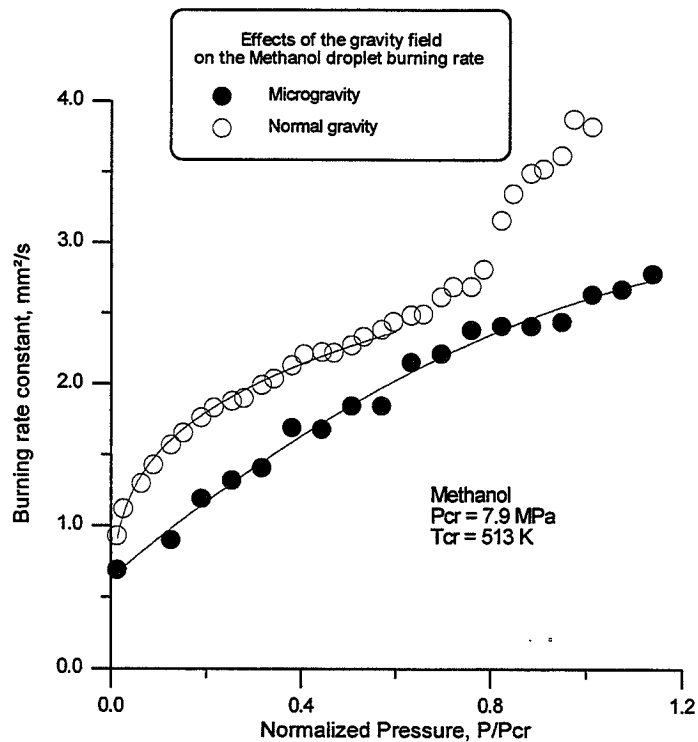
Fig. 3 Variation of the average burning rate versus reduced pressure. Comparison between the normal gravity and parabolic flight experiments with the French facility.
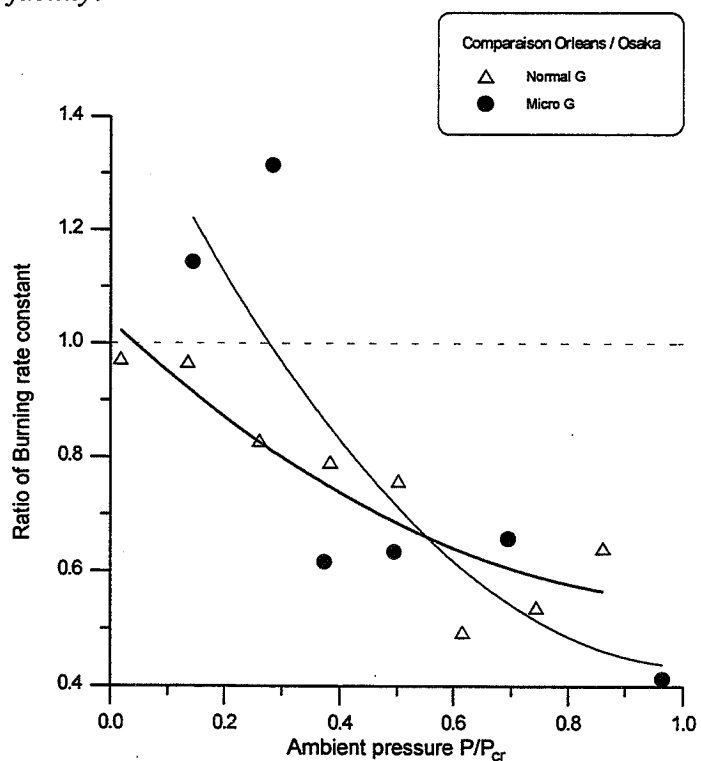
Fig.4 Comparison of the average burning rates obtained under normal and reduced gravity with the French and Japanese facilities, and the parabolic flights and the JAMIC drop shaft respectively.

508

Dispersed Fuels

Page intentionally left blank

HETEROGENEOUS COMBUSTION OF POROUS GRAPHITE PARTICLES IN MICROGRAVITY [1]

Harsha K. Chelliah
Department of Mechanical, Aerospace and Nuclear Engineering
University of Virginia, Charlottesville, VA 22903, USA
and
Fletcher J. Miller
Department of Mechanical and Aerospace Engineering
Case Western Reserve University, Cleveland, OH 44106, USA

Objectives

Recent theoretical investigations on graphite particle combustion have employed several levels of heterogeneous reaction models, ranging from global to elementary models, to describe the oxidation of carbon to gaseous products [1-5]. Unlike the counterpart homogeneous reaction models, these heterogeneous reaction models are not well developed because of the difficulties associated with decoupling the physical characteristics of the solid (e.g. surface area taking part in combustion) from the chemical kinetic data [6]. This is certainly true for *porous* graphite particle combustion, where heterogeneous and homogeneous reactions occur within the pores and play an important role in the overall oxidation process. As a result, there are considerable uncertainties of physical phenomena predicted using different heterogeneous kinetic models available in the literature. A good example, discussed later in this paper, is the predicted critical particle size below which the mass burning rate becomes exponentially small.

The main goal of this study is to understand the basic mechanism controlling such rapid changes in burning rates, by developing a model where physical contributions are decoupled from chemical rate constants in a consistent manner. Another important goal of the proposed study is to develop a truly intrinsic, detailed heterogeneous reaction model for porous graphite combustion at high-temperatures, and to derive a systematically reduced heterogeneous reaction model in terms of the elementary reaction rate constants of the detailed model. The validation of chemical kinetic models describing the heterogeneous and homogeneous combustion in and around a spherically symmetric porous graphite particle can be considerably simplified by experimental measurements obtained under microgravity conditions. A vital component of this study is to conduct such supporting experiments on particle burning rate and surface temperature using NASA microgravity facilities, in close coordination with the theoretical effort.

The basic understanding obtained and models developed as part of this project will be useful for optimal design of coal combustion devices. These models can also be extended to investigate the role of heterogeneous chemistry on pollutant formation pathways in combustion devices. The theoretical approach developed here, with pore diffusion effects decoupled from the chemical effects, can also be extended to understand the heterogeneous combustion of other porous fuels, for example, combustion of magnesium in a CO_2 environment for propulsion in the Martian atmosphere.

Approach

A theoretical model that can predict the burning rate of graphite particles, subject to the assumptions of spherically symmetric burning and quasi-steady surface regression, is already in place [4]. This model also assumes that the internal heterogeneous reactions can be lumped as a set of *ad hoc* semi-global reactions occurring at the external surface of the particle, similar to previous investigations [1, 2].

Currently, the above model is being extended to include (a) the two-phase combustion within the porous graphite (using a set of volume averaged equations and matching interface conditions with external homogeneous combustion) and (b) a reduced heterogeneous reaction model developed by introducing steady-state approximations to absorbed species at the surface. The predictions of mass burning rate and the surface temperature, with initial graphite particle sizes ranging from about 100 to 1500 μm and porosity up to about 40%, will be compared with experimental measurements planned under microgravity conditions. For these particles, the initial estimates indicate that the combustion durations range from about 2 to 22.5 sec. Hence, the supporting experiments can be performed using ground based NASA facilities, e.g. drop towers and the DC-9 aircraft. Important details of the theoretical and experimental aspects of the project are described below.

Theoretical Model

Figure 1 illustrates the typical transport and reactive processes, both heterogeneous and homogeneous, occurring near a spherical graphite particle. Under microgravity conditions, assuming a spherically symmetric flow field around the reacting particle, the conservation equations for mass, species and energy can be expressed as a function of the radial coordinate, r, simplifying the analyses considerably. The mathematical formulation of these conservation equations and numerical integration techniques are well known and described in detail elsewhere [5, 7, 8]. Here, only the essential details related to heterogeneous chemistry and pore diffusion are presented.

(i) Heterogeneous Reaction Models — (a) Detailed Reaction Model:
At sufficiently high surface temperatures (typically above 1000 K - although this value has been disputed recently [3]), the primary product of chemical reaction at the graphite surface is generally assumed to be CO. The overall surface reaction that forms CO, i.e. $2C + O_2 \rightarrow 2CO$, is postulated to occur through the following sequence of elementary surface reactions, $2C_f + O_2 \rightarrow 2C'(O)$ and $C'(O) + C_b \rightarrow CO + C_f$, where subscripts f and b identify the free-surface and bulk carbon sites, C(O) identifies adsorbed O-atom, and superscript $'$ identifies a mobile adsorbed site. At high temperature, the additional desorption path $C'(O) \rightarrow C(O)$ and $C(O) + C_b \rightarrow CO + C_f$ can contribute to the overall desorption rate. These oxidation reaction pathways of carbon have been extensively reviewed in Refs. [6]. Based on the published rate data, Mitchell et al. [3] have recently compiled an elementary adsorption-desorption surface reaction mechanism involving 16 species in 18 elementary reactions. This mechanism is listed in Table 1 and will be used here as the starting mechanism for the systematic development of the reduced heterogeneous reaction mechanism.

(b) Reduced Reaction Model:
Unlike gaseous species, the adsorbed surface species are neither convected or diffused in the direction normal to the surface. If the transport of mobile absorbed species is negligible, then the creation and destruction rates of these absorbed species should balance each other exactly, yielding steady-state approximations. Thus, the reduced heterogeneous reaction mechanism obtained with the application of steady-state approximation for absorbed species is an exact representation of the the elementary heterogeneous mechanism.

For the heterogeneous elementary mechanism listed in Table 1, by introducing the steady-state approximation for absorbed species $C'(O)$, $C(O)$, $C'(H)$, $C'(OH)$ and $C'(HO_2)$, an eight-step reduced surface reaction mechanism can be obtained, which is represented here by [5]

$$2C_b + O_2 \rightarrow 2CO, \quad \text{(I)} \qquad\qquad C_b + CO_2 \rightarrow 2CO, \quad \text{(II)}$$
$$C_b + H_2O \rightarrow CO + H_2, \quad \text{(III)} \qquad C_b + O \rightarrow CO, \quad \text{(IV)}$$
$$HO_2 + OH \rightarrow O_2 + H_2O, \quad \text{(V)} \qquad OH + OH \rightarrow O_2 + H_2, \quad \text{(VI)}$$
$$OH + H \rightarrow H_2O, \quad \text{(VII)} \qquad\qquad H + H \rightarrow H_2. \quad \text{(VIII)}$$
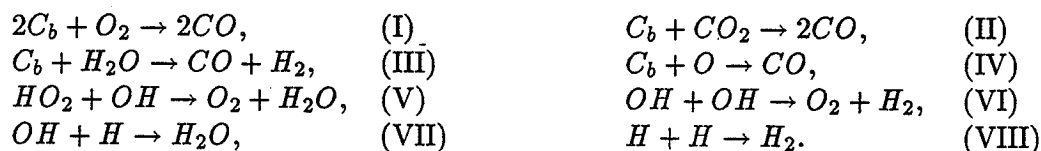
where the molar rates of the semi-global reactions I-VII are related to the elementary molar reaction rates ω_j as

$$\omega_I = \omega_1, \qquad\qquad\qquad \omega_{II} = \omega_2 - \omega_7,$$
$$\omega_{III} = \omega_3 + \omega_{18}, \qquad\qquad \omega_{IV} = \omega_8,$$
$$\omega_V = \omega_{11}, \qquad\qquad\qquad \omega_{VI} = \omega_{15},$$
$$\omega_{VII} = \omega_9 + \omega_{10} - \omega_{15} - \omega_{12} - \omega_{16} + \omega_{18}, \qquad \omega_{VIII} = \omega_{12} + \omega_{16} - \omega_{18}.$$

The steady-state relationships provide algebraic expressions for the concentration of surface intermediate species. Coupling between these expressions generally requires introduction of truncation approximations in order to obtain explicit expressions in terms of the known gas-phase species concentrations. Furthermore, these algebraic relations require information regarding the concentration of active surface sites, c_{C_f}. If the total number of active sites is conserved, then the following constraint must be satisfied $\sum_{i=1}^{N_s} Z_i = 1$, where Z_i is the fraction of sites occupied by species i. Since the surface concentration of ith species is given by $c_i = (S/N)Z_i$, where S is the surface density (assumed here as 10^{18} sites/cm^2 [3]) and N the Avogadro number (molecules/mole), the concentration of free-sites at the surface can be written as $c_{C_f} = S/N - \sum_{i=1, i \neq C_f}^{N_s} c_i$. Substitution of c_i's into the expression for c_{C_f} yields a quadratic equation for c_{C_f}, which can then be solved to obtain explicit expressions for the concentration of absorbed species [5].

The reactions (I)-(IV) indicated above correspond to consumption of carbon and production of CO, while reactions (V)-(VIII) correspond to recombination of gaseous reaction intermediates through adsorption-desorption reactions with carbon. In the elementary mechanism, the production of CO_2 by surface reactions is included in reaction 7, however, in the reduced surface mechanism the reaction 7 has been absorbed into ω_{II}. Hence, no explicit reaction for production of CO_2 is represented. Another important feature is that, for the starting elementary heterogeneous mechanism implemented, there is no reduced reaction of carbon with OH that leads to production of CO. Reaction 18 however does provide a reaction pathway to produce CO and, in fact, appears in the rate expression for ω_{III}. In contrast, *ad hoc* semi-global heterogeneous mechanisms discussed below have assumed explicit reaction of carbon with OH, producing CO.

(c) Semi-Global Reaction Model:
In most recent studies, the heterogeneous chemistry has been modeled by employing semi-global reaction models, as represented by reactions (I)-(IV) indicated above, but their rates were modeled by a set of overall rate constants. In estimating these rate constants, the internal reaction effects have been lumped into the specific reaction rate constants [2, 4]. Because such rate constants depend on the physical parameters of the graphite, physical phenomena predicted can be applicable only to the specific set of conditions.

To demonstrate the deficiencies of such semi-global rate constants, the mass burning rate ($\dot{m}$) and surface temperature (T_s) predictions of spherically symmetric graphite particles in a moist, hot oxidizing environment, using two sets of semi-global heterogeneous reaction models, are shown in Fig. 2. These predictions are obtained assuming quasi-steady particle regression rate. This figure indicates that when the semi-global rate constants corresponding to *non-porous* graphite kinetics are employed [4], $\dot{m}$ drops rapidly as particle diameter of 380 μm is approached. However, when rate data corresponding to porous graphite is employed, Fig. 2 shows that strong combustion conditions persist for much smaller porous graphite particles, assuming quasi-steady conditions. One goal of this investigation is to factor out surface area effects associated with such porous graphite, as described below, and obtain a truly intrinsic reduced heterogeneous reaction model.

(ii) Effects of Porosity and Two-Phase Modeling:
With increasing porosity of graphite, the gases diffuse further into the particle and as a result the internal surface area taking part in combustion can increase. By employing a set of volume average equations to describe the transport and chemical reactions within these pores, the physical effects can be decoupled from the finite-rate chemistry effects. Such an approach has already been implemented by the author to predict the combustion of porous graphite rods in a uniform flow field and is currently being implemented to the prediction of porous graphite particles under this project.

This effort requires utilization of interface conditions to match the two-phase solution describing the internal combustion and the external homogeneous combustion. The iteration procedure developed generally requires only a few iterations, typically less than 10, to match the interface conditions.

(iii) Effect of Particle Size on local Diffusion Time:
The rapid drop in mass burning rate observed in Fig. 2 for predictions with nonporous rate data can be investigated by estimating the chemical and physical time scales. Appropriate nondimensionalization of the governing equations shows that the characteristic diffusion time is proportional to the square of the particle size. In numerical calculations, the inverse of the scalar dissipation rate defined as $\tau = [2\alpha |dZ/dr|^2]^{-1}$, where α is the gas thermal diffusivity, provides a more convenient and rigorous method of obtaining a characteristic diffusion time of a burning graphite particle. For the overall reaction $CO + (1/2)O_2 \rightarrow CO_2$, the mixture fraction, Z, in the expression for τ can be obtained from [4]

$$Z = \frac{Z_{C,F}/W_C + Z_{O,F}/W_O - 2Z_{O,OX}/W_O + (2Z_{O,OX}/W_O)_2}{(Z_{C,F}/W_C + Z_{O,F}/W_O)_1 + (2Z_{O,OX}/W_O)_2},$$

where $Z_{j,F}$ the mass fraction of element j in the mixture associated with the fuel, and $Z_{j,OX}$ the mass fraction of element j in the mixture associated with the oxidizer. Subscripts 1 and 2 identify the conditions in the fuel and oxidizer stream, respectively.

Figure 3 shows a comparison between the four semi-global reaction rates for the nonporous case and the inverse diffusion time (τ^{-1}) estimated at the stoichiometric point, as a function of particle diameter. It is seen that as the critical particle size of about 380 μm is approached, the heterogeneous reaction rates decrease while the diffusion rate increases, leading to extinction of the chemical reactions. Similar analyses will be performed with the modifications introduced to decouple the surface area effects from the heterogeneous kinetic model as part of this project.

Experiments
We are in the process of building 1g apparatus and designing a drop/aircraft rig to perform oxidation rate and surface temperature measurements in low gravity. Similar to liquid fuel droplet experiments, the particle size regression rate is determined by imaging its silhouette onto a CCD array and tracking the digitized (from video tape) particle outline in four locations. Unique aspects of this experiment are the particle deployment, ignition and surface temperature measurement techniques. Only these details are discussed below.

(i) Particle Deployment:
In order to maintain the particle in the camera field-of-view during the experiment, as well as to hold it steady in the ignition region, the particle will be tethered on a 10 μm ceramic fiber. A method to drill holes in the particles using a mechanical drill of 12.5 μm diameter has already been developed. Both through-holes and single-ended holes have been tried; in the former case the fiber is threaded through the hole (see Fig. 4), in the latter it is pushed into the hole and held there with a dab of adhesive. In the case of the threaded fiber, the fiber itself is held at both ends by moderately tensioned strip springs; in the single-holed case it is cantilevered from a support.

(ii) Particle Ignition and Surface Temperature Measurements:
Ignition of the particle will be achieved using either hot wire type ignitors or by concentrated radiation. The latter method is preferred since that should lead to faster ignition, and will eliminate the disturbance of having a hot wire nearby which must be moved once ignition has been achieved. A 5W CO2 laser has been acquired for this purpose and is in the process of being setting up to ignite the particle. In addition, we plan to use concentrated light from projection bulbs in some experiments.

The surface temperature is an important parameter for heterogeneous kinetic model validation. In the present experiments, the surface temperature will be measured using a two-color optical pyrometer currently under development.

Future Work

On the modeling side, considerable progress has been made to decouple the surface area effects from heterogeneous kinetics. This effort needs to be combined with the detailed or reduced heterogeneous reaction models developed. In addition, for particles in the lower size range, the validity of the quasi-steady regression approximation must be evaluated by considering unsteady conservation equations.

Experiments at normal gravity conditions must be first performed to establish the compatibility of the particle deployment technique with different particle ignition methods planned. Once such studies are performed, experiments will be performed to gather mass burning rate and surface temperature data for model validations.

References

[1] Bradley, D., Dixon-Lewis, G., Habik, S.E., and Mushi, E.M.J., *Twentieth Symposium (International) on Combustion*, The Combustion Institute, p. 931 (1984).

[2] Cho, S.Y., Yetter, R. and Dryer, F.L., *J. Comp. Phys.* **102**, p. 160, 1992.

[3] Mitchell, R.E., Kee, R.J., Glarborg, P., and Coltrin, M.E., *Twenty-third Symposium (International) on Combustion*, The Combustion Institute, p.1169 (1991).

[4] Chelliah, H.K., *Comb. and Flame* **104**, pp. 81-94 (1996).

[5] Chelliah, H.K., "Numerical Modelling of Graphite Combustion using Elementary, Reduced and Semi-Global Heterogeneous Reaction Mechanisms," in *Modeling in Combustion Science*, (J. Buckmaster and T. Takeno, eds.), Lecture Notes in Physics, Springer-Verlag, Berlin, p. 130-147, 1995.

[6] Laurendeau, N.M., *Prog. Energy Comb. Sci.* **4**, p. 221 (1978).

[7] Williams, F.A., *Combustion Theory*, 2nd ed., Addison-Wesley, Menlo Park, CA, 1985.

[8] Smooke, M.D., *J. Comp. Phys.* **48**, p.72 (1982).

Table 1: Elementary surface reaction mechanism [3], where specific rate constants in the form of $k_j = A_j T^{\alpha_j} \exp(-E_j/RT)$

j	Reaction	A_j	α_j	E_j
1	$2C_f + O_2 \rightarrow 2C'(O)$	2.3×10^{16}	0	15000
2	$C_f + CO_2 \rightarrow C'(O) + CO$	4.8×10^9	0	30000
3	$C_f + H_2O \rightarrow C'(O) + H_2$	6.2×10^8	0	25000
4	$C'(O) \rightarrow C(O)$	5.0×10^{12}	0	70000
5	$C(O) + C_b \rightarrow CO + C_f$	2.0×10^{11}	0	60000
6	$C'(O) + C_b \rightarrow CO + C_f$	2.0×10^7	0	40000
7	$2C'(O) + C_b \rightarrow CO_2 + 2C_f$	4.0×10^{13}	0	35000
8	$C_f + O \rightarrow C'(O)$	2.0×10^9	0	1000
9	$C_f + H \rightarrow C'(H)$	2.0×10^8	0	1000
10	$C_f + OH \rightarrow C'(OH)$	2.0×10^8	0	1000
11	$C_f + HO_2 \rightarrow C'(HO_2)$	2.0×10^8	0	1000
12	$C'(H) + H \rightarrow H_2 + C_f$	2.0×10^9	0	1000
13	$C'(H) + OH \rightarrow H_2O + C_f$	2.0×10^9	0	1000
14	$C'(OH) + H \rightarrow H_2O + C_f$	2.0×10^9	0	1000
15	$C'(OH) + OH \rightarrow H_2 + O_2 + C_f$	2.0×10^9	0	1000
16	$C'(HO_2) + H \rightarrow H_2 + O_2 + C_f$	2.0×10^9	0	1000
17	$C'(HO_2) + OH \rightarrow H_2O + O_2 + C_f$	2.0×10^9	0	1000
18	$C'(OH) + C_f \rightarrow C'(O) + C'(H)$	1.0×10^{14}	0	20000

Units: mole, cubic centimeters, seconds, Kelvin and calories per mole
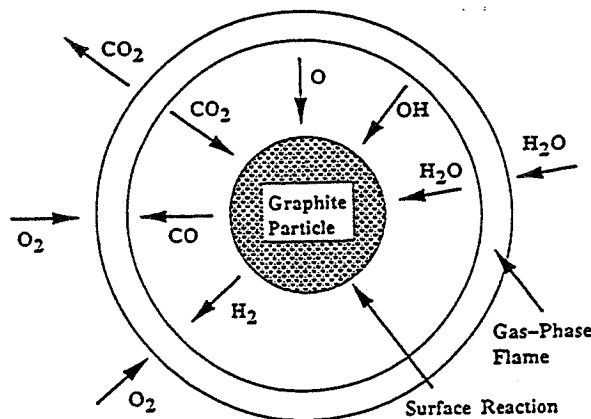
Figure 1: Illustration of the combustion process around a spherical graphite particle under idealized zero-g conditions.
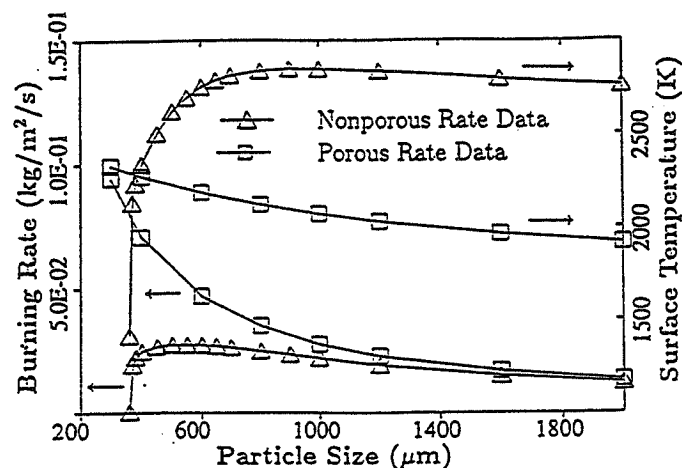

Figure 2: The mass burning rate and surface temperature predictions as a function of the particle diameter, burning in air ($Y_{O_2,\infty} = 0.232$, $Y_{N_2,\infty} = 0.762$, $Y_{H_2O,\infty} = 0.006$, $p=1$ atm, $T_\infty= 1400$ K); $\triangle$ = nonporous and $\square$ = porous semi-global rate constants.
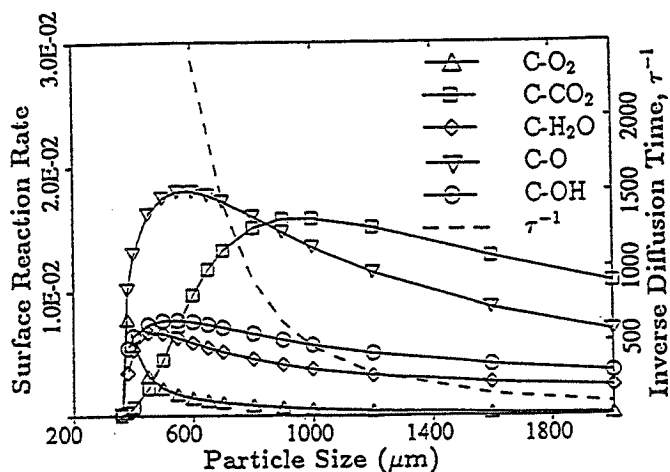

Figure 3: The semi-global surface reaction rates (kg/m^2/s) and the inverse diffusion time (s^{-1}) with nonporous rate data for conditions in Fig. 2.
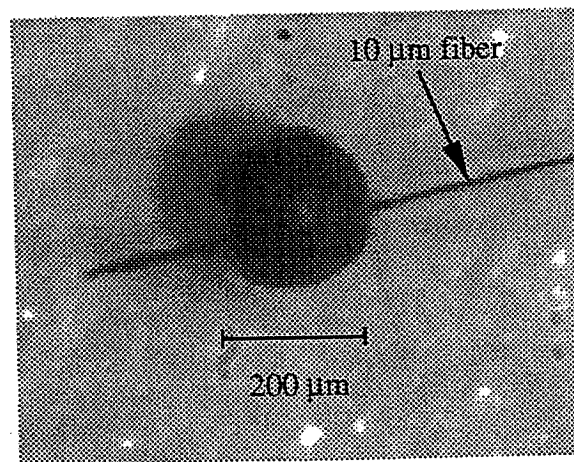
Figure 4: An image of $\sim$ 180 μm porous graphite particle with a 10 μm ceramic fiber threaded through it.

516

Detailed Studies on the Structure and Dynamics
of Reacting Dusty Flows at Normal and Microgravity

FOKION N. EGOLFOPOULOS AND CHARLES S. CAMPBELL
Department of Mechanical Engineering
University of Southern California
Los Angeles, California

Introduction

Two-phase reacting flows are substantially less understood compared to gas phase flows. While extensive work has been done on sprays, less attention has been given to the details of dusty reacting flows. Dusty flows are of particular interest for a wide range of applications. Particles can be present in a gas intentionally or unintentionally, and they can be inert or reacting. Inert particles can be also present in an otherwise reacting gas flow, and that can lead to flame cooling and modification of the extinction limits of a combustible mixture. Reacting solid particles can release substantial amounts of heat upon oxidation, and can be used either for propulsion (e.g. Al, B, Mg) or power generation (coal). Furthermore, accidents can occur when a reacting dust accumulates in air and which, in the presence of an ignition source, can cause explosion. Such explosions can occur during lumber milling, in grain elevators, and in mine galleries.

The addition of solid particles in a flowing gas stream can lead to strong couplings between the two phases, which can be of dynamic, thermal, and chemical nature. The dynamic coupling between the two phases is caused by the inertia which causes the phases to move with different velocities and in turn, leads to the development of forces and the modification of the velocity fields of both phases. In addition to the phase-interaction forces, thermophoretic, centrifugal, electrostatic, magnetic, and gravitational field forces can be exerted on the particles. The existence of electrostatic and magnetic forces critically depends on the presence of electric and magnetic fields as well as the physical properties of the particles, and is not frequently encountered in practical combustors. Furthermore, the centrifugal forces can be substantial only when strong flow rotation exists. On the other hand, the thermophoretic forces are caused by steep temperature gradients and can be important in reacting dusty flows. The gravitational forces are unavoidably present, and can play a substantial role in the overall dynamic response of the particle phase, especially for heavy particles. Indeed, existing experiments on dusty flows (e.g. [1]) indicate that global flame properties can be quite different when they are conducted at normal gravity and microgravity.

In assessing the thermal coupling, it must be first realized that as the thermal capacity of the solid phase is of the order of 10^3 times that of the gas phase, it will respond more slowly to the temperature changes induced by the flame and, through the interphasial thermal coupling, can slow the thermal response of the gas phase. Such temperature modifications can substantially affect the kinetics of each phase. The thermal equilibration process will depend on the thermal properties of the two phases. Similarly the emissivity of the solid phase is substantially higher compared to that of the gas phase and the radiative transfer from the particles are anticipated to be an important energy loss mechanism.

The ultimate challenge of this type of research is to better understand the chemical coupling between the two phases. The problem is complicated because the actual mechanisms leading to particle gasification can differ depending on the chemical composition of the particle. For example, carbon combustion in air is a surface reaction whose rate is controlled by the diffusion of oxidizing gaseous species towards the particle surface. On the other hand, powders such as Al, B, and Mg are first evaporated by the elevated temperatures and their vapor reacts with oxygen in the gas phase [2]. The chemical coupling between the two phases leads to particle size reduction, modification of the gas phase species composition, and the elevation of the temperature of both phases as a result of the exothermicity of both the surface and gas phase reactions. However, all particles begin this process as inert particles interacting with a combustion environment that must first be heated before they release volatiles and can themselves participate in the combustion process. Thus, one must first understand the more basic questions of the interactions of inert particles in a combustion environment.

The in-detail understanding of the dynamics and structure of dusty flows can be only advanced by considering first, simple flow geometries which (1) can be conveniently produced in the laboratory, (2) can be simulated with the use of detailed description of all the all physico-chemical processes in both phases, and (3) are of relevance to practical turbulent reacting flows. Past experience in gas phase combustion, has shown that the opposed jet, stagnation-type flows are likely candidates, given that the imposed strain rate is well-characterized, and that it allows for the in-depth understanding of the details of the pertinent physico-chemical processes.

Sung, Law and coworkers have recently conducted rigorous studies [3, 4] of the effect of strain rate and temperature gradients on the dynamics of small inert particles, as a way of understanding potential errors in experimental LDV measurements

that might arise from thermophoretic forces that cause the motion of the tracer particles to differ from that of the gas. These studies have included the detailed description of the particle Stokes drag and thermophoretic forces. Results have shown that depending on the particle size, strain rate, and temperature gradient, the particle velocity can substantially differ from the gas phase velocity which indeed compromises the fidelity of existing non-intrusive flow velocity measurement techniques. In these studies, the particle phase was not thermally coupled with the gas phase and was not allowed to affect the dynamics of the gas phase. Furthermore, the effect of gravity on the particle dynamics was not considered, as the focus of the study were the sub-micron sized particles, typically used as tracers, for which gravitational forces are negligible compared to fluid drag.

The dynamics and structure of reacting dusty flows can also have a strong dependence on the particle number density, n_p, defined as the number of solid particles per unit volume; such effects were not addressed in the previous studies [3, 4]. Nonetheless, the values of n_p observed in a combustion environment will in most cases be very small. This can be easily seen by realizing that a stoichiometric mixture of volatile particles and oxidizer requires delivering masses of the same order of each to the flame; but since the density of the solid is roughly three orders of magnitude larger than that of the surrounding gas, the volumetric loading will be of the order of 10^{-3}. Consequently, it is unlikely that particles will interact with one another and modeling information derived from studies on single particles in infinite fluids may be used with confidence.

Objectives

In view of the foregoing considerations, we have undertaken the task to conduct a long-term combined experimental and numerical study on the details of reacting dusty flows in which the effects of fluid mechanics, particle properties, steep temperature gradients, gas and particle detailed kinetics, and gravity are systematically addressed. More specifically we intend to undertake the following tasks:

1. Experimental determination of laminar flame speeds, extinction strain rates, and flammability limits for dusty flows at normal- and micro-gravity as functions of the particle type, particle initial diameter, particle initial number density, gas phase chemical composition, and ambient pressure.

2. Detailed numerical simulation of the experiments to the extent that current computational facilities allow. Results will be compared with experimental data and the adequacy of theoretical models will be assessed.

3. Provision of enhanced insight into the thermochemical coupling between the gas and solid phases as well as into the effects of the drag, gravitational, and thermophoretic particle forces on the overall burning response.

Experimental Approach

The counterflow configuration has already been experimentally implemented in microgravity facilities by the PI (FNE) for gaseous strained flames. The configuration includes two opposed nozzles from which the reactant streams emerge and impinge onto each other. The nozzles are of variable diameter ranging from 20 to 40 mm and they are surrounded by nitrogen coflow. The burner assembly is housed into a variable pressure chamber which operates between 0.1 and 10 atm. Ignition is obtained by using retractable electrodes and a powerful ignition circuit.

The conventional counterflow experimental configuration had to undergo some substantial modifications in order to appropriately handle and introduce the particles into the gas flow. Issues which are particularly important are the particle feeding especially under microgravity conditions, the establishment of a uniform particle loading and its accurate knowledge through direct calibration, the particle collection system, and the particle sizing.

The particle feeding system is a critical component of the overall design. In particular, it is necessary to design a system that will feed a uniform concentration of particles into a laminar flow. It will probably require several design iterations before a final design is decided upon. At the moment, we have implemented the design of Goroshin et al. [5], which with a few modifications would seem to best meet the requirements; our modified version is illustrated schematically in Fig. 1. In this design, the test powder is stored in a chamber directly behind the burner. A piston closes the far end of the chamber; pushing the piston forward feeds the material into the burner. Air seeded with submicron inert particles is then injected through a ring plenum surrounding the chamber, entering through a ring shaped jet that completely surrounds the chamber. The plenum itself is divided into two sections separated by a porous material. Air is injected into the outer plenum. The porous material generates enough pressure drop to evenly distribute the flow about the inner plenum and to ensure an even flow into the chamber. Moving the piston forward forces particles in front of the gas jets. The particles become entrained in the stream and most likely form into a cone centered in the chamber. The particle loading is largely controlled by the rate at which the piston moves forward.

The measurements to be conducted include the determination of the gas phase temperatures using thermocouples and the flow velocities, particle velocities, sizes, and number density by using the phase Doppler anemometry (PDA) technique along the

centerline of the counterflow. Given that these are simultaneous point measurements, a transverse mechanism will be designed to move the burners at a constant speed during the experiment. Thus, real time measurements of velocities and temperatures will be obtained throughout the centerline of the system. The unreacted particle collection will be obtained by passing all exhaust gases through appropriate filters. An overall schematic of the experimental configuration is shown in Fig. 2.

Numerical Approach

In this study, the particle number density is considered small enough so that the particles are very unlikely to encounter one another. The numerical simulations of the experiments will eventually include the integration of the axisymmetric steady conservation equations for both the gas and particle phases. While such an approach is one of the important later goals of the study, first a set of equations appropriate for the description of the system centerline was developed for both phases. By assuming that there is no property variation in the radial direction, a quasi-one-dimensional set of equations was derived for the gas phase, that is similar to the traditional gas phase formulation [6, 7]. The particle equations were formulated for each particle independently, as particles are not allowed to interact.

For inert particles, the gas phase continuity and species equations are identical to the ones of Refs. 6 and 7, but were modified by adding a term which represents the force exerted by the particles on the gas phase. The gas phase energy equation was also modified by including a term describing the conductive/convective heat exchange between the two phases. The axial particle momentum equation included the Stokes drag, thermophoretic, and gravitational contributions; the system configuration is assumed vertical (i.e., gravity points downwards). As the action of gravity and temperature gradients (and thus thermophoretic forces) only exist in the axial direction, the radial particle momentum equation included only the contribution of the Stokes drag. The particle energy equation included the contributions of conductive/convective heat exchange between the two phases, the radiative energy from the particle, and the energy which is radiated by the gas phase and is absorbed by the particles. Finally, a conservation equation for the particle number density was formulated.

The solution was obtained by simultaneously integrating the entire system of equations for both phases. A subtle point of the procedure was that, while the gas phase equations were integrated in a Eulerian frame of reference, the particle equations were integrated in a Lagrangian frame of reference. It was found that this is necessary, as it is possible for particles to reverse their direction of motion, which lead to singular behavior of the Eulerian solutions. Physically, this can be understood because the particle reversal means that at some locations there may be multiple solutions while particles may not reach other locations so that the particle velocity would be undefined. However, these present no problem for a Lagrangian formulation. Details on the equations formulation and solution procedure can be found in Ref. 8.

Summary of Research

Given the complexity which reacting particles introduce, as a first attempt, the dynamic, thermal, and gravitational effects introduced by chemically inert particles were studied. Thus, a systematic detailed numerical study is presented for inert Al_2O_3 particles embedded in strained, laminar premixed flames, which are stabilized in a stagnation-type flow configuration. Studies of chemically reacting particles will follow.

The numerical simulations were conducted for opposed-jet, atmospheric, laminar premixed H_2/air flames, with a nozzle separation distance of 1.4 cm (left nozzle located at x=-0.7 cm and right nozzle at x=+0.7 cm) and for equivalence ratios, ϕ, of 0.57 and 0.25. The nozzle exit velocities, u_{exit}, of the gas phase were identical for both nozzles and varied from as low as 14 cm/s to as high as 800 cm/s. The particles were injected from one nozzle only with a velocity equal to the gas phase velocity, u_{exit}.

The twin-burner assembly was considered to be vertical so that the gravitational forces would act along the direction of the system centerline. Given the unidirectional nature of gravity, its effect on the particle dynamics was considered for three cases. The first case was that of (+g), in which the particles were injected from the bottom nozzle with the gravity opposing the particle axial motion. The second case is that of (-g), in which the particles were injected from the top nozzle with the gravity favoring the particle axial motion. The third case is that of zero gravity (0-g). The (+g) and (-g) conditions can be easily produced in the laboratory under normal gravity conditions. The (0-g) conditions can and will be produced in special NASA facilities such as a drop tower and/or a parabolic-trajectory aircraft.

In all figures which follow, the particles were injected from the left nozzle at a spatial location x=-0.7 cm with a direction from left to right. By injecting particles from one nozzle only, an asymmetry was imposed to the system. This was intentional as it allows for the possibility of particle penetration into the opposing side of the (gas phase) stagnation plane which leads to a variety of dynamic and thermal phenomena. In the previous studies of Sung et al. [4, 5] only small particles were studied, which nearly follow the gas phase and always stagnate closely to the gas phase stagnation plane. Two identical premixed flames are established, symmetrically on each side of the stagnation plane.

In the present study, the particle diameter, d_p, was varied from 0.3 to 100 μm, which is the range of interest for our scheduled experiments. Finally, the injection number density at the nozzle exit, $n_{p,inj}$, was varied from values as low as 10 particles/cm^3 to values high enough to cool the flame to near-extinction.

Figure 3 depicts comparisons between gas phase velocity, u_g, and particle velocity, u_p, for $\phi=0.25$, $d_p=0.3$ and 5 μm, and for $u_{exit}=100$ cm/s. Results indicate that for $d_p=0.3$ μm, the particles follow closely the gas phase in the hydrodynamic zone, and that inside the flame zone the thermophoresis causes a reduction of the magnitude of u_p. Typically, both the 0.3 and 5.0 μm particles used to generate the data in Fig. 3, possess small particle inertia as is desirable for tracer particles used in LDV and PIV measurements, and it was shown that these particles can closely follow the gas phase, and they reach zero velocity at the stagnation plane of the gas phase. By further increasing the particle inertia, which may be accomplished either by increasing the injection velocity and/or the particle diameter, it is possible that the particles will penetrate the stagnation plane of the gas phase and stagnate at a different location. This is illustrated in Fig. 4 for the $\phi=0.57$ flame, $u_{exit}=400$ cm/s, and for various particle sizes. Figure 4 depicts that for $u_{exit}=400$ cm/s, the 10 and 20 μm particles penetrate the gas phase stagnation plane, and stagnate within the region of the opposing jet emerging from the upper burner. This leaves them with zero velocity in a region of reversed gas flow. Consequently, the particles reverse direction and again cross the gas phase stagnation plane where they may stagnate again and undergo a subsequent reversal. This results in an oscillating motion, but one that is strongly damped, so that the particles eventually stagnate on the gas phase stagnation plane. This behavior has been previously observed experimentally by Gomez and Chen [9] and numerically by Gutheil and Sirignano [10] for droplets in stagnation flow configurations. The results of Fig. 4 indicate that the 20 μm particles penetrate deeper into the opposing jet regime than do the 10 μm particles because of their increased inertia. Furthermore, the 50 μm particles have a high enough inertia to reach all the way to the opposing nozzle exit.

Scaling arguments based on the conservation equations indicate that the effect of gravity on the particle dynamics will be substantial for low convective velocities and for large particles. Simulations at (+g), (-g), and (0-g) were conducted for the $\phi=0.25$ flame with $u_{exit}=14$ cm/s and $d_p=5$, 10, 20, 50, and 100 μm and representing particle velocities are shown in Figs. 5 and 6. Figure 5 depicts that the velocity of a 20 μm particle does not follow the fluid motion (0-g curve) throughout the flow field. It can be seen that (+g) conditions result to a negative $d(u_p)/dx$ velocity gradient at the nozzle exit and the magnitude of this gradient was found to increase with d_p. Similarly, the (-g) conditions results in a positive $d(u_p)/dx$ gradient at the nozzle exit which again was found to increase with d_p. Figure 6 depicts that the gravity effect on u_p is even more dramatic for 50 μm particles. Under (+g) conditions, the particles stagnate at a short distance (~1 cm for the present conditions) from the nozzle exit before they reverse and eventually re-enter the nozzle. For (-g) and (0-g) conditions, however, the picture is different. The 50 μm particles penetrate deep into the flowfield, cross the gas phase stagnation plane, stagnate inside the opposing jet regime and subsequently reverse several times until they reach an equilibrium state. Notice that at (0-g) the equilibrium state lies on the stagnation plane, while for (-g) the equilibrium state lies to the right of the stagnation plane in the counterflowing stream where the velocity slip supports the particle against gravity. This may explain the substantial differences which have been observed for the burning rates of reacting dusty flows under normal- and micro-gravity conditions (e.g. [1]). The presence of gravity can affect the dynamic response of the particles and substantially modify the spatial distribution of the number density. For reacting particles, this is translated to a substantial modification of the rate at which (solid) fuel is supplied to the reaction zone and thus, one can expect the burning rate to be significantly affected.

The effect of gravity on the particle thermal state was also studied and results are shown in Fig. 7 for large particles and small injection velocities ($\phi=0.25$, $d_p=100$ μm and $u_{exit}=30$ cm/s). For (+g), these heavy particles stagnate well before they reach the gas phase stagnation plane and reverse towards the feed nozzle exit. During this excursion, the particles first are heated only to about 500 K, as they do not have a chance to interact with the hotter layers of the flame further downstream. During the return path, the particle cooling occurs gradually as the particle loses the heat retained by its large thermal capacity. At (0-g), the particles penetrate the gas phase stagnation plane and undergo several reversals. During these reversals, the particles follow a non-monotonic temperature variation, as they sequentially interact with hotter and colder gas layers. These results show that gravity might have a potentially strong effect on the particle thermodynamics as well as the particle dynamics.

The thermal effects on the gas phase was found to be significant as n_p increases. More specifically, by injecting particles at ambient temperature, the flames are cooled, and, as $n_{p,inj}$ was gradually increased, near extinction-conditions were observed. The cooling effect was found to be stronger for the left flame of the twin-flame assembly, as the left flame will interact first with the incoming cold particles (which are only injected from the left jet). It was also shown that this cooling effect was different for particles with small and large inertia, as the particles with large inertia penetrate deeper into the flowfield and can interact thermally with both jets. In Fig. 8, results are shown for the $\phi=0.57$ flame, with $u_{exit}=400$ cm/s, $d_p=50$ μm, and $n_{p,inj}=10$ and 7,010 particles/cm^3. For this case, the particle inertia is large enough that the particles can reach all the way to the opposing nozzle exit and thus, thermally affect the entire flowfield. For the $n_{p,inj}=10$ particles/cm^3 case, the T_g is unaffected, while for the $n_{p,inj}=7,010$ particles/cm^3 case, the T_g is substantially reduced throughout the flame assembly, with, as would be expected, a

520

more profound effect on the left side of the flame assembly. The T_p is also lower compared to the $n_{p,inj}=10$ particles/cm^3 case, again reflecting the reduction in flame temperature, and its value reduces gradually as it approaches the right nozzle. Thus, these particles remove thermal energy from the high-temperature regions of the gas phase, can transfer this energy to other parts of the flowfield, and can eventually preheat the flow coming from the right nozzle. This can be seen in Fig. 8, as the gas phase temperature of the jet emerging from the right nozzle, starts increasing well ahead of the flame, which is a result of the preheating by the particles.

Acknowledgments

References
1.   KOBAYASHI, H., ONO, N., OKUYAMA, Y., AND NIIOKA, T.: *Twenty-Fifth Symposium (International) on Combustion*, Combustion Institute, Pittsburgh, 1994, pp. 1693-1699.
2.   BALLAL, D.R.: *Proc. R. Soc. Lond.* A 385, pp. 21-51 (1983).
3.   SUNG, C.J., LAW, C.K., AND AXELBAUM, R.L.: *Combust. Sci. Tech.* 99, pp. 119-132 (1994).
4.   SUNG, C.J., KISTLER, J.S., NISHIOKA, M., AND LAW, C.K.: *Combust. Flame* 105, pp. 189-201 (1996).
5.   GOROSHIN, S., KLEINE, H., LEE, J.H.S. AND FROST, D. Microgravity Combustion of Dust Clouds. Quenching Distance Measurements. *Third International Microgravity Combustion Symposium*, NASA Lewis Research Center, Cleveland, Ohio, April 11-13, 1995.
6.   KEE, R.J., MILLER, J.A., EVANS, G.H., AND DIXON-LEWIS, G.: *Twenty-Second Symposium (International) on Combustion*, Combustion Institute, Pittsburgh, 1988, pp. 1479-1494.
7.   EGOLFOPOULOS, F.N. AND CAMPBELL, C.S.: *J. Fluid Mech.* 318, pp 1-29 (1996).
8.   EGOLFOPOULOS, F.N. AND CAMPBELL, C.S.: Dynamics and Structure of Dusty Reacting Flows: Inert Particles in Strained, Laminar, Premixed Flames. *Western States Section/Combustion Institute*, Fall Technical Meeting, University of Southern California, Los Angeles, California, October 28-29, 1996.
9.   GOMEZ, A. AND CHEN, G.: *Combust. Sci. Tech.* 96, pp. 47-59 (1994).
10.   GUTHEIL, E. AND SIRIGNANO, W.A.: Counterflow Spray Combustion Modeling with Detailed Transport and Detailed Chemistry. *Western States Section/The Combustion Institute*, Spring Technical Meeting, Arizona State University, Tempe, Arizona, March 10-12, 1996.
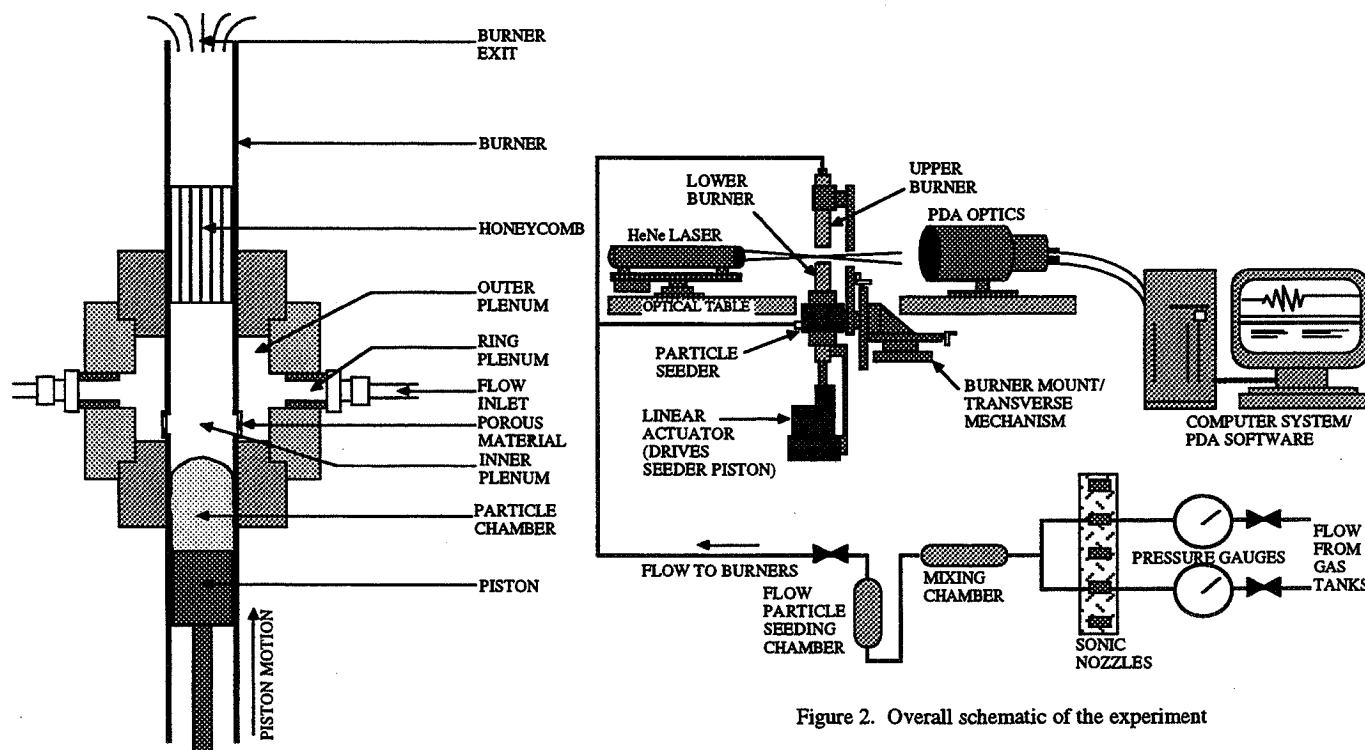
Figure 1. Schematic of the burner

Figure 2. Overall schematic of the experiment
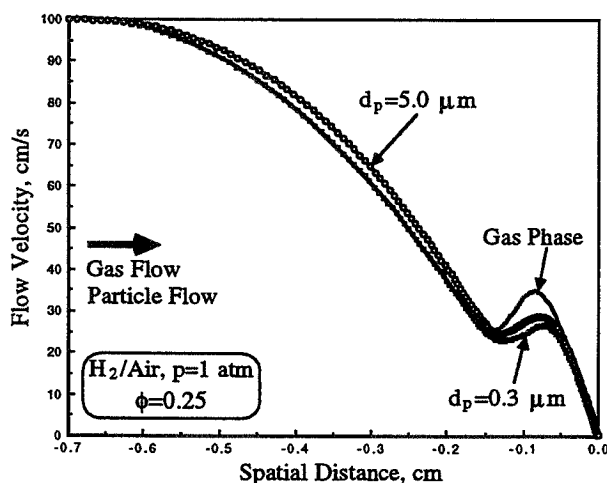
Figure 3. Effect of Stokes drag and thermophoresis on particle dynamics.
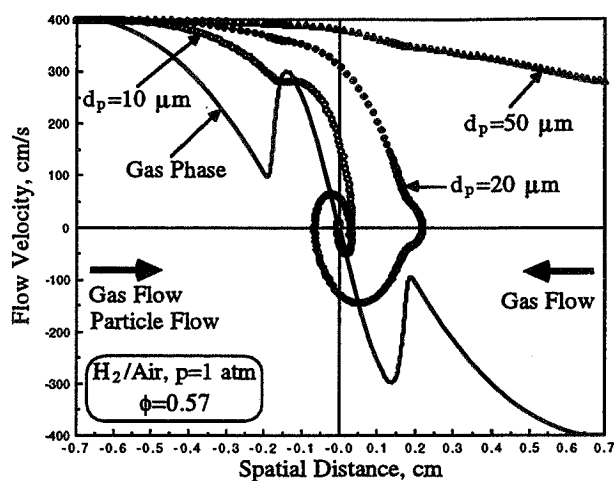
Figure 4. Effects of particle inertia on particle dynamics and the phenomenon of particle reversal.
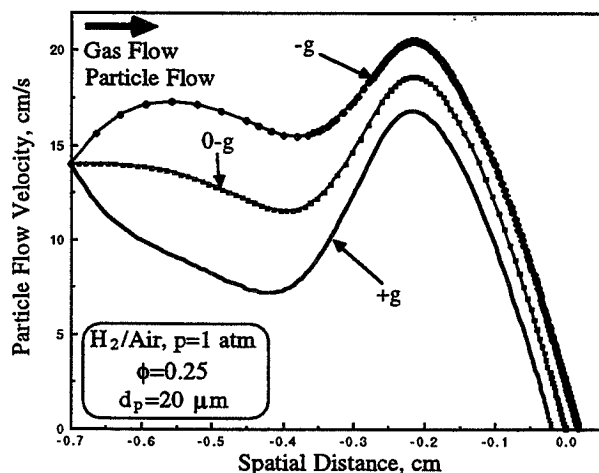
Figure 5. Effect of gravity on the particle dynamics.
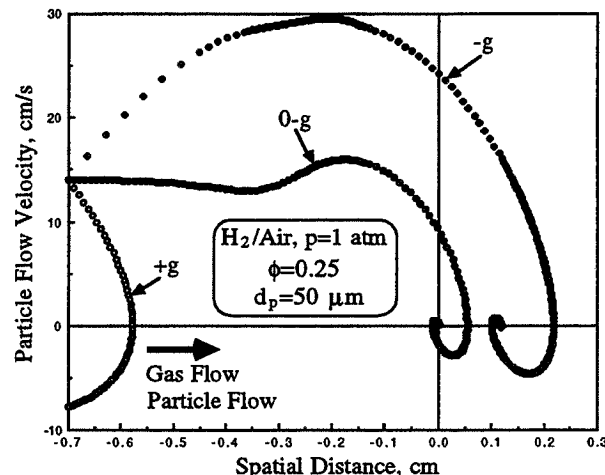
Figure 6. Effect of gravity on the particle dynamics.
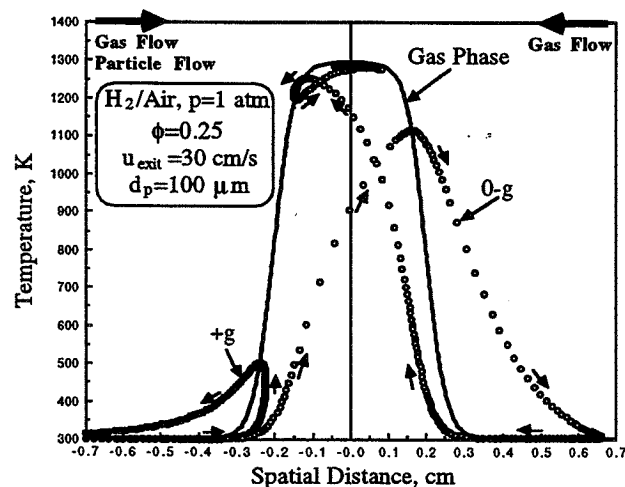
Figure 7. Effect of gravity on the particle thermal state. Arrows indicate the direction of particle motion.
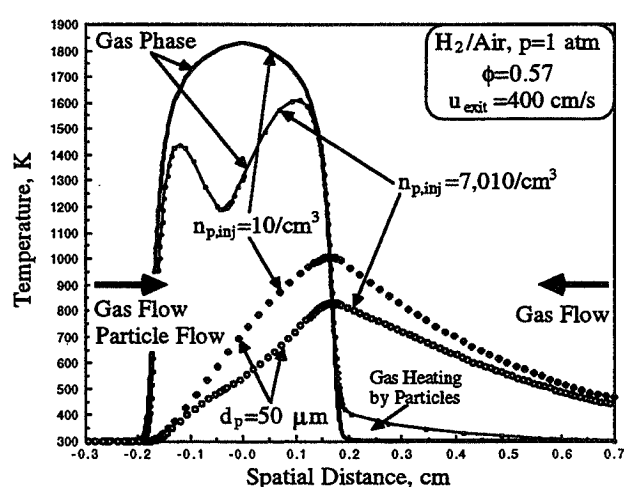
Figure 8. Effect of particle number density on the thermal states of the gas and particle phases.

RECENT DEVELOPMENTS IN SPRAY COMBUSTION: EXPERIMENTS AND MODELING

ALESSANDRO GOMEZ, Mitchell D. Smooke, Gung Chen, Adonios Karpetis and Lingping Gao
Yale Center for Combustion Studies
Department of Mechanical Engineering
Yale University, New Haven, CT 06520

Introduction

The current research program under NASA sponsorship (NAG3-1688) focuses on the study of fundamental aspects of spray diffusion flames at normal and reduced gravity. The objective of this program is to bridge the gap between classical single-droplet burning studies and practical spray flames, by using a variety of well-defined configurations, encompassing both laminar and turbulent spray diffusion flames. In the remainder of this article the main accomplishments in the two-year period (3-15-95 to 3-14-97) since the last International Microgravity Combustion Conference will be reviewed. A detailed account of the research activity is given in (refs. 1-10).

Laminar Co-flow Spray Diffusion Flames

The structure of axis-symmetric spray diffusion flames was examined by coupling a monodisperse electrostatic spray to a co-flow burner (refs. 1,2,5,8). Laminar flames of heptane were stabilized in a co-flow of air. As a result of changes in the liquid flow rate and applied voltage, the initial droplet size was varied by a factor of two (between 34 μm and 67 μm) and the initial droplet velocity by about 20% (between 4.3 m/s and 5.4 m/s). All flames burning in air resembled in many respects a conventional candle flame (Fig. 1a). Rather than burning, the majority of the droplets simply evaporated at low temperatures in the inner core of the flame, which appeared as a relatively dark region. This inner core was enveloped by a higher temperature region where soot was present. Outside of the sooty region, a flame characterized by a soft blue luminescence could be clearly seen in the lower half of the luminous combustion region. The flame was lifted off the burner by 3 mm, which is the distance required to vaporize enough fuel to establish a premixed stabilizing ring flame. Droplet life-history along the centerline of the flames showed that the droplets follow the d-square law with evaporation coefficients ranging between 0.53 to 0.59 mm^2/s. These values are a factor of two smaller than the evaporation coefficient of a droplet surrounded by an individual flame, which implies that the interactive effect between the droplets results in a flame enveloping a droplet cloud within which droplets evaporate *but do not burn*. Droplet interaction, however, was not intense enough to cause a departure from the d-square law.

To assess which type of group combustion mode applied, radial scans at selected heights were performed in which droplet diameter, velocity and number density, were measured by Phase Doppler techniques. The measured "primary" variables can be combined to derive parameters that are typically used in group combustion models. One such a parameter is l/D, the average ratio of the interdroplet spacing to droplet diameter, in which the numerator is computed from the inverse cubic root of the measured droplet number density, as if the droplets were disposed on a cubic lattice. Although this parameter can in principle be calculated at all measurement locations, for a meaningful evaluation only the region enveloped by the common blue flame was considered (Fig. 1a), in which the droplet relative standard deviation was sufficiently small (< 0.17). The resulting data are plotted in Fig. 2 (left ordinate, dashed lines). The ratio typically increases along the radial direction, which is a consequence of both the expanding nature of the spray, caused by the droplet coulombic repulsion, and the stronger evaporation at locations closer to the flame. Values of l/D range from 16 on the centerline to about 50 at the outermost location within the spray core enveloped by the flame. Most of the measured values, especially those in the upper portion of the evaporation region, are larger than the typical values that experiments on droplet streams and theoretical models of multiple droplet combustion report as upper limit for the droplets to start experiencing significant interactions (refs. 11, 12). Furthermore, the present values are much larger than the flame standoff distance for individual droplet burning or the critical l/D for the transition from merged to separated flames in droplet array studies (ref. 12). This fact shows that droplet *clouds* are more effective than droplet arrays at inhibiting oxygen penetration (ref. 8).

The presented measurements can also be related to theoretical models of cloud burning. Chiu and coworkers (ref. 13) developed a theory of cloud combustion under the assumptions of a spherically symmetric cloud burning/evaporating quasi-steadily in a purely diffusive environment and of unity Lewis number. They identified as controlling parameter of the burning regime a group combustion number, G, defined as

$$G \equiv 2\pi n D R_c^2$$

where n is the droplet number density, D is the droplet diameter and R_c is the cloud radius. For sufficiently large values of G, *total* or *external* group combustion prevails, with flame sharing by the entire cloud of droplets; for G< G_{cr}, a critical value for incipient group combustion, *individual* droplet burning occurs. In intermediate cases, *partial* or *internal* group combustion prevails, which is characterized by a cloud of droplets surrounded by a common flame in the core of the spray and individual droplets burning near the spray boundaries. Confidence in the selection of this controlling variable comes also from the fact that equivalent ones were identified independently by Labowsky and Rosner (ref. 14) and Sichel and Palaniswamy (ref. 15).

Conditions are not uniform throughout the spray in terms of either average diameter or concentration of the droplets in the cloud. Thus, first a *local* variable identical to G is defined in which the cloud radius R_c is formally replaced by r the radial coordinate, and local values of n and D are used from the experimental measurements. In Fig. 2 (right ordinate, solid lines) the radial distribution of this local G is plotted at selected heights. A vertical arrow on the first four scans marks the flame location. The G variable at first increases along r, it reaches a maximum and then it decreases farther away from the flame axis. The location of the maxima approximately coincide with that of the flame. Selecting the maximum as the *global* group combustion number of the spray would amount to using the flame radius, R_f, as macroscopic length scale in the definition of G. This experimentally determined G number based on the flame radius falls into a fairly narrow range between 0.46 and 0.35 in the first three scans, with a value of 0.3 in the fourth radial scan, which however is vitiated by somewhat broader size distributions. The uncertainty in this derived quantity is estimated at 19 %. This value is comfortably above the critical value for the transition from external group combustion regime to individual droplet burning. Farther downstream, as shown in Fig. 2 by solid curves without symbols, the local G number attains much smaller values. However, this is no indication of individual droplet burning. In fact, once a common envelope flame is established right above the ring stabilization region, it acts as a barrier for oxygen to penetrate into the flame core. Consequently, it is the bottom part of the flame that sets the stage for the burning mode of the bulk of the spray, as further elaborated in ref. 8.

An additional check that a G number based on flame radius is, indeed, the appropriate global parameter characterizing spray burning mode is to assess if, by changing its value relative to G_{cr}, the transition from one burning mode to another can be induced. To that end, the oxygen concentration in the free stream was increased without altering either the heptane flow rate or the applied voltage. In other words, the atomization conditions were kept constant, which implies that initial size, velocity and concentration of the droplets were unaffected, to a first approximation. As the oxygen concentration was raised in the oxidizer stream, the flame moved inward, closer to the centerline. Consequently, the relevant G number became smaller and smaller, while G_{cr}, that is a function of the oxygen mass fraction in the free stream, increased. Oxygen could penetrate farther and farther into the core of the spray and the percentage of droplets experiencing individual droplet combustion progressively increased. When the oxygen concentration reached the value of 0.62 on a molar basis, corresponding to a $G_{cr} \approx 0.2$, most soot could be eliminated and the flame, shown in Fig. 1b, appeared 30% shorter (flame height = 24.3 mm) than the base case, with the bottom part completely blue and the top half characterized by a faint orange luminosity. Unlike the base case flame in Fig. 1a, the oxygen-rich flame showed a multitude of blue streaks, that were evidently caused by individually burning droplets "radiating" from a common source.

Estimates of the Grashof number, Gr, based on the dimensions of the droplets used in these experiments (e.g., 50 μm) and the prevailing temperature fields (e.g., $\Delta T/T \cong 1.5$) yielded $75 \cdot 10^{-6}$, implying that gravity should play no role if droplets were to burn individually. On the other hand, if droplets burn as a cloud, as the previously discussed measurements indicate, the length scale that should appear at the numerator in Gr with a third power exponent is some characteristic size of the cloud that is of the same order of a flame dimension, since the Grashof number should be based on the size of the hot gas region which is convected by buoyancy. Such a dimension being on the order of one centimeter, Gr $\gg$ 1, in which case buoyancy is, indeed, expected to play a role. To assess such a role, the base case flame (Fig. 1a) was subsequently studied in microgravity in the drop tower at NASA-Lewis Research Center. Several changes in flame appearance were observed and can be explained by the virtual elimination of any buoyancy-induced flow in microgravity. The microgravity flames were found to be longer, similarly to the behavior of gaseous diffusion flames. Whereas the lower portion of the flame contour did not change significantly, the upper portion became wider. Blackbody radiation due to soot was also significantly enhanced under microgravity conditions, which resulted in much brighter flames. The fact that the flame base remained unchanged is a confirmation of the momentum-controlled nature of the flow field in the lower portion of the flame, as highlighted by gas velocity measurements (ref. 5). Farther up into the flame, when buoyancy effects are expected to take over in normal gravity, the elimination of such effects causes a decrease of the average velocity in the flame and an increase in residence times on the fuel side. From mass conservation, the decrease of average velocity within the upper portion of the flame must be accompanied by an increase in the average transversal dimension of the flame, which, in turn, translates in an increase in oxidizer diffusion time towards the flame centerline. Since flame length is defined by the condition of stoichiometric fluxes of fuel and oxidizer at the flame centerline, the general increase in characteristic times of the problem causes taller and wider flames, as observed. Soot, that is formed on the fuel side, has opportunity for further growth, which results in generally larger concentrations and brighter flames. Under certain conditions, soot oxidation in the upper part of the flame was not even complete and the flame opened up emitting a black streak of smoke. These observations confirm that the flames are under a mixed regime, with a momentum-controlled base and a buoyancy-controlled upper part.

In Fig. 3 some characteristic heights of five flames are plotted versus the fuel liquid flow rate. In particular, H_V is the height of the dark region where most of the evaporation occurred, whereas the other two heights are the luminous flame height at normal gravity and under microgravity conditions, respectively, all heights being measured from the burner plate. Similar to laminar gaseous diffusion flames, the luminous flame height at normal gravity is linearly proportional to the fuel flow rate over the examined range of liquid fuel flow rates. This finding is indirect confirmation of the fact that droplet evaporation is not controlling the overall flame structure. The dark region occupies a sizable portion of the flame, whose height ranges from 53 % to 76 % of the total luminous height, depending on the liquid flow rate. Despite the comparable size of H_V and $H_t(1g)$, the gaseous residence time and the droplet evaporation time are very different (ref. 5). Under microgravity conditions, the total height is still a monotonically increasing function of flow rate, but the dependence is no longer linear.

Laminar Counterflow Spray Diffusion Flames

The comparison of the experiments presented so far with theoretical models was somewhat contrived because the latter were conceived under idealized conditions that cannot be realized in the laboratory (e.g., spherical symmetry, no convection, etc.). Numerical modeling on the other hand, if properly validated, can provide a quantitative understanding of spray flames. Accordingly, a modeling effort was initiated. It was focused on the counterflow spray flame configuration that, being one-dimensional, offers significant simplifications from a computational standpoint. The steady-state, two-dimensional axisymmetric governing equations for the conservation of mass, chemical species, momentum and energy in the gas-phase were modified to include source/sink contributions accounting for the interaction with the fuel droplets (ref. 9). The statistical droplet size distribution, that had been experimentally measured by a Phase Doppler technique, was discretized into a number of sections. For each section, conservation equations were specified for mass, momentum and energy that enabled us to compute the source/sink terms in the gas-phase governing equations, through which the two phases were coupled (ref. 16). The spray was dilute enough that collisions between droplets were negligible. Droplets were assumed to be surrounded by a quasi-steady spherically symmetric film. The temperature within each droplet was spatially uniform but time varying, as it traveled towards the flame. The complexity of the system of gas equations was reduced by seeking a similarity solution, that, when substituted into the two-dimensional governing equations, yielded a nonlinear two-point boundary value problem in the axial direction. The combined gas/spray system was solved in a two step procedure, treating the spray and gas phase equations separately and solving iteratively. The chemical production rates, binary diffusion coefficients, mixture viscosity and mixture thermal conductivity were evaluated using vectorized and highly optimized transport and chemistry libraries. All calculations were performed in double precision on a IBM RS/6000 590 computer.

In the presence of a spray, such similarity solutions could only be derived under some restrictive assumptions on the liquid phase. Specifically, the model is limited to small slip velocities or small droplet Reynolds numbers. To achieve these conditions, a commercial ultrasonic nebulizer was coupled to the burner. Using helium as an inert on the fuel side to promote mixing of droplets and carrier gas, flat stable flames of either methanol or heptane were stabilized in the counterflow configuration. Experimental measurements provided the boundary conditions for the numerical code.

Figure 4 shows a comparison between experimental measurements and calculations of the gas-phase temperature in the spray flame, for which the kinetic mechanism in (ref. 18) was used. For quantitative comparison between experiments and calculations it was necessary that the velocity gradient at the boundary be carefully determined, without relying on a priori assumptions on the type of (plug versus potential) flow. The agreement between gas-phase temperature measurements and computations was very good throughout the domain. At the boundaries, adiabatic or nearly adiabatic conditions were verified experimentally. Farther downstream, the temperature increased and reached a calculated peak value of 1666 K at z=0.45 cm, to be compared with the measured 1638 K.

Figure 5 presents the total liquid mass concentration normalized with respect to the value at the fuel boundary as a function of the axial coordinate. The insets present droplet diameter distributions at selected axial locations. The leftmost one presents only the experimental size histogram, that was used as input in the numerical code to prescribe the liquid mass distribution in a total of nine diameter sections. The other two present a comparison between measurements (dashed bars) and computations (gray bars) farther downstream. The good agreement between measurements and computations in these figures shows that the droplet vaporization behavior is correctly represented. At z= 0.2 cm, the liquid fuel concentration was reduced to 1% of the initial value at the burner mouth. At this location the prevailing gas-phase temperature is only 865 K. Therefore, in the present flame no *direct* interaction between droplets and flame exist. Clearly, since the evaporation model was conceived for individual droplet evaporation (ref. 19), the spray is sufficiently dilute for droplet interactions not to cause significant effects. Noteworthy is that quasi-steady droplet evaporation applies also under transient temperature conditions, such as those experienced by the droplets in their path to complete vaporization.

As regards the role of gravity in this spray flame, the gas phase *per se* does not appear to be affected by buoyancy, except possibly at strain rates much lower than those of the present flame. In fact, the numerical code deals only with the radial component of the momentum equation, the axial component being replaced by a constant pressure approximation. On the other hand, droplet trajectories are affected by gravity. Since the velocity slip between the two phases is on the order of at most one or

two cm/s, the drag force acting on the droplets is not very large and the gravitational force is typically a non-negligible part of the total force acting on the droplet, especially for the large droplets in the size distribution. The present flame, however, is not very sensitive to gravitational details, since there is a separation of the order of two mm between the droplet vaporization plane, where most of the droplets disappear, and the flame location. It is anticipated that under conditions in which direct droplet-flame interaction occurs, that are currently under study, the flame structure will be much more sensitive to gravitational effects.

Although the present emphasis was not on the influence of liquid fuel dispersion on chemical species in flames, the successful validation of the code with respect to the physical variables suggests that it should be capable of addressing this issue, especially in the context of pollutant formation.

Turbulent Co-flow Spray Diffusion Flames

The objective of this part of the research program is the establishment of well-defined turbulent spray flames that capture general features of turbulent spray combustion. Such features are then studied by probing the flame with quantitative diagnostic techniques. To that end, a spray burner was designed, as sketched in Fig. 6, on the basis of the following two criteria. First, droplets were generated "gently" using an ultrasonic atomizer. As a result, the droplets had initially low momentum and were carried into the flame by a fraction of the air flow-rate that had been diverted around the atomizer stem. Since the velocity slip between droplets and gas was small, atomization effects on the structure of the spray flame were minimized. Second, efforts were made to maximize turbulence levels under burning conditions. The air was fed through holes in the periphery of a plate around the atomizer. A converging section at the top of the burner produced a recirculating pattern within the burner that ensured high levels of turbulence and at the same time stabilized the flame at the atomizer tip. Methanol was used as fuel in order to avoid soot production in the flame. The liquid flow-rate was 6.6 gr/min, while the air flow-rate was set at 80 l/min. The Re number under cold conditions was 21,000. Under burning conditions, some relaminarization inevitably occurred because of heat addition. Yet, the flame emerged from the burner surrounded by a highly turbulent and relatively cold air jet that ensured that turbulent conditions were maintained in the spray flame even at the burner exit. In addition to the measurements of droplet size and droplet and gas phase velocity by Phase Doppler techniques, gas phase temperature and nitrogen molar fraction were measured independently, using a recently developed spontaneous Raman spectroscopic technique, as detailed in (ref. 4).

The average and fluctuating gas velocities are plotted in Fig. 7. The average axial velocity $\overline{U}$ shows initially a dip at the centerline that persists up to $2D$, whereas all radial scans are "bell" shaped thereafter. This initial feature can only be attributed to the high local mass loading. In these dense areas of the spray a two-way coupling of momentum exists between the drops and the gas phase. The high liquid mass fractions result in gas deceleration. The subsequent acceleration of $\overline{U}$ on the centerline can be attributed to two factors: droplet vaporization, that provides a mass source locally, and momentum transport from the colder and faster turbulent air flow surrounding the spray flame. The fluctuating components u' shows good uniformity and small anisotropy in the second half of the measurement field. On the other hand, within the first two diameters from the burner mouth u' shows markedly high values that can be explained by radial mixing of large scale gas eddies that are convected axially by widely different velocities, consistently with the mechanism that explains the anisotropy of turbulent shear layers.

The results from the Raman spectroscopy, both in terms of average and RMS temperature are shown in Fig 8. The average temperature $\overline{T}$ shows a feature that is unexpected from the standpoint of gaseous jet flames. The temperature maximum occurs consistently at the spray centerline. Clearly, such result would be seemingly inconsistent with the concept of external or sheath combustion, which would suggest that the flame should be confined to the outer periphery of the spray. To verify that the flame location is on average away from the centerline, a line-of-sight emission measurement of excited CH radical at the exit of the burner was performed. Radial profiles of excited CH that were obtained from the Fourier-deconvolution of the line-of-sight measurements, showed that the flame never reaches the centerline, which confirms the prevalence of group combustion. Then, the only way to explain the temperature profiles of Fig. 8 is by considering the full convective-diffusive balance in the two-dimensional axisymmetric geometry. Further work in this area is currently in progress, as well as the analysis of passive scalar information.

Diagnostic Developments

New diagnostic methods were explored in two projects. In the first, a technique was developed for the determination of droplet size with an accuracy better than 1%, if the index of refraction is known and constant. The method entails imaging on a photodiode array the angular scattering intensity collected by a lens and applying a Fast Fourier Transform (FFT) to the array serial output to recover an effective frequency and phase corresponding to the number and position of the scattering lobes. In the second project, a single point Stokes/Antistokes spontaneous Raman thermometry technique for spray flames was developed. By using optical and acoustic techniques, interference effects from laser induced breakdown, droplet elastic light scattering and fluorescence were successfully screened out. Details of the two approaches are given in refs. 3 and 4, respectively.

526

References

1. Chen, G. and Gomez, A. "Group Combustion of a Dilute Spray in a Co-flow Laminar Diffusion Flame", Proceedings of the Third Asian-Pacific International Symposium on Combustion and Energy Utilization, Dec. 11-15, 1995, Hong Kong, Vol. 2, p. 384.
2. Chen, G. and Gomez, A. "On the Structure of a Co-flow Laminar Diffusion Flame", in "Recent Advances in Spray Combustion," (Kuo, K., Ed.), AIAA Progress Series, Ch. 8, AIAA, Washington, DC (1995).
3. Min, Sherman L. and Gomez, A., *Appl. Opt.* 35, p. 4919 (1996).
4. Karpetis, A. N. and Gomez, A., *Optics Letters* 21 (1996).
5. Chen, G. and Gomez, A., *Combust. Sci. and Tech.* 115, p. 177 (1996).
6. Tang, K. and Gomez, A., *J. Colloid and Interface Sci.* 184, p. 500 (1996).
7. Gomez, A. "Bridging the Gap between Single Droplet Burning and Practical Spray Flames," Invited Paper in the Proceedings of the Eastern States Section : The Combustion Institute, Fall Technical Meeting, Hilton Head, South Carolina, December 1996.
8. Chen, G. and Gomez, A. "Dilute Laminar Spray Diffusion Flames Near the Transition from Group Combustion to Individual Droplet Burning", to appear in *Combustion and Flame*, (1997).
9. Gao, L. P., D'Angelo, Y., Silverman, I., Gomez, A. and Smooke, M. D. "Quantitative Comparison of Detailed Numerical Computations and Experiments in Counterflow Spray diffusion Flames", to appear in ," *Proc. Twenty-sixth Int. Symposium on Combustion*, The Combustion Institute, (1997).
10. Gomez, A. and Chen, G. "Monodisperse Electrosprays: Combustion, Scale-up and Implications for Pollutant Formation", to appear in a volume in the Combustion Science and Technology Book Series (1997).
11. See, for example: Sangiovanni, J. J., & Dodge, L. G., Seventeenth Symposium (Int.) on Combustion, p. 455, The Combustion Institute (1979); Brzustowski, T. A., Twardus, E. M., Wojcick, S., & Sobiesiak, A., AIAA J., 17, p. 1234 (1979).
12. Miyasaka, K. and Law, C. K., Eighteenth Symposium (International) on Combustion, p. 283, The Combustion Institute, (1981).
13. Chiu, H. H., and Liu, T. M.,. Combust. Sci. and Tech., 17, p. 127 (1977); Chiu, H. H., Kim, H. Y., and Croke, E. J., Nineeenth Symposium (International) on Combustion, p. 971, The Combustion Institute, (1982).
14. Labowsky, M., and Rosner, D. E., in Evaporation-Combustion of Fuels (J. T. Zung, Ed.), American Chemical Society, p. 63 (1978).
15. Sichel, M., and Palaniswamy, S., Twentieth Symposium (International) on Combustion, p. 1789, The Combustion Institute, (1984).
16. Greenberg, J.B., Silverman, I. and Tambour, Y., Combust. Flame, 94, p. 90 (1993).
17. Seshadri, K., Trevino, C., and Smooke, M. D., Combust. Flame,76, p. 111 (1989).
18. Abramzon, B. and Sirignano, W.A., Int. J. Heat Mass Transfer, 32, p. 1605 (1989).

a)   b)

Figure 1

Figure 2

Figure 3

Figure 4

Figure 5

Figure 6

Figure 7

Figure 8

AUTHOR INDEX

REPORT DOCUMENTATION PAGE		Form Approved OMB No. 0704-0188

Public reporting burden for this collection of information is estimated to average 1 hour per response, including the time for reviewing instructions, searching existing data sources, gathering and maintaining the data needed, and completing and reviewing the collection of information. Send comments regarding this burden estimate or any other aspect of this collection of information, including suggestions for reducing this burden, to Washington Headquarters Services, Directorate for Information Operations and Reports, 1215 Jefferson Davis Highway, Suite 1204, Arlington, VA 22202-4302, and to the Office of Management and Budget, Paperwork Reduction Project (0704-0188), Washington, DC 20503.

1. AGENCY USE ONLY (Leave blank)	2. REPORT DATE May 1997	3. REPORT TYPE AND DATES COVERED Conference Publication	

4. TITLE AND SUBTITLE	5. FUNDING NUMBERS
Fourth International Microgravity Combustion Workshop	WU–963–80–0J
6. AUTHOR(S) Kurt R. Sacksteder, compiler	

7. PERFORMING ORGANIZATION NAME(S) AND ADDRESS(ES) National Aeronautics and Space Administration Lewis Research Center Cleveland, Ohio 44135–3191	8. PERFORMING ORGANIZATION REPORT NUMBER E–10678

9. SPONSORING/MONITORING AGENCY NAME(S) AND ADDRESS(ES) National Aeronautics and Space Administration Washington, D.C. 20546–0001	10. SPONSORING/MONITORING AGENCY REPORT NUMBER NASA CP–10194

11. SUPPLEMENTARY NOTES

Responsible person, Kurt R. Sacksteder, organization code 6711, (216) 433–2857.

12a. DISTRIBUTION/AVAILABILITY STATEMENT Unclassified - Unlimited Subject Category 29 This publication is available from the NASA Center for Aerospace Information, (301) 621–0390.	12b. DISTRIBUTION CODE

13. ABSTRACT (Maximum 200 words)

This Conference Publication contains 84 papers presented at the Fourth International Microgravity Combustion Workshop held in Cleveland, Ohio, from May 19 to 21, 1997. The purpose of the workshop was twofold: to exchange information about the progress and promise of combustion science in microgravity and to provide a forum to discuss which areas in microgravity combustion science need to be expanded profitably and which should be included in upcoming NASA Research Announcements (NRA).

14. SUBJECT TERMS			15. NUMBER OF PAGES 542
Microgravity; Combustion; Fires; Flammability			16. PRICE CODE A23

17. SECURITY CLASSIFICATION OF REPORT Unclassified	18. SECURITY CLASSIFICATION OF THIS PAGE Unclassified	19. SECURITY CLASSIFICATION OF ABSTRACT Unclassified	20. LIMITATION OF ABSTRACT

NSN 7540-01-280-5500

Standard Form 298 (Rev. 2-89)
Prescribed by ANSI Std. Z39-18
298-102